

Web of Science™

125 record(s) printed from Clarivate Web of Science

Record 1 of 125

Title: Strongly overdoped La_{2-x}Sr_xCuO₄: Evidence for Josephson-coupled grains of strongly correlated superconductor

Author(s): Li, YM (Li, Yangmu); Sapkota, A (Sapkota, A.); Lozano, PM (Lozano, P. M.); Du, ZY (Du, Zengyi); Li, H (Li, Hui); Wu, ZB (Wu, Zebin); Kundu, AK (Kundu, Asish K.); Koch, RJ (Koch, R. J.); Wu, LJ (Wu, Lijun); Winn, BL (Winn, B. L.); Chi, SX (Chi, Songxue); Matsuda, M (Matsuda, M.); Frontzek, M (Frontzek, M.); Bozin, ES (Bozin, E. S.); Zhu, YM (Zhu, Yimei); Bozovic, I (Bozovic, I.); Pasupathy, AN (Pasupathy, Abhay N.); Drozdov, IK (Drozdov, Ilya K.); Fujita, K (Fujita, Kazuhiro); Gu, GD (Gu, G. D.); Zaliznyak, IA (Zaliznyak, I. A.); Li, Q (Li, Qiang); Tranquada, JM (Tranquada, J. M.)

Source: PHYSICAL REVIEW B **Volume:** 106 **Issue:** 22 **Article Number:** 224515 **DOI:** 10.1103/PhysRevB.106.224515 **Published:** DEC 21 2022

Times Cited in Web of Science Core Collection: 0

Total Times Cited: 0

Usage Count (Last 180 days): 0

Usage Count (Since 2013): 0

Cited Reference Count: 156

Abstract: The interpretation of how superconductivity disappears in cuprates at large hole doping has been controversial. To address this issue, we present an experimental study of single-crystal and thin film samples of La_{2-x}Sr_xCuO₄ (LSCO) with $x = 0.25$. In particular, measurements of bulk susceptibility on LSCO crystals with $x = 0.25$ indicate an onset of diamagnetism at $T_{c1} = 38.5$ K, with a sharp transition to a phase with full bulk shielding at $T_{c2} = 18$ K, independent of field direction. Strikingly, the in-plane resistivity only goes to zero at T_{c2} . Inelastic neutron scattering on $x = 0.25$ crystals confirms the presence of low-energy incommensurate magnetic excitations with reduced strength compared to lower doping levels. The ratio of the spin gap to T_{c2} is anomalously large. Our results are consistent with a theoretical prediction for strongly overdoped cuprates by Spivak, Oretto, and Kivelson, in which superconductivity initially develops within disconnected self-organized grains characterized by a reduced hole concentration, with bulk superconductivity occurring only after superconductivity is induced by proximity effect in the surrounding medium of higher hole concentration. Beyond the superconducting-to-metal transition, local differential conductance measurements on an LSCO thin film suggest that regions with pairing correlations survive, but are too dilute to support superconducting order. Future experiments will be needed to test the degree to which these results apply to overdoped cuprates in general.

Accession Number: WOS:000905072900004

Language: English

Document Type: Article

KeyWords Plus: T-C SUPERCONDUCTIVITY; PHASE-SEPARATION; FLUCTUATING STRIPES; PAIRING INTERACTION; PENETRATION-DEPTH; OPTICAL-SPECTRA; TEMPERATURE; CUPRATE; DEPENDENCE; TRANSPORT

Addresses: [Li, Yangmu; Sapkota, A.; Lozano, P. M.; Du, Zengyi; Li, Hui; Wu, Zebin; Kundu, Asish K.; Koch, R. J.; Wu, Lijun; Bozin, E. S.; Zhu, Yimei; Bozovic, I.; Pasupathy, Abhay N.; Drozdov, Ilya K.; Fujita, Kazuhiro; Gu, G. D.; Zaliznyak, I. A.; Li, Qiang; Tranquada, J. M.] Brookhaven Natl Lab, Condensed Matter Phys & Mat Sci Div, Upton, NY 11973 USA.

[Lozano, P. M.; Li, Hui] SUNY Stony Brook, Dept Phys & Astron, Stony Brook, NY 11794 USA.

[Winn, B. L.; Chi, Songxue; Matsuda, M.; Frontzek, M.] Oak Ridge Natl Lab, Neutron Scattering Div, Oak Ridge, TN 37831 USA.

[Pasupathy, Abhay N.] Columbia Univ, Dept Phys, New York, NY 10027 USA.

[Li, Yangmu] Chinese Acad Sci, Inst Phys, Beijing Natl Lab Condensed Matter Phys, Beijing 100190, Peoples R China.

[Sapkota, A.] Iowa State Univ, Ames Lab, Ames, IA 50011 USA.

Corresponding Address: Tranquada, JM (corresponding author), Brookhaven Natl Lab, Condensed Matter Phys & Mat Sci Div, Upton, NY 11973 USA.

E-mail Addresses: jtran@bnl.gov

Affiliations: United States Department of Energy (DOE); Brookhaven National Laboratory; State University of New York (SUNY) System; State University of New York (SUNY) Stony Brook; United States Department of Energy (DOE); Oak Ridge National Laboratory; Columbia University; Chinese Academy of Sciences; Institute of Physics, CAS; Iowa State University; United States Department of Energy (DOE); Ames National Laboratory

Publisher: AMER PHYSICAL SOC

Publisher Address: ONE PHYSICS ELLIPSE, COLLEGE PK, MD 20740-3844 USA

Web of Science Index: Science Citation Index Expanded (SCI-EXPANDED)

Web of Science Categories: Materials Science, Multidisciplinary; Physics, Applied; Physics, Condensed Matter

Research Areas: Materials Science; Physics

IDS Number: 7K1UX

ISSN: 2469-9950

eISSN: 2469-9969

29-char Source Abbrev.: PHYS REV B

ISO Source Abbrev.: Phys. Rev. B

Source Item Page Count: 20

Funding:

Funding Agency	Grant Number
Office of Basic Energy Sciences, Materials Sciences and Engineering Division, U.S. Department of Energy (DOE)	
	DE-SC0012704
	DE-AC02-06CH11357

ACKNOWLEDGMENTS We thank S. A. Kivelson and M.-H. Julien for valuable comments. Work at Brookhaven is supported by the Office of Basic Energy Sciences, Materials Sciences and Engineering Division, U.S. Department of Energy (DOE) under Contract No. DE-SC0012704. A portion of this research used resources at the Spallation Neutron Source and the High Flux Isotope Reactor, DOE Office of Science User Facilities operated by Oak Ridge National Laboratory. Another portion of this re-search used resources of the Advanced Photon Source, a DOE Office of Science user facility operated by Argonne National Laboratory under Contract No. DE-AC02-06CH11357.

Open Access: Green Accepted

Output Date: 2023-01-27

Record 2 of 125

Title: Fluctuating Ru trimer precursor to a two-stage electronic transition in RuP

Author(s): Koch, RJ (Koch, Robert J.); Aryal, N (Aryal, Niraj); Ivashko, O (Ivashko, Oleh); Liu, Y (Liu, Yu); Abeykoon, M (Abeykoon, Milinda); Bauer, ED (Bauer, Eric D.); Zimmermann, MV (Zimmermann, Martin V.);

Yin, WG (Yin, Weiguo); Petrovic, C (Petrovic, Cedimir); Bozin, ES (Bozin, Emil S.)

Source: PHYSICAL REVIEW B **Volume:** 106 **Issue:** 21 **Article Number:** 214516 **DOI:** 10.1103/PhysRevB.106.214516 **Published:** DEC 19 2022

Times Cited in Web of Science Core Collection: 0

Total Times Cited: 0

Usage Count (Last 180 days): 0

Usage Count (Since 2013): 0

Cited Reference Count: 75

Abstract: Superconductivity in binary ruthenium pnictides occurs proximal to and upon suppression of a nonmagnetic ground state, preceded by a pseudogap phase associated with Fermi surface instability, and its critical temperature, T_c , is maximized around the pseudogap quantum critical point. By analogy with isoelectronic iron-based counterparts, antiferromagnetic fluctuations became "usual suspects" as putative mediators of superconducting pairing. Here we report on a high-temperature local symmetry breaking in RuP, the nonsuperconducting parent of the maximum- T_c branch of these novel superconductors, revealed by combined nanostructure-sensitive powder and single-crystal x-ray total scattering analyses. Large local distortions of Ru chains associated with orbital-charge trimerization, further assembled into hexamers, exist above the two-stage electronic transition in RuP. In the pseudogap regime the precursors order with distortions retaining their strength, whereas they acquire spin-singlet characteristics which dramatically enhances the distortion as the nonmagnetic ground state establishes. The precursors enable the nonmagnetic ground state and presumed complex oligomerization, and the relevance of pseudogap fluctuations for superconductivity emerges as a distinct prospect. As a transition metal system in which partial d-manifold filling combined with high crystal symmetry promotes electronic instabilities, this represents a further example of local electronic precursors underpinning the macroscopic collective behavior of quantum materials.

Accession Number: WOS:000903740800008

Language: English

Document Type: Article

KeyWords Plus: CHARGE-DENSITY-WAVE; CRITICAL-POINT; SCATTERING; PSEUDOGAP

Addresses: [Koch, Robert J.; Aryal, Niraj; Liu, Yu; Yin, Weiguo; Petrovic, Cedimir; Bozin, Emil S.] Brookhaven Natl Lab, Condensed Matter Phys & Mat Sci Div, Upton, NY 11973 USA.

[Ivashko, Oleh; Zimmermann, Martin V.] Deutsch Elektronen Synchrotron DESY, Notkestr 85, D-22607 Hamburg, Germany.

[Liu, Yu; Bauer, Eric D.] Los Alamos Natl Lab, Los Alamos, NM 87545 USA.

[Abeykoon, Milinda] Brookhaven Natl Lab, Photon Sci Div, Upton, NY 11973 USA.

Corresponding Address: Bozin, ES (corresponding author), Brookhaven Natl Lab, Condensed Matter Phys & Mat Sci Div, Upton, NY 11973 USA.

E-mail Addresses: bozin@bnl.gov

Affiliations: United States Department of Energy (DOE); Brookhaven National Laboratory; Helmholtz Association; Deutsches Elektronen-Synchrotron (DESY); United States Department of Energy (DOE); Los Alamos National Laboratory; United States Department of Energy (DOE); Brookhaven National Laboratory

Publisher: AMER PHYSICAL SOC

Publisher Address: ONE PHYSICS ELLIPSE, COLLEGE PK, MD 20740-3844 USA

Web of Science Index: Science Citation Index Expanded (SCI-EXPANDED)

Web of Science Categories: Materials Science, Multidisciplinary; Physics, Applied; Physics, Condensed Matter

Research Areas: Materials Science; Physics

IDS Number: 7I2RQ

ISSN: 2469-9950

eISSN: 2469-9969

29-char Source Abbrev.: PHYS REV B

ISO Source Abbrev.: Phys. Rev. B

Source Item Page Count: 9

Funding:

Funding Agency	Grant Number
U.S. Department of Energy, Office of Science, Office of Basic Energy Sciences (DOE-BES)	DE-SC0012704
U.S. Department of Energy, Office of Basic Energy Sciences, and Division of Materials Sciences and Engineering under the project "Quantum Fluctuations in Narrow Band Systems	

We gratefully acknowledge Olof G. for assistance with the single-crystal measurements, and J. D. Thompson for collecting the magnetic susceptibility data. Work at Brookhaven National Laboratory was supported by the U.S. Department of Energy, Office of Science, Office of Basic Energy Sciences (DOE-BES), under Contract No. DE-SC0012704. We acknowledge DESY (Hamburg, Germany), a member of the Helmholtz Association HGF, for the provision of experimental facilities. Parts of this research were carried out at beamline P21.1 at PETRA III. E.S.B. acknowledges the Stephenson Distinguished Visitor Programme for supporting his stay at DESY in Hamburg. This research was supported in part through the Maxwell computational resources operated at Deutsches Elektronen-Synchrotron DESY, Hamburg, Germany. Work at Los Alamos National Laboratory was performed under the auspices of the U.S. Department of Energy, Office of Basic Energy Sciences, and Division of Materials Sciences and Engineering under the project "Quantum Fluctuations in Narrow Band Systems."

Open Access: Green Submitted

Output Date: 2023-01-27

Record 3 of 125

Title: On single-crystal total scattering data reduction and correction protocols for analysis in direct space (vol A77, 611, 2021)

Author(s): Koch, RJ (Koch, Robert J.); Roth, N (Roth, Nikolaj); Liu, Y (Liu, Yu); Ivashko, O (Ivashko, Oleh); Dippel, AC (Dippel, Ann-Christin); Petrovic, C (Petrovic, Cedomir); Iversen, BB (Iversen, Bo B.); Zimmermann, MV (Zimmermann, Martin V.); Bozin, ES (Bozin, Emil S.)

Source: ACTA CRYSTALLOGRAPHICA A-FOUNDATION AND ADVANCES **Volume:** 78 **Pages:** 515-515 **DOI:** 10.1107/S2053273322009081 **Part:** 6 **Published:** NOV 2022

Times Cited in Web of Science Core Collection: 0

Total Times Cited: 0

Usage Count (Last 180 days): 1

Usage Count (Since 2013): 1

Cited Reference Count: 1

Accession Number: WOS:000885872600007

PubMed ID: 36318075

Language: English

Document Type: Correction

Author Keywords: pair distribution function analysis; PDF analysis; single-crystal 3D differential PDF; total scattering; data reduction; CuIr₂S₄

Addresses: [Koch, Robert J.; Liu, Yu; Petrovic, Cedomir; Bozin, Emil S.] Brookhaven Natl Lab, Condensed Matter Phys & Mat Sci Div, Upton, NY 11973 USA.

[Roth, Nikolaj; Iversen, Bo B.] Aarhus Univ, Dept Chem, Ctr Mat Crystallog, DK-8000 Aarhus, Denmark.

[Roth, Nikolaj; Iversen, Bo B.] Aarhus Univ, iNANO, DK-8000 Aarhus, Denmark.

[Ivashko, Oleh; Dippel, Ann-Christin; Zimmermann, Martin V.] Deutsches Elektronen Synchrotron DESY, D-22607 Hamburg, Germany.

Corresponding Address: Koch, RJ; Bozin, ES (corresponding author), Brookhaven Natl Lab, Condensed Matter Phys & Mat Sci Div, Upton, NY 11973 USA.

E-mail Addresses: rkoch177@gmail.com; bozin@bnl.gov

Affiliations: United States Department of Energy (DOE); Brookhaven National Laboratory; Aarhus University; Aarhus University; Helmholtz Association; Deutsches Elektronen-Synchrotron (DESY)

Author Identifiers:

Author	Web of Science ResearcherID	ORCID Number
Petrovic, Cedomir	A-8789-2009	0000-0001-6063-1881
Ivashko, Oleh		0000-0002-4869-8175
Bozin, Emil		0000-0002-6682-0365
v. Zimmermann, Martin		0000-0002-9320-6846

Publisher: INT UNION CRYSTALLOGRAPHY

Publisher Address: 2 ABBEY SQ, CHESTER, CH1 2HU, ENGLAND

Web of Science Index: Science Citation Index Expanded (SCI-EXPANDED)

Web of Science Categories: Chemistry, Multidisciplinary; Crystallography

Research Areas: Chemistry; Crystallography

IDS Number: 6I1FV

ISSN: 2053-2733

29-char Source Abbrev.: ACTA CRYSTALLOGR A

ISO Source Abbrev.: Acta Crystallogr. Sect. A

Source Item Page Count: 1

Open Access: Bronze

Output Date: 2023-01-27

Record 4 of 125

Title: Li-x(C5H5N)(y)Fe2-zSe2: A Defect-Resilient Expanded-Lattice High-Temperature Superconductor

Author(s): Deltsidis, A (Deltsidis, Alexandros); Simonelli, L (Simonelli, Laura); Vailakis, G (Vailakis, Georgios); Berdiell, IC (Berdiell, Izar Capel); Kopidakis, G (Kopidakis, Georgios); Krzton-Maziopa, A (Krzton-Maziopa, Anna); Bozin, ES (Bozin, Emil S.); Lappas, A (Lappas, Alexandros)

Source: INORGANIC CHEMISTRY **DOI:** 10.1021/acs.inorgchem.2c01906 **Early Access Date:** AUG 2022

Times Cited in Web of Science Core Collection: 0

Total Times Cited: 0

Usage Count (Last 180 days): 2

Usage Count (Since 2013): 2

Cited Reference Count: 77

Abstract: Two-dimensional iron chalcogenide intercalates display a remarkable correlation of the interlayer spacing with enhancement of the superconducting critical temperature (T_c). In this work, synchrotron X-ray absorption (XAS; at the Fe and Se K-edges) and emission (XES; at the Fe K beta) spectroscopies allow one to discuss how the important rise of T_c (similar to 44 K) in the molecule-intercalated $\text{Li}_x(\text{C}_5\text{H}_5\text{N})_y\text{Fe}_{2-z}\text{Se}_2$ relates to the electronic and local structural changes felt by the inorganic host upon doping (x). XES shows that widely separated layers of edge-sharing FeSe_4 tetrahedra carry low-spin moieties, with a local Fe magnetic moment slightly reduced compared to the parent beta- $\text{Fe}_{2-z}\text{Se}_2$. Pre-edge XAS expresses the progressively reduced mixing of metal 3d-4p states upon lithiation. Doping-mediated local lattice modifications, probed by conventional T_c optimization measures (cf. the anion height and FeSe_4 tetrahedra regularity), become less relevant when layers are spaced far away. On the basis of extended X-ray absorption fine structure, such distortions are compensated by a softer Fe network that relates to Fe-site vacancies, alleviating electron-lattice

correlations and superconductivity. Density functional theory (DFT) guided modification of the isolated Fe₂-zSe₂ (z, vacant sites) planes, resembling the host layers, identify that Fe-site deficiency occurs at low energy cost, giving rise to stretched Fe sheets, in accordance with experiments. The robust high-T_c in Li_x(C₅H₅N)_yFe₂-zSe₂, arises from the interplay of electron-donating spacers and the iron selenide layer's tolerance to defect chemistry, a tool to favorably tune its Fermi surface properties.

Accession Number: WOS:000842959000001

PubMed ID: 35913893

Language: English

Document Type: Article; Early Access

KeyWords Plus: TOTAL-ENERGY CALCULATIONS; LAYERED SUPERCONDUCTOR; PHASE-DIAGRAM; K-EDGE; IRON; SPECTROSCOPY; SPECTRA; NA

Addresses: [Deltsidis, Alexandros; Vailakis, Georgios; Berdiell, Izar Capel; Kopidakis, Georgios; Lappas, Alexandros] Fdn Res & Technol Hellas, Insti Elect Struct & Laser, Vassilika Vouton 71110, Heraklion, Greece. [Simonelli, Laura] ALBA Synchrotron Light Source, Cerdanyola Del Valles 08290, Spain.

[Deltsidis, Alexandros; Vailakis, Georgios; Kopidakis, Georgios] Univ Crete, Dept Mat Sci & Technol, Voutes 70013, Heraklion, Greece.

[Krzton-Maziopa, Anna] Warsaw Univ Technol, Fac Chem, PL-00664 Warsaw, Poland.

[Bozin, Emil S.] Brookhaven Natl Lab, Condensed Matter Phys & Mat Sci Dept, Upton, NY 11973 USA.

Corresponding Address: Lappas, A (corresponding author), Fdn Res & Technol Hellas, Insti Elect Struct & Laser, Vassilika Vouton 71110, Heraklion, Greece.

E-mail Addresses: lappas@iesl.forth.gr

Affiliations: Foundation for Research & Technology - Hellas (FORTH); University of Crete; Warsaw University of Technology; United States Department of Energy (DOE); Brookhaven National Laboratory

Author Identifiers:

Author	Web of Science ResearcherID	ORCID Number
Vailakis, Georgios	GRF-0549-2022	0000-0002-5497-886X
Deltsidis, Alexandros		0000-0001-8313-997X
Lappas, Alexandros	F-6771-2011	0000-0001-8486-0312
Simonelli, Laura		0000-0001-5331-0633

Publisher: AMER CHEMICAL SOC

Publisher Address: 1155 16TH ST, NW, WASHINGTON, DC 20036 USA

Web of Science Index: Science Citation Index Expanded (SCI-EXPANDED)

Web of Science Categories: Chemistry, Inorganic & Nuclear

Research Areas: Chemistry

IDS Number: 3X3RC

ISSN: 0020-1669

eISSN: 1520-510X

29-char Source Abbrev.: INORG CHEM

ISO Source Abbrev.: Inorg. Chem.

Source Item Page Count: 12

Funding:

Funding Agency	Grant Number
Office of Naval Research Global	N62909-17-1-2126
U.S. Department of Energy, Office of Science, Office of Basic Energy Sciences	DE-SC0012704
National Infrastructures for Research and Technology S.A.	

This material is based on research supported by the Office of Naval Research Global under Award N62909-17-1-2126. The spectroscopy experiments were performed at the BL22-CL?SS beamline at ALBA Synchrotron (Barcelona, Spain) in collaboration with the ALBA staff. Work at Brookhaven National Laboratory was supported by the U.S. Department of Energy, Office of Science, Office of Basic Energy Sciences, under Contract DE-SC0012704. First-principles calculations were performed with computational time granted from the National Infrastructures for Research and Technology S.A. (GRNET S.A.) in the National HPC facility ARIS under Project pa181005-NANOCOMPDESIGN.

Output Date: 2023-01-27

Record 5 of 125

Title: Hidden Local Symmetry Breaking in Silver Diamondoid Compounds is Root Cause of Ultralow Thermal Conductivity

Author(s): Xie, HY (Xie, Hongyao); Bozin, ES (Bozin, Emil S.); Li, Z (Li, Zhi); Abeykoon, M (Abeykoon, Milinda); Banerjee, S (Banerjee, Soham); Male, JP (Male, James P.); Snyder, GJ (Snyder, G. Jeffrey); Wolverton, C (Wolverton, Christopher); Billinge, SJL (Billinge, Simon J. L.); Kanatzidis, MG (Kanatzidis, Mercouri G.)

Source: ADVANCED MATERIALS **Volume:** 34 **Issue:** 24 **Article Number:** 2202255 **DOI:** 10.1002/adma.202202255 **Early Access Date:** MAY 2022 **Published:** JUN 2022

Times Cited in Web of Science Core Collection: 1

Total Times Cited: 1

Usage Count (Last 180 days): 35

Usage Count (Since 2013): 54

Cited Reference Count: 64

Abstract: Typically, conventional structure transitions occur from a low symmetry state to a higher symmetry state upon warming. In this work, an unexpected local symmetry breaking in the tetragonal diamondoid compound AgGaTe₂ is reported, which, upon warming, evolves continuously from an undistorted ground state to a locally distorted state while retaining average crystallographic symmetry. This is a rare phenomenon previously referred to as emphanisis. This distorted state, caused by the weak sd(3) orbital hybridization of tetrahedral Ag atoms, causes their displacement off the tetrahedron center and promotes a global distortion of the crystal structure resulting in strong acoustic-optical phonon scattering and an ultralow lattice thermal conductivity of 0.26 W m⁻¹ K⁻¹ at 850 K in AgGaTe₂. The findings explain the underlying reason for the unexpectedly low thermal conductivities of silver-based compounds compared to copper-based analogs and provide a guideline to suppressing heat transport in diamondoid and other materials.

Accession Number: WOS:000792325900001

PubMed ID: 35412675

Language: English

Document Type: Article

Author Keywords: chalcopyrites; emphanisis; thermal conductivity; thermoelectrics

KeyWords Plus: HIGH-THERMOELECTRIC PERFORMANCE; LOW-COST; CHALCOPYRITE; TEMPERATURE; EXPANSION; TERNARY; EFFICIENCY; FIGURE; MERIT; POWER

Addresses: [Xie, Hongyao; Kanatzidis, Mercouri G.] Northwestern Univ, Dept Chem, Evanston, IL 60208 USA.

[Bozin, Emil S.; Billinge, Simon J. L.] Brookhaven Natl Lab, Condensed Matter Phys & Mat Sci Div, Upton, NY 11973 USA.

[Li, Zhi; Male, James P.; Snyder, G. Jeffrey; Wolverton, Christopher] Northwestern Univ, Dept Mat Sci & Engn, Evanston, IL 60208 USA.

[Abeykoon, Milinda] Brookhaven Natl Lab, Photon Sci Div, Upton, NY 11973 USA.

[Banerjee, Soham] Deutsch Elektronen Synchrotron DESY, Notkestr 85, D-22607 Hamburg, Germany.
[Billinge, Simon J. L.] Columbia Univ, Dept Appl Phys & Appl Math, New York, NY 10027 USA.

Corresponding Address: Kanatzidis, MG (corresponding author), Northwestern Univ, Dept Chem, Evanston, IL 60208 USA.

E-mail Addresses: m-kanatzidis@northwestern.edu

Affiliations: Northwestern University; United States Department of Energy (DOE); Brookhaven National Laboratory; Northwestern University; United States Department of Energy (DOE); Brookhaven National Laboratory; Helmholtz Association; Deutsches Elektronen-Synchrotron (DESY); Columbia University

Author Identifiers:

Author	Web of Science ResearcherID	ORCID Number
Snyder, G. Jeffrey	E-4453-2011	0000-0003-1414-8682

Publisher: WILEY-V C H VERLAG GMBH

Publisher Address: POSTFACH 101161, 69451 WEINHEIM, GERMANY

Web of Science Index: Science Citation Index Expanded (SCI-EXPANDED)

Web of Science Categories: Chemistry, Multidisciplinary; Chemistry, Physical; Nanoscience & Nanotechnology; Materials Science, Multidisciplinary; Physics, Applied; Physics, Condensed Matter

Research Areas: Chemistry; Science & Technology - Other Topics; Materials Science; Physics

IDS Number: 2E6HJ

ISSN: 0935-9648

eISSN: 1521-4095

29-char Source Abbrev.: ADV MATER

ISO Source Abbrev.: Adv. Mater.

Source Item Page Count: 10

Funding:

Funding Agency	Grant Number
U.S. Department of Energy, Office of Science, and Office of Basic Energy Sciences	DE-SC0014520
U.S. Department of Energy, Office of Science, Office of Basic Energy Sciences (DOE-BES)	DE-SC0012704
DOE Office of Science	DE-SC0012704

This work was primarily supported by a grant from the U.S. Department of Energy, Office of Science, and Office of Basic Energy Sciences under Award number DE-SC0014520. Work at Brookhaven National Laboratory was supported by U.S. Department of Energy, Office of Science, Office of Basic Energy Sciences (DOE-BES) under Contract no. DE-SC0012704. The X-ray PDF measurements were conducted in part on beamline 28-ID-1 of the National Synchrotron Light Source II, a U.S. Department of Energy (DOE) Office of Science User Facility operated for the DOE Office of Science by Brookhaven National Laboratory under Contract no. DE-SC0012704. The authors also acknowledge DESY (Hamburg, Germany), a member of the Helmholtz Association HGF, for the provision of experimental facilities. Parts of this research were carried out PETRA III, beamline P21.1.

Output Date: 2023-01-27

Record 6 of 125

Title: In Situ Visualization of Local Distortions in the High-T(c)Molecule-Intercalated Li-x(C5H5N)(y)Fe(2-z)Se(2)Superconductor

Author(s): Berdiell, IC (Berdiell, Izar Capel); Pesko, E (Pesko, Edyta); Lator, E (Lator, Elijah); Deltsidis, A (Deltsidis, Alexandros); Krzton-Maziopa, A (Krzton-Maziopa, Anna); Abeykoon, AMM (Abeykoon, A. M. Milinda); Bozin, ES (Bozin, Emil S.); Lappas, A (Lappas, Alexandros)

Source: INORGANIC CHEMISTRY **Volume:** 61 **Issue:** 10 **Pages:** 4350-4360 **DOI:** 10.1021/acs.inorgchem.1c03610 **Published:** MAR 14 2022

Times Cited in Web of Science Core Collection: 2

Total Times Cited: 2

Usage Count (Last 180 days): 5

Usage Count (Since 2013): 13

Cited Reference Count: 50

Abstract: A time-resolved synchrotron X-ray total scattering study sheds light on the evolution of the different structural length scales involved during the intercalation of the layered iron-selenide host by organic molecular donors, aiming at the formation of the expanded-lattice $\text{Li}_x(\text{C}_5\text{H}_5\text{N})_y\text{Fe}_2\text{-zSe}_2$ hybrid superconductor. The intercalates are found to crystallize in the tetragonal ThCr_2Si_2 -type structure at the average level, however, with an enhanced interlayer iron-selenide spacing ($d = 16.2 \text{ \AA}$) that accommodates the heterocyclic molecular spacers. Quantitative atomic pair distribution function (PDF) analysis at variable times suggests distorted FeSe_4 tetrahedral local environments that appear swollen with respect to those in the parent beta- FeSe . Simultaneously acquired in situ synchrotron X-ray powder diffraction data disclose that secondary phases (α - Fe and Li_2Se) grow significantly when a higher lithium concentration is used in the solvothermal reaction or when the solution is aged. These observations are in line with the strongly reducing character of the intercalation medium's solvated electrons that mediate the defect chemistry of the expanded-lattice superconductor. In the latter, intralayer correlated local distortions indicate electron-donating aspects that reflect in somewhat enlarged Fe-Se bonds. They also reveal a degree of relief of chemical pressure associated with a large distance between Fe and Se sheets ("taller" anion height) and a stretched Fe-Fe square planar topology. The elongation of the latter, derived from the in situ PDF study, speaks for a plausible increase in the Fe-site vacancy concentration. The evolution of the local structural parameters suggests an optimum reaction window where kinetically stabilized phases resemble the distortions of the edge-sharing Fe-Se tetrahedra, required for a high- T_c in expanded-lattice iron-chalcogenides.

Accession Number: WOS:000780256600015

PubMed ID: 35212536

Language: English

Document Type: Article

KeyWords Plus: X-RAY; SUPERCONDUCTIVITY; PHOSPHIDES; ARSENIDES; LI

Addresses: [Berdiell, Izar Capel; Lator, Elijah; Deltsidis, Alexandros; Lappas, Alexandros] Fdn Res & Technol Hellas, Inst Elect Struct & Laser, Iraklion 71110, Greece.

[Pesko, Edyta; Krzton-Maziopa, Anna] Warsaw Univ Technol, Fac Chem, PL-00664 Warsaw, Poland.

[Deltsidis, Alexandros] Univ Crete, Dept Mat Sci & Technol, Iraklion 71003, Greece.

[Abeykoon, A. M. Milinda] Brookhaven Natl Lab, Photon Sci Div, Natl Synchrotron Light Source II, Upton, NY 11973 USA.

[Bozin, Emil S.] Brookhaven Natl Lab, Condensed Matter Phys & Mat Sci Div, Upton, NY 11973 USA.

Corresponding Address: Lappas, A (corresponding author), Fdn Res & Technol Hellas, Inst Elect Struct & Laser, Iraklion 71110, Greece.

E-mail Addresses: lappas@iesl.forth.gr

Affiliations: Foundation for Research & Technology - Hellas (FORTH); Warsaw University of Technology; University of Crete; United States Department of Energy (DOE); Brookhaven National Laboratory; United States Department of Energy (DOE); Brookhaven National Laboratory

Author Identifiers:

Author	Web of Science ResearcherID	ORCID Number
Lappas, Alexandros	F-6771-2011	0000-0001-8486-0312
Deltsidis, Alexandros		0000-0001-8313-997X

Publisher: AMER CHEMICAL SOC

Publisher Address: 1155 16TH ST, NW, WASHINGTON, DC 20036 USA

Web of Science Index: Science Citation Index Expanded (SCI-EXPANDED)

Web of Science Categories: Chemistry, Inorganic & Nuclear

Research Areas: Chemistry

IDS Number: 0J7BK

ISSN: 0020-1669

eISSN: 1520-510X

29-char Source Abbrev.: INORG CHEM

ISO Source Abbrev.: Inorg. Chem.

Source Item Page Count: 11

Funding:

Funding Agency	Grant Number
Office of Naval Research Global	N62909-17-1-2126
DOE Office of Basic Energy Sciences	
DOE Office of Science	DE-SC0012704

This research is supported by the Office of Naval Research Global under Award Number N62909-17-1-2126. The work used the beamline 28-ID-1 of the National Synchrotron Light Source II (NSLS-II), a U.S. Department of Energy (DOE) User Facility operated by Brookhaven National Laboratory (BNL). Work in the Condensed Matter Physics and Materials Science Division (CMPMSD) at BNL was supported by the DOE Office of Basic Energy Sciences. Activities at NSLS-II and CMPMSD were supported by the DOE Office of Science under contract no. DE-SC0012704. We thank Mr. George Papadakis for his assistance with the portable reactor for in situ total scattering studies, designed and manufactured at IESL-FORTH. We are grateful to Mr. John Trunk for the help provided during the preparation of the in situ experiments at NSLS-II.

Output Date: 2023-01-27

Record 7 of 125

Title: Cascade of Spin-State Transitions in the Intermetallic Marcasite FeP₂

Author(s): Du, QH (Du, Qianheng); Wang, YL (Wang, Yilin); Wei, Y (Wei, Yuan); Koch, RJ (Koch, Robert Joseph); Wu, LJ (Wu, Lijun); Zhang, WL (Zhang, Wenliang); Asmara, TC (Asmara, Teguh Citra); Hu, ZX (Hu, Zhixiang); Bozin, ES (Bozin, Emil S.); Zhu, YM (Zhu, Yimei); Schmitt, T (Schmitt, Thorsten); Kotliar, G (Kotliar, Gabriel); Petrovic, C (Petrovic, Cedomir)

Source: CHEMISTRY OF MATERIALS **Volume:** 34 **Issue:** 5 **Pages:** 2025-2033 **DOI:** 10.1021/acs.chemmater.1c02569 **Published:** MAR 8 2022

Times Cited in Web of Science Core Collection: 0

Total Times Cited: 0

Usage Count (Last 180 days): 9

Usage Count (Since 2013): 11

Cited Reference Count: 73

Abstract: Marcasite crystal structures show an interesting interplay of spin, orbital, and lattice degrees of freedom and host properties relevant for applications and fundamental science. Electronic correlations that arise in this context are critical for tuning conductivity which is of interest in electrochemical reactions in catalysis but are also important to understand high values of cryogenic thermopower in materials with 3d orbitals related to classical rare earth Kondo semiconductors. Here we show, by magnetic susceptibility, transport, thermodynamic, and X-ray absorption spectroscopy at Fe L_{2,3} edge measurements, that intermetallic marcasite FeP₂ exhibits a cascade of thermally induced spin-state transitions on cooling and a ground state with an energy gap due to d-p orbital hybridization. A small amount of P vacancy defects enhances conduction, giving rise to semimetal. The electronic structure calculations indicate the importance of strong electronic correlations and the nonlocal Coulomb interaction beyond local density approximation dynamical mean field theory. Our

results point to a possibility of Hund's rule and crystal field competition-induced orbital degeneracy lifting similar to that observed in LaCoO₃ perovskite. A relatively simple unit cell offers possibilities for further computationally guided modification of unconventional energy gap and atomic-defect-related conduction.

Accession Number: WOS:000812157200001

Language: English

Document Type: Article

KeyWords Plus: SCATTERING; SEMIMETAL; LACOO₃; CARBON; OXYGEN; FESB₂; GAP

Addresses: [Du, Qianheng; Wang, Yilin; Koch, Robert Joseph; Wu, Lijun; Hu, Zhixiang; Bozin, Emil S.; Zhu, Yimei; Kotliar, Gabriel; Petrovic, Cedomir] Brookhaven Natl Lab, Condensed Matter Phys & Mat Sci Div, Upton, NY 11973 USA.

[Wang, Yilin] Univ Sci & Technol China, Hefei Natl Lab Phys Sci Microscale, Hefei 230026, Anhui, Peoples R China.

[Wei, Yuan; Zhang, Wenliang; Asmara, Teguh Citra; Schmitt, Thorsten] Paul Scherrer Inst, Photon Sci Div, Swiss Light Source, CH-5232 Villigen, Switzerland.

[Du, Qianheng; Hu, Zhixiang; Petrovic, Cedomir] SUNY Stony Brook, Dept Mat Sci & Chem Engr, Stony Brook, NY 11790 USA.

[Kotliar, Gabriel] Rutgers State Univ, Dept Phys & Astron, Piscataway, NJ 08854 USA.

[Du, Qianheng] Argonne Natl Lab, Mat Sci Div, Lemont, IL 60439 USA.

Corresponding Address: Du, QH; Petrovic, C (corresponding author), Brookhaven Natl Lab, Condensed Matter Phys & Mat Sci Div, Upton, NY 11973 USA.

Du, QH; Petrovic, C (corresponding author), SUNY Stony Brook, Dept Mat Sci & Chem Engr, Stony Brook, NY 11790 USA.

Du, QH (corresponding author), Argonne Natl Lab, Mat Sci Div, Lemont, IL 60439 USA.

E-mail Addresses: qdu@anl.gov; petrovic@bnl.gov

Affiliations: United States Department of Energy (DOE); Brookhaven National Laboratory; Chinese Academy of Sciences; University of Science & Technology of China, CAS; Swiss Federal Institutes of Technology Domain; Paul Scherrer Institute; State University of New York (SUNY) System; State University of New York (SUNY) Stony Brook; Rutgers State University New Brunswick; United States Department of Energy (DOE); Argonne National Laboratory

Author Identifiers:

Author	Web of Science ResearcherID	ORCID Number
du, qian	GYJ-7090-2022	
Schmitt, Thorsten	A-7025-2010	
Zhu, Yimei		0000-0002-1638-7217

Publisher: AMER CHEMICAL SOC

Publisher Address: 1155 16TH ST, NW, WASHINGTON, DC 20036 USA

Web of Science Index: Science Citation Index Expanded (SCI-EXPANDED)

Web of Science Categories: Chemistry, Physical; Materials Science, Multidisciplinary

Research Areas: Chemistry; Materials Science

IDS Number: 2E3VH

ISSN: 0897-4756

eISSN: 1520-5002

29-char Source Abbrev.: CHEM MATER

ISO Source Abbrev.: Chem. Mat.

Source Item Page Count: 9

Funding:

Funding Agency	Grant Number

US DOE, Office of Science, Office of Basic Energy Sciences	DE-SC0012704
United States Department of Energy, Office of Science, Office of Basic Energy Sciences, as a part of the Computational Materials Science Program through the Center for Computational Design of Functional Strongly Correlated Materials and Theoretical Spectro	
National Energy Research Scientific Computing Center (NERSC), a U.S. Department of Energy Office of Science User Facility	DE-AC02-05CH11231
Swiss National Science Foundation	200021 178867
European Union's Horizon 2020 research and innovation programme under Marie Skłodowska-Curie grant	701647
European Union	884104

Work at Brookhaven National Laboratory was supported by US DOE, Office of Science, Office of Basic Energy Sciences, under contract DE-SC0012704 (Q.D., L.W., Y.Z., and C.P.) . Y.W. and G.K. were supported by the United States Department of Energy, Office of Science, Office of Basic Energy Sciences, as a part of the Computational Materials Science Program through the Center for Computational Design of Functional Strongly Correlated Materials and Theoretical Spectroscopy. This research used resources of the National Energy Research Scientific Computing Center (NERSC), a U.S. Department of Energy Office of Science User Facility operated under Contract No. DE-AC02-05CH11231. Synchrotron powder X-ray diffraction data were collected at the 28-ID-2 (XPD) beamline of National Synchrotron Light Source II at Brookhaven. The XAS measurements were performed at the ADDRESS beamline of the Swiss Light Source at the Paul Scherrer Institut. T.S., W.Z., and T.C.A. acknowledge support by the Swiss National Science Foundation through Grant Number 200021 178867. T.C.A. acknowledges funding from the European Union's Horizon 2020 research and innovation programme under Marie Skłodowska-Curie grant agreement no. 701647 (PSI-FEL-LOW-II-3i program) . Y.W. acknowledges funding from the European Union's Horizon 2020 research and innovation program under Marie Skłodowska-Curie grant agreement no. 884104 (PSI-FELLOW-III-3i) .

Output Date: 2023-01-27

Record 8 of 125

Title: Tailoring defects and nanocrystal transformation for optimal heating power in bimagnetic $\text{Co}_y\text{Fe}_{1-y}\text{O}@x\text{CoFe}_3\text{O}_4$ particles

Author(s): Antonaropoulos, G (Antonaropoulos, George); Vasilakaki, M (Vasilakaki, Marianna); Trohidou, KN (Trohidou, Kalliopi N.); Iannotti, V (Iannotti, Vincenzo); Ausanio, G (Ausanio, Giovanni); Abeykoon, M (Abeykoon, Milinda); Bozin, ES (Bozin, Emil S.); Lappas, A (Lappas, Alexandros)

Source: NANOSCALE **Volume:** 14 **Issue:** 2 **Pages:** 382-401 **DOI:** 10.1039/d1nr05172e **Early Access**

Date: NOV 2021 **Published:** JAN 6 2022

Times Cited in Web of Science Core Collection: 1

Total Times Cited: 1

Usage Count (Last 180 days): 4

Usage Count (Since 2013): 16

Cited Reference Count: 87

Abstract: The effects of cobalt incorporation in spherical heterostructured iron oxide nanocrystals (NCs) of sub-critical size have been explored by colloidal chemistry methods. Synchrotron X-ray total scattering methods suggest that cobalt (Co) substitution in rock salt iron oxide NCs tends to remedy their vacant iron sites, offering a higher degree of resistance to oxidative conversion. Self-passivation still creates a spinel-like shell, but with a higher volume fraction of the rock salt Co-containing phase in the core. The higher divalent metal stoichiometry in the rock salt phase, with increasing Co content, results in a population of unoccupied tetrahedral metal sites in the spinel part, likely through oxidative shell creation, involving an ordered defect-clustering mechanism, directly correlated to core stabilization. To shed light on the effects of Co-substitution

and atomic-scale defects (vacant sites), Monte Carlo simulations suggest that the designed NCs, with desirable, enhanced magnetic properties (cf. exchange bias and coercivity), are developed with magnetocrystalline anisotropy which increases due to a relatively low content of Co ions in the lattice. The growth of optimally performing candidates combines also a strongly exchange-coupled system, secured through a high volumetric ratio rock salt phase, interfaced by a not so defective spinel shell. In view of these requirements, specific absorption rate (SAR) calculations demonstrate that the rock salt core sufficiently protected from oxidation and the heterostructure preserved over time, play a key role in magnetically mediated heating efficacies, for potential use of such NCs in magnetic hyperthermia applications.

Accession Number: WOS:000732864500001

PubMed ID: 34935014

Language: English

Document Type: Article

KeyWords Plus: CORE-SHELL NANOPARTICLES; MAGNETIC-PROPERTIES; EXCHANGE-ANISOTROPY; SIZE; HYPERTHERMIA; SHAPE; FIELD; DEPENDENCE; MECHANISM; GROWTH

Addresses: [Antonaropoulos, George; Lappas, Alexandros] Fdn Res & Technol Hellas, Inst Elect Struct & Laser, Iraklion 71110, Greece.

[Antonaropoulos, George] Univ Crete, Dept Chem, Iraklion 71003, Greece.

[Vasilakaki, Marianna; Trohidou, Kalliopi N.] Natl Ctr Sci Res Demokritos, Inst Nanosci & Nanotechnol, Athens 15310, Greece.

[Iannotti, Vincenzo; Ausanio, Giovanni] Univ Naples Federico II, CNR SPIN, Piazzale V Tecchio 80, I-80125 Naples, Italy.

[Iannotti, Vincenzo; Ausanio, Giovanni] Univ Naples Federico II, Dept Phys E Pancini, Piazzale V Tecchio 80, I-80125 Naples, Italy.

[Abeykoon, Milinda] Brookhaven Natl Lab, Photon Sci Div, Natl Synchrotron Light Source 2, Upton, NY 11973 USA.

[Bozin, Emil S.] Brookhaven Natl Lab, Condensed Matter Phys & Mat Sci Div, Upton, NY 11973 USA.

Corresponding Address: Lappas, A (corresponding author), Fdn Res & Technol Hellas, Inst Elect Struct & Laser, Iraklion 71110, Greece.

E-mail Addresses: lappas@iesl.forth.gr

Affiliations: Foundation for Research & Technology - Hellas (FORTH); University of Crete; National Centre of Scientific Research "Demokritos"; Consiglio Nazionale delle Ricerche (CNR); Istituto Superconduttori, Materiali e Dispositivi Innovativi (SPIN-CNR); University of Naples Federico II; University of Naples Federico II; United States Department of Energy (DOE); Brookhaven National Laboratory; United States Department of Energy (DOE); Brookhaven National Laboratory

Author Identifiers:

Author	Web of Science ResearcherID	ORCID Number
Lappas, Alexandros	AFO-0640-2022	0000-0001-8486-0312
Antonaropoulos, George	AFL-1000-2022	
Lappas, Alexandros	F-6771-2011	0000-0001-8486-0312
Vasilakaki, Marianna	R-5308-2016	0000-0003-1832-7549
IANNOTTI, Vincenzo		0000-0001-7229-5045
Bozin, Emil		0000-0002-6682-0365
Trohidou, Kalliopi		0000-0002-6921-5419
Antonaropoulos, George		0000-0003-0214-8327

Publisher: ROYAL SOC CHEMISTRY

Publisher Address: THOMAS GRAHAM HOUSE, SCIENCE PARK, MILTON RD, CAMBRIDGE CB4 0WF, CAMBS, ENGLAND

Web of Science Index: Science Citation Index Expanded (SCI-EXPANDED)

Web of Science Categories: Chemistry, Multidisciplinary; Nanoscience & Nanotechnology; Materials Science,

Multidisciplinary; Physics, Applied

Research Areas: Chemistry; Science & Technology - Other Topics; Materials Science; Physics

IDS Number: YC3II

ISSN: 2040-3364

eISSN: 2040-3372

29-char Source Abbrev.: NANOSCALE

ISO Source Abbrev.: Nanoscale

Source Item Page Count: 20

Funding:

Funding Agency	Grant Number
DOE Office of Basic Energy Sciences	
DOE Office of Science	DE-SC0012704
European Union's Horizon 2020 Research and Innovation Programme: FET Proactive	731976

This research used the beamline 28-ID-2 of the National Synchrotron Light Source II, a U.S. Department of Energy (DOE) User Facility operated by Brookhaven National Laboratory (BNL). Work in the Condensed Matter Physics and Materials Science Division at BNL was supported by the DOE Office of Basic Energy Sciences. Both activities were supported by the DOE Office of Science under Contract No. DE-SC0012704. KNT and MV acknowledge the support received by the European Union's Horizon 2020 Research and Innovation Programme: FET Proactive under grant agreement No. 731976 MAGnetic nanoparticle based liquid ENergy materials for Thermoelectric device Applications (MAGENTA) www.magenta-h2020.eu.

Open Access: hybrid

Output Date: 2023-01-27

Record 9 of 125

Title: On single-crystal total scattering data reduction and correction protocols for analysis in direct space

Author(s): Koch, RJ (Koch, Robert J.); Roth, N (Roth, Nikolaj); Liu, Y (Liu, Yiu); Ivashko, O (Ivashko, Oleh); Dippel, AC (Dippel, Ann-Christin); Petrovic, C (Petrovic, Cedimir); Iversen, BB (Iversen, Bo B.); Zimmermann, MV (Zimmermann, Martin, V); Bozin, ES (Bozin, Emil S.)

Source: ACTA CRYSTALLOGRAPHICA A-FOUNDATION AND ADVANCES **Volume:** 77 **Pages:** 611-636 **DOI:** 10.1107/S2053273321010159 **Part:** 6 **Published:** NOV 2021

Times Cited in Web of Science Core Collection: 4

Total Times Cited: 4

Usage Count (Last 180 days): 3

Usage Count (Since 2013): 7

Cited Reference Count: 70

Abstract: Data reduction and correction steps and processed data reproducibility in the emerging single-crystal total-scattering-based technique of three-dimensional differential atomic pair distribution function (3D-Delta PDF) analysis are explored. All steps from sample measurement to data processing are outlined using a crystal of CuIr₂S₄ as an example, studied in a setup equipped with a high-energy X-ray beam and a flat-panel area detector. Computational overhead as pertains to data sampling and the associated data-processing steps is also discussed. Various aspects of the final 3D-Delta PDF reproducibility are explicitly tested by varying the data-processing order and included steps, and by carrying out a crystal-to-crystal data comparison. Situations in which the 3D-Delta PDF is robust are identified, and caution against a few particular cases which can lead to inconsistent 3D-Delta PDFs is noted. Although not all the approaches applied herein will be valid across all systems, and a more in-depth analysis of some of the effects of the data-processing steps may still be needed, the methods collected herein represent the start of a more systematic discussion about data processing and corrections in this field.

Accession Number: WOS:000715092000007

PubMed ID: 34726636

Language: English

Document Type: Article

Author Keywords: pair distribution function analysis; PDF analysis; single-crystal 3D differential PDF; total scattering; data reduction; CuIr₂S₄

KeyWords Plus: PAIR DISTRIBUTION FUNCTION; DIFFUSE-SCATTERING; AMORPHOUS-SILICON; DIFFRACTION; REFINEMENT; ROTATION; DETECTOR; PROGRAM; LIGHT

Addresses: [Koch, Robert J.; Liu, Yiu; Petrovic, Cedomir; Bozin, Emil S.] Brookhaven Natl Lab, Condensed Matter Phys & Mat Sci Div, Upton, NY 11973 USA.

[Roth, Nikolaj; Iversen, Bo B.] Aarhus Univ, Ctr Mat Crystallog, Dept Chem, DK-8000 Aarhus, Denmark.

[Roth, Nikolaj; Iversen, Bo B.] Aarhus Univ, iNANO, DK-8000 Aarhus, Denmark.

[Ivashko, Oleh; Dippel, Ann-Christin; Zimmermann, Martin, V] DESY, D-22607 Hamburg, Germany.

Corresponding Address: Koch, RJ; Bozin, ES (corresponding author), Brookhaven Natl Lab, Condensed Matter Phys & Mat Sci Div, Upton, NY 11973 USA.

E-mail Addresses: rkoch177@gmail.com; bozin@bnl.gov

Affiliations: United States Department of Energy (DOE); Brookhaven National Laboratory; Aarhus University; Aarhus University; Helmholtz Association; Deutsches Elektronen-Synchrotron (DESY)

Author Identifiers:

Author	Web of Science ResearcherID	ORCID Number
Iversen, Bo Brummerstedt	J-5831-2017	0000-0002-4632-1024
Liu, Yu	ABD-2488-2021	0000-0001-8886-2876
Bozin, Emil		0000-0002-6682-0365
Ivashko, Oleh		0000-0002-4869-8175
Petrovic, Cedomir	A-8789-2009	0000-0001-6063-1881

Publisher: INT UNION CRYSTALLOGRAPHY

Publisher Address: 2 ABBEY SQ, CHESTER, CH1 2HU, ENGLAND

Web of Science Index: Science Citation Index Expanded (SCI-EXPANDED)

Web of Science Categories: Chemistry, Multidisciplinary; Crystallography

Research Areas: Chemistry; Crystallography

IDS Number: WS3NN

ISSN: 2053-2733

29-char Source Abbrev.: ACTA CRYSTALLOGR A

ISO Source Abbrev.: Acta Crystallogr. Sect. A

Source Item Page Count: 26

Funding:

Funding Agency	Grant Number
U.S. Department of Energy, Office of Science, Office of Basic Energy Sciences (DOE-BES)	DESC0012704
Stephenson Distinguished Visitor Programme	
Maxwell computational resources operated at Deutsches Elektronen-Synchrotron DESY, Hamburg, Germany	
Villum Foundation	

Work at Brookhaven National Laboratory was supported by the U.S. Department of Energy, Office of Science, Office of Basic Energy Sciences (DOE-BES) under contract No. DESC0012704. We acknowledge DESY (Hamburg, Germany), a member of the Helmholtz Association HGF, for the provision of experimental

facilities. Parts of this research were carried out at beamline P21.1 at PETRA III. ESB acknowledges the Stephenson Distinguished Visitor Programme for supporting his stay at DESY in Hamburg. This research was supported in part through the Maxwell computational resources operated at Deutsches Elektronen-Synchrotron DESY, Hamburg, Germany. This research was also supported in part by the Villum Foundation.

Open Access: Green Submitted, Green Published

Output Date: 2023-01-27

Record 10 of 125

Title: Correlated disorder-to-order crossover in the local structure of $K_xFe_{2-y}Se_{2-z}S_z$ superconductor

Author(s): Bozin, ES (Bozin, E. S.); Koch, RJ (Koch, R. J.); Mangelis, P (Mangelis, P.); Lei, HC (Lei, H. C.); Neder, R (Neder, R.); McDonnell, M (McDonnell, M.); Feygenson, M (Feygenson, M.); Petrovic, C (Petrovic, C.); Lappas, A (Lappas, A.)

Source: ACTA CRYSTALLOGRAPHICA A-FOUNDATION AND ADVANCES **Meeting Abstract:** MS-18a-6 **Volume:** 77 **Pages:** C155-C155 **Supplement:** S **Published:** AUG 2021

Times Cited in Web of Science Core Collection: 0

Total Times Cited: 0

Usage Count (Last 180 days): 0

Usage Count (Since 2013): 0

Cited Reference Count: 1

Accession Number: WOS:000761714400150

Language: English

Document Type: Meeting Abstract

Author Keywords: iron-based superconductors; local atomic structure; correlated disorder; total scattering; neutron scattering

Addresses: [Bozin, E. S.; Koch, R. J.; Lei, H. C.; Petrovic, C.] Brookhaven Natl Lab, Upton, NY 11973 USA.
[Mangelis, P.; Lappas, A.] IESL FORTH, Iraklion, Greece.
[Neder, R.] Univ Erlangen Nurnberg, Erlangen, Germany.
[McDonnell, M.; Feygenson, M.] Oak Ridge Natl Lab, Oak Ridge, TN USA.

E-mail Addresses: bozin@bnl.gov

Affiliations: United States Department of Energy (DOE); Brookhaven National Laboratory; University of Erlangen Nuremberg; United States Department of Energy (DOE); Oak Ridge National Laboratory

Publisher: INT UNION CRYSTALLOGRAPHY

Publisher Address: 2 ABBEY SQ, CHESTER, CH1 2HU, ENGLAND

Web of Science Index: Science Citation Index Expanded (SCI-EXPANDED)

Web of Science Categories: Chemistry, Multidisciplinary; Crystallography

Research Areas: Chemistry; Crystallography

IDS Number: ZI6FI

ISSN: 2053-2733

29-char Source Abbrev.: ACTA CRYSTALLOGR A

ISO Source Abbrev.: Acta Crystallogr. Sect. A

Source Item Page Count: 1

Funding:

Funding Agency	Grant Number
U.S. Department of Energy, Office of Science, Office of Basic Energy Sciences (DOE-BES)	DE-SC0012704

Work at Brookhaven National Laboratory was supported by the U.S. Department of Energy, Office of Science, Office of Basic Energy Sciences (DOE-BES) under Contract No. DE-SC0012704. Alexandros Lappas acknowledges support by the U.S. Office of Naval Research Global, NICOP Grant Award No. N62909-17-1-2126. This research used resources at the Spallation Neutron Source, a U.S. Department of Energy Office of Science User Facility operated by the Oak Ridge National Laboratory

Output Date: 2023-01-27

Record 11 of 125

Title: The local structure fingerprint of dual orbital degeneracy lifting in a strongly correlated electron system

Author(s): Koch, RJ (Koch, R. J.); Sinclair, R (Sinclair, R.); McDonnell, MT (McDonnell, M. T.); Yu, R (Yu, R.); Abeykoon, M (Abeykoon, M.); Tucker, MG (Tucker, M. G.); Tselik, AM (Tselik, A. M.); Billinge, SJL (Billinge, S. J. L.); Zhou, HD (Zhou, H. D.); Yin, WG (Yin, W. -G.); Bozin, ES (Bozin, E. S.)

Source: ACTA CRYSTALLOGRAPHICA A-FOUNDATION AND ADVANCES **Meeting Abstract:** MS-37-6 **Volume:** 77 **Pages:** C268-C268 **Supplement:** S **Published:** AUG 2021

Times Cited in Web of Science Core Collection: 0

Total Times Cited: 0

Usage Count (Last 180 days): 1

Usage Count (Since 2013): 1

Cited Reference Count: 1

Accession Number: WOS:000761714400262

Language: English

Document Type: Meeting Abstract

Author Keywords: local structure; pair distribution function; total scattering

Addresses: [Koch, R. J.; Yu, R.; Tselik, A. M.; Billinge, S. J. L.; Yin, W. -G.; Bozin, E. S.] Brookhaven Natl Lab, Condensed Matter Phys & Mat Sci Div, Upton, NY 11973 USA.

[Sinclair, R.; Zhou, H. D.] Univ Tennessee, Dept Phys & Astron, Knoxville, TN 37996 USA.

[McDonnell, M. T.; Tucker, M. G.] Oak Ridge Natl Lab, Neutron Scattering Div, Oak Ridge, TN 37831 USA.

[Abeykoon, M.] Brookhaven Natl Lab, Photon Sci Div, Upton, NY 11973 USA.

[Billinge, S. J. L.] Columbia Univ, Dept Appl Phys & Appl Math, New York, NY 10027 USA.

E-mail Addresses: rkoch@bnl.gov

Affiliations: United States Department of Energy (DOE); Brookhaven National Laboratory; University of Tennessee System; University of Tennessee Knoxville; United States Department of Energy (DOE); Oak Ridge National Laboratory; United States Department of Energy (DOE); Brookhaven National Laboratory; Columbia University

Author Identifiers:

Author	Web of Science ResearcherID	ORCID Number
Tselik, Alexei	HJZ-5160-2023	0000-0002-7478-670X
Zhou, Haidong	O-4373-2016	0000-0002-1595-1912

Publisher: INT UNION CRYSTALLOGRAPHY

Publisher Address: 2 ABBEY SQ, CHESTER, CH1 2HU, ENGLAND

Web of Science Index: Science Citation Index Expanded (SCI-EXPANDED)

Web of Science Categories: Chemistry, Multidisciplinary; Crystallography

Research Areas: Chemistry; Crystallography

IDS Number: ZI6FI

ISSN: 2053-2733

29-char Source Abbrev.: ACTA CRYSTALLOGR A

ISO Source Abbrev.: Acta Crystallogr. Sect. A

Source Item Page Count: 1

Funding:

Funding Agency	Grant Number
U.S. Department of Energy, Office of Science, Office of Basic Energy Sciences (DOE-BES)	DE-SC0012704
U.S. Department of Energy	DE-SC-0020254
DOE Office of Science	DE-SC0012704

Work at Brookhaven National Laboratory was supported by U.S. Department of Energy, Office of Science, Office of Basic Energy Sciences (DOE-BES) under contract No. DE-SC0012704.

R.S. and H.Z. thank the support from the U.S. Department of Energy under award DE-SC-0020254. Neutron total scattering data were collected at the NOMAD beamline (BL-1B) at the Spallation Neutron Source, a U.S. Department of Energy Office of Science User Facility operated by the Oak Ridge National Laboratory.

X-ray PDF measurements were conducted on beamline 28-ID-1 of the National Synchrotron Light Source II, a U.S. Department of Energy (DOE) Office of Science User Facility operated for the DOE Office of Science by Brookhaven National Laboratory under Contract No. DE-SC0012704.

Output Date: 2023-01-27

Record 12 of 125

Title: Nanoscale distortions and ground state selection in geometrically frustrated magnets

Author(s): Lappas, A (Lappas, A.); Frandsen, BA (Frandsen, B. A.); Bozin, ES (Bozin, E. S.)

Source: ACTA CRYSTALLOGRAPHICA A-FOUNDATION AND ADVANCES **Meeting Abstract:** MS-45-6 **Volume:** 77 **Pages:** C317-C317 **Supplement:** S **Published:** AUG 2021

Times Cited in Web of Science Core Collection: 0

Total Times Cited: 0

Usage Count (Last 180 days): 1

Usage Count (Since 2013): 1

Cited Reference Count: 3

Accession Number: WOS:000761714400310

Language: English

Document Type: Meeting Abstract

Author Keywords: triangular lattice; antiferromagnetism; neutron diffraction; pair-distribution function analysis; phase transitions

Addresses: [Lappas, A.] Fdn Res & Technol Hellas, Inst Elect Struct & Laser, Iraklion 71110, Greece.

[Frandsen, B. A.] Brigham Young Univ, Dept Phys & Astron, Provo, UT 84602 USA.

[Bozin, E. S.] Brookhaven Natl Lab, Condensed Matter Phys & Mat Sci Div, Upton, NY 11973 USA.

E-mail Addresses: lappas@iesl.forth.gr

Affiliations: Foundation for Research & Technology - Hellas (FORTH); Brigham Young University; United States Department of Energy (DOE); Brookhaven National Laboratory

Publisher: INT UNION CRYSTALLOGRAPHY

Publisher Address: 2 ABBEY SQ, CHESTER, CH1 2HU, ENGLAND

Web of Science Index: Science Citation Index Expanded (SCI-EXPANDED)

Web of Science Categories: Chemistry, Multidisciplinary; Crystallography

Research Areas: Chemistry; Crystallography

IDS Number: ZI6FI

ISSN: 2053-2733

29-char Source Abbrev.: ACTA CRYSTALLOGR A

ISO Source Abbrev.: Acta Crystallogr. Sect. A

Source Item Page Count: 1

Funding:

Funding Agency	Grant Number
Brigham Young University	
U.S. DOE, Office of Science, Office of Basic Energy Sciences (DOE-BES)	DE-SC0012704

This research used resources at the Spallation Neutron Source, a DOE Office of Science User Facility operated by the Oak Ridge National Laboratory. B. A.F. acknowledges support from Brigham Young University. Work at Brookhaven National Laboratory was supported by U.S. DOE, Office of Science, Office of Basic Energy Sciences (DOE-BES) under Contract No. DE-SC0012704. A.L. thanks the Fulbright Foundation-Greece.

Output Date: 2023-01-27

Record 13 of 125

Title: Dual Orbital Degeneracy Lifting in a Strongly Correlated Electron System

Author(s): Koch, RJ (Koch, R. J.); Sinclair, R (Sinclair, R.); McDonnelle, MT (McDonnelle, M. T.); Yu, R (Yu, R.); Abeykoon, M (Abeykoon, M.); Tucker, MG (Tucker, M. G.); Tselik, AM (Tselik, A. M.); Billinge, SJL (Billinge, S. J. L.); Zhou, HD (Zhou, H. D.); Yin, WG (Yin, W-G); Bozin, ES (Bozin, E. S.)

Source: PHYSICAL REVIEW LETTERS **Volume:** 126 **Issue:** 18 **Article Number:** 186402 **DOI:** 10.1103/PhysRevLett.126.186402 **Published:** MAY 6 2021

Times Cited in Web of Science Core Collection: 8

Total Times Cited: 8

Usage Count (Last 180 days): 6

Usage Count (Since 2013): 27

Cited Reference Count: 69

Abstract: The local structure of NaTiSi₂O₆ is examined across its Ti-dimerization orbital-assisted Peierls transition at 210 K. An atomic pair distribution function approach evidences local symmetry breaking preexisting far above the transition. The analysis unravels that, on warming, the dimers evolve into a short range orbital degeneracy lifted (ODL) state of dual orbital character, persisting up to at least 490 K. The ODL state is correlated over the length scale spanning similar to 6 sites of the Ti zigzag chains. Results imply that the ODL phenomenology extends to strongly correlated electron systems.

Accession Number: WOS:000652838100007

PubMed ID: 34018766

Language: English

Document Type: Article

KeyWords Plus: METAL-INSULATOR-TRANSITION; PHASE-TRANSITION; NATISI2O6; SUPERCONDUCTIVITY; DIMERIZATION; FRUSTRATION; NEMATICITY; DISTORTION; SOFTWARE; BREAKING

Addresses: [Koch, R. J.; Yu, R.; Tselik, A. M.; Billinge, S. J. L.; Yin, W-G; Bozin, E. S.] Brookhaven Natl Lab, Condensed Matter Phys & Mat Sci Div, Upton, NY 11973 USA.

[Sinclair, R.; Zhou, H. D.] Univ Tennessee, Dept Phys & Astron, Knoxville, TN 37996 USA.

[McDonnelle, M. T.; Tucker, M. G.] Oak Ridge Natl Lab, Neutron Scattering Div, Oak Ridge, TN 37831 USA.

[Abeykoon, M.] Brookhaven Natl Lab, Photon Sci Div, Upton, NY 11973 USA.

[Billinge, S. J. L.] Columbia Univ, Dept Appl Phys & Appl Math, New York, NY 10027 USA.
[McDonnelle, M. T.] Oak Ridge Natl Lab, Comp Sci & Math Div, Oak Ridge, TN 37831 USA.
[Yu, R.] Chinese Acad Sci, Inst Phys, Beijing 100190, Peoples R China.

Corresponding Address: Koch, RJ; Yin, WG; Bozin, ES (corresponding author), Brookhaven Natl Lab, Condensed Matter Phys & Mat Sci Div, Upton, NY 11973 USA.

E-mail Addresses: rkoch@bnl.gov; wyin@bnl.gov; bozin@bnl.gov

Affiliations: United States Department of Energy (DOE); Brookhaven National Laboratory; University of Tennessee System; University of Tennessee Knoxville; United States Department of Energy (DOE); Oak Ridge National Laboratory; United States Department of Energy (DOE); Brookhaven National Laboratory; Columbia University; United States Department of Energy (DOE); Oak Ridge National Laboratory; Chinese Academy of Sciences; Institute of Physics, CAS

Author Identifiers:

Author	Web of Science ResearcherID	ORCID Number
Zhou, Haidong	O-4373-2016	0000-0002-1595-1912
Bozin, Emil	AAB-4551-2020	
Tselik, Alexei	HJZ-5160-2023	0000-0002-7478-670X
Tucker, Matt	C-9867-2016	0000-0002-2891-7086
Billinge, Simon		0000-0002-9734-4998
Yin, Weiguo	A-9671-2014	0000-0002-4965-5329

Publisher: AMER PHYSICAL SOC

Publisher Address: ONE PHYSICS ELLIPSE, COLLEGE PK, MD 20740-3844 USA

Web of Science Index: Science Citation Index Expanded (SCI-EXPANDED)

Web of Science Categories: Physics, Multidisciplinary

Research Areas: Physics

IDS Number: SF6BH

ISSN: 0031-9007

eISSN: 1079-7114

29-char Source Abbrev.: PHYS REV LETT

ISO Source Abbrev.: Phys. Rev. Lett.

Source Item Page Count: 6

Funding:

Funding Agency	Grant Number
U.S. Department of Energy, Office of Science, Office of Basic Energy Sciences (DOE-BES)	DE-SC0012704
U.S. Department of Energy	DE-SC-0020254
DOE Office of Science	DE-SC0012704

Work at Brookhaven National Laboratory was supported by U.S. Department of Energy, Office of Science, Office of Basic Energy Sciences (DOE-BES) under Contract No. DE-SC0012704. R. S. and H. Z. are thankful for the support from the U.S. Department of Energy under Award No. DE-SC-0020254. Neutron total scattering data were collected at the NOMAD beam line (BL-1B) at the Spallation Neutron Source, a U.S. Department of Energy Office of Science User Facility operated by the Oak Ridge National Laboratory. X-ray PDF measurements were conducted on beam line 28-ID-1 of the National Synchrotron Light Source II, a U.S. Department of Energy (DOE) Office of Science User Facility operated for the DOE Office of Science by Brookhaven National Laboratory under Contract No. DE-SC0012704.

Open Access: Green Submitted

Output Date: 2023-01-27

Record 14 of 125

Title: Comment on "Colossal Pressure-Induced Softening in Scandium Fluoride"

Author(s): Zaliznyak, A (Zaliznyak, A.); Bozin, E (Bozin, E.); Tkachenko, AV (Tkachenko, A. V.)

Source: PHYSICAL REVIEW LETTERS **Volume:** 126 **Issue:** 17 **Article Number:** 179601 **DOI:** 10.1103/PhysRevLett.126.179601 **Published:** APR 28 2021

Times Cited in Web of Science Core Collection: 0

Total Times Cited: 0

Usage Count (Last 180 days): 2

Usage Count (Since 2013): 8

Cited Reference Count: 4

Accession Number: WOS:000652836500018

PubMed ID: 33988444

Language: English

Document Type: Editorial Material

Addresses: [Zaliznyak, A.; Bozin, E.] Brookhaven Natl Lab, Condensed Matter Phys, Upton, NY 11973 USA.

[Zaliznyak, A.; Bozin, E.] Brookhaven Natl Lab, Div Mat Sci, Upton, NY 11973 USA.

[Tkachenko, A. V.] Brookhaven Natl Lab, CFN, Upton, NY 11973 USA.

Corresponding Address: Zaliznyak, A (corresponding author), Brookhaven Natl Lab, Condensed Matter Phys, Upton, NY 11973 USA.

Zaliznyak, A (corresponding author), Brookhaven Natl Lab, Div Mat Sci, Upton, NY 11973 USA.

E-mail Addresses: zaliznyak@bnl.gov

Affiliations: United States Department of Energy (DOE); Brookhaven National Laboratory; United States Department of Energy (DOE); Brookhaven National Laboratory; United States Department of Energy (DOE); Brookhaven National Laboratory

Author Identifiers:

Author	Web of Science ResearcherID	ORCID Number
Tkachenko, Alexei V	I-9040-2012	0000-0003-1291-243X
Bozin, Emil		0000-0002-6682-0365
Zaliznyak, Igor		0000-0002-8548-7924

Publisher: AMER PHYSICAL SOC

Publisher Address: ONE PHYSICS ELLIPSE, COLLEGE PK, MD 20740-3844 USA

Web of Science Index: Science Citation Index Expanded (SCI-EXPANDED)

Web of Science Categories: Physics, Multidisciplinary

Research Areas: Physics

IDS Number: SF6AR

ISSN: 0031-9007

eISSN: 1079-7114

29-char Source Abbrev.: PHYS REV LETT

ISO Source Abbrev.: Phys. Rev. Lett.

Source Item Page Count: 2

Funding:

Funding Agency	Grant Number

Office of Basic Energy Sciences (BES), Division of Materials Sciences and Engineering, U.S. Department of Energy (DOE)	DE-SC0012704
Scientific User Facilities Division, Office of Basic Energy Sciences, U.S. Department of Energy	DE-SC0012704

Work at Brookhaven National Laboratory was supported by Office of Basic Energy Sciences (BES), Division of Materials Sciences and Engineering, U.S. Department of Energy (DOE), under Award No. DE-SC0012704. Work at BNL's Center for Functional Nanomaterials (CFN) was sponsored by the Scientific User Facilities Division, Office of Basic Energy Sciences, U.S. Department of Energy, under the same award.

Open Access: Green Submitted, hybrid

Output Date: 2023-01-27

Record 15 of 125

Title: Charge density waves in cuprate superconductors beyond the critical doping

Author(s): Miao, H (Miao, H.); Fabbris, G (Fabbris, G.); Koch, RJ (Koch, R. J.); Mazzone, DG (Mazzone, D. G.); Nelson, CS (Nelson, C. S.); Acevedo-Esteves, R (Acevedo-Esteves, R.); Gu, GD (Gu, G. D.); Li, Y (Li, Y.); Yilimaz, T (Yilimaz, T.); Kaznatcheev, K (Kaznatcheev, K.); Vescovo, E (Vescovo, E.); Oda, M (Oda, M.); Kurosawa, T (Kurosawa, T.); Momono, N (Momono, N.); Assefa, T (Assefa, T.); Robinson, IK (Robinson, I. K.); Bozin, ES (Bozin, E. S.); Tranquada, JM (Tranquada, J. M.); Johnson, PD (Johnson, P. D.); Dean, MPM (Dean, M. P. M.)

Source: NPJ QUANTUM MATERIALS **Volume:** 6 **Issue:** 1 **Article Number:** 31 **DOI:** 10.1038/s41535-021-00327-4 **Published:** MAR 19 2021

Times Cited in Web of Science Core Collection: 34

Total Times Cited: 34

Usage Count (Last 180 days): 5

Usage Count (Since 2013): 28

Cited Reference Count: 52

Abstract: The unconventional normal-state properties of the cuprates are often discussed in terms of emergent electronic order that onsets below a putative critical doping of $x(c)$ approximate to 0.19. Charge density wave (CDW) correlations represent one such order; however, experimental evidence for such order generally spans a limited range of doping that falls short of the critical value $x(c)$, leading to questions regarding its essential relevance. Here, we use X-ray diffraction to demonstrate that CDW correlations in $\text{La}_{2-x}\text{Sr}_x\text{CuO}_4$ persist up to a doping of at least $x=0.21$. The correlations show strong changes through the superconducting transition, but no obvious discontinuity through $x(c)$ approximate to 0.19, despite changes in Fermi surface topology and electronic transport at this doping. These results demonstrate the interaction between CDWs and superconductivity even in overdoped cuprates and prompt a reconsideration of the role of CDW correlations in the high-temperature cuprate phase diagram.

Accession Number: WOS:000631560800004

Language: English

Document Type: Article

Addresses: [Miao, H.; Koch, R. J.; Mazzone, D. G.; Gu, G. D.; Li, Y.; Assefa, T.; Robinson, I. K.; Bozin, E. S.; Tranquada, J. M.; Johnson, P. D.; Dean, M. P. M.] Brookhaven Natl Lab, Condensed Matter Phys & Mat Sci Dept, Upton, NY 11973 USA.

[Fabbris, G.] Argonne Natl Lab, Adv Photon Source, Argonne, IL 60439 USA.

[Nelson, C. S.; Acevedo-Esteves, R.; Yilimaz, T.; Kaznatcheev, K.; Vescovo, E.] Brookhaven Natl Lab, Natl Synchrotron Light Source 2, Upton, NY 11973 USA.

[Oda, M.; Kurosawa, T.] Hokkaido Univ, Dept Phys, Sapporo, Hokkaido 0600810, Japan.

[Momono, N.] Muroran Inst Technol, Dept Sci & Informat, Muroran, Hokkaido 0508585, Japan.

[Robinson, I. K.] UCL, London Ctr Nanotechnol, Gower St, London WC1 6BT, England.

[Mazzone, D. G.] Paul Scherrer Inst, Lab Neutron Scattering & Imaging, CH-5232 Villigen, Switzerland.
[Assefa, T.] SLAC Natl Accelerator Lab, Stanford Inst Mat & Energy Sci, Menlo Pk, CA 94025 USA.

Corresponding Address: Miao, H; Dean, MPM (corresponding author), Brookhaven Natl Lab, Condensed Matter Phys & Mat Sci Dept, Upton, NY 11973 USA.

E-mail Addresses: hmiao@bnl.gov; mdean@bnl.gov

Affiliations: United States Department of Energy (DOE); Brookhaven National Laboratory; United States Department of Energy (DOE); Argonne National Laboratory; United States Department of Energy (DOE); Brookhaven National Laboratory; Hokkaido University; Muroran Institute of Technology; University of London; University College London; Swiss Federal Institutes of Technology Domain; Paul Scherrer Institute; Stanford University; United States Department of Energy (DOE); SLAC National Accelerator Laboratory

Author Identifiers:

Author	Web of Science ResearcherID	ORCID Number
Miao, Hu	AGX-0618-2022	
Dean, Mark PM	B-4541-2011	0000-0001-5139-3543
Fabbris, Gilberto	F-3244-2011	0000-0001-8278-4985
Bozin, Emil	AAB-4551-2020	
Assefa, Tadesse	ABD-2999-2021	0000-0003-3904-0846
Mazzone, Daniel	AAG-1497-2020	0000-0002-0421-0625
Tranquada, John M.	A-9832-2009	0000-0003-4984-8857
Robinson, Ian	A-4906-2010	0000-0003-4897-5221
Li, Yangmu		0000-0003-0886-2919
Nelson, Christie S.		0000-0002-0196-0340
Acevedo-Esteves, Raul		0000-0003-3668-7089
Miao, Hu		0000-0003-1078-5713

Publisher: NATURE RESEARCH

Publisher Address: HEIDELBERGER PLATZ 3, BERLIN, 14197, GERMANY

Web of Science Index: Science Citation Index Expanded (SCI-EXPANDED)

Web of Science Categories: Materials Science, Multidisciplinary; Quantum Science & Technology; Physics, Applied; Physics, Condensed Matter

Research Areas: Materials Science; Physics

IDS Number: RA6XU

eISSN: 2397-4648

29-char Source Abbrev.: NPJ QUANTUM MATER

ISO Source Abbrev.: npj Quantum Mater.

Source Item Page Count: 6

Funding:

Funding Agency	Grant Number
US Department of Energy (DOE), Office of Basic Energy Sciences	
US Department of Energy, Office of Basic Energy Sciences	DE-SC0012704
DOE Office of Science by Brookhaven National Laboratory	DE-SC0012704
DOE Office of Science by Argonne National Laboratory	DE-AC02-06CH11357

We thank N. Christensen, G. Kotliar, J. Q. Lin, V. Thampy, A. Tselik, and W. G. Yin for insightful discussions, and J. Jiang and S. S. Zhang for technical support. This material is based upon work supported by the US Department of Energy (DOE), Office of Basic Energy Sciences. Work at Brookhaven National Laboratory was supported by the US Department of Energy, Office of Basic Energy Sciences, under contract no. DESC0012704. X-ray and photoemission measurements used resources at the 4-ID and 21-ID-1 beamlines of

the National Synchrotron Light Source II, a US Department of Energy Office of Science User Facility operated for the DOE Office of Science by Brookhaven National Laboratory under contract no. DE-SC0012704. Additional X-ray measurements used resources at 4-ID-D in the Advanced Photon Source, a US Department of Energy (DOE) Office of Science User Facility operated for the DOE Office of Science by Argonne National Laboratory under contract no. DE-AC02-06CH11357.

Open Access: Green Submitted, gold, Green Published

Output Date: 2023-01-27

Record 16 of 125

Title: Imaging the Phase Transformation in Single Particles of the Lithium Titanate Anode for Lithium-Ion Batteries

Author(s): Assefa, TA (Assefa, Tadesse A.); Suzana, AF (Suzana, Ana F.); Wu, LL (Wu, Longlong); Koch, RJ (Koch, Robert J.); Li, LX (Li, Luxi); Cha, W (Cha, Wonsuk); Harder, RJ (Harder, Ross J.); Bozin, ES (Bozin, Emil S.); Wang, F (Wang, Feng); Robinson, IK (Robinson, Ian K.)

Source: ACS APPLIED ENERGY MATERIALS **Volume:** 4 **Issue:** 1 **Pages:** 111-118 **DOI:** 10.1021/acsaem.0c02010 **Early Access Date:** JAN 2021 **Published:** JAN 25 2021

Times Cited in Web of Science Core Collection: 7

Total Times Cited: 8

Usage Count (Last 180 days): 8

Usage Count (Since 2013): 28

Cited Reference Count: 45

Abstract: Lithium uptake and release in lithium titanate (LTO) anode materials during a discharge and charge cycle is one of the fundamental processes of a lithium-ion battery (LIB), still not fully understood at the microscopic level. During the discharge cycle, LTO undergoes a phase transformation between $\text{Li}_4\text{Ti}_5\text{O}_{12}$ and $\text{Li}_7\text{Ti}_5\text{O}_{12}$ states within a cubic crystal lattice. To reveal the details of the microscopic mechanism, it is necessary to track the sequence of phase transformations at different discharge/charge states under operating conditions. Here, we use in situ Bragg coherent diffraction imaging (BCDI) and in situ X-ray diffraction (XRD) experiments to examine the lithium insertion-induced materials phase transformation within a single LTO particle and a bulk battery analogue, respectively. BCDI analysis from (111) Bragg peak shows the two-phase transformation manifesting as a distinct image phase modulation within a single LTO nanoparticle occurring in the middle of the discharge region then subsiding toward the end of the discharge cycle. We observe the biggest phase variation at the two-phase stage, indicating the formation of phase domains of 200 nm in size during the discharge process. We also observe a lattice contraction of $>0.2\%$ in a single LTO nanoparticle at the (400) Bragg peak measurement, larger than that in the corresponding bulk material. Our observation of this phase transformation at a single-particle level has implications for the understanding of the microscopic/mesoscale picture of the phase transformation in anode and cathode LIBs materials.

Accession Number: WOS:000613720100015

Language: English

Document Type: Article

Author Keywords: coherent diffraction imaging; image phase variation; displacement field; battery material; lithium titanate anode

Addresses: [Assefa, Tadesse A.; Suzana, Ana F.; Wu, Longlong; Koch, Robert J.; Bozin, Emil S.; Wang, Feng; Robinson, Ian K.] Brookhaven Natl Lab, Condensed Matter Phys & Mat Sci Dept, Upton, NY 11793 USA. [Li, Luxi; Cha, Wonsuk; Harder, Ross J.] Argonne Natl Lab, Adv Photon Source, Argonne, IL 60439 USA. [Robinson, Ian K.] UCL, London Ctr Nanotechnol, London WC1E 6BT, England.

Corresponding Address: Assefa, TA; Robinson, IK (corresponding author), Brookhaven Natl Lab, Condensed Matter Phys & Mat Sci Dept, Upton, NY 11793 USA.

Robinson, IK (corresponding author), UCL, London Ctr Nanotechnol, London WC1E 6BT, England.

E-mail Addresses: tassefa@bnl.gov; irobinson@bnl.gov

Affiliations: United States Department of Energy (DOE); Brookhaven National Laboratory; United States Department of Energy (DOE); Argonne National Laboratory; University of London; University College London

Author Identifiers:

Author	Web of Science ResearcherID	ORCID Number
wu, longlong	T-3334-2019	0000-0002-1336-2743
Assefa, Tadesse	ABD-2999-2021	0000-0003-3904-0846
Bozin, Emil	AAB-4551-2020	
Robinson, Ian	A-4906-2010	0000-0003-4897-5221
Suzana, Ana		0000-0001-5736-7506

Publisher: AMER CHEMICAL SOC

Publisher Address: 1155 16TH ST, NW, WASHINGTON, DC 20036 USA

Web of Science Index: Science Citation Index Expanded (SCI-EXPANDED)

Web of Science Categories: Chemistry, Physical; Energy & Fuels; Materials Science, Multidisciplinary

Research Areas: Chemistry; Energy & Fuels; Materials Science

IDS Number: QA8VH

ISSN: 2574-0962

29-char Source Abbrev.: ACS APPL ENERG MATER

ISO Source Abbrev.: ACS Appl. Energ. Mater.

Source Item Page Count: 8

Funding:

Funding Agency	Grant Number
U.S. Department of Energy (DOE), Office of Basic Energy Sciences, Division of Materials Sciences and Engineering	DE-SC0012704
U.S. DOE Office of Science Facility, at the Brookhaven National Laboratory	DE-SC0012704
U.S. Department of Energy, Office of Energy Efficiency and Renewable Energy, Vehicle Technologies Office	DE-SC0012704
DOE Office of Science	DE-SC0012704
U.S. Department of Energy, Office of Science, Office of Basic Energy Sciences	DE-AC02-06CH11357
U.S. National Science Foundation	9724294
EPSRC	EP/I022562/1

We are very grateful for the help of Yao Shanshan with the sample preparation and help with in situ XRD measurements done at NSLS-II, 28-ID-2 beamline. We are also very grateful for the help of Jaiming Bai for the help with in situ XRD measurements done at NSLS-II, 28-ID-2 beamline. T.A.A. would like to thank Xiaojing Huang for his comments on the experimental results. The work at the Brookhaven National Laboratory was supported by the U.S. Department of Energy (DOE), Office of Basic Energy Sciences, Division of Materials Sciences and Engineering, under Contract no. DE-SC0012704. The sample characterization used the resources of the Centre for Functional Nanomaterials, which is a U.S. DOE Office of Science Facility, at the Brookhaven National Laboratory under Contract no. DE-SC0012704. F.W. acknowledges the support of the U.S. Department of Energy, Office of Energy Efficiency and Renewable Energy, Vehicle Technologies Office, under Contract no. DE-SC0012704. This research used the 28-ID-I (XPD) beamline of the National Synchrotron Light Source II, DOE Office of Science User Facilities operated for the DOE Office of Science by the Brookhaven National Laboratory under Contract no. DE-SC0012704. The experiments were carried out at Advanced Photon Source (APS) beamline 34ID-C, and the APS was supported by the U.S. Department of Energy, Office of Science, Office of Basic Energy Sciences, under Contract no. DE-AC02-06CH11357. The

beamline 34ID-C was built with U.S. National Science Foundation Grant no. NSF-DMR 9724294
Development of a Coherent X-Ray Diffraction Instrument.

Open Access: Green Submitted, Green Published, hybrid

Output Date: 2023-01-27

Record 17 of 125

Title: Two-orbital degeneracy lifted local precursor to a metal-insulator transition in MgTi₂O₄

Author(s): Yang, L (Yang, Long); Koch, RJ (Koch, Robert J.); Zheng, H (Zheng, Hong); Mitchell, JF (Mitchell, J. F.); Yin, WG (Yin, Weiguo); Tucker, MG (Tucker, Matthew G.); Billinge, SJL (Billinge, Simon J. L.); Bozin, ES (Bozin, Emil S.)

Source: PHYSICAL REVIEW B **Volume:** 102 **Issue:** 23 **Article Number:** 235128 **DOI:** 10.1103/PhysRevB.102.235128 **Published:** DEC 14 2020

Times Cited in Web of Science Core Collection: 10

Total Times Cited: 10

Usage Count (Last 180 days): 6

Usage Count (Since 2013): 30

Cited Reference Count: 63

Abstract: The MgTi₂O₄ spinel exhibits a metal-insulator transition on cooling below T_s approximate to 250 K, accompanied by Ti t(2g)(1) orbital ordering and spin-singlet dimerization with associated average symmetry reduction to tetragonal. By combining x-ray and neutron pair distribution function analyses to track the evolution of the local atomic structure across the transition we find that local tetragonality already exists in the metallic globally cubic phase at high temperature. Local distortions are observed up to at least 500 K, the highest temperature assessed in this study. Significantly, the high-temperature local state is not continuously connected to the orbitally ordered band insulator ground state and so the transition cannot be characterized as a trivial order-disorder type. The shortest Ti-Ti spin-singlet dimer bond lengths expand abruptly on warming across the transition, but remain shorter than those seen in the cubic average structure. These seemingly contradictory observations can be understood within the model of a local fluctuating two-orbital t(2g) orbital degeneracy lifted (ODL) precursor state derived from electron filling, Ti substructure topology, and point symmetry considerations. The ODL state in MgTi₂O₄ has a correlation length of about 1 nm at high temperature. We discuss that this extended character of the local distortions is consistent with the two-orbital nature of this state imposed by the charge filling and the bond charge repulsion. The MgTi₂O₄ spinel exemplifies multiorbital ODL state and presents the possibility of a widespread presence of such precursor states in scarcely studied high-temperature regimes of transition-metal-based quantum materials.

Accession Number: WOS:000598244300003

Language: English

Document Type: Article

Addresses: [Yang, Long; Billinge, Simon J. L.] Columbia Univ, Dept Appl Phys & Appl Math, New York, NY 10027 USA.

[Koch, Robert J.; Yin, Weiguo; Billinge, Simon J. L.; Bozin, Emil S.] Brookhaven Natl Lab, Condensed Matter Phys & Mat Sci Div, Upton, NY 11973 USA.

[Zheng, Hong; Mitchell, J. F.] Argonne Natl Lab, Mat Sci Div, Argonne, IL 60439 USA.

[Tucker, Matthew G.] Oak Ridge Natl Lab, Neutron Scattering Div, Oak Ridge, TN 37830 USA.

Corresponding Address: Bozin, ES (corresponding author), Brookhaven Natl Lab, Condensed Matter Phys & Mat Sci Div, Upton, NY 11973 USA.

E-mail Addresses: bozin@bnl.gov

Affiliations: Columbia University; United States Department of Energy (DOE); Brookhaven National Laboratory; United States Department of Energy (DOE); Argonne National Laboratory; United States Department of Energy (DOE); Oak Ridge National Laboratory

Author Identifiers:

Author	Web of Science ResearcherID	ORCID Number
Yang, Long	O-9037-2017	0000-0001-8731-0172
Bozin, Emil	AAB-4551-2020	
Mitchell, John F	A-1907-2012	
Tucker, Matt	C-9867-2016	0000-0002-2891-7086
Billinge, Simon		0000-0002-9734-4998
Bozin, Emil		0000-0002-6682-0365
Yin, Weiguo	A-9671-2014	0000-0002-4965-5329

Publisher: AMER PHYSICAL SOC

Publisher Address: ONE PHYSICS ELLIPSE, COLLEGE PK, MD 20740-3844 USA

Web of Science Index: Science Citation Index Expanded (SCI-EXPANDED)

Web of Science Categories: Materials Science, Multidisciplinary; Physics, Applied; Physics, Condensed Matter

Research Areas: Materials Science; Physics

IDS Number: PE3CB

ISSN: 2469-9950

eISSN: 2469-9969

29-char Source Abbrev.: PHYS REV B

ISO Source Abbrev.: Phys. Rev. B

Source Item Page Count: 13

Funding:

Funding Agency	Grant Number
U.S. Department of Energy (DOE), Office of Science, Office of Basic Energy Sciences	DE-SC0012704
ORNL Graduate Opportunity program - Neutron Science Directorate	
Scientific User Facilities Division, Office of Basic Energy Science, U.S. DOE	
U.S. DOE Office of Science, Basic Energy Sciences, Materials Science and Engineering Division	

Work at Brookhaven National Laboratory was supported by the U.S. Department of Energy (DOE), Office of Science, Office of Basic Energy Sciences under Contract No. DE-SC0012704. L.Y. and M.G.T. acknowledge support from the ORNL Graduate Opportunity program, which was funded by the Neutron Science Directorate, with support from the Scientific User Facilities Division, Office of Basic Energy Science, U.S. DOE. Work in the Materials Science Division at Argonne National Laboratory (sample synthesis and characterization) was sponsored by the U.S. DOE Office of Science, Basic Energy Sciences, Materials Science and Engineering Division. X-ray PDF measurements were conducted at 28-ID-1 and 28-ID-2 beamlines of the National Synchrotron Light Source II, a U.S. DOE Office of Science User Facility operated for the DOE Office of Science by Brookhaven National Laboratory. Neutron diffraction experiments were carried out at the NOMAD beamline of the Spallation Neutron Source, Oak Ridge National Laboratory, which was sponsored by the Scientific User Facilities Division, Office of Basic Energy Science, U.S. DOE.

Open Access: Green Submitted

Output Date: 2023-01-27

Record 18 of 125

Title: Pressure Induced Topological Quantum Phase Transition in Weyl Semimetal T-d-MoTe₂

Author(s): Guguchia, Z (Guguchia, Zurab); dos Santos, AM (dos Santos, Antonio M.); von Rohr, FO (von Rohr, Fabian O.); Molaison, JJ (Molaison, Jamie J.); Banerjee, S (Banerjee, Soham); Rhodes, D (Rhodes,

Daniel); Yin, JX (Yin, Jiabin); Khasanov, R (Khasanov, Rustem); Hone, J (Hone, James); Uemura, YJ (Uemura, Yasutomo J.); Hasan, MZ (Hasan, M. Zahid); Luetkens, H (Luetkens, Hubertus); Bozin, ES (Bozin, Emil S.); Amato, A (Amato, Alex)

Source: JOURNAL OF THE PHYSICAL SOCIETY OF JAPAN **Volume:** 89 **Issue:** 9 **Article Number:** 094707 **DOI:** 10.7566/JPSJ.89.094707 **Published:** SEP 15 2020

Times Cited in Web of Science Core Collection: 2

Total Times Cited: 2

Usage Count (Last 180 days): 1

Usage Count (Since 2013): 43

Cited Reference Count: 38

Abstract: We report the temperature and pressure ($p(\max)$ congruent to 1:5 GPa) evolution of the crystal structure of the Weyl semimetal T-d MoTe₂ by combination of neutron diffraction and the X-ray total scattering experiments. We find that the fundamental non-centrosymmetric structure T-d is fully suppressed and transforms into a centrosymmetric 1T' structure at a critical pressure of $p(\text{cr})$ similar to 1.2-1.4 GPa. This is strong evidence for a pressure induced quantum phase transition (QPT) between topological to a trivial electronic state. Although the topological QPT has strong effect on magnetoresistance, it is interesting that the superconducting (SC) critical temperature T_c , the superfluid density, and the SC gap all change smoothly and continuously across p_{cr} and no sudden effects are seen concomitantly with the suppression of the T-d structure. This implies that the T_c , and thus the SC pairing strength, is unaffected by the topological QPT. However, the QPT requires the change in the SC gap symmetry from non-trivial $s(\pm)$ to a trivial $s(++)$ state, which we discuss in this work. Our systematic characterizations of the structure and SC properties associated with the topological QPT provide deep insight into the pressure induced phase diagram in this topological quantum material.

Accession Number: WOS:000565913800027

Language: English

Document Type: Article

Addresses: [Guguchia, Zurab; Khasanov, Rustem; Luetkens, Hubertus; Amato, Alex] Paul Scherrer Inst, Lab Muon Spin Spect, CH-5232 Villigen, Switzerland.

[dos Santos, Antonio M.; Molaison, Jamie J.] Oak Ridge Natl Lab, Neutron Scattering Div, POB 2009, Oak Ridge, TN 37831 USA.

[von Rohr, Fabian O.] Univ Zurich, Dept Chem, CH-8057 Zurich, Switzerland.

[von Rohr, Fabian O.] Univ Zurich, Dept Phys, CH-8057 Zurich, Switzerland.

[Banerjee, Soham; Bozin, Emil S.] Brookhaven Natl Lab, Condensed Matter Phys & Mat Sci Div, Upton, NY 11973 USA.

[Rhodes, Daniel] Univ Wisconsin, Dept Mat Sci & Engr, 1509 Univ Ave, Madison, WI 53706 USA.

[Yin, Jiabin; Hasan, M. Zahid] Princeton Univ, Dept Phys, Lab Topol Quantum Matter & Spect, Princeton, NJ 08544 USA.

[Hone, James] Columbia Univ, Dept Mech Engr, New York, NY 10027 USA.

[Uemura, Yasutomo J.] Columbia Univ, Dept Phys, 538 W 120th St, New York, NY 10027 USA.

Corresponding Address: Guguchia, Z (corresponding author), Paul Scherrer Inst, Lab Muon Spin Spect, CH-5232 Villigen, Switzerland.

E-mail Addresses: zurab.guguchia@psi.ch

Affiliations: Swiss Federal Institutes of Technology Domain; Paul Scherrer Institute; United States Department of Energy (DOE); Oak Ridge National Laboratory; University of Zurich; University of Zurich; United States Department of Energy (DOE); Brookhaven National Laboratory; University of Wisconsin System; University of Wisconsin Madison; Princeton University; Columbia University; Columbia University

Author Identifiers:

Author	Web of Science ResearcherID	ORCID Number
Amato, Alex	H-7674-2013	0000-0001-9963-7498
Luetkens, Hubertus	G-1831-2011	0000-0002-5842-9788

Hone, James C	E-1879-2011	0000-0002-8084-3301
Yin, Jia-Xin	AAA-8548-2019	0000-0003-2661-4206
Bozin, Emil	AAB-4551-2020	
Guguchia, Zurab		0000-0002-0764-7574
dos Santos, Antonio M.	A-5602-2016	0000-0001-6900-0816

Publisher: PHYSICAL SOC JAPAN

Publisher Address: YUSHIMA URBAN BUILDING 5F, 2-31-22 YUSHIMA, BUNKYO-KU, TOKYO, 113-0034, JAPAN

Web of Science Index: Science Citation Index Expanded (SCI-EXPANDED)

Web of Science Categories: Physics, Multidisciplinary

Research Areas: Physics

IDS Number: NJ2YH

ISSN: 0031-9015

29-char Source Abbrev.: J PHYS SOC JPN

ISO Source Abbrev.: J. Phys. Soc. Jpn.

Source Item Page Count: 5

Funding:

Funding Agency	Grant Number
US DOE, Office of Science, Office of Basic Energy Sciences	DE-SC0012704
US NSF	DMR-1610633
Reimei Project of the Japan Atomic Energy Agency	
Swiss National Science Foundation (SNF)	PZ00P2-174015
Swiss National Science Foundation	PZ00P2-174015

A portion of this research used resources at the Spallation Neutron Source, a DOE Office of Science User Facility operated by the Oak Ridge National Laboratory. Work at Brookhaven National Laboratory was supported by US DOE, Office of Science, Office of Basic Energy Sciences under contract DE-SC0012704. Research at Columbia was supported by US NSF DMR-1610633 and the Reimei Project of the Japan Atomic Energy Agency. Z. Guguchia gratefully acknowledges the financial support by the Swiss National Science Foundation (SNF fellowship P300P2-177832). The work at the University of Zurich was supported by the Swiss National Science Foundation under Grant No. PZ00P2-174015. M.Z.H. acknowledges visiting scientist support from IQIM at the California Institute of Technology.

Open Access: Green Accepted, Green Submitted

Output Date: 2023-01-27

Record 19 of 125

Title: Three-dimensional Ising ferrimagnetism of Cr-Fe-Cr trimers in FeCr₂Te₄

Author(s): Liu, Y (Liu, Yu); Koch, RJ (Koch, R. J.); Hu, ZX (Hu, Zhixiang); Aryal, N (Aryal, Niraj); Stavitski, E (Stavitski, Eli); Tong, X (Tong, Xiao); Attenkofer, K (Attenkofer, Klaus); Bozin, ES (Bozin, E. S.); Yin, WG (Yin, Weiguo); Petrovic, C (Petrovic, C.)

Source: PHYSICAL REVIEW B **Volume:** 102 **Issue:** 8 **Article Number:** 085158 **DOI:** 10.1103/PhysRevB.102.085158 **Published:** AUG 31 2020

Times Cited in Web of Science Core Collection: 9

Total Times Cited: 9

Usage Count (Last 180 days): 4

Usage Count (Since 2013): 45

Cited Reference Count: 45

Abstract: We carried out a comprehensive study of magnetic critical behavior in single crystals of ternary chalcogenide FeCr₂Te₄ that undergoes a ferrimagnetic transition below T_c similar to 123 K. Detailed critical behavior analysis and scaled magnetic entropy change indicate a second-order ferrimagnetic transition. Critical exponents $\beta = 0.30(1)$ with T_c = 122.4(5) K, $\gamma = 1.22(1)$ with T_c = 122.8(1)K, and $\delta = 4.24(2)$ at T_c similar to 123 K suggest that the spins approach the three-dimensional Ising ($\beta = 0.325$, $\gamma = 1.24$, and $\delta = 4.82$) model coupled with attractive longrange interactions between spins that decay as J(r) approximate to r⁽⁻⁴⁾(88). Our results suggest that the ferrimagnetism in FeCr₂Te₄ is due to itinerant ferromagnetism among the antiferromagnetically coupled Cr-Fe-Cr trimers.

Accession Number: WOS:000564044900006

Language: English

Document Type: Article

KeyWords Plus: COLOSSAL MAGNETORESISTANCE; MAGNETIC-PROPERTIES; CRYSTALLINE; FERROMAGNETISM; MOSSBAUER; TRANSPORT; PRESSURE

Addresses: [Liu, Yu; Koch, R. J.; Hu, Zhixiang; Aryal, Niraj; Bozin, E. S.; Yin, Weiguo; Petrovic, C.] Brookhaven Natl Lab, Condensed Matter Phys & Mat Sci Dept, Upton, NY 11973 USA.

[Hu, Zhixiang; Petrovic, C.] SUNY Stony Brook, Dept Mat Sci & Chem Engr, Stony Brook, NY 11790 USA.
[Stavitski, Eli; Attenkofer, Klaus] Brookhaven Natl Lab, Natl Synchrotron Light Source II, Upton, NY 11973 USA.

[Tong, Xiao] Brookhaven Natl Lab, Ctr Funct Nanomat, Upton, NY 11973 USA.

Corresponding Address: Liu, Y (corresponding author), Brookhaven Natl Lab, Condensed Matter Phys & Mat Sci Dept, Upton, NY 11973 USA.

Affiliations: United States Department of Energy (DOE); Brookhaven National Laboratory; State University of New York (SUNY) System; State University of New York (SUNY) Stony Brook; United States Department of Energy (DOE); Brookhaven National Laboratory; United States Department of Energy (DOE); Brookhaven National Laboratory

Author Identifiers:

Author	Web of Science ResearcherID	ORCID Number
Liu, Yu	ABD-2488-2021	0000-0001-8886-2876
Attenkofer, Klaus	AAR-8772-2021	
Bozin, Emil	AAB-4551-2020	
Yin, Weiguo	A-9671-2014	0000-0002-4965-5329
Bozin, Emil		0000-0002-6682-0365
Attenkofer, Klaus		0000-0003-1588-3611
Aryal, Niraj		0000-0002-0968-6809

Publisher: AMER PHYSICAL SOC

Publisher Address: ONE PHYSICS ELLIPSE, COLLEGE PK, MD 20740-3844 USA

Web of Science Index: Science Citation Index Expanded (SCI-EXPANDED)

Web of Science Categories: Materials Science, Multidisciplinary; Physics, Applied; Physics, Condensed Matter

Research Areas: Materials Science; Physics

IDS Number: NG5TB

ISSN: 2469-9950

eISSN: 2469-9969

29-char Source Abbrev.: PHYS REV B

ISO Source Abbrev.: Phys. Rev. B

Source Item Page Count: 7

Funding:

Funding Agency	Grant Number
Office of Basic Energy Sciences, Materials Sciences and Engineering Division, U.S. Department of Energy (DOE)	DE-SC0012704
DOE Office of Science	DE-SC0012704
U.S. DOE Office of Science Facility, at BNL	DE-SC0012704

Work at Brookhaven National Laboratory (BNL) is supported by the Office of Basic Energy Sciences, Materials Sciences and Engineering Division, U.S. Department of Energy (DOE) under Contract No. DE-SC0012704. This research used the 28-ID-1 and 8-ID beamlines of the NSLS II, a U.S. DOE Office of Science User Facility operated for the DOE Office of Science by BNL under Contract No. DE-SC0012704. This research used resources of the Center for Functional Nanomaterials (CFN), which is a U.S. DOE Office of Science Facility, at BNL under Contract No. DE-SC0012704.

Open Access: Green Submitted

Output Date: 2023-01-27

Record 20 of 125

Title: Nanoscale degeneracy lifting in a geometrically frustrated antiferromagnet

Author(s): Frandsen, BA (Frandsen, Benjamin A.); Bozin, ES (Bozin, Emil S.); Aza, E (Aza, Eleni); Martinez, AF (Martinez, Antonio Fernandez); Feygenson, M (Feygenson, Mikhail); Page, K (Page, Katharine); Lappas, A (Lappas, Alexandros)

Source: PHYSICAL REVIEW B **Volume:** 101 **Issue:** 2 **Article Number:** 024423 **DOI:** 10.1103/PhysRevB.101.024423 **Published:** JAN 27 2020

Times Cited in Web of Science Core Collection: 8

Total Times Cited: 8

Usage Count (Last 180 days): 3

Usage Count (Since 2013): 25

Cited Reference Count: 52

Abstract: The local atomic and magnetic structures of the compounds $AMnO_2$ ($A = Na, Cu$), which realize a geometrically frustrated, spatially anisotropic triangular lattice of Mn spins, have been investigated by atomic and magnetic pair distribution function analysis of neutron total scattering data. Relief of frustration in $CuMnO_2$ is accompanied by a conventional cooperative symmetry-lowering lattice distortion driven by Neel order. In $NaMnO_2$, however, the distortion has a short-range nature. A cooperative interaction between the locally broken symmetry and short-range magnetic correlations lifts the magnetic degeneracy on a nanometer length scale, enabling long-range magnetic order in the Na derivative. The degree of frustration, mediated by residual disorder, contributes to the rather differing pathways to a single, stable magnetic ground state in these two related compounds. This study demonstrates how nanoscale structural distortions that cause local-scale perturbations can lift the ground-state degeneracy and trigger macroscopic magnetic order.

Accession Number: WOS:000509474900004

Language: English

Document Type: Article

KeyWords Plus: MATERIALS DIFFRACTOMETER; OXIDES; CREDNERITE

Addresses: [Frandsen, Benjamin A.] Brigham Young Univ, Dept Phys & Astron, Provo, UT 84602 USA.
[Bozin, Emil S.] Brookhaven Natl Lab, Condensed Matter Phys & Mat Sci Div, Upton, NY 11973 USA.
[Aza, Eleni; Martinez, Antonio Fernandez; Lappas, Alexandros] Fdn Res & Technol Hellas, Inst Elect Struct & Laser, Iraklion 71110, Greece.

[Aza, Eleni] Univ Ioannina, Dept Mat Sci & Engn, GR-45110 Ioannina, Greece.

[Feygenson, Mikhail; Page, Katharine] Oak Ridge Natl Lab, Neutron Scattering Div, Oak Ridge, TN 37831

USA.

[Feygenson, Mikhail] Forschungszentrum Julich, Julich Ctr Neutron Sci, D-52428 Julich, Germany.

[Page, Katharine] Univ Tennessee, Dept Mat Sci & Engr, Knoxville, TN 37996 USA.

Corresponding Address: Frandsen, BA (corresponding author), Brigham Young Univ, Dept Phys & Astron, Provo, UT 84602 USA.

E-mail Addresses: benfrandsen@byu.edu; bozin@bnl.gov; lappas@iesl.forth.gr

Affiliations: Brigham Young University; United States Department of Energy (DOE); Brookhaven National Laboratory; Foundation for Research & Technology - Hellas (FORTH); University of Ioannina; United States Department of Energy (DOE); Oak Ridge National Laboratory; Helmholtz Association; Research Center Julich; University of Tennessee System; University of Tennessee Knoxville

Author Identifiers:

Author	Web of Science ResearcherID	ORCID Number
Page, Katharine	AAO-6168-2020	0000-0002-9071-3383
Lappas, Alexandros	F-6771-2011	0000-0001-8486-0312
Bozin, Emil	AAB-4551-2020	
Page, Katharine	C-9726-2009	0000-0002-9071-3383
Lappas, Alexandros	AFO-0640-2022	0000-0001-8486-0312
Frandsen, Benjamin	AAJ-1680-2020	0000-0002-4047-9453
Bozin, Emil		0000-0002-6682-0365
Feygenson, Mikhail	H-9972-2014	0000-0002-0316-3265

Publisher: AMER PHYSICAL SOC

Publisher Address: ONE PHYSICS ELLIPSE, COLLEGE PK, MD 20740-3844 USA

Web of Science Index: Science Citation Index Expanded (SCI-EXPANDED)

Web of Science Categories: Materials Science, Multidisciplinary; Physics, Applied; Physics, Condensed Matter

Research Areas: Materials Science; Physics

IDS Number: KF8GI

ISSN: 2469-9950

eISSN: 2469-9969

29-char Source Abbrev.: PHYS REV B

ISO Source Abbrev.: Phys. Rev. B

Source Item Page Count: 9

Funding:

Funding Agency	Grant Number
Brigham Young University	
U.S. DOE, Office of Science, Office of Basic Energy Sciences (DOE-BES)	DE-SC0012704
Integrated Infrastructure Initiative ESTEEM2 (EU Seventh Framework Programme)	312483
U.S. DOE	DE-FG02-13ER41967
U.S. Department of Energy (DOE)	DE-AC05-00OR22725

This research used resources at the Spallation Neutron Source, a DOE Office of Science User Facility operated by the Oak Ridge National Laboratory. B.A.F. acknowledges support from Brigham Young University. Work at Brookhaven National Laboratory was supported by U.S. DOE, Office of Science, Office of Basic Energy Sciences (DOE-BES) under Contract No. DE-SC0012704. We thank the Science and Technology Facilities Council (STFC) for the provision of neutron beam time at the ISIS Facility. We acknowledge Dr. J. Neuefeind for assistance with the measurements at the NOMAD beamline and Dr. D. Keen for assistance on the GEM beamline. Access to the facilities of the Integrated Infrastructure Initiative ESTEEM2 (EU Seventh Framework

Programme with Reference No. 312483) is gratefully acknowledged. We are indebted to Prof. A. M. Abakumov for the TEM-based characterizations at EMAT. A.L. thanks the Fulbright Foundation-Greece. This work has been partially supported by U.S. DOE Grant No. DE-FG02-13ER41967. ORNL is managed by UT-Battelle, LLC, under Contract No. DE-AC05-00OR22725 for the U.S. Department of Energy (DOE). The U.S. government retains and the publisher, by accepting the article for publication, acknowledges that the U.S. government retains a nonexclusive, paid-up, irrevocable, worldwide license to publish or reproduce the published form of this manuscript, or allow others to do so for U.S. government purposes.

Open Access: Green Submitted

Output Date: 2023-01-27

Record 21 of 125

Title: Ultrafast x-ray diffraction study of melt-front dynamics in polycrystalline thin films

Author(s): Assefa, TA (Assefa, Tadesse A.); Cao, Y (Cao, Yue); Banerjee, S (Banerjee, Soham); Kim, S (Kim, Sungwon); Kim, D (Kim, Dongjin); Lee, H (Lee, Heemin); Kim, S (Kim, Sunam); Lee, JH (Lee, Jae Hyuk); Park, SY (Park, Sang-Youn); Eom, I (Eom, Intae); Park, J (Park, Jaeku); Nam, D (Nam, Daewoog); Kim, S (Kim, Sangsoo); Chun, SH (Chun, Sae Hwan); Hyun, H (Hyun, Hyojung); Kim, KS (Kim, Kyung Sook); Juhas, P (Juhas, Pavol); Bozin, ES (Bozin, Emil S.); Lu, M (Lu, Ming); Song, CY (Song, Changyong); Kim, H (Kim, Hyunjung); Billinge, SJL (Billinge, Simon J. L.); Robinson, IK (Robinson, Ian K.)

Source: SCIENCE ADVANCES **Volume:** 6 **Issue:** 3 **Article Number:** eaax2445 **DOI:** 10.1126/sciadv.aax2445 **Published:** JAN 2020

Times Cited in Web of Science Core Collection: 10

Total Times Cited: 10

Usage Count (Last 180 days): 4

Usage Count (Since 2013): 18

Cited Reference Count: 40

Abstract: Melting is a fundamental process of matter that is still not fully understood at the microscopic level. Here, we use time-resolved x-ray diffraction to examine the ultrafast melting of polycrystalline gold thin films using an optical laser pump followed by a delayed hard x-ray probe pulse. We observe the formation of an intermediate new diffraction peak, which we attribute to material trapped between the solid and melted states, that forms 50 ps after laser excitation and persists beyond 500 ps. The peak width grows rapidly for 50 ps and then narrows distinctly at longer time scales. We attribute this to a melting band originating from the grain boundaries and propagating into the grains. Our observation of this intermediate state has implications for the use of ultrafast lasers for ablation during pulsed laser deposition.

Accession Number: WOS:000510488100004

PubMed ID: 32010766

Language: English

Document Type: Article

KeyWords Plus: LATTICE-DYNAMICS; GOLD; RESISTIVITY; DEPENDENCE; ALUMINUM; METALS; NICKEL; MODEL

Addresses: [Assefa, Tadesse A.; Cao, Yue; Banerjee, Soham; Bozin, Emil S.; Billinge, Simon J. L.; Robinson, Ian K.] Brookhaven Natl Lab, Condensed Matter Phys & Mat Sci Dept, Upton, NY 11793 USA.

[Banerjee, Soham; Billinge, Simon J. L.] Columbia Univ, Dept Appl Phys & Appl Math, New York, NY 10027 USA.

[Kim, Sungwon; Kim, Dongjin; Kim, Hyunjung] Sogang Univ, Dept Phys, Seoul 04107, South Korea.

[Lee, Heemin; Song, Changyong] Pohang Univ Sci & Technol, Dept Phys, Pohang 37673, South Korea.

[Lee, Heemin; Song, Changyong] Pohang Univ Sci & Technol, POSTECH Photon Sci Ctr, Pohang 37673, South Korea.

[Kim, Sunam; Lee, Jae Hyuk; Park, Sang-Youn; Eom, Intae; Park, Jaeku; Nam, Daewoog; Kim, Sangsoo; Chun, Sae Hwan; Hyun, Hyojung; Kim, Kyung Sook] Pohang Accelerator Lab, Pohang 37673, Gyeongbuk, South Korea.

[Juhas, Pavol] Brookhaven Natl Lab, Computat Sci Initiat, Upton, NY 11793 USA.

[Lu, Ming] Brookhaven Natl Lab, Ctr Funct Nanomat, Upton, NY 11793 USA.

[Robinson, Ian K.] UCL, London Ctr Nanotechnol, London WC1 6BT, England.

[Cao, Yue] Argonne Natl Lab, Mat Sci Div, Argonne, IL 60439 USA.

Corresponding Address: Assefa, TA; Robinson, IK (corresponding author), Brookhaven Natl Lab, Condensed Matter Phys & Mat Sci Dept, Upton, NY 11793 USA.

Robinson, IK (corresponding author), UCL, London Ctr Nanotechnol, London WC1 6BT, England.

E-mail Addresses: tassefa@bnl.gov; irobinson@bnl.gov

Affiliations: United States Department of Energy (DOE); Brookhaven National Laboratory; Columbia University; Sogang University; Pohang University of Science & Technology (POSTECH); Pohang University of Science & Technology (POSTECH); Pohang University of Science & Technology (POSTECH); United States Department of Energy (DOE); Brookhaven National Laboratory; United States Department of Energy (DOE); Brookhaven National Laboratory; University of London; University College London; United States Department of Energy (DOE); Argonne National Laboratory

Author Identifiers:

Author	Web of Science ResearcherID	ORCID Number
Assefa, Tadesse	ABD-2999-2021	0000-0003-3904-0846
Bozin, Emil	AAB-4551-2020	
Kim, Hyunjung	AAI-7752-2020	0000-0001-6211-4888
Banerjee, Soham		0000-0001-9271-493X
Chun, Sae Hwan		0000-0001-8222-4849
Cao, Yue		0000-0002-3989-158X
Lee, Heemin		0000-0002-8727-210X
Robinson, Ian	A-4906-2010	0000-0003-4897-5221
Eom, Intae		0000-0002-3390-4052

Publisher: AMER ASSOC ADVANCEMENT SCIENCE

Publisher Address: 1200 NEW YORK AVE, NW, WASHINGTON, DC 20005 USA

Web of Science Index: Science Citation Index Expanded (SCI-EXPANDED)

Web of Science Categories: Multidisciplinary Sciences

Research Areas: Science & Technology - Other Topics

IDS Number: KH2OV

ISSN: 2375-2548

29-char Source Abbrev.: SCI ADV

ISO Source Abbrev.: Sci. Adv.

Source Item Page Count: 9

Funding:

Funding Agency	Grant Number
U.S. Department of Energy (DOE), Office of Basic Energy Sciences, Division of Materials Sciences and Engineering	DE-SC0012704
U.S. DOE Office of Science Facility, at BNL	DE-SC0012704
EPSRC	EP/I022562/1
National Research Foundation of Korea	NRF- 2014R1A2A1A10052454 2015R1A5A1009962 2016R1A6B2A02005468
Ministry of Science and ICT of Korea	2017-1st-FXS-007

The work at BNL was supported by the U.S. Department of Energy (DOE), Office of Basic Energy Sciences, Division of Materials Sciences and Engineering, under contract no. DE-SC0012704. The sample preparation used the resources of the Center for Functional Nanomaterials, which is a U.S. DOE Office of Science Facility, at BNL under contract no. DE-SC0012704. I.K.R. received support from EPSRC grant EP/I022562/1. S.K., D.K., and H.K. acknowledge the support from the National Research Foundation of Korea (NRF-2014R1A2A1A10052454, 2015R1A5A1009962, and 2016R1A6B2A02005468). C.S. is supported by NRF-2016R1A2B3010980. The experiments were carried out at the XSS end-station of the PAL-XFEL (proposal no. 2017-1st-FXS-007) funded by the Ministry of Science and ICT of Korea.

Open Access: Green Published, Green Submitted

Output Date: 2023-01-27

Record 22 of 125

Title: Quantum Liquid with Strong Orbital Fluctuations: The Case of a Pyroxene Family

Author(s): Feiguin, AE (Feiguin, A. E.); Tselik, AM (Tselik, A. M.); Yin, WG (Yin, Weiguo); Bozin, ES (Bozin, E. S.)

Source: PHYSICAL REVIEW LETTERS **Volume:** 123 **Issue:** 23 **Article Number:** 237204 **DOI:** 10.1103/PhysRevLett.123.237204 **Published:** DEC 3 2019

Times Cited in Web of Science Core Collection: 6

Total Times Cited: 6

Usage Count (Last 180 days): 2

Usage Count (Since 2013): 12

Cited Reference Count: 23

Abstract: We discuss quasi-one-dimensional magnetic Mott insulators from the pyroxene family where spin and orbital degrees of freedom remain tightly bound. We analyze their excitation spectrum and outline the conditions under which the orbital degrees of freedom become liberated so that the corresponding excitations become dispersive and the spectral weight shifts to energies much smaller than the exchange integral.

Accession Number: WOS:000500732100019

PubMed ID: 31868490

Language: English

Document Type: Article

Addresses: [Feiguin, A. E.] Northwestern Univ, Dept Phys, Boston, MA 02115 USA.

[Tselik, A. M.; Yin, Weiguo; Bozin, E. S.] Brookhaven Natl Lab, Condensed Matter Phys & Mat Sci Div, Upton, NY 11973 USA.

Corresponding Address: Feiguin, AE (corresponding author), Northwestern Univ, Dept Phys, Boston, MA 02115 USA.

Affiliations: Northwestern University; United States Department of Energy (DOE); Brookhaven National Laboratory

Author Identifiers:

Author	Web of Science ResearcherID	ORCID Number
Bozin, Emil	AAB-4551-2020	
Tselik, Alexei	HJZ-5160-2023	0000-0002-7478-670X
Yin, Weiguo	A-9671-2014	0000-0002-4965-5329
Bozin, Emil		0000-0002-6682-0365

Publisher: AMER PHYSICAL SOC

Publisher Address: ONE PHYSICS ELLIPSE, COLLEGE PK, MD 20740-3844 USA

Web of Science Index: Science Citation Index Expanded (SCI-EXPANDED)

Web of Science Categories: Physics, Multidisciplinary

Research Areas: Physics

IDS Number: JT1AY

ISSN: 0031-9007

eISSN: 1079-7114

29-char Source Abbrev.: PHYS REV LETT

ISO Source Abbrev.: Phys. Rev. Lett.

Source Item Page Count: 5

Funding:

Funding Agency	Grant Number
Office of Basic Energy Sciences, Material Sciences and Engineering Division, U.S. Department of Energy (DOE)	DE-SC0012704 DE-SC0014407

This work was supported by the Office of Basic Energy Sciences, Material Sciences and Engineering Division, U.S. Department of Energy (DOE) under Contracts No. DE-SC0012704 (A. M. T., W. Y., and E. S. B.) and No. DE-SC0014407 (A. E. F.).

Open Access: Green Submitted

Output Date: 2023-01-27

Record 23 of 125

Title: Vacancy-Driven Noncubic Local Structure and Magnetic Anisotropy Tailoring in $\text{Fe}_x\text{O}-\text{Fe}_3\text{-}\delta\text{O}_4$ Nanocrystals

Author(s): Lappas, A (Lappas, Alexandros); Antonaropoulos, G (Antonaropoulos, George); Brintakis, K (Brintakis, Konstantinos); Vasilakaki, M (Vasilakaki, Marianna); Trohidou, KN (Trohidou, Kalliopi N.); Iannotti, V (Iannotti, Vincenzo); Ausanio, G (Ausanio, Giovanni); Kostopoulou, A (Kostopoulou, Athanasia); Abeykoon, M (Abeykoon, Milinda); Robinson, IK (Robinson, Ian K.); Bozin, ES (Bozin, Emil S.)

Source: PHYSICAL REVIEW X **Volume:** 9 **Issue:** 4 **Article Number:** 041044 **DOI:** 10.1103/PhysRevX.9.041044 **Published:** NOV 27 2019

Times Cited in Web of Science Core Collection: 21

Total Times Cited: 21

Usage Count (Last 180 days): 3

Usage Count (Since 2013): 15

Cited Reference Count: 76

Abstract: In contrast to bulk materials, nanoscale crystal growth is critically influenced by size- and shape-dependent properties. However, it is challenging to decipher how stoichiometry, in the realm of mixed-valence elements, can act to control physical properties, especially when complex bonding is implicated by short- and long-range ordering of structural defects. Here, solution-grown iron-oxide nanocrystals (NCs) of the pilot wustite system are found to convert into iron-deficient rock-salt and ferro-spinel subdomains but attain a surprising tetragonally distorted local structure. Cationic vacancies within chemically uniform NCs are portrayed as the parameter to tweak the underlying properties. These lattice imperfections are shown to produce local exchange-anisotropy fields that reinforce the nanoparticles' magnetization and overcome the influence of (mite-size effects. The concept of atomic-scale defect control in subcritical-size NCs aspires to become a pathway to tailor-made properties with improved performance for hyperthermia heating over defect-free NCs.

Accession Number: WOS:000498886600001

Language: English

Document Type: Article

KeyWords Plus: FERRITE NANOPARTICLES; SHELL NANOPARTICLES; IRON-OXIDES; SIZE; WUSTITE; SHAPE; HYPERTHERMIA; SURFACE; FE₃O₄; RESONANCE

Addresses: [Lappas, Alexandros; Antonaropoulos, George; Brintakis, Konstantinos; Kostopoulou, Athanasia] Fdn Res & Technol Hellas, Inst Elect Struct & Laser, Iraklion 71110, Greece.

[Antonaropoulos, George] Univ Crete, Dept Chem, Iraklion 71003, Greece.

[Vasilakaki, Marianna; Trohidou, Kalliopi N.] Natl Ctr Sci Res Demokritos, Inst Nanosci & Nanotechnol, Athens 15310, Greece.

[Iannotti, Vincenzo; Ausanio, Giovanni] CNR, SPIN, Piazzale V Tecchio 80, I-80125 Naples, Italy.

[Iannotti, Vincenzo; Ausanio, Giovanni] Univ Naples Federico II, Dept Phys E Pancini, Piazzale V Tecchio 80, I-80125 Naples, Italy.

[Abeykoon, Milinda] Brookhaven Natl Lab, Photon Sci Div, Natl Synchrotron Light Source 2, Upton, NY 11973 USA.

[Robinson, Ian K.; Bozin, Emil S.] Brookhaven Natl Lab, Condensed Matter Phys & Mat Sci Dept, Upton, NY 11973 USA.

[Robinson, Ian K.] UCL, London Ctr Nanotechnol, London WC1E 6BT, England.

Corresponding Address: Lappas, A (corresponding author), Fdn Res & Technol Hellas, Inst Elect Struct & Laser, Iraklion 71110, Greece.

E-mail Addresses: lappas@iesl.forth.gr

Affiliations: Foundation for Research & Technology - Hellas (FORTH); University of Crete; National Centre of Scientific Research "Demokritos"; Consiglio Nazionale delle Ricerche (CNR); University of Naples Federico II; United States Department of Energy (DOE); Brookhaven National Laboratory; United States Department of Energy (DOE); Brookhaven National Laboratory; University of London; University College London

Author Identifiers:

Author	Web of Science ResearcherID	ORCID Number
Bozin, Emil	AAB-4551-2020	
Vasilakaki, Marianna	R-5308-2016	0000-0003-1832-7549
Vasilakaki, Marianna	AAL-3729-2021	0000-0003-1832-7549
Kostopoulou, Athanasia	T-5257-2017	
Antonaropoulos, George	AAV-8202-2021	0000-0003-0214-8327
Lappas, Alexandros	F-6771-2011	0000-0001-8486-0312
Antonaropoulos, George	AFL-1000-2022	
Lappas, Alexandros	AFO-0640-2022	0000-0001-8486-0312
Trohidou, Kalliopi		0000-0002-6921-5419
AUSANIO, Giovanni		0000-0003-3126-8504
Robinson, Ian	A-4906-2010	0000-0003-4897-5221

Publisher: AMER PHYSICAL SOC

Publisher Address: ONE PHYSICS ELLIPSE, COLLEGE PK, MD 20740-3844 USA

Web of Science Index: Science Citation Index Expanded (SCI-EXPANDED)

Web of Science Categories: Physics, Multidisciplinary

Research Areas: Physics

IDS Number: JQ3ZH

ISSN: 2160-3308

29-char Source Abbrev.: PHYS REV X

ISO Source Abbrev.: Phys. Rev. X

Source Item Page Count: 17

Funding:

Funding Agency	Grant Number
----------------	--------------

DOE Office of Basic Energy Sciences	
DOE Office of Science	DE-SC0012704
project "National Research Infrastructure on Nanotechnology, Advanced Materials and Micro/Nanoelectronics" - Operational Programme "Competitiveness, Entrepreneurship and Innovation" (National Strategic Reference Framework, GR/Hellenic Republic-NSRF 2014-20)	MIS 5002772
European Union (European Regional Development Fund)	
Fulbright Foundation-Greece	
EPSRC	EP/I022562/1

This research used the beamline 28-ID-2 of the National Synchrotron Light Source II, a U.S. Department of Energy (DOE) User Facility operated by Brookhaven National Laboratory (BNL). Work in the Condensed Matter Physics and Materials Science Department at BNL was supported by the DOE Office of Basic Energy Sciences. Both activities were supported by the DOE Office of Science under Contract No. DE-SC0012704. We acknowledge partial support of this work by the project "National Research Infrastructure on Nanotechnology, Advanced Materials and Micro/Nanoelectronics" (MIS 5002772), which is implemented under the "Action for the Strategic Development on the Research and Technological Sector," funded by the Operational Programme "Competitiveness, Entrepreneurship and Innovation" (National Strategic Reference Framework, GR/Hellenic Republic-NSRF 2014-2020) and co-financed by Greece and the European Union (European Regional Development Fund). A. L. thanks the Fulbright Foundation-Greece for support to conduct research at the Brookhaven National Laboratory, USA.

Open Access: Green Submitted, gold

Output Date: 2023-01-27

Record 24 of 125

Title: Entropic elasticity and negative thermal expansion in a simple cubic crystal

Author(s): Wendt, D (Wendt, David); Bozin, E (Bozin, Emil); Neuefeind, J (Neuefeind, Joerg); Page, K (Page, Katharine); Ku, W (Ku, Wei); Wang, LM (Wang, Limin); Fultz, B (Fultz, Brent); Tkachenko, AV (Tkachenko, Alexei V.); Zaliznyak, IA (Zaliznyak, Igor A.)

Source: SCIENCE ADVANCES **Volume:** 5 **Issue:** 11 **Article Number:** eaay2748 **DOI:** 10.1126/sciadv.aay2748 **Published:** NOV 2019

Times Cited in Web of Science Core Collection: 17

Total Times Cited: 18

Usage Count (Last 180 days): 6

Usage Count (Since 2013): 35

Cited Reference Count: 55

Abstract: While most solids expand when heated, some materials show the opposite behavior: negative thermal expansion (NTE). In polymers and biomolecules, NTE originates from the entropic elasticity of an ideal, freely jointed chain. The origin of NTE in solids has been widely believed to be different. Our neutron scattering study of a simple cubic NTE material, ScF₃, overturns this consensus. We observe that the correlation in the positions of the neighboring fluorine atoms rapidly fades on warming, indicating an uncorrelated thermal motion constrained by the rigid Sc-F bonds. This leads us to a quantitative theory of NTE in terms of entropic elasticity of a floppy network crystal, which is in remarkable agreement with experimental results. We thus reveal the formidable universality of the NTE phenomenon in soft and hard matter.

Accession Number: WOS:000499736100094

PubMed ID: 31701009

Language: English

Document Type: Article

KeyWords Plus: MADELUNG CONSTANTS; PHASE-TRANSITION; ENERGIES; DYNAMICS; SCF3

Addresses: [Wendt, David; Bozin, Emil; Ku, Wei; Wang, Limin; Zaliznyak, Igor A.] Brookhaven Natl Lab, Condensed Matter Phys & Mat Sci Div, Upton, NY 11973 USA.

[Neuefeind, Joerg; Page, Katharine] Oak Ridge Natl Lab, Neutron Scattering Div, Oak Ridge, TN 37831 USA.

[Fultz, Brent] CALTECH, Dept Appl Phys & Mat Sci, Pasadena, CA 91125 USA.

[Tkachenko, Alexei V.] Brookhaven Natl Lab, CFN, Upton, NY 11973 USA.

[Wendt, David] Stanford Univ, Stanford, CA 94305 USA.

[Ku, Wei] Shanghai Jiao Tong Univ, Tsung Dao Lee Inst, Shanghai 200240, Peoples R China.

[Ku, Wei] Shanghai Jiao Tong Univ, Sch Phys & Astron, Shanghai 200240, Peoples R China.

[Wang, Limin] GE Healthcare, Chicago, IL USA.

Corresponding Address: Zaliznyak, IA (corresponding author), Brookhaven Natl Lab, Condensed Matter Phys & Mat Sci Div, Upton, NY 11973 USA.

E-mail Addresses: zaliznyak@bnl.gov

Affiliations: United States Department of Energy (DOE); Brookhaven National Laboratory; United States Department of Energy (DOE); Oak Ridge National Laboratory; California Institute of Technology; United States Department of Energy (DOE); Brookhaven National Laboratory; Stanford University; Shanghai Jiao Tong University; Shanghai Jiao Tong University; General Electric

Author Identifiers:

Author	Web of Science ResearcherID	ORCID Number
Page, Katharine	C-9726-2009	0000-0002-9071-3383
Page, Katharine	AAO-6168-2020	0000-0002-9071-3383
Zaliznyak, Igor	AAW-2535-2020	0000-0002-8548-7924
Zaliznyak, Igor	E-8532-2014	0000-0002-8548-7924
Bozin, Emil	AAB-4551-2020	
Bozin, Emil		0000-0002-6682-0365
Tkachenko, Alexei	I-9040-2012	0000-0003-1291-243X
Wendt, David		0000-0003-4963-164X

Publisher: AMER ASSOC ADVANCEMENT SCIENCE

Publisher Address: 1200 NEW YORK AVE, NW, WASHINGTON, DC 20005 USA

Web of Science Index: Science Citation Index Expanded (SCI-EXPANDED)

Web of Science Categories: Multidisciplinary Sciences

Research Areas: Science & Technology - Other Topics

IDS Number: JR6MC

ISSN: 2375-2548

29-char Source Abbrev.: SCI ADV

ISO Source Abbrev.: Sci. Adv.

Source Item Page Count: 7

Funding:

Funding Agency	Grant Number
Office of Basic Energy Sciences, Division of Materials Sciences and Engineering, U.S. Department of Energy	DE-SC0012704
Scientific User Facilities Division, Office of Basic Energy Sciences, U.S. Department of Energy	

Work at Brookhaven National Laboratory (BNL) was supported by the Office of Basic Energy Sciences, Division of Materials Sciences and Engineering, U.S. Department of Energy, under contract no. DE-SC0012704. Work at BNL's Center for Functional Nanomaterials (CFN) is sponsored by the Scientific User

Facilities Division, Office of Basic Energy Sciences, U.S. Department of Energy, under the same contract. This research at ORNL's Spallation Neutron Source was sponsored by the Scientific User Facilities Division, Office of Basic Energy Sciences, U.S. Department of Energy.

Open Access: Green Published, gold, Green Submitted, Green Accepted

Output Date: 2023-01-27

Record 25 of 125

Title: Correlated disorder-to-order crossover in the local structure of $K_xFe_2-ySe_2-zSz$

Author(s): Mangelis, P (Mangelis, P.); Koch, RJ (Koch, R. J.); Lei, H (Lei, H.); Neder, RB (Neder, R. B.); McDonnell, MT (McDonnell, M. T.); Feygenson, M (Feygenson, M.); Petrovic, C (Petrovic, C.); Lappas, A (Lappas, A.); Bozin, ES (Bozin, E. S.)

Source: PHYSICAL REVIEW B **Volume:** 100 **Issue:** 9 **Article Number:** 094108 **DOI:** 10.1103/PhysRevB.100.094108 **Published:** SEP 16 2019

Times Cited in Web of Science Core Collection: 4

Total Times Cited: 4

Usage Count (Last 180 days): 0

Usage Count (Since 2013): 24

Cited Reference Count: 57

Abstract: A detailed account of the local atomic structure and disorder at 5 K across the phase diagram of the high-temperature superconductor $K_xFe_2-ySe_2-zSz$ ($0 \leq z \leq 2$) is obtained from neutron total scattering and associated atomic pair distribution function (PDF) approaches. Various model-independent and model-dependent aspects of the analysis reveal a high level of structural complexity on the nanometer length scale. Evidence is found for considerable disorder in the c-axis stacking of the $FeSe_{1-xS_x}$ slabs without observable signs of turbostratic character of the disorder. In contrast to the related $FeCh$ ($Ch = S, Se$)-type superconductors, substantial Fe-vacancies are present in $K_xFe_2-ySe_2-zSz$, deemed detrimental for superconductivity when ordered. Our study suggests that the distribution of vacancies significantly modifies the iron-chalcogen bond-length distribution, in agreement with observed evolution of the PDF signal. A crossoverlike transition is observed at a composition of z approximate to 1, from a correlated disorder state at the selenium end to a more vacancy-ordered (VO) state closer to the sulfur end of the phase diagram. The S-content-dependent measures of the local structure are found to exhibit distinct behavior on either side of this crossover, correlating well with the evolution of the superconducting state to that of a magnetic semiconductor toward the z approximate to 2 end. The behavior reinforces the idea of the intimate relationship of correlated Fe-vacancy order in the local structure and the emergent electronic properties.

Accession Number: WOS:000486625900002

Language: English

Document Type: Article

KeyWords Plus: SHORT-RANGE ORDER; PHASE-SEPARATION; RAY; SUPERCONDUCTIVITY

Addresses: [Mangelis, P.; Lappas, A.] Fdn Res & Technol Hellas, Inst Elect Struct & Laser, Iraklion 71110, Greece.

[Koch, R. J.; Lei, H.; Petrovic, C.; Bozin, E. S.] Brookhaven Natl Lab, Condensed Matter Phys & Mat Sci Dept, Upton, NY 11973 USA.

[Neder, R. B.] Friedrich Alexander Univ Erlangen Nurnberg, Inst Condensed Matter Phys, Staudtstr 3, D-91058 Erlangen, Germany.

[McDonnell, M. T.; Feygenson, M.] Oak Ridge Natl Lab, Neutron Scattering Div, POB 2009, Oak Ridge, TN 37831 USA.

[Lei, H.] Renmin Univ China, Dept Phys, Beijing, Peoples R China.

[Lei, H.] Renmin Univ China, Beijing Key Lab Optoelect Funct Mat & Micronano D, Beijing, Peoples R China.

[McDonnell, M. T.] Oak Ridge Natl Lab, Comp Sci & Math Div, POB 2009, Oak Ridge, TN 37831 USA.

[Feygenson, M.] Forschungszentrum Julich, JCNS, D-52425 Julich, Germany.

Corresponding Address: Koch, RJ (corresponding author), Brookhaven Natl Lab, Condensed Matter Phys & Mat Sci Dept, Upton, NY 11973 USA.

E-mail Addresses: rkoch@bnl.gov; lappas@iesl.forth.gr

Affiliations: Foundation for Research & Technology - Hellas (FORTH); United States Department of Energy (DOE); Brookhaven National Laboratory; University of Erlangen Nuremberg; United States Department of Energy (DOE); Oak Ridge National Laboratory; Renmin University of China; Renmin University of China; United States Department of Energy (DOE); Oak Ridge National Laboratory; Helmholtz Association; Research Center Julich

Author Identifiers:

Author	Web of Science ResearcherID	ORCID Number
Lappas, Alexandros	AFO-0640-2022	0000-0001-8486-0312
Bozin, Emil	AAB-4551-2020	
McDonnell, Marshall	AAF-3842-2020	0000-0002-3713-2117
Lappas, Alexandros	F-6771-2011	0000-0001-8486-0312
Mangelis, Panagiotis		0000-0001-5948-1177
Feygenson, Mikhail	H-9972-2014	0000-0002-0316-3265

Publisher: AMER PHYSICAL SOC

Publisher Address: ONE PHYSICS ELLIPSE, COLLEGE PK, MD 20740-3844 USA

Web of Science Index: Science Citation Index Expanded (SCI-EXPANDED)

Web of Science Categories: Materials Science, Multidisciplinary; Physics, Applied; Physics, Condensed Matter

Research Areas: Materials Science; Physics

IDS Number: IY8EC

ISSN: 2469-9950

eISSN: 2469-9969

29-char Source Abbrev.: PHYS REV B

ISO Source Abbrev.: Phys. Rev. B

Source Item Page Count: 12

Funding:

Funding Agency	Grant Number
U.S. Department of Energy, Office of Science, Office of Basic Energy Sciences (DOE-BES)	DE-SC0012704
U.S. Office of Naval Research Global, NICOP Grant	N62909-17-1-2126
U.S. Department of Energy	DE-AC05-00OR22725

Work at Brookhaven National Laboratory was supported by the U.S. Department of Energy, Office of Science, Office of Basic Energy Sciences (DOE-BES) under Contract No. DE-SC0012704. Alexandros Lappas acknowledges support by the U.S. Office of Naval Research Global, NICOP Grant Award No. N62909-17-1-2126. This research used resources at the Spallation Neutron Source, a U.S. Department of Energy Office of Science User Facility operated by the Oak Ridge National Laboratory. This paper has been co-authored by UT-Battelle, LLC under Contract No. DE-AC05-00OR22725 with the U.S. Department of Energy. The United States Government retains and the publisher, by accepting the article for publication, acknowledges that the United States Government retains a nonexclusive, paid-up, irrevocable, worldwide license to publish or reproduce the published form of this paper, or allow others to do so, for United States Government purposes. The Department of Energy will provide public access to these results of federally sponsored research in accordance with the DOE Public Access Plan [57].

Open Access: Green Submitted, hybrid

Record 26 of 125

Title: Local orbital degeneracy lifting as a precursor to an orbital-selective Peierls transition

Author(s): Bozin, ES (Bozin, E. S.); Yin, WG (Yin, W. G.); Koch, RJ (Koch, R. J.); Abeykoon, M (Abeykoon, M.); Hor, YS (Hor, Y. S.); Zheng, H (Zheng, H.); Lei, HC (Lei, H. C.); Petrovic, C (Petrovic, C.); Mitchell, JF (Mitchell, J. F.); Billinge, SJL (Billinge, S. J. L.)

Source: NATURE COMMUNICATIONS **Volume:** 10 **Article Number:** 3638 **DOI:** 10.1038/s41467-019-11372-w **Published:** AUG 13 2019

Times Cited in Web of Science Core Collection: 31

Total Times Cited: 31

Usage Count (Last 180 days): 2

Usage Count (Since 2013): 21

Cited Reference Count: 66

Abstract: Fundamental electronic principles underlying all transition metal compounds are the symmetry and filling of the d-electron orbitals and the influence of this filling on structural configurations and responses. Here we use a sensitive local structural technique, x-ray atomic pair distribution function analysis, to reveal the presence of fluctuating local-structural distortions at high temperature in one such compound, CuIr_2S_4 . We show that this hitherto overlooked fluctuating symmetry-lowering is electronic in origin and will modify the energy-level spectrum and electronic and magnetic properties. The explanation is a local, fluctuating, orbital-degeneracy-lifted state. The natural extension of our result would be that this phenomenon is likely to be widespread amongst diverse classes of partially filled nominally degenerate d-electron systems, with potentially broad implications for our understanding of their properties.

Accession Number: WOS:000480519200001

PubMed ID: 31409783

Language: English

Document Type: Article

KeyWords Plus: METAL-INSULATOR-TRANSITION; NEMATICITY; SUPERCONDUCTIVITY; SYMMETRY; POLARONS; CuIr_2S_4 ; STATE

Addresses: [Bozin, E. S.; Yin, W. G.; Koch, R. J.; Lei, H. C.; Petrovic, C.; Billinge, S. J. L.] Brookhaven Natl Lab, Condensed Matter Phys & Mat Sci Dept, Upton, NY 11973 USA.

[Abeykoon, M.] Brookhaven Natl Lab, Photon Sci Div, Upton, NY 11973 USA.

[Hor, Y. S.; Zheng, H.; Mitchell, J. F.] Argonne Natl Lab, Mat Sci Div, Argonne, IL 60439 USA.

[Billinge, S. J. L.] Columbia Univ, Dept Appl Phys & Appl Math, New York, NY 10027 USA.

[Hor, Y. S.] Missouri Univ Sci & Technol, Dept Phys, Rolla, MO 65409 USA.

[Lei, H. C.] Renmin Univ China, Dept Phys, Beijing 100872, Peoples R China.

[Lei, H. C.] Renmin Univ China, Beijing Key Lab Optoelect Funct Mat & Micronano D, Beijing 100872, Peoples R China.

Corresponding Address: Bozin, ES; Billinge, SJL (corresponding author), Brookhaven Natl Lab, Condensed Matter Phys & Mat Sci Dept, Upton, NY 11973 USA.

Billinge, SJL (corresponding author), Columbia Univ, Dept Appl Phys & Appl Math, New York, NY 10027 USA.

E-mail Addresses: bozin@bnl.gov; sb2896@columbia.edu

Affiliations: United States Department of Energy (DOE); Brookhaven National Laboratory; United States Department of Energy (DOE); Brookhaven National Laboratory; United States Department of Energy (DOE); Argonne National Laboratory; Columbia University; University of Missouri System; Missouri University of Science & Technology; Renmin University of China; Renmin University of China

Author Identifiers:

Author	Web of Science ResearcherID	ORCID Number
--------	-----------------------------	--------------

Bozin, Emil	AAB-4551-2020	
Mitchell, John F	A-1907-2012	
Abeykoon, Milinda		0000-0001-6965-3753
Billinge, Simon		0000-0002-9734-4998
Bozin, Emil		0000-0002-6682-0365
Yin, Weiguo	A-9671-2014	0000-0002-4965-5329

Publisher: NATURE PORTFOLIO

Publisher Address: HEIDELBERGER PLATZ 3, BERLIN, 14197, GERMANY

Web of Science Index: Science Citation Index Expanded (SCI-EXPANDED)

Web of Science Categories: Multidisciplinary Sciences

Research Areas: Science & Technology - Other Topics

IDS Number: IQ1OC

ISSN: 2041-1723

29-char Source Abbrev.: NAT COMMUN

ISO Source Abbrev.: Nat. Commun.

Source Item Page Count: 7

Funding:

Funding Agency	Grant Number
US DOE, Office of Science, Office of Basic Energy Sciences	DE-SC0012704
U.S. Department of Energy Office of Science, Basic Energy Sciences, Materials Science and Engineering Division	

Work at Brookhaven National Laboratory was supported by US DOE, Office of Science, Office of Basic Energy Sciences under contract DE-SC0012704. Work in the Materials Science Division of Argonne National Laboratory, was sponsored by the U.S. Department of Energy Office of Science, Basic Energy Sciences, Materials Science and Engineering Division. This research used 28-ID-2 beamline of the National Synchrotron Light Source II, a U.S. Department of Energy (DOE) Office of Science User Facility operated for the DOE Office of Science by Brookhaven National Laboratory.

Open Access: Green Published, gold, Green Submitted

Output Date: 2023-01-27

Record 27 of 125

Title: Room temperature local nematicity in FeSe superconductor

Author(s): Koch, RJ (Koch, R. J.); Konstantinova, T (Konstantinova, T.); Abeykoon, M (Abeykoon, M.); Wang, A (Wang, A.); Petrovic, C (Petrovic, C.); Zhu, Y (Zhu, Y.); Bozin, ES (Bozin, E. S.); Billinge, SJL (Billinge, S. J. L.)

Source: PHYSICAL REVIEW B **Volume:** 100 **Issue:** 2 **Article Number:** 020501 **DOI:** 10.1103/PhysRevB.100.020501 **Published:** JUL 3 2019

Times Cited in Web of Science Core Collection: 19

Total Times Cited: 19

Usage Count (Last 180 days): 2

Usage Count (Since 2013): 40

Cited Reference Count: 33

Abstract: We report pair distribution function measurements of the iron-based superconductor FeSe above and below the structural transition temperature. Structural analysis reveals a local orthorhombic distortion with a correlation length of about 4 nm at temperatures where an average tetragonal symmetry is observed. The

analysis further demonstrates that the local distortion is larger than the global distortion at temperatures where the average observed symmetry is orthorhombic. Our results suggest that the low-temperature macroscopic nematic state in FeSe forms from an imperfect ordering of orbital-degeneracy-lifted nematic fluctuations which persist up to at least 300 K.

Accession Number: WOS:000474365400002

Language: English

Document Type: Article

KeyWords Plus: DETECTOR; ORDER

Addresses: [Koch, R. J.; Konstantinova, T.; Wang, A.; Petrovic, C.; Zhu, Y.; Bozin, E. S.; Billinge, S. J. L.] Brookhaven Natl Lab, Condensed Matter Phys & Mat Sci Dept, Upton, NY 11973 USA.

[Konstantinova, T.; Zhu, Y.] SUNY Stony Brook, Dept Phys & Astron, Stony Brook, NY 11794 USA.

[Abeykoon, M.] Brookhaven Natl Lab, Photon Sci Div, Upton, NY 11973 USA.

[Billinge, S. J. L.] Columbia Univ, Dept Appl Phys & Appl Math, New York, NY 10027 USA.

[Wang, A.] Chongqing Univ, Sch Phys, Chongqing 400044, Peoples R China.

Corresponding Address: Koch, RJ (corresponding author), Brookhaven Natl Lab, Condensed Matter Phys & Mat Sci Dept, Upton, NY 11973 USA.

E-mail Addresses: rkoch@bnl.gov

Affiliations: United States Department of Energy (DOE); Brookhaven National Laboratory; State University of New York (SUNY) System; State University of New York (SUNY) Stony Brook; United States Department of Energy (DOE); Brookhaven National Laboratory; Columbia University; Chongqing University

Author Identifiers:

Author	Web of Science ResearcherID	ORCID Number
Wang, Aifeng	AAQ-2894-2020	0000-0003-2425-3259
Bozin, Emil	AAB-4551-2020	
Konstantinova, Tatiana		0000-0001-9736-4246

Publisher: AMER PHYSICAL SOC

Publisher Address: ONE PHYSICS ELLIPSE, COLLEGE PK, MD 20740-3844 USA

Web of Science Index: Science Citation Index Expanded (SCI-EXPANDED)

Web of Science Categories: Materials Science, Multidisciplinary; Physics, Applied; Physics, Condensed Matter

Research Areas: Materials Science; Physics

IDS Number: IH3AJ

ISSN: 2469-9950

eISSN: 2469-9969

29-char Source Abbrev.: PHYS REV B

ISO Source Abbrev.: Phys. Rev. B

Source Item Page Count: 5

Funding:

Funding Agency	Grant Number
US Department of Energy, Office of Science, Office of Basic Energy Sciences (DOE-BES)	DE-SC0012704
DOE Office of Science	DE-SC0012704

This work was supported by US Department of Energy, Office of Science, Office of Basic Energy Sciences (DOE-BES) under Contract No. DE-SC0012704. X-ray PDF measurements were conducted on beamline 28-ID-1 of the National Synchrotron Light Source II, a US Department of Energy (DOE) Office of Science User Facility operated for the DOE Office of Science by Brookhaven National Laboratory under Contract No. DE-SC0012704.

Open Access: hybrid, Green Submitted

Output Date: 2023-01-27

Record 28 of 125

Title: Unconventional Continuous Structural Disorder at the Order-Disorder Phase Transition in the Hexagonal Manganites

Author(s): Skjaervo, SH (Skjaervo, Sandra H.); Meier, QN (Meier, Quintin N.); Feygenson, M (Feygenson, Mikhail); Spaldin, NA (Spaldin, Nicola A.); Billinge, SJL (Billinge, Simon J. L.); Bozin, ES (Bozin, Emil S.); Selbach, SM (Selbach, Sverre M.)

Source: PHYSICAL REVIEW X **Volume:** 9 **Issue:** 3 **Article Number:** 031001 **DOI:** 10.1103/PhysRevX.9.031001 **Published:** JUL 1 2019

Times Cited in Web of Science Core Collection: 26

Total Times Cited: 26

Usage Count (Last 180 days): 1

Usage Count (Since 2013): 29

Cited Reference Count: 72

Abstract: The improper ferroelectricity in YMnO₃ and other related multiferroic hexagonal manganites is known to cause topologically protected ferroelectric domains that give rise to rich and diverse physical phenomena. The local structure and structural coherence across the ferroelectric transition, however, were previously not well understood. Here, we reveal the evolution of the local structure with temperature in YMnO₃ using neutron total scattering techniques, and we interpret them with the help of first-principles calculations and with a first-principles-based effective Hamiltonian. The results show that, at room temperature, the local and average structures are consistent with the established ferroelectric P6(3)cm symmetry. On heating, both local and average structural analyses show striking anomalies from about 800 K up to the Curie temperature and signatures of a locally more preserved structure than on average, consistent with increasing fluctuations of the order-parameter angle. These fluctuations result in an unusual local symmetry lowering into a continuum of structures on heating. This local symmetry breaking persists into the high-symmetry nonpolar phase, constituting an unconventional type of order-disorder transition, and we pinpoint it as the reason for the anomalous behavior near the phase transition. The hidden disorder revealed in YMnO₃ by total scattering is expected to find analogies in other materials with structural frustration or characteristic energy barriers of different magnitudes.

Accession Number: WOS:000473311000001

Language: English

Document Type: Article

Author Keywords: Condensed Matter Physics; Materials Science

KeyWords Plus: FERROELECTRICITY; CRYSTALLOGRAPHY; DISPLACIVE; SCATTERING; SYMMETRY; ORIGIN; YMNO3

Addresses: [Skjaervo, Sandra H.; Selbach, Sverre M.] NTNU Norwegian Univ Sci & Technol, Dept Mat Sci & Engr, NO-7491 Trondheim, Norway.

[Meier, Quintin N.; Spaldin, Nicola A.] Swiss Fed Inst Technol, Mat Theory, Wolfgang Pauli Str 27, CH-8093 Zurich, Switzerland.

[Feygenson, Mikhail] Forschungszentrum Julich, JCNS, D-52425 Julich, Germany.

[Feygenson, Mikhail] Oak Ridge Natl Lab, Chem & Engr Mat Div, Oak Ridge, TN 37831 USA.

[Billinge, Simon J. L.; Bozin, Emil S.] Brookhaven Natl Lab, Condensed Matter Phys & Mat Sci Dept, Upton, NY 11973 USA.

[Billinge, Simon J. L.] Columbia Univ, Dept Appl Phys & Appl Math, New York, NY 10027 USA.

Corresponding Address: Selbach, SM (corresponding author), NTNU Norwegian Univ Sci & Technol, Dept Mat Sci & Engr, NO-7491 Trondheim, Norway.

Bozin, ES (corresponding author), Brookhaven Natl Lab, Condensed Matter Phys & Mat Sci Dept, Upton, NY 11973 USA.

E-mail Addresses: bozin@bnl.gov; selbach@ntnu.no

Affiliations: Norwegian University of Science & Technology (NTNU); Swiss Federal Institutes of Technology Domain; ETH Zurich; Helmholtz Association; Research Center Julich; United States Department of Energy (DOE); Oak Ridge National Laboratory; United States Department of Energy (DOE); Brookhaven National Laboratory; Columbia University

Author Identifiers:

Author	Web of Science ResearcherID	ORCID Number
Bozin, Emil	AAB-4551-2020	
Spaldin, Nicola A	A-1017-2010	0000-0003-0709-9499
Feyngenson, Mikhail	H-9972-2014	0000-0002-0316-3265
Selbach, Sverre M.		0000-0001-5838-8632
Skjaervo, Sandra Helen		0000-0002-1532-2008
Meier, Quintin N.		0000-0001-5881-9551

Publisher: AMER PHYSICAL SOC

Publisher Address: ONE PHYSICS ELLIPSE, COLLEGE PK, MD 20740-3844 USA

Web of Science Index: Science Citation Index Expanded (SCI-EXPANDED)

Web of Science Categories: Physics, Multidisciplinary

Research Areas: Physics

IDS Number: IF8AY

ISSN: 2160-3308

29-char Source Abbrev.: PHYS REV X

ISO Source Abbrev.: Phys. Rev. X

Source Item Page Count: 16

Funding:

Funding Agency	Grant Number
U.S. DOE, Office of Science, Office of Basic Energy Sciences (DOE-BES)	DE-SC0012704
Research Council of Norway	231430
NTNU	
ETH Zurich	
European Research Council	291151

Experimental work was co-led by the groups at Brookhaven National Laboratory (BNL) and the Norwegian University of Science and Technology (NTNU). Theoretical work was led by ETH. Work at BNL was supported by U.S. DOE, Office of Science, Office of Basic Energy Sciences (DOE-BES) under Contract No. DE-SC0012704. The NTNU group acknowledges financial support from the Research Council of Norway (Project No. 231430) and NTNU. The ETH group was supported by ETH Zurich and Advanced Grant No. 291151 from the European Research Council. This research used resources at the Spallation Neutron Source, a DOE Office of Science User Facility operated by the Oak Ridge National Laboratory. Computational resources were provided by the Euler cluster at ETH, Zurich. Matt Tucker and Marshall McDonnell are acknowledged for assisting with the data collection for the neutron measurements. Matt Tucker is acknowledged for constructing TOPAS input files for reciprocal-space Rietveld refinements. Jorg Neufeind and Pavol Juhas are acknowledged for assisting with manual data reduction and quality testing. Peter M. Derlet is acknowledged for constructive feedback on the manuscript.

Open Access: Green Published, Green Submitted, gold

Output Date: 2023-01-27

Title: Photoinduced dynamics of nematic order parameter in FeSe

Author(s): Konstantinova, T (Konstantinova, T.); Wu, L (Wu, L.); Abeykoon, M (Abeykoon, M.); Koch, RJ (Koch, R. J.); Wang, AF (Wang, A. F.); Li, RK (Li, R. K.); Shen, X (Shen, X.); Li, J (Li, J.); Tao, J (Tao, J.); Zaliznyak, IA (Zaliznyak, I. A.); Petrovic, C (Petrovic, C.); Billinge, SJL (Billinge, S. J. L.); Wang, XJ (Wang, X. J.); Bozin, ES (Bozin, E. S.); Zhu, Y (Zhu, Y.)

Source: PHYSICAL REVIEW B **Volume:** 99 **Issue:** 18 **Article Number:** 180102 **DOI:** 10.1103/PhysRevB.99.180102 **Published:** MAY 28 2019

Times Cited in Web of Science Core Collection: 10

Total Times Cited: 10

Usage Count (Last 180 days): 1

Usage Count (Since 2013): 45

Cited Reference Count: 41

Abstract: Formation of electronic nematicity is a common thread of unconventional superconductors. We use ultrafast electron diffraction to probe the lattice interactions with electronic degrees of freedom in superconducting FeSe and find a significant lattice response to local nematicity. We observe that a perturbation by a laser pulse leads to a surprising enhancement of the high-symmetry crystalline order as a result of suppression of low-symmetry local lattice distortions, which are signatures of nematic fluctuations. The distortions are present at temperatures both below and above the nematic phase transition, as corroborated by our x-ray pair distribution function analysis and transmission electron microscopy measurements. Nonequilibrium lattice behavior of FeSe reveals two distinct time scales of nematic response to photoexcitation, 130(20) and 40(10) ps, corresponding to diffusive and percolative dynamics of nematic fluctuations respectively.

Accession Number: WOS:000469325500001

Language: English

Document Type: Article

KeyWords Plus: SUPERCONDUCTIVITY; DISORDER

Addresses: [Konstantinova, T.; Wu, L.; Abeykoon, M.; Koch, R. J.; Shen, X.; Li, J.; Tao, J.; Zaliznyak, I. A.; Petrovic, C.; Billinge, S. J. L.; Bozin, E. S.; Zhu, Y.] Brookhaven Natl Lab, Upton, NY 11973 USA.

[Konstantinova, T.; Zhu, Y.] SUNY Stony Brook, Stony Brook, NY 11794 USA.

[Wang, A. F.; Li, R. K.; Wang, X. J.] SLAC Natl Accelerator Lab, Menlo Pk, CA 94025 USA.

[Billinge, S. J. L.] Columbia Univ, New York, NY 10027 USA.

[Koch, R. J.] Chongqing Univ, Sch Phys, Chongqing 400044, Peoples R China.

Corresponding Address: Zhu, Y (corresponding author), Brookhaven Natl Lab, Upton, NY 11973 USA.

Zhu, Y (corresponding author), SUNY Stony Brook, Stony Brook, NY 11794 USA.

E-mail Addresses: zhu@bnl.gov

Affiliations: United States Department of Energy (DOE); Brookhaven National Laboratory; State University of New York (SUNY) System; State University of New York (SUNY) Stony Brook; Stanford University; United States Department of Energy (DOE); SLAC National Accelerator Laboratory; Columbia University; Chongqing University

Author Identifiers:

Author	Web of Science ResearcherID	ORCID Number
Shen, Xiaozhe	AAJ-9508-2020	0000-0002-6844-608X
Zaliznyak, Igor	AAW-2535-2020	0000-0002-8548-7924
Zaliznyak, Igor	E-8532-2014	0000-0002-8548-7924
Bozin, Emil	AAB-4551-2020	
Konstantinova, Tatiana		0000-0001-9736-4246

Publisher: AMER PHYSICAL SOC

Publisher Address: ONE PHYSICS ELLIPSE, COLLEGE PK, MD 20740-3844 USA

Web of Science Index: Science Citation Index Expanded (SCI-EXPANDED)

Web of Science Categories: Materials Science, Multidisciplinary; Physics, Applied; Physics, Condensed Matter

Research Areas: Materials Science; Physics

IDS Number: IA1MH

ISSN: 2469-9950

eISSN: 2469-9969

29-char Source Abbrev.: PHYS REV B

ISO Source Abbrev.: Phys. Rev. B

Source Item Page Count: 6

Funding:

Funding Agency	Grant Number
US Department of Energy (DOE), Office of Science, Office of Basic Energy Sciences (BES), Materials Science and Engineering Division	DE-SC0012704
DOE BES Scientific User Facilities Division Accelerator & Detector RD program	
LCLS Facility	
SLAC	DE-AC02-05-CH11231 DE-AC02-76SF00515

The authors thank A. F. Kemper, L. Classen, A. V. Chubukov, R. M. Konik, and A. M. Lindenberg for useful discussions and S. Lapidus for XPD measurements at the 11-BM beamline at APS. This research used the 28-ID-1 (PDF) beamline of the National Synchrotron Light Source II and the JEOL ARM 200 CF Microscope at BNL. Work at Brookhaven National Laboratory was supported by US Department of Energy (DOE), Office of Science, Office of Basic Energy Sciences (BES), Materials Science and Engineering Division under Contract No. DE-SC0012704. The UED work was performed at SLAC MeV-UED, which is supported in part by the DOE BES Scientific User Facilities Division Accelerator & Detector R&D program, the LCLS Facility, and SLAC under Contracts No. DE-AC02-05-CH11231 and No. DE-AC02-76SF00515.

Open Access: Green Submitted, hybrid

Output Date: 2023-01-27

Record 30 of 125

Title: Phase separation at the dimer-superconductor transition in Ir_{1-x}Rh_xTe₂

Author(s): Yu, R (Yu, R.); Banerjee, S (Banerjee, S.); Lei, H (Lei, H.); Abeykoon, M (Abeykoon, M.); Petrovic, C (Petrovic, C.); Guguchia, Z (Guguchia, Z.); Bozin, ES (Bozin, E. S.)

Source: PHYSICAL REVIEW B **Volume:** 98 **Issue:** 13 **Article Number:** 134506 **DOI:** 10.1103/PhysRevB.98.134506 **Published:** OCT 16 2018

Times Cited in Web of Science Core Collection: 4

Total Times Cited: 4

Usage Count (Last 180 days): 2

Usage Count (Since 2013): 35

Cited Reference Count: 84

Abstract: The detailed evolution of the local atomic structure across the (x, T) phase diagram of transition metal dichalcogenide superconductor Ir_{1-x}Rh_xTe₂ (0 ≤ x ≤ 0.3, 10 K ≤ T ≤ 300 K) is obtained from high-quality x-ray diffraction data using the atomic pair distribution function (PDF) method. The observed hysteretic thermal structural phase transition from a trigonal (P(3) over bar m1) to a triclinic (P(1) over bar) dimer phase

for low Rh content emphasizes the intimate connection between the lattice and electronic properties. For superconducting samples away from the dimer/superconductor phase boundary, structural transition is absent and the local structure remains trigonal down to 10 K. In the narrow range of compositions close to the boundary, PDF analysis reveals structural phase separation, suggestive of weak first-order character of the Rh-doping induced dimer-superconductor quantum phase transition. Samples from this narrow range show weak anomalies in electronic transport and magnetization, hallmarks of the dimer phase, as well as superconductivity albeit with incomplete diamagnetic screening. The results suggest that the dimer and superconducting orders exist in the mutually exclusive spatial regions.

Accession Number: WOS:000447463700007

Language: English

Document Type: Article

KeyWords Plus: CHARGE-DENSITY-WAVE; PAIR DISTRIBUTION FUNCTION; METAL DICHALCOGENIDES; T-C; IRTE2; ORDER; COMPETITION; SURFACE

Addresses: [Yu, R.; Lei, H.; Petrovic, C.; Guguchia, Z.; Bozin, E. S.] Brookhaven Natl Lab, Condensed Matter Phys & Mat Sci Dept, Upton, NY 11973 USA.

[Banerjee, S.] Columbia Univ, Dept Appl Phys & Appl Math, New York, NY 10027 USA.

[Abeykoon, M.] Brookhaven Natl Lab, Photon Sci Div, Upton, NY 11973 USA.

[Guguchia, Z.] Columbia Univ, Dept Phys, New York, NY 10027 USA.

[Yu, R.] Chinese Acad Sci, Inst Phys, Beijing 100190, Peoples R China.

[Lei, H.] Renmin Univ, Dept Phys, Beijing 100872, Peoples R China.

Corresponding Address: Bozin, ES (corresponding author), Brookhaven Natl Lab, Condensed Matter Phys & Mat Sci Dept, Upton, NY 11973 USA.

E-mail Addresses: bozin@bnl.gov

Affiliations: United States Department of Energy (DOE); Brookhaven National Laboratory; Columbia University; United States Department of Energy (DOE); Brookhaven National Laboratory; Columbia University; Chinese Academy of Sciences; Institute of Physics, CAS; Renmin University of China

Author Identifiers:

Author	Web of Science ResearcherID	ORCID Number
Bozin, Emil	AAB-4551-2020	
Guguchia, Zurab		0000-0002-0764-7574

Publisher: AMER PHYSICAL SOC

Publisher Address: ONE PHYSICS ELLIPSE, COLLEGE PK, MD 20740-3844 USA

Web of Science Index: Science Citation Index Expanded (SCI-EXPANDED)

Web of Science Categories: Materials Science, Multidisciplinary; Physics, Applied; Physics, Condensed Matter

Research Areas: Materials Science; Physics

IDS Number: GX1GR

ISSN: 2469-9950

eISSN: 2469-9969

29-char Source Abbrev.: PHYS REV B

ISO Source Abbrev.: Phys. Rev. B

Source Item Page Count: 9

Funding:

Funding Agency	Grant Number
US DOE, Office of Science, Office of Basic Energy Sciences (DOE-BES)	DE-SC0012704

Work at Brookhaven National Laboratory was supported by US DOE, Office of Science, Office of Basic Energy Sciences (DOE-BES) under Contract No. DE-SC0012704. We are grateful to J. Tranquada, S. Billinge,

I. Robinson, I. Zaliznyak, A. Lappas, and A. Tselik for fruitful discussions and critical comments.

Open Access: hybrid, Green Submitted

Output Date: 2023-01-27

Record 31 of 125

Title: Emphanitic anharmonicity in PbSe at high temperature and anomalous electronic properties in the Pb Q (Q = S, Se, Te) system

Author(s): Yu, RZ (Yu, Runze); Bozin, ES (Bozin, Emil S.); Abeykoon, M (Abeykoon, Milinda); Sangiorgio, B (Sangiorgio, Boris); Spaldin, NA (Spaldin, Nicola A.); Malliakas, CD (Malliakas, Christos D.); Kanatzidis, MG (Kanatzidis, Mercouri G.); Billinge, SJL (Billinge, Simon J. L.)

Source: PHYSICAL REVIEW B **Volume:** 98 **Issue:** 14 **Article Number:** 144108 **DOI:** 10.1103/PhysRevB.98.144108 **Published:** OCT 12 2018

Times Cited in Web of Science Core Collection: 17

Total Times Cited: 17

Usage Count (Last 180 days): 3

Usage Count (Since 2013): 35

Cited Reference Count: 52

Abstract: The temperature dependence of the local structure of PbSe has been investigated using pair distribution function (PDF) analysis of x-ray and neutron powder diffraction data and density functional theory (DFT) calculations. Observation of non-Gaussian PDF peaks at high temperature indicates the presence of significant anharmonicity, which can be modeled as Pb off-centering along [100] directions that grows on warming similar to the behavior seen in PbTe and PbS and sometimes called emphanisis. Interestingly, the emphanitic response is smaller in PbSe than in both PbS and PbTe indicating a nonmonotonic response with chalcogen atomic number in the Pb Q (Q = S, Se, Te) series. The DFT calculations indicate a correlation between band gap and the amplitude of [100] dipolar distortion, suggesting that emphanisis may be behind the anomalous composition and temperature dependencies of the band gaps in this series.

Accession Number: WOS:000447183100003

Language: English

Document Type: Article

KeyWords Plus: PAIR DISTRIBUTION FUNCTION; AUGMENTED-WAVE METHOD; ENERGY GAPS; BAND-GAP; DEPENDENCE; LEAD; SEMICONDUCTORS; CHALCOGENIDES; PERFORMANCE; AMPLITUDES

Addresses: [Yu, Runze; Bozin, Emil S.; Billinge, Simon J. L.] Brookhaven Natl Lab, Condensed Matter Phys & Mat Sci Dept, Upton, NY 11973 USA.

[Abeykoon, Milinda] Brookhaven Natl Lab, Photon Sci Div, Upton, NY 11973 USA.

[Sangiorgio, Boris; Spaldin, Nicola A.] Swiss Fed Inst Technol, Mat Theory, Wolfgang Pauli Str 27, CH-8093 Zurich, Switzerland.

[Malliakas, Christos D.; Kanatzidis, Mercouri G.] Northwestern Univ, Dept Chem, 2145 Sheridan Rd, Evanston, IL 60208 USA.

[Kanatzidis, Mercouri G.] Argonne Natl Lab, Div Mat Sci, 9700 S Cass Ave, Argonne, IL 60439 USA.

[Billinge, Simon J. L.] Columbia Univ, Dept Appl Phys & Appl Math, New York, NY 10027 USA.

Corresponding Address: Bozin, ES (corresponding author), Brookhaven Natl Lab, Condensed Matter Phys & Mat Sci Dept, Upton, NY 11973 USA.

E-mail Addresses: bozin@bnl.gov

Affiliations: United States Department of Energy (DOE); Brookhaven National Laboratory; United States Department of Energy (DOE); Brookhaven National Laboratory; Swiss Federal Institutes of Technology Domain; ETH Zurich; Northwestern University; United States Department of Energy (DOE); Argonne National Laboratory; Columbia University

Author Identifiers:

Author	Web of Science ResearcherID	ORCID Number
Bozin, Emil	AAB-4551-2020	
Spaldin, Nicola A	A-1017-2010	0000-0003-0709-9499

Publisher: AMER PHYSICAL SOC

Publisher Address: ONE PHYSICS ELLIPSE, COLLEGE PK, MD 20740-3844 USA

Web of Science Index: Science Citation Index Expanded (SCI-EXPANDED)

Web of Science Categories: Materials Science, Multidisciplinary; Physics, Applied; Physics, Condensed Matter

Research Areas: Materials Science; Physics

IDS Number: GW7WL

ISSN: 2469-9950

eISSN: 2469-9969

29-char Source Abbrev.: PHYS REV B

ISO Source Abbrev.: Phys. Rev. B

Source Item Page Count: 6

Funding:

Funding Agency	Grant Number
U.S. Department of Energy, Office of Science, Office of Basic Energy Sciences (DOE-BES)	DE-SC0012704
U.S. Department of Energy, Office of Science, Materials Sciences and Engineering	
DOE-BES	DE-SC0012704
ETH Zurich	
ERC Advanced Grant program	291151
Swiss National Supercomputing Centre (CSCS)	s624

Work at Brookhaven National Laboratory was supported by U.S. Department of Energy, Office of Science, Office of Basic Energy Sciences (DOE-BES) under Contract DE-SC0012704. Work at Argonne National Laboratory was supported by the U.S. Department of Energy, Office of Science, Materials Sciences and Engineering. The neutron diffraction measurements were carried out at NPDF instrument of the Lujan Neutron Scattering Center at Los Alamos National Laboratory, and the x-ray experiments were carried out at beamline 28-ID-2 (XPD) of the National Synchrotron Light Source II at Brookhaven National Laboratory. Use of the National Synchrotron Light Source II, Brookhaven National Laboratory, was supported by DOE-BES under Contract No. DE-SC0012704. B.S. and N.A.S. acknowledge support from ETH Zurich, the ERC Advanced Grant program (No. 291151), and the Swiss National Supercomputing Centre (CSCS) under Project ID s624.

Open Access: Green Submitted, hybrid

Output Date: 2023-01-27

Record 32 of 125

Title: Thermoelectric studies of Ir_{1-x}Rh_xTe₂ (0 ≤ x ≤ 0.3)

Author(s): Liu, Y (Liu, Yu); Lei, HC (Lei, Hechang); Wang, KF (Wang, Kefeng); Abeykoon, M (Abeykoon, Milinda); Warren, JB (Warren, J. B.); Bozin, E (Bozin, Emil); Petrovic, C (Petrovic, C.)

Source: PHYSICAL REVIEW B **Volume:** 98 **Issue:** 9 **Article Number:** 094519 **DOI:** 10.1103/PhysRevB.98.094519 **Published:** SEP 26 2018

Times Cited in Web of Science Core Collection: 8

Total Times Cited: 8

Usage Count (Last 180 days): 0

Usage Count (Since 2013): 40

Cited Reference Count: 40

Abstract: We report thermoelectric properties of Ir_{1-x}Rh_xTe₂ (0 ≤ x ≤ 0.3) alloy series where superconductivity at low temperatures emerges as the high-temperature structural transition (T_s) is suppressed. The isovalent ionic substitution of Rh into Ir has different effects on physical properties when compared to the anionic substitution of Se into Te, in which the structural transition is more stable with Se substitution. Rh substitution results in a slight reduction of lattice parameters and in an increase of number of carriers per unit cell. Weak-coupled BCS superconductivity in Ir_{0.8}Rh_{0.2}Te₂ that emerges at low temperature (T_c(zero) = 2.45 K) is most likely driven by electron-phonon coupling rather than dimer fluctuations mediated pairing.

Accession Number: WOS:000445724200005

Language: English

Document Type: Article

KeyWords Plus: CHARGE-DENSITY-WAVE; SUPERCONDUCTIVITY; TEMPERATURE; COMPETITION; IRTE2

Addresses: [Liu, Yu; Lei, Hechang; Wang, Kefeng; Bozin, Emil; Petrovic, C.] Brookhaven Natl Lab, Condensed Matter Phys & Mat Sci Dept, Upton, NY 11973 USA.

[Abeykoon, Milinda] Brookhaven Natl Lab, Photon Sci Div, Natl Synchrotron Light Source 2, Upton, NY 11973 USA.

[Warren, J. B.] Brookhaven Natl Lab, Instrumentat Div, Upton, NY 11973 USA.

[Lei, Hechang] Renmin Univ China, Dept Phys, Beijing 100872, Peoples R China.

[Lei, Hechang] Renmin Univ China, Beijing Key Lab Optoelect Funct Mat & Micronano D, Beijing 100872, Peoples R China.

[Wang, Kefeng] Univ Maryland, Ctr Nanophys & Adv Mat, Dept Phys, College Pk, MD 20742 USA.

Corresponding Address: Liu, Y (corresponding author), Brookhaven Natl Lab, Condensed Matter Phys & Mat Sci Dept, Upton, NY 11973 USA.

Affiliations: United States Department of Energy (DOE); Brookhaven National Laboratory; United States Department of Energy (DOE); Brookhaven National Laboratory; United States Department of Energy (DOE); Brookhaven National Laboratory; Renmin University of China; Renmin University of China; University System of Maryland; University of Maryland College Park

Author Identifiers:

Author	Web of Science ResearcherID	ORCID Number
Bozin, Emil	AAB-4551-2020	
Liu, Yu	ABD-2488-2021	0000-0001-8886-2876

Publisher: AMER PHYSICAL SOC

Publisher Address: ONE PHYSICS ELLIPSE, COLLEGE PK, MD 20740-3844 USA

Web of Science Index: Science Citation Index Expanded (SCI-EXPANDED)

Web of Science Categories: Materials Science, Multidisciplinary; Physics, Applied; Physics, Condensed Matter

Research Areas: Materials Science; Physics

IDS Number: GV0CL

ISSN: 2469-9950

eISSN: 2469-9969

29-char Source Abbrev.: PHYS REV B

ISO Source Abbrev.: Phys. Rev. B

Source Item Page Count: 6

Funding:

Funding Agency	Grant Number

This work has benefited from using the X7B beamline at the National Synchrotron Light Source at Brookhaven National Laboratory. We are indebted to Jonathan Hanson for his help with the x-ray diffraction experiment setup. Work at Brookhaven is supported by the US DOE under Contract No. DE-SC0012704.

Open Access: hybrid, Green Submitted

Output Date: 2023-01-27

Record 33 of 125

Title: On the Nanoscale Structure of $K(x)Fe_{2-y}Ch_2$ (Ch = S, Se): A Neutron Pair Distribution Function View

Author(s): Mangelis, P (Mangelis, Panagiotis); Lei, HC (Lei, Hechang); McDonnell, MT (McDonnell, Marshall T.); Feygenson, M (Feygenson, Mikhail); Petrovic, C (Petrovic, Cedomir); Bozin, ES (Bozin, Emil S.); Lappas, A (Lappas, Alexandros)

Source: CONDENSED MATTER **Volume:** 3 **Issue:** 3 **Article Number:** 20 **DOI:** 10.3390/condmat3030020 **Published:** SEP 2018

Times Cited in Web of Science Core Collection: 3

Total Times Cited: 3

Usage Count (Last 180 days): 0

Usage Count (Since 2013): 15

Cited Reference Count: 27

Abstract: Comparative exploration of the nanometer-scale atomic structure of $K(x)Fe_{2-y}Ch_2$ (Ch = S, Se) was performed using neutron total scattering-based atomic pair distribution function (PDF) analysis of 5 K powder diffraction data in relation to physical properties. Whereas $K_xFe_{2-y}Se_2$ is a superconductor with a transition temperature of about 32 K, the isostructural sulphide analogue is not, which instead displays a spin glass semiconducting behavior at low temperatures. The PDF analysis explores phase separated and disordered structural models as candidate descriptors of the low temperature data. For both materials, the nanoscale structure is well described by the iron (Fe)-vacancy-disordered $K(2)Fe_{(5-y)}Ch_5$ (I4/m) model containing excess Fe. An equally good description of the data is achieved by using a phase separated model comprised of I4/m vacancy-ordered and I4/mmm components. The I4/mmm component appears as a minority phase in the structure of both $K_xFe_{2-y}Se_2$ and $K_xFe_{2-y}S_2$, and with similar contribution, implying that the phase ratio is not a decisive factor influencing the lack of superconductivity in the latter. Comparison of structural parameters of the Fe-vacancy-disordered model indicates that the replacement of selenium (Se) by sulphur (S) results in an appreciable reduction in the Fe-Ch interatomic distances and anion heights, while simultaneously increasing the irregularity of $FeCh_4$ tetrahedra, suggesting the more significant influence of these factors. Structural features are also compared to the non-intercalated FeSe and FeS parent phases, providing further information for the discussion about the influence of the lattice degrees of freedom on the observed properties in layered iron chalcogenides.

Accession Number: WOS:000445304300008

Language: English

Document Type: Article

Author Keywords: neutron pair distribution function (PDF); intercalated iron superconductors; anion height; tetrahedron regularity

Keywords Plus: SUPERCONDUCTIVITY

Addresses: [Mangelis, Panagiotis; Lappas, Alexandros] Fdn Res & Technol Hellas, Inst Elect Struct & Laser, Iraklion 71110, Greece.

[Lei, Hechang; Petrovic, Cedomir; Bozin, Emil S.] Brookhaven Natl Lab, Condensed Matter Phys & Mat Sci Dept, Upton, NY 11973 USA.

[McDonnell, Marshall T.; Feygenson, Mikhail] Oak Ridge Natl Lab, Neutron Scattering Div, Oak Ridge, TN 37831 USA.

[Lei, Hechang] Renmin Univ, Dept Phys, Beijing 100872, Peoples R China.

[Feygenson, Mikhail] Forschungszentrum Julich, JCNS, D-52425 Julich, Germany.

Corresponding Address: Mangelis, P (corresponding author), Fdn Res & Technol Hellas, Inst Elect Struct & Laser, Iraklion 71110, Greece.

E-mail Addresses: mangelis@iesl.forth.gr; hlei@ruc.edu.cn; mcdonnellmt@ornl.gov; m.feygenson@fz-juelich.de; petrovic@bnl.gov; bozin@bnl.gov; lappas@iesl.forth.gr

Affiliations: Foundation for Research & Technology - Hellas (FORTH); United States Department of Energy (DOE); Brookhaven National Laboratory; United States Department of Energy (DOE); Oak Ridge National Laboratory; Renmin University of China; Helmholtz Association; Research Center Julich

Author Identifiers:

Author	Web of Science ResearcherID	ORCID Number
Lappas, Alexandros	AFO-0640-2022	0000-0001-8486-0312
Bozin, Emil	AAB-4551-2020	
McDonnell, Marshall	AAF-3842-2020	0000-0002-3713-2117
Lappas, Alexandros	F-6771-2011	0000-0001-8486-0312
Feygenson, Mikhail	H-9972-2014	0000-0002-0316-3265
Mangelis, Panagiotis		0000-0001-5948-1177

Publisher: MDPI

Publisher Address: ST ALBAN-ANLAGE 66, CH-4052 BASEL, SWITZERLAND

Web of Science Index: Emerging Sources Citation Index (ESCI)

Web of Science Categories: Physics, Condensed Matter

Research Areas: Physics

IDS Number: GU5DB

ISSN: 2410-3896

29-char Source Abbrev.: CONDENS MATTER

ISO Source Abbrev.: Condens. Matter

Source Item Page Count: 10

Open Access: Green Submitted, gold, Green Published

Output Date: 2023-01-27

Record 34 of 125

Title: Correlated local dipoles in PbTe

Author(s): Sangiorgio, B (Sangiorgio, Boris); Bozin, ES (Bozin, Emil S.); Malliakas, CD (Malliakas, Christos D.); Fechner, M (Fechner, Michael); Simonov, A (Simonov, Arkadiy); Kanatzidis, MG (Kanatzidis, Mercouri G.); Billinge, SJL (Billinge, Simon J. L.); Spaldin, NA (Spaldin, Nicola A.); Weber, T (Weber, Thomas)

Source: PHYSICAL REVIEW MATERIALS **Volume:** 2 **Issue:** 8 **Article Number:** 085402 **DOI:** 10.1103/PhysRevMaterials.2.085402 **Published:** AUG 6 2018

Times Cited in Web of Science Core Collection: 34

Total Times Cited: 34

Usage Count (Last 180 days): 1

Usage Count (Since 2013): 24

Cited Reference Count: 74

Abstract: We present a combined single-crystal x-ray diffuse scattering and ab initio molecular dynamics study of lead telluride, PbTe. Well-known for its thermoelectric and narrow-gap semiconducting properties, PbTe recently achieved further notoriety following the report of an unusual off-centering of the lead atoms, accompanied by a local symmetry breaking, on heating. This observation, which was named *emphanisis*, ignited considerable controversy regarding the details of the underlying local structure and the appropriate

interpretation of the total scattering experiments. In this study, we identify an unusual correlated local dipole formation extending over several unit cells with an associated local reduction of the cubic symmetry in both our x-ray diffuse scattering measurements and our molecular dynamics simulations. Importantly, when averaged spatially or temporally, the most probable positions for the ions are at the centers of their coordination polyhedra. Our results therefore clarify the nature of the local symmetry breaking, and reveal the source of the earlier controversy regarding the existence or absence of off-centering. Finally, we provide an interpretation of the behavior in terms of coupled soft optical and acoustic modes which is linked also to the high thermoelectric performance of PbTe.

Accession Number: WOS:000440830800002

Language: English

Document Type: Article

KeyWords Plus: MOLECULAR-DYNAMICS; DIFFUSE-SCATTERING; LONE-PAIR; BULK; PSEUDOPOTENTIALS; THERMOELECTRICS; CONVERGENCE; DISORDER

Addresses: [Sangiorgio, Boris; Fechner, Michael; Simonov, Arkadiy; Spaldin, Nicola A.; Weber, Thomas] Swiss Fed Inst Technol, Dept Mat, Vladimir Prelog Weg 5, CH-8093 Zurich, Switzerland.

[Bozin, Emil S.; Billinge, Simon J. L.] Brookhaven Natl Lab, Condensed Matter Phys & Mat Sci Dept, Upton, NY 11973 USA.

[Malliakas, Christos D.; Kanatzidis, Mercouri G.] Northwestern Univ Evanston, Dept Chem, Evanston, IL 60208 USA.

[Billinge, Simon J. L.] Columbia Univ, Dept Appl Phys & Appl Math, New York, NY 10027 USA.

Corresponding Address: Sangiorgio, B (corresponding author), Swiss Fed Inst Technol, Dept Mat, Vladimir Prelog Weg 5, CH-8093 Zurich, Switzerland.

Affiliations: Swiss Federal Institutes of Technology Domain; ETH Zurich; United States Department of Energy (DOE); Brookhaven National Laboratory; Northwestern University; Columbia University

Author Identifiers:

Author	Web of Science ResearcherID	ORCID Number
Bozin, Emil	AAB-4551-2020	
Spaldin, Nicola A	A-1017-2010	0000-0003-0709-9499
Fechner, Michael	J-7198-2018	
Weber, Thomas		0000-0003-1429-9915
Fechner, Michael		0000-0003-2774-7684

Publisher: AMER PHYSICAL SOC

Publisher Address: ONE PHYSICS ELLIPSE, COLLEGE PK, MD 20740-3844 USA

Web of Science Index: Science Citation Index Expanded (SCI-EXPANDED)

Web of Science Categories: Materials Science, Multidisciplinary

Research Areas: Materials Science

IDS Number: GP4JZ

ISSN: 2475-9953

29-char Source Abbrev.: PHYS REV MATER

ISO Source Abbrev.: Phys. Rev. Mater.

Source Item Page Count: 24

Funding:

Funding Agency	Grant Number
ETH Zurich	
ERC Advanced Grant program	291151
Swiss National Supercomputing Centre (CSCS)	s307 s624

B.S., M.F., and N.A.S. acknowledge support from ETH Zurich, the ERC Advanced Grant program (No. 291151), and the Swiss National Supercomputing Centre (CSCS) under project IDs s307, s624, and p504. We thank Joost Vande-Vondele for helpful discussions, in particular regarding the use of the CP2K code. T.W. thanks the staff of the X06SA beamline at the Swiss Light Source, Villigen, Switzerland for giving access to the beamline and for helping with the experiments. Work at Brookhaven National Laboratory was supported by U.S. Department of Energy, Office of Science, Office of Basic Energy Sciences (DOE-BES) under Contract No. DE-SC0012704.

Open Access: Green Submitted, hybrid

Output Date: 2023-01-27

Record 35 of 125

Title: Absence of local fluctuating dimers in superconducting Ir-1_x(Pt,Rh)_xTe-2

Author(s): Yu, RZ (Yu, Runze); Banerjee, S (Banerjee, S.); Lei, HC (Lei, H. C.); Sinclair, R (Sinclair, Ryan); Abeykoon, M (Abeykoon, M.); Zhou, HD (Zhou, H. D.); Petrovic, C (Petrovic, C.); Guguchia, Z (Guguchia, Z.); Bozin, ES (Bozin, E. S.)

Source: PHYSICAL REVIEW B **Volume:** 97 **Issue:** 17 **Article Number:** 174515 **DOI:** 10.1103/PhysRevB.97.174515 **Published:** MAY 18 2018

Times Cited in Web of Science Core Collection: 6

Total Times Cited: 6

Usage Count (Last 180 days): 2

Usage Count (Since 2013): 30

Cited Reference Count: 47

Abstract: The compound IrTe₂ is known to exhibit a transition to a modulated state featuring Ir-Ir dimers, with large associated atomic displacements. Partial substitution of Pt or Rh for Ir destabilizes the modulated structure and induces superconductivity. It has been proposed that quantum critical dimer fluctuations might be associated with the superconductivity. Here we test for such local dimer correlations and demonstrate their absence. X-ray pair distribution function approach reveals that the local structure of Ir_{0.95}Pt_{0.05}Te₂ and Ir_{0.8}Rh_{0.2}Te₂ dichalcogenide superconductors with compositions just past the dimer/superconductor boundary is explained well by a dimer-free model down to 10 K, ruling out the possibility of there being nanoscale dimer fluctuations in this regime. This is inconsistent with the proposed quantum-critical-point-like interplay of the dimer state and superconductivity, and precludes scenarios for dimer fluctuations mediated superconducting pairing.

Accession Number: WOS:000433010000003

Language: English

Document Type: Article

KeyWords Plus: ORDER; NANOSCALE; PDF

Addresses: [Yu, Runze; Lei, H. C.; Petrovic, C.; Guguchia, Z.; Bozin, E. S.] Brookhaven Natl Lab, Condensed Matter Phys & Mat Sci Dept, Upton, NY 11973 USA.

[Banerjee, S.] Columbia Univ, Dept Appl Phys & Appl Math, New York, NY 10027 USA.

[Sinclair, Ryan; Zhou, H. D.] Univ Tennessee, Dept Phys & Astron, Knoxville, TN 37996 USA.

[Abeykoon, M.] Brookhaven Natl Lab, Photon Sci Div, Upton, NY 11973 USA.

[Guguchia, Z.] Columbia Univ, Dept Phys, 538 W 120th St, New York, NY 10027 USA.

[Yu, Runze] Chinese Acad Sci, Inst Phys, Beijing 100190, Peoples R China.

[Lei, H. C.] Renmin Univ, Dept Phys, Beijing 100872, Peoples R China.

Corresponding Address: Bozin, ES (corresponding author), Brookhaven Natl Lab, Condensed Matter Phys & Mat Sci Dept, Upton, NY 11973 USA.

E-mail Addresses: bozin@bnl.gov

Affiliations: United States Department of Energy (DOE); Brookhaven National Laboratory; Columbia University; University of Tennessee System; University of Tennessee Knoxville; United States Department of Energy (DOE); Brookhaven National Laboratory; Columbia University; Chinese Academy of Sciences; Institute of Physics, CAS; Renmin University of China

Author Identifiers:

Author	Web of Science ResearcherID	ORCID Number
Bozin, Emil	AAB-4551-2020	
Zhou, Haidong	O-4373-2016	0000-0002-1595-1912
Guguchia, Zurab		0000-0002-0764-7574

Publisher: AMER PHYSICAL SOC

Publisher Address: ONE PHYSICS ELLIPSE, COLLEGE PK, MD 20740-3844 USA

Web of Science Index: Science Citation Index Expanded (SCI-EXPANDED)

Web of Science Categories: Materials Science, Multidisciplinary; Physics, Applied; Physics, Condensed Matter

Research Areas: Materials Science; Physics

IDS Number: GG9GW

ISSN: 2469-9950

eISSN: 2469-9969

29-char Source Abbrev.: PHYS REV B

ISO Source Abbrev.: Phys. Rev. B

Source Item Page Count: 8

Funding:

Funding Agency	Grant Number
US DOE, Office of Science, Office of Basic Energy Sciences (DOE-BES)	DE-SC00112704
	NSF-DMR-1350002

Work at Brookhaven National Laboratory was supported by US DOE, Office of Science, Office of Basic Energy Sciences (DOE-BES) under Contract No. DE-SC00112704. R.S. and H.D.Z. acknowledge support from Grant No. NSF-DMR-1350002. We are grateful to J. Tranquada, S. Billinge, I. Robinson, I. Zaliznyak, A. Lappas, and A. Tsvelik for fruitful discussions and critical comments.

Open Access: hybrid, Green Submitted

Output Date: 2023-01-27

Record 36 of 125

Title: Pressure tuning of structure, superconductivity, and novel magnetic order in the Ce-underdoped electron-doped cuprate $T' = \text{Pr}_{1.3-x}\text{La}_{0.7}\text{Ce}_x\text{CuO}_4$ ($x=0.1$)

Author(s): Guguchia, Z (Guguchia, Z.); Adachi, T (Adachi, T.); Shermadini, Z (Sheradini, Z.); Ohgi, T (Ohgi, T.); Chang, J (Chang, J.); Bozin, ES (Bozin, E. S.); von Rohr, F (von Rohr, F.); dos Santos, AM (dos Santos, A. M.); Molaison, JJ (Molaison, J. J.); Boehler, R (Boehler, R.); Koike, Y (Koike, Y.); Wieteska, AR (Wieteska, A. R.); Frandsen, BA (Frandsen, B. A.); Morenzoni, E (Morenzoni, E.); Amato, A (Amato, A.); Billinge, SJL (Billinge, S. J. L.); Uemura, YJ (Uemura, Y. J.); Khasanov, R (Khasanov, R.)

Source: PHYSICAL REVIEW B **Volume:** 96 **Issue:** 9 **Article Number:** 094515 **DOI:** 10.1103/PhysRevB.96.094515 **Published:** SEP 14 2017

Times Cited in Web of Science Core Collection: 5

Total Times Cited: 5

Usage Count (Last 180 days): 0

Usage Count (Since 2013): 26

Cited Reference Count: 66

Abstract: High-pressure neutron powder diffraction, muon-spin rotation, and magnetization studies of the structural, magnetic, and the superconducting properties of the Ce-underdoped superconducting (SC) electron-doped cuprate system with the Nd₂CuO₄ (the so-called T') structure T'-Pr_{1.3-x}La_{0.7}Ce_xCuO₄ with x = 0.1 are reported. A strong reduction of the in-plane and out-of-plane lattice constants is observed under pressure. However, no indication of any pressure-induced phase transition from T' to the K₂NiF₄ (the so-called T) structure is observed up to the maximum applied pressure of p = 11 GPa. Large and nonlinear increase of the short-range magnetic order temperature T_{so} in T'-Pr_{1.3-x}La_{0.7}Ce_xCuO₄ (x = 0.1) was observed under pressure. Simultaneous pressure causes a nonlinear decrease of the SC transition temperature T_c. All these experiments establish the short-range magnetic order as an intrinsic and competing phase in SC T'-Pr_{1.3-x}La_{0.7}Ce_xCuO₄ (x = 0.1). The observed pressure effects may be interpreted in terms of the improved nesting conditions through the reduction of the in-plane and out-of-plane lattice constants upon hydrostatic pressure.

Accession Number: WOS:000410860900003

Language: English

Document Type: Article

KeyWords Plus: STATIC ANTIFERROMAGNETIC CORRELATIONS; HIGH-TEMPERATURE SUPERCONDUCTOR; DENSITY-WAVE ORDER; GROUND-STATE; NEUTRON-SCATTERING; CRYSTAL-STRUCTURE; PHASE-DIAGRAM; TRANSPORT; FIELD; DEPENDENCE

Addresses: [Guguchia, Z.; Wieteska, A. R.; Uemura, Y. J.] Columbia Univ, Dept Phys, 538 W 120th St, New York, NY 10027 USA.

[Guguchia, Z.; Shermadini, Z.; Morenzoni, E.; Amato, A.; Khasanov, R.] Paul Scherrer Inst, Lab Muon Spin Spect, CH-5232 Villigen, Switzerland.

[Guguchia, Z.; Bozin, E. S.; Billinge, S. J. L.] Brookhaven Natl Lab, Condensed Matter Phys & Mat Sci Dept, Upton, NY 11973 USA.

[Adachi, T.] Sophia Univ, Dept Engn & Appl Sci, Chiyoda Ku, 7-1 Kioi Cho, Tokyo 1028554, Japan.

[Ohgi, T.; Koike, Y.] Tohoku Univ, Dept Appl Phys, Aoba Ku, 6-6-05 Aoba, Sendai, Miyagi 9808579, Japan.

[Chang, J.; von Rohr, F.] Univ Zurich, Inst Phys, Winterthurerstr 190, CH-8057 Zurich, Switzerland.

[dos Santos, A. M.; Molaison, J. J.; Boehler, R.] Oak Ridge Natl Lab, Neutron Sci Directorate, Oak Ridge, TN 37831 USA.

[Boehler, R.] Carnegie Inst Sci, Washington, DC 20005 USA.

[Frandsen, B. A.] Lawrence Berkeley Natl Lab, Div Mat Sci, Berkeley, CA 94720 USA.

[Billinge, S. J. L.] Columbia Univ, Dept Appl Phys & Appl Math, New York, NY 10027 USA.

Corresponding Address: Guguchia, Z (corresponding author), Columbia Univ, Dept Phys, 538 W 120th St, New York, NY 10027 USA.

Guguchia, Z (corresponding author), Paul Scherrer Inst, Lab Muon Spin Spect, CH-5232 Villigen, Switzerland.

Guguchia, Z (corresponding author), Brookhaven Natl Lab, Condensed Matter Phys & Mat Sci Dept, Upton, NY 11973 USA.

E-mail Addresses: zg2268@columbia.edu

Affiliations: Columbia University; Swiss Federal Institutes of Technology Domain; Paul Scherrer Institute; United States Department of Energy (DOE); Brookhaven National Laboratory; Sophia University; Tohoku University; University of Zurich; United States Department of Energy (DOE); Oak Ridge National Laboratory; Carnegie Institution for Science; United States Department of Energy (DOE); Lawrence Berkeley National Laboratory; Columbia University

Author Identifiers:

Author	Web of Science ResearcherID	ORCID Number
Santos, Antonio M dos	A-5602-2016	0000-0001-6900-0816
Bozin, Emil	AAB-4551-2020	
Morenzoni, Elvezio	R-3541-2019	0000-0002-9663-4213
Chang, Johan	F-1506-2014	0000-0002-4655-1516
Amato, Alex	H-7674-2013	0000-0001-9963-7498

Frandsen, Benjamin	AAJ-1680-2020	0000-0002-4047-9453
Boehler, Reinhard	L-3971-2016	0000-0003-0222-6997
Guguchia, Zurab		0000-0002-0764-7574
Khasanov, Rustem		0000-0002-4768-5524

Publisher: AMER PHYSICAL SOC

Publisher Address: ONE PHYSICS ELLIPSE, COLLEGE PK, MD 20740-3844 USA

Web of Science Index: Science Citation Index Expanded (SCI-EXPANDED)

Web of Science Categories: Materials Science, Multidisciplinary; Physics, Applied; Physics, Condensed Matter

Research Areas: Materials Science; Physics

IDS Number: FH0WI

ISSN: 2469-9950

eISSN: 2469-9969

29-char Source Abbrev.: PHYS REV B

ISO Source Abbrev.: Phys. Rev. B

Source Item Page Count: 11

Funding:

Funding Agency	Grant Number
Swiss National Science Foundation	P2ZHP2-161980
US NSF	DMR-1436095
NSF	DMR-1610633
REIMEI project of Japan Atomic Energy Agency	
U.S. Department of Energy, Office of Science, Office of Basic Energy Sciences (DOE-BES)	DE-SC00112704
Swiss National Science Foundation	
JSPS KAKENHI	23540399
MEXT KAKENHI	23108004
Division Of Materials Research	1436095

The mu SR experiments were carried out at the Swiss Muon Source (S mu S) Paul Scherrer Insitute, Villigen, Switzerland. A portion of this research used resources at the Spallation Neutron Source, a DOE Office of Science User Facility operated by the Oak Ridge National Laboratory. Z.G. gratefully acknowledges the financial support by the Swiss National Science Foundation (Early Postdoc Mobility SNFfellowship P2ZHP2-161980). Work at the Department of Physics of Columbia University is supported by US NSF DMR-1436095 (DMREF) and NSF DMR-1610633 as well as the REIMEI project of Japan Atomic Energy Agency. Work at Brookhaven National Laboratory was supported by the U.S. Department of Energy, Office of Science, Office of Basic Energy Sciences (DOE-BES) under Contract No. DE-SC00112704. Z.G. thanks H. Keller, A. Shengelaya, H. Luetkens, A.N. Pasupathy, and R.M. Fernandes for useful discussions. J.C. gratefully acknowledges financial support by the Swiss National Science Foundation. T.A. and Y.K. acknowledge support from JSPS KAKENHI Grant No. 23540399 and by MEXT KAKENHI Grant No. 23108004.

Open Access: Green Published, hybrid, Green Submitted

Output Date: 2023-01-27

Record 37 of 125

Title: Complementary approaches for the evaluation of biocompatibility of Y-90-labeled superparamagnetic citric acid (Fe,Er)(3)O-4 coated nanoparticles

Author(s): Antic, B (Antic, Bratislav); Boskovic, M (Boskovic, Marko); Nikodinovic-Runic, J (Nikodinovic-Runic, Jasmina); Ming, Y (Ming, Yue); Zhang, HG (Zhang, Hongguo); Bozin, ES (Bozin, Emil S.); Jankovic, D (Jankovic, Drina); Spasojevic, V (Spasojevic, Vojislav); Vranjes-Djuric, S (Vranjes-Djuric, Sanja)

Source: MATERIALS SCIENCE AND ENGINEERING C-MATERIALS FOR BIOLOGICAL APPLICATIONS **Volume:** 75 **Pages:** 157-164 **DOI:** 10.1016/j.msec.2017.02.023 **Published:** JUN 1 2017

Times Cited in Web of Science Core Collection: 4

Total Times Cited: 4

Usage Count (Last 180 days): 0

Usage Count (Since 2013): 34

Cited Reference Count: 27

Abstract: Magnetic nanoparticles (MNPs) are of immense interest for diagnostic and therapeutic applications in medicine. Design and development of new iron oxide-based MNPs for such applications is of rather limited breadth without reliable and sensitive methods to determine their levels in body tissues. Commonly used methods, such as ICP, are quite problematic, due to the inability to decipher the origin of the detected iron, i.e. whether it originates from the MNPs or endogenous from tissues and bodily fluids. One of the approaches to overcome this problem and to increase reliability of tracing MNPs is to partially substitute iron ions in the MNPs with Er. Here, we report on the development of citric acid coated (Fe,Er)(3)O₄ nanoparticles and characterization of their physico-chemical and biological properties by utilization of various complementary approaches. The synthesized MNPs had a narrow (6-7 nm) size distribution, as consistently seen in atomic pair distribution function, transmission electron microscopy, and DC magnetization measurements. The particles were found to be superparamagnetic, with a pronounced maximum in measured zero-field cooled magnetization at around 90 K. Reduction in saturation magnetization due to incorporation of 1.7% Er³⁺ into the Fe₃O₄ matrix was clearly observed. From the biological standpoint, citric acid coated (Fe,Er)(3)O₄ NPs were found to induce low toxicity both in human cell fibroblasts and in zebrafish (*Danio rerio*) embryos. Biodistribution pattern of the MNPs after intravenous administration in healthy Wistar rats was followed by the radiotracer method, revealing that Y-90-labeled MNPs were predominantly found in liver (75.33% ID), followed by lungs (16.70% ID) and spleen (2.83% ID). Quantitative agreement with these observations was obtained by ICP-MS elemental analysis using Er as the detected tracer. Based on the favorable physical, chemical and biological characteristics, citric acid coated (Fe,Er)(3)O₄ MNPs could be further considered for the potential application as a diagnostic and/or therapeutic agent. This work also demonstrates that combined application of these techniques is a promising tool for studies of pharmacokinetics of the new MNPs in complex biological systems. (C) 2017 Elsevier B.V. All rights reserved.

Accession Number: WOS:000400720800019

PubMed ID: 28415449

Language: English

Document Type: Article

Author Keywords: Magnetic nanoparticle; Biodistribution; Embryotoxicity; Radiolabeling; MNP

KeyWords Plus: MAGNETIC NANOPARTICLES; BIODISTRIBUTION; FUNCTIONALIZATION; PHARMACOKINETICS; TOXICITY

Addresses: [Antic, Bratislav; Boskovic, Marko; Jankovic, Drina; Spasojevic, Vojislav; Vranjes-Djuric, Sanja] Univ Belgrade, Vinca Inst Nucl Sci, POB 522, Belgrade 11001, Serbia.

[Nikodinovic-Runic, Jasmina] Univ Belgrade, Inst Mol Genet & Genet Engn, Vojvode Stepe 444a, Belgrade 11010, Serbia.

[Ming, Yue; Zhang, Hongguo] Beijing Univ Technol, Coll Mat Sci & Engn, Pingleyuan 100, Beijing 100124, Peoples R China.

[Bozin, Emil S.] Brookhaven Natl Lab, Condensed Matter Phys & Mat Sci Dept, Upton, NY 11973 USA.

Corresponding Address: Antic, B (corresponding author), Univ Belgrade, Vinca Inst Nucl Sci, POB 522, Belgrade 11001, Serbia.

Ming, Y (corresponding author), Beijing Univ Technol, Coll Mat Sci & Engn, Pingleyuan 100, Beijing 100124, Peoples R China.

E-mail Addresses: bantic@vinca.rs; yueming@bjut.edu.cn

Affiliations: University of Belgrade; University of Belgrade; Beijing University of Technology; United States Department of Energy (DOE); Brookhaven National Laboratory

Author Identifiers:

Author	Web of Science ResearcherID	ORCID Number
Nikodinovic-Runic, Jasmina	W-1277-2018	0000-0002-2553-977X
Bozin, Emil	AAB-4551-2020	
Nikodinovic-Runic, Jasmina	ABD-4022-2020	
Spasojevic, Vojislav		0000-0002-6134-8989
Jankovic, Drina		0000-0003-3938-2790
Boskovic, Marko		0000-0002-7466-9693
Antic, Bratislav		0000-0002-5693-6401
Vranjes-Djuric, Sanja		0000-0002-6340-2387

Publisher: ELSEVIER

Publisher Address: RADARWEG 29, 1043 NX AMSTERDAM, NETHERLANDS

Web of Science Index: Science Citation Index Expanded (SCI-EXPANDED)

Web of Science Categories: Materials Science, Biomaterials

Research Areas: Materials Science

IDS Number: EU0SE

ISSN: 0928-4931

eISSN: 1873-0191

29-char Source Abbrev.: MAT SCI ENG C-MATER

ISO Source Abbrev.: Mater. Sci. Eng. C-Mater. Biol. Appl.

Source Item Page Count: 8

Funding:

Funding Agency	Grant Number
Ministry of Education, Science and. Technological Development of the Republic of Serbia	III45015
International S&T Cooperation Program of China	2015DFG52020
MSTD, Republic of Serbia	OI173048
US DOE, Office of Science, Office of Basic Energy Sciences (DOE-BES)	DE-SC00112704

The Ministry of Education, Science and. Technological Development of the Republic of Serbia supported this work financially through the Project Grant No. III45015. The work of Y.M. and H.Z. was supported by International S&T Cooperation Program of China (2015DFG52020). JNR was partially supported by OI173048 (MSTD, Republic of Serbia). The author thanks Dr. Biljana Dojcinovic for helpful discussions concerning ICP-MS results and for help to perform ICP-MS experiments. Structural characterizations have benefited from X-ray diffraction data collected at X17A beam line of the National Synchrotron Light Source at Brookhaven National Laboratory. ESB acknowledges Milinda Abeykoon for help with X-ray data collection. Nanoparticle structural characterization work at Brookhaven National Laboratory was supported by the US DOE, Office of Science, Office of Basic Energy Sciences (DOE-BES), under Contract No. DE-SC00112704.

Open Access: Green Accepted, Green Submitted, Bronze

Output Date: 2023-01-27

Record 38 of 125

Title: Superconducting order from disorder in 2H-TaSe₂-xS_x

Author(s): Li, LJ (Li, Lijun); Deng, XY (Deng, Xiaoyu); Wang, Z (Wang, Zhen); Liu, Y (Liu, Yu); Abeykoon, M (Abeykoon, Milinda); Dooryhee, E (Dooryhee, Eric); Tomic, A (Tomic, Aleksandra); Huang, YN (Huang, Yanan); Warren, JB (Warren, John B.); Bozin, ES (Bozin, Emil S.); Billinge, SJL (Billinge, Simon J. L.); Sun, YP (Sun, Yuping); Zhu, YM (Zhu, Yimei); Kotliar, G (Kotliar, Gabriel); Petrovic, C (Petrovic, Cedomir)

Source: NPJ QUANTUM MATERIALS **Volume:** 2 **Article Number:** 11 **DOI:** 10.1038/s41535-017-0016-9 **Published:** FEB 24 2017

Times Cited in Web of Science Core Collection: 54

Total Times Cited: 54

Usage Count (Last 180 days): 4

Usage Count (Since 2013): 40

Cited Reference Count: 43

Abstract: We report on the emergence of robust superconducting order in single crystal alloys of TaSe_{2-x}S_x (0 ≤ x ≤ 2). The critical temperature of the alloy is surprisingly higher than that of the two end compounds TaSe₂ and TaS₂. The evolution of superconducting critical temperature T_c(x) correlates with the full width at half maximum of the Bragg peaks and with the linear term of the high-temperature resistivity. The conductivity of the crystals near the middle of the alloy series is higher or similar than that of either one of the end members 2H-TaSe₂ and/or 2H-TaS₂. It is known that in these materials superconductivity is in close competition with charge density wave order. We interpret our experimental findings in a picture where disorder tilts this balance in favor of superconductivity by destroying the charge density wave order.

Accession Number: WOS:000407417500001

Language: English

Document Type: Article

KeyWords Plus: CHARGE; DYNAMICS; 2H-NBSE2; 2H-TAS2

Addresses: [Li, Lijun; Wang, Zhen; Liu, Yu; Huang, Yanan; Bozin, Emil S.; Billinge, Simon J. L.; Zhu, Yimei; Kotliar, Gabriel; Petrovic, Cedomir] Brookhaven Natl Lab, Condensed Matter Phys & Mat Sci Dept, Upton, NY 11973 USA.

[Li, Lijun; Sun, Yuping] Chinese Acad Sci, Key Lab Mat Phys, Inst Solid State Phys, Hefei 230031, Anhui, Peoples R China.

[Deng, Xiaoyu; Kotliar, Gabriel] Rutgers State Univ, Dept Phys & Astron, Piscataway, NJ 08854 USA.

[Abeykoon, Milinda; Dooryhee, Eric] Brookhaven Natl Lab, Photon Sci Directorate, Upton, NY 11973 USA.

[Tomic, Aleksandra; Billinge, Simon J. L.] Columbia Univ, Dept Appl Phys & Appl Math, New York, NY 10027 USA.

[Warren, John B.] Brookhaven Natl Lab, Instrumentat Div, Upton, NY 11973 USA.

[Huang, Yanan] Chinese Acad Sci, High Magnet Field Lab, Hefei 230031, Peoples R China.

Corresponding Address: Li, LJ (corresponding author), Brookhaven Natl Lab, Condensed Matter Phys & Mat Sci Dept, Upton, NY 11973 USA.

E-mail Addresses: lilijun@issp.ac.cn; petrovic@bnl.gov

Affiliations: United States Department of Energy (DOE); Brookhaven National Laboratory; Chinese Academy of Sciences; Hefei Institutes of Physical Science, CAS; Rutgers State University New Brunswick; United States Department of Energy (DOE); Brookhaven National Laboratory; Columbia University; United States Department of Energy (DOE); Brookhaven National Laboratory; Chinese Academy of Sciences; Hefei Institutes of Physical Science, CAS

Author Identifiers:

Author	Web of Science ResearcherID	ORCID Number
Bozin, Emil	AAB-4551-2020	
Z, Z	GPT-1884-2022	
Z, Z	HHN-3970-2022	
Z, Z	GWQ-2914-2022	
Z, Z	GXZ-4805-2022	

Liu, Yu | ABD-2488-2021 | 0000-0001-8886-2876

Publisher: NATURE PUBLISHING GROUP

Publisher Address: MACMILLAN BUILDING, 4 CRINAN ST, LONDON N1 9XW, ENGLAND

Web of Science Index: Science Citation Index Expanded (SCI-EXPANDED)

Web of Science Categories: Materials Science, Multidisciplinary; Quantum Science & Technology; Physics, Applied; Physics, Condensed Matter

Research Areas: Materials Science; Physics

IDS Number: FD3EY

eISSN: 2397-4648

29-char Source Abbrev.: NPJ QUANTUM MATER

ISO Source Abbrev.: npj Quantum Mater.

Source Item Page Count: 7

Funding:

Funding Agency	Grant Number
U.S. DOE	DESC00112704
National Natural Science Foundation of China	11404342
U.S. Department of Energy, Office of Science, Office of Basic Energy Sciences	DE-SC0012704
AFOSR MURI program	
U.S. Department of energy, Office of Science, Basic Energy Sciences, Computational Materials Science Program	

Work at Brookhaven is supported by the U.S. DOE under Contract No. DESC00112704. Work at Institute of Solid State Physics of CAS is supported by the National Natural Science Foundation of China, Grant No. 11404342. Use of the National Synchrotron Light Source II, Brookhaven National Laboratory, was supported by the U.S. Department of Energy, Office of Science, Office of Basic Energy Sciences, under Contract No. DE-SC0012704. X.D. is supported by AFOSR MURI program. Y.L. and G.K. are supported by U.S. Department of energy, Office of Science, Basic Energy Sciences as a part of the Computational Materials Science Program.

Open Access: Green Published, gold, Green Submitted

Output Date: 2023-01-27

Record 39 of 125

Title: Cuproiridsite - orbital parts unknown

Author(s): Bozin, ES (Bozin, Emil S.)

Source: ACTA CRYSTALLOGRAPHICA A-FOUNDATION AND ADVANCES **Volume:** 73 **Pages:** A121-A121 **DOI:** 10.1107/S0108767317098798 **Supplement:** S **Published:** 2017

Times Cited in Web of Science Core Collection: 0

Total Times Cited: 0

Usage Count (Last 180 days): 0

Usage Count (Since 2013): 0

Cited Reference Count: 0

Accession Number: WOS:000477683800121

Language: English

Document Type: Meeting Abstract

Addresses: [Bozin, Emil S.] Brookhaven Natl Lab, Upton, NY 11973 USA.

Affiliations: United States Department of Energy (DOE); Brookhaven National Laboratory

Author Identifiers:

Author	Web of Science ResearcherID	ORCID Number
Bozin, Emil	AAB-4551-2020	

Publisher: INT UNION CRYSTALLOGRAPHY**Publisher Address:** 2 ABBEY SQ, CHESTER, CH1 2HU, ENGLAND**Web of Science Index:** Science Citation Index Expanded (SCI-EXPANDED)**Web of Science Categories:** Chemistry, Multidisciplinary; Crystallography**Research Areas:** Chemistry; Crystallography**IDS Number:** VI3TU**ISSN:** 2053-2733**29-char Source Abbrev.:** ACTA CRYSTALLOGR A**ISO Source Abbrev.:** Acta Crystallogr. Sect. A**Source Item Page Count:** 1**Open Access:** Bronze**Output Date:** 2023-01-27

Record 40 of 125**Title:** PbTe studied by 3D-Delta PDF analysis and ab-initio simulations**Author(s):** Weber, T (Weber, Thomas); Sangiorgio, B (Sangiorgio, Boris); Billinge, S (Billinge, Simon); Bozin, E (Bozin, Emil); Malliakas, C (Malliakas, Christos); Kanatzidis, M (Kanatzidis, Mercouri); Simonov, A (Simonov, Arkadiy); Spaldin, N (Spaldin, Nicola)**Source:** ACTA CRYSTALLOGRAPHICA A-FOUNDATION AND ADVANCES **Meeting Abstract:** MS076.O03 **Volume:** 73 **Pages:** C1044-C1044 **DOI:** 10.1107/S2053273317085308 **Supplement:** S **Published:** 2017**Times Cited in Web of Science Core Collection:** 0**Total Times Cited:** 0**Usage Count (Last 180 days):** 0**Usage Count (Since 2013):** 1**Cited Reference Count:** 3**Accession Number:** WOS:000481522001047**Language:** English**Document Type:** Meeting Abstract**Author Keywords:** PbTe; 3D-Delta PDF; ab-initio simulation**Addresses:** [Weber, Thomas; Sangiorgio, Boris; Spaldin, Nicola] Swiss Fed Inst Technol, Dept Mat, Zurich, Switzerland.

[Billinge, Simon] Columbia Univ, Dept Appl Phys & Appl Math, New York, NY USA.

[Bozin, Emil] Columbia Univ, BNL Xray Grp, New York, NY USA.

[Malliakas, Christos; Kanatzidis, Mercouri] Northwestern Univ, Dept Chem, Evanston, IL USA.

[Simonov, Arkadiy] Univ Oxford, Inorgan Chem Lab, Oxford, England.

E-mail Addresses: thomas.weber@mat.ethz.ch**Affiliations:** Swiss Federal Institutes of Technology Domain; ETH Zurich; Columbia University; Columbia University; Northwestern University; University of Oxford**Author Identifiers:**

Author	Web of Science ResearcherID	ORCID Number
Spaldin, Nicola A	A-1017-2010	0000-0003-0709-9499
Bozin, Emil	AAB-4551-2020	

Publisher: INT UNION CRYSTALLOGRAPHY

Publisher Address: 2 ABBEY SQ, CHESTER, CH1 2HU, ENGLAND

Web of Science Index: Science Citation Index Expanded (SCI-EXPANDED)

Web of Science Categories: Chemistry, Multidisciplinary; Crystallography

Research Areas: Chemistry; Crystallography

IDS Number: VI3XK

ISSN: 2053-2733

29-char Source Abbrev.: ACTA CRYSTALLOGR A

ISO Source Abbrev.: Acta Crystallogr. Sect. A

Source Item Page Count: 1

Open Access: Bronze

Output Date: 2023-01-27

Record 41 of 125

Title: Multiband electronic transport in α -Yb(1-x)Sr(x)AlB₄ [x=0, 0.19(3)] single crystals

Author(s): Ryu, H (Ryu, Hyejin); Abeykoon, M (Abeykoon, Milinda); Bozin, E (Bozin, Emil); Matsumoto, Y (Matsumoto, Yosuke); Nakatsuji, S (Nakatsuji, S.); Petrovic, C (Petrovic, C.)

Source: JOURNAL OF PHYSICS-CONDENSED MATTER **Volume:** 28 **Issue:** 42 **Article Number:** 425602 **DOI:** 10.1088/0953-8984/28/42/425602 **Published:** OCT 26 2016

Times Cited in Web of Science Core Collection: 0

Total Times Cited: 0

Usage Count (Last 180 days): 0

Usage Count (Since 2013): 21

Cited Reference Count: 31

Abstract: We report on the evidence for the multiband electronic transport in α -YbAlB₄ and α -Yb_{0.81(2)}Sr_{0.19(3)}AlB₄. Multiband transport reveals itself below 10 K in both compounds via Hall effect measurements, whereas anisotropic magnetic ground state sets in below 3 K in α -Yb_{0.81(2)}Sr_{0.19(3)}AlB₄. Our results show that Sr²⁺ substitution enhances conductivity, but does not change the quasiparticle mass of bands induced by heavy fermion hybridization.

Accession Number: WOS:000383990600002

Language: English

Document Type: Article

Author Keywords: superconductivity; electronic transport; magnetism

KeyWords Plus: PHYSICAL-PROPERTIES; HIGH-PRESSURE; SUPERCONDUCTIVITY; BEHAVIOR; YB

Addresses: [Ryu, Hyejin; Abeykoon, Milinda; Bozin, Emil; Petrovic, C.] Brookhaven Natl Lab, Condensed Matter Phys & Mat Sci Dept, Upton, NY 11973 USA.

[Ryu, Hyejin; Petrovic, C.] SUNY Stony Brook, Dept Phys & Astron, Stony Brook, NY 11794 USA.

[Matsumoto, Yosuke; Nakatsuji, S.; Petrovic, C.] Univ Tokyo, Inst Solid State Phys, Kashiwa, Chiba 2778581, Japan.

[Ryu, Hyejin] EO Lawrence Berkeley Natl Lab Berkeley, Adv Light Source, Berkeley, CA 94720 USA.

Corresponding Address: Petrovic, C (corresponding author), Brookhaven Natl Lab, Condensed Matter Phys & Mat Sci Dept, Upton, NY 11973 USA.

Petrovic, C (corresponding author), SUNY Stony Brook, Dept Phys & Astron, Stony Brook, NY 11794 USA.

Petrovic, C (corresponding author), Univ Tokyo, Inst Solid State Phys, Kashiwa, Chiba 2778581, Japan.

E-mail Addresses: petrovic@bnl.gov

Affiliations: United States Department of Energy (DOE); Brookhaven National Laboratory; State University of New York (SUNY) System; State University of New York (SUNY) Stony Brook; University of Tokyo; United States Department of Energy (DOE); Lawrence Berkeley National Laboratory

Author Identifiers:

Author	Web of Science ResearcherID	ORCID Number
Bozin, Emil	AAB-4551-2020	
Matsumoto, Yosuke	N-6566-2018	0000-0001-8522-7113
Nakatsuji, Satoru		0000-0001-9134-659X

Publisher: IOP PUBLISHING LTD

Publisher Address: TEMPLE CIRCUS, TEMPLE WAY, BRISTOL BS1 6BE, ENGLAND

Web of Science Index: Science Citation Index Expanded (SCI-EXPANDED)

Web of Science Categories: Physics, Condensed Matter

Research Areas: Physics

IDS Number: DW900

ISSN: 0953-8984

eISSN: 1361-648X

29-char Source Abbrev.: J PHYS-CONDENS MAT

ISO Source Abbrev.: J. Phys.-Condes. Matter

Source Item Page Count: 5

Funding:

Funding Agency	Grant Number
U.S. DOE	DE-SC00112704
JSPS, Japan	25707030
ISSP at the University of Tokyo	
Grants-in-Aid for Scientific Research	16H04011

Work at Brookhaven is supported by the U.S. DOE under Contract No. DE-SC00112704. This work has benefited from using the X7B beamline of the NSLS at Brookhaven Laboratory. We thank John B Warren for help with scanning electron microscopy measurements, and Jonathan Hanson for help with x-ray measurements. This work is partially supported by Grant-in-Aid for Scientific Research (No. 25707030) from JSPS, Japan. CP acknowledges ISSP at the University of Tokyo for its hospitality and financial support.

Open Access: Green Submitted

Output Date: 2023-01-27

Record 42 of 125

Title: Magnetotransport study of Dirac fermions in YbMnBi₂ antiferromagnet

Author(s): Wang, AF (Wang, Aifeng); Zaliznyak, I (Zaliznyak, I.); Ren, WJ (Ren, Weijun); Wu, LJ (Wu, Lijun); Graf, D (Graf, D.); Garlea, VO (Garlea, V. O.); Warren, JB (Warren, J. B.); Bozin, E (Bozin, E.); Zhu, YM (Zhu, Yimei); Petrovic, C (Petrovic, C.)

Source: PHYSICAL REVIEW B **Volume:** 94 **Issue:** 16 **Article Number:** 165161 **DOI:** 10.1103/PhysRevB.94.165161 **Published:** OCT 24 2016

Times Cited in Web of Science Core Collection: 59

Total Times Cited: 60

Usage Count (Last 180 days): 13

Usage Count (Since 2013): 97

Cited Reference Count: 48

Abstract: We report quantum transport and Dirac fermions in YbMnBi₂ single crystals. YbMnBi₂ is a layered material with anisotropic conductivity and magnetic order below 290 K. Magnetotransport properties, nonzero Berry phase, and small cyclotron mass indicate the presence of Dirac fermions. Angular-dependent magnetoresistance indicates a possible quasi-two-dimensional Fermi surface, whereas the deviation from the nontrivial Berry phase expected for Dirac states suggests the contribution of parabolic bands at the Fermi level or spin-orbit coupling.

Accession Number: WOS:000390034000006

Language: English

Document Type: Article

KeyWords Plus: TOPOLOGICAL INSULATORS; ULTRAHIGH MOBILITY; SEMIMETAL CD₃AS₂; GRAPHENE; WEYL; MAGNETORESISTANCE; ARCS

Addresses: [Wang, Aifeng; Zaliznyak, I.; Ren, Weijun; Wu, Lijun; Bozin, E.; Zhu, Yimei; Petrovic, C.] Brookhaven Natl Lab, Condensed Matter Phys & Mat Sci Dept, Upton, NY 11973 USA.

[Ren, Weijun] Chinese Acad Sci, Shenyang Natl Lab Mat Sci, Inst Met Res, Shenyang 110016, Peoples R China.

[Graf, D.] Florida State Univ, Natl High Magnet Field Lab, Tallahassee, FL 32306 USA.

[Garlea, V. O.] Oak Ridge Natl Lab, Quantum Condensed Matter Div, Oak Ridge, TN 37831 USA.

[Warren, J. B.] Brookhaven Natl Lab, Instrument Div, Upton, NY 11973 USA.

Corresponding Address: Wang, AF (corresponding author), Brookhaven Natl Lab, Condensed Matter Phys & Mat Sci Dept, Upton, NY 11973 USA.

Affiliations: United States Department of Energy (DOE); Brookhaven National Laboratory; Chinese Academy of Sciences; Institute of Metal Research, CAS; State University System of Florida; Florida State University; United States Department of Energy (DOE); Oak Ridge National Laboratory; United States Department of Energy (DOE); Brookhaven National Laboratory

Author Identifiers:

Author	Web of Science ResearcherID	ORCID Number
Zaliznyak, Igor	AAW-2535-2020	0000-0002-8548-7924
Graf, David	X-2245-2018	0000-0001-6195-0462
Wang, Aifeng	AAQ-2894-2020	0000-0003-2425-3259
Zaliznyak, Igor	E-8532-2014	0000-0002-8548-7924
Ren, Wei Jun	C-6551-2008	0000-0003-2894-7442
Bozin, Emil	AAB-4551-2020	
li, bing	GWQ-9617-2022	
Garlea, Vasile Ovidiu	A-4994-2016	0000-0002-5322-7271

Publisher: AMER PHYSICAL SOC

Publisher Address: ONE PHYSICS ELLIPSE, COLLEGE PK, MD 20740-3844 USA

Web of Science Index: Science Citation Index Expanded (SCI-EXPANDED)

Web of Science Categories: Materials Science, Multidisciplinary; Physics, Applied; Physics, Condensed Matter

Research Areas: Materials Science; Physics

IDS Number: EF0RQ

ISSN: 2469-9950

eISSN: 2469-9969

29-char Source Abbrev.: PHYS REV B

ISO Source Abbrev.: Phys. Rev. B

Source Item Page Count: 6

Funding:

Funding Agency	Grant Number
U.S. Department of Energy-BES, Division of Materials Science and Engineering	DE-SC0012704
NSF	DMR-0654118
state of Florida	
Scientific User Facilities Division, Office of Basic Energy Sciences, U.S. Department of Energy	

V.O.G. gratefully acknowledge H. Cao for the support during the neutron diffraction experiment. Work at BNL was supported by the U.S. Department of Energy-BES, Division of Materials Science and Engineering, under Contract No. DE-SC0012704. Work at the National High Magnetic Field Laboratory is supported by the NSF Cooperative Agreement No. DMR-0654118, and by the state of Florida. Work at the Oak Ridge National Laboratory was sponsored by the Scientific User Facilities Division, Office of Basic Energy Sciences, U.S. Department of Energy. X-ray scattering data were collected at the 28-ID-C x-ray powder diffraction beam line at National Synchrotron Light Source II at Brookhaven National Laboratory.

Open Access: hybrid, Green Submitted

Output Date: 2023-01-27

Record 43 of 125

Title: Interlayer electronic transport in CaMnBi₂ antiferromagnet

Author(s): Wang, AF (Wang, Aifeng); Graf, D (Graf, D.); Wu, LJ (Wu, Lijun); Wang, KF (Wang, Kefeng); Bozin, E (Bozin, E.); Zhu, YM (Zhu, Yimei); Petrovic, C (Petrovic, C.)

Source: PHYSICAL REVIEW B **Volume:** 94 **Issue:** 12 **Article Number:** 125118 **DOI:** 10.1103/PhysRevB.94.125118 **Published:** SEP 12 2016

Times Cited in Web of Science Core Collection: 17

Total Times Cited: 17

Usage Count (Last 180 days): 2

Usage Count (Since 2013): 52

Cited Reference Count: 34

Abstract: We report interlayer electronic transport in CaMnBi₂ single crystals. Quantum oscillations and angular magnetoresistance suggest coherent electronic conduction and valley polarized conduction of Dirac states. The small cyclotron mass, high mobility of carriers, and nontrivial Berry's phase are consistent with the presence of Dirac fermions on the side wall of the warped cylindrical Fermi surface. Similarly to SrMnBi₂, which features an anisotropic Dirac cone, our results suggest that magnetic-field-induced changes in interlayer conduction are also present in layered bismuth-based materials with a zero-energy line in momentum space created by the staggered alkaline earth atoms.

Accession Number: WOS:000383145300004

Language: English

Document Type: Article

KeyWords Plus: MAGNETORESISTANCE; BISMUTH; ANISOTROPY; GRAPHENE; ANGLE

Addresses: [Wang, Aifeng; Wu, Lijun; Wang, Kefeng; Bozin, E.; Zhu, Yimei; Petrovic, C.] Brookhaven Natl Lab, Condensed Matter Phys & Mat Sci Dept, Upton, NY 11973 USA.

[Graf, D.] Florida State Univ, Natl High Magnet Field Lab, Tallahassee, FL 32306 USA.

[Wang, Kefeng] Univ Maryland, Dept Phys, College Pk, MD 20742 USA.

Corresponding Address: Wang, KF (corresponding author), Brookhaven Natl Lab, Condensed Matter Phys & Mat Sci Dept, Upton, NY 11973 USA.

Wang, KF (corresponding author), Univ Maryland, Dept Phys, College Pk, MD 20742 USA.

Affiliations: United States Department of Energy (DOE); Brookhaven National Laboratory; State University System of Florida; Florida State University; University System of Maryland; University of Maryland College Park

Author Identifiers:

Author	Web of Science ResearcherID	ORCID Number
Graf, David	X-2245-2018	0000-0001-6195-0462
Wang, Aifeng	AAQ-2894-2020	0000-0003-2425-3259
Bozin, Emil	AAB-4551-2020	

Publisher: AMER PHYSICAL SOC

Publisher Address: ONE PHYSICS ELLIPSE, COLLEGE PK, MD 20740-3844 USA

Web of Science Index: Science Citation Index Expanded (SCI-EXPANDED)

Web of Science Categories: Materials Science, Multidisciplinary; Physics, Applied; Physics, Condensed Matter

Research Areas: Materials Science; Physics

IDS Number: DV7VF

ISSN: 2469-9950

eISSN: 2469-9969

29-char Source Abbrev.: PHYS REV B

ISO Source Abbrev.: Phys. Rev. B

Source Item Page Count: 6

Funding:

Funding Agency	Grant Number
U.S. DOE-BES, Division of Materials Science and Engineering	DE-SC0012704
Scientific User Facilities Division, BES, U.S. DOE	
NSF	DMR-0654118
state of Florida	

Work at BNL was supported by the U.S. DOE-BES, Division of Materials Science and Engineering, under Contract No. DE-SC0012704. The experiment at ORNL Spallation Neutron Source was sponsored by the Scientific User Facilities Division, BES, U.S. DOE. Work at the National High Magnetic Field Laboratory was supported by the NSF Cooperative Agreement No. DMR-0654118 and by the state of Florida.

Open Access: Green Submitted, hybrid

Output Date: 2023-01-27

Record 44 of 125

Title: Nonpercolative nature of the metal-insulator transition and persistence of local Jahn-Teller distortions in the rhombohedral regime of $\text{La}_{1-x}\text{Ca}_x\text{MnO}_3$

Author(s): Shatnawi, M (Shatnawi, Mouath); Bozin, ES (Bozin, Emil S.); Mitchell, JF (Mitchell, J. F.); Billinge, SJL (Billinge, Simon J. L.)

Source: PHYSICAL REVIEW B **Volume:** 93 **Issue:** 16 **Article Number:** 165138 **DOI:** 10.1103/PhysRevB.93.165138 **Published:** APR 25 2016

Times Cited in Web of Science Core Collection: 11

Total Times Cited: 11

Usage Count (Last 180 days): 1

Usage Count (Since 2013): 52

Cited Reference Count: 59

Abstract: Evolution of the average and local crystal structure of Ca-doped LaMnO₃ has been studied across the metal to insulator (MI) and the orthorhombic to rhombohedral (OR) structural phase transitions over a broad temperature range for two Ca concentrations ($x = 0.18, 0.22$). Combined Rietveld and high real space resolution atomic pair distribution function (PDF) analysis of neutron total scattering data was carried out with aims of exploring the possibility of nanoscale phase separation (PS) in relation to MI transition, and charting the evolution of local Jahn-Teller (JT) distortion of MnO₆ octahedra across the OR transition at T-S similar to 720 K. The study utilized explicit two-phase PDF structural modeling, revealing that away from T-MI there is no evidence for nanoscale phase coexistence. The local JT distortions disappear abruptly upon crossing into the metallic regime both with doping and temperature, with only a small temperature-independent signature of quenched disorder being observable at low temperature as compared to CaMnO₃. The results hence do not support the percolative scenario for the MI transition in La_{1-x}CaxMnO₃ based on PS, and question its ubiquity in the manganites. In contrast to LaMnO₃ that exhibits long-range orbital correlations and sizable octahedral distortions at low temperature, the doped samples with compositions straddling the MI boundary exhibit correlations (in the insulating regime) limited to only similar to 1 nm with observably smaller distortions. In the $x = 0.22$ sample local JT distortions are found to persist across the OR transition and deep into the R phase (up to similar to 1050 K), where they are crystallographically prohibited. Their magnitude and subnanometer spatial extent remain unchanged.

Accession Number: WOS:000374950300010

Language: English

Document Type: Article

KeyWords Plus: ELECTRONIC PHASE-SEPARATION; COLOSSAL MAGNETORESISTANCE; CHARGE LOCALIZATION; FERROMAGNETIC PHASE; MAGNETIC PHASE; MANGANITES; TRANSPORT; DIFFRACTION; COEXISTENCE

Addresses: [Shatnawi, Mouath] Hashemite Univ, Dept Phys, Zarqa 13115, Jordan.

[Bozin, Emil S.; Billinge, Simon J. L.] Brookhaven Natl Lab, Dept Condensed Matter Phys & Mat Sci, Upton, NY 11973 USA.

[Mitchell, J. F.] Argonne Natl Lab, Div Mat Sci, 9700 S Cass Ave, Argonne, IL 60439 USA.

[Billinge, Simon J. L.] Columbia Univ, Dept Appl Phys & Appl Math, New York, NY 10027 USA.

Corresponding Address: Bozin, ES (corresponding author), Brookhaven Natl Lab, Dept Condensed Matter Phys & Mat Sci, Upton, NY 11973 USA.

E-mail Addresses: bozin@bnl.gov

Affiliations: Hashemite University; United States Department of Energy (DOE); Brookhaven National Laboratory; United States Department of Energy (DOE); Argonne National Laboratory; Columbia University

Author Identifiers:

Author	Web of Science ResearcherID	ORCID Number
Bozin, Emil	AAB-4551-2020	
Mitchell, John F	A-1907-2012	

Publisher: AMER PHYSICAL SOC

Publisher Address: ONE PHYSICS ELLIPSE, COLLEGE PK, MD 20740-3844 USA

Web of Science Index: Science Citation Index Expanded (SCI-EXPANDED)

Web of Science Categories: Materials Science, Multidisciplinary; Physics, Applied; Physics, Condensed Matter

Research Areas: Materials Science; Physics

IDS Number: DK5HF

ISSN: 2469-9950

eISSN: 2469-9969

29-char Source Abbrev.: PHYS REV B

ISO Source Abbrev.: Phys. Rev. B

Source Item Page Count: 10

Funding:

Funding Agency	Grant Number
U.S. DOE, Office of Science, Office of Basic Energy Sciences (DOE-BES)	DE-SC00112704
U.S. Department of Energy Office of Science, Basic Energy Sciences	
Materials Science and Engineering Division	
	DE-AC52-06NA25396

Work at Brookhaven National Laboratory was supported by U.S. DOE, Office of Science, Office of Basic Energy Sciences (DOE-BES) under Contract DE-SC00112704. Work in the Materials Science Division of Argonne National Laboratory (sample preparation and characterization) was sponsored by the U.S. Department of Energy Office of Science, Basic Energy Sciences, Materials Science and Engineering Division. Neutron PDF experiments were carried out on NPDF at LANSCE, funded by DOE BES; Los Alamos National Laboratory is operated by Los Alamos National Security LLC under Contract No. DE-AC52-06NA25396. E.S.B. gratefully acknowledges T.E. Proffen and J. Siewenie for assistance with the NPDF measurements.

Open Access: Green Submitted, hybrid

Output Date: 2023-01-27

Record 45 of 125

Title: Thermal evolution of antiferromagnetic correlations and tetrahedral bond angles in superconducting FeTe_{1-x}Sex

Author(s): Xu, ZJ (Xu, Zhijun); Schneeloch, JA (Schneeloch, J. A.); Wen, JS (Wen, Jinsheng); Bozin, ES (Bozin, E. S.); Granroth, GE (Granroth, G. E.); Winn, BL (Winn, B. L.); Feyngenson, M (Feyngenson, M.); Birgeneau, RJ (Birgeneau, R. J.); Gu, GD (Gu, Genda); Zaliznyak, IA (Zaliznyak, I. A.); Tranquada, JM (Tranquada, J. M.); Xu, GY (Xu, Guangyong)

Source: PHYSICAL REVIEW B **Volume:** 93 **Issue:** 10 **Article Number:** 104517 **DOI:** 10.1103/PhysRevB.93.104517 **Published:** MAR 14 2016

Times Cited in Web of Science Core Collection: 5

Total Times Cited: 5

Usage Count (Last 180 days): 0

Usage Count (Since 2013): 40

Cited Reference Count: 85

Abstract: It has recently been demonstrated that dynamical magnetic correlations measured by neutron scattering in iron chalcogenides can be described with models of short-range correlations characterized by particular choices of four-spin plaquettes, where the appropriate choice changes as the parent material is doped towards superconductivity. Here we apply such models to describe measured maps of magnetic scattering as a function of two-dimensional wave vectors obtained for optimally superconducting crystals of FeTe_{1-x}Sex. We show that the characteristic antiferromagnetic wave vector evolves from that of the bicollinear structure found in underdoped chalcogenides (at high temperature) to that associated with the stripe structure of antiferromagnetic iron arsenides (at low temperature); these can both be described with the same local plaquette, but with different interplaquette correlations. While the magnitude of the low-energy magnetic spectral weight is substantial at all temperatures, it actually weakens somewhat at low temperature, where the charge carriers become more itinerant. The observed change in spin correlations is correlated with the dramatic drop in the electronic scattering rate and the growth of the bulk nematic response upon cooling. Finally, we also present powder neutron diffraction results for lattice parameters in FeTe_{1-x}Sex indicating that the tetrahedral bond angle tends to increase towards the ideal value upon cooling, in agreement with the increased screening of the crystal field by more itinerant electrons and the correspondingly smaller splitting of the Fe 3d orbitals.

Accession Number: WOS:000372404400008

Language: English

Document Type: Article

KeyWords Plus: MAGNETIC ORDER; SPIN DYNAMICS; IRON; NEMATICITY; FRUSTRATION; ANISOTROPY; STATE

Addresses: [Xu, Zhijun; Birgeneau, R. J.] Univ Calif Berkeley, Dept Phys, Berkeley, CA 94720 USA.

[Xu, Zhijun; Birgeneau, R. J.] Univ Calif Berkeley, Lawrence Berkeley Natl Lab, Div Mat Sci, Berkeley, CA 94720 USA.

[Schneeloch, J. A.; Bozin, E. S.; Gu, Genda; Zaliznyak, I. A.; Tranquada, J. M.; Xu, Guangyong] Brookhaven Natl Lab, Condensed Matter Phys & Mat Sci Dept, Upton, NY 11973 USA.

[Schneeloch, J. A.] SUNY Stony Brook, Dept Phys & Astron, Stony Brook, NY 11794 USA.

[Wen, Jinsheng] Nanjing Univ, Natl Lab Solid State Microstruct, Ctr Superconducting Phys & Mat, Nanjing 210093, Jiangsu, Peoples R China.

[Wen, Jinsheng] Nanjing Univ, Dept Phys, Nanjing 210093, Jiangsu, Peoples R China.

[Granroth, G. E.] Oak Ridge Natl Lab, Neutron Data Anal & Visualizat Div, Oak Ridge, TN 37831 USA.

[Winn, B. L.] Oak Ridge Natl Lab, Quantum Condensed Matter Div, Oak Ridge, TN 37831 USA.

[Feyngenson, M.] Oak Ridge Natl Lab, Chem & Engn Mat Div, Oak Ridge, TN 37831 USA.

Corresponding Address: Xu, GY (corresponding author), Brookhaven Natl Lab, Condensed Matter Phys & Mat Sci Dept, Upton, NY 11973 USA.

E-mail Addresses: gxu@bnl.gov

Affiliations: University of California System; University of California Berkeley; United States Department of Energy (DOE); Lawrence Berkeley National Laboratory; University of California System; University of California Berkeley; United States Department of Energy (DOE); Brookhaven National Laboratory; State University of New York (SUNY) System; State University of New York (SUNY) Stony Brook; Nanjing University; Nanjing University; United States Department of Energy (DOE); Oak Ridge National Laboratory; United States Department of Energy (DOE); Oak Ridge National Laboratory; United States Department of Energy (DOE); Oak Ridge National Laboratory

Author Identifiers:

Author	Web of Science ResearcherID	ORCID Number
Bozin, Emil	AAB-4551-2020	
Xu, Guangyong	A-8707-2010	0000-0003-1441-8275
xu, zhijun	A-3264-2013	0000-0001-7486-2015
Zaliznyak, Igor	E-8532-2014	0000-0002-8548-7924
Granroth, Garrett E	G-3576-2012	0000-0002-7583-8778
Wen, Jinsheng	F-4209-2010	0000-0001-5864-1466
Zaliznyak, Igor	AAW-2535-2020	0000-0002-8548-7924
Tranquada, John M.	A-9832-2009	0000-0003-4984-8857
Feyngenson, Mikhail	H-9972-2014	0000-0002-0316-3265

Publisher: AMER PHYSICAL SOC

Publisher Address: ONE PHYSICS ELLIPSE, COLLEGE PK, MD 20740-3844 USA

Web of Science Index: Science Citation Index Expanded (SCI-EXPANDED)

Web of Science Categories: Materials Science, Multidisciplinary; Physics, Applied; Physics, Condensed Matter

Research Areas: Materials Science; Physics

IDS Number: DG9LL

ISSN: 2469-9950

eISSN: 2469-9969

29-char Source Abbrev.: PHYS REV B

ISO Source Abbrev.: Phys. Rev. B

Source Item Page Count: 9

Funding:

Funding Agency	Grant Number
Office of Basic Energy Sciences, US Department of Energy	DE-SC00112704 DE-AC02-05CH11231
NSFC	11374143 NCET-13-0282
Division of Scientific User Facilities of the same office	

We are grateful for stimulating discussions with Wei Ku, Ian Fisher, Adriana Moreo, Elbio Dagotto, and Ming Yi. The work at Brookhaven National Laboratory was supported by the Office of Basic Energy Sciences, US Department of Energy, under Contract No. DE-SC00112704. Z.J.X. and R.J.B. are also supported by the Office of Basic Energy Sciences, US Department of Energy, through Contract No. DE-AC02-05CH11231. Research at Oak Ridge National Laboratory was sponsored by the Division of Scientific User Facilities of the same office. The work at Nanjing University was supported by NSFC No. 11374143, and NCET-13-0282.

Open Access: Green Published, hybrid, Green Submitted

Output Date: 2023-01-27

Record 46 of 125

Title: Charge-screening role of c-axis atomic displacements in YBa₂Cu₃O_{6+x} and related superconductors

Author(s): Bozin, ES (Bozin, E. S.); Huq, A (Huq, A.); Shen, B (Shen, Bing); Claus, H (Claus, H.); Kwok, WK (Kwok, W. K.); Tranquada, JM (Tranquada, J. M.)

Source: PHYSICAL REVIEW B **Volume:** 93 **Issue:** 5 **Article Number:** 054523 **DOI:** 10.1103/PhysRevB.93.054523 **Published:** FEB 29 2016

Times Cited in Web of Science Core Collection: 14

Total Times Cited: 14

Usage Count (Last 180 days): 0

Usage Count (Since 2013): 24

Cited Reference Count: 105

Abstract: The importance of charge reservoir layers for supplying holes to the CuO₂ planes of cuprate superconductors has long been recognized. Less attention has been paid to the screening of the charge transfer by the intervening ionic layers. We address this issue in the case of YBa₂Cu₃O_{6+x}, where CuO chains supply the holes for the planes. We present a simple dielectric-screening model that gives a linear correlation between the relative displacements of ions along the c axis, determined by neutron powder diffraction, and the hole density of the planes. Applying this model to the temperature-dependent shifts of ions along the c axis, we infer a charge transfer of 5-10% of the hole density from the planes to the chains on warming from the superconducting transition to room temperature. Given the significant coupling of c-axis displacements to the average charge density, we point out the relevance of local displacements for screening charge modulations and note recent evidence for dynamic screening of in-plane quasiparticles. This line of argument leads us to a simple model for atomic displacements and charge modulation that is consistent with images from scanning-tunneling microscopy for underdoped Bi₂Sr₂CaCu₂O_{8+delta}.

Accession Number: WOS:000371391800005

Language: English

Document Type: Article

KeyWords Plus: DENSITY-WAVE ORDER; T-C; PSEUDOGAP STATE; CUO CHAINS; PHASE; TRANSITION; NEMATICITY; SYMMETRY; PHONONS; FLUCTUATIONS

Addresses: [Bozin, E. S.; Tranquada, J. M.] Brookhaven Natl Lab, Condensed Matter Phys & Mat Sci Dept, Upton, NY 11973 USA.

[Huq, A.] Oak Ridge Natl Lab, Chem & Engrn Mat Div, Oak Ridge, TN 37831 USA.

[Shen, Bing; Claus, H.; Kwok, W. K.] Argonne Natl Lab, Mat Sci Div, 9700 S Cass Ave, Argonne, IL 60439 USA.

Corresponding Address: Bozin, ES (corresponding author), Brookhaven Natl Lab, Condensed Matter Phys & Mat Sci Dept, Upton, NY 11973 USA.

Affiliations: United States Department of Energy (DOE); Brookhaven National Laboratory; United States Department of Energy (DOE); Oak Ridge National Laboratory; United States Department of Energy (DOE); Argonne National Laboratory

Author Identifiers:

Author	Web of Science ResearcherID	ORCID Number
Huq, Ashfia	J-8772-2013	0000-0002-8445-9649
Bozin, Emil	AAB-4551-2020	
Tranquada, John M.	A-9832-2009	0000-0003-4984-8857
Kwok, Wai-Kwong		0000-0003-0030-084X

Publisher: AMER PHYSICAL SOC

Publisher Address: ONE PHYSICS ELLIPSE, COLLEGE PK, MD 20740-3844 USA

Web of Science Index: Science Citation Index Expanded (SCI-EXPANDED)

Web of Science Categories: Materials Science, Multidisciplinary; Physics, Applied; Physics, Condensed Matter

Research Areas: Materials Science; Physics

IDS Number: DF5KY

ISSN: 2469-9950

eISSN: 2469-9969

29-char Source Abbrev.: PHYS REV B

ISO Source Abbrev.: Phys. Rev. B

Source Item Page Count: 11

Funding:

Funding Agency	Grant Number
Center for Emergent Superconductivity, an Energy Frontier Research Center - Office of Basic Energy Sciences (BES), Division of Materials Sciences and Engineering, U.S. Department of Energy (DOE)	
BES, U.S. DOE	DE-SC00112704
Scientific User Facilities Division, BES, U.S. DOE	

We thank J. C. Davis, M. R. Norman, and W. G. Yin for helpful discussions. This project was conceived and samples were prepared with support from the Center for Emergent Superconductivity, an Energy Frontier Research Center funded by Office of Basic Energy Sciences (BES), Division of Materials Sciences and Engineering, U.S. Department of Energy (DOE). Work at Brookhaven was supported by the BES, U.S. DOE, through Contract No. DE-SC00112704. The experiment at ORNL's Spallation Neutron Source was sponsored by the Scientific User Facilities Division, BES, U.S. DOE.

Open Access: Green Submitted, hybrid

Output Date: 2023-01-27

Record 47 of 125

Title: Sustained phase separation and spin glass in Co-doped $K_xFe_{2-y}Se_2$ single crystals

Author(s): Ryu, H (Ryu, Hyejin); Wang, KF (Wang, Kefeng); Opacic, M (Opacic, M.); Lazarevic, N (Lazarevic, N.); Warren, JB (Warren, J. B.); Popovic, ZV (Popovic, Z. V.); Bozin, ES (Bozin, Emil S.); Petrovic, C (Petrovic, C.)

Source: PHYSICAL REVIEW B **Volume:** 92 **Issue:** 17 **Article Number:** 174522 **DOI:** 10.1103/PhysRevB.92.174522 **Published:** NOV 19 2015

Times Cited in Web of Science Core Collection: 4

Total Times Cited: 4

Usage Count (Last 180 days): 1

Usage Count (Since 2013): 34

Cited Reference Count: 45

Abstract: We present Co substitution effects in $K_xFe_{2-y-z}Co_zSe_2$ ($0.06 \leq z \leq 1.73$) single-crystal alloys. By 3.5% of Co doping superconductivity is suppressed, whereas phase separation of semiconducting $K_2Fe_4Se_5$ and superconducting/metallic $K_xFe_2Se_2$ is still present. We show that the arrangement and distribution of the superconducting phase (stripe phase) are connected with the arrangement of K, Fe, and Co atoms. Semiconducting spin glass is found in proximity to the superconducting state, persisting for large Co concentrations. At high Co concentrations a ferromagnetic metallic state emerges above the spin glass. This is coincident with changes of the unit cell and arrangement and connectivity of the stripe conducting phase.

Accession Number: WOS:000364997100005

Language: English

Document Type: Article

KeyWords Plus: IRON; SUPERCONDUCTIVITY

Addresses: [Ryu, Hyejin; Wang, Kefeng; Bozin, Emil S.; Petrovic, C.] Brookhaven Natl Lab, Condensed Matter Phys & Mat Sci Dept, Upton, NY 11973 USA.

[Ryu, Hyejin; Petrovic, C.] SUNY Stony Brook, Dept Phys & Astron, Stony Brook, NY 11794 USA.

[Opacic, M.; Lazarevic, N.; Popovic, Z. V.] Univ Belgrade, Inst Phys Belgrade, Ctr Solid State Phys & New Mat, Belgrade 11080, Serbia.

[Warren, J. B.] Brookhaven Natl Lab, Instrument Div, Upton, NY 11973 USA.

Corresponding Address: Ryu, H (corresponding author), EO Lawrence Berkeley Natl Lab, Adv Light Source, Berkeley, CA 94720 USA.

Affiliations: United States Department of Energy (DOE); Brookhaven National Laboratory; State University of New York (SUNY) System; State University of New York (SUNY) Stony Brook; University of Belgrade; United States Department of Energy (DOE); Brookhaven National Laboratory

Author Identifiers:

Author	Web of Science ResearcherID	ORCID Number
Lazarević, Nenad Z	O-1076-2018	0000-0001-6310-9511
Lazarević, Nenad	C-3254-2012	0000-0001-6310-9511
Bozin, Emil	AAB-4551-2020	

Publisher: AMER PHYSICAL SOC

Publisher Address: ONE PHYSICS ELLIPSE, COLLEGE PK, MD 20740-3844 USA

Web of Science Index: Science Citation Index Expanded (SCI-EXPANDED)

Web of Science Categories: Materials Science, Multidisciplinary; Physics, Applied; Physics, Condensed Matter

Research Areas: Materials Science; Physics

IDS Number: CW4WK

ISSN: 2469-9950

eISSN: 2469-9969

29-char Source Abbrev.: PHYS REV B

ISO Source Abbrev.: Phys. Rev. B

Source Item Page Count: 7

Funding:

Funding Agency	Grant Number
U.S. DOE	DE-SC00112704
Center for Emergent Superconductivity, an Energy Frontier Research Center - U.S. DOE, Office for Basic Energy Science	
Serbian Ministry of Education, Science and Technological Development	ON171032 III45018

M. Abeykoon and J. Hanson are gratefully acknowledged for experimental assistance at the X7B beamline of NSLS at BNL. Work at Brookhaven is supported by the U.S. DOE under Contract No. DE-SC00112704 and in part by the Center for Emergent Superconductivity, an Energy Frontier Research Center funded by the U.S. DOE, Office for Basic Energy Science (K.W. and C.P.). This work was also supported by the Serbian Ministry of Education, Science and Technological Development under Projects No. ON171032 and No. III45018.

Open Access: Green Submitted, hybrid

Output Date: 2023-01-27

Record 48 of 125

Title: Insulating and metallic spin glass in Ni-doped $K_xFe_{2-y}Se_2$ single crystals

Author(s): Ryu, H (Ryu, Hyejin); Abeykoon, M (Abeykoon, Milinda); Wang, KF (Wang, Kefeng); Lei, HC (Lei, Hechang); Lazarevic, N (Lazarevic, N.); Warren, JB (Warren, J. B.); Bozin, ES (Bozin, E. S.); Popovic, ZV (Popovic, Z. V.); Petrovic, C (Petrovic, C.)

Source: PHYSICAL REVIEW B **Volume:** 91 **Issue:** 18 **Article Number:** 184503 **DOI:** 10.1103/PhysRevB.91.184503 **Published:** MAY 4 2015

Times Cited in Web of Science Core Collection: 7

Total Times Cited: 7

Usage Count (Last 180 days): 0

Usage Count (Since 2013): 27

Cited Reference Count: 59

Abstract: We report electron doping effects by Ni in $K_xFe_{2-\delta}Ni_ySe_2$ ($0.06 \leq y \leq 1.44$) single-crystal alloys. A rich ground-state phase diagram is observed. A small amount of Ni (similar to 4%) suppressed superconductivity below 1.8 K, inducing insulating spin-glass magnetic ground state for higher Ni content. With further Ni substitution, metallic resistivity is restored. For high Ni concentration in the lattice the unit cell symmetry is high symmetry $I4/mmm$ with no phase separation whereas both $I4/m + I4/mmm$ space groups were detected in the phase separated crystals when concentration of Ni < Fe. The absence of superconductivity coincides with the absence of crystalline Fe vacancy order.

Accession Number: WOS:000353771600003

Language: English

Document Type: Article

KeyWords Plus: SUPERCONDUCTIVITY; MAGNETISM

Addresses: [Ryu, Hyejin; Abeykoon, Milinda; Wang, Kefeng; Lei, Hechang; Bozin, E. S.; Popovic, Z. V.; Petrovic, C.] Brookhaven Natl Lab, Condensed Matter Phys & Mat Sci Dept, Upton, NY 11973 USA.

[Ryu, Hyejin; Petrovic, C.] SUNY Stony Brook, Dept Phys & Astron, Stony Brook, NY 11794 USA.

[Lazarevic, N.; Popovic, Z. V.] Univ Belgrade, Inst Phys Belgrade, Ctr Solid State Phys & New Mat, Belgrade 11080, Serbia.

[Warren, J. B.] Brookhaven Natl Lab, Instrument Div, Upton, NY 11973 USA.

Corresponding Address: Ryu, H (corresponding author), EO Lawrence Berkeley Natl Lab, Adv Light Source, Berkeley, CA 94720 USA.

Affiliations: United States Department of Energy (DOE); Brookhaven National Laboratory; State University of New York (SUNY) System; State University of New York (SUNY) Stony Brook; University of Belgrade; United States Department of Energy (DOE); Brookhaven National Laboratory

Author Identifiers:

Author	Web of Science ResearcherID	ORCID Number
Lazarević, Nenad Z	O-1076-2018	0000-0001-6310-9511
Lazarević, Nenad	C-3254-2012	0000-0001-6310-9511
Bozin, Emil	AAB-4551-2020	
LEI, Hechang	H-3278-2016	0000-0003-0850-8514
Petrovic, Cedomir	A-8789-2009	0000-0001-6063-1881

Publisher: AMER PHYSICAL SOC

Publisher Address: ONE PHYSICS ELLIPSE, COLLEGE PK, MD 20740-3844 USA

Web of Science Index: Science Citation Index Expanded (SCI-EXPANDED)

Web of Science Categories: Materials Science, Multidisciplinary; Physics, Applied; Physics, Condensed Matter

Research Areas: Materials Science; Physics

IDS Number: CH1HH

ISSN: 2469-9950

eISSN: 2469-9969

29-char Source Abbrev.: PHYS REV B

ISO Source Abbrev.: Phys. Rev. B

Source Item Page Count: 6

Funding:

Funding Agency	Grant Number
U.S. DOE	DE-AC02-98CH10886
Center for Emergent Superconductivity, an Energy Frontier Research Center - U.S. DOE, Office for Basic Energy Science	
Ministry of Education, Science, and Technological Development of Republic of Serbia	ON171032 III45018

Work at Brookhaven is supported by the U.S. DOE under Contract No. DE-AC02-98CH10886 and in part by the Center for Emergent Superconductivity, an Energy Frontier Research Center funded by the U.S. DOE, Office for Basic Energy Science (K.W and C.P.). This work was also supported by the Ministry of Education, Science, and Technological Development of Republic of Serbia under Projects No. ON171032 and No. III45018.

Open Access: hybrid, Green Submitted

Output Date: 2023-01-27

Record 49 of 125

Title: Reconciliation of local and long-range tilt correlations in underdoped $\text{La}_{2-x}\text{Ba}_x\text{CuO}_4$ ($0 \leq x \leq 0.155$)

Author(s): Bozin, ES (Bozin, Emil S.); Zhong, RD (Zhong, Ruidan); Knox, KR (Knox, Kevin R.); Gu, GD (Gu, Genda); Hill, JP (Hill, John P.); Tranquada, JM (Tranquada, John M.); Billinge, SJL (Billinge, Simon J. L.)

Source: PHYSICAL REVIEW B **Volume:** 91 **Issue:** 5 **Article Number:** 054521 **DOI:** 10.1103/PhysRevB.91.054521 **Published:** FEB 26 2015

Times Cited in Web of Science Core Collection: 23

Total Times Cited: 23

Usage Count (Last 180 days): 0

Usage Count (Since 2013): 35

Cited Reference Count: 80

Abstract: A long-standing puzzle regarding the disparity of local and long-range CuO₆ octahedral tilt correlations in the underdoped regime of La_{2-x}Ba_xCuO₄ is addressed by utilizing complementary neutron powder diffraction and inelastic neutron scattering (INS) approaches. This system is of interest because of the strong depression of the bulk superconducting transition at $x = 1/8$ in association with charge and spin stripe order. The latter unidirectional order is tied to Cu-O bond-length anisotropy present in the so-called low-temperature tetragonal (LTT) phase. On warming, the lattice exhibits two sequential structural transitions, involving changes in the CuO₆ tilt pattern, first to the low-temperature orthorhombic (LTO) and then the high-temperature tetragonal (HTT) phase. Despite the changes in static order, inspection of the instantaneous local atomic structure suggests that the LTT-type tilts persist through the transitions. Analysis of the INS spectra for the $x = 1/8$ composition reveals the dynamic nature of the LTT-like tilt fluctuations within the LTO and HTT phases. Within the low-temperature phase, the Cu-O bond-length splitting inferred from lattice symmetry and fitted atomic position parameters reaches a maximum of 0.3% at $x = 1/8$, suggesting that electron-phonon coupling may contribute to optimizing the structure to stabilize stripe order. This splitting is much too small to be resolved in the pair distribution function, and in fact we do not resolve any enhancement of the instantaneous bond-length distribution in association with stripe order. This study exemplifies the importance of a systematic approach using complementary techniques when investigating systems exhibiting a large degree of complexity and subtle structural responses.

Accession Number: WOS:000350207200009

Language: English

Document Type: Article

KeyWords Plus: STRUCTURAL PHASE-TRANSITION; HIGH-TC SUPERCONDUCTIVITY; SOFT-PHONON BEHAVIOR; NEUTRON-SCATTERING; CUO2 PLANE; LATTICE INSTABILITIES; TETRAGONAL PHASE; OCTAHEDRAL TILTS; C SUPPRESSION; ORDER

Addresses: [Bozin, Emil S.; Zhong, Ruidan; Knox, Kevin R.; Gu, Genda; Hill, John P.; Tranquada, John M.; Billinge, Simon J. L.] Brookhaven Natl Lab, Dept Condensed Matter Phys & Mat Sci, Upton, NY 11973 USA. [Zhong, Ruidan] SUNY Stony Brook, Dept Mat Sci & Engr, Stony Brook, NY 11790 USA. [Billinge, Simon J. L.] Columbia Univ, Dept Appl Phys & Appl Math, New York, NY 10027 USA.

Corresponding Address: Bozin, ES (corresponding author), Brookhaven Natl Lab, Dept Condensed Matter Phys & Mat Sci, Upton, NY 11973 USA.

E-mail Addresses: bozin@bnl.gov

Affiliations: United States Department of Energy (DOE); Brookhaven National Laboratory; State University of New York (SUNY) System; State University of New York (SUNY) Stony Brook; Columbia University

Author Identifiers:

Author	Web of Science ResearcherID	ORCID Number
Zhong, Ruidan	D-5296-2013	0000-0003-1652-9454
Tranquada, John M.	A-9832-2009	0000-0003-4984-8857
Bozin, Emil	AAB-4551-2020	

Publisher: AMER PHYSICAL SOC

Publisher Address: ONE PHYSICS ELLIPSE, COLLEGE PK, MD 20740-3844 USA

Web of Science Index: Science Citation Index Expanded (SCI-EXPANDED)

Web of Science Categories: Materials Science, Multidisciplinary; Physics, Applied; Physics, Condensed Matter

Research Areas: Materials Science; Physics

IDS Number: CC2XB

ISSN: 2469-9950

eISSN: 2469-9969

29-char Source Abbrev.: PHYS REV B

ISO Source Abbrev.: Phys. Rev. B

Source Item Page Count: 13

Funding:

Funding Agency	Grant Number
US DOE, Office of Science, Office of Basic Energy Sciences (DOE-BES)	DE-SC00112704
DOE BES	
DOE	DE-AC52-06NA25396
Scientific User Facilities Division, Office of Basic Energy Sciences, US Department of Energy	

Work at Brookhaven National Laboratory was supported by US DOE, Office of Science, Office of Basic Energy Sciences (DOE-BES), under Contract No. DE-SC00112704. Neutron PDF experiments were carried out on NPDF at LANSCE, funded by DOE BES; Los Alamos National Laboratory is operated by Los Alamos National Security LLC under DOE Contract No. DE-AC52-06NA25396. Inelastic neutron scattering experiments were carried out on HYSPEC at Spallation Neutron Source at ORNL, sponsored by the Scientific User Facilities Division, Office of Basic Energy Sciences, US Department of Energy. J.M.T. and R.D.Z. are grateful to B. L. Winn and M. Graves-Brook for assistance with the HYSPEC measurements. E.S.B. gratefully acknowledges T. E. Proffen and J. Siewenie for assistance with the NPDF measurements.

Open Access: Green Submitted, hybrid

Output Date: 2023-01-27

Record 50 of 125

Title: Evolution of symmetry-broken states in the pseudo-gap regimes of nickelates and cuprates

Author(s): Bozin, E (Bozin, Emil)

Source: ACTA CRYSTALLOGRAPHICA A-FOUNDATION AND ADVANCES **Meeting Abstract:** KN-5 **Volume:** 71 **Pages:** S4-S4 **DOI:** 10.1107/S2053273315099921 **Supplement:** S **Published:** 2015

Times Cited in Web of Science Core Collection: 0

Total Times Cited: 0

Usage Count (Last 180 days): 0

Usage Count (Since 2013): 1

Cited Reference Count: 0

Accession Number: WOS:000480363600008

Language: English

Document Type: Meeting Abstract

Author Keywords: superconductivity; neutron scattering; nanoscale; pair distribution function; broken symmetry states

Addresses: [Bozin, Emil] Brookhaven Natl Lab, Condensed Matter Phys & Mat Sci Dept, Upton, NY USA.

E-mail Addresses: bozin@bnl.gov

Author Identifiers:

Author	Web of Science ResearcherID	ORCID Number
Bozin, Emil	AAB-4551-2020	

Publisher: INT UNION CRYSTALLOGRAPHY

Publisher Address: 2 ABBEY SQ, CHESTER, CH1 2HU, ENGLAND

Web of Science Index: Science Citation Index Expanded (SCI-EXPANDED)

Web of Science Categories: Chemistry, Multidisciplinary; Crystallography

Research Areas: Chemistry; Crystallography

IDS Number: VI3WG

ISSN: 2053-2733

29-char Source Abbrev.: ACTA CRYSTALLOGR A

ISO Source Abbrev.: Acta Crystallogr. Sect. A

Source Item Page Count: 1

Output Date: 2023-01-27

Record 51 of 125

Title: Intra-unit-cell nematic charge order in the titanium-oxypnictide family of superconductors

Author(s): Frandsen, BA (Frandsen, Benjamin A.); Bozin, ES (Bozin, Emil S.); Hu, HF (Hu, Hefei); Zhu, YM (Zhu, Yimei); Nozaki, Y (Nozaki, Yasumasa); Kageyama, H (Kageyama, Hiroshi); Uemura, YJ (Uemura, Yasutomo J.); Yin, WG (Yin, Wei-Guo); Billinge, SJL (Billinge, Simon J. L.)

Source: NATURE COMMUNICATIONS **Volume:** 5 **Article Number:** 5761 **DOI:** 10.1038/ncomms6761 **Published:** DEC 2014

Times Cited in Web of Science Core Collection: 25

Total Times Cited: 25

Usage Count (Last 180 days): 0

Usage Count (Since 2013): 55

Cited Reference Count: 50

Abstract: Understanding the role played by broken-symmetry states such as charge, spin and orbital orders in the mechanism of emergent properties, such as high-temperature superconductivity, is a major current topic in materials research. That the order may be within one unit cell, such as nematic, was only recently considered theoretically, but its observation in the iron-pnictide and doped cuprate superconductors places it at the forefront of current research. Here, we show that the recently discovered BaTi₂Sb₂O superconductor and its parent compound BaTi₂As₂O form a symmetry-breaking nematic ground state that can be naturally explained as an intra-unit-cell nematic charge order with d-wave symmetry, pointing to the ubiquity of the phenomenon. These findings, together with the key structural features in these materials being intermediate between the cuprate and iron-pnictide high-temperature superconducting materials, render the titanium oxypnictides an important new material system to understand the nature of nematic order and its relationship to superconductivity.

Accession Number: WOS:000347611800002

PubMed ID: 25482113

Language: English

Document Type: Article

KeyWords Plus: DENSITY-WAVE; PHASE; INSTABILITY; PHYSICS; STATES

Addresses: [Frandsen, Benjamin A.; Uemura, Yasutomo J.] Columbia Univ, Dept Phys, New York, NY 10027 USA.

[Bozin, Emil S.; Hu, Hefei; Zhu, Yimei; Yin, Wei-Guo; Billinge, Simon J. L.] Brookhaven Natl Lab, Condensed Matter Phys & Mat Sci Dept, Upton, NY 11973 USA.

[Nozaki, Yasumasa; Kageyama, Hiroshi] Kyoto Univ, Grad Sch Engn, Dept Energy & Hydrocarbon Chem, Nishikyo Ku, Kyoto 6158510, Japan.

[Billinge, Simon J. L.] Columbia Univ, Dept Appl Phys & Appl Math, New York, NY 10027 USA.

Corresponding Address: Billinge, SJL (corresponding author), Brookhaven Natl Lab, Condensed Matter Phys & Mat Sci Dept, Upton, NY 11973 USA.

E-mail Addresses: sb2896@columbia.edu

Affiliations: Columbia University; United States Department of Energy (DOE); Brookhaven National Laboratory; Kyoto University; Columbia University

Author Identifiers:

Author	Web of Science ResearcherID	ORCID Number
Kageyama, Hiroshi	A-4602-2010	
Yin, Weiguo	A-9671-2014	0000-0002-4965-5329
Bozin, Emil	AAB-4551-2020	
Frandsen, Benjamin	AAJ-1680-2020	0000-0002-4047-9453

Publisher: NATURE PUBLISHING GROUP

Publisher Address: MACMILLAN BUILDING, 4 CRINAN ST, LONDON N1 9XW, ENGLAND

Web of Science Index: Science Citation Index Expanded (SCI-EXPANDED)

Web of Science Categories: Multidisciplinary Sciences

Research Areas: Science & Technology - Other Topics

IDS Number: AY5KU

ISSN: 2041-1723

29-char Source Abbrev.: NAT COMMUN

ISO Source Abbrev.: Nat. Commun.

Source Item Page Count: 7

Funding:

Funding Agency	Grant Number
U.S. Department of Energy, Office of Basic Energy Sciences	DE-AC02-98CH10886
U.S. National Science Foundation (NSF) Partnership for International Research and Education (PIRE) Super-PIRE project	OISE-0968226
NSF	DMR-1105961
Japan Atomic Energy Agency Reimei project	
Friends of Todai Inc	
FIRST program	
Japan Society of the Promotion of Science (JSPS)	
DOE Office of Basic Energy Sciences	
DOE	DE-AC52-06NA25396
Direct For Mathematical & Physical Scien	1105961
Office Of Internatl Science &Engineering	0968226

Work at Brookhaven National Laboratory was supported by the U.S. Department of Energy, Office of Basic Energy Sciences, under contract No. DE-AC02-98CH10886. Work at Columbia University was supported by the U.S. National Science Foundation (NSF) Partnership for International Research and Education (PIRE) Super-PIRE project (grant OISE-0968226). Y.J.U. also acknowledges support from NSF DMR-1105961, the Japan Atomic Energy Agency Reimei project, and the Friends of Todai Inc. The work at Kyoto University was supported by the FIRST program, Japan Society of the Promotion of Science (JSPS). Neutron scattering experiments were carried out on NPDF at LANSCE, funded by DOE Office of Basic Energy Sciences. LANL is operated by Los Alamos National Security LLC under DOE Contract No. DE-AC52-06NA25396.

Open Access: Green Submitted, Bronze

Output Date: 2023-01-27

Record 52 of 125

Title: Nanoscale phase coexistence at the metal-insulator transition in Cu(Ir_{1-x}Cr_x)₂S₄

Author(s): Bozin, E (Bozin, E.); Knox, K (Knox, K.); Juhas, P (Juhas, P.); Hor, Y (Hor, Y.); Mitchell, J (Mitchell, J.); Billinge, S (Billinge, S.)

Source: ACTA CRYSTALLOGRAPHICA A-FOUNDATION AND ADVANCES **Meeting Abstract:** MS90.O04 **Volume:** 70 **Pages:** C1351-C1351 **DOI:** 10.1107/S2053273314086483 **Supplement:** S **Published:** AUG 2014

Times Cited in Web of Science Core Collection: 0

Total Times Cited: 0

Usage Count (Last 180 days): 0

Usage Count (Since 2013): 1

Cited Reference Count: 1

Accession Number: WOS:000519606301354

Language: English

Document Type: Meeting Abstract

Author Keywords: iridates; nanoscale phase separation; metal-insulator transition

Addresses: [Bozin, E.; Knox, K.; Juhas, P.; Billinge, S.] Brookhaven Natl Lab, Condensed Matter Phys & Mat Sci Dept, Upton, NY 11973 USA.

[Hor, Y.; Mitchell, J.] Argonne Natl Lab, Mat Sci Dept, Argonne, IL USA.

[Billinge, S.] Columbia Univ, Appl Phys & Appl Math Dept, New York, NY USA.

Affiliations: United States Department of Energy (DOE); Brookhaven National Laboratory; United States Department of Energy (DOE); Argonne National Laboratory; Columbia University

Author Identifiers:

Author	Web of Science ResearcherID	ORCID Number
Bozin, Emil	AAB-4551-2020	

Publisher: INT UNION CRYSTALLOGRAPHY

Publisher Address: 2 ABBEY SQ, CHESTER, CH1 2HU, ENGLAND

Web of Science Index: Science Citation Index Expanded (SCI-EXPANDED)

Web of Science Categories: Chemistry, Multidisciplinary; Crystallography

Research Areas: Chemistry; Crystallography

IDS Number: VI8ST

ISSN: 2053-2733

29-char Source Abbrev.: ACTA CRYSTALLOGR A

ISO Source Abbrev.: Acta Crystallogr. Sect. A

Source Item Page Count: 1

Open Access: Bronze

Output Date: 2023-01-27

Record 53 of 125

Title: Local Symmetry Breaking in the High Temperature Regime of SnTe

Author(s): Knox, K (Knox, K.); Bozin, E (Bozin, E.); Malliakas, C (Malliakas, C.); Kanatzidis, M (Kanatzidis, M.); Billinge, S (Billinge, S.)

Source: ACTA CRYSTALLOGRAPHICA A-FOUNDATION AND ADVANCES **Meeting Abstract:** MS55.O03 **Volume:** 70 **Pages:** C857-C857 **DOI:** 10.1107/S2053273314091426 **Supplement:** S **Published:** AUG 2014

Times Cited in Web of Science Core Collection: 0

Total Times Cited: 0

Usage Count (Last 180 days): 0

Usage Count (Since 2013): 2

Cited Reference Count: 3

Accession Number: WOS:000519606300858

Language: English

Document Type: Meeting Abstract

Author Keywords: PDF; Symmetry breaking; SnTe

Addresses: [Knox, K.; Bozin, E.; Billinge, S.] Brookhaven Natl Lab, Condensed Matter Phys, Upton, NY 11973 USA.

[Malliakas, C.; Kanatzidis, M.] Northwestern Univ, Dept Chem, Evanston, IL USA.

[Billinge, S.] Columbia Univ, Dept Appl Phys, New York, NY 10027 USA.

Affiliations: United States Department of Energy (DOE); Brookhaven National Laboratory; Northwestern University; Columbia University

Author Identifiers:

Author	Web of Science ResearcherID	ORCID Number
Bozin, Emil	AAB-4551-2020	

Publisher: INT UNION CRYSTALLOGRAPHY

Publisher Address: 2 ABBEY SQ, CHESTER, CH1 2HU, ENGLAND

Web of Science Index: Science Citation Index Expanded (SCI-EXPANDED)

Web of Science Categories: Chemistry, Multidisciplinary; Crystallography

Research Areas: Chemistry; Crystallography

IDS Number: VI8ST

ISSN: 2053-2733

29-char Source Abbrev.: ACTA CRYSTALLOGR A

ISO Source Abbrev.: Acta Crystallogr. Sect. A

Source Item Page Count: 1

Open Access: Bronze

Output Date: 2023-01-27

Record 54 of 125

Title: Probing IrTe₂ crystal symmetry by polarized Raman scattering

Author(s): Lazarevic, N (Lazarevic, N.); Bozin, ES (Bozin, E. S.); Scepanovic, M (Scepanovic, M.); Opacic, M (Opacic, M.); Lei, HC (Lei, Hechang); Petrovic, C (Petrovic, C.); Popovic, ZV (Popovic, Z. V.)

Source: PHYSICAL REVIEW B **Volume:** 89 **Issue:** 22 **Article Number:** 224301 **DOI:** 10.1103/PhysRevB.89.224301 **Published:** JUN 16 2014

Times Cited in Web of Science Core Collection: 13

Total Times Cited: 13

Usage Count (Last 180 days): 1

Usage Count (Since 2013): 81

Cited Reference Count: 25

Abstract: Polarized Raman scattering measurements on IrTe₂ single crystals carried out over the 15-640 K temperature range, and across the structural phase transition, reveal different insights regarding the crystal symmetry. In the high temperature regime three Raman active modes are observed at all of the studied temperatures above the structural phase transition, rather than two as predicted by the factor group analysis for

the assumed $P(3)$ over $\bar{m}1$ symmetry. This indicates that the actual symmetry of the high temperature phase is lower than previously thought. The observation of an additional E-g mode at high temperature can be explained by doubling of the original trigonal unit cell along the c axis and within the $P(3)$ over $\bar{c}1$ symmetry. In the low temperature regime (below 245 K) the other Raman modes appear as a consequence of the symmetry lowering phase transition and the corresponding increase of the primitive cell. All of the modes observed below the phase transition temperature can be assigned within the monoclinic crystal symmetry. The temperature dependence of the Raman active phonons in both phases is mainly driven by anharmonicity effects. The results call for reconsideration of the crystallographic phases of IrTe₂.

Accession Number: WOS:000337730000001

Language: English

Document Type: Article

KeyWords Plus: BAND-STRUCTURE; TRANSITION; BONDS

Addresses: [Lazarevic, N.; Scepanovic, M.; Opacic, M.; Popovic, Z. V.] Univ Belgrade, Ctr Solid State Phys & New Mat, Inst Phys Belgrade, Belgrade 11080, Serbia.

[Bozin, E. S.; Lei, Hechang; Petrovic, C.] Brookhaven Natl Lab, Condensed Matter Phys & Mat Sci Dept, Upton, NY 11973 USA.

Corresponding Address: Lazarevic, N (corresponding author), Univ Belgrade, Ctr Solid State Phys & New Mat, Inst Phys Belgrade, Pregrevica 118, Belgrade 11080, Serbia.

Affiliations: University of Belgrade; United States Department of Energy (DOE); Brookhaven National Laboratory

Author Identifiers:

Author	Web of Science ResearcherID	ORCID Number
LEI, Hechang	H-3278-2016	0000-0003-0850-8514
Petrovic, Cedomir	A-8789-2009	0000-0001-6063-1881
Scepanovic, Maja J	F-6720-2010	0000-0002-6791-5622
Lazarević, Nenad	C-3254-2012	0000-0001-6310-9511
Lazarević, Nenad Z	O-1076-2018	0000-0001-6310-9511
Bozin, Emil	AAB-4551-2020	

Publisher: AMER PHYSICAL SOC

Publisher Address: ONE PHYSICS ELLIPSE, COLLEGE PK, MD 20740-3844 USA

Web of Science Index: Science Citation Index Expanded (SCI-EXPANDED)

Web of Science Categories: Materials Science, Multidisciplinary; Physics, Applied; Physics, Condensed Matter

Research Areas: Materials Science; Physics

IDS Number: AJ5NF

ISSN: 2469-9950

eISSN: 2469-9969

29-char Source Abbrev.: PHYS REV B

ISO Source Abbrev.: Phys. Rev. B

Source Item Page Count: 6

Funding:

Funding Agency	Grant Number
Serbian Ministry of Education, Science and Technological Development	ON171032 III45018
Serbian-Germany bilateral project "Interplay of Fe-vacancy ordering and spin fluctuations in iron-based high temperature superconductors."	

We gratefully acknowledge discussions with R. Hackl. This work was supported by the Serbian Ministry of Education, Science and Technological Development under Projects No. ON171032 and No. III45018, as well as the Serbian-Germany bilateral project "Interplay of Fe-vacancy ordering and spin fluctuations in iron-based high temperature superconductors." Part of this work was carried out at the Brookhaven National Laboratory which is, as well as the NSLS facility, operated for the Office of Basic Energy Sciences, US Department of Energy by Brookhaven Science Associates, under Contract No. DE-AC02-98CH10886.

Open Access: Green Submitted

Output Date: 2023-01-27

Record 55 of 125

Title: Low-temperature structural and transport anomalies in Cu₂Se (vol 89, 195209, 2014)

Author(s): Chi, H (Chi, Hang); Kim, H (Kim, Hyoungchul); Thomas, JC (Thomas, John C.); Shi, GS (Shi, Guangsha); Sun, K (Sun, Kai); Abeykoon, M (Abeykoon, Milinda); Bozin, ES (Bozin, Emil S.); Shi, XY (Shi, Xiaoya); Li, Q (Li, Qiang); Shi, X (Shi, Xun); Kioupakis, E (Kioupakis, Emmanouil); Van der Ven, A (Van der Ven, Anton); Kaviani, M (Kaviani, Massoud); Uher, C (Uher, Ctirad)

Source: PHYSICAL REVIEW B **Volume:** 89 **Issue:** 23 **Article Number:** 239904 **DOI:** 10.1103/PhysRevB.89.239904 **Published:** JUN 12 2014

Times Cited in Web of Science Core Collection: 0

Total Times Cited: 0

Usage Count (Last 180 days): 0

Usage Count (Since 2013): 63

Cited Reference Count: 1

Accession Number: WOS:000338650300006

Language: English

Document Type: Correction

Author Identifiers:

Author	Web of Science ResearcherID	ORCID Number
Bozin, Emil	AAB-4551-2020	
Shi, Xun	A-1764-2019	0000-0002-8086-6407
Kioupakis, Emmanouil	L-4504-2013	

Publisher: AMER PHYSICAL SOC

Publisher Address: ONE PHYSICS ELLIPSE, COLLEGE PK, MD 20740-3844 USA

Web of Science Index: Science Citation Index Expanded (SCI-EXPANDED)

Web of Science Categories: Materials Science, Multidisciplinary; Physics, Applied; Physics, Condensed Matter

Research Areas: Materials Science; Physics

IDS Number: AK8AU

ISSN: 1098-0121

eISSN: 1550-235X

29-char Source Abbrev.: PHYS REV B

ISO Source Abbrev.: Phys. Rev. B

Source Item Page Count: 1

Output Date: 2023-01-27

Record 56 of 125**Title:** Low-temperature structural and transport anomalies in Cu₂Se**Author(s):** Chi, H (Chi, Hang); Kim, H (Kim, Hyoungchul); Thomas, JC (Thomas, John C.); Shi, GS (Shi, Guangsha); Sun, K (Sun, Kai); Abeykoon, M (Abeykoon, Milinda); Bozin, ES (Bozin, Emil S.); Shi, XY (Shi, Xiaoya); Li, Q (Li, Qiang); Shi, X (Shi, Xun); Kioupakis, E (Kioupakis, Emmanouil); Van der Ven, A (Van der Ven, Anton); Kaviany, M (Kaviany, Massoud); Uher, C (Uher, Ctirad)**Source:** PHYSICAL REVIEW B **Volume:** 89 **Issue:** 19 **Article Number:** 195209 **DOI:** 10.1103/PhysRevB.89.195209 **Published:** MAY 28 2014**Times Cited in Web of Science Core Collection:** 50**Total Times Cited:** 50**Usage Count (Last 180 days):** 3**Usage Count (Since 2013):** 201**Cited Reference Count:** 35

Abstract: Through systematic examination of symmetrically nonequivalent configurations, first-principles calculations have identified a new ground state of Cu₂Se, which is constructed by repeating sextuple layers of Se-Cu-Cu-Cu-Cu-Se. The layered nature is in accord with electron and x-ray diffraction studies at and below room temperature and also is consistent with transport properties. Magnetoresistance measurements at liquid helium temperatures exhibit cusp-shaped field dependence at low fields and evolve into quasilinear field dependence at intermediate and high fields. These results reveal the existence of weak antilocalization effect, which has been analyzed using a modified Hikami, Larkin, and Nagaoka model, including a quantum interference term and a classical quadratic contribution. Fitting parameters suggest a quantum coherence length L of 175 nm at 1.8 K. With increasing temperature, the classical parabolic behavior becomes more dominant, and L decreases as a power law of $T^{-0.83}$.

Accession Number: WOS:000336755200004**Language:** English**Document Type:** Article**KeyWords Plus:** THERMOELECTRIC PERFORMANCE; PHASE-TRANSITIONS; MAGNETORESISTANCE**Addresses:** [Chi, Hang; Uher, Ctirad] Univ Michigan, Dept Phys, Ann Arbor, MI 48109 USA.

[Kim, Hyoungchul; Kaviany, Massoud] Univ Michigan, Dept Mech Engn, Ann Arbor, MI 48109 USA.

[Thomas, John C.; Shi, Guangsha; Sun, Kai; Kioupakis, Emmanouil; Van der Ven, Anton] Univ Michigan, Dept Mat Sci & Engn, Ann Arbor, MI 48109 USA.

[Abeykoon, Milinda; Bozin, Emil S.; Shi, Xiaoya; Li, Qiang] Brookhaven Natl Lab, Condensed Matter Phys & Mat Sci Dept, Upton, NY 11973 USA.

[Shi, Xun] Chinese Acad Sci, Shanghai Inst Ceram, State Key Lab High Performance Ceram & Superfine, Shanghai 200050, Peoples R China.

[Van der Ven, Anton] Univ Calif Santa Barbara, Dept Mat, Santa Barbara, CA 93106 USA.

[Kim, Hyoungchul] Korea Inst Sci & Technol, High Temp Energy Mat Res Ctr, Seoul 136791, South Korea.

Corresponding Address: Uher, C (corresponding author), Univ Michigan, Dept Phys, Ann Arbor, MI 48109 USA.**E-mail Addresses:** cuher@umich.edu**Affiliations:** University of Michigan System; University of Michigan; University of Michigan System; University of Michigan; University of Michigan System; University of Michigan; United States Department of Energy (DOE); Brookhaven National Laboratory; Chinese Academy of Sciences; Shanghai Institute of Ceramics, CAS; University of California System; University of California Santa Barbara; Korea Institute of Science & Technology (KIST)**Author Identifiers:**

Author	Web of Science ResearcherID	ORCID Number
Kioupakis, Emmanouil	L-4504-2013	

Thomas, John C	A-2764-2009	0000-0002-3162-0152
Bozin, Emil	AAB-4551-2020	
shi, xun	B-4499-2009	0000-0002-3806-0303
Chi, Hang	F-1537-2011	0000-0002-1299-1150
Shi, Xun	A-1764-2019	0000-0002-8086-6407
Thomas, John C.	W-4621-2019	0000-0002-3162-0152
Kioupakis, Emmanouil		0000-0003-1880-6443

Publisher: AMER PHYSICAL SOC

Publisher Address: ONE PHYSICS ELLIPSE, COLLEGE PK, MD 20740-3844 USA

Web of Science Index: Science Citation Index Expanded (SCI-EXPANDED)

Web of Science Categories: Materials Science, Multidisciplinary; Physics, Applied; Physics, Condensed Matter

Research Areas: Materials Science; Physics

IDS Number: AI3IS

ISSN: 2469-9950

eISSN: 2469-9969

29-char Source Abbrev.: PHYS REV B

ISO Source Abbrev.: Phys. Rev. B

Source Item Page Count: 5

Funding:

Funding Agency	Grant Number
Center for Solar and Thermal Energy Conversion, an Energy Frontier Research Center - U.S. Department of Energy, Office of Science, Basic Energy Sciences	DE-SC-0000957
National Science Foundation	DMR-9871177
DOE, Office of Science, Division of Materials Science	DE-AC02-98CH10886
National Natural Science Foundation of China (NSFC)	51121064 51222209

This work was supported as part of the Center for Solar and Thermal Energy Conversion, an Energy Frontier Research Center funded by the U.S. Department of Energy, Office of Science, Basic Energy Sciences under Award No. DE-SC-0000957. The JEOL 2010F TEM was funded by the National Science Foundation (Grant No. DMR-9871177) and operated by the Electron Microbeam Analysis Laboratory at the University of Michigan. Work at Brookhaven National Laboratory was supported by the DOE, Office of Science, Division of Materials Science (Contract No. DE-AC02-98CH10886). Work at the Shanghai Institute of Ceramics was supported by the National Natural Science Foundation of China (NSFC) (Award No. 51121064 and 51222209).

Output Date: 2023-01-27

Record 57 of 125

Title: Cu(Ir_{1-x}Cr_x)(₂)S-4: a model system for studying nanoscale phase coexistence at the metal-insulator transition

Author(s): Bozin, ES (Bozin, E. S.); Knox, KR (Knox, K. R.); Juhas, P (Juhas, P.); Hor, YS (Hor, Y. S.); Mitchell, JF (Mitchell, J. F.); Billinge, SJL (Billinge, S. J. L.)

Source: SCIENTIFIC REPORTS **Volume:** 4 **Article Number:** 4081 **DOI:** 10.1038/srep04081 **Published:** FEB 12 2014

Times Cited in Web of Science Core Collection: 13

Total Times Cited: 13

Usage Count (Last 180 days): 0

Usage Count (Since 2013): 53

Cited Reference Count: 66

Abstract: Increasingly, nanoscale phase coexistence and hidden broken symmetry states are being found in the vicinity of metal-insulator transitions (MIT), for example, in high temperature superconductors, heavy fermion and colossal magnetoresistive materials, but their importance and possible role in the MIT and related emergent behaviors is not understood. Despite their ubiquity, they are hard to study because they produce weak diffuse signals in most measurements. Here we propose $\text{Cu}(\text{Ir}_{1-x}\text{Cr}_x)_2\text{S}_4$ as a model system, where robust local structural signals lead to key new insights. We demonstrate a hitherto unobserved coexistence of an Ir^{4+} charge-localized dimer phase and Cr-ferromagnetism. The resulting phase diagram that takes into account the short range dimer order is highly reminiscent of a generic MIT phase diagram similar to the cuprates. We suggest that the presence of quenched strain from dopant ions acts as an arbiter deciding between the competing ground states.

Accession Number: WOS:000331290100007

PubMed ID: 24518384

Language: English

Document Type: Article

KeyWords Plus: PAIR DISTRIBUTION FUNCTION; NEUTRON-DIFFRACTION; STRIPE ORDER; SUPERCONDUCTOR; THIOSPINEL; INHOMOGENEITY; TEMPERATURE; CuIr_2S_4 ; HOLES; SPINS

Addresses: [Bozin, E. S.; Knox, K. R.; Juhas, P.; Billinge, S. J. L.] Brookhaven Natl Lab, Condensed Matter Phys & Mat Sci Dept, Upton, NY 11973 USA.

[Hor, Y. S.; Mitchell, J. F.] Argonne Natl Lab, Div Mat Sci, Argonne, IL 60439 USA.

[Billinge, S. J. L.] Columbia Univ, Dept Appl Phys & Appl Math, New York, NY 10027 USA.

Corresponding Address: Bozin, ES (corresponding author), Brookhaven Natl Lab, Condensed Matter Phys & Mat Sci Dept, Upton, NY 11973 USA.

E-mail Addresses: bozin@bnl.gov

Affiliations: United States Department of Energy (DOE); Brookhaven National Laboratory; United States Department of Energy (DOE); Argonne National Laboratory; Columbia University

Author Identifiers:

Author	Web of Science ResearcherID	ORCID Number
Bozin, Emil	AAB-4551-2020	
Juhas, Pavol	Q-7225-2019	0000-0001-8751-4458
Mitchell, John F	A-1907-2012	
San Hor, Yew	S-1429-2017	0000-0002-1417-4357
Billinge, Simon		0000-0002-9734-4998

Publisher: NATURE PUBLISHING GROUP

Publisher Address: MACMILLAN BUILDING, 4 CRINAN ST, LONDON N1 9XW, ENGLAND

Web of Science Index: Science Citation Index Expanded (SCI-EXPANDED)

Web of Science Categories: Multidisciplinary Sciences

Research Areas: Science & Technology - Other Topics

IDS Number: AA7PT

ISSN: 2045-2322

29-char Source Abbrev.: SCI REP-UK

ISO Source Abbrev.: Sci Rep

Source Item Page Count: 6

Funding:

Funding Agency	Grant Number
----------------	--------------

U.S. Department of Energy Office of Science (DOE-OS)	DE-AC02-98CH10886
U.S. DOE-OS	DE-AC02-06CH11357

Work at Brookhaven National Laboratory (data collection, analysis and modeling) is supported by the U.S. Department of Energy Office of Science (DOE-OS) under Contract no. DE-AC02-98CH10886. Work at Argonne National Laboratory, which is operated by UChicago Argonne LLC, and the Advanced Photon Source (APS) facility, (materials synthesis and characterization) is supported under the U.S. DOE-OS Contract No. DE-AC02-06CH11357. This work has benefited from using the 11-IDC beamline of the APS.

Open Access: gold, Green Published, Green Submitted

Output Date: 2023-01-27

Record 58 of 125

Title: Physical properties of $K_xNi_{2-y}Se_2$ single crystals

Author(s): Lei, HC (Lei, Hechang); Abeykoon, M (Abeykoon, Milinda); Wang, KF (Wang, Kefeng); Bozin, ES (Bozin, Emil S.); Ryu, H (Ryu, Hyejin); Graf, D (Graf, D.); Warren, JB (Warren, J. B.); Petrovic, C (Petrovic, C.)

Source: JOURNAL OF PHYSICS-CONDENSED MATTER **Volume:** 26 **Issue:** 1 **Article Number:** 015701 **DOI:** 10.1088/0953-8984/26/1/015701 **Published:** JAN 8 2014

Times Cited in Web of Science Core Collection: 10

Total Times Cited: 10

Usage Count (Last 180 days): 0

Usage Count (Since 2013): 71

Cited Reference Count: 41

Abstract: We have synthesized $K_{0.95}(1)Ni_{1.86}(2)Se_2$ single crystals. The single crystals contain K and Ni deficiencies not observed in KNi_2Se_2 polycrystals. Unlike KNi_2Se_2 polycrystals, the superconductivity is absent in single crystals. The detailed physical property study indicates that the $K_{0.95}Ni_{1.86}Se_2$ single crystals exhibit heavy-fermion-like characteristics. The transition to a heavy fermion state below T similar to 30 K results in an enhancement of the electron-like carrier density whereas the magnetic susceptibility shows little anisotropy and suggests the presence of both itinerant and localized Ni orbitals.

Accession Number: WOS:000328194600022

PubMed ID: 24292376

Language: English

Document Type: Article

KeyWords Plus: LAYERED SUPERCONDUCTOR; MAGNETIZATION

Addresses: [Lei, Hechang; Abeykoon, Milinda; Wang, Kefeng; Bozin, Emil S.; Ryu, Hyejin; Petrovic, C.] Brookhaven Natl Lab, Condensed Matter Phys & Mat Sci Dept, Upton, NY 11973 USA.

[Ryu, Hyejin; Petrovic, C.] SUNY Stony Brook, Dept Phys & Astron, Stony Brook, NY 11794 USA.

[Graf, D.] Florida State Univ, NHMFL Phys, Tallahassee, FL 32310 USA.

[Warren, J. B.] Brookhaven Natl Lab, Instrumentat Div, Upton, NY 11973 USA.

Corresponding Address: Lei, HC (corresponding author), Tokyo Inst Technol, Frontier Res Ctr, Midori Ku, 4259 Nagatsuta, Yokohama, Kanagawa 2268503, Japan.

E-mail Addresses: petrovic@bnl.gov

Affiliations: United States Department of Energy (DOE); Brookhaven National Laboratory; State University of New York (SUNY) System; State University of New York (SUNY) Stony Brook; State University System of Florida; Florida State University; United States Department of Energy (DOE); Brookhaven National Laboratory

Author Identifiers:

Author	Web of Science ResearcherID	ORCID Number
Petrovic, Cedomir	A-8789-2009	0000-0001-6063-1881

Graf, David	X-2245-2018	0000-0001-6195-0462
Bozin, Emil	AAB-4551-2020	
Wang, Kefeng	E-7683-2011	0000-0002-8449-9720
LEI, Hechang	H-3278-2016	0000-0003-0850-8514

Publisher: IOP PUBLISHING LTD

Publisher Address: TEMPLE CIRCUS, TEMPLE WAY, BRISTOL BS1 6BE, ENGLAND

Web of Science Index: Science Citation Index Expanded (SCI-EXPANDED)

Web of Science Categories: Physics, Condensed Matter

Research Areas: Physics

IDS Number: 268TX

ISSN: 0953-8984

eISSN: 1361-648X

29-char Source Abbrev.: J PHYS-CONDENS MAT

ISO Source Abbrev.: J. Phys.-Condes. Matter

Source Item Page Count: 7

Funding:

Funding Agency	Grant Number
US DOE	DE-AC02-98CH10886
DOE NNSA	DEFG52-10NA29659
NSF	DMR-0654118
State of Florida	

Work at Brookhaven is supported by the US DOE under Contract No. DE-AC02-98CH10886. This work has benefited from using the X7B beamline of the National Synchrotron Light Source at Brookhaven National Laboratory (MA and EB). Work at the National High Magnetic Field Laboratory is supported by the DOE NNSA DEFG52-10NA29659 (DG), by the NSF Cooperative Agreement No. DMR-0654118, and by the State of Florida.

Open Access: Green Submitted

Output Date: 2023-01-27

Record 59 of 125

Title: Local off-centering symmetry breaking in the high-temperature regime of SnTe

Author(s): Knox, KR (Knox, K. R.); Bozin, ES (Bozin, E. S.); Malliakas, CD (Malliakas, C. D.); Kanatzidis, MG (Kanatzidis, M. G.); Billinge, SJL (Billinge, S. J. L.)

Source: PHYSICAL REVIEW B **Volume:** 89 **Issue:** 1 **Article Number:** 014102 **DOI:** 10.1103/PhysRevB.89.014102 **Published:** JAN 3 2014

Times Cited in Web of Science Core Collection: 68

Total Times Cited: 68

Usage Count (Last 180 days): 1

Usage Count (Since 2013): 63

Cited Reference Count: 51

Abstract: The local structure of SnTe has been studied using atomic pair distribution function analysis of x-ray and neutron data. Evidence is found for a locally distorted high-temperature state, which emerges on warming from an undistorted rocksalt structure. The structural distortion appears rapidly over a relatively narrow temperature range from 300 to 400 K. A similar effect has been reported in PbTe and PbS and dubbed

emphanisis; here we report on emphanisis in a compound that does not contain Pb. The analysis suggests that this effect is unrelated to the low-temperature ferroelectric state in SnTe.

Accession Number: WOS:000332171500001

Language: English

Document Type: Article

KeyWords Plus: STRUCTURAL PHASE-TRANSITIONS; MOSSBAUER-SPECTROSCOPY; LEAD CHALCOGENIDES; CRYSTAL-STRUCTURE; PHONON MODE; PBTE; SCATTERING; DISORDER; ORDER; MONOCHALCOGENIDES

Addresses: [Knox, K. R.; Bozin, E. S.; Billinge, S. J. L.] Brookhaven Natl Lab, Dept Condensed Matter Phys & Mat Sci, Upton, NY 11973 USA.

[Malliakas, C. D.; Kanatzidis, M. G.] Northwestern Univ, Dept Chem, Evanston, IL 60208 USA.

[Malliakas, C. D.; Kanatzidis, M. G.] Argonne Natl Lab, Div Mat Sci, Argonne, IL 60439 USA.

[Billinge, S. J. L.] Columbia Univ, Dept Appl Phys & Appl Math, New York, NY 10027 USA.

Corresponding Address: Knox, KR (corresponding author), Brookhaven Natl Lab, Dept Condensed Matter Phys & Mat Sci, Upton, NY 11973 USA.

Affiliations: United States Department of Energy (DOE); Brookhaven National Laboratory; Northwestern University; United States Department of Energy (DOE); Argonne National Laboratory; Columbia University

Author Identifiers:

Author	Web of Science ResearcherID	ORCID Number
Bozin, Emil	AAB-4551-2020	
Billinge, Simon		0000-0002-9734-4998

Publisher: AMER PHYSICAL SOC

Publisher Address: ONE PHYSICS ELLIPSE, COLLEGE PK, MD 20740-3844 USA

Web of Science Index: Science Citation Index Expanded (SCI-EXPANDED)

Web of Science Categories: Materials Science, Multidisciplinary; Physics, Applied; Physics, Condensed Matter

Research Areas: Materials Science; Physics

IDS Number: AC0FZ

ISSN: 2469-9950

eISSN: 2469-9969

29-char Source Abbrev.: PHYS REV B

ISO Source Abbrev.: Phys. Rev. B

Source Item Page Count: 5

Funding:

Funding Agency	Grant Number
US DOE, Office of Science, Office of Basic Energy Sciences (DOE-BES)	DE-AC02-98CH10886
DOE-BES	DE-AC02-06CH11357
DOE BES	
Los Alamos National Security LLC	DE-AC52-06NA25396

Data collection, analysis, and modeling were supported by US DOE, Office of Science, Office of Basic Energy Sciences (DOE-BES) under Contract No. DE-AC02-98CH10886. NSLS is operated by BNL under the same Contract No. Sample preparation and characterization were supported by DOE-BES under Contract No. DE-AC02-06CH11357. Neutron PDF experiments were carried out on NPDF at LANSCE, funded by DOE BES; Los Alamos National Laboratory is operated by Los Alamos National Security LLC under Contract No. DE-AC52-06NA25396.

Output Date: 2023-01-27

Record 60 of 125**Title:** Local structural evidence for strong electronic correlations in spinel LiRh₂O₄**Author(s):** Knox, KR (Knox, K. R.); Abeykoon, AMM (Abeykoon, A. M. M.); Zheng, H (Zheng, H.); Yin, WG (Yin, W. -G.); Tselik, AM (Tselik, A. M.); Mitchell, JF (Mitchell, J. F.); Billinge, SJL (Billinge, S. J. L.); Bozin, ES (Bozin, E. S.)**Source:** PHYSICAL REVIEW B **Volume:** 88 **Issue:** 17 **Article Number:** 174114 **DOI:** 10.1103/PhysRevB.88.174114 **Published:** NOV 25 2013**Times Cited in Web of Science Core Collection:** 15**Total Times Cited:** 15**Usage Count (Last 180 days):** 0**Usage Count (Since 2013):** 61**Cited Reference Count:** 30

Abstract: The local structure of the spinel LiRh₂O₄ has been studied using atomic-pair distribution function analysis of powder x-ray diffraction data. This measurement is sensitive to the presence of short Rh-Rh bonds that form due to dimerization of Rh⁴⁺ ions on the pyrochlore sublattice, independent of the existence of long-range order. We show that structural dimers exist in the low-temperature phase, as previously supposed, with a bond shortening of Δr similar to 0.15 angstrom. The dimers persist up to 350 K, well above the insulator-metal transition, with Δr decreasing in magnitude on warming. Such behavior is inconsistent with the Fermi-surface nesting-driven Peierls transition model. Instead, we argue that LiRh₂O₄ should properly be described as a strongly correlated system.

Accession Number: WOS:000327314700004**Language:** English**Document Type:** Article**KeyWords Plus:** TRANSITION; MANGANITES; CUIR2S4

Addresses: [Knox, K. R.; Abeykoon, A. M. M.; Yin, W. -G.; Tselik, A. M.; Billinge, S. J. L.; Bozin, E. S.] Brookhaven Natl Lab, Dept Condensed Matter Phys & Mat Sci, Upton, NY 11973 USA.
[Zheng, H.; Mitchell, J. F.] Argonne Natl Lab, Div Mat Sci, Argonne, IL 60439 USA.
[Billinge, S. J. L.] Columbia Univ, Dept Appl Phys & Appl Math, New York, NY 10027 USA.

Corresponding Address: Knox, KR (corresponding author), Brookhaven Natl Lab, Dept Condensed Matter Phys & Mat Sci, Upton, NY 11973 USA.

E-mail Addresses: kknnox@bnl.gov

Affiliations: United States Department of Energy (DOE); Brookhaven National Laboratory; United States Department of Energy (DOE); Argonne National Laboratory; Columbia University

Author Identifiers:

Author	Web of Science ResearcherID	ORCID Number
Tselik, Alexei	HJZ-5160-2023	0000-0002-7478-670X
Yin, Weiguo	A-9671-2014	0000-0002-4965-5329
Mitchell, John F	A-1907-2012	
Bozin, Emil	AAB-4551-2020	
Billinge, Simon		0000-0002-9734-4998

Publisher: AMER PHYSICAL SOC**Publisher Address:** ONE PHYSICS ELLIPSE, COLLEGE PK, MD 20740-3844 USA**Web of Science Index:** Science Citation Index Expanded (SCI-EXPANDED)**Web of Science Categories:** Materials Science, Multidisciplinary; Physics, Applied; Physics, Condensed Matter**Research Areas:** Materials Science; Physics**IDS Number:** 256MJ

ISSN: 1098-0121

eISSN: 1550-235X

29-char Source Abbrev.: PHYS REV B

ISO Source Abbrev.: Phys. Rev. B

Source Item Page Count: 6

Funding:

Funding Agency	Grant Number
U.S. Department of Energy, Office of Science, Office of Basic Energy Sciences (DOE-BES)	DE-AC02-06CH11357
DOE-BES	DE-AC02-98CH10886

Sample preparation and characterization work at Argonne National Laboratory was supported by the U.S. Department of Energy, Office of Science, Office of Basic Energy Sciences (DOE-BES) under Contract No. DE-AC02-06CH11357. PDF x-ray experiments, data analysis, and modeling were carried out at Brookhaven National Laboratory, supported by DOE-BES under Contract No. DE-AC02-98CH10886. Use of the National Synchrotron Light Source, Brookhaven National Laboratory, was supported by the DOE-BES under Contract No. DE-AC02-98CH10886.

Open Access: Green Submitted

Output Date: 2023-01-27

Record 61 of 125

Title: New Layered Fluorosulfide SrFBiS₂

Author(s): Lei, HC (Lei, Hechang); Wang, KF (Wang, Kefeng); Abeykoon, M (Abeykoon, Milinda); Bozin, ES (Bozin, Emil S.); Petrovic, C (Petrovic, Cedomir)

Source: INORGANIC CHEMISTRY **Volume:** 52 **Issue:** 18 **Pages:** 10685-10689 **DOI:** 10.1021/ic4018135 **Published:** SEP 16 2013

Times Cited in Web of Science Core Collection: 73

Total Times Cited: 73

Usage Count (Last 180 days): 2

Usage Count (Since 2013): 85

Cited Reference Count: 36

Abstract: We have synthesized a new layered BiS₂-based compound, SrFBiS₂. This compound has a similar structure to LaOBiS₂. It is built up by stacking up SrF layers and NaCl-type BiS₂ layers alternatively along the c axis. Electric transport measurement indicates that SrFBiS₂ is a semiconductor. Thermal transport measurement shows that SrFBiS₂ has a small thermal conductivity and large Seebeck coefficient. First principle calculations are in agreement with experimental results and show that SrFBiS₂ is very similar to LaOBiS₂, which becomes a superconductor with F doping. Therefore, SrFBiS₂ may be a parent compound of new superconductors.

Accession Number: WOS:000330098300057

PubMed ID: 23987520

Language: English

Document Type: Article

KeyWords Plus: SUPERCONDUCTIVITY

Addresses: [Lei, Hechang; Wang, Kefeng; Abeykoon, Milinda; Bozin, Emil S.; Petrovic, Cedomir] Brookhaven Natl Lab, Condensed Matter Phys & Mat Sci Dept, Upton, NY 11973 USA.

Corresponding Address: Petrovic, C (corresponding author), Brookhaven Natl Lab, Condensed Matter Phys & Mat Sci Dept, Upton, NY 11973 USA.

E-mail Addresses: petrovic@bnl.gov

Affiliations: United States Department of Energy (DOE); Brookhaven National Laboratory

Author Identifiers:

Author	Web of Science ResearcherID	ORCID Number
Bozin, Emil	AAB-4551-2020	
LEI, Hechang	H-3278-2016	0000-0003-0850-8514
Petrovic, Cedomir	A-8789-2009	0000-0001-6063-1881
Wang, Kefeng	E-7683-2011	0000-0002-8449-9720

Publisher: AMER CHEMICAL SOC

Publisher Address: 1155 16TH ST, NW, WASHINGTON, DC 20036 USA

Web of Science Index: Science Citation Index Expanded (SCI-EXPANDED)

Web of Science Categories: Chemistry, Inorganic & Nuclear

Research Areas: Chemistry

IDS Number: 295EB

ISSN: 0020-1669

eISSN: 1520-510X

29-char Source Abbrev.: INORG CHEM

ISO Source Abbrev.: Inorg. Chem.

Source Item Page Count: 5

Funding:

Funding Agency	Grant Number
U.S. DOE	DE-ACO2-98CH10886
Center for Emergent Superconductivity, an Energy Frontier Research Center	
U.S. DOE, Office for Basic Energy Science	

We thank John Warren for help with SEM measurements. Work at Brookhaven is supported by the U.S. DOE under Contract No. DE-ACO2-98CH10886 and in part by the Center for Emergent Superconductivity, an Energy Frontier Research Center funded by the U.S. DOE, Office for Basic Energy Science (HI. and C.P.). This work benefited from usage of X17A beamline of the National Synchrotron Light Source at Brookhaven National Laboratory. We gratefully acknowledge Zhong Zhong and Jonathan Hanson for their help with the X17A experiment setup.

Open Access: Green Submitted

Output Date: 2023-01-27

Record 62 of 125

Title: Evidence for Short-Range-Ordered Charge Stripes Far above the Charge-Ordering Transition in La_{1.67}Sr_{0.33}NiO₄

Author(s): Abeykoon, AMM (Abeykoon, A. M. Milinda); Bozin, ES (Bozin, Emil S.); Yin, WG (Yin, Wei-Guo); Gu, GD (Gu, Genda); Hill, JP (Hill, John P.); Tranquada, JM (Tranquada, John M.); Billinge, SJL (Billinge, Simon J. L.)

Source: PHYSICAL REVIEW LETTERS **Volume:** 111 **Issue:** 9 **Article Number:** 096404 **DOI:** 10.1103/PhysRevLett.111.096404 **Published:** AUG 30 2013

Times Cited in Web of Science Core Collection: 23

Total Times Cited: 23

Usage Count (Last 180 days): 0

Usage Count (Since 2013): 41

Cited Reference Count: 43

Abstract: The temperature evolution of structural effects associated with charge order (CO) and spin order in $\text{La}_{1.67}\text{Sr}_{0.33}\text{NiO}_4$ has been investigated using neutron powder diffraction. We report an anomalous shrinking of the c/a lattice parameter ratio that correlates with T-CO. The sign of this change can be explained by the change in interlayer Coulomb energy between the static-stripe-ordered state and the fluctuating-stripe-ordered state or the charge-disordered state. In addition, we identify a contribution to the mean-square displacements of Ni and in-plane O atoms whose width correlates quite well with the size of the pseudogap extracted from the reported optical conductivity, with a non-Debye-like component that persists below and well above T-CO. We infer that dynamic charge-stripe correlations survive to T similar to $2T(\text{CO})$.

Accession Number: WOS:000323716400005

PubMed ID: 24033056

Language: English

Document Type: Article

KeyWords Plus: FLUCTUATING STRIPES; NEUTRON-SCATTERING; SUPERCONDUCTORS; $\text{La}_{5/3}\text{Sr}_{1/3}\text{NiO}_4$; PSEUDOGAP; PHASES

Addresses: [Abeykoon, A. M. Milinda; Bozin, Emil S.; Yin, Wei-Guo; Gu, Genda; Hill, John P.; Tranquada, John M.; Billinge, Simon J. L.] Brookhaven Natl Lab, Condensed Matter Phys & Mat Sci Dept, Upton, NY 11973 USA.

[Billinge, Simon J. L.] Columbia Univ, Dept Appl Phys & Appl Math, New York, NY 10027 USA.

Corresponding Address: Abeykoon, AMM (corresponding author), Brookhaven Natl Lab, Condensed Matter Phys & Mat Sci Dept, Upton, NY 11973 USA.

Affiliations: United States Department of Energy (DOE); Brookhaven National Laboratory; Columbia University

Author Identifiers:

Author	Web of Science ResearcherID	ORCID Number
Yin, Weiguo	A-9671-2014	0000-0002-4965-5329
Bozin, Emil	AAB-4551-2020	
Tranquada, John M.	A-9832-2009	0000-0003-4984-8857
Billinge, Simon		0000-0002-9734-4998

Publisher: AMER PHYSICAL SOC

Publisher Address: ONE PHYSICS ELLIPSE, COLLEGE PK, MD 20740-3844 USA

Web of Science Index: Science Citation Index Expanded (SCI-EXPANDED)

Web of Science Categories: Physics, Multidisciplinary

Research Areas: Physics

IDS Number: 208XS

ISSN: 0031-9007

29-char Source Abbrev.: PHYS REV LETT

ISO Source Abbrev.: Phys. Rev. Lett.

Source Item Page Count: 5

Funding:

Funding Agency	Grant Number
Office of Basic Energy Sciences, Division of Materials Sciences and Engineering, U.S. Department of Energy	DE-AC02-98CH10886
DOE Office of Basic Energy Sciences	
DOE	DE-AC52-06NA25396

This work was supported by the Office of Basic Energy Sciences, Division of Materials Sciences and Engineering, U.S. Department of Energy through account No. DE-AC02-98CH10886. This work has benefited from the use of NPDF at LANSCE, funded by DOE Office of Basic Energy Sciences. LANL is operated by Los Alamos National Security LLC under DOE Contract No. DE-AC52-06NA25396.

Open Access: Green Submitted

Output Date: 2023-01-27

Record 63 of 125

Title: Thermal Evolution of Cation Distribution/Crystallite Size and Their Correlation with the Magnetic State of Yb-Substituted Zinc Ferrite Nanoparticles

Author(s): Vucinic-Vasic, M (Vucinic-Vasic, M.); Bozin, ES (Bozin, E. S.); Bessais, L (Bessais, L.); Stojanovic, G (Stojanovic, G.); Kozmidis-Luburic, U (Kozmidis-Luburic, U.); Abeykoon, M (Abeykoon, M.); Jancar, B (Jancar, B.); Meden, A (Meden, A.); Kremenovic, A (Kremenovic, A.); Antic, B (Antic, B.)

Source: JOURNAL OF PHYSICAL CHEMISTRY C **Volume:** 117 **Issue:** 23 **Pages:** 12358-12365 **DOI:** 10.1021/jp403459t **Published:** JUN 13 2013

Times Cited in Web of Science Core Collection: 23

Total Times Cited: 23

Usage Count (Last 180 days): 0

Usage Count (Since 2013): 19

Cited Reference Count: 22

Abstract: Evolution of the structural and magnetic properties of ZnFe_{1.95}Yb_{0.05}O₄ nanoparticles, prepared via a high-energy ball milling route and exposed to further thermal annealing/heating, was assessed in detail and correlation of these properties explored. Inversion, heating of the sample to similar to 500 degrees C is found to rapidly alter the cation distribution from mixed to normal, in agreement with the known cation preferences. Under the same conditions the crystallite size only slowly grows. By further thermal treatment appreciably. An interrelationship among the lattice parameter, octahedral site occupancy, and crystallite size has been established. The observations are (a) both the site occupancy of Fe³⁺ at octahedral 16d spinel sites (N-16d(Fe³⁺)) and the cubic lattice parameter rapidly increase with an initial increase of the crystallite size, (b) the lattice parameter increases with increasing occupancy, N-16d(Fe³⁺), and (c) there appears to be a critical nanoparticle diameter (approximately 15 nm) above which both the site occupancy and lattice parameter values are saturated. The magnetic behavior of the annealed samples appears to be correlated to the evolution of both the cation distribution and crystallite size, as follows. As-prepared samples and those annealed at lower temperatures show superparamagnetic behavior at room temperature, presumably as a consequence of the Fe³⁺ distribution and strong Fe³⁺(8a)-O-Fe³⁺(16d) superexchange interactions. Samples with a nanoparticle diameter greater than 12 nm and with almost normal distributions exhibit the paramagnetic state. The coercive field is found to decrease with an increase of the crystallite size. Partial Yb³⁺/Fe³⁺ substitution is found to increase the inversion parameter and saturation magnetization. Detailed knowledge of the thermal evolution of structural/microstructural parameters allows control over the cation distribution and crystallite size and hence the magnetic properties of nanoferrites.

Accession Number: WOS:000320640500054

Language: English

Document Type: Article

Keywords Plus: MICROSTRUCTURE

Addresses: [Vucinic-Vasic, M.; Stojanovic, G.; Kozmidis-Luburic, U.] Univ Novi Sad, Fac Tech Sci, Novi Sad 21000, Serbia.

[Bozin, E. S.; Abeykoon, M.] Brookhaven Natl Lab, Condensed Matter Phys & Mat Sci Dept, Upton, NY 11973 USA.

[Bessais, L.] CNRS, UMR 7075, ICPME, F-94230 Thiais, France.

[Bessais, L.] Univ Paris 06, F-94230 Thiais, France.

[Jancar, B.] Jozef Stefan Inst, Ljubljana 1000, Slovenia.

[Meden, A.] Univ Ljubljana, Fac Chem & Chem Technol, Ljubljana 1000, Slovenia.

[Kremenovic, A.; Antic, B.] Univ Belgrade, Inst Nucl Sci Vinca, POB 522, Belgrade 11001, Serbia.

[Kremenovic, A.] Univ Belgrade, Fac Min & Geol, Crystallog Lab, Belgrade 11001, Serbia.

Corresponding Address: Antic, B (corresponding author), Univ Belgrade, Inst Nucl Sci Vinca, POB 522, Belgrade 11001, Serbia.

E-mail Addresses: bantic@vinca.rs

Affiliations: University of Novi Sad; United States Department of Energy (DOE); Brookhaven National Laboratory; Centre National de la Recherche Scientifique (CNRS); Universite Paris-Est-Creteil-Val-de-Marne (UPEC); UDICE-French Research Universities; Sorbonne Universite; Slovenian Academy of Sciences & Arts (SASA); Jozef Stefan Institute; University of Ljubljana; University of Belgrade; University of Belgrade

Author Identifiers:

Author	Web of Science ResearcherID	ORCID Number
Kremenovic, A	AAL-7534-2020	0000-0001-8845-2332
Bessais, Lotfi	I-5423-2013	0000-0001-7236-1604
Bozin, Emil	AAB-4551-2020	
Stojanović, Goran M	R-5402-2016	0000-0003-2098-189X
Antic, Bratislav		0000-0002-5693-6401

Publisher: AMER CHEMICAL SOC

Publisher Address: 1155 16TH ST, NW, WASHINGTON, DC 20036 USA

Web of Science Index: Science Citation Index Expanded (SCI-EXPANDED)

Web of Science Categories: Chemistry, Physical; Nanoscience & Nanotechnology; Materials Science, Multidisciplinary

Research Areas: Chemistry; Science & Technology - Other Topics; Materials Science

IDS Number: 167OE

ISSN: 1932-7447

eISSN: 1932-7455

29-char Source Abbrev.: J PHYS CHEM C

ISO Source Abbrev.: J. Phys. Chem. C

Source Item Page Count: 8

Funding:

Funding Agency	Grant Number
Serbian Ministry of Education and Science	III45015
U.S. Department of Energy, Office of Science, Office of Basic Energy Sciences	DE-AC02-98CH10886
U.S. Department of Energy, Office of Science	DE-AC02-06CH11357

The Serbian Ministry of Education and Science has financially supported this work under Contract No. III45015. Work at Brookhaven National Laboratory was supported by the U.S. Department of Energy, Office of Science, Office of Basic Energy Sciences, under Contract No. DE-AC02-98CH10886. This work benefited from usage of the 11-IDC beamline of the APS at ANL. Use of the APS is supported by the U.S. Department of Energy, Office of Science, under Contract No. DE-AC02-06CH11357.

Output Date: 2023-01-27

Record 64 of 125

Title: An integrated study of thermal treatment effects on the microstructure and magnetic properties of Zn-ferrite nanoparticles

Author(s): Antic, B (Antic, Bratislav); Perovic, M (Perovic, Marija); Kremenovic, A (Kremenovic, Aleksandar); Blanusa, J (Blanusa, Jovan); Spasojevic, V (Spasojevic, Vojislav); Vulic, P (Vulic, Predrag);

Bessais, L (Bessais, Lotfi); Bozin, ES (Bozin, Emil S.)

Source: JOURNAL OF PHYSICS-CONDENSED MATTER **Volume:** 25 **Issue:** 8 **Article Number:** 086001 **DOI:** 10.1088/0953-8984/25/8/086001 **Published:** FEB 27 2013

Times Cited in Web of Science Core Collection: 22

Total Times Cited: 22

Usage Count (Last 180 days): 2

Usage Count (Since 2013): 50

Cited Reference Count: 57

Abstract: The evolution of the magnetic state, crystal structure and microstructure parameters of nanocrystalline zinc-ferrite, tuned by thermal annealing of similar to 4 nm nanoparticles, was systematically studied by complementary characterization methods. Structural analysis of neutron and synchrotron x-ray radiation data revealed a mixed cation distribution in the nanoparticle samples, with the degree of inversion systematically decreasing from 0.25 in an as-prepared nanocrystalline sample to a non-inverted spinel structure with a normal cation distribution in the bulk counterpart. The results of DC magnetization and Mossbauer spectroscopy experiments indicated a superparamagnetic relaxation in similar to 4 nm nanoparticles, albeit with different freezing temperatures T_f of 27.5 K and 46 K, respectively. The quadrupole splitting parameter decreases with the annealing temperature due to cation redistribution between the tetrahedral and octahedral sites of the spinel structure and the associated defects. DC magnetization measurements indicated the existence of significant interparticle interactions among nanoparticles ('superspins'). Additional confirmation for the presence of interparticle interactions was found from the fit of the $T_f(H)$ dependence to the AT line, from which a value of the anisotropy constant of $K_{\text{eff}} = 5.6 \times 10^5 \text{ erg cm}^{-3}$ was deduced. Further evidence for strong interparticle interactions was found from AC susceptibility measurements, where the frequency dependence of the freezing temperature $T_f(f)$ was satisfactorily described by both Vogel-Fulcher and dynamic scaling theory, both applicable for interacting systems. The parameters obtained from these fits suggest collective freezing of magnetic moments at T_f .

Accession Number: WOS:000314780400024

PubMed ID: 23343510

Language: English

Document Type: Article

KeyWords Plus: CLUSTER GLASS BEHAVIOR; FINE-PARTICLE SYSTEM; SPIN-GLASS; FIELD-DEPENDENCE; ZNFE2O4; HYDROLYSIS; DYNAMICS

Addresses: [Antic, Bratislav; Perovic, Marija; Blanusa, Jovan; Spasojevic, Vojislav] Univ Belgrade, Condensed Matter Phys Lab, Inst Nucl Sci Vinca, Belgrade 11001, Serbia.

[Kremenovic, Aleksandar; Vulic, Predrag] Univ Belgrade, Fac Min & Geol, Crystallog Lab, Belgrade 11001, Serbia.

[Bessais, Lotfi] Univ Paris 12, CNRS, UMR 7182, CMTR, ICMPE, F-94320 Thiais, France.

[Bozin, Emil S.] Brookhaven Natl Lab, Condensed Matter Phys & Mat Sci Dept, Upton, NY 11973 USA.

Corresponding Address: Antic, B (corresponding author), Univ Belgrade, Condensed Matter Phys Lab, Inst Nucl Sci Vinca, POB 522, Belgrade 11001, Serbia.

E-mail Addresses: bantic@vinca.rs

Affiliations: University of Belgrade; University of Belgrade; Centre National de la Recherche Scientifique (CNRS); CNRS - Institute of Chemistry (INC); Universite Paris-Est-Creteil-Val-de-Marne (UPEC); United States Department of Energy (DOE); Brookhaven National Laboratory

Author Identifiers:

Author	Web of Science ResearcherID	ORCID Number
Vulic, Predrag	B-3884-2008	0000-0002-4806-4551
Bessais, Lotfi	I-5423-2013	0000-0001-7236-1604
Kremenovic, A	AAL-7534-2020	0000-0001-8845-2332
Perović, Marija	AHD-2573-2022	

Bozin, Emil	AAB-4551-2020	
Spasojevic, Vojislav		0000-0002-6134-8989
Blanusa, Jovan		0000-0003-4930-9730
Perovic, Marija		0000-0002-0088-7612
Antic, Bratislav		0000-0002-5693-6401

Publisher: IOP Publishing Ltd

Publisher Address: TEMPLE CIRCUS, TEMPLE WAY, BRISTOL BS1 6BE, ENGLAND

Web of Science Index: Science Citation Index Expanded (SCI-EXPANDED)

Web of Science Categories: Physics, Condensed Matter

Research Areas: Physics

IDS Number: 087RR

ISSN: 0953-8984

eISSN: 1361-648X

29-char Source Abbrev.: J PHYS-CONDENS MAT

ISO Source Abbrev.: J. Phys.-Condes. Matter

Source Item Page Count: 13

Funding:

Funding Agency	Grant Number
Serbian Ministry of Education and Science	III 45015
US DOE	DE-AC02-98CH10886 DE-AC02-06CH11357
LANSCE at Los Alamos National Laboratory	DEAC52-06NA25396

The Serbian Ministry of Education and Science has financially supported this work under contract No. III 45015. We would like to thank Professor Vladimir Srdic for sample preparation. The work at the Brookhaven National Laboratory was supported by the US DOE under Contract No. DE-AC02-98CH10886. The experiments at the Advanced Photon Source at the Argonne National Laboratory were supported by the US DOE Contract No. DE-AC02-06CH11357, and those at LANSCE at Los Alamos National Laboratory under Contract No. DEAC52-06NA25396.

Output Date: 2023-01-27

Record 65 of 125

Title: Crystal-Field Splitting and Correlation Effect on the Electronic Structure of $A(2)IrO(3)$

Author(s): Gretarsson, H (Gretarsson, H.); Clancy, JP (Clancy, J. P.); Liu, X (Liu, X.); Hill, JP (Hill, J. P.); Bozin, E (Bozin, Emil); Singh, Y (Singh, Yogesh); Manni, S (Manni, S.); Gegenwart, P (Gegenwart, P.); Kim, J (Kim, Jungho); Said, AH (Said, A. H.); Casa, D (Casa, D.); Gog, T (Gog, T.); Upton, MH (Upton, M. H.); Kim, HS (Kim, Heung-Sik); Yu, J (Yu, J.); Katukuri, VM (Katukuri, Vamshi M.); Hozoi, L (Hozoi, L.); van den Brink, J (van den Brink, Jeroen); Kim, YJ (Kim, Young-June)

Source: PHYSICAL REVIEW LETTERS **Volume:** 110 **Issue:** 7 **Article Number:** 076402 **DOI:** 10.1103/PhysRevLett.110.076402 **Published:** FEB 13 2013

Times Cited in Web of Science Core Collection: 193

Total Times Cited: 194

Usage Count (Last 180 days): 6

Usage Count (Since 2013): 241

Cited Reference Count: 41

Abstract: The electronic structure of the honeycomb lattice iridates Na_2IrO_3 and Li_2IrO_3 has been investigated using resonant inelastic x-ray scattering (RIXS). Crystal-field-split d-d excitations are resolved in

the high-resolution RIXS spectra. In particular, the splitting due to noncubic crystal fields, derived from the splitting of $j(\text{eff}) = 3/2$ states, is much smaller than the typical spin-orbit energy scale in iridates, validating the applicability of $j\text{eff}$ physics in $\text{A}(\text{2})\text{IrO}(\text{3})$. We also find excitonic enhancement of the particle-hole excitation gap around 0.4 eV, indicating that the nearest-neighbor Coulomb interaction could be large. These findings suggest that both Na_2IrO_3 and Li_2IrO_3 can be described as spin-orbit Mott insulators, similar to the square lattice iridate Sr_2IrO_4 . DOI: 10.1103/PhysRevLett.110.076402

Accession Number: WOS:000314870300006

PubMed ID: 25166387

Language: English

Document Type: Article

KeyWords Plus: X-RAY-SCATTERING; SPIN; SEPARATION; Li_2IrO_3 ; Sr_2CuO_3

Addresses: [Gretarsson, H.; Clancy, J. P.; Kim, Young-June] Univ Toronto, Dept Phys, Toronto, ON M5S 1A7, Canada.

[Liu, X.; Hill, J. P.; Bozin, Emil] Brookhaven Natl Lab, CMP&MS Dept, Upton, NY 11973 USA.

[Singh, Yogesh] Indian Inst Sci Educ & Res Mohali, Sect 81, Sas Nagar, Punjab, India.

[Manni, S.; Gegenwart, P.] Univ Gottingen, Inst Phys 1, D-37077 Gottingen, Germany.

[Kim, Jungho; Said, A. H.; Casa, D.; Gog, T.; Upton, M. H.] Argonne Natl Lab, Adv Photon Source, Argonne, IL 60439 USA.

[Kim, Heung-Sik; Yu, J.] Seoul Natl Univ, Dept Phys & Astron, Seoul 151747, South Korea.

[Katukuri, Vamshi M.; Hozoi, L.; van den Brink, Jeroen] IFW Dresden, Inst Theoret Solid State Phys, D-01069 Dresden, Germany.

Corresponding Address: Gretarsson, H (corresponding author), Univ Toronto, Dept Phys, 60 St George St, Toronto, ON M5S 1A7, Canada.

E-mail Addresses: yjkim@physics.utoronto.ca

Affiliations: University of Toronto; United States Department of Energy (DOE); Brookhaven National Laboratory; Indian Institute of Science Education & Research (IISER) - Mohali; University of Gottingen; United States Department of Energy (DOE); Argonne National Laboratory; Seoul National University (SNU); Institute for Integrative Nanosciences (IIN); Leibniz Institute for Solid State & Materials Research Dresden

Author Identifiers:

Author	Web of Science ResearcherID	ORCID Number
Bozin, Emil	AAB-4551-2020	
Katukuri, Vamshi Mohan	J-4048-2015	0000-0001-9355-0594
Kim, Young-June	G-7196-2011	0000-0002-1172-8895
Gretarsson, Hlynur	M-5141-2017	
Manni, Soham	G-1455-2016	0000-0001-6279-3497
Casa, Diego M	F-9060-2016	
Singh, Yogesh	AAD-9310-2019	
van den Brink, Jeroen	E-5670-2011	0000-0001-6594-9610
Gegenwart, Philipp	A-7291-2017	0000-0003-4180-3785
singh, yogesh	F-7160-2016	
Yu, Jaejun	CAF-9846-2022	0000-0003-0460-3565
Kim, HeungSik	J-3149-2019	0000-0003-0691-7605
van den Brink, Jeroen	Y-3931-2019	
Upton, Mary		0000-0002-9929-0487
Liu, Xuerong		0000-0001-7688-1156
Clancy, James Patrick		0000-0002-6569-7369

Publisher: AMER PHYSICAL SOC

Publisher Address: ONE PHYSICS ELLIPSE, COLLEGE PK, MD 20740-3844 USA

Web of Science Index: Science Citation Index Expanded (SCI-EXPANDED)

Web of Science Categories: Physics, Multidisciplinary

Research Areas: Physics

IDS Number: 088XD

ISSN: 0031-9007

eISSN: 1079-7114

29-char Source Abbrev.: PHYS REV LETT

ISO Source Abbrev.: Phys. Rev. Lett.

Source Item Page Count: 5

Funding:

Funding Agency	Grant Number
NSERC	
CFI	
OMRI	
Computational Materials and Chemical Sciences Network (CMCSN) Program of the Division of Materials Science and Engineering, U.S. Department of Energy	DE-SC0007091
U.S. DOE Office of Science	DE-AC02-06CH11357
DOE, Office of Science, Division of Materials Science	DE-AC02-98CH10886
KOFST through the Brainpool Program	
NRF through the ARP	R17-2008-033-01000-0
KISTI Supercomputing Center through the strategic support program for supercomputing application research	KSC-2010-S00-0005
Erasmus Mundus Eurindia Project	

We would like to thank Y. B. Kim and S. Bhattacharjee for fruitful discussions and Doug Robinson for technical assistance during the PDF measurements. Research at the University of Toronto was supported by the NSERC, CFI, and OMRI. This research benefited from the RIXS Collaboration, which is supported by the Computational Materials and Chemical Sciences Network (CMCSN) Program of the Division of Materials Science and Engineering, U.S. Department of Energy, Grant No. DE-SC0007091. Use of the APS was supported by the U.S. DOE Office of Science, under Contract No. DE-AC02-06CH11357. Work performed at Brookhaven National Laboratory was supported by the DOE, Office of Science, Division of Materials Science, under Contract No. DE-AC02-98CH10886. Y.-J. Kim was supported by the KOFST through the Brainpool Program. H.-S. Kim and J. Yu were supported by the NRF through the ARP (R17-2008-033-01000-0). H.-S. Kim would like to acknowledge the support from the KISTI Supercomputing Center through the strategic support program for supercomputing application research (No. KSC-2010-S00-0005). S. Manni acknowledges support from the Erasmus Mundus Eurindia Project.

Open Access: Green Submitted, hybrid

ESI Highly Cited Paper: Y

ESI Hot Paper: N

Output Date: 2023-01-27

Record 66 of 125

Title: Metastability and Structural Polymorphism in Noble Metals: The Role of Composition and Metal Atom Coordination in Mono- and Bimetallic Nanoclusters

Author(s): Sanchez, SI (Sanchez, Sergio I.); Small, MW (Small, Matthew W.); Bozin, ES (Bozin, Emil S.); Wen, JG (Wen, Jian-Guo); Zuo, JM (Zuo, Jian-Min); Nuzzo, RG (Nuzzo, Ralph G.)

Source: ACS NANO **Volume:** 7 **Issue:** 2 **Pages:** 1542-1557 **DOI:** 10.1021/nm305314m **Published:** FEB 2013

Times Cited in Web of Science Core Collection: 33

Total Times Cited: 33

Usage Count (Last 180 days): 1

Usage Count (Since 2013): 158

Cited Reference Count: 73

Abstract: This study examines structural variations found in the atomic ordering of different transition metal nanoparticles synthesized via a common, kinetically controlled protocol: reduction of an aqueous solution of metal precursor salt(s) with NaBH₄ at 273 K in the presence of a capping polymer ligand. These noble metal nanoparticles were characterized at the atomic scale using spherical aberration-corrected scanning transmission electron microscopy (C-s-STEM). It was found for monometallic samples that the third row, face-centered-cubic (fcc), transition metal [(3M)-Ir, Pt, and Au] particles exhibited more coherently ordered geometries than their second row, fcc, transition metal [(2M)-Rh, Pd, and Ag] analogues. The former exhibit growth habits favoring crystalline phases with specific facet structures while the latter samples are dominated by more disordered atomic arrangements that include complex systems of facets and twinning. Atomic pair distribution function (PDF) measurements further confirmed these observations, establishing that the 3M clusters exhibit longer ranged ordering than their 2M counterparts. The assembly of intracolumn bimetallic nanoparticles (Au-Ag, Pt-Pd, and Ir-Rh) using the same experimental conditions showed a strong tendency for the 3M atoms to template long-ranged, crystalline growth of 2M metal atoms extending up to over 8 nm beyond the 3M core.

Accession Number: WOS:000315618700075

PubMed ID: 23273019

Language: English

Document Type: Article

Author Keywords: nanoparticle; atomic structure; noble metals; bimetallic; core-shell; pair distribution function; aberration corrected electron microscopy

KeyWords Plus: SURFACE-TENSION; SHAPE CONTROL; PALLADIUM NANOPARTICLES; GOLD NANOPARTICLES; CATALYTIC-ACTIVITY; SIZE; NANOCRYSTALS; DISORDER; NANOSTRUCTURES; HYDROGENATION

Addresses: [Sanchez, Sergio I.; Small, Matthew W.; Wen, Jian-Guo; Nuzzo, Ralph G.] Univ Illinois, Dept Chem, Urbana, IL 61801 USA.

[Sanchez, Sergio I.; Small, Matthew W.; Wen, Jian-Guo; Nuzzo, Ralph G.] Univ Illinois, Frederick Seitz Mat Res Lab, Urbana, IL 61801 USA.

[Zuo, Jian-Min; Nuzzo, Ralph G.] Univ Illinois, Dept Mat Sci & Engn, Urbana, IL 61801 USA.

[Bozin, Emil S.] Brookhaven Natl Lab, Condensed Matter Phys & Mat Sci Dept, Upton, NY 11973 USA.

Corresponding Address: Nuzzo, RG (corresponding author), Univ Illinois, Dept Chem, Urbana, IL 61801 USA.

E-mail Addresses: r-nuzzo@illinois.edu

Affiliations: University of Illinois System; University of Illinois Urbana-Champaign; University of Illinois System; University of Illinois Urbana-Champaign; United States Department of Energy (DOE); Brookhaven National Laboratory

Author Identifiers:

Author	Web of Science ResearcherID	ORCID Number
Bozin, Emil	AAB-4551-2020	
Zuo, Jian-Min		0000-0002-5151-3370

Publisher: AMER CHEMICAL SOC

Publisher Address: 1155 16TH ST, NW, WASHINGTON, DC 20036 USA

Web of Science Index: Science Citation Index Expanded (SCI-EXPANDED)

Web of Science Categories: Chemistry, Multidisciplinary; Chemistry, Physical; Nanoscience & Nanotechnology; Materials Science, Multidisciplinary

Research Areas: Chemistry; Science & Technology - Other Topics; Materials Science

IDS Number: 099KA

ISSN: 1936-0851

eISSN: 1936-086X

29-char Source Abbrev.: ACS NANO

ISO Source Abbrev.: ACS Nano

Source Item Page Count: 16

Funding:

Funding Agency	Grant Number
United States Department of Energy	DE-FG02-03ER15476 DE-FG02-07ER46453 DE-FG02-07ER46471
United States Department of Energy, Office of Science, Office of Basic Energy Sciences	DE-AC02-06CH11357
	DE-AC02-98CH10886

This work was sponsored in part by the United States Department of Energy Grant No. DE-FG02-03ER15476. Experiments were conducted in part at the Frederick Seitz Materials Research Laboratory Central Facilities, University of Illinois at Urbana-Champaign, which is partially supported by the United States Department of Energy under Grand Nos. DE-FG02-07ER46453 and DE-FG02-07ER46471. Work at Brookhaven National Laboratory, which is operated for the U.S. Department of Energy by Brookhaven Science Associates, is supported by Grant No. DE-AC02-98CH10886. Research was also carried out at the Advanced Photon Source (APS) at Argonne National Laboratory. Use of APS was supported by the United States Department of Energy, Office of Science, Office of Basic Energy Sciences, under Grant No. DE-AC02-06CH11357

Open Access: Green Submitted

Output Date: 2023-01-27

Record 67 of 125

Title: Confirmation of disordered structure of ultrasmall CdSe nanoparticles from X-ray atomic pair distribution function analysis

Author(s): Yang, XH (Yang, Xiaohao); Masadeh, AS (Masadeh, Ahmad S.); McBride, JR (McBride, James R.); Bozin, ES (Bozin, Emil S.); Rosenthal, SJ (Rosenthal, Sandra J.); Billinge, SJL (Billinge, Simon J. L.)

Source: PHYSICAL CHEMISTRY CHEMICAL PHYSICS **Volume:** 15 **Issue:** 22 **Pages:** 8480-8486 **DOI:** 10.1039/c3cp00111c **Published:** 2013

Times Cited in Web of Science Core Collection: 55

Total Times Cited: 55

Usage Count (Last 180 days): 1

Usage Count (Since 2013): 57

Cited Reference Count: 36

Abstract: The atomic pair distribution function (PDF) analysis of X-ray powder diffraction data has been used to study the structure of small and ultra-small CdSe nanoparticles. A method is described that uses a wurtzite and zinc-blende mixed phase model to account for stacking faults in CdSe particles. The mixed-phase model successfully describes the structure of nanoparticles larger than 2 nm yielding a stacking fault density of about 30%. However, for ultrasmall nanoparticles smaller than 2 nm, the models cannot fit the experimental PDF

showing that the structure is significantly modified from that of larger particles and the bulk. The observation of a significant change in the average structure at ultra-small size is likely to explain the unusual properties of the ultrasmall particles such as their white light emitting ability.

Accession Number: WOS:000319006100005

PubMed ID: 23525376

Language: English

Document Type: Article

KeyWords Plus: WHITE-LIGHT EMISSION; DIFFRACTION DATA; NANOCRYSTALS; TRANSFORMATION

Addresses: [Yang, Xiaohao; Billinge, Simon J. L.] Columbia Univ, Dept Appl Phys & Appl Math, New York, NY 10027 USA.

[Masadeh, Ahmad S.] Univ Jordan, Dept Phys, Amman 11942, Jordan.

[McBride, James R.; Rosenthal, Sandra J.] Vanderbilt Univ, Dept Chem, Nashville, TN 37235 USA.

[Bozin, Emil S.; Billinge, Simon J. L.] Brookhaven Natl Lab, Condensed Matter Phys & Mat Sci Dept, Upton, NY 11973 USA.

Corresponding Address: Billinge, SJL (corresponding author), Columbia Univ, Dept Appl Phys & Appl Math, New York, NY 10027 USA.

E-mail Addresses: sb2896@columbia.edu

Affiliations: Columbia University; University of Jordan; Vanderbilt University; United States Department of Energy (DOE); Brookhaven National Laboratory

Author Identifiers:

Author	Web of Science ResearcherID	ORCID Number
Yang, Xiaohao	H-3977-2013	0000-0001-6136-3575
McBride, James	D-2934-2012	0000-0003-0161-7283
Bozin, Emil	AAB-4551-2020	
Billinge, Simon		0000-0002-9734-4998

Publisher: ROYAL SOC CHEMISTRY

Publisher Address: THOMAS GRAHAM HOUSE, SCIENCE PARK, MILTON RD, CAMBRIDGE CB4 0WF, CAMBS, ENGLAND

Web of Science Index: Science Citation Index Expanded (SCI-EXPANDED)

Web of Science Categories: Chemistry, Physical; Physics, Atomic, Molecular & Chemical

Research Areas: Chemistry; Physics

IDS Number: 145HN

ISSN: 1463-9076

eISSN: 1463-9084

29-char Source Abbrev.: PHYS CHEM CHEM PHYS

ISO Source Abbrev.: Phys. Chem. Chem. Phys.

Source Item Page Count: 7

Funding:

Funding Agency	Grant Number
Center for Re-Defining Photovoltaic Efficiency Through Molecule Scale Control, an Energy Frontier Research Center	
U.S. Department of Energy, Office of Science, Office of Basic Energy Sciences	DE-SC0001085
U.S. DOE, Office of Science, Office of Basic Energy Sciences	W-31-109-Eng-38

We would like to acknowledge help from Pavol Juhas, Mouath Shatnawi, HyunJeong Kim and Christos Malliakas for help in collecting data. The X-ray data collection and analysis were supported as part of the Center for Re-Defining Photovoltaic Efficiency Through Molecule Scale Control, an Energy Frontier Research Center funded by the U.S. Department of Energy, Office of Science, Office of Basic Energy Sciences under Award Number DE-SC0001085. Data were collected at the 6IDD beamline of the MUCAT sector at the Advanced Photon Source (APS). Use of the APS is supported by the U.S. DOE, Office of Science, Office of Basic Energy Sciences, under Contract No. W-31-109-Eng-38.

Output Date: 2023-01-27

Record 68 of 125

Title: Iron chalcogenide superconductors at high magnetic fields

Author(s): Lei, HC (Lei, Hechang); Wang, KF (Wang, Kefeng); Hu, RW (Hu, Rongwei); Ryu, H (Ryu, Hyejin); Abeykoon, M (Abeykoon, Milinda); Bozin, ES (Bozin, Emil S.); Petrovic, C (Petrovic, Cedomir)

Source: SCIENCE AND TECHNOLOGY OF ADVANCED MATERIALS **Volume:** 13 **Issue:** 5 **Article Number:** 054305 **DOI:** 10.1088/1468-6996/13/5/054305 **Published:** OCT 2012

Times Cited in Web of Science Core Collection: 46

Total Times Cited: 46

Usage Count (Last 180 days): 2

Usage Count (Since 2013): 97

Cited Reference Count: 151

Abstract: Iron chalcogenide superconductors have become one of the most investigated superconducting materials in recent years due to high upper critical fields, competing interactions and complex electronic and magnetic phase diagrams. The structural complexity, defects and atomic site occupancies significantly affect the normal and superconducting states in these compounds. In this work we review the vortex behavior, critical current density and high magnetic field pair-breaking mechanism in iron chalcogenide superconductors. We also point to relevant structural features and normal-state properties.

Accession Number: WOS:000314425100009

PubMed ID: 27877518

Language: English

Document Type: Review

Author Keywords: iron chalcogenide superconductors; upper critical fields; vortex physics; critical current density

KeyWords Plus: LAYERED SUPERCONDUCTOR; GRAIN-BOUNDARIES; TEMPERATURE; LIFEAS; ORDER; ANISOTROPY; SPIN

Addresses: [Lei, Hechang; Wang, Kefeng; Hu, Rongwei; Ryu, Hyejin; Abeykoon, Milinda; Bozin, Emil S.; Petrovic, Cedomir] Brookhaven Natl Lab, Condensed Matter Phys & Mat Sci Dept, Upton, NY 11973 USA. [Ryu, Hyejin; Petrovic, Cedomir] SUNY Stony Brook, Dept Phys & Astron, Stony Brook, NY 11794 USA.

Corresponding Address: Lei, HC (corresponding author), Brookhaven Natl Lab, Condensed Matter Phys & Mat Sci Dept, Upton, NY 11973 USA.

E-mail Addresses: hlei@bnl.gov; petrovic@bnl.gov

Affiliations: United States Department of Energy (DOE); Brookhaven National Laboratory; State University of New York (SUNY) System; State University of New York (SUNY) Stony Brook

Author Identifiers:

Author	Web of Science ResearcherID	ORCID Number
Bozin, Emil	AAB-4551-2020	
LEI, Hechang	H-3278-2016	0000-0003-0850-8514
Wang, Kefeng	E-7683-2011	0000-0002-8449-9720
Petrovic, Cedomir	A-8789-2009	0000-0001-6063-1881

Publisher: TAYLOR & FRANCIS LTD

Publisher Address: 2-4 PARK SQUARE, MILTON PARK, ABINGDON OR14 4RN, OXON, ENGLAND

Web of Science Index: Science Citation Index Expanded (SCI-EXPANDED)

Web of Science Categories: Materials Science, Multidisciplinary

Research Areas: Materials Science

IDS Number: 082WW

ISSN: 1468-6996

eISSN: 1878-5514

29-char Source Abbrev.: SCI TECHNOL ADV MAT

ISO Source Abbrev.: Sci. Technol. Adv. Mater.

Source Item Page Count: 23

Funding:

Funding Agency	Grant Number
US Department of Energy by Brookhaven Science Associates	DE-Ac02-98CH10886
US Department of Energy, Office of Science, Office of Basic Energy Sciences as part of the Energy Frontier Research Center (EFRC), Center for Emergent Superconductivity (CES)	
NSF	DMR-0084173
State of Florida	
US Department of Energy	

We thank T P Murphy, E S Choi, D Graf and S W Tozer for useful discussions and experiment support at NHMFL and J B Warren for help with scanning electron microscopy measurement at Brookhaven Nation Laboratory. This work was carried out at the Brookhaven National Laboratory, which is operated for the US Department of Energy by Brookhaven Science Associates DE-Ac02-98CH10886. This work was in part supported by the US Department of Energy, Office of Science, Office of Basic Energy Sciences as part of the Energy Frontier Research Center (EFRC), Center for Emergent Superconductivity (CES) (HL and CP). A portion of this work was performed at the National High Magnetic Field Laboratory, which is supported by NSF Cooperative Agreement no DMR-0084173, by the State of Florida, and by the US Department of Energy.

Open Access: Green Published

Output Date: 2023-01-27

Record 69 of 125

Title: Local structure of ReO₃ at ambient pressure from neutron total-scattering study

Author(s): Bozin, ES (Bozin, E. S.); Chatterji, T (Chatterji, T.); Billinge, SJL (Billinge, S. J. L.)

Source: PHYSICAL REVIEW B **Volume:** 86 **Issue:** 9 **Article Number:** 094110 **DOI:** 10.1103/PhysRevB.86.094110 **Published:** SEP 18 2012

Times Cited in Web of Science Core Collection: 11

Total Times Cited: 11

Usage Count (Last 180 days): 0

Usage Count (Since 2013): 32

Cited Reference Count: 32

Abstract: A hypothesis that the local rotations of ReO₆ octahedra persist in the crystallographically untilted ambient phase of ReO₃ is examined by the high-resolution neutron time-of-flight total scattering based atomic pair distribution function analysis. Three candidate models were tested, Pm (3) over barm, P4/mbm, and Im (3)

over bar, for the local structure of ReO₃ at ambient pressure and 12 K, and both quantitative and qualitative assessments of the data were performed. No evidence for large local octahedral rotations was found, suggesting that the local and the average structures are the same (Pm (3) over bar) as normally assumed.

Accession Number: WOS:000308864900001

Language: English

Document Type: Article

KeyWords Plus: X-RAY-ABSORPTION; PHASE; TRANSITION; LATTICE

Addresses: [Bozin, E. S.; Billinge, S. J. L.] Brookhaven Natl Lab, Dept Condensed Matter Phys & Mat Sci, Upton, NY 11973 USA.

[Billinge, S. J. L.] Columbia Univ, Dept Appl Phys & Appl Math, New York, NY 10027 USA.

[Chatterji, T.] Inst Max Von Laue Paul Langevin, F-38042 Grenoble 9, France.

Corresponding Address: Bozin, ES (corresponding author), Brookhaven Natl Lab, Dept Condensed Matter Phys & Mat Sci, Upton, NY 11973 USA.

Affiliations: United States Department of Energy (DOE); Brookhaven National Laboratory; Columbia University; Institut Laue-Langevin (ILL)

Author Identifiers:

Author	Web of Science ResearcherID	ORCID Number
Bozin, Emil	AAB-4551-2020	
Billinge, Simon		0000-0002-9734-4998
Chatterji, Tapan		0000-0002-2303-8904

Publisher: AMER PHYSICAL SOC

Publisher Address: ONE PHYSICS ELLIPSE, COLLEGE PK, MD 20740-3844 USA

Web of Science Index: Science Citation Index Expanded (SCI-EXPANDED)

Web of Science Categories: Materials Science, Multidisciplinary; Physics, Applied; Physics, Condensed Matter

Research Areas: Materials Science; Physics

IDS Number: 007BX

ISSN: 2469-9950

eISSN: 2469-9969

29-char Source Abbrev.: PHYS REV B

ISO Source Abbrev.: Phys. Rev. B

Source Item Page Count: 4

Funding:

Funding Agency	Grant Number
Office of Science, US Department of Energy (OS-DOE)	DE-AC02-98CH10886
DOE Office of Basic Energy Sciences	
DOE	DE-AC52-06NA25396

E.S.B. acknowledges useful discussions with John Provis, Efrain Rodriguez, and Anna Llobet. Work at Brookhaven National Laboratory was supported by the Office of Science, US Department of Energy (OS-DOE), under Contract No. DE-AC02-98CH10886. This work has benefited from the use of NPDF at the Lujan Center at Los Alamos Neutron Science Center, funded by DOE Office of Basic Energy Sciences. Los Alamos National Laboratory is operated by Los Alamos National Security LLC under DOE Contract No. DE-AC52-06NA25396.

Open Access: Green Submitted, hybrid

Output Date: 2023-01-27

Record 70 of 125**Title:** Magnetism in La₂O₃(Fe_{1-x}Mn_x)₂Se-2 tuned by Fe/Mn ratio**Author(s):** Lei, HC (Lei, Hechang); Bozin, ES (Bozin, Emil S.); Llobet, A (Llobet, A.); Ivanovski, V (Ivanovski, V.); Koteski, V (Koteski, V.); Belosevic-Cavor, J (Belosevic-Cavor, J.); Cekic, B (Cekic, B.); Petrovic, C (Petrovic, C.)**Source:** PHYSICAL REVIEW B **Volume:** 86 **Issue:** 12 **Article Number:** 125122 **DOI:** 10.1103/PhysRevB.86.125122 **Published:** SEP 17 2012**Times Cited in Web of Science Core Collection:** 16**Total Times Cited:** 17**Usage Count (Last 180 days):** 0**Usage Count (Since 2013):** 34**Cited Reference Count:** 33**Abstract:** We report the evolution of structural and magnetic properties in La₂O₃(Fe_{1-x}Mn_x)₂Se-2. Heat capacity and bulk magnetization indicate an increased ferromagnetic component of the long-range magnetic order and possible increased degree of frustration. Atomic disorder on Fe(Mn) sites suppresses the temperature of the long-range order whereas intermediate alloys show a rich magnetic phase diagram.**Accession Number:** WOS:000308867200005**Language:** English**Document Type:** Article**KeyWords Plus:** BOND-VALENCE PARAMETERS; OXYCHALCOGENIDES; SUPERCONDUCTIVITY; SPIN**Addresses:** [Lei, Hechang; Bozin, Emil S.; Petrovic, C.] Brookhaven Natl Lab, Condensed Matter Phys & Mat Sci Dept, Uptown, NY 11973 USA.

[Llobet, A.] Los Alamos Natl Lab, Lujan Neutron Scattering Ctr, Los Alamos, NM 87545 USA.

[Ivanovski, V.; Koteski, V.; Belosevic-Cavor, J.; Cekic, B.] Univ Belgrade, Inst Nucl Sci Vinca, Belgrade 11001, Serbia.

Corresponding Address: Lei, HC (corresponding author), Brookhaven Natl Lab, Condensed Matter Phys & Mat Sci Dept, Uptown, NY 11973 USA.**Affiliations:** United States Department of Energy (DOE); Brookhaven National Laboratory; United States Department of Energy (DOE); Los Alamos National Laboratory; University of Belgrade**Author Identifiers:**

Author	Web of Science ResearcherID	ORCID Number
Ivanovski, Valentin	AAT-8089-2020	0000-0001-7036-7631
Bozin, Emil	AAB-4551-2020	
Llobet, Anna	B-1672-2010	0000-0002-7490-4630
Petrovic, Cedomir	A-8789-2009	0000-0001-6063-1881
Belosevic -Cavor, Jelena		0000-0002-8457-1577

Publisher: AMER PHYSICAL SOC**Publisher Address:** ONE PHYSICS ELLIPSE, COLLEGE PK, MD 20740-3844 USA**Web of Science Index:** Science Citation Index Expanded (SCI-EXPANDED)**Web of Science Categories:** Materials Science, Multidisciplinary; Physics, Applied; Physics, Condensed Matter**Research Areas:** Materials Science; Physics**IDS Number:** 007CU**ISSN:** 2469-9950**eISSN:** 2469-9969**29-char Source Abbrev.:** PHYS REV B

ISO Source Abbrev.: Phys. Rev. B

Source Item Page Count: 7

Funding:

Funding Agency	Grant Number
US Department of Energy (DOE) by Bookcases Science Associates	DE-Ac02-98CH10886
DOE Office of Basic Energy Sciences	
DOE	DE-AC52-06NA25396
Serbian Ministry of Education and Science	45018

Part of this work was carried out at Brookhaven National Laboratory which is operated for the US Department of Energy (DOE) by Bookcases Science Associates under Grant No. DE-Ac02-98CH10886. A portion of this work benefited from the use of a high-intensity powder diffractometer at the Lujan Center at Los Alamos Neutron Science Center, funded by DOE Office of Basic Energy Sciences. Los Alamos National Laboratory is operated by Los Alamos National Security LLC under DOE Contract No. DE-AC52-06NA25396. This work was also supported by Grant No. 45018 from the Serbian Ministry of Education and Science.

Open Access: Green Submitted, hybrid

Output Date: 2023-01-27

Record 71 of 125

Title: Electronic thermoelectric power factor and metal-insulator transition in FeSb₂

Author(s): Jie, Q (Jie, Qing); Hu, RW (Hu, Rongwei); Bozin, E (Bozin, Emil); Llobet, A (Llobet, A.); Zaliznyak, I (Zaliznyak, I.); Petrovic, C (Petrovic, C.); Li, Q (Li, Q.)

Source: PHYSICAL REVIEW B **Volume:** 86 **Issue:** 11 **Article Number:** 115121 **DOI:** 10.1103/PhysRevB.86.115121 **Published:** SEP 14 2012

Times Cited in Web of Science Core Collection: 34

Total Times Cited: 34

Usage Count (Last 180 days): 2

Usage Count (Since 2013): 79

Cited Reference Count: 42

Abstract: We show that synthesis-induced metal-insulator transition (MIT) for electronic transport along the orthorhombic c axis of FeSb₂ single crystals has greatly enhanced electrical conductivity while keeping the thermopower at a relatively high level. By this means, the thermoelectric power factor is enhanced to a new record high S^{-2} similar to $8000 \mu\text{W K}^{-2} \text{cm}^{-1}$ at 28 K. We find that the large thermopower in FeSb₂ can be rationalized within the correlated electron model with two bands having large quasiparticle disparity, whereas MIT is induced by subtle structural differences. The results in this work testify that correlated electrons can produce extreme power factor values.

Accession Number: WOS:000308736700001

Language: English

Document Type: Article

KeyWords Plus: KONDO INSULATOR; TRANSPORT-PROPERTIES; SEEBECK COEFFICIENT; CE; PR; LA

Addresses: [Jie, Qing; Hu, Rongwei; Bozin, Emil; Zaliznyak, I.; Petrovic, C.; Li, Q.] Brookhaven Natl Lab, Condensed Matter Phys & Mat Sci Dept, Upton, NY 11973 USA.

[Llobet, A.] Los Alamos Natl Lab, Manuel Lujan Jr Neutron Scattering Ctr, Los Alamos, NM 87545 USA.

Corresponding Address: Jie, Q (corresponding author), Boston Coll, Dept Phys, Chestnut Hill, MA 02467 USA.

E-mail Addresses: petrovic@bnl.gov; qiangli@bnl.gov

Affiliations: United States Department of Energy (DOE); Brookhaven National Laboratory; United States Department of Energy (DOE); Los Alamos National Laboratory

Author Identifiers:

Author	Web of Science ResearcherID	ORCID Number
Bozin, Emil	AAB-4551-2020	
Zaliznyak, Igor	AAW-2535-2020	0000-0002-8548-7924
Petrovic, Cedomir	A-8789-2009	0000-0001-6063-1881
Llobet, Anna	B-1672-2010	0000-0002-7490-4630
Jie, Qing	N-8673-2013	
Zaliznyak, Igor	E-8532-2014	0000-0002-8548-7924

Publisher: AMER PHYSICAL SOC

Publisher Address: ONE PHYSICS ELLIPSE, COLLEGE PK, MD 20740-3844 USA

Web of Science Index: Science Citation Index Expanded (SCI-EXPANDED)

Web of Science Categories: Materials Science, Multidisciplinary; Physics, Applied; Physics, Condensed Matter

Research Areas: Materials Science; Physics

IDS Number: 005FU

ISSN: 2469-9950

eISSN: 2469-9969

29-char Source Abbrev.: PHYS REV B

ISO Source Abbrev.: Phys. Rev. B

Source Item Page Count: 6

Funding:

Funding Agency	Grant Number
US DOE-OS	DE-AC02-06CH11357
DOE BES	

We thank T. M. Rice and Simon Billinge for useful discussions and Milinda Abeykoon and Pavol Juhas for help with x-ray experiments. This work was carried out at the Brookhaven National Laboratory, which is operated for the US Department of Energy by Brookhaven Science Associates DE-Ac02-98CH10886. The Advanced Photon Source at Argonne National Laboratory, operated by UChicago Argonne LLC, is supported under the US DOE-OS Contract No. DE-AC02-06CH11357. Neutron PDF experiments were carried out on HIPD at LANSCE, funded by DOE BES; LANL is operated by Los Alamos National Security LLC under DE-AC52-06NA25396.

Open Access: Green Submitted

Output Date: 2023-01-27

Record 72 of 125

Title: Lattice dynamics reveals a local symmetry breaking in the emergent dipole phase of PbTe

Author(s): Jensen, KMO (Jensen, Kirsten M. O.); Bozin, ES (Bozin, Emil S.); Malliakas, CD (Malliakas, Christos D.); Stone, MB (Stone, Matthew B.); Lumsden, MD (Lumsden, Mark D.); Kanatzidis, MG (Kanatzidis, Mercouri G.); Shapiro, SM (Shapiro, Stephen M.); Billinge, SJL (Billinge, Simon J. L.)

Source: PHYSICAL REVIEW B **Volume:** 86 **Issue:** 8 **Article Number:** 085313 **DOI:** 10.1103/PhysRevB.86.085313 **Published:** AUG 20 2012

Times Cited in Web of Science Core Collection: 52

Total Times Cited: 52

Usage Count (Last 180 days): 0

Usage Count (Since 2013): 50

Cited Reference Count: 19

Abstract: Local symmetry breaking in complex materials is emerging as an important contributor to materials properties but is inherently difficult to study. Here we follow up an earlier structural observation of such a local symmetry broken phase in the technologically important compound PbTe with a study of the lattice dynamics using inelastic neutron scattering (INS). We show that the lattice dynamics are responsive to the local symmetry broken phase, giving key insights in the behavior of PbTe, but also revealing INS as a powerful tool for studying local structure. The new result is the observation of the unexpected appearance upon warming of a new zone center phonon branch in PbTe. In a harmonic solid the number of phonon branches is strictly determined by the contents and symmetry of the unit cell. The appearance of the new mode indicates a crossover to a dynamic lower symmetry structure with increasing temperature. No structural transition is seen crystallographically, but the appearance of the new mode in inelastic neutron scattering coincides with the observation of local Pb off-centering dipoles observed in the local structure. The observation resembles relaxor ferroelectricity, but since there are no inhomogeneous dopants in pure PbTe this anomalous behavior is an intrinsic response of the system. We call such an appearance of dipoles out of a nondipolar ground-state "emphanisis" meaning the appearance out of nothing. It cannot be explained within the framework of conventional phase transition theories such as soft-mode theory and challenges our basic understanding of the physics of materials.

Accession Number: WOS:000307724000005

Language: English

Document Type: Article

KeyWords Plus: LEAD-TELLURIDE; ENERGY; SCATTERING

Addresses: [Jensen, Kirsten M. O.] Univ Aarhus, Dept Chem & iNano, Ctr Mat Crystallog, DK-8000 Aarhus C, Denmark.

[Bozin, Emil S.; Shapiro, Stephen M.; Billinge, Simon J. L.] Brookhaven Natl Lab, Condensed Matter Phys & Mat Sci Dept, Upton, NY 11973 USA.

[Malliakas, Christos D.; Kanatzidis, Mercouri G.] Northwestern Univ, Dept Chem, Evanston, IL 60208 USA.

[Stone, Matthew B.; Lumsden, Mark D.] Oak Ridge Natl Lab, Quantum Condensed Matter Div, Oak Ridge, TN 37831 USA.

[Kanatzidis, Mercouri G.] Argonne Natl Lab, Div Mat Sci, Argonne, IL 60439 USA.

[Billinge, Simon J. L.] Columbia Univ, Dept Appl Phys & Appl Math, New York, NY 10027 USA.

Corresponding Address: Jensen, KMO (corresponding author), Univ Aarhus, Dept Chem & iNano, Ctr Mat Crystallog, DK-8000 Aarhus C, Denmark.

Affiliations: Aarhus University; United States Department of Energy (DOE); Brookhaven National Laboratory; Northwestern University; United States Department of Energy (DOE); Oak Ridge National Laboratory; United States Department of Energy (DOE); Argonne National Laboratory; Columbia University

Author Identifiers:

Author	Web of Science ResearcherID	ORCID Number
Jensen, Kirsten Marie Ørnsbj M. Ø.	I-9367-2012	0000-0003-0291-217X
Lumsden, Mark	F-5366-2012	0000-0002-5472-9660
Stone, Matthew	G-3275-2011	0000-0001-7884-9715
BL18, ARCS	A-3000-2012	
Bozin, Emil	AAB-4551-2020	
Billinge, Simon		0000-0002-9734-4998

Publisher: AMER PHYSICAL SOC

Publisher Address: ONE PHYSICS ELLIPSE, COLLEGE PK, MD 20740-3844 USA

Web of Science Index: Science Citation Index Expanded (SCI-EXPANDED)

Web of Science Categories: Materials Science, Multidisciplinary; Physics, Applied; Physics, Condensed Matter

Research Areas: Materials Science; Physics

IDS Number: 991TH

ISSN: 1098-0121

29-char Source Abbrev.: PHYS REV B

ISO Source Abbrev.: Phys. Rev. B

Source Item Page Count: 7

Funding:

Funding Agency	Grant Number
Office of Science, US Department of Energy (OS-DOE)	DE-AC02-98CH10886
Revolutionary Materials for Solid State Energy Conversion, an Energy Frontier Research Center	
US Department of Energy, Office of Science, Office of Basic Energy Sciences	DE-SC0001054
Scientific User Facilities Division, Office of Basic Energy Sciences, US Department of Energy	

We would like to thank Simon Johnsen for help with growing the crystal and Nicola Spaldin and Petros Souvatzis for helpful discussions. Work in the Billinge group was supported by the Office of Science, US Department of Energy (OS-DOE), under Contract No. DE-AC02-98CH10886. Work in the Kanatzidis group was supported as part of the Revolutionary Materials for Solid State Energy Conversion, an Energy Frontier Research Center funded by the US Department of Energy, Office of Science, Office of Basic Energy Sciences under Award No. DE-SC0001054. The neutron scattering measurements were carried out at the HFIR and SNS at Oak Ridge National Laboratory was sponsored by the Scientific User Facilities Division, Office of Basic Energy Sciences, US Department of Energy.

Open Access: Green Submitted

Output Date: 2023-01-27

Record 73 of 125

Title: Vacancy-induced nanoscale phase separation in $K_xFe_{2-y}Se_2$ single crystals evidenced by Raman scattering and powder x-ray diffraction

Author(s): Lazarevic, N (Lazarevic, N.); Abeykoon, M (Abeykoon, M.); Stephens, PW (Stephens, P. W.); Lei, HC (Lei, Hechang); Bozin, ES (Bozin, E. S.); Petrovic, C (Petrovic, C.); Popovic, ZV (Popovic, Z. V.)

Source: PHYSICAL REVIEW B **Volume:** 86 **Issue:** 5 **Article Number:** 054503 **DOI:** 10.1103/PhysRevB.86.054503 **Published:** AUG 6 2012

Times Cited in Web of Science Core Collection: 43

Total Times Cited: 43

Usage Count (Last 180 days): 0

Usage Count (Since 2013): 38

Cited Reference Count: 19

Abstract: Polarized Raman scattering spectra of $K_xFe_{2-y}Se_2$ were analyzed in terms of peculiarities of both $I4/m$ and $I4/mmm$ space group symmetries. The presence of the Raman active modes from both space group symmetries (16 Raman-active modes of the $I4/m$ phase and two Raman-active modes of the $I4/mmm$ phase) confirmed the existence of two crystallographic domains with different space group symmetry in a $K_xFe_{2-y}Se_2$ sample. High-resolution synchrotron powder x-ray diffraction structural refinement of the same sample confirmed the two-phase description, and determined the atomic positions and occupancies for both domains.

Accession Number: WOS:000307269800004

Language: English

Document Type: Article

KeyWords Plus: ORDER

Addresses: [Lazarevic, N.; Popovic, Z. V.] Univ Belgrade, Inst Phys Belgrade, Ctr Solid State Phys & New Mat, Belgrade 11080, Serbia.

[Abeykoon, M.; Lei, Hechang; Bozin, E. S.; Petrovic, C.] Brookhaven Natl Lab, Condensed Matter Phys & Mat Sci Dept, Upton, NY 11973 USA.

[Stephens, P. W.] SUNY Stony Brook, Dept Phys & Astron, Stony Brook, NY 11794 USA.

[Stephens, P. W.] Brookhaven Natl Lab, Photon Sci Directorate, Upton, NY 11973 USA.

Corresponding Address: Lazarevic, N (corresponding author), Univ Belgrade, Inst Phys Belgrade, Ctr Solid State Phys & New Mat, Pregrevica 118, Belgrade 11080, Serbia.

Affiliations: University of Belgrade; United States Department of Energy (DOE); Brookhaven National Laboratory; State University of New York (SUNY) System; State University of New York (SUNY) Stony Brook; United States Department of Energy (DOE); Brookhaven National Laboratory

Author Identifiers:

Author	Web of Science ResearcherID	ORCID Number
Bozin, Emil	AAB-4551-2020	
Petrovic, Cedomir	A-8789-2009	0000-0001-6063-1881
LEI, Hechang	H-3278-2016	0000-0003-0850-8514
Lazarević, Nenad Z	O-1076-2018	0000-0001-6310-9511
Lazarević, Nenad	C-3254-2012	0000-0001-6310-9511

Publisher: AMER PHYSICAL SOC

Publisher Address: ONE PHYSICS ELLIPSE, COLLEGE PK, MD 20740-3844 USA

Web of Science Index: Science Citation Index Expanded (SCI-EXPANDED)

Web of Science Categories: Materials Science, Multidisciplinary; Physics, Applied; Physics, Condensed Matter

Research Areas: Materials Science; Physics

IDS Number: 985MD

ISSN: 2469-9950

eISSN: 2469-9969

29-char Source Abbrev.: PHYS REV B

ISO Source Abbrev.: Phys. Rev. B

Source Item Page Count: 5

Funding:

Funding Agency	Grant Number
Serbian Ministry of Education and Science	ON171032 III45018
US Department of Energy (DOE)	DE-AC02-98CH10886
Center for Emergent Superconductivity	
DOE Office for Basic Energy Science	

This work was supported by the Serbian Ministry of Education and Science under Projects No. ON171032 and No. III45018. Work at Brookhaven is supported by the US Department of Energy (DOE) under Contract No. DE-AC02-98CH10886 (M.A. and E.S.B.) and in part by the Center for Emergent Superconductivity, an Energy Frontier Research Center funded by the DOE Office for Basic Energy Science (H.L. and C.P.).

Open Access: hybrid

Output Date: 2023-01-27

Record 74 of 125

Title: Quantitative nanostructure characterization using atomic pair distribution functions obtained from laboratory electron microscopes

Author(s): Abeykoon, M (Abeykoon, Milinda); Malliakas, CD (Malliakas, Christos D.); Juhas, P (Juhas, Pavol); Bozin, ES (Bozin, Emil S.); Kanatzidis, MG (Kanatzidis, Mercouri G.); Billinge, SJL (Billinge, Simon J. L.)

Source: ZEITSCHRIFT FUR KRISTALLOGRAPHIE-CRYSTALLINE MATERIALS **Volume:** 227 **Issue:** 5 **Pages:** 248-256 **DOI:** 10.1524/zkri.2012.1510 **Published:** 2012

Times Cited in Web of Science Core Collection: 37

Total Times Cited: 37

Usage Count (Last 180 days): 2

Usage Count (Since 2013): 56

Cited Reference Count: 37

Abstract: Quantitatively reliable atomic pair distribution functions (PDFs) have been obtained from nanomaterials in a straightforward way from a standard laboratory transmission electron microscope (TEM). The approach looks very promising for making electron derived PDFs (ePDFs) a routine step in the characterization of nanomaterials because of the ubiquity of such TEMs in chemistry and materials laboratories. No special attachments such as energy filters were required on the microscope. The methodology for obtaining the ePDFs is described as well as some opportunities and limitations of the method.

Accession Number: WOS:000305099900004

Language: English

Document Type: Article

Author Keywords: Pair distribution function; Electron diffraction; Nanomaterials; Polycrystalline films

KeyWords Plus: X-RAY-DIFFRACTION; AMORPHOUS MATERIALS; SCALE STRUCTURE; NANOPARTICLES; NANOCRYSTALS

Addresses: [Abeykoon, Milinda; Bozin, Emil S.; Billinge, Simon J. L.] Brookhaven Natl Lab, Condensed Matter Phys & Mat Sci Dept, Upton, NY 11973 USA.

[Malliakas, Christos D.; Kanatzidis, Mercouri G.] Northwestern Univ, Dept Chem, Evanston, IL 60208 USA.

[Juhas, Pavol; Billinge, Simon J. L.] Columbia Univ, Dept Appl Phys & Appl Math, New York, NY 10027 USA.

[Kanatzidis, Mercouri G.] Argonne Natl Lab, Div Mat Sci, Chicago, IL 60439 USA.

Corresponding Address: Billinge, SJL (corresponding author), Brookhaven Natl Lab, Condensed Matter Phys & Mat Sci Dept, POB 5000, Upton, NY 11973 USA.

E-mail Addresses: sb2896@columbia.edu

Affiliations: United States Department of Energy (DOE); Brookhaven National Laboratory; Northwestern University; Columbia University; United States Department of Energy (DOE); Argonne National Laboratory

Author Identifiers:

Author	Web of Science ResearcherID	ORCID Number
Bozin, Emil	AAB-4551-2020	
Juhas, Pavol	Q-7225-2019	0000-0001-8751-4458
Billinge, Simon		0000-0002-9734-4998

Publisher: WALTER DE GRUYTER GMBH

Publisher Address: GENTHINER STRASSE 13, D-10785 BERLIN, GERMANY

Web of Science Index: Science Citation Index Expanded (SCI-EXPANDED)

Web of Science Categories: Crystallography

Research Areas: Crystallography

IDS Number: 956OV

ISSN: 2194-4946

eISSN: 2196-7105

29-char Source Abbrev.: Z KRIST-CRYST MATER

ISO Source Abbrev.: Z. Krist.-Cryst. Mater.

Source Item Page Count: 9

Funding:

Funding Agency	Grant Number
DOE-BES	DE-AC02-98CH10886
NSF	DMR-1104965

We would like to acknowledge helpful discussions with Michael Thorpe. We also thank Jon Hanson for allowing access to the X7B beamline at NSLS, which is supported by DOE-BES under contract No DE-AC02-98CH10886. Work in the Billinge group was supported by DOE-BES through account DE-AC02-98CH10886. Work in the Kanatzidis group was supported by NSF through grant DMR-1104965.

Open Access: Green Submitted

Output Date: 2023-01-27

Record 75 of 125

Title: Phase Diagram of $K_xFe_2-Se_y(2)-S_z(z)$ and the Suppression of its Superconducting State by an Fe₂-Se/S Tetrahedron Distortion

Author(s): Lei, HC (Lei, Hechang); Abeykoon, M (Abeykoon, Milinda); Bozin, ES (Bozin, Emil S.); Wang, KF (Wang, Kefeng); Warren, JB (Warren, J. B.); Petrovic, C (Petrovic, C.)

Source: PHYSICAL REVIEW LETTERS **Volume:** 107 **Issue:** 13 **Article Number:** 137002 **DOI:** 10.1103/PhysRevLett.107.137002 **Published:** SEP 19 2011

Times Cited in Web of Science Core Collection: 65

Total Times Cited: 66

Usage Count (Last 180 days): 1

Usage Count (Since 2013): 45

Cited Reference Count: 25

Abstract: We report structurally tuned superconductivity in a $K_xFe_2-Se_y(2)-S_z(z)$ ($0 \leq z \leq 2$) phase diagram. Superconducting T_c is suppressed as S is incorporated into the lattice, eventually vanishing at 80% of S. The magnetic and conductivity properties can be related to stoichiometry on a poorly occupied Fe₁ site and the local environment of a nearly fully occupied Fe₂ site. The decreasing T_c coincides with the increasing Fe₁ occupancy and the overall increase in Fe stoichiometry from $z = 0$ to $z = 2$. Our results indicate that the irregularity of the Fe₂-Se/S tetrahedron is an important controlling parameter that can be used to tune the ground state in the new superconductor family.

Accession Number: WOS:000295005200027

PubMed ID: 22026891

Language: English

Document Type: Article

KeyWords Plus: CS

Addresses: [Lei, Hechang; Abeykoon, Milinda; Bozin, Emil S.; Wang, Kefeng; Petrovic, C.] Brookhaven Natl Lab, Condensed Matter Phys & Mat Sci Dept, Upton, NY 11973 USA.

[Warren, J. B.] Brookhaven Natl Lab, Instrumentat Div, Upton, NY 11973 USA.

Corresponding Address: Lei, HC (corresponding author), Brookhaven Natl Lab, Condensed Matter Phys & Mat Sci Dept, Upton, NY 11973 USA.

Affiliations: United States Department of Energy (DOE); Brookhaven National Laboratory; United States Department of Energy (DOE); Brookhaven National Laboratory

Author Identifiers:

Author	Web of Science ResearcherID	ORCID Number
Petrovic, Cedomir	A-8789-2009	0000-0001-6063-1881
LEI, Hechang	H-3278-2016	0000-0003-0850-8514
Wang, Kefeng	E-7683-2011	0000-0002-8449-9720
Bozin, Emil	AAB-4551-2020	

Publisher: AMER PHYSICAL SOC

Publisher Address: ONE PHYSICS ELLIPSE, COLLEGE PK, MD 20740-3844 USA

Web of Science Index: Science Citation Index Expanded (SCI-EXPANDED)

Web of Science Categories: Physics, Multidisciplinary

Research Areas: Physics

IDS Number: 821WN

ISSN: 0031-9007

eISSN: 1079-7114

29-char Source Abbrev.: PHYS REV LETT

ISO Source Abbrev.: Phys. Rev. Lett.

Source Item Page Count: 5

Funding:

Funding Agency	Grant Number
U.S. DOE	DE-AC02-98CH10886
Center for Emergent Superconductivity, an Energy Frontier Research Center	
U.S. DOE, Office for Basic Energy Science	

We thank Jonathan Hanson for help with the XRD experiment. Work at Brookhaven is supported by the U.S. DOE under Contract No. DE-AC02-98CH10886 and, in part, by the Center for Emergent Superconductivity, an Energy Frontier Research Center funded by the U.S. DOE, Office for Basic Energy Science.

Open Access: Green Submitted, hybrid

Output Date: 2023-01-27

Record 76 of 125

Title: Antiferromagnetism in semiconducting $\text{KFe}_{0.85}\text{Ag}_{1.15}\text{Te}_2$ single crystals

Author(s): Lei, HC (Lei, Hechang); Bozin, ES (Bozin, Emil S.); Wang, KF (Wang, Kefeng); Petrovic, C (Petrovic, C.)

Source: PHYSICAL REVIEW B **Volume:** 84 **Issue:** 6 **Article Number:** 060506 **DOI:** 10.1103/PhysRevB.84.060506 **Published:** AUG 16 2011

Times Cited in Web of Science Core Collection: 22

Total Times Cited: 22

Usage Count (Last 180 days): 0

Usage Count (Since 2013): 37

Cited Reference Count: 27

Abstract: We have synthesized single crystals of $\text{K}_{1.00(3)}\text{Fe}_{0.85(2)}\text{Ag}_{1.15(2)}\text{Te}_{2.0(1)}$. The material crystallizes in the ThCr_2Si_2 structure with $I4/mmm$ symmetry and without K and Fe/Ag deficiencies, unlike in $\text{K}_x\text{Fe}_{2-y}\text{Se}_2$ and $\text{K}_x\text{Fe}_{2-y}\text{S}_2$. Transport, magnetic, and heat-capacity measurements indicate that $\text{KFe}_{0.85}\text{Ag}_{1.15}\text{Te}_2$ is a semiconductor with long-range antiferromagnetic transition at $T_N = 35$ K.

Accession Number: WOS:000293918200001

Language: English

Document Type: Article

KeyWords Plus: SUPERCONDUCTIVITY; CS

Addresses: [Lei, Hechang; Bozin, Emil S.; Wang, Kefeng; Petrovic, C.] Brookhaven Natl Lab, Condensed Matter Phys & Mat Sci Dept, Upton, NY 11973 USA.

Corresponding Address: Lei, HC (corresponding author), Brookhaven Natl Lab, Condensed Matter Phys & Mat Sci Dept, Upton, NY 11973 USA.

Affiliations: United States Department of Energy (DOE); Brookhaven National Laboratory

Author Identifiers:

Author	Web of Science ResearcherID	ORCID Number
Wang, Kefeng	E-7683-2011	0000-0002-8449-9720
LEI, Hechang	H-3278-2016	0000-0003-0850-8514
Bozin, Emil	AAB-4551-2020	
Petrovic, Cedomir	A-8789-2009	0000-0001-6063-1881

Publisher: AMER PHYSICAL SOC

Publisher Address: ONE PHYSICS ELLIPSE, COLLEGE PK, MD 20740-3844 USA

Web of Science Index: Science Citation Index Expanded (SCI-EXPANDED)

Web of Science Categories: Materials Science, Multidisciplinary; Physics, Applied; Physics, Condensed Matter

Research Areas: Materials Science; Physics

IDS Number: 807RU

ISSN: 1098-0121

eISSN: 1550-235X

29-char Source Abbrev.: PHYS REV B

ISO Source Abbrev.: Phys. Rev. B

Source Item Page Count: 4

Funding:

Funding Agency	Grant Number
US DOE	DE-AC02-98CH10886
US DOE, Office for Basic Energy Science	

We thank John Warren for help with scanning electron microscopy measurements and Jonathan Hanson for help with x-ray measurements. Work at Brookhaven is supported by the US DOE under Contract No. DE-AC02-98CH10886 and in part by the Center for Emergent Superconductivity, an Energy Frontier Research Center funded by the US DOE, Office for Basic Energy Science.

Open Access: hybrid, Green Submitted

Output Date: 2023-01-27

Record 77 of 125

Title: Synthesis, crystal structure, and magnetism of beta-Fe_{1.00(2)}Se_{1.00(3)} single crystals (vol 83, 224502, 2011)

Author(s): Hu, RW (Hu, Rongwei); Lei, HC (Lei, Hechang); Abeykoon, M (Abeykoon, Milinda); Bozin, ES (Bozin, Emil S.); Billinge, SJL (Billinge, Simon J. L.); Warren, JB (Warren, J. B.); Siegrist, T (Siegrist, Theo); Petrovic, C (Petrovic, C.)

Source: PHYSICAL REVIEW B **Volume:** 84 **Issue:** 1 **Article Number:** 019903 **DOI:** 10.1103/PhysRevB.84.019903 **Published:** JUL 22 2011

Times Cited in Web of Science Core Collection: 0

Total Times Cited: 0

Usage Count (Last 180 days): 0

Usage Count (Since 2013): 11

Cited Reference Count: 1

Accession Number: WOS:000293004800006

Language: English

Document Type: Correction

Author Identifiers:

Author	Web of Science ResearcherID	ORCID Number
Bozin, Emil	AAB-4551-2020	
Petrovic, Cedomir	A-8789-2009	0000-0001-6063-1881
Bozin, Emil	E-4679-2011	
Hu, Rongwei	E-7128-2012	
Billinge, Simon		0000-0002-9734-4998

Publisher: AMER PHYSICAL SOC

Publisher Address: ONE PHYSICS ELLIPSE, COLLEGE PK, MD 20740-3844 USA

Web of Science Index: Science Citation Index Expanded (SCI-EXPANDED)

Web of Science Categories: Materials Science, Multidisciplinary; Physics, Applied; Physics, Condensed Matter

Research Areas: Materials Science; Physics

IDS Number: 795VK

ISSN: 1098-0121

29-char Source Abbrev.: PHYS REV B

ISO Source Abbrev.: Phys. Rev. B

Source Item Page Count: 1

Output Date: 2023-01-27

Record 78 of 125

Title: Synthesis, crystal structure, and magnetism of beta-Fe_{1.00(2)}Se_{1.00(3)} single crystals

Author(s): Hu, RW (Hu, Rongwei); Lei, HC (Lei, Hechang); Abeykoon, M (Abeykoon, Milinda); Bozin, ES (Bozin, Emil S.); Billinge, SJL (Billinge, Simon J. L.); Warren, JB (Warren, J. B.); Siegrist, T (Siegrist, Theo); Petrovic, C (Petrovic, C.)

Source: PHYSICAL REVIEW B **Volume:** 83 **Issue:** 22 **Article Number:** 224502 **DOI:** 10.1103/PhysRevB.83.224502 **Published:** JUN 20 2011

Times Cited in Web of Science Core Collection: 55

Total Times Cited: 56

Usage Count (Last 180 days): 4

Usage Count (Since 2013): 78

Cited Reference Count: 42

Abstract: Understanding iron-based superconductors requires high-quality impurity-free single crystals. So far they have been elusive for beta-FeSe and extraction of intrinsic materials properties has been compromised by several magnetic-impurity phases. Here, we report synchrotron-clean beta-FeSe superconducting single crystals grown via LiCl/CsCl flux method. Phase purity yields evidence for a defect-induced weak ferromagnetism that

coexists with superconductivity below T_c . In contrast to Fe_{1+y}Te-based superconductors, our results reveal that the interstitial Fe(2) site is not occupied and that all contribution to density of states at the Fermi level must come from in-plane Fe(1).

Accession Number: WOS:000291797600008

Language: English

Document Type: Article

KeyWords Plus: SUPERCONDUCTIVITY

Addresses: [Hu, Rongwei; Lei, Hechang; Abeykoon, Milinda; Bozin, Emil S.; Billinge, Simon J. L.; Petrovic, C.] Brookhaven Natl Lab, Condensed Matter Phys & Mat Sci Dept, Upton, NY 11973 USA.

[Billinge, Simon J. L.] Columbia Univ, Dept Appl Phys & Appl Math, New York, NY 10027 USA.

[Warren, J. B.] Brookhaven Natl Lab, Instrumentat Div, Upton, NY 11973 USA.

[Siegrist, Theo] Florida State Univ, Dept Chem & Biochem Engr, Tallahassee, FL 32310 USA.

[Siegrist, Theo] Florida State Univ, Natl High Magnet Field Lab, Tallahassee, FL 32310 USA.

Corresponding Address: Hu, RW (corresponding author), US DOE, Ames Lab, Ames, IA 50011 USA.

E-mail Addresses: petrovic@bnl.gov

Affiliations: United States Department of Energy (DOE); Brookhaven National Laboratory; Columbia University; United States Department of Energy (DOE); Brookhaven National Laboratory; State University System of Florida; Florida State University; State University System of Florida; Florida State University

Author Identifiers:

Author	Web of Science ResearcherID	ORCID Number
Petrovic, Cedomir	A-8789-2009	0000-0001-6063-1881
Bozin, Emil	AAB-4551-2020	
Bozin, Emil	E-4679-2011	
Hu, Rongwei	E-7128-2012	
Siegrist, Theo	R-3855-2019	0000-0001-5368-1442
LEI, Hechang	H-3278-2016	0000-0003-0850-8514
Billinge, Simon		0000-0002-9734-4998

Publisher: AMER PHYSICAL SOC

Publisher Address: ONE PHYSICS ELLIPSE, COLLEGE PK, MD 20740-3844 USA

Web of Science Index: Science Citation Index Expanded (SCI-EXPANDED)

Web of Science Categories: Materials Science, Multidisciplinary; Physics, Applied; Physics, Condensed Matter

Research Areas: Materials Science; Physics

IDS Number: 779RD

ISSN: 2469-9950

eISSN: 2469-9969

29-char Source Abbrev.: PHYS REV B

ISO Source Abbrev.: Phys. Rev. B

Source Item Page Count: 8

Funding:

Funding Agency	Grant Number
US Department of Energy, Office of Science, Office of Basic Energy Sciences as part of the Energy Frontier Research Center (EFRC)	
Center for Emergent Superconductivity (CES)	
NSF	DMR-0654118
state of Florida	

We thank Sang-Wook Cheong and Hai-Hu Wen for useful discussions and J. C. Hanson for help with XRD measurements. This work was carried out at the Brookhaven National Laboratory, which is operated for the US Department of Energy by Brookhaven Science Associates DE-Ac02-98CH10886. This work was in part supported by the US Department of Energy, Office of Science, Office of Basic Energy Sciences as part of the Energy Frontier Research Center (EFRC), and Center for Emergent Superconductivity (CES). A portion of this work was performed at the National High Magnetic Field Laboratory, which is supported by NSF Cooperative Agreement No. DMR-0654118, by the state of Florida, and by the DOE.

Open Access: Green Submitted, hybrid

Output Date: 2023-01-27

Record 79 of 125

Title: Spin-glass behavior of semiconducting $K_xFe_{2-y}S_2$

Author(s): Lei, HC (Lei, Hechang); Abeykoon, M (Abeykoon, Milinda); Bozin, ES (Bozin, Emil S.); Petrovic, C (Petrovic, C.)

Source: PHYSICAL REVIEW B **Volume:** 83 **Issue:** 18 **Article Number:** 180503 **DOI:** 10.1103/PhysRevB.83.180503 **Published:** MAY 16 2011

Times Cited in Web of Science Core Collection: 48

Total Times Cited: 48

Usage Count (Last 180 days): 0

Usage Count (Since 2013): 35

Cited Reference Count: 28

Abstract: We report the discovery of $K_xFe_{2-y}S_2$ single crystals, isostructural to $K_xFe_{2-y}Se_2$ superconductors. The sulfide compound is a small gap semiconductor and shows spin-glass behavior below 32 K. Our results indicate that stoichiometry, defects, and the local environment of $FeCh$ ($Ch = S, Se$) tetrahedra have important effects on the physical properties of isostructural and isoelectronic $K(x)Fe_{2-y}Ch_2$ compounds.

Accession Number: WOS:000290709300001

Language: English

Document Type: Article

KeyWords Plus: SUPERCONDUCTIVITY; HEAT; CUMN

Addresses: [Lei, Hechang; Abeykoon, Milinda; Bozin, Emil S.; Petrovic, C.] Brookhaven Natl Lab, Condensed Matter Phys & Mat Sci Dept, Upton, NY 11973 USA.

Corresponding Address: Lei, HC (corresponding author), Brookhaven Natl Lab, Condensed Matter Phys & Mat Sci Dept, Upton, NY 11973 USA.

Affiliations: United States Department of Energy (DOE); Brookhaven National Laboratory

Author Identifiers:

Author	Web of Science ResearcherID	ORCID Number
Bozin, Emil	E-4679-2011	
LEI, Hechang	H-3278-2016	0000-0003-0850-8514
Petrovic, Cedomir	A-8789-2009	0000-0001-6063-1881
Bozin, Emil	AAB-4551-2020	

Publisher: AMER PHYSICAL SOC

Publisher Address: ONE PHYSICS ELLIPSE, COLLEGE PK, MD 20740-3844 USA

Web of Science Index: Science Citation Index Expanded (SCI-EXPANDED)

Web of Science Categories: Materials Science, Multidisciplinary; Physics, Applied; Physics, Condensed Matter

Research Areas: Materials Science; Physics

IDS Number: 765LY

ISSN: 1098-0121

29-char Source Abbrev.: PHYS REV B

ISO Source Abbrev.: Phys. Rev. B

Source Item Page Count: 4

Funding:

Funding Agency	Grant Number
US Department of Energy (DOE)	DE-AC02-98CH10886
DOE Office for Basic Energy Science	

We thank S. L. Bud'ko for discussions, John Warren for help with scanning electron microscopy measurements, and John Hanson for help in facilitating the X7B experiment. The work at Brookhaven is supported by the US Department of Energy (DOE) under Contract No. DE-AC02-98CH10886 and in part by the Center for Emergent Superconductivity, an Energy Frontier Research Center funded by the DOE Office for Basic Energy Science.

Open Access: Green Submitted

Output Date: 2023-01-27

Record 80 of 125

Title: Heterogeneity and Disorder in Ti_{1-x}FeyO_{2-d} Nanocrystal Rutile-Based Flowerlike Aggregates: Detection of Anatase

Author(s): Kremenovic, A (Kremenovic, Aleksandar); Antic, B (Antic, Bratislav); Blanusa, J (Blanusa, Jovan); Comor, M (Comor, Mirjana); Colomban, P (Colomban, Philippe); Mazerolles, L (Mazerolles, Leo); Bozin, ES (Bozin, Emil S.)

Source: JOURNAL OF PHYSICAL CHEMISTRY C **Volume:** 115 **Issue:** 11 **Pages:** 4395-4403 **DOI:** 10.1021/jp109437b **Published:** MAR 24 2011

Times Cited in Web of Science Core Collection: 15

Total Times Cited: 15

Usage Count (Last 180 days): 0

Usage Count (Since 2013): 11

Cited Reference Count: 54

Abstract: Here we report results of systematic investigation of heterogeneity and disorder in Ti_{1-x}FeyO_{2-d} nanorod rutile-based flowerlike aggregates. It was found that Ti_{1-x}FeyO_{2-d} aggregates are composed of two crystalline phases: rutile as a dominant and anatase as a minor phase. Flowerlike aggregates were found to grow from an isometric core ca. 5-10 nm in diameter that was built from anatase and rutile nanorods ca. 5 x 100 nm that were grown on the anatase surface having base plane (001) intergrowth with an anatase plane. The direction of rutile nanorods growth, i.e., direction of the nanorod elongation, was [001]. Highly nonisometric rutile crystals produce anisotropic X-ray powder diffraction line broadening and doubling of vibrational bands in Raman spectra. Both these techniques confirmed nonisometric character of rutile crystals and gave a quantitative measure of crystal shape anisotropy in excellent agreement with high-resolution transmission electron microscopy measurements. In addition, from the atomic pair distribution function and Raman spectral analyses the level of vacancy concentration was determined in rutile and anatase phases of investigated samples.

Accession Number: WOS:000288401200006

Language: English

Document Type: Article

KeyWords Plus: TEMPERATURE SYNTHESIS; RAMAN-SPECTROSCOPY; RHODAMINE-B; THIN-FILMS; TiO₂; SIZE; PHASE; PHOTODEGRADATION; NANOMATERIALS; NANORODS

Addresses: [Kremenovic, Aleksandar; Antic, Bratislav; Blanusa, Jovan; Comor, Mirjana; Bozin, Emil S.] Univ Belgrade, Inst Nucl Sci Vinca, Belgrade 11001, Serbia.

[Kremenovic, Aleksandar] Univ Belgrade, Fac Min & Geol, Crystallog Lab, Belgrade 11000, Serbia.

[Colomban, Philippe] CNRS, UMR 7075, LADIR, F-94230 Thiais, France.

[Colomban, Philippe] Univ Paris 06, F-94230 Thiais, France.

[Mazerolles, Leo] CNRS, UMR 7182, ICMPE, F-94320 Thiais, France.

[Mazerolles, Leo] Univ Paris Est Creteil, F-94320 Thiais, France.

[Bozin, Emil S.] Brookhaven Natl Lab, Condensed Matter Phys & Mat Sci Dept, Upton, NY 11973 USA.

Corresponding Address: Kremenovic, A (corresponding author), Univ Belgrade, Inst Nucl Sci Vinca, POB 522, Belgrade 11001, Serbia.

E-mail Addresses: akremen@EUnet.rs

Affiliations: University of Belgrade; University of Belgrade; Centre National de la Recherche Scientifique (CNRS); UDICE-French Research Universities; Sorbonne Universite; Centre National de la Recherche Scientifique (CNRS); CNRS - Institute of Chemistry (INC); Universite Paris-Est-Creteil-Val-de-Marne (UPEC); Universite Paris-Est-Creteil-Val-de-Marne (UPEC); United States Department of Energy (DOE); Brookhaven National Laboratory

Author Identifiers:

Author	Web of Science ResearcherID	ORCID Number
Bozin, Emil	E-4679-2011	
Colomban, Philippe	H-8973-2019	0000-0001-6099-5423
Bozin, Emil	AAB-4551-2020	
Kremenovic, A	AAL-7534-2020	0000-0001-8845-2332
Blanusa, Jovan		0000-0003-4930-9730
Comor, Mirjana		0000-0002-7222-4500
Antic, Bratislav		0000-0002-5693-6401

Publisher: AMER CHEMICAL SOC

Publisher Address: 1155 16TH ST, NW, WASHINGTON, DC 20036 USA

Web of Science Index: Science Citation Index Expanded (SCI-EXPANDED)

Web of Science Categories: Chemistry, Physical; Nanoscience & Nanotechnology; Materials Science, Multidisciplinary

Research Areas: Chemistry; Science & Technology - Other Topics; Materials Science

IDS Number: 735GK

ISSN: 1932-7447

eISSN: 1932-7455

29-char Source Abbrev.: J PHYS CHEM C

ISO Source Abbrev.: J. Phys. Chem. C

Source Item Page Count: 9

Funding:

Funding Agency	Grant Number
Serbian Ministry of Science	III 45015
Office of Basic Energy Sciences, US Department of Energy	DE-AC02-98CH10886
DOE	DE-AC02-06CH11357

The Serbian Ministry of Science has financially supported this work under Contract No. III 45015. E.B. thanks Simon Billinge for discussions. Work at BNL was supported by the Office of Basic Energy Sciences, US Department of Energy, under Contract No. DE-AC02-98CH10886. Advanced Photon Source at the Argonne National Laboratory is supported under DOE Contract No. DE-AC02-06CH11357.

Output Date: 2023-01-27

Record 81 of 125

Title: Detailed Mapping of the Local Ir⁴⁺ Dimers through the Metal-Insulator Transitions of CuIr₂S₄ Thiospinel by X-Ray Atomic Pair Distribution Function Measurements

Author(s): Bozin, ES (Bozin, E. S.); Masadeh, AS (Masadeh, A. S.); Hor, YS (Hor, Y. S.); Mitchell, JF (Mitchell, J. F.); Billinge, SJL (Billinge, S. J. L.)

Source: PHYSICAL REVIEW LETTERS **Volume:** 106 **Issue:** 4 **Article Number:** 045501 **DOI:** 10.1103/PhysRevLett.106.045501 **Published:** JAN 24 2011

Times Cited in Web of Science Core Collection: 22

Total Times Cited: 22

Usage Count (Last 180 days): 0

Usage Count (Since 2013): 38

Cited Reference Count: 36

Abstract: The evolution of the short-range structural signature of the Ir⁴⁺ dimer state in CuIr₂S₄ thiospinel has been studied across the metal-insulator phase transitions as the metallic state is induced by temperature, Cr doping, and x-ray fluence. An atomic pair distribution function (PDF) approach reveals that there are no local dimers that survive into the metallic phase when this is invoked by temperature and doping. The PDF shows Ir⁴⁺ dimers when they exist, regardless of whether or not they are long-range ordered. At 100 K, exposure to a 98 keV x-ray beam melts the long-range dimer order within a few seconds, though the local dimers remain intact. This shows that the metallic state accessed on warming and doping is qualitatively different from the state obtained under x-ray irradiation.

Accession Number: WOS:000286736700009

PubMed ID: 21405330

Language: English

Document Type: Article

KeyWords Plus: SUPERCONDUCTIVITY; PDF

Addresses: [Bozin, E. S.; Billinge, S. J. L.] Brookhaven Natl Lab, Condensed Matter Phys & Mat Sci Dept, Upton, NY 11973 USA.

[Masadeh, A. S.] Michigan State Univ, Dept Phys & Astron, E Lansing, MI 48824 USA.

[Masadeh, A. S.] Univ Jordan, Dept Phys, Amman 11942, Jordan.

[Hor, Y. S.; Mitchell, J. F.] Argonne Natl Lab, Div Mat Sci, Argonne, IL 60439 USA.

[Billinge, S. J. L.] Columbia Univ, Dept Appl Phys & Appl Math, New York, NY 10027 USA.

Corresponding Address: Bozin, ES (corresponding author), Brookhaven Natl Lab, Condensed Matter Phys & Mat Sci Dept, Upton, NY 11973 USA.

E-mail Addresses: bozin@bnl.gov

Affiliations: United States Department of Energy (DOE); Brookhaven National Laboratory; Michigan State University; University of Jordan; United States Department of Energy (DOE); Argonne National Laboratory; Columbia University

Author Identifiers:

Author	Web of Science ResearcherID	ORCID Number
Bozin, Emil	E-4679-2011	
San Hor, Yew	S-1429-2017	0000-0002-1417-4357
Bozin, Emil	AAB-4551-2020	
Mitchell, John F	A-1907-2012	
Billinge, Simon		0000-0002-9734-4998

Publisher: AMER PHYSICAL SOC

Publisher Address: ONE PHYSICS ELLIPSE, COLLEGE PK, MD 20740-3844 USA

Web of Science Index: Science Citation Index Expanded (SCI-EXPANDED)

Web of Science Categories: Physics, Multidisciplinary

Research Areas: Physics

IDS Number: 713KK

ISSN: 0031-9007

eISSN: 1079-7114

29-char Source Abbrev.: PHYS REV LETT

ISO Source Abbrev.: Phys. Rev. Lett.

Source Item Page Count: 4

Funding:

Funding Agency	Grant Number
U.S. Department of Energy Office of Science (DOE-OS)	DE-AC02-98CH10886 DE-AC02-06CH11357

We would like to thank P. Chupas and K. Chapman for their help in data collection. Work in the Billinge group was supported by the U.S. Department of Energy Office of Science (DOE-OS) under Contract No. DE-AC02-98CH10886. J.F.M.'s work at Argonne National Laboratory (ANL), which is operated by UChicago Argonne LLC, and the APS facility, are supported under the U.S. DOE-OS Contract No. DE-AC02-06CH11357.

Open Access: hybrid

Output Date: 2023-01-27

Record 82 of 125

Title: NiO/Ni nanocomposite (micro)structure evolution induced by thermal annealing and milling

Author(s): Antic, B (Antic, Bratislav); Kremenovic, A (Kremenovic, Aleksandar); Jovic, N (Jovic, Natasa); Blanus, J (Blanus, Jovan); Jancar, B (Jancar, Bostjan); Bozin, ES (Bozin, Emil S.)

Source: ACTA CRYSTALLOGRAPHICA A-FOUNDATION AND ADVANCES **Meeting Abstract:** MS18.P07 **Volume:** 67 **Pages:** C323-C324 **DOI:** 10.1107/S0108767311091872 **Supplement:** S **Published:** 2011

Times Cited in Web of Science Core Collection: 1

Total Times Cited: 1

Usage Count (Last 180 days): 0

Usage Count (Since 2013): 0

Cited Reference Count: 0

Accession Number: WOS:000484219401303

Language: English

Document Type: Meeting Abstract

Author Keywords: nano-1; powder-2; magnetic-3

Addresses: [Antic, Bratislav; Kremenovic, Aleksandar; Jovic, Natasa; Blanus, Jovan] Inst Nucl Sci Vinca, Lab Condensed Matter Phys, Belgrade, Serbia.

[Jancar, Bostjan] Inst Josef Stefan, Adv Mat Dept, Ljubljana, Slovenia.

[Bozin, Emil S.] Brookhaven Natl Lab, Condensed Matter Phys & Mat Sci Dept, Upton, NY 11973 USA.

E-mail Addresses: bantic@vinca.rs

Affiliations: University of Belgrade; Slovenian Academy of Sciences & Arts (SASA); Jozef Stefan Institute; United States Department of Energy (DOE); Brookhaven National Laboratory

Publisher: INT UNION CRYSTALLOGRAPHY

Publisher Address: 2 ABBEY SQ, CHESTER, CH1 2HU, ENGLAND

Web of Science Index: Science Citation Index Expanded (SCI-EXPANDED)

Web of Science Categories: Chemistry, Multidisciplinary; Crystallography

Research Areas: Chemistry; Crystallography

IDS Number: VI4FT

ISSN: 2053-2733

29-char Source Abbrev.: ACTA CRYSTALLOGR A

ISO Source Abbrev.: Acta Crystallogr. Sect. A

Source Item Page Count: 2

Funding:

Funding Agency	Grant Number
SCOPES project	IZ73Z0_1 27961

The SNF has financially supported this work under SCOPES project (Grant No. IZ73Z0_1 27961).

Open Access: Bronze

Output Date: 2023-01-27

Record 83 of 125

Title: Pair-distribution function analysis of the structural valence transition in Cp*Yb-2(4,4'-Me-2-bipy)

Author(s): Booth, CH (Booth, C. H.); Bauer, ED (Bauer, E. D.); Bozin, ES (Bozin, E. S.); Billinge, SJL (Billinge, S. J. L.); Walter, MD (Walter, M. D.)

Edited by: Ronning F; Batista C

Source: INTERNATIONAL CONFERENCE ON STRONGLY CORRELATED ELECTRON SYSTEMS (SCES 2010) **Book Series:** Journal of Physics Conference Series **Volume:** 273 **Article Number:** 012149 **DOI:** 10.1088/1742-6596/273/1/012149 **Published:** 2011

Times Cited in Web of Science Core Collection: 0

Total Times Cited: 0

Usage Count (Last 180 days): 0

Usage Count (Since 2013): 4

Cited Reference Count: 18

Abstract: The Cp*Yb-2(L) class of compounds, where Cp*=pentamethylcyclopentadienyl = C₅Me₅ and L is either a 1,4-diazabutadiene or bipy = 2,2'-bipyridine related ligand, have provided excellent analogies to the Kondo state on the nanoscale. Cp*Yb-2(4,4'-Me-2-bipy) furthers this analogy by demonstrating a valence transition as the sample is cooled below 200 K. Here, pair-distribution function (PDF) analysis of x-ray powder diffraction data demonstrate that the Cp*Yb-2(4,4'-Me-2-bipy) molecule is virtually unchanged through the valence transition. However, the molecule's stacking arrangement is altered through the valence transition.

Accession Number: WOS:000291224100149

Language: English

Document Type: Proceedings Paper

Conference Title: International Conference on Strongly Correlated Electron Systems (SCES 2010)

Conference Date: JUN 27-JUL 02, 2010

Conference Location: Santa Fe, NM

Conference Sponsors: Natl High Magnet Field Lab, Dept Energy Natl Labs, Quantum Design, ICAM-I2CAM

KeyWords Plus: DECAMETHYLYTTERBOCENE; BIPYRIDINES; COMPLEXES

Addresses: [Booth, C. H.; Walter, M. D.] Univ Calif Berkeley, Lawrence Berkeley Lab, Div Chem Sci, Berkeley, CA 94720 USA.

[Bauer, E. D.] Los Alamos Natl Lab, Mat Phys & Applicat Div, Los Alamos, NM 87545 USA.

[Bozin, E. S.; Billinge, S. J. L.] Columbia Univ, Dept Appl Phys & Appl Math, New York, NY 10027 USA.

[Bozin, E. S.; Billinge, S. J. L.] Brookhaven Natl Lab, Condensed Matter Phys & Mat Sci Dept, Upton, NY 11973 USA.

Corresponding Address: Booth, CH (corresponding author), Univ Calif Berkeley, Lawrence Berkeley Lab, Div Chem Sci, Berkeley, CA 94720 USA.

E-mail Addresses: chbooth@lbl.gov

Affiliations: United States Department of Energy (DOE); Lawrence Berkeley National Laboratory; University of California System; University of California Berkeley; United States Department of Energy (DOE); Los Alamos National Laboratory; Columbia University; United States Department of Energy (DOE); Brookhaven National Laboratory

Author Identifiers:

Author	Web of Science ResearcherID	ORCID Number
Bozin, Emil	E-4679-2011	
Bozin, Emil	AAB-4551-2020	
Bauer, Eric D	D-7212-2011	
Walter, Marc	E-4479-2012	0000-0002-4682-8749
Billinge, Simon		0000-0002-9734-4998
Booth, Corwin	A-7877-2008	0000-0001-6827-0080

Publisher: IOP PUBLISHING LTD

Publisher Address: DIRAC HOUSE, TEMPLE BACK, BRISTOL BS1 6BE, ENGLAND

Web of Science Index: Conference Proceedings Citation Index - Science (CPCI-S)

Web of Science Categories: Physics, Condensed Matter

Research Areas: Physics

IDS Number: BVD96

ISSN: 1742-6588

eISSN: 1742-6596

29-char Source Abbrev.: J PHYS CONF SER

Source Item Page Count: 4

Funding:

Funding Agency	Grant Number
Director, Office of Science (OS)	
Office of Basic Energy Sciences (OBES), of the U.S. Department of Energy (DOE)	DE-AC02-05CH11231
DOE	DE-AC02-98CH10886 AC02-06CH11357

Work at Lawrence Berkeley National Laboratory was supported by the Director, Office of Science (OS), Office of Basic Energy Sciences (OBES), of the U.S. Department of Energy (DOE) under Contract No. DE-AC02-05CH11231. Work in the Billinge group was supported by the DOE under contract No. DE-AC02-98CH10886. The APS facility at Argonne is supported by DOE Contract DE-AC02-06CH11357. Work at Los Alamos was supported by the DOE.

Open Access: gold, Green Submitted

Output Date: 2023-01-27

Record 84 of 125

Title: Entropically Stabilized Local Dipole Formation in Lead Chalcogenides

Author(s): Bozin, ES (Bozin, Emil S.); Malliakas, CD (Malliakas, Christos D.); Souvatzis, P (Souvatzis, Petros); Proffen, T (Proffen, Thomas); Spaldin, NA (Spaldin, Nicola A.); Kanatzidis, MG (Kanatzidis, Mercouri G.); Billinge, SJL (Billinge, Simon J. L.)

Source: SCIENCE **Volume:** 330 **Issue:** 6011 **Pages:** 1660-1663 **DOI:** 10.1126/science.1192759 **Published:** DEC 17 2010

Times Cited in Web of Science Core Collection: 270

Total Times Cited: 274

Usage Count (Last 180 days): 8

Usage Count (Since 2013): 197

Cited Reference Count: 19

Abstract: We report the observation of local structural dipoles that emerge from an undistorted ground state on warming, in contrast to conventional structural phase transitions in which distortions emerge on cooling. Using experimental and theoretical probes of the local structure, we demonstrate this behavior in binary lead chalcogenides, which were believed to adopt the ideal, undistorted rock-salt structure at all temperatures. The behavior is consistent with a simple thermodynamic model in which the emerging dipoles are stabilized in the disordered state at high temperature due to the extra configurational entropy despite the fact that the undistorted structure has lower internal energy. Our findings shed light on the anomalous electronic and thermoelectric properties of the lead chalcogenides. Similar searches may show that the phenomenon is more widespread.

Accession Number: WOS:000285390500062

PubMed ID: 21164012

Language: English

Document Type: Article

Addresses: [Bozin, Emil S.; Billinge, Simon J. L.] Brookhaven Natl Lab, Condensed Matter Phys & Mat Sci Dept, Upton, NY 11973 USA.

[Malliakas, Christos D.; Kanatzidis, Mercouri G.] Northwestern Univ, Dept Chem, Evanston, IL 60208 USA.

[Souvatzis, Petros] Los Alamos Natl Lab, Div Theoret, Los Alamos, NM 87545 USA.

[Proffen, Thomas] Los Alamos Natl Lab, Lujan Neutron Scattering Ctr, Los Alamos, NM 87545 USA.

[Spaldin, Nicola A.] ETH, Dept Mat, Zurich, Switzerland.

[Kanatzidis, Mercouri G.] Argonne Natl Lab, Div Mat Sci, Argonne, IL 60439 USA.

[Billinge, Simon J. L.] Columbia Univ, Dept Appl Phys & Appl Math, New York, NY 10027 USA.

Corresponding Address: Billinge, SJL (corresponding author), Brookhaven Natl Lab, Condensed Matter Phys & Mat Sci Dept, Upton, NY 11973 USA.

E-mail Addresses: sb2896@columbia.edu

Affiliations: United States Department of Energy (DOE); Brookhaven National Laboratory; Northwestern University; United States Department of Energy (DOE); Los Alamos National Laboratory; United States Department of Energy (DOE); Los Alamos National Laboratory; Swiss Federal Institutes of Technology Domain; ETH Zurich; United States Department of Energy (DOE); Argonne National Laboratory; Columbia University

Author Identifiers:

Author	Web of Science ResearcherID	ORCID Number
Proffen, Thomas	B-3585-2009	0000-0002-1408-6031
Spaldin, Nicola A	A-1017-2010	0000-0003-0709-9499
Bozin, Emil	E-4679-2011	
Bozin, Emil	AAB-4551-2020	
Billinge, Simon		0000-0002-9734-4998

Publisher: AMER ASSOC ADVANCEMENT SCIENCE

Publisher Address: 1200 NEW YORK AVE, NW, WASHINGTON, DC 20005 USA

Web of Science Index: Science Citation Index Expanded (SCI-EXPANDED)

Web of Science Categories: Multidisciplinary Sciences

Research Areas: Science & Technology - Other Topics

IDS Number: 695RO

ISSN: 0036-8075

eISSN: 1095-9203

29-char Source Abbrev.: SCIENCE

ISO Source Abbrev.: Science

Source Item Page Count: 4

Funding:

Funding Agency	Grant Number
U.S. Department of Energy, Office of Basic Energy Sciences (DOE-BES)	DE-AC02-98CH10886
Office of Naval Research	
NSF	DMR-0940420

S.J.B. and E. B. thank J. Richardson for his early support and enthusiasm for the project and dedicate the paper to him. We acknowledge useful discussions with A. Millis, P. Allen, R. Cohen, C. Farrow, and J. Hill. Work in the Billinge group was supported by the U.S. Department of Energy, Office of Basic Energy Sciences (DOE-BES), under contract DE-AC02-98CH10886. Work in the Kanatzidis group was supported by the Office of Naval Research. Work in the Spaldin group was supported by the NSF under award DMR-0940420. The neutron diffraction measurements were carried out at the Lujan Center at Los Alamos National Laboratory, and the x-ray experiments were carried out at the Advanced Photon Source, Argonne National Laboratory, both of which are supported by DOE-BES, and the calculations were performed at the San Diego Supercomputer Center, which is supported by NSF.

Output Date: 2023-01-27

Record 85 of 125

Title: Advances in Structural Studies of Materials Using Scattering Probes

Author(s): Huq, A (Huq, Ashfia); Welberry, R (Welberry, Richard); Bozin, E (Bozin, Emil)

Source: MRS BULLETIN **Volume:** 35 **Issue:** 7 **Pages:** 520-530 **DOI:** 10.1557/mrs2010.601 **Published:** JUL 2010

Times Cited in Web of Science Core Collection: 2

Total Times Cited: 2

Usage Count (Last 180 days): 0

Usage Count (Since 2013): 8

Cited Reference Count: 72

Abstract: X-ray and neutron diffraction have been two key techniques for structural characterization of materials since their inception. If single crystals of the materials of interest cannot be synthesized, one has to resort to powder diffraction. This results in the loss of three-dimensional orientation information of the crystal, and one has to contend with the one-dimensional information that is inherent to powder diffraction, making it harder to analyze the data. The structural study of contemporary materials and their remarkable properties is a challenging problem, particularly when properties of interest result from interplay of multiple degrees of freedom. Very often these are associated with structural defects or relate to different length scales in a material. The signature of the defect-related phenomenon is visible as diffuse scattering in the diffraction pattern, and the signals associated with diffuse scattering are orders of magnitude smaller than Bragg scattering. Given these limitations, it is crucial to have high-resolution and high-intensity data along with the ability to carry out theoretical interpretation that goes beyond periodic lattice formalism of crystallography. Great advances have been achieved due to the advent of synchrotron and neutron sources, along with the availability of high-speed computational algorithms allowing materials scientists to work with a very small amount of sample (both single crystal and powder) and analyze vast amounts of data to unravel detailed structural descriptions that were not previously possible. This article presents some of these great advances in using scattering probes for materials characterization.

Accession Number: WOS:000279980400018

Language: English

Document Type: Article

KeyWords Plus: PAIR DISTRIBUTION FUNCTION; X-RAY SCATTERING; DIFFUSE-SCATTERING; CRYSTAL-STRUCTURES; HIGH-RESOLUTION; REFINEMENT; LITHIUM; SUPERCONDUCTIVITY; TRANSITION; EXPANSION

Author Identifiers:

Author	Web of Science ResearcherID	ORCID Number
Bozin, Emil	AAB-4551-2020	
Welberry, Thomas R	H-7847-2014	0000-0002-6906-9191
Huq, Ashfia	J-8772-2013	0000-0002-8445-9649
Bozin, Emil	E-4679-2011	

Publisher: SPRINGER HEIDELBERG

Publisher Address: TIERGARTENSTRASSE 17, D-69121 HEIDELBERG, GERMANY

Web of Science Index: Science Citation Index Expanded (SCI-EXPANDED)

Web of Science Categories: Materials Science, Multidisciplinary; Physics, Applied

Research Areas: Materials Science; Physics

IDS Number: 626QA

ISSN: 0883-7694

eISSN: 1938-1425

29-char Source Abbrev.: MRS BULL

ISO Source Abbrev.: MRS Bull.

Source Item Page Count: 11

Funding:

Funding Agency	Grant Number
U.S. Department of Energy	DE-AC05-000R22725 DE-AC02-98CH10886
Australian Research Council	
Australian Partnership for Advanced Computing	

A.H. acknowledges support by the U.S. Department of Energy (DE-AC05-000R22725) with UT-Battelle, LLC. R.W. gratefully acknowledges support of the Australian Research Council and the Australian Partnership for Advanced Computing. E.B. acknowledges support by the U.S. Department of Energy (DE-AC02-98CH10886).

Output Date: 2023-01-27

Record 86 of 125

Title: Nanoscale disorder and local electronic properties of CaCu₃Ti₄O₁₂: An integrated study of electron, neutron, and x-ray diffraction, x-ray absorption fine structure, and first-principles calculations

Author(s): Zheng, JC (Zheng, Jin-Cheng); Frenkel, AI (Frenkel, A. I.); Wu, L (Wu, L.); Hanson, J (Hanson, J.); Ku, W (Ku, W.); Bozin, ES (Bozin, E. S.); Billinge, SJL (Billinge, S. J. L.); Zhu, YM (Zhu, Yimei)

Source: PHYSICAL REVIEW B **Volume:** 81 **Issue:** 14 **Article Number:** 144203 **DOI:** 10.1103/PhysRevB.81.144203 **Published:** APR 1 2010

Times Cited in Web of Science Core Collection: 58

Total Times Cited: 60

Usage Count (Last 180 days): 2

Usage Count (Since 2013): 59

Cited Reference Count: 67

Abstract: We report a combined experimental and theoretical study of CaCu₃Ti₄O₁₂. Based on our experimental observations of nanoscale regions of Ca-Cu antisite defects in part of the structure, we carried out

density-functional theory (DFT) calculations that suggest a possible electronic mechanism to explain the gigantic dielectric response in this material. The defects are evident in atomically resolved transmission electron microscopy measurements, with supporting evidence from a quantitative analysis of the electron diffraction and DFT which suggests that such defects are reasonable on energetic grounds. To establish the extent of the defects, bulk average measurements of the local structure were carried out: extended x-ray absorption fine structure (EXAFS), atomic pair-distribution function analysis of neutron powder-diffraction data, and single-crystal x-ray crystallography. The EXAFS data are consistent with the presence of the nanoclustered defects with an estimate of less than 10% of the sample being disordered while the neutron powder-diffraction experiments place an upper of similar to 5% on the proportion of the sample in the defective state. Because of the difficulty of quantifying nanoscale defects at such low levels, further work will be required to establish that this mechanism is operative in CaCu₃Ti₄O₁₂ but it presents a nontraditional plausible avenue for understanding colossal dielectric behavior.

Accession Number: WOS:000277210200061

Language: English

Document Type: Article

KeyWords Plus: HIGH-DIELECTRIC-CONSTANT; CHARGE-TRANSFER; SCATTERING; ORDER; PEROVSKITES; ACCURATE; CRYSTALS; DENSITY; CU

Addresses: [Zheng, Jin-Cheng; Wu, L.; Hanson, J.; Ku, W.; Bozin, E. S.; Billinge, S. J. L.; Zhu, Yimei] Brookhaven Natl Lab, Dept Condensed Matter Phys & Mat Sci, Upton, NY 11973 USA.

[Frenkel, A. I.] Yeshiva Univ, Dept Phys, New York, NY 10016 USA.

[Bozin, E. S.; Billinge, S. J. L.] Columbia Univ, Dept Appl Phys & Appl Math, New York, NY 10027 USA.

Corresponding Address: Zhu, YM (corresponding author), Brookhaven Natl Lab, Dept Condensed Matter Phys & Mat Sci, Upton, NY 11973 USA.

E-mail Addresses: zhu@bnl.gov

Affiliations: United States Department of Energy (DOE); Brookhaven National Laboratory; Yeshiva University; Columbia University

Author Identifiers:

Author	Web of Science ResearcherID	ORCID Number
Bozin, Emil	AAB-4551-2020	
Hanson, jonathan C	E-3517-2010	
Bozin, Emil	E-4679-2011	
Zheng, JC	G-3383-2010	0000-0002-6292-3236
Frenkel, Anatoly	D-3311-2011	0000-0002-5451-1207
Hanson, Jonathan		0000-0003-0686-3985
Billinge, Simon		0000-0002-9734-4998

Publisher: AMER PHYSICAL SOC

Publisher Address: ONE PHYSICS ELLIPSE, COLLEGE PK, MD 20740-3844 USA

Web of Science Index: Science Citation Index Expanded (SCI-EXPANDED)

Web of Science Categories: Materials Science, Multidisciplinary; Physics, Applied; Physics, Condensed Matter

Research Areas: Materials Science; Physics

IDS Number: 590FN

ISSN: 2469-9950

eISSN: 2469-9969

29-char Source Abbrev.: PHYS REV B

ISO Source Abbrev.: Phys. Rev. B

Source Item Page Count: 19

Funding:

Funding Agency	Grant Number
U.S. Department of Energy, Office of Basic Energy Science	DE-FG02-03ER15476 DE-AC02-98CH10886
DOE-CMSN	

We thank Morrel H. Cohen, David Vanderbilt, Weiguo Yin, and Peter Stephens for stimulating discussions. A. I. F. acknowledges support by the U.S. Department of Energy, Office of Basic Energy Science, Grant No. DE-FG02-03ER15476. Work at Brookhaven was supported by the U.S. Department of Energy, Office of Basic Energy Science, under Contract No. DE-AC02-98CH10886 and DOE-CMSN.

Output Date: 2023-01-27

Record 87 of 125

Title: Thermal annealing effect on cation inversion and particle size of Zn-ferrite.

Author(s): Antic, B (Antic, B.); Kremenovic, A (Kremenovic, A.); Blanusa, J (Blanusa, J.); Bessais, L (Bessais, L.); Bozin, ES (Bozin, E. S.)

Source: ACTA CRYSTALLOGRAPHICA A-FOUNDATION AND ADVANCES **Meeting Abstract:** FA2-MS14-P **Volume:** 66 **Pages:** S156-S156 **DOI:** 10.1107/S0108767310096509 **Supplement:** S **Published:** 2010

Times Cited in Web of Science Core Collection: 0

Total Times Cited: 0

Usage Count (Last 180 days): 0

Usage Count (Since 2013): 0

Cited Reference Count: 0

Accession Number: WOS:000483128900349

Language: English

Document Type: Meeting Abstract

Author Keywords: nanoparticles; microstructure analysis; cation distribution

Addresses: [Antic, B.; Blanusa, J.] Vinca Inst, Belgrade, Serbia.

[Kremenovic, A.] Univ Belgrade, Belgrade, Serbia.

[Bessais, L.] Inst Chim & Hateriaux Paris Est, Paris, France.

[Bozin, E. S.] Columbia Univ, New York, NY USA.

E-mail Addresses: bantic@vinca.rs

Affiliations: University of Belgrade; University of Belgrade; Columbia University

Author Identifiers:

Author	Web of Science ResearcherID	ORCID Number
Kremenovic, A	AAL-7534-2020	0000-0001-8845-2332
Bozin, Emil	AAB-4551-2020	
Bessais, Lotfi	I-5423-2013	0000-0001-7236-1604

Publisher: INT UNION CRYSTALLOGRAPHY

Publisher Address: 2 ABBEY SQ, CHESTER, CH1 2HU, ENGLAND

Web of Science Index: Science Citation Index Expanded (SCI-EXPANDED)

Web of Science Categories: Chemistry, Multidisciplinary; Crystallography

Research Areas: Chemistry; Crystallography

IDS Number: VI4CD

ISSN: 2053-2733

29-char Source Abbrev.: ACTA CRYSTALLOGR A

ISO Source Abbrev.: Acta Crystallogr. Sect. A

Source Item Page Count: 1

Open Access: Bronze

Output Date: 2023-01-27

Record 88 of 125

Title: Characterisation of amorphous and nanocrystalline molecular materials by total scattering

Author(s): Billinge, SJL (Billinge, Simon J. L.); Dykhne, T (Dykhne, Timur); Juhas, P (Juhas, Pavol); Bozin, E (Bozin, Emil); Taylor, R (Taylor, Ryan); Florence, AJ (Florence, Alastair J.); Shankland, K (Shankland, Kenneth)

Source: CRYSTENGGCOMM **Volume:** 12 **Issue:** 5 **Pages:** 1366-1368 **DOI:** 10.1039/b915453a **Published:** 2010

Times Cited in Web of Science Core Collection: 64

Total Times Cited: 65

Usage Count (Last 180 days): 1

Usage Count (Since 2013): 52

Cited Reference Count: 15

Abstract: The use of high-energy X-ray total scattering coupled with pair distribution function analysis produces unique structural fingerprints from amorphous and nanostructured phases of the pharmaceuticals carbamazepine and indomethacin. The advantages of such facility-based experiments over laboratory-based ones are discussed and the technique is illustrated with the characterisation of a melt-quenched sample of carbamazepine as a nanocrystalline (4.5 nm domain diameter) version of form III.

Accession Number: WOS:000277091700003

Language: English

Document Type: Article

KeyWords Plus: INDOMETHACIN; DIFFRACTION; POLYMORPHS

Addresses: [Billinge, Simon J. L.; Dykhne, Timur; Juhas, Pavol; Bozin, Emil] Columbia Univ, Dept Appl Phys & Appl Math, New York, NY 10027 USA.

[Billinge, Simon J. L.; Bozin, Emil] Brookhaven Natl Lab, Condensed Matter Phys & Mat Sci Dept, Upton, NY 11973 USA.

[Taylor, Ryan; Florence, Alastair J.] Univ Strathclyde, Strathclyde Inst Pharm & Biomed Sci, Solid State Res Grp, Glasgow G4 0NR, Lanark, Scotland.

[Shankland, Kenneth] Univ Reading, Sch Pharm, Reading RG6 6AD, Berks, England.

Corresponding Address: Billinge, SJL (corresponding author), Columbia Univ, Dept Appl Phys & Appl Math, New York, NY 10027 USA.

E-mail Addresses: sb2896@columbia.edu

Affiliations: Columbia University; United States Department of Energy (DOE); Brookhaven National Laboratory; University of Strathclyde; University of Reading

Author Identifiers:

Author	Web of Science ResearcherID	ORCID Number
Juhas, Pavol	Q-7225-2019	0000-0001-8751-4458
Bozin, Emil	E-4679-2011	
Juhas, Pavol	A-6544-2008	0000-0001-8751-4458
Shankland, Kenneth	H-5943-2013	0000-0001-6566-0155
Bozin, Emil	AAB-4551-2020	
Florence, Alastair		0000-0002-9706-8364
Billinge, Simon		0000-0002-9734-4998

Publisher: ROYAL SOC CHEMISTRY

Publisher Address: THOMAS GRAHAM HOUSE, SCIENCE PARK, MILTON RD, CAMBRIDGE CB4 0WF, CAMBS, ENGLAND

Web of Science Index: Science Citation Index Expanded (SCI-EXPANDED)

Web of Science Categories: Chemistry, Multidisciplinary; Crystallography

Research Areas: Chemistry; Crystallography

IDS Number: 588RQ

eISSN: 1466-8033

29-char Source Abbrev.: CRYSTENGCOMM

ISO Source Abbrev.: Crystengcomm

Source Item Page Count: 3

Funding:

Funding Agency	Grant Number
EPSRC	EP/E036244/1
Engineering and Physical Sciences Research Council	EP/E036244/1

Open Access: Green Accepted

Output Date: 2023-01-27

Record 89 of 125

Title: Characterisation of amorphous and nanocrystalline molecular materials by total scattering (vol 12, pg 1366, 2010)

Author(s): Billinge, SJL (Billinge, Simon J. L.); Dykhne, T (Dykhne, Timur); Juhas, P (Juhas, Pavol); Bozin, E (Bozin, Emil); Taylor, R (Taylor, Ryan); Florence, AJ (Florence, Alastair J.); Shankland, K (Shankland, Kenneth)

Source: CRYSTENGCOMM **Volume:** 12 **Issue:** 12 **Pages:** 4444-4444 **Published:** 2010

Times Cited in Web of Science Core Collection: 0

Total Times Cited: 0

Usage Count (Last 180 days): 0

Usage Count (Since 2013): 6

Cited Reference Count: 1

Accession Number: WOS:000284266200073

Language: English

Document Type: Correction

Author Identifiers:

Author	Web of Science ResearcherID	ORCID Number
Bozin, Emil	AAB-4551-2020	
Bozin, Emil	E-4679-2011	
Billinge, Simon		0000-0002-9734-4998

Publisher: ROYAL SOC CHEMISTRY

Publisher Address: THOMAS GRAHAM HOUSE, SCIENCE PARK, MILTON RD, CAMBRIDGE CB4 0WF, CAMBS, ENGLAND

Web of Science Index: Science Citation Index Expanded (SCI-EXPANDED)

Web of Science Categories: Chemistry, Multidisciplinary; Crystallography

Research Areas: Chemistry; Crystallography

IDS Number: 680VV

ISSN: 1466-8033

29-char Source Abbrev.: CRYSTENGCOMM

ISO Source Abbrev.: Crystengcomm

Source Item Page Count: 1

Output Date: 2023-01-27

Record 90 of 125

Title: Quantitative structure refinement from the ARCS chopper spectrometer

Author(s): Bozin, ES (Bozin, E. S.); Juhas, P (Juhas, P.); Zhou, W (Zhou, W.); Stone, MB (Stone, M. B.); Abernathy, DL (Abernathy, D. L.); Huq, A (Huq, A.); Billinge, SJL (Billinge, S. J. L.)

Book Group Author(s): IOP

Source: INTERNATIONAL CONFERENCE ON NEUTRON SCATTERING 2009 **Book Series:** Journal of Physics Conference Series **Volume:** 251 **Article Number:** 012080 **DOI:** 10.1088/1742-6596/251/1/012080 **Published:** 2010

Times Cited in Web of Science Core Collection: 2

Total Times Cited: 2

Usage Count (Last 180 days): 0

Usage Count (Since 2013): 2

Cited Reference Count: 21

Abstract: The new wide angular-range chopper spectrometer ARCS at the Spallation Neutron Source at Oak Ridge National Laboratory has been successfully used in white-beam mode, with no Fermi chopper, to obtain neutron powder diffraction based atomic pair distribution functions (PDFs). Obtained PDF patterns of Si, Ni, and Al₂O₃ were refined using the PDFfit method and the results compared to data collected at the NPDF diffractometer at Los Alamos National Laboratory. High quality resulting fits are presented, demonstrating that reliable powder diffraction data can be obtained from ARCS when operated in this configuration.

Accession Number: WOS:000291982100080

Language: English

Document Type: Proceedings Paper

Conference Title: International Conference on Neutron Scattering 2009

Conference Date: MAY 03-07, 2009

Conference Location: Knoxville, TN

KeyWords Plus: PAIR DISTRIBUTION FUNCTION

Addresses: [Bozin, E. S.; Juhas, P.; Zhou, W.; Billinge, S. J. L.] Columbia Univ, Dept Appl Phys & Appl Math, New York, NY 10027 USA.

[Bozin, E. S.; Billinge, S. J. L.] Brookhaven Natl Lab, Condensed Matter Phys & Mat Sci Dept, Upton, NY 11973 USA.

[Stone, M. B.; Abernathy, D. L.; Huq, A.] Oak Ridge Natl Lab, Neutron Scattering Sci Div, Oak Ridge, TN 37831 USA.

Corresponding Address: Bozin, ES (corresponding author), Columbia Univ, Dept Appl Phys & Appl Math, New York, NY 10027 USA.

E-mail Addresses: sb2896@columbia.edu

Affiliations: Columbia University; United States Department of Energy (DOE); Brookhaven National Laboratory; United States Department of Energy (DOE); Oak Ridge National Laboratory

Author Identifiers:

Author	Web of Science ResearcherID	ORCID Number
Bozin, Emil	AAB-4551-2020	

Stone, Matthew	G-3275-2011	0000-0001-7884-9715
BL18, ARCS	A-3000-2012	
Abernathy, Douglas L	A-3038-2012	0000-0002-3533-003X
Huq, Ashfia	J-8772-2013	0000-0002-8445-9649
Juhas, Pavol	Q-7225-2019	0000-0001-8751-4458
Billinge, Simon		0000-0002-9734-4998

Publisher: IOP PUBLISHING LTD

Publisher Address: DIRAC HOUSE, TEMPLE BACK, BRISTOL BS1 6BE, ENGLAND

Web of Science Index: Conference Proceedings Citation Index - Science (CPCI-S)

Web of Science Categories: Biophysics; Instruments & Instrumentation; Materials Science, Multidisciplinary; Physics, Condensed Matter

Research Areas: Biophysics; Instruments & Instrumentation; Materials Science; Physics

IDS Number: BVN68

ISSN: 1742-6588

eISSN: 1742-6596

29-char Source Abbrev.: J PHYS CONF SER

Source Item Page Count: 6

Funding:

Funding Agency	Grant Number
Office of Science, U.S. Department of Energy	DE-AC02-98CH10886
NSF	DMR-0520547
DOE Office of Basic Energy Sciences	
DOE	DE-AC52-06NA25396
Scientific User Facilities Division, Office of Basic Energy Sciences, U. S. Department of Energy	

We thank Thomas Proffen for providing standard data from NPDF that is used in this study. Work in the Billinge-group was supported by the Office of Science, U.S. Department of Energy, under contract no. DE-AC02-98CH10886. DANSE software was developed under NSF award DMR-0520547. This work has benefited from the use of NPDF at the Lujan Center at Los Alamos Neutron Science Center, funded by DOE Office of Basic Energy Sciences. Los Alamos National Laboratory is operated by Los Alamos National Security LLC under DOE Contract DE-AC52-06NA25396. The research at Oak Ridge National Laboratory's Spallation Neutron Source was sponsored by the Scientific User Facilities Division, Office of Basic Energy Sciences, U. S. Department of Energy.

Open Access: gold

Output Date: 2023-01-27

Record 91 of 125

Title: Effects of Thermal Annealing on Structural and Magnetic Properties of Lithium Ferrite Nanoparticles

Author(s): Jovic, NG (Jovic, Natasa G.); Masadeh, AS (Masadeh, Ahmad S.); Kremenovic, AS (Kremenovic, Aleksandar S.); Antic, BV (Antic, Bratislav V.); Blanus, JL (Blanus, Jovan L.); Cvjeticanin, ND (Cvjeticanin, Nikola D.); Goya, GF (Goya, Gerardo F.); Antisari, MV (Antisari, Marco Vittori); Bozin, ES (Bozin, Emil S.)

Source: JOURNAL OF PHYSICAL CHEMISTRY C **Volume:** 113 **Issue:** 48 **Pages:** 20559-20567 **DOI:** 10.1021/jp907559y **Published:** DEC 3 2009

Times Cited in Web of Science Core Collection: 74

Total Times Cited: 76

Usage Count (Last 180 days): 0

Usage Count (Since 2013): 35

Cited Reference Count: 39

Abstract: Pure, crystalline, similar to 10 nm lithium ferrite phase ($\text{Li}_{0.5}\text{Fe}_{2.5}\text{O}_4$), was Successfully synthesized at very low temperature using a modified combustion method. The crystal structure and microstructure evolution of this system upon annealing were monitored by a careful investigation of X-ray diffractograms collected on a synchrotron source. Comparative analysis of the results obtained from the full profile Rietveld method (in reciprocal space) and the pair distribution function method (in direct space) was carried Out. Nanocrystalline samples exhibit similar crystal structure, on average, with a partial ordering of Li^+ and Fe^{3+} ions between octahedral 4b and 12d sites on the spinel crystal lattice (space group $\text{P4}(3)32$). After annealing at 973 K, cation distribution changes to a completely ordered, resembling that which is seen in the bulk lithium ferrite. The PDF analysis reveals abnormally high values of oxygen atomic displacement parameters in tetrahedral 8c sites (OI) indicating a significant disordering of the OI network and suggests migration of lithium ions from 4b sites to the outer layers of nanoparticles. Analysis of room temperature Mossbauer spectra has shown that the hyperfine field for Fe^{3+} ions in tetrahedral 8c sites is the most sensitive on increasing the particle size and improving the crystallinity. From the differential thermal analysis, it was found that a lower driving force is required to induce an order-disorder phase transition in nanocrystalline samples, compared to the bulk-like sample, presumably due to the higher crystal disordering in these samples.

Accession Number: WOS:000272038600007

Language: English

Document Type: Article

KeyWords Plus: LOW-TEMPERATURE SYNTHESIS; MICROSTRUCTURE; RELAXATION; DISORDER

Addresses: [Jovic, Natasa G.; Kremenovic, Aleksandar S.; Antic, Bratislav V.; Blanusa, Jovan L.] Inst Vinca, Lab Theoret & Condensed Matter Phys, Belgrade 11001, Serbia.

[Masadeh, Ahmad S.] Michigan State Univ, Dept Phys & Astron, E Lansing, MI 48824 USA.

[Masadeh, Ahmad S.] Univ Jordan, Dept Phys, Amman 11942, Jordan.

[Kremenovic, Aleksandar S.] Inst Vinca, Crystallog Lab, Fac Min & Geol, Belgrade 11000, Serbia.

[Cvjeticanin, Nikola D.] Fac Phys Chem, Belgrade 11000, Serbia.

[Goya, Gerardo F.] Univ Zaragoza, Aragon Inst Nanosci, Zaragoza, Spain.

[Goya, Gerardo F.] Univ Zaragoza, Dept Condensed Matter Phys, Zaragoza, Spain.

[Antisari, Marco Vittori] ENEA, FIM Dept, CR Casaccia, I-00060 Rome, Italy.

[Bozin, Emil S.] Columbia Univ, Dept Appl Phys & Appl Math, New York, NY 10027 USA.

Corresponding Address: Jovic, NG (corresponding author), Inst Vinca, Lab Theoret & Condensed Matter Phys, POB 522, Belgrade 11001, Serbia.

E-mail Addresses: natasaj@vinca.rs

Affiliations: University of Belgrade; Michigan State University; University of Jordan; University of Belgrade; University of Belgrade; University of Zaragoza; University of Zaragoza; Italian National Agency New Technical Energy & Sustainable Economics Development; Columbia University

Author Identifiers:

Author	Web of Science ResearcherID	ORCID Number
Kremenovic, A	AAL-7534-2020	0000-0001-8845-2332
Bozin, Emil	AAB-4551-2020	
Goya, G.F.	B-1915-2008	0000-0003-1558-9279
Bozin, Emil	E-4679-2011	
JOVIĆ ORSINI, Nataša	ABC-7664-2021	0000-0003-1613-3361
Jović Orsini, Nataša	C-3983-2017	0000-0003-1613-3361
Blanusa, Jovan		0000-0003-4930-9730
Antic, Bratislav		0000-0002-5693-6401

Publisher: AMER CHEMICAL SOC

Publisher Address: 1155 16TH ST, NW, WASHINGTON, DC 20036 USA

Web of Science Index: Science Citation Index Expanded (SCI-EXPANDED)

Web of Science Categories: Chemistry, Physical; Nanoscience & Nanotechnology; Materials Science, Multidisciplinary

Research Areas: Chemistry; Science & Technology - Other Topics; Materials Science

IDS Number: 522ZJ

ISSN: 1932-7447

eISSN: 1932-7455

29-char Source Abbrev.: J PHYS CHEM C

ISO Source Abbrev.: J. Phys. Chem. C

Source Item Page Count: 9

Funding:

Funding Agency	Grant Number
The Serbian Ministry of Science	141027
National Science Foundation (NSF)	DMR-0304391 DMR-0703940
DOE	DE-AC02-06CH11357
Spanish MICINN	

The Serbian Ministry of Science has financially supported this work through the project No. 141027. A.S.M. and E.S.B. thank SJL Billinge for useful discussions. Parts of this work were also supported by National Science Foundation (NSF) Grant Nos. DMR-0304391 and DMR-0703940. HEXRPD data were collected at the 6ID-D beamline at the Advanced Photon Source at the Argonne National Laboratory supported under DOE Contract No. DE-AC02-06CH11357. G.F.G. acknowledges financial help from Spanish MICINN through the Ramon y Cajal program.

Output Date: 2023-01-27

Record 92 of 125

Title: Superconductivity, magnetism, and stoichiometry of single crystals of $\text{Fe}_{1+y}(\text{Te}_{1-x}\text{S}_x)(z)$

Author(s): Hu, RW (Hu, Rongwei); Bozin, ES (Bozin, Emil S.); Warren, JB (Warren, J. B.); Petrovic, C (Petrovic, C.)

Source: PHYSICAL REVIEW B **Volume:** 80 **Issue:** 21 **Article Number:** 214514 **DOI:** 10.1103/PhysRevB.80.214514 **Published:** DEC 2009

Times Cited in Web of Science Core Collection: 93

Total Times Cited: 93

Usage Count (Last 180 days): 0

Usage Count (Since 2013): 38

Cited Reference Count: 52

Abstract: We report synthesis of high-quality $\text{Fe}_{1+y}(\text{Te}_{1-x}\text{S}_x)(z)$ single crystals and a comprehensive study of structural, magnetic, and transport properties. We demonstrate the very small upper critical field anisotropy of $\text{Fe}_{1+y}(\text{Te}_{1-x}\text{S}_x)(z)$, $\gamma(H) = H - c_2(c) / H - c_2(\text{perpendicular to } c)$. The value of $\gamma(H)$ reaches 1.05 at $T = 0.65T(C)$ for $\text{Fe}_{1.12}\text{Te}_{0.83}\text{S}_{0.11}$ while still maintaining large values of upper critical field. There is high sensitivity to material stoichiometry which includes vacancies on the Te(S) site. Our results reveal competition and coexistence of magnetic order and percolative superconductivity for $x \geq 0.03$ while zero resistivity is achieved for $x \geq 0.1$.

Accession Number: WOS:000273228200089

Language: English

Document Type: Article

Author Keywords: electrical resistivity; iron compounds; magnetic anisotropy; magnetic moments; magnetic superconductors; magnetic susceptibility; percolation; spin density waves; stoichiometry; tellurium compounds; vacancies (crystal)

KeyWords Plus: SPIN; PURITY; PHASE; HEAT

Addresses: [Hu, Rongwei; Bozin, Emil S.; Petrovic, C.] Brookhaven Natl Lab, Condensed Matter Phys & Mat Sci Dept, Upton, NY 11973 USA.

[Bozin, Emil S.] Columbia Univ, Dept Appl Phys & Appl Math, New York, NY 10027 USA.

[Warren, J. B.] Brookhaven Natl Lab, Instrumentat Div, Upton, NY 11973 USA.

Corresponding Address: Hu, RW (corresponding author), US DOE, Ames, IA 50011 USA.

Affiliations: United States Department of Energy (DOE); Brookhaven National Laboratory; Columbia University; United States Department of Energy (DOE); Brookhaven National Laboratory

Author Identifiers:

Author	Web of Science ResearcherID	ORCID Number
Petrovic, Cedomir	A-8789-2009	0000-0001-6063-1881
Bozin, Emil	AAB-4551-2020	
Bozin, Emil	E-4679-2011	
Hu, Rongwei	E-7128-2012	

Publisher: AMER PHYSICAL SOC

Publisher Address: ONE PHYSICS ELLIPSE, COLLEGE PK, MD 20740-3844 USA

Web of Science Index: Science Citation Index Expanded (SCI-EXPANDED)

Web of Science Categories: Materials Science, Multidisciplinary; Physics, Applied; Physics, Condensed Matter

Research Areas: Materials Science; Physics

IDS Number: 539BK

ISSN: 2469-9950

eISSN: 2469-9969

29-char Source Abbrev.: PHYS REV B

ISO Source Abbrev.: Phys. Rev. B

Source Item Page Count: 8

Funding:

Funding Agency	Grant Number
U. S. Department of Energy by Brookhaven Science Associates	DE-Ac0298CH10886
U.S. Department of Energy, Office of Science, Office of Basic Energy Sciences	DEAC02-06CH11357
Office of Basic Energy Sciences of the U. S. Department of Energy	

We are grateful for helpful discussions with Paul Canfield, Sergey Bud'ko, Simon Billinge, and Myron Strongin. This work was carried out at the Brookhaven National Laboratory, which is operated for the U.S. Department of Energy by Brookhaven Science Associates (Grant No. DE-Ac0298CH10886). Use of the Advanced Photon Source was supported by the U.S. Department of Energy, Office of Science, Office of Basic Energy Sciences, under Contract No. DEAC02-06CH11357. This work was supported by the Office of Basic Energy Sciences of the U. S. Department of Energy.

Open Access: Green Submitted

Output Date: 2023-01-27

Title: Atomic pair distribution function analysis from the ARCS chopper spectrometer at the Spallation Neutron Source

Author(s): Bozin, ES (Bozin, E. S.); Juhas, P (Juhas, P.); Zhou, W (Zhou, W.); Stone, MB (Stone, M. B.); Abernathy, DL (Abernathy, D. L.); Huq, A (Huq, A.); Billinge, SJL (Billinge, S. J. L.)

Source: JOURNAL OF APPLIED CRYSTALLOGRAPHY **Volume:** 42 **Pages:** 724-725 **DOI:** 10.1107/S0021889809023504 **Part:** 4 **Published:** AUG 2009

Times Cited in Web of Science Core Collection: 6

Total Times Cited: 6

Usage Count (Last 180 days): 2

Usage Count (Since 2013): 9

Cited Reference Count: 4

Abstract: Neutron powder-diffraction-based atomic pair distribution functions (PDFs) are reported from the new wide-angular-range chopper spectrometer ARCS at the Spallation Neutron Source at Oak Ridge National Laboratory. The spectrometer was run in white-beam mode with no Fermi chopper. The PDF patterns of Ni and Al₂O₃ were refined using the PDFfit method and the results compared with data collected at the NPDF diffractometer at Los Alamos National Laboratory. The resulting fits are of high quality, demonstrating that quantitatively reliable powder diffraction data can be obtained from ARCS when operated in this configuration.

Accession Number: WOS:000268068000021

Language: English

Document Type: Article

Addresses: [Bozin, E. S.; Juhas, P.; Zhou, W.; Billinge, S. J. L.] Columbia Univ, Dept Appl Phys & Appl Math, New York, NY 10027 USA.

[Bozin, E. S.; Billinge, S. J. L.] Brookhaven Natl Lab, Condensed Matter Phys & Mat Sci Dept, Upton, NY 11973 USA.

[Stone, M. B.; Abernathy, D. L.; Huq, A.] Oak Ridge Natl Lab, Neutron Scattering Sci Div, Oak Ridge, TN 37831 USA.

Corresponding Address: Billinge, SJL (corresponding author), Columbia Univ, Dept Appl Phys & Appl Math, New York, NY 10027 USA.

E-mail Addresses: sb2896@columbia.edu

Affiliations: Columbia University; United States Department of Energy (DOE); Brookhaven National Laboratory; United States Department of Energy (DOE); Oak Ridge National Laboratory

Author Identifiers:

Author	Web of Science ResearcherID	ORCID Number
Abernathy, Douglas L	A-3038-2012	0000-0002-3533-003X
Huq, Ashfia	J-8772-2013	0000-0002-8445-9649
Bozin, Emil	E-4679-2011	
Juhas, Pavol	A-6544-2008	0000-0001-8751-4458
Bozin, Emil	AAB-4551-2020	
Stone, Matthew	G-3275-2011	0000-0001-7884-9715
Juhas, Pavol	Q-7225-2019	0000-0001-8751-4458
BL18, ARCS	A-3000-2012	
Billinge, Simon		0000-0002-9734-4998

Publisher: INT UNION CRYSTALLOGRAPHY

Publisher Address: 2 ABBEY SQ, CHESTER, CH1 2HU, ENGLAND

Web of Science Index: Science Citation Index Expanded (SCI-EXPANDED)

Web of Science Categories: Chemistry, Multidisciplinary; Crystallography

Research Areas: Chemistry; Crystallography

IDS Number: 47100

eISSN: 1600-5767

29-char Source Abbrev.: J APPL CRYSTALLOGR

ISO Source Abbrev.: J. Appl. Crystallogr.

Source Item Page Count: 2

Funding:

Funding Agency	Grant Number
US Department of Energy	DE-AC02-98CH10886

Work in the Billinge group was supported by the Office of Basic Energy Sciences, US Department of Energy, under contract No. DE-AC02-98CH10886. This research at Oak Ridge National Laboratory's Spallation Neutron Source was sponsored by the Scientific User Facilities Division, Office of Basic Energy Sciences, US Department of Energy.

Open Access: Green Submitted

Output Date: 2023-01-27

Record 94 of 125

Title: Phase separation and nanostructuring in the thermoelectric material $\text{PbTe}_{1-x}\text{S}_x$ studied using the atomic pair distribution function technique

Author(s): Lin, H (Lin, He); Bozin, ES (Bozin, E. S.); Billinge, SJL (Billinge, S. J. L.); Androulakis, J (Androulakis, J.); Malliakas, CD (Malliakas, C. D.); Lin, CH (Lin, C. H.); Kanatzidis, MG (Kanatzidis, M. G.)

Source: PHYSICAL REVIEW B **Volume:** 80 **Issue:** 4 **Article Number:** 045204 **DOI:** 10.1103/PhysRevB.80.045204 **Published:** JUL 2009

Times Cited in Web of Science Core Collection: 17

Total Times Cited: 17

Usage Count (Last 180 days): 2

Usage Count (Since 2013): 39

Cited Reference Count: 36

Abstract: The average and local structures of the $(\text{PbTe})_{(1-x)}(\text{PbS})_x$ system of thermoelectric materials has been studied using the Rietveld and atomic pair distribution function methods. Samples with $0.25 \leq x$ are macroscopically phase separated. Phase separation was suppressed in a quenched $x = 0.5$ sample which, nonetheless, exhibited a partial spinodal decomposition. The promising thermoelectric material with $x = 0.16$ showed intermediate behavior. Combining TEM and bulk scattering data suggests that the sample is a mixture of PbTe-rich material and a partially spinodally decomposed phase similar to the quenched 50% sample. This confirms that, in the bulk, this sample is inhomogeneous on a nanometer length scale, which may account for its enhanced thermoelectric figure of merit.

Accession Number: WOS:000268618100052

Language: English

Document Type: Article

KeyWords Plus: PROFILE REFINEMENT; TEMPERATURE; TELLURIUM; SULPHUR; SPACE; PBS

Addresses: [Lin, He] Michigan State Univ, Dept Phys & Astron, E Lansing, MI 48824 USA.

[Bozin, E. S.; Billinge, S. J. L.] Columbia Univ, Dept Appl Phys & Appl Math, New York, NY 10027 USA.

[Bozin, E. S.; Billinge, S. J. L.] Brookhaven Natl Lab, Dept Condensed Matter Phys & Mat Sci, Upton, NY 11973 USA.

[Androulakis, J.; Malliakas, C. D.; Lin, C. H.; Kanatzidis, M. G.] Northwestern Univ, Dept Chem, Evanston, IL 60208 USA.

Corresponding Address: Lin, H (corresponding author), Michigan State Univ, Dept Phys & Astron, E Lansing, MI 48824 USA.

E-mail Addresses: sb2896@columbia.edu

Affiliations: Michigan State University; Columbia University; United States Department of Energy (DOE); Brookhaven National Laboratory; Northwestern University

Author Identifiers:

Author	Web of Science ResearcherID	ORCID Number
Bozin, Emil	AAB-4551-2020	
Bozin, Emil	E-4679-2011	
Billinge, Simon		0000-0002-9734-4998

Publisher: AMER PHYSICAL SOC

Publisher Address: ONE PHYSICS ELLIPSE, COLLEGE PK, MD 20740-3844 USA

Web of Science Index: Science Citation Index Expanded (SCI-EXPANDED)

Web of Science Categories: Materials Science, Multidisciplinary; Physics, Applied; Physics, Condensed Matter

Research Areas: Materials Science; Physics

IDS Number: 478WA

ISSN: 2469-9950

eISSN: 2469-9969

29-char Source Abbrev.: PHYS REV B

ISO Source Abbrev.: Phys. Rev. B

Source Item Page Count: 8

Funding:

Funding Agency	Grant Number
National Science Foundation (NSF)	DMR-0304391 DMR-0703940
Office of Naval Research	
U.S. Department of Energy, Office of Science, Office of Basic Energy Sciences	DE-ACO2-06CH11357 W-7405-Eng-82

We acknowledge Pavol Juhas, Ahmad Masadeh, Hyun-Jeong Kim, and Asel Sartbaeva for their valuable assistance with the data collection. Work in the Billinge group was supported in part by National Science Foundation (NSF) under Grants No. DMR-0304391 and No. DMR-0703940 and in the Kanatzidis group by the Office of Naval Research. Data were collected at the 6IDD beamline in the Midwest Universities Collaborative Access Team (MUCAT) sector at the APS. Use of the Advanced Photon Source was supported by the U.S. Department of Energy, Office of Science, Office of Basic Energy Sciences, under Contract No. DE-ACO2-06CH11357. The MUCAT sector at the APS is supported by the U.S. DOE, Office of Science, Office of Basic Energy Sciences, through the Ames Laboratory under Contract No. W-7405-Eng-82.

Output Date: 2023-01-27

Record 95 of 125

Title: Local and average structures of the spin-glass pyrochlore Y₂Mo₂O₇ from neutron diffraction and neutron pair distribution function analysis

Author(s): Greedan, JE (Greedan, J. E.); Gout, D (Gout, Delphine); Lozano-Gorrin, AD (Lozano-Gorrin, A. D.); Derahkshan, S (Derahkshan, Shahab); Proffen, T (Proffen, Th.); Kim, HJ (Kim, H. -J.); Bozin, E (Bozin, E.); Billinge, SJL (Billinge, S. J. L.)

Source: PHYSICAL REVIEW B **Volume:** 79 **Issue:** 1 **Article Number:** 014427 **DOI:** 10.1103/PhysRevB.79.014427 **Published:** JAN 2009

Times Cited in Web of Science Core Collection: 40

Total Times Cited: 42

Usage Count (Last 180 days): 1

Usage Count (Since 2013): 48

Cited Reference Count: 37

Abstract: The observation of canonical spin-glass behavior in the pyrochlore oxide $Y_2Mo_2O_7$ has been a subject of considerable interest as the original structural studies were interpreted in terms of a well-ordered crystallographic model. It is widely held that the stabilization of the spin-glass state requires some level of positional disorder along with frustration. Recent reports from local probe measurements, extended x-ray-absorption fine structure (EXAFS) and Y-89 NMR, have been interpreted in terms of disorder involving the Mo-Mo distances (EXAFS) and multiple Y sites (NMR). This work reports results from temperature-dependent (15-300 K) neutron diffraction (ND) and neutron pair distribution function studies which can provide from the same data set information on both the average and local structures. The principal findings are that: (1) there is no crystallographic phase transition over the temperature region studied within the resolution of the ND data; (2) the diffraction data are well fitted using a fully ordered model but with large and anisotropic displacement parameters for three of the four atomic sites; (3) the pairwise real-space correlation function $G(r)$ shows clear evidence that the principal source of disorder is associated with the Y-O1 atom pairs rather than the Mo-Mo pairs, in disagreement with the interpretation of the EXAFS results; (4) fits to the $G(r)$ improve significantly when anisotropic displacements for all sites are included; (5) inclusion of a split-site position parameter for O1 improves, slightly, both the $G(r)$ fits and the Rietveld fits to the ND data; and (6) for all models the fits become worse as the temperature decreases and as the fitting range decreases. These results are qualitatively consistent with the Y-89 NMR observations and perhaps recent muon-spin-relaxation studies. The issue of static versus dynamic disorder is not resolved, definitively. An estimate of the distribution of exchange constants due to the disorder is made using spin-dimer analysis and compared with the Saunders-Chalker model for the generation of spin-glass behavior from "weak" disorder on geometrically frustrated lattices.

Accession Number: WOS:000262977900074

Language: English

Document Type: Article

Author Keywords: exchange interactions (electron); frustration; neutron diffraction; spin glasses; yttrium compounds

KeyWords Plus: DYNAMICS; BEHAVIOR; CRISTOBALITE; TRANSITION; SYSTEMS; PHASES; SIO2

Addresses: [Greedan, J. E.; Lozano-Gorrin, A. D.; Derakhshan, Shahab] McMaster Univ, Dept Chem, Hamilton, ON L8S 4M1, Canada.

[Greedan, J. E.; Lozano-Gorrin, A. D.; Derakhshan, Shahab] McMaster Univ, Brockhouse Inst Mat Res, Hamilton, ON L8S 4M1, Canada.

[Gout, Delphine] Forschungszentrum Julich, Julich Ctr Neutron Sci SNS, D-52425 Julich, Germany.

[Gout, Delphine] Oak Ridge Natl Lab, Oak Ridge, TN 38371 USA.

[Proffen, Th.; Kim, H. -J.] Los Alamos Natl Lab, Manuel Lujan Jr Neutron Scattering Ctr, Los Alamos, NM 87545 USA.

[Bozin, E.; Billinge, S. J. L.] Columbia Univ, Dept Appl Phys & Appl Math, New York, NY 10027 USA.

[Bozin, E.; Billinge, S. J. L.] Brookhaven Natl Lab, Condensed Matter & Mat Sci Dept, Upton, NY 11973 USA.

Corresponding Address: Greedan, JE (corresponding author), McMaster Univ, Dept Chem, 1280 Main St W, Hamilton, ON L8S 4M1, Canada.

Affiliations: McMaster University; McMaster University; Helmholtz Association; Research Center Julich; United States Department of Energy (DOE); Oak Ridge National Laboratory; United States Department of Energy (DOE); Los Alamos National Laboratory; Columbia University; United States Department of Energy (DOE); Brookhaven National Laboratory

Author Identifiers:

Author	Web of Science ResearcherID	ORCID Number
Bozin, Emil	AAB-4551-2020	
Bozin, Emil	E-4679-2011	
Lozano-Gorrin, Antonio	AAY-8759-2020	

Proffen, Thomas	B-3585-2009	0000-0002-1408-6031
Kim, Hyunjeong	L-6966-2018	0000-0001-5018-3173
Billinge, Simon		0000-0002-9734-4998

Publisher: AMER PHYSICAL SOC

Publisher Address: ONE PHYSICS ELLIPSE, COLLEGE PK, MD 20740-3844 USA

Web of Science Index: Science Citation Index Expanded (SCI-EXPANDED)

Web of Science Categories: Materials Science, Multidisciplinary; Physics, Applied; Physics, Condensed Matter

Research Areas: Materials Science; Physics

IDS Number: 401XX

ISSN: 2469-9950

eISSN: 2469-9969

29-char Source Abbrev.: PHYS REV B

ISO Source Abbrev.: Phys. Rev. B

Source Item Page Count: 10

Funding:

Funding Agency	Grant Number
Natural Sciences and Engineering Research Council	
Los Alamos Neutron Science Center	
DOE Office of Basic Energy Sciences	
Los Alamos National Laboratory is operated by Los Alamos National Security LLC	DE-AC5206NA25396

J.E.G. thanks the Natural Sciences and Engineering Research Council of Canada for support through a Discovery Grant. A. D. L.-G. thanks the Spanish Ministry of Education for support. The authors thank I. P. Swinson for helpful discussions. This work benefited from the use of NPDF at the Lujan Center at Los Alamos Neutron Science Center, funded by DOE Office of Basic Energy Sciences. Los Alamos National Laboratory is operated by Los Alamos National Security LLC under DOE Contract No. DE-AC5206NA25396. The upgrade of NPDF was funded by NSF through Grant No. DMR00-76488. Work by the Billinge group was supported by the Office of Science, U. S. Department of Energy, under Contract No. DE-AC02-98CH10886.

Output Date: 2023-01-27

Record 96 of 125

Title: Magnetic Structure of ZnFe₂O₄

Author(s): Kremenovic, A (Kremenovic, Aleksandar); Vulic, P (Vulic, Predrag); Antic, B (Antic, Bratislav); Bozin, ES (Bozin, Emil S.); Blanusa, J (Blanusa, Jovan)

Source: ACTA CRYSTALLOGRAPHICA A-FOUNDATION AND ADVANCES **Meeting Abstract:** FA2-MS09-P **Volume:** 65 **Pages:** S218-S218 **DOI:** 10.1107/S0108767309095488 **Supplement:** S **Published:** 2009

Times Cited in Web of Science Core Collection: 0

Total Times Cited: 0

Usage Count (Last 180 days): 0

Usage Count (Since 2013): 1

Cited Reference Count: 2

Accession Number: WOS:000480362900452

Language: English

Document Type: Meeting Abstract

Author Keywords: magnetic structure; time-of-flight diffraction; ferrite

Addresses: [Kremenovic, Aleksandar; Antic, Bratislav; Blanusa, Jovan] INS Vinca, Belgrade, Serbia.

[Kremenovic, Aleksandar; Vulic, Predrag] Univ Belgrade, FMG, Belgrade, Serbia.

[Bozin, Emil S.] Columbia Univ, New York, NY USA.

E-mail Addresses: akremen@EUnet.rs

Affiliations: University of Belgrade; University of Belgrade; Columbia University

Author Identifiers:

Author	Web of Science ResearcherID	ORCID Number
Kremenovic, A	AAL-7534-2020	0000-0001-8845-2332
Bozin, Emil	AAB-4551-2020	

Publisher: INT UNION CRYSTALLOGRAPHY

Publisher Address: 2 ABBEY SQ, CHESTER, CH1 2HU, ENGLAND

Web of Science Index: Science Citation Index Expanded (SCI-EXPANDED)

Web of Science Categories: Chemistry, Multidisciplinary; Crystallography

Research Areas: Chemistry; Crystallography

IDS Number: VI3WE

ISSN: 2053-2733

29-char Source Abbrev.: ACTA CRYSTALLOGR A

ISO Source Abbrev.: Acta Crystallogr. Sect. A

Source Item Page Count: 1

Funding:

Funding Agency	Grant Number
Office of Science, U.S. Department of Energy	DE-AC02-98CH10886

Work at Columbia was supported by the Office of Science, U.S. Department of Energy, under contract no. DE-AC02-98CH10886.

Open Access: Bronze

Output Date: 2023-01-27

Record 97 of 125

Title: Structure of CaMnO₃ in the range 10 K ≤ T ≤ 550 K from neutron time-of-flight total scattering

Author(s): Bozin, ES (Bozin, E. S.); Sartbaeva, A (Sartbaeva, A.); Zheng, H (Zheng, H.); Wells, SA (Wells, S. A.); Mitchell, JF (Mitchell, J. F.); Proffen, T (Proffen, Th.); Thorpe, MF (Thorpe, M. F.); Billinge, SJL (Billinge, S. J. L.)

Source: JOURNAL OF PHYSICS AND CHEMISTRY OF SOLIDS **Volume:** 69 **Issue:** 9 **Special Issue:** SI **Pages:** 2146-2150 **DOI:** 10.1016/j.jpcs.2008.03.029 **Published:** SEP 2008

Times Cited in Web of Science Core Collection: 30

Total Times Cited: 30

Usage Count (Last 180 days): 0

Usage Count (Since 2013): 18

Cited Reference Count: 25

Abstract: The local and average structure of the Ca endmember of the La_{1-x}CaxMnO₃ series has been investigated. Neutron powder diffraction-based high real-space resolution atomic pair distribution function (PDF) analysis, yielding the local atomic structure, and the corresponding Rietveld analysis yielding the average crystal structure show that the two structural scales are in accord in this material, and that the MnO₆ octahedral units are regular for all temperatures studied. Quantitative values of structural parameters are reported for a wide temperature range, important for both experimental and theoretical considerations of hole

and electron doped branches of the rich phase diagram of $\text{La}_{1-x}\text{Ca}_x\text{MnO}_3$. (C) 2008 Elsevier Ltd. All rights reserved.

Accession Number: WOS:000260142000004

Language: English

Document Type: Article; Proceedings Paper

Conference Title: 4th International Conference on Study of Matter at Extreme Conditions

Conference Date: APR 15-20, 2007

Conference Location: Miami Beach, FL

Conference Sponsors: Ctr Study Matter Extreme Condit, Florida Int Univ

Author Keywords: Oxides; Neutron scattering; Crystal structure

KeyWords Plus: DIFFRACTION

Addresses: [Bozin, E. S.; Billinge, S. J. L.] Michigan State Univ, Dept Phys & Astron, 4250 Biomed Phys Sci, E Lansing, MI 48824 USA.

[Sartbaeva, A.; Wells, S. A.; Thorpe, M. F.] Arizona State Univ, Dept Phys, Tempe, AZ 85283 USA.

[Zheng, H.; Mitchell, J. F.] Argonne Natl Lab, Div Mat Sci, Argonne, IL 60439 USA.

[Proffen, Th.] Los Alamos Natl Lab, LANSCE LC, Los Alamos, NM 87545 USA.

Corresponding Address: Bozin, ES (corresponding author), Michigan State Univ, Dept Phys & Astron, 4250 Biomed Phys Sci, E Lansing, MI 48824 USA.

E-mail Addresses: bozin@pa.msu.edu

Affiliations: Michigan State University; Arizona State University; Arizona State University-Tempe; United States Department of Energy (DOE); Argonne National Laboratory; United States Department of Energy (DOE); Los Alamos National Laboratory

Author Identifiers:

Author	Web of Science ResearcherID	ORCID Number
Sartbaeva, Asel	K-9890-2019	0000-0003-1017-0161
Proffen, Thomas	B-3585-2009	0000-0002-1408-6031
Wells, Stephen	L-2064-2014	
Mitchell, John F	A-1907-2012	
Sartbaeva, Asel	I-5914-2013	
Bozin, Emil	E-4679-2011	
Bozin, Emil	AAB-4551-2020	
Billinge, Simon		0000-0002-9734-4998
Wells, Stephen		0000-0002-3920-3644

Publisher: PERGAMON-ELSEVIER SCIENCE LTD

Publisher Address: THE BOULEVARD, LANGFORD LANE, KIDLINGTON, OXFORD OX5 1GB, ENGLAND

Web of Science Index: Science Citation Index Expanded (SCI-EXPANDED); Conference Proceedings Citation Index - Science (CPCI-S)

Web of Science Categories: Chemistry, Multidisciplinary; Physics, Condensed Matter

Research Areas: Chemistry; Physics

IDS Number: 361QK

ISSN: 0022-3697

eISSN: 1879-2553

29-char Source Abbrev.: J PHYS CHEM SOLIDS

ISO Source Abbrev.: J. Phys. Chem. Solids

Source Item Page Count: 5

Output Date: 2023-01-27

Record 98 of 125

Title: Study of the negative thermal expansion of cuprite-type structures by means of temperature-dependent pair distribution function analysis: Preliminary results

Author(s): Dapiaggi, M (Dapiaggi, Monica); Kim, H (Kim, HyunJeong); Bozin, ES (Bozin, Emil S.); Billinge, SJL (Billinge, Simon J. L.); Artioli, G (Artioli, Gilberto)

Source: JOURNAL OF PHYSICS AND CHEMISTRY OF SOLIDS **Volume:** 69 **Issue:** 9 **Special Issue:** SI **Pages:** 2182-2186 **DOI:** 10.1016/j.jpcs.2008.03.030 **Published:** SEP 2008

Times Cited in Web of Science Core Collection: 11

Total Times Cited: 11

Usage Count (Last 180 days): 0

Usage Count (Since 2013): 15

Cited Reference Count: 16

Abstract: Copper (I) and silver (I) oxides crystallize with the same structure, and both show a wide range of negative thermal expansion (NTE): Cu₂O contracts with temperature up to about 200 K and then expands, while Ag₂O has a NTE up to its decomposition temperature at about 450 K. Here we report a careful temperature-dependent pair distribution function (PDF) analysis that showed that copper oxide, at about 200 K, exhibits geometric distortions of the tetrahedral units, probably related to a change in the solid angle of the polyhedra. Silver oxide, on the other hand, showed the same distortions even at the lowest temperature measured (10 K): structural refinements of the PDF confirmed the presence of local distortions (below 10 angstrom) at all temperatures. (C) 2008 Elsevier Ltd. All rights reserved.

Accession Number: WOS:000260142000012

Language: English

Document Type: Article; Proceedings Paper

Conference Title: 4th International Conference on Study of Matter at Extreme Conditions

Conference Date: APR 15-20, 2007

Conference Location: Miami Beach, FL

Conference Sponsors: Ctr Study Matter Extreme Condit, Florida Int Univ

Author Keywords: oxides; Neutron scattering; Thermal expansion

KeyWords Plus: BEHAVIOR; EXAFS

Addresses: [Dapiaggi, Monica] Univ Milan, Dipartimento Sci Terra, I-20133 Milan, Italy.

[Kim, HyunJeong; Bozin, Emil S.; Billinge, Simon J. L.] Michigan State Univ, Dept Phys & Astron, E Lansing, MI 48824 USA.

[Artioli, Gilberto] Univ Padua, Dipartimento Geosci, I-35137 Padua, Italy.

Corresponding Address: Dapiaggi, M (corresponding author), Univ Milan, Dipartimento Sci Terra, Via Botticelli 23, I-20133 Milan, Italy.

E-mail Addresses: monica.dapiaggi@unimi.it

Affiliations: University of Milan; Michigan State University; University of Padua

Author Identifiers:

Author	Web of Science ResearcherID	ORCID Number
Kim, Hyunjeong	L-6966-2018	0000-0001-5018-3173
Bozin, Emil	AAB-4551-2020	
Dapiaggi, Monica	A-2479-2014	0000-0002-7815-3213
Artioli, Gilberto	F-2149-2015	0000-0002-8693-7392
Bozin, Emil	E-4679-2011	
Billinge, Simon		0000-0002-9734-4998

Publisher: PERGAMON-ELSEVIER SCIENCE LTD

Publisher Address: THE BOULEVARD, LANGFORD LANE, KIDLINGTON, OXFORD OX5 1GB, ENGLAND

Web of Science Index: Science Citation Index Expanded (SCI-EXPANDED); Conference Proceedings Citation Index - Science (CPCI-S)

Web of Science Categories: Chemistry, Multidisciplinary; Physics, Condensed Matter

Research Areas: Chemistry; Physics

IDS Number: 361QK

ISSN: 0022-3697

eISSN: 1879-2553

29-char Source Abbrev.: J PHYS CHEM SOLIDS

ISO Source Abbrev.: J. Phys. Chem. Solids

Source Item Page Count: 5

Open Access: Green Submitted

Output Date: 2023-01-27

Record 99 of 125

Title: Local lattice dynamics in the Mg_{0.5}Al_{0.5}B₂ superconductor

Author(s): Campi, G (Campi, G.); Proffen, T (Proffen, T.); Qiu, X (Qiu, X.); Bozin, ES (Bozin, E. S.); Billinge, SJL (Billinge, S. J. L.); Agrestini, S (Agrestini, S.); Saini, NL (Saini, N. L.); Bianconi, A (Bianconi, A.)

Source: JOURNAL OF SUPERCONDUCTIVITY AND NOVEL MAGNETISM **Volume:** 20 **Issue:** 7-8 **Pages:** 505-510 **DOI:** 10.1007/s10948-007-0277-9 **Published:** NOV 2007

Times Cited in Web of Science Core Collection: 3

Total Times Cited: 3

Usage Count (Last 180 days): 0

Usage Count (Since 2013): 12

Cited Reference Count: 34

Abstract: We have studied temperature evolution of the local as well as the average crystal structure of MgB₂ and Mg_{0.5}Al_{0.5}B₂ using real-space atomic pair distribution function (PDF) measured by high resolution neutron powder diffraction in a wide temperature range of T=10-600 K. The mean square relative displacements (MSRD) of atomic B-B, B-Mg (B-Al) pairs are compared with mean-square displacements (MSD) to calculate atomic correlations. In spite of the enhanced atomic disorder in Mg_{0.5}Al_{0.5}B₂, where the boron-boron, and boron-magnesium pair motions are found to be small, we find that the same atomic correlations in MgB₂ assume even slightly lower values and remain nearly constant in a wide temperature range of 0-600 K. This anomalous behavior and its physical interpretation provoke new questions on our understanding to the local lattice dynamics in this material.

Accession Number: WOS:000250835800005

Language: English

Document Type: Article; Proceedings Paper

Conference Title: 5th International Conference on Stripes and High T_c Superconductivity

Conference Date: DEC 17-22, 2006

Conference Location: Rome, ITALY

Author Keywords: MgB₂; neutron diffraction

KeyWords Plus: DENSITY; MGB2

Addresses: CNR, Ist Cristallograf, I-00016 Monterotondo, Italy.

Los Alamos Natl Lab, Lujan Neutron Scattering Ctr, Los Alamos, NM 87545 USA.

Michigan State Univ, Dept Phys & Astron, E Lansing, MI 48824 USA.

Univ Roma La Sapienza, Dipartimento Fis, I-00185 Rome, Italy.

Corresponding Address: Campi, G (corresponding author), CNR, Ist Cristallograf, Via Salaria Km 29-300, I-00016 Monterotondo, Italy.

E-mail Addresses: gaetano.campi@ic.cur.it

Affiliations: Consiglio Nazionale delle Ricerche (CNR); Istituto Di Cristallografia (IC-CNR); United States Department of Energy (DOE); Los Alamos National Laboratory; Michigan State University; Sapienza University Rome

Author Identifiers:

Author	Web of Science ResearcherID	ORCID Number
Bozin, Emil	AAB-4551-2020	
Bozin, Emil	E-4679-2011	
Proffen, Thomas	B-3585-2009	0000-0002-1408-6031
Saini, Naurang	J-7918-2013	0000-0003-3684-1517
Bianconi, Antonio	J-3997-2013	0000-0001-9795-3913
Campi, Gaetano	H-1981-2018	0000-0001-9845-9394
Agrestini, Stefano		0000-0002-3625-880X
Billinge, Simon		0000-0002-9734-4998

Publisher: SPRINGER

Publisher Address: ONE NEW YORK PLAZA, SUITE 4600, NEW YORK, NY, UNITED STATES

Web of Science Index: Science Citation Index Expanded (SCI-EXPANDED); Conference Proceedings Citation Index - Science (CPCI-S)

Web of Science Categories: Physics, Applied; Physics, Condensed Matter

Research Areas: Physics

IDS Number: 229WB

ISSN: 1557-1939

eISSN: 1557-1947

29-char Source Abbrev.: J SUPERCOND NOV MAGN

ISO Source Abbrev.: J. Supercond. Nov. Magn

Source Item Page Count: 6

Output Date: 2023-01-27

Record 100 of 125

Title: Quadrupolar ordering in LaMnO₃ revealed from scattering data and geometric modeling

Author(s): Sartbaeva, A (Sartbaeva, A.); Wells, SA (Wells, S. A.); Thorpe, MF (Thorpe, M. F.); Bozin, ES (Bozin, E. S.); Billinge, SJL (Billinge, S. J. L.)

Source: PHYSICAL REVIEW LETTERS **Volume:** 99 **Issue:** 15 **Article Number:** 155503 **DOI:** 10.1103/PhysRevLett.99.155503 **Published:** OCT 12 2007

Times Cited in Web of Science Core Collection: 34

Total Times Cited: 35

Usage Count (Last 180 days): 0

Usage Count (Since 2013): 10

Cited Reference Count: 29

Abstract: Many strongly correlated materials display quadrupolar (Jahn-Teller) distortion of the local octahedral structural units. It is common for these distortions to be observed by probes of local structure but absent in the crystallographic average structure. The ordering of these quadrupoles is important in determining the properties of manganites and cuprates, and the nature of the disorder in these structures has been an

unsolved problem. We combine high resolution scattering data and novel geometrical modeling techniques to obtain a detailed picture of the local atomic structure, and also to extract the quadrupolar order parameter associated with the distorted octahedra. We show that in LaMnO₃, quadrupoles undergo a strong first-order phase transition at 730 K, but with nonzero order parameter remaining in the high-temperature phase.

Accession Number: WOS:000250140600038

PubMed ID: 17995180

Language: English

Document Type: Article

KeyWords Plus: CHARGE

Addresses: Arizona State Univ, Dept Phys & Astron, Tempe, AZ 85287 USA.

Michigan State Univ, Dept Phys & Astron, E Lansing, MI 48824 USA.

Corresponding Address: Sartbaeva, A (corresponding author), Arizona State Univ, Dept Phys & Astron, Tempe, AZ 85287 USA.

Affiliations: Arizona State University; Arizona State University-Tempe; Michigan State University

Author Identifiers:

Author	Web of Science ResearcherID	ORCID Number
Bozin, Emil	AAB-4551-2020	
Bozin, Emil	E-4679-2011	
Sartbaeva, Asel	I-5914-2013	
Wells, Stephen	L-2064-2014	
Sartbaeva, Asel	K-9890-2019	0000-0003-1017-0161
Billinge, Simon		0000-0002-9734-4998
Wells, Stephen		0000-0002-3920-3644

Publisher: AMER PHYSICAL SOC

Publisher Address: ONE PHYSICS ELLIPSE, COLLEGE PK, MD 20740-3844 USA

Web of Science Index: Science Citation Index Expanded (SCI-EXPANDED)

Web of Science Categories: Physics, Multidisciplinary

Research Areas: Physics

IDS Number: 220EV

ISSN: 0031-9007

eISSN: 1079-7114

29-char Source Abbrev.: PHYS REV LETT

ISO Source Abbrev.: Phys. Rev. Lett.

Source Item Page Count: 4

Output Date: 2023-01-27

Record 101 of 125

Title: Quantitative size-dependent structure and strain determination of CdSe nanoparticles using atomic pair distribution function analysis

Author(s): Masadeh, AS (Masadeh, A. S.); Bozin, ES (Bozin, E. S.); Farrow, CL (Farrow, C. L.); Paglia, G (Paglia, G.); Juhas, P (Juhas, P.); Billinge, SJL (Billinge, S. J. L.); Karkamkar, A (Karkamkar, A.); Kanatzidis, MG (Kanatzidis, M. G.)

Source: PHYSICAL REVIEW B **Volume:** 76 **Issue:** 11 **Article Number:** 115413 **DOI:**

10.1103/PhysRevB.76.115413 **Published:** SEP 2007

Times Cited in Web of Science Core Collection: 165

Total Times Cited: 166

Usage Count (Last 180 days): 1

Usage Count (Since 2013): 69

Cited Reference Count: 63

Abstract: The size-dependent structure of CdSe nanoparticles, with diameters ranging from 2 to 4 nm, has been studied using the atomic pair distribution function (PDF) method. The core structure of the measured CdSe nanoparticles can be described in terms of the wurtzite atomic structure with extensive stacking faults. The density of faults in the nanoparticles is similar to 50%. The diameter of the core region was extracted directly from the PDF data and is in good agreement with the diameter obtained from standard characterization methods, suggesting that there is little surface amorphous region. A compressive strain was measured in the Cd-
Se bond length that increases with decreasing particle size being 0.5% with respect to bulk CdSe for the 2 nm diameter particles. This study demonstrates the size-dependent quantitative structural information that can be obtained even from very small nanoparticles using the PDF approach.

Accession Number: WOS:000249786400104

Language: English

Document Type: Article

KeyWords Plus: LOCAL-STRUCTURE; SCATTERING; TRANSFORMATION; NANOCRYSTALS; DIFFRACTION; DISORDER; REFINEMENT; PROGRAM; EXAFS

Addresses: Michigan State Univ, Dept Phys & Astron, E Lansing, MI 48824 USA.

Michigan State Univ, Dept Chem, E Lansing, MI 48824 USA.

Corresponding Address: Billinge, SJL (corresponding author), Michigan State Univ, Dept Phys & Astron, E Lansing, MI 48824 USA.

E-mail Addresses: billinge@pa.msu.edu

Affiliations: Michigan State University; Michigan State University

Author Identifiers:

Author	Web of Science ResearcherID	ORCID Number
Bozin, Emil	AAB-4551-2020	
Juhas, Pavol	Q-7225-2019	0000-0001-8751-4458
Bozin, Emil	E-4679-2011	
Juhas, Pavol	A-6544-2008	0000-0001-8751-4458
Billinge, Simon		0000-0002-9734-4998

Publisher: AMER PHYSICAL SOC

Publisher Address: ONE PHYSICS ELLIPSE, COLLEGE PK, MD 20740-3844 USA

Web of Science Index: Science Citation Index Expanded (SCI-EXPANDED)

Web of Science Categories: Materials Science, Multidisciplinary; Physics, Applied; Physics, Condensed Matter

Research Areas: Materials Science; Physics

IDS Number: 215CR

ISSN: 2469-9950

eISSN: 2469-9969

29-char Source Abbrev.: PHYS REV B

ISO Source Abbrev.: Phys. Rev. B

Source Item Page Count: 11

Open Access: Green Submitted

Output Date: 2023-01-27

Record 102 of 125

Title: PDFfit2 and PDFgui: computer programs for studying nanostructure in crystals

Author(s): Farrow, CL (Farrow, C. L.); Juhas, P (Juhas, P.); Liu, JW (Liu, J. W.); Bryndin, D (Bryndin, D.); Bozin, ES (Bozin, E. S.); Bloch, J (Bloch, J.); Proffen, T (Proffen, Th); Billinge, SJL (Billinge, S. J. L.)

Source: JOURNAL OF PHYSICS-CONDENSED MATTER **Volume:** 19 **Issue:** 33 **Article Number:** 335219 **DOI:** 10.1088/0953-8984/19/33/335219 **Published:** AUG 22 2007

Times Cited in Web of Science Core Collection: 1323

Total Times Cited: 1326

Usage Count (Last 180 days): 7

Usage Count (Since 2013): 225

Cited Reference Count: 28

Abstract: PDFfit2 is a program as well as a library for real-space refinement of crystal structures. It is capable of fitting a theoretical three-dimensional (3D) structure to atomic pair distribution function data and is ideal for nanoscale investigations. The fit system accounts for lattice constants, atomic positions and anisotropic atomic displacement parameters, correlated atomic motion, and experimental factors that may affect the data. The atomic positions and thermal coefficients can be constrained to follow the symmetry requirements of an arbitrary space group. The PDFfit2 engine is written in C++ and is accessible via Python, allowing it to inter-operate with other Python programs. PDFgui is a graphical interface built on the PDFfit2 engine. PDFgui organizes fits and simplifies many data analysis tasks, such as configuring and plotting multiple fits. PDFfit2 and PDFgui are freely available via the Internet.

Accession Number: WOS:000248185900020

PubMed ID: 21694142

Language: English

Document Type: Article; Proceedings Paper

Conference Title: 3rd Workshop on Reverse Monte Carlo Methods

Conference Date: SEP 28-30, 2006

Conference Location: Budapest, HUNGARY

KeyWords Plus: DIFFRACTION; DISORDER

Addresses: Michigan State Univ, Dept Phys & Astron, E Lansing, MI 48824 USA.

Univ Regensburg, Inst Theoret Phys, D-93040 Regensburg, Germany.

Los Alamos Natl Lab, Manuel Lujan Jr Neutron Scattering Ctr, Los Alamos, NM 87545 USA.

Michigan State Univ, Dept Comp Sci & Engn, E Lansing, MI 48824 USA.

Corresponding Address: Farrow, CL (corresponding author), Michigan State Univ, Dept Phys & Astron, E Lansing, MI 48824 USA.

E-mail Addresses: billinge@pa.msu.edu

Affiliations: Michigan State University; University of Regensburg; United States Department of Energy (DOE); Los Alamos National Laboratory; Michigan State University

Author Identifiers:

Author	Web of Science ResearcherID	ORCID Number
Bozin, Emil	E-4679-2011	
Juhas, Pavol	Q-7225-2019	0000-0001-8751-4458
Juhas, Pavol	A-6544-2008	0000-0001-8751-4458
Bozin, Emil	AAB-4551-2020	
Proffen, Thomas	B-3585-2009	0000-0002-1408-6031
Billinge, Simon		0000-0002-9734-4998

Publisher: IOP Publishing Ltd

Publisher Address: TEMPLE CIRCUS, TEMPLE WAY, BRISTOL BS1 6BE, ENGLAND

Web of Science Index: Science Citation Index Expanded (SCI-EXPANDED); Conference Proceedings Citation Index - Science (CPCI-S)

Web of Science Categories: Physics, Condensed Matter

Research Areas: Physics

IDS Number: 192FJ

ISSN: 0953-8984

eISSN: 1361-648X

29-char Source Abbrev.: J PHYS-CONDENS MAT

ISO Source Abbrev.: J. Phys.-Condes. Matter

Source Item Page Count: 7

Output Date: 2023-01-27

Record 103 of 125

Title: Nanoscale alpha-structural domains in the phonon-glass thermoelectric material beta-Zn₄Sb₃

Author(s): Kim, HJ (Kim, H. J.); Bozin, ES (Bozin, E. S.); Haile, SM (Haile, S. M.); Snyder, GJ (Snyder, G. J.); Billinge, SJL (Billinge, S. J. L.)

Source: PHYSICAL REVIEW B **Volume:** 75 **Issue:** 13 **Article Number:** 134103 **DOI:** 10.1103/PhysRevB.75.134103 **Published:** APR 2007

Times Cited in Web of Science Core Collection: 30

Total Times Cited: 30

Usage Count (Last 180 days): 0

Usage Count (Since 2013): 26

Cited Reference Count: 22

Abstract: A study of the local atomic structure of the promising thermoelectric material beta-Zn₄Sb₃, using atomic pair distribution function (PDF) analysis of x-ray- and neutron-diffraction data, suggests that the material is nanostructured. The local structure of the beta phase closely resembles that of the low-temperature alpha phase. The alpha structure contains ordered zinc interstitial atoms which are not long range ordered in the beta phase. A rough estimate of the domain size from a visual inspection of the PDF is less than or similar to 10 nm. It is probable that the nanoscale domains found in this study play an important role in the exceptionally low thermal conductivity of beta-Zn₄Sb₃.

Accession Number: WOS:000246074800023

Language: English

Document Type: Article

KeyWords Plus: PAIR DISTRIBUTION FUNCTION; MERIT; FIGURE; ZN₄SB₃; ZINC

Addresses: Michigan State Univ, Dept Phys & Astron, E Lansing, MI 48824 USA.

CALTECH, Dept Mat Sci, Pasadena, CA 91125 USA.

Corresponding Address: Billinge, SJL (corresponding author), Michigan State Univ, Dept Phys & Astron, E Lansing, MI 48824 USA.

E-mail Addresses: billinge@pa.msu.edu

Affiliations: Michigan State University; California Institute of Technology

Author Identifiers:

Author	Web of Science ResearcherID	ORCID Number
Bozin, Emil	E-4679-2011	
Snyder, G. Jeffrey	E-4453-2011	0000-0003-1414-8682
Bozin, Emil	AAB-4551-2020	
Haile, Sossina M	I-3448-2015	
Snyder, G J	I-2263-2015	
Kim, Hyunjeong	L-6966-2018	0000-0001-5018-3173
Billinge, Simon		0000-0002-9734-4998

Publisher: AMER PHYSICAL SOC

Publisher Address: ONE PHYSICS ELLIPSE, COLLEGE PK, MD 20740-3844 USA

Web of Science Index: Science Citation Index Expanded (SCI-EXPANDED)

Web of Science Categories: Materials Science, Multidisciplinary; Physics, Applied; Physics, Condensed Matter

Research Areas: Materials Science; Physics

IDS Number: 162GL

ISSN: 1098-0121

29-char Source Abbrev.: PHYS REV B

ISO Source Abbrev.: Phys. Rev. B

Source Item Page Count: 4

Open Access: Green Accepted

Output Date: 2023-01-27

Record 104 of 125

Title: Understanding the insulating phase in colossal magnetoresistance manganites: Shortening of the Jahn-Teller long-bond across the phase diagram of $\text{La}_{1-x}\text{Ca}_x\text{MnO}_3$

Author(s): Bozin, ES (Bozin, E. S.); Schmidt, M (Schmidt, M.); DeConinck, AJ (DeConinck, A. J.); Paglia, G (Paglia, G.); Mitchell, JF (Mitchell, J. F.); Chatterji, T (Chatterji, T.); Radaelli, PG (Radaelli, P. G.); Proffen, T (Proffen, Th.); Billinge, SJL (Billinge, S. J. L.)

Source: PHYSICAL REVIEW LETTERS **Volume:** 98 **Issue:** 13 **Article Number:** 137203 **DOI:** 10.1103/PhysRevLett.98.137203 **Published:** MAR 30 2007

Times Cited in Web of Science Core Collection: 60

Total Times Cited: 60

Usage Count (Last 180 days): 0

Usage Count (Since 2013): 19

Cited Reference Count: 40

Abstract: The detailed evolution of the magnitude of the local Jahn-Teller (JT) distortion in $\text{La}_{1-x}\text{Ca}_x\text{MnO}_3$ is obtained across the phase diagram for $0 \leq x \leq 0.5$ from high-quality neutron diffraction data using the atomic pair distribution function method. A local JT distortion is observed in the insulating phase for all Ca concentrations studied. However, in contrast with earlier local structure studies, its magnitude is not constant, but decreases continuously with increasing Ca content. This observation is at odds with a simple small-polaron picture for the insulating state.

Accession Number: WOS:000245331500068

PubMed ID: 17501235

Language: English

Document Type: Article

KeyWords Plus: PAIR DISTRIBUTION FUNCTION; NEUTRON-DIFFRACTION; ELECTRONIC-STRUCTURE; CHARGE LOCALIZATION; DOPED MANGANITES; LOCAL-STRUCTURE; SPECTROSCOPY; DISTORTIONS; TRANSITION; SEPARATION

Addresses: Michigan State Univ, Dept Phys & Astron, E Lansing, MI 48824 USA.

Rutherford Appleton Lab, CCLRC, ISIS, Didcot OX11 0QX, Oxon, England.

Argonne Natl Lab, Div Mat Sci, Argonne, IL 60439 USA.

Inst Max Von Laue Paul Langevin, F-38042 Grenoble 9, France.

Los Alamos Natl Lab, Manuel Lujan Jr Neutron Scattering Ctr, Los Alamos, NM 87545 USA.

Corresponding Address: Bozin, ES (corresponding author), Michigan State Univ, Dept Phys & Astron, E Lansing, MI 48824 USA.

Affiliations: Michigan State University; UK Research & Innovation (UKRI); Science & Technology Facilities Council (STFC); STFC Rutherford Appleton Laboratory; United States Department of Energy (DOE); Argonne National Laboratory; Institut Laue-Langevin (ILL); United States Department of Energy (DOE); Los Alamos National Laboratory

Author Identifiers:

Author	Web of Science ResearcherID	ORCID Number
Mitchell, John F	A-1907-2012	
Radaelli, Paolo G	C-2952-2011	0000-0002-6717-035X
Proffen, Thomas	B-3585-2009	0000-0002-1408-6031
Bozin, Emil	AAB-4551-2020	
Bozin, Emil	E-4679-2011	
Billinge, Simon		0000-0002-9734-4998
DeConinck, Adam		0000-0003-2592-8983
Chatterji, Tapan		0000-0002-2303-8904

Publisher: AMERICAN PHYSICAL SOC

Publisher Address: ONE PHYSICS ELLIPSE, COLLEGE PK, MD 20740-3844 USA

Web of Science Index: Science Citation Index Expanded (SCI-EXPANDED)

Web of Science Categories: Physics, Multidisciplinary

Research Areas: Physics

IDS Number: 152AD

ISSN: 0031-9007

29-char Source Abbrev.: PHYS REV LETT

ISO Source Abbrev.: Phys. Rev. Lett.

Source Item Page Count: 4

Open Access: Green Submitted

Output Date: 2023-01-27

Record 105 of 125

Title: Utilizing total scattering to study the Jahn-Teller transition in La_{1-x}CaxMnO₃

Author(s): Bozin, ES (Bozin, E. S.); Qiu, X (Qiu, X.); Worhatch, RJ (Worhatch, R. J.); Paglia, G (Paglia, G.); Schmidt, M (Schmidt, M.); Radaelli, PG (Radaelli, P. G.); Mitchell, JF (Mitchell, J. F.); Chatterji, T (Chatterji, T.); Proffen, T (Proffen, Th.); Billinge, SJL (Billinge, S. J. L.)

Source: ZEITSCHRIFT FUR KRISTALLOGRAPHIE **Pages:** 429-434 **Supplement:** 26 **Part:** 2 **Published:** 2007

Times Cited in Web of Science Core Collection: 3

Total Times Cited: 3

Usage Count (Last 180 days): 0

Usage Count (Since 2013): 7

Cited Reference Count: 24

Abstract: Total scattering based atomic pair distribution function (PDF) analysis, with the advent of high data throughput neutron powder diffractometers, helps understanding the nature of the Jahn-Teller (JT) phase transition in La_{1-x}CaxMnO₃ colossal magnetoresistive (CMR) manganites. The JT distortion of the MnO₆ octahedra, is long-range ordered in the orthorhombic (O) phase, but disappears in the pseudo-cubic (O') phase crystallographically. An anomalous unit cell volume contraction occurs at the transition. The PDF study indicates that the distortion persists locally deep in the O' phase, contrary to the crystallographic view. Simultaneously, local structural features observed in PDF at 10.3 angstrom, sensitive to the oxygen sublattice changes, evolve dramatically across the transition. The same effect is observed irrespective of the way the O-O'

phase boundary is crossed: it is seen both in the temperature series data for $x=0$, and in the doping series data at 310 K and at 550 K.

Accession Number: WOS:000253340900036

Language: English

Document Type: Article

Author Keywords: total scattering; atomic pair distribution function; CMR manganites

KeyWords Plus: NEUTRON-DIFFRACTION

Addresses: [Bozin, E. S.; Qiu, X.; Worhatch, R. J.; Paglia, G.; Billinge, S. J. L.] Michigan State Univ, Dept Phys & Astron, E Lansing, MI 48824 USA.

[Schmidt, M.; Radaelli, P. G.] CCLRC Rutherford Appleton Lab, ISIS, Didcot OX11 0QX, Oxon, England.

[Mitchell, J. F.] Argonne Natl Lab, Div Mat Sci, Argonne, IL 60439 USA.

[Chatterji, T.] Inst Max Von Laue Paul Langevin, F-38042 Grenoble 9, France.

[Proffen, Th.] Los Alamos Natl Lab, Lujan Neutron Scattering Ctr, Los Alamos, NM 87545 USA.

Corresponding Address: Bozin, ES (corresponding author), Michigan State Univ, Dept Phys & Astron, E Lansing, MI 48824 USA.

E-mail Addresses: bozin@pa.msu.edu

Affiliations: Michigan State University; UK Research & Innovation (UKRI); Science & Technology Facilities Council (STFC); STFC Rutherford Appleton Laboratory; United States Department of Energy (DOE); Argonne National Laboratory; Institut Laue-Langevin (ILL); United States Department of Energy (DOE); Los Alamos National Laboratory

Author Identifiers:

Author	Web of Science ResearcherID	ORCID Number
Bozin, Emil	E-4679-2011	
Bozin, Emil	AAB-4551-2020	
Radaelli, Paolo G	C-2952-2011	0000-0002-6717-035X
Proffen, Thomas	B-3585-2009	0000-0002-1408-6031
Mitchell, John F	A-1907-2012	
Billinge, Simon		0000-0002-9734-4998
Chatterji, Tapan		0000-0002-2303-8904

Publisher: WALTER DE GRUYTER GMBH

Publisher Address: GENTHINER STRASSE 13, D-10785 BERLIN, GERMANY

Web of Science Index: Science Citation Index Expanded (SCI-EXPANDED)

Web of Science Categories: Crystallography

Research Areas: Crystallography

IDS Number: 265EC

ISSN: 0044-2968

29-char Source Abbrev.: Z KRISTALLOGR

ISO Source Abbrev.: Z. Kristall.

Source Item Page Count: 6

Output Date: 2023-01-27

Record 106 of 125

Title: Local structural aspects of the orthorhombic to pseudo-cubic phase transformation in $\text{La}_{1-x}\text{Ca}_x\text{MnO}_3$

Author(s): Bozin, ES (Bozin, E. S.); Qiu, X (Qiu, X.); Schmidt, M (Schmidt, M.); Paglia, G (Paglia, G.); Mitchell, JF (Mitchell, J. F.); Radaelli, PG (Radaelli, P. G.); Proffen, T (Proffen, Th.); Billinge, SJL (Billinge, S. J. L.)

Source: PHYSICA B-CONDENSED MATTER **Volume:** 385 **Special Issue:** SI **Pages:** 110-112 **DOI:** 10.1016/j.physb.2006.05.137 **Part:** 1 **Published:** NOV 15 2006

Times Cited in Web of Science Core Collection: 10

Total Times Cited: 10

Usage Count (Last 180 days): 0

Usage Count (Since 2013): 3

Cited Reference Count: 13

Abstract: The local and intermediate structure of $\text{La}_{1-x}\text{Ca}_x\text{MnO}_3$ has been studied in the orthorhombic (O) and pseudo-cubic (O') phases, both as a function of temperature ($x = 0.00$), and as a function of Ca content (at 310K). Neutron powder diffraction-based high real space resolution atomic pair distribution function (PDF) analysis shows that the Jahn Teller distortion of the MnO_6 octahedra persists locally deep in the O' phase in both cases studied, contrary to the average crystallographic view. The O to O' structural phase transformation does have a local structural signature evidenced as a dramatic change in a PDF peak at 10.3 angstrom sensitive to the rotations of the MnO_6 octahedra, providing further evidence that the nature of the transformation is orbital order to disorder regardless of whether the phase boundary is crossed as a function of T or x. (c) 2006 Elsevier B.V. All rights reserved.

Accession Number: WOS:000243096400033

Language: English

Document Type: Article; Proceedings Paper

Conference Title: 8th International Conference (ICNS 2005)

Conference Date: NOV 27-DEC 02, 2005

Conference Location: Sydney, AUSTRALIA

Conference Sponsors: Australian Govt, Dept Educ, Sci & Training, Australian Nucl Sci & Technol Org, ISIS, Cooperat Res Ctr Polymers, INVAP S E, Inst Laue Langevin

Author Keywords: local structure; manganites; Jahn-Teller distortion

KeyWords Plus: NEUTRON-DIFFRACTION; TRANSITION

Addresses: Michigan State Univ, Dept Phys & Astron, E Lansing, MI 48824 USA.

Rutherford Appleton Lab, ISIS Facil, Didcot OX11 0QX, Oxon, England.

Polish Acad Sci, Inst Mol Phys, PL-60179 Poznan, Poland.

Argonne Natl Lab, Div Sci Mat, Argonne, IL 60439 USA.

Los Alamos Natl Lab, LANSCE12, Los Alamos, NM 87545 USA.

Corresponding Address: Bozin, ES (corresponding author), Michigan State Univ, Dept Phys & Astron, E Lansing, MI 48824 USA.

E-mail Addresses: bozin@pa.msu.edu

Affiliations: Michigan State University; UK Research & Innovation (UKRI); Science & Technology Facilities Council (STFC); STFC Rutherford Appleton Laboratory; Polish Academy of Sciences; Institute of Molecular Physics of the Polish Academy of Sciences; United States Department of Energy (DOE); Argonne National Laboratory; United States Department of Energy (DOE); Los Alamos National Laboratory

Author Identifiers:

Author	Web of Science ResearcherID	ORCID Number
Mitchell, John F	A-1907-2012	
Bozin, Emil	AAB-4551-2020	
Proffen, Thomas	B-3585-2009	0000-0002-1408-6031
Bozin, Emil	E-4679-2011	
Radaelli, Paolo G	C-2952-2011	0000-0002-6717-035X
Billinge, Simon		0000-0002-9734-4998

Publisher: ELSEVIER

Publisher Address: RADARWEG 29, 1043 NX AMSTERDAM, NETHERLANDS

Web of Science Index: Science Citation Index Expanded (SCI-EXPANDED); Conference Proceedings Citation Index - Science (CPCI-S)

Web of Science Categories: Physics, Condensed Matter

Research Areas: Physics

IDS Number: 120PF

ISSN: 0921-4526

eISSN: 1873-2135

29-char Source Abbrev.: PHYSICA B

ISO Source Abbrev.: Physica B

Source Item Page Count: 3

Output Date: 2023-01-27

Record 107 of 125

Title: Geometric simulation of perovskite frameworks with Jahn-Teller distortions: Applications to the cubic manganites

Author(s): Sartbaeva, A (Sartbaeva, A.); Wells, SA (Wells, S. A.); Thorpe, MF (Thorpe, M. F.); Bozin, ES (Bozin, E. S.); Billinge, SJL (Billinge, S. J. L.)

Source: PHYSICAL REVIEW LETTERS **Volume:** 97 **Issue:** 6 **Article Number:** 065501 **DOI:** 10.1103/PhysRevLett.97.065501 **Published:** AUG 11 2006

Times Cited in Web of Science Core Collection: 22

Total Times Cited: 22

Usage Count (Last 180 days): 0

Usage Count (Since 2013): 15

Cited Reference Count: 29

Abstract: A new approach is presented for modeling perovskite frameworks with disordered Jahn-Teller (JT) distortions and has been applied to study the elastic response of the LaMnO₃ structure to defects in the JT ordering. Surprisingly, antiphase domain boundary defects in the pattern of ordered JT octahedra, along the [110] and [1 (1) over bar 0] bonding directions, are found to produce 1D stripe patterns rotated 45 degrees along a(*) directions, similar to stripe structures observed in these systems. Geometric simulation is shown to be an efficient and powerful approach for finding relaxed atomic structures in the presence of disorder in networks of corner-shared JT-distorted octahedra such as the perovskites. Geometric modeling rapidly relaxes large supercells (thousands of octahedra) while preserving the local coordination chemistry, and shows great promise for studying these complex systems.

Accession Number: WOS:000239690900024

PubMed ID: 17026173

Language: English

Document Type: Article

KeyWords Plus: ATOMISTIC SIMULATIONS; CHARGE; SPECTROSCOPY; TRANSITION; STRIPES; OXIDES; QUARTZ; LAMNO3

Addresses: Arizona State Univ, Dept Phys & Astron, Tempe, AZ 85287 USA.

Michigan State Univ, Dept Phys & Astron, E Lansing, MI 48824 USA.

Corresponding Address: Sartbaeva, A (corresponding author), Arizona State Univ, Dept Phys & Astron, Tempe, AZ 85287 USA.

Affiliations: Arizona State University; Arizona State University-Tempe; Michigan State University

Author Identifiers:

Author	Web of Science ResearcherID	ORCID Number
Bozin, Emil	AAB-4551-2020	

Sartbaeva, Asel	I-5914-2013	
Wells, Stephen	L-2064-2014	
Bozin, Emil	E-4679-2011	
Sartbaeva, Asel	K-9890-2019	0000-0003-1017-0161
Wells, Stephen		0000-0002-3920-3644
Billinge, Simon		0000-0002-9734-4998

Publisher: AMERICAN PHYSICAL SOC

Publisher Address: ONE PHYSICS ELLIPSE, COLLEGE PK, MD 20740-3844 USA

Web of Science Index: Science Citation Index Expanded (SCI-EXPANDED)

Web of Science Categories: Physics, Multidisciplinary

Research Areas: Physics

IDS Number: 072RO

ISSN: 0031-9007

29-char Source Abbrev.: PHYS REV LETT

ISO Source Abbrev.: Phys. Rev. Lett.

Source Item Page Count: 4

Output Date: 2023-01-27

Record 108 of 125

Title: Fine-scale nanostructure in gamma-Al₂O₃

Author(s): Paglia, G (Paglia, Gianluca); Bozin, ES (Bozin, Emil S.); Billinge, SJL (Billinge, Simon J. L.)

Source: CHEMISTRY OF MATERIALS **Volume:** 18 **Issue:** 14 **Pages:** 3242-3248 **DOI:**

10.1021/cm060277j **Published:** JUL 11 2006

Times Cited in Web of Science Core Collection: 92

Total Times Cited: 94

Usage Count (Last 180 days): 1

Usage Count (Since 2013): 73

Cited Reference Count: 49

Abstract: We have applied a local structural technique, atomic pair distribution function (PDF) analysis of powder diffraction data to gamma-Al₂O₃, to obtain a quantitative structure. Refinements of the PDF support previous findings that nonspinel model representations are more suitable to describe the average structure of gamma-Al₂O₃, as opposed to the spinel model. Surprisingly, also we find a previously unknown fine-scale nanostructure with a domain size similar to 1 nm. Modeling suggests that within these nanodomains the oxygen sublattice is modified from the average structure and retains aspects of the boehmite precursor that reflects a stacking fault in the gamma-Al₂O₃ matrix. This results in a novel and unexpected view of the gamma-Al₂O₃ structure because earlier controversies about it centered on the arrangement of Al ions among different cation sites, whereas the oxygen sublattice arrangement was rarely questioned. This average oxygen sublattice structure is recovered in our models on longer length scales by introducing aperiodic arrays of stacking faults. The use of gamma-Al₂O₃ in catalysis depends sensitively on its nanoporosity and defect structure. Here we present a new view which may allow for additional understanding and optimization of its functional properties.

Accession Number: WOS:000238727000011

Language: English

Document Type: Article

KeyWords Plus: GAMMA-ALUMINA SYSTEM; BOEHMITE; DEHYDRATION; REFINEMENT; TEMPERATURE; DISORDER; HYDROGEN; PHASE; ETA

Addresses: Michigan State Univ, Dept Phys & Astron, E Lansing, MI 48824 USA.

Corresponding Address: Billinge, SJL (corresponding author), Michigan State Univ, Dept Phys & Astron, E Lansing, MI 48824 USA.

E-mail Addresses: billinge@pa.msu.edu

Affiliations: Michigan State University

Author Identifiers:

Author	Web of Science ResearcherID	ORCID Number
Bozin, Emil	E-4679-2011	
Bozin, Emil	AAB-4551-2020	
Billinge, Simon		0000-0002-9734-4998

Publisher: AMER CHEMICAL SOC

Publisher Address: 1155 16TH ST, NW, WASHINGTON, DC 20036 USA

Web of Science Index: Science Citation Index Expanded (SCI-EXPANDED)

Web of Science Categories: Chemistry, Physical; Materials Science, Multidisciplinary

Research Areas: Chemistry; Materials Science

IDS Number: 059IR

ISSN: 0897-4756

eISSN: 1520-5002

29-char Source Abbrev.: CHEM MATER

ISO Source Abbrev.: Chem. Mat.

Source Item Page Count: 7

Output Date: 2023-01-27

Record 109 of 125

Title: Study of temperature dependent atomic correlations in MgB₂

Author(s): Campi, G (Campi, G.); Cappelluti, E (Cappelluti, E.); Proffen, T (Proffen, Th.); Qiu, X (Qiu, X.); Bozin, ES (Bozin, E. S.); Billinge, SJL (Billinge, S. J. L.); Agrestini, S (Agrestini, S.); Saini, NL (Saini, N. L.); Bianconi, A (Bianconi, A.)

Source: EUROPEAN PHYSICAL JOURNAL B **Volume:** 52 **Issue:** 1 **Pages:** 15-21 **DOI:** 10.1140/epjb/e2006-00269-7 **Published:** JUL 2006

Times Cited in Web of Science Core Collection: 28

Total Times Cited: 28

Usage Count (Last 180 days): 0

Usage Count (Since 2013): 12

Cited Reference Count: 36

Abstract: We have studied temperature evolution of the local as well as the average crystal structure of MgB₂ using real-space atomic pair distribution function (PDF) measured by high resolution neutron powder diffraction in a wide temperature range of T=10-600 K. We find small positive correlation factors for the B-B and B-Mg pairs, determined by mean-square displacements (MSD) and the mean-square relative displacements (MSRD). We analyze the PDF using both Einstein and force constant models finding a good agreement between the experimental data and the two models. This indicates that B and Mg atomic correlations are not sensitive to the details of phonon dispersion.

Accession Number: WOS:000238848700003

Language: English

Document Type: Article

KeyWords Plus: MICRO-STRAIN; T-C; SUPERCONDUCTIVITY; SCATTERING; DENSITY

Addresses: CNR, Ist Cristallog, Sez Monterotondo, Area Ric Roma Montelibretti, I-00016 Monterotondo, RM, Italy.

CNR, INFN, Ist Sistemi Complessi, I-00185 Rome, Italy.

Univ Roma La Sapienza, Dipartimento Fis, I-00185 Rome, Italy.

Los Alamos Natl Lab, Manuel Lujan Jr Neutron Scattering Ctr, Los Alamos, NM 87545 USA.

Michigan State Univ, Dept Phys & Astron, E Lansing, MI 48824 USA.

Corresponding Address: Campi, G (corresponding author), CNR, Ist Cristallog, Sez Monterotondo, Area Ric Roma Montelibretti, POB 10, I-00016 Monterotondo, RM, Italy.

E-mail Addresses: gaetano.campi@roma1.infn.it

Affiliations: Consiglio Nazionale delle Ricerche (CNR); Istituto Di Cristallografia (IC-CNR); Consiglio Nazionale delle Ricerche (CNR); Istituto dei Sistemi Complessi (ISC-CNR); Istituto Nazionale per la Fisica della Materia (INFN-CNR); Sapienza University Rome; United States Department of Energy (DOE); Los Alamos National Laboratory; Michigan State University

Author Identifiers:

Author	Web of Science ResearcherID	ORCID Number
Saini, Naurang	J-7918-2013	0000-0003-3684-1517
Cappelluti, Emmanuele	U-4946-2019	
Proffen, Thomas	B-3585-2009	0000-0002-1408-6031
Bozin, Emil	E-4679-2011	
Bozin, Emil	AAB-4551-2020	
Bianconi, Antonio	J-3997-2013	0000-0001-9795-3913
Agrestini, Stefano		0000-0002-3625-880X
Campi, Gaetano	H-1981-2018	0000-0001-9845-9394
Billinge, Simon		0000-0002-9734-4998

Publisher: SPRINGER

Publisher Address: ONE NEW YORK PLAZA, SUITE 4600, NEW YORK, NY, UNITED STATES

Web of Science Index: Science Citation Index Expanded (SCI-EXPANDED)

Web of Science Categories: Physics, Condensed Matter

Research Areas: Physics

IDS Number: 061CL

ISSN: 1434-6028

eISSN: 1434-6036

29-char Source Abbrev.: EUR PHYS J B

ISO Source Abbrev.: Eur. Phys. J. B

Source Item Page Count: 7

Open Access: Green Submitted

Output Date: 2023-01-27

Record 110 of 125

Title: Accurate structure determination of Mo₆SyIz nanowires from atomic pair distribution function (PDF) analysis

Author(s): Paglia, G (Paglia, G); Bozin, ES (Bozin, ES); Vengust, D (Vengust, D); Mihailovic, D (Mihailovic, D); Billinge, SJL (Billinge, SJL)

Source: CHEMISTRY OF MATERIALS **Volume:** 18 **Issue:** 1 **Pages:** 100-106 **DOI:** 10.1021/cm051833x **Published:** JAN 10 2006

Times Cited in Web of Science Core Collection: 25

Total Times Cited: 25

Usage Count (Last 180 days): 4

Usage Count (Since 2013): 15

Cited Reference Count: 29

Abstract: The structure of the recently discovered systematically reproducible Mo₆SyI₇ nanowires has been determined from the atomic pair distribution function (PDF) analysis of powder X-ray diffraction data. This total scattering approach was required because the nanowires are not perfectly crystalline and, therefore, the structure cannot be obtained crystallographic ally. Several nanotube and nanowire models were fit to the PDF data. The resulting best-fit model structure consists of nanowires Of Mo-6 octahedra that are bridged by sulfur and terminated on the outside by iodine. This demonstrates the power of total scattering methods in accurately resolving structural issues in nanostructured materials where traditional crystallographic methods fail.

Accession Number: WOS:000234587800014

Language: English

Document Type: Article

KeyWords Plus: REFINEMENT; SOLUBILITY; DISORDER

Addresses: Michigan State Univ, Dept Phys & Astron, E Lansing, MI 48824 USA.

Josef Stefan Inst, SI-1000 Ljubljana, Slovenia.

Univ Ljubljana, Fac Math & Phys, SI-1000 Ljubljana, Slovenia.

Corresponding Address: Paglia, G (corresponding author), Michigan State Univ, Dept Phys & Astron, E Lansing, MI 48824 USA.

E-mail Addresses: paglia@msu.edu

Affiliations: Michigan State University; Slovenian Academy of Sciences & Arts (SASA); Jozef Stefan Institute; University of Ljubljana

Author Identifiers:

Author	Web of Science ResearcherID	ORCID Number
Bozin, Emil	AAB-4551-2020	
Bozin, Emil	E-4679-2011	
Mihailovic, Dragan	H-6753-2014	0000-0003-2074-2899
Billinge, Simon		0000-0002-9734-4998

Publisher: AMER CHEMICAL SOC

Publisher Address: 1155 16TH ST, NW, WASHINGTON, DC 20036 USA

Web of Science Index: Science Citation Index Expanded (SCI-EXPANDED)

Web of Science Categories: Chemistry, Physical; Materials Science, Multidisciplinary

Research Areas: Chemistry; Materials Science

IDS Number: 002CA

ISSN: 0897-4756

eISSN: 1520-5002

29-char Source Abbrev.: CHEM MATER

ISO Source Abbrev.: Chem. Mat.

Source Item Page Count: 7

Output Date: 2023-01-27

Record 111 of 125

Title: Nominal doping and partition of doped holes between planar and apical orbitals in La_{2-x}Sr_xCuO₄

Author(s): Bozin, ES (Bozin, ES); Billinge, SJL (Billinge, SJL)

Source: PHYSICAL REVIEW B **Volume:** 72 **Issue:** 17 **Article Number:** 174427 **DOI:** 10.1103/PhysRevB.72.174427 **Published:** NOV 2005

Times Cited in Web of Science Core Collection: 10

Total Times Cited: 10

Usage Count (Last 180 days): 0

Usage Count (Since 2013): 5

Cited Reference Count: 20

Abstract: By considering both the average structural parameters obtained from Rietveld refinement of neutron powder diffraction data, and the local structural parameters obtained from the atomic pair distribution function, we have tested the recent hypothesis of Perry [Phys. Rev. B 65, 144501 (2002)] that doping in a $\text{La}_{2-x}\text{Sr}_x\text{CuO}_4$ system occurs as localized defects of predominantly $\text{Cu}(3z)(2-r)(2)\text{-Op}(z)$ character associated with the Sr dopants accompanied by a local destruction of the Jahn-Teller distortion. While the structural parameters behave qualitatively according to the prediction of this model, a quantitative analysis indicates that doped holes predominantly appear in the planar $\text{Cu}(x)(2-y)(2)\text{-Op}(x,y)$ band as is normally assumed. However, a small amount of the doped charge does enter the $\text{Cu}(3z)(2-r)(2)\text{-Op}(z)$ orbitals and this should be taken into account when theoretical phase diagrams are compared to experiment. We present a calibration curve, $p=x[1.00(1)-0.45(7)x]$, for the planar charge doping, p , vs strontium content, x , for the $\text{La}_{2-x}\text{Sr}_x\text{CuO}_4$ system.

Accession Number: WOS:000233603500093

Language: English

Document Type: Article

KeyWords Plus: STATES

Addresses: Michigan State Univ, Dept Phys & Astron, E Lansing, MI 48824 USA.

Corresponding Address: Bozin, ES (corresponding author), Michigan State Univ, Dept Phys & Astron, E Lansing, MI 48824 USA.

E-mail Addresses: bozin@pa.msu.edu

Affiliations: Michigan State University

Author Identifiers:

Author	Web of Science ResearcherID	ORCID Number
Bozin, Emil	AAB-4551-2020	
Bozin, Emil	E-4679-2011	
Billinge, Simon		0000-0002-9734-4998

Publisher: AMER PHYSICAL SOC

Publisher Address: ONE PHYSICS ELLIPSE, COLLEGE PK, MD 20740-3844 USA

Web of Science Index: Science Citation Index Expanded (SCI-EXPANDED)

Web of Science Categories: Materials Science, Multidisciplinary; Physics, Applied; Physics, Condensed Matter

Research Areas: Materials Science; Physics

IDS Number: 988LU

ISSN: 2469-9950

eISSN: 2469-9969

29-char Source Abbrev.: PHYS REV B

ISO Source Abbrev.: Phys. Rev. B

Source Item Page Count: 6

Open Access: Green Submitted

Output Date: 2023-01-27

Record 112 of 125

Title: Nanoscale clusters in the high performance thermoelectric AgPbmSbTe_{m+2}

Author(s): Lin, H (Lin, H); Bozin, ES (Bozin, ES); Billinge, SJL (Billinge, SJL); Quarez, E (Quarez, E); Kanatzidis, MG (Kanatzidis, MG)

Source: PHYSICAL REVIEW B **Volume:** 72 **Issue:** 17 **Article Number:** 174113 **DOI:** 10.1103/PhysRevB.72.174113 **Published:** NOV 2005

Times Cited in Web of Science Core Collection: 59

Total Times Cited: 60

Usage Count (Last 180 days): 0

Usage Count (Since 2013): 35

Cited Reference Count: 19

Abstract: The local structure of the AgPbmSbTem+2 series of thermoelectric materials has been studied using the atomic pair distribution function (PDF) method. Three candidate-models were attempted for the structure of this class of materials using either a one- or a two-phase modeling procedure. Combining modeling the PDF with HRTEM data we show that AgPbmSbTem+2 contains nanoscale inclusions with composition close to AgPb3SbTe5 randomly embedded in a PbTe matrix.

Accession Number: WOS:000233603500046

Language: English

Document Type: Article

KeyWords Plus: REFINEMENT

Addresses: Michigan State Univ, Dept Phys & Astron, E Lansing, MI 48824 USA.

Michigan State Univ, Dept Chem, E Lansing, MI 48824 USA.

Corresponding Address: Lin, H (corresponding author), Michigan State Univ, Dept Phys & Astron, E Lansing, MI 48824 USA.

E-mail Addresses: billinge@pa.msu.edu

Affiliations: Michigan State University; Michigan State University

Author Identifiers:

Author	Web of Science ResearcherID	ORCID Number
QUAREZ, Eric	K-5440-2015	0000-0001-7887-892X
Bozin, Emil	AAB-4551-2020	
Bozin, Emil	E-4679-2011	
Billinge, Simon		0000-0002-9734-4998

Publisher: AMER PHYSICAL SOC

Publisher Address: ONE PHYSICS ELLIPSE, COLLEGE PK, MD 20740-3844 USA

Web of Science Index: Science Citation Index Expanded (SCI-EXPANDED)

Web of Science Categories: Materials Science, Multidisciplinary; Physics, Applied; Physics, Condensed Matter

Research Areas: Materials Science; Physics

IDS Number: 988LU

ISSN: 2469-9950

eISSN: 2469-9969

29-char Source Abbrev.: PHYS REV B

ISO Source Abbrev.: Phys. Rev. B

Source Item Page Count: 7

Open Access: Green Submitted

Output Date: 2023-01-27

Title: Temperature dependent total scattering structural study of CaCu₃Ti₄O₁₂

Author(s): Bozin, ES (Bozin, ES); Petkov, V (Petkov, V); Barnes, PW (Barnes, PW); Woodward, PM (Woodward, PM); Vogt, T (Vogt, T); Mahanti, SD (Mahanti, SD); Billinge, SJL (Billinge, SJL)

Source: JOURNAL OF PHYSICS-CONDENSED MATTER **Volume:** 16 **Issue:** 44 **Special Issue:** SI **Pages:** S5091-S5102 **DOI:** 10.1088/0953-8984/16/44/007 **Published:** NOV 10 2004

Times Cited in Web of Science Core Collection: 40

Total Times Cited: 40

Usage Count (Last 180 days): 0

Usage Count (Since 2013): 14

Cited Reference Count: 34

Abstract: X-ray and neutron powder diffraction data as a function of temperature are analysed for the colossal dielectric constant material CaCu₃Ti₄O₁₂. The local structure is studied using atomic pair distribution function analysis. No evidence is found for enlarged oxygen or Ti displacement parameters suggesting that short range octahedral tilt disorder and off-centre Ti displacements are minimal. However, an unusual temperature dependence for the atomic displacement parameters of calcium and copper is observed. Temperature dependent modelling of the structure, using bond valence concepts, suggests that the calcium atoms become underbonded below approximately 260 K, which provides a rationale for the unusually high Ca displacement parameters at low temperature.

Accession Number: WOS:000225708800008

Language: English

Document Type: Article; Proceedings Paper

Conference Title: Workshop in Honor of Mike Thorpes 60th Birthday on Flexibility in Complex Materials: Glasses, Amorphous and Proteins

Conference Date: AUG 07-10, 2004

Conference Location: St Adele, CANADA

KeyWords Plus: HIGH-DIELECTRIC-CONSTANT; X-RAY; PROGRAM; PEROVSKITES

Addresses: Michigan State Univ, Dept Phys & Astron, E Lansing, MI 48824 USA.

Michigan State Univ, Ctr Fundamental Mat Res, E Lansing, MI 48824 USA.

Cent Michigan Univ, Dept Phys, Mt Pleasant, MI 48859 USA.

Ohio State Univ, Dept Chem, Columbus, OH 43210 USA.

Brookhaven Natl Lab, Dept Phys, Upton, NY 11973 USA.

Corresponding Address: Bozin, ES (corresponding author), Michigan State Univ, Dept Phys & Astron, E Lansing, MI 48824 USA.

Affiliations: Michigan State University; Michigan State University; Central Michigan University; University System of Ohio; Ohio State University; United States Department of Energy (DOE); Brookhaven National Laboratory

Author Identifiers:

Author	Web of Science ResearcherID	ORCID Number
Vogt, Thomas	A-1562-2011	0000-0002-4731-2787
Bozin, Emil	AAB-4551-2020	
Bozin, Emil	E-4679-2011	
M Woodward, Patrick	AGN-8481-2022	

Publisher: IOP Publishing Ltd

Publisher Address: TEMPLE CIRCUS, TEMPLE WAY, BRISTOL BS1 6BE, ENGLAND

Web of Science Index: Science Citation Index Expanded (SCI-EXPANDED); Conference Proceedings Citation Index - Science (CPCI-S)

Web of Science Categories: Physics, Condensed Matter

Research Areas: Physics

IDS Number: 879IE

ISSN: 0953-8984

eISSN: 1361-648X

29-char Source Abbrev.: J PHYS-CONDENS MAT

ISO Source Abbrev.: J. Phys.-Condes. Matter

Source Item Page Count: 12

Open Access: Green Submitted, Green Published

Output Date: 2023-01-27

Record 114 of 125

Title: Reciprocal-space instrumental effects on the real-space neutron atomic pair distribution function

Author(s): Qiu, XY (Qiu, XY); Bozin, ES (Bozin, ES); Juhas, P (Juhas, P); Proffen, T (Proffen, T); Billinge, SJL (Billinge, SJL)

Source: JOURNAL OF APPLIED CRYSTALLOGRAPHY **Volume:** 37 **Pages:** 110-116 **DOI:** 10.1107/S0021889803026670 **Part:** 1 **Published:** FEB 2004

Times Cited in Web of Science Core Collection: 90

Total Times Cited: 91

Usage Count (Last 180 days): 0

Usage Count (Since 2013): 25

Cited Reference Count: 20

Abstract: An atomic pair distribution function (PDF) neutron powder diffraction round-robin experiment was performed on six diffractometers at three spallation sources. Instrument-specific effects on the real-space PDF were investigated, such as finite measurement range, the instrument resolution and the asymmetric shape of diffraction peaks. Two illustrative samples, a perfectly long-range-ordered element, Pb, and a locally strained alloy ZnSe_{0.5}Te_{0.5}, were measured at low temperatures. Various aspects of the PDF were explored, either qualitatively by direct comparison or quantitatively via structural modelling. Future implementation of modelling codes incorporating some of these instrumental effects are also discussed.

Accession Number: WOS:000188225100017

Language: English

Document Type: Article

KeyWords Plus: LOCAL-STRUCTURE

Addresses: Michigan State Univ, Dept Phys & Astron, E Lansing, MI 48824 USA.
Los Alamos Natl Lab, Los Alamos, NM 87545 USA.

Corresponding Address: Billinge, SJL (corresponding author), Michigan State Univ, Dept Phys & Astron, E Lansing, MI 48824 USA.

E-mail Addresses: billinge@pa.msu.edu

Affiliations: Michigan State University; United States Department of Energy (DOE); Los Alamos National Laboratory

Author Identifiers:

Author	Web of Science ResearcherID	ORCID Number
Juhas, Pavol	A-6544-2008	0000-0001-8751-4458
Juhas, Pavol	Q-7225-2019	0000-0001-8751-4458
Bozin, Emil	AAB-4551-2020	
Proffen, Thomas	B-3585-2009	0000-0002-1408-6031
Bozin, Emil	E-4679-2011	

Publisher: INT UNION CRYSTALLOGRAPHY

Publisher Address: 2 ABBEY SQ, CHESTER, CH1 2HU, ENGLAND

Web of Science Index: Science Citation Index Expanded (SCI-EXPANDED)

Web of Science Categories: Chemistry, Multidisciplinary; Crystallography

Research Areas: Chemistry; Crystallography

IDS Number: 764UU

eISSN: 1600-5767

29-char Source Abbrev.: J APPL CRYSTALLOGR

ISO Source Abbrev.: J. Appl. Crystallogr.

Source Item Page Count: 7

Output Date: 2023-01-27

Record 115 of 125

Title: Structural response to local charge order in underdoped but superconducting $\text{La}_{2-x}(\text{Sr},\text{Ba})_x\text{CuO}_4$

Author(s): Billinge, SJL (Billinge, SJL); Gutmann, M (Gutmann, M); Bozin, ES (Bozin, ES)

Source: INTERNATIONAL JOURNAL OF MODERN PHYSICS B **Volume:** 17 **Issue:** 18-20 **Pages:** 3640-3647 **DOI:** 10.1142/S021797920302154X **Part:** 2 **Published:** AUG 10 2003

Times Cited in Web of Science Core Collection: 7

Total Times Cited: 7

Usage Count (Last 180 days): 0

Usage Count (Since 2013): 2

Cited Reference Count: 41

Abstract: Results are presented of a local structural study of the nearest neighbor Cu-O distance distribution in underdoped but superconducting $\text{La}_{1.875}\text{Sr}_{0.125}\text{CuO}_4$, $\text{La}_{1.85}\text{Ba}_{0.15}\text{CuO}_4$ and $\text{La}_{1.85}\text{Sr}_{0.15}\text{CuO}_4$. Atomic pair distribution function analysis of neutron powder diffraction data has been carried out to obtain local structural information over a wide temperature range. We observe an anomalous increase in the Cu-O bond length distribution at low temperature that may be associated with the presence of an inhomogeneous charge distribution. The increase at low temperature has an onset temperature which correlates with observations of charge and spin freezing seen by other probes.

Accession Number: WOS:000185634800038

Language: English

Document Type: Article; Proceedings Paper

Conference Title: 4th International Conference on New Theories, Discoveries and Applications of Superconductors and Related Materials

Conference Date: JAN 16-21, 2003

Conference Location: SAN DIEGO, CA

KeyWords Plus: ABSORPTION FINE-STRUCTURE; T-C SUPERCONDUCTIVITY; NEUTRON-DIFFRACTION; TETRAGONAL PHASE; NORMAL-STATE; TEMPERATURE; TRANSITION; $\text{LA}_{2-x}\text{SR}_x\text{CUO}_4$; FLUCTUATIONS; REFINEMENT

Addresses: Michigan State Univ, Dept Phys & Astron, E Lansing, MI 48824 USA.

Michigan State Univ, Ctr Fundamental Mat Res, E Lansing, MI 48824 USA.

Corresponding Address: Billinge, SJL (corresponding author), Michigan State Univ, Dept Phys & Astron, E Lansing, MI 48824 USA.

Affiliations: Michigan State University; Michigan State University

Author Identifiers:

Author	Web of Science ResearcherID	ORCID Number
Bozin, Emil	E-4679-2011	
Bozin, Emil	AAB-4551-2020	

Publisher: WORLD SCIENTIFIC PUBL CO PTE LTD

Publisher Address: 5 TOH TUCK LINK, SINGAPORE 596224, SINGAPORE

Web of Science Index: Science Citation Index Expanded (SCI-EXPANDED); Conference Proceedings Citation Index - Science (CPCI-S)

Web of Science Categories: Physics, Applied; Physics, Condensed Matter; Physics, Mathematical

Research Areas: Physics

IDS Number: 727AX

ISSN: 0217-9792

eISSN: 1793-6578

29-char Source Abbrev.: INT J MOD PHYS B

ISO Source Abbrev.: Int. J. Mod. Phys. B

Source Item Page Count: 8

Open Access: Green Submitted

Output Date: 2023-01-27

Record 116 of 125

Title: Improved measures of quality for the atomic pair distribution function

Author(s): Peterson, PF (Peterson, PF); Bozin, ES (Bozin, ES); Proffen, T (Proffen, T); Billinge, SJL (Billinge, SJL)

Source: JOURNAL OF APPLIED CRYSTALLOGRAPHY **Volume:** 36 **Pages:** 53-64 **DOI:** 10.1107/S0021889802018708 **Part:** 1 **Published:** FEB 2003

Times Cited in Web of Science Core Collection: 83

Total Times Cited: 84

Usage Count (Last 180 days): 0

Usage Count (Since 2013): 36

Cited Reference Count: 26

Abstract: The introduction of neutron spallation-source instruments, such as the General Materials Diffractometer (GEM) at ISIS, allows measurement of pair distribution function (PDF) data at significantly higher rates than previously possible. As a result of the increased rate, a single experiment can produce over a hundred individual runs. Manual processing of all these data using traditional methods becomes inconvenient and inefficient. This article presents quality criteria that help produce automated direct Fourier transformed PDFs of quality similar to hand-processed data, and compares optimization methods.

Accession Number: WOS:000180457300009

Language: English

Document Type: Article

KeyWords Plus: NEUTRON-SCATTERING; X-RAY; PROGRAM; NORMALIZATION; INTENSITIES; REFINEMENT; SCALE

Addresses: Michigan State Univ, Dept Phys & Astron, E Lansing, MI 48824 USA.

Michigan State Univ, Ctr Fundamental Mat Res, E Lansing, MI 48824 USA.

Los Alamos Natl Lab, Los Alamos, NM 87544 USA.

Corresponding Address: Billinge, SJL (corresponding author), Michigan State Univ, Dept Phys & Astron, E Lansing, MI 48824 USA.

E-mail Addresses: billinge@pa.msu.edu

Affiliations: Michigan State University; Michigan State University; United States Department of Energy (DOE); Los Alamos National Laboratory

Author Identifiers:

Author	Web of Science ResearcherID	ORCID Number
--------	-----------------------------	--------------

Bozin, Emil	AAB-4551-2020	
Peterson, Peter	S-3056-2019	0000-0002-1353-0348
Bozin, Emil	E-4679-2011	
Proffen, Thomas	B-3585-2009	0000-0002-1408-6031

Publisher: INT UNION CRYSTALLOGRAPHY

Publisher Address: 2 ABBEY SQ, CHESTER, CH1 2HU, ENGLAND

Web of Science Index: Science Citation Index Expanded (SCI-EXPANDED)

Web of Science Categories: Chemistry, Multidisciplinary; Crystallography

Research Areas: Chemistry; Crystallography

IDS Number: 636LK

ISSN: 1600-5767

29-char Source Abbrev.: J APPL CRYSTALLOGR

ISO Source Abbrev.: J. Appl. Crystallogr.

Source Item Page Count: 12

Output Date: 2023-01-27

Record 117 of 125

Title: Temperature evolution of the local atomic structure in oxygen isotope substituted Pr_{0.525}La_{0.175}Ca_{0.3}MnO₃

Author(s): Gutmann, M (Gutmann, M); Bozin, ES (Bozin, ES); Billinge, SJL (Billinge, SJL); Babushkina, NA (Babushkina, NA); Belova, LM (Belova, LM); Kaul, AR (Kaul, AR); Gorbenko, OY (Gorbenko, OY)

Source: APPLIED PHYSICS A-MATERIALS SCIENCE & PROCESSING **Volume:** 74 **Pages:** S892-S894 **DOI:** 10.1007/s003390201672 **Supplement:** S **Part:** 1 **Published:** DEC 2002

Times Cited in Web of Science Core Collection: 1

Total Times Cited: 1

Usage Count (Last 180 days): 0

Usage Count (Since 2013): 2

Cited Reference Count: 10

Abstract: The local atomic structure of two oxygen isotope substituted samples Of Pr_{0.525}La_{0.175}Ca_{0.3}MnO₃ with O-16 and O-18 has been studied as a function of temperature using the pair-distribution function (PDF) obtained from pulsed neutron diffraction. The sample containing O-16 undergoes an insulator-metal (IM) transition below 100 K while the sample substituted with O-18 remains insulating at all temperatures. We find from the PDF that the shape of the MnO₆ octahedra changes from being elongated, due to a Jahn-Teller distortion, to a more regular shape below the IM transition in the O-16 sample, whereas the O-18 sample remains distorted at all temperatures.

Accession Number: WOS:000181499600298

Language: English

Document Type: Article; Proceedings Paper

Conference Title: International Conference on Neutron Scattering

Conference Date: SEP 09-13, 2001

Conference Location: MUNICH, GERMANY

KeyWords Plus: LA1-XCAXMNO3; DIFFRACTION; MANGANITES; REFINEMENT; EXCHANGE; CHARGE

Addresses: Rutherford Appleton Lab, ISIS Facil, Didcot OX11 0QX, Oxon, England.

Michigan State Univ, Dept Phys, E Lansing, MI 48824 USA.

RRC Kurchatov Inst, Moscow 123182, Russia.

Moscow MV Lomonosov State Univ, Dept Chem, Moscow 119899, Russia.

Corresponding Address: Gutmann, M (corresponding author), Rutherford Appleton Lab, ISIS Facil, Didcot OX11 0QX, Oxon, England.

Affiliations: UK Research & Innovation (UKRI); Science & Technology Facilities Council (STFC); STFC Rutherford Appleton Laboratory; Michigan State University; National Research Centre - Kurchatov Institute; Lomonosov Moscow State University

Author Identifiers:

Author	Web of Science ResearcherID	ORCID Number
Bozin, Emil	AAB-4551-2020	
Kaul, Andrey	AAU-6918-2020	
Belova, Lyubov	A-9868-2011	0000-0003-4889-4210
Bozin, Emil	E-4679-2011	

Publisher: SPRINGER-VERLAG

Publisher Address: 175 FIFTH AVE, NEW YORK, NY 10010 USA

Web of Science Index: Conference Proceedings Citation Index - Science (CPCI-S); Science Citation Index Expanded (SCI-EXPANDED)

Web of Science Categories: Materials Science, Multidisciplinary; Physics, Applied

Research Areas: Materials Science; Physics

IDS Number: 654MA

ISSN: 0947-8396

29-char Source Abbrev.: APPL PHYS A-MATER

ISO Source Abbrev.: Appl. Phys. A-Mater. Sci. Process.

Source Item Page Count: 3

Output Date: 2023-01-27

Record 118 of 125

Title: Structure of V₂O₅ center dot nH(2)O xerogel solved by the atomic pair distribution function technique

Author(s): Petkov, V (Petkov, V); Trikalitis, PN (Trikalitis, PN); Bozin, ES (Bozin, ES); Billinge, SJL (Billinge, SJL); Vogt, T (Vogt, T); Kanatzidis, MG (Kanatzidis, MG)

Source: JOURNAL OF THE AMERICAN CHEMICAL SOCIETY **Volume:** 124 **Issue:** 34 **Pages:** 10157-10162 **Article Number:** UNSP JA026143Y **DOI:** 10.1021/ja026143y **Published:** AUG 28 2002

Times Cited in Web of Science Core Collection: 370

Total Times Cited: 374

Usage Count (Last 180 days): 4

Usage Count (Since 2013): 143

Cited Reference Count: 31

Abstract: A long-standing issue regarding the local and long-range structure of V₂O₅.nH(2)O xerogel has been successfully addressed. The full three-dimensional structure of the lamellar turbostratic V₂O₅.nH(2)O xerogel was determined by the atomic pair distribution function technique. We show that on the atomic scale the slabs of the xerogel can be described well as almost perfect pairs (i.e., bilayers) of single V₂O₅ layers made of square pyramidal VO₅ units. These slabs are separated by water molecules and stack along the z-axis of a monoclinic unit cell (space group C2/m) with parameters a = 11.722(3) Angstrom, b = 3.570(3) Angstrom, c = 11.520(3) Angstrom, and beta = 88.65degrees. The stacking sequence shows signatures of turbostratic disorder and a structural coherence limited to 50 Angstrom.

Accession Number: WOS:000177576000042

PubMed ID: 12188680

Language: English

Document Type: Article

KeyWords Plus: HYDRATED VANADIUM-OXIDES; LOCAL-STRUCTURE; CONDUCTIVE POLYMER; LAYERED STRUCTURES; NANOCOMPOSITES; PROGRAM; REFINEMENT; BRONZES

Addresses: Michigan State Univ, Dept Chem, E Lansing, MI 48824 USA.

Michigan State Univ, Dept Phys & Astron, E Lansing, MI 48824 USA.

Michigan State Univ, Ctr Fundamental Mat Res, E Lansing, MI 48824 USA.

Brookhaven Natl Lab, Dept Phys, Upton, NY 11973 USA.

Corresponding Address: Kanatzidis, MG (corresponding author), Michigan State Univ, Dept Chem, E Lansing, MI 48824 USA.

E-mail Addresses: kanatzid@cem.msu.edu

Affiliations: Michigan State University; Michigan State University; Michigan State University; United States Department of Energy (DOE); Brookhaven National Laboratory

Author Identifiers:

Author	Web of Science ResearcherID	ORCID Number
Trikalitis, Pantelis N	E-5696-2011	
Bozin, Emil	AAB-4551-2020	
Vogt, Thomas	A-1562-2011	0000-0002-4731-2787
Bozin, Emil	E-4679-2011	
Trikalitis, Pantelis		0000-0002-6286-2955

Publisher: AMER CHEMICAL SOC

Publisher Address: 1155 16TH ST, NW, WASHINGTON, DC 20036 USA

Web of Science Index: Science Citation Index Expanded (SCI-EXPANDED)

Web of Science Categories: Chemistry, Multidisciplinary

Research Areas: Chemistry

IDS Number: 586GJ

ISSN: 0002-7863

eISSN: 1520-5126

29-char Source Abbrev.: J AM CHEM SOC

ISO Source Abbrev.: J. Am. Chem. Soc.

Source Item Page Count: 6

Output Date: 2023-01-27

Record 119 of 125

Title: Local structure as a probe of stripes and its relation to T*

Author(s): Billinge, SJL (Billinge, SJL); Gutmann, M (Gutmann, M); Bozin, ES (Bozin, ES)

Source: PHYSICA C **Volume:** 341 **Pages:** 1795-1796 **DOI:** 10.1016/S0921-4534(00)01077-7 **Part:** 3 **Published:** NOV 2000

Times Cited in Web of Science Core Collection: 0

Total Times Cited: 0

Usage Count (Last 180 days): 0

Usage Count (Since 2013): 1

Cited Reference Count: 13

Abstract: We describe atomic pair distribution function (PDF) analysis measurements of the local structure from a range of HTS materials. These are analyzed to search for the presence of, and characterize the nature of, fluctuating stripe phases in the bulk of superconducting HTS samples. We find evidence for the presence of local stripe phases in La_{2-x}Sr_xCuO₄ and YBa₂Cu₃O_{6+δ}. At least in the 214 system of cuprates, we have evidence of a correlation between local charge inhomogeneities and T*, the pseudo-gap closing temperature.

Accession Number: WOS:000165855900140

Language: English

Document Type: Article; Proceedings Paper

Conference Title: International Conference on Materials and Mechanisms of Superconductivity High Temperature Superconductors VI

Conference Date: FEB 20-25, 2000

Conference Location: HOUSTON, TEXAS

KeyWords Plus: LA2-XSRXCUO4; TEMPERATURE; SUPERCONDUCTORS

Addresses: Michigan State Univ, Dept Phys & Astron, E Lansing, MI 48824 USA.

Michigan State Univ, Ctr Fundamental Mat Res, E Lansing, MI 48824 USA.

Corresponding Address: Billinge, SJL (corresponding author), Michigan State Univ, Dept Phys & Astron, E Lansing, MI 48824 USA.

Affiliations: Michigan State University; Michigan State University

Author Identifiers:

Author	Web of Science ResearcherID	ORCID Number
Bozin, Emil	E-4679-2011	
Bozin, Emil	AAB-4551-2020	

Publisher: ELSEVIER SCIENCE BV

Publisher Address: PO BOX 211, 1000 AE AMSTERDAM, NETHERLANDS

Web of Science Index: Conference Proceedings Citation Index - Science (CPCI-S); Science Citation Index Expanded (SCI-EXPANDED)

Web of Science Categories: Physics, Applied; Physics, Condensed Matter

Research Areas: Physics

IDS Number: 382YX

ISSN: 0921-4534

29-char Source Abbrev.: PHYSICA C

ISO Source Abbrev.: Physica C

Source Item Page Count: 2

Output Date: 2023-01-27

Record 120 of 125

Title: Local structural evidence for inhomogeneous charge distribution in CuO₂ planes of superconducting La_{2-x}ST_xCuO₄

Author(s): Bozin, ES (Bozin, ES); Billinge, SJL (Billinge, SJL); Kwei, GH (Kwei, GH); Takagi, H (Takagi, H)

Source: PHYSICA C **Volume:** 341 **Pages:** 1793-1794 **DOI:** 10.1016/S0921-4534(00)01074-1 **Part:**

3 **Published:** NOV 2000

Times Cited in Web of Science Core Collection: 7

Total Times Cited: 7

Usage Count (Last 180 days): 0

Usage Count (Since 2013): 0

Cited Reference Count: 4

Abstract: Local structural evidence is found supporting the presence of charge inhomogeneities in the CuO₂ planes of underdoped La_{2-x}Sr_xCuO₄, using high-resolution PDF analysis of neutron powder diffraction data. Broadening of the in-plane Cu-O bond distribution as a function of doping up to optimal doping is observed. Thereafter the peak abruptly sharpens. The result suggests a crossover from a charge inhomogeneous state below optimal doping to a homogeneous charge state above optimal doping.

Accession Number: WOS:000165855900139

Language: English

Document Type: Article; Proceedings Paper

Conference Title: International Conference on Materials and Mechanisms of Superconductivity High Temperature Superconductors VI

Conference Date: FEB 20-25, 2000

Conference Location: HOUSTON, TEXAS

Addresses: Michigan State Univ, Dept Phys & Astron, E Lansing, MI 48824 USA.

Michigan State Univ, Ctr Fundamental Mat Res, E Lansing, MI 48824 USA.

Univ Calif Los Alamos Natl Lab, Los Alamos, NM 87545 USA.

Univ Tokyo, Inst Solid State Phys, Minato Ku, Tokyo 106, Japan.

Corresponding Address: Bozin, ES (corresponding author), Michigan State Univ, Dept Phys & Astron, E Lansing, MI 48824 USA.

Affiliations: Michigan State University; Michigan State University; United States Department of Energy (DOE); Los Alamos National Laboratory; University of Tokyo

Author Identifiers:

Author	Web of Science ResearcherID	ORCID Number
Takagi, Hidenori	B-2935-2010	
Bozin, Emil	AAB-4551-2020	
Bozin, Emil	E-4679-2011	
TAKAGI, HIDENORI	Q-1041-2019	0000-0001-5700-3761

Publisher: ELSEVIER SCIENCE BV

Publisher Address: PO BOX 211, 1000 AE AMSTERDAM, NETHERLANDS

Web of Science Index: Conference Proceedings Citation Index - Science (CPCI-S); Science Citation Index Expanded (SCI-EXPANDED)

Web of Science Categories: Physics, Applied; Physics, Condensed Matter

Research Areas: Physics

IDS Number: 382YX

ISSN: 0921-4534

29-char Source Abbrev.: PHYSICA C

ISO Source Abbrev.: Physica C

Source Item Page Count: 2

Output Date: 2023-01-27

Record 121 of 125

Title: Microscopic charge inhomogeneities in underdoped La_{2-x}Sr_xCuO₄: Local structural evidence underdoped

Author(s): Billinge, SJL (Billinge, SJL); Bozin, ES (Bozin, ES); Gutmann, M (Gutmann, M); Takagi, H (Takagi, H)

Source: JOURNAL OF SUPERCONDUCTIVITY **Volume:** 13 **Issue:** 5 **Pages:** 713-722 **DOI:** 10.1023/A:1007801928742 **Published:** OCT 2000

Times Cited in Web of Science Core Collection: 13

Total Times Cited: 13

Usage Count (Last 180 days): 0

Usage Count (Since 2013): 0

Cited Reference Count: 47

Abstract: We present local structural evidence for the existence of charge inhomogeneities at low temperature in underdoped and optimally doped $\text{La}_{2-x}\text{Sr}_x\text{CuO}_4$. The inhomogeneities disappear for x greater than or equal to 0.2. The evidence for the charge inhomogeneities comes from an anomalous increase in the inplane Cu-O bond length distribution in the underdoped samples as well as evidence for CuO₆ octahedral tilt inhomogeneities in the intermediate range structure. Preliminary analysis of the temperature dependence of this phenomenon indicates that the inhomogeneities set in at temperatures in the range $60 \text{ K} < T < \infty < 130 \text{ K}$, which depends on doping.

Accession Number: WOS:000165458900010

Language: English

Document Type: Article; Proceedings Paper

Conference Title: International Conference on Major Trends in Superconductivity in the New Millennium

Conference Date: MAR 31-APR 06, 2000

Conference Location: KLOSTERS, SWITZERLAND

Author Keywords: charge inhomogeneities; underdoped $\text{La}_{2-x}\text{Sr}_x\text{CuO}_4$; local structure

KeyWords Plus: HIGH-TEMPERATURE SUPERCONDUCTORS; COPPER-OXIDE SUPERCONDUCTORS; ABSORPTION FINE-STRUCTURE; ATOMIC-SCALE STRUCTURE; T-C SUPERCONDUCTIVITY; X-RAY; LATTICE-DISTORTIONS; NEUTRON-SCATTERING; OCTAHEDRAL TILTS; STRIPED PHASE

Addresses: Michigan State Univ, Dept Phys & Astron, E Lansing, MI 48824 USA.

Michigan State Univ, Ctr Fundamental Mat Res, E Lansing, MI 48824 USA.

Univ Tokyo, Inst Solid State Phys, Minato Ku, Tokyo 106, Japan.

Corresponding Address: Billinge, SJL (corresponding author), Michigan State Univ, Dept Phys & Astron, E Lansing, MI 48824 USA.

Affiliations: Michigan State University; Michigan State University; University of Tokyo

Author Identifiers:

Author	Web of Science ResearcherID	ORCID Number
TAKAGI, HIDENORI	Q-1041-2019	0000-0001-5700-3761
Bozin, Emil	AAB-4551-2020	
Bozin, Emil	E-4679-2011	
Takagi, Hidenori	B-2935-2010	

Publisher: KLUWER ACADEMIC/PLENUM PUBL

Publisher Address: 233 SPRING ST, NEW YORK, NY 10013 USA

Web of Science Index: Conference Proceedings Citation Index - Science (CPCI-S); Science Citation Index Expanded (SCI-EXPANDED)

Web of Science Categories: Physics, Applied; Physics, Condensed Matter

Research Areas: Physics

IDS Number: 376LK

ISSN: 0896-1107

29-char Source Abbrev.: J SUPERCOND

ISO Source Abbrev.: J. Supercond.

Source Item Page Count: 10

Output Date: 2023-01-27

Record 122 of 125

Title: Neutron diffraction evidence of microscopic charge inhomogeneities in the CuO(2) plane of superconducting $\text{La}_{2-x}\text{Sr}_x\text{CuO}_4$ ($0 \leq x \leq 0.30$)

Author(s): Bozin, ES (Bozin, ES); Kwei, GH (Kwei, GH); Takagi, H (Takagi, H); Billinge, SJL (Billinge, SJL)

Source: PHYSICAL REVIEW LETTERS **Volume:** 84 **Issue:** 25 **Pages:** 5856-5859 **DOI:** 10.1103/PhysRevLett.84.5856 **Published:** JUN 19 2000

Times Cited in Web of Science Core Collection: 152

Total Times Cited: 153

Usage Count (Last 180 days): 0

Usage Count (Since 2013): 15

Cited Reference Count: 21

Abstract: High-resolution atomic pair distribution functions have been obtained using neutron powder diffraction data from $\text{La}(2-x)\text{Sr}(x)\text{CuO}(4)$ over the range of doping $0 \leq x \leq 0.30$ at 10 K. Despite the average structure getting less orthorhombic, we see a broadening of the in-plane Cu-O bond distribution as a function of doping up to optimal doping. Thereafter the peak abruptly sharpens. The peak broadening can be well explained by a local microscopic coexistence of doped and undoped material. This suggests a crossover from a charge inhomogeneous state at and below optimal doping to a homogeneous charge state above optimal doping.

Accession Number: WOS:000087653300042

PubMed ID: 10991072

Language: English

Document Type: Article

KeyWords Plus: HIGH-TEMPERATURE SUPERCONDUCTORS; C SUPERCONDUCTIVITY

Addresses: Michigan State Univ, Dept Phys & Astron, E Lansing, MI 48824 USA.

Michigan State Univ, Ctr Fundamental Mat Res, E Lansing, MI 48824 USA.

Los Alamos Natl Lab, Los Alamos, NM 87545 USA.

Univ Tokyo, Dept Adv Mat Sci, Bunkyo Ku, Tokyo 1138656, Japan.

Corresponding Address: Bozin, ES (corresponding author), Michigan State Univ, Dept Phys & Astron, E Lansing, MI 48824 USA.

Affiliations: Michigan State University; Michigan State University; United States Department of Energy (DOE); Los Alamos National Laboratory; University of Tokyo

Author Identifiers:

Author	Web of Science ResearcherID	ORCID Number
Bozin, Emil	AAB-4551-2020	
Bozin, Emil	E-4679-2011	
Takagi, Hidenori	B-2935-2010	
TAKAGI, HIDENORI	Q-1041-2019	0000-0001-5700-3761

Publisher: AMER PHYSICAL SOC

Publisher Address: ONE PHYSICS ELLIPSE, COLLEGE PK, MD 20740-3844 USA

Web of Science Index: Science Citation Index Expanded (SCI-EXPANDED)

Web of Science Categories: Physics, Multidisciplinary

Research Areas: Physics

IDS Number: 325AC

ISSN: 0031-9007

29-char Source Abbrev.: PHYS REV LETT

ISO Source Abbrev.: Phys. Rev. Lett.

Source Item Page Count: 4

Open Access: Green Submitted

Output Date: 2023-01-27

Title: Charge-stripe ordering from local octahedral tilts: Underdoped and superconducting La_{2-x}Sr_xCuO₄ (0 ≤ x ≤ 0.30)

Author(s): Bozin, ES (Bozin, ES); Billinge, SJL (Billinge, SJL); Kwei, GH (Kwei, GH); Takagi, H (Takagi, H)

Source: PHYSICAL REVIEW B **Volume:** 59 **Issue:** 6 **Pages:** 4445-4454 **DOI:** 10.1103/PhysRevB.59.4445 **Published:** FEB 1 1999

Times Cited in Web of Science Core Collection: 119

Total Times Cited: 119

Usage Count (Last 180 days): 0

Usage Count (Since 2013): 15

Cited Reference Count: 55

Abstract: The local structure of La_{2-x}Sr_xCuO₄, for 0 less than or equal to x less than or equal to 0.30, has been investigated using the atomic pair distribution function (PDF) analysis of neutron powder-diffraction data. The local octahedral tilts are studied to look for evidence of [110] symmetry [i.e., low-temperature tetragonal (LTT) symmetry] tilts locally, even though the average tilts have [010] symmetry [i.e., low-temperature orthorhombic (LTO) symmetry] in these compounds. We argue that this observation would suggest the presence of local charge-stripe order. We show that the tilts are locally LTO in the undoped phase, in agreement with the average crystal structure. At nonzero doping the PDF data are consistent with the presence of local tilt disorder in the form of a mixture of LTO and LTT local tilt directions and a distribution of local tilt magnitudes. We present topological tilt models which qualitatively explain the origin of tilt disorder in the presence of charge stripes and show that the PDF data are well explained by such a mixture of locally small and large amplitude tilts.

Accession Number: WOS:000078699400068

Language: English

Document Type: Article

KeyWords Plus: HIGH-TEMPERATURE SUPERCONDUCTORS; EARTH-DOPED LA2-XSRXCuO4; T-C SUPERCONDUCTIVITY; PHASE-TRANSITIONS; LA2-XBAXCuO4; DIFFRACTION; HOLES; SPINS; LA1-XCAXMNO3; SCATTERING

Addresses: Michigan State Univ, Dept Phys & Astron, E Lansing, MI 48824 USA.

Michigan State Univ, Ctr Fundamental Mat Res, E Lansing, MI 48824 USA.

Los Alamos Natl Lab, Los Alamos, NM 87545 USA.

Univ Tokyo, Inst Solid State Phys, Minato Ku, Tokyo 106, Japan.

Corresponding Address: Bozin, ES (corresponding author), Michigan State Univ, Dept Phys & Astron, E Lansing, MI 48824 USA.

Affiliations: Michigan State University; Michigan State University; United States Department of Energy (DOE); Los Alamos National Laboratory; University of Tokyo

Author Identifiers:

Author	Web of Science ResearcherID	ORCID Number
Bozin, Emil	E-4679-2011	
TAKAGI, HIDENORI	Q-1041-2019	0000-0001-5700-3761
Takagi, Hidenori	B-2935-2010	
Bozin, Emil	AAB-4551-2020	

Publisher: AMER PHYSICAL SOC

Publisher Address: ONE PHYSICS ELLIPSE, COLLEGE PK, MD 20740-3844 USA

Web of Science Index: Science Citation Index Expanded (SCI-EXPANDED)

Web of Science Categories: Materials Science, Multidisciplinary; Physics, Applied; Physics, Condensed Matter

Research Areas: Materials Science; Physics

IDS Number: 168NP

ISSN: 2469-9950

eISSN: 2469-9969

29-char Source Abbrev.: PHYS REV B

ISO Source Abbrev.: Phys. Rev. B

Source Item Page Count: 10

Open Access: Green Submitted

Output Date: 2023-01-27

Record 124 of 125

Title: Understanding the role of the local structure in the second order structural phase transition of $\text{La}(2-x)\text{A}(x)\text{CuO}(4)$ ($\text{A} = \text{Ba}, \text{Sr}$)

Author(s): Bozin, ES (Bozin, ES); Billinge, SJL (Billinge, SJL); Kwei, GH (Kwei, GH)

Source: SOLID STATE PHENOMENA **Volume:** 61-2 **Pages:** 271-274 **Published:** 1998

Times Cited in Web of Science Core Collection: 1

Total Times Cited: 1

Usage Count (Last 180 days): 1

Usage Count (Since 2013): 2

Cited Reference Count: 14

Abstract: We have studied the local atomic structure of $\text{La}(2-x)\text{A}(x)\text{CuO}(4)$ ($\text{A} = \text{Ba}, \text{Sr}$) through the high-temperature tetragonal (HTT) to low temperature orthorhombic (LTO) structural phase transition using the atomic pair distribution function technique. Although long-range ordered tilts disappear in the average structure, we show that significant local tilts persist. We propose an order-disorder model which reconciles both the local and long-range structural observations.

Accession Number: WOS:000075589100052

Language: English

Document Type: Article

Author Keywords: local structure; structural phase transition; pair distribution function; neutron powder diffraction; high temperature superconductors

KeyWords Plus: NEUTRON-POWDER-DIFFRACTION; SUPERCONDUCTIVITY; LA2-XBAXCUO4; LA2-XSRXCUO4

Addresses: Michigan State Univ, Dept Phys & Astron, E Lansing, MI 48824 USA.

Michigan State Univ, Ctr Fundamental Mat Res, E Lansing, MI 48824 USA.

Univ Calif Los Alamos Natl Lab, Los Alamos, NM 87545 USA.

Corresponding Address: Bozin, ES (corresponding author), Michigan State Univ, Dept Phys & Astron, E Lansing, MI 48824 USA.

Affiliations: Michigan State University; Michigan State University; United States Department of Energy (DOE); Los Alamos National Laboratory

Author Identifiers:

Author	Web of Science ResearcherID	ORCID Number
Bozin, Emil	E-4679-2011	
Bozin, Emil	AAB-4551-2020	

Publisher: TRANS TECH-SCITEC PUBLICATIONS LTD

Publisher Address: BRANDRAIN 6, CH-8707 UETIKON A.S., SWITZERLAND

Web of Science Index: Science Citation Index Expanded (SCI-EXPANDED)

Web of Science Categories: Materials Science, Multidisciplinary; Physics, Applied; Physics, Condensed Matter

Research Areas: Materials Science; Physics

IDS Number: 114BK

ISSN: 1012-0394

29-char Source Abbrev.: SOLID STATE PHENOM

ISO Source Abbrev.: Solid State Phenom.

Source Item Page Count: 4

Output Date: 2023-01-27

Record 125 of 125

Title: Re-examination of the second-order structural phase transition in $\text{La}(2-x)\text{A}(x)\text{CuO}(4)$ ($\text{A} = \text{Ba}, \text{Sr}$)

Author(s): Bozin, ES (Bozin, ES); Billinge, SJL (Billinge, SJL); Kwei, GH (Kwei, GH)

Source: PHYSICA B **Volume:** 241 **Pages:** 795-797 **DOI:** 10.1016/S0921-4526(97)00720-5 **Published:** DEC 1997

Times Cited in Web of Science Core Collection: 10

Total Times Cited: 10

Usage Count (Last 180 days): 1

Usage Count (Since 2013): 5

Cited Reference Count: 8

Abstract: In the high temperature tetragonal phase of $\text{La}_{1.85}\text{Ba}_{0.15}\text{CuO}_4$ (LBCO) and $\text{La}_{1.875}\text{Sr}_{0.125}\text{CuO}_4$ (LSCO), the average octahedral tilts disappear at high temperature. However, we show that, locally, tilts remain at temperatures well above the orthorhombic to tetragonal phase transition. We have used full profile refinement of the real-space atomic pair distribution function (PDF) obtained from pulsed neutron powder diffraction measurements. Our modeling indicates that order-disorder models of the octahedral tilts give significantly better agreement with the data than displacive models. (C) 1998 Published by Elsevier Science B.V. All rights reserved.

Accession Number: WOS:000074062600231

Language: English

Document Type: Article; Proceedings Paper

Conference Title: International Conference on Neutron Scattering

Conference Date: AUG 17-21, 1997

Conference Location: TORONTO, CANADA

Author Keywords: local structure; pair distribution function analysis; structural phase transition; high temperature superconductors

KeyWords Plus: NEUTRON-POWDER-DIFFRACTION

Addresses: Michigan State Univ, Dept Phys & Astron, E Lansing, MI 48824 USA.

Michigan State Univ, Ctr Fundamental Mat Res, E Lansing, MI 48824 USA.

Univ Calif Los Alamos Natl Lab, Los Alamos, NM 87545 USA.

Corresponding Address: Bozin, ES (corresponding author), Michigan State Univ, Dept Phys & Astron, E Lansing, MI 48824 USA.

Affiliations: Michigan State University; Michigan State University; United States Department of Energy (DOE); Los Alamos National Laboratory

Author Identifiers:

Author	Web of Science ResearcherID	ORCID Number
Bozin, Emil	E-4679-2011	
Bozin, Emil	AAB-4551-2020	

Publisher: ELSEVIER SCIENCE BV

Publisher Address: PO BOX 211, 1000 AE AMSTERDAM, NETHERLANDS

Web of Science Index: Conference Proceedings Citation Index - Science (CPCI-S); Science Citation Index Expanded (SCI-EXPANDED)

Web of Science Categories: Physics, Condensed Matter

Research Areas: Physics

IDS Number: ZT224

ISSN: 0921-4526

29-char Source Abbrev.: PHYSICA B

ISO Source Abbrev.: Physica B

Source Item Page Count: 3

Output Date: 2023-01-27

End of File

PDFfit2 and PDFgui: computer programs for studying nanostructure in crystals

To cite this article: C L Farrow *et al* 2007 *J. Phys.: Condens. Matter* **19** 335219

View the [article online](#) for updates and enhancements.

You may also like

- [Review of Particle Physics](#)
K.A. Olive
- [Electrochemical Study and Material Characterization of \$x\text{SiO}_2\(1-x\)\text{Sn}_3\text{Co}_3\text{C}_{40}\$ Composite Anode Material for Lithium-Ion Batteries](#)
Bo Liu, Ali Abouimrane, Yang Ren et al.
- [PDF4LHC recommendations for LHC Run II](#)
Jon Butterworth, Stefano Carrazza, Amanda Cooper-Sarkar et al.

PDFfit2 and PDFgui: computer programs for studying nanostructure in crystals

C L Farrow¹, P Juhas¹, J W Liu¹, D Bryndin^{1,4}, E S Božin¹, J Bloch²,
Th Proffen³ and S J L Billinge¹

¹ Department of Physics and Astronomy, Michigan State University, East Lansing,
MI 48824-2320, USA

² Institute for Theoretical Physics, University of Regensburg, 93040 Regensburg, Germany

³ Lujan Neutron Scattering Center, Los Alamos National Laboratory, Los Alamos,
NM 87545, USA

⁴ Department of Computer Science and Engineering, Michigan State University, East Lansing,
MI 48824, USA

E-mail: billinge@pa.msu.edu

Received 29 March 2007

Published 4 July 2007

Online at stacks.iop.org/JPhysCM/19/335219

Abstract

PDFfit2 is a program as well as a library for real-space refinement of crystal structures. It is capable of fitting a theoretical three-dimensional (3D) structure to atomic pair distribution function data and is ideal for nanoscale investigations. The fit system accounts for lattice constants, atomic positions and anisotropic atomic displacement parameters, correlated atomic motion, and experimental factors that may affect the data. The atomic positions and thermal coefficients can be constrained to follow the symmetry requirements of an arbitrary space group. The PDFfit2 engine is written in C++ and is accessible via Python, allowing it to inter-operate with other Python programs. PDFgui is a graphical interface built on the PDFfit2 engine. PDFgui organizes fits and simplifies many data analysis tasks, such as configuring and plotting multiple fits. PDFfit2 and PDFgui are freely available via the Internet.

(Some figures in this article are in colour only in the electronic version)

1. Introduction

Increasingly materials scientists and chemists are interested in complex materials which have structure on the nanometre length-scale. Examples are discrete nanoparticles [1], crystals with embedded nanoscale structures [2–4], and nanoporous materials with molecules or nanoparticles intercalated inside the pores [5, 6]. It is difficult to study structure on the nanoscale quantitatively using diffraction methods, because the diffraction gives no sharp Bragg peaks but only broad diffuse features in the scattering. Total scattering, in which both Bragg and diffuse components of the scattering are analysed together, is growing in popularity

for the study of this kind of problem [2, 7]. One approach to analysing the data is to use reverse Monte Carlo [8], the subject of this journal supplement. An alternative approach is to Fourier transform the data to real space to obtain the atomic pair distribution function (PDF) and analyse the data directly in real space [9].

A popular approach for this is to use the profile fitting refinement program PDFfit [10, 11]. This approach assumes that the structure can be described by a relatively small number of atoms in a unit cell, which may be the crystallographic unit cell or it may be a supercell to accommodate symmetry lowering local distortions. The refined parameters are in direct analogy with those determined crystallographically: lattice parameters and unit cell angles, atomic fractional coordinates and anisotropic atomic displacement parameters (ADPs); however, they correspond to the relevant values in the *local* structure. This allows direct comparison between the local structure in a distorted crystal and the average structure determined from the Bragg peaks alone. In the absence of local disorder, the values determined crystallographically and those determined from total scattering studies will be the same. This is not the case in the interesting materials, where the local structure disagrees with the average structure [2, 7, 12]. Here we report a significant redesign and modification of the successful software program PDFfit [13], including a new user-friendly graphical user interface (GUI) with labour-saving data and structure plotting capabilities.

1.1. PDF technique

The pair distribution function method was originally developed to study the structure of materials with no long-range order, such as liquids and glasses [14]. The technique is now increasingly applied for investigations of disorder in crystalline materials and for studies of nanomaterials [2]. It is complementary to traditional crystallographic analysis, which assumes a perfect periodic material and considers only intensities from Bragg reflections. The PDF method does not require periodic order in the sample—instead it uses the whole measured spectrum, including Bragg and diffuse components, to extract the total scattering structure function, $S(Q)$, which contains coherent scattering intensities from the material [9].

The experimental atomic pair distribution function, $G(r)$, is obtained by Fourier transformation of $S(Q)$,

$$G(r) = \frac{2}{\pi} \int_0^{\infty} Q[S(Q) - 1] \sin(Qr) dQ, \quad (1)$$

where Q is the magnitude of the scattering vector. For elastic scattering, $Q = 4\pi \sin(\theta)/\lambda$, with 2θ being the scattering angle and λ the wavelength of the measured radiation. The $G(r)$ function is related to the atomic structure through the relation,

$$G(r) = 4\pi r [\rho(r) - \rho_0], \quad (2)$$

where ρ_0 is the atomic number density of the material and $\rho(r)$ is the atomic pair density which gives the mean weighted density of neighbour atoms at radial distance r from an atom at the origin. Thus,

$$\rho(r) = \frac{1}{4\pi r^2 N} \sum_i \sum_{j \neq i} \frac{b_i b_j}{\langle b \rangle^2} \delta(r - r_{ij}), \quad (3)$$

where the indices i and j go over all N atoms in the sample, b_i is the scattering factor of atom i , $\langle b \rangle$ is the average scattering factor, and r_{ij} is the distance between atoms i and j . Full details on the determination of an experimental PDF can be found elsewhere [9].

For a known structure model, the experimental PDF can be calculated using

$$G_{\text{calc}}(r) = \frac{1}{Nr} \sum_i \sum_{j \neq i} \left[\frac{b_i b_j}{\langle b \rangle^2} \delta(r - r_{ij}) \right] - 4\pi r \rho_0. \quad (4)$$

There are many methods of extracting structural information from measured PDFs. These range from the simple analysis of peak positions, widths and intensities to extract bonding information directly [9, 15, 16], reverse Monte Carlo analysis of large structure models [17, 18], and emerging *ab initio* structure solution methods [19], to the common down-hill least-square refinement as implemented in the PDFfit program [10, 11], and PDFfit2 described here.

2. PDFfit2

PDFfit2 is a major upgrade to PDFfit [10], and inherits many of its features. PDFfit is capable of fitting a theoretical three-dimensional structure to an experimentally determined PDF. It can simultaneously fit multiple structures, accounting for different structural phases in a material. PDFfit has a constraint system that allows the expression of structure variables as simple functions of fitted parameters. PDFfit structure variables include lattice constants, data and phase scale factors, atomic site occupation, anisotropic ADPs, and atomic vibrational correlations. PDFfit has a built-in FORTRAN-style command language that understands simple `for` loops and some built-in arithmetic functions.

The original PDFfit was written in FORTRAN-77, which imposes some limitations on the program. For example, it uses fixed-size arrays for internal storage. This precludes the analysis of structures with large cells without modifying the code. Though the constraint system is powerful, it requires that a constraint equation be accompanied by its first derivative. This places the burden of determining the derivatives on the user, which can introduce errors that lead to instability in the convergence. Furthermore, the code is monolithic, not easily extensible, and hard to integrate with external programs.

The primary focus of PDFfit2 development was to remedy the limitations of PDFfit while extending its functionality. The old PDFfit engine has been completely rewritten in C++, and many bugs have been fixed. The new engine uses dynamic memory allocation so that the size of the structure or extent of the fit-range of the PDF is limited only by the physical memory available. The constraint system has also been upgraded. The program *automatically* computes the analytical derivatives of the constraints that are required by the minimization routine. This simplifies user input and reduces the possibility of errors. In addition, new fitting parameters for handling dynamic atomic correlations and experimental resolution have been introduced as well.

Instead of rewriting the PDFfit command interpreter, which is used to define the fitting problem and to control and run the refinement, its functions are carried out using the Python language⁴. Python is a powerful, cross-platform, open-source interpreted programming language (i.e. it does not need to be compiled to run, similar to scripting) that emphasizes object-oriented and modular design. PDFfit2 scripts written in Python syntax take the place of PDFfit macros, and the Python interpreter can handle everything that the old interpreter could and more. Using Python as an interpreter allows PDFfit2 to be combined with and enhanced by other Python libraries. We make use of this capability with PDFgui as described below.

3. PDFgui

The PDFfit2 engine can be used either directly from the Python command line or as part of larger and more complex software applications. The first application built on PDFfit2 is PDFgui, a graphical environment for PDF fitting.

⁴ Python Software Foundation.

3.1. Design principles

PDFgui has been designed to provide users with an easy-to-use yet powerful interface for fitting structure models to PDF data. It makes use of an object-oriented, component-based architecture, which makes it highly extensible and maintainable. This allows for powerful usability features such as real-time plotting and remote execution of the fitting program whilst visualizing the results locally. PDFgui has been designed with multi-tasking in mind. It is multi-threaded, so that the work being done by the PDFfit2 engine does not interfere with the tasks of the user interface.

PDFgui is written in the Python programming language. Python features a relaxed and friendly syntax, supports ‘write once, run anywhere’ portability, and has extensive libraries and modules for virtually every task. Software codes written in a variety of programming languages can be bound into Python, which allows them to be used together. Python is becoming a popular choice in the scientific computation community.

PDFgui’s interface is built using wxPython [20], the Python package for wxWidgets, which is a mature cross-platform GUI library. Graphical applications written in wxPython provide a look and feel native to the platform on which they are run. PDFgui is designed to run on Windows, Mac OS, Linux, and all major Unix systems.

3.2. Capabilities

PDFgui contains all of the functionality of PDFfit2 along with additional enhancements for usability. Mundane tasks are handled by the program and difficult tasks are made simple. PDFgui can manage multiple fits at once. Each fit can have multiple experimental data sets and structure models. Fits in a sequence can call upon other fits for their starting parameters, and configured fits can be queued to run while the user is away. All the initial, final, and intermediate data are stored in a platform-independent project file that can be loaded on any computer. All management tasks, such as fit creation, configuration, modification, and visualization, can be done through the graphical interface.

PDFgui supports space group operations. Users can define an asymmetric unit and let PDFgui expand it to a full cell with all symmetry-related positions. PDFgui can also generate symmetry constraints for atom positions and anisotropic ADPs. Users just need to specify the space group, and the program will identify equivalent sites and generate constraint equations for their coordinates and temperature factors to keep the structure consistent with the symmetry requirements. This can be done either for all atoms in the structure or for an arbitrary subset—for example, when it is known that only a certain species shows a local distortion. The code for space group definitions was provided by the Python Macromolecular Library (mmLib) [21]. PDFgui also supports supercell expansion of a normal unit cell.

PDFgui uses the matplotlib [22] Python package for two-dimensional (2D) plotting of data and results. Matplotlib has a friendly interface, so the user can quickly and easily view the results of a fitting. PDFgui lets users plot data from a series of fits and plot it against selected metadata (temperature, doping, etc), plot the results of several fits in the same window, plot the PDF in real time as the fitting is running, plot the parameters or variables in real time as the refinement evolves, and save plots in common image formats or export the data to a text file. PDFgui uses AtomEye [23] for 3D visualization. The modular nature of PDFgui allows for other alternatives in the future, such as PyMOL [24].

PDFgui supports built-in macros for advanced fits. For example, for a set of experimental data from one system at different temperatures or doping levels, PDFgui can expand a template fit to a series of related fits. Another PDFgui macro makes it easy to set up boxcar fits, where the same model is fitted over different r -ranges of the PDF data.

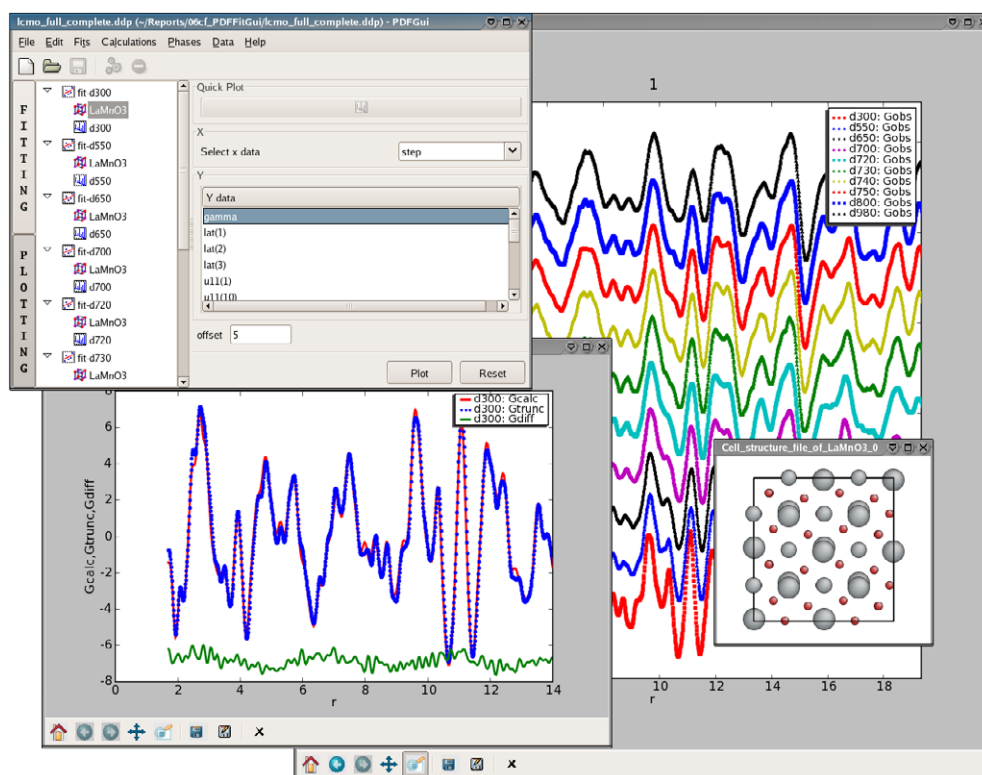


Figure 1. The PDFgui plot window, plots of the LaMnO₃ PDF fit at 300 K and the data at all temperatures, and the refined structure at 300 K.

3.3. Example

The capabilities of PDFgui are demonstrated here on an example fitting of a temperature series of neutron PDF data from LaMnO₃. The specifics of using PDFgui and PDFfit2 are detailed in the respective user manuals, available with the code.

LaMnO₃ has a perovskite structure consisting of corner-shared MnO₆ octahedral units [25, 26]. At room temperature this material takes on orthorhombic symmetry (space group *Pbnm*) where the Jahn–Teller (JT) distorted MnO₆ octahedra contain four short and two long Mn–O bonds and the JT long-bonds are ordered in space in a checker-board fashion [13]. As temperature is increased through 750 K, a structural phase transition occurs to a pseudo-cubic phase, without a change in space group [27]. Using neutron powder diffraction data collected at the NPDF diffractometer [28] at the Lujan Center at Los Alamos National Laboratory, PDFgui was used to create a temperature series fit to investigate the orthorhombic to pseudo-cubic phase transition. More detail about this analysis can be found in [29] and [30]. The average crystallographic structure for LaMnO₃ was used as a starting point for the fits. In practice, this can be done by typing in the asymmetric unit, or loading it from a CIF-format file and letting the program expand it.

Each fit in the series was part of the same project and configured identically. The La and Mn atoms were constrained to have isotropic thermal factors, as were the axial and polar oxygen atoms. Using the PDFfit2 constraint mechanism allows one to include explicitly known

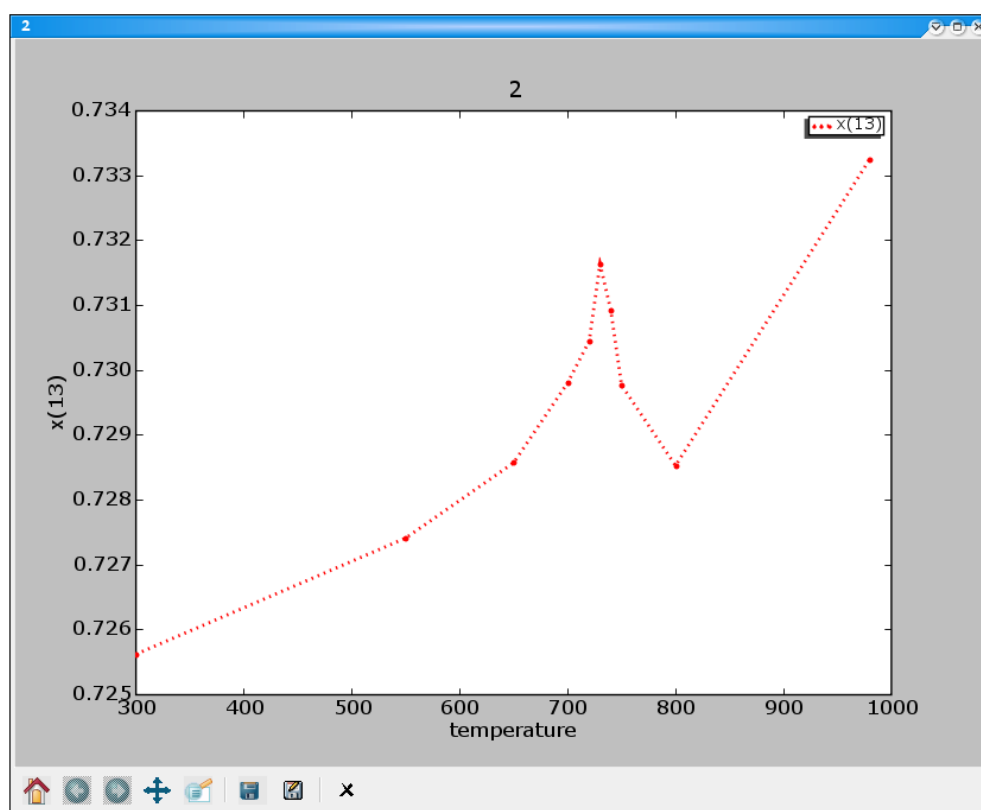


Figure 2. The full PDFgui plot window showing the fractional x -coordinate of an axial oxygen versus temperature.

correlations between the physical parameters of the fit and leads to less uncertainty in the resulting refinement. To speed up the convergence of the fits, the starting values used for a given temperature were taken from the converged values of the previous temperature in the series. Chaining fits together in such a way places the fitting parameters in the basin of attraction for the minimum in the parameter space. Figure 1 shows the fit organization and plot interface of PDFgui, a stacked plot of all of the project data, a plot of the 300 K fit results, and the refined structure from the 300 K fit.

One of the goals of this series of fits was to track the orientation of the MnO_6 octahedra. A major strength of PDFgui is the ability to plot any structure variable or a parameter used in a fit. This allows users to easily and creatively investigate the complex correlations among the fit parameters, without having to manually mine data out of output files. An example of this can be seen in figure 2. The figure shows a screen shot of a PDFgui plot window displaying the refined fractional x -coordinate of one of the planar oxygens. The expected structural phase transition is clearly indicated by a spike in the value of this parameter at the transition temperature.

4. Availability

PDFfit2 and PDFgui are open source and distributed under a BSD license. They run on Windows, Linux, and all major Unix systems. The source code is freely available. For more

information, please contact professor Simon Billinge (billinge@pa.msu.edu) or consult the web page [31]. News of updates and releases will be posted at this website and on the total-scattering e-mail list. Instructions for joining the e-mail list can be found on the web page.

Acknowledgments

We would like to acknowledge HyunJeong Kim, He Lin and Wenduo Zhou for help and useful discussions during the development and all the Billinge group members for help in testing. PDFgui was developed as part of the Distributed Analysis of Neutron Scattering Data (DANSE) project, which is funded by the US National Science Foundation (NSF) under DMR-0520547. The PDFfit2 development was funded by the NSF under contract DMR-0304391.

References

- [1] Gilbert B, Huang F, Zhang H, Waychunas G A and Banfield J F 2004 *Science* **305** 651–4
- [2] Billinge S J L and Kanatzidis M G 2004 *Chem. Commun.* **749–60**
- [3] Lin H, Božin E S, Billinge S J L, Quarez E and Kanatzidis M G 2005 *Phys. Rev. B* **72** 174113
- [4] Vensky S, Kienle L, Dinnebier R E, Masadeh A S, Billinge S J L and Jansen M 2005 *Z. Kristallogr.* **220** 231–44
- [5] Petkov V, Billinge S J L, Vogt T, Ichimura A S and Dye J L 2002 *Phys. Rev. Lett.* **89** 075502
- [6] Billinge S J L, McKimney E J, Shatnawi M, Kim H, Petkov V, Wermeille D and Pinnavaia T J 2005 *J. Am. Chem. Soc.* **127** 8492–8
- [7] Tucker M G, Squires M P, Dove M T and Keen D A 2001 *J. Phys.: Condens. Matter* **13** 403–23
- [8] McGreevy R L and Pusztai L 1988 *Mol. Simul.* **1** 359–67
- [9] Egami T and Billinge S J L 2003 *Underneath the Bragg Peaks: Structural Analysis of Complex Materials* (Oxford: Pergamon, Elsevier)
- [10] Proffen T and Billinge S J L 1999 *J. Appl. Crystallogr.* **32** 572–5
- [11] Billinge S J L 1998 *Local Structure from Diffraction* ed Billinge S J L and M F Thorpe (New York: Plenum) p 137
- [12] Tucker M G, Goodwin A L, Dove M T, Keen D A, Wells S A and Evans J S O 2005 *Phys. Rev. Lett.* **95** 255501
- [13] Proffen T, DiFrancesco R G, Billinge S J L, Brosha E L and Kwei G H 1999 *Phys. Rev. B* **60** 9973
- [14] Warren B E 1990 *X-ray Diffraction* (New York: Dover)
- [15] Wright A C 1998 *Glass Phys. Chem.* **24** 148–79
- [16] Jeong I-K, Proffen T, Mohiuddin-Jacobs F and Billinge S J L 1999 *J. Phys. Chem. A* **103** 921–4
- [17] McGreevy R L 2001 *J. Phys.: Condens. Matter* **13** R877–913
- [18] Toby B H and Egami T 1992 *Acta Crystallogr. A* **48** 336–46
- [19] Juhas P, Cherba D M, Duxbury P M, Punch W F and Billinge S J L 2006 *Nature* **440** 655–8
- [20] <http://www.wxpython.org>
- [21] Painter J and Merritt E A 2004 *J. Appl. Crystallogr.* **37** 174–8
- [22] <http://matplotlib.sourceforge.net>
- [23] Li J 2003 *Modelling Simul. Mater. Sci.* **11** 173–7
- [24] DeLano W L 2002 *The PyMOL User's Manual* (San Carlos, CA: DeLano Scientific) <http://www.pymol.org>
- [25] Elemans J B A A, Van Laar B, Van der Veen K R and Loopstra B O 1971 *J. Solid State Chem.* **3** 238–42
- [26] Rodriguez-Carvajal J, Hennion M, Moussa F, Moudén A H, Pinsard L and Revcolevschi A 1998 *Phys. Rev. B* **57** R3189–92
- [27] Chatterji T, Fauth F, Ouladdiaf B, Mandal P and Ghosh B 2003 *Phys. Rev. B* **68** (5) 052406
- [28] Proffen T, Egami T, Billinge S J L, Cheetham A K, Louca D and Parise J B 2002 *Appl. Phys. A* **74** s163–5
- [29] Qiu X, Proffen Th, Mitchell J F and Billinge S J L 2005 *Phys. Rev. Lett.* **94** 177203
- [30] Božin E S, Qiu X, Schmidt M, Paglia G, Mitchell J F, Radaelli P G, Proffen T and Billinge S J L 2006 *Physica B* **385/386** 110–2
- [31] <http://www.diffpy.org>

Local Lattice Dynamics in the $\text{Mg}_{0.5}\text{Al}_{0.5}\text{B}_2$ Superconductor

G. Campi · T. Proffen · X. Qiu · E.S. Bozin ·
S.J.L. Billinge · S. Agrestini · N.L. Saini · A. Bianconi

Received: 3 July 2007 / Accepted: 3 July 2007 / Published online: 14 September 2007
© Springer Science+Business Media, LLC 2007

Abstract We have studied temperature evolution of the local as well as the average crystal structure of MgB_2 and $\text{Mg}_{0.5}\text{Al}_{0.5}\text{B}_2$ using real-space atomic pair distribution function (PDF) measured by high resolution neutron powder diffraction in a wide temperature range of $T = 10\text{--}600$ K. The mean square relative displacements (MSRD) of atomic B–B, B–Mg (B–Al) pairs are compared with mean-square displacements (MSD) to calculate atomic correlations. In spite of the enhanced atomic disorder in $\text{Mg}_{0.5}\text{Al}_{0.5}\text{B}_2$, where the boron–boron, and boron–magnesium pair motions are found to be small, we find that the same atomic correlations in MgB_2 assume even slightly lower values and remain nearly constant in a wide temperature range of 0–600 K. This anomalous behavior and its physical interpretation provoke new questions on our understanding to the local lattice dynamics in this material.

Keywords MgB_2 · Neutron diffraction

G. Campi (✉)
Istituto di Cristallografia, CNR, Via Salaria Km 29,300,
00016 Monterotondo Rome, Italy
e-mail: gaetano.campi@ic.cur.it

T. Proffen
Lujan Neutron Scattering Center, Los Alamos National
Laboratory, Los Alamos, NM 87545, USA

X. Qiu · E.S. Bozin · S.J.L. Billinge
Department of Physics and Astronomy, Michigan State
University, East Lansing, MI 48824, USA

S. Agrestini · N.L. Saini · A. Bianconi
Dipartimento di Fisica, Università di Roma La Sapienza,
P. le Aldo Moro 2, 00185 Rome, Italy

1 Introduction

MgB_2 is the simplest system to investigate the quantum mechanism of the formation of a superconducting condensate with a critical temperature of $T_c \sim 40$ K [1], a factor two higher than in all other known intermetallic superconductors. There is now a general consensus about MgB_2 being a high T_c multiband superconductor where the electron-phonon interaction constructs a weak pairing in the π channel and a strong pairing in the σ -channel [2–13]. This strong electron-phonon coupling, driven by the interaction between electronic carriers in the 2D σ band with boron $p_{x,y}$ character and the zone center E_{2g} phonon mode [12–17], is reflected in a Kohn anomaly in the phonon dispersion related to the size of the small 2D tubular Fermi surfaces [18]. The proximity of the Fermi level to the Van Hove singularity (VHs) and to the band edge discloses a new scenario where the large amplitude of the expected boron zero point lattice fluctuations [7, 12, 15, 19–21] induces large fluctuations of the same order of the separation between the VHs, the gap edge and the Fermi level itself. Although the amplitude of the lattice fluctuations seems thus to be highly relevant for the superconductivity in MgB_2 , there is a lack of experimental information on this key point. Furthermore, although the average structure (P6/mmm) of the MgB_2 system has been exhaustively investigated, there is not yet any study on the local structure, since the usual X-ray local probes, as EXAFS, is limited by poor scattering amplitude due to light atoms.

In view of this, we have investigated the local as well as the average structure of MgB_2 and $\text{Mg}_{0.5}\text{Al}_{0.5}\text{B}_2$ using high resolution neutron diffraction to obtain the pair distribution function (PDF). We focused here on the atomic pairs correlations founded by comparing the mean-square displacements (MSD) and the mean-square relative displace-

ments (MSRD) of the boron–boron ($\rho_{\text{B-B}}$), and boron–magnesium (aluminium) ($\rho_{\text{B-Mg/Al}}$) pair motions. Comparing the atomic correlations in MgB_2 and $\text{Mg}_{0.5}\text{Al}_{0.5}\text{B}_2$, we have been able to investigate the effects on the local structure of the two main microscopic mechanisms for the T_c decrease produced by the Al substitution [4]: (i) the filling of the electronic states in the 2D σ band of $p_{x,y}$ -orbitals within the boron layers and the resulting decrease in the density of states at the Fermi level, and (ii) the increased disorder of the inter-band scattering induced by lattice disorder on the atomic scale. We find that in both MgB_2 and $\text{Mg}_{0.5}\text{Al}_{0.5}\text{B}_2$, the atomic correlations for B–B ($\rho_{\text{B-B}}$) and B–Mg/Al ($\rho_{\text{B-Mg/Al}}$) bonds show small (~ 0.2) positive and anomalous nearly temperature independent behavior.

2 Experimental

Polycrystalline samples of MgB_2 and $\text{Mg}_{0.5}\text{Al}_{0.5}\text{B}_2$ were synthesized at high temperature by direct reaction of the elements in a tantalum crucible under argon atmosphere using pure ^{11}B isotopes. Time-of-flight neutron powder diffraction data were collected on the NPDF diffractometer at the Manuel Lujan, Jr., Neutron Scattering Center (LANSCE) at Los Alamos National Laboratory. The NPDF diffractometer, with its high neutron flux and backscattering detector modules provides a high resolution [22], permitting access to a wide range of momentum transfer with sufficient counting statistics making it ideal for PDF studies. The powdered samples were sealed inside extruded cylindrical vanadium containers. These were mounted on the stage of a cryofurnace with and without heat-shield for $T < 300$ K and $T > 300$ K, respectively. The scattering data from the empty cryofurnace, with and without heat-shield, an empty container mounted on the cryofurnace, and the empty instrument were also collected, allowing us to assess and subtract instrumental backgrounds. The scattering from a vanadium rod was also measured to allow the data to be normalized for the incident spectrum and detector efficiencies. We collected each diffraction spectrum up to the high momentum transfer of $Q = 40 \text{ \AA}^{-1}$ in 3 hours. The high resolution diffraction spectrum so obtained presents both the Bragg peaks and the diffuse scattering. While the Bragg peaks reflect the long-range order of the crystalline samples, the oscillating diffuse scattering contains local structural information including the correlated dynamics [23, 24]. The PDF is obtained from a Fourier transform of the powder diffraction spectrum (Bragg peaks + diffuse scattering) [25]. It consists of a series of peaks, the positions of which give the distances of atom pairs in the real space, while the ideal width of these peaks is due both to relative thermal atomic motion and to static disorder.

This permits the study of the effects of lattice fluctuations on PDF peak widths and yields information on both

mean-square displacements and the mean-square relative displacements of atom pairs and their correlations. Standard data corrections [25] were carried out using the program PDFGETN [26]. After being corrected, the data were normalized by the total scattering cross section of the sample to yield the total scattering structure function $S(Q)$. Afterwards, the total scattering structure function $S(Q)$ is converted to the PDF, $G(r)$, by means of a sine Fourier transform according to the relation:

$$G(r) = 4\pi r(\rho(r) - \rho_0) = \frac{2}{\pi} \int_0^\infty Q[S(Q) - 1] \sin(Qr) dQ. \quad (1)$$

We modeled the PDF using a structural model that takes advantage of the definition of the radial distribution function RDF $R(r)$, namely:

$$R(r) = \sum_i \sum_{i \neq j} \frac{b_i b_j}{\langle b^2 \rangle} \delta(r - r_{ij}), \quad (2)$$

where b_i is the scattering length of the i th atom, $\langle b \rangle$ is the scattering length averaged over the sample composition, $r_{ij} = |\mathbf{r}_i - \mathbf{r}_j|$ is the distance between the i th and the j th atoms, and the sums are taken over all the atoms in the sample. Before being compared to the data, the calculated $G(r)$ is convoluted with a termination function, $\sin(Q_{\text{max}}r)/r$ to account for the effects of the finite data collection range. Fundamental lattice information, such as the average crystal structure, the lattice constants, a scale factor, and the refined atomic (thermal) displacement parameters, can now be extracted from the PDF by using the PDF refinement program PDFFIT [27] that is based on a least-squares approach to fit the PDF profile. The mean square displacement of atom i along the major axes x , y and z , $\sigma^2(i_x)$, $\sigma^2(i_y)$, $\sigma^2(i_z)$, are defined as

$$\sigma^2(i_\alpha) = \langle [\mathbf{u}_i \cdot \hat{\mathbf{r}}_\alpha]^2 \rangle, \quad (3)$$

where \mathbf{u}_i is the lattice displacement of atom i from its average position 28 and $\hat{\mathbf{r}}_\alpha$ is the unit vector pointing along the direction $\alpha = x, y, z$. Due to the geometry of these compounds, the two boron atoms for the unit cell are equivalent and $\sigma^2(i_x) = \sigma^2(i_y)$ for all the atoms, so that only four parameters were needed, namely, $\sigma^2(\text{B}_{xy})$, $\sigma^2(\text{B}_z)$, $\sigma^2(\text{Mg}_{xy})$, and $\sigma^2(\text{Mg}_z)$. We found the same mean square displacements for Mg and Al atom in $\text{Mg}_{0.5}\text{Al}_{0.5}\text{B}_2$.

3 Results

In Fig. 1, we have shown the reduced scattering structure function $Q[S(Q) - 1]$ for the MgB_2 and $\text{Mg}_{0.5}\text{Al}_{0.5}\text{B}_2$ at

Fig. 1 The reduced structure function $Q[S(Q) - 1]$ for MgB_2 (left panel) and $\text{Mg}_{0.5}\text{Al}_{0.5}\text{B}_2$ (right panel) measured at 300 K

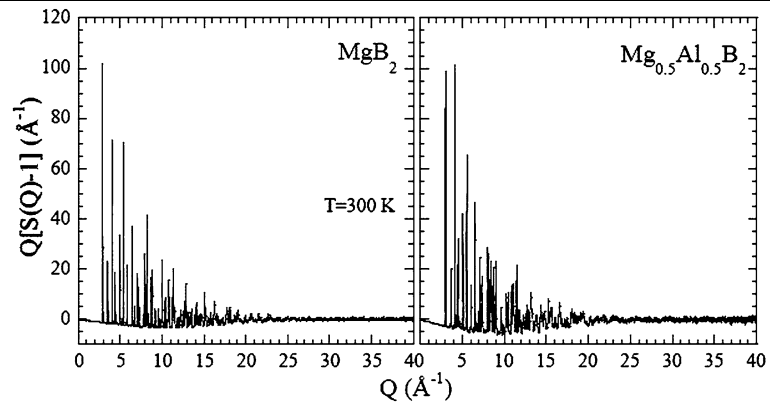
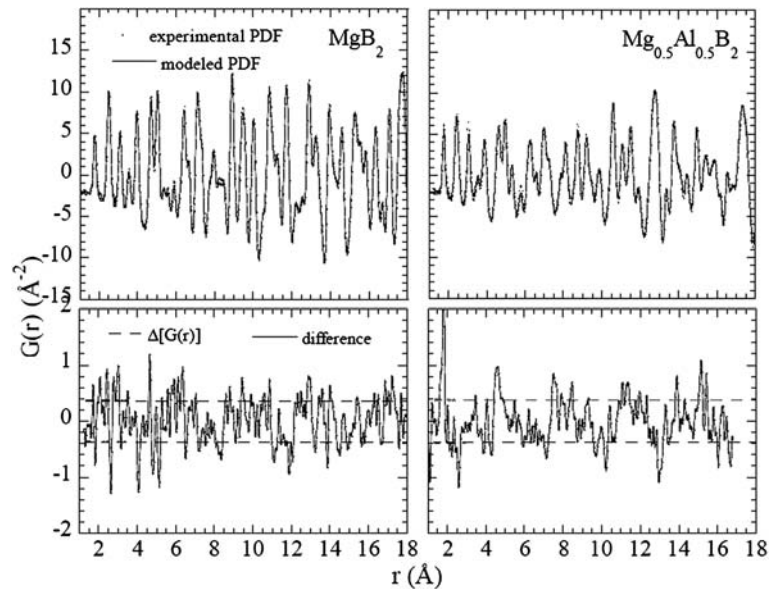


Fig. 2 (Upper panels) The PDF, $G(r)$, obtained from (1) for MgB_2 (left panel) and $\text{Mg}_{0.5}\text{Al}_{0.5}\text{B}_2$ (right panel) measured at 300 K (dots), with the structure refinement curves obtained by a least-squares approach (solid lines). (Lower panels) The difference curves (solid lines) of the experimental PDFs with the modeled fits and the standard deviations on the data $\Delta[G(r)]$ (dashed lines) are shown. We can observe that most of the fluctuations in the difference curves are within $\Delta[G(r)]$



$T = 300$ K, while the corresponding reduced PDFs, $G(r)$, obtained using (1), are shown in the upper panels of Fig. 2.

The features of the NPDF diffractometer allowed us to obtain high quality PDFs as can be noted by inspecting the modeled fit (solid line) of the $G(r)$ in the upper panels (Fig. 2). This can be seen also in the lower panels of Fig. 2 where most of the fluctuations in the difference curves (solid lines) are within the standard deviation of the data $\Delta[G(r)]$ (dashed lines above and below the difference curves). The PDFs have been fit over the range 1–18 Å using a hexagonal crystal structure (space group P6/mmm), obtaining very good fits at all temperatures. The Bragg peaks are clearly persistent up to 25 Å⁻¹, reflecting both the long-range order of the crystalline samples and the small amount of positional (vibrational or static) disorder of the atoms around their average positions. The lattice parameters at $T = 300$ K for MgB_2 ($T_c \sim 39$ K) and $\text{Mg}_{0.5}\text{Al}_{0.5}\text{B}_2$ were found to be $a = 3.08505(4)$ Å, $c = 3.5218(1)$ Å and $a = 3.05457(5)$ Å, $c = 3.37863(10)$ Å, respectively. The mean square displacements $\sigma^2(\text{B}_{xy})$, $\sigma^2(\text{B}_z)$, $\sigma^2(\text{Mg}_{xy}/\text{Al}_{xy})$, and $\sigma^2(\text{Mg}_z/\text{Al}_z)$

for MgB_2 (open circles) and $\text{Mg}_{0.5}\text{Al}_{0.5}\text{B}_2$ (open squares) are shown in Fig. 3.

In order to extract information about the phonon spectrum, we fit each MSD with a simple Einstein model

$$\sigma^2(i_\alpha) = \frac{\hbar}{m_i \omega_{i\alpha}} \left[\frac{1}{2} + n[\omega(i_\alpha)] \right] + \sigma_0^2(i_\alpha), \quad (4)$$

where $\sigma_0^2(i_\alpha)$ takes into account the static disorder, M_i is atomic mass of the atom i and $\omega(i_\alpha)$ provided an estimate of the vibrational frequency of the atom i along the direction α . The quantity $n[x]$ is the Bose thermal factor $n[x] = [\exp(x/k_B T) - 1]^{-1}$. The good fits indicate that a simple Einstein model seems to describe quite well the lattice vibrations in these compounds. Moreover, the Einstein fits were obtained by simply using nominal atomic masses $M_{\text{Mg}} = 24.3$ a.m.u. for $\sigma^2(\text{Mg})$, $M_{\text{B}} = 10.81$ a.m.u. for $\sigma^2(\text{B})$ and $M_{\text{Al}} = 26.98$ a.m.u. for $\sigma^2(\text{Al})$. This means that we are implicitly assuming the magnesium and boron vibrations being decoupled. A more quantitative check of this assumption, obtained calculating the phonon dispersion of MgB_2 within

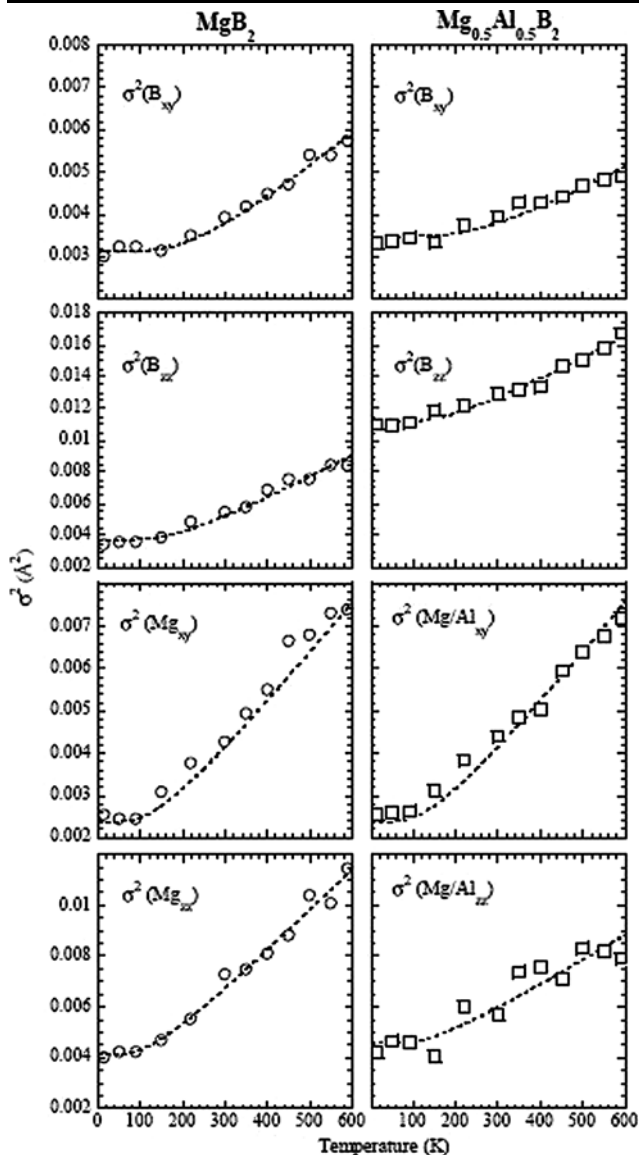


Fig. 3 Anisotropic in plane $\sigma^2(B_{xy})$, $\sigma^2(Mg_{xy}/Al_{xy})$ and along the c -axis $\sigma^2(B_z)$, $\sigma^2(Mg_z/Al_z)$ mean-square displacements for the B and Mg(Al) atoms, as a function of the temperature in MgB_2 (circles in left column panels) and $Mg_{0.5}Al_{0.5}B_2$ (squares in right column panel). The open circles and squares represent the PDFFIT refined values, while the dotted lines represent the modelled data in the Einstein model. The error bars in the mean-square displacements are smaller than the size of the used symbols

a force constant shell model, can be found in [29]. The values of the fitting parameters, $\omega(i_\alpha)$ and $\sigma_0^2(i_\alpha)$, are reported in Table 1, and the σ^2 vs. T fitting curves are represented by dotted lines in the Fig. 3. The different values of $\omega(i_\alpha)$ represent the different energy range of the phonon spectra associated with the boron and magnesium (aluminium) in-plane and out-of-plane lattice vibrations, and they are in good agreement with the corresponding spectra reported in [30]. Upon inspection of the σ_0 values, one will note the larger static disorder term σ_0 for the B and Mg(Al) atoms motion

Table 1 Effective phonon frequencies $\omega(i_\alpha)$ and static disorder contributions $\sigma_0^2(i_\alpha)$ for the in-plane and out-of-plane B and Mg/Al displacements as obtained by the Einstein model fit (4) of $\sigma^2(i_\alpha)$

	MgB_2	$Mg_{0.5}Al_{0.5}B_2$
$\omega(B_{xy})$ (K)	703 ± 10	876 ± 46
$\omega(B_{zz})$ (K)	572 ± 15	560 ± 23
$\omega(Mg/Al_{xy})$ (K)	398 ± 6	400 ± 13
$\omega(Mg/Al_{zz})$ (K)	350 ± 9	415 ± 31
$\sigma_0^2(B_{xy})$ (\AA^2)	$(5.11 \pm 5.11) \times 10^{-5}$	0.0011 ± 0.0002
$\sigma_0^2(B_{zz})$ (\AA^2)	$(9.10 \pm 9.10) \times 10^{-5}$	0.0074 ± 0.0004
$\sigma_0^2(Mg/Al_{xy})$ (\AA^2)	$(7.35 \pm 7.35) \times 10^{-5}$	0.0002 ± 0.0002
$\sigma_0^2(Mg/Al_{zz})$ (\AA^2)	0.0013 ± 0.0003	0.0024 ± 0.0004

in $Mg_{0.5}Al_{0.5}B_2$ than in MgB_2 where we find contribution of the disorder only for the magnesium out-of-plane lattice vibration ($\sigma^2(Mg_z) \sim 0.0013 \text{ \AA}^2$) while it is found to be negligible for the other modes.

The PDF technique is sensitive to the correlations in the atomic dynamics that contain some additional details about the underlying interatomic potentials [23, 24, 28, 31, 32]. Here, we explore the motional correlations in the two compounds using the PDF data. The Gaussian width σ_{ij} of the PDF peaks is directly related to the mean-square relative displacement (MSRD) of atomic pairs projected onto the vector joining the atom pairs 28, that is

$$\sigma_{ij}^2 = \langle [(\mathbf{u}_i - \mathbf{u}_j) \cdot \hat{\mathbf{r}}_{ij}]^2 \rangle, \quad (5)$$

where \mathbf{u}_i and \mathbf{u}_j are the lattice displacements of atoms i and j from their average positions, $\hat{\mathbf{r}}_{ij}$ is the unit vector connecting atoms i and j , and the angular brackets indicate an ensemble average [28]. As a general consideration, we would like to stress once more that while $\sigma_0^2(i_\alpha)$ probes the absolute magnitude of the single atom mean-square displacement, σ_{ij}^2 provides information about the correlation between the lattice displacements of atom pairs. Let us consider for instance the case of σ_{B-B}^2 which involves only boron in-plane lattice fluctuations. We can identify three limiting behaviors for this quantity: (i) perfectly in-phase lattice motion; (ii) perfectly opposite-phase motion; and (iii) completely independent motion. In the first case, it is easy to see that $\sigma_{B-B}^2 = 0$, while $\sigma_{B-B}^2 = 2\sigma^2(B_{xy})$ when the nearest neighbor boron lattice displacements are uncorrelated, and $\sigma_{B-B}^2 = 4\sigma^2(B_{xy})$ when they have opposite phase. To formalize this, we rearrange (5) as

$$\sigma_{ij}^2 = \langle [\mathbf{u}_i \cdot \hat{\mathbf{r}}_{ij}]^2 \rangle + \langle [\mathbf{u}_j \cdot \hat{\mathbf{r}}_{ij}]^2 \rangle - 2\langle (\mathbf{u}_i \cdot \hat{\mathbf{r}}_{ij})(\mathbf{u}_j \cdot \hat{\mathbf{r}}_{ij}) \rangle. \quad (6)$$

Here, the first two terms are related to mean-square thermal displacement of atoms i and j projected along $\hat{\mathbf{r}}_{ij}$, while the third term is a displacement correlation function, which carries information about the motional correlations. It is now

Fig. 4 Mean-square relative lattice displacements σ_{B-B}^2 (a), σ_{B-Mg}^2 (b), as extracted from the width of the PDF peaks and the corresponding correlation function ρ_{B-B} (c), ρ_{B-Mg} (d) (open circles) for MgB₂. The filled diamonds represent lattice displacements σ_{B-B}^2 , σ_{B-Mg}^2 for completely uncorrelated lattice motion, i.e., $\rho_{ij} = 0$

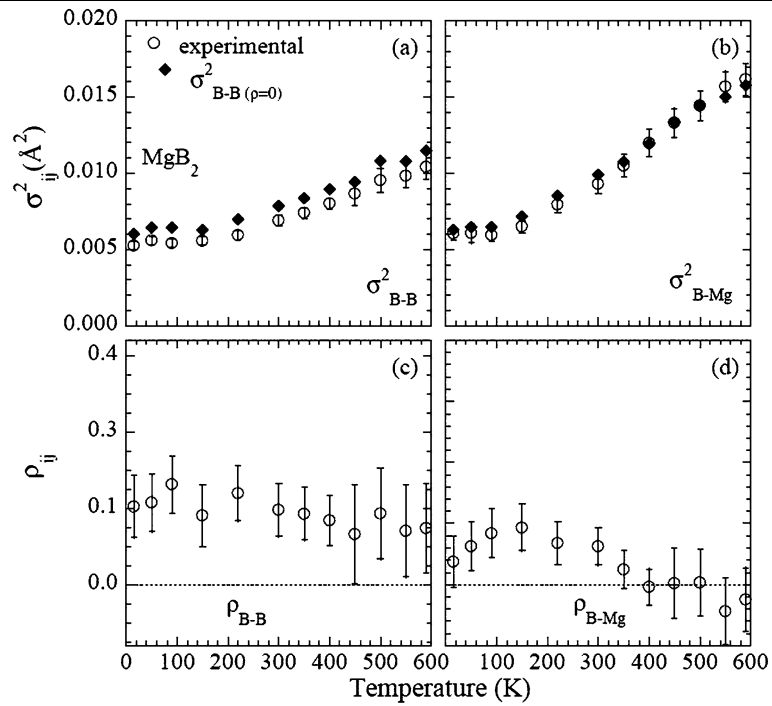
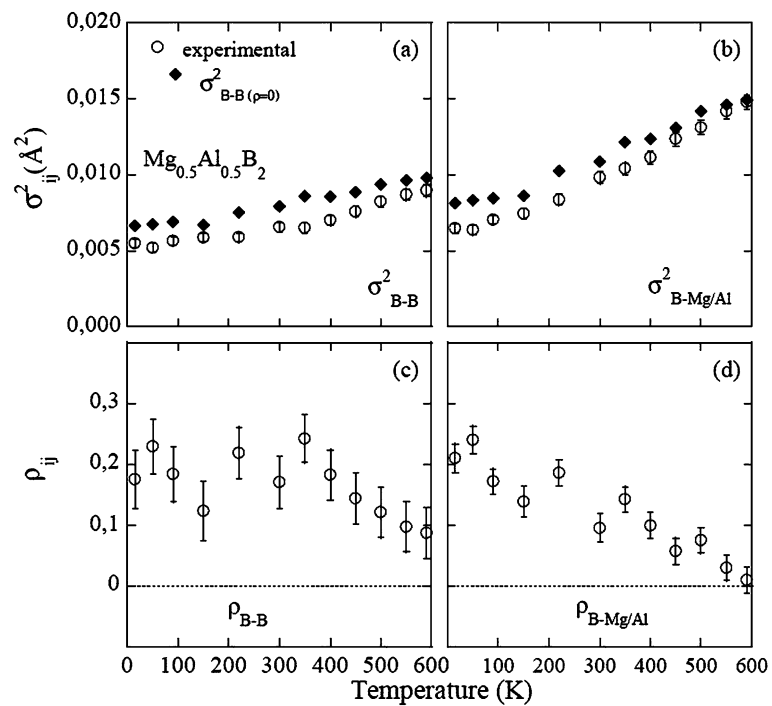


Fig. 5 The same quantities of Fig. 4, namely, mean-square relative lattice displacements σ_{B-B}^2 (a), $\sigma_{B-Mg/Al}^2$ (b), with the corresponding correlation function ρ_{B-B} (c), $\rho_{B-Mg/Al}$ (d) (open circles) and lattice displacements σ_{B-B}^2 , $\sigma_{B-Mg/Al}^2$ for completely uncorrelated lattice motion, i.e., $\rho_{ij} = 0$ are here illustrated for the Mg_{0.5}Al_{0.5}B₂



useful to quantify the degree of correlation by introducing the dimensionless correlation parameter ρ_{ij} defined as [23, 24, 31, 33]:

$$\sigma_{ij}^2 = \sigma^2(i_j) + \sigma^2(j_i) - 2\sigma(i_j)\sigma(j_i)\rho_{ij}, \quad (7)$$

where $\sigma^2(i_j) = \langle [\mathbf{u}_i \cdot \hat{\mathbf{r}}_{ij}]^2 \rangle$. Positive values of ρ describe a situation where the atoms move in phase, so that the re-

sulting value of σ_{ij}^2 is smaller than for the uncorrelated case. On the other hand, a predominance of opposite phase atomic vibrations should result in $\rho < 0$ and in a PDF peak width σ_{ij}^2 larger than the uncorrelated case. It is important to note that the correlation function ρ_{ij} in (7) expresses the degree of correlation between the total atomic displacements. Using (7), the correlation parameter can be calculated from the total width of the PDF peak as:

$$\rho_{ij} = \frac{(\sigma^2(i_j) + \sigma^2(j_i)) - \sigma_{ij}^2}{2\sigma(i_j)\sigma(j_i)}. \quad (8)$$

In our analysis, we focus on the width of the nearest neighbor boron-boron PDF peak, σ_{B-B}^2 , and on the nearest neighbor magnesium (aluminium)-boron peak, $\sigma_{B-Mg/Al}^2$. These are well resolved single-component peaks in the PDF whose width directly yields correlated dynamical information [24]. The Gaussian widths σ_{B-B}^2 , $\sigma_{B-Mg/Al}^2$, as measured by the PDF data are shown in the upper panels of Figs. 4 and 5 (open circles) for MgB_2 and $Mg_{0.5}Al_{0.5}B_2$. The correlation factor ρ_{ij} as extracted from the PDF data σ_{B-B}^2 , $\sigma_{B-Mg/Al}^2$ and from the single atom mean-square lattice displacements $\sigma^2(i_\alpha)$ is shown in the lower panels of Figs. 4 (MgB_2) and 5 ($Mg_{0.5}Al_{0.5}B_2$). We find a positive correlation factor for both $\rho_{B-B} \sim 0, 1$, and $\rho_{B-Mg/Al} \sim 0, 1$, indicating a slight predominance of the in-phase B–B and B–Mg/Al lattice displacements in this experimental probe. Positive values of ρ_{ij} are commonly reported in a variety of materials. The intuitive explanation is that the in-phase phonon modes (acoustic, low optical branch modes) are generally less stiff than the opposite-phase optical ones. Our reported values of ρ_{B-B} ; $\rho_{B-Mg/Al} \sim 0.1$ are, however, much smaller than the correlation factors commonly found in other covalently bonded materials [23, 24, 31, 33].

4 Conclusion

In this work, we have investigated local lattice properties of the MgB_2 and $Mg_{0.5}Al_{0.5}B_2$ compounds paying special attention on the lattice dynamics and the correlations in the B–B and B–Mg/Al first neighbor atomic pair motion. We have used the real space PDF obtained from high resolution neutron diffraction to study the effects of the lattice vibrations on the PDF peak widths. The PDF peaks in well ordered crystals, such as the present case, yield important information about the underlying atomic potentials through the correlated local lattice dynamics. The analysis of the PDF peak linewidths permits to evaluate the correlation for both the nearest neighbor B–B and B–Mg/Al atomic pairs. We find a small positive correlation factor $\rho_{B-B} \sim 0.1$ and $\rho_{B-Mg/Al} \sim 0.1$, nearly temperature independent, indicating a weakly prevalent in-phase relative atomic motion.

References

- Nagamatsu, J., Nakagawa, N., Muranaka, T., Zenitali, Y., Akimitsu, J.: *Nature* **410**, 63 (2001)
- Agrestini, S., Di Castro, D., Sansone, M., Saini, N.L., Saccone, A., De Negri, S., Giovannini, M., Colapietro, M., Bianconi, A.: *J. Phys. Condens. Matter* **13**, 11689 (2001)
- Imada, M.: *J. Phys. Soc. Jpn.* **70**, 1218 (2001)
- Bianconi, A., Di Castro, D., Agrestini, S., Campi, G., Saini, N.L., Saccone, A., De Negri, S., Giovannini, M.: *J. Phys. Condens. Matter* **13**, 7383 (2001)
- Yamaji, K.: *J. Phys. Soc. Jpn.* **70**, 1476 (2001)
- Ord, T., Kristoffel, N.: *Physica C* **370**, 17 (2002)
- Bouquet, F., Fisher, R.A., Phillips, N.E., Hinks, D.G., Jorgensen, J.D.: *Phys. Rev. Lett.* **87**, 047001 (2001)
- Szabo, P., Samuely, P., Kacmarcik, J., Klein, T., Marcus, J., Fruchart, D., Miraglia, S., Marcenat, C., Jansen, A.G.M.: *Phys. Rev. Lett.* **87**, 137005 (2001)
- Giubileo, F., Roditchev, D., Sacks, M., Lassey, R., Thanh, D.X., Klein, J.: *Phys. Rev. Lett.* **87**, 177008 (2001)
- Tsuda, S., Yokoya, T., Takano, Y., Kito, H., Matsushita, A., Yin, F., Itoh, J., Harima, H., Shin, S.: *Phys. Rev. Lett.* **91**, 127001 (2003)
- Gonnelli, R.S., Daghero, D., Ummerino, G.A., Stepanov, V.A., Jun, J., Kazakov, S.M., Karpinski, J.: *Phys. Rev. Lett.* **89**, 247004 (2003)
- Liu, A.Y., Mazin, I.I., Kortus, J.: *Phys. Rev. Lett.* **87**, 087005 (2001)
- Choi, H.J., Roundy, D., Sun, H., Cohen, M.L., Louie, S.G.: *Phys. Rev. B* **66**, 020513 (2002); *ibid. Nature* **418** 758 (2002)
- An, J.M., Pickett, W.E.: *Phys. Rev. Lett.* **86**, 4366 (2001)
- Yildirim, T., Gulseren, O., Lynn, J.W., Brown, C.M., Udovic, T.J., Huang, Q., Rogado, N., Regan, K.A., Hayward, M.A., Slusky, J.S., He, T., Haas, M.K., Khalifah, P., Inumaru, K., Cava, R.J.: *Phys. Rev. Lett.* **87**, 037001 (2001)
- Bohnen, K.-P., Heid, R., Renker, B.: *Phys. Rev. Lett.* **86**, 5771 (2001)
- Kong, Y., Dolgov, O.V., Jepsen, O., Andersen, O.K.: *Phys. Rev. B* **64**, 020501 (2001)
- Shukla, A., Calandra, M., d'Astuto, M., Lazzeri, M., Mauri, F., Bellin, C., Krisch, M., Karpinski, J., Kazakov, S.M., Jun, J., Daghero, D., Parlinski, K.: *Phys. Rev. Lett.* **90**, 095506 (2003)
- Boeri, L., Bachelet, G.B., Cappelluti, E., Pietronero, L.: *Phys. Rev. B* **65**, 214501 (2002)
- Bianconi, A., Agrestini, S., Di Castro, D., Campi, G., Zangari, G., Saini, N.L., Saccone, A., De Negri, S., Giovannini, M., Profeta, G., Continenza, A., Satta, G., Massidda, S., Cassetta, A., Pifferi, A., Colapietro, M.: *Phys. Rev. B* **65**, 174515 (2002)
- Boeri, L., Cappelluti, E., Pietronero, L.: *Phys. Rev. B* **71**, 012501 (2005)
- Proffen, T., Egami, T., Billinge, S.J.L., Cheetham, A.K., Louca, D., Parise, J.B.: *Appl. Phys. A: Mater. Sci. Process.* **74**, S163 (2002)
- Jeong, I.-K., Proffen, T., Mohiuddin-Jacobs, F., Billinge, S.J.L.: *J. Phys. Chem. A* **103**, 921 (1999)
- Jeong, I.-K., Hefner, R.H., Graf, M.J., Billinge, S.J.L.: *Phys. Rev. B* **67**, 104301 (2003)
- Egami, T., Billinge, S.J.L.: *Underneath the Bragg Peaks: Structural Analysis of Complex Materials*. Pergamon, Oxford (2003)
- Peterson, P.F., Gutmann, M., Proffen, T., Billinge, S.J.L.: *J. Appl. Crystallogr.* **33**, 1192 (2000)
- Proffen, T., Billinge, S.J.L.: *J. Appl. Crystallogr.* **32**, 572 (1999)
- Thorpe, M.F., Levashov, V.A., Lei, M., Billinge, S.J.L.: In: Billinge, S.J.L., Thorpe, M.F. (eds.) *From Semiconductors to Proteins: Beyond the Average Structure*, p. 105. Kluwer/Plenum, New York (2002)
- Campi, G., Capelluti, E., Proffen, T., Qiu, X., Bozin, E.S., Billinge, S.J.L., Agrestini, S., Saini, N.L., Bianconi, A.: *Eur. Phys. J. B* **52**, 15–21 (2006)
- Osborn, R., Goremychkin, E.A., Kolesnikov, A.I., Hinks, D.G.: *Phys. Rev. Lett.* **87**, 017005 (2001)
- Chung, J.S., Thorpe, M.F.: *Phys. Rev. B* **55**, 1545 (1997)
- Graf, M.J., Jeong, I.K., Starr, D.L., Hefner, R.H.: *Phys. Rev. B* **68**, 064305 (2003)
- Booth, C.H., Bridges, F., Bauer, E.D., Li, G.G., Boyce, J.B., Claesson, T., Chu, C.W., Xiong, Q.: *Phys. Rev. B* **52**, R15745 (1995)

Nanoscale α -structural domains in the phonon-glass thermoelectric material β -Zn₄Sb₃H. J. Kim,¹ E. S. Božin,¹ S. M. Haile,² G. J. Snyder,² and S. J. L. Billinge^{1,*}¹Department of Physics and Astronomy, Michigan State University, East Lansing, Michigan 48824-1116, USA²Department of Materials Science, California Institute of Technology, Pasadena, California 91125, USA

(Received 8 January 2007; published 18 April 2007)

A study of the local atomic structure of the promising thermoelectric material β -Zn₄Sb₃, using atomic pair distribution function (PDF) analysis of x-ray- and neutron-diffraction data, suggests that the material is nanostructured. The local structure of the β phase closely resembles that of the low-temperature α phase. The α structure contains ordered zinc interstitial atoms which are not long range ordered in the β phase. A rough estimate of the domain size from a visual inspection of the PDF is $\lesssim 10$ nm. It is probable that the nanoscale domains found in this study play an important role in the exceptionally low thermal conductivity of β -Zn₄Sb₃.

DOI: 10.1103/PhysRevB.75.134103

PACS number(s): 72.20.Pa, 61.10.Nz, 61.12.Ld, 73.50.Lw

Thermoelectric materials allow for direct conversion of heat into electrical energy and vice versa. They hold great technological promise for solid-state refrigeration and power generation¹ if the dimensionless figure of merit, ZT , can be pushed above 2. The materials' challenge is to minimize thermal conductivity without reducing the electrical conductivity, i.e., to produce strong scattering of phonons, but not electrons. The simple and nominally stoichiometric β -Zn₄Sb₃ (Ref. 2) is an excellent example of such a phonon-glass³ thermoelectric material and presents a model system for studying this phenomenon, but the mechanism for the low thermal conductivity is not established.^{2,4-6} Here, we show that interstitial Zn atoms^{2,5} not only provide point defects but also force a local structural rearrangement on the nanometer scale in β -Zn₄Sb₃. These nanodomains should effectively scatter the long wavelength phonons that are important for heat transport.⁷⁻¹⁰ This strongly supports the view that nanoscale structural modulations are an important ubiquitous component in emerging high ZT materials.⁷⁻¹²

The $ZT=S^2\sigma T/\kappa$, where S , σ , and κ are the Seebeck coefficient, electrical conductivity, and thermal conductivity, respectively, of β -Zn₄Sb₃ exceeds unity above 540 K.² It crystallizes in space group $R\bar{3}c$ (Fig. 1). Several different structural defects have been proposed to exist in the lattice such as Zn and Sb mixed sites¹³ and an occupational deficiency on Zn sites.⁴ The recent proposal of interstitial Zn atom defects in the crystal structure of β -Zn₄Sb₃ (Refs. 2 and 5) would increase phonon scattering and therefore ZT . However, such point defects are expected to scatter short-wavelength phonon more effectively than mid- to long-wavelength phonons,^{7,10} the major agents of heat conduction in alloys.⁷ The point defects alone are unlikely to explain the exceptionally low thermal conductivity. We used the atomic pair distribution function (PDF) analysis^{14,15} of x-ray and neutron scattering data to study the local structure in β -Zn₄Sb₃. The PDF method, a local structural probe that yields the probability of finding an atom at a distance r away from another atom, has been successfully applied to solve the structures of disordered crystals.¹⁵ The high-symmetry rhombohedral structure and nominally stoichiometric composition of β -Zn₄Sb₃ hides an interesting underlying complexity that is revealed by these local structural measurements. By comparing the experimental PDF of Zn₄Sb₃ with

PDFs calculated from several structural models, we show that, locally, the material retains its low-symmetry low-temperature form^{16,17} and the higher-symmetry average structure is due to averaging of these nanometer scale local domains. Temperature-dependent measurements through the α - β transition support this picture. We have estimated the domain size at less than 10 nm from a comparison of low- and high-temperature PDFs determined over a wide range of r . Interestingly, the length scale of this intrinsically self-organized nanodomains observed in the high ZT β form of the material is comparable to the length scale of nanoscale superstructures^{11,12} or defects⁷⁻¹⁰ introduced in newly engineered high ZT materials to efficiently scatter mid-to long-wavelength phonons. This is a report on nanoscale domains in β -Zn₄Sb₃, and the compelling similarity in the order of domains size to nanoscale structural modulations in other high ZT materials strongly suggests their important role in very low thermal conductivity of β -Zn₄Sb₃.⁷

Two Zn₄Sb₃ samples (I and II) were prepared at different times by direct reaction of the elements. Neutron-powder diffraction measurements were carried out on sample I at 15 and 300 K using the NPDF diffractometer at the Lujan Center at Los Alamos National Laboratory. X-ray powder-diffraction data for sample II were collected at room temperature and over a range of temperatures to 150 K at the 6-IDD station at the Advanced Photon Source at Argonne National Laboratory. The x-ray energies were 87.006 keV

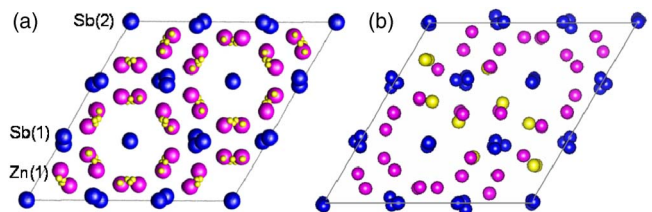


FIG. 1. (Color online) The crystal structure of Zn₄Sb₃. (a) Projection down the c axis of the crystal structure of β -Zn₄Sb₃ in space group $R\bar{3}c$. There are three distinct atomic positions, 36Zn(1), 18Sb(1), and 12Sb(2). Possible Zn interstitial sites in the interstitial model are indicated with light small circles. (b) The interstitial atoms have full occupancy and become ordered in the α phase (light blue circles). To help with comparison, only a part of a triclinic supercell is shown.

($\lambda=0.14248 \text{ \AA}$) for the 300 K data and 129.77 keV ($\lambda=0.095541 \text{ \AA}$) for the low-temperature measurements. Data were collected using the rapid acquisition PDF technique.¹⁸ Both neutron and x-ray data were processed to obtain the PDFs (Refs. 14 and 18) using programs PDFGETN (Ref. 19) and PDFGETX2,²⁰ respectively.

Three structural models based on the $R\bar{3}c$ framework and the α -phase superstructure were used for this study (Fig. 1): the mixed occupancy,¹³ vacancy,⁴ and interstitial² models. The α -phase superstructure, here named the α -structural model, accounts for superlattice peaks arising from ordered Zn interstitial defects below $T \approx 260 \text{ K}$.^{16,17} All the sites in the low-temperature α -structural model are fully occupied.

The structural modeling was carried out using the program PDFFIT2.²¹ Each model was taken as an initial structure, then lattice parameters, atomic coordinates, and isotropic displacement parameters (U_{iso}) were refined using a least-squares approach until the difference between the experimental and calculated PDFs was minimized. The atomic coordinates were constrained to retain the symmetry of the $R\bar{3}c$ space group for the mixed occupancy, vacancy, and interstitial models. For the α -structural model, the space group $C\bar{1}$ was used and the atomic coordinates were fixed to the values from the literature.¹⁶ For all the models, only two parameters were assigned for U_{iso} : one for Zn atoms and the other for Sb atoms regardless of different crystallographic sites. The refinement range was $1.5 < r < 20.0 \text{ \AA}$.

The PDF obtained from 15 K neutron data is shown in Fig. 2(a). The excellent signal-to-noise ratio of the data is evident from the negligibly small ripples on the base line of the PDF below 2 \AA compared to the PDF peaks. The first sharp peak at 2.7 \AA derives from the nearest-neighbor pairs of Zn–Zn, Zn–Sb, and Sb–Sb in the rhombohedral unit cell [Fig. 1(a)]. The calculated PDF from the refined α -structural model is plotted over the data with the difference shown in the curve below it. The refined values of the structural parameters are summarized in Table I. The model is in excellent agreement with the data without refinement of atomic coordinates, directly indicating that the local structure agrees well with the average structure in the α phase.

Now, we focus on the PDF of β -Zn₄Sb₃. The results of structural modeling on the neutron PDF at 300 K using the mixed occupancy, vacancy, and interstitial models are summarized in Table I. Reasonably good fits are obtained from each of the models with agreement factor, R_w ,²¹ of around 0.15 for mixed occupancy and vacancy models and lower for the interstitial model which has two to three times more refinable parameters. These fits are obtained at the expense of enlarged atomic displacement factors on the Zn sites, though the interstitial model does better in this regard. Enlarged atomic displacement factors may signify the presence of loosely coordinated “rattler ions”²² or alternatively nonthermal disorder that is not incorporated explicitly in the models.

The R_w^b values in Table I show how the results changed when U_{iso} was fixed to a smaller value of 0.01 \AA^2 , a value between the refined 15 and 300 K values and appropriate for a temperature in the vicinity of the structural phase transition, for both Zn and Sb atoms. Now, the insufficiency of each model emerges due to the sharpening of PDF peaks by

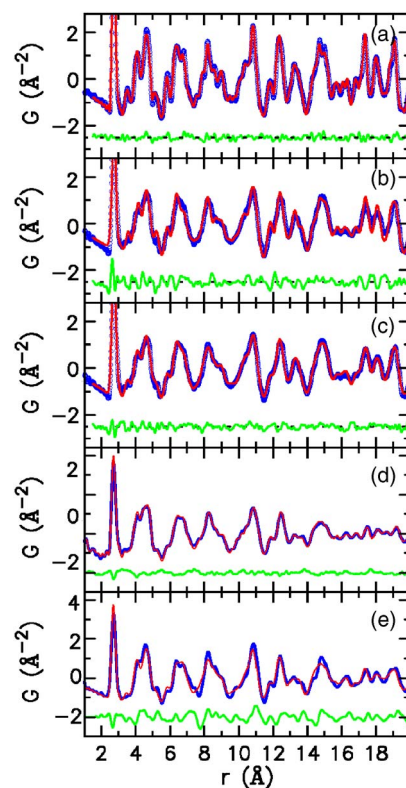


FIG. 2. (Color online) PDF refinement results and the change in PDF over α - β transition. (a) The experimental neutron PDF obtained at 15 K (blue circles) together with the calculated PDF from the refined α model (red line). (b) 300 K neutron data with the calculated PDF from the refined β -phase interstitial model. (c) The same data as (b) but this time the calculated PDF of the α -structural model. The PDFs in (b) and (c) were calculated with a fixed U_{iso} of 0.01 \AA^2 . In each case, the difference between the calculated and measured PDFs is plotted below the data. The good agreement in (c) indicates that the α -structural model explains the *local* structure of β -Zn₄Sb₃ with a smaller value of U_{iso} whereas the interstitial model does not (b). [(d) and (e)] Comparison of the change in PDF expected as the sample goes from the α to β phase. The PDF in the α phase is shown in light red line and the β phase in dark blue line. The difference is plotted below. (d) *Experimental* x-ray PDFs in β (270 K, dark blue line) and α (220 K, light red line) phases. (e) The *calculated* PDFs based on the average structures. U_{iso} used for the calculation is 0.01 \AA^2 for both interstitial and α -structural models. The observed changes in the local structure are much smaller than expected from the crystal structure models.

the small U_{iso} value. The case of the interstitial model is shown in Fig. 2(b). The results imply that the local structure of β -Zn₄Sb₃ is somehow more distorted than the three models suggest.

We also tried the α -structural model for the *local* structure of the 300 K data. It provides as good a fit as the other models did with just U_{iso} being refined. With fewer parameters, the resultant R_w value is comparable to the other models (Table I). The most interesting result was obtained when U_{iso} was fixed to 0.01 \AA^2 during the refinement [Fig. 2(c)]. Even though U_{iso} was fixed, a good fit was still obtained; the fluctuation in the difference curve is not significant and, most of all, the R_w value does not change much (Table I), implying

TABLE I. Refined structural parameters from various models. Lattice parameters and isotropic displacement parameters (U_{iso}) were refined for all models. The atomic coordinates (not reported here) were refined only for mixed occupancy, vacancy, and interstitial models being constrained to keep the $R\bar{3}c$ symmetry. The refinement range was $1.5 < r < 20.0$ Å.

	Mixed occupancy		Vacancy		Interstitial		α structural		
	Neutron (300 K)	X ray (300 K)	Neutron (300 K)	X ray (300 K)	Neutron (300 K)	X ray (300 K)	Neutron (300 K)	X ray (300 K)	Neutron (15 K)
a (Å)	12.2508(5)	12.231(2)	12.2444(5)	12.244(1)	12.2433(5)	12.234(2)	32.730(7)	32.576 (3)	32.553(5)
b (Å)							12.249(3)	12.220(6)	12.236(2)
c (Å)	12.432(1)	12.468(3)	12.430(1)	12.472(1)	12.427(1)	12.464(1)	10.896(3)	10.945(1)	10.872(2)
β							98.97(1)	99.25(1)	98.99(1)
Zn U_{iso} (Å ²)	0.0333(2)	0.0459(1)	0.0315(2)	0.0731(3)	0.0269(2)	0.0292(3)	0.0176(1)	0.0285(2)	0.0052(1)
Sb U_{iso} (Å ²)	0.01191(9)	0.0151(1)	0.0147(1)	0.0110(3)	0.0140(1)	0.0166(1)	0.0098(1)	0.0126(1)	0.00281(7)
n^a	9	9	9	9	18	18	6	6	6
R_w	0.153501	0.14236	0.150178	0.162943	0.110834	0.123122	0.116389	0.138129	0.083549
R_w^b	0.268002	0.242116	0.258401	0.291704	0.230391	0.227926	0.133564	0.159292	

^aNumber of parameters used.

^bResults with U_{iso} for both Zn and Sb atoms fixed to 0.01 Å².

that in the β phase the α -like structure is preserved locally. This result suggests that the enlarged U_{iso} on Zn sites in the β model is due to the averaging of different local environments in the cubic model and interstitials are not rattler ions.

As a further check of this hypothesis, we measured the temperature dependence of the local structure through the α - β phase transition at 260 K. Indeed, there is no significant change in the x-ray PDF on crossing the transition [Fig. 2(d)], compared to the expected change based on the α and β models [Fig. 2(e)], indicating that locally the structure is not changing even though there is a change in the average symmetry at this transition.

It is interesting to investigate what aspect of the α model makes it better for the low- r region of the PDF of β -Zn₄Sb₃ than the interstitial model even though they have similar numbers of Zn interstitial atoms. The improvement in fit is unlikely to be explained by the ordering arrangement of interstitial atoms in the α model since the defects themselves are only 10% in the fully occupied $R\bar{3}c$ framework^{2,16} and the consequent effect is small in the PDF. The reason seems to lie in the local coordination of the interstitial atoms in the respective models. The interstitial model provides possible Zn interstitial sites in a highly symmetric $R\bar{3}c$ structural frame [Fig. 1(a)] but not their influence of relaxing the positions of neighboring atoms. Accordingly, large U_{iso} values are necessary for the interstitial model to get sufficiently broad PDF peaks. However, the lower-symmetry atomic arrangement in the α model [Fig. 1(b)] correctly captures the perturbed environment of the interstitial atoms. Since the local structure does not change at the α - β -phase transition, the Zn interstitial defects persist but lose their long-range order forming the α -like domains in the β phase.

When point defects are discovered in a material, particularly charged point defects that require other charge balancing defects, one should expect local structural distortions or rearrangements that will lead either to long-range order and a superstructure or to short-range-ordered nanometer size do-

main that are not detected with traditional diffraction techniques. In the Zn₄Sb₃ case, the Zn interstitials order at low temperature, resulting in a new crystallographic phase and a superstructure in the diffraction pattern.^{16,17} This tendency to order locally will reduce Coulombic and elastic strain energies. At high temperature, the defects prefer to disorder to increase the entropy, but the strong tendency toward local ordering persists, resulting in nanoscale domains, or short-range order with a finite coherence length, such as was found here.

In the β phase, the local α -like domains must be oriented

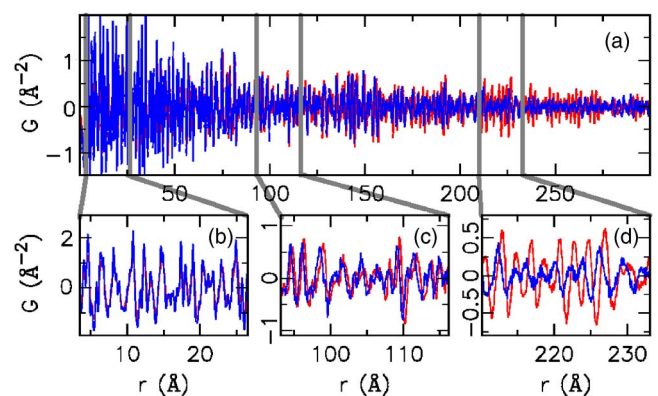


FIG. 3. (Color online) Comparison of 15 and 300 K PDFs in different r regions. (a) Comparison of low- (15 K, dark blue line) and high-temperature (300 K, light red line) neutron PDFs of Zn₄Sb₃ plotted over a wide range of r to 300 Å. (b)–(d) are the same data but plotted on expanded r scales. Note that at low r , the 300 K PDF has broader and lower peaks, but at high r the situation is reversed. PDF peaks broaden with temperature due to increased thermal motion as evident at low r (b). The PDF peaks are sharper and higher at room temperature in the high- r region (d) because the 300 K data are from the high-symmetry β phase. A rough estimate of the size of the local α domains can be obtained from where the behavior switches over (c).

in such a way that crystallographically the interstitial atoms appear in a randomly distributed way over three possible interstitial sites in the average $R\bar{3}c$ structure. However, the similarity of the local structure suggests that locally the interstitial atoms avoid each other in the β phase, resulting in short-range defect ordering that resembles the α phase. The rhombohedral β structure is incomplete as a local structure as it has atomic distances that are unphysically short. This work confirms that the actual local structure contains reasonable atomic distances (such as those in the α phase with no indication of a Zn–Zn bond⁵) and that nanoscale domains must exist. We would like to estimate the domain size, or coherence length, of this local order. At low r , the PDF is probing below this domain length scale and finds an α -like local structure; however, the PDF at high r (consistent with the average x-ray-diffraction measurements²) averages over a longer length scale and results in the different average structure of β -Zn₄Sb₃. A striking feature found in a comparison of the 300 and 15 K neutron PDFs is an inversion of the relative PDF peak heights in the region between 60 and 120 Å (Fig. 3). Below 60 Å, the PDF peaks in the 15 K data are taller than those in the 300 K data [Fig. 3(b)], as expected due to the reduced thermal motion. However, above 120 Å, the opposite is observed [Fig. 3(d)]. If there is no phase change, the PDF peaks will broaden with increasing temperature at all distances r , but this is not observed. The anomalous T dependence is explained due to the fact that at higher r the PDF reflects the higher symmetry of the β struc-

ture and higher symmetry results in sharper PDF peaks. The fact that the low- r peaks broaden with increasing temperature and do not sharpen at the phase transition is a strong evidence that the local symmetry is lower than the average symmetry. We can roughly estimate the diameter of the lower-symmetry domains from the crossover in peak-broadening behavior. The crossover happens in the region of 60–120 Å [Fig. 3(c)]. We therefore estimate the α -domain size to be of the order of, but probably somewhat less than, 10 nm, where the effects on the PDF of the higher average symmetry start to dominate. A more thorough study is necessary to estimate the exact domain size.

We have investigated the local structure of Zn₄Sb₃ using the PDF technique. The result shows that the structure of β -Zn₄Sb₃ at 300 K is composed of nanoscaled α -like domains. Like other recently developed high ZT thermoelectric materials, the exceptionally low thermal conductivity of β -Zn₄Sb₃ may be attributed to these nanoscale structural domains.

The authors gratefully acknowledge F. Gascoin, Th. Proffen, D. Robinson, D. Wermeille, X. Qiu, and A. Masadeh for experimental help and S. D. Mahanti for useful discussions. This work was supported by the NSF through Grant No. DMR-0304391. The Lujan Center, APS, and the MUCAT sector at APS are funded by DOE through Contract Nos. W-7405-ENG-36, W-31-109-ENG-38, and W-7405-ENG-82, respectively.

*Electronic address: billinge@pa.msu.edu

¹F. J. DiSalvo, *Science* **285**, 703 (1999).

²G. J. Snyder, M. Christensen, E. Nishibori, T. Caillat, and B. B. Iversen, *Nat. Mater.* **3**, 458 (2004).

³G. A. Slack, in *CRC Handbook of Thermoelectrics*, edited by D. M. Rowe (CRC, Boca Raton, FL, 1995), Chap. 34.

⁴Y. Mozharivskyj, A. O. Pecharsky, S. Bud'ko, and G. J. Miller, *Chem. Mater.* **16**, 1580 (2004).

⁵F. Cargnoni, E. Nishibori, P. Rabiller, L. Bertini, G. J. Snyder, M. Christensen, C. Gatti, and B. B. Iversen, *Chem.-Eur. J.* **10**, 3862 (2004).

⁶S. Bhattacharya, R. P. Hermann, V. Keppens, T. M. Tritt, and G. J. Snyder, *Phys. Rev. B* **74**, 134108 (2006).

⁷W. Kim, J. Zide, A. Gossard, D. Klenov, S. Stemmer, A. Shakouri, and A. Majumdar, *Phys. Rev. Lett.* **96**, 045901 (2006).

⁸K. F. Hsu, S. Loo, F. Guo, W. Chen, J. S. Dyck, C. Uher, T. Hogan, E. K. Polychroniadis, and M. G. Kanatzidis, *Science* **303**, 818 (2004).

⁹H. Lin, E. S. Božin, S. J. L. Billinge, E. Quarez, and M. G. Kanatzidis, *Phys. Rev. B* **72**, 174113 (2005).

¹⁰J. Androulakis, K. F. Hsu, R. Pcionek, H. Kong, C. Uhr, J. J. D'Angelo, A. Downey, T. Hogan, and M. G. Kanatzidis, *Adv. Mater. (Weinheim, Ger.)* **18**, 1170 (2006).

¹¹L. D. Hicks and M. S. Dresselhaus, *Phys. Rev. B* **47**, 12727

(1993).

¹²R. Venkatasubramanian, E. Siivola, T. Colpitts, and B. O'Quinn, *Nature (London)* **413**, 597 (2001).

¹³H. W. Mayer, I. Mikhail, and K. Schubert, *J. Less-Common Met.* **59**, 43 (1978).

¹⁴T. Egami and S. J. L. Billinge, *Underneath the Bragg Peaks: Structural Analysis of Complex Materials* (Pergamon, England, 2003).

¹⁵S. J. L. Billinge and M. G. Kanatzidis, *Chem. Commun. (Cambridge)* **2004** (7), 749.

¹⁶J. Nylén, M. Andersson, S. Lidin, and U. Häussermann, *J. Am. Chem. Soc.* **126**, 16306 (2004).

¹⁷A. S. Mikhaylushkin, J. Nylén, and U. Häussermann, *Chem.-Eur. J.* **11**, 4912 (2005).

¹⁸P. J. Chupas, X. Qiu, J. C. Hanson, P. L. Lee, C. P. Grey, and S. J. L. Billinge, *J. Appl. Crystallogr.* **36**, 1342 (2003).

¹⁹P. F. Peterson, M. Gutmann, T. Proffen, and S. J. L. Billinge, *J. Appl. Crystallogr.* **33**, 1192 (2000).

²⁰X. Qiu, J. W. Thompson, and S. J. L. Billinge, *J. Appl. Crystallogr.* **37**, 678 (2004).

²¹T. Proffen and S. J. L. Billinge, *J. Appl. Crystallogr.* **32**, 572 (1999).

²²B. C. Sales, B. Chakoumakos, D. Mandrus, and J. W. Sharp, *J. Solid State Chem.* **146**, 528 (1999).

Quantitative size-dependent structure and strain determination of CdSe nanoparticles using atomic pair distribution function analysis

A. S. Masadeh, E. S. Božin, C. L. Farrow, G. Paglia, P. Juhas, and S. J. L. Billinge*

Department of Physics and Astronomy, Michigan State University, East Lansing, Michigan 48824-1116, USA

A. Karkamkar and M. G. Kanatzidis

Department of Chemistry, Michigan State University, East Lansing, Michigan 48824-1116, USA

(Received 9 April 2007; revised manuscript received 3 August 2007; published 12 September 2007)

The size-dependent structure of CdSe nanoparticles, with diameters ranging from 2 to 4 nm, has been studied using the atomic pair distribution function (PDF) method. The core structure of the measured CdSe nanoparticles can be described in terms of the wurtzite atomic structure with extensive stacking faults. The density of faults in the nanoparticles is $\sim 50\%$. The diameter of the core region was extracted directly from the PDF data and is in good agreement with the diameter obtained from standard characterization methods, suggesting that there is little surface amorphous region. A compressive strain was measured in the Cd–Se bond length that increases with decreasing particle size being 0.5% with respect to bulk CdSe for the 2 nm diameter particles. This study demonstrates the size-dependent quantitative structural information that can be obtained even from very small nanoparticles using the PDF approach.

DOI: [10.1103/PhysRevB.76.115413](https://doi.org/10.1103/PhysRevB.76.115413)

PACS number(s): 61.46.Df, 61.10.–i, 78.66.Hf, 61.46.–w

I. INTRODUCTION

Semiconductor nanoparticles are of increasing interest for both applied and fundamental research. Wurtzite-structured cadmium selenide is an important II–VI semiconducting compound for optoelectronics.¹ CdSe quantum dots are the most extensively studied quantum nanostructure because of their size-tunable properties, and they have been used as a model system for investigating a wide range of nanoscale electronic, optical, optoelectronic, and chemical processes.² CdSe also provided the first example of self-assembled semiconductor nanocrystal superlattices.³ With a direct band gap of 1.8 eV, CdSe quantum dots have been used for laser diodes,⁴ nanosensing,⁵ and biomedical imaging.⁶ In fundamental research, particles with a diameter in the 1–5 nm range are of particular importance since they cover the transition regime between the bulk and molecular domains where quantum size effects play an important role. Significant deviation from bulk properties are expected for particles with diameter below 5 nm and were observed in many cases^{6,7} as well as in this study.

Accurate determination of atomic scale structure, homogeneous and inhomogeneous strain, structural defects, and geometrical particle parameters such as diameter and shape is important for understanding the fundamental mechanisms and processes in nanostructured materials. However, difficulties are experienced when standard methods are applied to small nanoparticles. In this domain, the presumption of a periodic solid, which is the basis of a crystallographic analysis, breaks down. Quantitative determinations of the nanoparticle structure require methods that go beyond crystallography. This was noted early on in a seminal study by Bawendi *et al.*⁸ where they used the Debye equation, which is not based on a crystallographic assumption, to simulate semiquantitatively the scattering from some CdSe nanoparticles. However, despite the importance of knowing the nanoparticle structure quantitatively with high accuracy, this

work has not been followed up with application of modern local structural methods^{9,10} until recently.^{11–16} In this study, we return to the archetypal CdSe nanoparticles to investigate the extent of information about the size-dependent structure of nanoparticles from the atomic pair distribution function (PDF) method. This is a local structural technique that yields quantitative structural information on the nanoscale from x-ray and neutron powder diffraction data.¹⁰ Recent developments in both data collection^{17,18} and modeling^{19,20} make this a potentially powerful tool in the study of nanoparticles. Additional extensions to the modeling are necessary for nanoparticles, and some of these have been successfully demonstrated.^{11,12,21}

In this paper, we present a detailed analysis of the structural information available from PDF data on (2–4 nm) CdSe nanoparticles. The PDF method is demonstrated here as a key tool that can yield precise structural information about the nanoparticles such as the atomic structure size of the core, the degree of crystallinity, local bonding, the degree of the internal disorder, and the atomic structure of the core region, as a function of the nanoparticle diameter. Three CdSe nanoparticle samples with different diameters that exhibit different optical spectra have been studied. The purpose of this paper is not only to explain the PDF data of CdSe nanoparticles through a modeling process but also to systematically investigate the sensitivity of the PDF data to subtle structural modifications in nanoparticles relative to the bulk material.

The measurement of the nanoparticle size can lead to significantly different results when performed by different methods, and there is no consensus as to which is the most reliable.^{22,23} It is also not clear that a single diameter is sufficient to fully specify even a spherical particle since the presence of distinct crystalline core and disordered surface regions has been postulated.⁸

Powder diffraction is a well established method for structural and analytical studies of crystalline materials, but the

applicability to such small particles of standard powder diffraction based on crystallographic methods is questionable and likely to be semiquantitative at best. Palosz *et al.*²⁴ have shown that the conventional tools developed for the elaboration of powder diffraction data are not directly applicable to nanocrystals.²⁴ There have been some reports^{8,23,25} in the past few years extracting nanoparticle diameter from x-ray diffraction (XRD) using the Scherrer formula, which is a phenomenological approach that considers the finite size broadening of Bragg peaks.²⁶ This approach will decrease in accuracy with decreasing particle size, and for particle sizes in the range of a few nanometers, the notion of a Bragg peak becomes moot.²⁴ At this point, the Debye formula²⁷ becomes the more appropriate way to calculate the scattering.⁸ The inconsistencies between the nanoparticle diameter determined from the standard characterization methods and the diameter obtained by applying the Scherrer formula have been observed by several authors.^{8,23,28}

Previous studies of CdSe nanoparticle structure have demonstrated the sensitivity of the XRD pattern to the presence of planar disorder and thermal effects due to nanosize effects.^{8,29} The diffraction patterns of CdSe nanoparticles smaller than 2.0 nm have been observed to appear markedly different from those of the larger diameters (see Ref. 29, Fig. 11), the large attenuation and broadening in the Bragg reflections in these small nanoparticles, making the distinction between wurtzite and zinc blende hard using conventional XRD methods. Murray *et al.*²⁹ reported that the combination of x-ray studies and transmission electron micrograph (TEM) imaging yields a description of the average CdSe nanoparticle structure. Strict classification of the CdSe nanoparticles structure as purely wurtzite or zinc blende is potentially misleading.²⁹ Bawendi *et al.*⁸ reported that CdSe nanoparticles are best fitted by a mixture of crystalline structures intermediate between zinc blende and wurtzite. Here, we apply the PDF method to CdSe nanoparticles and refine quantitative structural parameters to a series of CdSe nanoparticles of different sizes.

Strain in nanosystems has been observed before in different studies, as well as in this study. Using combined PDF and extended x-ray-absorption fine structure (EXAFS) methods, Gilbert *et al.*¹¹ observed a compressive strain compared to the bulk in ZnS nanocrystals. Using an electric-field-induced resonance method, Chen *et al.*³⁰ detected the enhancement of Young's modulus of ZnO nanowires along the axial direction when the diameters are decreased. Very recently, Ouyang *et al.*³¹ developed an analytical model for the size-induced strain and stiffness of a nanocrystal from the perspective of thermodynamics and a continuum medium approach. It was found theoretically that the elastic modulus increases with the inverse of crystal size and the vibration frequency is higher than that of the bulk.³¹ Experimentally, the CdQ ($Q = S, Se, Te$) first-neighbor distances have been studied using both XRD and EXAFS methods.³² The distances were found smaller than those in the bulk compounds by less than 1.0%. Herron *et al.*³³ studied CdS nanocrystals and showed a bond contraction of $\sim 0.5\%$ compared to the bulk. Carter *et al.*³⁴ studied a series of CdSe nanoparticles using the EXAFS method. In the first shell around both the Se and Cd atoms, they found essentially no change in the first-neighbor dis-

tance. Chauré *et al.*³⁵ studied the strain in nanocrystalline CdSe thin films, using Raman scattering, and observed a peak shift with a decrease in particle size, which was attributed to the increase in stress with decreasing particle size.³⁵

Local structural deviations or disorder mainly affect the diffuse scattering background. The XRD experiments probe for the presence of periodic structure, which are reflected in the Bragg peaks. In order to have information about both long-range order and local-structure disorder, a technique that takes both the Bragg and the diffuse scattering need to be used, such as the PDF technique. Here, we apply the PDF method to study the structure, size, and strain in CdSe nanoparticles as a function of nanoparticle diameter. The core structure of the CdSe nanoparticles can be described by a mixture of crystalline structures intermediate between zinc blende and wurtzite, which is wurtzite containing a stacking fault density (SFD) of up to $\sim 50\%$, with no clear evidence of a disordered surface region, certainly down to 3 nm diameter. The structural parameters are reported quantitatively. We measure a size-dependent strain on the Cd-Se bond which reaches 0.5% at the smallest particle size. The size of the well-ordered core extracted directly from the data agrees with the size determined from other methods.

II. EXPERIMENTAL DETAILS

A. Sample preparation

CdSe nanoparticles were synthesized from cadmium acetate, selenium, trioctyl phosphine, and trioctyl phosphine oxide. 64 g of trioctylphosphine oxide (TOPO) containing cadmium acetate was heated to 360 °C under flowing argon. Cold stock solution (38.4 ml) of (Se:trioctylphosphine = 2:100 by mass) was quickly injected into the rapidly stirred, hot TOPO solution. The temperature was lowered to 300 °C by the injection. At various time intervals, 5–10 ml aliquots of the reaction mixture were removed and precipitated in 10 ml of methanol. The color of the sample changed from bright yellow to orange to red to brown with a time interval variation from 20 to 1200 s. Three nanoparticle sizes, CdSe I (small), CdSe II (medium), and CdSe III (large), were used for this study, as well as a bulk CdSe sample for reference.

The samples were further purified by dissolving and centrifuging in methanol to remove excess TOPO. This process also resulted in a narrower particle size distribution. The TEM images (Fig. 1) show uniformly sized nanoparticles with no signs of aggregation. The ultraviolet visible (UV-vis) absorption and photoluminescence (PL) spectra of the aliquots were recorded by redissolving the nanocrystals in toluene. The spectra are shown in Fig. 2.

The band-gap values obtained for the measured samples can be correlated with the diameter of the nanoparticles based on the table provided in the supplementary information of Peng *et al.*³⁶ using the data on exciton peaks measured with UV-vis light absorption and photoluminescence peaks. The particle sizes were measured by TEM as well. The measured values of particle diameter using these various methods are summarized in Table I.

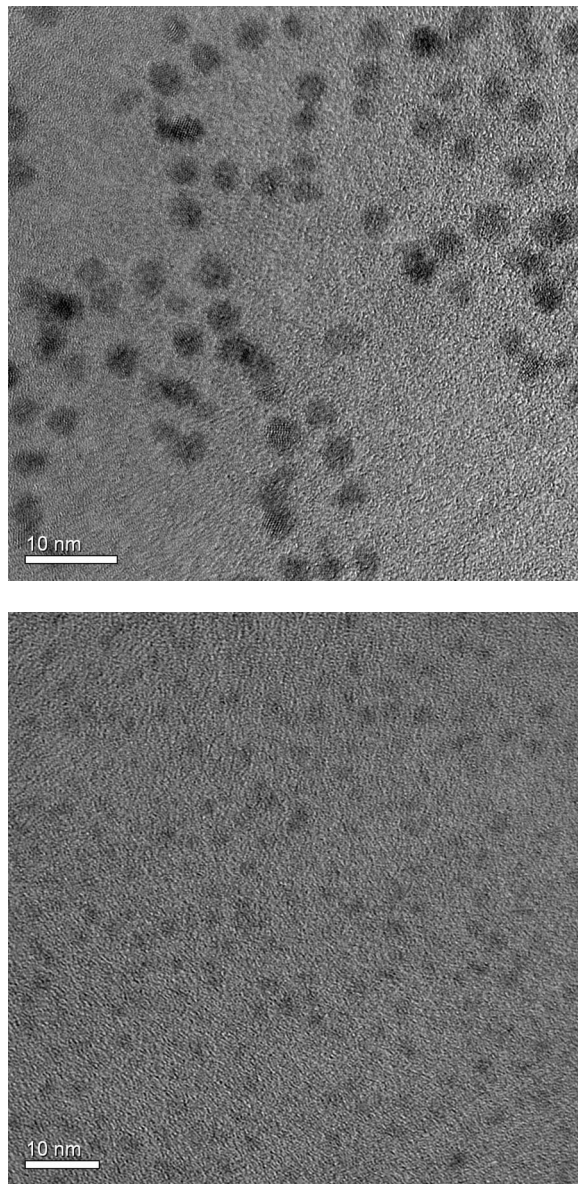


FIG. 1. TEM image of CdSe nanocrystal prepared using the method described in the text. CdSe obtained by 1200 s (top) and 15 s (bottom) nucleation. The line bar is 10 nm in size in both images.

B. Atomic Pair distribution function method

The atomic PDF analysis of x-ray and neutron powder diffraction data is a powerful method for studying the structure of nanostructured materials.^{9,10,37–40} Recently, it has been explicitly applied to study the structure of discrete nanoparticles.^{11,12,40–42} The PDF method can yield precise structural and size information, provided that special care is applied to the measurement and to the method used for analyzing the data. The atomic PDF $G(r)$ is defined as

$$G(r) = 4\pi r[\rho(r) - \rho_0], \quad (1)$$

where $\rho(r)$ is the atomic pair density, ρ_0 is the average atomic number density, and r is the radial distance.⁴³ The

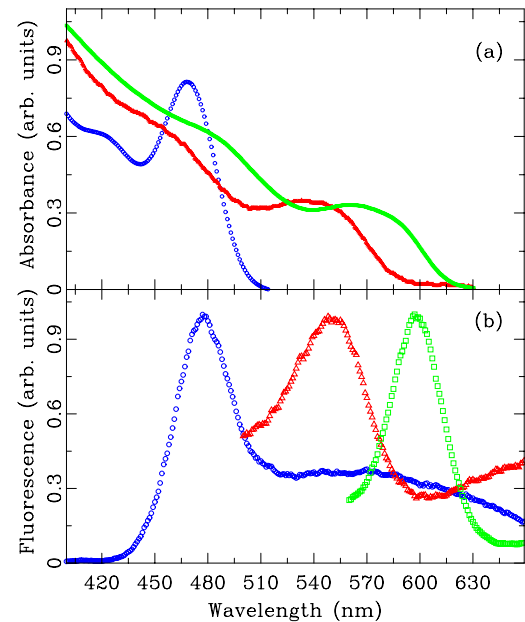


FIG. 2. (Color online) (a) Room temperature UV-vis absorption and (b) photoluminescence spectra from the sample of CdSe nanocrystals: (○) CdSe I, (△) CdSe II, and (□) CdSe III.

PDF yields the probability of finding pairs of atoms separated by a distance r . It is obtained by a sine Fourier transformation of the reciprocal space total scattering structure function $S(Q)$, according to

$$G(r) = \frac{2}{\pi} \int_0^{\infty} Q[S(Q) - 1] \sin QrdQ, \quad (2)$$

where $S(Q)$ is obtained from a diffraction experiment. This approach is widely used for studying liquids and amorphous and crystalline materials but has recently also been successfully applied to nanocrystalline materials.¹⁰

C. High-energy x-ray diffraction experiments

X-ray powder diffraction experiments to obtain the PDF were performed at the 6IDD beamline at the Advanced Photon Source at Argonne National Laboratory. Diffraction data were collected using the recently developed rapid acquisition pair distribution function (RAPDF) technique¹⁷ that benefits from two-dimensional (2D) data collection. Unlike TEM,

TABLE I. CdSe nanoparticle diameter as determined using various methods.

	CdSe III	CdSe II	CdSe I
Nucleation time (s)	1200	630	15
Diameter (nm)			
TEM	3.5(2)	2.7(2)	2.0(2)
UV-vis	3.5(4)	2.9(3)	≤1.90
PL	3.6(4)	2.9(3)	≤2.1
PDF	3.7(1)	3.1(1)	2.2(2)

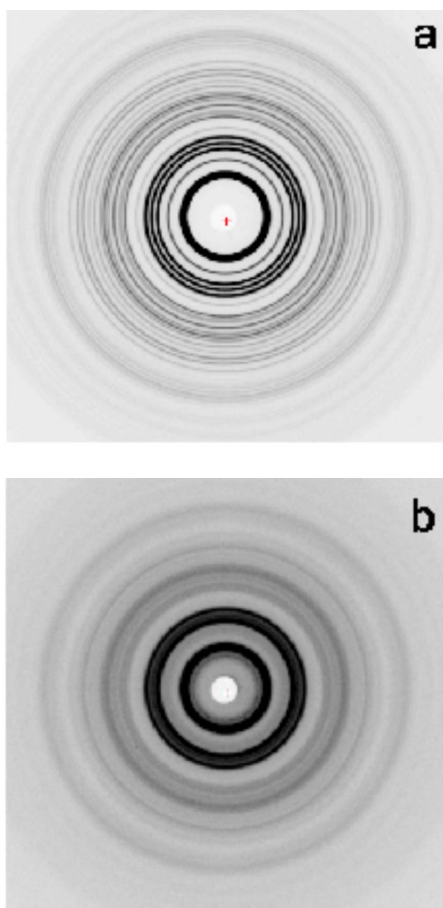


FIG. 3. (Color online) Two-dimensional XRD raw data collected using the image plate detector from (a) CdSe bulk and (b) nanoparticle CdSe III samples.

XRD probes a large number of crystallites that are randomly oriented. The powder samples were packed in a flat plate with thickness of 1.0 mm sealed between Kapton tapes. Data were collected at room temperature with an x-ray energy of 87.005 keV ($\lambda=0.14248$ Å). An image plate camera (Mar345) with a diameter of 345 mm was mounted orthogonally to the beam path with a sample to detector distance of 208.857 mm, as calibrated by using a silicon standard sample.¹⁷ The image plate was exposed for 10 s and this was repeated five times for a total data collection time of 50 s. The RAPDF approach avoids detector saturation while allowing sufficient statistics to be obtained. This approach also avoids sample degradation in the beam that was observed for the TOPO coated nanoparticles during longer exposures, on the scale of hours, that were required using conventional point-detector approaches. To reduce the background scattering, lead shielding was placed before the sample with a small opening for the incident beam.

Examples of the raw 2D data are shown in Fig. 3. These data were integrated and converted to intensity versus 2θ using the software FIT2D,⁴⁴ where 2θ is the angle between the incident and scattered x-ray beams. The integrated data were normalized by the average monitor counts. The data were corrected and normalized⁹ using the program PDFGETX2 (Ref.

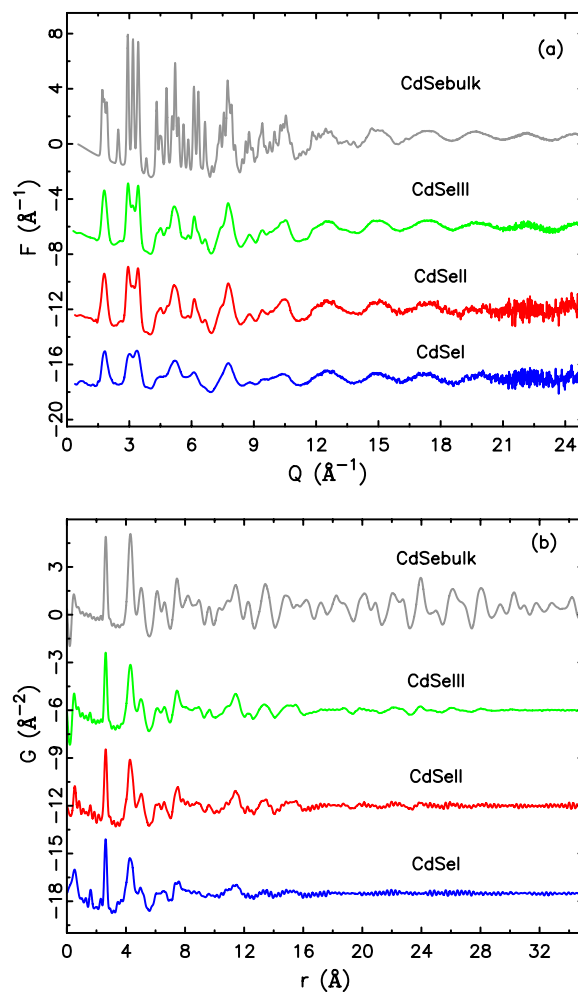


FIG. 4. (Color online) (a) The experimental reduced structure function $F(Q)$ of CdSe nanoparticle with different diameters and (b) the corresponding PDF $G(r)$ obtained by Fourier transformation of the data in (a) with $Q_{max}=25.0$ Å⁻¹, from top to bottom: bulk, CdSe III, CdSe II, and CdSe I.

45) to obtain the total scattering structure function $S(Q)$ and the PDF $G(r)$, which are shown in Figs. 4(a) and 4(b), respectively. The scattering signal from the surfactant (TOPO) was measured independently and subtracted as a background in the data reduction.

In the Fourier transform step to get from $S(Q)$ to the PDF $G(r)$, the data are truncated at a finite maximum value of the momentum transfer, $Q=Q_{max}$. Different values of Q_{max} may be chosen. Here, a $Q_{max}=25.0$ Å⁻¹ was found to be optimal. Q_{max} is optimized such as to avoid large termination effects and to reasonably minimize the introduced noise level as the signal to noise ratio decreases with the Q value.

Structural information was extracted from the PDFs using a full-profile real-space local-structure refinement method⁴⁶ analogous to Rietveld refinement.⁴⁷ We used an updated version⁴⁸ of the program PDFFIT (Ref. 19) to fit the experimental PDFs. Starting from a given structure model and given a set of parameters to be refined, PDFFIT searches for the best structure that is consistent with the experimental PDF data. The residual function (R_w) is used to quantify the

agreement of the calculated PDF from model to experimental data,

$$R_w = \sqrt{\frac{\sum_{i=1}^N \omega(r_i) [G_{obs}(r_i) - G_{calc}(r_i)]^2}{\sum_{i=1}^N \omega(r_i) G_{obs}^2(r_i)}}. \quad (3)$$

Here, the weight $\omega(r_i)$ is set to unity which is justified because in $G(r)$, the statistical uncertainty on each point is approximately equal.^{49,50}

The structural parameters of the model were unit cell parameters, anisotropic atomic displacement parameters (ADPs), and the fractional coordinate z of the Se and/or Cd atom. Nonstructural parameters that were refined were a correction for the finite instrumental resolution (σ_Q), low- r correlated motion peak sharpening factor (δ),^{51,52} and scale factor. When estimating the particle size, a new version of the fitting program with particle size effects included as a refinable parameter⁵³ was used. The sample resolution broadening was determined from a refinement to the crystalline CdSe and the silicon standard sample and fixed, and the particle diameter refined, as described below. Good agreement between these results was obtained.

III. RESULTS AND DISCUSSION

The reduced structure functions for the bulk and nanocrystalline samples are shown plotted over a wide range of Q in Fig 4(a). All of the patterns show significant intensity up to the highest values of Q , highlighting the value of measured data over such a wide Q range. All of the diffraction patterns have peaks in similar positions reflecting the similarity of the basic structures, but as the nanoparticles get smaller, the diffraction features become broadened out due to finite size effects.²⁶

The PDFs are shown in Fig. 4(b). What is apparent is that, in real space, the PDF features at low r are comparably sharp in all the samples. The finite size effects do not broaden features in real space. The finite particle size is evident in a falloff in the intensity of structural features with increasing r . Later, we will use this to extract the average particle size in the material. The structure apparent in the $G(r)$ function comes from the atomic order within the nanoparticle. The value of r where these ripples disappear indicates the particle core region diameter, or at least the diameter of any coherent structural core of the nanoparticle. By direct observation (Fig. 9), we can put a lower limit on the particle diameters to be 3.6, 2.8, and 1.6 nm for CdSe III, II and I, respectively, where the ripples can be seen to die out by visual inspection. These numbers will be quantified more accurately later.

A. Nanoparticle structure

Features in the PDF at low r reflect the internal structure of the nanoparticles. The nanoparticle PDFs have almost the same features as in the bulk in the region below 8.0 Å, reflecting the fact that they share a similar atomic structure on

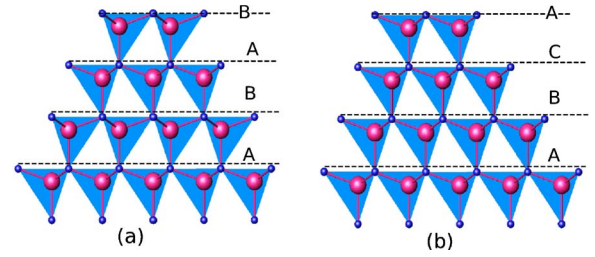


FIG. 5. (Color online) Fragments from the (a) wurtzite structure, space group ($P6_3mc$) and (b) zinc-blende structure, space group ($F\bar{4}3m$).

average. In the finite nano-size regime, local structural deviations from the average bulk structure are expected.

A large number of semiconductor alloys, especially some sulfides and selenides, do not crystallize in the cubic zinc-blende structure but in the hexagonal wurtzite structure.⁵⁴ Both wurtzite and zinc-blende structures are based on the stacking of identical two-dimensional planar units translated with respect to each other, in which each atom is tetrahedrally coordinated with four nearest neighbors. The layer stacking is described as $ABABAB\dots$ along the $[001]$ axis for wurtzite and as $ABCABC\dots$ along the $[111]$ axis for zinc blende. As can be seen in Fig. 5, each cadmium and selenium are tetrahedrally coordinated in both structures. However, the next nearest and more distant coordination sequences are different in the two structures.

The largest changes in structure are expected in the smallest nanoparticles. In these small nanoparticles, the proportion of atoms on the surface is large, making the notion of a well-ordered crystalline core moot. The fractions of atoms involved in the surface atoms were estimated as 0.6, 0.45, and 0.35 for 2, 3, and 4 nm nanoparticle diameters, respectively. This was estimated by taking different spherical cuts from the bulk structure, then counting the atom with coordination number 4 as the core atom and the one with less than 4 as the surface atom. For the smallest particles, the small number of atoms in the core makes it difficult to define a core crystal structure, making the distinction between wurtzite and zinc blende difficult using the conventional XRD methods as the nanoparticle size decreases.²⁹ The principle difference between these structures is the topology of the CdSe_4 connections, which may also be becoming defective in the small nanoparticles.

Two structure models, wurtzite (space group $P6_3mc$) and zinc blende (space group $F\bar{4}3m$), were fit to the PDF data. The results of the full-profile fitting to the PDF data are shown in Fig. 6. In this figure, we compare fits to the (a) wurtzite and (b) zinc-blende structure models using isotropic atomic displacement factors (U_{iso}) in both models. The wurtzite structure gives superior fits for the bulk structure. However, for all the nanoparticle sizes, the fits of wurtzite and zinc blende are comparable as evident from the difference curves in Fig. 6 and the R_w values reported in Table II. This indicates that classification of the CdSe nanoparticle structure as purely wurtzite or zinc blende is misleading²⁹ and it is better described as being intermediate between the two structures, as has been reported earlier.⁸

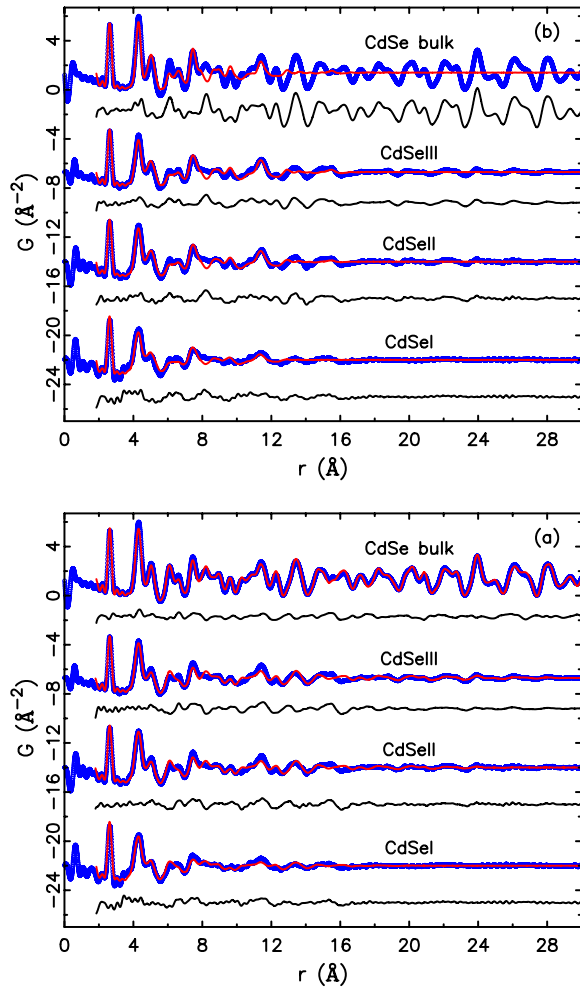


FIG. 6. (Color online) The experimental PDF $G(r)$ with $Q_{max} = 19.0 \text{ \AA}^{-1}$ (blue solid dots) and the calculated PDF from the refined structural model (red solid line), with the difference curve offset below (black solid line). PDF data are fitted using (a) the wurtzite structure model with space group $P6_3mc$ and (b) the zinc-blende model with space group $F\bar{4}3m$. In both models, isotropic atomic displacement factors (U_{iso}) are used.

Introducing anisotropic ADPs ($U_{11}=U_{22}\neq U_{33}$) into the wurtzite model resulted in better fits to the data. The refined parameters are reproduced in Table III and the fits are shown in Fig. 7(a). The values for the nanoparticles are rather close to the values in the bulk wurtzite structure. The model with anisotropic ADPs resulted in lower R_w . There is a general increase in the ADPs with decreasing particle size. This re-

TABLE II. The refined residual (R_w) values obtained from PDF analysis assuming the wurtzite and zinc blende structure models with space groups $P6_3mc$ and $F\bar{4}3m$, respectively. In both models, isotropic atomic displacement factors (U_{iso}) are used.

	CdSe bulk	CdSe III	CdSe II	CdSe I
Wurtzite (R_w)	0.16	0.31	0.28	0.31
Zinc blende (R_w)	0.52	0.32	0.30	0.35

fects the inhomogeneous strain accommodation in the nanoparticles, as we will discuss below. However, the values of the ADPs along the z direction for Se atoms (U_{33}) are four times larger in the nanoparticles compared with the bulk where they are already unphysically large. The fact that this parameter is large on the Se site and small on the Cd site is not significant since we can change the origin of the unit cell to place a Cd ion at the $(1/3, 2/3, z)$ position and the enlarged U_{33} shifts to the Cd site in this case.

The unphysically large U_{33} value on the Se site is likely to be due to the presence of faults in the basal plane stacking. For example, similar unphysical enlargements of perpendicular thermal factors in PDF measurements are explained by the presence of turbostratic disorder in layered carbons,⁵⁵ which is a similar effect to faults in the $ABABAB$ wurtzite stacking. Also, the presence of stacking faults in the nanoparticles has been noted previously.⁸ It is noteworthy that this parameter is enlarged in EXAFS analyses of bulk wurtzite structures, probably for the same reason.^{32,56,57} We suspect that the enlargement in this parameter (U_{33}) is related to the stacking fault density present in the bulk and that is increasing in the nanoparticles.

To test this idea, we simulated PDF data using the wurtzite structure containing different stacking fault densities. The stacking faults were simulated for different densities (0.167, 0.25, 0.333, and 0.5) by creating wurtzite superlattices with different stacking sequences along the C axis. The program DISCUS (Ref. 58) was used to create the stacking fault models and PDFGUI (Ref. 48) was used to generate the corresponding PDFs. The PDFs were simulated with all the ADPs fixed at $U_{ii}=0.0133 \text{ \AA}^2$, the value observed in the experimental bulk data collected at room temperature (see Table III).

To see if this results in enlarged U_{33} values, we refined the simulated data containing stacking faults using the wurtzite model without any stacking faults. Indeed, the refined Se site U_{33} increased monotonically with increasing stacking fault density. The results are plotted in Fig. 8.

Figure 8 can be considered as a calibration curve of stacking fault density in the wurtzite structure, based on the enlargement in the ADPs along the z direction U_{33} . From this, we can estimate a stacking fault density of $\sim 35\%$ for our bulk CdSe sample and $\sim 50\%$ for each of the nanoparticles.

It is then possible to carry out a refinement using a structural model that contains an appropriate stacking fault density. The PDF data of bulk CdSe were therefore fitted with a wurtzite model with a 33% density, and the nanoparticle PDF fitted with a model with 50% of stacking faults. The refinements give excellent fits, as is evident in Fig. 7(b). The results are presented in Table III. The enlarged U_{33} parameter on the Se site is no longer present and it is now possible to refine physically reasonable values for that parameter. As well as resulting in physically reasonable ADPs, the quality of the fits to the data is excellent, though the R_w value is slightly larger in the nanoparticles.

Attempts to characterize the structure changes using direct measurements such as TEM technique for such small CdSe nanoparticles⁵⁹ were unsuccessful due to the poor contrast. However, in the present study, we were successful in exploring the local atomic structure for CdSe nanoparticles, in real space, at different length scales. The PDF fits clearly

TABLE III. The refined parameter values obtained from PDF analysis assuming the wurtzite structure, space group $P6_3mc$, with different stacking fault densities (SFDs).

Stacking fault density (%)	CdSe bulk		CdSe III		CdSe II		CdSe I	
	0.0	33.0	0.0	50.0	0.0	50.0	0.0	50.0
a (Å)	4.3014(4)	4.3012(4)	4.2997(9)	4.2987(9)	4.3028(9)	4.3015(9)	4.2930(9)	4.2930(8)
c (Å)	7.0146(9)	7.0123(9)	7.0145(4)	7.0123(4)	6.9987(9)	6.9975(9)	6.9405(9)	6.9405(7)
Se Z-frac.	0.3774(3)	0.3771(3)	0.3761(9)	0.3759(9)	0.3751(6)	0.3747(6)	0.3685(9)	0.3694(9)
Cd $U_{11}=U_{22}$ (Å ²)	0.0108(2)	0.0102(2)	0.0146(7)	0.0149(7)	0.0149(6)	0.0112(5)	0.0237(9)	0.0213(8)
U_{33} (Å ²)	0.0113(3)	0.0112(3)	0.0262(9)	0.0241(9)	0.0274(9)	0.0271(9)	0.0261(9)	0.0281(9)
Se $U_{11}=U_{22}$ (Å ²)	0.0109(9)	0.0102(9)	0.0077(7)	0.0138(7)	0.0083(7)	0.0121(7)	0.0110(9)	0.0191(9)
U_{33} (Å ²)	0.0462(9)	0.0115(9)	0.1501(9)	0.02301(9)	0.1628(9)	0.0265(9)	0.1765(9)	0.0311(9)
NP ^a diameter (nm)	∞	∞	3.7(1)	3.7(1)	3.1(1)	3.1(1)	2.4(2)	2.2(2)
R_w	0.12	0.09	0.20	0.14	0.18	0.15	0.27	0.21

^aNP refers to nanoparticle.

indicate that the structure can be described in terms of locally distorted wurtzite structure containing $\sim 50\%$ stacking fault density (i.e., intermediate between wurtzite and zinc blende) even for the 2 nm diameter particles, Fig. 7.

Interestingly, there is little evidence in our data for a significant surface modified region. This surface region is sometimes thought of as being an amorphouslike region. Amorphous structures appear in the PDF with sharp first-neighbor peaks but rapidly diminish and broaden higher neighbor peaks. Thus, in the presence of a surface amorphous region, we might expect to see extra intensity at the first-peak position when the wurtzite model is scaled to fit the higher- r features coming just from the crystalline core. As evident in Fig. 7, this is not observed. Furthermore, as we will describe below, the diameter of the crystalline core that we refine from the PDF agrees well with other estimates of nanoparticle size, suggesting that there is no surface amorphous region in these nanoparticles. The good agreement in the intensity of the first PDF peak also presents a puzzle in the opposite direction since we might expect surface atoms to be undercoordinated, which would result in a decrease in the intensity of this peak. It is possible that the competing effects of surface amorphous behavior and surface under coordination perfectly balance each other out, and this cannot be ruled out, though it seems unlikely that it would work perfectly at all nanoparticle diameters. This is also not supported by the nanoparticle size determinations described below.

B. Nanoparticle size

We describe here how we extracted more accurate nanoparticle diameters. This determination is important since the physical properties are size dependent. It is also important to use complementary techniques to determine particle size as different techniques are more dependent on different aspects of the nanoparticle structure, for example, whether or not the technique is sensitive to any amorphous surface layer on the nanoparticle. More challenges are expected in accurate size determination as the nanoparticle diameter decreases, due to poor contrast near the surface of the nanoparticle.

In the literature, CdSe nanoparticles with a diameter of 2.0 nm have been considered to be an especially stable size with an associated band edge absorption centered at 414 nm,⁶⁰ that size was observed earlier^{29,61} with an estimated diameter of ≤ 2.0 nm. There are some reported difficulties in determining the diameter of such small CdSe nanoparticles. Attempts to characterize the structure changes by TEM and x-ray diffraction techniques⁵⁹ were unsuccessful due to the small diameter of the particles relative to the capping material.

If we assume the nanoparticle to have a spherical shape (a reasonable approximation based on the TEM in Fig. 1) cut from the bulk, then the measured PDF will look like the PDF of the bulk material that has been attenuated by an envelope function given by the PDF of a homogeneous sphere as follows:⁶²

$$G(r, d)_s = G(r)f(r, d), \quad (4)$$

where $G(r)$ is given in Eq. (1) and $f(r, d)$ is a sphere envelope function given by

$$f(r, d) = \left[1 - \frac{3r}{2d} + \frac{1}{2} \left(\frac{r}{d} \right)^3 \right] \Theta(d - r), \quad (5)$$

where d is the diameter of the homogeneous sphere and $\Theta(x)$ is the Heaviside step function, which is equal to 0 for negative x and 1 for positive.

The approach is as follows. First, we refine the bulk CdSe data using PDFFIT. This gives us a measure of the PDF intensity falloff due to the finite resolution of the measurement.⁹ Then, the measured value of the finite resolution was kept as an unrefined parameter after that, while all the other structural and nonstructural parameters were refined. To measure the PDF intensity falloff due to the finite particle size, the refined PDF is attenuated, during the refinement, by the envelope function [Eq. (5)], which has one refined parameter, the particle diameter. The fitted results are shown in Fig. 9 and the resulting values of particle diameter from the PDF refinement are recorded in Table I. The insets show the calculated and measured PDFs on an expanded scale. The ac-

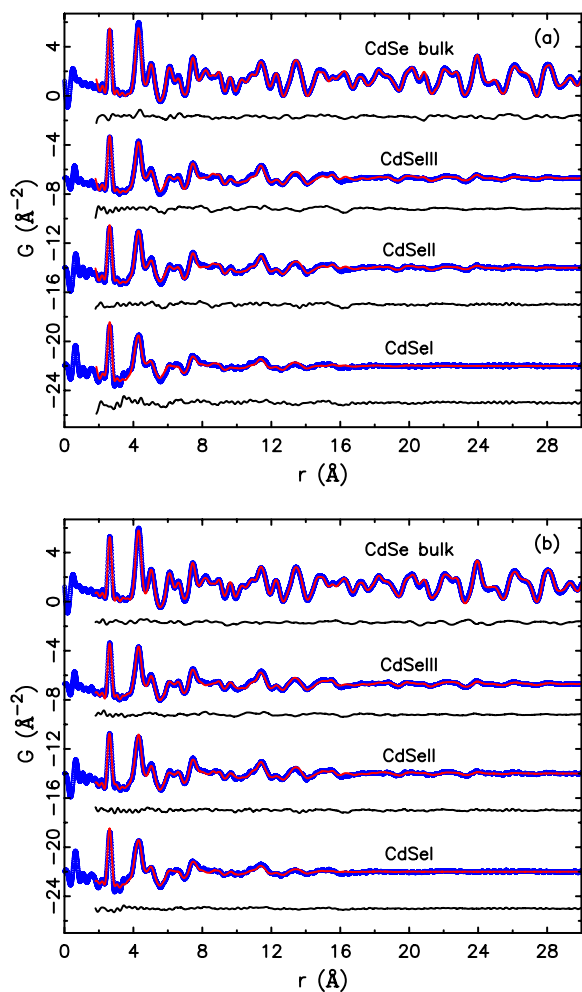


FIG. 7. (Color online) The experimental PDF $G(r)$ with $Q_{max} = 19.0 \text{ \AA}^{-1}$ (blue solid dots) and the calculated PDF from the refined structural model (red solid line), with the difference curve offset below (black solid line). PDF data are fitted using the wurtzite structure model (a) with no stacking fault and (b) with 33% stacking fault density for bulk and 50% for all nanoparticle sizes. In both cases, anisotropic atomic displacement factors (U_{aniso}) are used.

accuracy of determining the nanoparticle size can be evaluated directly from this figure. Features in the measured PDFs that correspond to the wurtzite structure are clearly seen disappearing smoothly attenuated by the spherical PDF envelope function. The procedure is least successful in the smallest nanoparticles, where the spherical particle approximation on the model results in features that extend beyond those in the data. In this case, the spherical approximation may not be working so well.

The particle diameters determined from the PDF are consistent with those obtained from TEM, UV-vis, and photoluminescence measurements. In particular, an accurate determination of the average diameter of the smallest particles is possible in the region where UV-vis and photoluminescence measurements lose their sensitivity.²³ In this analysis, we have not considered particle size distributions, which are small in these materials. The good agreement between the data and the fits justify this, though some of the differences

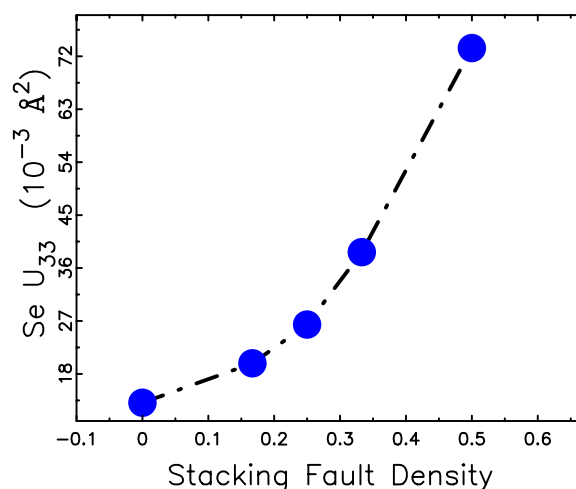


FIG. 8. (Color online) The enlargement in the ADPs along the z direction for Se site U_{33} , as a function of the stacking fault density.

at high r may result from this and could contribute an error to the particle size. Several additional fits to the data were performed to test the sphericity of the nanoparticles. Attempts were made to fit the PDF with oblate and prolate spheroid nanoparticle form factors. These fits resulted in ellipticities very close to 1, and large uncertainties in the refined ellipticity and particle diameters, which suggests that the fits are over parametrized. Another series of fits attempted to profile the PDF with a log-normal distribution of spherical nanoparticles. Allowing the mean nanoparticle diameter and log-normal width to vary resulted in nonconvergent fits, which implies that the particle sizes are not log-normal distributed. Therefore, there appears to be little evidence for significant ellipticity, nor a significant particle size distribution, as fits assuming undistributed spherical particles give the best results.

The simple fitting of a wurtzite structure with $\sim 50\%$ SFD to the data will result in an estimate of the coherent structural core of the nanoparticle that has a structure which can be described by a mixture of crystalline structures intermediate between zinc blende and wurtzite. Comparing the nanoparticle core diameter extracted from PDF analysis with the diameter determined from the standard characterization methods yields information about the existence of a surface amorphous region. The agreement between the core diameter extracted from PDF and that determined from the standard methods (Table I) indicates that within our measurement uncertainties, there is no significant heavily disordered surface region in these nanoparticles, even at the smallest diameter of 2 nm (Fig. 9). In contrast with ZnS nanoparticles,¹¹ the heavily disordered surface region is about 40% of the nanoparticle diameter for a diameter of 3.4 nm, the surface region thickness being around 1.4 nm.¹¹

C. Internal strain

The local bonding of the tetrahedral Cd-Se building unit was investigated vs nanoparticle diameter. The nearest neighbor peaks at $r=2.6353(3) \text{ \AA}$ come from covalently bonded

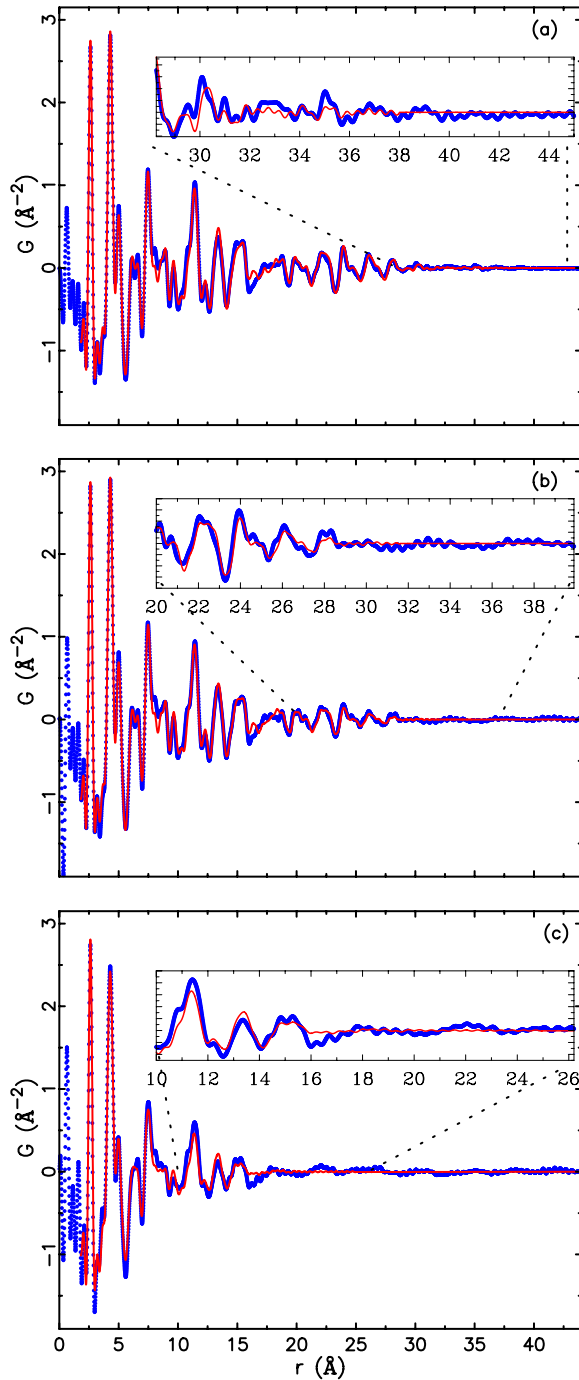


FIG. 9. (Color online) The experimental PDF $G(r)$ shown as solid dots. Sphere envelope function [Eq. (5)] is used to transform the calculated PDF of bulk CdSe, using wurtzite structure containing 50% stacking fault density, to give a best fit replication of the PDF of CdSe nanoparticles (red solid line). The inset shows an expanded scale for the high- r region of experimental $G(r)$ on the top of simulated PDF data for different diameters of CdSe nanoparticles (solid line): (a) CdSe III, (b) CdSe II, (c) CdSe I. Dashed lines are guides for the eyes.

Cd-Se pairs. The positions and the width of these peaks have been determined by fitting a Gaussian [Fig. 10(a)] and the results presented in Table IV. The results indicate that there

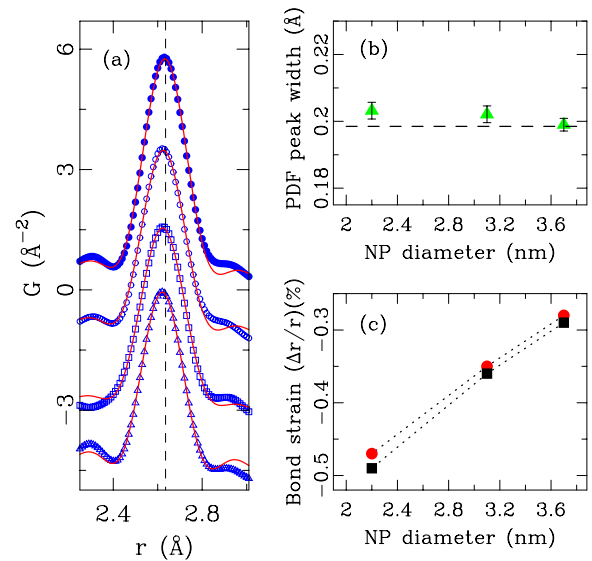


FIG. 10. (Color online) (a) The first PDF peak, (●) bulk, (○) CdSe III, (□) CdSe II, and (△) CdSe I fitted with one Gaussian (—). Dashed line represents the position of first PDF peak in the bulk data. (b)(▲) The first PDF peak width vs nanoparticle size obtained from one Gaussian fit. Dashed line represents the width of first PDF peak in the bulk data. (c) Strain in Cd-Se bond ($\Delta r/r$) (%) vs nanoparticle size. (■) Bond values obtained from the local-structure fitting and (●) obtained from one Gaussian fit to the first PDF peak. Dotted curves are guides for the eyes.

is a significant compressive strain on this near-neighbor bond length, and it is possible to measure it with the PDF with high accuracy. The bond length of Cd-Se pairs shorten as the nanoparticle diameter decreases, suggesting the presence of an internal stress in the nanoparticles. The Cd-Se bond lengths extracted from the PDF structural refinement are also in good agreement with those obtained from the first-peak Gaussian fit, as shown in Fig. 10(c). Thus, we have a model independent and a model dependent estimate of the strain that are in quantitative agreement. The widths of the first PDF peaks have also been extracted vs nanoparticle diameter from the Gaussian fits (Table IV). They remain comparably sharp as the nanoparticles get smaller, as shown in Fig. 10(b). Apparently, there is no size-dependent inhomogeneous strain measurable on the first peak. However, peaks at higher r do indicate significant broadening [Fig. 4(b)], suggesting that there is some relaxation taking place through bond bending. This is reflected in enlarged thermal factors that are refined in the nanoparticle samples. This is similar to what is observed in semiconductor alloys where most of the structural relaxation takes place in relatively lower energy bond-bending distortions.^{63,64}

TABLE IV. The first PDF peak position (FPP) and width (FPW) for different CdSe nanoparticle sizes and the bulk.

	CdSe bulk	CdSe III	CdSe II	CdSe I
PDF FPP (Å)	2.6353(3)	2.6281(3)	2.6262(3)	2.6233(3)
PDF FPW (Å)	0.1985(09)	0.1990(19)	0.2021(25)	0.2032(25)

IV. CONCLUSION

The PDF is used to address the size and structural characterization of a series of CdSe nanoparticles prepared by the method mentioned in the text. The core structure of the measured CdSe nanoparticles was found to possess a well-defined atomic arrangement that can be described in terms of locally disordered wurtzite structure that contains $\sim 50\%$ stacking fault density, and quantitative structural parameters are presented.

The diameter of the CdSe nanoparticles was extracted from the PDF data and is in good agreement with the diameter obtained from standard characterization methods, indicating that within our measurement uncertainties, there is no significant heavily disordered surface region in these nanoparticles, even at the smallest diameter of 2 nm. In contrast with ZnS nanoparticles,¹¹ the heavily disordered surface region is about 40% of the nanoparticle diameter for a diameter of 3.4 nm, the surface region thickness being around 1.4 nm.¹¹

Compared with the bulk PDF, the nanoparticle PDF peaks are broader in the high- r region due to strain and structural defects in the nanoparticles. The nearest neighbor peaks at

$r=2.6353(3)$ Å which come from covalently bonded Cd-Se pairs shorten as the nanoparticle diameter decreases, resulting in a size-dependent strain on the Cd-Se bond that reaches 0.5% at the smallest particle size.

ACKNOWLEDGMENTS

We would like to acknowledge help from Didier Wermeille, Doug Robinson, Mouath Shatnawi, Moneeb Shatnawi, and He Lin for help in collecting data. We are grateful to Christos Malliakas for the valuable assistance with the transmission electron microscopy. Many thanks to Hyun-Jeong Kim for useful discussion. We are grateful to Reinhard Neder for the valuable help with the stacking fault simulation. This work was supported in part by National Science Foundation (NSF) Grant No. DMR-0304391. Data were collected at the 6IDD beamline of the MUCAT sector at the Advanced Photon Source (APS). Use of the APS is supported by the U.S. DOE, Office of Science, Office of Basic Energy Sciences, under Contract No. W-31-109-Eng-38. The MUCAT sector at the APS is supported by the U.S. DOE, Office of Science, Office of Basic Energy Sciences, through the Ames Laboratory under Contract No. W-7405-Eng-82.

*billinge@pa.msu.edu

¹G. Hodes, A. Albu-Yaron, F. Decker, and P. Motisuke, *Phys. Rev. B* **36**, 4215 (1987).

²S. H. Tolbert and P. A. Alivisatos, *Science* **265**, 373 (1994).

³C. B. Murray, C. R. Kagan, and M. G. Bawendi, *Science* **270**, 1335 (1995).

⁴V. L. Colvin, M. C. Schlamp, and A. P. Alivisatos, *Nature (London)* **370**, 354 (1994).

⁵P. T. Tran, E. R. Goldman, G. P. Anderson, J. M. Mauro, and H. Mattoussi, *Phys. Status Solidi B* **229**, 427 (2002).

⁶M. Bruchez, M. Moronne, P. Gin, S. Weiss, and A. P. Alivisatos, *Science* **281**, 2013 (1998).

⁷L. S. Li and A. P. Alivisatos, *Phys. Rev. Lett.* **90**, 097402 (2003).

⁸M. G. Bawendi, A. R. Kortan, M. L. Steigerwald, and L. E. Brus, *J. Chem. Phys.* **91**, 7282 (1989).

⁹T. Egami and S. J. L. Billinge, *Underneath the Bragg Peaks: Structural Analysis of Complex Materials* (Pergamon, New York/Elsevier, Oxford, 2003).

¹⁰S. J. L. Billinge and M. G. Kanatzidis, *Chem. Commun. (Cambridge)* **2004**, 749.

¹¹B. Gilbert, F. Huang, H. Zhang, G. A. Waychunas, and J. F. Banfield, *Science* **305**, 651 (2004).

¹²R. B. Neder and V. I. Korsunskiy, *J. Phys.: Condens. Matter* **17**, S125 (2005).

¹³R. C. Howell, T. Proffen, and S. D. Conradson, *Phys. Rev. B* **73**, 094107 (2006).

¹⁴K. Page, T. Proffen, H. Terrones, M. Terrones, L. Lee, Y. Yang, S. Stemmer, R. Seshadri, and A. K. Cheetham, *Chem. Phys. Lett.* **393**, 385 (2004).

¹⁵V. Petkov, M. Gateshki, J. Choi, E. G. Gillan, and Y. Ren, *J. Mater. Chem.* **15**, 4654 (2005).

¹⁶M. Gateshki, V. Petkov, G. Williams, S. K. Pradhan, and Y. Ren,

Phys. Rev. B **71**, 224107 (2005).

¹⁷P. J. Chupas, X. Qiu, J. C. Hanson, P. L. Lee, C. P. Grey, and S. J. L. Billinge, *J. Appl. Crystallogr.* **36**, 1342 (2003).

¹⁸T. Proffen, T. Egami, S. J. L. Billinge, A. K. Cheetham, D. Louca, and J. B. Parise, *Appl. Phys. A: Mater. Sci. Process.* **74**, s163 (2002).

¹⁹T. Proffen and S. J. L. Billinge, *J. Appl. Crystallogr.* **32**, 572 (1999).

²⁰M. G. Tucker, M. P. Squires, M. T. Dove, and D. A. Keen, *J. Phys.: Condens. Matter* **13**, 403 (2001).

²¹C. Kumpf *et al.*, *J. Chem. Phys.* **123**, 224707 (2005).

²²J. N. Wickham, A. B. Herhold, and A. P. Alivisatos, *Phys. Rev. Lett.* **84**, 4515 (2000).

²³J. Nanda, S. Sapra, D. D. Sarma, N. Chandrasekharan, and G. Hodes, *Chem. Mater.* **12**, 1018 (2000).

²⁴B. Palosz, E. Grzanka, S. Gierlotka, S. Stel'Makh, R. Pielaszek, U. Bismayer, J. Neuefeind, H. P. Weber, and W. Palosz, *Acta Phys. Pol. A* **102**, 57 (2002).

²⁵H. Borchert, E. V. Shevchenko, A. Robert, I. Mekis, A. Kornowski, G. Grubel, and H. Weller, *Langmuir* **21**, 1931 (2005).

²⁶A. Guinier, *X-ray Diffraction in Crystals, Imperfect Crystals, and Amorphous Bodies* (Freeman, San Francisco, 1963).

²⁷P. Debye, *Ann. Phys.* **46**, 809 (1915).

²⁸Z. Kaszkar, *Z. Kristallogr.* **23**, 147 (2006).

²⁹C. B. Murray, D. J. Norris, and M. G. Bawendi, *J. Am. Chem. Soc.* **115**, 8706 (1993).

³⁰C. Q. Chen, Y. Shi, Y. S. Zhang, J. Zhu, and Y. J. Yan, *Phys. Rev. Lett.* **96**, 075505 (2006).

³¹G. Ouyang, X. L. Li, X. Tan, and G. W. Yang, *Appl. Phys. Lett.* **89**, 031904 (2006).

³²M. A. Marcus, L. E. Brus, C. Murray, M. G. Bawendi, A. Prasad, and A. P. Alivisatos, *Nanostruct. Mater.* **1**, 323 (1992).

- ³³N. Herron, J. C. Calabrese, W. E. Farneth, and Y. Wang, *Science* **259**, 1426 (1993).
- ³⁴A. C. Carter, C. E. Bouldin, K. M. Kemmer, M. I. Bell, J. C. Woicik, and S. A. Majetich, *Phys. Rev. B* **55**, 13822 (1997).
- ³⁵S. Chaure, N. B. Chaure, and R. K. Pandey, *Physica E (Amsterdam)* **28**, 439 (2005).
- ³⁶X. G. Peng, J. Wickham, and A. P. Alivisatos, *J. Am. Chem. Soc.* **120**, 5343 (1998).
- ³⁷V. Petkov, S. J. L. Billinge, J. Heising, and M. G. Kanatzidis, *J. Am. Chem. Soc.* **122**, 11571 (2000).
- ³⁸V. Petkov, P. N. Trikalitis, E. S. Božin, S. J. L. Billinge, T. Vogt, and M. G. Kanatzidis, *J. Am. Chem. Soc.* **124**, 10157 (2002).
- ³⁹V. Petkov, P. Y. Zavalij, S. Lutta, M. S. Whittingham, V. Parvanov, and S. Shastri, *Phys. Rev. B* **69**, 085410 (2004).
- ⁴⁰P. Juhas, D. M. Cherba, P. M. Duxbury, W. F. Punch, and S. J. L. Billinge, *Nature (London)* **440**, 655 (2006).
- ⁴¹H. Z. Zhang, B. Gilbert, F. Huang, and J. F. Banfield, *Nature (London)* **424**, 1025 (2003).
- ⁴²V. Petkov, Y. Peng, G. Williams, B. Huang, D. Tomalia, and Y. Ren, *Phys. Rev. B* **72**, 195402 (2005).
- ⁴³B. E. Warren, *X-ray Diffraction* (Dover, New York, 1990).
- ⁴⁴A. P. Hammersley, S. O. Svenson, M. Hanfland, and D. Hauserman, *High Press. Res.* **14**, 235 (1996).
- ⁴⁵X. Qiu, J. W. Thompson, and S. J. L. Billinge, *J. Appl. Crystallogr.* **37**, 678 (2004).
- ⁴⁶S. J. L. Billinge, in *Local Structure From Diffraction*, edited by S. J. L. Billinge and M. F. Thorpe (Plenum, New York, 1998), p. 137.
- ⁴⁷H. M. Rietveld, *J. Appl. Crystallogr.* **2**, 65 (1969).
- ⁴⁸C. L. Farrow, P. Juhas, J. W. Liu, D. Bryndin, E. S. Božin, J. Bloch, T. Proffen, and S. J. L. Billinge, *J. Phys.: Condens. Matter* **19**, 335219 (2007).
- ⁴⁹B. H. Toby and S. J. L. Billinge, *Acta Crystallogr., Sect. A: Found. Crystallogr.* **60**, 315 (2004).
- ⁵⁰B. H. Toby and T. Egami, *Acta Crystallogr., Sect. A: Found. Crystallogr.* **48**, 336 (1992).
- ⁵¹I.-K. Jeong, T. Proffen, F. Mohiuddin-Jacobs, and S. J. L. Billinge, *J. Phys. Chem. A* **103**, 921 (1999).
- ⁵²I. K. Jeong, R. H. Heffner, M. J. Graf, and S. J. L. Billinge, *Phys. Rev. B* **67**, 104301 (2003).
- ⁵³C. Farrow (unpublished).
- ⁵⁴I. Kikuma and M. Furukoshi, *J. Cryst. Growth* **71**, 136 (1985).
- ⁵⁵V. Petkov, R. G. DiFrancesco, S. J. L. Billinge, M. Acharya, and H. C. Foley, *Philos. Mag. B* **79**, 1519 (1999).
- ⁵⁶M. A. Marcus, W. Flood, M. Stiegerwald, L. Brus, and M. Bawendi, *J. Phys. Chem.* **95**, 1572 (1991).
- ⁵⁷J. Rockenberger, L. Troger, A. L. Rogach, M. Tischer, M. Grundmann, H. Weller, and A. Eychmuller, *Phys. Chem. Chem. Phys.* **102**, 1561 (1998).
- ⁵⁸Th. Proffen and R. B. Neder, *J. Appl. Crystallogr.* **30**, 171 (1997).
- ⁵⁹C. Landes, M. Braun, C. Burda, and M. El-Sayed, *Nano Lett.* **1**, 667 (2001).
- ⁶⁰X. B. Chen, A. C. Samia, Y. B. Lou, and C. Burda, *J. Am. Chem. Soc.* **127**, 4372 (2005).
- ⁶¹L. Qu, Z. Peng, and X. Peng, *Nano Lett.* **1**, 333 (2001).
- ⁶²K. Kodama, S. Iikubo, T. Taguchi, and S. Shamoto, *Acta Crystallogr., Sect. A: Found. Crystallogr.* **62**, 444 (2006).
- ⁶³V. Petkov, I.-K. Jeong, J. S. Chung, M. F. Thorpe, S. Kycia, and S. J. L. Billinge, *Phys. Rev. Lett.* **83**, 4089 (1999).
- ⁶⁴I.-K. Jeong, F. Mohiuddin-Jacobs, V. Petkov, S. J. L. Billinge, and S. Kycia, *Phys. Rev. B* **63**, 205202 (2001).

Understanding the Insulating Phase in Colossal Magnetoresistance Manganites: Shortening of the Jahn-Teller Long-Bond across the Phase Diagram of $\text{La}_{1-x}\text{Ca}_x\text{MnO}_3$

E. S. Božin,¹ M. Schmidt,² A. J. DeConinck,¹ G. Paglia,¹ J. F. Mitchell,³ T. Chatterji,⁴ P. G. Radaelli,² Th. Proffen,⁵ and S. J. L. Billinge¹

¹*Department of Physics and Astronomy, Michigan State University, East Lansing, Michigan 48824-2320, USA*

²*ISIS, CCLRC Rutherford Appleton Laboratory, Chilton-Didcot, OX11 0QX, Oxfordshire, United Kingdom*

³*Materials Science Division, Argonne National Laboratory, Argonne, Illinois 60439, USA*

⁴*Institute Laue-Langevin, Boîte Postale 156, 38042 Grenoble Cedex 9, France*

⁵*Lujan Neutron Scattering Center, Los Alamos National Laboratory, Los Alamos, New Mexico 87545, USA*

(Received 19 September 2006; published 27 March 2007)

The detailed evolution of the magnitude of the local Jahn-Teller (JT) distortion in $\text{La}_{1-x}\text{Ca}_x\text{MnO}_3$ is obtained across the phase diagram for $0 \leq x \leq 0.5$ from high-quality neutron diffraction data using the atomic pair distribution function method. A local JT distortion is observed in the insulating phase for all Ca concentrations studied. However, in contrast with earlier local structure studies, its magnitude is not constant, but *decreases* continuously with increasing Ca content. This observation is at odds with a simple small-polaron picture for the insulating state.

DOI: [10.1103/PhysRevLett.98.137203](https://doi.org/10.1103/PhysRevLett.98.137203)

PACS numbers: 75.47.Gk, 61.12.-q, 71.38.-k, 75.47.Lx

Doped transition metal oxides are of fundamental interest for their electronic properties that exhibit various types of colossal responses such as high-temperature superconductivity, colossal magnetoresistance (CMR), and ferroelectricity [1], which are still not fully understood. A recent concept that may be relevant for many of these systems is the observation of nanoscale inhomogeneities that are thought to be intrinsic. These can take the form of nanoscale checkerboard [2,3] or stripe patterns [4], or less ordered structures [5–8] that are related to electronic phase separation. Phase separation is also found theoretically in computational models, which have been used to explain the large changes in conductivity with temperature and doping [9]. However, the ubiquity and fundamental importance of electronic inhomogeneities to the colossal effects is not completely established [10]. For example, local-probe experiments where no electronic inhomogeneities are observed have been made on samples that show a colossal response [11,12] and some observed inhomogeneities have been related to disorder in the chemical dopant ions [13].

One approach for establishing a correlation between inhomogeneities and electronic properties is to study the complete phase diagram of interesting systems. We set out to examine the local structure of the $\text{La}_{1-x}\text{Ca}_x\text{MnO}_3$ (LCMO) manganite family. This is an archetypal system for such studies because of the strong electron-phonon coupling, through the JT effect, resulting in a large structural response to electronic phase separation. We probe this using the atomic pair distribution function (PDF) measured from neutron powder diffraction data. The signature of the metallic phase in local structural probes is the absence of a JT-long-bond [14,15]. When the charges are localized in a polaronic insulating phase, the JT-long-bond is seen [14–18]. A two phase fit of an undistorted and distorted phase to the low- r region of the PDF can thus yield a quantitative

measure of the phase fraction of each phase as a function of T and x in the system $\text{La}_{1-x}\text{Ca}_x\text{MnO}_3$ [19]. Unexpectedly, we found that the *length* of the Jahn-Teller long-bond in the insulating phase decreases continuously with increasing doping in this system, contrary to the canonical understanding [17,18,20,21]. Here we report for the first time extensive, high real-space resolution PDF data as a function of temperature and doping from $0 \leq x \leq 0.5$ on well characterized samples in the $\text{La}_{1-x}\text{Ca}_x\text{MnO}_3$ system using new high-resolution, high-throughput, time-of-flight neutron diffractometers. We rule out the existence of fully JT distorted long-bonds at 2.16 Å in the CMR compositions that would be expected in a simple single-site small-polaron scenario for the phase above T_c . The smooth continuous decrease in the length of the JT-long-bond is most easily explained in a delocalized or large polaron picture.

A series of 13 powdered LCMO samples with compositions spanning $0 \leq x \leq 0.5$ range were prepared using standard solid state synthesis methods and annealed to ensure oxygen stoichiometry [22] and characterized by resistivity and magnetization measurements. Two additional finely pulverized single crystal samples ($x = 0.075, 0.1$), grown by the floating zone method utilizing image furnace, were also used to increase coverage of the phase space under the study. Neutron powder diffraction measurements were carried out at the GEM diffractometer at the ISIS facility at the Rutherford Appleton Laboratory in the UK and at the NPDF diffractometer at Los Alamos Neutron Scattering Center. The samples, of approximately 6 grams each, were loaded into extruded vanadium containers and sealed under He atmosphere. The data were collected for all the samples at a consistent set of 7 temperatures between 10 K and 550 K using a closed cycle He refrigerator. The data were processed to obtain PDFs [23] using the program PDFGETN [24] by a sine Fourier trans-

form of the total scattering structure function $F(Q)$ up to a value of Q_{\max} of 35 \AA^{-1} . This high Q_{\max} , coupled with the good statistics from GEM and NPDF, result in high-quality PDFs with minimal spurious low- r ripples and negligible termination ripples, as evident in Fig. 1. The PDF analysis reported here involves both direct data evaluation and structural modeling using the program PDFFIT [25]. Results of complementary average crystal structure modeling, carried out using the program GSAS [26], are also presented. All refinements were carried out using the O or O' structural models in the $Pbnm$ space group with isotropic displacement parameters [27]. Our analysis does not address the ordering of localized charges such as observed in the charge ordered state at $x = 0.5$ [28].

The results of the average crystal structure evaluation is summarized in Figs. 2(a) and 3. In the orthorhombic O phase [29], the *local JT* distortion amplitude (the length of the JT-long-bond) is the same as the average long range ordered value. The distortion is constant with temperature for fixed Ca content, but decreases linearly with increasing Ca content. Upon crossing into the pseudocubic O' phase, the average JT distortion disappears abruptly [Fig. 2(a) and 3]. However, this effect is accompanied by the anomalous increase of the isotropic thermal parameters on oxygen sites, Fig. 2(d). This is consistent with the understanding that the pseudocubic O' phase in the insulating state consists of orbitally disordered, JT distorted, octahedra [30,31], and that this picture can be extended to finite doping. In the ferromagnetic metallic (FM) phase, the Rietveld refined JT-long-bond disappears, but there is no significant enlargement of the refined oxygen thermal parameter showing that the local JT-long-bond is also absent [14]. Structural refinements to the PDF data over a wide range of r ($r_{\max} = 20 \text{ \AA}$) mimic the Rietveld results rather closely [Fig. 2(b) and 2(e)]. This shows that the average structure result is already obtained for a PDF refinement over a 20 \AA range, suggesting that the size of local orbital ordering correlations is limited to this range.

The size and shape of the local MnO_6 octahedra can be obtained by fitting the PDF over a narrow r range of 6 \AA . The length of the local long Mn-O bond has been obtained

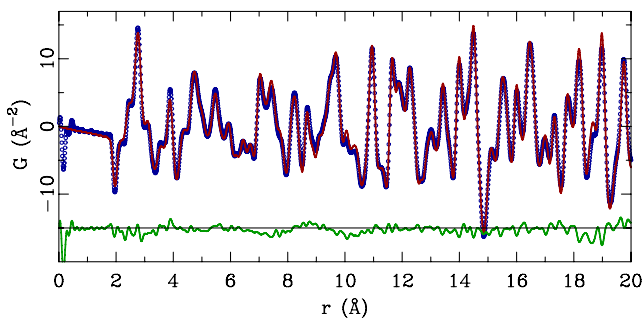


FIG. 1 (color online). \circ are the $G(r)$ of $x = 0.22$ sample at 10 K; solid red line is the calculated $G(r)$ from the crystal structure model. The difference curve is shown offset below.

for all compositions and temperatures studied, and is shown as a contour plot in Fig. 2(c). The color scale has been set such that a fully shortened long-bond of 1.96 \AA shows up as black. The presence of color therefore indicates a finite local JT distortion. There is a striking resemblance between the contour plot of the local JT-long-bond in Fig. 2(c) and the electronic phase diagram of this manganite that is superimposed. The position of the phase transition lines were verified from magnetization and resistivity measurements of the samples used in this study.

First, we note that the *local JT* distortion is present in the entire insulating part of the phase diagram, but that it is effectively removed for the metallic compositions at lowest temperatures. Second, it is seen that the *magnitude* of the local JT distortion has a relatively strong doping dependence at lower Ca concentrations, with the bond length versus concentration curve flattening at higher Ca doping levels.

Selected constant temperature cuts are shown in Fig. 3(a)–3(c), for 550 K, 250 K, and 10 K, respectively. The square symbols show the behavior of the average structure. The JT-long-bond decreases with doping in the orbitally ordered O phase, but then abruptly shortens at the structural phase transition, indicated by the dotted line in the figure. In contrast, the local JT bond is insensitive to the

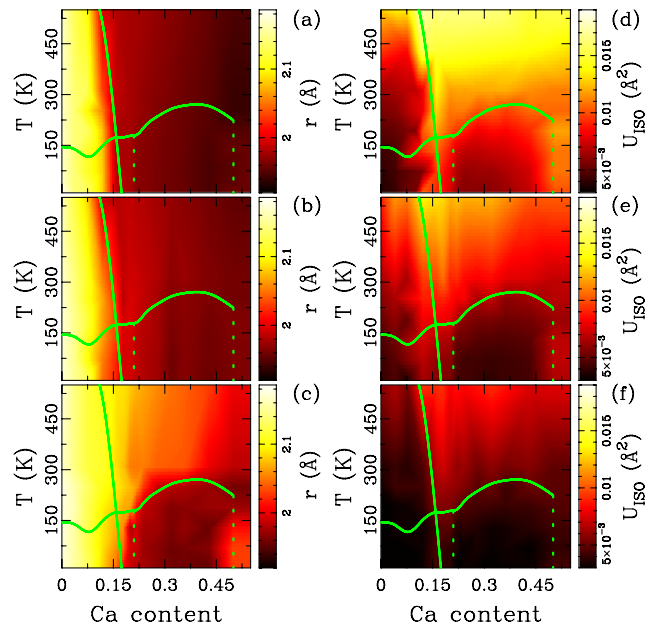


FIG. 2 (color online). Contour plot of the JT distortion (long Mn-O distance) in (x, T) parameter space as obtained from (a) Rietveld analysis and PDF analyses over (b) 20 \AA and (c) 6 \AA ranges, respectively. Contour plot of the isotropic displacement parameter of oxygen, $U_{\text{iso}}(\text{O}2)$ in $Pbnm$ setting, as obtained from (d) Rietveld analysis, and PDF analyses over (e) 20 \AA and (f) 6 \AA ranges. In all the panels the solid curves indicate T_{JT} and T_c phase lines, while dotted vertical lines indicate IM phase boundaries, as determined from the sample characterization measurements.

structural transition, but disappears abruptly when the sample goes through the insulator-metal (IM) transition. This is consistent with the widely held current view [14,15]. What is less expected is the observation that the *length* of the local JT-long-bond shortens with increasing doping in the insulating state. In a single-site small-polaron picture the insulating state consists of distinct Mn^{3+} and Mn^{4+} sites. The $4+$ sites are presumed to have regular, undistorted, MnO_6 octahedra and the $3+$ sites to be JT distorted with 2.16 \AA long bonds, as in the undoped LaMnO_3 end member, and this was supported by experimental evidence [15,17,18]. We investigate these refinement results in greater detail below.

Figure 4 shows some representative PDF data bracketing the IM transition. We show the nearest-neighbor doublet of the PDF from $\text{La}_{1-x}\text{Ca}_x\text{MnO}_3$ with $x = 0.18$ and $x = 0.22$. The former sample remains in the insulating state at all temperatures; the latter is a ferromagnetic metal below $\sim 180 \text{ K}$, and paramagnetic insulator at higher temperature. Thus, a comparison of the curves in Fig. 4(b) shows the effect of changing composition without crossing the IM transition. The changes are very small. In Fig. 4(a) the metal insulator (MI) is crossed at constant temperature. The changes to the nearest-neighbor doublet on crossing the MI transition are evident with a sharp, single-valued peak giving way to a peak with a well-defined shoulder on the high- r side. This is the appearance of the JT-long-bond in the insulating phase. Notable, however, is the absence of intensity at the position of the undoped JT-long-bond at $r = 2.16 \text{ \AA}$, indicated by a vertical dashed line in the figure. This clearly shows the absence of any fully distorted JT octahedra in the structure. The difference curve in Fig. 4(a) also shows the appearance of intensity on the low- r side of the shortest bond in the insulating phase. Figure 4(c) and 4(d) shows the model fits to the metallic and insulating PDFs, giving a sense of the quality of fits to the local PDF that were obtained in our determination of the phase diagram in Figs. 2 and 3.

The main result of the current study is the clear demonstration of an absence of any Mn-O long-bonds of the fully JT distorted 2.16 \AA length in the doped samples, as would be expected in a simple-minded small-polaron picture. Our result disagrees with the canonical understanding from earlier experimental studies [15,17,18], though is consistent with the observations of a number of less well-known studies [32,33]. The observation could be explained in a homogeneous picture where the electron density is uniformly distributed over all Mn sites in the insulating state. In this case, the electron density in the orbitals, and therefore the driving force for the JT distortion, decreases continuously with increasing hole doping. It is harder to explain in a small-polaron picture where localized Mn^{4+} sites exist in a fully distorted Mn^{3+} background. In this scenario, one source of long-bond shortening could be elastic strain in the lattice because of the disordered polar-

ons. This is unlikely to explain our observation. The energy scale for octahedral rotations is much smaller than for stretching the covalent bonds [34] and most elastic strain accommodation is expected to occur in the octahedral rotations. This is indeed the case when orbital disorder sets in at constant doping as a function of temperature [30]. Also, we note that there is a negative deviation from Vegard's law [35], indicated by the dashed line in Fig. 3, in the average length of the long-bond. Elastic

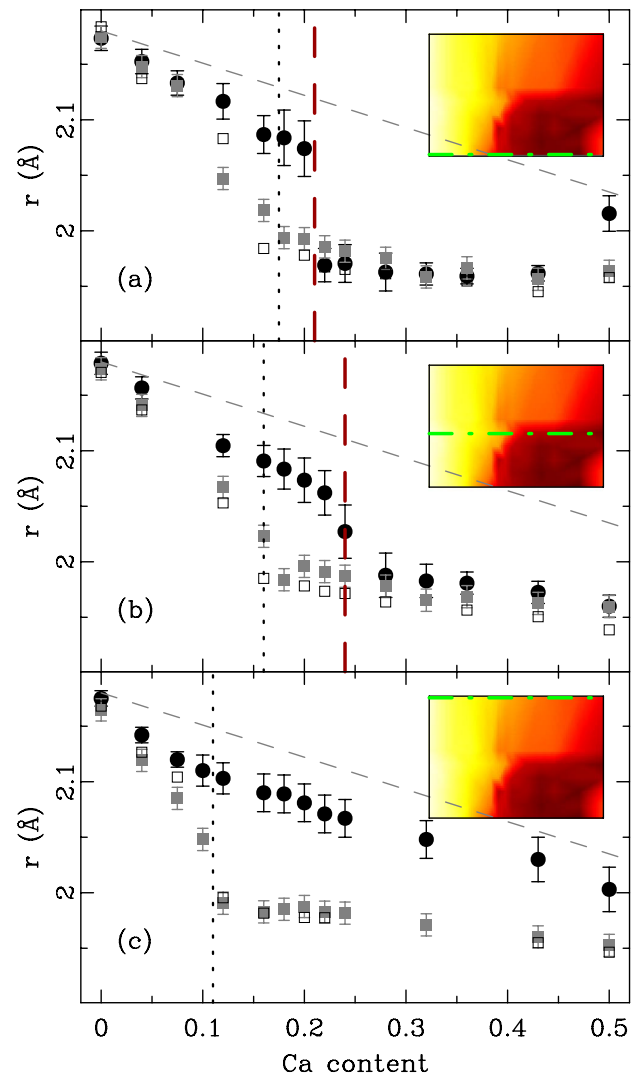


FIG. 3 (color online). Length of the longest Mn-O distance in the MnO_6 octahedron vs doping at (a) 10 K, (b) 250 K, and (c) 550 K. \square denote Rietveld result; \blacksquare and \bullet show results of PDF refinements over 20 \AA and 6 \AA ranges, respectively. Sloping dashed lines denote Vegard's law [35] behavior for Mn-O long-bond interpolating between the values for LaMnO_3 and CaMnO_3 . Dashed vertical lines mark the IM transition, while the dotted vertical lines denote the orthorhombic to pseudocubic phase transition. The insets reproduce Fig. 2(c) showing the temperature of the data shown in the panel. Symbols indicate measured compositions.

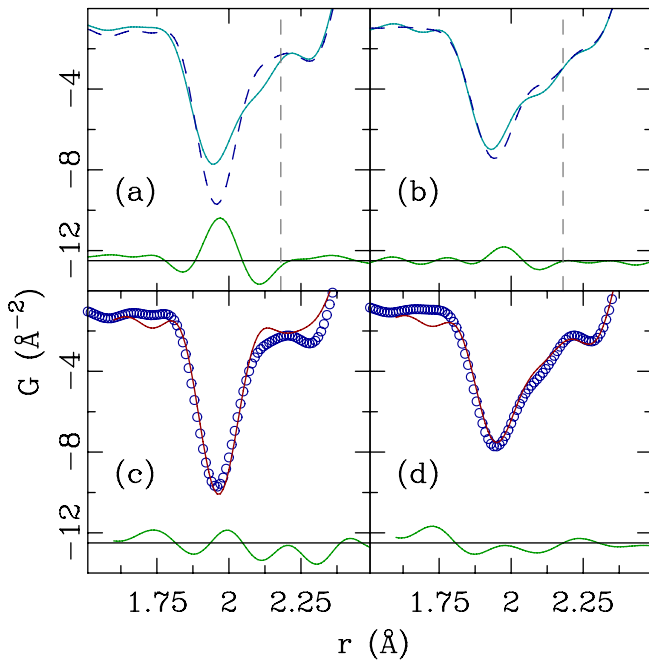


FIG. 4 (color online). Experimental PDFs, $G(r)$, of $x = 0.18$ (solid line) and $x = 0.22$ (dashed line) samples at (a) 10 K and (b) 190 K, with difference curves underneath. Both data sets are in the insulating phase in (b) but straddle the IM boundary in (a). A JT long-bond appears in the insulating phase but is shorter than that in the undoped end member, indicated by the vertical dashed lines. (c) and (d) show representative $r_{\max} = 6 \text{ \AA}$ PDF fits (solid lines) to the 10 K data (\circ) shown in (a). Difference curves are offset below.

relaxation in covalently bonded alloys analogous to the manganites results in a characteristic Z plot [36,37] of bond-length versus composition that is clearly not seen here. A principle strain relaxation mode through octahedral rotations is also indicated by enlarged U_{iso} values in the insulating region of the phase diagram, as evident in Fig. 2(d). We also note that oxygen K edge spectroscopy indicates an increasing importance of oxygen ligand hole states with doping [38,39], indicating a clear change in the local electronic structure induced by doping.

It is not possible from our current data to tell unambiguously whether or not the sample is phase separated into metallic and insulating regions. Phase separation would imply a transfer of intensity from the position of the long-bond to that of the short-bond. What we show here is that the length of the long-bond decreases with doping. The long-bond starts to overlap with the short-bond at higher doping making an extraction of the integrated area of the peak uncertain. However, we note that modeling the local structure with a homogeneous model in $Pbnm$ setting as we have done, with 4 short and 2 long-bonds at all doping levels in the insulating region, results in rather good fits as evident in Figs. 1 and 4(d). Enlarged oxygen U_{iso} values in $0.12 \leq x \leq 0.17$ range are evident in Fig. 2(d)–2(f) where phase separation has been observed [40].

We acknowledge discussions with S. D. Mahanti, P. M. Duxbury, T. A. Kaplan, and P. Juhás. Work at MSU was supported by the NSF under Grant No. DMR-0304391, Argonne by DOE under Contract No. DE-AC02-06CH11375, and Los Alamos under Contract No. DE-AC52-06NA25396.

- [1] A. J. Millis, *Nature (London)* **392**, 147 (1998).
- [2] S. Komiyama *et al.*, *Phys. Rev. Lett.* **94**, 207004 (2005).
- [3] T. Hanaguri *et al.*, *Nature (London)* **430**, 1001 (2004).
- [4] J. M. Tranquada *et al.*, *Nature (London)* **375**, 561 (1995).
- [5] M. Fath *et al.*, *Science* **285**, 1540 (1999).
- [6] M. Uehara *et al.*, *Nature (London)* **399**, 560 (1999).
- [7] T. Becker *et al.*, *Phys. Rev. Lett.* **89**, 237203 (2002).
- [8] J. C. Loudon and P. A. Midgley, *Phys. Rev. Lett.* **96**, 027214 (2006).
- [9] E. Dagotto, *Science* **309**, 257 (2005).
- [10] G. C. Milward *et al.*, *Nature (London)* **433**, 607 (2005).
- [11] R. Akiyama *et al.*, *Appl. Phys. Lett.* **79**, 4378 (2001).
- [12] K. Matsuba *et al.*, *Physica (Amsterdam)* **388C**, 281 (2003).
- [13] K. McElroy *et al.*, *Science* **309**, 1048 (2005).
- [14] S. J. L. Billinge *et al.*, *Phys. Rev. Lett.* **77**, 715 (1996).
- [15] C. H. Booth *et al.*, *Phys. Rev. Lett.* **80**, 853 (1998).
- [16] P. G. Radaelli *et al.*, *Phys. Rev. B* **54**, 8992 (1996).
- [17] D. Louca *et al.*, *Phys. Rev. B* **56**, R8475 (1997).
- [18] S. J. L. Billinge *et al.*, *Phys. Rev. B* **62**, 1203 (2000).
- [19] T. Proffen and S. J. L. Billinge, *Appl. Phys. A* **74**, s1770 (2002).
- [20] E. Dagotto *et al.*, *Phys. Rep.* **344**, 1 (2001).
- [21] N. E. Massa *et al.*, *J. Magn. Magn. Mater.* **233**, 91 (2001).
- [22] B. Dabrowski *et al.*, *J. Solid State Chem.* **146**, 448 (1999).
- [23] P. F. Peterson *et al.*, *J. Appl. Crystallogr.* **36**, 53 (2003).
- [24] P. F. Peterson *et al.*, *J. Appl. Crystallogr.* **33**, 1192 (2000).
- [25] T. Proffen and S. J. L. Billinge, *J. Appl. Crystallogr.* **32**, 572 (1999).
- [26] A. C. Larson and R. B. Von Dreele, Los Alamos Laboratory Report No. LAUR-86-748, 1987.
- [27] T. Proffen *et al.*, *Phys. Rev. B* **60**, 9973 (1999).
- [28] P. G. Radaelli *et al.*, *Phys. Rev. B* **55**, 3015 (1997).
- [29] E. O. Wollan and W. C. Koehler, *Phys. Rev.* **100**, 545 (1955).
- [30] X. Qiu *et al.*, *Phys. Rev. Lett.* **94**, 177203 (2005).
- [31] J. Rodriguez-Carvajal *et al.*, *Phys. Rev. B* **57**, R3189 (1998).
- [32] S. J. Hibble *et al.*, *J. Phys. Condens. Matter* **11**, 9221 (1999).
- [33] R. Bindu *et al.*, *J. Phys. Condens. Matter* **17**, 6393 (2005).
- [34] M. N. Iliev *et al.*, *Phys. Rev. B* **57**, 2872 (1998).
- [35] L. Vegard, *Z. Phys.* **5**, 17 (1921).
- [36] J. C. Mikkelsen and J. B. Boyce, *Phys. Rev. Lett.* **49**, 1412 (1982).
- [37] I.-K. Jeong *et al.*, *Phys. Rev. B* **63**, 205202 (2001).
- [38] J. van Elp and A. Tanaka, *Phys. Rev. B* **60**, 5331 (1999).
- [39] G. Zampieri *et al.*, *Phys. Rev. B* **58**, 3755 (1998).
- [40] M. Pissas *et al.*, *Phys. Rev. B* **72**, 064425 (2005).

Quadrupolar Ordering in LaMnO_3 Revealed from Scattering Data and Geometric Modeling

A. Sartbaeva, S. A. Wells, and M. F. Thorpe

Department of Physics and Astronomy, Arizona State University, Tempe, Arizona 85287-1504, USA

E. S. Božin and S. J. L. Billinge

Department of Physics and Astronomy, Michigan State University, East Lansing, Michigan 48824-2320, USA

(Received 1 May 2007; published 10 October 2007)

Many strongly correlated materials display quadrupolar (Jahn-Teller) distortion of the local octahedral structural units. It is common for these distortions to be observed by probes of local structure but absent in the crystallographic average structure. The ordering of these quadrupoles is important in determining the properties of manganites and cuprates, and the nature of the disorder in these structures has been an unsolved problem. We combine high resolution scattering data and novel geometrical modeling techniques to obtain a detailed picture of the local atomic structure, and also to extract the quadrupolar order parameter associated with the distorted octahedra. We show that in LaMnO_3 , quadrupoles undergo a strong first-order phase transition at 730 K, but with nonzero order parameter remaining in the high-temperature phase.

DOI: [10.1103/PhysRevLett.99.155503](https://doi.org/10.1103/PhysRevLett.99.155503)

PACS numbers: 61.43.Bn, 61.50.Ah, 71.70.Ej, 75.40.Mg

Extracting detailed structural information from solids that have both long-range order (Bragg peaks) and local disorder (diffuse scattering) is one of the most challenging problems in characterizing complex materials [1]. Here we show how it is possible to combine high resolution neutron scattering data out to large scattering wave vectors, with modeling that preserves the local stereochemistry. The latter requires the introduction of various penalty functions for distortions from perfect crystallinity and is done by a new technique involving geometrical simulation that we have developed. This new combined experiment and modeling approach is illustrated here with LaMnO_3 where the MnO_6 octahedra can distort uniaxially and arrange themselves in a quadrupolar ordering pattern.

In manganite perovskites and layered cuprates [2–5], strong Jahn-Teller (JT) coupling [5–12] gives rise to a variety of interesting magnetic, electronic, and structural phenomena such as charge and orbital ordering, ferromagnetism, phase separation, and of course colossal magnetoresistance (CMR) [2–4,13,14] and superconductivity [15,16]. In the undoped end member LaMnO_3 , crystallographic methods indicate that above about 730 K, the JT distortion ceases to exist [17–19]. The transition is characterized as first order based on the observation of a coexistence of the low and high temperature phases over a range of temperatures and an anomalous volume collapse is observed [19]. However, studies sensitive to local structure [20–22] indicate that locally the octahedra remain JT distorted above the transition and only disappear on average. Although LaMnO_3 has been investigated using experimental techniques including neutron diffraction [17], transport and SQUID [22], XANES, and EXAFS [21], all of which have led to important insights, none of these has led to a comprehensive structural model or a full description of the nature of the JT phase transition. Here, we have

been successful in combining pair distribution function (PDF) data [20] with new geometrical modeling techniques [23,24] to describe both the short- and long-range order at all temperatures, and most importantly to extract the quadrupolar order parameter. Surprisingly, weak long-range quadrupolar ordering persists above the first-order phase transition at around 730 K up to the highest temperatures studied (1150 K).

Qiu *et al.* [20] studied LaMnO_3 using data collected at the NPDF diffractometer at Los Alamos National Laboratory. Structural parameters were initially refined using PDFFIT [25]. Models were refined for the data over different length scales r . Fits confined to the low- r region yielded the local (JT-distorted) structure, whereas fits over wider ranges of r gradually crossed over to the average crystallographic structures, suggesting that the nature of the high-temperature state is that of orientationally disordered, JT-distorted, octahedra with a short-range local ordering persisting at all temperatures.

To obtain more complete structural models of LaMnO_3 that fully reconcile the local and the average structures we represent the structure with a large supercell. For each temperature point our starting model was a $16 \times 16 \times 12$ supercell of the PDF-refined crystal structure, with cell edges of about 90 Å, containing 61 440 atoms (12 288 octahedra). We then refined the atomic positions within this supercell so as to fit its PDF to the experimental PDF, using a simulated-annealing algorithm. In each round of the algorithm, a randomly selected atom is moved, the $G(r)$ of the new structure is calculated and compared to the experimental $G(r)$, and changes that improve the fit are accepted, while those that worsen the fit are accepted or rejected based on a Metropolis criterion. We perform simulated annealing by gradually lowering the pseudotemperature in the Metropolis criterion.

In practice, fitting based only on $G(r)$ can give unphysical results [26] and some form of constraint must be used to ensure that local chemical bonding and steric exclusion are properly maintained. It is usual to apply harmonic constraints [26] to bond lengths and angles, so that the cost function includes not only the mismatch between experimental and simulated $G(r)$, but also the cost of stretching constraints. However, this approach can be used only if equilibrium values for bond lengths are known; since the pattern of JT distortions in the high-temperature structures is not known, we cannot define ideal Mn-O bond lengths in advance.

We have made use of a new form of geometric constraint based on the technique of geometric modeling [23,24,27,28], where the constraints in a bonded group of atoms (here, an MnO_6 unit) are represented using a rigid “template” which has the ideal geometry of the group. The template may be a regular octahedron or a JT-distorted octahedron with long Mn-O bond of 2.16 Å and a short bond of 1.94 Å [23]. The template shape is chosen based on the aspect ratio of the Mn-O bonds, allowing a JT distortion to develop to fit the data. The application of these templates is shown in Fig. 1. Every time an atom is moved, the template is fitted over the atoms of the group. The distortion of the group from the template geometry is measured by the mismatch of O atoms from template vertices. If the mismatch exceeds a defined tolerance, the move is immediately rejected for violation of bonding geometry. We allowed a tolerance of 0.3 Å, to allow for normal thermal variation in the bond lengths. Conformers

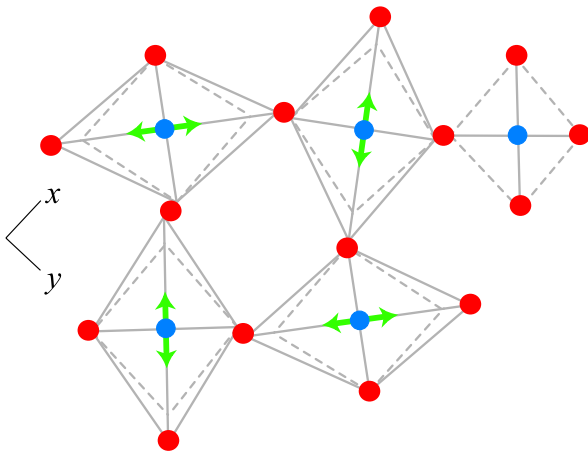
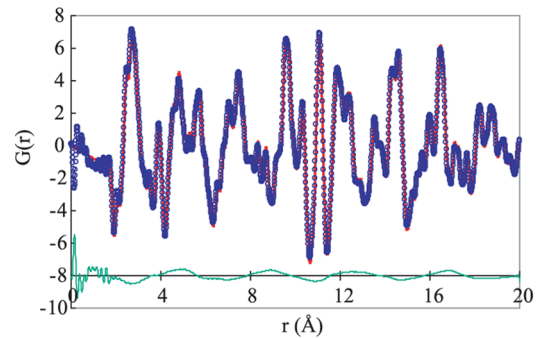


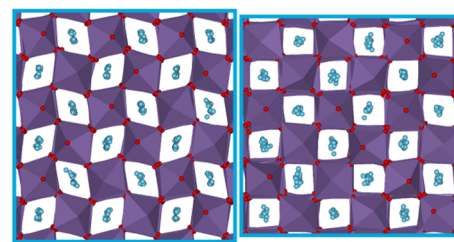
FIG. 1 (color online). Schematic representation of the structure of LaMnO_3 in the xy plane showing the checkerboard arrangement of JT-distorted octahedra in the xy plane with long and short bonds; the direction of JT distortion is emphasized by green (light gray) arrows. A regular octahedron is shown on the right and has all short bonds. Mn ions are in the middle of octahedra, and O ions are at the vertices of octahedra. La atoms are omitted for clarity. Ideal geometric templates for JT-distorted octahedra (gray lines) are superimposed over each octahedron.

are also rejected if two atoms are unacceptably close to each other, e.g., a severe steric clash between an interstitial La and an O atom. If the system passes these geometric tests, the simulated-annealing algorithm then determines whether to accept or reject the move based on its fit to the data.

In Fig. 2(a) we show the PDF $G(r)$ at 300 K and fit to data. It is notable that we fit both the long-range data and the short-range data (showing splitting of the first Mn-O peak due to the JT distortion) equally well. The fits are comparably good at all temperatures. The width of a peak indicates a distribution of interatomic distances in the model. In Fig. 2(b), we show portions of the fitted structures at 300 and 1050 K. The JT distortion of an octahedron is a quadrupolar (rather than dipolar) distortion, described by a quadrupole moment q . We analyzed our structures by obtaining the quadrupole moment of each octahedron. The five components of q are defined in terms of the components x, y, z of the six Mn-O bond vectors in each octahedron, as follows:



(a)



(b)

FIG. 2 (color online). (a) Representative fit of $G(r)$ [red (or dark gray) line] to the data [blue (or gray) circles] for LaMnO_3 at 300 K. The difference is offset below in green (or light gray). (b) Slices of the fitted models for 300 and 1050 K showing arrangement of MnO_6 octahedra. La ions (light gray or cyan) are interstitial atoms in the channels. At 300 K, there is a checkerboard arrangement of octahedra and La ions are relatively ordered in the channels. At 1050 K—the average structure appears cubiclike, the octahedra are very buckled and La ions are disordered in the channels. The different sizes of the images are due to a small degree of negative thermal expansion [19].

$$\begin{aligned}
 q_1 &= 2 \sum_{i=1}^6 x_i y_i; & q_2 &= 2 \sum_{i=1}^6 y_i z_i; & q_3 &= 2 \sum_{i=1}^6 z_i x_i; \\
 q_4 &= \sum_{i=1}^6 (x_i^2 - y_i^2); & q_5 &= \frac{1}{\sqrt{3}} \sum_{i=1}^6 (2z_i^2 - x_i^2 - y_i^2).
 \end{aligned}
 \tag{1}$$

The correlation between two quadrupole moments q and q' at different sites is given by

$$C = \frac{3}{16(b^2 - a^2)^2} (q_1 q'_1 + q_2 q'_2 + q_3 q'_3 + q_4 q'_4 + q_5 q'_5),
 \tag{2}$$

where a and b are the average length of short and long bonds in JT octahedra. In our normalization we used values of $a = 1.94 \text{ \AA}$ and $b = 2.16 \text{ \AA}$ as obtained previously by diffraction methods [12,17,20]. We also define a normalized magnitude for the quadrupole moment on a single site as

$$P^2 = \frac{3}{16(b^2 - a^2)^2} \left(\sum_{j=1}^5 q_j^2 \right),
 \tag{3}$$

so that a JT-distorted octahedron with bond lengths a and b will have a magnitude $P \approx 1$.

For octahedra with these bond lengths, the correlation factor C has values of $+1$ for alignment (long bonds parallel) and $-1/2$ for antialignment (long bonds perpendicular), and so is asymmetric by definition. Two other factors in the LaMnO_3 system also make this correlation function asymmetric. In the low-temperature ordered form, the long axes of all octahedra lie in the xy plane and so the q_5 component tends to be negative for all octahedra. Also,

the octahedra are tilted so that the long axes of adjacent octahedra are not exactly perpendicular. Both factors produce a positive bias on C . We therefore define a symmetrized correlation C' by subtracting from each individual quadrupole moment q [Eq. (1)], the average quadrupole moment $\langle q \rangle$ for all octahedra in the model. C' lies approximately in the range

$$-1 < C' < +1,
 \tag{4}$$

where $+1$ signifies alignment and -1 antialignment.

Since in low-temperature, ordered LaMnO_3 , the octahedra are ordered in the xy plane, we specifically consider the correlation in this plane, which we will call C'_{xy} . For each octahedron, we obtain its correlation C'_{xy} with its nearest-neighbor octahedra (those with which it shares a vertex) in the xy plane, with its second-nearest neighbors, and so on. We examine the distribution of these correlations for all octahedra in each model, from first neighbors out to tenth. In the fully ordered structure we expect the distribution of C'_{xy} for odd neighbors to peak around -1 , and for even neighbors to peak around $+1$.

In Fig. 3 we show the distributions of C'_{xy} at several temperatures. At 300 K, the distributions for all odd neighbors are peaked around $C'_{xy} \approx -1$, and those for even neighbors are peaked around $C'_{xy} \approx +1$. At 700 K (just below the transition) the peaks have moved closer together and are broader. At 750 K (just above the transition) and 1050 K, the distributions for odd and even neighbors are almost superimposed on each other with mean correlations close to zero. At first sight it appears that all ordering is lost at high temperatures, despite the persistence of the JT distortion in each octahedron individually.

We examine the transition in more detail by extracting the mean value of C'_{xy} for each set of neighbors (first, second, third, and so on). At 300 K, the correlation is equally strong for all neighbors; odd neighbors (from 1st to 9th) are strongly anticorrelated, with $\langle C'_{xy} \rangle$ close to -1 , and even neighbors (from 2nd to 10th) are strongly correlated. At higher temperatures, however, a different pattern emerges. First, $\langle C'_{xy} \rangle$ for first neighbors is more negative than $\langle C'_{xy} \rangle$ for odd neighbors at longer range, indicating a stronger anticorrelation of first neighbors. As first neighbors share one oxygen atom in common in an $\text{Mn}_A\text{-O-Mn}_B$ bridge, if the $\text{Mn}_A\text{-O}$ distance is shorter it is intrinsically more likely that the O-Mn_B distance is longer. This also is in agreement with the observation of Qiu *et al.* [20] that small domains of order similar to the low-temperature ordered structure persist above the phase transition. More surprisingly, long-range ordering is not completely lost even at very high temperatures; an alternation in $\langle C'_{xy} \rangle$ between odd and even neighbors is visible even at the highest temperatures, although the magnitude is quite small (at 1050 K, $-0.011 < \langle C'_{xy} \rangle < 0.019$, i.e., less than $1/50$ of that seen at low temperature).

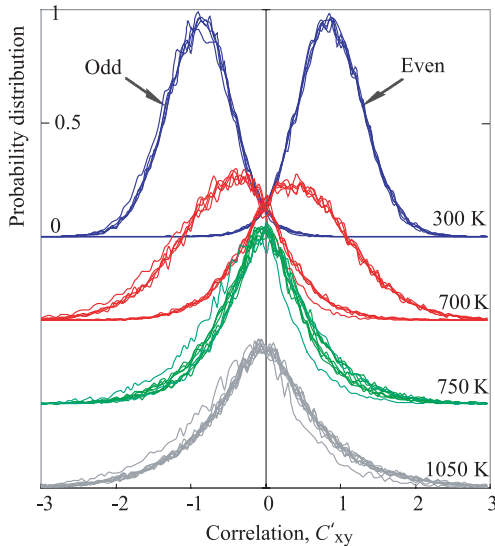


FIG. 3 (color online). Distribution of xy -plane correlation C'_{xy} at 300, 700, 750, and 1050 K. Below the JT transition the distributions for odd and even neighbors are quite distinct, while above the transition the distributions are almost superimposed.

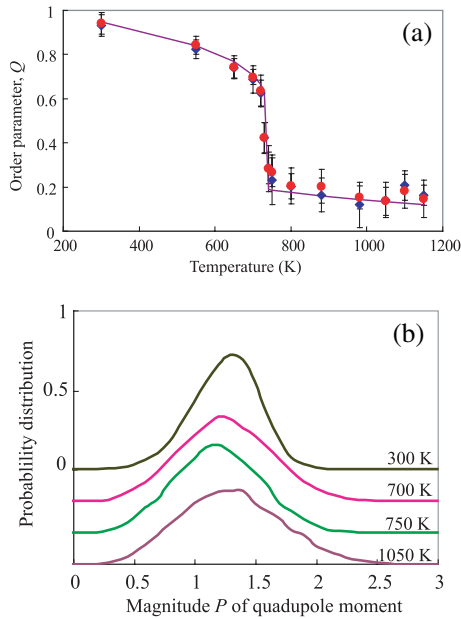


FIG. 4 (color online). (a) Order parameter Q vs temperature. Red (dark gray) and blue (gray) dots are determined from even and odd neighbors, respectively. (b) Probability distribution of quadrupole magnitudes, P , at selected temperatures.

From the behavior of the mean correlation, we obtain an order parameter Q describing long-range quadrupolar ordering. If the ordering on a site is proportional to the order parameter, then the correlation between sites is proportional to Q^2 . Thus we estimate Q as $\sqrt{|\langle C'_{xy} \rangle|}$ for neighbors, in the xy plane, at long range (i.e., not including first neighbors). In Fig. 4(a) we show this order parameter for all temperatures. We observe strong long-range order at lower temperatures and weak but nonzero long-range ordering at high temperatures, with a sharp (first-order) transition between the two at around 730 K. This is very similar to the form of quadrupolar ordering transition for $S = \frac{3}{2}$ Ising systems studied by Sivardière and Blume [29]. The distribution of magnitudes P [Eq. (3)] of individual quadrupole moments of octahedra [Fig. 4(b)] shows that the full amplitude JT distortions persist up to the highest temperatures studied, consistent with earlier observations [20,21], and the drop in Q at high temperatures is due to a change in ordering, not to a loss of JT distortion on individual sites. It might appear disconcerting that the order parameter does not go to zero at the phase transition, but this is known to occur in quadrupolar systems. The existence of a field that couples to the order parameter (for example, an external magnetic field in a ferromagnet) will guarantee that the order parameter never goes to zero, and therefore destroys the critical point when the transition is second order. For quadrupolar ordering in, say, a spin $S = 1$ system, the field that couples to the order parameter Q is a crystal field term like DS_z^2 , where S_z is the z component

of the spin. A first-order phase transition can then occur where Q jumps at the transition and then has a tail at high temperatures [29]. In this case the field that couples to Q is generated internally by strain in the sample. Here we extract the order parameter directly from the PDF measurement bypassing the need to write down a Hamiltonian for the system.

Our results suggest the correlation of quadrupole distortions is the correct microscopic order parameter to describe the Jahn-Teller phase transition in LaMnO_3 . The integrated experiment and modeling approach developed in this work, which involves incorporating local stereochemical constraints on the scattering data using geometrical simulation, should prove to be of wide validity in manganites, cuprates, and other materials with coupled local Jahn-Teller distortions.

- [1] T. Egami *et al.*, *Underneath the Bragg Peaks: Structural Analysis of Complex Materials* (Pergamon, Elsevier, New York, 2003).
- [2] T. Saitoh *et al.*, Phys. Rev. B **62**, 1039 (2000).
- [3] *Colossal-Magnetoresistive Oxides* edited by Y. Tokura (Gordon and Breach, New York, 2000).
- [4] A. P. Ramirez, J. Phys. Condens. Matter **9**, 8171 (1997).
- [5] K. H. Ahn and A. J. Millis, Phys. Rev. B **58**, 3697 (1998).
- [6] H. A. Jahn *et al.*, Proc. R. Soc. A **161**, 220 (1937).
- [7] J. B. Goodenough, Phys. Rev. **100**, 564 (1955).
- [8] J. C. Loudon *et al.*, Phys. Rev. Lett. **94**, 097202 (2005).
- [9] G. C. Milward *et al.*, Nature (London) **433**, 607 (2005).
- [10] A. J. Millis, Phys. Rev. B **53**, 8434 (1996).
- [11] *Nanoscale Phase Separation and Colossal Magnetoresistance*, edited by E. Dagotto (Springer-Verlag, Berlin, 2003).
- [12] T. Proffen *et al.*, Phys. Rev. B **60**, 9973 (1999).
- [13] S. J. L. Billinge *et al.*, Phys. Rev. B **62**, 1203 (2000).
- [14] E. S. Božin *et al.*, Phys. Rev. Lett. **98**, 137203 (2007).
- [15] S. Fujita *et al.*, *Theory of High-Temperature Superconductivity* (Kluwer Academic Publishers, Dordrecht, The Netherlands, 2001).
- [16] T. Egami, J. Supercond. Novel Magnetism **19**, 203 (2006).
- [17] J. Rodríguez-Carvajal *et al.*, Phys. Rev. B **57**, R3189 (1998).
- [18] C. P. Adams *et al.*, Phys. Rev. Lett. **85**, 3954 (2000).
- [19] T. Chatterji *et al.*, Phys. Rev. B **68**, 052406 (2003).
- [20] X. Qiu *et al.*, Phys. Rev. Lett. **94**, 177203 (2005).
- [21] M. Sanchez *et al.*, Phys. Rev. Lett. **90**, 045503 (2003).
- [22] J.-S. Zhou *et al.*, Phys. Rev. B **60**, R15002 (1999).
- [23] A. Sartbaeva *et al.*, Phys. Rev. Lett. **97**, 065501 (2006).
- [24] A. Sartbaeva *et al.*, Nat. Mater. **5**, 962 (2006).
- [25] T. Proffen *et al.*, J. Appl. Crystallogr. **32**, 572 (1999).
- [26] R. L. McGreevy, Nucl. Instrum. Methods Phys. Res., Sect. A **354**, 1 (1995).
- [27] S. A. Wells *et al.*, J. Phys. Condens. Matter **14**, 4567 (2002).
- [28] S. A. Wells *et al.*, Phys. Biol. **2**, S127 (2005).
- [29] J. Sivardière *et al.*, Phys. Rev. B **5**, 1126 (1972).

Utilizing total scattering to study the Jahn-Teller transition in $\text{La}_{1-x}\text{Ca}_x\text{MnO}_3$

E. S. Božin^{1,*}, X. Qiu¹, R. J. Worhatch¹, G. Paglia¹,
M. Schmidt², P. G. Radaelli², J. F. Mitchell³, T. Chatterji⁴,
Th. Proffen⁵, and S. J. L. Billinge¹

¹Department of Physics and Astronomy, Michigan State University, East Lansing, MI 48824-2320, USA

²ISIS, CCLRC Rutherford Appleton Laboratory, Chilton-Didcot, OX11 0QX, Oxfordshire, United Kingdom

³Material Science Division, Argonne National Laboratory, Argonne, IL 60439, USA

⁴Institute Laue-Langevin, Boîte Postale 156, 38042 Grenoble Cedex 9, France

⁵Lujan Neutron Scattering Center, Los Alamos National Laboratory, Los Alamos, NM 87545, USA

* Contact author; e-mail: bozin@pa.msu.edu

Keywords: total scattering, atomic pair distribution function, CMR manganites

Abstract. Total scattering based atomic pair distribution function (PDF) analysis, with the advent of high data throughput neutron powder diffractometers, helps understanding the nature of the Jahn-Teller (JT) phase transition in $\text{La}_{1-x}\text{Ca}_x\text{MnO}_3$ colossal magnetoresistive (CMR) manganites. The JT distortion of the MnO_6 octahedra, is long-range ordered in the orthorhombic (O) phase, but disappears in the pseudo-cubic (O') phase crystallographically. An anomalous unit cell volume contraction occurs at the transition. The PDF study indicates that the distortion persists *locally* deep in the O' phase, contrary to the crystallographic view. Simultaneously, local structural features observed in PDF at 10.3 Å, sensitive to the oxygen sublattice changes, evolve dramatically across the transition. The same effect is observed irrespective of the way the O-O' phase boundary is crossed: it is seen both in the temperature series data for $x=0$, and in the doping series data at 310 K and at 550 K.

Introduction

The hole-doped $\text{La}_{1-x}\text{Ca}_x\text{MnO}_3$ (LCMO) series have been the subject of significant interest for decades due to the complex interplay between the spin, charge, orbital and lattice degrees of freedom [1-6]. The parent LaMnO_3 (LMO) has an A-type antiferromagnetic ground state, with long-range ordered JT distorted MnO_6 octahedra, exhibiting four shorter (~ 1.94 Å) and two longer (~ 2.17 Å) Mn-O bonds, and has orthorhombic (O) symmetry (s.g. *Pbnm*) [7, 8]. When heated above $T_{JT} \sim 750$ K, the structure becomes pseudo-cubic (O'), but the system retains the same space group [9]. At this JT-transition a loss of long-range orbital order is

observed, and the JT-distortions disappear crystallographically. The temperature of the O-O' transition abruptly lowers with Ca doping, and it becomes as low as 35 K at $x=0.2$ [9]. Although the insulating pseudo-cubic phase is of great importance, as it hosts the ferromagnetism and CMR effect, its exact nature is still not fully understood [10-13]. The JT-transition is argued to be order-disorder in character [12, 14], but the exact mechanism is still debated [15-17]. The local JT distortion in the undoped endmember, as recently shown, remains with full magnitude all the way up to the highest temperature and the rhombohedral phase [15]. The same study suggested that the ground-state-like orbital order remains within clusters ~ 16 Å in diameter above the T_{JT} . The nature of the O-O' transition appears to have the same origin when the phase line is crossed both vs temperature at fixed doping, and vs doping at fixed temperature [18]. Here we extend these results to the case when the phase line is crossed as a function of doping at 550 K temperature, deep in the insulating phase. The results agree with those obtained for 310 K. Using the same set of data crystallographic results are further obtained for the evolution of the unit cell volume with doping at 550 K. Anomalous volume contraction is observed upon crossing into the pseudo-cubic O' phase along the doping axis, in agreement with earlier T-dependent studies at fixed doping [14, 16].

Experimental

The local structural information is obtained by the real-space atomic pair distribution function (PDF) analysis of the neutron diffraction data collected at NPDF diffractometer at LANSCE, and at GEM diffractometer at ISIS. The temperature dependence of the $x=0$ sample was carried out at 14 temperatures from 300 K up to 1150 K at NPDF. At the same instrument data were collected for 13 samples spanning $0 \leq x \leq 0.5$ doping range at 550 K. The data at 310 K for the same doping range were collected at GEM. Sample preparation and the measurement details including data processing methodology are specified elsewhere [15, 19, 20]. The experimental PDF, $G(r)$, is obtained through a sine Fourier transform of the total scattering structure function, $S(Q)$, where Q is the momentum transfer, via

$$G(r) = \frac{2}{\pi} \int_0^{\infty} F(Q) \sin(Qr) dQ, \quad (1)$$

using the program PDFGETN [21]. The radial distribution function (RDF), $R(r)$, is related to $G(r)$ through a series of simple arithmetic operations [20]. Both functions are peaked at distances separating pairs of atoms. We show here PDFs that were obtained using high resolution total scattering data up to a very high value of momentum transfer, $Q_{MAX}=35 \text{ \AA}^{-1}$. The full profile refinements of experimental PDFs is obtained using the modelling program PDFFIT [22], while the Rietveld refinements on the diffraction patterns of the same data is carried out using the program GSAS [23, 24] to obtain the crystallographic values.

Results

The data presented here are a subset of an extensive set of data collected at high throughput neutron diffraction instruments to accurately evaluate local structural properties across the phase diagram of LCMO [19]. The advent of modern synchrotron based high flux sources allows for new, previously undetected structural details to emerge. Figure 1 shows detailed

phase diagram of LCMO as mapped out by the O2 isotropic crystallographic displacement parameter. The ridge centred at around $x=0.175$ at low T tracks the O-O' phase boundary.

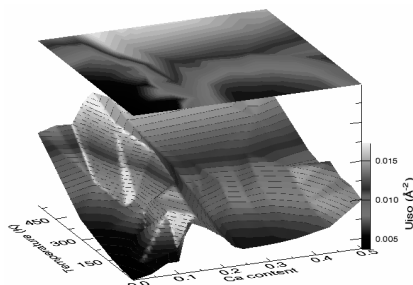


Figure 1. Phase diagram of LCMO CMR manganites mapped out by the isotropic displacement parameter of O2, as obtained from crystallographic modelling using *Pbnm* space group settings. The ridge centred at around $x=0.175$ in the 3D plot corresponds to the Jahn-Teller transition.

Typical PDF, $G(r)$, of the $x=0$ sample is shown in figure 2. The nearest neighbour doublet at $\sim 2 \text{ \AA}$ corresponds to the 4 shorter and 2 longer Mn-O bonds. The peaks are negative due to

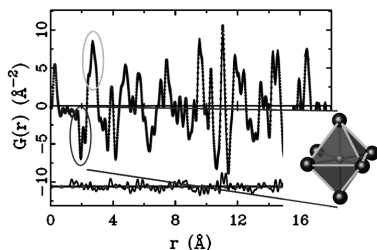


Figure 2. Typical atomic PDF, $G(r)$, of the LCMO system. Symbols represent the data, solid line is the crystallographic model, and the difference curve is offset below. The circled peaks at 2.0 \AA and 2.75 \AA in PDF correspond to the MnO_6 octahedra locally, to the Mn-O and O-O distances respectively.

the negative neutron scattering length of Mn. Set of positive PDF peaks centred at $\sim 2.75 \text{ \AA}$ contains O-O bond length contributions. These PDF features, circled in figure 2, capture the local behaviour of the MnO_6 octahedra, and allow systematic tracking of the JT-distortion evolution with temperature and/or doping. New high data throughput neutron powder diffractometers, such as NPDF and GEM, make it feasible to systematically evaluate the local structural behaviour in this manner. In figure 3 (a) and (b) we summarize the results of the evolution of the JT distortion with temperature in $x=0$ sample, and with doping at 310 K respectively, using the $R(r)$ representation of the PDF. The vertical dashed lines indicate the length of the Mn-O bonds in the ground state of LMO. The dashed profiles denote the O-O' phase transition boundaries in the two cases. There is no appreciable change of the local JT distortion upon crossing into the O' phase, evident in the figures. Moreover, the peaks near

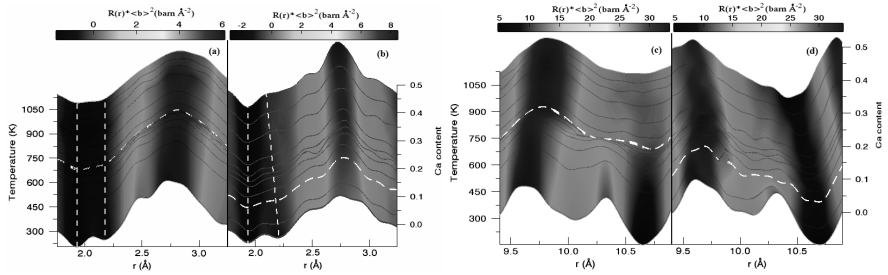


Figure 3. Radial distribution function (RDF), $R(r)$, depicting the evolution of the JT distortion with (a) temperature in the $x=0$ sample, and with (b) doping at 310K. The vertical dashed lines indicate the positions of the short and long Mn-O bonds in the undoped endmember at 10K. Dashed profiles denote the Jahn-Teller phase boundary. (c) and (d) show the same RDFs with emphasis on the features at slightly higher r -values. Notable is a dramatic change in the 10.3 \AA peak across the phase boundary marked with dashed lines.

2.75 \AA do not change discontinuously either. The changes that can be noticed are those that are due to the thermal broadening, figure 3 (a), and due to the scattering length change, as Ca doping changes, figure 3 (b). However in both cases the RDF profiles evolve continuously. Rather dramatic change in the local structure is observed around 10.3 \AA , figure 3 (c) and (d). There is an abrupt change in this peak intensity on crossing the JT phase line. It has been demonstrated that this effect is related to the rearrangements within the oxygen sublattice [18]. Quantification of these observations, by fitting the PDF profiles over relatively narrow r -range, further showed that the local JT distortion remains unchanged across the Jahn-Teller transition, while the features sensitive to oxygen rotations that correspond to further-neighbour correlations change dramatically and vanish in the pseudo-cubic phase [18].

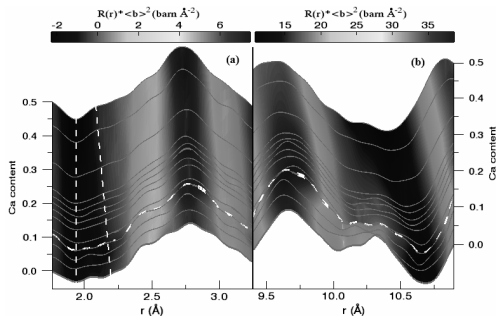


Figure 4. The RDFs of the series of LCMO samples obtained for 550K. All the structural features previously observed as a function of temperature at fixed doping ($x=0$), and as a function of doping at fixed temperature ($T=310\text{K}$) are reproduced deep in the insulating phase.

Note that there is a systematic gradual shift of the intensity of the 2.17 Å long bond peak towards lower r -values. This, however, continues smoothly across the JT-transition [19].

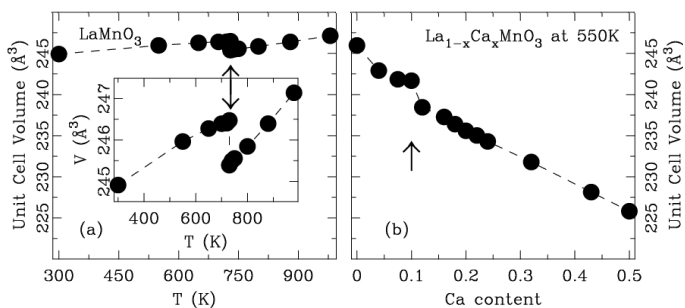


Figure 5. Evolution of the unit cell volume, as obtained from the Rietveld refinement, (a) with temperature at fixed doping ($x=0$), and (b) with doping at fixed temperature ($T=550\text{K}$). Anomalous unit cell volume reduction is observed at the phase transition (indicated by the arrows) in both cases. Inset to (a) shows the $x=0$ data in more detail. Dashed lines are guide for the eyes

Figure 4 shows doping evolution at 550 K of the structural features from figure 3. Apart from the apparent shift of the phase boundary towards lower x , compared to 310 K, the result is in accord with the earlier findings. In figure 5 (a) the temperature dependence of the crystallographic unit cell volume is shown across the $T_{JT}\sim 750\text{K}$ for $x=0$ sample, and on the same scale in figure 5 (b) the doping dependence of the volume at 550 K across the $x_{JT}\sim 0.1$. The anomalous volume collapse, presumably due to the repacking of the structure at the transition [14, 16], is observed in both cases. ΔV is estimated to be around 1.1Å^3 (0.41% change across the transition) in the $x=0$ sample in agreement with earlier results, and about 3.2Å^3 (1.34% change) when the phase boundary is crossed along the doping axis at 550 K. .

Concluding remarks

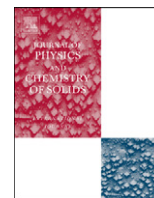
The neutron powder diffraction based atomic PDF analysis is a powerful tool in accurately tracking the structural evolution of complex materials. The local JT distortion as a function of doping at 550 K persists in the O' phase, while dramatic changes associated with the rearrangement in the oxygen sublattice at T_{JT} are observed. The volume collapse upon crossing into the O' phase along the doping axis at 550 K is observed from the same set of data using Rietveld refinement results. This effect is comparable, but slightly larger than that observed in T-dependence for the $x=0$ sample.

References

1. Millis, A.J., 1996, *Phys. Rev. B*, **53**, 8483.
2. Ramirez, A.P., 1997, *J. Phys. Condens. Matter*, **9**, 8171.
3. Salamon, M.B. & Jaime, M., 2001, *Rev. Mod. Phys.*, **73**, 583.

4. Milward, G.C., Calderón, M.J. & Littlewood, P.B., 2005, *Nature*, **433**, 607.
5. Dagotto, E., 2005, *Science*, **309**, 257.
6. Schlottmann, P., 2006, *Phys. Rev. B*, **73**, 214428.
7. Wollan, E.O. & Koehler, W.C., 1955, *Phys. Rev.*, **100**, 545.
8. Rodríguez-Carvajal, J., Hennion, M., Moussa, F., Moudden, A. H., Pinsard, L. & Revcolevschi, A., 1998, *Phys. Rev. B*, **57**, R3189.
9. Kim, K.H, Uehara, M., Kiryukhin, V. & Cheong, S.-W., 2002, in *Colossal Magnetoresistive Manganites*, edited by T. Chatterji (Dordrecht: Kluwer–Academic).
10. Tovar, M., Alejandro, G., Butera, A., Caneiro, A., Causa, M.T., Prado, F. & Sánchez, R.D., 1999, *Phys. Rev. B*, **60**, 10199.
11. Zhou, J.-S. & Goodenough, J. B., 1999, *Phys. Rev. B*, **60**, R15002.
12. Zhou, J.-S. & Goodenough, J. B., 2003, *Phys. Rev. B*, **68**, 144406.
13. Mandal, P., Bandyopadhyay, B. & Ghosh, B., 2001, *Phys. Rev. B*, **64**, R180405.
14. Chatterji, T., Fauth, F., Ouladdiaf, B., Mandal, P. & Ghosh, B., 2003, *Phys. Rev. B*, **68**, 052406.
15. Qiu, X., Proffen, Th., Mitchell, J.F. & Billinge, S.J.L., 2005, *Phys. Rev. Lett.*, **94**, 177203.
16. Chatterji, T., Riley, D., Fauth, F., Mandal, P. & Gosh, B., 2006, *Phys. Rev. B*, **73**, 094444.
17. Ahmed, M.R. & Gehring, G.A., 2006, *Phys. Rev. B*, **74**, 014420.
18. Božin, E.S., et al., 2006, *Physica B*, **385**, 110.
19. Božin, E.S., Schmidt, DeConinck, A.J., M., Paglia, G., Mitchell, J.F., Chatterji, T., Radaelli, P.G., Proffen, Th. & Billinge, S.J.L., 2007, *Phys. Rev. Lett.* (in press).
20. Egami, T. & Billinge, S.J.L., 2003, *Underneath the Bragg peaks: structural analysis of complex materials* (Oxford, England: Pergamon Press).
21. Peterson, P.F., Gutmann, M., Proffen, Th. & Billinge, S.J.L., 2000, *J. Appl. Crystallogr.*, **33**, 1192.
22. Proffen, Th. & Billinge, S. J. L., 1999, *J. Appl. Crystallogr.*, **32**, 572.
23. Larson, A.C. & Von Dreele, R.B., 2000, *General Structure Analysis System (GSAS)*, Los Alamos National Laboratory Report LAUR 86-748.
24. Toby, B.H., 2001, *J. Appl. Cryst.*, **34**, 210.

Acknowledgements. This work was supported by the NSF under grant DMR-0304391. Argonne National Laboratory (ANL) is supported by UChicago Argonne, LLC, Operator of ANL. ANL, a U.S. DOE Office of Science laboratory, is operated under Contract No. DE-AC02-06CH11357. This work has benefited from the use of NPDF at the Lujan Center at Los Alamos Neutron Science Center, funded by DOE Office of Basic Energy Sciences. Los Alamos National Laboratory is operated by Los Alamos National Security LLC under DOE Contract DE-AC52-06NA25396.



Structure of CaMnO_3 in the range $10\text{ K} \leq T \leq 550\text{ K}$ from neutron time-of-flight total scattering

E.S. Božin^{a,*}, A. Sartbaeva^b, H. Zheng^c, S.A. Wells^b, J.F. Mitchell^c, Th. Proffen^d, M.F. Thorpe^b, S.J.L. Billinge^a

^a Department of Physics and Astronomy, Michigan State University, 4250 Biomedical Physical Sciences, East Lansing, MI 48824-2320, USA

^b Department of Physics, Arizona State University, Tempe, AZ 85283, USA

^c Material Science Division, Argonne National Laboratory, Argonne, IL 60439, USA

^d Los Alamos National Laboratory, LANSCE-LC, MS H805, Los Alamos, NM 87545, USA

ARTICLE INFO

Keywords:

A. Oxides
C. Neutron scattering
D. Crystal structure

ABSTRACT

The local and average structure of the Ca endmember of the $\text{La}_{1-x}\text{Ca}_x\text{MnO}_3$ series has been investigated. Neutron powder diffraction-based high real-space resolution atomic pair distribution function (PDF) analysis, yielding the local atomic structure, and the corresponding Rietveld analysis yielding the average crystal structure show that the two structural scales are in accord in this material, and that the MnO_6 octahedral units are regular for all temperatures studied. Quantitative values of structural parameters are reported for a wide temperature range, important for both experimental and theoretical considerations of hole and electron doped branches of the rich phase diagram of $\text{La}_{1-x}\text{Ca}_x\text{MnO}_3$.

© 2008 Elsevier Ltd. All rights reserved.

1. Introduction

Colossal responses, such as high-temperature superconductivity, colossal magnetoresistance (CMR) and ferroelectricity, have brought doped transition metal oxides into focus during the past two decades [1]. This is not only due to their importance for potential applications, but also as these materials represent an extremely fertile ground for verification of various fundamental physical concepts.

The manganite-based perovskite $\text{La}_{1-x}\text{Ca}_x\text{MnO}_3$ family in particular has been the subject of enhanced interest as it exhibits a complex interplay of orbital, electronic, and magnetic degrees of freedom [2]. This system is of great value to the oxide community as it is dopable over the full range of Ca concentrations between 0 and 1. The appearance of the insulator-to-metal phase transition and the CMR effect for Ca-doping between 0.2 and 0.5 are certainly among the most prominent features, whose mechanisms are still not fully understood. The importance of the atomic structure to understand the CMR properties of manganites, especially that on a nanometer lengthscale, has been established [3,4]. However, the lack of complete understanding of the exact role that local structure plays extends to the present time [5,6]. Knowledge of accurate values of the structural parameters of the La and Ca endmembers over a broad temperature range is

essential both for numerical studies [7] and for experimental considerations such as those aimed to quantify the phase fractions as part of an effort to verify (or otherwise) the phase separation scenario [8]. While the rich structure of the La endmember has been studied in detail over an extremely wide temperature range [2,9–11], the structure of the Ca endmember has been quantified less extensively and for fewer temperatures [12].

In this paper we report the results of a neutron total scattering experiment on CaMnO_3 over a wide temperature range, bridging the gap and complementing the detailed structural work carried out over the same temperature range for a dense series of Ca concentrations in the hole-doped branch of the phase diagram [6]. This provides important (and so far missing) experimental information allowing for the quantification of microscopic phase separation in $\text{La}_{1-x}\text{Ca}_x\text{MnO}_3$, among other things.

2. Experimental

Powder CaMnO_3 sample was synthesized using standard solid state reaction from high purity CaCO_3 and MnO_2 starting materials. The mixed powder was ground and fired in air at 900, 1000, and 1050 °C, successively, with intermediate grindings. Finally, the powder was pressed into a pellet and fired at 1070 °C. The as-made pellet was annealed at 500 °C, under 2650 psi O_2 pressure, with 0.1 C/min cooling rate to room temperature. The final high pressure treatment was necessary to suppress the occurrence of the Marokite impurity phase and to optimize

* Corresponding author. Tel.: +1 517 355 9200; fax: +1 517 353 4500.
E-mail address: bozin@pa.msu.edu (E.S. Božin).

the oxygen stoichiometry. The crystallographic behavior was confirmed by means of X-ray diffraction characterization.

Time-of-flight (TOF) neutron diffraction measurements were carried out on the NPDF diffractometer at LANSCE at Los Alamos National Laboratory. The local structural information is accessed by means of the real-space atomic pair distribution function (PDF) analysis of the neutron diffraction data collected at seven temperatures from 10 K up to 550 K. Approximately 5 g of finely pulverized sample was sealed in an extruded cylindrical vanadium tube with He exchange gas. The sample was cooled using a closed-cycle He refrigerator. The data were corrected for experimental effects and normalized [13] to obtain the total scattering function $S(Q)$ [14], where $Q = |\mathbf{Q}| = |\mathbf{k} - \mathbf{k}_0|$ represents the momentum transfer magnitude for the scattering. The PDF function, $G(r)$, is then obtained by a Fourier transformation according to

$$G(r) = \frac{2}{\pi} \int_0^{\infty} Q[S(Q) - 1] \sin(Qr) dQ. \quad (1)$$

A typical total scattering structure function, $F(Q)$, and the corresponding PDF, $G(r)$, are shown in Fig. 1. The function $G(r)$ gives the probability of finding an atom at a distance r from another atom. This function is obtained directly from the Fourier transform of the neutron diffraction data and is used to investigate features of the local structure of a material. The radial distribution function (RDF), $R(r)$, relates to $G(r)$ through a series of simple arithmetic operations [13]. Both $G(r)$ and $R(r)$ functions are peaked at distances separating pairs of atoms. The PDFs presented here used high resolution total scattering data up to a very high value of momentum transfer ($Q_{MAX} = 35 \text{ \AA}^{-1}$) and were reduced from the raw data using the PDFgetN program package [15].

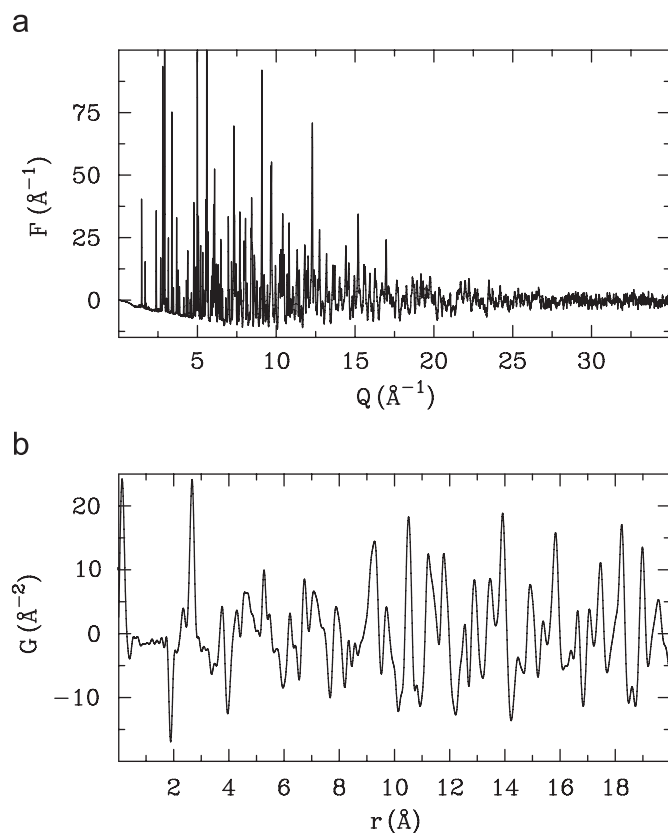


Fig. 1. Reduced total scattering structure function, $F(Q) = Q(S(Q) - 1)$, of CaMnO_3 at 10 K (a) and corresponding atomic pair distribution function, $G(r)$, (b) obtained through a Fourier transform. Upper limit of integration in the transform, Q_{max} , was set to 35 \AA^{-1} .

3. Modeling

Structural modeling was carried out in reciprocal and in direct space. The Rietveld refinements were done using the GSAS program [16] controlled by EXPGUI [17]. Structural refinements in direct space were performed using the PDFfit2 modeling engine controlled by PDFgui [18]. The PDF modeling was carried out over a 19.5 \AA r -range using the constraints of the orthorhombic $Pnma$ space group, with 16 parameters refined. These are three lattice parameters and seven fractional coordinates as permitted by symmetry, four isotropic atomic displacement parameters (ADPs), correlated motion parameter δ_2 associated with the quadratic term [13], and a scale factor. The Rietveld refinements were done with the same set of parameters, except for the one pertaining to the correlated motion, and in addition six background parameters using GSAS background function 4 (expansion of the exponential), and two peak profile parameters. Very good fits were obtained for all the data sets. Example refinements are shown in Fig. 2: Rietveld fits for 425 and 130 K data are presented in Fig. 2(a) and (b), respectively, while the PDF fits of the data at the same two temperatures are shown in panels (c) and (d), respectively.

We have recently [19] investigated the structure of LaMnO_3 by fitting large structural models to PDF data, using simulated-annealing combined with geometric constraints [20], which allows for the presence or absence of Jahn–Teller (JT) distortions in the MnO_6 octahedra to be studied. Here we apply the same approach to CaMnO_3 . For each temperature point our starting model was a $16 \times 16 \times 12$ supercell of the PDF-refined crystal structure, with cell edges of about 90 \AA , containing 61 440 atoms (12 288 octahedra). This starting structure was refined following

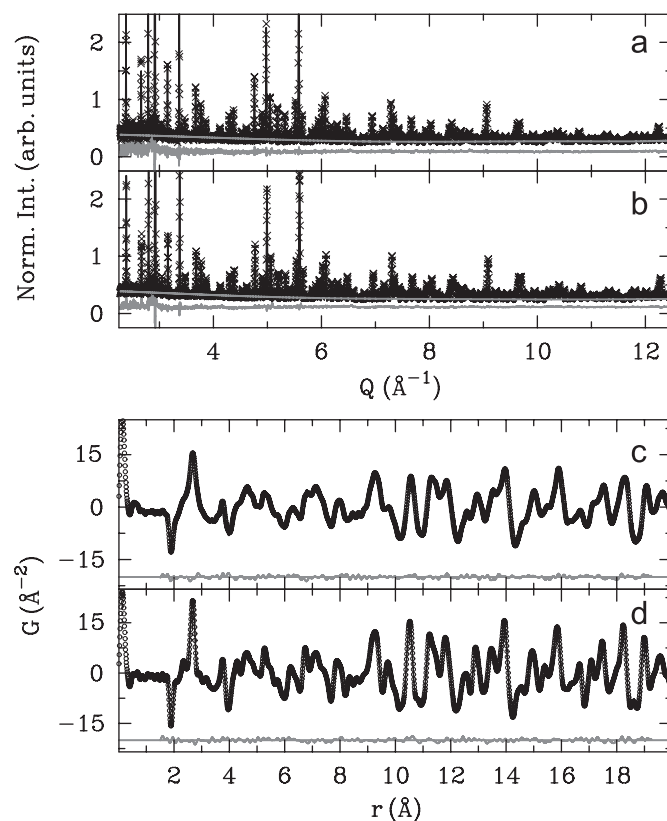


Fig. 2. Typical orthorhombic model refinements of the total scattering data. (a) 425 K and (b) 130 K Rietveld refinements. (c) 425 K and (d) 130 K PDFfit refinements. In all cases, symbols are the data, solid line is the refined profile, and the offset gray line is the difference curve. The gray line in the Rietveld plots underneath the data is the calculated background function.

the procedure described in Ref. [19]. Such large models can give unphysical results [21] and constraints must be used to ensure that local chemical bonding and steric exclusion are properly maintained. Our geometrically constrained refinement approach constrains the bonding geometry of the MnO₆ octahedra using a system of geometric templates [20,22,23] which allow each octahedron to adopt either regular or JT distorted geometry, as described in more detail in Ref. [19]. From the fully converged models we obtained the distribution of quadrupole distortions of the octahedra to look for evidence in the data for the existence of JT distortions. The five components of a quadrupole q are defined in terms of the components x, y, z of the six MnO bond vectors in each octahedron, as follows:

$$\begin{aligned} q_1 &= 2 \sum_{i=1}^6 x_i y_i, & q_2 &= 2 \sum_{i=1}^6 y_i z_i, \\ q_3 &= 2 \sum_{i=1}^6 z_i x_i, & q_4 &= \sum_{i=1}^6 (x_i^2 - y_i^2), \\ q_5 &= \frac{1}{\sqrt{3}} \sum_{i=1}^6 (2z_i^2 - x_i^2 - y_i^2). \end{aligned} \quad (2)$$

4. Results and discussion

The results of the refinements for all temperatures are reported in Table 1. Excellent agreement is observed between the PDF and Rietveld refined parameters, confirming that there are no significant local structural distortions in this material, as expected. The refined fractional coordinates are largely within the estimated uncertainties, which gives confidence in their accuracy given that they are being refined using different techniques. The ADPs are consistently lower in the PDF refinements. We might expect that the PDF data give more accurate ADPs because the data-range that is probed is wider and the refined ADPs are not correlated with a fitted background function. The fact that they are so small in the PDF refinements is a good indicator that there is little in the way of local structural disorder in this material. The refined lattice parameters are close between the PDF and Rietveld refinements, but are consistently overestimated by ~ 0.004 Å in the PDF results. This is a known problem with PDF data derived from TOF neutron data that has asymmetric diffraction peak

profiles [24] and this aberration has not been corrected in the current fits, so the Rietveld refined lattice parameters should be considered as the accurate values.

A parameter of interest in the manganites is the MnO bond-length, which is highly sensitive to the electronic state of the manganese [3,6]. In Table 2 we reproduce the values of this bond-length determined from the Rietveld refinements. The peaks corresponding to the nearest neighbor MnO correlations appear negative due to negative neutron scattering length of manganese. The presence of the JT distortion is clearly apparent in the LaMnO₃ data with a broad peak from the four shorter bonds centered around 1.92 Å and a completely resolved peak at 2.16 Å coming from the two long bonds. In the case of CaMnO₃ the peak has clearly collapsed to a single Gaussian and shifted to shorter- r . This shows that the octahedra have become regular in the Mn⁴⁺ case, with an average bond length that is shorter than the short-bonds of the Mn³⁺ in LaMnO₃. This is expected as Mn⁴⁺ in a cubic crystal field is not a JT ion [1]. This is reflected in the refined bond-lengths shown in Table 2.

The length of the longer MnO bonds is seen to decrease continuously with Ca doping [6]. In a charge-segregated model this behavior is expected to occur in the average bond-length, but not the bond-length determined locally, for example, from the PDF. The current result gives us a well-defined endmember value against which to compare the doping dependent behavior in La_{1-x}Ca_xMnO₃. The model was orthorhombic, allowing for three independent bond-lengths. However, all three values refined to approximately the same length of roughly 1.90 Å. This is slightly shorter than the average of the “short” MnO bonds in the MnO₆ octahedra of LaMnO₃ where the Mn is in the 3+ state. These bonds are 1.92 and 1.97 Å, respectively, at 20 K [10] giving an average value of 1.945 Å. This compares with the average MnO bond-length of 1.90 Å at 10 K in CaMnO₃ found here. The unstrained MnO₆ octahedra for Mn⁴⁺ charge-state are therefore smaller. If, in the doped systems, holes localize to make locally 4+ sites in a background of 3+ ions, this will result in a local strain.

It is interesting to compare the nature of the PDF in the region of the first few coordination shells to see the effect on the PDF of changing the shape of the MnO₆ octahedron as we go from Mn³⁺ to Mn⁴⁺. Fig. 3 shows a comparison of the low- r region of the RDFs, $R(r)$, for LaMnO₃ (gray profile) and CaMnO₃ (black profile) at 10 K temperature.

Table 1
PDF and Rietveld refinement results for CaMnO₃

T (K)	Rietveld					PDF				
	10	130	300	425	550	10	130	300	425	550
a (Å)	5.2757(1)	5.2782(1)	5.2816(1)	5.2850(1)	5.2884(1)	5.2790(2)	5.2808(2)	5.2834(3)	5.2856(10)	5.2917(6)
b (Å)	7.4398(1)	7.4435(1)	7.4567(1)	7.4666(2)	7.4761(2)	7.4438(3)	7.4482(3)	7.4624(5)	7.4781(13)	7.4803(8)
c (Å)	5.2555(1)	5.2577(1)	5.2671(1)	5.2748(1)	5.2820(1)	5.2583(2)	5.2609(2)	5.2716(3)	5.2756(8)	5.2870(4)
Ca x	0.0348(2)	0.0348(2)	0.0327(2)	0.0310(3)	0.0293(3)	0.0342(1)	0.0344(1)	0.0331(1)	0.0310(3)	0.0294(2)
Ca z	0.9936(4)	0.9939(4)	0.9946(4)	0.9943(7)	0.9945(6)	0.9935(1)	0.9931(1)	0.9944(2)	0.9918(6)	0.9922(3)
O1 x	0.4896(2)	0.4894(2)	0.4901(2)	0.4906(4)	0.4910(4)	0.4883(1)	0.4877(1)	0.4879(1)	0.4871(3)	0.4865(2)
O1 z	0.0674(3)	0.0671(2)	0.0661(3)	0.0658(4)	0.0653(4)	0.0673(1)	0.0671(1)	0.0649(2)	0.0669(4)	0.0644(2)
O2 x	0.2867(2)	0.2875(1)	0.2872(2)	0.2869(2)	0.2863(2)	0.2870(1)	0.2873(1)	0.2876(1)	0.2862(3)	0.2867(2)
O2 y	0.0347(1)	0.0342(1)	0.0337(1)	0.0328(2)	0.0321(1)	0.0345(1)	0.0346(1)	0.0342(1)	0.0323(2)	0.0313(1)
O2 z	0.7122(2)	0.7115(1)	0.7120(2)	0.7125(2)	0.7133(2)	0.7116(1)	0.7109(1)	0.7109(1)	0.7120(3)	0.7120(2)
Ca U_{iso} (Å ²)	0.0042(2)	0.0047(1)	0.0078(2)	0.0098(3)	0.0118(3)	0.0030(1)	0.0036(1)	0.0058(1)	0.0081(2)	0.0095(2)
Mn U_{iso} (Å ²)	0.0028(2)	0.0029(1)	0.0043(1)	0.0052(2)	0.0059(2)	0.0017(1)	0.0022(1)	0.0034(1)	0.0035(2)	0.0049(1)
O1 U_{iso} (Å ²)	0.0044(2)	0.0048(1)	0.0070(2)	0.0083(2)	0.0102(2)	0.0036(1)	0.0039(1)	0.0057(1)	0.0063(2)	0.0073(1)
O2 U_{iso} (Å ²)	0.0047(1)	0.0050(1)	0.0073(1)	0.0091(2)	0.0108(2)	0.0037(1)	0.0043(1)	0.0065(1)	0.0085(1)	0.0100(1)
R_w	0.038	0.034	0.042	0.072	0.085	0.094	0.073	0.077	0.126	0.084

All refinements were carried out using a structural model with orthorhombic symmetry (space group Pnma), with O1 occupying 4c ($x, 0.25, z$), and O2 occupying 8d (x, y, z) positions. Ca was at ($x, 0.25, x$) and Mn at (0.5, 0.0, 0.0) site.

Table 2
MnO distances and Mn–O2–Mn angles for $10\text{K} \leq T \leq 550\text{K}$ temperature range obtained from the Rietveld refinements

T (K)	$r(\text{MnO})_{\text{short}}$ (Å)	$r(\text{MnO})_{\text{medium}}$ (Å)	$r(\text{MnO})_{\text{long}}$ (Å)	$\theta(\text{Mn-O2-Mn})$ (deg)
10	1.89421(28)	1.8971(9)	1.9026(9)	156.98(5)
70	1.89454(27)	1.8976(8)	1.9027(8)	156.94(5)
130	1.89485(24)	1.8985(8)	1.9036(8)	156.89(4)
190	1.89563(23)	1.9000(7)	1.9034(8)	156.89(4)
250	1.89661(25)	1.8995(8)	1.9045(8)	157.05(5)
300	1.89715(25)	1.9003(8)	1.9045(8)	157.18(5)
425	1.89920(40)	1.9013(14)	1.9050(14)	157.55(7)
550	1.90120(40)	1.9025(14)	1.9047(14)	158.00(7)

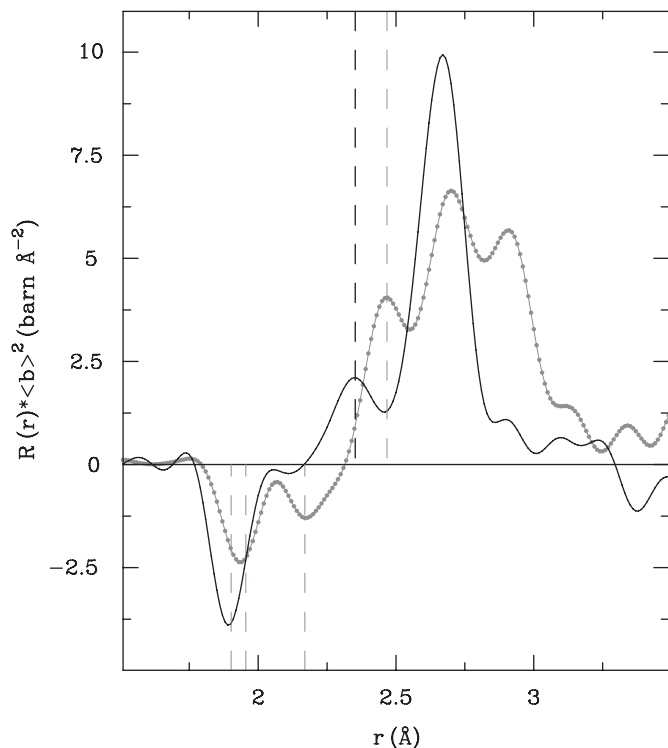


Fig. 3. Comparison of the radial distribution function, $R(r)$, for CaMnO_3 (solid black line) and LaMnO_3 (dotted gray line) at 10 K temperature. The figure shows the RDF peaks that describe the MnO_6 octahedron. The set of negative peaks at around 2 and 2.17 Å belong to the MnO bonds constituting the octahedron. The peaks are negative due to the negative neutron scattering length of Mn. Vertical dashed lines below $r = 2.25\text{Å}$ denote the positions of the MnO distances refined from LaMnO_3 . The two vertical dashed lines above $r = 2.25\text{Å}$ mark the position of the nearest LaO and CaO distances in the structures of the La and Ca endmembers, respectively.

Significant changes are also seen in the 2.75 and 2.85 Å oxygen–oxygen correlations that appear as a single peak in the CaMnO_3 data but are split into a multiplet in the JT distorted LaMnO_3 case. It is also worth noticing that the LaO peak at $\sim 2.48\text{Å}$ shifts considerably, becoming a CaO peak centered at $\sim 2.36\text{Å}$ for the Ca endmember. This is expected based on the relative size of La and Ca [25]. The intensity of the LaO RDF peak is twice that of the CaO peak due to the fact that the scattering length of La is nearly twice that of Ca, and the RDF peak intensity is scaled with the scattering lengths of the contributing atomic pairs.

The octahedra in the average crystal structure are regular and have no significant quadrupole distortions. In the case of LaMnO_3 , there is a discrepancy at high temperatures between the average and local structures [11]. In our large models refined using geometrically constrained refinement [19] we observed large

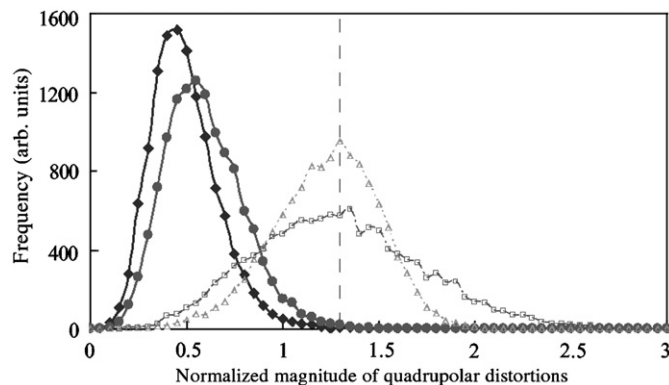


Fig. 4. Distribution of magnitudes of quadrupole distortions for the octahedra in large models of LaMnO_3 at 300 K (open, dashed, triangles) and 1050 K (open, dashed, squares), and for CaMnO_3 at 130 K (closed, solid, rhombus) and 425 K (closed, solid, circles). The magnitudes are normalized and dimensionless such that an octahedron with two long bonds of 2.16 Å and four short bonds of 1.94 Å would have a distortion of 1. In LaMnO_3 both distributions peak at around 1.3, indicating a strong JT distortion, and the width increases with temperature. In CaMnO_3 , the distortions are much smaller and the peak positions increase slightly with temperature. This is consistent with the distortions in the CaMnO_3 models being due to thermal variations in atomic positions, with no systematic JT distortion. The dashed line indicates the position of average quadrupole distortions for LaMnO_3 at 1.3, which does not move with temperature.

quadrupoles on all octahedra due to the persistence of the JT distortion. The distribution of quadrupole distortions in LaMnO_3 displayed a peak at a large value appropriate to the fully JT-distorted octahedron seen in the low-temperature crystal structure. The width of the distribution increased with temperature, but the position of the peak did not move. However, in CaMnO_3 we find the distribution of quadrupole distortion peaks at a much lower value, as shown in Fig. 4. Both the peak position and the width of the distribution increase with temperature. Thermal variations in atomic positions produce small quadrupolar distortions of octahedra. From the width of the thermal variation in MnO bond lengths, we can estimate the average magnitude of these small distortions. The FWHM of the distributions of MnO bond lengths are approximately 0.11 Å at 130 K and 0.16 Å at 425 K. From Eq. (2) this gives an average quadrupole of ~ 0.3 at 130 K and 0.5 at 425 K, consistent with our refined results (Fig. 4). The geometrically constrained refinement [19] therefore supports structural results that show, for example, at 130 K a small static distortion of $\sim 0.009\text{Å}$ coupled with thermal motion amplitude of $\sim 0.08\text{Å}$.

5. Summary

In summary, structural parameters for CaMnO_3 , in the Pnma space group, over the $10\text{K} \leq T \leq 550\text{K}$ temperature range are presented, as obtained from neutron time-of-flight total scattering experiments. Results of Rietveld and PDF analyses are in accord, showing that the MnO_6 octahedral units are regular across the temperature range studied. The evolution of the MnO bond lengths is discussed as the sample goes from pure Mn^{3+} in LaMnO_3 to Mn^{4+} in CaMnO_3 .

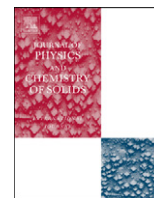
Acknowledgments

Work at MSU and ASU was supported by the NSF under Grant no. DMR-0304391. Work at Argonne National Laboratory is

supported under Contract no. DE-AC02-06CH1137. Beamtime on NPDF at Lujan Center at Los Alamos National Laboratory was funded under DOE Contract no. DEAC52-06NA25396. Simulations were run on the Saguaro High-Performance Computing Facility at ASU.

References

- [1] A.J. Millis, Lattice effects in magnetoresistive manganese perovskites, *Nature* 392 (1998) 147.
- [2] E.O. Wollan, W.C. Koehler, Neutron-diffraction study of the magnetic properties of the series of perovskite-type compounds $\text{La}_{1-x}\text{Ca}_x\text{MnO}_3$, *Phys. Rev.* 100 (1955) 545–563.
- [3] S.J.L. Billinge, R.G. DiFrancesco, G.H. Kwei, J.J. Neumeier, J.D. Thompson, Direct observation of lattice polaron formation in the local structure of $\text{La}_{1-x}\text{Ca}_x\text{MnO}_3$, *Phys. Rev. Lett.* 77 (1996) 715–718.
- [4] C.H. Booth, F. Bridges, G.H. Kwei, J.M. Lawrence, A.L. Cornelius, J.J. Neumeier, Direct relationship between magnetism and MnO_6 distortions in $\text{La}_{1-x}\text{Ca}_x\text{MnO}_3$, *Phys. Rev. Lett.* 80 (4) (1998) 853–856.
- [5] E.S. Božin, X. Qiu, M. Schmidt, G. Paglia, J.F. Mitchell, P.G. Radaelli, Th. Proffen, S.J.L. Billinge, Local structural aspects of the orthorhombic to pseudo-cubic phase transformation in $\text{La}_{1-x}\text{Ca}_x\text{MnO}_3$, *Physica B* 385–386 (2006) 110–112.
- [6] E.S. Božin, M. Schmidt, A.J. DeConinck, G. Paglia, J.F. Mitchell, T. Chatterji, P.G. Radaelli, Th. Proffen, S.J.L. Billinge, Understanding the insulating phase in CMR manganites: shortening of the Jahn–Teller long-bond across the phase diagram of $\text{La}_{1-x}\text{Ca}_x\text{MnO}_3$, *Phys. Rev. Lett.* 98 (2007) 137203.
- [7] E. Dagotto, Complexity in strongly correlated electronic systems, *Science* 309 (2005) 257–262.
- [8] Th. Proffen, S.J.L. Billinge, Probing the local structure of doped manganites using the atomic pair distribution function, *Appl. Phys. A* 74 (2002) 1770.
- [9] J. Rodriguez-Carvajal, M. Hennion, F. Moussa, A.H. Moudden, L. Pinsard, A. Revcolevschi, Neutron-diffraction study of the Jahn–Teller transition in stoichiometric LaMnO_3 , *Phys. Rev. B* 57 (1998) R3189–R3192.
- [10] Th. Proffen, R.G. DiFrancesco, S.J.L. Billinge, E.L. Brosha, G.H. Kwei, Measurement of the local Jahn–Teller distortion in $\text{LaMnO}_{3.006}$, *Phys. Rev. B* 60 (1999) 9973.
- [11] X. Qiu, Th. Proffen, J.F. Mitchell, S.J.L. Billinge, Orbital correlations in the pseudocubic O and rhombohedral R-phases of LaMnO_3 , *Phys. Rev. Lett.* 94 (2005) 177203.
- [12] C.D. Ling, E. Grando, J.J. Neumeier, J.W. Lynn, D.N. Argyriou, Inhomogeneous magnetism in La-doped CaMnO_3 : I, Mesoscopic phase separation due to lattice-coupled ferromagnetic interactions, *Phys. Rev. B* 68 (2003) 134439.
- [13] T. Egami, S.J.L. Billinge, *Underneath the Bragg Peaks: Structural Analysis of Complex Materials*, Pergamon Press, Elsevier, Oxford, England, 2003.
- [14] B.E. Warren, *X-ray Diffraction*, Dover, New York, 1990.
- [15] P.F. Peterson, M. Gutmann, Th. Proffen, S.J.L. Billinge, PDFgetN: a user-friendly program to extract the total scattering structure function and the pair distribution function from neutron powder diffraction data, *J. Appl. Crystallogr.* 33 (2000) 1192.
- [16] A.C. Larson, R.B. Von Dreele, General structure analysis system, Report No. LAUR-86-748, Los Alamos National Laboratory, Los Alamos, NM, 2000.
- [17] B.H. Toby, Expgui, a graphical user interface for GSAS, *J. Appl. Crystallogr.* 34 (2001) 201–213.
- [18] C.L. Farrow, P. Juhas, J.W. Liu, D. Bryndin, E.S. Božin, J. Bloch, Th. Proffen, S.J.L. Billinge, PDFfit2 and PDFgui: computer programs for studying nanostructure in crystals, *J. Phys. Condens. Matter* 19 (2007) 335219.
- [19] A. Sartbaeva, S.A. Wells, M.F. Thorpe, E.S. Božin, S.J.L. Billinge, Quadrupolar ordering in LaMnO_3 revealed from scattering data and geometric modeling, *Phys. Rev. Lett.* 99 (2007) 155503.
- [20] A. Sartbaeva, S.A. Wells, M.F. Thorpe, E.S. Božin, S.J.L. Billinge, Geometric simulation of perovskite frameworks with Jahn–Teller distortions: applications to the cubic manganites, *Phys. Rev. Lett.* 94 (2006) 065501.
- [21] R.L. McGreevy, RMC: progress, problems and prospects, *Nucl. Instrum. Methods Phys. Res. A* 354 (1995) 1–16.
- [22] S.A. Wells, M.T. Dove, M.G. Tucker, Finding best-fit polyhedral rotations with geometric algebra, *J. Phys. Condens. Matter* 14 (2002) 4567–4584.
- [23] A. Sartbaeva, S.A. Wells, M.M.J. Treacy, M.F. Thorpe, The flexibility window in zeolites, *Nat. Mater.* 12 (2006) 962–965.
- [24] I. Jeong, M.J. Graf, R.H. Heffner, Effects of Bragg peak profiles and nanoparticle sizes on the real-space pair distribution function, *J. Appl. Crystallogr.* 38 (2005) 55–61.
- [25] R.D. Shannon, Revised effective ionic radii and systematic studies of interatomic potentials, *Acta Cryst. A* 32 (1976) 751.



Study of the negative thermal expansion of cuprite-type structures by means of temperature-dependent pair distribution function analysis: Preliminary results

Monica Dapiaggi^{a,*}, HyunJeong Kim^b, Emil S. Božin^b, Simon J.L. Billinge^b, Gilberto Artioli^c

^a Dipartimento di Scienze della Terra, Università degli Studi di Milano, via Botticelli 23, I20133 Milano, Italy

^b Department of Physics and Astronomy, Michigan State University, East Lansing, MI 48824-1116, USA

^c Dipartimento di Geoscienze, Università degli Studi di Padova, via Giotto 1, I35137 Padova, Italy

ARTICLE INFO

Keywords:

- A. oxides
- C. Neutron scattering
- D. Thermal expansion

ABSTRACT

Copper (I) and silver (I) oxides crystallize with the same structure, and both show a wide range of negative thermal expansion (NTE): Cu₂O contracts with temperature up to about 200 K and then expands, while Ag₂O has a NTE up to its decomposition temperature at about 450 K. Here we report a careful temperature-dependent pair distribution function (PDF) analysis that showed that copper oxide, at about 200 K, exhibits geometric distortions of the tetrahedral units, probably related to a change in the solid angle of the polyhedra. Silver oxide, on the other hand, showed the same distortions even at the lowest temperature measured (10 K): structural refinements of the PDF confirmed the presence of local distortions (below 10 Å) at all temperatures.

© 2008 Elsevier Ltd. All rights reserved.

1. Introduction

The simple cuprite structure is shared by cuprite (Cu₂O) and silver (I) oxide (Ag₂O) and it can be described by two interpenetrated chains of corner sharing M₄O tetrahedra, where M represents the metal atom. Both compounds show a wide range of negative thermal expansion (NTE): cuprite contracts with temperature up to about 200 K and then expands (but extremely slowly), while Ag₂O has an NTE up to its decomposition temperature at about 450 K. These materials have been investigated extensively by coupling the anisotropic displacement parameters (ADPs) measured by diffraction to an accurate EXAFS analysis of higher-order cumulants in the whole accessible temperature range (for the latest results see Refs. [1,2]). The tetrahedral units in the structure proved to be much stiffer against stretching than against bond-bending distortions that bring the metal atoms towards each other. The bridging metal atoms show a strong anisotropy in thermal vibrations, larger in the direction perpendicular to the bond than parallel to it. Many of the NTE materials have a similar anisotropy in the measured ADPs, indicating the presence of low-frequency rigid unit modes (RUMs) that can cause rotations of the polyhedral units but that keeps them rigid. In many framework structures, such as ZrW₂O₈ (NTE

from 0.3 to 1050 K) [3], RUMs are thought to be the origin of NTE, though the full situation may be more complex [4,5]. In other framework structures, the correlation between RUMs and transverse atomic motion cannot be clearly recognized, even though transverse vibrations of bridging atoms surely play a relevant role in NTE. The cuprite structure is one of the latter: the bridging atoms show a strong anisotropy in thermal motion, but the structure shows a complex local behavior of the metal atoms, with a positive thermal expansion of M–O bonds, coupled with a NTE of only 6 of the 12s nearest neighbors (M–M) [2]. Up to now, no simple model was found to explain NTE in these materials. There are many factors that can influence their thermal behavior. Although most of them are certainly of vibrational origin, an influence of geometric distortions on NTE cannot be excluded. The presence of static disorder in Ag₂O [1] was already demonstrated by the large intercept at 0 K of ADPs determined from diffraction. On the other hand, Cu₂O showed no static disorder whatsoever (the intercept at 0 K was comparable with zero point motion [6]). All these results suggest the necessity of studying geometric distortions in the cuprite structure. Here we report preliminary results from a temperature-dependent pair distribution function (PDF) analysis. The PDF analysis based on total scattering approach was chosen due to the possibility of studying structural distortions at short range as well as at long range, even though they are not detectable with crystallographic techniques. Moreover, PDF results can be compared directly with EXAFS results, allowing the use of these techniques in a complementary and critical way.

* Corresponding author. Tel.: +39 2 50315576; fax: +39 2 50315597.
E-mail address: monica.dapiaggi@unimi.it (M. Dapiaggi).

This paper aims to present the preliminary data obtained from PDF analysis and to insert them in the scientific background of NTE materials.

2. Experiments and data reduction

Total scattering neutron diffraction experiments were performed at the beamline GEM at ISIS (Rutherford Appleton Laboratory, Chilton, UK) [7], with a cryofurnace, from 10 to 375 K every 25 K for Ag_2O and up to 300 K every 50 K for Cu_2O . Commercially available Cu_2O sample was purchased from Aldrich, CAS no. 1317-39-1 (purity 97%), while the Ag_2O sample was obtained from Riedel-de-Haën, CAS no. 20667-12-3 (purity 99.5%). The Ag_2O sample did not show any sign of the phase transition observed in other Ag_2O samples [8,9]. A high-purity vanadium rod, extruded vanadium container, and the sample environment were also collected in order to correct and normalize the data [10]. At each temperature, data were collected for about 5 h. The nominal maximum Q attainable at GEM is about 100 \AA^{-1} [7]. However, the data were used up to $Q_{\text{max}} = 40 \text{ \AA}^{-1}$ for Cu_2O , and only up to $Q = 20 \text{ \AA}^{-1}$ for Ag_2O ; the reason for the latter is that data statistics did not allow the use of the high Q range data. Although a longer acquisition time might have solved the problem, the experimental decision was to collect as many temperatures as possible in order to have a detailed temperature dependence. Data reduction was performed with the software PDFGetN [11]. Data analyses and simulations were carried out with the softwares PDFfit2 and PDFgui [12]. However, when the two compounds are compared directly, a Q_{max} of 20 \AA^{-1} was used for both of them in order to obtain a fair assessment of their differences or similarities.

3. Cuprite structure and its PDF peaks

The cuprite structure is fairly simple, although shared only by two materials: Cu_2O and Ag_2O . It belongs to space group $Pn\bar{3}m$, with the metal (M) atoms occupying the positions (4b) and the oxygen atoms occupying the positions (2a). The cuprite structure is made by two interpenetrating lattices, one face-centered cubic (FCC) sublattice of metal atoms and one body-centered cubic (BCC) sublattice of oxygen atoms. Each M atom is linearly coordinated to two O atoms, while each O atom is tetrahedrally coordinated to four M atoms. Alternatively, the cuprite structure can be considered as a framework of two interpenetrating networks of corner shared M_4O tetrahedra with the cristobalite-type topology. Fig. 1 shows the two networks differentiated by color, being one with red oxygen atoms and cyan metal atoms, and the other with purple oxygen atoms and blue metal atoms.

In order to better understand the features in the $G(r)$, it is necessary to briefly explain the relationship between each PDF peak and the actual atomic distances.

For this reason, the partial PDFs have been calculated [12], based on the Cu_2O structure, for the distances Cu–Cu, Cu–O, and O–O. The same partials have been also calculated using only one network of the two in the structure, to be able to differentiate distances from atoms belonging to the same network from those belonging to different networks. The partial PDFs were weighted by appropriate weighting factors related to scattering properties of the atomic species involved [10]. The results of this can be seen in Fig. 2, with the top part showing the partial for one network only and the bottom part showing the partials for the whole structure. Each diagram also contains the total $G(r)$, simulated under exactly the same conditions, for a quicker comparison. According to the figure, the first peak in the PDF represents the 4

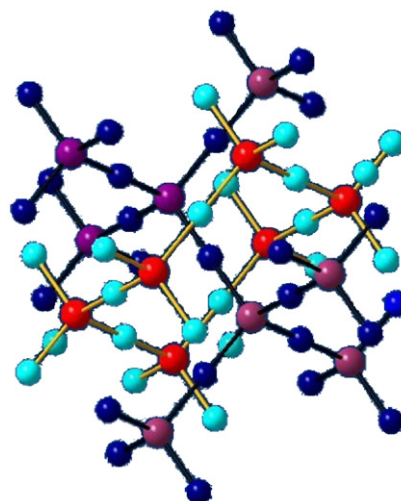


Fig. 1. Sketch of the cuprite structure: the two different interpenetrating networks can be clearly distinguished by color, being one with red oxygen atoms and cyan metal atoms, and the other with purple oxygen atoms and blue metal atoms.

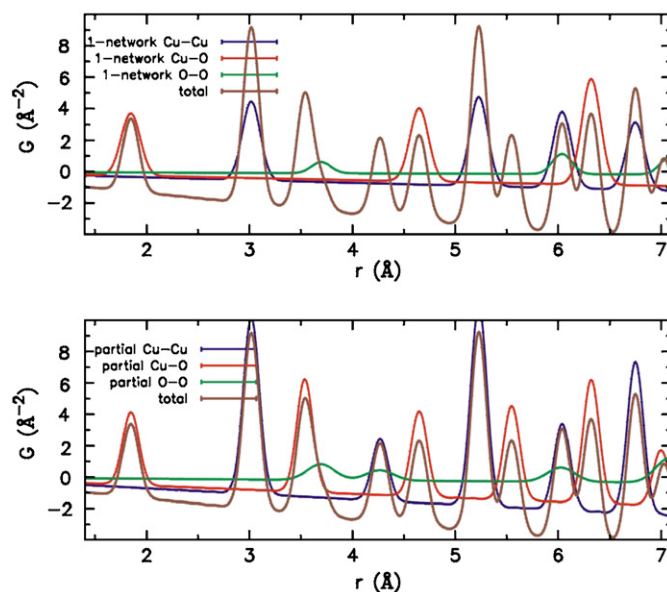


Fig. 2. Partial PDFs for Cu–Cu, Cu–O and O–O bonds in the cuprite structure. The upper part of the figure shows the partial PDFs from just one of the two-cuprite networks. The lower part of the figures shows the partial PDFs for the whole structure.

Table 1

Summary of the relationship between interatomic distances and PDF peaks: in the line with “same” one can find interactions between atoms belonging to the same network, in the line with “other” one can find interactions between atoms belonging to different networks

Distance	1.8 Å	3 Å	3.5 Å	4.2 Å	4.6 Å
M–M		Same+other		Other	
M–O	Same		Other		Same
O–O			Same		

M–O distances within the tetrahedron; the second peak corresponds to 12 M–M distances, of which 6 are within the same network and the other 6 to interactions between atoms belonging to different networks. The third peak is a combination of 6 M–O

distances belonging to interactions on different networks and of O–O distances in the same network. A summary of this is shown in Table 1.

4. Results of the PDF analysis and comparison with EXAFS data

The position of the first peak in PDF, $G(r)$, constituted by the 4 M–O distances within the tetrahedron, can be used for a direct comparison with EXAFS data [2], which gives the temperature dependence of this M–O bond length. The peak position in the $G(r)$ was evaluated by fitting a Gaussian profile to the data, while the EXAFS data were taken from Ref. [2]. As can be seen in Fig. 3, the temperature dependence of this distance is the same from both the techniques and its absolute value is very similar for both the techniques, as expected. It is interesting to note that the Ag–O bond expands more than Cu–O bond. In order to be able to directly compare the results for the two materials, the PDFs were calculated using the same Q_{\max} for both (20 \AA^{-1}).

Fig. 4 shows the low- r region of the $G(r)$ of copper (top) and silver (bottom) oxides at selected temperatures. As can be seen from the figure, the first peak is very sharp for both the samples and its shape does not change with temperature, meaning that the 4 distances are still all equal with raising temperature, i.e. there is no measurable distortion of these bond lengths in the tetrahedron. The positions of the other peaks are not so straightforward to understand and to compare with EXAFS results, due to their composite nature. For example, the second peak (at about 3 Å for Cu_2O and 3.3 Å for Ag_2O) comes from contributions from interactions of atoms in the same network and in different networks, while the third one (at about 3.5 Å for Cu_2O and 4 Å for Ag_2O) is a combination of M–O and O–O interactions. These different contributions may have different behavior with temperature (as already demonstrated by EXAFS for the second shell [2]), and therefore, care should be employed in comparing results regarding these PDF peaks.

We now look at the behavior of the PDF of the two oxides with temperature in more detail.

4.1. Cu_2O

Fig. 4 (upper part) shows selected $G(r)$ of Cu_2O at different temperatures. Besides what was already said about the first peak,

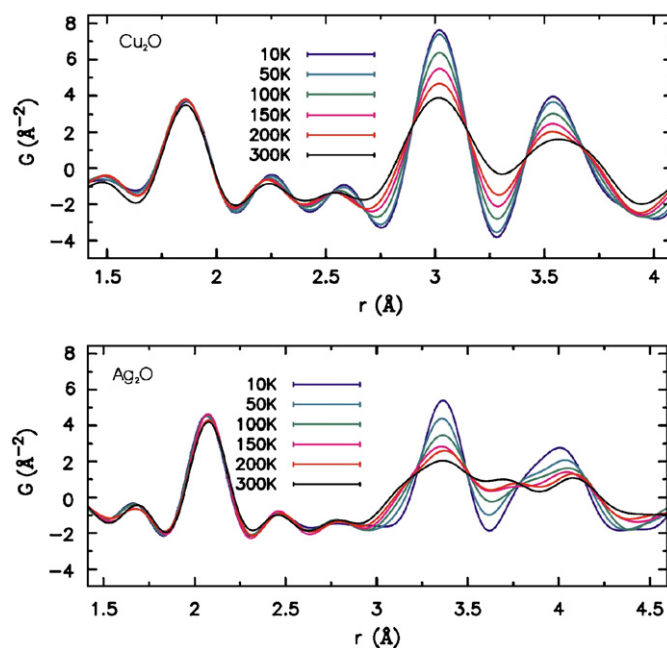


Fig. 4. Comparison of the first three PDF peaks for Cu_2O and Ag_2O at selected temperatures between 10 and 300 K. For both the oxides, the $G(r)$ were obtained with $Q_{\max} = 20 \text{ \AA}^{-1}$, for a reasonable comparison.

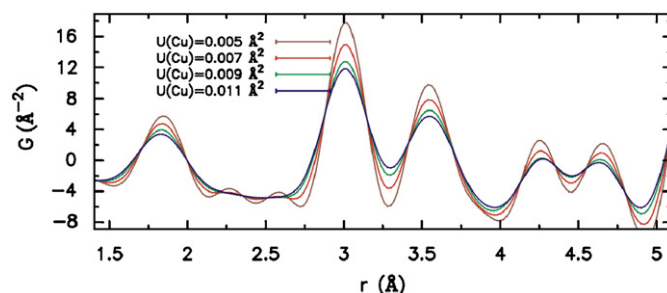


Fig. 5. Effects of thermal factors on the simulated PDF of the Cu_2O structure, with (i) $U(\text{Cu}) = U(\text{O}) = 0.005 \text{ \AA}^2$, (ii) $U(\text{Cu}) = U(\text{O}) = 0.007 \text{ \AA}^2$, (iii) $U(\text{Cu}) = U(\text{O}) = 0.009 \text{ \AA}^2$ and (iv) $U(\text{Cu}) = U(\text{O}) = 0.011 \text{ \AA}^2$. The simulations are made with $Q_{\max} = 20 \text{ \AA}^{-1}$. These results can be compared with the experimental PDFs shown in Fig. 4.

let us now look at the second peak (6+6 Cu–Cu distances): the peak intensity and the peak shape change rapidly with temperature, producing a broader and less intense peak at higher temperatures. In general, the reasons for peak broadening and reduced peak intensity can be found in a purely dynamic disorder (thermal effect), or in geometric distortions (static disorder) that lead to a spread of distances, hence in a broader peak in $G(r)$. A combination of the two effects is also possible. However, the variations in the PDF are far larger than expected for a pure thermal effect (U_{iso} for the PDF measured at 300 K was 0.015 \AA^2 for copper and 0.018 \AA^2 for oxygen, and still the fit was rather poor ($R_w = 0.181$)). In Fig. 5 the $G(r)$ s of the Cu_2O structure were calculated with different sets of thermal parameters, similar to those obtained from Rietveld analysis of the same data. The thermal parameters used were: $U_{\text{iso}}(\text{Cu}) = U_{\text{iso}}(\text{O}) = 0.005 \text{ \AA}^2$, (ii) $U_{\text{iso}}(\text{Cu}) = U_{\text{iso}}(\text{O}) = 0.007 \text{ \AA}^2$, (iii) $U_{\text{iso}}(\text{Cu}) = U_{\text{iso}}(\text{O}) = 0.009 \text{ \AA}^2$, (iv) $U_{\text{iso}}(\text{Cu}) = U_{\text{iso}}(\text{O}) = 0.011 \text{ \AA}^2$. Two main observations can be made from the comparison between the experimental and the simulated data: (1) the decrease in intensity of the third peak is much larger in the experimental PDF than in the simulated PDF; (2) in the

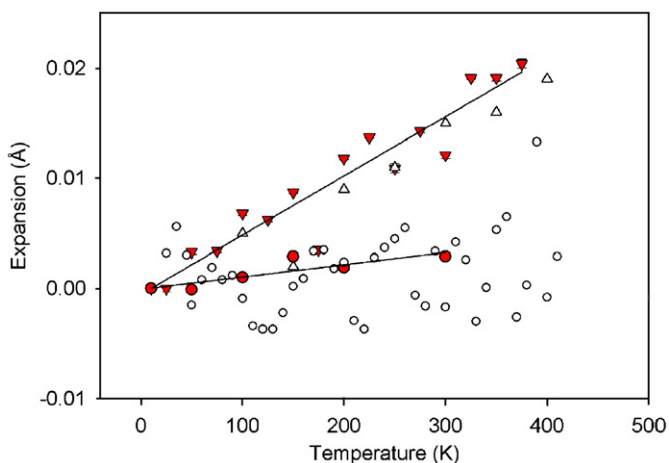


Fig. 3. Comparison between the thermal expansion of the M–O bond (first shell) as measured by EXAFS and PDF. The EXAFS data are taken from Ref. [2]. The lines are best fit lines for PDF data only, to make the graph more readable. Filled symbols are from the PDF, open symbols are from EXAFS. Silver oxide results are plotted as triangles and cuprite as circles.

third peak, a shoulder starts to appear on the high- r side at about 200 K, and further develops at 300 K. This shoulder is not an artefact from the Fourier transform procedure: various checks were made by FT the data with different Q_{\max} , and the shoulder never disappeared. The third peak is dominated by 6 Cu–O distance between atoms belonging to different networks as shown in Fig. 2. These effects on the PDF can be due to a distortion in the tetrahedral units, with the solid angle of the tetrahedron changing, and thus producing two different Cu–Cu distances. This may affect the structure, at least locally, causing the development of the shoulder in the high- r region of the third peak (two different Cu–O distances).

4.2. Ag_2O

Fig. 4 (lower part) shows selected $G(r)$ s of Ag_2O at different temperatures. Even at the lowest temperature (10 K), the second peak in the $G(r)$ is almost of the same height as the first one, and the broadening (and decrease in intensity) of the second and third peak is much faster with temperature than for copper oxide. Shoulders appear on both side of the second peak, while the shoulder on the high- r side of the third peak is already present at 10 K and grows very fast with temperature, becoming soon more

intense than the original distance at about 4 Å (or moving to higher r with temperature). The origin of these effects on the PDF peaks may be related, also in this case, to a distortion in the tetrahedral units spreading locally in the structure. A structural refinement of the $G(r)$ with PDFgui [12] starting from the undistorted crystal structure of Ag_2O taken from literature [13], showed that, even at the lowest temperature measured, there were some discrepancies between the “crystallographic” structure and the PDF data (Fig. 6). As can be seen in the figure, the low- r region (below 8–10 Å) shows a larger difference curve, revealing the presence of distortions in the local region unexplained by the crystallographic model used. As it can be seen in the figure, the fit in the higher r region proves to be much more satisfactory, showing that the distortions tend to affect the structure locally, within a few coordination shells. In the case of copper oxide, on the other hand, the PDF can be fitted with very good results by using the “crystallographic” structure, at least up to the temperature at which the first distortion starts to appear. The effect, however, is much smaller than in the case of silver oxide, as it can be clearly evinced from the bottom part of Fig. 6.

5. Discussion: dynamic disorder vs static disorder

The results of the comparison between EXAFS and diffraction allow a better understanding of the dynamics of the cuprite structure, showing that neither the Cu–O bond nor the Ag–O bond are strong enough to form structural units behaving rigidly with temperature [1]. This was also confirmed by inelastic neutron scattering and lattice dynamics calculations [14]. The tetrahedral units tend to deform with temperature, and a certain degree of static disorder is present in the silver oxide structure. Moreover, Mittal and coworkers [14] showed that Cu–O and Cu–Cu bonds are stiffer than Ag–O and Ag–Ag, as already evidenced by the larger displacement correlation function found for copper oxide first and second coordination shells [1,2]. The atom dynamics is almost fully understood: what needs developing and further study is the possible effect of static disorder on the vibrational properties of these materials, and hence on its thermal expansion behavior.

The analysis of the temperature-dependent PDF for copper and silver oxides illustrates the presence of geometric distortions in the structure of both oxides that develop with temperature, although starting at different temperatures in the two cases. For copper oxide, the distortion appears for the first time at around 200 K, corresponding to the inversion in the thermal expansion behavior. The presence of this distortion is not in contradiction with the fact that Cu_2O ADPs showed a 0 K intercept compatible with zero point motion, as the deformation begins at high temperature, and no sign of static disorder is present in the low-temperature region [6]. In Ag_2O , on the other hand, probably the same tetrahedral distortion appears at very low temperature (it is present even at 10 K), confirming the strong contribution of static disorder to the APDs at low temperature in silver oxide. These distortions become more distinct and a further spread in distances can be seen in the PDF at higher temperatures, clear signs of a larger degree of deformation in the structure. The specific nature of these distortions can only be supposed at present, as further analysis is necessary in order to better characterize which atoms are involved and how the structure evolves with temperature. Past studies can provide a good starting point, especially EXAFS data on the different thermal behavior of M–M distances contributing to the second shell. This can play a key role in understanding if the distortion comes from a bending of the M–M bond, i.e. a change in the solid angle of the tetrahedral units or from a shortening of the distance between the two networks.

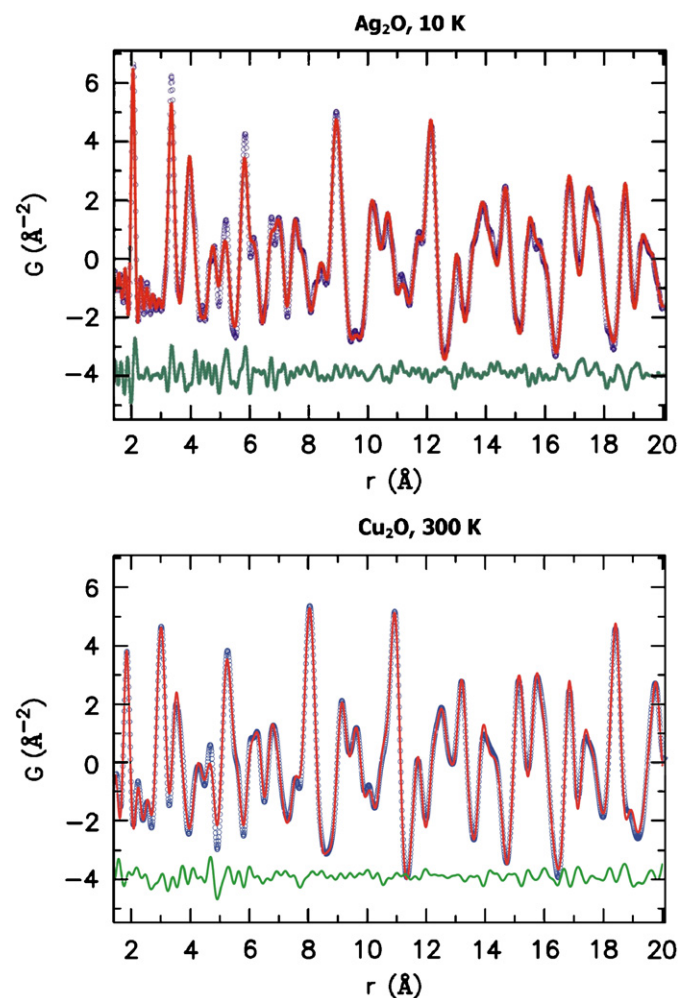


Fig. 6. PDF fits of the cuprite structure. The top part shows the fit of Ag_2O at $T = 10$ K, and the bottom part shows the fit of Cu_2O at $T = 300$ K. The red curve represents the best fit: for Ag_2O isotropic thermal factor for Ag and O equal to 0.012 \AA^2 were used, while for Cu_2O isotropic thermal factors were refined. The blue dots represent the data points for $Q_{\max} = 20 \text{ \AA}^{-1}$. The green curve underneath the graph represents the difference between the experimental and the calculated $G(r)$.

What is clear from PDF analysis is that the four M–O bonds within the tetrahedron, all remain equal with temperature for both the oxides. Moreover, a comparison between the shape of the first peak compared to the others shows that in the experimental PDF (Fig. 4) the first peak is much sharper than the others, while it is not in the simulated ones (Fig. 5), where motion correlations are neglected [15,16]. This confirms the results of the EXAFS-diffraction approach [1,2], as well as those from lattice dynamics calculations [14]. From these preliminary results, it is still not clear which is the relationship of the structural distortions with the thermal behavior of the two oxides, but there seems to be a correlation between the appearance of the first signs of distortion in Cu₂O and the inversion temperature (at 200 K Cu₂O starts to expand), so copper oxide thermal behavior is not coming only from normal atom dynamics, as supposed until now. The structural distortions in silver oxide are much more evident even at very low temperature and suggest that the local structure has lower symmetry than the average structure. This can certainly play a role in the thermal expansion of the structure, when coupled with the strong transverse vibrations of bridging atoms typical of this structure, but also can play a role in the appearance of the phase transition at low temperature, observed in other Ag₂O samples. A more detailed study of the PDF evolution with temperature is necessary to better understand the nature of the distortions and their relationship with the thermal behavior of the materials.

Acknowledgments

The authors would like to thank ISIS for providing the beam time at GEM (experiment number 510070), and P.G. Radaelli (ISIS) for his help during data collection. M.D. and G.A. would also like to thank W.I.F. David (ISIS) for sharing some of his beam time, and for many helpful discussions. M.D.'s work in the Billinge group was funded by the US National Science Foundation through Grant DMR-0703940.

References

- [1] G. Artioli, M. Dapiaggi, P. Fornasini, A. Sanson, F. Rocca, M. Merli, Negative thermal expansion in cuprite-type compounds: a combined synchrotron XRPD, EXAFS, and computational study of Cu₂O and Ag₂O, *J. Phys. Chem. Solids* 67 (2006) 1918–1922.
- [2] A. Sanson, F. Rocca, G. Dalba, P. Fornasini, R. Grisenti, M. Dapiaggi, G. Artioli, Negative thermal expansion and local dynamics in Cu₂O and Ag₂O, *Phys. Rev. B: Condens. Matter Mater. Phys.* 73 (2006) 214305/1–214305/13.
- [3] T.A. Mary, J.S.O. Evans, T. Vogt, A.W. Sleight, Negative thermal expansion from 0.3 to 1050 K in ZrW₂O₈, *Science* 272 (1996) 90–92.
- [4] D. Cao, F. Bridges, G.R. Kowach, A.P. Ramirez, Frustrated soft modes and negative thermal expansion in ZrW₂O₈, *Phys. Rev. Lett.* 89 (2002) 215902.
- [5] D. Cao, F. Bridges, G.R. Kowach, A.P. Ramirez, Correlated atomic motions in the negative thermal expansion material ZrW₂O₈ a local structure study, *Phys. Rev. B: Condens. Matter Mater. Phys.* 68 (2003) 014303.
- [6] M. Dapiaggi, W. Tiano, G. Artioli, A. Sanson, P. Fornasini, The thermal behavior of cuprite: an XRD–EXAFS combined approach, nuclear instruments & methods in physics research, Sect. B: Beam Interact. Mater. Atoms 200 (2003) 231–236.
- [7] A.C. Hannon, Results on disordered materials from the general materials diffractometer, GEM, at ISIS, nuclear instruments & methods in physics research, Sect. A: Accel., Spectrometers Detectors Assoc. Equip. 551 (2005) 88–107.
- [8] W. Tiano, 2002, Laurea Thesis.
- [9] B.J. Kennedy, Y. Kubota, K. Kato, Negative thermal expansion and phase transition behaviour in Ag₂O, *Solid State Commun.* 136 (2005) 177–180.
- [10] T. Egami, S.J.L. Billinge, Underneath the Bragg peaks: structural analysis of complex materials, in: R.W. Cahn (Ed.), Pergamon Materials Series, vol. 7, Pergamon, 2003.
- [11] P.F. Peterson, M. Gutmann, T. Proffen, S.J.L. Billinge, PDFgetN: a user-friendly program to extract the total scattering structure function and the pair distribution function from neutron powder diffraction data, *J. Appl. Crystallogr.* 33 (2000) 1192.
- [12] C.L. Farrow, P. Juhas, J.W. Liu, D. Bryndin, J. Bloch, T. Proffen, S.J.L. Billinge, PDFfit2 and PDFgui: computer programs for studying nanostructure in crystals, *J. Phys.: Condens. Matter* 19 (2007) 335219.
- [13] P. Niggli, Die Kristallstruktur einiger oxyde I, *zeitschrift fuer kristallographie, kristallgeometrie, kristallphysik, Kristallchemie* 57 (1922) 253–299.
- [14] R. Mittal, S.R. Chaplot, S.K. Mishra, P.P. Bose, Inelastic neutron scattering and lattice dynamical calculation of negative thermal expansion compounds Cu₂O and Ag₂O, *Phys. Rev. B: Condens. Matter Mater. Phys.* 75 (2007) 174303(1)–174303(8).
- [15] I.K. Jeong, R.H. Heffner, M.J. Graf, S.J.L. Billinge, Lattice dynamics and correlated atomic motion from the atomic pair distribution function, *Phys. Rev. B: Condens. Matter Mater. Phys.* 67 (2003) 104301.
- [16] I.K. Jeong, T. Proffen, F. Mohiuddin-Jacobs, S.J.L. Billinge, Measuring correlated atomic motion using X-ray diffraction, *J. Phys. Chem. A* 103 (1999) 921–924.

Atomic pair distribution function analysis from the ARCS chopper spectrometer at the Spallation Neutron Source

E. S. Božin,^{a,b} P. Juhás,^a W. Zhou,^a M. B. Stone,^c D. L. Abernathy,^c A. Huq^c and S. J. L. Billinge^{a,b*}

^aDepartment of Applied Physics and Applied Mathematics, Columbia University, New York, New York 10027, USA, ^bCondensed Matter Physics and Materials Science Department, Brookhaven National Laboratory, Upton, New York 11973, USA, and ^cNeutron Scattering Sciences Division, Oak Ridge National Laboratory, Tennessee 37831, USA. Correspondence e-mail: sb2896@columbia.edu

Neutron powder-diffraction-based atomic pair distribution functions (PDFs) are reported from the new wide-angular-range chopper spectrometer ARCS at the Spallation Neutron Source at Oak Ridge National Laboratory. The spectrometer was run in white-beam mode with no Fermi chopper. The PDF patterns of Ni and Al₂O₃ were refined using the PDFfit method and the results compared with data collected at the NPDF diffractometer at Los Alamos National Laboratory. The resulting fits are of high quality, demonstrating that quantitatively reliable powder diffraction data can be obtained from ARCS when operated in this configuration.

© 2009 International Union of Crystallography
Printed in Singapore – all rights reserved

1. Introduction

Neutron powder diffraction measurements can be carried out routinely using time-of-flight (TOF) instruments at spallation sources such as the NPDF at the Los Alamos Neutron Science Center (LANSCE). Here we show that quantitatively reliable PDFs can also be obtained from the ARCS chopper spectrometer at the Spallation Neutron Source at Oak Ridge National Laboratory when operated without a Fermi chopper. The Fermi chopper mechanism at ARCS is mounted on a motorized translation table, allowing one to switch easily between two installed Fermi chopper slit packages and an open 'white-beam' position. This feature, together with the demonstration that quantitatively reliable structural information can be obtained from ARCS, means that it becomes straightforward to analyze structure and dynamics from the same sample without dismounting it from the instrument.

2. Experimental

No routines currently exist for a complete time-focusing of diffraction data from ARCS, and so the data were histogrammed to produce the one-dimensional powder diffraction pattern using a generic TOF to *d* space conversion. This results in data with degraded resolution and with poorly defined peak shapes. Although the data could not be refined using the Rietveld method, we successfully acquired and refined atomic pair distribution functions (PDFs) to obtain quantitative structural information.

Data were collected on two different commercially available standard samples: Ni and Al₂O₃. For comparison, data from Ni were obtained from the NPDF diffractometer at LANSCE. The samples were loose powders of between 3 and 8.3 g in weight sealed in extruded vanadium tubes. A vanadium rod measurement was also performed to obtain incident spectrum information. A typical reduced total scattering structure function, $F(Q) = Q[S(Q) - 1]$, where $S(Q)$ is the total scattering structure function and Q is the

momentum transfer, from ARCS is shown in Fig. 1(a), with the corresponding $F(Q)$ function from NPDF shown in Fig. 1(b) for comparison. The resulting PDFs are shown in Figs. 1(c) and 1(d), with model fits obtained using *PDFgui* (Farrow *et al.*, 2007) superimposed. The details of the PDF method are provided elsewhere (Egami & Billinge, 2003).

Simple visual comparison of the ARCS and the NPDF PDFs demonstrates that the ARCS data are of high quality. Furthermore, all ARCS data sets could be successfully refined, including the more complicated Al₂O₃ structure. The quantitative results of the refinements are presented in Table 1.

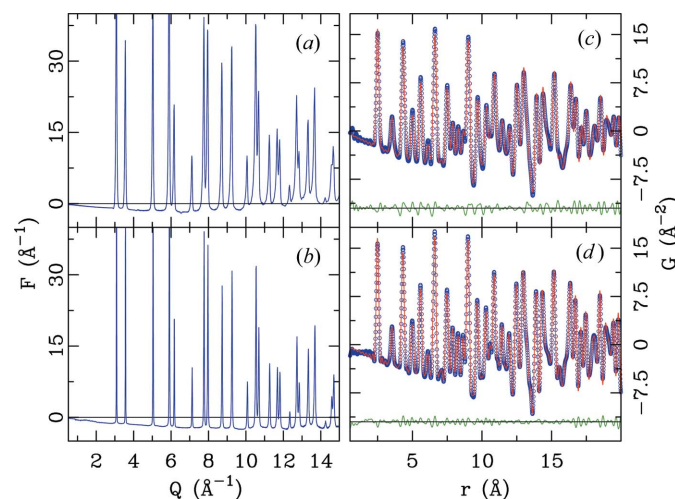


Figure 1
Total scattering function $F(Q)$ of Ni from data collected at (a) ARCS and (b) NPDF. Data were collected at room temperature for 30 min at both instruments. Corresponding experimental PDFs (open symbols), *PDFgui* fits of the structural models (solid lines) and associated difference curves (offset for clarity) for (c) ARCS and (d) NPDF.

Table 1

Parameters from the PDF refinements of ARCS Ni and Al₂O₃ data at 300 K, compared with NPDF and literature values (Lewis *et al.*, 1982), respectively.

Ni (space group $Fm\bar{3}m$) with Ni at (0, 0, 0). Al₂O₃ (space group $R\bar{3}c$) with Al at (0, 0, z) and O at $(x, 0, \frac{1}{4})$. The parameter δ_2 accounts for the correlated atomic motion effect that sharpens the near-neighbor PDF peak.

Parameter	Ni (ARCS)	Ni (NPDF)	Al ₂ O ₃ (ARCS)	Al ₂ O ₃ (literature)
a (Å)	3.5372 (2)	3.5270 (2)	4.7801 (14)	4.7602 (4)
c (Å)	–	–	13.0502 (16)	12.9933 (17)
z_{Al}	–	–	0.3521 (1)	0.35216 (1)
x_{O}	–	–	0.3071 (1)	0.30624 (4)
$U_{\text{iso}}^{\text{Ni}}$ (Å ²)	0.0072 (2)	0.0053 (2)	–	–
$U_{\text{iso}}^{\text{Al}}$ (Å ²)	–	–	0.0055 (2)	0.00347 (3)
$U_{\text{iso}}^{\text{O}}$ (Å ²)	–	–	0.0061 (3)	0.00419 (3)
δ_2 (Å ²)	2.74 (4)	2.77 (2)	1.79 (11)	–
Scale	0.57 (2)	1.03 (3)	1.37 (2)	–
Q_d (Å ⁻¹)	0.046 (11)	0.017 (4)	0.046	–
r_w	0.108	0.067	0.109	–

As is evident from Table 1, quantitative structural parameters can be refined from the ARCS PDF with high accuracy. Interestingly, the peak width in the ARCS PDF also appears to be larger than that for the NPDF data for the same upper limit of integration in the PDF Fourier transform Q_{max} . This effect is known to appear when data

have a Q -dependent peak broadening (Toby & Egami, 1992) but appears to be particularly marked in the ARCS data. If it is not accounted for in the model, this broadening results in an overestimate for atomic displacement parameters from ARCS, as is evident in Table 1. Notably, the fit gives a very good value for the agreement factor r_w , which is a standard qualitative goodness of fit measure (Egami & Billinge, 2003).

Work in the Billinge group was supported by the Office of Basic Energy Sciences, US Department of Energy, under contract No. DE-AC02-98CH10886. This research at Oak Ridge National Laboratory's Spallation Neutron Source was sponsored by the Scientific User Facilities Division, Office of Basic Energy Sciences, US Department of Energy.

References

- Egami, T. & Billinge, S. J. L. (2003). *Underneath the Bragg Peaks: Structural Analysis of Complex Materials*. Oxford: Pergamon Press, Elsevier.
- Farrow, C. L., Juhás, P., Liu, J. W., Bryndin, D., Božin, E. S., Bloch, J., Proffen, T. & Billinge, S. J. L. (2007). *J. Phys. Condens. Mater.* **19**, 335219.
- Lewis, J., Schwarzenbach, D. & Flack, H. D. (1982). *Acta Cryst.* **A38**, 733–739.
- Toby, B. H. & Egami, T. (1992). *Acta Cryst.* **A48**, 336–346.

Effects of Thermal Annealing on Structural and Magnetic Properties of Lithium Ferrite Nanoparticles

Nataša G. Jović,^{*,†} Ahmad S. Masadeh,^{‡,§} Aleksandar S. Kremenović,^{†,||} Bratislav V. Antić,[†] Jovan L. Blanuša,[†] Nikola D. Cvjetičanin,[⊥] Gerardo F. Goya,[#] Marco Vittori Antisari,[∇] and Emil S. Božin[○]

Institute “Vinča”, Laboratory of Theoretical and Condensed Matter Physics, P.O. Box 522, 11001 Belgrade, Serbia, Department of Physics and Astronomy, Michigan State University, East Lansing, Michigan 48824, Department of Physics, University of Jordan, Amman 11942, Jordan, Faculty of Mining and Geology, Laboratory for Crystallography, University of Belgrade, Đušina 7, 11000 Belgrade, Serbia, Faculty of Physical Chemistry, Studentski Trg 12-14, 11000 Belgrade, Serbia, Aragon Institute of Nanoscience & Condensed Matter Physics Department, University of Zaragoza, Zaragoza, Spain, ENEA, FIM Department, C.R. Casaccia, Via Anguillarese 301, 00060 Roma, Italy, Department of Applied Physics and Applied Mathematics, Columbia University, New York, New York 10027

Received: August 5, 2009; Revised Manuscript Received: October 12, 2009

Pure, crystalline, ~10 nm lithium ferrite phase (Li_{0.5}Fe_{2.5}O₄), was successfully synthesized at very low temperature using a modified combustion method. The crystal structure and microstructure evolution of this system upon annealing were monitored by a careful investigation of X-ray diffractograms collected on a synchrotron source. Comparative analysis of the results obtained from the full profile Rietveld method (in reciprocal space) and the pair distribution function method (in direct space) was carried out. Nanocrystalline samples exhibit similar crystal structure, on average, with a partial ordering of Li⁺ and Fe³⁺ ions between octahedral 4b and 12d sites on the spinel crystal lattice (space group *P4₃32*). After annealing at 973 K, cation distribution changes to a completely ordered, resembling that which is seen in the bulk lithium ferrite. The PDF analysis reveals abnormally high values of oxygen atomic displacement parameters in tetrahedral 8c sites (O1) indicating a significant disordering of the O1 network and suggests migration of lithium ions from 4b sites to the outer layers of nanoparticles. Analysis of room temperature Mössbauer spectra has shown that the hyperfine field for Fe³⁺ ions in tetrahedral 8c sites is the most sensitive on increasing the particle size and improving the crystallinity. From the differential thermal analysis, it was found that a lower driving force is required to induce an order–disorder phase transition in nanocrystalline samples, compared to the bulk-like sample, presumably due to the higher crystal disordering in these samples.

1. Introduction

Lithium ferrite Li_{0.5}Fe_{2.5}O₄ spinel has been of great technological interest in many electromagnetic devices for a long time. High electrical resistivity, low eddy current losses, low magnetic losses, and very good thermal and chemical stability make lithium ferrite a material of great importance for microwave applications.¹ This soft ferrite material with high Curie temperature, square loop properties, and high saturation magnetization has also been used in ferrite-core memory systems. Thermal stability and safety of lithium ferrite make this material suitable for application in Li-ion batteries as a cathode material,² and recently as a potential gas sensor element.³ Furthermore, due to the low fabrication cost, lithium ferrite has been increasingly used as a replacement for the more expensive yttrium iron garnet (YIG) in mass-scale microwave devices.

Bulk lithium ferrite is an inverse spinel that typically crystallizes in two polymorphic forms. The ordered α -phase (space group *P4₃32*) is characterized by the presence of 1:3 ordering of Li⁺ and Fe³⁺ ions on the octahedral sublattice in spinel structure, with corresponding cation distribution (Fe³⁺)_{8a}[(Li⁺)_{0.5}]_{4b}(Fe³⁺)_{1.5}]_{12d}. The disordered β -phase (space group *Fd $\bar{3}m$*) possesses a random distribution of Li⁺ and Fe³⁺ ions over the octahedral sites with cations distribution (Fe³⁺)_{8a}[Li⁺)_{0.5}Fe³⁺)_{1.5}]_{16d}. The order–disorder phase transition in bulk Li_{0.5}Fe_{2.5}O₄ occurs in the temperature range 1008–1028 K.⁴

In nanomaterials, the cation distribution can differ significantly from that in a bulk counterpart.⁵ The large surface-to-volume ratio in nanoparticles has significant influence on their physical and chemical behavior. The atoms at the surface of the particles display an incomplete coordination shell which can result in ionic displacements, changes in the lattice parameters, and even provoke a nanoparticles' core/shell structure.^{6,7}

In the study reported here, the pure nanocrystalline lithium ferrite phase has been successfully synthesized at very low temperature using the citrate gel precursor method. The study has been focused on the following issues: (i) the synthesis route, (ii) the evolution of the crystal structure and microstructure with changing annealing conditions, observed by X-ray powder diffraction and differential thermal analysis (DTA) methods, (iii)

* Corresponding author. Phone: +381 11 80 65 828. Fax: +381 11 80 65 829. E-mail: natasaj@vinca.rs.

[†] Institute “Vinča”.

[‡] Michigan State University.

[§] University of Jordan.

^{||} University of Belgrade.

[⊥] Faculty of Physical Chemistry.

[#] University of Zaragoza.

[∇] ENEA.

[○] Columbia University.

the comparative analysis of crystal structure and microstructural parameters obtained using Rietveld profile method and the atomic pair distribution function (PDF) approach, and (iv) changes of the Mössbauer parameters with increasing annealing temperature (i.e., crystallite size).

2. Experimental Section

2.1. Synthesis Procedure. A series of nanocrystalline lithium ferrite samples, $\text{Li}_{0.5}\text{Fe}_{2.5}\text{O}_4$, was synthesized by a modified combustion method using citric acid as a fuel for combustion reaction. Lithium nitrate and iron(III) nitrate nonahydrate were used as starting materials. Aqueous solutions of metal nitrates were mixed with 5 mol % of lithium ions in excess comparing the required stoichiometric molar ratio. The lithium cations were added in excess in order to avoid the formation of hematite that was found to appear as a second phase when the cation molar ratio followed stoichiometric ratio. In the next step, the citric acid was added to the precursor solution with the metal to citric molar ratio of 1: 1. The solution was mixed and then slowly dried in an oven at 353 K for 12 h in order to undergo dehydration. After cooling down to room temperature the dried gel was sintered at 453 K for 12 h in order to induce gel decomposition. As-prepared sample (S1) was further annealed in air for 4 h at 573 K (S2), 673 K (S3), and 973 K (S4).

2.2. Experimental Methods. In order to check the stoichiometry of the samples, chemical quantitative analysis was performed using inductively coupled plasma optical emission spectroscopy (ICP-OES), Spectroflame ICP, 2.5KW, 27 MHz. The ICP-OES analysis was performed by measuring the intensity of radiation of the specific wavelengths emitted by each element. The samples were dispersed in liquid and introduced into the plasma in the form of aerosol, where they were vaporized, atomized, and excited.

Thermal analysis (DTA/TGA) was used to check the end of the decomposition process and to study changes of the order–disorder structural phase transition temperature with annealing. Measurements were done in air, in the temperature range from 300 to 1123 K, with a heating/cooling rate of 20 K/min, using TA SDT 2960 instrument.

Structural and microstructural analysis of nanocrystalline lithium ferrites (S1, S2 and S3) have been carried out using synchrotron based high-energy X-ray powder diffraction data (HEXRPD), whereas the X-ray powder diffraction data (XRPD) of bulk-like sample (S4) was collected on a Bruker D8 diffractometer in the angular range $13\text{--}113^\circ$ (2θ) with a step of 0.017° and a counting time of 10 s per step. The particle size and shape of the sample S1 were determined by transmission electron microscopy (TEM) with a FEI TECNAI G2 30F microscope operated at 300 kV. To this purpose the powder particles have been dispersed on a holey carbon support film.

The HEXRPD experiments were performed at the 6-ID-D beamline at the Advanced Photon Source at Argonne National Laboratory, Argonne, Illinois. Diffraction data were collected using the recently developed rapid acquisition pair distribution function (RAPDF) technique^{8a} that benefits from two-dimensional (2D) data collection. The powder samples were packed in Kapton capillaries with diameter of 1.0 mm, sealed at both ends. The data were collected at room temperature with an X-ray energy of 86.8406 keV ($\lambda = 0.142773 \text{ \AA}$) selected using Si (331) monochromator. Incident beam size was $0.6 \times 0.6 \text{ mm}$. An image plate (IP) camera (Mar345) with a diameter of 345 mm was mounted orthogonally to the beam path with a sample to detector distance of 230.274 mm, as calibrated by using ceria standard sample.^{8a} Each sample was exposed for 120 s and this

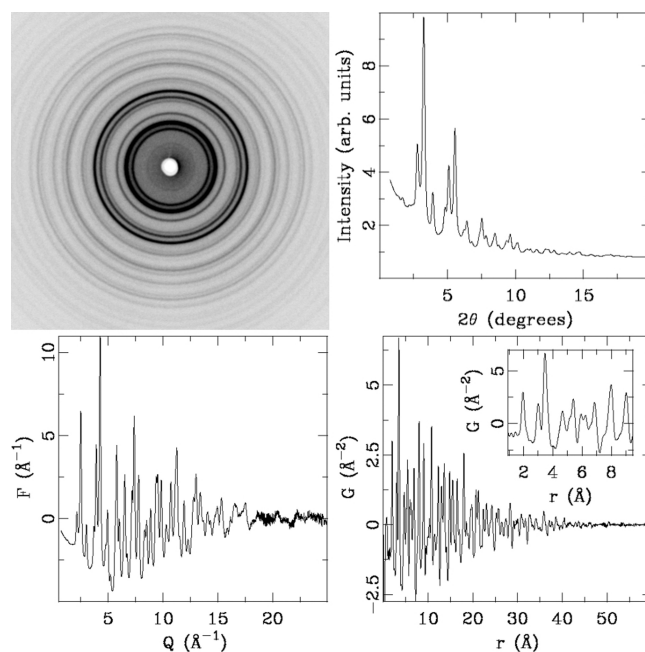


Figure 1. Experimental data obtained at 6-ID-D at APS for S1 sample at 300 K: 2D diffraction pattern (upper left), corresponding integrated 1D diffraction pattern (upper right), total scattering structure function, $F(Q)$, (lower left), and the atomic PDF (lower right). The inset shows a close-up to the low- r region in the PDF. The PDF intensity at high- r diminishes both as a result of the finite size of the nanoparticles, and due to the limited resolution of the 2D measurement.

was repeated 5 times for a total data collection time of 600 s. The RAPDF approach avoids detector saturation while allowing sufficient statistics to be obtained. To reduce the background scattering, lead shielding was placed before the sample with a small opening for the incident beam. Examples of the raw 2D data, for S1 sample are shown in top left panel of Figure 1. These data were integrated and converted to intensity versus 2θ using the software FIT2D,^{8b} where 2θ is the angle between the incident and scattered X-ray beams. Example for S1 is shown in top right panel of Figure 1. The integrated data were normalized by the average monitor counts. The data were corrected and normalized^{8c} using the program PDFgetX2^{8d} to obtain the total scattering structure function, $F(Q)$ and its Sine Fourier transform, i.e. the atomic PDF, $G(r)$, which are shown respectively in bottom left and bottom right panels of Figure 1 for sample S1. In the Fourier transform of $F(Q)$ to get the PDF, $G(r)$, the data are truncated at a finite maximum value of the momentum transfer, $Q = Q_{\text{max}}$. Q_{max} is optimized such as to avoid large termination effects and to reasonably minimize the introduced noise level as the signal-to-noise ratio decreases with the increased Q value. Here, a $Q_{\text{max}} = 27.0 \text{ \AA}^{-1}$ was found to be optimal.

Structural and microstructural analysis have been done from as collected XRPD data using the Rietveld profile refinement method^{9a,b} incorporated into the program Fullprof^{9c,d} and the PDF approach, using the program PDFgui.^{8e} The obtained results were compared.

Mössbauer spectra were recorded at room temperature using MS4 Mössbauer spectrometer, operating in constant acceleration mode. The source was ^{57}Co in Rh matrix. The velocity calibration was done using natural iron foil.

3. Results and Discussion

3.1. Synthesis. The chemical composition of samples S1 and S4 has been checked by ICP-OES analysis. In the as-prepared

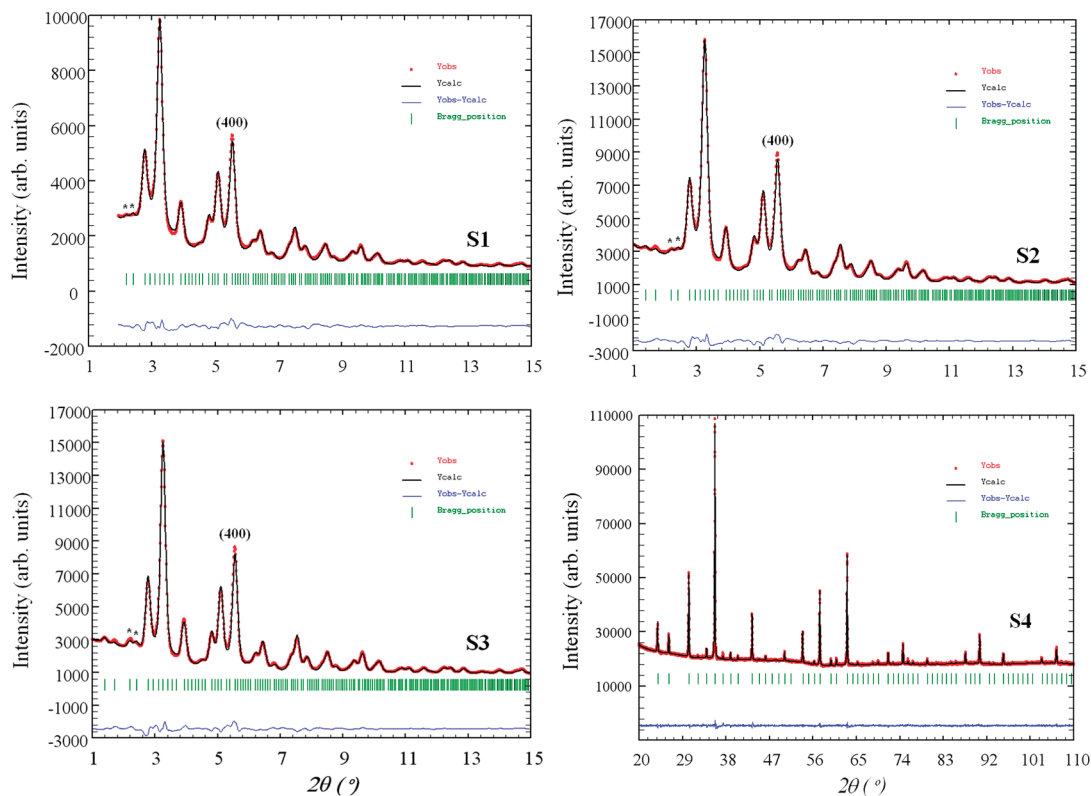


Figure 2. HEXRPD patterns of lithium ferrite: as-prepared (S1), annealed at 573 K (S2), and 673 K (S3), and XRPD pattern of sample annealed at 973 K (S4). Superstructure reflexions (210) and (211) are denoted by asterisk. Experimental data (Y_{obs}), refined XRPD spectrum (Y_{calc}) (S.G. $P4_332$), their differences ($Y_{\text{obs}} - Y_{\text{calc}}$), and the Bragg reflections' positions are shown in figure. Note that the data for S4 sample were collected in an experimental setup having much higher resolution than that used for S1, S2, and S3 samples and that the diffractograms are not directly comparable.

sample (S1), a deviation from the stoichiometry has been found, whereas in the sample S4 the molar ratio of Li/Fe ions with (1.68 ± 0.04) wt % of Li^+ and (65 ± 2) wt % of Fe^{3+} ions, corresponds to the required stoichiometric ratio for pure lithium ferrite phase. DTA analysis of sample S1 revealed that a mass lost of about 17% occurs in sample S1 with annealing up to 1123 K. This suggests the presence of some non decomposed organic part in the sample after thermal treatment of precursor gel at 453 K. Notable mass change is absent in samples S2 and S3.

The HEXRPD patterns of samples S1, S2, and S3 are shown in Figure 2. Their characteristic feature is the presence of low intensity superstructure reflections (210) and (211), which confirms that the samples crystallize in (at least partially) ordered spinel structure, S.G. $P4_332$. The presence of any other crystalline phase was not observed from the XRPD patterns. It is relatively common to find some impurity phase, usually hematite ($\alpha\text{-Fe}_2\text{O}_3$), during the synthesis route via citrate precursor gel decomposition¹⁰ or via oxalate precursor route.¹¹ We have found that the formation of $\alpha\text{-Fe}_2\text{O}_3$ (~ 4 wt %) can be avoided by the use of an overstoichiometric solution where 5 wt % of lithium ions were added in excess during formation of precursor gel.

Detailed analysis of $\text{Li}_{0.5}\text{Fe}_{2.5}\text{O}_4$ preparation by the citrate gel precursor method has been recently reported.¹² It was pointed out that the decomposition/oxidation rate of anhydrous precursor can be crucial in order to avoid formation of impurities and that it can be controlled by setting up the pH value of the precursor. Higher pH value allows for a higher oxidation rate, which is necessary to obtain pure lithium ferrite phase, but at the same time it significantly increases the particles size. By

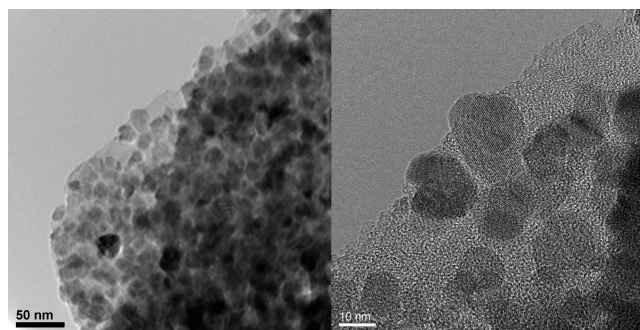


Figure 3. HRTEM micrographs of sample S1.

keeping pH value near 1 and by adding some lithium in excess we have managed to obtain pure lithium ferrite phase.

3.2. Crystal Structure and Microstructure of Nanocrystalline $\text{Li}_{0.5}\text{Fe}_{2.5}\text{O}_4$. **3.2.1. TEM Analysis.** High-resolution TEM (HRTEM) analysis provided more detailed structural information. From the HRTEM micrographs of sample S1, shown in Figure 3, we can see that the ferrite particles have globular morphology with the particle sizes laying in the range 10–20 nm. These values are something higher than the one determined by HEXRPD (~ 5 nm for samples S1 and S2, ~ 9 nm for sample S3; see lately in the text). Since the HEXRPD is sensitive to the size of the optically coherent volume, this discrepancy can indicate the presence of some residual defects in the S1 sample, which is fully recovered in samples heat treated at the highest temperature. Despite the possible presence of defects, HRTEM images also show that the particles seem to be single-crystalline in the nature. For soft ferrites, like lithium ferrite, it has been found that the critical particle size below which they are single-domain is about 30–40 nm.¹³

TABLE 1: Lattice Constant, the Fractional Coordinates of Oxygen O2 at the General 24e and Oxygen O1 at the Special 8c Positions, As Well As Lithium/Iron at the 12d and Iron at the 8c Sites, and the Average Crystallite (Particle) Size and the Max-Strain for Nanocrystalline $\text{Li}_{0.5}\text{Fe}_{2.5}\text{O}_4$ Annealed at 453 K (S1), 573 K (S2), and 673 K (S3), Obtained Using Rietveld (FP) and the Atomic PDF Approaches

sample	method	a (Å)	O2x (24e)	O2y (24e)	O2z (24e)	O1x (8c)	Li2/Fe2y (12d)	Fe3x (8c)	average crystallite size (Å)
S1	FP	8.3466(3)	0.1099(10)	0.1294(9)	0.3787(11)	0.3851(11)	0.3627(3)	0.9915(3)	54
	PDF	8.3499(38)	0.1180(11)	0.1207(10)	0.3809(15)	0.3731(14)	0.3669(5)	0.9973(5)	57(1)
FP: $\chi^2 = 1.15$, $R_{\text{Bragg}} = 2.74$, $R_p = 1.95$; PDF: Reduced $\chi^2 = 0.035$; $R_w = 0.134$; Max-strain (10^{-4}) = 34.0(0.5) ^a									
S2	FP	8.3205(3)	0.1101(10)	0.1300(8)	0.3781(12)	0.3842(11)	0.3638(3)	0.9930(3)	54
	PDF	8.3243(6)	0.1194(10)	0.1208(9)	0.3804(13)	0.3813(12)	0.3681(5)	0.9983(5)	59(1)
FP: $\chi^2 = 2.22$, $R_{\text{Bragg}} = 2.63$, $R_p = 2.34$; PDF: Reduced $\chi^2 = 0.045$; $R_w = 0.118$; Max-strain (10^{-4}) = 29.2(0.4) ^a									
S3	FP	8.3337(2)	0.1120(11)	0.1321(8)	0.3774(10)	0.3837(12)	0.3660(3)	0.9942(3)	87
	PDF	8.3385(14)	0.1143(9)	0.1239(7)	0.3804(12)	0.3718(12)	0.3692(5)	0.9992(5)	94(1)
FP: $\chi^2 = 1.93$, $R_{\text{Bragg}} = 3.02$, $R_p = 2.28$; PDF: Reduced $\chi^2 = 0.046$; $R_w = 0.101$; Max-strain (10^{-4}) = 28.8(0.4) ^a									

^a Numbers in parentheses have meaning of degree of anisotropy (not standard deviation).

3.2.2. Rietveld vs PDF Method. The comparative crystal structure and microstructure analysis of $\text{Li}_{0.5}\text{Fe}_{2.5}\text{O}_4$ samples annealed at different temperatures have been performed by two methods: by full profile Rietveld refinement using program Fullprof (¹³c), and by the PDF method.^{8c,14} The two complementary approaches were chosen, as it is well-known that crystal structure analysis of nanoparticle materials is subject to numerous difficulties when using conventional powder diffraction methods alone. These methods can become insufficient or even break down as the diffuse scattering becomes significant at the nanoscale, while the Bragg scattering, the one that crystallography relies upon, gets diminished. As an alternative, the total scattering based atomic PDF method is one of the promising experimental approaches in nanoscale structure determination, particularly when used in combination with other techniques that provide highly complementary information.^{14b}

The full profile Rietveld method allows the average structure determination from the Bragg peaks position and intensity, and the microstructure determination (size-strain analysis) from the peak profile analysis.^{9a,b} XRPD peak profiles are modeled by the Thomson-Cox-Hasting modified pseudo-Voigt (TCH-pV) function and the instrumental resolution function is used to estimate the microstructural parameters (the average crystallite size and microstrain). The Fullprof program package allows for an estimate the average crystallite size and microstrain by averaging the values obtained for apparent size and maximum strain calculated for each crystal direction [hkl] given by expressions:^{9c} Apparent size = $1/\beta_{\text{size}}$ (Å) and Max-strain = $(\beta_{\text{strain}}d_{hkl}/2) (\times 10^{-4})$. In the case of isotropic size and strain models, both β_{size} and β_{strain} were obtained from TCH-pV functions parameters according to procedure described in ref 9c.

In the diffraction patterns of nanocrystalline materials diffuse scattering is more dominant than in those of crystalline materials, hence using PDF analysis of neutron and X-ray total scattering data comes as a natural choice for studying the structure of nanostructured materials.^{8a,c,14a} Recently, the structure of discrete nanoparticles has been successfully studied using this approach.¹⁵⁻¹⁹ If special care is applied to the measurement and to the approach used for analyzing the data, the PDF method can yield precise structure and size information. The atomic PDF, $G(r)$, is defined as $G(r) = 4\pi r[\rho(r) - \rho_0]$, where $\rho(r)$ is the atomic pair density, ρ_0 is the average atomic number density, and r is the radial distance.^{8c} The PDF yields the probability of finding pairs of atoms separated by a distance r . It is obtained by a Sine Fourier transformation of the reciprocal space total scattering structure function, $F(Q) = Q[S(Q) - 1]$, according to $G(r) = (2/\pi)\int_0^\infty F(Q)$

$\sin(Qr) dQ$, where $S(Q)$ is obtained from a diffraction experiment. This approach is widely used for studying liquids, amorphous, and crystalline materials, and has recently also been successfully applied to characterize nanocrystalline materials.^{14c}

3.2.3. Rietveld Approach. The HEXRPD patterns of nanocrystalline lithium ferrite annealed at 453, 573, and 673 K (S1, S2, and S3, respectively) are shown in Figure 2. As already mentioned, all samples were found to crystallize in a cubic spinel structure, and the presence of superstructure reflections indicates cation ordering within the octahedral sublattice (S.G. $P4_332$). Compared to diffraction pattern of standard powder (CeO_2), broadening of diffraction peaks due to the small crystallite size and the effects of strain is observed. The Rietveld refinement has been performed within the space group $P4_332$ using the Fullprof program. The isotropic size and strain model^{9c} is applied, and the results of refinements are presented in Table 1.

The starting model for crystal structure refinement of samples S1, S2, and S3 was based on a bulk-like cation distribution model in which the tetrahedral, 8c sites are occupied only by Fe^{3+} ions and the rest of Fe^{3+} ions and all Li^+ ions are distributed between two distinct octahedral sites, 4b and 12d, in the space group $P4_332$. The best refinements were obtained when a partial mixing of Li^+ and Fe^{3+} ions between two octahedral sites, 4b and 12d, was allowed. Since Li scatters X-rays poorly compared to the heavier elements present in the structure, Li occupation is followed indirectly, by keeping Li occupation numbers constrained with those of Fe ions in order to preserve the proper Li/Fe ratio.

The refined patterns showed very good agreement with experimental data (Figure 2), except for a small difference between experimental and calculated intensity of (440) reflection. There can be several possible reasons for this deviation, all of them being specific to this material: the presence of short-range disordering along the [110] direction (direction of cation ordering in an ordered spinel structure), anisotropic microstrain due to dislocations, phase boundaries or stacking faults (the latter leads to asymmetric peaks),²⁰ and also surface relaxation effects, when the broad and even asymmetric tails can arise from the departure from crystalline order of the surface layers.^{6b}

Following the model described above, we have found an insignificant change in the cation distribution with annealing up to 673 K. The occupancy of 4b site by lithium in all nanocrystalline samples was found to vary around 60% of overall Li content, and so the cation distribution can be represented by the formula $(\text{Fe}^{3+})_{8c}[(\text{Li}^+_{0.3}\text{Fe}^{3+}_{0.2})_{4b}(\text{Li}^+_{0.2}\text{Fe}^{3+}_{1.3})_{12d}]$. The samples S1, S2, and S3 may be therefore regarded as a partially

ordered. These results reflect the importance of particular synthesis route for nanoparticle lithium ferrite. For instance, it was found that the citrate gel method used with ammonia solution added into the precursor, produces a random distribution of Li^+ ions over the octahedral and tetrahedral sites, S.G. $Fd\bar{3}m$.²¹ After annealing at 973 K, a totally ordered lithium ferrite (Fe^{3+})_{8c}[(Li^+)_{0.5}]_{4b}(Fe^{3+})_{1.5}]_{12d} has been obtained (sample S4).

The important structure and microstructure parameters obtained from Rietveld method are summarized in Table 1. When analyzed in terms of annealing temperature, these results show some differences in behavior of structural (unit cell and atomic parameters) and microstructural (size and strain) parameters. While microstructure parameters seem to change in adequate manner (increase of particle size with temperature and decrease of average microstrain), the values of structure parameters, in particular the cell constants show a nonuniform change with annealing temperature.

Compared to the bulk form of fully ordered lithium ferrite (S4), the cell constants of S1 and S2 were found to be over- and underestimated, respectively. Similar values of these parameters were also obtained by PDF method (for comparison, they are also given in Table 1). Apart from the possible limitations of the applied structural model itself (bulk-like description of the crystal structure), the explanation for discrepancy between unit cell values of S1 and S2 can also be found in specific behavior of the microstructure parameters for these two samples. Their values reveal that annealing at 573 K does not induce significant change in particle size but predominantly results in the reduction of microstrain, which is known to increase the lattice constant in nanosized samples compared to their bulk counterpart.⁷ Thus the higher defect concentration and/or the mixing effects of both micro- and macrostrain are likely to contribute to the increased value for S1 cell constant. However, as annealing at 573 K leads to decreased value of unit cell constant in S2, this value is found to be somewhat smaller than the one related to bulk lithium ferrite, which suggests that this effect is not possible to explain only in terms of average defect relaxation estimated from the Rietveld analysis. The PDF analysis, on the other hand, reveals existence of oxygen disordering in the samples, and provides additional insight into the short-range structure that is generally out of the scope of the Rietveld method. We describe these results below.

3.2.4. PDF Approach. Here, we apply the PDF method to study the structure and size in lithium ferrite nanoparticles, where the size is controlled by adjusting the temperature in the annealing step of the synthesis, as described. Figure 4 features experimental PDFs, shown as open circles, for the three samples used. From Figure 4 is apparent that, in direct space, the PDF features at low r are comparably sharp in all the samples. Unlike in the reciprocal space, the direct space features are not broadened due to the finite size effects. The finite particle size produces a falloff in the intensity of structural features with increasing interatomic spacing r , similar to one that can be seen in the lower right panel of Figure 1. The structure apparent in the $G(r)$ function, as that seen in Figure 4, comes from the atomic order within the nanoparticle. In case of high reciprocal resolution measurements on nanoparticle samples, the value of r where the PDF signal disappears indicates the particle core region diameter, or at least the diameter of any coherent structural core of the nanoparticle. Features in the PDF at low r reflect the internal structure of the nanoparticles. Inspection of the experimental PDF data in Figure 4 reveals that nanoparticles have almost the same features, reflecting the fact that they

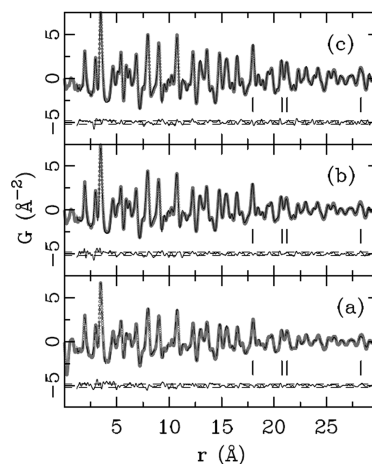


Figure 4. PDFgui refinements of the $P4_32$ model to the experimental PDF data for (a) S1 sample, (b) S2 sample, and (c) S3 sample, over a wide r -range. Data are shown as open symbols, model profiles as solid lines, and corresponding difference curves are shown offset below for clarity. Dashed horizontal lines denote estimated experimental uncertainty at 2σ level. All profiles shown in panels (b) and (c) are placed on the same scale as in (a) for easier comparison. Vertical tick marks denote selected features discussed in the text.

share a similar atomic structure on average. In the finite nanosize regime, local structural changes are expected: the largest changes in structure are expected in the smallest nanoparticles. In such nanoparticles, the contribution of surface atoms is large, making it difficult to define well-ordered crystalline core. It should be noted here that the effect of limited reciprocal space resolution of the measurement also yields a similar falloff of the PDF intensity, producing a Gaussian envelope to the experimental PDF. In studying crystalline materials, distinct are sample (grain size effect) and resolution limited measurements, depending on which of the effects is predominant.^{8c} Since the resolution effects necessarily come to play when IP detectors are used, and are relevant in case of intermediate size nanoparticles, such as these studied here, measurements on silicon crystalline standard were carried out to account for this, as explained below.

Using the PDF approach, it is possible to obtain size-dependent quantitative structural information, and through a structure modeling process refine reliable structural parameters, even in cases of very small nanoparticles.¹⁹ Structural information was extracted from the PDFs using a full-profile real-space least-squares refinement approach, analogous to the Rietveld refinement. We used the program PDFgui^{8c} to fit the experimental PDFs. Starting from a given structure model and given a set of parameters to be refined, PDFgui searches for the best structure that is consistent with the experimental PDF data. The residual function, R_w , is used to quantify the agreement of the calculated PDF from model to experimental data, and is minimized in the refinement process. The structural parameters of the model (cubic, $P4_32$) were: lattice parameter, fractional coordinates observing $P4_32$ symmetry constraints, isotropic atomic displacement parameters (ADPs), and the site occupancy of Li atom. The modeling program takes into account both the particle size and the finite resolution effects, through corresponding fitting parameters.^{8c,14c} The resolution damping factor, Q_{damp} , which defines PDF Gaussian dampening envelope ($0.5e^{-(Q_{\text{damp}} \cdot r)^2}$) due to limited Q -resolution,^{8c,e} was determined from a refinement to the silicon standard data and fixed, and the nanoparticle diameter was refined. PDF data obtained for Si standard (325 mesh) are shown in Figure 5a with dampening envelope superimposed, highlighting the effect of the resolution

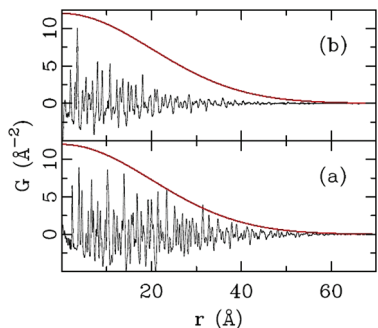


Figure 5. Effect of reciprocal space resolution on PDF. (a) Silicon standard PDF (solid line profile) and PDF Gaussian dampening envelope (thick solid line) scaled to track the data. (b) PDF of sample S1 (solid line profile) with the same envelope as shown in (a). Data shown in (a) and (b) are on the same scale. See text for details.

of IP measurement on data. For comparison, PDF data for S1 sample are shown in Figure 5b, demonstrating sensitivity to additional dampening observable in these data originating from the finite size of the nanoparticles. This is particularly obvious in the 30–50 Å region, where PDF peaks of Si are much stronger than PDF peaks of S1 sample. Good agreement, with low values of R_w , between the model and the data was achieved for all three samples. The fits are shown in Figure 4 as model PDFs (solid lines) superimposed on data, with the difference curves offset for clarity. Vertical tick marks label selected features in the PDF, allowing for visual comparison of these PDF peaks. Notably, higher- r features are more dampened and additionally broadened for samples S1 and S2, compared to that for sample S3, landing confidence that different nanoparticle sizes can be distinguished and assessed from the modeling process despite resolution effects. The obtained structural parameters are reported in Table 1.

Determining accurately the occupancy of Li represents a challenge for the reasons already stated in the previous section. PDF refinements were carried over two ranges, narrow (up to ~ 10 Å) and broad (spanning available PDF data up to ~ 50 Å). Notably, in all PDF refinements, the occupancy of Li on octahedral 4b site refined to lower values compared to 0.50 observed in the bulk counterpart. This was persistently observed for all three samples, indicating that an appreciable amount of Li ions occupy the octahedral 12d sites. Broad range fits were initially unstable, due to correlation between Li occupancy and ADP parameters of lithium and oxygen ions. Therefore, in the final refinements over a broad range, the Li occupancy was set to 0.2(1), as obtained from more stable fits for S3, and fixed for all three samples, which gave satisfactory fits. Interestingly, when the refinements were carried over a narrow range, the observed Li occupancy on the 4b site indicated even smaller values (below 0.1), suggesting a possibility that some of the Li ions escape to the outer layers of the nanoparticles. An idea about the sensitivity of PDF to this effect can be gained from Figure 6a, where two model PDFs for Li occupancy observed in the bulk, and that reported in this study are compared. Quantifying this, however, is beyond the sensitivity of our measurement.

We also found a significant difference in the fractional coordinates of oxygen ions in 8c site (O1) and 24e site (O2) depending on whether PDF or Fullprof methods were used. In conjecture with this is another observation that we made: an anomalous increase of the O1 isotropic ADP parameters to unphysical values, for all three samples, whereas the ADPs of other sites were having considerably smaller values, albeit still

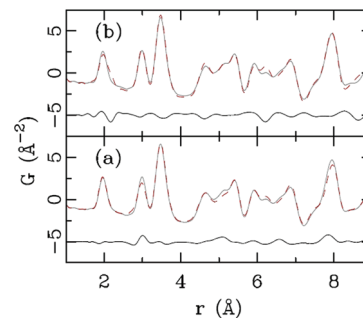


Figure 6. Effect of disorder on PDF. (a) Model PDF (solid line profile) for S1 sample with the occupancy of Li on octahedral 4b site set to 0.50 as observed in the bulk counterpart, and model PDF (dashed line profile) with the occupancy of Li set to 0.1. (b) Model PDF (solid line profile) for S1 sample with ADP of O1 set to observed unphysically large values, and model PDF (dashed line profile) with ADP of O1 set to physically reasonable values comparable to that obtained for O2. In both panels difference curves are offset for clarity. See text for details.

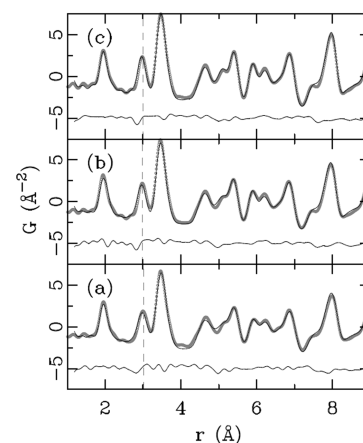


Figure 7. PDFgui refinements of the $P4_332$ model to the experimental PDF data for the (a) S1, (b) S2, and (c) S3 samples, over a narrow r -range. Dashed vertical lines denote position of the second PDF peak in the data, to emphasize the data-model mismatch, as also evident in the difference curve. All profiles shown in panels (b) and (c) are placed on the same scale as in (a) for easier comparison. See text for details.

enhanced. This is suggesting significant disorder in the O1 network, that appears to be the largest for the smallest nanoparticle (S1), with ADP of O1 being $0.148(5)$ Å², compared to $0.128(5)$ Å² and $0.140(5)$ Å² for S2 and S3 samples, respectively. For comparison, observed ADP values for O2 site are 1 order of magnitude smaller, being $0.012(1)$, $0.010(1)$, and $0.011(1)$ Å² for S1, S2, and S3, respectively. Illustration of the effect of disorder in the O1 sublattice is provided in Figure 6b by comparing model PDFs corresponding to anomalously increased and more physical values of O1 ADPs.

From the PDF fits over the narrow r -range (Figure 7), apparent discrepancies between the model and the data in the PDF peak position of certain peaks can be observed. The figure features fits to the data of the (a) S1, (b) S2, and (c) S3 samples. For easier comparison, all of the profiles in the later two panels were rescaled such to be on the same scale as these shown in panel (a). Vertical dashed lines denote the position of the second PDF peak of the data, emphasizing that there is an offset between the data and the model peak, also evident in the difference curve. Such mismatch also occurs for some other PDF peaks, as evident from the difference curves. This is consistent with there being a shell region where the interatomic

TABLE 2: Cation–Anion Distances Which Correspond to the Refined Crystal Structure Parameters by the Rietveld (FP) and PDF Methods^a

sample	method	$\langle d_{8c-O^{2-}} \rangle$ (Å)	$d_{4b-O^{2-}}$ (Å)	$\langle d_{12d-O^{2-}} \rangle$ (Å)
S1	FP	1.892(10)	2.151(12)	2.014(12)
	PDF	1.863(11)	2.053(10)	2.060(10)
S2	FP	1.886(10)	2.126(10)	2.011(10)
	PDF	1.880(8)	2.047(9)	2.035(9)
S3	FP	1.870(10)	2.145(9)	2.022(10)
	PDF	1.856(8)	2.078(9)	2.052(9)
$(Fe^{3+})_{8c}[(Li^{+}_{0.3}Fe^{3+}_{0.2})_{4b}(Li^{+}_{0.2}Fe^{3+}_{1.3})_{12d}]O_4$	calc.	1.87	2.178	2.059

^a Label “calc.” denotes values of cation–anion distances related to the given cation distribution and Shannon–Prewitt effective ionic radii.

distances are different than those in the core. There is no evidence in PDF that the shell is amorphous, which would manifest itself as a set of glass-like PDF features in the difference curve, with sharp near-neighbor distances, and a disordered hump at higher values of r . The data are more consistent with the shell being crystalline, with somewhat disordered structure, but similar to that of the core. The resolution (falloff) effects hamper the ability to estimate the spatial extent of the core and shell regions from the PDF analysis.

3.2.5. Analysis of Cation–Anion Distances. As two methods (Rietveld and PDF) give an appreciable mismatch in fractional coordinates of oxygen ions in 8c (O1) and 24e sites (O2) (Table 1), we compared the cation–anion distances (given in Table 2), which correspond to the refined crystal structure parameters obtained by Rietveld (FP) and PDF methods, with the values calculated from the effective ionic radii and refined cation distribution.²² The average cation–anion distances for 8c and 12d sites obtained by Fullprof and PDF are in agreement within three estimated standard deviations (ESD), whereas notable deviation is found for 4b site. Further, the average cation(8c)–anion distance (obtained by Fullprof and PDF) match pretty well value 1.87 Å calculated from Shannon effective ionic radii in the case that 8c site is occupied only by Fe^{3+} ions. The average cation(12d)–anion distances are also in agreement with value calculated taking into account the cation distribution $((Li^{+}_{0.2}Fe^{3+}_{1.3})_{12d})$ and ionic radii. This supports obtained refinement results when so-called bulk-like model was applied in nanocrystalline lithium ferrites. Some discrepancies are found only for 4b site where the cation(4b)–anion distances appears somewhat shorter (especially those obtained by PDF), from the predicted value calculated concerning the cation distribution $((Li^{+}_{0.3}Fe^{3+}_{0.2})_{4b})$. Regarding the value of Li^{+} and Fe^{3+} (high spin) ionic radii in octahedral coordination, this discrepancy could be an indication of some migration of Li ions from 4b sites to outer surface layers.

3.3. Mössbauer Spectroscopy of $Li_{0.5}Fe_{2.5}O_4$. Fe^{57} Mössbauer spectra for all samples were recorded at room temperature (Figure 8). The Mössbauer spectrum of sample S4 could be fitted with two overlapping sextets, assigned to Fe^{3+} ions at tetrahedral (A) and octahedral (B) sites. The Mössbauer parameters (isomer shift $\delta \cong 0.22$ and 0.37 mm s⁻¹, and hyperfine fields $B_{hyp} = 50.3$ and 51.0 T for A and B sites, respectively) are in agreement with previous results of $H_A = 50.0$ T, $\delta_A \cong 0.20$ and $H_B = 50.6$ T, $\delta_B \cong 0.37$ mm s⁻¹ for A and B sites, respectively.²³ Dormann et al.^{24a} have suggested that zero-field Mössbauer spectra of lithium ferrite taken at $T = 78$ K can be used to determine the relative Fe ion occupation

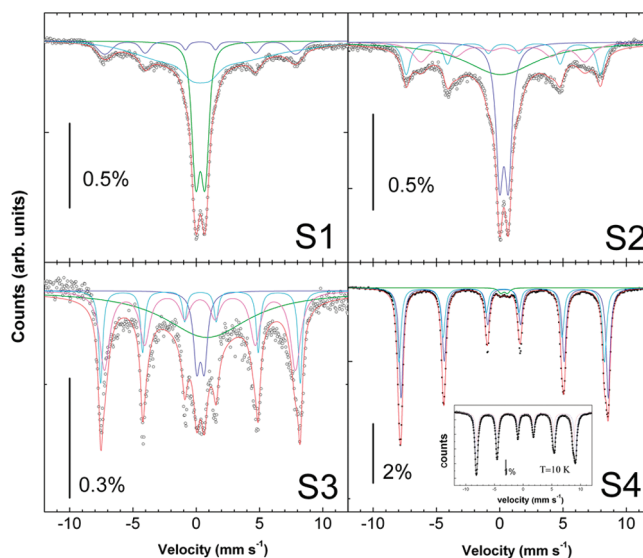


Figure 8. Mössbauer spectra of all samples (S1–S4) collected at room temperature.

at A and B sites. The ratio of spectral areas corresponding to Fe^{3+} at A and B sites was obtained from Mössbauer data taken at $T = 10$ K (see the inset of Figure 8), and the obtained value was in agreement with the ordered $(Fe^{3+}_{8c})_{tet}[(Li^{+}_{0.5})_{4b}(Fe^{3+}_{1.5})_{12d}]_{oct}$ cation distribution inferred from Rietveld refinement sample S4.

The room temperature Mössbauer spectra recorded for samples with smaller particle size (namely, S1, S2, and S3) could be fitted using two sextets and one broad doublet, the latter originating from the superparamagnetic relaxation of the smallest nanoparticles. This coexistence of sextets/doublets is typical for samples of ultrafine particles with size distributions, due to the exponential dependence of the relaxation time τ with particle volume.

For particles having relaxation times τ larger than the Larmor precession time $\tau_L \approx 10^{-8}$ s of the resonant ^{57}Fe nucleus, the later can sense the magnetic hyperfine interactions resulting in a magnetically split sextet. On the other hand, particles having $\tau < \tau_L$ will fluctuate many times during the time scale of the ^{57}Fe excited state, averaging all interactions to zero and leaving the quadrupolar interactions alone. Near the condition $\tau \approx \tau_L$ (i.e., the blocking temperature T_B for Mössbauer time window) the typical Mössbauer spectrum usually consists of a paramagnetic doublet superimposed on a magnetic hyperfine sextet, the latter exhibiting broad absorption lines and reduced hyperfine splitting. Since there are no theoretical models for the resulting Mössbauer spectra for $\tau \approx \tau_L$ (neither lineshapes nor hyperfine field behavior), the interpretation of any hyperfine parameter from spectra near T_B must be done with caution.

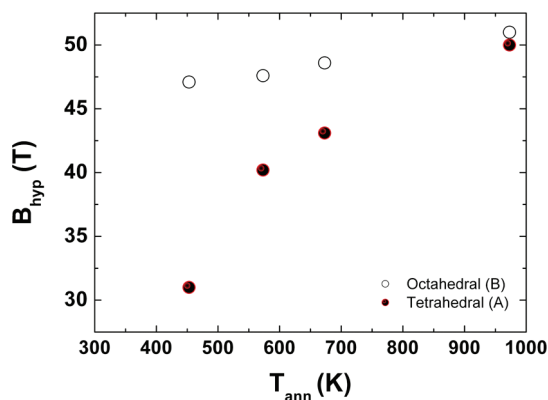
In our samples, the intensity of the central doublet originating from superparamagnetic relaxation of smaller particles decreases with increasing the annealing temperature and the magnetically split sextet becomes the major fraction of the ^{57}Fe signal, as expected from the growth of the average particle size. Concurrently, the spectral lines narrow for samples with higher annealing temperatures, due to the increase of average particle sizes and/or improved crystallinity of the particles. Table 3 summarizes the fitted Mössbauer parameters for lithium ferrite. It is worth mentioning that no indication of Fe^{2+} spectral component was detected in our samples.

The Mössbauer parameters obtained for bulk-like sample S4, namely 50.3 and 51.0 T (A and B sites, respectively) are in

TABLE 3: Hyperfine Parameters Obtained from Fits to the ^{57}Fe Mössbauer Spectra Collected at Room Temperature for Samples S1–S4^a

sample	component	δ (mm s ⁻¹)	QS (mm s ⁻¹)	B_{hyp} (T)
S1	doublet	0.33	0.74	
	sextet A	0.27		31
	sextet B	0.33		46.9
S2	doublet	0.33	0.69	
	sextet A	0.27		40.1
	sextet B	0.30		47.6
S3	doublet	0.33	0.59	
	sextet A	0.29		46.8
	sextet B	0.33		48.6
S4	sextet A	0.22	-0.03	50.3
	sextet B	0.37	0.01	51.0

^a The parameters are isomer shift (δ), quadrupole splitting (QS), and hyperfine field (B_{hyp}).

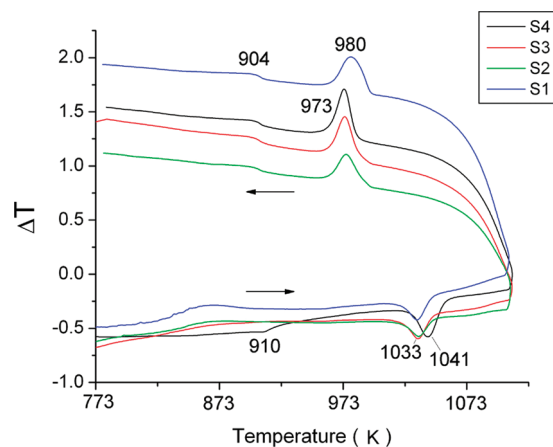
**Figure 9.** Hyperfine fields (B_{hyp}), for Fe^{3+} ions at tetrahedral (A) and octahedral (B) sites in spinel lattice.

agreement with previous reports on this system.²³ It is interesting to note that the evolution of hyperfine fields of A and B sites for Fe^{3+} ions with annealing temperatures are quite different (Figure 9). Indeed, the hyperfine field of the tetrahedral site shows a marked decrease for samples annealed at lower temperatures, reflecting larger sensitivity to changes in the local environment and/or to relaxation effects of the single-domain particles.

For NPs with different cation distributions at the cores and surface layers, fitting of the Mössbauer spectra by using multiple sextets (up to five) is impractical.²³ The complexity of the spectra in nanocrystalline $\text{Li}_{0.5}\text{Fe}_{2.5}\text{O}_4$ samples is due not only to relaxation effects near the SPM transition, but also due to the complex cation distribution. Previous studies have proposed detailed models for fitting substituted bulk lithium ferrite (e.g., Cr-doped $\text{Li}_{0.5}\text{Fe}_{2.5}\text{O}_4$) using multiple sets of subspectra, based on a model of supertransferred hyperfine field contributions at each Fe site.²⁴ In any case, the observed broadening of the sextet lines are the previous stage before SPM relaxation takes place, and therefore it seems more plausible to relate both the observed hyperfine field decrease and line broadening to Néel relaxation effects in single-domain nanoparticles.

3.4. Order–Disorder Phase Transition in $\text{Li}_{0.5}\text{Fe}_{2.5}\text{O}_4$

DTA analysis was used to investigate structural phase transitions (S.G. $P4_332 \leftrightarrow Fd\bar{3}m$), in all prepared samples, and the corresponding DTA curves are shown in Figure 10. DTA graph shows that each sample exhibits discernible endothermic peak which appears at $T_f'' = 1033$ K in nanocrystalline samples (S1, S2, and S3) and at $T_f'' = 1041$ K in bulk-like lithium ferrite (S4). This endothermic transition observed in heating regime, corresponds to the exothermic transition in cooling regime which

**Figure 10.** DTA curves of samples S1, S2, S3, and S4 measured in heating and cooling regimes (shown in the range of temperature 773–1110 K).

appears at $T_f'' = 980$ K in sample S1, and $T_f'' = 973$ K in samples S2, S3, and S4. Both observed types of transition peaks are due to reversible order–disorder phase transition in lithium ferrite and are shifted relative to each other (so-called thermal hysteresis) in heating/cooling regime: $\Delta T = T_f'' - T_f'' \approx 53$ K for sample S1, ≈ 60 K for S2 and S3, and ≈ 68 K for S4, and these observations are consistent with the reported data.²⁵ Hence, lower driving force is necessary to induce order–disorder phase transition in nanocrystalline samples compared to their bulk counterpart, and consequently the temperature of phase transition in bulk sample is 8 K above the transition temperature in nanocrystalline samples.

DTA curves also exhibit a flexure at approximately 904 K, which can be related to a magnetic phase transition (ferrimagnetic \leftrightarrow paramagnetic). This transition occurs at the same temperature in all samples and is close to that one obtained from DSC measurements (920 K).²⁶ Literature value of the Néel temperature of lithium ferrite is usually in the range of $T_N = 913$ –953 K.²⁷

4. Conclusions

In this paper we have analyzed certain aspects of synthesis of lithium ferrite obtained from citrate precursor gel decomposition at very low temperature, discussing the evolution of the crystal structure/microstructure parameters and Mössbauer parameters with annealing. The addition of 5 wt % of lithium in excess in citrate precursor enables the preparation of nanocrystalline lithium ferrite phase at 453 K, free from impurity ferric oxides. It has been found that annealing of the samples up to 673 K resulted in a similar atomic structure on average with almost unchanged cation distributions. Based on the analysis of the cation–anion distances, and within the precision given by XRPD technique, we suggest the possible migration of lithium ions from 4b sites to outer layers of particles. PDF analysis reveals an anomalous increase of the oxygen O1 isotropic ADP parameters to unphysical values, suggesting significant disordering in the O1 network. Mössbauer spectra of samples annealed at lower temperatures show decreased hyperfine field values, as expected from thermal fluctuations in small particles. With increasing annealing temperatures, the particles increase their average size and hyperfine fields increase to the bulk values. Taking into account that the nearest neighbor coordination of the iron in tetrahedral (A) sites is much more influenced by the oxygen O1 anions than the octahedral (B) sites in spinel structure, we can conclude that thermal annealing

of lithium ferrite powder mainly activated relaxations of the oxygen sublattices and does not change significantly the cation distribution up to 673 K. After annealing at 973 K, XRPD and Mössbauer experiments reveal that the sample S4 has a totally ordered cation distribution and bulk-like properties. The DTA analysis indicates that lower driving force is necessary to induce order–disorder phase transition in nanocrystalline samples compared to the bulk-like sample due to higher crystal disordering.

Acknowledgment. The Serbian Ministry of Science has financially supported this work through the project No. 141027. A.S.M. and E.S.B. thank SJL Billinge for useful discussions. Parts of this work were also supported by National Science Foundation (NSF) Grant Nos. DMR-0304391 and DMR-0703940. HEXRPD data were collected at the 6ID-D beamline at the Advanced Photon Source at the Argonne National Laboratory supported under DOE Contract No. DE-AC02-06CH11357. G.F.G. acknowledges financial help from Spanish MICINN through the Ramon y Cajal program.

References and Notes

- (1) Baba, P. D.; Argentina, G. M.; Courtney, W. E.; Dionne, G. F.; Temme, D. H. *IEEE Trans. Magn.* **1972**, *MAG-8*, 83–94.
- (2) Wang, X.; Gao, L.; Li, L.; Zheng, H.; Zhang, Z.; Yu, W.; Qian, Y. *Nanotechnology* **2005**, *16*, 2677–2680.
- (3) Relescu, N.; Doroftei, C.; Relescu, E.; Popa, P. D. *Sens. Actuators B* **2008**, *133*, 420–425.
- (4) Kato, E. *Bull. Chem. Soc. Jpn.* **1958**, *31*, 113–117.
- (5) Antic, B.; Kremenovic, A.; Nikolic, A. S.; Stoiljkovic, M. *J. Phys. Chem. B* **2004**, *108*, 12646.
- (6) (a) Nunes, A. C.; Yang, L. *Surf. Sci.* **1998**, *399*, 225–233. (b) Nunes, A. C.; Lin, D. *J. Appl. Crystallogr.* **1995**, *28*, 274–278.
- (7) Widatallah, H. M.; Johnson, C.; Gismelseed, A. M.; Al-Omari, I. A.; Stewart, S. J.; Al-Harathi, S. H.; Thomas, S.; Sitepu, H. *J. Phys. D: Appl. Phys.* **2008**, *41*, 165006.
- (8) (a) Chupas, P. J.; Qiu, X.; Hanson, J. C.; Lee, P. L.; Grey, C. P.; Billinge, S. J. L. *J. Appl. Crystallogr.* **2003**, *36*, 1342–1347. (b) Hammersley, A. P.; Svenson, S. O.; Hanfland, M.; Hauserman, D. *High Press. Res.* **1996**, *14*, 235. (c) Egami T.; Billinge, S. J. L. *Underneath the Bragg Peaks: Structural Analysis of Complex Materials*; Cahn, R. W., Eds.; Pergamon: New York, 2003. (d) Qiu, X.; Thompson, J. W.; Billinge, S. J. L. *J. Appl. Crystallogr.* **2004**, *37*, 678. (e) Farrow, C. L.; Juhás, P.; Liu, J. W.; Bryndin, D.; Bozin, E. S.; Bloch, J.; Proffen, Th.; Billinge, S. J. L. *J. Phys. Condens. Matter* **2007**, *19*, 335219.
- (9) (a) Rietveld, H. M. *J. Appl. Crystallogr.* **1969**, *2*, 65–71. (b) Young, R. A. *The Rietveld Method*; Oxford University Press: New York, 1993. (c) Rodriguez-Carvajal J. FullProf computer program 2008 (<http://www.ill.eu/sites/fullprof/index.html>). (d) Rodriguez-Carvajal, J. Recent Developments of the Program FULLPROF, in Commission on Powder Diffraction (IUCr). *Newsletter* **2001**, *26*, 12–19. (<http://journals.iucr.org/iucr-top/comm/cpd/Newsletters/>).
- (10) Verma, S.; Karande, J.; Patidar, A.; Joy, P. A. *Mater. Lett.* **2005**, *59*, 2630–2633.
- (11) Hessien, M. M. *J. Magn. Magn. Mater.* **2008**, *320*, 2800–2807.
- (12) Verma, S.; Joy, P. A. *Mater. Res. Bull.* **2008**, *43*, 3447–3456.
- (13) Verma, S.; Joy, P. A. *J. Phys. D: Appl. Phys.* **2005**, *98*, 124312.
- (14) (a) Billinge, S. J. L. *J. Solid State Chem.* **2008**, *181*, 1698–1703. (b) Billinge, S. J. L.; Levin, I. *Science* **2007**, *316*, 561–565. (c) Billinge, S. J. L.; Kanatzidis, M. G. *Chem. Commun.* **2004**, 749–760.
- (15) Gilbert, B.; Huang, F.; Zhang, H.; Waychunas, G. A.; Banfield, J. F. *Science* **2004**, *305*, 651.
- (16) Neder, R. B.; Korsunskiy, V. I. *J. Phys.: Condens. Matter* **2005**, *17*, S125.
- (17) Zhang, H. Z.; Gilbert, B.; Huang, F.; Banfield, J. F. *Nature* **2003**, *424*, 1025.
- (18) Petkov, V.; Peng, Y.; Williams, G.; Huang, B.; Tomalia, D.; Ren, Y. *Phys. Rev. B* **2005**, *72*, 195402.
- (19) Masadeh, A. S.; Bozin, E. S.; Farrow, C. L.; Paglia, G.; Juhás, P.; Karkamkar, A.; Kanatzidis, M. G.; Billinge, S. J. L. *Phys. Rev. B* **2007**, *76*, 115413.
- (20) Leoni, M.; Scardi, P. Surface Relaxation Effects in Nanocrystalline Powders. In *Diffraction Analysis of the Microstructure of Materials*; Scardi, P., Mittemeijer, E. J., Eds.; Springer Verlag: Berlin, 2003.
- (21) Dey, S.; Roy, A.; Das, D.; Ghose, J. *J. Magn. Magn. Mater.* **2004**, *270*, 224–229.
- (22) Shannon, R. D. *Acta Crystallogr.* **1976**, *A32*, 751–767.
- (23) Kuznetsov, M. V.; Pankhurst, Q. A.; Parkin, I. P. *J. Phys. D: Appl. Phys.* **1998**, *31*, 2886.
- (24) (a) Dormann, J. L.; Tomas, A.; Nogue, M. *Phys. Status Solidi A* **1983**, *77*, 611. (b) Dormann, J. L. *Rev. Phys. Appl.* **1980**, *15*, 1113.
- (25) Vucinic-Vasic, M.; Antic, B.; Blanus, J.; Rakic, S.; Kremenovic, A.; Nikolic, A. S.; Kapor, A. *App. Phys. A* **2006**, *82*, 49–54.
- (26) Visnevskii, I. I.; Alapin, B. G.; L'isak, C. V.; Skripak, V. N. *Kristallografiya* **1968**, *9*, 1079.
- (27) (a) Guillot, M. Magnetic properties of Ferrites. In *Electronic and Magnetic Properties of Metals and Ceramics*; Buschow, K. H. J., Eds.; VCH: Germany, 1994. (b) White, G. O.; Patton, C. E. *J. Magn. Magn. Mater.* **1978**, *9*, 299.

JP907559Y



Local and average structures of the spin-glass pyrochlore $Y_2Mo_2O_7$ from neutron diffraction and neutron pair distribution function analysis

J. E. Greedan,¹ Delphine Gout,² A. D. Lozano-Gorrin,¹ Shahab Derakhshan,¹ Th. Proffen,³ H.-J. Kim,³ E. Božin,⁴ and S. J. L. Billinge⁴

¹*Department of Chemistry and Brockhouse Institute for Materials Research, McMaster University, Hamilton, Canada L8S 4M1*

²*Jülich Center for Neutron Science–SNS, Forschungszentrum Jülich, 52425 Jülich, Germany and Oak Ridge National Laboratory, P.O. Box 2008, Oak Ridge, Tennessee 38371, USA*

³*Lujan Neutron Scattering Center, Los Alamos National Laboratory, Los Alamos, New Mexico 87545, USA*

⁴*Department of Applied Physics and Applied Mathematics, Columbia University, New York, New York 10027, USA and Condensed Matter and Materials Science Department, Brookhaven National Laboratory, Upton, New York 11973, USA*

(Received 18 November 2008; revised manuscript received 11 December 2008; published 21 January 2009)

The observation of canonical spin-glass behavior in the pyrochlore oxide $Y_2Mo_2O_7$ has been a subject of considerable interest as the original structural studies were interpreted in terms of a well-ordered crystallographic model. It is widely held that the stabilization of the spin-glass state requires some level of positional disorder along with frustration. Recent reports from local probe measurements, extended x-ray-absorption fine structure (EXAFS) and ^{89}Y NMR, have been interpreted in terms of disorder involving the Mo-Mo distances (EXAFS) and multiple Y sites (NMR). This work reports results from temperature-dependent (15–300 K) neutron diffraction (ND) and neutron pair distribution function studies which can provide from the same data set information on both the average and local structures. The principal findings are that: (1) there is no crystallographic phase transition over the temperature region studied within the resolution of the ND data; (2) the diffraction data are well fitted using a fully ordered model but with large and anisotropic displacement parameters for three of the four atomic sites; (3) the pairwise real-space correlation function $G(r)$ shows clear evidence that the principal source of disorder is associated with the Y-O1 atom pairs rather than the Mo-Mo pairs, in disagreement with the interpretation of the EXAFS results; (4) fits to the $G(r)$ improve significantly when anisotropic displacements for all sites are included; (5) inclusion of a split-site position parameter for O1 improves, slightly, both the $G(r)$ fits and the Rietveld fits to the ND data; and (6) for all models the fits become worse as the temperature decreases and as the fitting range decreases. These results are qualitatively consistent with the ^{89}Y NMR observations and perhaps recent muon-spin-relaxation studies. The issue of static versus dynamic disorder is not resolved, definitively. An estimate of the distribution of exchange constants due to the disorder is made using spin-dimer analysis and compared with the Saunders-Chalker model for the generation of spin-glass behavior from “weak” disorder on geometrically frustrated lattices.

DOI: [10.1103/PhysRevB.79.014427](https://doi.org/10.1103/PhysRevB.79.014427)

PACS number(s): 75.50.Lk, 61.05.fm

I. INTRODUCTION

Geometrically frustrated materials with nearest-neighbor antiferromagnetic (AF) constraints can exhibit a variety of ground states including long-range but complex-order, spin-liquid and spin-glass (SG) behaviors. If the constraints are ferromagnetic and accompanied by strong axial anisotropy, the spin-ice state may be stabilized. Materials with the pyrochlore structure, mostly oxides, have been central to investigations of such phenomena and the voluminous literature has been reviewed recently.¹ Among the known pyrochlore oxides for which there is no obvious compositional disorder, there are only a few examples of the SG ground state. The best studied of these is $Y_2Mo_2O_7$, which was first tentatively characterized as a spin glass with $T_f=22$ K on the basis of low-temperature dc susceptibility results in 1986,² although high-temperature data had been reported as early as 1975.^{3,4} Subsequent work has established that $Y_2Mo_2O_7$ does indeed behave as a nearly ideal spin glass from nonlinear susceptibility, heat-capacity, ac susceptibility, elastic and inelastic neutron-scattering, muon-spin-relaxation, and neutron spin-echo data, for example.^{5–11} There appears to be little doubt that $Y_2Mo_2O_7$ is a spin glass; indeed the critical exponents

extracted from the analysis of the nonlinear dc susceptibility agree well with those found in classical disordered spin-glass systems.⁵ It is a widely held tenet that in order for the SG state to be stable, both frustration and positional disorder must be present, simultaneously. This is certainly the case in the classical spin glasses such as dilute solid solutions of iron in gold, Fe_xAu_{1-x} , with $x \sim 0.05$, where the randomness of the Fe sites and the Ruderman-Kittel-Kasuya-Yosida (RKKY) exchange mechanism combine to produce the spin-glass state. Another class of spin glasses can be obtained by dilution of the magnetic sites of an antiferromagnetic or a ferromagnetic insulator with a diamagnetic substituent. Among many examples are the antiferromagnets $Fe_xZn_{1-x}F_2$ and $Fe_xMg_{1-x}TiO_3$, where a SG state obtains for x values near the percolation threshold.^{12,13} In other cases, $Eu_xSr_{1-x}S$, for example, a SG state emerges for x values ($x \sim 0.5$) well above the percolation limit ($x \sim 0.2$).¹⁴ Here, competing nearest-neighbor ferromagnetic and next-nearest-neighbor antiferromagnetic interactions are key factors. In all of the above examples, significant levels of positional disorder induce magnetic frustration in the relevant systems. For the pyrochlore oxides in which dilution effects are clearly not present, another mechanism must be operable.

TABLE I. Description of the $A_2B_2O_7$ pyrochlore structure in $Fd3m$.

Atom	Wyckoff site	Point symmetry	Minimal coordinates
A	16d	$-3m$	1/2 1/2 1/2
B	16c	$-3m$	0 0 0
O1	48f	mm	x 1/8 1/8
O2	8b	$-43m$	3/8 3/8 3/8

Before proceeding further, it is highly relevant to consider the existing structural evidence from neutron diffraction (ND) which measures, of course, the average structure. The formal description of the pyrochlore structure for materials, mostly oxides with composition $A_2B_2O_7$, is within space group $Fd3m$ as shown in Table I. There are four occupied positions, the choice with A in 16d, B in 16c, O1 in 48f, and O2 in 8b is now considered standard, although in earlier literature other origins have been used.¹⁵

In the original neutron powder diffraction study, the fully ordered model was refined for $Y_2Mo_2O_7$ with Y in 16d, Mo in 16c, and O2 in 8b, and the lone positional parameter for O1 in 48f was found to be $x=0.3382(1)$ with the cubic lattice constant $a_0=10.230(1)$ Å.¹⁶ Some disorder models involving O2 were explored but these gave no improvement on the ideal model. Anisotropic displacement parameters were refined for the Y site and these gave an ellipsoid flattened normal to the local axis which is a $\langle 111 \rangle$ -type direction within the unit cell. All interatomic distances were reasonable for the fully ordered model, being in excellent agreement with the sum of the effective ionic radii.

Of course all real materials will contain various types of defects, generally at low levels. Concentrations can be difficult to measure but recent computational results for pyrochlore oxides suggest values on the order of 1%.¹⁷ For $Y_2Mo_2O_7$ the calculated antisite (Y/Mo exchange) defect level is 1.1% and the oxygen vacancy level is 0.4%. Are such defect concentrations sufficient to induce spin-glass behavior? This seems somewhat unlikely on the basis that only a few nominally stoichiometric pyrochlores are actually spin glasses and the defect levels are calculated to be similar for all oxide materials of this structure type. One known case for which spin-glass behavior results from very low levels of substitutional disorder is that of Cd-doped $ZnCr_2O_4$.¹⁸ Here, Cd substitution for Zn at the 3% level is sufficient to destroy the Néel order in $ZnCr_2O_4$. For this material, the Cr^{3+} sublattice has pyrochlore topology and in the pure phase undergoes a tetragonal distortion which presumably lifts the ground-state degeneracy and selects an AF long-range-order (LRO) ground state with $T_N=14$ K. It is argued that the large size mismatch between Cd^{2+} and Zn^{2+} , 0.78 Å versus 0.60 Å, respectively,¹⁹ induces random strains which, in the presence of strong magnetoelastic coupling, can result in the spin-glass ground state. Interestingly, substitution of diamagnetic Ga^{3+} on the Cr^{3+} sites is much less effective, with the SG state appearing only at concentrations approaching 20% Ga. Ga^{3+} and Cr^{3+} have nearly identical radii for sixfold coordination, 0.62 Å.

Saunders and Chalker²⁰ attempted to explain the occurrence of the SG ground state in geometrically frustrated mag-

nets with “weak” disorder levels. In this approach, weak disorder is defined as $\Delta \ll J$, where J is the average exchange constant and Δ is its fluctuation. The model considered is the classical Heisenberg antiferromagnet with near-neighbor exchange on a pyrochlore lattice. The central results are that the spin-glass correlation function is finite at large distances for a range of Δ and that the spin-freezing temperature $T_f \propto \Delta$ but is independent of J . Quantitative application of these ideas to actual systems is not straightforward as the relationship of $\Delta(J)$ to a specific disorder or defect mechanism will be complex and perhaps not easily established.

Nonetheless, it is still important to identify the nature of the disorder in materials such as $Y_2Mo_2O_7$ in a first effort to understand its unique behavior. Recently, there have been two studies, both involving local probes, which provide some evidence for disorder in this material. Extended x-ray-absorption fine structure (EXAFS) data for both Mo and Y edges have been interpreted in terms of a large static variance in the Mo-Mo distances, $\Delta^2=0.026(5)$ Å², which is ~ 10 times larger than the variances found for Mo-O1, Mo-Y, and Y-Y distances, for example.²¹ This implies a fluctuation in the Mo-Mo bond distance of 0.16(2) Å, which is $\sim 4\%$ of the equilibrium Mo-Mo distance. It has been widely suggested that this disorder level may explain the spin-glass ground state but no quantitative link has been established. In another study ⁸⁹Y NMR data show a large number of resonances when $Y_2Mo_2O_7$ is cooled below 200 K.²² This can be interpreted as evidence for a local multiplicity of Y sites, in contrast to the average structure value of one. As the Weiss temperature for this material is -200 K, the suggestion was made that the disorder was somehow “frustration driven” but no evidence has yet been presented for a true phase transition as seen for the case of $ZnCr_2O_4$ described above. Subsequent muon spin relaxation (μ SR) studies in applied fields have attempted to measure the distribution of local magnetic fields seen by the muon in $Y_2Mo_2O_7$ which was equated with the distribution in exchange constants.²³ It was concluded that this distribution increases rapidly below 40 K. Another study, not on $Y_2Mo_2O_7$ but instead on isostructural $Yb_2Mo_2O_7$, is worth mentioning. ¹⁷⁰Yb Mössbauer-effect data must be interpreted in terms of a distribution of electric field gradients at the Yb site, suggesting some type of disorder on the A site.²⁴ Interestingly, a similar disorder but of lesser magnitude is noted for ferromagnetic $Gd_2Mo_2O_7$.

There is in these studies the usual dichotomy between the information obtained from diffraction probes which determine the average structure and the local probes where the structural information is restricted to very short length scales, often that between nearest neighbors. It is, thus, challenging to reconcile the two types of data to provide a consistent interpretation. Ideally, one would like to use a method which could, from the same data set, provide information on both the local and average structure. The neutron pair distribution function (NPDF) method meets this criterion.²⁵ In this approach diffraction data, $S(Q)$, are collected to very large momentum transfers, $Q \sim 30-40$ Å⁻¹. Fourier transformation of suitably normalized data can then yield the real-space pairwise distribution function, $G(r)$, from which local structure information can be extracted. Of course the same $S(Q)$ data can be analyzed using conventional Rietveld crystallo-

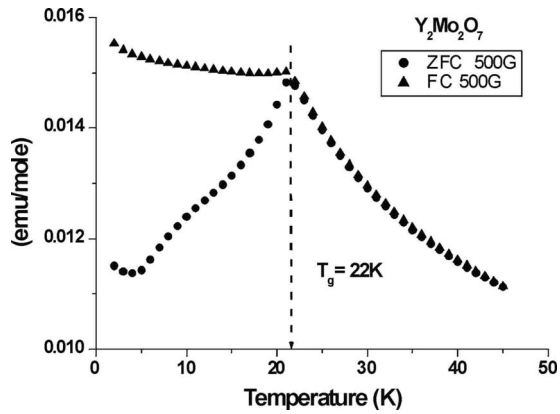


FIG. 1. Low-temperature dc magnetic susceptibility for the $Y_2Mo_2O_7$ sample used in these studies.

graphic tools to yield the average structure. Recent advances in instrumentation, especially at spallation neutron sources, and corresponding developments in data analysis codes have now made this technique more widely accessible.^{26,27} In the following, ND and NPDF data are used to characterize both the average and local structure of $Y_2Mo_2O_7$ over a wide temperature range, 15–300 K, which includes those for which the EXAFS and NMR studies were done and extending well into the spin-glass regime.

II. EXPERIMENTAL

A. Sample preparation and characterization

$Y_2Mo_2O_7$ was prepared from starting materials, MoO_2 (99.9%) and Y_2O_3 (99.99%). Y_2O_3 was fired at 1000 °C for 8 h. before weighing. The mixture was ground and mixed well in a mortar and pestle, then pelletized and fired at 1300 °C for 48 h in a buffer gas mixture $CO/CO_2=1$ as described in a previous report.²⁸ The material was determined to be single phase from x-ray powder diffraction using

a Guinier-Hägg camera. Magnetic-susceptibility data were collected using a Quantum Design superconducting quantum interference device (SQUID) magnetometer.

B. Neutron scattering and data handling

Neutron-scattering data were collected on the instrument NPDF at the M. Lujan Jr. Center for Neutron Scattering at the Los Alamos Neutron Science Center. This instrument has been described elsewhere.²⁶ The sample of ~ 5 g was contained in a vanadium can which was placed in a Displex closed-cycle refrigerator. Background corrections were determined by measuring the empty sample chamber, empty Displex, and empty vanadium sample can. Detector efficiency was normalized by measuring a vanadium rod. Data were collected to a limit of $Q=45 \text{ \AA}^{-1}$ at several temperatures between 300 and 15 K. Data for neutron diffraction analysis were obtained by truncating the data at $Q=9 \text{ \AA}^{-1}$, while for PDF analysis, the truncation limit was taken as $Q=35 \text{ \AA}^{-1}$ based on inspection of the noise level in the data. Standard data corrections were carried out using PDF_{getN}.²⁵ Corrected data were normalized by the total scattering cross section of the sample to yield the total scattering structure factor $S(Q)$, where Q is the scattering or momentum transfer vector, $Q=4\pi \sin \theta/\lambda$. The $G(r)$ was obtained by a sine Fourier transform according to

$$G(r) = 4\pi r[\rho(r) - \rho_0] = 2/\pi \int_0^\infty Q[S(Q) - 1]\sin(Qr)dQ,$$

where $\rho(r)$ is the atomic pair density and ρ_0 is the average atomic number density. The ND data were refined using the GSAS package and the refinements of $G(r)$ were done with PDFFIT and PDFGUI, the latter permitting the refinement of anisotropic atomic displacement factors (ADFs).²⁷

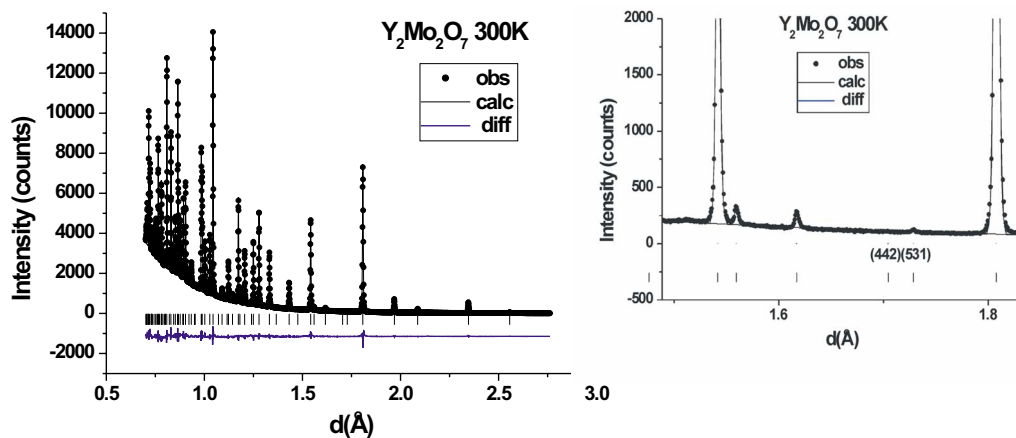


FIG. 2. (Color online) (Left) A Rietveld fit for the neutron diffraction data for $Y_2Mo_2O_7$ at 300 K on the fully ordered model using ADFs for all atoms. $R_{wp}=4.01\%$. The black circles are the data, the solid line is the model, and the lower curve is the difference plot. Bragg-peak positions are shown by the vertical tic marks. (Right) The region including the 442 reflection position showing the absence of this reflection. The very weak but allowed 531 reflection is also marked.

TABLE II. Rietveld refinement results with anisotropic ADFs for $Y_2Mo_2O_7$ at various temperatures.

T (K)	a_0 (Å)	$x(O1)$	R_{wp}
300	10.23025(2)	0.337689(29)	0.0407
225	10.22129(2)	0.33788(4)	0.0468
200	10.21859(2)	0.337811(33)	0.0419
150	10.21352(2)	0.337852(30)	0.0444
100	10.21014(2)	0.338031(33)	0.0498
50	10.20828(2)	0.338047(31)	0.0480
25	10.20759(2)	0.338071(32)	0.0492
20	10.20759(2)	0.338080(32)	0.0487
15	10.20753(2)	0.338088(32)	0.0482

III. RESULTS AND DISCUSSION

A. Magnetic characterization

Magnetic-susceptibility data taken at 0.05 T are shown in Fig. 1. Note the divergence between the data collected in zero-field-cooled and field-cooled modes at 22 K which can be taken as the spin-glass freezing temperature T_F . These data are consistent with several other determinations shown in the literature and indicate that this sample is equivalent in terms of magnetic properties to typical samples of $Y_2Mo_2O_7$.

B. Neutron diffraction: The average structure

The only structural study previously published¹⁶ was based on data taken at a low-flux reactor-based source with modest resolution, so it is of considerable interest to analyze data of superior resolution and extended Q range as afforded here. Initially, the data sets at each temperature were refined using both isotropic and anisotropic ADFs on the fully ordered model. A typical result is shown in Fig. 2, left panel, from which it is clear that the fit is excellent. Figure 2, right panel, demonstrates the absence of the 442 reflection, the significance of which is discussed later in this section. The refinement results are listed in Tables II–IV for anisotropic ADFs and the temperature dependence of the anisotropic

ADFs is shown in Fig. 3, left panel, while the ellipsoids are indicated in Fig. 3, right panel.

First the anisotropic refinement results at 300 K can be compared directly with those for other pyrochlores, for example, $Y_2Sn_2O_7$, obtained also from neutron powder data as shown in Table V.²⁹ These results were obtained at a reactor source to $Q_{max}=8.1 \text{ \AA}^{-1}$ comparable to those of the present work for which $Q_{max}=9.1 \text{ \AA}^{-1}$. The effective radii for Sn^{4+} (0.69 Å) and Mo^{4+} (0.65 Å) are comparable.¹⁹

Note that, except for the O2 site, the diagonal displacement factors for $B=Mo$ are significantly larger, by factor of 2 or 3, than those for the $B=Sn$ pyrochlore. The shapes of the ellipsoids at the B site are different as well, with negative off-diagonal values for $B=Sn$ which are positive for $B=Mo$. Thus, the Sn ellipsoid is a disklike slightly flattened sphere, while for $B=Mo$, it is an elongated cigar shape (Fig. 3, right panel). Considering relative magnitudes among ADFs for $Y_2Mo_2O_7$, $U_{11}(O1)$ is the largest of all by nearly a factor of 2. Examination of the temperature dependence of the displacements (Fig. 3, left panel) indicates normal behavior for most, but U_{11} for O1 remains very large and U_{11} for Mo shows nearly no temperature dependence. Thus, in spite of the excellent apparent fit of the fully ordered model to the data, it is clear that all of the atomic displacement factors are large and show considerable anisotropy except of course for O2, for which the site symmetry constrains the ellipsoid to be spherical. Before leaving this discussion, it is worth noting that the 442 reflection, which has been linked with static atomic displacements in pyrochlores, is not observed in the neutron data (Fig. 2, right panel). For example, pyrochlores with so-called lone pair active ions on the A site, e.g., $Bi_2Ti_2O_7$ or $Sn_2Ta_2O_7$, for which a clear static distortion has been demonstrated, always show a 442 reflection.^{30,31} In these cases the lone pair ion is disordered over the 96g sites and O2 is partially distributed over 32e. The origin of this correlation is that additional systematic absences arise in $Fd3m$ with isotropic atoms in Wyckoff sites $a-d$ and f which forbid 442 but for atoms in any other site these additional extinctions do not hold. Apparently, anisotropic atoms in these special sites also allow 442 in principle but in the case of $Y_2Mo_2O_7$, it is absent in spite of large-amplitude anisotropic behavior at all of these sites except of course 8b. Finally, the absence of 442 argues against disorder of O2 in 32e.

TABLE III. Anisotropic ADFs $U_{ij} \times 10^2 \text{ \AA}^2$ for $Y_2Mo_2O_7$ at various temperatures.

T (K)	$U_{11}(Y)$	$U_{12}(Y)$	$U_{11}(Mo)$	$U_{12}(Mo)$	$U_{11}(O1)$	$U_{22}(O1)$	$U_{23}(O1)$	$U_{11}(O2)$
300	0.856(9)	-0.224(9)	1.14(1)	0.61(1)	1.85(2)	0.96(1)	0.16(1)	0.56(2)
225	0.648(9)	-0.19(1)	0.99(1)	0.69(2)	1.64(2)	0.70(1)	0.16(2)	0.35(2)
200	0.722(8)	-0.18(1)	1.15(1)	0.75(2)	1.72(2)	0.82(1)	0.11(1)	0.46(2)
150	0.732(7)	-0.162(9)	1.27(1)	0.80(1)	1.73(2)	0.868(9)	0.06(1)	0.50(2)
100	0.511(8)	-0.16(1)	1.11(1)	0.81(2)	1.45(2)	0.677(9)	0.03(1)	0.34(2)
50	0.497(7)	-0.130(9)	1.14(1)	0.84(2)	1.48(2)	0.680(9)	0.03(1)	0.35(2)
25	0.491(7)	-0.14(1)	1.14(1)	0.83(2)	1.47(2)	0.691(9)	0.03(1)	0.35(2)
20	0.471(7)	-0.140(9)	1.12(1)	0.82(2)	1.44(2)	0.667(9)	0.03(1)	0.35(2)
15	0.471(7)	-0.136(9)	1.11(1)	0.83(2)	1.45(2)	0.66(1)	0.03(1)	0.32(2)

TABLE IV. Selected interatomic distances (\AA) for $\text{Y}_2\text{Mo}_2\text{O}_7$ from Rietveld refinements.

T (K)	Y-O1	Y-O2	Mo-O1	Y-Y/Mo-Mo
300	2.4552(2)	2.21491(1)	2.0187(1)	3.61694(1)
225	2.4517(3)	2.21297(1)	2.0178(2)	3.61377(1)
200	2.4515(2)	2.21239(1)	2.0170(2)	3.62182(1)
150	2.4500(2)	2.21129(1)	2.0162(1)	3.61102(1)
100	2.4480(2)	2.21056(1)	2.0163(2)	3.60983(1)
50	2.4474(2)	2.21016(1)	2.0160(2)	3.60917(1)
25	2.4471(2)	2.21001(1)	2.0160(2)	3.60893(1)
20	2.4470(2)	2.21001(1)	2.0160(2)	3.60893(1)
15	2.4469(2)	2.20999(1)	2.0161(2)	3.60891(1)

The average structure data can also be used to examine the possibility of a crystallographic phase transition, frustration driven or otherwise, within the temperature range investigated. For example, the data of Fig. 3 show some scatter but no discontinuity in the ADFs as the temperature is lowered, nor is there any other discontinuity such as in the cell constant or the $x(\text{O1})$. Figure 4 shows a comparison of data from the 148° backscattering detector bank for 300 and 20 K. Within the resolution of these data, $\Delta d/d \sim 1.5 \times 10^{-3}$, there is no evidence for new reflections or peak splitting or broadening which would signal a crystallographic phase transition to a lower symmetry as the temperature decreases to below the observed T_F .

C. Pair distribution function analysis: The local structure

The $G(r)$ shows sharp features out to quite long distances, indicating a high degree of crystallinity for the sample. In these studies a $r_{\text{max}} = 20 \text{ \AA}$ has been chosen for fitting and is displayed in Fig. 6. The weak ripples below about 2 \AA are unphysical, coming from errors in the data analysis.³² They are small, indicating the good quality of the data, and are insignificant in the physical region of the PDF above 1.8 \AA . There is merit in examining the region of small r which includes the nearest-neighbor pairwise distances for this material. Figure 5 displays the $G(r)$ out to 3.8 \AA , showing six

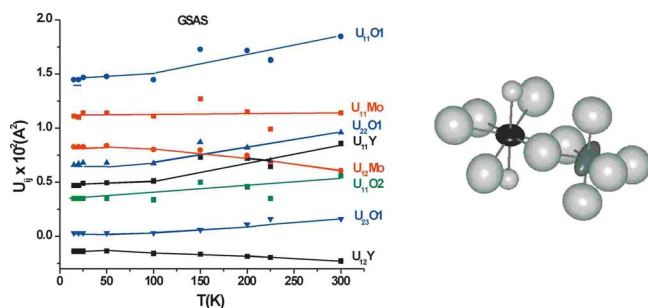


FIG. 3. (Color online) (Right) Temperature dependence of the anisotropic displacement factors for $\text{Y}_2\text{Mo}_2\text{O}_7$. The lines are guides for the eyes. (Left) The ADF ellipsoids at 300 K. Y is black, Mo is dark gray, O1 is large and white, and O2 is small and white.

TABLE V. Comparison of anisotropic displacement factors (10^{-2} \AA^2) for $\text{Y}_2\text{B}_2\text{O}_7$ pyrochlores at 300 K; $B = \text{Sn, Mo}$.

Parameter (Site)	$B = \text{Sn}$	$B = \text{Mo}$
$U_{11} = U_{22} = U_{33}$ (Y)	0.54(2)	0.856(9)
$U_{12} = U_{13} = U_{23}$ (Y)	-0.09(2)	-0.224(9)
$U_{11} = U_{22} = U_{33}$ (Sn, Mo)	0.27(2)	1.14(1)
$U_{12} = U_{13} = U_{23}$ (Sn, Mo)	-0.03(2)	0.61(1)
U_{11} (O1)	0.64(3)	1.85(2)
$U_{22} = U_{33}$ (O1)	0.56(2)	0.96(1)
U_{23} (O1)	0.23(2)	0.16(1)
$U_{11} = U_{22} = U_{33}$ (O2)	0.49(4)	0.56(2)

resolved peaks, each of which can be assigned unambiguously as indicated by comparison of the peak maxima with the interatomic distances refined from the Rietveld analysis (Table IV).

Note that the peaks for Y-O1 and O1-O1 which correspond to a difference of 0.16 \AA are sufficiently well resolved to be readily identified. At this stage it is of interest to compare the interpretation of the EXAFS data in terms of a static splitting of the Mo site with magnitude of $\sim 0.16 \text{ \AA}$ directly to the $G(r)$. Unfortunately, due to the cubic symmetry, two atom pairs contribute to the peak at 3.62 \AA , Y-Y and Mo-Mo, each involving six neighbors. The total intensity of a peak in the $G(r)$ is given by $I_{\text{tot}} = \sum_{ab} N_{ab} b_a b_b$, where N_{ab} is the number of contributing atom pairs and b_a and b_b are the scattering lengths of the atoms in the pair. The relative contribution of a given pair to the total peak intensity is thus $N_{ab} b_a b_b / I_{\text{tot}}$. On this basis the Mo-Mo pairs account for 41% of the peak intensity at 3.62 \AA , a significant fraction. Note that there is no evidence for two observable peaks in the $G(r)$ at this distance. The EXAFS analysis found no unusual behavior of the Y-Y correlation, so in spite of the coincidence of the two atom pairs in the $G(r)$, one could expect to see Mo site splitting manifested in the form of discernable shoulders or at least a strong deviation from a Gaussian peak shape, which is also not evident. From another point of view, one can compare the relative widths of the Mo-O1 and Mo-Mo peaks between the $G(r)$ and the EXAFS fits. In the latter experiment the ratio of the variances, Δ^2 , for Mo-Mo/Mo-O1 is given as ~ 11 , which implies that the ratio of the peak widths should be ~ 3.3 . Inspection of Fig. 5 shows that this is not observed; in fact the actual ratio is 1.5 at 300 K, which reduces to 1.1 at 15 K. Thus, the observed $G(r)$ does not appear to support a disorder model involving a split static Mo position of the magnitude needed to explain the EXAFS data. In addition one can compare the relative peak heights in the $G(r)$ data which should scale according to the equation given earlier, assuming a common peak width. Note that the Y-O1 ($x6$) peak is actually less intense than the Mo-O1 peak ($x6$) and even less intense than the Y-O2 peak ($x2$), whereas one would expect the relative peak height ratios to be $3/2.7/1$ for the three atom pairs in the order listed. This indicates that, even without any fitting of the $G(r)$ data, attention is focused on the Y-O1 pairs as the principal origin of short-range disorder in this material. While the EXAFS data do

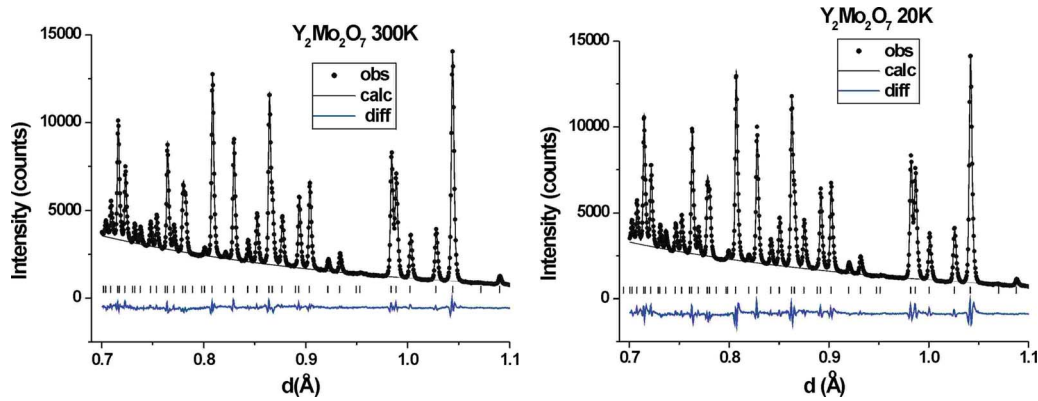


FIG. 4. (Color online) Comparison of neutron diffraction data at short d spacings for $\text{Y}_2\text{Mo}_2\text{O}_7$ at 300 K (left) and 20 K (right) showing the absence of a structural phase transition.

show anomalous behavior associated with the Mo-Mo pairs, this may be traced to the very large degree of anisotropy associated with the Mo ADF, but there is no clear evidence from the $G(r)$ for a static splitting. Of course much more definitive conclusions can be extracted from a detailed modeling of the NPDF data.

The $G(r)$ data were fitted using three models. The first involved the fully ordered model and isotropic ADFs, U_{iso} , for all atoms, and the results for 300 and 15 K are shown in Fig. 6. Clearly, the result at 300 K is poor with an agreement index $R_w = 12\%$. Insight into the problems with this model is afforded by viewing the short- r regime, shown at the top right in Fig. 6. Here, as anticipated already, it is clear that the major area of poor fit involves the Y-O1 and O1-O1 sites. Clearly, the Y-O1 peak is strongly overestimated in the fit. While a difference peak occurs at Mo-Mo/Y-Y/Mo-Y, it is of the opposite sense, i.e., the data peak is actually sharper than the fitted peak, again a counterindication with respect to the EXAFS-derived model. Essentially the same situation is found at low temperature. Figure 6 bottom shows comparable data at 15 K, below T_f . Note that R_w is larger at 15 K, almost 16%. The data of Fig. 6 are not inconsistent with the large-amplitude anisotropic displacement parameters for the O1, Y, and Mo sites determined from the Rietveld analysis of the average structure.

Thus, the $G(r)$ data were fitted using anisotropic ADFs, U_{aniso} , for all atoms. The results at 300 and 15 K are shown in Fig. 7. Note first that R_w drops to 8% at 300 K and 10% at 15 K, both significant improvements to the fits. As seen in the short- r data, fits around the Y-O1 and Mo-Mo/Y-Y distances are much better. The total number of fitting parameters is now increased to 13 from 9 in the isotropic ADF model.

At this stage a static disorder model in which the O1 site was split was implemented. From the dimensions of the O1 ellipsoid, extreme x values of 0.329 and 0.346 were chosen as starting parameters and the O1 sites were divided into two groups of 24. This refinement in which all atoms were refined anisotropically showed a slight improvement in the fit at 300 K but results in the same R_w value as for the anisotropic ADF model at 15 K shown in Fig. 8. The number of refined parameters is now 16. The fitted values for $x(\text{O1})$ are 0.3305(12) and 0.3465(13).

Such a model can be checked using the diffraction data. To that end a refinement was attempted using a split O1 site in 48f. The starting x value was that from the fully ordered model. The results show that two independent x parameters can be refined with values of 0.3289(1) and 0.3466(1), very similar to those found from the PDF fit to the $G(r)$ data described above. However, it was not possible to refine simultaneously both the x values and the ADFs for each site. ADFs were refined separately, holding the x values constant, giving U_{11} and U_{22} values for the thermal ellipsoid of the O1 site which are now comparable, 0.0094(1) and 0.0089(1) \AA^2 , respectively. A major implication of the split-site model is that there are now two Y-O1 distances, 2.5165 and 2.3847 \AA , with a mean value of 2.4556 \AA and a standard deviation $\sigma = 0.0609$, and two Mo-O1 distances, 1.9805 and 2.0606 \AA , with a mean value of 2.023 \AA and $\sigma = 0.0376$. Such σ values would not result in resolvable features in the $G(r)$ as the observed full widths at half maximum (FWHMs) of the Mo-O peak and the Mo-Mo peak are 0.14 and 0.19 \AA , respectively, at 300 K.

As has been noted previously, the R_w values for the fits to $G(r)$ increase for the same model as the temperature decreases. The global result for all models including the average structure is shown in Fig. 9. The common feature is that all agreement indices do increase with decreasing temperature but the behavior is different for each model. The average structure model shows the smallest effect with an increase from 4.07% at 300 K to 4.82% at 15 K, an overall change of 18%. The PDFFIT for the isotropic ADF model increases from 12.01% to 15.97%, a 33% change over the same range but

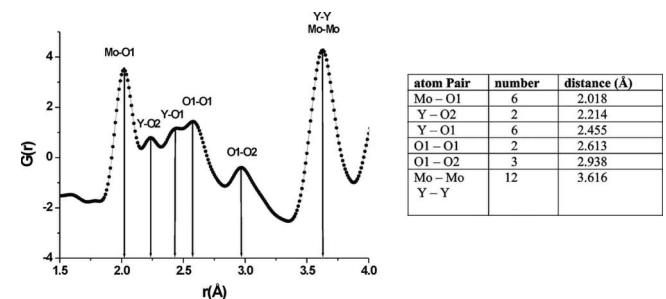


FIG. 5. The short- r region of $G(r)$ for $\text{Y}_2\text{Mo}_2\text{O}_7$ at 300 K. Peak assignments are indicated.

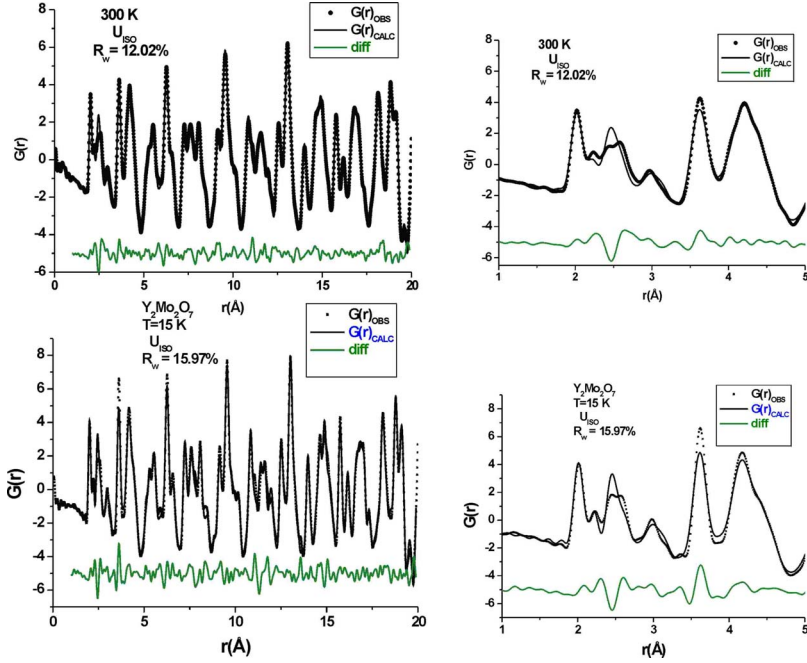


FIG. 6. (Color online) Fits to the $G(r)$ at 300 and 15 K: the fully ordered model with isotropic ADF. Top: 300 K; bottom: 15 K. Left: 0–20 Å; right: 1–5 Å.

R_w increases gradually to ~ 100 K and is then constant. For the other two models, there is a more discontinuous jump in R_w below 100 K for the all aniso models and below 50 K for the O1 split-site model. The overall changes are different, 22% for the former and 44% for the latter. Clearly, all models are less accurate at low temperature. These observations may be consistent with the recent μ SR studies, mentioned above, which find a significant increase in the distribution of local fields below 40 K.²³

Fits to the $G(r)$ were also carried out in which the range of r over which the fitting was done was varied. The minimum r value, r_{min} , was fixed at 1 Å and r_{max} was increased systematically to 20 Å. The results for the split-O1-site model are shown in Fig. 10 for both 300 and 15 K. Note that

R_w decreases sharply in both cases as r_{max} is increased for both temperatures. At 300 K R_w reaches an approximately constant value beyond $r_{max} \sim 10-12$ Å, while at 15 K R_w appears to be constant above $r_{max} \sim 8-10$ Å. Both results suggest that the disorder in this material extends to at least 8 Å, which is beyond the nearest-neighbor distance range.

D. Spin-dimer analysis

It is clearly of great interest to compare the implications of the disorder models investigated here with the criteria of Saunders and Chalker²⁰ for the emergence of the spin-glass ground state due to weak disorder in a pyrochlore lattice. A computational estimation of relative strengths of spin inter-

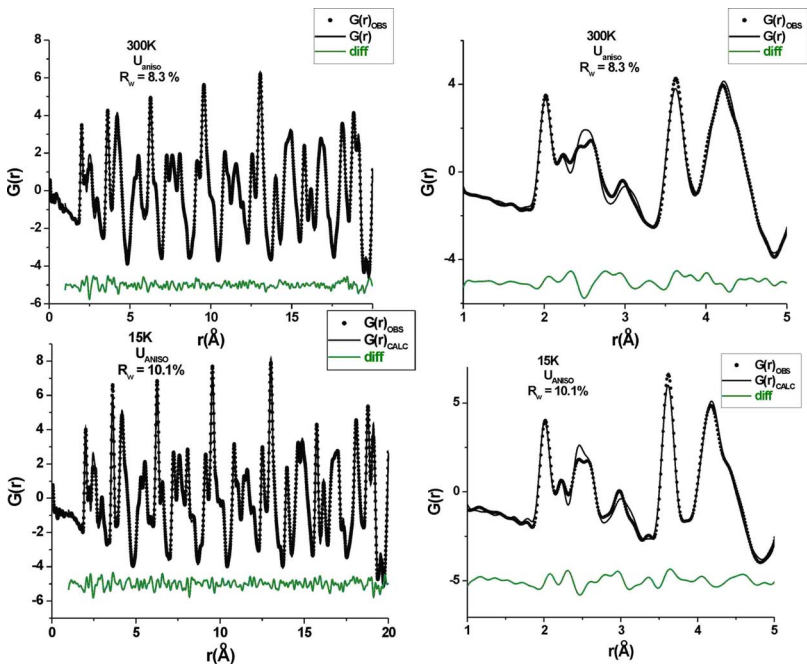


FIG. 7. (Color online) Fits to the $G(r)$ at 300 and 15 K for the fully ordered model with anisotropic ADF for all atoms. Top: 300 K; bottom: 15 K. Left: 0–20 Å; right: 1–5 Å.

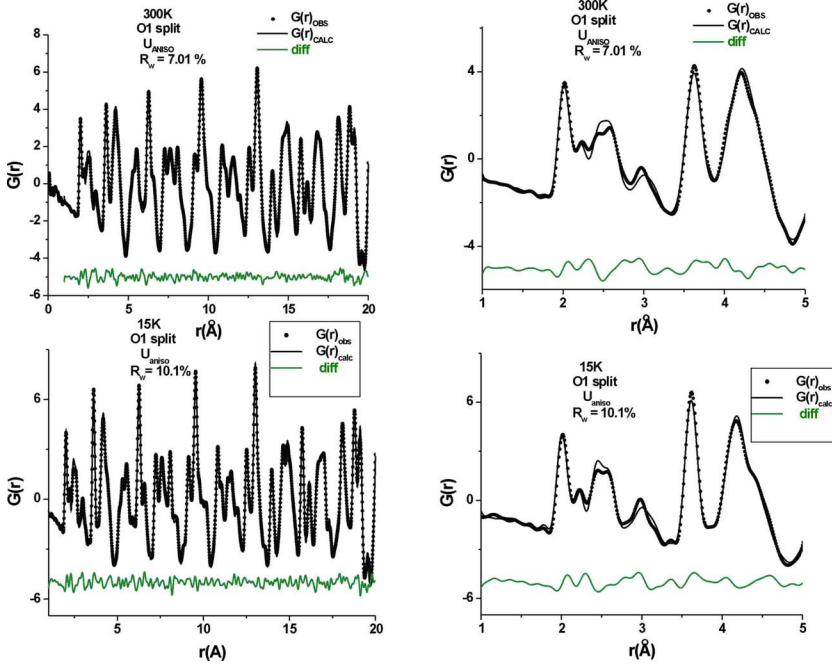


FIG. 8. (Color online) Fits to the $G(r)$ at 300 and 15 K: the split-O1-site model with anisotropic ADF. Top: 300 K; bottom: 15 K. Left: 0–20 Å; right: 1–5 Å.

actions among different magnetic ions and through different pathways was obtained using extended Hückel spin-dimer analysis.³³ The strengths of spin interaction manifested in the exchange constant J are related to the hopping energies among different magnetic sites, Δe , as well as the electron correlation energy U resulting from accommodation of two electrons within the same orbital. These quantities are related through the formula

$$J = -2 \frac{(\Delta e)^2}{U}. \quad (1)$$

When comparing J values of different interaction pathways involving the same magnetic ion, the correlation energy, U , is constant and therefore the difference in the $(\Delta e)^2$ value determines the significance of a particular spin interaction relative to the other possible pathways. In these computations three different interaction pathways between two nearest-neighbor Mo sites were considered based on the x positional value for O1 for the average structure and the two extreme values for the split-site model. The values of the intersite hopping energies Δe were acquired by employing the CAESAR package³⁴ assuming that all three t_{2g} Mo 4d orbitals contributed equally to the superexchange interaction. The variation in the Mo-O1-Mo angle and $(\Delta e)^2$ as a function of x is shown in Table VI.

It is clear from Table VI that $\langle \Delta e \rangle^2$ and, thus J , are strong functions of $x(\text{O1})$ and that disorder at this level will lead to a large distribution of exchange constant values, ΔJ , with $\Delta J/J > 0.1$. Thus, in the Saunders-Chalker context it seems clear that a spin-glass ground state for $\text{Y}_2\text{Mo}_2\text{O}_7$ can be understood.

IV. SUMMARY AND CONCLUSIONS

The main conclusions from this work pertinent to the average structure of $\text{Y}_2\text{Mo}_2\text{O}_7$ are that: (1) neutron diffraction

data of relatively high resolution can be fitted very well by a fully ordered model with anisotropic ADFs, but (2) the ADFs are indeed highly anisotropic in comparison to isostructural $\text{Y}_2\text{Sn}_2\text{O}_7$, and (3) there is no evidence for a true crystallographic phase transition over the range of 300–15 K within the resolution of the data.

Conclusions relevant to the local structure are that: (1) there is significant disorder associated with the Y-O1 pairs which would be qualitatively consistent with ^{89}Y NMR results reported previously, (2) there is no evidence for a disorder model involving the Mo-Mo pairs proposed previously from EXAFS data, (3) either a dynamic disorder model (anisotropic ADFs) or a static split-O1-site model results in dramatic improvements in fits of the $G(r)$, (4) fits of the local

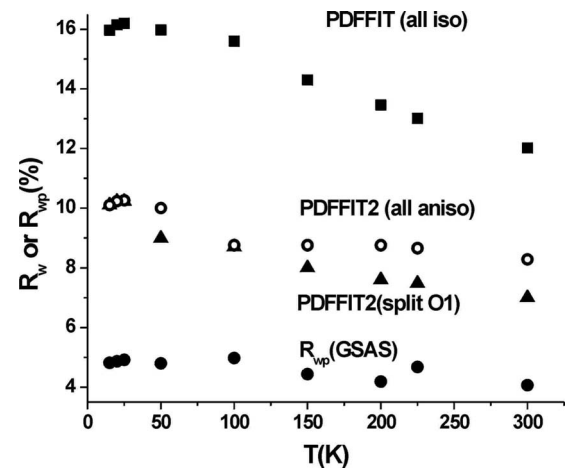


FIG. 9. The evolution of agreement indices R_w and R_{wp} for various models as a function of temperature. R_{wp} (GSAS) refers to the average structure fit of the diffraction data. PDFFIT2(split O1), PDFFIT2(all aniso), and PDFFIT(all iso) correspond to the three models tried for the local structure. Below 50 K the R_w values for the (split O1) and (all aniso) models are numerically the same.

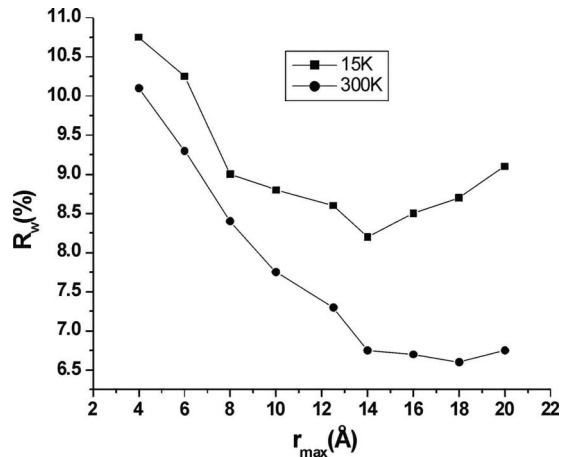


FIG. 10. Comparison of the agreement index R_w as a function of increasing r_{\max} with $r_{\min}=1$ Å for 30 and 15 K.

structure always become worse as the temperature is decreased for any model, and (5) the range of the disorder extends to 8–12 Å, well beyond nearest neighbors.

The present results are also consistent with the observed spin-glass ground state. In either the static or dynamic disorder model, there is a significant variation in the parameters which determine the nearest-neighbor superexchange interaction in $Y_2Mo_2O_7$ as shown by application of the simple spin-dimer model. While not quantitatively accurate, this model is generally reliable in assessing relative changes. The conclusion here is that the criterion of Saunders and Chalker²⁰ would appear to be satisfied quantitatively for $Y_2Mo_2O_7$.

To conclude, at least three further questions should be addressed. First, is there genuine static disorder in $Y_2Mo_2O_7$ or large-amplitude dynamic disorder? Both models provide an improved fit to the $G(r)$, with the split-site model being slightly better at high temperatures, albeit with the advantage of three additional free parameters. However, both models appear to give equivalent fits at low temperature. Thus, the NPDF analysis does not provide a clear basis for choice. This situation has elements similar to the well-studied case of the β -cristobalite form of SiO_2 which has been conveniently summarized.³⁵ β -cristobalite is a high-temperature quenchable form of silica and, coincidentally, crystallizes in $Fd3m$. In the fully ordered model, Si is in $8a$ and O is in $16c$. However, this requires an unusually short Si-O bond length and a linear Si-O-Si bond angle, which is considered somewhat unlikely. The displacements for the O site are large and anisotropic as well. Early alternative models involved disordering O over the 96 h sites with partial occupancy.³⁶ Refinements of this model led to a six-domain hypothesis with lower tetragonal symmetry and equal distribution of the domains to recover the $Fd3m$ symmetry. This interpretation has been questioned and molecular-dynamics simulations along with inelastic-neutron-scattering, Raman, and infrared data appear to rule out a static disorder model and support a dynamic disorder alternative.³⁵ Nonetheless, ND data for $Y_2Mo_2O_7$, specifically the very weak variation in the ADFs for O1 and Mo with temperature, suggest strongly the presence of a static component to the disorder. At the very least

TABLE VI. The variation in Mo-O1-Mo angle and $\langle \Delta e \rangle^2$ with \times for O1 in $Y_2Mo_2O_7$.

$x(O1)$	Mo-O1-Mo (deg)	$\langle \Delta e \rangle^2$ (meV) ²
0.3289	131.9	23579
0.3384	126.9	14212
0.3466	122.7	10546

the data are consistent with a very flat and probably anharmonic potential for the Y-O1 atom pairs. At this stage it is not yet possible to refine anharmonic ADFs within the existing PDFFIT codes. Thus, as the true situation for $Y_2Mo_2O_7$ remains elusive, new data from inelastic-neutron-scattering, Raman, and infrared spectroscopies would be very helpful in resolving this question.

Second, is there any evidence that geometric magnetic frustration plays a causal role in the structural disorder found in this material? At first glance the answer would appear to be no. Data at 300 K indicate that disorder exists in both the average and local structures even at this relatively high temperature. However, fits to the local structure, regardless of model, become significantly worse as the temperature is decreased. For the most realistic local structure models, seemingly discontinuous changes in R_w occur below the range of 100–50 K. Thus, it is impossible to rule out some rather subtle role for magnetic frustration but a detailed model for this is certainly not obvious.

Third and finally, the structures, both average and local, of very few pyrochlore oxides have been studied at the depth presented here. Is local disorder of the type found for $Y_2Mo_2O_7$ commonplace among pyrochlore oxides or is the rare-earth molybdate series unique? That most magnetic pyrochlore materials do not exhibit spin-glass behavior would seem to argue for the latter, but in fact the knowledge base here is very shallow and more work would appear to be warranted.

ACKNOWLEDGMENTS

J.E.G. thanks the Natural Sciences and Engineering Research Council of Canada for support through a Discovery Grant. A.D.L.-G. thanks the Spanish Ministry of Education for support. The authors thank I. P. Swinson for helpful discussions. This work benefited from the use of NPDF at the Lujan Center at Los Alamos Neutron Science Center, funded by DOE Office of Basic Energy Sciences. Los Alamos National Laboratory is operated by Los Alamos National Security LLC under DOE Contract No. DE-AC52-06NA25396. The upgrade of NPDF was funded by NSF through Grant No. DMR 00-76488. Work by the Billinge group was supported by the Office of Science, U.S. Department of Energy, under Contract No. DE-AC02-98CH10886.

- ¹J. S. Gardner, M. J. P. Gingras, and J. E. Greedan, *Rev. Mod. Phys.* (to be published).
- ²J. E. Greedan, M. Sato, Xu Yan, and F. S. Razavi, *Solid State Commun.* **59**, 895 (1986).
- ³P. H. Hubert, *Bull. Soc. Chim. Fr.* **11**, 2385 (1974).
- ⁴P. H. Hubert, *Bull. Soc. Chim. Fr.* **111**, 2463 (1975).
- ⁵M. J. P. Gingras, C. V. Stager, N. P. Raju, B. D. Gaulin, and J. E. Greedan, *Phys. Rev. Lett.* **78**, 947 (1997).
- ⁶J. S. Gardner, B. D. Gaulin, S.-H. Lee, C. Broholm, N. P. Raju, and J. E. Greedan, *Phys. Rev. Lett.* **83**, 211 (1999).
- ⁷N. P. Raju, E. Gmelin, and R. K. Kremer, *Phys. Rev. B* **46**, 5405 (1992).
- ⁸S. R. Dunsiger, R. F. Kiefl, K. H. Chow, B. D. Gaulin, M. J. P. Gingras, J. E. Greedan, A. Keren, K. Kojima, G. M. Luke, W. A. MacFarlane, N. P. Raju, J. E. Sonier, Y. J. Uemura, and W. D. Wu, *Phys. Rev. B* **54**, 9019 (1996).
- ⁹K. Miyoshi, Y. Nishimura, K. Honda, K. Fujiwara, and J. Takeuchi, *J. Phys. Soc. Jpn.* **69**, 3517 (2000).
- ¹⁰J. S. Gardner, G. Ehlers, R. H. Heffner, and F. Mezei, *J. Magn. Mater.* **226-230**, 460 (2001).
- ¹¹J. S. Gardner, G. Ehlers, S. T. Bramwell, and B. D. Gaulin, *J. Phys.: Condens. Matter* **16**, S643 (2004).
- ¹²F. C. Montenegro, S. M. Rezende, and M. D. Coutinho-Fihlo, *J. Appl. Phys.* **63**, 3755 (1988).
- ¹³H. Kato, K. Iwai, A. Ito, and Y. Nakagawa, *J. Magn. Mater.* **140-144**, 1801 (1995).
- ¹⁴K. Binder, W. Kinzel, H. Maletta, and D. Stauffer, *J. Magn. Mater.* **15-18**, 189 (1980).
- ¹⁵M. A. Subramanian and A. W. Sleight, in *Handbook on the Physics and Chemistry of Rare Earths*, edited by K. A. Gschneidner, Jr. and L. Eyring (Elsevier Science, New York, 1993), Vol. 16, p. 225.
- ¹⁶J. N. Reimers, J. E. Greedan, and M. Sato, *J. Solid State Chem.* **72**, 390 (1988).
- ¹⁷L. Minervini, R. Grimes, Y. Tabira, R. L. Withers, and K. Sickafus, *Philos. Mag. A* **82**, 123 (2002).
- ¹⁸W. Ratcliff, S. H. Lee, C. Broholm, S. W. Cheong, and Q. Huang, *Phys. Rev. B* **65**, 220406(R) (2002).
- ¹⁹R. D. Shannon, *Acta Crystallogr., Sect. A: Cryst. Phys., Diffr., Theor. Gen. Crystallogr.* **32**, 751 (1976).
- ²⁰T. E. Saunders and J. T. Chalker, *Phys. Rev. Lett.* **98**, 157201 (2007).
- ²¹C. H. Booth, J. S. Gardner, G. H. Kwei, R. H. Heffner, F. Bridges, and M. A. Subramanian, *Phys. Rev. B* **62**, R755 (2000).
- ²²A. Keren and J. S. Gardner, *Phys. Rev. Lett.* **87**, 177201 (2001).
- ²³E. Sagi, O. Ofer, A. Keren, and J. S. Gardner, *Phys. Rev. Lett.* **94**, 237202 (2005).
- ²⁴J. A. Hodges, P. Bonville, A. Forget, J. P. Sanchez, P. Vulliet, M. Rams, and K. Krolas, *Eur. Phys. J. B* **33**, 173 (2003).
- ²⁵S. J. L. Billinge, *Z. Kristallogr.* **219**, 117 (2004).
- ²⁶T. Proffen, T. Egami, S. J. L. Billinge, A. K. Cheetham, D. Loluca, and J. Parise, *Appl. Phys. A: Mater. Sci. Process.* **74**, S163 (2002).
- ²⁷C. L. Farrow, P. Juhas, J. W. Liu, D. Bryndin, E. S. Bozin, J. Bloch, Th. Proffen, and S. J. L. Billinge, *J. Phys.: Condens. Matter* **19**, 335219 (2007).
- ²⁸M. Sato, Xu Yan, and J. E. Greedan, *Z. Anorg. Allg. Chem.* **540**, 177 (1986).
- ²⁹B. J. Kennedy, B. A. Hunter, and C. J. Howard, *J. Solid State Chem.* **130**, 58 (1997).
- ³⁰T. Birchall and A. W. Sleight, *J. Solid State Chem.* **13**, 118 (1975).
- ³¹A. L. Hector and S. B. Wiggin, *J. Solid State Chem.* **177**, 139 (2004).
- ³²T. Egami and S. J. L. Billinge, *Underneath the Bragg Peaks: Structural Analysis of Complex Materials* (Plenum, Oxford, 2003).
- ³³M. H. Whangbo, H. J. Koo, and D. J. Dai, *J. Solid State Chem.* **176**, 417 (2003).
- ³⁴J. Ren, W. Liang, and M. H. Whangbo, *Crystal and Electronic Structure Analysis Using CAESAR, 2005* (<http://www.primeC.com>).
- ³⁵I. P. Swainson and M. T. Dove, *J. Phys.: Condens. Matter* **7**, 1771 (1995).
- ³⁶D. M. Hatch and M. Ghose, *Phys. Chem. Miner.* **17**, 554 (1991); A. F. Wright and A. J. Leadbetter, *Philos. Mag.* **31**, 1391 (1975).

Phase separation and nanostructuring in the thermoelectric material $\text{PbTe}_{1-x}\text{S}_x$ studied using the atomic pair distribution function technique

He Lin

Department of Physics and Astronomy, Michigan State University, East Lansing, Michigan 48824, USA

E. S. Božin and S. J. L. Billinge*

*Department of Applied Physics and Applied Mathematics, Columbia University, New York, New York 10027, USA**and Department of Condensed Matter Physics and Materials Science, Brookhaven National Laboratory, Upton, New York 11973, USA*

J. Androulakis, C. D. Malliakas, C. H. Lin, and M. G. Kanatzidis

Department of Chemistry, Northwestern University, Evanston, Illinois 60208, USA

(Received 15 December 2006; revised manuscript received 15 June 2009; published 10 July 2009)

The average and local structures of the $(\text{PbTe})_{1-x}(\text{PbS})_x$ system of thermoelectric materials has been studied using the Rietveld and atomic pair distribution function methods. Samples with $0.25 \leq x$ are macroscopically phase separated. Phase separation was suppressed in a quenched $x=0.5$ sample which, nonetheless, exhibited a partial spinodal decomposition. The promising thermoelectric material with $x=0.16$ showed intermediate behavior. Combining TEM and bulk scattering data suggests that the sample is a mixture of PbTe-rich material and a partially spinodally decomposed phase similar to the quenched 50% sample. This confirms that, in the bulk, this sample is inhomogeneous on a nanometer length scale, which may account for its enhanced thermoelectric figure of merit.

DOI: [10.1103/PhysRevB.80.045204](https://doi.org/10.1103/PhysRevB.80.045204)

PACS number(s): 61.05.C-, 72.15.Jf, 73.50.Lw, 73.63.Bd

I. INTRODUCTION

Thermoelectric materials are the subject of intense research because of their potential for efficient power generation and cooling. The efficiency of the thermoelectric material is measured by the figure of merit, ZT , defined by several interdependent physical parameters.¹ It is difficult to get a high- ZT material due to the competing requirements for optimizing the interdependent parameters. Many efforts have focused on reducing the thermal conductivity κ , without sacrificing electrical conductivity, σ . κ is the sum of the lattice thermal conductivity κ_{lat} and the electronic thermal conductivity κ_{ele} . Theoretical and experimental studies suggest that materials that show nanophase separation appear to be promising in achieving high performance.²⁻⁷

The material with composition $\text{PbTe}_{0.84}\text{S}_{0.16}$ shows a very low room-temperature lattice thermal conductivity of 0.4 W/m K and a ZT value significantly higher than that of PbTe (Fig. 1) and PbS.⁸ The thermal conductivity is only 28% of that observed in the PbTe system, which is remarkable given that the two are isostructural and $\text{PbTe}_{0.84}\text{S}_{0.16}$ has only 16 at. % of S substituted on the Te site. Understanding the origin of this remarkable reduction in κ for a small doping change should give important insights into the thermoelectric problem.

Early studies on the $(\text{PbTe})_{1-x}(\text{PbS})_x$ system showed that phase separation occurs at low temperature over almost the whole composition range.^{9,10} A miscibility gap exists over a wide range of composition and extends almost up to the melting point of the alloy. There are no apparent intermediate compounds and the phase separation occurs into phases which are almost pure PbTe and PbS over the whole alloy range. Theoretical work¹⁰ supports such a picture and the calculated phase diagram using a thermodynamic model

agreed with the previous experimental data. Earlier work¹¹⁻¹³ suggested a smaller range for the miscibility gap in the phase diagram and this discrepancy was attributed to the subtle difference in chemical processing⁹ and quenching rate. It is apparent from the high-resolution transmission electron microscopy (HRTEM) images that phase separation occurs on several different length scales in $\text{PbTe}_{0.84}\text{S}_{0.16}$ and that naturally forming striped nanostructures due to spinodal decomposition are evident in portions of the sample. Here we investigate this question further using bulk diffraction probes of the average and local atomic structure. We address two questions. First, can we confirm that the nanoscale phase separation is a bulk property and can we characterize the average chemical composition and structure of the spinodal domain? We have also extended the study to other composi-

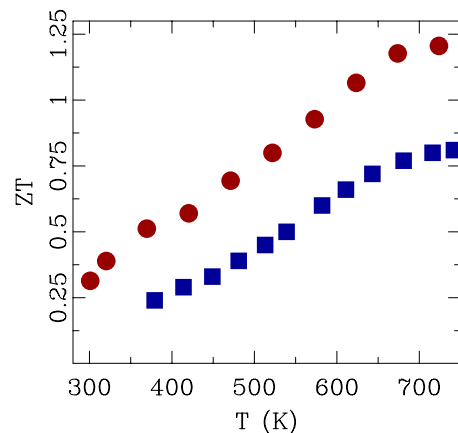


FIG. 1. (Color online) Comparison of temperature dependencies of measured thermoelectric figure of merit, ZT , for PbTe (solid blue squares) and $\text{PbTe}_{0.84}\text{S}_{0.16}$ (solid red circles).

tions in the phase diagram to see how these effects evolve with changing composition.

The atomic pair distribution function (PDF) analysis of x-ray diffraction data is a useful method for studying nanophase-separated samples.^{14,15} In the PDF approach, both Bragg and diffuse scattering are analyzed and it yields the bulk average local atomic structure. Recently it was successfully used to study the thermoelectric material $\text{Ag}_x\text{Pb}_m\text{SbTe}_{m+2}$, where silver- and antimony-rich nanoscale clusters were found to be coherently embedded in the PbTe matrix as a bulk property.¹⁶

We have used both PDF and Rietveld methods to study the $(\text{PbTe})_{1-x}(\text{PbS})_x$ system. We find phase separation occurring over the whole composition range. Refinements from both Rietveld and PDF methods show that the $x=0.25, 0.5$, and 0.75 samples are macroscopically separated into phases that are almost pure PbS and PbTe. This does not happen in the important 16% PbS doped sample. However, taking all the evidence together we suggest that the 16% sample is a nanoscale mixture of a PbTe-rich phase with a partially spinodally decomposed phase of nominally 50% composition. Such a phase was stabilized and observed in a quenched $x=0.5$ sample in this study. This offers the opportunity in the future for engineering nanostructures and microstructures with favorable thermoelectric properties by controlling the thermal history in these materials.

II. EXPERIMENTAL METHODS

Powder samples in the $(\text{PbTe})_{1-x}(\text{PbS})_x$ series were made with different compositions $x=0, 0.16, 0.25, 0.50, 0.75$, and 1. The samples were produced by mixing appropriate ratios of high-purity elemental starting materials with a small molar percentage of PbI_2 , an n -type dopant. The initial loads were sealed in fused silica tubes under vacuum and fired at 1273 K for 6 h followed by rapid cooling to 773 K and held there over a period of 72 h. One $x=0.5$ sample was also quenched rapidly to room temperature. More details of sample synthesis can be found elsewhere.⁸ The thermoelectric figure of merit of the 16% sample was measured as a function of temperature. Thermopower and electrical-conductivity properties were measured simultaneously under helium atmosphere using a ZEM-3 Seebeck coefficient/electrical resistivity measurement system (ULVAC-RIKO, Japan). The thermal conductivity was determined using the flash diffusivity method on a LFA 457/2/G Microflash NETZSCH and ZT was obtained by combining these values. As evident in Fig. 1, the 16% sample has a significantly enhanced ZT compared to that of PbTe being $\sim 50\%$ higher despite the small level of doping.

Finely powdered samples were packed in flat plates with a thickness of 1.0 mm sealed between kapton tape windows. X-ray powder-diffraction data were collected using the rapid acquisition pair distribution function method,¹⁷ which benefits from very-high-energy x rays and a two-dimensional (2D) detector. The experiments were conducted using synchrotron x rays with an energy of 86.727 keV ($\lambda = 0.14296 \text{ \AA}$) at the 6-ID-D beam line at the Advanced Photon Source (APS) at Argonne National Laboratory. The data

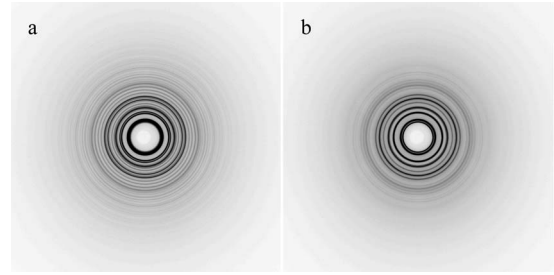


FIG. 2. Raw x-ray powder-diffraction data from the 2D detector for the $x=0.50$ $(\text{PbTe})_{1-x}(\text{PbS})_x$ sample. Data from the (a) unquenched and (b) quenched samples are shown for comparison. The one-dimensional integrated powder-diffraction patterns obtained from these data are shown in Fig. 3(a) and on an expanded scale in Fig. 5. The white circle in the center of each 2D diffractogram represents a shadow from the beam stop.

were collected using a circular image plate camera (Mar345) 345 mm in diameter. The camera was mounted orthogonally to the beam path with a sample-to-detector distance of 210.41 mm.

In order to avoid saturation of the detector, each room-temperature measurement was carried out in multiple exposures. Each exposure lasted 5 s and each sample was exposed five times to improve the counting statistics. Two representative 2D diffraction images for unquenched and quenched $\text{PbTe}_{0.5}\text{S}_{0.5}$ samples are shown in Figs. 2(a) and 2(b), respectively. The excellent powder statistics giving uniform rings are evident. All the samples yielded similar quality images. The 2D data sets from each sample were combined and integrated using the program FIT2D (Ref. 18) before further processing.

Data from an empty container were also collected to subtract the container scattering. The corrected total scattering structure function, $S(Q)$, was obtained using standard corrections^{15,17} with the program PDFGETX2.¹⁹ Finally, the PDF was obtained by Fourier transformation of $S(Q)$ according to $G(r) = \frac{2}{\pi} \int_0^{Q_{\max}} Q[S(Q) - 1] \sin(Qr) dQ$, where Q is the magnitude of the scattering vector. A $Q_{\max} = 26.0 \text{ \AA}^{-1}$ was used. Fig. 3, shows $F(Q) = Q[S(Q) - 1]$ and $G(r)$ for all the samples. The good statistics and overall quality of the data are apparent in Fig. 3(a). The low spurious ripples at low r in the $G(r)$ functions are also testament to the quality of the data.²⁰ Note that $G(r)$ has been plotted all the way to $r=0$ in these plots, which is a stringent test of this.

III. MODELING

Both PDF (using the PDFGUI program^{21,22}) and Rietveld²³ (using the TOPAS academic program²⁴) refinements were carried out on the system. The models used in the fits are described below.

One of the main purposes of this study is to determine the phase composition of the phase-separated sample as a function of composition. When phase separation is long ranged, Rietveld refinement can be used to estimate the relative abundance of the phase components.^{25–30}

Phase segregation can also be determined from the

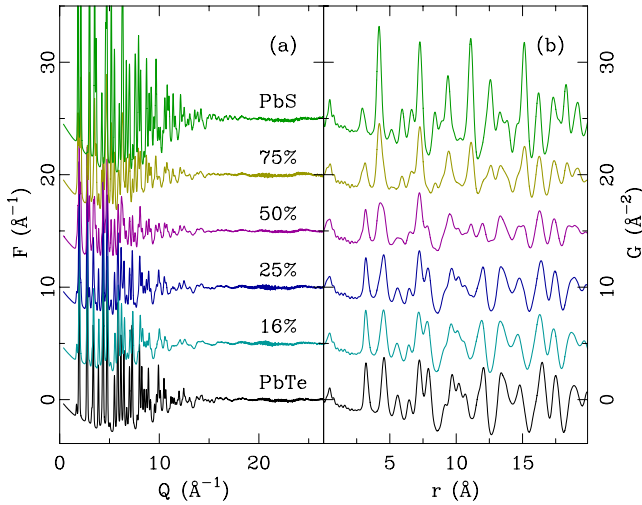


FIG. 3. (Color online) Experimental (a) $F(Q)$ and (b) $G(r)$ for all unquenched samples. In the Fourier transform, Q_{\max} was set to 26.0 \AA^{-1} . The data are offset for clarity. The compositions of the $(\text{PbTe})_{1-x}(\text{PbS})_x$ samples are indicated in panel (a). From top to bottom: $x=1.00$ (green), $x=0.75$ (yellow), $x=0.50$ (magenta), $x=0.25$ (blue), $x=0.16$ (cyan), and $x=0.00$ (black).

PDF.^{16,31} In PDFGUI, each phase in a multiphase fit has its own scale factor in the refinement. The scale factor reflects both the relative phase fraction of the phases and the average scattering power of each phase, which depends on the chemical compositions of each phase. The conversion from scale factor to atomic fraction is done using the equations derived in Ref. 16.

For each sample, we explored different models. The structure is of the rock-salt-type space group $Fm-3m$. First we start from a homogeneous (solid-solution) model where the anions are assumed to be randomly distributed on the sites of the anionic sublattice. In this model, S atoms substitute the Te site randomly without breaking the symmetry. The only structural parameters refined are the lattice constants and the atomic displacement factors.

The next model we tried was a simple two-phase model in which a phase separation into a PbTe-rich and PbS-rich phase was assumed. The phase diagram for this system shows a miscibility gap at low temperature over a wide composition range.^{9,10} The two phases that coexist have compositions rather close to the pure end members and there is limited solid solubility. Based on this, and in an effort to keep the modeling as simple as possible, we modeled the phase separation as a mixture of pure PbTe and PbS, however, allowing the lattice constants to vary as would be expected if the phases were not the pure end members. The parameters that were allowed to vary in these fits were lattice constants, atomic displacement factors, and phase-specific scale factors which reflect the relative abundance of each phase. More complicated phase-separated models were also tried where the composition of the phases was varied as described below.

IV. RESULTS

First we carried out PDF and Rietveld refinements on the undoped end members of the series, PbS and PbTe. The level

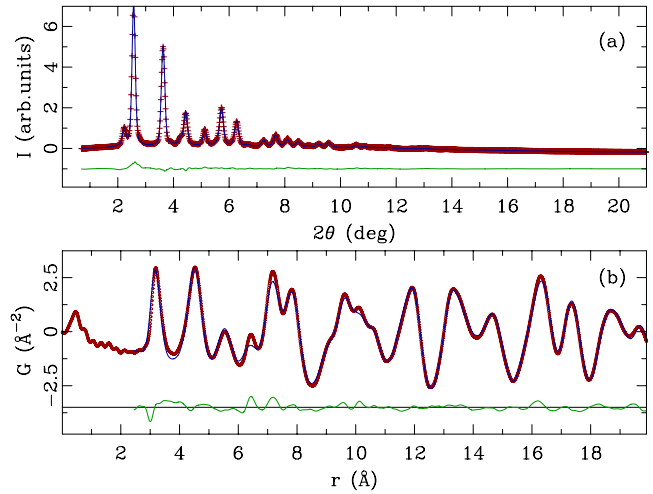


FIG. 4. (Color online) Representative refinements of the PbTe data using (a) Rietveld and (b) PDF approaches. Symbols represent data and solid lines are the model fits. The difference curves are offset for clarity.

of agreement of Rietveld and PDFGUI refinements can be seen in Fig. 4 and Table I. These fits give a baseline for the quality of the fits for materials without disorder. The fits are acceptable and the refined parameters are in good agreement with literature values for PbTe, though outside the estimated errors. The PDF and Rietveld refinements are also only in semiquantitative agreement with each other. The parameter estimates were made on the same data sets but using different methods and systematic errors are not accounted for in the error estimates. Even in these nominally pure materials, the refined atomic displacement factors are rather large,³² which is in agreement with previous work,³³ though this behavior is not really understood.

Now we consider the chemically mixed systems. The existence of phase separation can be qualitatively verified in our samples by looking at the diffraction patterns in Fig. 5. The top curve is PbS and the bottom curve is PbTe and the vertical dashed lines are at the positions of the main Bragg peaks of these phases. For compositions $x=0.25, 0.50,$ and $0.75,$ a coexistence of PbS and PbTe diffraction patterns is

TABLE I. Refinement results from PbS and PbTe compared with literature values.

	Literature ^a	Rietveld	PDF
R_w		0.040	0.085
a_{PbTe} (Å)	6.4541(9)	6.4776(3)	6.465(3)
U_{Pb} (Å ²)	0.0204(3)	0.033(5)	0.032(4)
U_{Te} (Å ²)	0.0141(2)	0.009(9)	0.014(4)
R_w		0.044	0.082
a_{PbS} (Å)	5.9315(7)	5.9460(3)	5.940(3)
U_{Pb} (Å ²)	0.0163(3)	0.023(3)	0.0185(5)
U_{S} (Å ²)	0.0156(5)	0.018(4)	0.030(5)

^aReference 32.

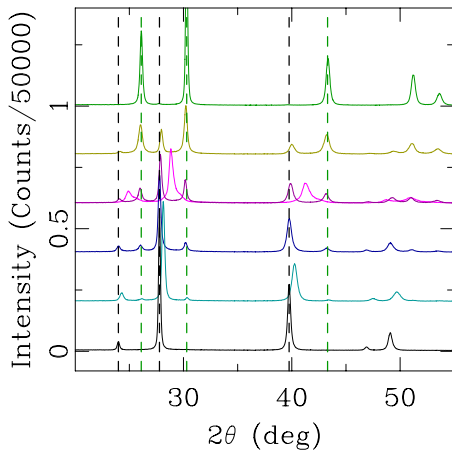


FIG. 5. (Color online) Powder diffraction patterns from laboratory x-ray source of all the $(\text{PbTe})_{1-x}(\text{PbS})_x$ samples studied. From top to bottom: $x=1.00$ (green), $x=0.75$ (yellow), $x=0.50$ (light and dark magenta), $x=0.25$ (blue), $x=0.16$ (cyan), and $x=0.00$ (black). The data corresponding to the quenched $x=0.50$ sample (light magenta) is superimposed on top of those of the unquenched sample (dark magenta) without being offset. The other data are offset for clarity. Vertical dashed lines indicate positions of several characteristic Bragg peaks in the end-member data to allow for easier comparison.

clearly evident as the diffraction patterns are qualitatively recognizable as a linear superposition of the end-member patterns. Diffraction peaks appear at precisely the positions of the end-member Bragg peaks. The same is true for the annealed $x=0.5$ sample (dark magenta). On the other hand, the *quenched* $x=0.5$ sample has a diffraction pattern that resembles the PbTe pattern but shifted significantly to higher scattering angles. This is what would be expected for a solid solution, rather than phase separated, sample suggesting that quenching the sample suppresses phase separation.

The situation is slightly less clear for the $x=0.16$ sample which resembles closely the pure PbTe diffraction pattern. The effects of phase separation would be difficult to see in this case because of the small PbS component. However, careful inspection of the curve indicates that the main peaks are shifted to higher scattering angles, in analogy with the quenched $x=0.5$ sample. Thus, this sample appears to be a solid solution on the macroscale probed in a diffraction pattern.

We would like to consider evidence in the *local* structure for phase separation. The PDFs of the samples with diffraction patterns presented in Fig. 5 are shown in Fig. 6 arranged in the same way and with the same colors as in Fig. 5. The samples that are macroscopically phase separated [$x=0.25$, 0.5 (annealed), and 0.75] also show phase separation in the local structure as expected, the curves having the qualitative appearance of a mixture of the end-member PDFs.

The behavior of peaks in the PDF in solid solutions has been discussed previously.^{34,35} The nearest-neighbor peaks retain the character of the end members, albeit with a small strain relaxation. However, peaks at higher r , from the second neighbor onwards, appear broadened because of inhomogeneous strain in the sample but are peaked at the average

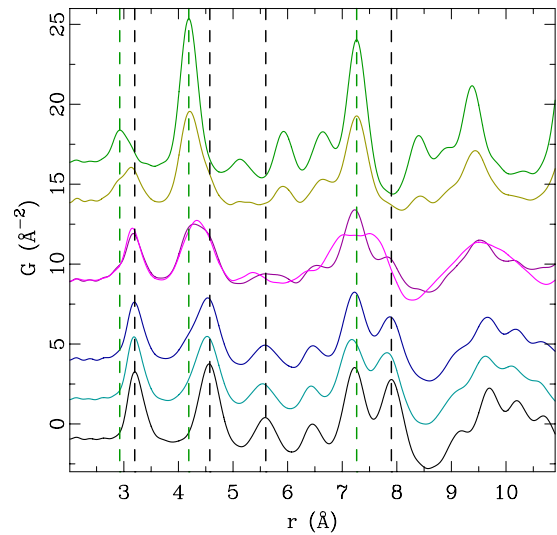


FIG. 6. (Color online) Experimental PDFs for various $(\text{PbTe})_{1-x}(\text{PbS})_x$ samples on expanded scale. The PDFs, from top to bottom, correspond to $x=1.00$ (green), $x=0.75$ (yellow), $x=0.50$ (magenta), quenched $x=0.50$ (bright magenta), $x=0.25$ (blue), $x=0.16$ (cyan), and $x=0.00$ (black). The data corresponding to the quenched $x=0.50$ sample (light magenta) is superimposed on top of those of the unquenched sample (dark magenta) without being offset. The other data are offset for clarity. Vertical dashed lines indicate positions of a few selected characteristic PDF features of the end members for easier comparison.

position expected from the average structure for the solid solution.

To investigate the phase-separation phenomenon more quantitatively, we carried out two-phase refinements for the macroscopically phase-separated samples on both the diffraction data and the PDF. Fig. 7 shows representative fits from the $x=0.50$ sample. The refined parameters are reproduced in Table II. In the table the n and n_0 refer to the refined fraction of the sample in the PbTe phase and the expected

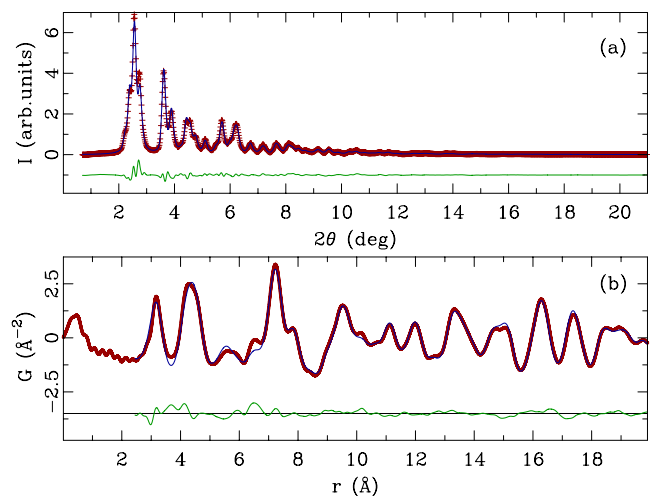


FIG. 7. (Color online) Representative refinements of the $x=0.50$ sample data using (a) Rietveld and (b) PDF approach. Symbols represent data and solid lines are the model fits. The difference curves are offset for clarity.

TABLE II. Refinement results for two-phase fitting to $(\text{PbTe})_{1-x}(\text{PbS})_x$. Rietveld and PDF refer to Rietveld and PDF fits, respectively, where the composition of the two phases was fixed to PbTe and PbS. n and n_0 refer to the refined and expected (based on stoichiometry) phase fractions for the PbS-rich phase

	$x=0.25$		$x=0.5$		$x=0.75$	
	Rietveld	PDF	Rietveld	PDF	Rietveld	PDF
R_w	0.034	0.118	0.047	0.151	0.034	0.100
n/n_0	0.19/0.25	0.20/0.25	0.50/0.50	0.49/0.50	0.71/0.75	0.85/0.75
C	6.4669(3)	6.446(3)	6.4418(3)	6.414(3)	6.4301(3)	6.415(3)
U_{Pb} (\AA^2)	0.037(6)	0.040(4)	0.041(6)	0.040(5)	0.040(7)	0.040(5)
U_{Te} (\AA^2)	0.015(6)	0.016(4)	0.0052(6)	0.019(4)	0.033(7)	0.02(4)
a_{PbS} (\AA)	5.9768(3)	5.97(1)	5.9841(3)	5.953(4)	5.9738(3)	5.956(3)
U_{Pb} (\AA^2)	0.044(8)	0.027(5)	0.034(7)	0.025(4)	0.024(6)	0.023(3)
U_{S} (\AA^2)	0.073(8)	0.03(5)	-0.0027(7)	0.031(4)	0.0065(6)	0.029(3)

fraction based on the stoichiometry and assuming phase separation into pure PbTe and PbS, respectively. The two-phase fits of pure PbS and PbTe are good (“Rietveld” and “PDF” columns in the table), as indicated by the low residuals. The refined atomic displacement parameters (ADPs) are also in good agreement with the end-member refinements, though the refinements of this parameter are somewhat unstable on the PbS phase when it is the minority phase as it does not contribute strongly to the scattering in that case. The result, that relatively large ADPs are needed on the Pb site in PbTe and on the S site in PbS, is reproduced in the two-phase fits of the phase-separated samples.

The lattice parameters of the PbTe in the phase-separated samples are consistently shorter than those for the pure material and are consistently longer than those for the PbS phase component. This effect is real and reflects the fact that the phases in the phase-separated samples are actually solid solutions with finite amounts of S in the PbTe and Te in the PbS phase, respectively. We can make a rough estimation of the composition of the phase-separated phases by considering their refined lattice parameters and assuming that Vegard’s law^{36,37} is obeyed in the vicinity of the end-member compositions. In this case, the formula for the lattice parameter in the solid solution of composition $\text{PbTe}_{(1-y)}\text{S}_y$ is $a_y = y(a_{\text{PbTe}}) + (1-y)a_{\text{PbS}}$. Thus, we can estimate the compositions of the solid solutions in the phase-separated phases from the Rietveld refined lattice parameters. We find that in the $x=0.25$ phases, $y=0.94$ for the PbS-rich phase and $y=0.05$ for the PbTe-rich phase. This verifies that the composition of the phases in the two-phase mixture is indeed very near PbTe and PbS. The values determined from the $x=0.5$ and 0.75 samples give nearly the same result with the estimated composition of the PbTe-rich phase as $y=0.895$ and that of PbS $y=0.03$. These numbers are consistent with estimates from TEM evidence of a solid-solubility limit of 3%.⁸

The powder-diffraction data are relatively insensitive to small changes in chemical composition of the particular phases³¹ which explains the good fit to the data with the end-member PbS and PbTe compositions, albeit with modified lattice constants. However, for completeness, we have carried out two-phase refinements to the phase-separated

data using the nominal compositions for the two phases that were determined above. The fits were comparable in quality to those where the compositions of the two phases were limited to pure PbTe and PbS, but the refined parameters were not significantly different.

The agreement of the refined with the nominal composition, n/n_0 , is best in the $x=0.50$ sample in both the PDF and Rietveld data. It is less good, though acceptable for the 0.25 and 0.75. Due to the relative insensitivity to chemical composition, we expect rather large error bars on these quantities and do not ascribe significance to the differences. The agreement between the Rietveld and PDF results shows that the phase separation is macroscopic since we get the same result in both the local and average structures.

We now consider the samples that appear from the qualitative analysis of the data to be solid solutions, $x=0.5$ (quenched) and $x=0.16$. In Fig. 8 we consider the $x=0.5$ sample. In this figure, model PDFs of the undoped end members are reproduced as curves (a) and (b) for reference and the positions of their main peaks are marked. The quenched data are shown as gray symbols in the curves (c) and the annealed data in the curves (d). The magenta lines are simulated PDFs. In (c) the simulated PDF is from a homogeneous solid-solution virtual-crystal model with the right nominal composition and lattice parameter. It agrees well with the data. In (d) the simulated PDF is a linear combination of the PbTe and PbS PDFs. In each case, the ADPs of the simulations have been adjusted to give the best agreement with the data. The simulations fit rather well indicating that this picture of phase separation (annealed) vs solid solution (quenched) is a good explanation for the bulk behavior for the $x=0.5$ sample. Quantitative refinement results for the quenched 50% sample are reproduced in Table III. The fits are good with low R_w ’s and reasonable refined parameters. The refined lattice parameter is between the end-member values as expected and the ADP on the Pb site is further enlarged from the end-member values as expected due to disorder in the alloy.

In the quenched $x=0.5$ sample, the solid solution is not thermodynamically stable but can be metastably trapped by the rapid quench. The quench is mostly successful at sup-

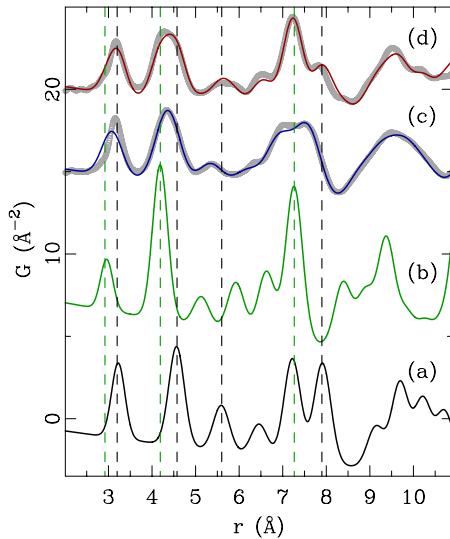


FIG. 8. (Color online) PDFs of converged models for (a) $x=0.00$ and (b) $x=1.00$ $(\text{PbTe})_{1-x}(\text{PbS})_x$ samples. Comparison of the data for (c) quenched and (d) unquenched $x=0.50$ samples (open symbols) with the solid solution (c) and mixture (d) models (solid lines), respectively. See text for details. Vertical dashed lines indicate positions of selected PDF features characteristic for the end-member compositions, for easier comparison.

pressing phase separation as discussed above. However, it is not completely successful, as TEM images of the quenched $x=0.5$ sample indicate that the sample has compositional modulations, as shown in Fig. 9(b). The striped nature of these modulations suggests that there is an arrested spinodal decomposition taking place in the 50% doped sample that would result in sinusoidal compositional modulations about the nominal 50% composition. The amplitude of the modulations is not known, but the good agreement of the homogeneous solid-solution model to the PDF and Rietveld data suggest that the variation in composition around the nominal 50% is not too large. Thus we understand the quenched 50% sample to be close to an ideal metastable solid solution, but with an arrested spinodal decomposition that gives rise to nanoscale compositional modulations.

Of greater interest from both a technological and scientific viewpoint is the behavior of the $x=0.16$ sample that shows especially good thermoelectricity, as is evident in Fig. 1. As discussed above, the diffraction data in Fig. 5 suggests that the sample is macroscopically a solid solution even though it lies outside the range of solid solubility suggested by the phase diagrams^{9,10} and inferred from the composition of the

TABLE III. Refinement results from both PDF and Rietveld for the quenched 50% sample from a homogeneous solid-solution model.

	Rietveld	PDF
R_w	0.047	0.163
a (Å)	6.2571(4)	6.217(3)
U_{Pb} (Å ²)	0.055(5)	0.062(3)
$U_{\text{Te,S}}$ (Å ²)	0.017(5)	0.054(3)

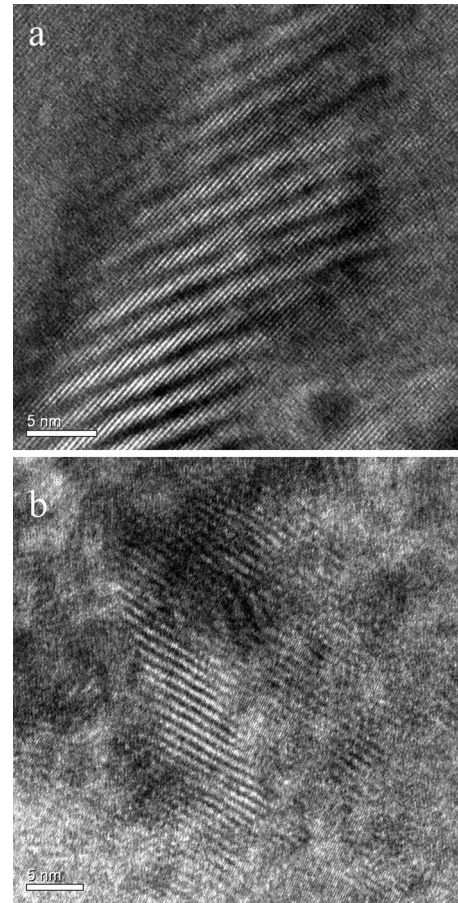


FIG. 9. HRTEM images of (a) $x=0.16$ and (b) quenched $x=0.50$ $(\text{PbTe})_{1-x}(\text{PbS})_x$ samples.

PbTe -rich phase of the phase-separated compositions in our own refinements (25%, 50%, and 75% sample).

We tried fitting two-phase and homogeneous models to both the diffraction and PDF data. The results are shown in Table IV with representative fits shown in Fig. 10. As expected from the qualitative analysis of the data discussed above, the single-phase solid-solution model (model A) provides acceptable fits to the data. The refined lattice parameters are shorter than pure PbTe . According to the Vegard's law analysis, the refined lattice parameter gives a nominal composition for this sample of 0.14 (Rietveld)/0.12 (PDF), in reasonable agreement with the actual composition. Enlarged ADPs are found on the Pb sublattice with smaller ADPs on the Te lattice, as was the case for the PbTe end member. As expected for a solid solution, the ADPs are enlarged with respect to PbTe .

We also tried the simple model of phase separation into pure PbTe and PbS end members. The results appear in Table IV as model B. The Rietveld fit is significantly worse as measured by R_w . In the case of the PDF fit, the R_w is comparable but the refinement reduced the phase fraction of the second phase and adjusted the lattice parameter of the majority phase, moving the refinement back toward the solid-solution result. This refinement also returned unphysical negative atomic displacement factors on the minority phase. The solid-solution model is clearly preferred over full phase

TABLE IV. Rietveld and PDF refinement results from three different models for the $\text{PbTe}_{0.84}\text{S}_{0.16}$ sample: model A is solid-solution model, model B is a simple two-phase mixture of PbTe and PbS and model C is a mixture of pure PbTe phase plus a solid solution of composition $\text{PbTe}_{0.5}\text{-PbS}_{0.5}$. n and n_0 refer to the refined and expected (based on stoichiometry) phase fractions for the PbS-rich phase.

	Model A		Model B		Model C		
	Rietveld	PDF	Rietveld	PDF	Rietveld	PDF	
	R_w	0.046	0.121	0.052	0.121	0.031	0.114
	n/n_0			0.14/0.16	0.037/0.16	0.31/0.32	0.24/0.32
PbTe	a (Å)	6.4264(5)	6.403(3)	6.4233(4)	6.403(24)	6.4203(4)	6.416(3)
	U_{Pb} (Å ²)	0.047(5)	0.047(3)	0.035(6)	0.035(3)	0.028(6)	0.036(4)
	U_{Te} (Å ²)	0.0061(6)	0.019(3)	0.023(6)	0.029(4)	0.016(6)	0.025(5)
Second Phase	a (Å)			5.900(1)	5.942(4)	6.1673(3)	6.255(3)
	U_{Pb} (Å ²)			0.018(8)	0.021(6)	0.253(8)	0.064(6)
	$U_{\text{S,Te}}$ (Å ²)			0.013(8)	-0.0024(6)	0.253(8)	0.070(6)

separation from the bulk diffraction measurements.

The TEM images from the 16% sample [Ref. 8 and Fig. 9(a)] suggest that it is two phased, with one phase being homogeneous and the other resembling the quenched $x=0.5$ sample with arrested spinodal decomposition appearing as stripey fringes. A model that simulated this situation was successfully compared to the PDF data, as shown from model C in Table IV. This model assumed that the nominally 16% sample is phase separated into regions that are pure PbTe and regions that resemble the quenched 50% sample, i.e., they are nominally $x=0.5$ solid solutions but also exhibiting spinodal decomposition as suggested by the TEM images. Thus, model C is a phase separation into pure PbTe and a solid solution of composition $\text{PbTe}_{0.5}\text{S}_{0.5}$. This model gives the lowest R_w 's for fits to the 16% compound in both the Rietveld and PDF refinements. The phase fractions were free to vary but refined to values that are close to those expected. The lattice constants refined to reasonable values. The majority-phase lattice constant was close to that of the PbTe-

rich phase in the two-phase refinements in Table II. In the case of the minority phase, the lattice constant lay between pure PbTe and PbS consistent with a nominal 50% composition. The ADPs are slightly large in the PbTe-rich phase but physically reasonable. In the minority phase, the ADPs are unphysical in the Rietveld refinement suggesting that this parameter is not well determined in the refinement. However, in the PDF refinement they are more reasonable but very large. This is perfectly consistent with the fact that this minority phase itself actually has a compositional variation due to the spinodal effects. This is one of many possible such models but it shows that the data are at least consistent with a phase separation into Te-rich and Te-poor regions and some level of spinodal decomposition in the sulfur-rich regions. The data are *not* consistent with a full phase separation into almost pure PbTe and PbS expected from the phase diagram as shown by the samples with higher S content.

V. SUMMARY

This work confirmed the phase-separation tendency of the PbTe/PbS system. It also showed that phase separation can be effectively, but not completely, suppressed by quenching at 50% composition, where a partial spinodal decomposition appears to be taking place, at least in a portion of the sample.

However, the main result is an improvement in our understanding of the state of the thermoelectrically promising 16% sample. Measurements of the bulk average structure, and the bulk local structure, indicate that it is not phase separated into PbTe-rich and PbS-poor end members like the other similarly processed samples in the series. Taken together with the TEM data in Ref. 8 and additional data shown here, the best explanation is that this sample prefers a phase separation into a PbTe-rich phase and a PbTe-poor phase. Such a nanoscale phase separation is thought to be important in producing the enhanced ZT that is observed in this material evident in Fig. 1. Interestingly, in this case the effect appeared not after a quench but after an anneal suggesting that

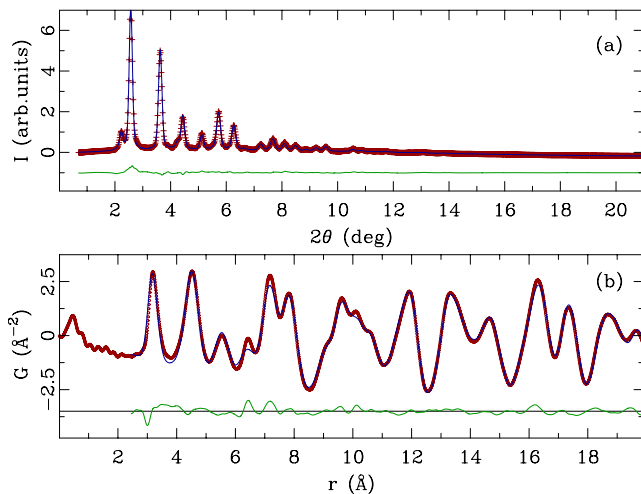


FIG. 10. (Color online) Representative refinements of the $x=0.16$ sample data using (a) Rietveld and (b) PDF approach. Symbols represent data and solid lines are the model fits. The difference curves are offset for clarity.

it is the thermodynamically preferred state, though this needs to be investigated further. It is possible that the thermodynamically stable state is fully phase separated as in the higher doped samples. In that case the phase separation may be suppressed even at low quench rates because of a low thermodynamic driving force that is not great enough to overcome kinetic constraints. Also of interest is to explore further the nature of the PbTe-rich component, which, as preliminary TEM investigations⁸ indicate, also contains nanostructured regions with nanoscale nuclei of a second phase present.

The other important observation from this work is that quenching is very important in determining the phase separation and resulting nanoscale microstructure. This suggests that in this system, it may be possible to engineer κ and, therefore, ZT in the bulk material by appropriate heat treatments. This is a promising route for future research.

ACKNOWLEDGMENTS

We acknowledge Pavol Juhas, Ahmad Masadeh, Hyun-Jeong Kim, and Asel Sartbaeva for their valuable assistance with the data collection. Work in the Billinge group was supported in part by National Science Foundation (NSF) under Grants No. DMR-0304391 and No. DMR-0703940 and in the Kanatzidis group by the Office of Naval Research. Data were collected at the 6IDD beamline in the Midwest Universities Collaborative Access Team (MUCAT) sector at the APS. Use of the Advanced Photon Source was supported by the U.S. Department of Energy, Office of Science, Office of Basic Energy Sciences, under Contract No. DE-AC02-06CH11357. The MUCAT sector at the APS is supported by the U.S. DOE, Office of Science, Office of Basic Energy Sciences, through the Ames Laboratory under Contract No. W-7405-Eng-82.

*sb2896@columbia.edu; <http://slapper.apam.columbia.edu:8083/Plone>

¹ $ZT = \sigma S^2 T / \kappa$ where T is the operating temperature of the device, S is the thermopower, and σ and κ are the electrical and thermal conductivities of the material, respectively.

²T. C. Harman, P. J. Taylor, M. P. Walsh, and B. E. LaForge, *Science* **297**, 2229 (2002).

³T. C. Harman, M. P. Walsh, B. E. LaForge, and G. W. Turner, *J. Electron. Mater.* **34**, L19 (2005).

⁴K. F. Hsu, S. Loo, F. Guo, W. Chen, J. S. Dyck, C. Uher, T. Hogan, E. K. Polychroniadis, and M. G. Kanatzidis, *Science* **303**, 818 (2004).

⁵W. Kim, J. Zide, A. Gossard, D. Klenov, S. Stemmer, A. Shakouri, and A. Majumdar, *Phys. Rev. Lett.* **96**, 045901 (2006).

⁶J. R. Sootsman, H. Kong, C. Uher, J. J. D'Angelo, C.-I. Wu, T. P. Hogan, T. Caillat, and M. G. Kanatzidis, *Angew. Chem., Int. Ed.* **47**, 8618 (2008).

⁷C. J. Vineis, T. C. Harman, S. D. Calawa, M. P. Walsh, R. E. Reeder, R. Singh, and A. Shakouri, *Phys. Rev. B* **77**, 235202 (2008).

⁸J. Androulakis, C. H. Lin, H. J. Kong, C. Uher, C. I. Wu, T. Hogan, B. A. Cook, T. Caillat, K. M. Paraskevopoulos, and M. Kanatzidis, *J. Am. Chem. Soc.* **129**, 9780 (2007).

⁹M. S. Darrow, W. B. White, and R. Roy, *Trans. Metall. Soc. AIME* **236**, 654 (1966).

¹⁰V. Leute and N. Volkmer, *Z. Phys. Chem.* **144**, 145 (1985).

¹¹S. Yamamoto, *Sci. Rep. Tohoku Univ., Ser. 1*, **40**, 11 (1956).

¹²N. D. Sindeyeva and A. A. Godovikov, *Dokl. Akad. Nauk SSSR* **127**, 431 (1959).

¹³A. Y. Malevskiy, *Dokl. Akad. Nauk SSSR* **152**, 191 (1963).

¹⁴S. J. L. Billinge and M. G. Kanatzidis, *Chem. Commun. (Cambridge)* **2004**, 749 (2004).

¹⁵T. Egami and S. J. L. Billinge, *Underneath the Bragg Peaks: Structural Analysis of Complex Materials* (Pergamon, Elsevier, Oxford, England, 2003).

¹⁶H. Lin, E. S. Božin, S. J. L. Billinge, E. Quarez, and M. G. Kanatzidis, *Phys. Rev. B* **72**, 174113 (2005).

¹⁷P. J. Chupas, X. Qiu, J. C. Hanson, P. L. Lee, C. P. Grey, and S. J. L. Billinge, *J. Appl. Crystallogr.* **36**, 1342 (2003).

¹⁸A. P. Hammersley, ESRF Internal Report No. ESRF98HA01T 1998 (unpublished).

¹⁹X. Qiu, J. W. Thompson, and S. J. L. Billinge, *J. Appl. Crystallogr.* **37**, 678 (2004).

²⁰P. F. Peterson, E. S. Božin, T. Proffen, and S. J. L. Billinge, *J. Appl. Crystallogr.* **36**, 53 (2003).

²¹C. L. Farrow, P. Juhás, J. W. Liu, D. Bryndin, E. S. Božin, J. Bloch, T. Proffen, and S. J. L. Billinge, *J. Phys.: Condens. Matter* **19**, 335219 (2007).

²²T. Proffen and S. J. L. Billinge, *J. Appl. Crystallogr.* **32**, 572 (1999).

²³H. M. Rietveld, *J. Appl. Crystallogr.* **2**, 65 (1969).

²⁴A. A. Coelho, TOPAS general profile and structure analysis software for powder diffraction data, <http://members.optusnet.com.au/~alancoelho/>

²⁵P. E. Werner, S. Salome, G. Malmros, and J. O. Thomas, *J. Appl. Crystallogr.* **12**, 107 (1979).

²⁶R. J. Hill and C. J. Howard, *J. Appl. Crystallogr.* **20**, 467 (1987).

²⁷D. L. Bish and S. A. Howard, *J. Appl. Crystallogr.* **21**, 86 (1988).

²⁸B. H. O'Connor and M. D. Raven, *Powder Diffr.* **3**, 2 (1988).

²⁹R. J. Hill, *Powder Diffr.* **6**, 74 (1991).

³⁰R. A. Young, *The Rietveld Method*, International Union of Crystallography Monographs on Crystallography (Oxford University Press, Oxford, 1993) Vol. 5.

³¹T. Proffen, V. Petkov, S. J. L. Billinge, and T. Vogt, *Z. Kristallogr.* **217**, 47 (2002).

³²I.-K. Jeong, T. Proffen, F. Mohiuddin-Jacobs, and S. J. L. Billinge, *J. Phys. Chem. A* **103**, 921 (1999).

³³Y. Noda, K. Masumoto, S. Ohba, Y. Saito, K. Toriumi, Y. Iwata, and I. Shibuya, *Acta Crystallogr. C: Cryst. Struct. Commun.* **43**, 1443 (1987).

³⁴V. Petkov, I. K. Jeong, J. S. Chung, M. F. Thorpe, S. Kycia, and S. J. L. Billinge, *Phys. Rev. Lett.* **83**, 4089 (1999).

³⁵I.-K. Jeong, F. Mohiuddin-Jacobs, V. Petkov, S. J. L. Billinge, and S. Kycia, *Phys. Rev. B* **63**, 205202 (2001).

³⁶L. Vegard, *Z. Phys.* **5**, 17 (1921).

³⁷M. F. Thorpe and E. J. Garboczi, *Phys. Rev. B* **42**, 8405 (1990).

Superconductivity, magnetism, and stoichiometry of single crystals of $\text{Fe}_{1+y}(\text{Te}_{1-x}\text{S}_x)_z$

Rongwei Hu,^{1,*} Emil S. Bozin,^{1,2} J. B. Warren,³ and C. Petrovic¹

¹*Condensed Matter Physics and Materials Science Department, Brookhaven National Laboratory, Upton, New York 11973, USA*

²*Department of Applied Physics and Applied Mathematics, Columbia University, New York, New York 10027, USA*

³*Instrumentation Division, Brookhaven National Laboratory, Upton, New York 11973, USA*

(Received 21 August 2009; revised manuscript received 15 November 2009; published 11 December 2009)

We report synthesis of high-quality $\text{Fe}_{1+y}(\text{Te}_{1-x}\text{S}_x)_z$ single crystals and a comprehensive study of structural, magnetic, and transport properties. We demonstrate the very small upper critical field anisotropy of $\text{Fe}_{1+y}(\text{Te}_{1-x}\text{S}_x)_z$, $\gamma_H = H_{c2}^{\parallel c} / H_{c2}^{\perp c}$. The value of γ_H reaches 1.05 at $T = 0.65T_C$ for $\text{Fe}_{1.12}\text{Te}_{0.83}\text{S}_{0.11}$ while still maintaining large values of upper critical field. There is high sensitivity to material stoichiometry which includes vacancies on the Te(S) site. Our results reveal competition and coexistence of magnetic order and percolative superconductivity for $x \geq 0.03$ while zero resistivity is achieved for $x \geq 0.1$.

DOI: [10.1103/PhysRevB.80.214514](https://doi.org/10.1103/PhysRevB.80.214514)

PACS number(s): 74.62.Bf, 74.10.+v, 74.20.Mn, 74.70.Dd

I. INTRODUCTION

The discovery of superconductivity in quaternary iron-based layered superconductor $\text{LaFeAsO}_{1-x}\text{F}_x$ with $T_C = 26$ K stimulated an intense search for superconductors with higher T_C in this materials class.¹ Shortly after, the critical temperatures were raised up to 55 K in materials of the ZrCuSiAs structure type,² and superconductivity had been discovered in $\text{Ba}_{1-x}\text{K}_x\text{Fe}_2\text{As}$ and LiFeAs .^{3,4} Superconductivity in the PbO -type FeSe opened another materials space in the search for iron-based superconductors.⁵ This was followed by the discovery of superconductivity in polycrystalline $\text{FeTe}_{1-x}\text{Se}_x$ and $\text{FeTe}_{1-x}\text{S}_x$.^{6,7} Binary iron chalcogenide superconductors share the most prominent characteristics of iron arsenide compounds: a square-planar lattice of Fe with tetrahedral coordination similar to LaFeAsO or LiFeAs , and Fermi-surface topology.⁸ They crystallize in a simple crystal structure which is amenable to modeling by band-structure calculations.^{5,7-12}

Iron pnictide superconductors exhibit Cooper pairing in proximity to a magnetic ground state, similar to all exotic superconductors: cuprate oxides, heavy fermion intermetallics and organics. The magnetism in these materials is strongly influenced by subtle crystal structure changes.^{1,13,14} FeSe hosts high T_C 's of up to 37 K under pressure and an isotropic superconducting (SC) state. Its crystal structure changes from high-temperature tetragonal $P4/nmm$ to low-temperature orthorhombic $Cmmm$ at 70 K.^{15,16} In $\text{Fe}_{1.08}\text{Te}$ transition to monoclinic space group $P21/m$ with commensurate antiferromagnetic (AF) order occurs between 65 and 75 K, whereas $\text{Fe}_{1.14}\text{Te}$ exhibits weaker first-order transition to orthorhombic space group $Pmmm$ and incommensurate AF order from 55 to 63 K.⁹

It was noted, however, that it would be desirable to have isotropic superconductors with high T_C and ability to carry high critical currents for power applications.¹⁷ In this work we report the synthesis of $\text{Fe}_{1+y}(\text{Te}_{1-x}\text{S}_x)_z$ superconducting single crystals for $x = (0-0.15)$, $y = (0-0.14)$, and $z = (0.94-1)$. We demonstrate small values of $\gamma_H = H_{c2}^{\parallel c} / H_{c2}^{\perp c}$ while still maintaining large values of the upper critical field and critical currents. We examine the evolution of superconductivity and magnetism with S doping and provide experimen-

tal evidence for structural parameters at the magnetic/superconducting boundary.

II. EXPERIMENTAL METHOD

Single crystals of $\text{Fe}_{1+y}(\text{Te}_{1-x}\text{S}_x)_z$ were grown from Te-S self-flux using a high-temperature flux method.^{18,19} Elemental Fe, Te, and S were sealed in quartz tubes under partial argon atmosphere. The sealed ampoule was heated to a soaking temperature of 430–450 °C for 24 h, followed by a rapid heating to the growth temperature at 850–900 °C, and then slowly cooled to 800–840 °C. The excess flux was removed from crystals by decanting. Platelike crystals up to $11 \times 10 \times 2$ mm³ can be grown. Elemental analysis and microstructure was performed using energy-dispersive x-ray spectroscopy in a JEOL JSM-6500 scanning electron microscope. The average stoichiometry was determined by examination of multiple points on the crystals. Total scattering data from finely pulverized crystals were obtained at 80 K at 11-ID-B beamline of the Advanced Photon Source synchrotron using 58.26 keV x-rays ($\lambda = 0.2128$ Å) selected by a Si 311 monochromator. Two-dimensional (2D) patterns for samples in 1mm diameter Kapton tubes were collected using a MAR345 2D detector, placed perpendicular to the primary beam path, 188.592 mm away from the sample. An Oxford Cryosystem cryostream was used for temperature regulation. Details on experimental procedures, data processing, the atomic pair-distribution function (PDF) method, and structural modeling can be found elsewhere.²⁰⁻²² Flux-free rectangular shaped crystals with the largest surface orthogonal to \hat{c} axis of tetragonal structure were selected for four-probe resistivity measurements with current flowing parallel to the \hat{a} axis of tetragonal structure. Thin Pt wires were attached to electrical contacts made with Epotek H20E silver epoxy. Sample dimensions were measured with an optical microscope Nikon SMZ-800 with 10 μm resolution. Magnetization and resistivity measurements were carried out in a Quantum Design MPMS-5 (magnetic property measurement system) and a PPMS-9 (physical property measurement system) for temperatures from 1.8 to 350 K.

III. RESULTS

Typical synchrotron data (symbols), with fully converged $P4/nmm$ structural model superimposed (solid lines), and

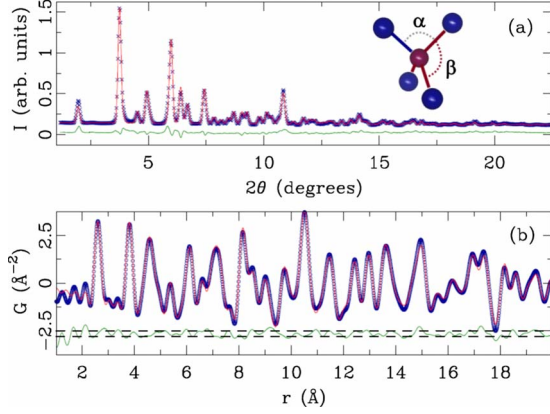


FIG. 1. (Color online) (a) $\text{Fe}_{1+y}(\text{Te}_{1-x}\text{S}_x)_z$ synchrotron Rietveld and (b) PDF refinement results taken at $T=80$ K. Inset shows two Te-Fe-Te bond angles illustrated on the FeTe_4 tetrahedron.

corresponding difference curves (offset for clarity) are presented in Fig. 1, featuring $\text{Fe}_{1.12}\text{Te}_{0.83}\text{S}_{0.11}$. Panel (a) features a Rietveld refinement with a corresponding PDF refinement shown in (b). The PDF is peaked at positions corresponding to the observed interatomic distances. Excellent fits with low agreement factors are obtained for all studied $\text{Fe}_{1+y}(\text{Te}_{1-x}\text{S}_x)_z$ samples. Initial PDF fits assumed ideal stoichiometry, and revealed slightly enhanced atomic displacement parameters, suggesting either Te(S) deficiency, or excess Fe content, or both. To explore this, in final $P4/nmm$ models where S shared site with Te, Fe/Te/S ratios were kept fixed at values obtained from scanning electron microscopy (SEM), while stoichiometry was refined. Additionally, Fe was allowed to occupy two sites, Fe(1) (0,0,0) and Fe(2)(0.5,0,z). Total Fe content in the refinements was constrained to respect the SEM ratio while the relative occupancy of the two Fe sites was allowed to vary. Results are reported in Table I. Undoped FeTe crystallizes with excess Fe variably occupying interstitial Fe(2) site and full occupancies of Fe(1) and Te sites. With contraction of the unit cell due to sulfur doping we observe both excess Fe and vacancies on Te(S) site. With reduction in the unit cell due to an increase in sulfur stoichiometry (x) excess Fe(y) decreases so that for highest $x=0.15$ we observe the smallest deviation from ideal stoichiometry. Both Fe(1) and Fe(2) sites are still occupied for high x values (Table I).

TABLE I. Structural parameters from PDF refinement at $T=80$ K, magnetic and superconducting properties of $\text{Fe}_{1+y}(\text{Te}_{1-x}\text{S}_x)_z$. Transition temperatures T_1 and T_2 are from $\partial(\chi T/\partial T)$ data. Temperatures of T_C onset and zero resistance are from resistivity data.

$\text{Fe}_{1+y}(\text{Te}_{1-x}\text{S}_x)_z$	V (\AA^3)	c/a	Occ(Fe1)	Occ(Fe2)	α	Θ (K)	μ (μ_B)	T_2 (K)	T_1 (K)	T_C^{onset} (K)	T_C (K)
$\text{Fe}_{1.14(2)}\text{Te}_{1.01(1)}$	91.150(4)	1.642(1)	1.04(2)	0.10(2)	117.46(1)	-191(4)	3.92(2)	59(1)	70(1)		
$\text{Fe}_{1.09(2)}\text{Te}_{1.00(1)}$	91.017(4)	1.640(1)	1.02(2)	0.07(2)			3.73(1)	59(1)	66(1)		
$\text{Fe}_{1.12(3)}\text{Te}_{0.97(1)}\text{S}_{0.03(2)}$	90.558(4)	1.637(1)	1.00(3)	0.12(3)	117.57(1)	-175(1)	3.83(1)	41(1)	44(1)	6.5(1)	
$\text{Fe}_{1.13(3)}\text{Te}_{0.85(1)}\text{S}_{0.10(2)}$	90.032(5)	1.632(1)	1.00(4)	0.13(4)	117.33(1)	-186(4)	3.56(2)	21(1)	23(1)	8.5(1)	2.0(1)
$\text{Fe}_{1.12(3)}\text{Te}_{0.83(1)}\text{S}_{0.11(2)}$	90.095(4)	1.632(1)	1.06(4)	0.07(4)	117.30(1)	-162(3)	3.38(2)		20(1)	8.6(1)	3.5(1)
$\text{Fe}_{1.06(3)}\text{Te}_{0.88(1)}\text{S}_{0.14(2)}$	90.097(4)	1.632(1)	0.95(4)	0.11(4)	117.32(1)	-156(6)	3.36(3)		23.5(1)	8.7(1)	7.0(1)
$\text{Fe}_{0.98(4)}\text{Te}_{0.90(1)}\text{S}_{0.15(2)}$	89.900(5)	1.632(1)	0.82(4)	0.16(4)	117.21(1)	-167(7)	3.34(6)		19(1)	8.8(5)	

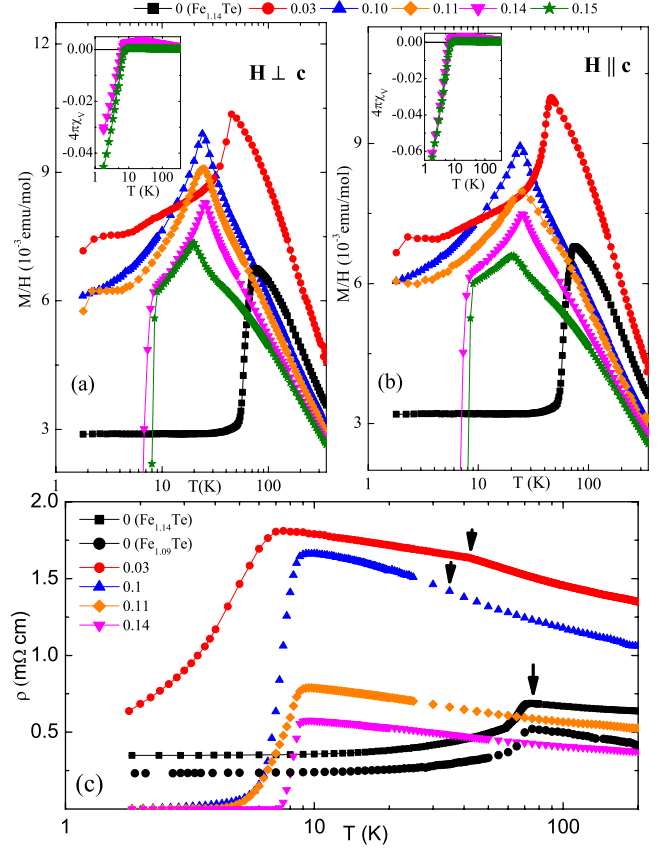


FIG. 2. (Color online) (a) Magnetic susceptibility as a function of temperature for $H \perp c$ and (b) $H \parallel c$. Insets show the Meissner volume fraction of $x=0.14$ and $x=0.15$. (c) In-plane resistivity in zero field for $\text{Fe}_{1+y}(\text{Te}_{1-x}\text{S}_x)_z$. Arrows show positions of peaks in $\partial\rho/\partial T$ that correspond to anomalies in magnetization associated with SDW transitions [(a) and (b)].

Figures 2(a) and 2(b) shows the anisotropic temperature dependence of magnetic susceptibility for $\text{Fe}_{1+y}(\text{Te}_{1-x}\text{S}_x)_z$ for a magnetic field of 1000 Oe applied in the ab plane and along c axis. The peak at 70 K for $\text{Fe}_{1.14(2)}\text{Te}$ corresponds to an AF transition presumably coupled with structural and first order.²³ The transition spans about 20 K for both field orientations. The magnetic susceptibility is isotropic above 70 K and $\chi^{\parallel c}/\chi^{\perp c}$ increases from 1 to 1.1 below the transition. The transition temperature is suppressed with sulfur doping down

to 20 K by $x=0.15$. A diamagnetic signal is observed for $x \geq 0.14$ [Figs. 2(a) and 2(b) insets], in apparent coexistence with a magnetic state. The volume fraction $4\pi\chi_v$ reaches $-0.06 \sim -0.09$ at 0 K by linear extrapolation. Magnetic susceptibility is Curie-Weiss type above 200 K. The effective moments estimated are between the low-spin ($2.94\mu_B$, $S=1$) and high-spin ($4.9\mu_B$, $S=2$) values of an $\text{Fe}^{2+}(3d^6)$ in a tetragonal crystal field (Table I). The high-temperature effective moments decrease with the S doping and with the reduction in excess Fe. Negative Curie-Weiss temperatures attest to the antiferromagnetic coupling between moments (Table I).

The in-plane electrical resistivity in zero field is shown in Fig. 2(c). Residual resistivity values at low temperatures for pure Fe_{1+y}Te and crystals with the highest sulfur concentration x are comparable to single crystals grown by Bridgeman method,²⁴ but smaller by a factor of 3–4 than in polycrystalline materials⁷ due to the absence of grain boundaries and secondary phases. The grain boundaries are not transparent as in MgB_2 where intrinsic low values of ρ_0 in high-quality polycrystals are often lower than in crystals.²⁵ Therefore grain boundaries cannot be neglected when measuring resistivity on polycrystals of iron chalcogenide superconductors. The resistivity of Fe_{1+y}Te above the magnetic transition is poorly metallic, in agreement with measurements on polycrystals and an optical conductivity study which did not find a semiconducting gap.^{7,26} This is an important distinction from the metallic resistivity above T_c in iron-based superconductors of ThCr_2Si_2 , ZrCuSiAs structure, or even FeSe .^{5,27–30} The magnitude of the resistivity, ρ , becomes larger with small doping for $x=0.03$ but decreases with the increase in S concentration. Two distinct contributions to ρ are observed in the low-temperature phase at the temperature of the magnetization anomaly: semiconducting and metallic or semimetallic [arrows Fig. 2(c)]. For $x=0.03$ a small decrease in temperature slope in ρ is observed whereas the resistivity of $x=0.1$ sample shows an increase, indicating that a part of the Fermi surface is destroyed. This can be understood within the framework of density-functional theory (DFT) calculations that predict a metal with “nesting” cylindrical Fermi surfaces which are separated by a wave vector corresponding to spin-density wave (SDW) low-temperature ground state.⁸ With further increase in x , the resistivity anomaly at the magnetic transition is smaller and broader when compared to $x=0$. Though all samples for $x \geq 0.03$ show a clear onset of superconductivity; zero resistivity is observed for $x \geq 0.10$ [Fig. 2(c)].

The temperature dependence of resistivity with a magnetic field applied perpendicular and parallel to c axis for the superconducting sample $x=0.14$ is shown in Fig. 3(a). The residual resistivity of the normal state $\rho_0=0.58$ m Ω cm of our crystals is smaller than in polycrystalline $\text{FeTe}_{1-x}\text{S}_x$.⁷ It is comparable to residual resistivity observed in $\text{NdFeAsO}_{0.7}\text{F}_{0.3}$ (~ 0.2 m Ω cm) (Ref. 31) or $(\text{Ba}_{0.55}\text{K}_{0.45})\text{Fe}_2\text{As}_2$ (~ 0.4 m Ω cm) (Ref. 28) single crystals. Transition width of our crystals ($\Delta T_c = T_{\text{onset}} - T_{\text{zero } \rho} = 1.8$ K) is smaller than that in Ref. 7 ($\Delta T_c = 2$ K). The small shift of the transition temperature with magnetic field indicates a large zero-temperature upper critical field. The upper critical field H_{c2} is estimated as the field corresponding

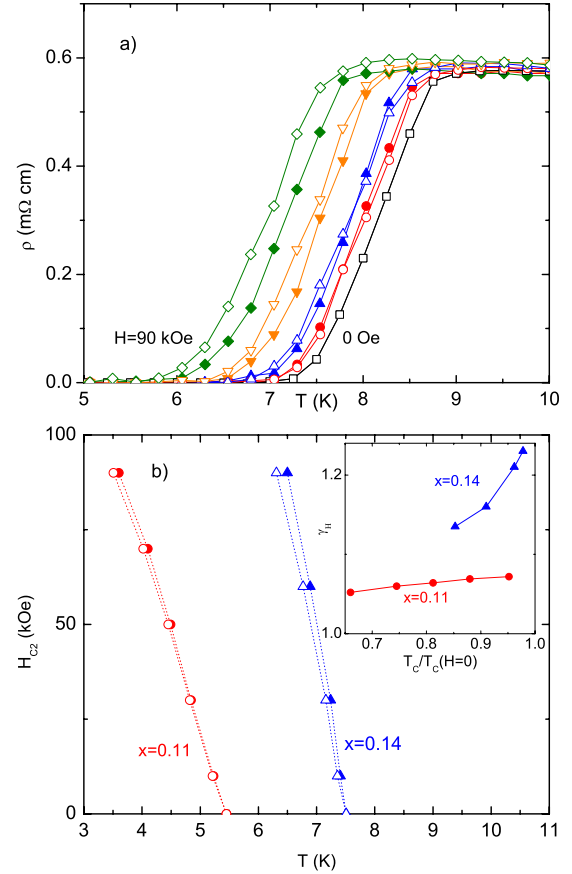


FIG. 3. (Color online) (a) In-plane resistivity for $x=0.14$ of two field orientations, $H \perp c$ (solid symbols) and $H \parallel c$ (open symbols). The applied magnetic field increases gradually from 0 Oe (the rightmost curve), 10 kOe, 30 kOe, 60 kOe to 90 kOe (the leftmost curve). (b) The upper critical fields for $x=0.11$ and $x=0.14$, $H \perp c$ (solid symbols) and $H \parallel c$ (open symbols). Dotted lines are guides to the eye. Inset shows the anisotropy in the upper critical field $\gamma_H = H_{c2}^{\parallel c} / H_{c2}^{\perp c}$.

to the 90% of resistivity drop. An estimate for $H_{c2}(T=0)$ is given by weak-coupling formula for conventional superconductors in the Werthamer-Helfand-Hohenberg model (Table II): $H_{c2o}(0) \sim -0.7H_c'(T_c)T_c$.³² The superconducting coherence length $\xi(0)$ [$\xi^2 = \Phi_0 / 2\pi H_{c2}$] is around 3 nm. The anisotropy $\gamma_H = H_{c2}^{\parallel c} / H_{c2}^{\perp c}$ decreases with a temperature decrease approaching a value close to unity. By $T_c / T_c(0) \approx 0.65$ [Fig. 3(b) inset], $\gamma_H = 1.05$, for $x=0.11$. These values indicate that $\text{Fe}_{1+y}(\text{Te}_{1-x}\text{S}_x)_z$ is a high-field isotropic superconductor with γ_H smaller than that in Ref. 32 [$\gamma_H > 1.5$ at $0.5T_c(H=0)$] or in Ref. 33 [$\gamma_H \sim 1.3$ at $0.5T_c(H=0)$].

To determine the anisotropy of the critical current, we analyze the magnetic measurements using an extended Bean model.^{34,35} Considering a rectangular prism-shaped crystal of dimension $c < a < b$, when a magnetic field is applied along the crystalline c axis, the in-plane critical current density J_c^{ab} is given by

$$J_c^{ab} = \frac{20}{a} \frac{\Delta M_c}{(1 - a/3b)}$$

in which ΔM_c is the width of the magnetic hysteresis loop for increasing and decreasing field. When the magnetic field

TABLE II. Upper critical field at zero temperature and corresponding coherence length for two superconducting samples.

	$H_{c2}^{\perp c}(T_c)$	$H_{c2}^{\perp c}(0)$ (T)	$H_{c2}^{\parallel c}(T_c)$	$H_{c2}^{\parallel c}(0)$ (T)	$\xi^{\perp c}(0)$ (nm)	$\xi^{\parallel c}(0)$ (nm)
$\text{Fe}_{1.12(3)}\text{Te}_{0.83(1)}\text{S}_{0.11(2)}$	-4.9	19	-4.6	18	4.3	4.3
$\text{Fe}_{1.06(3)}\text{Te}_{0.88(1)}\text{S}_{0.14(2)}$	-10.7	56	-8.4	44	2.4	2.7

is applied along the b axis and parallel to the ab plane, both of the in-plane j_c^{ab} and the crossplane j_c^c are involved in the Bean model. For a crystal in our measurements with $a = 1.245$ mm, $b = 1.285$ mm, and $c = 0.732$ mm,

$$j_c^c = \frac{c}{3a} \frac{j_c^{ab}}{(1 - 20\Delta M_b/cj_c^{ab})}.$$

Because of the large volume fraction of the normal and magnetic state, a magnetic background is superposed on the hysteresis loop. Moreover, as shown in Fig. 4(b) inset, the hysteretic magnetization loop for the sample $x=0.14$ sustains above the superconducting transition temperature at 7.5 K and vanishes above the antiferromagnetic transition at 25 K. It implies a magnetic structure of $\text{FeTe}_{1-x}\text{S}_x$ where a ferro-

magnetic component coexists with an antiferromagnetic moment. Density-functional calculation on FeTe by Subedi *et al.*⁸ does indicate that besides the SDW, FeTe is close to a ferromagnetic instability, similar to LaFeAsO. In order to estimate the ΔM only due to flux pinning, we take the hysteresis loop immediately above superconducting transition at 8 K as the ferromagnetic background and subtract it from other loops below 7.5 K. The identical hysteresis loops at 8 and 9 K in the normal state justifies our rationale to use them as a temperature-independent background. Figure 4(a) shows hysteresis loops for $H \parallel c$ and $H \perp c$ at 1.8 K after background removal. The magnetically deduced in-plane and interplane critical current density are displayed in Fig. 4(b). The ratio of j_c^{ab}/j_c^c is roughly about 4. The critical current densities for both directions are 10^5 – 10^6 A/cm², comparable to MgB_2 , $\text{Ba}(\text{Fe}_{1-x}\text{Co}_x)_2\text{As}_2$ in the same temperature range.³⁶

Figure 5(a) gives the temperature-dependent specific heat C_p and M/H for $\text{Fe}_{1.14(2)}\text{Te}$ and $\text{Fe}_{1.09(2)}\text{Te}$ below 90 K. Both crystals show two lambda anomalies at magnetic/structural transition around $T_1 = 70$ K and $T_2 = 59$ K for $\text{Fe}_{1.14(2)}\text{Te}$ and around $T_1 = 66$ K and $T_2 = 59$ K for $\text{Fe}_{1.09(2)}\text{Te}$. Above and below the transition region there is no difference in $C_p(T)$. A magnetic field of 90 kOe shifts both transition in both samples for $\Delta T = 1$ K. The entropy $\Delta S = 2.2$ J/mol associated with the transition is independent of the iron stoichiometry y [Fig. 5(b)]. This is smaller than estimated change in entropy in $\text{Fe}_{1.07}\text{Te}$ of $\Delta S \sim 3.2$ J/mole(K).²³ The discrepancy is probably due to conventional PPMS heat-capacity setup which introduces sizeable error in the vicinity of the first-order phase transition.³⁷ Nevertheless, we can still compare the change in ΔS for Fe_{1+y}Te crystals with different y caused by AF contribution which dominates ΔS in the transition region.²³ Assuming that total entropy is lost on the spin-state transition $\Delta S = R \ln[(2S_H + 1)/(2S_L + 1)]$ and using $\mu_{eff}^H = \sqrt{4S(S+1)}$, high-temperature effective moment is $\mu_{eff}^H(\text{Fe}_{1.14(2)}\text{Te}) = 3.92\mu_B$, $\mu_{eff}^H(\text{Fe}_{1.09(2)}\text{Te}) = 3.73\mu_B$, we obtain the moment value below magnetic transitions in the ordered state $\mu_{eff}^H(\text{Fe}_{1.14(2)}\text{Te}) = 1.3\mu_B$ and $\mu_{eff}^H(\text{Fe}_{1.09(2)}\text{Te}) = 1.2\mu_B$. Larger relative entropy change for higher y is related to the occupancy of iron in the interstitial sites which is expected to be strongly magnetic.¹¹ Interestingly, these numbers are very close to values for a spin moment of $1.3\mu_B$ associated with SDW transition calculated by DFT calculations.⁸

The low-temperature C_p data for $\text{Fe}_{1.14}\text{Te}$ can be fitted to the $C(T) = \gamma T + \beta T^3$ power law below 15 K with $\gamma = 32$ mJ/mole K² and $\beta = 0.49$ mJ/mole K⁴ from which a $\theta_D = 228$ K can be obtained [Fig. 5(c)]. Specific heat shows a broad feature around T_c [Fig. 5(c) inset] for superconducting samples similar to other iron pnictides.²⁸ Due to high upper

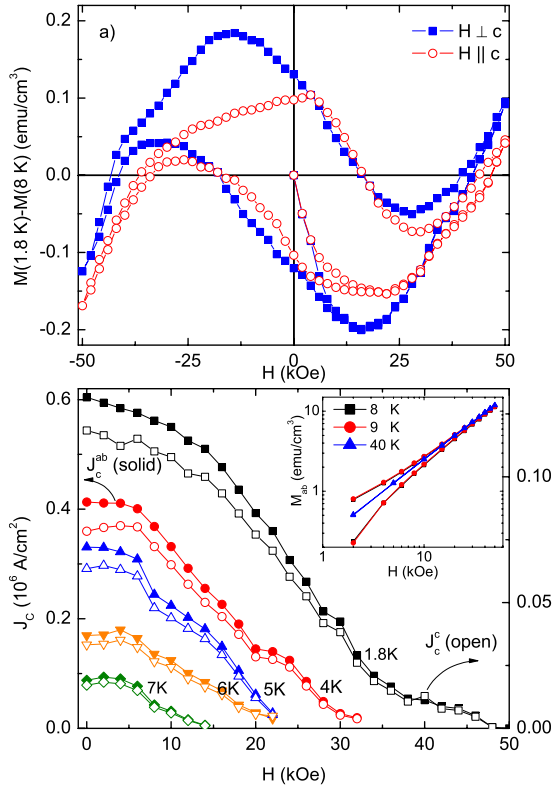


FIG. 4. (Color online) (a) Magnetization hysteresis loops of $x = 0.14$ for 1.8 K after ferromagnetic background subtraction for $H \parallel c$ (open symbols) and $H \perp c$ (solid symbols). (b) In-plane (to left axis) and interplane (to right axis) critical currents for $x=0.14$. Inset shows the magnetization at 8, 9, and 40 K. Only the positive field magnetization is shown on log-log scale and the virgin curves of the loops at 8 and 9 K are omitted for clarity.

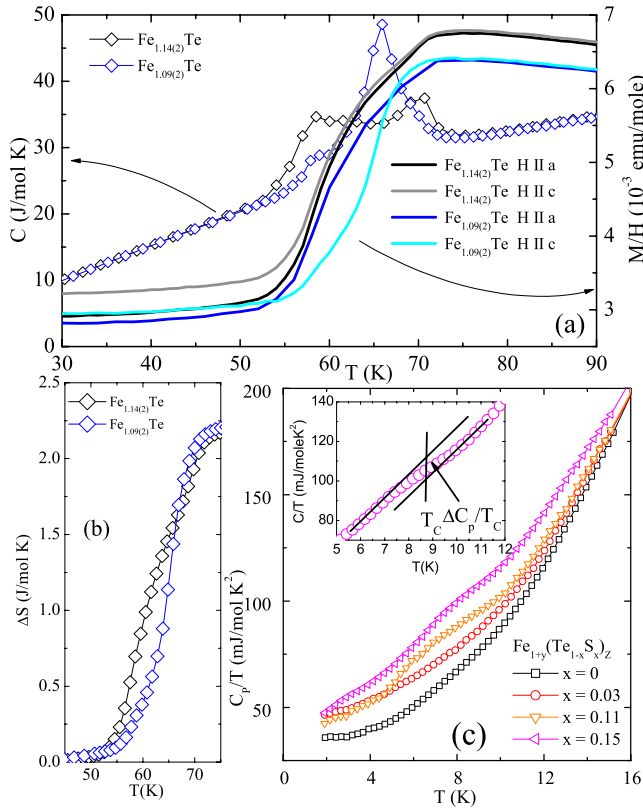


FIG. 5. (Color online) (a) Magnetization and heat capacity C_p at SDW transition of $\text{Fe}_{1.14(2)}\text{Te}$ and $\text{Fe}_{1.09(2)}\text{Te}$. (b) Entropy balance around the transition. (c) Low-temperature heat capacity with discontinuity in C_p/T at T_c for $x=0.15$ sample shown in the inset. Clear jumps associated with superconducting transitions are seen for $x \geq 0.11$.

critical fields and apparent coexistence of superconductivity and long-range magnetic order in our crystals, a reliable estimate of the normal-state contribution to electronic specific heat γ is rather difficult. Additional uncertainty in testing traditional isotropic weak-coupling BCS value of $\Delta C_p / \gamma T_c$ in $\text{Fe}_{1+y}(\text{Te}_{1-x}\text{S}_x)_z$ is introduced by the percolative nature of superconductivity with up to 7% superconducting volume fraction (Fig. 2). Therefore we restrict ourselves to an estimate of the C_p/T discontinuity associated with superconducting transition for material with the highest sulfur concentration and consequently the most pronounced jump in specific heat.³⁸ For $x=0.15$ it is about 12 mJ/mole K² at $T_c=8.8$ K, comparable to what is observed in $\text{Ba}(\text{Fe}_{1-x}\text{Co}_x)_2\text{As}_2$ and $\text{Ba}(\text{Fe}_{1-x}\text{Ni}_x)_2\text{As}_2$ single crystals.³⁸

Closer inspection of the $(\partial\chi T / \partial T)$ (Ref. 39) and $\partial\rho / \partial T$ data (Fig. 6) for $\text{Fe}_{1.14(2)}\text{Te}$ and $\text{Fe}_{1.09(2)}\text{Te}$ unveils two transitions at temperatures T_1 and T_2 that correspond to specific-heat anomalies in Fig. 5(a) (Table I). With sulfur substitution both transitions are clearly observed only up to $x \leq 0.1$ (Fig. 6). For higher sulfur concentration only one broad anomaly can be observed (Fig. 6 insets). Two successive transitions were reproduced on independently grown crystals within the same batch and in different batches. The exact temperatures of transitions T_1 and T_2 did vary from batch to batch.

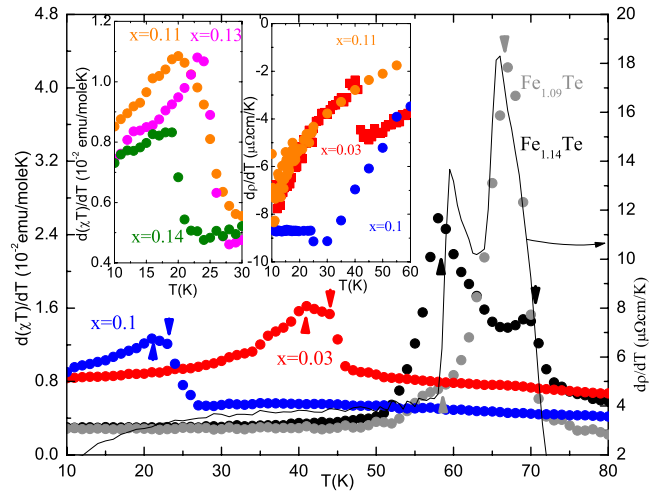


FIG. 6. (Color online) $\text{Fe}_{1.14(2)}\text{Te}$ and $\text{Fe}_{1.09(2)}\text{Te}$ as well as sulfur-doped samples for $x \leq 0.1$ show two clear magnetization anomalies around SDW transition, as seen in derivatives $d(\chi T) / dT$ and $d\rho / dT$ (inset). For higher sulfur content anomalies are broader (insets) and cannot be distinguished.

IV. DISCUSSION

The AF SDW in pure Fe_{1+y}Te is accompanied by a lattice distortion for all investigated values of y as in the undoped Fe-As superconductors.^{27,40–43} DFT calculations have found that excess Fe donates charge as Fe^+ to FeTe layers with strong tendency of moment formation on the excess Fe site.¹¹ By comparing our $C(T)$ data with the specific heat data taken on $\text{Fe}_{1.06}\text{Te}$ crystals⁴⁴ it can be seen that the clarity of the two step anomaly increases with the increase in y in Fe_{1+y}Te . It is absent for $\text{Fe}_{1.05}\text{Te}$ and $\text{Fe}_{1.06}\text{Te}$,^{40,44} visible for $\text{Fe}_{1.09}\text{Te}$ and rather pronounced for $\text{Fe}_{1.14}\text{Te}$ with similar entropy under both transitions [Figs. 5(a) and 5(b)]. Magnetic measurements $(\partial\chi T / \partial T)$ closely match thermodynamic data (Figs. 5 and 6). Whereas temperature of lower temperature transition T_2 (59 K) does not change with change in y , Fe_{1+y}Te with higher content of excess Fe y has transition T_1 at higher temperature (70 and 66 K, Table I). The Fermi level in Fe_{1+y}Te lies exactly at the sharp peak of the excess Fe density of states $N(E_F)$; therefore higher T_1 may be magnetically driven based on the Stoner criterion $N(E_F)I > 1$.¹¹ Increased ρ values for $\text{Fe}_{1.14}\text{Te}$ when compared to $\text{Fe}_{1.09}\text{Te}$ are also consistent with this (Fig. 2). Higher level of excess Fe y corresponds to larger size mismatch between cylindrical electron and hole Fermi surfaces. Therefore T_2 and T_1 transitions may correspond to successive SDW Fermi-surface nesting of individual electron-hole cylindrical pieces.^{8,11} Recent work shows that the magnetic order in parent compounds of iron-based superconductors is established below temperature of structural transition with up to 20 K difference in temperature of transition, as seen in $\text{CeFe}_{1-x}\text{Co}_x\text{AsF}$.^{42,45} It is unlikely that two transitions seen in our crystals correspond to individual magnetic and structural transitions since they have the same sensitivity to magnetic field.

Our findings are summarized in the electronic and structural phase diagrams shown in Fig. 7. The lattice contraction with isoelectronic sulfur substitution corresponds to a posi-

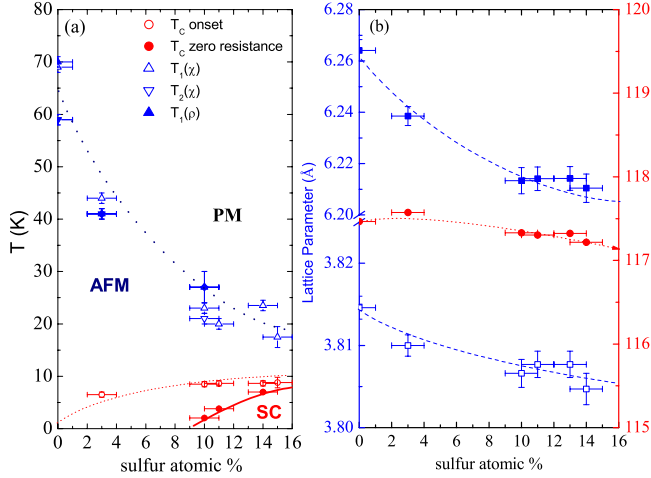


FIG. 7. (Color online) (a) Electronic phase diagram of $\text{Fe}_{1+y}(\text{Te}_{1-x}\text{S}_x)_z$, showing paramagnetic (PM), antiferromagnetic and SC ground states. Blue triangles pointing up and down correspond to T_2 and T_1 transitions, respectively. For $x=0$ both can easily be identified. Red circles denote onset of superconducting transition in ρ and zero resistance. Transition for $x=0.15$ was estimated from heat-capacity measurement. (b) Structural parameters at $T=80$ K.

tive chemical pressure. The magnetic transition is suppressed from the $\sim 58\text{--}70$ K region to about 20 K. Signatures of percolative superconductivity were observed for all $x \geq 0.3$. Zero resistivity in fully percolating path was observed for $x \geq 0.1$. The superconducting transition width decreases with the increase in x and T_c . Clearly, there is a competition between magnetic SDW order and the superconducting state since with increase in sulfur content x , $dT_{1,2}/dx$ and dT_c/dx have opposite signs.

Having delineated the evolution of magnetic and superconducting properties, it is natural to ask what is the correlation with the structural parameters. The unit-cell parameters a and c of $P4/nmm$ crystal structure decrease smoothly at $T=80$ K as sulfur is substituted in the place of tellurium (Table I). The c/a ratio decreases to nearly constant value for $x \geq 0.1$ up to $x=0.15$. After $x=0.15$ we have observed formation of FeS in the hexagonal NiAs type of structure in the same range of synthesis parameters. Close inspection of the tetrahedral angle α at $T=80$ K [Fig. 7(b)] reveals an extremum near the superconducting percolation threshold. The angle α increases up to $x=0.03$ and then decreases with further sulfur increase. The tetrahedral angle α therefore seems to be intimately connected with electronic transport properties which will be discussed next.

Both $x=0$ crystals are metallic in the low-temperature phase [Fig. 2(c)]. On the other hand, two successive transitions have also been reported in $\text{FeTe}_{0.92}$ under high pressure in the intermediate regime between $P=(1\text{--}1.8)$ GPa,⁴⁶ as well as two distinct types of transport below the magnetic and structural transition: metallic for $\text{FeTe}_{0.9}$ and semiconducting for $\text{FeTe}_{0.82}$.¹⁰ We note that semiconducting contribution to ρ below the magnetization anomaly for $x=0.10$ and $x=0.11$ (Fig. 2) coincides with Te(S) vacancies from synchrotron x-ray refinement (Fig. 1, Table I). Crystals with no Te(S) vacancies within error bars have metallic or semime-

talic contributions to ρ . This is in agreement with photoemission studies that showed no visible energy gaps at the electron and hole Fermi surface for $y < 0.05$ in Fe_{1+y}Te .⁴⁷ Increase in resistivity at the SDW AF transition signals small gap opening at the Fermi surface. The band structure of FeTe features intersecting elliptical cylindrical electron portions at the Brillouin-zone corners compensated by hole sections with higher effective mass at the zone center.⁸ Our findings show that the details of the nesting condition depend rather sensitively on the tetrahedral angle α and vacancies on the ligand site. This points to importance of hybridization between Te p and Fe d bands in addition to excess stoichiometry y on Fe site.¹² Our results strongly suggest that nanoscale inhomogeneity seems to be the key factor governing magnetic and electronic transport properties in $\text{Fe}_{1+y}(\text{Te}_{1-x}\text{S}_x)_z$.

Finally we comment on the percolative nature of superconductivity found in our crystals. Superconducting volume fraction increases with sulfur stoichiometry x . The $4\pi\chi_v$ reaches up to -0.07 at $T=1.8$ K ($\sim 0.26T_c$) for the highest x crystals where zero resistivity was observed to approach the T_c onset (Fig. 7). This is in good agreement with the polycrystalline data in Ref. 7. This signals granular superconducting state coexisting with SDW order, taking only a fraction of sample volume and stabilizing to fully percolating superconducting path by $x=0.14$. Similar coexistence was observed in other iron-based superconductors, $\text{CaFe}_{1-x}\text{Co}_x\text{AsF}$, $\text{SmFeAsO}_{1-x}\text{F}_x$, SrFe_2As_2 , and BaFe_2As_2 .^{41,45,48} For example, in the underdoped region of $\text{Ba}_{1-x}\text{K}_x\text{Fe}_2\text{As}_2$ the superconducting volume fraction has been reported to be $(23 \pm 3)\%$ of $-1/4\pi$ at $\sim 0.06T_c$ increasing up to 50% for nearly optimally doped material.^{28,49,50} Since SDW magnetic order and superconductivity compete for the same Fermi surface, percolative nature of superconductivity may be associated with intrinsic mesoscopic real-space phase separation as in cuprate oxides or $\text{CaFe}_{1-x}\text{Co}_x\text{AsF}$.^{45,51,52} Consequently superconductivity may be mediated by magnetic fluctuations, consistent with small values of electron-phonon coupling constant found in doped Fe_{1+x}Te and FeSe .⁸

V. CONCLUSION

In conclusion, we have performed combined and comprehensive study of structural, magnetic and superconducting properties of $\text{Fe}_{1+y}(\text{Te}_{1-x}\text{S}_x)_z$ single crystals. Magnetic transition decreases from $\sim 58\text{--}70$ K to about 20 K for $x=0.15$. We have shown that the increase in excess Fe y in Fe_{1+y}Te results in two anomalies in thermodynamic, magnetization, and transport properties. Electronic transport is rather sensitive to possible vacancies on Te(S) site. $\text{Fe}_{1+y}(\text{Te}_{1-x}\text{S}_x)_z$ are isotropic high-field superconductors with one of the smallest values of $\gamma_H = H_{c2}^{\parallel c} / H_{c2}^{\perp c}$ observed so far in iron-based superconducting materials. Moreover, anisotropy in the superconducting state decreases with increased sulfur content. Filamentary superconductivity is observed for all x in apparent coexistence with magnetism. Microscopic measurements such as muon-spin rotation (μSR) are needed to

confirm real-space phase separation and/or coexistence of superconductivity and magnetism. By utilizing high-pressure synthesis techniques even higher T_C 's, upper critical fields and smaller γ_H may be simultaneously obtained. Since FeTe_{1-x}S_x superconductors consist of relatively inexpensive and nontoxic elements, materials based on FeTeS with full volume fraction may be useful for future high-field power applications. In addition, higher S doping level would enable the answer to the question if maximal T_C occurs at the point where magnetism disappears as in cuprate oxides and other complex iron arsenide superconductors.

We are grateful for helpful discussions with Paul Canfield, Sergey Bud'ko, Simon Billinge, and Myron Strongin. This work was carried out at the Brookhaven National Laboratory, which is operated for the U.S. Department of Energy by Brookhaven Science Associates (Grant No. DE-Ac02-98CH10886). Use of the Advanced Photon Source was supported by the U. S. Department of Energy, Office of Science, Office of Basic Energy Sciences, under Contract No. DE-AC02-06CH11357. This work was supported by the Office of Basic Energy Sciences of the U.S. Department of Energy.

*Present address: Ames Laboratory US DOE and Department of Physics and Astronomy, Iowa State University, Ames, IA 50011, USA.

- ¹Y. Kamihara, T. Watanabe, M. Hirano, and H. Hosono, *J. Am. Chem. Soc.* **130**, 3296 (2008).
- ²Z.-A. Ren, W. Lu, J. Yang, W. Yi, X.-L. Shen, Zheng-Cai, G.-C. Che, X.-L. Dong, L.-L. Sun, F. Zhou, and Z.-X. Zhao, *Chin. Phys. Lett.* **25**, 2215 (2008).
- ³M. Rotter, M. Tegel, and D. Johrendt, *Phys. Rev. Lett.* **101**, 107006 (2008).
- ⁴X. C. Wang, Q. Q. Liu, Y. X. LV, W. B. Gao, L. X. Yang, R. C. Yu, F. Y. Li, and C. Q. Jin, *Solid State Commun.* **148**, 538 (2008).
- ⁵F.-C. Hsu, J.-Y. Luo, K.-W. Yeh, T.-K. Chen, T.-W. Huang, P. M. Wu, Y.-C. Lee, Y.-L. Huang, Y.-Y. Chu, D.-C. Yan, and M.-K. Wu, *Proc. Natl. Acad. Sci. U.S.A.* **105**, 14262 (2008).
- ⁶K. W. Yeh, T. W. Huang, Y. L. Huang, T. K. Chen, F. C. Hsu, P. M. Wu, Y. C. Lee, Y. Y. Chu, C. L. Chen, J. Y. Luo, D. C. Yan, and M. K. Wu, *EPL* **84**, 37002 (2008).
- ⁷Y. Mizuguchi, F. Tomioka, S. Tsuda, T. Yamaguchi, and Y. Takano, *Appl. Phys. Lett.* **94**, 012503 (2009).
- ⁸A. Subedi, L. Zhang, D. J. Singh, and M. H. Du, *Phys. Rev. B* **78**, 134514 (2008).
- ⁹W. Bao, Y. Qiu, Q. Huang, M. A. Green, P. Zajdel, M. R. Fitzsimmons, M. Zhernenkov, S. Chang, M. Fang, B. Qian, E. K. Vehstedt, J. Yang, H. M. Pham, L. Spinu, and Z. Q. Mao, *Phys. Rev. Lett.* **102**, 247001 (2009).
- ¹⁰M. H. Fang, H. M. Pham, B. Qian, T. J. Liu, E. K. Vehstedt, Y. Liu, L. Spinu, and Z. Q. Mao, *Phys. Rev. B* **78**, 224503 (2008).
- ¹¹L. Zhang, D. J. Singh, and M. H. Du, *Phys. Rev. B* **79**, 012506 (2009).
- ¹²M. J. Han and S. Y. Savrasov, *Phys. Rev. Lett.* **103**, 067001 (2009).
- ¹³I. I. Mazin and M. D. Johannes, *Nat. Phys.* **5**, 141 (2009).
- ¹⁴M. R. Norman, *Phys.* **1**, 21 (2008).
- ¹⁵S. Margadonna, Y. Takabayashi, Y. Ohishi, Y. Mizuguchi, Y. Takano, T. Kagayama, T. Nakagawa, M. Takata, and K. Prassides, *Phys. Rev. B* **80**, 064506 (2009).
- ¹⁶S. Margadonna, Y. Takabayashi, M. T. McDonald, K. Kasperkiewicz, Y. Mizuguchi, Y. Takano, A. N. Fitch, E. Suard, and K. Prassides, *Chem. Commun. (Cambridge)* **2008**, 5607.
- ¹⁷Report on of the Basic Energy Sciences, U.S. Department of Energy, Superconductivity, Washington, DC, 2006.
- ¹⁸P. C. Canfield and Z. Fisk, *Philos. Mag.* **B 65**, 1117 (1992).
- ¹⁹Z. Fisk and J. P. Remeika, in *Handbook on the Physics and Chemistry of Rare Earths*, edited by K. A. Gschneider and J. Eyring (Elsevier, Amsterdam, 1989), Vol. 12.
- ²⁰P. J. Chupas, X. Qiu, J. C. Hanson, P. L. Lee, C. P. Grey, and S. J. L. Billinge, *J. Appl. Crystallogr.* **36**, 1342 (2003).
- ²¹T. Egami and S. J. L. Billinge, *Underneath the Bragg Peaks: Structural Analysis of Complex Materials* (Pergamon, New York/Elsevier, Oxford, England, 2003).
- ²²C. L. Farrow, P. Juhas, J. W. Liu, D. Bryndin, E. S. Bozin, J. Bloch, Th. Proffen, and S. J. L. Billinge, *J. Phys.: Condens. Matter* **19**, 335219 (2007).
- ²³S. Li, C. de la Cruz, Q. Huang, Y. Chen, J. W. Lynn, J. Hu, Y.-L. Huang, F.-C. Hsu, K.-W. Yeh, M.-K. Wu, and P. Dai, *Phys. Rev. B* **79**, 054503 (2009).
- ²⁴B. C. Sales, A. S. Sefat, M. A. McGuire, R. Y. Jin, D. Mandrus, and Y. Mozharivskiy, *Phys. Rev. B* **79**, 094521 (2009).
- ²⁵R. A. Ribeiro, S. L. Bud'ko, C. Petrovic, and P. C. Canfield, *Physica C* **382**, 194 (2002).
- ²⁶G. F. Chen, Z. G. Chen, J. Dong, W. Z. Hu, G. Li, X. D. Zhang, P. Zheng, J. L. Luo, and N. L. Wang, *Phys. Rev. B* **79**, 140509(R) (2009).
- ²⁷M. Rotter, M. Tegel, D. Johrendt, I. Schellenberg, W. Hermes, and R. Pöttgen, *Phys. Rev. B* **78**, 020503(R) (2008).
- ²⁸N. Ni, S. L. Bud'ko, A. Kreyssig, S. Nandi, G. E. Rustan, A. I. Goldman, S. Gupta, J. D. Corbett, A. Kracher, and P. C. Canfield, *Phys. Rev. B* **78**, 014507 (2008).
- ²⁹A. S. Sefat, R. Jin, M. A. McGuire, B. C. Sales, D. J. Singh, and D. Mandrus, *Phys. Rev. Lett.* **101**, 117004 (2008).
- ³⁰G. Wu, Y. L. Xie, H. Chen, M. Zhong, R. H. Liu, B. C. Shi, Q. J. Li, X. F. Wang, T. Wu, Y. J. Yan, J. J. Ying, and X. H. Chen, *J. Phys.: Condens. Matter* **21**, 142203 (2009).
- ³¹J. Jaroszynski, F. Hunte, L. Balicas, Y.-j. Jo, I. Raičević, A. Gurevich, D. C. Larbalestier, F. F. Balakirev, L. Fang, P. Cheng, Y. Jia, and H. H. Wen, *Phys. Rev. B* **78**, 174523 (2008).
- ³²N. R. Werthamer, E. Helfand, and P. C. Hohenberg, *Phys. Rev.* **147**, 295 (1966).
- ³³A. Yamamoto, J. Jaroszynski, C. Tarantini, L. Balicas, J. Jiang, A. Gurevich, D. C. Larbalestier, R. Jin, A. S. Sefat, M. A. McGuire, B. C. Sales, D. K. Christen, and D. Mandrus, *Appl. Phys. Lett.* **94**, 062511 (2009).
- ³⁴C. P. Bean, *Phys. Rev. Lett.* **8**, 250 (1962).
- ³⁵E. M. Gyorgy, R. B. van Dover, K. A. Jackson, L. F. Schneem-

- eyer, and J. V. Waszczak, *Appl. Phys. Lett.* **55**, 283 (1989).
- ³⁶M. A. Tanatar, N. Ni, C. Martin, R. T. Gordon, H. Kim, V. G. Kogan, G. D. Samolyuk, S. L. Bud'ko, P. C. Canfield, and R. Prozorov, *Phys. Rev. B* **79**, 094507 (2009).
- ³⁷J. C. Lashley, M. F. Hundley, A. Migliori, J. L. Sarrao, P. G. Pagliuso, T. W. Darling, M. Jaime, J. C. Cooley, W. L. Hults, L. Morales, D. J. Thoma, J. L. Smith, J. Boerio-Goates, B. F. Woodfield, G. R. Stewart, R. A. Fisher, and N. E. Phillips, *Cryogenics* **43**, 369 (2003).
- ³⁸S. L. Bud'ko, N. Ni, and P. C. Canfield, *Phys. Rev. B* **79**, 220516(R) (2009).
- ³⁹M. E. Fisher, *Philos. Mag.* **7**, 1731 (1962).
- ⁴⁰G. F. Chen, Z. Li, D. Wu, G. Li, W. Z. Hu, J. Dong, P. Zheng, J. L. Luo, and N. L. Wang, *Phys. Rev. Lett.* **100**, 247002 (2008).
- ⁴¹A. J. Drew, Ch. Niedermayer, P. J. Baker, F. L. Pratt, S. J. Blundell, T. Lancaster, R. H. Liu, G. Wu, X. H. Chen, I. Watanabe, V. K. Malik, A. Dubroka, M. Rossle, K. W. Kim, C. Baines, and C. Bernhard, *Nature Mater.* **8**, 310 (2009).
- ⁴²C. de la Cruz, Q. Huang, J. W. Lynn, J. Li, W. Ratcliff, J. L. Zarestky, H. A. Mook, G. F. Chen, J. L. Luo, N. L. Wang, and P. Dai, *Nature (London)* **453**, 899 (2008).
- ⁴³H.-H. Klauss, H. Luetkens, R. Klingeler, C. Hess, F. J. Litterst, M. Kraken, M. M. Korshunov, I. Eremin, S.-L. Drechsler, R. Khasanov, A. Amato, J. Hamann-Borrero, N. Leps, A. Kondrat, G. Behr, J. Werner, and B. Büchner, *Phys. Rev. Lett.* **101**, 077005 (2008).
- ⁴⁴S. L. Bud'ko, P. C. Canfield, A. S. Sefat, B. C. Sales, M. A. McGuire, and D. Mandrus, *Phys. Rev. B* **80**, 134523 (2009).
- ⁴⁵Y. Xiao, Y. Su, R. Mittal, T. Chatterji, T. Hansen, C. M. N. Kumar, S. Matsuishi, H. Hosono, and Th. Brueckel, *Phys. Rev. B* **79**, 060504(R) (2009).
- ⁴⁶Hironari Okada, Hiroyuki Takahashi, Yoshikazu Mizuguchi, Yoshihiko Takano, and Hiroki Takahashi, *J. Phys. Soc. Jpn.* **78**, 083709 (2009).
- ⁴⁷Y. Xia, D. Qian, L. Wray, D. Hsieh, G. F. Chen, J. L. Luo, N. L. Wang, and M. Z. Hasan, *Phys. Rev. Lett.* **103**, 037002 (2009).
- ⁴⁸E. Colombier, S. L. Bud'ko, N. Ni, and P. C. Canfield, *Phys. Rev. B* **79**, 224518 (2009).
- ⁴⁹T. Goko, A. A. Aczel, E. Baggio-Saitovitch, S. L. Bud'ko, P. C. Canfield, J. P. Carlo, G. F. Chen, P. Dai, A. C. Hamman, W. Z. Hu, H. Kageyama, G. M. Luke, J. L. Luo, B. Nachumi, N. Ni, D. Reznik, D. R. Sanchez-Candela, A. T. Savici, K. J. Sikes, N. L. Wang, C. R. Wiebe, T. J. Williams, T. Yamamoto, W. Yu, and Y. J. Uemura, *Phys. Rev. B* **80**, 024508 (2009).
- ⁵⁰J. T. Park, D. S. Inosov, Ch. Niedermayer, G. L. Sun, D. Haug, N. B. Christensen, R. Dinnebier, A. V. Boris, A. J. Drew, L. Schulz, T. Shapoval, U. Wolff, V. Neu, X. Yang, C. T. Lin, B. Keimer, and V. Hinkov, *Phys. Rev. Lett.* **102**, 117006 (2009).
- ⁵¹J. D. Jorgensen, B. Dabrowski, S. Pei, D. G. Hinks, L. Soderholm, B. Morosin, J. E. Schirber, E. L. Venturini, and D. S. Ginley, *Phys. Rev. B* **38**, 11337 (1988).
- ⁵²S. H. Pan, J. P. O'Neil, R. L. Badzey, C. Chamon, H. Ding, J. R. Engelbrecht, Z. Wang, H. Eisaki, S. Uchida, A. K. Gupta, K.-W. Ng, E. W. Hudson, K. M. Lang, and J. C. Davis, *Nature (London)* **413**, 282 (2001).

Characterisation of amorphous and nanocrystalline molecular materials by total scattering†

Simon J. L. Billinge,^{*ab} Timur Dykhne,^a Pavol Juhás,^a Emil Božin,^{ab} Ryan Taylor,^c Alastair J. Florence^c and Kenneth Shankland^d

Received 28th July 2009, Accepted 7th October 2009

First published as an Advance Article on the web 19th October 2009

DOI: 10.1039/b915453a

The use of high-energy X-ray total scattering coupled with pair distribution function analysis produces unique structural fingerprints from amorphous and nanostructured phases of the pharmaceuticals carbamazepine and indomethacin. The advantages of such facility-based experiments over laboratory-based ones are discussed and the technique is illustrated with the characterisation of a melt-quenched sample of carbamazepine as a nanocrystalline (4.5 nm domain diameter) version of form III.

The majority of active pharmaceutical ingredients (APIs) are marketed as crystalline forms for reasons of stability. However, the formation, stability and performance of amorphous solids are also of significant interest within pharmaceutical research and development. Whilst the amorphous state can confer desirable properties to an API, such as increased aqueous solubility,¹ the inadvertent production of non-crystalline material during processing can also lead to uncontrolled variability in physical and chemical attributes. The potential for commercial exploitation of amorphous APIs is often complicated by their tendency to revert to a more thermodynamically favourable, and less soluble, crystalline state. Although the identification, characterisation and quantification of amorphous pharmaceuticals has received considerable attention, little is known about local ordering in amorphous APIs due to the lack of reliable experimental probes. The powerful tools of crystallography begin to lose their power for structures on the nanoscale; conventional X-ray powder diffraction (XRPD) patterns become broad and featureless in these cases (Fig. 1) and are not useful for differentiating between different local molecular packing arrangements.² Accordingly, XRPD is generally used simply to identify such samples as non-crystalline (*i.e.* ‘X-ray amorphous’).

It has recently been suggested that Fourier transforming conventional laboratory XRPD data‡ to obtain the atomic distribution function (PDF)^{3,4} allows more structural information to be extracted.⁵ The PDF, $G(r)$, yields the probability of finding an atom at a distance r from any reference atom and so provides information on

local structure in real space. However, this approach is intrinsically limited by the relatively low momentum transfer magnitude Q ($4\pi\sin\theta/\lambda$) values typically accessible in the laboratory environment, resulting in a PDF of limited real-space resolution. For an accurate PDF across a wide range of r , data should be collected with low instrumental background and good counting statistics to high Q . These requirements can be met by combining high-energy (synchrotron) X-rays with imaging plate detectors.

In this work, a high-energy XRPD method known as total scattering,³ coupled with Fourier transformation and PDF analysis, is applied to individual X-ray amorphous samples§ of the anti-epileptic drug carbamazepine (CBZ; Fig. 1) and the non-steroidal anti-inflammatory drug indomethacin (IND). This approach is referred to as the total scattering pair distribution function (TSPDF) method to differentiate it from the approach of obtaining the PDF from conventional laboratory XRPD data.⁵ The TSPDF method has been widely applied to inorganic materials to study amorphous structures⁶ and more recently crystalline and nanocrystalline systems,^{3,7} but its application to molecular systems has to date been very limited.

Total scattering data were collected¶ from melt-quenched samples of CBZ and IND as well as polycrystalline samples of CBZ I and III⁸ and α^9 and γ^{10} IND. The short wavelength used (0.137 Å), combined with an appropriate data collection strategy enables data to be recorded over a sufficiently high Q -range to provide the necessary resolution in real-space for quantitative structural analysis to be

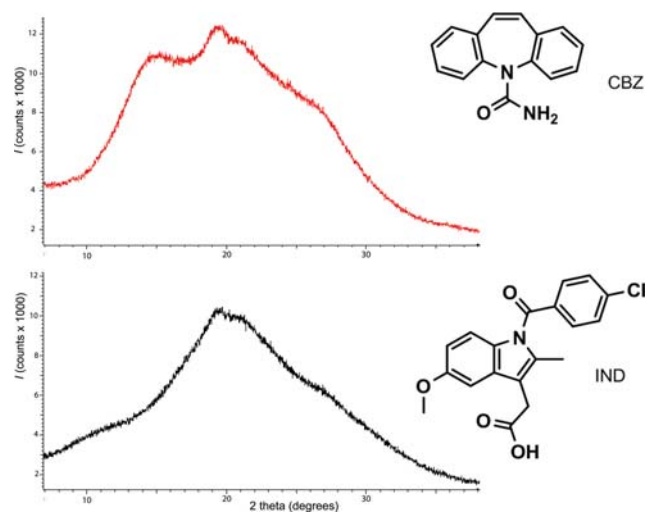


Fig. 1 Molecular structures and laboratory Cu $K\alpha_1$ XRPD patterns for X-ray amorphous melt-quenched samples of CBZ (top) and IND (bottom).

^aDepartment of Applied Physics and Applied Mathematics, Columbia University, New York, NY, 10027, USA. E-mail: sb2896@columbia.edu; Fax: +1 212-854-8257; Tel: +1 212-854-2918

^bCondensed Matter Physics and Materials Science Department, Brookhaven National Laboratory, Upton, NY, 11973, USA

^cSolid-State Research Group, Strathclyde Institute of Pharmacy and Biomedical Sciences, University of Strathclyde, Glasgow, UK G4 0NR

^dSchool of Pharmacy, University of Reading, Reading, UK RG6 6AD

† Electronic supplementary information (ESI) available: Sample preparation, data processing and PolySNAP comparisons of CBZ TSPDF data. See DOI: 10.1039/b915453a

attempted. In these data, a useable $Q_{\max} = 20 \text{ \AA}^{-1}$ was achieved, equating to a real-space resolution of 0.31 \AA . Further processing was carried out on all data sets to obtain the total scattering reduced structure function, $F(Q)$, and the TSPDF, $G(r)$, using the program PDFgetX2.¹¹ A summary of data processing steps is provided as ESI.† The total scattering data, presented as $F(Q)$, and the resultant TSPDFs for the amorphous and polycrystalline samples of CBZ are shown in Fig. 2.

$F(Q)$ for the melt-quenched sample (Fig. 2(b)), measured over a wide enough range of momentum transfer and properly normalized (see ESI),† is rich in information content compared to a conventional laboratory-based XRPD measurement (*e.g.* Fig. 1). Close inspection shows no clear Bragg diffraction, confirming a lack of long-range order in the sample. $F(Q)$ clearly distinguishes the polycrystalline samples CBZ III and I (Fig. 2(a) and (c), respectively) with the melt-quenched sample showing a closer resemblance to that of CBZ III than CBZ I.

Transforming $F(Q)$ to $G(r)$ (*i.e.* the TSPDF; see ESI)† allows interpretation and comparison to be carried out in real space. There is a striking resemblance between the TSPDF of CBZ III and the melt-quenched sample. Full-profile comparisons of the TSPDFs in the range dominated by inter-molecular interactions, 3–20 \AA , for the three samples using PolySNAP¹² yielded a correlation co-efficient of 0.8389 for the melt-quenched and CBZ III TSPDFs (perfect match = 1.0; see ESI).† The next closest similarity was observed for melt-quenched CBZ and form I, but yielding a correlation coefficient of only 0.5164.

Given such close agreement between the melt-quenched and form III TSPDFs, the structural similarity between these samples was explored in more detail. The TSPDF of CBZ-III was modified by attenuating the TSPDF peaks in the high- r region to simulate the effects of reducing the range of structural coherence (or long range ordering) on the data, assuming spherical particles. If the internal atomic arrangement of a nanocrystalline domain resembles that of a bulk crystalline analog, its TSPDF resembles that of the bulk except that the amplitude of the TSPDF peaks is attenuated with increasing r due to the loss of far-neighbour correlations outside the particle. This can be modelled by multiplying the crystalline PDF with the auto-correlation of the shape function of the particle as done here (see ESI).†

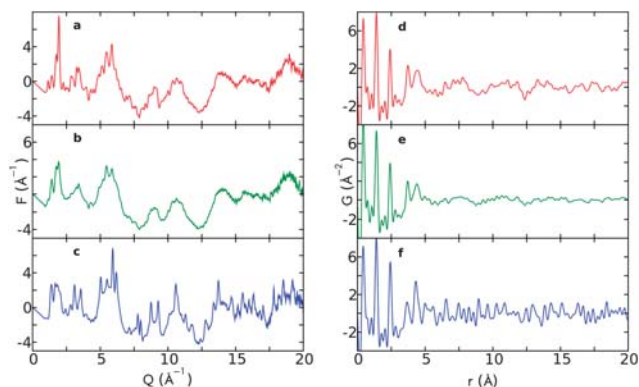


Fig. 2 Total scattering diffraction patterns and TSPDFs of CBZ. Panels (a) and (d) correspond to CBZ III, (b) and (e) to the melt-quenched sample and (c) and (f) to CBZ I; (a), (b), (c) show the total scattering data in the form of $F(Q)$ (see ESI)† whilst (d), (e), (f) are in the form of the TSPDF, $G(r)$.

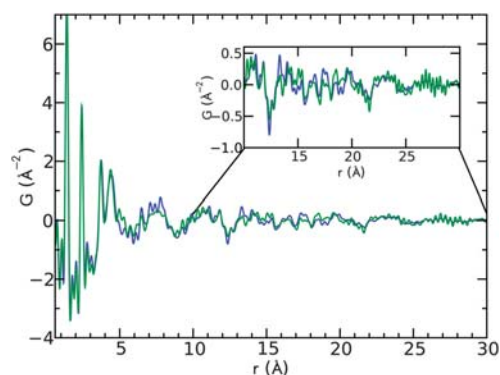


Fig. 3 Comparison of TSPDF from the melt-quenched amorphous sample (green) and CBZ III (blue), modified as if it were a 4.5 nm nanoparticle (see text for details). PolySNAP correlation coefficient 0.8601.

The overlay shown in Fig. 3 was obtained using a nanocrystalline domain diameter of 4.5 nm. The excellent agreement between the attenuated TSPDF from CBZ III and the melt-quenched CBZ TSPDF is definitive proof that the local packing in the melt-quenched sample is that of form III with a range of structural coherence of 4.5 nm. It is interesting to ask whether the sample is made up of discrete 4.5 nm nanocrystallites of form III or whether it is truly a homogeneous amorphous structure with short-range molecular CBZ III-like packing. The data suggest the former since the sharpness of features in the TSPDFs is preserved with increasing r whilst their amplitude is simply reduced, which is not the behaviour seen in truly amorphous samples. We thus conclude that the structure of the melt-quenched CBZ used in the measurement is actually nanocrystalline CBZ III with an average particle diameter of 4.5 nm. Although the TSPDF of the melt-quenched sample is well explained by CBZ III attenuated by the PDF characteristic function for a sphere, we cannot rule out that there is a dispersion of nanoparticle sizes centered around the value of 4.5 nm. For example, narrow dispersions with $\sim 10\%$ polydispersity are well explained using the characteristic function for a single sphere.

A similar analysis has also been carried out on a melt-quenched sample of IND, and the results are shown in Fig. 4. Again, $F(Q)$ shows the melt-quenched IND sample to be X-ray amorphous (no evident Bragg diffraction) and rich in structural information. The highest correlation coefficient from full-profile comparisons of the TSPDFs of melt-quenched, α and γ IND in PolySNAP was 0.6770, returned for the melt-quenched and α -IND phases. This is significantly lower than the highest value obtained for the CBZ TSPDF comparisons. All other coefficients were less than 0.5 (ESI).† Thus, the TSPDFs indicate that the local structure of the melt-quenched IND sample at 100 K is largely distinct from the α and γ crystalline forms. This contrasts with the suggestion based on crystallization and spectroscopic evidence that below T_g (315 K)¹³ amorphous IND has a local structure, with dimeric hydrogen bonding, similar to the γ form.¹⁴ Linear combinations of the α and γ crystalline phases also do not give good agreement with the TSPDF from the melt-quenched sample. Further comparisons with the δ form of IND were not possible at the time of writing as neither a crystal structure nor experimental TSPDF were available.¹⁵ However, this result clearly shows that the TSPDF can readily characterise distinct local molecular packing arrangements in the amorphous IND sample. We note

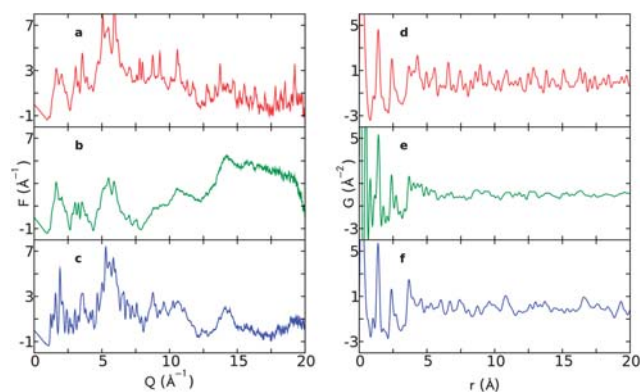


Fig. 4 Total scattering diffraction patterns and TSPDFs of IND samples. (a) and (d), contain patterns from IND α , (b) and (e) from the melt-quenched sample and (c) and (f), IND γ . The column (a), (b), (c) shows the synchrotron total scattering data in the form of $F(Q)$ and the second column, (d), (e), (f), contains the total scattering data in the form of the TSPDF, $G(r)$.

that, as with the CBZ, oscillations in the PDF are apparent over the whole r -range shown and clearly extend beyond 20 Å, which shows that the melt-quenched IND sample we studied is also nanocrystalline rather than truly amorphous.

The key to obtaining useful TSPDF curves is not the use of synchrotron radiation *per se* but collecting data to high Q with good statistics. This is possible from laboratory based diffractometers that have Ag ($\lambda = 0.556$ Å) or Mo ($\lambda = 0.7107$ Å) sources, where the fact that λ is a factor of ~ 2 – 3 times smaller than that of a Cu source means that higher Q values can be accessed for any given diffraction angle. The current data were Fourier transformed with a Q_{\max} of 20 Å⁻¹, which is certainly accessible with a Ag lab diffractometer, although a suitably configured Mo instrument would offer significant practical advantages such as higher incident flux, increased X-ray scattering and higher detector efficiency. That said, synchrotron measurements are advantageous because the requisite statistics can be obtained over the whole Q -range in a short time (in this case 30 min) compared to many hours on a laboratory-based source. Future developments in high intensity, short wavelength laboratory X-ray sources will certainly help close this particular gap.

These results have a number of important implications. They show that TSPDF data can be used to unambiguously differentiate between different forms of amorphous or nanocrystalline molecular solids. As such, TSPDF is an approach that can take the ‘fingerprinting’ role for amorphous pharmaceuticals that XRPD takes for polycrystalline pharmaceuticals. This opens the door to future studies exploring the effects of processing or storage on amorphous materials and of phase stability in molecular dispersions, for example. There can also be sufficient information in the TSPDF to enable the fitting of well-defined structural models for the molecular conformation and

packing arrangements in amorphous and nanocrystalline samples. Clearly this would have particular application in the case of the melt-quenched IND TSPDF presented here, however the development of such models is beyond the scope of the current work. This capability offers the potential to revolutionise the study of amorphous samples, by illuminating the basic science underpinning the structure of non-crystalline molecular materials to add to the wealth of thermodynamic and spectroscopic literature available. Also, by tracking the evolution of structure of melt-quenched glasses for example, this tool may help identify new crystalline polymorphs *via* an amorphous or nanocrystalline route.

Notes and references

‡ Typically Cu K α radiation, $\lambda = 1.54$ Å; $2\theta = 60^\circ$; $Q_{\max} = 4.1$ Å⁻¹.

§ Data were collected from amorphous samples of CBZ and IND prepared by a melt-quenching method. For further details of the sample preparation see ESI.†

¶ Data were collected at 100 K at beamline 11ID-B at the Advanced Photon Source (APS) using the rapid acquisition PDF method. Samples were sealed in 1 mm diameter Kapton capillaries and irradiated with X-rays of wavelength $\lambda = 0.1370$ Å. A large area 2D image plate detector (MAR345) was placed centered on and perpendicular to the incident beam 198 mm behind the sample. Sufficient statistics in the high Q -range were obtained using multiple exposures of the image plate, exposing for 300 s, between 5 and 8 times for each data point. The separate exposures were summed together before further processing, resulting in an integrated exposure time of 30 min per sample. 1D powder diffraction patterns were obtained by integrating around the Scherrer rings on the image plate images, correcting for beam polarization effects using the program Fit2D. Data were collected to $Q = 31$ Å⁻¹ and Fourier transformed using data to 20 Å⁻¹ to generate TSPDFs to $r = 30$ Å. Further details in ESI.†

- 1 B. C. Hancock and M. Parks, *Pharmacol. Res.*, 2000, **17**, 397–404.
- 2 S. J. L. Billinge and I. Levin, *Science*, 2007, **316**, 561–565.
- 3 Takeshi Egami and S. J. L. Billinge, *Underneath the Bragg peaks: structural analysis of complex materials*, Pergamon, Amsterdam, London, 2003.
- 4 B. E. Warren, *X-Ray Diffraction*, Dover, New York, 1990.
- 5 S. Bates, G. Zografi, D. Engers, K. Morris, K. Crowley and A. Newman, *Pharmacol. Res.*, 2006, **23**, 2333–2349.
- 6 A. C. Wright, *Phys. Chem. Glasses*, 1998, **24**, 148–179.
- 7 S. J. L. Billinge, *J. Solid State Chem.*, 2008, **181**, 1695–1700.
- 8 A. L. Grzesiak, M. D. Lang, K. Kim and A. J. Matzger, *J. Pharm. Sci.*, 2003, **92**, 2260–2271.
- 9 X. M. Chen, K. R. Morris, U. J. Griesser, S. R. Byrn and J. G. Stowell, *J. Am. Chem. Soc.*, 2002, **124**, 15012–15019.
- 10 P. J. Cox and P. L. Manson, *Acta Crystallogr., Sect. E: Struct. Rep. Online*, 2003, **59**, o986–O988.
- 11 Xiangyun Qiu, Jeroen W. Thompson and Simon J. L. Billinge, *J. Appl. Crystallogr.*, 2004, **37**, 678.
- 12 G. Barr, W. Dong and C. J. Gilmore, *J. Appl. Crystallogr.*, 2004, **37**, 658–664.
- 13 V. Andronis and G. Zografi, *J. Non-Cryst. Solids*, 2000, **271**, 236–248.
- 14 E. Y. Shalaev and G. Zografi, in *Amorphous Food and Pharmaceutical Systems*, ed. Harry Ed Levine, Royal Society of Chemistry, Cambridge, 2002, pp. 11–30.
- 15 L. Borka, *Acta Pharma. Suec.*, 1974, **11**, 295–303.

OPEN ACCESS

Quantitative structure refinement from the ARCS chopper spectrometer

To cite this article: E S Božin *et al* 2010 *J. Phys.: Conf. Ser.* **251** 012080

View the [article online](#) for updates and enhancements.

You may also like

- [Effectiveness of ARCS Based Economic E-Book to Improve Learning Motivation and Learning Outcomes](#)
Kartika Yunita Saputri, Sigit Santoso and Aniek Hindrayani
- [Research on Human Resource Development and Training Design Based on ARCS Model](#)
Yi Xia
- [An interactive web-based tool to guide the preparation of neutron imaging experiments at oak ridge national laboratory](#)
Yuxuan Zhang, Jean-C Bilheux, Hassina Z Bilheux et al.

ECS Toyota Young Investigator Fellowship



For young professionals and scholars pursuing research in batteries, fuel cells and hydrogen, and future sustainable technologies.

At least one \$50,000 fellowship is available annually.
More than \$1.4 million awarded since 2015!



Application deadline: January 31, 2023

Learn more. Apply today!

Quantitative structure refinement from the ARCS chopper spectrometer

E S Božin,^{1,2} P Juhás,¹ W Zhou,¹ M B Stone,³ D L Abernathy,³
A Huq,³ and S J L Billinge^{1,2}

¹Department of Applied Physics and Applied Mathematics, Columbia University, New York, New York, 10027, USA

²Condensed Matter Physics and Materials Science Department, Brookhaven National Laboratory, Upton, New York, 11973, USA

³Neutron Scattering Sciences Division, Oak Ridge National Laboratory, Oak Ridge, Tennessee, 37831, USA

E-mail: sb2896@columbia.edu

Abstract. The new wide angular-range chopper spectrometer ARCS at the Spallation Neutron Source at Oak Ridge National Laboratory has been successfully used in white-beam mode, with no Fermi chopper, to obtain neutron powder diffraction based atomic pair distribution functions (PDFs). Obtained PDF patterns of Si, Ni, and Al₂O₃ were refined using the PDFfit method and the results compared to data collected at the NPDF diffractometer at Los Alamos National Laboratory. High quality resulting fits are presented, demonstrating that reliable powder diffraction data can be obtained from ARCS when operated in this configuration.

1. Introduction

Time-of-flight (TOF) instruments at spallation sources, such as the NPDF [1] at the Los Alamos Neutron Science Center (LANSCE) or the general materials diffractometer (GEM) [2] at ISIS, are routinely utilized to carry out neutron powder diffraction measurements. It is less common to exploit chopper spectrometers to obtain powder diffraction data suitable for structure refinements, since their primary role is inelastic neutron scattering measurements to obtain information about a system's dynamics. However, if operated without the monochromating Fermi chopper in the primary beam, a chopper spectrometer resembles the configuration of a TOF powder diffractometer. If there is no appropriate detector coverage at large scattering angles, the Q -resolution and Q -range, where Q is the magnitude of the scattering vector, may be insufficient for PDF analysis. However, the ARCS spectrometer at SNS has high detector coverage over a wide angular range, scattering angles between 2 and 135 degrees, resulting in an acceptable Q -resolution for the higher-angle detectors. The ARCS spectrometer is situated on a relatively short flight-path (13.6 m primary, and 3.0-3.4 m secondary) at the Spallation Neutron Source (SNS) at Oak Ridge National Laboratory (ORNL) in Tennessee, currently the brightest spallation neutron source in the world. The Fermi chopper mechanism at ARCS is mounted on a motorized translation table, allowing one to easily switch between two installed Fermi chopper slit packages and an open 'white-beam' position. This feature means that it becomes straightforward to analyze structure and dynamics from the same sample without dismounting it from the instrument. Here we present in greater detail the preliminary experiments, which

demonstrate this capability on ARCS, that were reported in an earlier brief communication [3]. Quantitative structural information could be obtained from ARCS by obtaining reliable atomic pair distribution functions (PDFs) from the data [4] and refining models to them using the PDFgui software [5]. Here we describe in greater detail the procedure and the results.

Complete time-focussing of diffraction data from ARCS is not achievable at present due to lack of appropriate software routines. The data presented here were histogrammed to produce the 1D powder diffraction pattern using a generic TOF to d -space conversion protocol, without applying standard second order corrections. As a consequence, the data have a degraded resolution, and with poorly defined peak shapes. Attempts were made to refine the data by the Rietveld method using Fullprof [6, 7] and GSAS [8, 9] with poor results. Because the data were not fully time-focussed and inherently low resolution, the time was not spent to explore this issue any further and we concentrated on obtaining structure refinements from atomic pair distribution functions (PDFs) obtained from the data [4, 10] since the PDF is not very sensitive to details of the profile function. Successful refinements were performed as described below, demonstrating that this approach can be used even in the absence of software codes that do the full time-focussing, which is a significant challenge from a diffractometer of the complexity of ARCS. The data from Si and Ni samples are benchmarked against data from similar samples collected at the NPDF diffractometer at LANSCE with comparable statistics. NPDF is currently the highest resolution neutron powder diffractometer situated at a spallation source in the US [1] and is also a highly successful PDF instrument [11, 12, 13, 14, 15]. Finally, data for a corundum Al_2O_3 sample were collected and the PDF successfully refined, demonstrating the capability for carrying out research-quality diffraction experiments on nontrivial systems at the ARCS instrument.

2. Experimental

In this study we collected neutron TOF data at ARCS at SNS on three different commercially available standard samples: Ni, Si, and Al_2O_3 . In addition, data from neutron TOF powder diffraction measurements on Ni and Si, carried out using the high-resolution NPDF diffractometer at LANSCE, are presented. All data were collected at room temperature.

For the ARCS experiment, loose powder samples (3.0 grams of Si, 8.3 grams of Ni, and 3.8 grams of Al_2O_3) were sealed in extruded vanadium tubes (1.11 cm in diameter, approximately 5.08 cm in height, and with wall thickness of 0.015 cm). Data for all the samples, as well as for the empty vanadium container (background), were collected for about 30 minutes each. A vanadium rod measurement was also performed to obtain incident spectrum information. The experiments were carried out using a neutron beam produced by 1.25 coulombs of charge impinging on a liquid mercury target surrounded by a decoupled water moderator [16]. In the case of standard NPDF measurements, to obtain the total scattering structure function, $S(Q)$, raw data are corrected for experimental effects, such as sample absorption and multiple scattering, and normalized by the incident spectrum [4], using the program PDFgetN [17]. The data from ARCS were converted from scattering events as a function of TOF and detector position to histogrammed intensity as a function of d -spacing with bin sizes 0.0005 Å for $0.0625 \leq d \leq 0.25$ Å, 0.001 Å for $0.25 \leq d \leq 1.5$ Å, and 0.005 Å for $1.5 \leq d \leq 12.0$ Å using Distributed Data Analysis for Neutron Scattering Experiments (DANSE) software. Variable bin sizes were chosen because of the variation in resolution as a function of d -spacing. To get $S(Q)$, these data were minimally processed, using custom made programs to correct for the background parasitic scattering and to normalize by the incident spectrum only, without any other standard correction. This works because many of the corrections are the same for the sample and the vanadium standard and cancel during the normalization. We note that even with this coarse data treatment, it is possible to obtain useful structural information of reasonably high quality. A typical total scattering function of data collected at ARCS is shown in Figure 1(a), with the corresponding $F(Q)$ function from NPDF shown in Figure 1(b). The structure function from ARCS is accurate

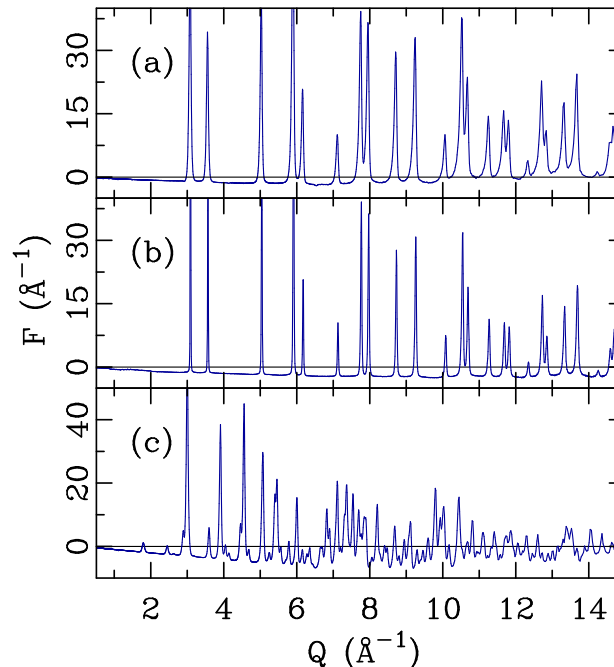


Figure 1. Total scattering function $F(Q)=Q[S(Q)-1]$ of Ni from data collected at (a) ARCS and (b) NPDF, and Al_2O_3 obtained from ARCS data (c). All data were collected at room temperature for 30 minutes.

and measured with good statistics though clearly of much lower resolution than that from NPDF. The total scattering function of Al_2O_3 data collected at ARCS is shown in Figure 1 (c).

The PDF, $G(r)$, is obtained from the structure function, $F(Q)$, by a Fourier transformation according to $G(r) = \frac{2}{\pi} \int_{Q_{min}}^{\infty} Q[S(Q) - 1] \sin Qr dQ$, where Q is the magnitude of the scattering vector and Q_{min} is a value of Q beyond the limit of the small angle scattering but below the limit of the lowest wide-angle scattering and $S(Q)$ is the properly corrected and normalized powder diffraction intensity [18]. The PDF gives the probability of finding an atom at a distance r away from another atom. The PDFs presented in this study were produced using various upper limits of integration in the Fourier transform, Q_{max} , as follows: Ni data $Q_{max} = 25.0 \text{ \AA}^{-1}$, Si data $Q_{max} = 20.5 \text{ \AA}^{-1}$, and Al_2O_3 data $Q_{max} = 35.0 \text{ \AA}^{-1}$. The upper Q -limits in these cases are dictated by factors such as signal to noise ratio, as well as by the imperfections at higher momentum transfers resulting from incomplete data processing procedures that were used.

Assessment of the structure information was carried out via refinements of the experimental PDFs, using the program PDFgui [5]. The details of the PDF method are provided elsewhere [4, 10].

3. Results and Discussion

Here we show the quality of PDFs that can be obtained from ARCS and compare them to PDFs from NPDF. Representative experimental PDFs of Si and Ni are shown in Figure 2 (open symbols), obtained using the same value of Q_{max} for both instruments. Simple visual comparison of the ARCS and the NPDF PDFs demonstrates that the ARCS data is of high quality. Furthermore, all ARCS datasets could be successfully refined. In Figure 2 fully converged structure models (solid lines) are plotted on top of the data. Standard structural models were used for Si ($Fd\bar{3}m$), and Ni ($Fm\bar{3}m$). The corresponding difference curves are shown offset for clarity.

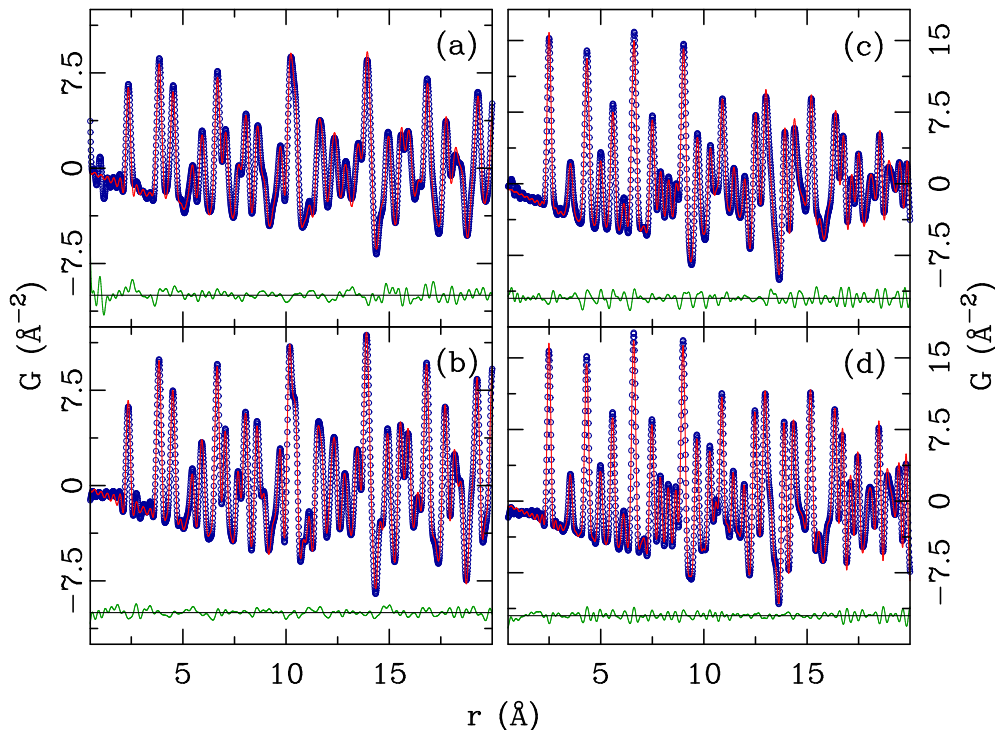


Figure 2. Experimental PDFs (open symbols), PDFgui fits of the structural models (solid lines) and corresponding difference curves (offset for clarity): (a) Si data collected at ARCS, (b) Si data collected at NPDF, (c) Ni data collected at ARCS, and (d) Ni data collected at NPDF. See text for details.

Refinements of Si, Figure 2(a) and (b), give lattice parameters of $5.4515(2)$ Å and $5.4361(2)$ Å, and U_{iso}^{Si} of $0.0086(6)$ Å² and $0.0060(7)$ Å² for ARCS and NPDF data respectively, with corresponding goodness of fit, r_W , of 0.120 and 0.086. The quantitative results for the other samples are reported elsewhere [3]. In PDF refinements the Q_{damp} parameter [5], which attenuates the PDF with increasing r , is the parameter that is most affected by the instrumental resolution. This parameter, as refined for the Ni standard, is markedly larger for ARCS ($0.046(11)$ Å⁻¹) than it is for NPDF data ($0.017(4)$ Å⁻¹) [3]. This is illustrated in Figure 3 where two datasets for Si, one from ARCS and the other from NPDF are plotted on top of each other over a wide range of r . The PDF from the ARCS data clearly damps out more quickly with increasing- r due to the lower resolution of these ARCS data. To emphasize this, a dashed line is shown that depicts the Gaussian envelope function that is multiplied with the model-PDF to simulate this effect in the calculated PDFs. However, a significant signal persists up to 60 Å, which is beyond the range over which most PDF refinements are carried out. This suggests that powder diffraction data from ARCS are quite appropriate for PDF analysis.

Interestingly, the PDF peak width in the ARCS data also appears to be larger than that for the NPDF data for the same Q_{max} used. This effect is known to appear when data have a Q -dependent peak broadening [19, 20] but appears to be particularly marked in these ARCS data. If it is not accounted for in the model, this results in an overestimate for atomic displacement parameters. It is also apparent that there exists a small but systematic offset of about $+0.01$ Å in the lattice parameters obtained from the refinement of ARCS data of both Si and Ni [3], compared to those obtained for NPDF data. This is presumably an artifact that comes about due to the inadequate TOF conversion used in our procedure. In a real experiment this is readily

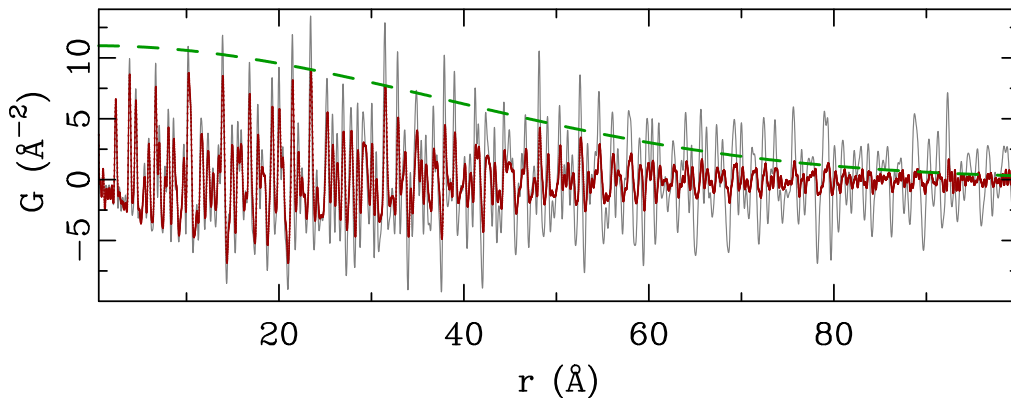


Figure 3. Comparison of experimental PDF data for Si 640c standard obtained at ARCS (red solid line) and NPDF (gray solid line) at room temperature, processed using the same value of Q_{max} . Thick dashed green line depicts the effect of diminishing PDF profile of ARCS data due to limited reciprocal space resolution.

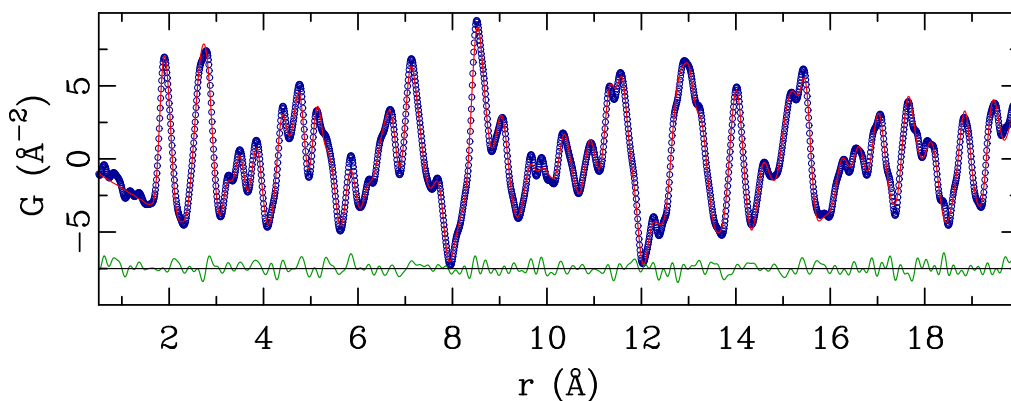


Figure 4. PDFgui fit of the Al_2O_3 structural model to ARCS data collected at room temperature. The data are shown as open symbols and the calculated curve as a solid line. Offset below is the difference curve.

corrected for using a calibration measurement such as carried out here.

In Figure 4 we show an example of a structural refinement to data from corundum Al_2O_3 , which has more structural parameters than the simple Ni and Si structures. The results [3] are in reasonable quantitative agreement with the literature values [21].

4. Summary

We have refined the first powder diffraction data from the ARCS chopper spectrometer instrument at the Spallation Neutron Source, operating in white-beam mode. The PDF data have been obtained and also refined using PDFgui. The refinements were compared to similar refinements from an established neutron powder diffractometer, NPDF at LANSCE. They yielded high quality fits and quantitatively reliable structural data, although some systematic offsets have been identified. Thus, we verify that high quality powder diffraction data, suitable also for nano-scale structure determination using the PDF, can be obtained from ARCS when used in white-beam mode without the Fermi chopper operating. This may be useful, for example, when it is desired to measure both structure and dynamics of a sample *in situ* without removing

it from the instrument. The ARCS Fermi chopper is able to be remotely removed from the beam to switch between white-beam diffraction and monochromatic dynamics measurements quickly.

Acknowledgements

We thank Thomas Proffen for providing standard data from NPDF that is used in this study. Work in the Billinge-group was supported by the Office of Science, U.S. Department of Energy, under contract no. DE-AC02-98CH10886. DANSE software was developed under NSF award DMR-0520547. This work has benefited from the use of NPDF at the Lujan Center at Los Alamos Neutron Science Center, funded by DOE Office of Basic Energy Sciences. Los Alamos National Laboratory is operated by Los Alamos National Security LLC under DOE Contract DE-AC52-06NA25396. The research at Oak Ridge National Laboratory's Spallation Neutron Source was sponsored by the Scientific User Facilities Division, Office of Basic Energy Sciences, U. S. Department of Energy.

References

- [1] Proffen T, Egami T, Billinge S J L, Cheetham A K, Louca D and Parise J B 2002 *Appl. Phys. A* **74** s163–s165
- [2] Williams W G, Ibberson R M, Day P and Enderby J E 1998 *Physica B* **241-243** 234–236
- [3] Božin E S, Juhás P, Zhou W, Stone M B, Abernathy D L, Huq A and Billinge S J L 2009 *J. Appl. Crystallogr.* In press. Preprint at arXiv:0903.1268v2
- [4] Egami T and Billinge S J L 2003 *Underneath the Bragg peaks: structural analysis of complex materials* (Oxford, England: Pergamon Press, Elsevier)
- [5] Farrow C L, Juhás P, Liu J W, Bryndin D, Božin E S, Bloch J, Proffen T and Billinge S J L 2007 *J. Phys: Condens. Mat.* **19** 335219
- [6] Rodriguez-Carvajal J 1990 *Abstracts of the Satellite Meeting on Powder Diffraction of the XV Congress of the IUCr, Toulouse, France*
- [7] Rodriguez-Carvajal J 1993 *Physica B* **192** 55–69
- [8] Larson A C and Von Dreele R B 2000 General structure analysis system report No. LAUR-86-748, Los Alamos National Laboratory, Los Alamos, NM 87545
- [9] Toby B H 2001 *J. Appl. Crystallogr.* **34** 201–213
- [10] Billinge S J L 2008 *Powder diffraction: theory and practice* ed Dinnebier R E and Billinge S J L (London, England: Royal Society of Chemistry) pp 464 – 493
- [11] E S Božin, Schmidt M, DeConinck A J, Paglia G, Mitchell J F, Chatterji T, Radaelli P G, Proffen T and Billinge S J L 2007 *Phys. Rev. Lett.* **98** 137203
- [12] Sundaram N, Jiang Y, Anderson I E, Belanger D P, Booth C H, Bridges F, Mitchell J F, Proffen T and Zheng H 2009 *Phys. Rev. Lett.* **102** 026401
- [13] Greedan J E, Gout D, Lozano A D, Derakhshan S, Th Proffen, H-J Kim, Božin E S and Billinge S J L 2009 *Phys. Rev. B* **79** 014427
- [14] Page K, Kolodiazhnyi T, Proffen T, Cheetham A K and Seshadri R 2008 *Phys. Rev. Lett.* **101** 205502
- [15] Kim Y, Cadars S, Shayib R, Proffen T, Feigerle C S, Chmelka B F and Seshadri R 2008 *Phys. Rev. B* **78** 195205
- [16] Mason T E, Abernathy D, Anderson I, Ankner J, Egami T, Ehlers G, Ekkebus A, Granroth G, Hagen M, Herwig K, Hodges J, Hoffmann C, Horak C, Horton L, Klose F, Larese J, Mesecar A, Myles D, Neufeind J, Ohl M, Tulk C, Wang X and Zhao J 2006 *Physica B* **385-395** 955–960
- [17] Peterson P F, Gutmann M, Proffen T and Billinge S J L 2000 *J. Appl. Crystallogr.* **33** 1192–1192
- [18] Farrow C L and Billinge S J L 2009 *Acta Crystallogr. A* **65** 232–239
- [19] Toby B H and Egami T 1992 *Acta Crystallogr. A* **48** 336–46
- [20] Qiu X, Božin E S, Juhás P, Proffen T and Billinge S J L 2004 *J. Appl. Crystallogr.* **37** 110–116
- [21] Lewis J, Schwarzenbach D and Flack H D 1982 *Acta Crystallogr.* **38** 733

Advances in Structural Studies of Materials Using Scattering Probes

Ashfia Huq, Richard Welberry, and Emil Bozin

Abstract

X-ray and neutron diffraction have been two key techniques for structural characterization of materials since their inception. If single crystals of the materials of interest cannot be synthesized, one has to resort to powder diffraction. This results in the loss of three-dimensional orientation information of the crystal, and one has to contend with the one-dimensional information that is inherent to powder diffraction, making it harder to analyze the data. The structural study of contemporary materials and their remarkable properties is a challenging problem, particularly when properties of interest result from interplay of multiple degrees of freedom. Very often these are associated with structural defects or relate to different length scales in a material. The signature of the defect-related phenomenon is visible as diffuse scattering in the diffraction pattern, and the signals associated with diffuse scattering are orders of magnitude smaller than Bragg scattering. Given these limitations, it is crucial to have high-resolution and high-intensity data along with the ability to carry out theoretical interpretation that goes beyond periodic lattice formalism of crystallography. Great advances have been achieved due to the advent of synchrotron and neutron sources, along with the availability of high-speed computational algorithms allowing materials scientists to work with a very small amount of sample (both single crystal and powder) and analyze vast amounts of data to unravel detailed structural descriptions that were not previously possible. This article presents some of these great advances in using scattering probes for materials characterization.

Introduction

Understanding and predicting properties of emerging complex functional materials requires detailed knowledge of their atomic-scale structure. Structure solution has traditionally been carried out using single-crystal analysis; only in the absence of single crystals were polycrystalline (powder) samples studied. However, with the emergence of powerful techniques to get quantitative structural information from powders, such as the Rietveld method (described in the next section), this trend is changing. Structural studies and refinement from powders are often the methods of choice and have had many successes in materials science. The powder method is especially powerful when employed for detailed parametric studies across rich

phase diagrams of materials, for *in situ* studies of chemical processes, or when observing materials in operation, often in special environments that would be difficult to implement for single-crystal experiments. Traditional crystallography has serious limitations for the structural study of nanoscale materials, primarily due to the presence of only a few Bragg reflections that crystallography relies on and the diffraction pattern being dominated by diffuse scattering features. In this case, a recent development, the total scattering approach, can be used. This utilizes both Bragg and diffuse scattering signals and yields information on different length scales, making it a versatile technique to study complex systems, such as heterogeneous bulk materials, nanoporous media, and nanometer-

size clusters such as nanoparticles, nanotubes, and nanorods. We are interested in defects and nanoscale substructures in bulk crystals. The greatest amount of information about the nanostructure can be obtained from a direct study of the single-crystal diffuse scattering. In this article, we will highlight some recent advances in materials characterization using advanced x-ray and neutron scattering sources and focus on powder diffraction, total scattering, and single-crystal diffuse scattering.

Rietveld Analysis and Structure Solution from X-Ray and Neutron Powder Diffraction

Many materials in technological applications are polycrystalline and are most appropriately studied in powder form. Rietveld¹ described a structure refinement method that, instead of using integrated intensities from individual peaks, applied a least squares method for full powder pattern matching. This revolutionized the field of structural characterization of materials using powder diffraction, as it allowed the user to handle the overlap problem inherent in a powder diffraction experiment and still extract useful quantitative structural information from materials of interest. Traditionally, powder diffraction techniques were used predominantly for phase identification and quantitative phase analysis. Rietveld refinement led to a much wider application of the technique to determine structures of complex oxides, zeolites, and small organic molecules. Recent advances in x-ray and neutron sources and optics deliver higher resolution and flux to a sample. Combined with rapid improvements in computing, this makes it possible to carry out real-time diffraction measurements, which allows us to access processes in seconds, combine stroboscopic techniques to study kinetics of structural changes on a microscopic level on time scales of microseconds, study materials under extreme conditions of temperature and pressure, and routinely determine crystal and magnetic structures of ever more complex systems. The following sections will highlight some of these advances in the field of x-ray and neutron powder diffraction.

Correlated Electron Materials

Powder diffraction has been an essential structural characterization tool for the study of strongly correlated electron materials, as often synthesis of single crystals of new materials is not possible. A primary example of this is the contribution made by Jorgensen et al., who published authoritative and highly cited papers²⁻⁴ on high T_c superconductors in the past 30 years.

Their seminal work on the structure of YBCO using neutron powder diffraction showed that the structure did not contain CuO_6 octahedra, as was expected. They were also the first to find phase separation in $\text{La}_2\text{CuO}_{4+\delta}$, which led to the hypothesis of the much-debated electronic phase segregation in high T_c superconductors. One of the more recent exciting developments in this field was the discovery of superconductivity in iron pnictides and iron chalcogenides.⁵ Based on our knowledge of BCS- (Bardeen, Cooper, and Schrieffer theory) and high T_c superconductors, it was thought that iron with its typical ferromagnetic properties is not compatible with superconductivity. While the first crystal structure analysis of the parent compound LaOFeP was carried out in 1995,⁶ two publications^{7,8} from Hosono's group at the Tokyo Institute of Technology pointed out that these compounds doped with F are superconductors with $T_c = 26$ K. The superconducting transition temperature for this family of compounds doubled within two months with other rare earth metal substitutions. Three other families with parental prototype 122 (BaFe_2As_2), 111 (LiFeAs), and 11 (FeSe) joined the original 1111 (LaFeAsO) compounds within six months. Neutron powder diffraction-probed structural and magnetic phase transitions of both the parent compound LaOFeAs and fluorine doped⁹ $\text{La}_{1-x}\text{F}_x\text{FeAs}$ were performed. These studies revealed that LaOFeAs undergoes an abrupt structural distortion below 155 K, changing the symmetry from tetragonal to monoclinic at low temperatures. At 137 K, it develops long-range spin density wave (SDW)-type antiferromagnetic order, with a small moment but simple magnetic structure. Doping the system with fluorine suppresses both the magnetic order and the structural distortion in favor of superconductivity. Neutron diffraction continues to play a significant role in understanding the structure and transport properties of this family of materials.

Neutron powder diffraction is the tool of choice to solve the magnetic structure of materials and has made invaluable contributions to spintronic materials.¹⁰ Representational analysis based on group-theory techniques aids greatly in the determination of magnetic structures. The incorporation of this tool into existing refinement programs¹¹ simplifies its use for the general users carrying out rigorous analysis of experimental data.¹² In addition, global optimization techniques, such as simulated annealing, allow the solution of complex magnetic structures with several inequivalent sites in the unit cell

and with low magnetic symmetry. For example, Chapon et al.^{13,14} first proposed the microscopic magnetoelectric coupling mechanism for YMn_2O_5 based on the in-plane magnetic structure determination (Figure 1). Recent advances in magnetic structure determination from neutron diffraction also can be found in Reference 15.

In Situ Time-Resolved Powder Diffraction

Materials are often employed under nonambient conditions. Powder diffraction is uniquely useful in studying such materials in realistic environments, making the *in situ* approach an ever-growing field in materials characterization. Early experiments to obtain kinetic insight into industrially relevant problems, such as the hydration of cement, were carried out at neutron sources.¹⁶ Large penetration depth and sensitivity to lighter elements, especially mobile species such as hydrogen and oxygen, in the presence of heavier elements make neutron diffraction an ideal tool to probe energy storage materials, catalysts, gas absorption phenomena, and other

chemical processes such as materials synthesis. However, the advent of synchrotron sources that are capable of producing x-rays with very high photon energies now allows penetration of x-rays through thick walls of stainless steel vessels, making it possible to mimic realistic reaction conditions to follow and obtain faster dynamic information, thus allowing diffraction studies of engineering materials.

For example, materials can be studied even as they undergo solid-state synthesis. In a recent publication,¹⁷ Readman et al. showed conclusively for the first time that cubic $\gamma\text{-ZrMo}_2\text{O}_8$, a negative thermal expansion material, can be synthesized directly from its constituent oxides. Prior to this work, it was assumed that the cubic phase of ZrMo_2O_8 is thermodynamically metastable at all temperatures. However, when using beamline ID11 at the European Synchrotron Radiation Facility (ESRF), the authors were able to show the route to synthesis of this material by full quantitative Rietveld analysis of the intermediate reaction products formed on time scales down to 0.1 seconds. In addition to this fast data

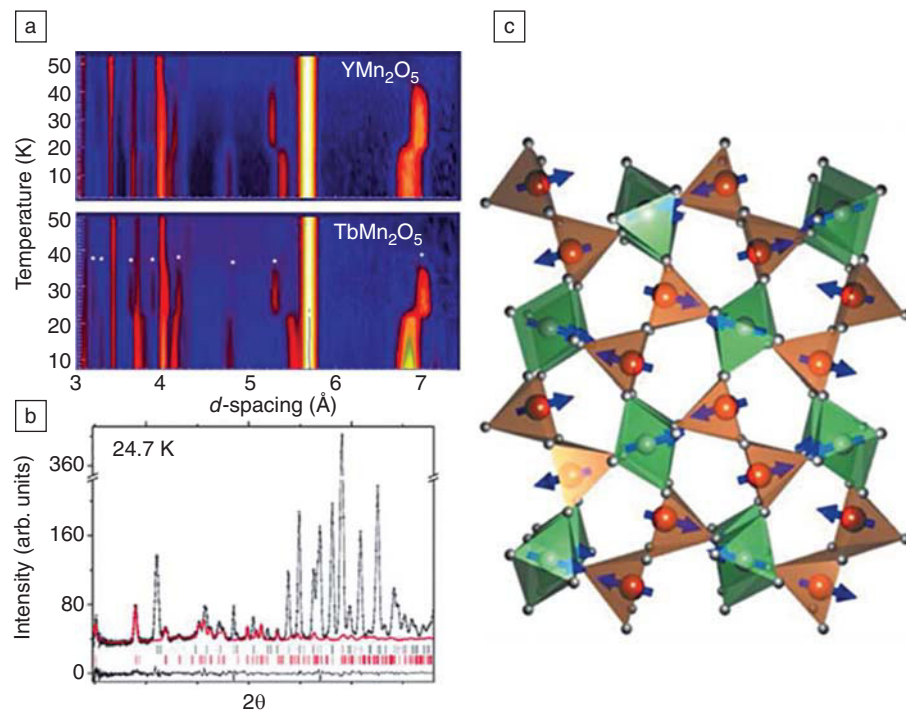


Figure 1. (a) Thermodiffractograms obtained with 1 K temperature steps from the multiferroic compounds YMn_2O_5 and TbMn_2O_5 obtained using the GEM neutron diffraction instrument. The diffraction intensities are color coded, with the brightest color corresponding to the highest intensity. Reprinted with permission from Reference 13. ©2008, IOP Publishing. (b) Powder diffractogram obtained on YMn_2O_5 in the ferroelectric commensurate magnetic phase. Rietveld refinement of the magnetic scattering shown as a red line, deduced from models obtained by a simulated annealing procedure. Reprinted with permission from Reference 14. ©2006, American Physical Society. (c) The in-plane magnetic arrangement of the Mn^{3+} and Mn^{4+} spins. Reprinted with permission from Reference 10. ©2009, Elsevier.

collection, a combination of techniques, such as thermo-gravimetric analysis, residual gas analysis, and powder diffraction, now allow a very attractive multi-probe approach to study the processes involved in solid-state synthesis.

In situ studies are also important in battery systems. When a battery is charged or discharged, the redox reactions change the molecular or crystalline structure of the electrode materials, often affecting their stability and reducing their lifetime. Recently, Nishimura et al. combined high-temperature powder neutron diffraction data and a maximum entropy method to reveal the first experimental evidence of a curved one-dimensional chain for lithium motion in the important battery cathode material LiFePO_4 .¹⁸ Figure 2 shows that the lithium distribution is along the [010] crystallographic direction.

X-ray and neutron powder diffraction contribute to our understanding of other energy materials also, such as hydrogen storage systems,^{19–24} where they shed light on the mechanisms of hydrogen absorption and desorption. A combined synchrotron and neutron diffraction study of a 2:1 mixture of lithium amide and magnesium hydride, a potential hydrogen storage material, revealed the formation of an unknown phase $\text{Li}_2\text{Mg}(\text{NH})_2$ during dehydrogenation (Figure 3).²¹ Various structural phase transitions of this material also were observed at elevated temperature (closer to the expected performance conditions).

These structures were determined using powder diffraction, and, based on the observation of disordering of Li, Mg, and cation vacancies, reaction pathways for hydrogen storage were elucidated.

Similar *in situ* studies also have helped reveal high-temperature thermal and chemical properties of fuel cell and membrane materials, such as $\text{Ba}_{0.5}\text{Sr}_{0.5}\text{Co}_{0.8}\text{Fe}_{0.2}\text{O}_{3-\delta}$ under realistic operation conditions of these cells.^{25,26} *In situ* time-resolved measurements also have been successfully used to carry out parametric studies of materials under varying temperature,^{27–29} pressure,^{30–32} and magnetic field^{33–35} to elucidate their physical and chemical properties under varying environments.

Stroboscopic Measurements

The discussion so far has been centered on *in situ* time-resolved measurements of processes, which are not necessarily reversible. In these cases, sufficient counting statistics are needed, and the time slice required for each diffractogram is determined by the amount of sample, its scattering power, complexity of structure, and x-ray/neutron flux available. Hence, the speed of the observed phenomenon must be comparable to the counting time. However, if the process of interest is reversible, which means that it can be reproducibly cycled, then it is possible to collect data with much better time resolution (i.e., the shortest possible time slice of the phenomenon to be observed by

using stroboscopy). The technique holds tremendous promise to study kinetic behaviors of systems such as spinodal decomposition in ionic crystals, stress-induced phase transition into the incommensurate phase of quartz,³⁶ or dynamic piezoelectric response in ferroelectric materials.³⁷

Ab Initio Structure Determination from Powder Diffraction

Single crystal x-ray diffraction is the most widely used and powerful technique for solving crystal structures; however, many materials of interest are available only as microcrystalline powders. Compared to about 40,000 structures/year solved from single crystal data, only 200/year are solved from powder data.³⁸ The information contained in a powder diffraction pattern is intrinsically more limited, since the three-dimensional intensity information of single-crystal diffraction data is compressed to one dimension. However, there is a significant interest in both basic science and commercial enterprise to be able to solve the structure of these materials, and great strides have been made in that field over the last decade. Classical methods, such as the Patterson method, and direct methods have more recently been joined by a maximum entropy approach, global optimization techniques such as simulated annealing, genetic algorithm, and the charge flipping approach. Several books have been published recently discussing the various

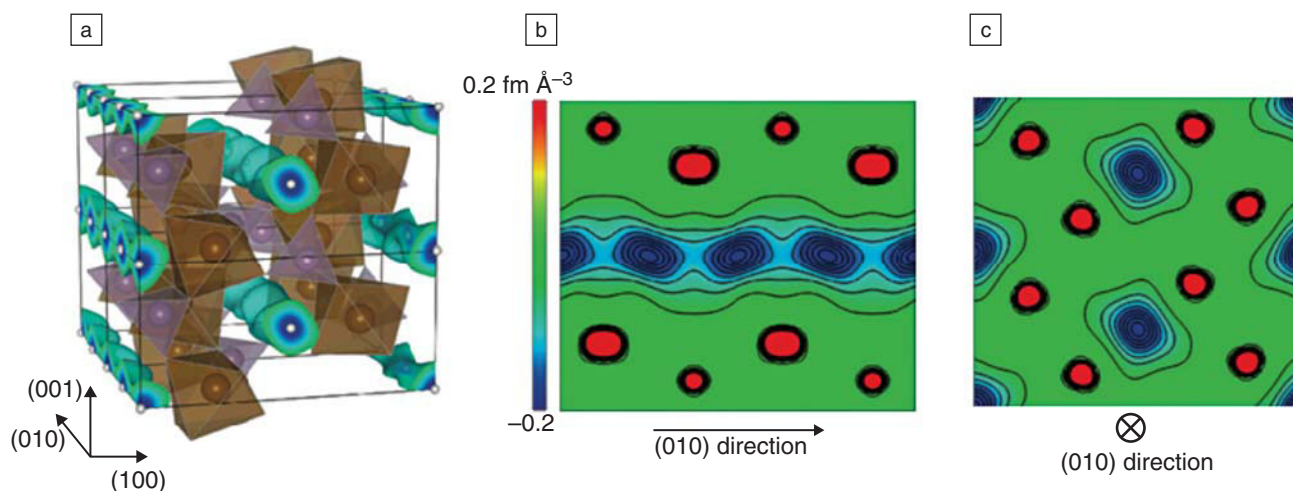


Figure 2. Nuclear distribution of lithium calculated by the maximum entropy method (MEM) using neutron powder diffraction data measured for $\text{Li}_{0.6}\text{FePO}_4$. The classical static atom models with harmonic vibration were no longer appropriate to describe the dynamic disorder of lithium in $\text{Li}_{0.6}\text{FePO}_4$ at 620 K; the MEM nuclear density distribution provided much information on the time and spatial average of the complicated dynamic disorder arising from lithium diffusion. (a) Three-dimensional Li nuclear density data, plotted as blue contours at which the coherent nuclear scattering density is $-0.15 \text{ fm } \text{\AA}^{-3}$. Brown octahedra represent FeO_6 , and the purple tetrahedra represent PO_4 units. (b) Two-dimensional contour map sliced on the (001) plane at $z = 0.5$. Lithium delocalizes along the curved one-dimensional chain along the [010] direction, whereas Fe, P, and O remain near their original positions. (c) Two-dimensional contour map sliced on the (010) plane at $y = 0$; all atoms remain near their original positions. Reprinted with permission from Reference 18. ©2008, Nature Publishing Group.

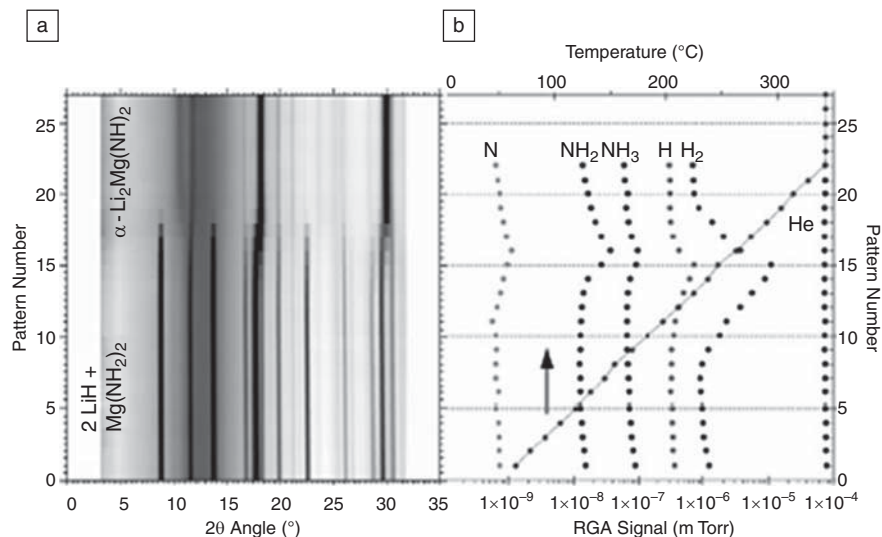


Figure 3. (a) *In situ* x-ray diffraction and (b) simultaneous residual gas analysis (RGA) of the evolved gases during the second heating of a mixture of $\text{Mg}(\text{NH}_2)_2 + 2\text{LiH}$ to form $\alpha\text{-Li}_2\text{Mg}(\text{NH})_2$. The y-axis shows how the pattern is changing with time as the material is getting heated, so a diffraction pattern is collected at a regular interval. Reprinted with permission from Reference 21. ©2008, Elsevier. The dark lines in (a) represent the Bragg lines as a function of heating, while the gases evolving due to the formation of new material are identified using an RGA in (b).

methodologies to solve complex structures from powder diffraction, and dedicated structure determination from powder diffraction software is now available for the general user.^{39–41} More recently, Oszlányi and Sütő presented a rather simple structure solution algorithm termed charge flipping.⁴² This method then was adopted for powder data by Baerlocher et al.⁴³ and other structure solution programs. This algorithm has been successfully used to determine various complex framework structures, such as zeolite catalyst SSZ-74.⁴⁴

Powder diffraction is extending its contributions even further from standard structural chemistry into molecular biology and medicine. The World Health Organization estimates that each year, 300–500 million cases of malaria occur, and more than one million die of the disease, especially in developing countries. Nevertheless, neither the mechanism by which the malaria parasite detoxifies and sequesters heme nor how current anti-malaria drugs work are well understood. The heme group released from the digestion of the hemoglobin of infected red blood cells forms insoluble aggregate materials known as β -hematin or malarial pigment. It was thought that these aggregates are polymers, and the action of chloroquine or other related drugs is to inhibit a proposed polymerization enzyme. However, Pagola et al.⁴⁵ determined the structure of β -hematin by using simulated annealing techniques from synchrotron x-ray data. It was established that these molecules do not form polymers but

dimers, which aggregate into chains through hydrogen bonding in the crystal. This observation is forcing researchers to rethink the mechanism by which current drugs work and possibly may help in the design of new ones.

Remarkably, powder diffraction is also having an effect in the complex world of protein crystallography. The first protein crystal structure determination from high-resolution x-ray powder diffraction data took place in 2000 by Von Dreele et al.⁴⁶ A molecular replacement method adapted for Rietveld refinement was used to refine this 1630-atom protein—a variant of T_3R_3 human insulin-zinc complex—by combining 7981 stereochemical restraints with a 4800 step synchrotron x-ray powder pattern. Since then, there have been many developments in experimental methods, software, and refinement strategies.⁴⁷

Total Scattering Approach and Atomic Pair Distribution Function Analysis

Atomic order of interest in emerging complex functional materials is often limited to the nanometer length scale, where crystallography, the basis of Rietveld refinement, fails.⁴⁸ In these cases, the total scattering approach can be used. This approach treats Bragg and diffuse scattering on an equal basis. In recent years, the analysis of the total scattering data has become an invaluable tool to study nanocrystalline, nanoporous, and disordered crystalline materials. As a Fourier

sine transform of the reduced total scattering structure function, $F(Q)$, where Q is the momentum transfer, the atomic pair distribution function (PDF), $G(r)$, where r is the interatomic distance, utilizes both Bragg and diffuse scattering and, hence, yields the direct-space information of atomic arrangements on various length scales.⁴⁹ With advances on the experimental and modeling software frontiers and their synergy, the applicability scope of the PDF method is extensive.

Nanocrystals

With reduction to nanometer size, materials exhibit novel or enhanced size-tunable properties compared to their bulk counterparts, with a broad range of promising applications such as nanosensors, biomedical imaging, optoelectronic devices, energy materials, and catalysts. In this domain, the presumption of a periodic solid, which is the basis of a crystallographic analysis, breaks down. Since the PDF probes atomic correlations independent of translational symmetry, it is well suited for nanoscale materials characterization. It allows access to a wealth of information: accurate determination of atomic-scale structure, homogeneous and inhomogeneous strain, structural defects, geometrical particle parameters such as diameter and shape, and core-shell structure assessment, important for understanding the fundamental mechanisms and processes in novel nanostructured materials. Appreciable effort has been made recently to accurately account for the finite size effects^{50,51} and enable modeling of the PDF for nanocrystalline materials.^{52–54} The rich level of detail that can be obtained from the PDF is summarized in a recent study of quantitative size-dependent structure and strain determination of CdSe nanoparticles with diameters ranging from 2 to 4 nm.⁵⁵ CdSe quantum dots are extensively studied nanostructures that have size-tunable properties and form a model system for investigating a wide range of nanoscale electronic, optical, optoelectronic, and chemical processes. Figure 4a shows a transmission electron microscopy (TEM) image of 2 nm CdSe nanoparticles, with the corresponding x-ray diffraction pattern exhibiting few broad features in the raw data, clearly insufficient for carrying out conventional Rietveld refinement. However, the reduced total scattering structure function, $F(Q) = Q(S(Q) - 1)$, which is the momentum transfer Q -weighted version of the diffraction pattern, where $S(Q)$ is total scattering structure function, amplifies the features at high values of Q that are nonobservable and provides means for utilizing this information for structural assessment. In Figure 4b and 4c, $F(Q)$ and $G(r)$ are

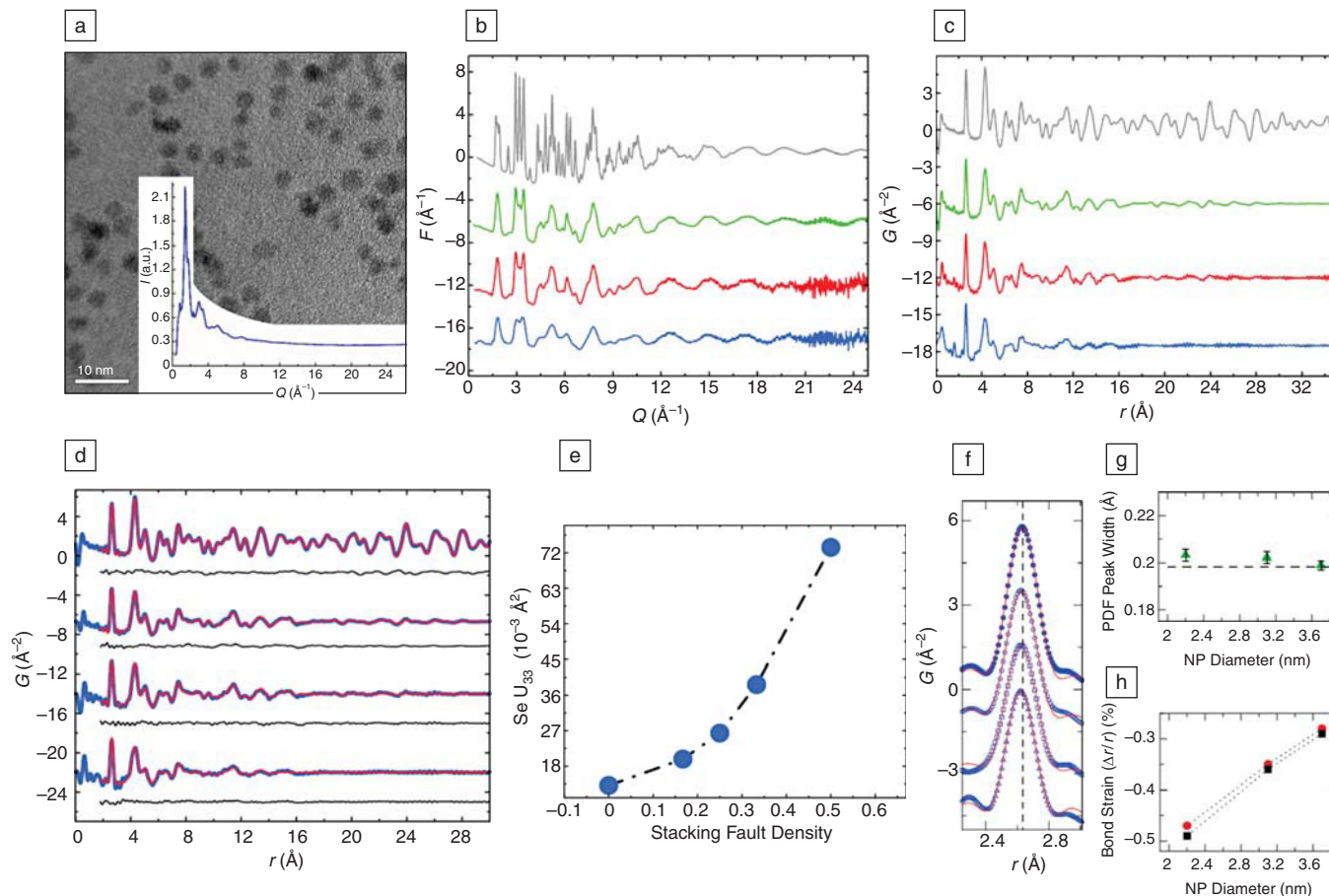


Figure 4. (a) Transmission electron microscopy image of 2-nm-diameter CdSe nanoparticles. Inset shows corresponding diffraction pattern featuring only a few broad intensity (I) peaks at low values of momentum transfer Q . (b) Reduced total scattering function $F(Q)$ for, from top to bottom, bulk, 4-nm, 3-nm, and 2-nm diameter CdSe, with (c) respective atomic pair distribution functions (PDFs) $G(r)$. (d) PDF data fitted with the wurtzite structure model incorporating appropriate stacking fault density. Corresponding difference curves are shown in black, offset below the data (blue) and model (red) curves. (e) The enlargement in the atomic displacement parameters along the z direction for Se site U_{33} as a function of the stacking fault density. (f) The first PDF peak with Gaussian fit for the sequence of samples as in (b). Dashed line represents the position of first PDF peak in the bulk data. (g) Inhomogeneous strain assessment from the first peak widths as a function of nanoparticle (NP) diameter.⁵⁵ (h) Homogeneous strain in Cd–Se bond ($\Delta r/r$) (%) as a function of NP diameter.⁵⁵

shown for bulk CdSe (top) and small CdSe nanoparticles of various sizes. The data in this form for these materials can be assessed and compared on an equal footing through a process of structural modeling using versatile and user-friendly modeling software such as PDFgui.⁵³ Using this, it was shown that the core structure of the measured CdSe nanoparticles can be described in terms of the wurtzite structure with extensive stacking faults (Figure 4d). The presence of stacking faults causes an anomalous increase of the atomic displacement parameters (ADPs) in the original wurtzite model. By assessing the enhancement of ADPs caused by various stacking fault densities using simulations, it was possible to come up with a calibration curve (Figure 4e) that enabled the density of faults in the nanoparticles to be estimated at $\sim 50\%$ level. The diameter of the nanoparticle core was

extracted directly from modeling the PDF data and is in good agreement with the diameter obtained from standard characterization methods (TEM, ultraviolet-visible absorption spectroscopy, and photoluminescence), suggesting that there is little surface amorphous region. The PDF also provides a means to assess inhomogeneous and homogeneous strain information from the width and position of the Cd–Se neighbor PDF peak (Figure 4f), respectively. The widths of the first PDF peaks remain comparably sharp as the nanoparticles get smaller (Figure 4g), indicating that there is little size-dependent inhomogeneous strain. However, the bond length of Cd–Se pairs shortens as the nanoparticle diameter decreases (Figure 4h), indicating the presence of a homogeneous compressive strain that is nanoparticle size dependent, being 0.5% with respect to bulk CdSe for the

2-nm-diameter particles. This study demonstrates the size-dependent quantitative structural information that can be obtained from very small nanoparticles using the PDF approach.

Rapid Acquisition PDF Measurements

Recent years have brought a particularly important breakthrough for application of the PDF approach, with utilization of an image-plate detector coupled with high-energy synchrotron x-ray radiation. This resulted in reducing the data collection time by at least four orders of magnitude in so-called rapid acquisition PDF setup, with access to a high Q range, excellent counting statistics, and highly reproducible data.⁵⁶ This not only enabled high data throughput experiments but also opened up new avenues for x-ray PDF studies of nano-sized

and bulk materials not possible before, such as *in situ*⁵⁷ and under extreme conditions.⁵⁸ While determination of the crystal structure using single-crystal or powder diffraction measurements at nonambient conditions is done routinely, PDF studies at high-pressure of material classes addressed here have been rather modest, since the pressure cells impose a number of compromises on the experiments, and since the diffuse scattering is inherently low intensity. Further advancements came with application of an amorphous silicon (a-Si)-based area detector with efficient readout capabilities, allowing for high-sensitivity and fast time-resolved PDF measurements.⁵⁹ The most compelling applications of the a-Si detectors lie in time-resolved measurements and parametric studies, rather than in static measurements under ambient conditions, enabling one to observe materials at work, such as determining the kinetics of chemical processes. This capability affects a broad class of problems in fields such as solid-state chemistry and catalysis. An impressive demonstration of this capability is given in a study of PtO₂ reduction.⁵¹ Data were collected during the *in situ* reduction of Pt^{IV}O₂ to metallic Pt⁰ at 473 K under hydrogen gas flow (4% in helium), using the maximum ultrafast readout mode of an a-Si detector (30 Hz). Data suitable for PDF analysis were obtained for each frame.

The 200 PDFs (Figure 5a) cover the reduction process from initiation to completion. While the intensity of the peaks in the PDF corresponding to Pt–O and Pt···Pt distances in Pt^{IV}O₂ (starting material) decrease from the initial values until indistinguishable from background over a six second period (Figure 5b), the peak corresponding to the nearest-neighbor Pt–Pt distance in the metallic Pt⁰ product appears and grows in intensity. Refinement of a face-centered cubic model to the experimental PDFs corresponding to the Pt⁰ product yielded fits with excellent agreement. The a-Si detector improves the relative ease, reliability, speed, and efficiency with which high-quality x-ray PDF data may be obtained, with resolutions matching those routinely achieved at spallation neutron sources.

Nanoporous Materials

High data throughput instruments enable measurements with excellent counting statistics, allowing weak scattering or dilute features to be investigated. This is particularly advantageous for differential PDF methods, through which relatively weak contributions to the total PDF (a few wt%), such as arising from adsorbed guest species, are studied. The

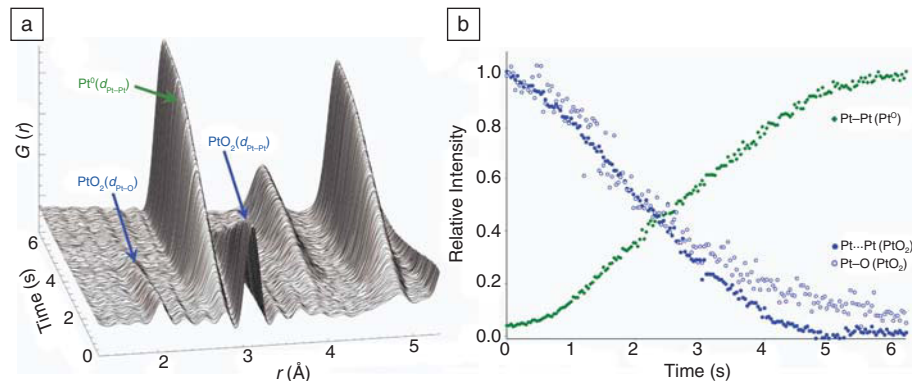


Figure 5. (a) A series of 200 pair distribution functions (PDFs) collected over a period of 6 s for the *in situ* reduction of Pt^{IV}O₂ to metallic Pt⁰ under hydrogen gas. (b) The relative PDF peak intensities corresponding to the Pt···Pt and Pt–O bond lengths in the starting material and product extracted from the PDFs obtained during this reaction.⁵⁷ *G*, atomic pair distribution function; *r*, interatomic distance.

problem of determining the structure of loaded nanoporous materials is often handled through either multiphase refinements or assessment of differential PDF.^{49,59,60} A typical experiment consists of two measurements, one on an empty and another on a loaded nanoporous material, where a difference is taken and studied. An example of using PDF to study porous coordination framework materials, capable of reversible H₂ sorption that is of current interest for potential mobile energy-storage applications, is given in the recent study of H₂-loaded Prussian blue analogue.⁶¹ This study made direct observation of adsorbed H₂-framework interactions in the nanoporous Mn^{II}₃[Co^{III}(CN)₆]₂, where the relative importance of accessible coordination sites and van der Waals interactions were addressed through differential x-ray and neutron pair distribution function analysis at 77 K. Figure 6a and 6b show the data for empty and loaded frameworks using x-ray and a neutron probe, respectively. Experimental differential PDFs are shown offset for clarity. Differential PDFs calculated for a model with a short-range binding interaction with Mn^{II} fail to reproduce the features in the experimental data (bottom of Figure 6c and 6d). This is particularly evident in the x-ray differential, which contains a large contribution from the H-metal correlations. On the other hand, calculated differentials based on a model consistent with van der Waals interactions, in which the guest H₂/D₂ is located at the center of the pore, (1/4,1/4,1/4), largely reproduce the observed peak positions and intensities of the x-ray and neutron differential PDFs. The capability of addressing this type of situation is of great importance for materials scientists.

Characterizing Short-Range Fluctuations in Bulk Materials

Finally, in bulk materials, the PDF allows assessment and comparison of structural information on different length scales from the same measurement. This is of particular importance for understanding properties of materials with a nanoscale structure that *differs* from crystallographic average. High data throughput neutron and x-ray total scattering measurements, coupled with new PDF modeling software capable of handling a large volume of data,⁵³ give an opportunity to study the structure of materials on variable length scales with an unprecedented level of detail. These studies include the evolution of local fluctuations across phase diagrams, allowing for important observations to be made systematically, consistently, and in “one go.” An example of one such case is given in a recent study of nanometer length-scale fluctuations in La_{1-x}Ca_xMnO₃ (Figure 7). This material exhibits an extremely rich phase diagram over a wide range of Ca concentration and temperature and is a host to the colossal magnetoresistance effect and metal-to-insulator phase transition at which material transforms from the ferromagnetic metallic (FM) to the paramagnetic insulating (PI) state on heating.⁶² Atomic PDF profiles, such as these shown in Figure 7a, reveal important local structural fluctuations. Although the average structure appears “regular” (Figure 7b), local fluctuations are present in the material that mark themselves in the Rietveld refinement through an unphysical increase of the ADPs (Figure 7c). The PDF approach provides insight into the nature of these fluctuations (Figure 7d), characterized by local distortions of MnO₆ octahedra that decrease

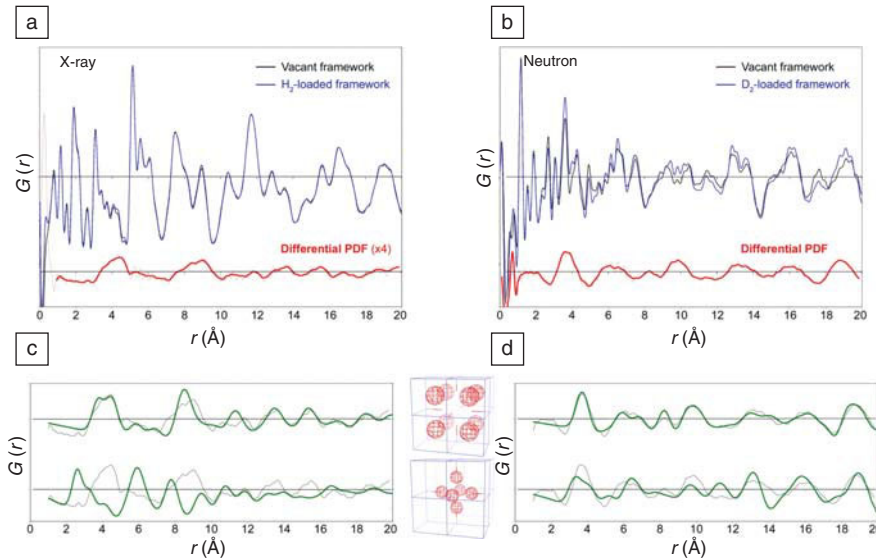


Figure 6. Direct observation of interactions between adsorbed H_2 and the nanoporous $\text{Mn}^{\text{II}}_3[\text{Co}^{\text{III}}(\text{CN})_6]_2$ framework host. The pair distribution functions (PDFs) for the (a) empty and H_2 -loaded or (b) D_2 -loaded Prussian blue analogue framework and the corresponding differential PDFs from the (a) x-ray and (b) neutron scattering data. The differentials, raw (dotted) and r -averaged over normalization ripples (continuous), are shown underneath. (c) Calculated x-ray and (d) neutron differential PDFs for models consistent with van der Waals interactions (top) and consistent with binding at the accessible Mn^{II} sites (bottom). The two models are depicted in the sketches between the panels (c) and (d). The experimental differentials (gray) are given for comparison.⁶¹

with increased Ca content in the insulating phase, rectifying an earlier understanding of the material and setting the limits for theoretical considerations. The synergy of high data throughput instruments and high-performance computing capabilities brings studies of local fluctuations in complex bulk materials to a new level.

Single-Crystal Diffuse Scattering

Although the pair distribution function provides rich information on nanoscale structures in bulk crystals, the information content is fundamentally limited by the extensive orientational averaging that takes place in the powder. If single crystals are available, the diffuse scattering can be analyzed directly, with both orientational and distance information unambiguously accessible, offering perhaps the most definitive means of elucidating the nanoscale structure.

Historically, the development of methods to interpret and analyze diffuse scattering has lagged well behind the development of conventional average structure determination. The reasons for this are that diffuse scattering intensities are much weaker than Bragg peaks, making the experimental observation vastly more demanding and time consuming. However, the advent of

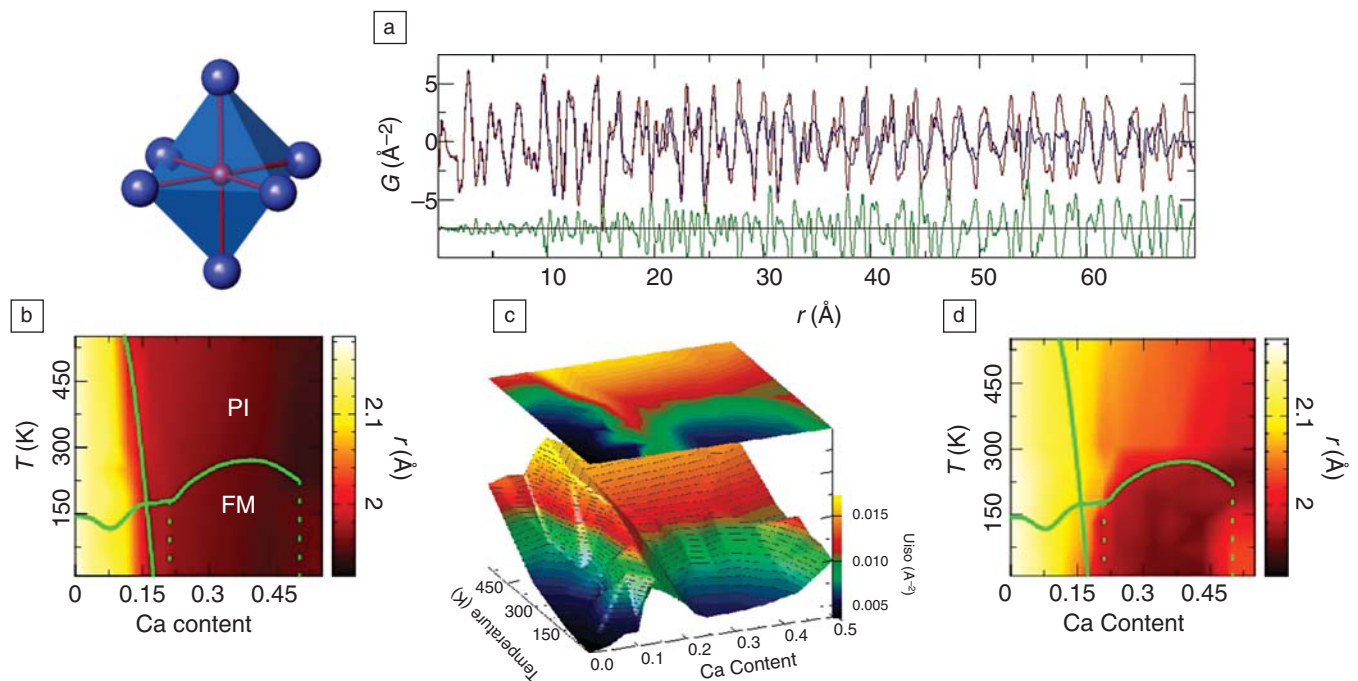


Figure 7. Jahn-Teller distortion of the MnO_6 octahedral unit, comprising four short and two long Mn–O bonds, making the unit irregular. (a) Experimental neutron pair distribution functions (PDFs) for 700 K (blue) and 750 K (red) bracing the orbital order-to-disorder Jahn-Teller transition that occurs at 720 K in LaMnO_3 . The difference curve (green) reveals that the distortion persists *locally* in the crystallographically undistorted high-temperature phase, and that structure over a ~ 1 nm length scale remains unchanged. Parametric evolution of (b) the length of the long Mn–O bond across the phase diagram of $\text{La}_{1-x}\text{Ca}_x\text{MnO}_3$, and (c) the atomic displacement parameters (U_{iso}) of general position oxygen from Rietveld refinement. (d) Parametric evolution of the length of the long Mn–O bond from short-range PDF refinement.⁶² PI, paramagnetic insulating phase; FM, ferromagnetic metallic phase.

intense synchrotron sources and various kinds of area detectors means that this aspect of the problem is largely solved, and it is now possible to obtain high-quality three-dimensional diffuse scattering data relatively routinely.^{63,64} The second reason is that the sheer diversity of different types of disorder that occur in nature has made it difficult to formulate a solution strategy that will work for all problems.

Although interpretation and analysis of diffuse scattering from single crystals remains a challenging problem, many advances have been made. In particular, the use of Monte Carlo (MC) computer simulations of a model structure has become a powerful and well-accepted technique for this purpose.⁶⁵⁻⁶⁸ The method consists of comparing diffraction patterns calculated from a computer model of the disordered structure with measured x-ray or neutron diffuse intensities. The advantage of the method is that it can be applied generally to all systems, regardless of their complexity or the magnitude of the atomic displacements that might be present. The only limitation is the extent to which the MC energy can be made to provide a realistic representation of the real system energy. At one extreme, a very simplified model may be useful in providing a qualitative demonstration of particular effects,⁶⁹ while at the other extreme, a quantitative and detailed description of a disordered structure can be obtained.⁷⁰

Some Theoretical Considerations
Intensity as a Function of Pair Correlations. Although Monte Carlo (MC) models may be used without any knowledge of basic diffraction theory, in building or formulating such models, it is important to recognize some basic properties of diffraction patterns that arise directly from the theory. First, and most importantly, remember that the diffracted intensity is the Fourier transform of the “pair correlation” function. For example, for a simple binary alloy, a general expression for the scattered intensity may be written,

$$I(\mathbf{k}) = \sum_m \sum_{m'} f_m f_{m'} \exp[i\mathbf{k} \cdot (\mathbf{r}_m + \mathbf{u}_m - \mathbf{r}_{m'} - \mathbf{u}_{m'})]. \quad (1)$$

This clearly shows that the summation is over all pairs of atoms m and m' in the crystal. These atoms have scattering factors f_m and $f_{m'}$, respectively. The reciprocal space vector is \mathbf{k} ; \mathbf{r}_m and $\mathbf{r}_{m'}$ are real space vectors defining the average sites of the atoms; and \mathbf{u}_m and $\mathbf{u}_{m'}$ are individual atomic displacements away from these average sites. In Equation 1, there is clearly no contribution from higher-body terms, such as triplets or quadruplets of atomic sites.

In some systems in which the basic MC potential is legitimately comprised of “pair interactions,” the correlation function, and hence the intensity, will clearly reflect these basic interactions. However, if multi-body interactions are important, they can still be used in the MC energy, but the scattered intensity will not bear any simple relationship to them. The intensity will, rather, reflect the pair correlations that have been induced by the application of the multi-body interaction. A striking example of this is shown in Figure 8.

Diffuse Components. A second important aspect of diffraction theory to consider when building or formulating MC models is to recognize that the scattered intensity can be expressed in terms of different components of intensity, which naturally arise when Equation 1 is expanded in terms of powers of the atomic displacements, \mathbf{u}_m .

$$I_{\text{total}} = I_0 + I_1 + I_2 \dots + \text{higher order terms} \quad (2)$$

I_0 is the so-called short-range order term and is not dependent on the displacements, \mathbf{u}_m . This term arises when there is

occupational disorder of the atomic sites of the average structure. I_1 is the size-effect term that takes into account that interatomic vectors, $\mathbf{r}_N = \mathbf{r}_m - \mathbf{r}_{m'}$, that are nominally of equal length in the average lattice, have different lengths depending on whether the vector joins sites occupied by A–A, A–B, B–A, or B–B. N in \mathbf{r}_N is a number identifying the vector between two different atom positions. This component includes all terms that are linear in the displacements \mathbf{u}_m . I_2 is the Huang scattering and first-order TDS (thermal diffuse scattering) component and includes all terms that are quadratic in the displacements \mathbf{u}_m . Huang scattering is the name given to the intensity around Bragg peaks that arises as a result of the strain fields induced by point defects in a lattice. The different components may be distinguished in a diffraction pattern, as they have different dependencies on the scattering vector $\mathbf{q} = 4\pi\sin(\theta)/\lambda$, where λ is the wavelength, and 2θ is the diffraction angle. Close to the origin, only I_0 is non-zero, while at progressively higher values of \mathbf{q} , other terms become increasingly important. Figure 9 shows an example

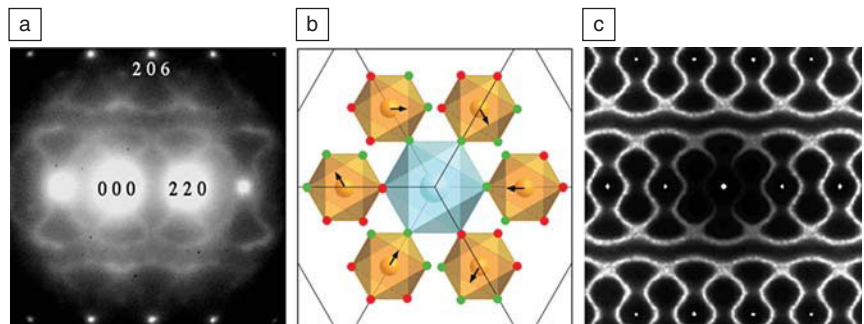


Figure 8. Diffuse scattering in $\text{K}_3\text{MoO}_3\text{F}_3$. (a) Observed electron diffraction pattern viewed down [331]. (b) Polyhedral representation of the structure. The displacements of the Mo ions within the six octahedra surrounding any K octahedron are subject to a six-body constraint. (c) Corresponding diffraction pattern calculated from Monte Carlo model using the multibody interactions only. Reprinted with permission from Reference 71. ©2003, Elsevier.

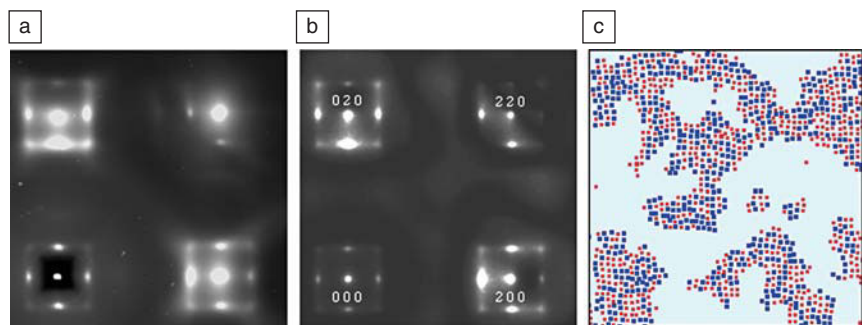


Figure 9. Diffuse x-ray scattering in wüstite, Fe_{1-x}O . (a) Observed x-ray pattern. (b) Pattern computed from a Monte Carlo model. (c) Small sample of the model showing the inhomogeneous distribution of defects. Reprinted with permission from Reference 72. ©1997, Springer.

where the effect of I_0 is clearly visible near the origin, while at higher q , the effect of I_1 , in particular, comes to dominate.

An important aspect of this separation into different components is that the even components, I_0 , I_2 , I_4 , consist of sums of terms involving cosines and so are functions that are always symmetric about the Bragg peak positions. Conversely, the odd components, I_1 , I_3 , I_5 , consist of sums of terms involving sines and hence are functions that are antisymmetric about the Bragg peak positions. Of particular importance is the size-effect term I_1 , the presence of which produces a marked and very characteristic asymmetry in the scattering patterns. Although this asymmetry was first noticed in powder diffraction profiles, the effects in three-dimensional diffuse scattering are distinctive and more informative. The degree of asymmetry allows the magnitude of the size effect to be determined along with the length and orientation of the vector along which it is acting.

Examples

The three examples given in this section have been chosen to illustrate the diverse range of diffuse scattering effects that are observed in materials. The examples also show that MC simulation of a model structure is a general method that can be used to interpret and analyze the observed data to give detailed information of the nanoscale structure.

Potassium Molybdenum Oxy-Fluoride, $K_3MoO_3F_3$. This is a prime example where the complex diffuse scattering patterns can

be modeled using multisite interactions alone. The MC model is simple and consists of two multisite chemical constraints. Around each Mo, there are six anion sites forming an octahedron. It is assumed that in each octahedron, there are 3O and 3F ions and, moreover, these occur in threes on opposite triangular faces. The Mo ions then are displaced away from the middle of the octahedron toward the 3O ions that would otherwise be very under bonded. Any single $(MoO_3F_3)^{3-}$ ion thus has a resulting dipole moment that is oriented in one of eight different directions (Figure 8b). The second simple constraint specifies that the net dipole of the six $(MoO_3F_3)^{3-}$ ions surrounding any potassium ion should be zero. This is all that is needed to reproduce the observed scattering. For further details, see References 66 and 71. It should be noted that a model *could* be constructed using pair interactions, but this would require many interactions and give little physical or chemical insight.

Non-Stoichiometric Oxide Wüstite, $Fe_{1-x}O$. The example of wüstite shown in Figure 9 is instructive. Around the origin of the diffraction pattern, as in Figure 9a, there is a motif of scattering comprising a weak diffuse square, with stronger elongated peaks at the centers of each side of the square and weaker peaks at the corners. These peaks are incommensurate with the basic FeO rock salt lattice, and their distance from the origin corresponds to the reciprocal of the spacing between defects. The same motif occurs around all other Bragg peaks, but now it is modified

by the size-effect terms that arise because of local relaxation of the basic FeO lattice around the defects. Each motif is now highly asymmetric, with the intensity of the low-angle side of the Bragg peaks much stronger than on the high-angle side. Figure 9b shows a corresponding pattern calculated from a MC model. This qualitatively reproduces all of the different effects observed in the x-ray data. Figure 9c shows a small representative portion of the distribution of defects from which Figure 9b was calculated. For further details on this system, see References 66 and 72.

Pentachloronitrobenzene, $C_6Cl_5NO_2$ (PCNB). PCNB is an example that shows diffuse scattering and requires for its understanding all three types of component: I_0 , I_1 , and I_2 . The basic disorder in this system derives from the fact that each molecular site in the crystal contains the molecule in one of six possible orientations. In the *average* structure, the six substituent sites around a benzene ring comprise 5/6 Cl and 1/6 NO_2 (i.e., the nitro group may occur in one of six positions). On average, the molecular planes lie perpendicular to the c -axis. When viewed down the c -axis (Figure 10a), the diffraction pattern shows broad regions of diffuse scattering that reflect the form of the short-range order term I_0 . In this section, the scattering around any given Bragg peak is symmetric, showing that the size effect is negligible. On the other hand, the view from a direction normal to the c -axis (Figure 10b) shows a series of

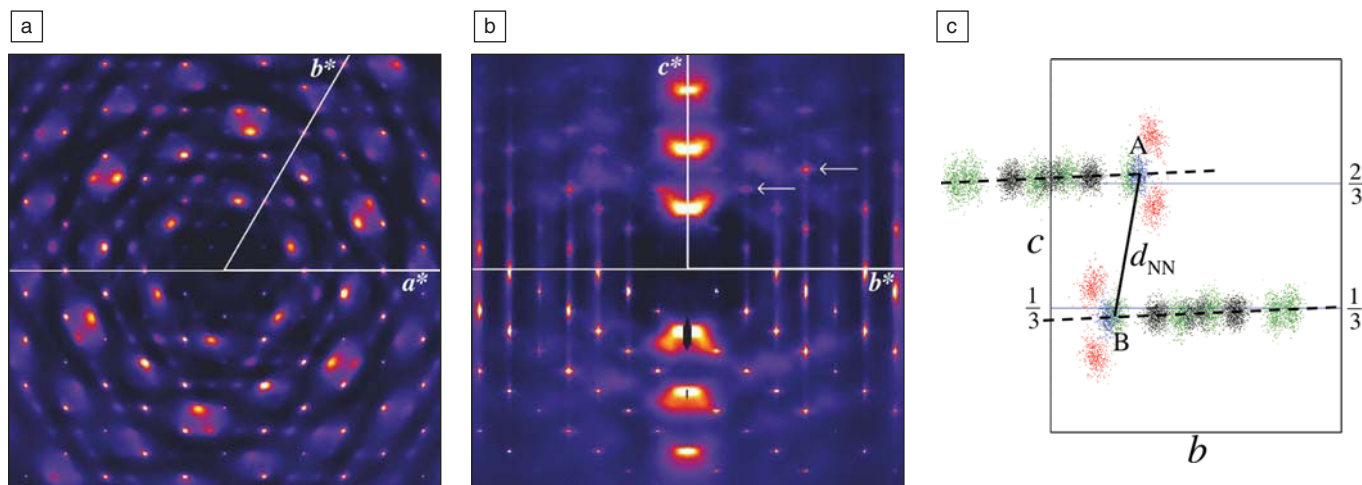


Figure 10. Diffuse x-ray scattering in pentachloronitrobenzene (PCNB). (a) $hk0$ section; asterisks indicate reciprocal lattice vectors. (b) Ok_l section. In (a) and (b), the lower half is observed x-ray data, and the top half is calculated from a Monte Carlo model. (c) Scatter plot of the atom positions in the Monte Carlo model for all unit cells in which the sites A and B are occupied by nitrogen. Note that d_{NN} , the nitrogen-nitrogen distance, is greater than the length of the average vector, resulting in a tilting of the molecular planes. Reprinted with permission from Reference 73. ©2007, Wiley.

strong diffuse peaks that are very asymmetric. This originates from a strong size effect that occurs whenever two molecules in neighboring layers have substituent sites in close proximity that both contain a nitro group. Figure 10c shows a scatter plot of the atom positions in the MC model for all unit cells in which the sites A and B are occupied by nitrogen. Note that d_{NN} , the nitrogen-nitrogen distance, is greater than the length of the average vector, resulting in a tilting of the molecular planes. A second distinctive feature of Figure 10b is the set of vertical rods of scattering that run along the columns of Bragg peaks. These derive from the I_2 component and are due to concerted lateral movements of the planes of molecules normal to the c -axis. For further details on this system, see Reference 73.

Summary

In this article, the advances that have been made in a range of scattering-based techniques have been described. Together these provide a powerful set of tools for materials characterization. Selected examples have been shown to illustrate the trends in development, the demands set by the complexity of the materials properties, and the impact on contemporary materials science.

Three main areas have been covered. The first of these is the use of Rietveld refinement in powder diffraction, including *ab initio* structure determination and the ability to perform time-resolved studies. Second is the use of total scattering via pair distributions function analysis, which has extended the range of materials that may be studied from conventional powder samples to nanoparticles, single crystals, and even amorphous materials. Last is the analysis of diffuse scattering from single crystals, which arguably offers the most definitive means of elucidating nanoscale structure with both orientational and distance information unambiguously accessible.

It is anticipated that the synergy of these highly complementary methods and analysis tools will play an increasingly important role in the future of materials science research. With the development of even brighter sources, better detectors, faster and more efficient computational resources, and analysis software tools, it will be possible to unravel finer detail from a wider range of materials.

Acknowledgments

A.H. acknowledges support by the U.S. Department of Energy (DE-AC05-000R22725) with UT-Battelle, LLC. R.W. gratefully acknowledges support of the


Australian Research Council and the Australian Partnership for Advanced Computing. E.B. acknowledges support by the U.S. Department of Energy (DE-AC02-98CH10886).

References

- H.M. Rietveld, *J. Appl. Crystallogr.* **2**, 65 (1969).
- J.D. Jorgensen, M.A. Beno, D.G. Hinks, L. Soderholm, R.L. Hitterman, J.D. Grace, I.K. Schuller, C.U. Segre, K. Zhang, M.S. Kleefisch, *Phys. Rev. B* **36**, 3608 (1987).
- J.D. Jorgensen, B.W. Veal, A.P. Paulikas, L.J. Nowicki, G.W. Crabtree, H. Claus, W.K. Kwok, *Phys. Rev. B* **41**, 1863 (1990).
- J.D. Jorgensen, H.B. Schuttler, D.G. Hinks, D.W. Capone, K. Zhang, M.B. Brodsky, D.J. Scalapino, *Phys. Rev. B* **58**, 1024 (1987).
- C. Day, *Physics Today* **62**, 36 (2009).
- B.I. Zimmer, W. Jeitschko, J.H. Albering, R. Glaum, M. Reehuis, *J. Alloys Compd.* **229**, 238 (1995).
- Y. Kamihara, H. Hiramatsu, M. Hirano, R. Kawamura, H. Yanagi, T. Kamiya, H. Hosono, *J. Am. Chem. Soc.* **128**, 10012 (2008).
- Y. Kamihara, T. Watanabe, M. Hirano, H. Hosono, *J. Am. Chem. Soc.* **130**, 3296 (2008).
- C. de la Cruz, Q. Huang, J.W. Lynn, J. Li, W. Ratcliff II, J.L. Zarestky, H.A. Mook, G.F. Chen, J.L. Luo, N.L. Wang, P. Dai, *Nature* **453**, 899 (2008).
- C.H. Marrows, L.C. Chapon, S. Langridge, *Mater. Today* **12**, 70 (2009).
- A.S. Wills, *Phys. B* **276**, 680 (2000).
- A. Poole, E. Lelievre-Berna, A.S. Wills, *Phys. B* **404**, 2535 (2009).
- P.G. Radaelli, L.C. Chapon, *J. Phys.: Condens. Matter* **20**, 434213 (2008).
- L.C. Chapon, P.G. Radaelli, G.R. Blake, S. Park, W.-W. Cheong, *Phys. Rev. Lett.* **96**, 097601 (2006).
- J. Rodriguez-Carvajal, *Phys. B* **192**, 55 (1993).
- A.N. Christensen, M.S. Lehmann, J. Pannetier, *J. Appl. Crystallogr.* **18**, 170 (1985).
- J.E. Readman, S.E. Lister, L. Peters, J. Wright, J.S.O. Evans, *J. Am. Chem. Soc.* **131**, 17560 (2009).
- S. Nishimura, G. Kobayashi, K. Ohoyama, R. Kanno, M. Yashima, A. Yamada, *Nat. Mater.* **7**, 707 (2008).
- H.W. Brinks, B.C. Hauback, P. Norby, H. Fjellvag, *J. Alloys Compd.* **351**, 222 (2003).
- U. Bosenberg, S. Doppiu, L. Mosegaard, G. Barkhordarian, N. Eigen, A. Borgschulte, T.R. Jensen, Y. Cerenius, O. Gutfleisch, T. Klassen, M. Dornheim, R. Bormann, *Acta Mater.* **55**, 3951 (2007).
- J. Rissenbeek, Y. Gao, J. Hanson, Q. Huang, C. Jones, B. Toby, *J. Alloys Compd.* **454**, 233 (2008).
- Z.T. Xiong, C.K. Yong, G.T. Wu, P. Chen, W. Shaw, A. Karkamkar, M.O. Jones, S.R. Johnson, P.P. Edwards, W.I.F. David, *Nat. Mater.* **7**, 138 (2008).
- A. Huq, J.W. Richardson, E.R. Maxey, D. Chandra, W.M. Chien, *J. Alloys Compd.* **436**, 256 (2007).
- E. Weidner, D.J. Bull, I.L. Shabalin, S.G. Keens, M.T.F. Telling, D.K. Ross, *Chem. Phys. Lett.* **444**, 76 (2007).
- S. McIntosh, J.F. Vente, W.G. Haije, D.H.A. Blank, H.J.M. Bouwmeester, *Chem. Mater.* **18**, 2187 (2006).

- Y. Li, E.R. Maxey, J.W. Richardson, *J. Am. Ceram. Soc.* **88**, 1244 (2005).
- R. Ali, M. Yashima, *J. Solid State Chem.* **178**, 2867 (2005).
- G.W. Stinton, J.S.O. Evans, *J. Appl. Crystallogr.* **40**, 87 (2007).
- W.I.F. David, J.S.O. Evans, A.W. Sleight, *Europhys. Lett.* **46**, 661 (1999).
- M. Ahart, M. Somayazulu, R.E. Cohen, P. Ganesh, P. Dera, H. Mao, R.J. Hemley, Y. Ren, P. Liermann, Z. Wu, *Nature* **451**, 31 (2008).
- C.G. Salzman, P.G. Radaelli, A. Hallbrucker, E. Mayer, J.L. Finney, *Science* **311**, 1758 (2006).
- Y. Ding, D. Haskel, Y. Tseng, E. Kaneshita, M. Veenendaal, J.F. Mitchell, S.V. Sinogeikin, V. Prakapenka, H. Mao, *Phys. Rev. Lett.* **102**, 237201 (2009).
- M. Kenzelmann, A.B. Harris, A. Aharony, O. Entin-Wohlman, T. Yildirim, Q. Huang, S. Park, G. Lawes, C. Broholm, N. Rogado, R.J. Cava, K.H. Kim, G. Jorge, A.P. Ramirez, *Phys. Rev. B* **74**, 014429 (2006).
- K. Koyama, K. Watanabe, T. Kanomata, R. Kainuma, K. Oikawa, K. Ishida, *Appl. Phys. Lett.* **88**, 132505 (2006).
- V.K. Pecharsky, Y. Mudryk, K.A. Gschneidner Jr., *Z. Kristallogr.* **26**, 139 (2007).
- G. Eckold, H. Gibhardt, D. Caspary, P. Elter, K. Elisbihani, *Z. Kristallogr.* **218**, 144 (2003).
- J.L. Jones, M. Hoffman, J.E. Daniels, A.J. Studer, *Appl. Phys. Lett.* **89**, 092901 (2006).
- A. Le Bail, L.M.D. Cranswick, K. Adil, A. Altomare, M. Avdeev, R. Cerny, C. Cuocci, C. Giacovazzo, I. Halasz, S.H. Lapidus, J.N. Louwen, A. Moliterni, L. Palatinus, R. Rizzi, E.C. Schilder, P.W. Stephens, K.H. Stone, J. van Mechelen, *Powder Diffr.* **24**, 254 (2009).
- W.I.F. David, K. Shankland, L.L. McCusker, Ch. Baerlocher, *Structure Determination from Powder Diffraction Data* (Oxford University Press, Oxford, UK, 2002).
- A. Clearfield, J.H. Reibenspies, N. Bhuvanesh, *Principles and Applications of Powder Diffraction* (Blackwell, Oxford, UK, 2008).
- R.E. Dinnebier, S.J.L. Billinge, *Powder Diffraction—Theory and Practice* (RSC, Cambridge, 2008).
- G. Oszlányi, A. Sütő, *Acta Crystallogr., Sect. A: Found. Crystallogr.* **60**, 134 (2004).
- Ch. Baerlocher, L.B. McCusker, L. Palatinus, *Z. Kristallogr.* **222**, 47 (2007).
- Ch. Baerlocher, D. Xie, L.B. McCusker, S.-J. Hwang, I.Y. Chan, K. Ong, A.W. Burton, S.I. Zones, *Nat. Mater.* **7**, 631 (2008).
- S. Pagola, P.W. Stephens, D.S. Bohle, A.D. Kosar, S.K. Madsen, *Nature* **404**, 307 (2000).
- R.B. Von Dreele, P.W. Stephens, G.D. Smith, R.H. Blessing, *Acta Crystallogr., Sect. D: Biol. Crystallogr.* **56**, 1549 (2000).
- I. Margiolaki, J.P. Wright, *Acta Crystallogr., Sect. A: Found. Crystallogr.* **64**, 169 (2007).
- S.J.L. Billinge, I. Levin, *Science* **316**, 561 (2007).
- T. Egami, S.J.L. Billinge, *Underneath the Bragg Peaks: Structural Analysis of Complex Materials* (Pergamon Press Elsevier, Oxford, UK, 2003).
- K. Kodama, S. Iikubo, T. Taguchi, S.-I. Shamoto, *Acta Crystallogr., Sect. A: Found. Crystallogr.* **62**, 444 (2006).
- V.I. Korsunskiy, R.B. Neder, A. Hofmann, S. Dembski, C. Graf, E. Rühlb, *J. Appl. Crystallogr.* **40**, 975 (2007).

52. P. Juhás, D.M. Cherba, P.M. Duxbury, W.F. Punch, S.J.L. Billinge, *Nature* **440**, 655 (2006).
53. C.L. Farrow, P. Juhas, J.W. Liu, D. Bryndin, E.S. Bozin, J. Bloch, Th. Proffen, S.J.L. Billinge, *J. Phys: Condens. Mater.* **19**, 335219 (2007).
54. C.L. Farrow, S.J.L. Billinge, *Acta Crystallogr., Sect. A: Found. Crystallogr.* **65**, 232, (2009).
55. A.S. Masadeh, E.S. Bozin, C.L. Farrow, G. Paglia, P. Juhas, S.J.L. Billinge, A. Karkamkar, M.G. Kanatzidis, *Phys. Rev. B* **76**, 115413 (2007).
56. P.J. Chupas, X. Qiu, J.C. Hanson, P.L. Lee, C.P. Grey, S.J.L. Billinge, *J. Appl. Crystallogr.* **36**, 1342 (2003).
57. P.J. Chupas, K.W. Chapman, P.L. Lee, *J. Appl. Crystallogr.* **40**, 463 (2007).
58. L. Ehm, S.M. Antao, J. Chen, D.R. Locke, F.M. Michel, C.D. Martin, T. Yu, J.B. Parise, P.L. Lee, P.J. Chupas, S.D. Shastri, Q. Guo, *Powder Diffr.* **22**, 108 (2007).
59. P. Armand, M.-L. Saboungi, D.L. Price, L. Iton, C. Cramer, M. Grimsditch, *Phys. Rev. Lett.* **79**, 2061 (1997).
60. M. Shatnawi, G. Paglia, J.L. Dye, K.C. Cram, M. Lefenfeld, S.J.L. Billinge, *J. Am. Chem. Soc.* **129**, 1386 (2007).
61. K.W. Chapman, P.J. Chupas, E.R. Maxey, J.W. Richardson, *Chem. Commun.* 4013 (2006).
62. E.S. Bozin, M. Schmidt, A.J. DeConinck, G. Paglia, J.F. Mitchell, T. Chatterji, P.G. Radaelli, Th. Proffen, S.J.L. Billinge, *Phys. Rev. Lett.* **98**, 137203 (2007).
63. T.R. Welberry, D.J. Goossens, A.P. Heerdegen, P.L. Lee, *Z. Kristallogr.* **222**, 1052 (2005).
64. E.J. Chan, T.R. Welberry, D.J. Goossens, A.P. Heerdegen, A.G. Beasley, P.J. Chupas, *Acta Crystallogr., Sect. B: Struct. Sci.* **65**, 382 (2009).
65. T.R. Welberry, B.D. Butler, *J. Appl. Crystallogr.* **27**, 205 (1994).
66. T.R. Welberry, *Diffuse X-ray Scattering and Models of Disorder*, IUCr Monographs on Crystallography (Oxford University Press, Oxford, UK, 2004).
67. T. Weber, H.-B. Bürgi, *Acta Crystallogr., Sect. A: Found. Crystallogr.* **58**, 526 (2002).
68. T. Weber, M.A. Estermann, H.-B. Bürgi, *Acta Crystallogr., Sect. B: Struct. Sci.* **57**, 579 (2001).
69. T.R. Welberry, *Acta Crystallogr., Sect. A: Found. Crystallogr.* **57**, 244 (2001).
70. T.R. Welberry, D.J. Goossens, A.J. Edwards, W.I.F. David, *Acta Crystallogr., Sect. A: Found. Crystallogr.* **57**, 101, (2001).
71. R.L. Withers, T.R. Welberry, F.J. Brink, L. Norén. *J. Solid State Chem.* **170**, 211 (2003).
72. T.R. Welberry, A.G. Christy, *Phys. Chem. Miner.* **24**, 24 (1997).
73. L.H. Thomas, T.R. Welberry, D.J. Goossens, A.P. Heerdegen, M.J. Gutmann, S.J. Teat, P.L. Lee, C.C. Wilson, J.M. Cole, *Acta Crystallogr., Sect. B: Struct. Sci.* **63**, 663 (2007). □



XIX International Materials Research Congress IMRC 2010
A joint meeting of the **Sociedad Mexicana de Materiales** and the **Materials Research Society**
August 15–19, 2010 • Cancun, Mexico • www.mrs.org/IMRC2010
For more information see page 541

High Resolution RBS

National Electrostatics Corporation has added Ångstrom level, High Resolution RBS to the RC43 Analysis System for nanotechnology applications. A single Pelletron instrument can now provide RBS, channeling RBS, microRBS, PIXE, ERDA, NRA, and HR-RBS capability, collecting up to four spectra simultaneously.

Pelletron accelerators are available with ion beam energies from below 1 MeV in to the 100 MeV region.

www.pelletron.com

Phone: 608-831-7600

E-mail: nec@pelletron.com

Full wafer version of the model RC43 analysis end station with High Resolution RBS Detector.

National Electrostatics Corp.



Nanoscale disorder and local electronic properties of $\text{CaCu}_3\text{Ti}_4\text{O}_{12}$: An integrated study of electron, neutron, and x-ray diffraction, x-ray absorption fine structure, and first-principles calculations

Jin-Cheng Zheng,¹ A. I. Frenkel,² L. Wu,¹ J. Hanson,¹ W. Ku,¹ E. S. Božin,^{1,3} S. J. L. Billinge,^{1,3} and Yimei Zhu^{1,*}

¹*Department of Condensed Matter Physics and Materials Science, Brookhaven National Laboratory, Upton, New York 11973, USA*

²*Physics Department, Yeshiva University, New York, New York 10016, USA*

³*Department of Applied Physics and Applied Mathematics, Columbia University, New York, New York 10027, USA*

(Received 17 October 2009; revised manuscript received 26 February 2010; published 29 April 2010)

We report a combined experimental and theoretical study of $\text{CaCu}_3\text{Ti}_4\text{O}_{12}$. Based on our experimental observations of nanoscale regions of Ca-Cu antisite defects in part of the structure, we carried out density-functional theory (DFT) calculations that suggest a possible electronic mechanism to explain the gigantic dielectric response in this material. The defects are evident in atomically resolved transmission electron microscopy measurements, with supporting evidence from a quantitative analysis of the electron diffraction and DFT which suggests that such defects are reasonable on energetic grounds. To establish the extent of the defects, bulk average measurements of the local structure were carried out: extended x-ray absorption fine structure (EXAFS), atomic pair-distribution function analysis of neutron powder-diffraction data, and single-crystal x-ray crystallography. The EXAFS data are consistent with the presence of the nanoclustered defects with an estimate of less than 10% of the sample being disordered while the neutron powder-diffraction experiments place an upper of $\sim 5\%$ on the proportion of the sample in the defective state. Because of the difficulty of quantifying nanoscale defects at such low levels, further work will be required to establish that this mechanism is operative in $\text{CaCu}_3\text{Ti}_4\text{O}_{12}$ but it presents a nontraditional plausible avenue for understanding colossal dielectric behavior.

DOI: [10.1103/PhysRevB.81.144203](https://doi.org/10.1103/PhysRevB.81.144203)

PACS number(s): 77.84.-s, 77.22.-d, 71.20.-b

I. INTRODUCTION

Extensive studies of perovskite $\text{CaCu}_3\text{Ti}_4\text{O}_{12}$ (CCTO) have been carried out in recent years due to its unusually high dielectric constant ($\epsilon_0 \sim 10^5$) in kilohertz radio-frequency region¹⁻³ across a wide range of temperatures (ϵ_0 remains almost constant between 100 and 600 K). Although high static dielectric constant was observed in many ferroelectric or relaxor materials, such as SrTiO_3 (Ref. 4) and other related perovskite compounds,⁵ such high dielectric constant is normally associated with a ferroelectric phase transition and is strongly temperature dependent. The temperature dependence of these dielectric properties significantly limits the application of the materials for wireless communication and microelectronic devices, therefore, there is significant technological interest in the development of new materials such as CCTO that exhibit a temperature-independent giant dielectric constant over a wide temperature range.

The intriguing dielectric properties of CCTO are not well understood. Density-functional theory- (DFT-) based calculations suggest that the dielectric constant of the ideal crystal should be about 40,⁶ which is at least four orders of magnitude smaller than that observed experimentally.¹⁻³ As a consequence, the intrinsic nature of the dielectric behavior of CCTO has been challenged and many extrinsic models have been proposed, based on percolating or nonpercolating conducting layers and internal barrier layer capacitance (IBLC).⁷ Such models might be plausible for polycrystalline materials which consist of a large number of grain boundaries that can act as either conducting or insulating layers for current to percolate. For single crystals, there exist no grain boundaries,

thus the IBLC mechanism has to be based on other planar defects, such as twin boundaries. From a crystallographic point of view, it is probable to have twins in CCTO, nevertheless, the long-expected twin domains have never been observed in any form of CCTO.⁸ Furthermore, in single crystal, sintered ceramic and thin films of CCTO, the type and density of the defects are very different,⁸ yet all show similar dielectric behavior, the origin of which has become a long-standing mystery.⁹

In this work, we report our study to shed light on the mechanism of the unusual dielectric properties of CCTO, by using advanced characterization tools which include transmission electron microscopy (TEM) [quantitative electron diffraction (QED) and high-resolution transmission electron microscopy (HRTEM) imaging], synchrotron x-ray diffraction (XRD), x-ray absorption near-edge structure (XANES), extended x-ray absorption fine structure (EXAFS), neutron powder diffraction and atomic pair-distribution function (PDF) analysis, and first-principles calculations based on DFT. From electron diffraction and HRTEM and EXAFS, we find significant indication for off-stoichiometric nanoscale regions containing Cu-Ca antisite defects existing within the stoichiometric ordered matrix of the single crystal. DFT calculations show that the ordered and disordered phases possess different local electronic properties, which we suggest gives rise to the huge dielectric response in the system. Single-crystal x-ray diffraction and powder neutron diffraction with PDF analysis provide place an upper bound on the quantity of the sample in this state of $\sim 5\%$. More work is required to establish that this mechanism is operative in CCTO, the electronic mechanism based on the presence of nanoscale regions of chemical disorder presents a different

approach to study the colossal dielectric-response property.

The rest of the paper is organized as follows. Description of methodology (i.e., experimental and theoretical methods) is given in Sec. II with the results presented in Sec. III. Discussions on the possible origin of the unusual dielectric response in CCTO based on our analyses are presented in Sec. IV with a brief summary being presented in Sec. V.

II. METHODS

Large single crystals of CCTO were made by S. Wakimoto of University of Toronto. The crystals were grown by the travelling-solvent floating-zone method in an image furnace. Details of the crystal growth have been published previously.³ The same crystals were studied previously by neutron scattering and optical conductivity.³ The size of the crystal rods for neutron scattering was about 1 cm with a diameter of about 3 mm and the size of the crystals for the optical inferred measurement about a 3 mm disks with 1 mm in thickness. The crystals used for the present study of TEM, XRD, and EXAFS, were cut from the large crystal batch.

A. Quantitative electron diffraction and imaging

The electron microscopy study including high-resolution imaging and quantitative diffraction was carried out using a 300 kV field-emission microscope with a postcolumn energy filter and a 200 kV aberration-corrected microscope with an in-column filter at Brookhaven National Laboratory (BNL). All images were recorded on a 14-bit charge-coupled device camera while diffraction data were on 20-bit imaging plates to improve the dynamic range of diffraction-intensity acquisition. TEM samples were prepared using a standard procedure, consisting of mechanical slicing, polishing, dimpling, and thinning. The final stage of the thinning involves 5 kV Ar-ion milling (Fischione Instrument) at 10° glancing angle and liquid nitrogen temperature. Extreme care was taken to avoid any damage during the sample preparation process.

Electron imaging covered a wide magnification range from $1000\times$ to $2\,000\,000\times$. Low magnification was mainly used to search for areas of interest, including defects and domain interfaces. Two-beam diffraction conditions were used for image contrast analysis. High magnifications ($200\,000\times$ and above) were used to retrieve local structural information, such as local symmetry and atomic disorder, based on many-beam phase-contrast theory. Qualitative and quantitative image analyses were assisted with high-resolution image simulation using BNL computer codes based on multislice algorithms.

To understand the bonding characteristics and valence-electron distribution in CCTO, a unique quantitative electron-diffraction approach, the paralleling recording of dark-field images (PARODI) method,^{10–14} was used to accurately measure the structure factors of low-order reflections. The measurement is model independent. In the PARODI setting, we focus the incident electron beam above the sample, rather than on the sample as in conventional converged beam electron diffraction (cCBED),^{15,16} thus illuminating an area of tens to hundreds of nanometers in diameter and generating

a disk pattern of Bragg reflections. The intensity oscillation in each reflection, also called Pendellösung fringes or shadow images, reflects the change in incident-beam direction as well as thickness variation in the illuminated area.

The low-order structure factors were determined through a refinement procedure by comparing experiment with calculation based on Bloch-wave dynamic diffraction theory. The initial calculations usually start from electron structure factors (ESFs) of the procrystals [i.e., a hypothetical crystal with atoms having the electron distribution of free atoms; also so-called independent atom model (IAM)]. Then iterative calculations were carried out by adjusting values of structure factors until the difference between calculated and experimental patterns reaches minimum. To ensure that this minimum is not a saddle local minimum, we tested it by selecting several different starting points and recalculating structure factors iteratively until we reach the same lowest minimum. The structure factors obtained in this way are regarded as *measured* structure factors.

Although PARODI is more technically demanding than cCBED, there are several advantages^{10–14} of using PARODI method for crystals with a large unit cell (as the case of CCTO): (1) many reflections can be recorded simultaneously, ensuring the same condition of the exposure and the crystallographic direction of the incident beam for all reflections; (2) the defocused beam minimizes possible radiation damage in comparison with cCBED; and (3) due to the strong dynamical coupling of the different diffracted beams, the data points in each reflection obtained from different thicknesses of the illuminated area are independent data sets, thus the ratio of the number of observations vs the number of variables is dramatically increased and the reliability of refinement process is enhanced subsequently. In the present study of CCTO, the electron-diffraction measurements were carried out at 90 K using a Gatan liquid N₂ holder as well as at room temperature (RT).

B. Synchrotron x-ray diffraction

The singly-crystal XRD was performed at beam line X7B at the National Synchrotron Light Source (NSLS), BNL. The wavelength ($\lambda=0.9222\text{ \AA}$) was determined by the powder pattern of LaB₆, and other instrument parameters were determined using the program FIT2D.¹⁷ A high-quality whisker (see below) with an estimated size of $0.05\times 0.02\times 0.05\text{ mm}$ was cut from a large single-crystal piece of CCTO, then mounted on the end of a glass fiber with 5 min epoxy. The data were collected with a MAR345 image-plate detector. A set of different hemispheres of data were collected with different scan rates and scan ranges to obtain the largest possible range of intensities. The minimum d spacing was 0.92 \AA (maximum q of 6.82). The intensities were extracted and merged from the image-plate data with the program suite HKL.¹⁸ An additional oblique incidence correction was applied.¹⁸ The traditional refinement was carried out with the SHELXTL program.¹⁹

Similar to the electron diffraction, the XRD experiments were also carried out at both room temperature and 90 K, using an Oxford Cryo-cooler system. The lattice parameters,

temperature factors, and atomic coordinates, and *A*-site disorder were refined. To obtain the best structure factors for the structure, we selected a crystal which had sharp spots and which had almost no diffraction that could not be attributed to a single crystal. However, several samples were rejected which had diffraction spots from multiple crystals and even powderlike rings. The process of “selecting” a good crystal for single-crystal diffraction study may preclude selecting a crystal which exhibits the defects observed from much smaller samples such as those with TEM or powder diffraction.

Electrons and x rays are complementary probes. Since x rays see total electron density in crystals, it is difficult for x rays to distinguish valence and core electrons if the number of core electrons is large. Stevens and Coppens proposed a simple suitability criterion²⁰ for charge-density analyses using x ray, $S = V/\Sigma n^2 \gg 5 \sim 0.1 \text{ \AA}^3 e^{-2}$, where V is the volume of the unit cell and n is the number of core electrons. For CCTO, $V = 402 \text{ \AA}^3$, $\Sigma n^2 = 5280e^2$, $S = 0.08 \text{ \AA}^3 e^{-2}$, which is much smaller than the typical values suitable for charge-density study using x rays. Thus, x rays may be extremely useful to retrieve the basic structure of CCTO, it may not be the best method for studying its bonding characteristics and charge-density distributions. In addition, the proposed disorder of the Ca and Cu cations (see below) and the limited range of data we acquired would normally restrict the interpretation of the valence-electron distribution.

On the other hand, incident electrons interact with electrostatic potential, thus at small scattering angle they are more sensitive to valence-electron distribution than x rays due to the near cancellation of the scattering from the positive nucleus and negative electron charges.²¹ Nevertheless, due to high energy of the incident electrons we use, usually only very limited low-index reflections ($\sin \theta/\lambda < 0.6 \text{ \AA}^{-1}$) can be recorded with sufficient quality. We thus took the advantage of the *complementarity* of electrons and x rays by combining the measured structure factor of low-order reflections from electron diffraction and high-order reflections from x-ray diffraction as a full data set. Multipole refinement model of Hansen and Coppens²² were then used to refine the measured structure factors for charge-density analysis via computer codes of VALRAY (Ref. 23),

$$\rho_{\text{atomic}}(\mathbf{r}) = P_{\text{core}}\rho_{\text{core}}(r) + P_{\text{val}}\kappa^3\rho_{\text{val}}(\kappa r) + \sum_{l=1}^{l_{\text{max}}} \alpha^3 R_l(\alpha r) \sum_{m=1}^l P_{lm\pm} Y_{lm\pm}(\theta, \phi), \quad (1)$$

where $\rho_{\text{core}}(r)$ and $\rho_{\text{val}}(r)$ are the spherical atomic core charge density and spherical valence charge density (monopole), respectively. P_{core} and $\rho_{\text{val}}(r)$ are the electron population of core and valence parts. The last term is the multipole contribution. The Roothaan-Hartree-Fock atomic wave functions²⁴ were used to describe the core and valence charge densities of isolated atoms.

C. X-ray absorption spectroscopy: XANES and EXAFS

X-ray spectroscopy measurements (both the XANES and the EXAFS), were carried out to probe the local structure

and electronic properties of the CCTO powder grounded from the same single crystal that was used in other measurements described here. The details of the techniques using these x-ray spectroscopy methods to study local structure of materials can be found in Refs. 25–32. XANES experiments (beamline X11A at NSLS) were mainly focused on the Ti *K* edge to examine its possible off-center displacement while the EXAFS data were collected for all three cations (*K* edge of Cu, Ti at beamline X11A and Ca at beamline X15B, NSLS) to measure the cation short-range order. The EXAFS spectra were analyzed concurrently for all three edges by using UWXAFS package³³ that implements multiple data set refinement with a nonlinear least square fit of FEFF6 theory³⁴ to the data. All coordination numbers between the Ti, Cu, and Ca central atoms and their nearest neighbors, their bond lengths and the mean-squared disorder in the bond lengths were varied in the fit.

One of the unique advantages of EXAFS study is its sensitivity to the local coordination numbers of nearest neighbors and, therefore, short-range order of alloys, which can be analyzed with equal facility for ordered and disordered structures. Several constraints described below were applied to unlike pairs (Cu-Ca, Ti-Ca, and Ti-Cu) to minimize uncertainties in the best-fit values of the structural parameters and increase confidence in the results.³⁵ In CCTO, the coordination numbers of Ti-Cu and Ti-Ca bonds, $N_{\text{Ti-Cu}}$ and $N_{\text{Ti-Ca}}$, do not depend on the degree or randomness of the distribution of Cu and Ca in the *I3m* lattice because the total numbers of these bonds in the sample must be in the ratio defined by a 3:1 stoichiometry, even if there are macroscopic compositional fluctuations. Thus, $N_{\text{Ti-Cu}}$ and $N_{\text{Ti-Ca}}$ were fixed in the fits to 6 and 2, respectively. Furthermore, Ti is a common atom in the titanate perovskite ATiO_3 lattice, and each *A* atom (i.e., Cu or Ca) must have eight Ti neighbors. Thus, the coordination numbers $N_{\text{Cu-Ti}}$ and $N_{\text{Ca-Ti}}$ were fixed to 8. There are two Cu-Ca bonds and four Cu-Cu bonds per Cu atom, i.e., $N_{\text{Cu-Ca}} : N_{\text{Cu-Cu}} = 1:2$ in the *Im* $\bar{3}$ structure. However, if the Ca and Cu atoms occupied their sites randomly, with the probabilities $\alpha_{\text{Ca}} = 0.25$ and $\alpha_{\text{Cu}} = 0.75$ (i.e., $N_{\text{Cu-Ca}} : N_{\text{Cu-Cu}} = 1:3$), then the average numbers of Cu-Ca and Cu-Cu bonds would be $N_{\text{Cu-Ca}} = 1.5$ and $N_{\text{Cu-Cu}} = 4.5$ (since the second-nearest-neighbor coordination number of Cu must remain 6 in both cases). Thus, $N_{\text{Cu-Ca}} = 2$ corresponds to the ideal ordered $\text{CaCu}_3\text{Ti}_4\text{O}_{12}$ system, and $N_{\text{Cu-Ca}} = 1.5$ to the random alloy ($\text{Ca}_{0.25}\text{Cu}_{0.75}\text{TiO}_3$). Analogously, for Ca, in the ideal system the coordination numbers should be $N_{\text{Ca-Cu}} = 6$ and $N_{\text{Ca-Ca}} = 0$. In the random alloy, they should be 4.5 and 1.5, respectively. EXAFS measurement is sensitive to the variation in coordination numbers within such limits, and, using careful analysis employing multiple-edge, multiple data-set refinement, one can resolve between different possible models of short-range order in alloys.^{27,30,35–37} Fits were also made using a model with no antisite defects for comparison.

As a result of all constraints applied to the structural variables in our EXAFS analysis, and performing concurrent refinement of the Cu *K*-, Ca *K*-, and Ti *K*-edge data, we had the total of 43 relevant independent data points and as few as 18 adjustable parameters in the fits.

D. Neutron powder diffraction and atomic pair-distribution function measurements

To search for further evidence of cation sublattice disorder as a bulk effect, we considered neutron powder-diffraction data, applying a PDF analysis to the data. CCTO has been the subject of a number of structural studies.^{2,38–45} We therefore refined various models incorporating antisite defects similar to those observed in TEM and EXAFS measurements⁴⁶ against the existing data that were reported in Ref. 9. These are time-of-flight neutron powder-diffraction data collected at the Special Environment Powder Diffractometer (SEPD) at the Intense Pulsed Neutron Source (IPNS) at Argonne National Laboratory. The data were subsequently analyzed by Fourier transformation and atomic PDF analysis. Details of the data collection and analysis can be found in Ref. 9.

The strength of the PDF technique is that it takes into account both Bragg and diffuse scattering, and yields structural information on both long-range order and local structural disorder in materials. The PDF function $G(r)$ gives the number of atoms in a spherical shell of unit thickness at a distance r from a reference atom. It peaks at characteristic distances separating pairs of atoms and thus reflects the atomic structure.⁴⁷ Structural information is obtained from the PDF data through a modeling procedure similar to the traditional reciprocal-space-based Rietveld method.⁴⁸ However, it is carried out in real space and yields the local structure rather than the average crystal structure.⁴⁷ From the refinements, different structural information can be extracted, such as lattice parameters, average atomic positions and amplitudes of their thermal motion, atomic displacements, site occupancies, and magnitudes of local octahedral tilts. The PDF analysis reported here involves structural modeling using the program PDFGUL.⁴⁹ In cases where the average and local structure are the same (i.e., well-ordered crystals), the structural parameters obtained from Rietveld and PDF analysis are the same.⁵⁰ However, when the local structure deviates from the average structure the parameters from the PDF will reflect the local structure and the Rietveld parameters the periodically averaged values.

We focused on neutron-diffraction data because there is more contrast between the Ca ($b_{\text{Ca}}=4.70$ fm) and Cu ($b_{\text{Cu}}=7.718$ fm) scattering lengths than with x rays ($f_{\text{Ca}}=20$ and $f_{\text{Cu}}=29$, respectively). Replacing Cu on Ca sites and vice versa has the effect of changing the integrated intensity of peaks in the PDF associated with those positions, though the effects can be small.⁵¹ The antisite defects will also result in displacive disorder of oxygen ions surrounding these sites so enlarged oxygen atomic displacement parameters (ADPs), (and to a lesser extent enlarged cation ADPs) would be consistent with the presence of such disorder.

E. First-principles calculations

The first-principles calculations were based on DFT.⁵² We used both full potential and pseudopotential methods to calculate the structural, electronic, and magnetic properties of stoichiometric and off-stoichiometric (Ca-rich or Cu-rich) CCTO. For the pseudopotential calculations, we used the

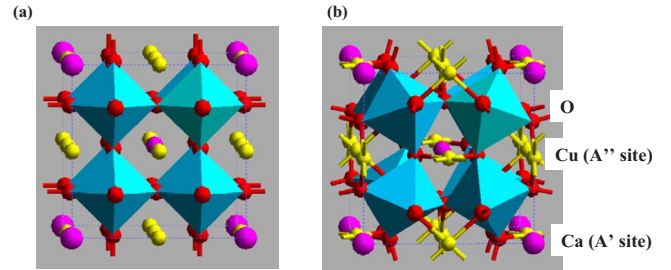


FIG. 1. (Color online) Structural model of CCTO. (a) Ideal perovskite structure and (b) with TiO_6 octahedra tilted.

SIESTA code⁵³ that is a fully self-consistent DFT method based on a linear combination of an atomic orbitals basis set with linear scaling. For full-potential calculations, we employed an augmented plane-wave plus local-orbital (APW+lo) method (implemented in WIEN2K package) (Ref. 54) in DFT framework. The configurations of spin ordering in the large unit cell (40-atom) for the stoichiometric and off-stoichiometric Ca-rich or Cu-rich CCTO were optimized by pseudopotential method, and then the related electronic and magnetic properties were obtained by full-potential calculations. Several types of exchange-correlation potential, such as local spin-density approximation (LSDA) (Ref. 55) and generalized gradient approximation [GGA–Perdew–Burke–Ernzerhof (PBE) (Ref. 56)], were employed. We also used the LDA+ U self-interaction corrected⁵⁷ method to take into account the strongly correlated effects in CCTO.

III. RESULTS

A. Basic crystal structure

The space group of the ideal CCTO structure is $Im\bar{3}$ (No. 204 in the International Crystallography Table) in a primitive unit cell (20 atoms per cell), or $Pm\bar{3}$ (No. 200) in a more conventional unit cell used in the literature (a double primitive unit cell, 40 atoms per cell) to include the antiferromagnetic (AFM) ordering at Cu sites, as shown in Fig. 1. The cubic crystal cell has a lattice constant $a=7.39$ Å at 300 K with Wyckoff positions Ca(0,0,0), Cu(0,0.5,0.5), Ti(0.25,0.25,0.25), and O(0.3032, 0.1792, 0).⁹ For the doubled unit cell, coppers with spin up (Cu1) and spin down (Cu2) are located at (0.5, 0, 0.5) and (0,0,0.5) sites, respectively, with a $Pm\bar{3}$ symmetry.

Our synchrotron x-ray diffraction data revealed a measurable difference in intensity between the 103 and 013 type of reflections (also 105 and 015, and the $h0l$ and $0hl$ family in general), suggestive of an untwinned crystal structure since a $Im\bar{3}$ crystal with twinning these reflections should be equivalent. This is consistent with our previous TEM studies.⁸ Although early neutron and x-ray diffraction experiments suggested CCTO was twinned, an exhaustive search for twin domains or variants using various electron microscopy imaging and diffraction methods in single crystals, bulk ceramics, and thin films was unsuccessful.⁸ It was argued that the failure of finding twinning using TEM is due to a scale issue since neutrons and x rays have a much larger beam size and

TABLE I. Summary of the refinement results by SHELXTL program. Temp=temperature, refl=reflections, R1=R factor 1, wR2=weighted R factor 2, GooF=goodness of fitting, Scale*=scale to bring F_{calc} (calculated structure factors) on the scale of the F_{obs} (observed structure factors).

Temp (K)	No. refl	R1	wR2	GooF	Scale*	Extinction parameter
300	58	0.023	0.075	1.32	0.490(8)	0.011(2)
90	53	0.019	0.082	1.48	0.489(9)	0.005(1)

if the twin domains in CCTO are larger than the electron-beam diameter one can easily miss them. It is important to note that modern electron microscopes offer a wide range of beam sizes, typically from 0.1 nm to 0.1 mm. This flexibility allows us to detect domains and defects of different length scales, thus revealing the symmetry of the crystal on different length scales, which may be lower than that observed by crystallographic x-ray or neutron experiment, which often probe with larger coherence volumes. Electron microscopists routinely use low magnifications, say 10 000 \times , to look for macroscopic structural features such as grains and twins based on diffraction or mass/thickness contrast in an electron microscope. If twin domains are 0.01 mm in size, then at 10 000 \times across the viewing chamber (20 cm \times 20 cm) of a microscope one would see two twin domains on the screen even without moving the sample (In fact, many microscopes can be operated down to 100x). Under various magnifications, using both imaging and diffraction modes in TEM, we have not observed twins in CCTO. (If the twin domains are smaller than 0.05 mm in size, we would not miss them.) We thus conclude that there exist no twins in CCTO, at least for all the samples we have examined. If the size of the twins is on the order of the crystal size, the low density of twins would have little effect on the properties of the materials. The absence of twins with appropriate sizes brings into question the applicability of the IBLC model for explaining the dielectric behavior of single-crystal CCTO.

Table I summarizes the refinement results of XRD using the SHELXTL program. In general, the fitting for space group $Im\bar{3}$ was quite good, especially for the strong reflections. A comparison between observed and calculated intensity of the Bragg reflections (structure factors squared) are shown in Fig. 2 for 300 and 90 K. Slight changes in lattice parameters are observed but no phase transitions are present in this temperature range. The temperature dependence of the structural parameters is quite small. For example, the coordinates of the oxygen atoms change in x and y directions are $0.1 \pm 0.16\%$ and $-0.2 \pm 0.3\%$, respectively, for a temperature range of 210 K. The change in the 141.5 $^\circ$ bonding angle of Ti-O-Ti due to the tilt of TiO_6 octahedra (from the original 180 $^\circ$ for the ideal cubic perovskite) with temperature is also very small, only 0.05 $^\circ$ (namely, 0.04%) for $\Delta T=210$ K. The structure factor obtained at 90 and 300 K was used for multipole refinement analysis and will be discussed in the following sections.

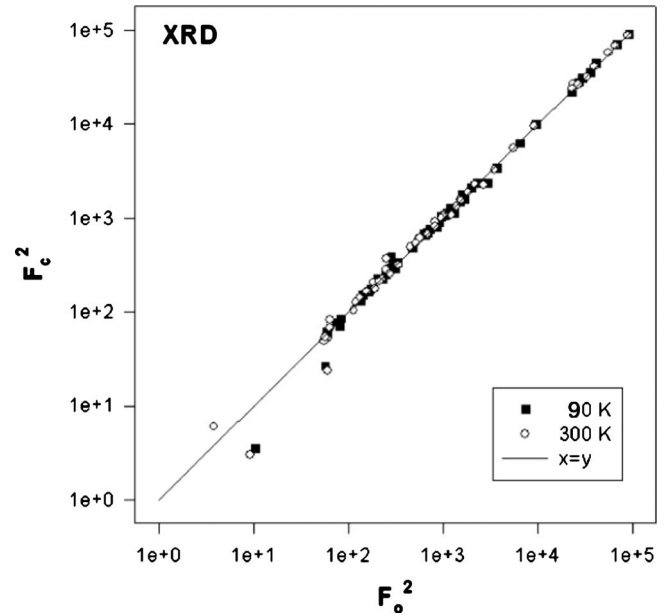


FIG. 2. Comparison of structure factor squared between calculation (F_c^2) and observation (F_o^2) in structural refinements using SHELXTL program. Solid square is for 90 K and open circle is for 300 K.

B. Low-order structure factors

1. Experimental measurements

Table II lists the nuclear charge, the atomic Debye-Waller factor, and the critical scattering vectors [$s_c(\text{\AA}^{-1})$] for the element of O, Ca, Ti, and Cu that form CCTO. The critical scattering vector defines the scattering angle for a particular element below which the electron probe is more sensitive than x ray to measure the variation in the charge distribution.²¹ In our electron-diffraction experimental setup, the scattering angle ($\sin \theta/\lambda$) of the six low-index reflections measurable with high accuracy (110, 200, 211, 220, 400, 422) all are smaller than s_c of Ca, Ti, and Cu (see Table III). Only the scattering vector of (422) reflection is larger than s_c of oxygen. This suggests it is crucial to use electron diffraction, rather than x ray, to accurately measure the structure factor of these six low-index reflections to understand the bonding characteristics and the valance-electron distribution in CCTO.

TABLE II. Atomic Debye-Waller Factor in CCTO at 90 K and 300 K, and estimated critical scattering vectors [$s_c(\text{\AA}^{-1})$] from standard or parameterized tables of x-ray scattering factors for atoms (or ions).

Element	Nuclear charge	s_c	Debye-Waller factor	
			90 K	300 K
O	8	0.3	0.30	0.40
Ca	20	0.35	0.38	0.45
Ti	22	0.35	0.25	0.37
Cu	29	0.45	0.22	0.44

TABLE III. Electron-structure factors of the six innermost reflections in CCTO at 90 and 300 K, where experimental observations were compared with DFT calculations (LDA+ U , $U=4$ eV) and a hypothetical crystal assembled by neutral atoms, namely, independent atom model (IAM) or procrystal. Please note the large deviation of the (110) structure factor between DFT calculation and experiment at 300 K, and the same calculated value at 90 and 300 K due to the insensitivity of the low-order reflection to atomic position and Debye-Waller factors. R_1 and R_2 are defined by Eqs. (2) and (3), respectively.

Index (hkl)	$\sin(\theta)/\lambda$ (Å)	$T=90$ K			$T=300$ K		
		ED measurements	LDA+ U ($U=4$ eV)	IAM	ED measurements	LDA+ U ($U=4$ eV)	IAM
110	0.09568	1.06 ± 0.12	1.17	3.38	0.63 ± 0.37	1.17	3.35
200	0.13531	-10.29 ± 0.42	-9.47	-11.50	-9.80 ± 0.19	-9.22	-11.53
211	0.16572	-3.21 ± 0.40	-2.76	-2.56	-2.93 ± 0.25	-2.67	-2.47
220	0.19135	48.92 ± 0.91	49.12	45.88	49.07 ± 2.18	48.90	45.66
400	0.27061	50.13 ± 1.32	50.58	50.05	47.44 ± 1.40	50.11	49.59
422	0.33143	37.56 ± 0.75	37.13	36.77	36.93 ± 1.05	36.57	36.22
$R_1(\%)$			1.63	5.35		3.12	7.62
$R_2(\%)$			5.80	43.23		17.91	79.75

As described in Sec. II A, the quantitative electron-diffraction (PARODI) approach was used for the measurements. An example of the experimental PARODI patterns of the $h00$ systematic row with 000, ± 200 , and ± 400 reflections of CCTO is shown in Fig. 3(a). Please note the intensity oscillation in each disk is due to the dynamic scattering of incident electrons. Figure 3(b) is the comparison with the best-fit calculations. To simplify the analysis, we searched for a wedge area with a linear increase in thickness, t . In Fig. 3(a), the top-right edge of the reflection disks is the vacuum area ($t=0$) and the thickness of the illuminated area increases from top right to bottom left with $t_{\max}=170$ nm. To keep the number of variables to a minimum, we only vary structure factors, crystal thickness (t_{\max}), and crystal orientation in the fitting process. The line scans [as marked in (a)] of the ex-

perimental and calculated intensity profile from the same area, red lines and open circles, respectively, are plotted in Fig. 3(c), showing excellent agreement between experiment and calculation. The resulting six low-order ESFs from the fitting procedure are listed in Table III for two different temperatures, 90 and 300 K.

2. Comparison of various theoretical approaches

Low-order structure factors are numerical parameters of a material property and very sensitive to chemical-bonding characteristics. Thus, they are very suitable for comparing and testing theoretical calculations from different models. In Table III, we also list the calculated ESFs using DFT (LDA+ U) and IAM (independent atom model) corrected with temperature effects for 90 and 300 K.⁹ The differences between calculated ESFs using DFT and IAM as well as measured ESFs are plotted in Fig. 4. The difference between ED measurements and DFT is in blue and IAM is in red in 90 K [Fig. 4(a)] and 300 K [Fig. 4(c)]. The sequence of the data points in the figure with the increase in scattering angle is (110), (200), (211), (220), (400), and (422) reflections. Figures 4(b) and 4(d) plot the relative changes in the ESFs in percentage, normalized by the ED measurements. Although the differences are somewhat reflection dependent due to the symmetry of the charge distribution, the trend is quite clear. The deviations from the experiment based on both IAM and DFT models are approaching zero at high scattering angles [(400) and (422) reflections] whilst being significant at small scattering angles. This is due to the fact that low-order ESFs are very sensitive to charge redistribution and bonding properties, due to the near cancellation of the scattering from the positively charged nucleus and the negatively charged electrons.^{14,21}

The ESFs calculated by DFT are in better agreement with ED measurements than those calculated by IAM, as evidenced from Fig. 4 and the R factors [see Eqs. (2) and (3) below] in Table III. This is expected because in IAM calculations, the valence-charge rearrangements are totally ig-

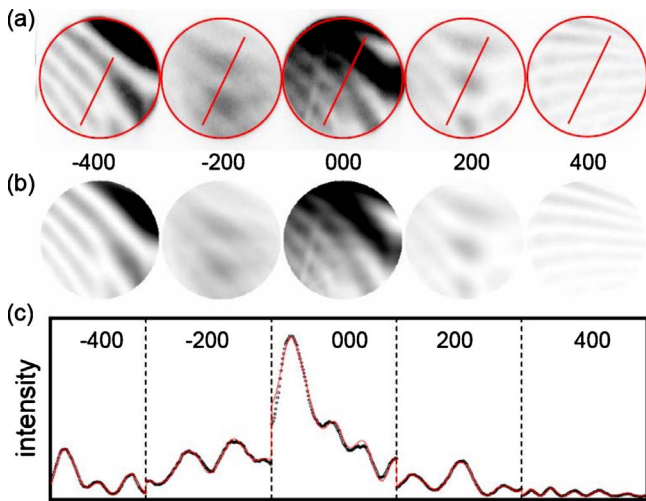


FIG. 3. (Color online) (a) Parallel recording of dark-field images (PARODI) of CCTO at $h00$ systematical row. (b) Calculation based on Bloch-wave method. (c) Line scan of the intensity profile from the experiment pattern in (a). The open circles are experiment while the red curves are calculation after refining the structure factors of 200 and 400.

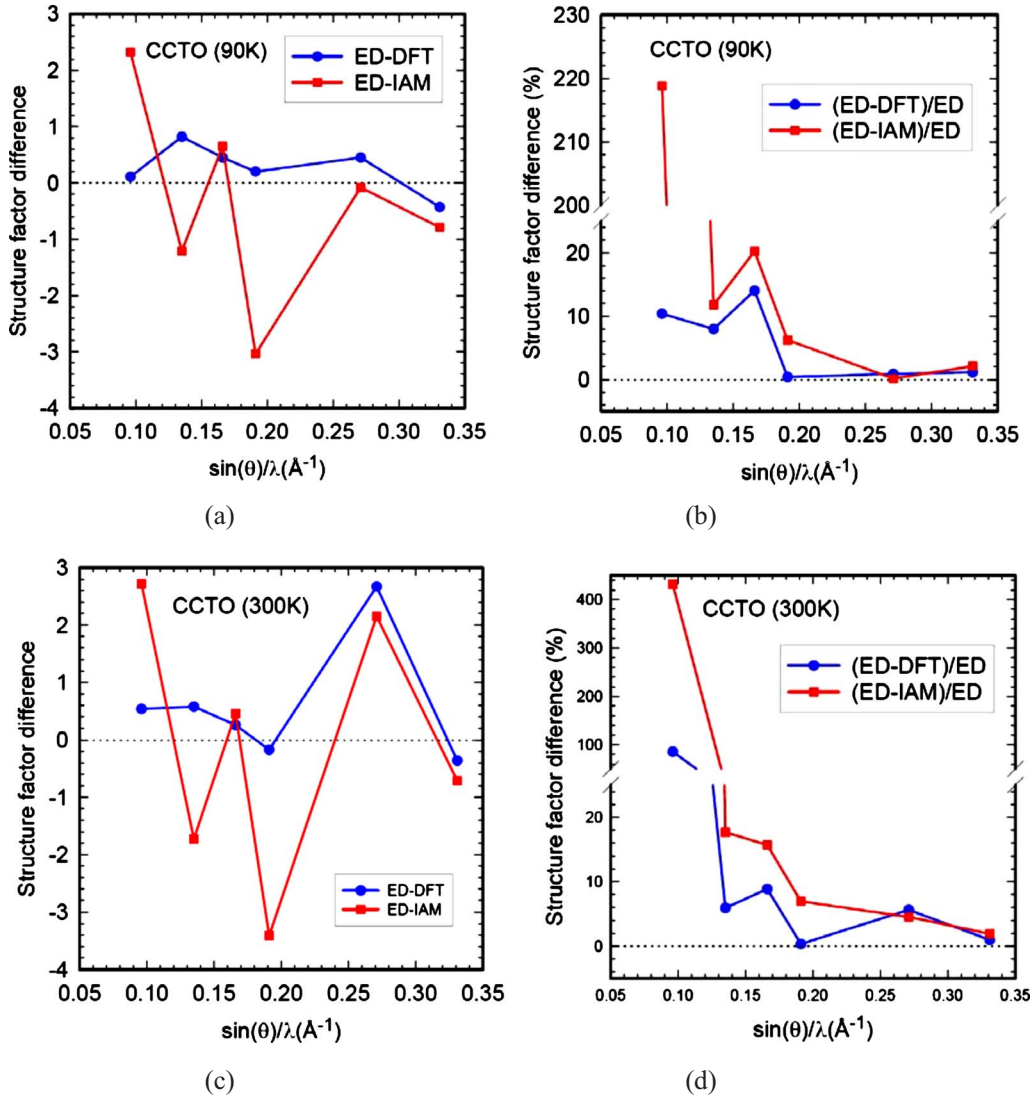


FIG. 4. (Color online) The difference of electron-structure factors of the six low-index reflections in CCTO obtained from different approaches for two different temperatures, (a)–(b): 90 K and (c)–(d): 300 K. (a) and (c): difference of structure factors between quantitative electron-diffraction (ED) measurements and density-functional theory (DFT) calculations (blue) and between ED and independent-atom-model (IAM) calculations (red). (b) and (d): relative changes in structure factor in percentage (%) normalized by the ED measurement. The sequence of data points in the figures from small to large scattering angle is (110), (200), (211), (220), (400), and (422) reflections.

nored while in DFT calculations, the valence-electron redistributions due to chemical bonding and charge transfer between ions are taken into account. The accuracy of ESF calculations by DFT depends on the approximations used for the exchange and correlation potentials, as well as the convergence control in calculations. The full-potential DFT calculations can give very accurate charge density in many complex systems including transition-metal oxides if strongly correlated effects are properly considered.

We further examine the effects on structure factors due to different magnetic configurations, i.e., paramagnetic (PM), ferromagnetic (FM), and AFM as well as exchange-correlation functionals (e.g., LDA or GGA). The results are listed in Table IV. In order to compare quantitatively these effects on ESFs, two different R factors were used. They were defined as

$$R_1 = \left(\frac{\sum_{i=1}^n |F_{(cal)}^i - F_{(ED)}^i|}{\sum_{i=1}^n |F_{(ED)}^i|} \right) 100(\%), \quad (2)$$

$$R_2 = \frac{1}{n} \left(\frac{\sum_{i=1}^n |F_{(cal)}^i - F_{(ED)}^i|}{|F_{(ED)}^i|} \right) 100(\%), \quad (3)$$

where $F_{(ED)}^i$ and $F_{(cal)}^i$ are i th measured and calculated (i.e., LDA+ U or IAM) ESFs, respectively; and n is the number of ESFs. R_1 , commonly used as goodness of fit,⁵⁸ is the summation of the differences between calculation and measurement divided by the total sum of measured ESFs. R_1 thus is more sensitive to the absolute values (and summation) of ESF differences, dominating for large values of ESFs, but not sensitive to relative changes in individual ESFs. It is

TABLE IV. Electron-structure factor of CCTO (40 atoms) calculated by DFT with 90 K lattice parameters and using 90 K Debye-Waller factor. [The experimental atomic positions are Ca(0,0,0), Cu(0,0.5,0.5), Ti(0.25,0.25,0.25), O(0.3028,0.1789,0) and the experimental lattice constant is 7.382 Å at 90 K.) PM: paramagnetic, FM: ferromagnetic, and AFM: antiferromagnetic.

(hkl)	GGA(PM)	LDA(PM)	LDA(FM)	LDA(AFM)
110	1.24	1.23	1.20	1.20
200	-9.12	-9.17	-9.16	-9.16
211	-2.74	-2.78	-2.79	-2.79
220	49.11	49.05	49.12	49.11
400	50.47	50.60	50.61	50.61
422	37.08	37.14	37.14	37.14
$R_1(\%)$	1.87	1.81	1.85	1.84
$R_2(\%)$	7.56	7.11	6.63	6.62

good for a large data set with large error bars such as those from x-ray measurements but is not sufficient to describe the characteristics in small data sets such as those obtained by ED even with much better accuracy. Therefore, in order to take into account the relative changes in every ESF, we also adopted R_2 , as defined in Eq. (3), which is similar to the R factor we used previously.²¹ The advantage of R_2 is that it treats the difference in percentage for each ESF equally, thus it is more sensitive to the relative changes in individual ESFs.

The differences in ESFs due to the different exchange-correlation functionals are within 0.1% for R_1 , which are often smaller than the error bar in the experiment measurement. This suggests that LDA or GGA calculation result in very similar structure factors and charge densities in CCTO. Different magnetic configurations only give about 0.05% differences in R_1 . The R_1 for LDA+ U with an antiferromagnetic configuration has 1.63% deviation from ED measurements, adjusted for 90 K lattice constants and Debye-Waller factors (Table V). This is much smaller than the 5.35% from IAM. The R factors (R_1 and R_2) are slightly reduced with the increase in U in LDA+ U until U reaches beyond 6 eV. This is consistent with the fact that CCTO is a strongly correlated

TABLE V. Effects of U in LDA+ U on electron-structure factors (90 K lattice parameters) using 90 K Debye-Waller factor.

hkl	$U=0$ eV	$U=4$ eV	$U=6$ eV	$U=8$ eV
110	1.20	1.17	1.14	1.08
200	-9.16	-9.47	-9.46	-9.06
211	-2.79	-2.76	-2.75	-2.75
220	49.11	49.12	49.13	49.15
400	50.61	50.58	50.57	50.55
422	37.14	37.13	37.12	37.12
$R_1(\%)$	1.84	1.63	1.63	1.85
$R_2(\%)$	6.62	5.80	5.40	5.11

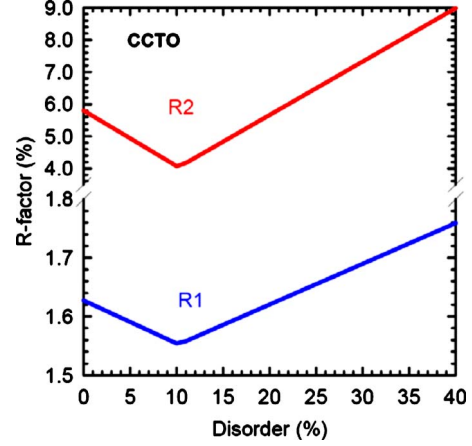


FIG. 5. (Color online) R factor as a function of Ca/Cu disorder in CCTO at 90 K. DFT calculations using LDA+ U with $U=4$ eV.

system. For a comparison between experimental and calculated ESFs using the R_2 definition, the R factors are larger than R_1 because of the larger relative changes in SF of the (110), (211), and (200) reflections.

Overall, we found that, by comparing the R factors, improvement of exchange-correlation functionals (e.g., from LDA to GGA), the addition of strongly correlated effects (e.g., including U in LDA) or consideration of magnetic configurations (e.g., FM and AFM), does not improve the agreement between ED experiments and DFT calculations much. The discrepancy between the two with the best choice of U ($U=4$ eV) is still about $R_1=1.6\%$ ($R_2=5.8\%$) at 90 K and $R_1=3\%$ ($R_2=18\%$) at 300 K (Table III). This can be attributed the fact that the improvement of DFT calculations only gives about 0.2% reduction in R factors with the (110) structure factors being identical. This is because the low-order ESFs are not sensitive to the atomic positions, or the variation in temperature,²¹ the more accurate determination of Debye-Waller factors will not further reduce the R factors. Nevertheless, at 300 K, the (110) ESF shows remarkable deviation from the calculation, in comparison with that at 90 K. Unexpectedly, when we induce 10% of Ca/Cu antisite disorder into the structure (see Sec. III D), the R factors of the six low-order ESFs are reduced considerably, R_2 reduced by 45% and R_1 reduced by 5%, as shown in Fig. 5. The improvement of the R factors at 300 K is more significant.⁴⁶ Due to the small value of the (110) ESF and large measurement error, the accurate assessment of the R factors improvement at 300 K is difficult to make but the trend is very clear. A few hundred percent of reduction in the R factors can be reached for room temperature if only the (110) reflection is considered.

C. Charge-density maps

Charge-density maps were obtained from multipole refinement of electron and x-ray structure factors. The latter are the Fourier component of the charge density. In our study, we combined structure factors of low-order reflections measured by electron diffraction with those of high-order reflections measured by x ray. Total 58 independent reflec-

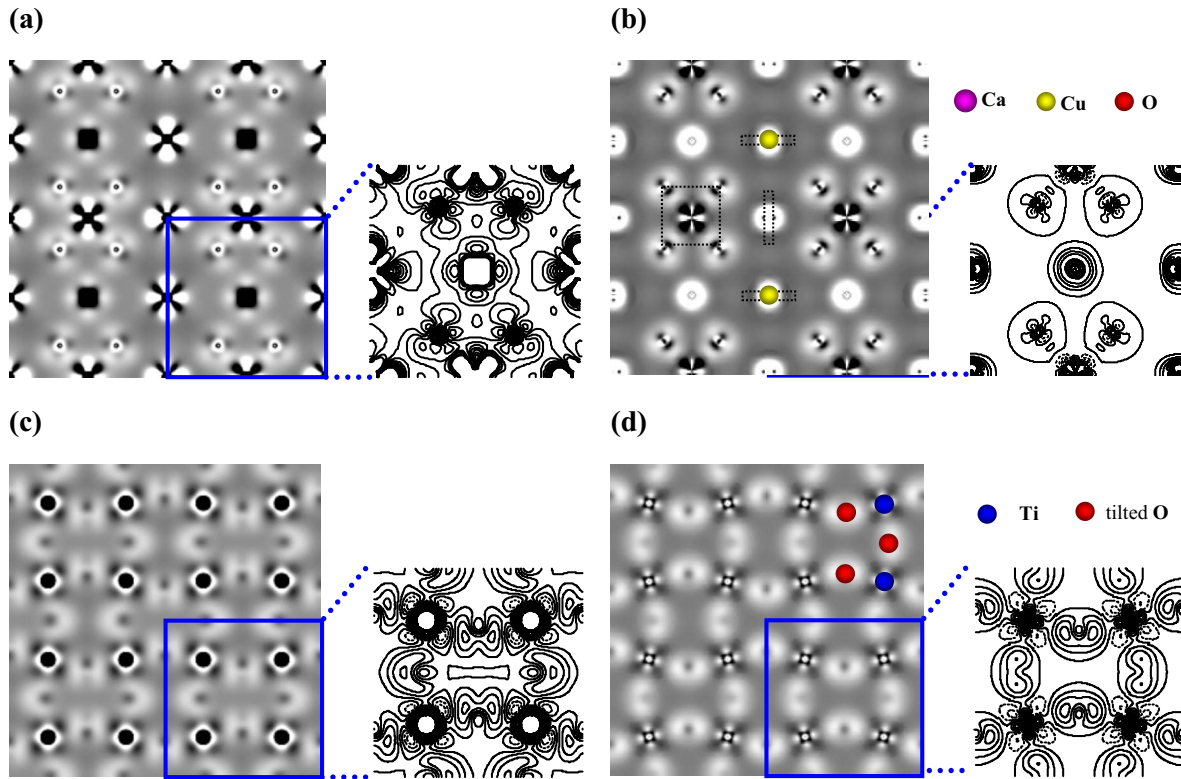


FIG. 6. (Color online) Deformation charge-density maps of CCTO derived from experimental measurements [(a) and (c)] and DFT calculations (LDA+ U) [(b) and (d)] in the (001) planes for the Cu-Ca-O plane ($z=0$) in [(a) and (b)] and Ti-Ti plane ($z=0.25$) in [(b) and (d)]. The experimental results were obtained by combining structure factors of 58 reflections measured by electron diffraction (the six innermost reflections) and x-ray diffraction via multipole refinement. The square and rectangles in (b) represent the CuO_4 square in-plane and out-of-plane (with plane normal along the [100] and [010] direction). Enlarged contour plots from the marked area are shown on the right. Since in (d), the TiO_6 octahedra are tilted, the O atoms are not in the $z=0.25$ plane. Detailed comparison of the density map between experiment and calculation is not possible due to the limited number of reflections used in experiment (see text). The major feature in difference is the Ca site in (a) and (b): the calculation shows a close-shell orbital with a spherical symmetry while the experimental map shows some orbital anisotropy, suggesting possible Cu occupancy on the Ca site.

tions for 300 K and 53 for 90 K, corresponding to about 700 reflections if multiplicity is considered, were used to map the three-dimensional (3D) charge-density distributions in CCTO. Since total charge density is dominated by the core electrons which are not of great interest, we plot either valence-electron distribution if the core electron distribution is used as a reference or deformation map if the charge density of a procrystal (a hypothetical crystal formed by neutral atoms) is used as a reference. Figures 6(a) and 6(b) are the 90 K experimental deformation charge-density maps of CCTO in the (001) plane, the Cu/Ca-O basal plane ($z=0$) and the Ti-Ti plane ($z=0.25$), respectively, obtained after multipole refinements. For comparison, we also include those from DFT calculations within the local spin-density approximation (LDA+ U) for ideal stoichiometric CCTO. The experimental map [Fig. 6(a)] clearly shows the bonding valence states, the electron density in the CuO squares and surrounding the Ca^{2+} ions in the basal plane ($z=0$). The magnetically active and orbital-ordered (OO) Cu d states exhibit well-defined t_{2g} symmetry [pointing toward the (110) directions], and form antibonds with neighboring O p states, in agreement with the calculation. Detailed comparison between experiment and calculation is not possible (details of the density map in calculation come from the infinitely large

number of high-order reflections), due to the truncation error (limited number of reflections used) in experiment. We thus focus our attention on the main features, especially those extended to a large distance, in the distribution maps. As we can clearly observe in Fig. 6(a) that both experimental and calculated maps show open-shell d -electron orbitals for the Cu site with a fourfold symmetry. In contrast, at the Ca site, the calculation shows a close-shell orbital with a spherical symmetry while the experimental map shows some fourfold symmetry (orbital anisotropy with a weak e_g symmetry). This observation suggests possible $3d$ orbitals occupying on the Ca site, a result of local Ca and Cu switching or antisite disorder, as we reported previously. Although in our quantitative ED experiments, the probe size used was quite small (<5 nm), the areas of the crystal used for the measurement were rather thick (~ 100 nm). Should both ordered and disordered regions exist, we expect that the experimental map reflects an overlap of both. This is the significant outcome of our charge-density study. On the other hand, we did not observe any noticeable anomaly of the density map in the Ti-Ti plane ($z=0.5$). The agreement between experiment and calculation for the Ti sites [Fig. 6(b)] appears much better than Ca and Cu sites, suggesting less disorder for Ti.

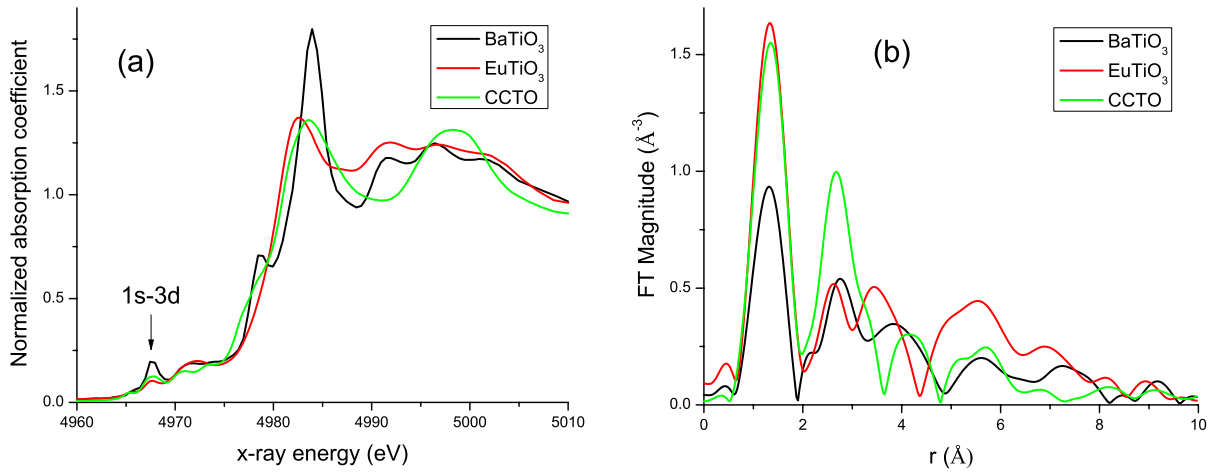


FIG. 7. (Color online) (a) XANES of Ti K edge in CCTO and two reference samples: BaTiO₃ (with 0.23 Å Ti atom static off-center displacement) and EuTiO₃ (with Ti atom being on the inversion symmetry center). The CCTO signal is similar to EuTiO₃ in the $1s\ 3d$ transition region, shown by the arrow. The nonzero signals in CCTO and EuTiO₃ are due to dynamic off-center displacements, which are much smaller than the static displacements in BaTiO₃. The BaTiO₃ and EuTiO₃ data are taken from Ref. 31. (b) Fourier-transform magnitudes of the Ti K -edge EXAFS. The magnitude in the first peak (corresponding to the first nearest-neighbor Ti-O contributions) is smaller in BaTiO₃ compared to EuTiO₃ and CCTO. In all cases, Ti is octahedrally coordinated by oxygens but in EuTiO₃, the disorder in Ti-O distances is purely thermal while in BaTiO₃, it is thermal and configurational (due to the split of six oxygens in two groups of three oxygens each); thus, the Debye-Waller factor term causes the signal in BaTiO₃ to be lower than in EuTiO₃. The similarity between the signal in EuTiO₃ and CCTO means that the Ti environment is also more symmetric in CCTO than in the room-temperature phase of BaTiO₃.

D. Local structure

1. Ti displacement

We examined the possible cation displacement in CCTO using synchrotron x-ray absorption spectroscopy by comparing CCTO with BaTiO₃ and EuTiO₃. It is well known that the off-center displacement of Ti ion in TiO₆ octahedron gives rise to ferroelectricity in BaTiO₃.³¹ Ti is the most common “shifter” in titanate perovskites (e.g., BaTiO₃, PbTiO₃, SrTiO₃, and EuTiO₃). To study the possible Ti off-center displacement, we studied both XANES and EXAFS data in CCTO. Our XANES results demonstrate no enhancement (typical for systems with Ti off-center displacements) of the signal in the $1s\ 3d$ transition region (~ 4968 eV) below the Ti K -edge rise. The very presence of such a signal allowed in the past to evaluate the magnitude of such displacements in similar compounds.^{26,30,31}

Figure 7(a) show the comparison of the Ti K edge in CCTO with two reference samples: BaTiO₃ (with 0.23 Å Ti atom static off-center displacement) and EuTiO₃ (with Ti atom being on the inversion symmetry center).³¹ The CCTO signal is similar to EuTiO₃ in the $1s\ 3d$ transition region, as marked by an arrow. The nonzero signals in CCTO and EuTiO₃ are due to dynamic off-center displacements, which are much smaller than the static displacements in BaTiO₃. The BaTiO₃ and EuTiO₃ data are taken from Ref. 31. Our results suggest that Ti atoms are not displaced off-center of their oxygen coordination environments, which thus form relatively rigid structural units which can only rotate but not change their 3D shape. This is in agreement with a neutron PDF study which showed no evidence for Ti off-centering displacements in the local structure.⁹ This is further supported by analysis of the Debye-Waller effects in the EX-

AFS. Figure 7(b) is the Fourier-transform magnitudes of the Ti K -edge EXAFS of the three samples. The magnitude of the first peak (corresponding to the first nearest-neighbor Ti-O contributions) is smaller in BaTiO₃ compared to EuTiO₃ and CCTO. In all cases, Ti is octahedrally coordinated by oxygens but in EuTiO₃, the disorder in Ti-O distances is purely thermal while in BaTiO₃, it is both thermal and configurational (due to the split of six oxygen atoms in two groups of three atoms each); thus, the Debye-Waller factor term causes the signal in BaTiO₃ to be lower than in EuTiO₃. The similarity between the signal in EuTiO₃ and CCTO suggests that the Ti environment is also more symmetric in CCTO than in the room-temperature phase of BaTiO₃. We thus conclude that there is no significant off-center Ti displacement in our CCTO single crystals.

The possibility of displacements of Cu and Ca atoms was also investigated using their K -edge XANES data. No evident off-center displacement of either Cu or Ca was observed. For the possible swap of Ca and Cu due to the local disorder, the Cu-O environment can be strongly disordered and one might expect that on the Ca site, due to its small size, Cu would not be located at the center of the Ca site. However, we did not gather any evidence of a preferred direction of Cu displacement: such evidence will be obtained by our EXAFS analysis.

2. Antisite (Ca/Cu) disorder

To further explore local disorder suggested by the charge-density study (Sec. III C), we conducted an EXAFS study. EXAFS reveals information about the short-range-order environment around selected atoms, including the number of their nearest neighbors, their types, average bond lengths, and their mean-squared relative displacements. Figure 8

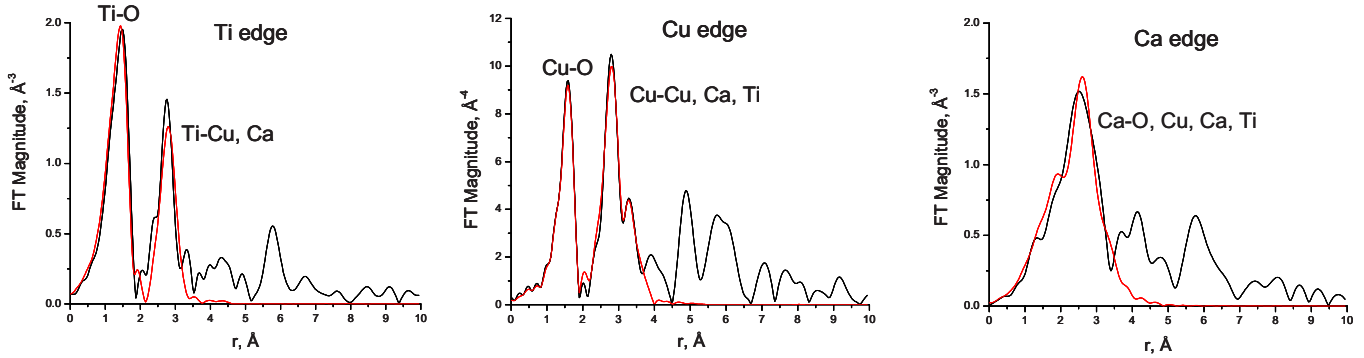


FIG. 8. (Color online) The Ti *K*, Cu *K*, and Ca *K* edges of the EXAFS data and their theoretical fits.

shows the EXAFS data of Ti, Cu, and Ca *K*-edge superimposed on their theoretical fits. As explained above, the best-fit values of $N_{\text{Cu-Ca}}$ and $N_{\text{Ca-Cu}}$ can either communicate partial order (when $1.5 < N_{\text{Cu-Ca}} < 2$ and $4.5 < N_{\text{Ca-Cu}} < 6$) coupled with the preservation of the long-range order or reveal macroscopic compositional fluctuations (when $N_{\text{Cu-Ca}}$ and $N_{\text{Ca-Cu}}$ are outside of the above ranges) without long-range order.⁵⁹ The coordination numbers, based on the best-fit results and obtained by concurrent EXAFS modeling of Ti, Ca, and Cu data, as well as the bond lengths are summarized in Table VI. We found that the Cu-Ca and Ca-Cu coordination numbers, $N_{\text{Cu-Ca}} = 2.8 \pm 1.0$ and $N_{\text{Ca-Cu}} = 2.4 \pm 1.6$, respectively, obtained by EXAFS significantly deviate from those (2.0 and 6.0, respectively) expected in the idealized, homogeneous CCTO with the $Im\bar{3}$ structure. Such deviation cannot be explained by randomizing Cu and Ca at their sites within the same unit cell (in the random alloy $N_{\text{Ca-Ca}} = 1.5$ and $N_{\text{Ca-Cu}} = 4.5$). Thus, our conclusion from this observation is that the randomization occurred at the length scale of a few unit cells (some—Cu rich and some—Ca rich), rendering a possibility of forming nanoscale regions with antisite chemical disorder. We would like to emphasize that the signature of the nanoscale disorder is not the Cu-Ca and Ca-Cu coordination numbers alone but also the differences in the Ti-Cu and Ti-Ca distances, as well as the Cu-Cu, Cu-Ca, and Ca-Ca distances

not observed by XRD measurements, which were obtained independently from the coordination numbers. Indeed, in a homogeneous alloy, the Cu-Ca and Ti-Ca distances should be longer than Cu-Cu and Ti-Cu, respectively, due to the larger size of Ca ion relative to Cu. In this system, we obtain the opposite effect (Table VI). All the information available from EXAFS, therefore, points to a structural disorder that is inconsistent with the ideal $Im\bar{3}$ structure. We found no evidence of enhanced (compared to thermal disorder) values of Cu-O, Ti-O, or Ca-O bond-length disorder, thus ruling out measurable oxygen-atom disorder and, in turn, its possible role in conductivity.

As a control, a model of stoichiometric CCTO without defects was also fit simultaneously to all of the available edge data. Although the reduced chi squared for the fit of this model to the multiple data sets was comparable with that for the previous model where antisite defects were allowed, the latter model resulted in a worse fit quality for Cu *K* edge, the one most sensitive to the Cu/Ca substitution. Indeed, the Ca *K*-edge data were the worst quality with the lowest k_{max} (and thus the worst spatial resolution of all the data), and the Ti *K*-edge data are not sensitive to Ca/Ca substitution since Ti is the common atom in this system.

Here we explore in greater detail the model that contains the Ca/Cu antisite defects. In this model, the deviations in

TABLE VI. Structural results obtained from multiple-edge EXAFS data analysis compared with DFT data (pseudopotential LSDA calculations).

Bond	N_{exp}	$N_{\text{th}}(x=0)$	$N_{\text{th}}(x=1)$	N_{DFT}	R_{DFT} (Å)	R_{EXAFS} (Å)	R_{XRD} (Å)	σ^2 (Å ²)
Ti-O	6	6	6	6	1.953	1.96(2)	1.964	0.0072(28)
Cu-O	4	4	4	4	1.968	1.971(4)	1.971	0.0041(3)
Cu-O	4	4	4	4	2.786	2.80(5)	2.789	0.015(10)
Cu-O	4	4	4	4		3.25(1)	3.269	0.013(30)
Ca-O	12	12	12	12	2.552	2.56(3)	2.606	0.024(6)
Ti-Cu	6	6	6	5	3.194	3.22(2)	3.206	0.0079(10)
Ti-Ca	2	2	2	3	3.205	3.17(4)	3.206	0.0043(35)
Cu-Cu	2.8(1)	4.5	4	4 or 2	3.704	3.77(2)	3.703	0.0040(20)
Cu-Ca	3.2(1)	1.5	2	4 or 6	3.679	3.70(2)	3.703	0.0038(29)
Ca-Cu	2.4(1.6)	4.5	6	4 or 6	3.679	3.70(2)	3.703	0.0038(29)
Ca-Ca		1.5	0	2	3.739			

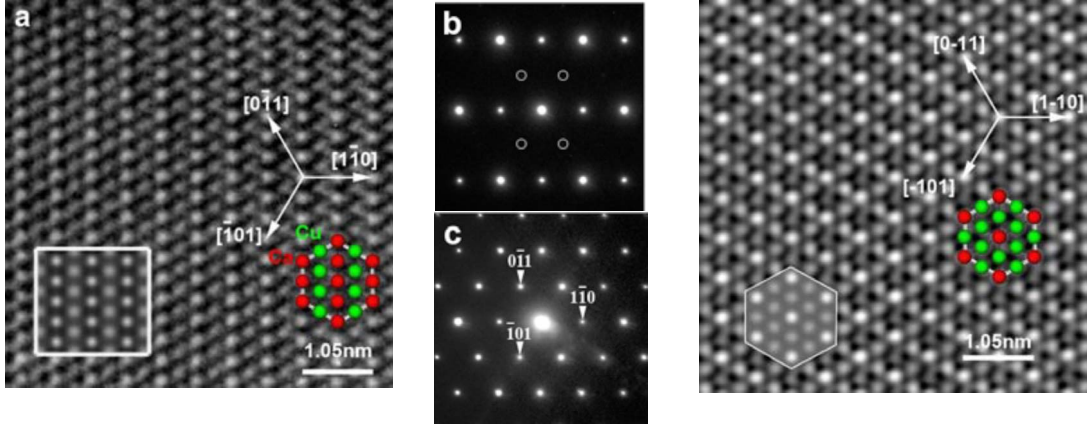


FIG. 9. (Color online) (a) High-resolution image of an unusually large Ca-rich region in CCTO taken along the $[111]$ projection. The boxed area is the simulation using the model on the right. (b) Electron-diffraction pattern from the Ca-rich area showing broken a threefold symmetry. Open circles represent the missing $0-11$ and -101 reflections. (c) Electron-diffraction pattern from a stoichiometric region of CCTO showing a threefold symmetry. (d) High-resolution image of perfect CCTO observed along the same orientation as (a) The boxed area is the simulation using the model on the right (for simplicity, only Ca and Cu are drawn).

coordination numbers from those expected in homogeneous CCTO indicate the presence of a Ca-rich phase $\text{Ca}_x\text{Cu}_{1-x}\text{TiO}_3$, where $x > 0.25$, as well as Cu-rich phase where $x < 0.25$, suggesting the presence of local compositional and structural disorder with Ca on the Cu sites. Both types of phases must be present in the sample, along with the stoichiometric phase ($x=0.25$), since our measurements show that the overall sample composition is stoichiometric ($x=0.25$). Since both Cu and Ca edge analyses points to the presence of Ca-rich regions, we suggest that the Cu-rich regions are more disordered, or have reduced dimensionality, than the Ca-rich ones, which might reflect the smaller size of the Cu ion relative to Ca. This conclusion is consistent with our TEM observations. Figure 9(a) shows a high-resolution image from an unusually large Ca-rich region in the CCTO single crystal taken along the $[111]$ projection. The boxed area is the simulation using the model on the right. A corresponding electron-diffraction pattern from the area is shown in Fig. 9(b), with a clear broken threefold symmetry, similar to the observations reported previously. The open circles represent the missing $(0-11)$ and (-101) reflections, being con-

sistent with the image. For comparison, in Fig. 9(c) we include the $(111)^*$ diffraction pattern from the stoichiometric ordered CCTO with threefold symmetry. The corresponding high-resolution image is shown in Fig. 9(d). The model and the simulation of the structure are also included.

Although we observed a Ca-rich region using electron diffraction and imaging, we have not convincingly detected the Cu-rich regions. There were two reasons: (1) as EXAFS suggested that the Cu-rich must be low dimensional, i.e., a small Cu-rich disordered region embedded in the ordered matrix is difficult to see in a projected image, especially considering the small difference in scattering amplitude between Ca and Cu; and (2) from a diffraction point of view, the substitution of Ca with Cu does not significantly alter the crystal symmetry and change the extinction of the reflections and is thus difficult to detect in diffraction. Our TEM spectroscopy measurements [energy dispersive x-ray (EDX) and electron-energy-loss spectroscopy (EELS)] of Cu-rich regions were inconclusive. This can be attributed to their low dimension, thus low-concentration difference from the matrix through the sample thickness.

TABLE VII. Summary of the PDF refinement results obtained by PDFGUI program for 300 K neutron data. Crystallographic $Im\bar{3}$ model refinement yields $a=7.4011(3)$ Å, $x(\text{O})=0.3027(2)$, $y(\text{O})=0.1789(2)$, $U_{\text{ISO}}(\text{Ca})=0.0050(6)$ Å², $U_{\text{ISO}}(\text{Cu})=0.0050(2)$ Å², $U_{\text{ISO}}(\text{Ti})=0.0044(2)$ Å², and $U_{\text{ISO}}(\text{O})=0.0047(1)$ Å². Three models including chemical disorder with respect to crystallographic stoichiometric model are compared. Refined parameters in these models are replacement (or off-stoichiometry) parameter, d , $U_{\text{iso}}(\text{Ca})$, and $U_{\text{iso}}(\text{Cu})$. Structural parameters are kept fixed to crystallographic values. Denotations are listed as follows: Crystallographic=crystallographic with nominal stoichiometry, Antisite=chemical disorder on Cu and Ca sites with nominal stoichiometry, E-Cu=excess Cu on Ca site (nonstoichiometric), E-Ca=excess Ca on Cu site (nonstoichiometric). See text for details.

Parameter\model	Crystallographic	Antisite	E-Cu	E-Ca
$U_{\text{ISO}}(\text{Ca})$ (Å ²)	0.0050(6)	0.0056(7)	0.0044(7)	0.0053(6)
$U_{\text{ISO}}(\text{Cu})$ (Å ²)	0.0050(2)	0.0048(2)	0.0050(3)	0.0048(2)
d		0.07(3)	-0.11(6)	0.09(3)
R_w	0.1351	0.1347	0.1348	0.1343

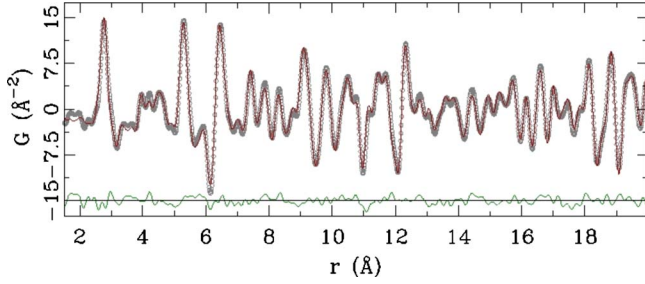


FIG. 10. (Color online) Typical CCTO PDF model fit: experimental PDF at 300 K (open circles), antisite model (solid line), and corresponding difference curve (offset for clarity).

In short, although we did not observe Ti-related disorder, we do find that a model with a disordered phase with Cu/Ca substitution, suggested by the TEM and electron-diffraction results, is consistent with the EXAFS data. Similar nanoscale phases were previously established with EXAFS in analogous systems.^{29,60}

E. Analysis of neutron PDF data

The neutron powder-diffraction PDF results from the RT refinements based on the method we discussed in Sec. II D are tabulated in Table VII. To model the data we used the crystallographic ($Im\bar{3}$) model. This was refined to the PDF data to obtain structural parameters, in agreement with the previous study.⁹ Then several models incorporating antisite disorder were attempted to allow the exchange of Ca and Cu ions. The antisite model preserved the nominal stoichiometry by only allowing switches of Cu and Ca ions. We also tried models where Cu was allowed to reside on Ca sites, Cu_{Ca} , and vice versa, without changing the composition of the unaffected site that results in a change in overall stoichiometry of the sample. In each case, a defect parameter, d , was defined. For the antisite model $d = O(\text{Cu}_{\text{Ca}})$, where $O(X_Y)$ is the occupancy of X atoms on Y -atom sites, with the further constraints $O(\text{Cu}_{\text{Cu}}) = 1 - d$, $O(\text{Ca}_{\text{Cu}}) = 0.33d$, and $O(\text{Ca}_{\text{Ca}}) = 1 - 0.33d$. This retains the overall stoichiometry because there are three copper sites for every Ca site. We also tried two models for uncompensated antisite defects. The E-Cu model has $d = O(\text{Cu}_{\text{Ca}})$ with the further constraint $O(\text{Ca}_{\text{Ca}}) = 1 - d$ to ensure full occupancy of the Ca site by either Ca or Cu, and the occupancies of the copper sites set to 1. For completeness we also define an E-Ca model with $d = O(\text{Ca}_{\text{Cu}})$, $O(\text{Ca}_{\text{Ca}}) = 1 - d$ and the Cu site fully occupied with copper. Refinements were first carried out with $d = 0$, which is the ideal crystallographic model. This process reproduced the results presented in Ref. 9, with all refined parameters being within two standard deviations of the values reported in Ref. 9) as expected. The parameter d was then allowed to refine in addition to the free variables from the crystallographic models. Refinements were carried out over a range of r to 20 Å on data with the following temperatures: 50, 100, 150, and 200 K, and room temperature. For temperatures at 300 K and below, we expect negligible diffusion of cations and so the cation distribution in the samples must be the same at all temperatures. However, the complementary data sets provide

TABLE VIII. Refined values of the defect parameter, d (see text for details) for the different models and different measurement temperatures refined.

T (K)	Antisite	E-Ca	E-Cu
300	0.07(3)	0.09(3)	-0.11(6)
200	0.01(3)	0.04(3)	-0.11(6)
150	-0.01(3)	0.02(3)	-0.10(6)
100	-0.01(3)	0.01(3)	-0.09(6)
50	-0.04(3)	-0.02(3)	-0.06(6)

independent measurements and should give consistent results for d .

A typical CCTO PDF model with antisite disorder fit with the experimental data at 300 K is shown in Fig. 10. The refined values of the defect parameter, d , for all temperatures and models are summarized in Table VIII. For the 300 K data, the agreement factors are slightly improved for all the antisite models with small positive disorder parameters, d , refined for the antisite and E-Ca models (Ca defects on Cu sites). However, the refinements to the lower-temperature data sets all converge to d values that are not significantly different from zero, suggesting that the neutron-diffraction data of the powder sample do not support the presence of significant antisite defects within the precision of the measurement. Based on the estimated errors in the refinement, the uncertainty on the refined d parameter is $\sim 3\%$, which may be considered as a lower-bound because it does not take into account systematic errors and parameter correlations in the refinement which both contribute to the uncertainty. The neutron data therefore do not contradict the TEM and EXAFS observations but they do place an upper bound on the extent of the effect. It is difficult to put a precise numerical value on this bound but based on the estimated uncertainties on the data we suggest it is certainly less than 10% and probably about $\sim 5\%$. We note that in the case of the antisite defects, the PDF d parameter and EXAFS x parameter are defined the same way. The PDF data are not good enough to differentiate between stoichiometric and nonstoichiometric models for the antisite disorder and for the same reason, no models with short-range ordering of the defects were tried.

F. Formation energy of nonstoichiometric phases

The antisite disorder of Ca and Cu in CCTO seems unfavorable from chemical intuition based on their ionic radii (i.e., 0.57 Å for a 4-coordinate Cu^{2+} vs 1.34 Å for a 12-coordinate Ca^{2+}) and bond length (1.967 Å for Cu-O bond length vs 2.602 Å for Ca-O). To understand the energetics of various phases in CCTO, we calculated the total energy of three different phases, stoichiometric, Ca-rich, and Cu-rich phases, and compared their formation energies to examine their stabilities using LDA-based pseudopotential calculations. The formation energy for different phases can be defined as

$$E_{\text{form}}(\text{Ca}_x\text{Cu}_{8-x}\text{Ti}_8\text{O}_{24}) = E_{\text{tot}}(\text{Ca}_x\text{Cu}_{8-x}\text{Ti}_8\text{O}_{24}) - xE_{\text{tot}}(\text{CaO}) - (8-x)E_{\text{tot}}(\text{CuO}) - 8E_{\text{tot}}(\text{TiO}_2).$$

Here, $\text{Ca}_x\text{Cu}_{8-x}\text{Ti}_8\text{O}_{24}$ represents the general form of system

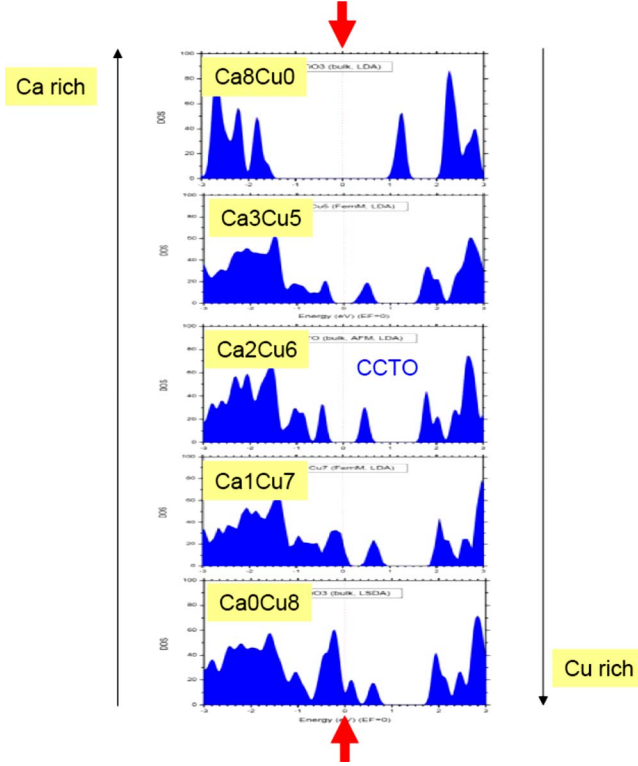


FIG. 11. (Color online) Density of states of $\text{Ca}_x\text{Cu}_{8-x}\text{Ti}_8\text{O}_{24}$ as a function of composition calculated using pseudopotential localized spin-density approximation LSDA with optimized geometry (top to bottom: $x=8, 3, 2, 1$, and 0). Stoichiometric $\text{Ca}_2\text{Cu}_6\text{Ti}_8\text{O}_{24}$ corresponds to $x=2$. Note, for $x \geq 2$ (top three phases), the system exhibits an insulating behavior with an energy gap near the Fermi level. For $x < 2$, the system becomes metallic.

for various compositions ($x=1, 2$, and 3), E_{form} and E_{tot} is the formation energy and the total energy, respectively. We use CaO, CuO, and rutile TiO_2 as starting oxides that are commonly used in synthesis. We have

$$\begin{aligned} E_{\text{form}}(\text{Ca}_2\text{Cu}_6\text{Ti}_8\text{O}_{24}) &= E_{\text{tot}}(\text{Ca}_2\text{Cu}_6\text{Ti}_8\text{O}_{24}) - 2E_{\text{tot}}(\text{CaO}) \\ &\quad - 6E_{\text{tot}}(\text{CuO}) - 8E_{\text{tot}}(\text{TiO}_2) \\ &= -2.20 \text{ (eV/40 atom cell)}, \end{aligned}$$

$$\begin{aligned} E_{\text{form}}(\text{Ca}_3\text{Cu}_5\text{Ti}_8\text{O}_{24}) &= E_{\text{tot}}(\text{Ca}_3\text{Cu}_5\text{Ti}_8\text{O}_{24}) - 3E_{\text{tot}}(\text{CaO}) \\ &\quad - 5E_{\text{tot}}(\text{CuO}) - 8E_{\text{tot}}(\text{TiO}_2) \\ &= -2.39 \text{ (eV/40 atom cell)}, \end{aligned}$$

$$\begin{aligned} E_{\text{form}}(\text{Ca}_1\text{Cu}_7\text{Ti}_8\text{O}_{24}) &= E_{\text{tot}}(\text{Ca}_1\text{Cu}_7\text{Ti}_8\text{O}_{24}) - E_{\text{tot}}(\text{CaO}) \\ &\quad - 7E_{\text{tot}}(\text{CuO}) - 8E_{\text{tot}}(\text{TiO}_2) \\ &= +0.40 \text{ (eV/40 atom cell)}. \end{aligned}$$

The results suggest that the formation of stoichiometric and Ca-rich CCTO are energetically favorable while that of the formation of Cu-rich CCTO is unfavorable. This means that the Ca-rich phase can grow bigger in size than the Cu-rich phase. In our calculations, the entire structure was re-

laxed without imposing any displacement constraints. The result is in full agreement with our EXAFS and TEM data that due to the small size of the Cu-rich phase we mainly observe only Ca-rich phase from the overall stoichiometric crystal (see Sec. III D 2).

G. Electronic properties of $\text{Ca}_x\text{Cu}_{8-x}\text{Ti}_8\text{O}_{24}$ ($0 \leq x \leq 8$)

The total density of states of off-stoichiometric CCTO, i.e., $\text{Ca}_x\text{Cu}_{8-x}\text{Ti}_8\text{O}_{24}$ ($0 \leq x \leq 8$), as a function of x were studied using pseudopotential LSDA (localized spin-density approximation) with optimized crystal geometry. The results are plotted in Fig. 11. (Note that the finite bandwidth of the Cu orbitals near the Fermi level results artificially from the periodicity of the disordered Cu in the calculation.) The AFM bulk stoichiometric $\text{Ca}_2\text{Cu}_6\text{Ti}_8\text{O}_{24}$ (i.e., $x=2$) phase clearly shows a ~ 0.5 eV band gap and is in good agreement with previous pseudopotential LSDA calculations.⁶ From Ca-rich to Cu-rich phases, Fig. 11 clearly shows an increasing amount of Cu d orbitals residing near the Fermi level. For the Ca-rich phases (namely, with composition of $x > 2$), there is an energy gap at the Fermi level and the gap remains till $x=2$, i.e., stoichiometric CCTO. On the other hand, as soon as Cu starts to occupy the Ca sites to form various Cu-rich phases (lower two panels), the associated d orbitals start to pile up at the Fermi level. The same trend is reproduced upon inclusion of a strong local interaction in Cu atoms via LSDA+ U (Ref. 57) calculations within the full-potential linear APW methods.⁵⁴ In the LSDA+ U calculations for stoichiometric antiferromagnetic CCTO, the Cu $3d$ states are more localized and the band gap is broadened to about 2 eV, which is in good agreement with experimental observations (> 1.5 eV).⁶¹ For the Cu-rich CCTO (e.g., for $x=1$, namely, $\text{Ca}_1\text{Cu}_7\text{Ti}_8\text{O}_{24}$), the LSDA+ U calculations also show Cu states at the Fermi level from the Cu located in the Ca sites.

IV. DISCUSSION

A. Ca/Cu disorder

Our EXAFS and TEM results clearly suggest that there is a local Ca/Cu disorder in the CCTO single crystals that we studied. The obvious question we have was why neutron and x-ray diffraction experiments did not unambiguously identify but only give some evidence of such an antisite disorder.

In the $Im\bar{3}$ CCTO structure, the substitution of Cu at Ca sites and Ca at Cu sites result in changes only in the intensity of the ooe class of reflections (o and e refers to odd and even numbers, respectively) but does not result in any change to the eee reflections. Consequently, the normal least-squares refinement parameters for the entire data set are not very sensitive to the substitution when only limited numbers of reflections are collected. The change in agreement factors (goodness of fit) with and without 5% substitution is quite small. Even at 10% of substitution (20% of disordered regions), the agreement factor changes only from 1.32 to 2.24. To show the effects of the substitution on major reflections in the x-ray data, in Fig. 12 we plot calculated intensity vs 2θ scattering angles of powder diffraction for CCTO using MATERIALS STUDIO software with a wavelength $\lambda=0.154$ nm.

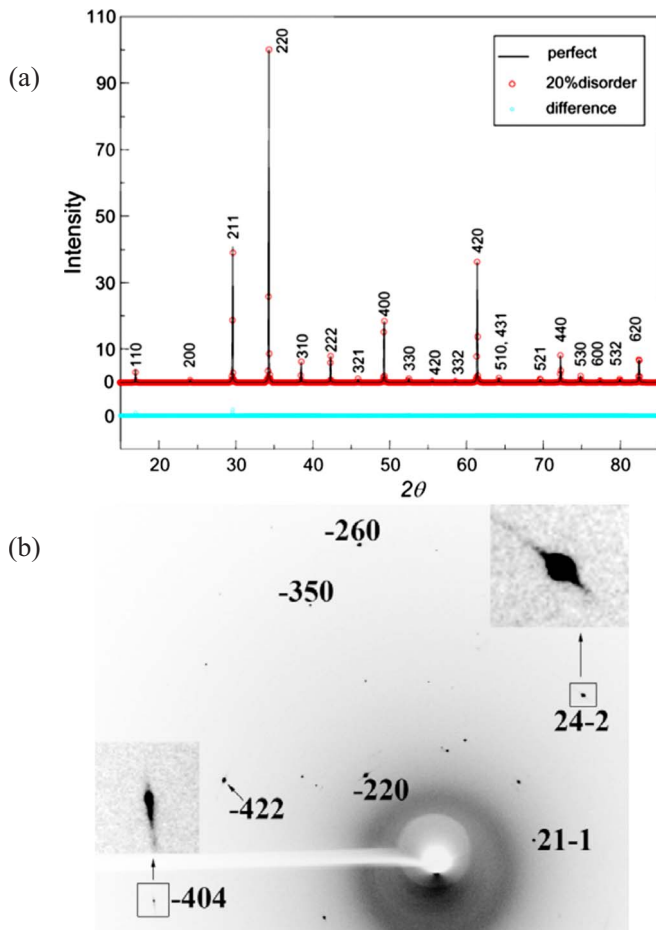


FIG. 12. (Color online) (a) Calculated intensity vs scattering angles of powder x-ray diffraction (XRD) pattern for CCTO using MATERIALS STUDIO software with wavelength $\lambda=0.154$ nm. The solid lines are for perfect CCTO, the open circles are for CCTO with 10% swap of Ca with Cu, i.e., 20% of disordered regions. The difference, calculated by subtracting the intensity of disordered from that of perfect CCTO, is shown in blue. Note, visible difference only shown at the 110 and 211 reflections. Our accurate measurements of the structure factor of the two reflections suggest they deviate from the DFT calculation of the perfect CCTO. (b) X-ray diffraction pattern of CCTO single crystal recorded at room temperature, showing diffuse scattering surrounding some of the Bragg peaks.

The solid lines are for ideal stoichiometric CCTO, the crosses are for CCTO with a 10% swap of Ca with Cu, i.e., 20% of disordered regions. The difference, calculated by subtracting the intensity of the disordered from that of perfect CCTO, is shown in blue. The largest discrepancies are at the 110 and 211 reflections (our accurate measurements of the structure factor of the two reflections using PARODI also suggest they deviate from the DFT calculation of the perfect CCTO). It is evident that a small percentage of disorder in CCTO has a subtle change in the overall x-ray diffraction data. This is to be expected because of the small difference between Ca and Cu x-ray scattering factors.

In the refinement using perfect CCTO, the R1 and wR2 are 0.023 and 0.075, respectively. By simply introducing 5%

exchange between Ca and Cu (corresponding to 10% disorder) without refinement the R1 increases to 0.028 while wR2 to 0.091. After further refinement, the R1 actually decreases to 0.018 while wR2 to 0.046. We note although the change in the R factors is not significant, it indeed indicates the possible existence of the disordered phase. We plan to perform an additional x-ray experiment with much high-order reflections [including diffuse scattering analysis, see Fig. 12(b)] to accurately determine the amount of the disordered phases.

It is interesting to note that at room temperature, our measurements using EXAFS, TEM, and PDF all point to the existence of small percent of Ca/Cu antisite disorder in CCTO, in particular, with detectable Ca-rich regions and undetectable Cu-rich regions. This is consistent with our DFT calculations based on the energy ground of the two phases. At lower temperatures, the Ca/Cu disorder seems much less measurable (90 K for TEM and 50–200 K for PDF measurements) and PDF analysis was inconclusive on the existence of the Ca/Cu disorder (see Sec. III E). The observed variation in Ca/Cu disorder at different temperatures may be an important factor that can be associated with low-temperature-dependent dielectric properties of CCTO, which shows a reduction in dielectric constant for certain frequencies at 100 K and below.

At current stage, it is not clear what the origin of the variation in Ca/Cu disorder at different temperatures is. Temperature-dependent EXAFS, QED, and high-resolution EELS measurements to explore temperature-dependent electronic structure and the dielectric function at much lower temperatures than 100 K as well as theoretical dynamical calculations such as molecular-dynamics simulations may help to address this question. Further studies can also include a joint EXAFS/PDF analysis on new data obtained from diffraction and spectroscopy measurements on identical samples, as suggested in Ref. 62. In the following, we discuss the possible mechanism of Ca/Cu disorder induced enhancement of dielectric response.

B. Temperature effects on ionicity and charge transfer

Structure factors measured by quantitative electron diffraction at different temperatures were used to understand the temperature effects in the CCTO. To cancel the Debye-Waller factor term, all the structure factors were converted to 0 K for comparison. We noticed that the structure factor of the (200) reflection increases $\sim 2\%$, from 18.96 at RT to 19.38 at 90 K. By comparing the hypothetical pure ionic and neutral-atom (procrystal) models, our calculations show that among the six measurable low-order structure factors in CCTO, only the (200) reflection is very sensitive to temperature. The (200) reflection is a measure of the degree of octahedral tilting in the double perovskite structure. The strong T dependence of this peak indicates a destruction of the long-range order of the octahedral tilts, via thermal fluctuations, and thus the weakening of the associated orbital ordering among the t_{2g} electrons. Such an observation is also seen in the PDF analyses.⁹ As discussed below in more detail, such disruption of orbital ordering recovers the near degeneracy of the Cu electrons (in this case moving the t_{2g} states close to

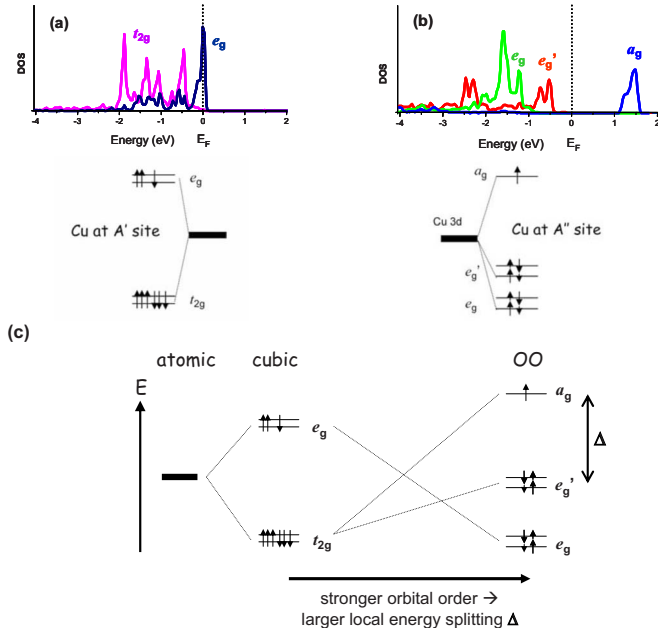


FIG. 13. (Color online) Local symmetry consideration of Cu orbitals showing the influence of antisite Ca/Cu order on the electronic structure in CCTO ($A'A''Ti_4O_{12}$). (a) Cubic symmetry (i.e., Cu at the A' site, or $Ca_3Cu_5Ti_8O_{24}$) and (b) lower symmetry (i.e., Cu at the A'' site as the ideal or ordered $CaCu_3Ti_4O_{12}$). The former hosts one hole in the triply degenerate t_{2g} complex and pins the chemical potential while the latter hosts one hole in the nondegenerate a_g orbital and allows the formation of a Mott insulator. The corresponding density of states obtained from DFT (LDA+ U) calculations are also included, showing in perfect agreement with the local symmetry consideration [40-atom unit cell (space group $Pm\bar{3}$) in an AFM ground state for (b) and replacing Ca atom at the face center with Cu after relaxation for (a)]. (c) Evolution of local-orbital structure via lowering of the symmetry, from spherical (atomic) to cubic and to the orbital-ordered (OO) case. Clearly, the local energy splitting, Δ , of a_g and e'_g increases with strengthened orbital ordering.

the chemical potential from both above and below) which in turn would give a large electronic enhancement of the dielectric response and could provide a natural explanation of the experimentally observed increase in dielectric constant at higher temperature.

C. Electronic origin of giant dielectric response in CCTO

Our combined experimental and theoretical study leads to an interesting observation of large enhancement of dielectric response in CCTO via *electronic* contributions that are currently unnoticed in the literature. The above EXAFS and diffraction analyses provide strong evidence of nanoscale phase separations in CCTO with a mixture of stoichiometric (ordered) and nonstoichiometric (disordered) regions. The formation of these regions is further confirmed theoretically by their low formation energies obtained in our DFT calculations. In addition, the DFT results indicate a significant difference in the electronic structure in Cu-rich systems, fa-

voring accumulation of Cu d states at the Fermi level (Fig. 11).

This interesting result of numerical calculations can be understood from the following robust local symmetry consideration. As illustrated in Fig. 13(a), under the local cubic point-group symmetry (as in the A' site), the five d orbitals of Cu splits into two sets, double-degenerate e_g and triple-degenerate t_{2g} . Therefore, the single hole in Cu^{2+} (d^9 configuration) resides in a complex of degenerate orbitals, pinning the chemical potential right in the middle of the degenerate orbitals, as shown in the local density of states of the A' -site Cu obtained in our DFT calculation. In contrast, the threefold degenerate t_{2g} orbitals further split into two distinct sets, a_g and e'_g for Cu located in the A'' sites, as shown in Fig. 13(b). This allows the system to lower its energy by having the hole in the highest nondegenerate a_g level, providing an opportunity for the formation of a Mott insulator based on our DFT calculation.

The apparent reason for the lower point-group symmetry of A'' site is the asymmetric positioning of the surrounding oxygen atoms associated with the TiO_6 octahedral tilting/distortion. However, recent first-principles theoretical studies of similar octahedral tilting/distortion in $LaMnO_3$,⁶³ Ca doped $LaMnO_3$,⁶⁴ and orbital ordering in Fe pnictides⁶⁵ revealed that even without the external lattice effects, the strong interactions among the $3d$ electrons make such a orbital degenerate system highly vulnerable against “orbital ordering,” a spontaneous symmetry breaking with asymmetric orbital polarization and arrangement. Therefore, it is most likely that the octahedral tilting/distortion owes its microscopic origin, at least in part, to the underlying orbital ordering of the electrons.

The above robust symmetry consideration dictates that the A'' -Cu should have partially filled degenerate orbital at the chemical potential if the symmetry were not broken by the orbital ordering (accompanied by the octahedral tilting/distortion). In that case, CCTO would have been a metal with divergent dielectric constant in the first place. It is precisely the splitting of the orbital degeneracy due to the orbital ordering that allows the insulating behavior of the system via the formation of a Mott insulator. Therefore, the electronic response of the system is expected to be unconventional and extreme caution must be exercised to avoid treating the system as a regular band insulator, such as the titanates, for example.

This microscopic insight suggests an interesting “extrinsic” feature that might explain the unusually large dielectric response. Since the insulating nature of the system is derived from the orbital ordering, any local disruption of the orbital ordering and the octahedral tilting/distortion, say via the introduction of A' -Cu or A'' -Ca, would significantly reduce the local energy splitting, Δ , of the a_g and e'_g orbitals, as illustrated in Fig. 13(c). In addition, as discussed above, in the orbital-ordered structure, A' site has higher local point-group symmetry and can introduce degenerate orbitals right at the chemical potential ($\Delta \rightarrow 0$). Taking into account the first-moment sum rule, the dynamical spectral weight of the interorbital excitations across the gap is proportional to $1/\Delta$ while the Kramers-Kronig transform dictates the low-frequency dielectric function to be proportional to the dy-

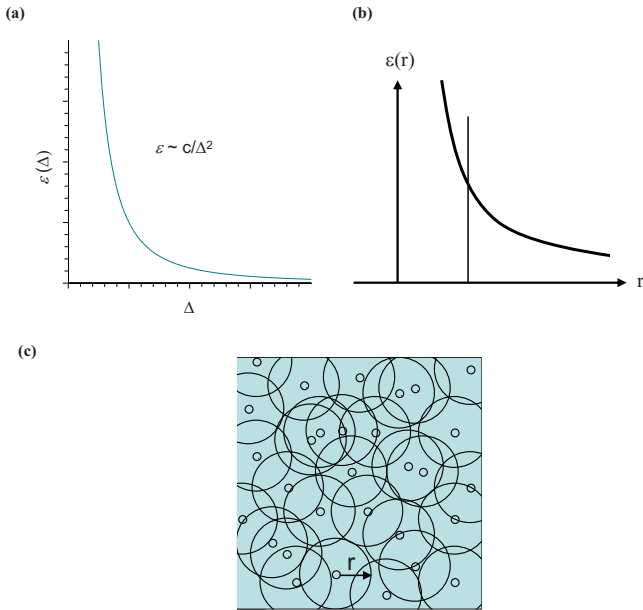


FIG. 14. (Color online) Illustration of enhancement of electronic dielectric response via proximity effects around A' -Cu. (a) $1/\Delta^2$ enhancement of the local dielectric constant for Cu atoms with disrupted orbital ordering. (b) The proximity effects of the dielectric constant around A' -Cu. At short distance ($r \rightarrow 0$) from the A' -Cu sites, the dielectric constant diverges quickly as the gap shrinks. (c) The proximity effects in a system with randomly distributed chemical disorder (disordered bubbles). If the occurrence of A' -Cu spreads throughout the sample without much clustering, as suggested by our EXAFS analysis, there can be very little region left unaffected by the proximity effects, giving rise to a significant enhancement of the total dielectric constant.

namical spectral weight multiplied by inverse of the excitation frequency. Together, one expects qualitatively a significant enhancement of the dielectric constant proportional to $1/\Delta^2$, as shown in Fig. 14(a).

Following the above rigorous analysis, we suggest the following inhomogeneous picture of enhanced *electronic* dielectric response. Near A' -Cu, the local dielectric response should be greatly enhanced from coupling to the degenerate orbitals of A' -Cu ($\Delta \rightarrow 0$) and the variation in significantly reduced Δ resulting from disruption of orbital ordering of the surrounding A'' -Cu. The local dielectric response consists of a profile of singularly large value centered at each A' -Cu, with a smooth decay at larger distance [Fig. 14(b)]. Formulated in a continuous model, it is apparent the bulk dielectric function $\epsilon_{\text{tot}}^{-1} = \frac{1}{V} \int \epsilon^{-1}(x) d^3x$ is ultimately controlled by the regions with small local response. As illustrated in Fig. 14(c), given a random distribution of A' -Cu and A'' -Ca and a large enough radius of the enhancement, the bulk dielectric response can be boosted easily by several order of magnitudes. That is, the above proximity effect can lead to a large dielectric response, given only a very small portions of the bulk that are far from all the A' -Cu sites, as indicated by our EXAFS data, to possess small enough local dielectric response that contribute to the integral.

This picture also naturally resolves a puzzling dilemma existing in some of the conventional extrinsic pictures⁷ in-

volving metallic domains with insulating boundaries in which a very small volume fraction ($\sim 10^{-3}$) of insulator is needed while the insulating boundaries have to fully cover the metallic domains in order to keep the system insulating. If such picture were to be realized, an insulating “blocking layer” to make the sample insulating would be unavoidable, which however was not observed in any of our measurements. This difficulty does not enter in our picture since the region near A' -Cu are still well insulating ($\Delta > 0$) in terms of transport (determined by states at the chemical potential) but with large dielectric response (controlled by all low-energy states with $\Delta \ll 1$).

Our interpretation also provides a natural scenario for the well-known puzzle why the dielectric response of $\text{CdCa}_3\text{Ti}_4\text{O}_{12}$ is found two orders of magnitude lower than CCTO.⁶¹ Cd and Ca are isoelectronic in these systems, with a very similar chemical size, and thus pure-phase Cd-CTO and CCTO have almost identical electronic structure, as confirmed by a previous theoretical study.⁴¹ It is thus a great surprise that their dielectric response is so different. Now, since disorder in materials is controlled by complicated non-equilibrium process of crystal growth, the disorder in these two similar materials can be very different. Our picture suggests that either the degree of disordered A' -Cu is less in CdCTO or the disordered A' -Cu atoms form larger cluster (thus leaving larger volume fraction with small dielectric response). Future experimental verification of this issue will provide an unambiguous confirmation of our picture.

We note that the above novel picture of extrinsic effect is based on the proximity effect of metallic behavior in terms of dielectric response, not transport, of a disordered orbital-ordered Mott insulator, and is substantially different from the physics in a conventional band insulator such as conventional ferroelectric compounds. The validity of this strongly correlated picture can be experimentally verified by, for example, direct observation of these low-energy excitations via large- q inelastic x-ray scattering, which is capable of probing transition in atomic length scale or local dielectric profile with high-resolution low-energy electron-energy-loss spectroscopy measurement. Similar idea can be applied to the search for high dielectric materials by introducing disorders in other families of strongly correlated degenerate Mott insulators, such as the manganites or the vanadium oxides.

V. CONCLUSIONS

In summary, using experimental techniques that are sensitive to local disorder, we found that there exist small amount of off-stoichiometric nanoscale regions in CCTO single crystals. The measurement and detection are not trivial largely due to the low concentration and small size of the defect regions. Nonetheless, theoretical calculations based on density-functional theory suggest a large metal-like local *electronic* dielectric response near the disordered Cu atoms, as a consequence of the recovery of degeneracy of the open t_{2g} shell and the disruption of the long-range orbital order. Bulk measurements of local structure indicate that the defective regions constitute $< 10\%$ of the sample. Because of the

difficulty of quantifying nanoscale defects at such low levels, further work will be required to establish that this mechanism is operative in $\text{CaCu}_3\text{Ti}_4\text{O}_{12}$. However, our results demonstrate that local atomic substitution or disorder can induce a dramatic change in the local dielectric behavior in strongly correlated systems with orbital freedom, and point to an innovative way in searching for fascinating properties in correlated materials, including perovskite transition-metal oxides.

ACKNOWLEDGMENTS

We thank Morrel H. Cohen, David Vanderbilt, Weiguo Yin, and Peter Stephens for stimulating discussions. A.I.F. acknowledges support by the U.S. Department of Energy, Office of Basic Energy Science, Grant No. DE-FG02-03ER15476. Work at Brookhaven was supported by the U.S. Department of Energy, Office of Basic Energy Science, under Contract No. DE-AC02-98CH10886 and DOE-CMSN.

*Corresponding author. zhu@bnl.gov

- ¹M. A. Subramanian, D. Li, N. Duan, B. Reisner, and A. W. Sleight, *J. Solid State Chem.* **151**, 323 (2000).
- ²A. P. Ramirez, M. A. Submananian, M. Gardel, G. Blumberg, D. Li, T. Vogt, and S. M. Shapiro, *Solid State Commun.* **115**, 217 (2000).
- ³C. C. Homes, T. Vogt, S. M. Shapiro, S. Wakimoto, and A. P. Ramirez, *Science* **293**, 673 (2001).
- ⁴H. C. Li, W. Si, A. D. West, and X. X. Xi, *Appl. Phys. Lett.* **73**, 464 (1998).
- ⁵G. A. Samara and L. A. Boatner, *Phys. Rev. B* **61**, 3889 (2000).
- ⁶L. He, J. B. Neaton, M. H. Cohen, D. Vanderbilt, and C. C. Homes, *Phys. Rev. B* **65**, 214112 (2002).
- ⁷M. H. Cohen, J. B. Neaton, L. He, and D. Vanderbilt, *J. Appl. Phys.* **94**, 3299 (2003).
- ⁸L. Wu, Y. Zhu, S. Park, S. Shapiro, G. Shirane, and J. Tafto, *Phys. Rev. B* **71**, 014118 (2005).
- ⁹E. S. Božin, V. Petkov, P. W. Barnes, P. M. Woodward, T. Vogt, S. D. Mahanti, and S. J. L. Billinge, *J. Phys.: Condens. Matter* **16**, S5091 (2004).
- ¹⁰Y. Zhu and J. Tafto, *Philos. Mag. B* **75**, 785 (1997).
- ¹¹J. Taftø, Y. Zhu, and L. Wu, *Acta Crystallogr., Sect. A: Found. Crystallogr.* **54**, 532 (1998).
- ¹²L. Wu, Y. Zhu, and J. Tafto, *Micron* **30**, 357 (1999).
- ¹³Y. Zhu, L. Wu, and J. Tafto, *Microsc. Microanal.* **9**, 442 (2003).
- ¹⁴L. Wu, Y. Zhu, T. Vogt, H. Su, and J. W. Davenport, *Phys. Rev. B* **69**, 064501 (2004).
- ¹⁵J. M. Zuo, M. O’Keeffe, P. Rez, and J. C. H. Spence, *Phys. Rev. Lett.* **78**, 4777 (1997).
- ¹⁶J. M. Zuo, M. Kim, M. O’Keeffe, and J. C. H. Spence, *Nature (London)* **401**, 49 (1999).
- ¹⁷A. P. Hammersley (1994) FIT2D program; A. P. Hammersley, ESRF Internal Report No. EXP/AH/95-01, 1995 (unpublished).
- ¹⁸Z. Otwinowski and W. Minor, *Methods in Enzymology*, Macromolecular Crystallography Part A Vol. 276, edited by C. W. Carter, Jr. and R. M. Sweet (Academic Press, New York, 1997), pp. 307–326; J. Zaleski, G. Wu, and P. Coppens, *J. Appl. Crystallogr.* **31**, 302 (1998).
- ¹⁹G. M. Sheldrick, *SHELXTL Reference Manual* (Bruker AXS, Madison, Wisconsin, 1993).
- ²⁰E. D. Stevens and P. Coppens, *Acta Crystallogr., Sect. A: Cryst. Phys., Diffr., Theor. Gen. Crystallogr.* **32**, 915 (1976).
- ²¹J.-C. Zheng, L. Wu, Y. Zhu, and J. W. Davenport, *J. Appl. Crystallogr.* **38**, 648 (2005).
- ²²H. K. Hansen and P. Coppens, *Acta Crystallogr., Sect. A: Cryst. Phys., Diffr., Theor. Gen. Crystallogr.* **34**, 909 (1978).
- ²³R. F. Stewart, M. A. Spaceman, and C. Flensburg, *VALRAY User’s Manual* (Carnegie Mellon University and University of Copenhagen, Pittsburgh, PA, 2000).
- ²⁴E. Clementi and C. Roetti, in *Atomic Data and Nuclear Data Tables*, edited by K. Way (Academic Press, New York, 1974), Vol. 14, pp. 177–478.
- ²⁵A. Frenkel, E. A. Stern, A. Voronel, M. Qian, and M. Newville, *Phys. Rev. Lett.* **71**, 3485 (1993).
- ²⁶A. I. Frenkel, M. H. Frey, and D. A. Payne, *J. Synchrotron Radiat.* **6**, 515 (1999).
- ²⁷A. I. Frenkel, V. Sh. Machavariani, A. Rubshtein, Yu. Rosenberg, A. Voronel, and E. A. Stern, *Phys. Rev. B* **62**, 9364 (2000).
- ²⁸P. Pfalzer, J. Will, A. Naterprov, M. Klemm, S. Horn, A. I. Frenkel, S. Calvin, and M. L. denBoer, *Phys. Rev. B* **66**, 085119 (2002).
- ²⁹A. I. Frenkel, D. M. Fanning, D. L. Adler, I. K. Robinson, and J. O. Cross, *The 5th Williamsburg Workshop on First-Principles Calculations for Ferroelectrics*, Williamsburg, Virginia, 1–4 February 1998, AIP Conf. Proc. No. 436 (AIP, New York, 1998), p. 96.
- ³⁰A. I. Frenkel, D. M. Pease, G. Giniewicz, E. A. Stern, D. L. Brewster, M. Daniel, and J. Budnick, *Phys. Rev. B* **70**, 014106 (2004).
- ³¹A. I. Frenkel, Y. Feldman, V. Lyahovitskaya, E. Wachtel, and I. Lubomirsky, *Phys. Rev. B* **71**, 024116 (2005).
- ³²A. I. Frenkel, D. M. Pease, J. Budnick, P. Metcalf, E. A. Stern, P. Shanthakumar, and T. Huang, *Phys. Rev. Lett.* **97**, 195502 (2006).
- ³³E. A. Stern, M. Newville, B. Ravel, Y. Yacoby, and D. Haskel, *Physica B* **208-209**, 117 (1995).
- ³⁴S. I. Zabinsky, J. J. Rehr, A. Ankudinov, R. C. Albers, and M. J. Eller, *Phys. Rev. B* **52**, 2995 (1995).
- ³⁵A. V. Kolobov, P. Fons, A. I. Frenkel, A. L. Ankudinov, J. Tomimaga, and T. Uruga, *Nature Mater.* **3**, 703 (2004).
- ³⁶P. Shanthakumar, M. Balasubramanian, D. Pease, A. I. Frenkel, D. Potrepka, J. Budnick, W. A. Hines, and V. Kraizman, *Phys. Rev. B* **74**, 174103 (2006).
- ³⁷M. S. Nashner, A. I. Frenkel, D. L. Adler, J. R. Shapley, and R. G. Nuzzo, *J. Am. Chem. Soc.* **119**, 7760 (1997).
- ³⁸B. Bochu, M. N. Deschizeaux, J. C. Joubert, A. Collomb, J. Chenavas, and M. Marezio, *J. Solid State Chem.* **29**, 291 (1979).
- ³⁹Y. J. Kim, S. Wakimoto, S. M. Shapiro, P. M. Gehring, and A. P. Ramirez, *Solid State Commun.* **121**, 625 (2002).
- ⁴⁰S. G. Ebbinghaus, A. Weidenkaff, and R. J. Cava, *J. Solid State Chem.* **167**, 126 (2002).

- ⁴¹L. X. He, J. B. Neaton, D. Vanderbilt, and M. H. Cohen, *Phys. Rev. B* **67**, 012103 (2003).
- ⁴²S. H. Byeon, M. W. Lufaso, J. B. Parise, P. M. Woodward, and T. Hansen, *Chem. Mater.* **15**, 3798 (2003).
- ⁴³D. Capsoni, M. Bini, V. Massarotti, G. Chiodelli, M. C. Mozzatic, and C. B. Azzoni, *J. Solid State Chem.* **177**, 4494 (2004).
- ⁴⁴S. Y. Chung, *Appl. Phys. Lett.* **87**, 052901 (2005).
- ⁴⁵W. Wong-Ng, J. Suh, and J. A. Kaduk, *Powder Diffr.* **20**, 193 (2005).
- ⁴⁶Y. Zhu, J. C. Zheng, L. Wu, A. I. Frenkel, J. Hanson, P. Northrup, and W. Ku, *Phys. Rev. Lett.* **99**, 037602 (2007).
- ⁴⁷T. Egami and S. J. L. Billinge, *Underneath the Bragg Peaks: Structural Analysis of Complex Materials* (Pergamon, New York/Elsevier, Oxford, 2003).
- ⁴⁸R. A. Young, *The Rietveld Method, International Union of Crystallography Monographs on Crystallography* (Oxford University Press, Oxford, 1993), Vol. 5.
- ⁴⁹C. L. Farrow, P. Juhas, J. W. Liu, D. Bryndin, E. S. Božin, J. Bloch, Th. Proffen, and S. J. L. Billinge, *J. Phys.: Condens. Matter* **19**, 335219 (2007).
- ⁵⁰Th. Proffen, R. G. DiFrancesco, S. J. L. Billinge E. L. Brosha, and G. H. Kwei, *Phys. Rev. B* **60**, 9973 (1999).
- ⁵¹T. Proffen, V. Petkov, S. J. L. Billinge, and T. Vogt, *Z. Kristallogr.* **217**, 47 (2002).
- ⁵²P. Hohenberg and W. Kohn, *Phys. Rev.* **136**, B864 (1964); W. Kohn and L. J. Sham, *ibid.* **140**, A1133 (1965).
- ⁵³J. M. Soler, E. Artacho, J. D. Gale, A. García, J. Junquera, P. Ordejón, and D. Sánchez-Portal, *J. Phys.: Condens. Matter* **14**, 2745 (2002).
- ⁵⁴P. Blaha, K. Schwarz, G. K. H. Madsen, D. Kvasnicka, and J. Luitz, *WIEN2K, An Augmented Plane Wave PlusLocal Orbitals Program for Calculating Crystal Properties* (Vienna University of Technology, Vienna, Austria, 2001).
- ⁵⁵J. P. Perdew and Y. Wang, *Phys. Rev. B* **45**, 13244 (1992).
- ⁵⁶J. P. Perdew, K. Burke, and M. Ernzerhof, *Phys. Rev. Lett.* **77**, 3865 (1996).
- ⁵⁷V. I. Anisimov, I. V. Solovyev, M. A. Korotin, M. T. Czyżyk, and G. A. Sawatzky, *Phys. Rev. B* **48**, 16929 (1993).
- ⁵⁸J. M. Zuo, *Rep. Prog. Phys.* **67**, 2053 (2004).
- ⁵⁹J. M. Cowley, *Phys. Rev.* **138**, A1384 (1965).
- ⁶⁰E. Prouzet, E. Husson, N. DeMathan, and A. Morell, *J. Phys.: Condens. Matter* **5**, 4889 (1993).
- ⁶¹C. C. Homes, T. Vogt, S. M. Shapiro, S. Wakimoto, M. A. Subramanian, and A. P. Ramirez, *Phys. Rev. B* **67**, 092106 (2003).
- ⁶²S. J. L. Billinge and I. Levin, *Science* **316**, 561 (2007).
- ⁶³W.-G. Yin and W. Ku, *Phys. Rev. Lett.* **96**, 116405 (2006).
- ⁶⁴D. Volja, W.-G. Yin, and W. Ku, *EPL* **89**, 27008 (2010).
- ⁶⁵C.-C. Lee, W.-G. Yin, and W. Ku, *Phys. Rev. Lett.* **103**, 267001 (2009).

Entropically Stabilized Local Dipole Formation in Lead Chalcogenides

Emil S. Božin,¹ Christos D. Malliakas,² Petros Souvatzis,³ Thomas Proffen,⁴ Nicola A. Spaldin,⁵ Mercuri G. Kanatzidis,^{2,6} Simon J. L. Billinge^{1,7*}

We report the observation of local structural dipoles that emerge from an undistorted ground state on warming, in contrast to conventional structural phase transitions in which distortions emerge on cooling. Using experimental and theoretical probes of the local structure, we demonstrate this behavior in binary lead chalcogenides, which were believed to adopt the ideal, undistorted rock-salt structure at all temperatures. The behavior is consistent with a simple thermodynamic model in which the emerging dipoles are stabilized in the disordered state at high temperature due to the extra configurational entropy despite the fact that the undistorted structure has lower internal energy. Our findings shed light on the anomalous electronic and thermoelectric properties of the lead chalcogenides. Similar searches may show that the phenomenon is more widespread.

Ferroelectric materials are characterized by a spontaneous alignment of static local dipole moments leading to a net electric polarization that can be switched by an applied electric field (*I*). Above their critical Curie temperature, T_c , they undergo a phase transition to a higher symmetry, nonpolar state, which by analogy with ferromagnets is called paraelectric. Although the question of whether the paraelectric phase consists of fluctuating local dipole moments or entirely centrosymmetric arrangements of atoms remains open (and likely depends on material, temperature, and length scale), the transition from paraelectric to ferroelectric on cooling always involves a lowering in symmetry that is well described within the traditional Landau picture of phase transitions, for example, in BaTiO_3 (*2*). In PbTe and PbS , we have observed the existence at high temperature of such a paraelectric phase of disordered, fluctuating dipoles, but the ground state rather than being the ferroelectric state is a dielectric with no local dipoles. There is no macroscopic symmetry change associated with the spontaneous local dipole formation, so the behavior is invisible to conventional crystallographic techniques. We detect the local atomic off-centering at high temperature using recently developed local structural probes.

Lead chalcogenides such as PbTe and the mineral galena (PbS) have been known and exploited since ancient times (*3*). They are particularly important today, with PbTe currently the leading thermoelectric material in applications just above room temperature (*4*). Despite

their long history, their nanoscale structure has only recently been studied in detail (*5–7*), motivated by the realization that intrinsic nanoscale structural modulations are helpful in producing low thermal conductivity and, therefore, high thermoelectric figures of merit (*4, 8*). Such studies of the nanostructure have been enabled by powerful synchrotron-based local structure probes, such as atomic pair distribution function (PDF) analysis (*9, 10*). The PDF is obtained by Fourier transforming appropriately collected and corrected x-ray or neutron powder diffraction data (*9*) and has peaks at positions corresponding to interatomic distances in the solid. We show in Fig. 1B the PDF of the simple rock-salt structure (Fig. 1A) that the lead chalcogenides were previously believed to adopt at all temperatures. Because both Bragg and diffuse scattering signals are used, the PDF yields local structural information rather than just the average crystallographic structure.

Our main results, obtained from temperature-dependent neutron diffraction studies, are summarized in Fig. 1, C to I. Because PbTe and PbS behave qualitatively similarly, we present only the PbTe results in the figure; data for PbS are contained in figs. S1 and S2 in the supporting online material (*11*). The dramatic effect of temperature on the structure of PbTe is evident in the powder diffraction pattern, shown in the form of the corrected and normalized diffraction intensity function $F(Q)$ (*11*) in Fig. 1C. This figure also serves to illustrate the high quality and good statistics of the neutron powder diffraction data collected over a wide range of momentum transfer, Q ($Q = 4\pi\sin\theta/\lambda$, where θ is the Bragg angle and λ the wavelength of the x-rays or neutrons). The dramatic loss of intensity in the Bragg peaks at high Q in the 500 K data (red) compared with the 15 K data (blue) is clear. The attenuation is due in part to the usual Debye-Waller effects (*12*) from increased thermal motion; however, the extent of the changes is extraordinarily large. In Fig. 1, D and E, we show the PDFs at 15 K and 500 K, respectively; the effect of temperature on the PDFs is anomalous, with notable broadening

evident at 500 K compared with 15 K. (The scale in Fig. 1E is one-fifth that in Fig. 1D.)

To study the temperature-induced local structural effects in more detail, we next analyze the temperature dependence of the low- r region, where r is the interatomic pair separation distance, of the PDF (Fig. 1F), where measured PDFs are shown every 50 K from 15 K to 500 K. The PDF peak broadening is reflected in the drop in the maxima of the peaks. Particularly striking is the drop in the nearest-neighbor peak, which occurs as rapidly as those in the higher-neighbor peaks. This strong broadening of the nearest-neighbor PDF peak does not occur in conventional materials. This is because of the highly correlated dynamics of nearest-neighbor atoms (*13*), which results in the relative motion of directly bonded atom pairs having a much smaller temperature dependence than the higher-neighbor pairs.

In Fig. 1, G and H, we show the Pb-Te nearest-neighbor peak on an expanded scale. At 15 K (Fig. 1G), the peak appears as a sharp, single-Gaussian function with small ripples coming from the finite Q range of the Fourier transform, so-called termination ripples (*9*). The red line is a calculated PDF peak with a pure Gaussian line-shape, convoluted with a sinc function to simulate the effects of the finite Fourier transform (*9*). This is characteristic of a single average bond length with harmonic motion taking place around that position, indicating that the ground state of PbTe at 15 K is ideal rock-salt in both the local and average structures, as expected. However, at 500 K (Fig. 1H), the peak is considerably broadened and qualitatively non-Gaussian, with extra intensity apparent on the high- r side of the peak. This unambiguously indicates the appearance of nonharmonic effects with increasing temperature.

We have quantified the asymmetry of this peak, and in Fig. 1I we plot the temperature dependence of a PDF peak asymmetry parameter, ΔR_{ASYMM} (*11*). It has a value of zero for a perfectly symmetric peak such as a Gaussian, and its numerical value increases as the peak becomes more asymmetric. As evident in Fig. 1I, the asymmetric nature of the first PDF peak increases continuously from 15 K to ~ 250 K, where it saturates.

The non-Gaussian asymmetry can be interpreted either in terms of strong anharmonicity in a single-welled potential probed by the atomic motions or by the appearance of multiple, incompletely resolved, short and long bond lengths under the nearest-neighbor PDF peak, characteristic of quasistatic structural dipoles in materials studied using the PDF (*14, 15*). Figure 1F points to the latter interpretation because it is evident that higher-neighbor peaks are also losing their Gaussian character at high temperature. Despite being globally rock-salt, characteristic of lone-pair-inactive Pb^{2+} compounds (*6*), the local structure behaves like that in ferroelectrically distorted lone-pair-active Pb^{2+} compounds such as PbTiO_3 (*14*). The off-centered ions are disordered

¹Condensed Matter Physics and Materials Science Department, Brookhaven National Laboratory, Upton, NY 11973, USA. ²Department of Chemistry, Northwestern University, Evanston, IL 60208, USA. ³Theoretical Division, Los Alamos National Laboratory, Los Alamos, NM 87545, USA. ⁴Lujan Neutron Scattering Center, Los Alamos National Laboratory, Los Alamos, NM 87545, USA. ⁵Department of Materials, ETH, Zurich, Switzerland. ⁶Materials Science Division, Argonne National Laboratory, Argonne, IL 60439, USA. ⁷Department of Applied Physics and Applied Mathematics, Columbia University, New York, NY 10027, USA.

*To whom correspondence should be addressed. E-mail: sb2896@columbia.edu

among symmetry-equivalent displaced sites similar to the Ti in the high-temperature phases of BaTiO₃ (14). Although the PDF does not yield information directly on the dynamics, it is likely that the local dipole moments are fluctuating between the symmetry equivalent displaced sites.

Further confirmation of this unexpected result has been obtained by modeling the PDF using a least-squares fitting procedure (11). In Fig. 2A, the reduced χ^2 (goodness of fit) values of a number of competing models are shown as a function of temperature. Undistorted models give the best agreement at low temperature, but above 100 K

distorted models give better agreement, with a model including displacements along (100) crystallographic directions being clearly preferred.

In Fig. 2, B and C, we show the T dependence of Pb isotropic atomic displacement parameters (ADPs) and the lattice parameter, respectively, refined from the simplest undistorted model. In this model, any off-centering must be accommodated in the refined ADP. The temperature dependence of both lattice parameters and the ADPs are linear, as expected, in the high-temperature region. In contrast, both properties show a downward deviation from this linear

behavior below room temperature, precisely in the region where the PDF peak asymmetry is changing. This cannot be explained in any harmonic or quasiharmonic model for the lattice dynamics, such as the Debye model (16), shown as solid lines in the figure. The combined temperature dependences of the PDF peak asymmetry and the ADPs suggest that local ferroelectric-like Pb²⁺ off-center displacements, absent at $T = 0$ K, gradually emerge over the temperature range up to 250 K. At higher temperatures, the displaced ions show more conventional dynamics, resulting in a linear ADP and lattice expansion. The amplitude of the Pb²⁺ ion off-centering distortion, refined in the favored (100)-displacements model, is shown in Fig. 2E. The refined distortion saturates at a maximum value of 0.24 Å. This is comparable in magnitude to ferroelectric displacements in, for example, BaTiO₃ (2). The vicinity of a ferroelectric instability is also implicated in first-principles electronic structure calculations (7), including our recently developed self-consistent ab initio lattice dynamical (SCAILD) method (17), as evident in fig. S3 (11).

Although the behavior observed in the PDF is highly unusual—we know of no other observation of local dipoles emerging from an undistorted ground state on heating—we rationalize it using a simple thermodynamic argument. In Fig. 3A, we plot the familiar schematic of the thermodynamic free energy, F , versus temperature for a series of phases.

The curves slope downward with increasing temperature, T , due to the increased contribution of the entropy term in the free energy at higher temperature: $F = U - TS$, where U is the internal energy. Phases with higher entropies, S , slope down more steeply and may cross below phases, with lower internal energy becoming the stable phase at high temperature. This is the classic explanation of the solid-liquid phase transition. In Fig. 3A, we represent the free energy of an ordered ferroelectric phase as a light blue line and that of the disordered paraelectric phase in olive green. In the absence of competing phases, the ferroelectric phase transition occurs at T_F , where these lines cross as indicated in the figure. Above T_F , the stable state is the paraelectric phase.

Another metastable state may exist that is undistorted but has a higher internal energy than the distorted phase. This is represented as a dashed gray line in Fig. 3B. Its configurational entropy should be the same as the ordered ferroelectric phase (light blue curve), so in the schematic we give these a similar slope, although factors such as vibrational entropy differences will change this somewhat in practice. Because it is higher in energy and has a similar slope, the free energy of this phase never crosses the ferroelectric phase, and it is never the stable state. However, consider the special situation in which this competing undistorted state is very close but slightly lower in energy than the ferroelectric state at $T = 0$. This situation is depicted as the red line in the figure. In this case,

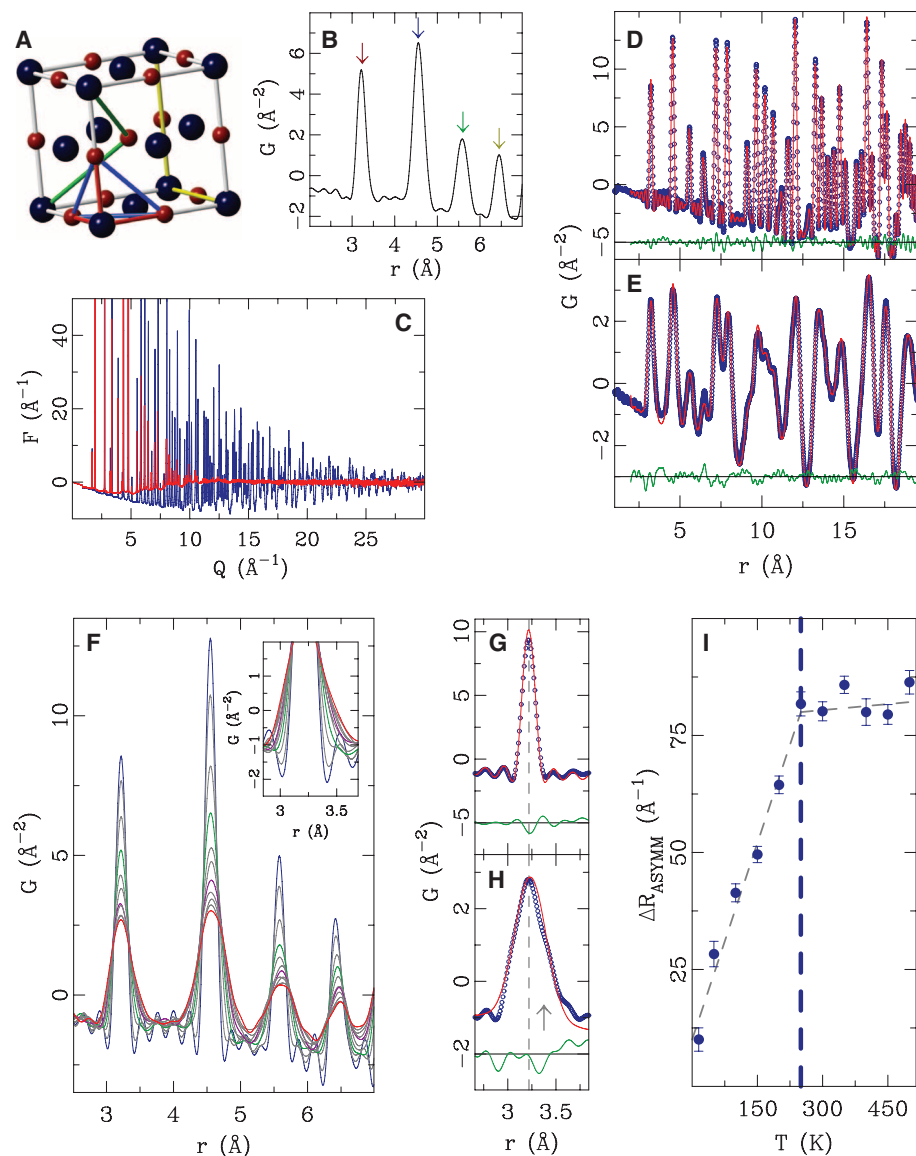


Fig. 1. (A) The rock-salt structure of PbTe with various interatomic distances color coded and (B) the respective PDF peaks marked with arrows using the same color code to illustrate how the PDF is built up from atom-pair distances in the structure. (C) Experimental total scattering structure function $F(Q)$ at $T = 15$ K (blue) and $T = 500$ K (red), with the corresponding PDFs (open symbols) shown in (D) and (E). The PDF of the rock-salt structure model is superimposed as a solid red line, with the difference curve (green) offset for clarity. (F) A stack of experimental PDFs from 15 K (blue) to 500 K (red) in ~ 50 K increments. The 150 K data set is highlighted in green, and the 300 K data are in purple. The inset focuses on the behavior of the nearest-neighbor PDF peak. (G) Fit of the rock-salt crystallographic model to the nearest-neighbor PDF peak data at 15 K and (H) at 500 K. (I) Asymmetry of the near-neighbor PDF peak.

the ground state is undistorted, but on warming the stable state becomes the paraelectric phase, and local fluctuating dipoles emerge out of an undistorted ground state. This crossover is indicated by T_E in the figure. These thermodynamic arguments do not explain the phenomenon, but they give an intuitive rationalization for this be-

havior and suggest that it may be more widespread than in the PbQ compounds studied here.

The thermodynamic arguments do not address the microscopic mechanisms that could give rise to this situation, nor do they address the precise nature of the transition from the undistorted to the paraelectric phase, that is, whether

it is an abrupt transition or a diffuse crossover. The short-range nature of the dipole fluctuations suggests the latter, although characterizing this will require further study. Although there is no change in crystal symmetry, so it is not possible to identify a macroscopic order parameter, there is evidence for the transition in a macroscopic structural parameter: An anomaly is evident in the temperature dependence of the lattice parameter (Fig. 2B), which shows a similar negative deviation from linear behavior at 250 K.

The structural effects we report should be considered in future explanations of the peculiar properties of these materials; for example, the very low lattice thermal conductivity (*18*) at elevated temperatures. The ferroelectric-like moment fluctuations would also explain the well-known strong temperature dependence of carrier scattering, which is unique in PbQ and not found in other semiconductors such as Si, Ge, and Bi₂Te₃. This dependence causes the rapid degradation of carrier mobility with rising temperature with a $T^{-2.5}$ dependence (*19*). Generally, the power exponent for the mobility in semiconductors is $\sim T^{-1.5}$, and it is due to the increase in vibrational amplitude of the lattice. The high power exponent in PbQ implies additional scattering mechanisms for the carriers that would come from the local off-centering fluctuations of the Pb²⁺ ions. Similarly, our electronic structure calculations (*11*) find an enhanced band gap for the locally distorted structure, indicating that the observed anomalous increase in the band gap, E_g , with increasing temperature observed in PbTe (*20*), may be explained by the appearance of the local distortions.

The emergence of structural dipoles from normal, undistorted states in materials may be more ubiquitous than currently recognized. There are some similarities of the present situation to the search for a hidden broken symmetry in the pseudogap phase of high-temperature superconductors, where a short-range nematic orbital ordering may be relevant but is only apparent in probes of local structure (*21*). The PDF is a powerful experimental tool for probing these effects. Finally, we may now begin to contemplate new ways to control these fluctuations through appropriate chemical modifications that could lead to large increases in the thermoelectric performance of PbTe-based materials. We suggest in particular that new thermoelectrics should be sought among materials that, like PbTe, are close to a ferroelectric instability. It is remarkable that binary compounds with such simple structures, which have been known about and exploited for thousands of years, can still harbor surprises when studied using modern experimental and theoretical tools.

References and Notes

1. F. Jona, G. Shirane, *Ferroelectric Crystals* (Dover, New York, 1993).
2. G. H. Kwei, A. C. Lawson, S. J. L. Billinge, S.-W. Cheong, *J. Phys. Chem.* **97**, 2368 (1993).
3. P. Walter *et al.*, *Nano Lett.* **6**, 2215 (2006).

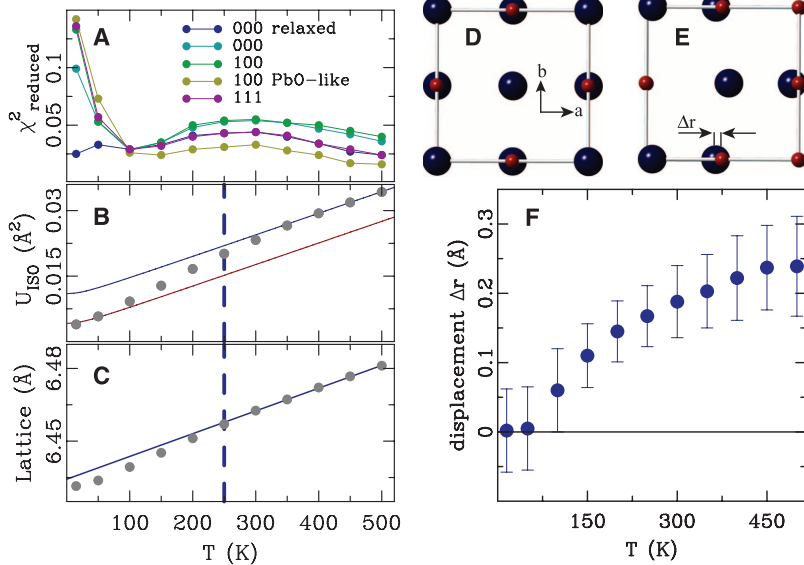


Fig. 2. (A) Reduced χ^2 of best fits for competing models of the local structure (*11*). (B) The gray dots are the isotropic ADPs for Pb refined from the undistorted model. The solid lines represent the behavior expected from the Debye model, using the same Debye temperature, but with different offset parameters, accounting for static disorder, for the red and blue lines. (C) The PbTe lattice parameter (gray dots) as obtained from Rietveld refinement. The vertical dashed line indicates the temperature 250 K where the asymmetry of the nearest-neighbor peak saturates (Fig. 1). (D) Schematic of the rock-salt structure shown in projection down the c axis, showing Pb (blue) and Te (red). (E) Same view of the proposed model for the distorted rock-salt structure above room temperature. The amplitude of the Pb displacements have been highly exaggerated to show the displacements more clearly. (F) Amplitude of Pb local off-centering refined from the $\langle 100 \rangle$ displaced model.

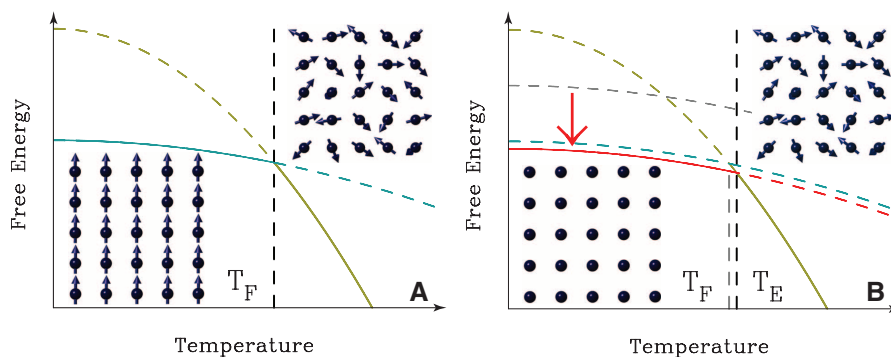


Fig. 3. Schematics of the temperature dependence of the thermodynamic free energy F . (A) The light blue curve represents $F(T)$ for a ferroelectric state with ordered dipole moments (shown schematically as blue arrows), and the olive green curve is for the paraelectric state where the dipoles are fluctuating and only short-range ordered at best. It is more steeply sloping because of the extra configurational entropy. Where these curves cross is the ferroelectric transition temperature, labeled T_F . The blue arrows show schematically the ordered dipole moments in the ferroelectric phase and disordered moments in the paraelectric phase. (B) As in (A) but superimposed are additional free-energy curves for putative undistorted states. The gray dashed curve represents $F(T)$ for a metastable undistorted state. The red curve shows the case where the competing undistorted state is slightly lower in energy than the ferroelectric state. In this case, there is a crossover from an undistorted to a paraelectric phase at a temperature T_E , as shown schematically. In the insets, the blue dots indicate the absence of dipoles at low temperature and the blue arrows the disordered fluctuating dipoles at high temperature.

4. Z. H. Dughaish, *Physica B* **322**, 205 (2002).
5. H. Lin, E. S. Bozin, S. J. L. Billinge, E. Quarez, M. G. Kanatzidis, *Phys. Rev. B* **72**, 174113 (2005).
6. U. V. Waghmare, N. A. Spaldin, H. C. Kandpal, R. Seshadri, *Phys. Rev. B* **67**, 125111 (2003).
7. J. M. An, A. Subedi, D. J. Singh, *Solid State Commun.* **148**, 417 (2008).
8. J. R. Sootsman *et al.*, *Angew. Chem. Int. Ed.* **47**, 8618 (2008).
9. T. Egami, S. J. L. Billinge, *Underneath the Bragg Peaks: Structural Analysis of Complex Materials* (Pergamon Press, Elsevier, Oxford, England, 2003).
10. S. J. L. Billinge, I. Levin, *Science* **316**, 561 (2007).
11. Materials and methods are available as supporting material on Science Online.
12. B. E. Warren, *X-ray Diffraction* (Dover, New York, 1990).
13. I.-K. Jeong, T. Proffen, F. Mohiuddin-Jacobs, S. J. L. Billinge, *J. Phys. Chem. A* **103**, 921 (1999).
14. G. H. Kwei, S. J. L. Billinge, S.-W. Cheong, J. G. Saxton, *Ferroelectrics* **164**, 57 (1995).
15. H. D. Rosenfeld, T. Egami, *Ferroelectrics* **164**, 133 (1995).
16. P. Debye, *Ann. Phys.-Berlin* **39**, 789 (1912).
17. P. Souvatzi, O. Eriksson, M. I. Katsnelson, S. P. Rudin, *Phys. Rev. Lett.* **100**, 095901 (2008).
18. A. F. Joffé, *Can. J. Phys.* **34**, (12A), 1342 (1956).
19. B. A. E. Yu, I. Ravich, I. A. Smirnov, *Semiconducting Lead Chalcogenides*, vol. 5 (Plenum, New York, 1970).
20. R. N. Tauber, A. A. Machonis, I. B. Cadoff, *J. Appl. Phys.* **37**, 4855 (1966).
21. T. M. Chuang *et al.*, *Science* **327**, 181 (2010).
22. S.J.B. and E.B. thank J. Richardson for his early support and enthusiasm for the project and dedicate the paper to him. We acknowledge useful discussions with A. Millis, P. Allen, R. Cohen, C. Farrow, and J. Hill. Work in the Billinge group was supported by the U.S. Department of Energy, Office of Basic Energy Sciences (DOE-BES), under contract DE-AC02-98CH10886. Work in the Kanatzidis group was supported by the Office of Naval

Research. Work in the Spaldin group was supported by the NSF under award DMR-0940420. The neutron diffraction measurements were carried out at the Lujan Center at Los Alamos National Laboratory, and the x-ray experiments were carried out at the Advanced Photon Source, Argonne National Laboratory, both of which are supported by DOE-BES, and the calculations were performed at the San Diego Supercomputer Center, which is supported by NSF.

Supporting Online Material

www.sciencemag.org/cgi/content/full/330/6011/1660/DC1

Materials and Methods

SOM Text

Figs. S1 to S4

References

24 May 2010; accepted 16 November 2010

10.1126/science.1192759

Large Variations in Southern Hemisphere Biomass Burning During the Last 650 Years

Z. Wang,¹ J. Chappellaz,² K. Park,¹ J. E. Mak^{1*}

We present a 650-year Antarctic ice core record of concentration and isotopic ratios ($\delta^{13}\text{C}$ and $\delta^{18}\text{O}$) of atmospheric carbon monoxide. Concentrations decreased by ~25% (14 parts per billion by volume) from the mid-1300s to the 1600s then recovered completely by the late 1800s. $\delta^{13}\text{C}$ and $\delta^{18}\text{O}$ decreased by about 2 and 4 per mil (‰), respectively, from the mid-1300s to the 1600s then increased by about 2.5 and 4‰ by the late 1800s. These observations and isotope mass balance model results imply that large variations in the degree of biomass burning in the Southern Hemisphere occurred during the last 650 years, with a decrease by about 50% in the 1600s, an increase of about 100% by the late 1800s, and another decrease by about 70% from the late 1800s to present day.

Carbon monoxide (CO) plays a key role in the chemistry of the troposphere, largely determining the oxidation potential of the atmosphere through its interaction with hydroxyl radical (OH). CO also interacts with atmospheric methane, a gas whose preindustrial variability is the topic of continuing debate (1, 2). Little is known about the variability of CO before the industrial age (3) or about the anthropogenic impact on its budget, although both affect atmospheric CH_4 and O_3 budgets and related climate-chemistry interactions.

The main sources of atmospheric CO include atmospheric oxidation of methane and nonmethane hydrocarbons (NMHCs), biomass burning, and fossil fuel combustion (4). These sources account for about 90% of today's global CO budget (4). Stable isotopic ratios ($\delta^{13}\text{C}$ and $\delta^{18}\text{O}$) in atmospheric CO help to resolve the relative contribu-

tions of these sources and thus to better estimate the global CO budget (5). To date, no isotopic ratios from CO in ice have been reported, and few CO mixing ratio measurements have been reported (1, 3, 6). Through use of a recently developed analytical technique (7), we present measurements of CO concentration ([CO]), $\delta^{13}\text{C}$, and $\delta^{18}\text{O}$ from a South Pole ice core [89°57'S 17°36'W; 2800 m above sea level (asl)] and from the D47 ice core (67°23'S 154°03'E; 1550 m asl) in Antarctica (Fig. 1).

The combined changes in [CO], $\delta^{13}\text{C}$, and $\delta^{18}\text{O}$ during the past 650 years should reflect variations in both total CO flux and a shift in relative source strengths over time. [CO] shows a decreasing trend from 53 ± 5 parts per billion by volume (ppbv) in the mid-1300s to a minimum of 38 ± 5 ppbv in the 1600s. CO mixing ratio then increases to a relatively constant value of 55 ± 5 ppbv in the late 1800s. Good agreement was observed between our [CO] data and previous measurements on Antarctic ice samples (3, 6). Trends in both $\delta^{13}\text{C}$ and $\delta^{18}\text{O}$ look similar to the [CO] record up to the late 1800s. $\delta^{13}\text{C}$ [Vienna Pee Dee belemnite (VPDB)] and $\delta^{18}\text{O}$ [Vienna standard mean ocean water (VSMOW)], respectively, decreased from $-28.0 \pm 0.3\text{‰}$ and $0.6 \pm 0.7\text{‰}$ in the mid-1300s to $-30.2 \pm 0.3\text{‰}$ and $-3.4 \pm 0.7\text{‰}$ in the 1600s,

then increased to $-27.4 \pm 0.3\text{‰}$ and $0.8 \pm 0.7\text{‰}$ by the late 1800s. Minimum values of [CO], $\delta^{13}\text{C}$, and $\delta^{18}\text{O}$ roughly coincide with the Little Ice Age (LIA; circa 1500–1800), as defined in the Northern Hemisphere.

Observations from Berkner Island (79°32.90'S 45°40.7'W; 890 m asl) firm and present day samples are also shown in Fig. 1. The slight decrease of [CO] from the late 1800s to present day is thus accompanied by large shifts in both $\delta^{13}\text{C}$ and $\delta^{18}\text{O}$, which is a result of variations in relative source strengths during the past century. In particular, methane-derived CO, which is dependent upon methane concentration and depleted in both $\delta^{13}\text{C}$ and $\delta^{18}\text{O}$, increased dramatically—by 13 ppbv—during this time (Fig. 2). Because there was little difference in overall [CO] between the late 1800s and present day, contributions from other CO sources must have decreased by a similar amount. Data from Berkner Island firm air show an increase in [CO] and a decrease in $\delta^{13}\text{C}$ since 1970 (8), reflecting the increase in atmospheric methane (9).

The contribution from fossil fuel combustion is negligible before the 1900s according to historic CO_2 emissions data (10). In addition, simulations from the Model for Ozone and Related chemical Tracers (MOZART-4) (11) show the fossil fuel combustion contribution to today's CO budget in Antarctica is only 2 to 3 ppbv. Thus, the main sources of CO able to explain our signals are biomass burning and NMHC oxidation.

We can use isotopic compositions to help distinguish combustion-derived CO (such as biomass burning) from noncombustion-derived CO (such as hydrocarbon oxidation). C^{18}O is a useful tracer for this because of large differences in the oxygen isotopic composition between combustion and noncombustion sources of CO (12). The $\delta^{18}\text{O}$ signature from combustion sources is significantly enriched as compared with the $\delta^{18}\text{O}$ signature from hydrocarbon oxidation processes (12, 13). The $\delta^{18}\text{O}$ value for biomass burning-derived CO is generally between 15 and 22‰, depending on specific combustion conditions (13–15).

We used an isotope mass balance model to estimate the ratio of combustion to noncombustion

¹Institute for Terrestrial and Planetary Atmospheres/School of Marine and Atmospheric Sciences, Stony Brook University, Stony Brook, NY 11794–5000, USA. ²Laboratoire de Glaciologie et Géophysique de l'Environnement (LGGE), CNRS, University of Grenoble, BP 96, 38402 St. Martin d'Hères Cedex, France.

*To whom correspondence should be addressed. E-mail: john.mak@stonybrook.edu

OPEN ACCESS

Pair-distribution function analysis of the structural valence transition in $\text{Cp}^*_2\text{Yb}(4,4'\text{-Me}_2\text{-bipy})$

To cite this article: C H Booth *et al* 2011 *J. Phys.: Conf. Ser.* **273** 012149

View the [article online](#) for updates and enhancements.

You may also like

- [Spin-crossover behavior of bis\(dihydrobis\(4-methylpyrazol-1-yl-borate\)\)-\(2,2-bipyridine\)iron and analogous complexes in the bulk and in thin films: Elucidating the influence of –interactions on the type of spin transition](#)
Sascha Ossinger, Christian Näther and Felix Tuzcek
- [Tunable spin-state bistability in a spin crossover molecular complex](#)
Xuanyuan Jiang, Guanhua Hao, Xiao Wang et al.
- [Photoluminescence and scintillation properties of \$\text{Yb}^{2+}\$ -doped \$\text{SrCl}_2\text{Br}_x\$ \(\$x = 0, 1.6, 2.0\$ \) crystals](#)
Kohei Mizoi, Miki Arai, Yutaka Fujimoto et al.

ECS Toyota Young Investigator Fellowship



For young professionals and scholars pursuing research in batteries, fuel cells and hydrogen, and future sustainable technologies.

At least one \$50,000 fellowship is available annually.
More than \$1.4 million awarded since 2015!



Application deadline: January 31, 2023

Learn more. Apply today!

Pair-distribution function analysis of the structural valence transition in $\text{Cp}_2^*\text{Yb}(4,4'\text{-Me}_2\text{-bipy})$

C H Booth¹, E D Bauer², E S Bozin^{3,4}, S J L Billinge^{3,4} and M D Walter¹

¹Chemical Sciences Division, Lawrence Berkeley National Laboratory, Berkeley, California 94720, USA

²Materials Physics and Applications Division, Los Alamos National Laboratory, Los Alamos, New Mexico 87545, USA

³Department of Applied Physics and Applied Mathematics, Columbia University, New York, New York 10027, USA

⁴Condensed Matter Physics and Materials Science Department, Brookhaven National Laboratory, Upton, NY 11973, USA

E-mail: chbooth@lbl.gov

Abstract. The $\text{Cp}_2^*\text{Yb}(L)$ class of compounds, where Cp^* =pentamethylcyclopentadienyl = C_5Me_5 and L is either a 1,4-diazabutadiene or bipy = 2,2'-bipyridine related ligand, have provided excellent analogies to the Kondo state on the nanoscale. $\text{Cp}_2^*\text{Yb}(4,4'\text{-Me}_2\text{-bipy})$ furthers this analogy by demonstrating a valence transition as the sample is cooled below 200 K. Here, pair-distribution function (PDF) analysis of x-ray powder diffraction data demonstrate that the $\text{Cp}_2^*\text{Yb}(4,4'\text{-Me}_2\text{-bipy})$ molecule is virtually unchanged through the valence transition. However, the molecule's stacking arrangement is altered through the valence transition.

In 1989, Neumann and Fulde [1] conjectured that a molecular analogue to the Kondo effect occurs in certain Ce- and Yb-based organometallic molecules. The theory of such effects (see Ref. [2] and references therein) indicates the traditional role of many-body interactions in Kondo systems is reduced to, essentially, including specific configuration interactions (CIs) to the single-electron theory using, for instance, the Complete Active Space Self-Consistent Field (CASSCF) approach. According to such methods, intermediate valence (IV) occurs in the ground state when open and closed shell singlet configurations mix, thereby lowering the combined open-shell singlet state below the triplet state [2]. For example, CASSCF calculations in $\text{Cp}_2^*\text{Yb}(\text{bipy})$ indicate that the open-shell $f_{\uparrow}^{13}\pi_{\downarrow}^*1$ configuration interacts with, primarily, the closed-shell $f_{\uparrow,\downarrow}^{14}\pi^*0$ configuration to form an open-shell singlet below the triplet configuration [2], where Cp^* = pentamethylcyclopentadienyl = C_5Me_5 , Me = methyl = CH_3 , and bipy = 2,2'-bipyridine = $(\text{C}_5\text{H}_4\text{N})_2$. This result is in contrast to lower-order calculations from Density Functional Theory (DFT) that indicate a triplet $f_{\uparrow}^{13}\pi_{\uparrow}^*1$ in the ground state in $\text{Cp}_2^*\text{Yb}(\text{bipy})$ [2]. The IV ground state in the CASSCF calculation has an f -hole occupancy of about $n_f = 0.8$, consistent with Yb L_{III} -edge x-ray absorption near-edge structure (XANES) experiments [2, 3]. In analogy to the Kondo effect, the singlet interactions are made possible both by symmetry and the more extended nature of the f -orbital in Yb and the π^* orbital in the aromatic bipy ligand, which plays the role of a quantum-confined metallic band in an intermetallic nanoparticle [4, 5]. The Kondo analogy has also worked very well for guiding many other aspects of the research

[2, 6]. These studies therefore have broad implications for fields such as solid-state physics, materials science, and organometallic chemistry, and may have future implications for nanoscale devices, which have spurred recent interest in understanding the Kondo effect on the nanoscale.

The Me-substituted $\text{Cp}_2^*\text{Yb}(\text{bipy})$ complexes demonstrate one of the more dramatic differences between bulk and nanoscale Kondo behavior in that the first excited state need not be a triplet. However, the $\text{Cp}_2^*\text{Yb}(4,4'\text{-Me}_2\text{-bipy})$ molecule (Fig. 1) also undergoes a first-order +10% valence transition when cooling below 200 K [3, 7]. Here, we address the low temperature structure of the molecule using the pair-distribution function (PDF) technique to determine whether the molecule is isomorphic through the transition, in analogy to the isomorphic valence transition in YbInCu_4 [8] and the α - γ transition in elemental cerium [9, 10].

Synthesis details for the $\text{Cp}_2^*\text{Yb}(4,4'\text{-Me}_2\text{-bipy})$ complex are reported in Ref. [7]. In preparation for the x-ray scattering experiments, the air-sensitive single crystals were powdered in an inert atmosphere glove box. The finely powdered sample was packed into a 5 mm diameter hole in a 1 mm thick aluminum plate, and then sealed between aluminized mylar windows. The sample was then shipped to the Advanced Photon Source (APS) at Argonne National Laboratory in a nitrogen-filled jar. The sample was removed from the jar and then placed into a displax just prior to measurement at the 6ID-D beamline of MuCAT. Measurements were made at many temperatures between 50 K and 300 K. X-ray powder-diffraction data were collected using the rapid acquisition pair distribution function method [11]. The experiments were conducted using synchrotron x-rays with a wavelength of 0.12634 Å using a circular image plate camera (Mar345) 345 mm in diameter. The camera was mounted orthogonally to the beam path with a sample-to-detector distance of 240.464 mm. Other details of data collection and analysis are as described previously [12]. The corrected total scattering structure function, $S(Q)$, was obtained using standard corrections [13] with the program PDFGETX2 [14]. Finally, the PDF was obtained by Fourier transformation of $S(Q)$ according to $G(r) = \frac{2}{\pi} \int_0^{Q_{\text{max}}} Q[S(Q) - 1] \sin(Qr) dQ$, where Q is the magnitude of the scattering vector. A $Q_{\text{max}} = 15.0 \text{ \AA}^{-1}$ was used. Fig. 2 shows $G(r)$ for several selected temperatures. Fits are performed using the PDFGUI analysis package [15].

From room temperature to just above the transition, the changes in the PDF data from temperature to temperature are small, consistent with thermally-induced variations. At the transition, a clearly resolved change occurs, as illustrated in Fig. 2, where in the 10 K above the transition the data overlap well (Fig. 2a), yet in the next 10 K (Fig. 2b), the changes in the local structure are easily discernible, especially starting at about 9 Å. However, below 9 Å, the local structure is nearly unaffected. Note that the intermolecular Yb-Yb distance is about 9 Å in these crystals, while the longest intramolecular distances are about 11 Å and the shortest intermolecular distances are about 4 Å. We can therefore conclude simply from these data and with no fitting that the main structural change occurs in the molecular stacking.

Two questions remain unanswered: (1) can we resolve an actual change in the molecule's morphology, and (2) what is the change in the packing arrangement? To answer these questions,

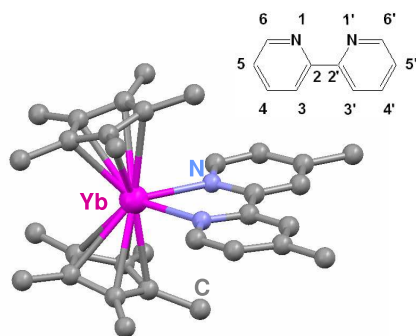


Figure 1. The $\text{Cp}_2^*\text{Yb}(4,4'\text{-Me}_2\text{-bipy})$ molecule and the position numbering scheme for bipyridine. The $\text{Cp}_2^*\text{Yb}(4,4'\text{-Me}_2\text{-bipy})$ molecule crystallizes into the $P2_1/c$ space group above 200 K.

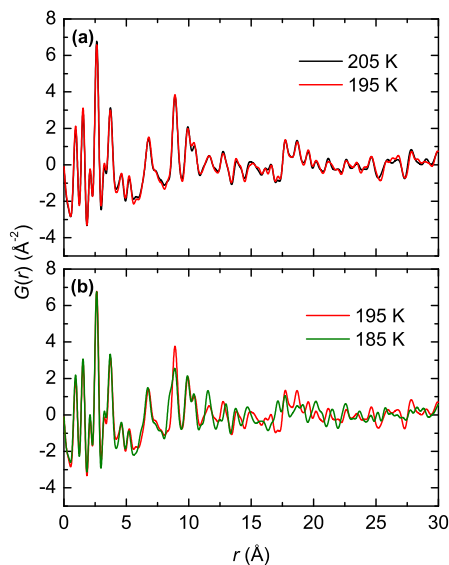


Figure 2. The PDF at two temperatures 10 K apart (a) above and (b) through the transition.

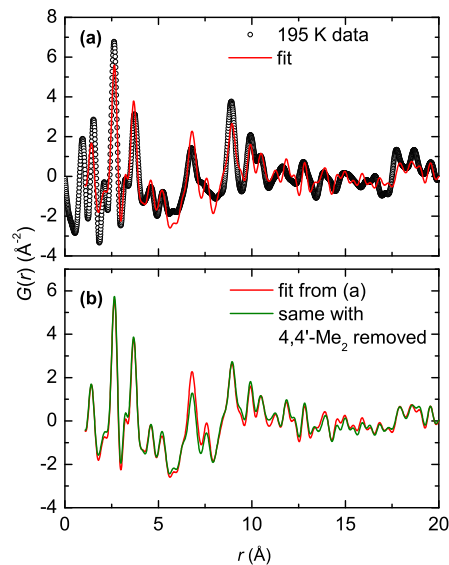


Figure 3. (a) Data and fit to the single crystal structure. (b) Fit from (a) with and without the 4,4'-Me₂ removed.

a detailed fit should be performed. Unfortunately, attempts to fit structural models to the low temperature data, even including a wide variety of constraints, did not produce satisfactory results. It is possible to fit the high-temperature-phase data to the nominal crystal structure [7] by only allowing a single mean-squared displacement parameter u^2 for each atomic species, the three lattice parameters, a scale factor, and a damping factor to vary. Such a fit is shown in Fig. 3a. Clearly, the high-temperature-phase data represent the structure from the much more accurate single-crystal diffraction results well.

Fortunately, we can demonstrate the sensitivity of the data (if not the fit) to possible changes in the molecule's morphology through the transition using these fit results. A relatively small change in the morphology, at least as far as the x-ray scattering is concerned, would be to eliminate a C atom from the molecule. In Fig. 3b, the effect of removing the Me carbons at the 4,4' sites on the bipy is illustrated by taking the fit result shown in Fig. 3a and simply deleting these Me groups. The $G(r)$ is nearly unaffected, except at the Yb-Me distance of about 7 Å. This example, of course, illustrates the change from two carbon atoms; in any case, there is no change observed on this scale below 9 Å in the data spanning the phase transition (Fig. 2b). Consequently, we conclude that the molecule's morphology is unaffected by the valence transition. Changes in the bond lengths due to the change in valence can be observed in these data, but are more accurately presented in fits to extended x-ray absorption fine-structure (EXAFS) data described elsewhere [3].

Although the molecule has the same morphology in the high and low temperature phases, it is possible, if not likely, that the change in packing produces a different crystal symmetry than $P2_1/c$. A likely alternative is a $Pbca$ structure, such as occurs for $Cp_2^*Yb(bipy)$, $Cp_2^*Yb(5,5'-Me_2-bipy)$, and others [3]. As mentioned above, fits using the $Pbca$ structure are inconclusive. Attempts to fit these data using Rietveld refinement also failed to produce a unique answer, since the data can be fit using either space group if enough parameters are allowed to vary.

The molecule itself is therefore isomorphic through the valence transition, but based on the changes in packing, the most likely conclusion regarding the crystal structure is that it is not isomorphic through the transition. It remains unclear whether the valence transition is driven

by the Kondo effect or not. As the low-temperature structure may well be in the *Pbca* space group, the change in structure could be driven by steric effects. The observed valence transition would then be an indication that intermolecular, Van der Waals interactions are important in these molecules, although we note that CASSCF calculations on isolated molecules obtain an n_f that is generally well within 10% of the measured values. The changing intermolecular interaction could, in any case, have an effect on the overall π^* charge density, and so the change in valence could be a manifestation of a charge-density induced change to the f -orbital coupling. This scenario would be very similar to one suggested for YbInCu_4 , except that in that case the change in density is thought to be due to a sharp band edge near the Fermi level [16].

Another possibility is that intermolecular effects are insignificant, and the valence transition is somehow analogous to that which occurs in the α - γ transition in cerium [9, 10]. Of course, even here, there remains a controversy regarding the basic physics underlying the volume collapse in elemental cerium. The two general possibilities at present are the so-called Kondo Volume Collapse model (KVM) [17], and the Mott transition model [18]. With regard to the role of the Kondo effect, the KVM achieves a volume change by exploiting nonlinearities in the pressure/volume relationship in the Kondo impurity model [17]. Although the possibility of a Mott transition exists in cerium, it is unlikely that there is some local equivalent possibility in $\text{Cp}_2^*\text{Yb}(4,4'\text{-Me}_2\text{-bipy})$ given the observed IV in both the high temperature and the low temperature phases. Therefore, CI-induced IV behavior appears to play an important role in generating the valence transition in $\text{Cp}_2^*\text{Yb}(4,4'\text{-Me}_2\text{-bipy})$, either through structural-induced changes in charge density or through a KVM-like mechanism.

Acknowledgments

Work at Lawrence Berkeley National Laboratory was supported by the Director, Office of Science (OS), Office of Basic Energy Sciences (OBES), of the U.S. Department of Energy (DOE) under Contract No. DE-AC02-05CH11231. Work in the Billinge group was supported by the DOE under contract No. DE-AC02-98CH10886. The APS facility at Argonne is supported by DOE Contract DE-AC02-06CH11357. Work at Los Alamos was supported by the DOE.

References

- [1] Neumann C S and Fulde P 1989 *Z. Phys. B* **74** 277
- [2] Booth C H, Walter M D, Kazhdan D, Hu Y J, Lukens W W, Bauer E D, Maron L, Eisenstein O and Andersen R A 2009 *J. Am. Chem. Soc.* **131** 6480
- [3] Booth C H *et al.* Intermediate-valence tautomerism in decamethylterbocene complexes of methyl-substituted bipyridines (*Preprint* http://lise.lbl.gov/chbooth/papers/Me_bipy.pdf)
- [4] Thimm W B, Kroha J and von Delft J 1999 *Phys. Rev. Lett.* **82** 2143
- [5] Schlottmann P 2002 *Phys. Rev. B* **65** 024420
- [6] Booth C H, Walter M D, Daniel M, Lukens W W and Andersen R A 2005 *Phys. Rev. Lett.* **95** 267202
- [7] Walter M D, Berg D J and Andersen R A 2006 *Organometallics* **25** 3228
- [8] Felner I and Nowik I 1986 *Phys. Rev. B* **33** 617
- [9] Lawrence J M, Riseborough R S and Parks R D 1981 *Rep. Prog. Phys.* **44** 1
- [10] McMahan A K, Huscroft C, Scalettar R T and Pollock E L 1998 *J. Comput.-Aid. Mater. Des.* **5** 131
- [11] Chupas P J, Qiu X, Hanson J C, Lee P L, Grey C P and Billinge S J L 2003 *J. Appl. Crystallogr.* **36** 1342
- [12] Lin H, Božin E S, Billinge S J L, Androulakis J, Malliakas C D, Lin C H and Kanatzidis M G 2009 *Phys. Rev. B* **80** 045204
- [13] Egami T and S J L Billinge 2003 *Underneath the Bragg peaks: Structural analysis of complex materials* (Amsterdam: Pergamon)
- [14] Qiu X, Thompson J W and Billinge S J L 2004 *J. Appl. Crystallogr.* **37** 678
- [15] Farrow C L, Juhás P, Liu J W, Bryndin D, Božin E S, Bloch J, Proffen T and Billinge S J L 2007 *J. Phys.: Condens. Matter* **19** 335219
- [16] Figueroa E, Lawrence J M, Sarrao J L, Fisk Z, Hundley M F and Thompson J D 1998 *Solid State Commun.* **106** 347
- [17] Allen J W and Martin R M 1982 *Phys. Rev. Lett.* **49** 1106
- [18] Johansson B 1974 *Phil. Mag.* **30** 469

Heterogeneity and Disorder in $\text{Ti}_{1-x}\text{Fe}_y\text{O}_{2-d}$ Nanocrystal Rutile-Based Flowerlike Aggregates: Detection of Anatase

Aleksandar Kremenović,^{*,†,‡} Bratislav Antić,[†] Jovan Blanuša,[†] Mirjana Čomor,[†] Philippe Colombar,[§] Leo Mazerolles,^{||} and Emil S. Bozin^{†,⊥}

[†]Institute of Nuclear Sciences “Vinča”, University of Belgrade, P.O. Box 522, 11001 Belgrade, Serbia

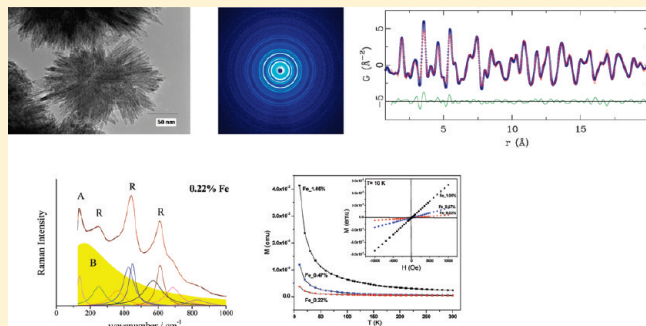
[‡]Faculty of Mining and Geology, Laboratory for Crystallography, University of Belgrade, Djusina 7, 11000 Belgrade, Serbia

[§]LADIR, UMR 7075 CNRS, and Université Pierre and Marie Curie, 94230 Thiais, France

^{||}ICMPE, UMR 7182 CNRS, and Université Paris Est Créteil, 94320 Thiais, France

[⊥]Condensed Matter Physics and Material Science Department, Brookhaven National Laboratory, Upton, New York 11973, United States

ABSTRACT: Here we report results of systematic investigation of heterogeneity and disorder in $\text{Ti}_{1-x}\text{Fe}_y\text{O}_{2-d}$ nanorod rutile-based flowerlike aggregates. It was found that $\text{Ti}_{1-x}\text{Fe}_y\text{O}_{2-d}$ aggregates are composed of two crystalline phases: rutile as a dominant and anatase as a minor phase. Flowerlike aggregates were found to grow from an isometric core ca. 5–10 nm in diameter that was built from anatase and rutile nanorods ca. 5×100 nm that were grown on the anatase surface having base plane (001) intergrowth with an anatase plane. The direction of rutile nanorods growth, i.e., direction of the nanorod elongation, was [001]. Highly nonisometric rutile crystals produce anisotropic X-ray powder diffraction line broadening and doubling of vibrational bands in Raman spectra. Both these techniques confirmed nonisometric character of rutile crystals and gave a quantitative measure of crystal shape anisotropy in excellent agreement with high-resolution transmission electron microscopy measurements. In addition, from the atomic pair distribution function and Raman spectral analyses the level of vacancy concentration was determined in rutile and anatase phases of investigated samples.



1. INTRODUCTION

Because of its wide range of potential technological applications, such as for pigments, cosmetic products, photovoltaic cells, and catalysis, titanium dioxide, TiO_2 , has been the focus of intense research.^{1,2} As a well-known photocatalyst, its photocatalytic characteristics are greatly influenced due to the advent of nanotechnology. With a size reduction to nanoscale, not only the surface area of titanium dioxide particle increases dramatically, which is important for the activity, but also the system exhibits additional effects in optical properties and size quantization. Reduction in size commonly involves modification of the structure and introduces nonstoichiometric conditions. Defect concentration highly depends on the distance from the center of the crystal, with the regions closer to the surface retaining more vacancies. Furthermore, the atoms at the surface tend to react with the atmosphere (protonation, sulfur and nitrogen adsorption, etc.). Another marked effect of the reduced size comes from the increased surface to volume ratio, and the number of atoms near the surface becomes dominant compared to the number of atoms in the bulk.^{3,4} Consequently, it is of great importance to be able to characterize in as much detail as possible the exact nature

of the nanomaterial, to understand the origin of its properties, and ultimately to gain control over tunability of these properties. Therefore, nano- TiO_2 is applicable in a number of branches of traditional industry,⁵ such as materials for environmental treatment, antimicrobial materials, and self-cleaning materials, and could find applications as UV-block sunscreen and UV-block paint. Most of the unique optical properties of TiO_2 are derived from its remarkably high value of refractive index,⁵ which expresses the ability of a material to bend and scatter the light. From a crystallographic point of view, bulk TiO_2 crystallizes in three main forms: anatase (space group $I4_1/amd$), rutile (space group $P4_2/mnm$), and brookite (space group $Pbca$). Two other existing structural forms, known as columbite and baddeleyite, are stabilized only under high pressure.⁶ Quite generally, structure and microstructure (shape, size, surface morphology, and anisotropy) determine the physical and chemical properties of a material. On the other hand, structure and microstructure

Received: October 1, 2010

Revised: January 31, 2011

Published: March 01, 2011

depend on the preparation conditions. For example, it was found that the electrical conductivity of nanocrystalline TiO₂ films exhibits a pronounced dependence on crystallite size.^{7–9} Wu et al. synthesized and used titania films to assist photodegradation of Rhodamine B in water.^{10–12} They have shown that the efficiency depends on both preparation method and thermal treatment of synthesized titania. The efficiency of TiO₂ nanopowders in the photocatalysis was also related to synthesis procedure.¹³ One of the aim of this study was synthesis of Fe-doped TiO₂ nanopowders.

While microstructure parameters strongly affect properties of nanosized materials, nonstoichiometry can also have a profound influence on some physical properties, such as electronic transport properties.^{14,15} In TiO₂, nonstoichiometry may be due to oxygen vacancies and excess titanium on interstitial sites or Ti vacancies.

Ion doping (or partial ion substitution) of TiO₂ can influence a deviation from stoichiometry by forming oxygen vacancies and appearance of cation deficit/surplus with a change in cation valence. For example, in TiO₂ doped by 3d ions an increase in the photocatalytic activity has been observed.¹⁶ By incorporation of Fe³⁺ in host TiO₂ the light absorption of pure TiO₂ is significantly shifted from UV toward the visible spectral region.^{8,17}

Crystalline structure, size, and shape of the particles strongly influence the possible application of TiO₂. Although for photocatalytic applications anatase displays higher efficiency than rutile, a combination of anatase and rutile seems to be the best.¹⁸ However, because of its wide band gap (3.0–3.2 eV)¹⁸ which requires UV radiation for excitation, commercial photocatalytic application of TiO₂ is still moderate. Further, fast recombination of photogenerated e⁻–h⁺ pairs lowers the quantum yield below 10%. The photocatalytic efficiency of titanium dioxide could be enhanced by doping with various elements,^{2,16,17,19–22} e.g., Cr³⁺, Ni²⁺, or Fe³⁺ ions. Incorporating these ions in titania crystal structure could shift the absorption threshold above 450 nm, resulting in absorption in the visible part of the spectrum.¹⁶ Moreover, the shape of titanium dioxide nanocrystals greatly influences e⁻–h⁺ recombination rate. For example, in nanorods charge carriers are free to move along the length of the elongated nanocrystal, which is not the case for nanospheres. Therefore, charge carriers delocalization is higher and, consequently, the probability of their recombination is lower.⁹

This study is focused on synthesis and characterization of elongated TiO₂ nanocrystals, nanorods with rutile crystalline structure doped with Fe³⁺ ions. The aim of the research presented here on pure and Fe-doped TiO₂ nanorods is determination of materials composition, structure, and microstructure (particle size, morphology, microstrain, and defects concentration), as they provide important insights for better understanding of their properties, essential for applications. To achieve this, we carried out HRTEM, Raman spectroscopy, X-ray diffraction (Rietveld and atomic pair distribution function (PDF) methods), and SQUID magnetic measurements.

2. EXPERIMENTAL SECTION

2.1. Sample Preparation. All chemicals used were of p.a. purity and were used without further purification. Triply distilled water was used for aqueous solutions. TiO₂ nanopowders doped with iron ions were prepared by a modified synthetic procedure of Abazović et al.²³ An appropriate amount of FeCl₃ (Aldrich), in order to get samples with 0.25, 0.50, and 1.00 of iron ions in TiO₂, was dissolved in 200 mL of triply distilled water. Then, 5 mL of TiCl₄ (Fluka) prechilled to –20 °C was added dropwise

into solution containing FeCl₃ under stirring. After 2 h of stirring at room temperature, the obtained dispersions were heated and kept at 60–70 °C for 24 h with continuous stirring. The resulting precipitates were dialyzed against water until test reaction for Cl⁻ ions was negative. After centrifugation of dispersions, transparent solutions were decanted and precipitates were dried in vacuum at room temperature. Pure TiO₂ powder was synthesized in the same manner, without FeCl₃ in the reaction solution. Concentration of Fe³⁺ ions was determined by inductively coupled plasma optical emission spectroscopy (Spectroflame ICP, 2.5 kW, 27 MHz). ICP-OES measurements were performed by measuring the intensity of radiation at the specific wavelengths emitted by each element. Obtained concentrations were 0.22, 0.47, and 1.05 at. % of Fe³⁺ in TiO₂ matrix.

2.2. Characterization Techniques. High-resolution transmission electron microscopy (HRTEM) measurements of the samples were carried out using a TOPCON 002B electron microscope operating at 200 kV. The samples were prepared by ultrasonication in ethanol and deposition on a conventional carbon-covered copper HRTEM grid. After drying, the samples were examined by HRTEM.

Synchrotron X-ray experiments were performed at room temperature at the 6-ID-D beamline at the Advanced Photon Source at Argonne National Laboratory, Argonne, IL. Diffraction data were collected using the rapid acquisition pair distribution function (RAPDF) technique²⁴ that benefits from two-dimensional (2D) data collection. The powder samples were packed in Kapton capillaries with diameter of 1.0 mm, sealed at both ends. The data were collected at room temperature with an X-ray energy of 98.65 keV ($\lambda = 0.126 \text{ \AA}$) selected using Si (331) monochromator. Incident beam size was 0.5 × 0.5 mm. An image plate detector (General Electrics)²⁵ with active area of 410 mm × 410 mm was mounted orthogonally to the beam path with a sample-to-detector distance of 268.62 mm, as calibrated by using ceria standard sample.²⁴ Each sample was exposed for 10 s, and this was repeated six times for a total data collection time of 60 s to obtain good counting statistics. The RAPDF approach is described in detail elsewhere.²⁴ The data were corrected and normalized²⁶ using the program PDFgetX2²⁷ to obtain the total scattering structure function, $F(Q)$, and its sine Fourier transform, the atomic PDF, $G(r)$.

The dc magnetization was measured in the temperature region of 1.8–300 K, and in an applied field of 500 Oe using an MPMS XL-5 SQUID magnetometer. Hysteresis loops were measured in zero-field-cooled regime over (–50 kOe, 50 kOe) at temperatures of 10 K.

A high-sensitivity multichannel notch-filtered INFINITY spectrograph (Jobin-Yvon-Horiba SAS, Longjumeau, France) equipped with a Peltier cooled CCD matrix detector was used to record Raman spectra between ~150 and 2000 cm⁻¹, using 532 and 632 nm exciting lines (YAG and He–Ne lasers). Backscattering illumination and collection of the scattered light were made through an Olympus confocal microscope (long focus Olympus ×10 and ×50 objective, total magnification ×100 and ×500). Special attention was paid to the power of illumination used (0.1–2 mW). The examination was carried out on small particle aggregates, in a procedure preferentially used for dark material.

3. RESULTS AND DISCUSSION

3.1. Morphology and Microstructure by HRTEM. Electron transmission microscopy was used in order to characterize size

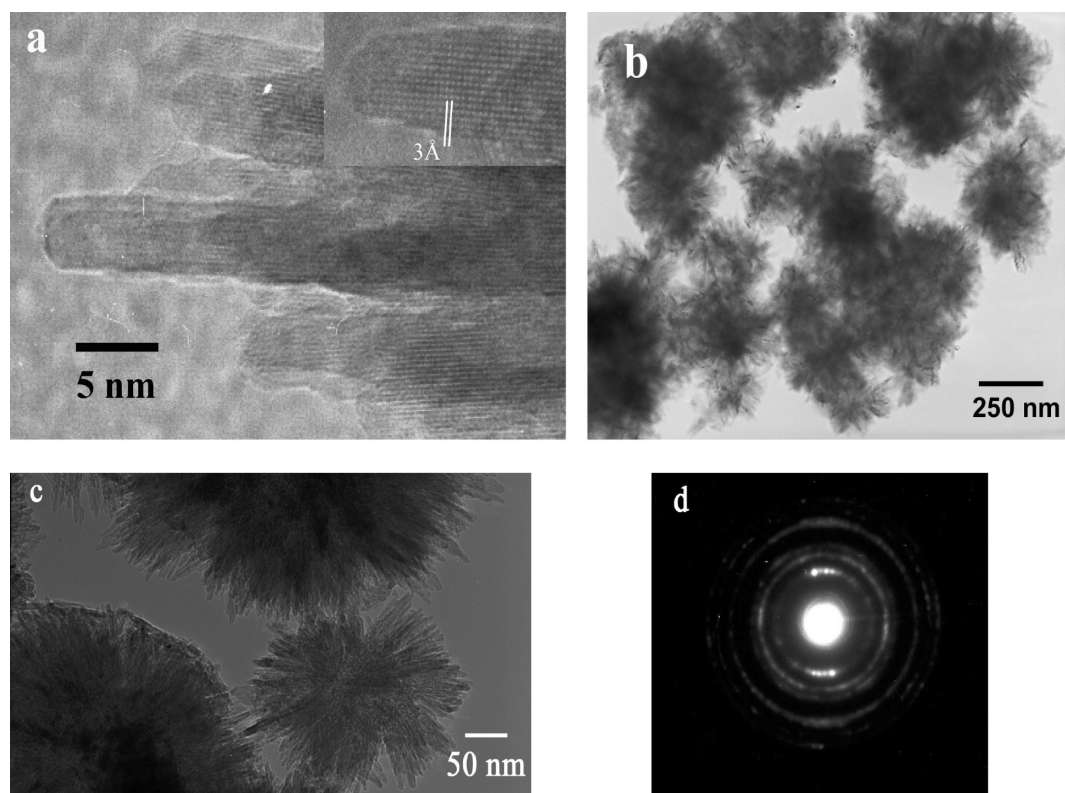


Figure 1. HRTEM images (a–c) and SAED pattern (d) of TiO_2 doped with 0.22 at. % of Fe.

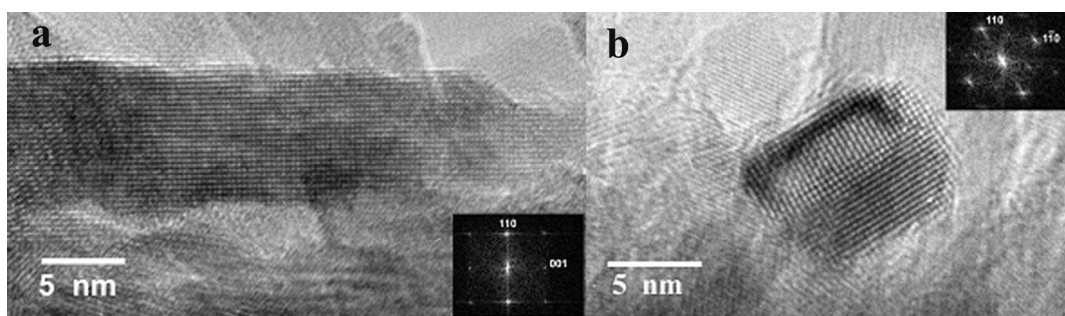


Figure 2. HRTEM images (Fourier transform in the inset) of longitudinal (a) and transversal (b) sections of a nanorod for TiO_2 doped with 0.22 at. % of Fe.

and morphology of nanocrystallites. Rodlike shapes of nanocrystallites were observed (Figure 1a), typical for rutile phase of TiO_2 . High-resolution electron microscopy is a very good method for revealing crystal defects such as stacking faults. Our observations on different areas (Figure 1a and Figure 2 are examples) revealed neither dislocations nor stacking faults inside the crystal structure of nanorods. The average length of nanorods was $\sim 80 \pm 20$ nm, with average diameter of $\sim 7 \pm 2$ nm for samples containing 0.22 at. % of Fe. Similar results were obtained for the other Fe concentrations studied, indicating that in the investigated region Fe content did not significantly modify the crystalline morphology and nanorod dimensions. Nanorods of rutile samples display a flowerlike structure (Figure 1b,c). The selected area electron diffraction (SAED) pattern (Figure 1d) indicated that nano-objects are crystalline. Here, it is worth mentioning results of Wu et al. on synthesis of titania thin films with a dual structure, that is, flowerlike rutile aggregates sitting on

top of an anatase layer, that were fabricated simply by oxidizing metallic Ti plates.¹⁰

The interplanar distance of ~ 3 Å corresponds to (001) planes of rutile structure, which indicates that the preferred particle growth direction is [001], in agreement with results of Rietveld analysis (for details see results in section 3.2). Theoretical calculation by Oliver et al. showed that the (001) surface has the highest surface energy; the [001] is favored growth direction.²⁸ The same conclusion for rutile nanocrystals was drawn from experimental results of Zhang et al.²⁹ No crystalline or amorphous phase containing Fe (pure Fe or its oxide) was detected from the HRTEM examinations.

The HRTEM image in Figure 2a and its Fourier transform (similar to a local microdiffraction) in the inset show that these needles are grown parallel to the *c*-axis of the rutile structure. Observation of a transverse section of these needles (Figure 2b) reveals facets corresponding to (110) planes.

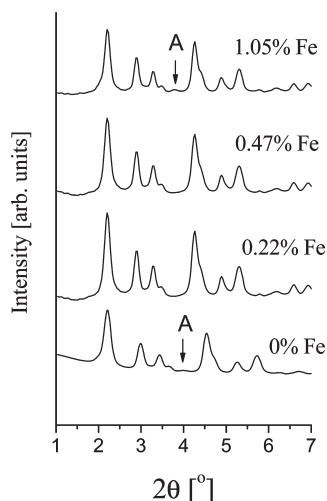


Figure 3. Part of synchrotron X-ray diffraction patterns of pure TiO₂ and Fe-doped TiO₂ samples (A denotes anatase contribution).

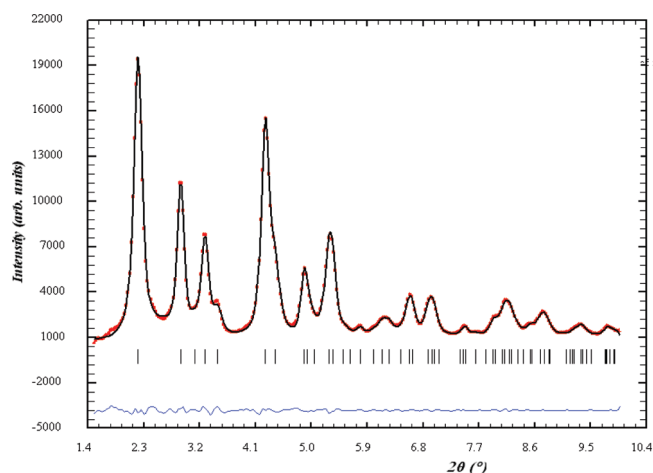


Figure 4. Rietveld fit for TiO₂ doped with 0.22 at. % of Fe ($R_{wp} \sim 3\%$). The difference (bottom) curve between experimental and calculated values is offset for clarity. Ticks mark reflections for rutile.

3.2. Structure and Microstructure Analysis in Reciprocal Space: Rietveld and Size–Strain Analysis. The analysis of obtained XRPD patterns (Figure 3) shows that all samples predominantly crystallized in rutile form with a small amount of anatase phase that could be noticed only in pure TiO₂ and TiO₂ doped with 1.05 at. % of Fe. The patterns were analyzed by FullProf program 30 started initially with standard Rietveld refinement procedure. However, an attempt to fully implement Rietveld refinement in order to refine all crystal structure parameters was unsuccessful in this case; this was attributed to the difficulties in integrated intensity calculations for highly anisotropic particles. To avoid these problems, further analysis was done by using FullProf in profile matching mode with the chosen “needlelike” crystallite size line broadening model.³⁰ The refinement based on this model has shown very good agreement with experiment (Figure 4). The profile of diffraction peaks was described by Thompson–Cox–Hastings approximation of Voigt function comprising the size and strain calculations based on integral breadths.^{31,32} The instrumental full width at half-maximum (fwhm) was derived from XRPD pattern of standard CeO₂ powder sample for microstructure analysis.³³

Table 1. Unit Cell Parameters, Average Strain, and Crystallite Size for Pure and Fe-Doped TiO₂ Nanocrystals

unit cell/strain/size	pure	0.22 at. % Fe	0.47 at. % Fe	1.05 at. % Fe
<i>a</i> [Å]	4.6055 (3)	4.6149 (3)	4.6139 (3)	4.6078 (3)
<i>c</i> [Å]	2.9543 (3)	2.9536 (3)	2.9545 (2)	2.9569 (2)
average strain 10^{-4}	20.26 (2)	25.36 (3)	28.1 (2)	30.842 (2)
size [Å]				
along [110]	102	51	53	68
along [001]	23000 ^a	16000 ^a	22000 ^a	12000 ^a
along [103]	488	245	246	326

^a Resolution limited. These micrometer-scale values are out of XRD measurement scope and should not be regarded as reliable.

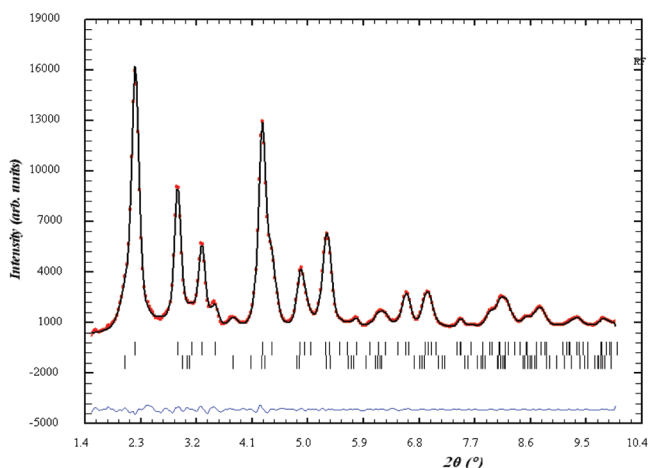


Figure 5. Rietveld fit for TiO₂ doped with 1.05 at. % of Fe ($R_{wp} \sim 3\%$). The difference (bottom) curve between experimental and calculated values is offset for clarity. Reflection positions are represented by vertical ticks (first row denotes rutile phase and second row anatase phase).

The results obtained for cell parameters and microstructure (crystallite size and average microstrain) are summarized in Table 1. It was not possible to calculate average particle size due to the fact that fwhms of certain reflections were similar to the instrumental fwhm, so in these directions (close to [001]) it was not possible to extract the actual particle size (these values are indicated in Table 1 as “resolution limited”). Thus, instead of the average size values, dimensions along three directions are stated in Table 1: [110] direction, for which the smallest size value was found in all samples, indicates the direction corresponding to the cylinder diameter (assuming cylindrical particle shape as observed by TEM); the second one is size along direction [001], the value of which was too large to be correctly evaluated by XRD, indicating the preferential particle growth along [001] direction; the third direction listed in Table 1 is [103], for which the size value was found to be the largest among all nonorthogonal directions to [110]. This value can be used as an indicator of crystallite length along [001] since the real value along [001] cannot be precisely determined.

Table 1 shows that the isotropic microstrain increases uniformly with the iron content increase. However, crystallite size changes nonuniformly with the Fe content increase. It was shown that smallest crystallites were formed in samples doped with 0.22 and 0.47 at. % of iron. As expected, the largest crystallite size was found in pure TiO₂. However, further increase of iron content above 0.47 at. % did not induce further decrease of size; on the

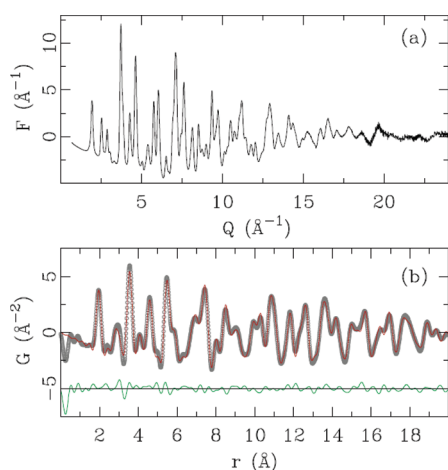


Figure 6. (a) Representative experimental total scattering function, $F(Q)$, and (b) corresponding atomic PDF, $G(r)$ (open symbols), with rutile structure model (solid line). Difference curve is offset for clarity. The data are shown for pure TiO_2 nanocrystal at room temperature, with $Q_{\text{max}} = 24 \text{ \AA}^{-1}$ used in Fourier transform.

Table 2. Structure Parameters from PDF Refinements of Rutile $P4_2/mmm$ Model over 1.2–20 Å Range^a

parameter	pure	0.22 at. % Fe	0.47 at. % Fe	1.05 at. % Fe
a [Å]	4.6058 (4)	4.6076 (4)	4.6063 (4)	4.6037 (4)
c [Å]	2.9559 (5)	2.9549 (4)	2.9558 (4)	2.9568 (4)
$x(\text{O})$	0.3068 (2)	0.3067 (2)	0.3069 (2)	0.3056 (2)
$U_{\text{iso}}(\text{Ti})$ [Å ²]	0.00746 (5)	0.00627 (5)	0.00604 (5)	0.00588 (5)
$U_{\text{iso}}(\text{O})$ [Å ²]	0.01319 (4)	0.01304 (4)	0.01339 (4)	0.01649 (4)
occupancy (O)	0.90 (1)	0.98 (1)	0.98 (1)	0.95 (1)
R_w [%]	14.0	14.8	14.6	14.5
with anatase R_w [%]	13.0			13.2
anatase fraction [%]	5 (3)			6 (3)

^a Ti is at 2a (0,0,0) position while O is at 4f ($x, x, 0$). Anatase $I4_1/amd$ phase was used as a secondary phase to fit data for pure and 1.05 at. % Fe-doped samples.

contrary, 1.05 at. % Fe doped sample showed the largest particle size among all three doped samples.

The amount of anatase phase was also found not to be in regular correspondence with the iron content. The diffraction patterns of samples doped with 0.22 and 0.47 at. % of iron did not show the presence of anatase detectable by X-ray diffraction, and these were refined as single phase patterns (Figure 4). On the other hand, pure TiO_2 and 1.05 at. % Fe doped samples gave diffraction patterns with notable presence of anatase phase. They were refined as two-phase patterns (for illustration, refined pattern of 1.05 at. % doped sample is shown in Figure 5), and the amount of anatase ratio is estimated to 4.6% and 6% for pure and 1.05 at. % Fe-doped sample, respectively.

The crystal structures of rutile and anatase are in agreement with literature.⁶ Because of very small amount of Fe, it was not possible to refine reliably Fe content and its distribution in doped samples. Irregular unit cell parameter change with Fe concentration increase could indicate large crystallite macrostrain or random substitution of Ti by Fe. Large crystallite size anisotropy is in accord with HRTEM results. Rather small strain anisotropy indicates absence of dislocations and stacking faults, again in

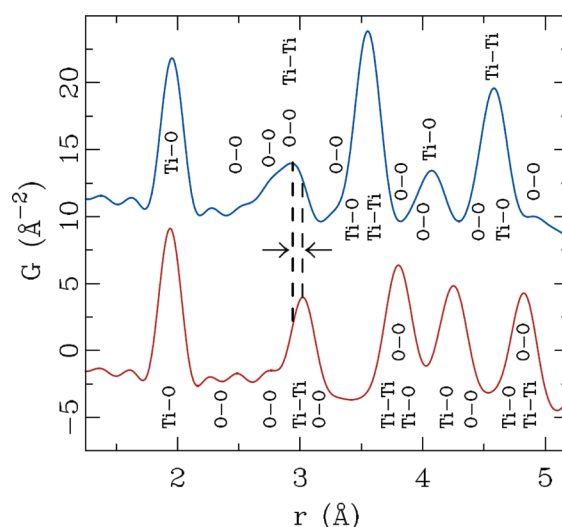


Figure 7. Simulated PDF profiles based on room temperature rutile (top) and anatase (bottom) models. Specific pair contributions are labeled for reference close to peaks that they contribute to. After the second well-pronounced PDF peak, higher- r peaks for the two structures are completely out of registry. Notably, the second pronounced PDF peaks in both profiles are very close in position, with offset indicated by arrows and dashed lines. The largest discrepancy between the rutile model and the data, observable from the difference curve in Figure 6b, is precisely in this range.

accord with HRTEM results. However, the presence of point defects in Fe-doped TiO_2 could be expected.

3.3. Structure Parameters from PDF Analysis in Direct Space. Total X-ray scattering data of all the samples were considered in direct space via the PDF approach, using the program PDFgui.³⁴ Total scattering structure $F(Q)$ is Q -weighted structure function that enhances the signal at higher momentum transfer, Q , compared to low Q (see Figure 6a). When Fourier transformed, these data can be fit using the least-squares approach (Figure 6b). This allowed overcoming the difficulties of determining structural parameters using the Rietveld method. Data for all the samples are consistent with rutile structure, and refined parameters are reported in Table 2. The starting values for lattice parameters were those obtained from Rietveld refinement, and these were allowed to further vary in the PDF modeling procedure. Small but observable discrepancies between the lattice parameters observed by Rietveld and PDF methods can be attributed to the fact that the former method depends on Bragg intensities alone, while the later utilizes both Bragg and diffuse scattering components and essentially yields different structural information. Oxygen occupancy is also refined, indicating that the pure and 1.05 at. % Fe samples are slightly oxygen deficient (ca. 10% for pure and 5% for 1.05 at. % Fe-doped TiO_2 ; see Table 2), while 0.22 at. % Fe and 0.47 at. % Fe samples are nearly stoichiometric. In addition, since some presence of anatase was observed in pure sample and sample with 1.05 at. % Fe, as mentioned earlier, after completing the refinement of the rutile model refinement, anatase was added as a second phase using initial value for parameters from the literature,^{35,36} and phase fraction was estimated, which is consistent with the results of Rietveld refinement, and contributed to a small but observable improvement of R_w values. The same wide-range modeling was attempted for the other two Fe-doped samples, but this gave unstable fits with larger value of R_w than the single-phase rutile model.

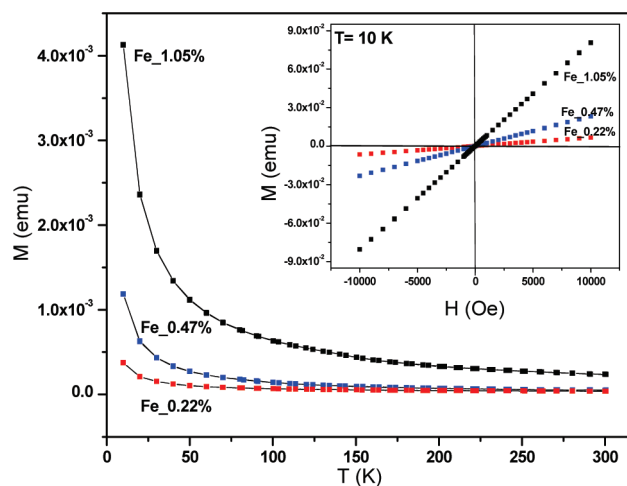


Figure 8. Magnetization versus temperature for $\text{TiO}_2\text{:Fe}$ samples measured after zero field cooling. Inset: magnetization versus magnetic field.

Typical fit of rutile model is shown in Figure 6b. The model works rather well, with only a noticeable mismatch in the low- r region, around 3 Å. This type of discrepancy is often observed in cases of nanocrystals when there are appreciable surface reconstruction effects. However, another possible source of the discrepancy could be the presence of highly amorphous anatase phase. If we consider the second PDF peak, the discrepancy in the fit, Figure 6b, is such that the data PDF has extra intensity at the high- r side of the peak, with respect to the model PDF. Interestingly, the same type of mismatch is observed in the second PDF peak of model profiles calculated for rutile and anatase, based on literature values for the two crystallographic phases of TiO_2 (Figure 7). To further test whether this is consistent with the data, we have carried out a two phase refinement over a narrow r -range from 1.2 to 4.0 Å where this discrepancy is observed. While parameters for rutile phase were fixed to values obtained from single-phase fits (Table 2), anatase parameters were varied. The results are summarized in section 3.6.

3.4. Fe Ion Distribution. From the magnetic point of view Fe-doped or substituted TiO_2 belongs to diluted magnetic semiconductors (DMS). Among different DMS, the 3d ions ZnO and TiO_2 in hosts are of importance as potential materials for spintronics.³⁷ However, to be applicable in this sense, they need to show the ferromagnetic behavior at room temperature. A number of recent publications deal with magnetic ion-doped TiO_2 and ZnO.³⁸ There are some published experimental results regarding room temperature magnetism for these materials, followed by many propositions on causes of high-temperature ferromagnetism in a magnetic ion-doped TiO_2 and ZnO.³⁹ However, our magnetization measurements versus temperature and field have shown characteristics of typical paramagnetic behavior for all Fe-doped samples (Figure 8). The presence of Fe ion clusters was not detected, which is not completely surprising having in mind very low Fe concentration in the samples studied.

3.5. Raman Spectroscopy. From Figure 9 it is evident that all samples studied were composed only from rutile and anatase (although the latter in small fraction).^{40–44} Evidently, anatase/rutile ratio is highest in pure TiO_2 and TiO_2 with 1.05 at. % of Fe, in agreement with the results of Rietveld and PDF refinements. Although the anatase content is similar for pure and 1.05% Fe batch (~5–6% in volume, Table 2), strong differences are

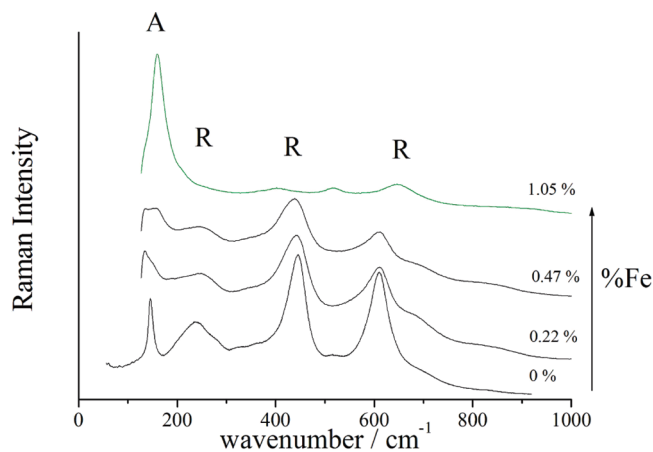


Figure 9. Raman spectra of pure and iron-doped TiO_2 nanocrystals (A = anatase; R = rutile).

observed in their Raman spectra: The spectrum of the latter compound is dominated by the anatase signature, but the main peak is broadened (fwhm = 33 cm^{-1} instead of 11 cm^{-1}) and shifted from 146 to 159 cm^{-1} . A possible explanation of this observation is that the broad and diffuse background-like X-ray scattering observed below $3^\circ 2\theta$ in Figure 3 for pure TiO_2 corresponds to amorphous anatase and that the true anatase content is in fact much higher than reported in Table 1. By comparison with pure TiO_2 where standard crystalline anatase signature is observed, we can conclude that anatase content in 0.22 and 0.47% Fe: TiO_2 is less than 1% in volume. Careful examination of the Raman signature of these two compounds shows unusual features: Rayleigh wings extend at least up to ~400 and 800 cm^{-1} . Such Raman feature is observed for disordered compounds such as substituted zirconia, especially those obtained from sol–gel route,⁴⁵ Al_2TiO_5 nanopowders prepared by high-energy ball milling,⁴⁶ and in glassy silicates (the so-called “boson peak”).⁴ The common feature of these materials is the presence of defects (oxygen vacancies and substituted atoms, stacking faults and $\text{Fe}^{2+}/\text{Fe}^{3+}$ distribution, compensating cations and depolymerization, etc.) which breaks the periodicity and the propagation of the phonons and hence make active at the zone center modes of the whole Brillouin zone. In our case the small needle section, the Ti/Fe substitution, and presence of oxygen vacancies can hinder the propagation of the phonons and induce a vibrational distribution of state signature. The size effect is expected to be the dominant effect.

By comparing fwhm of the Raman bands, it is evident that fwhm increase as Fe content increases. This is likely due to the phonon breaking by Fe ions and vacancies that are formed during the replacement of Ti^{4+} by Fe. Additionally, increase of the background intensity with increasing Fe content is evident. This could be ascribed again to the phonon breaking by Fe ions and vacancies that are formed during replacement of Ti^{4+} by Fe^{3+} or Fe^{2+} . In order to make appropriate fits of Raman spectra, not only the bands of vibrations belonging to anatase and rutile were fit by pure Lorentzian profiles but also fit of a “boson-like” peak was added in order to take into account vibrations that represent a disordered part of the material (Figure 10).⁴⁷ Evidently, boson-like peak intensity increases with the increase of the Fe content, indicating that disordered part of the structure increases as the Fe concentration increases. However, the rutile/anatase ratio did not change systematically with change of the Fe content. This

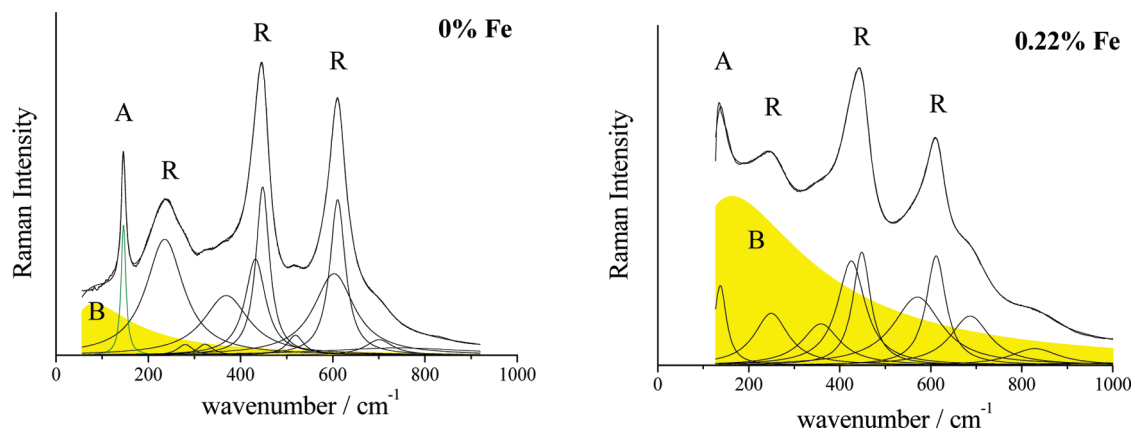


Figure 10. Raman spectra of pure TiO_2 nanocrystals and TiO_2 nanocrystals doped with 0.22 at. % of Fe (A = anatase contribution, R = rutile contribution, B = “boson-like” contribution).

suggests that the range of Fe concentrations between 0.2 and 0.5 at. % could be optimal for preparation of pure rutile specimen (or maximizes the rutile contribution to the structure).

By comparing our results with recent results of Zukerman et al.⁴⁸ and Swamy et al.⁴⁹ in regard to crystallite size measured from Raman spectroscopy, it could be found that our result for pure anatase is in agreement with their predictions giving ca. 5–10 nm crystallite size on average. This is also in line with the results obtained from PDF analysis (for details see sections 3.3 and 3.6).

The investigated rutile nanorods are elongated in one direction, and the average crystallite size and form are presumably too complex to be defined by Raman spectroscopy. Notably, Mazza et al.⁴⁴ demonstrated that the phonon confinement model is not adequate for explaining the features of the lattice dynamics of rutile nanocrystals of any form. However, a simple and effective procedure can be applied for this purpose if calibration diagrams produced by Swamy⁴² (see Figures 4 and 5 in ref 42) are utilized properly. Considering a highly anisotropic object, we could expect that Raman spectrum for such an object is composed of two convoluted bands originating from two different directions each. These bands should be close to each other, different in fwhm, and with equal intensity. Results of fits presented in Figure 10 for pure TiO_2 are in good agreement with this prediction for two most intense rutile bands centered at ca. 445 and 605 cm^{-1} . For both vibration bands two peaks with equal intensity within experimental error were obtained (Table 3). Therefore, the results of our fit indicate that investigated rutile crystals are highly anisotropic, with two dominant dimensions of ca. 5 and 100 nm.

For iron-doped samples the calibration curves could not be used since both position and fwhm of the used Raman mode depend on the iron content as well as on the vacancy concentration.⁴⁴ This issue is more pronounced for highly anisotropic crystals, such as these that we investigated. Notably, Wang et al.¹ recorded Raman spectra on a mixed anatase/rutile nanopowders, both pure and doped with iron. In 1% Fe-doped and 2% Fe-doped specimens they found a shift in position of the main anatase band with respect to pure compounds from 146.2 to 149.7 cm^{-1} and to 155.6 cm^{-1} , respectively. This is an indication that anatase in our specimen, considering the position of main vibrational band at 159 cm^{-1} , contains between 2 and 3% of iron. We speculate that in the synthesis process Fe from the reaction volume prefers to be taken by anatase, rather than rutile.

Table 3. Results of Fit Presented in Figure 10 (Errors in Parentheses)

center of gravity [cm^{-1}]		fwhm [cm^{-1}]	
0% Fe	0.22% Fe	0% Fe	0.22% Fe
448.1 (6)	448 (2)	18 (1)	24 (4)
432 (4)	425 (8)	27 (3)	37 (7)
610.5 (2)	611.7 (6)	>20.3 (9)	26 (3)
603 (2)	570 (9)	53 (6)	65 (13)

3.6. Formation, Location, Structure, and Morphology of Anatase.

Structural and Raman spectroscopy results showed that samples crystallized predominantly in rutile form. It was shown that at the nanoscale anatase phase is thermodynamically more stable than rutile, while in bulk form rutile is the more stable phase.^{50,51} Consequently, the applied synthesis method enables one to obtain rutile—thermodynamically stable TiO_2 —even in nanoparticle form. It should also be noted that TiO_2 doped with Fe favors rutile formation. As it is evident that even pure TiO_2 crystallized predominantly in rutile form, this indicates that doping is not the dominant factor in the crystallization process.

Through HRTEM assessment of the structure no anatase was observed. Both Rietveld and intermediate range PDF analyses showed that anatase could only be observed if its quantity is greater than ca. 5% (Table 3). Further, results of PDF refinements over a narrow r -range are consistent with presence of small fraction of nearly amorphous anatase in all investigated samples. The total scattering-based PDF approach, which includes both Bragg and diffuse scattering components into consideration, has the advantage over Rietveld approach, in that it can probe both intermediate and short-range order in a material, i.e., well-crystalline and “amorphous-like” material. The results of short-range PDF analysis point to a conclusion that small amount of anatase observed in the nanocrystal system is poorly crystalline. Higher content of anatase in predominantly rutile structure is systematically obtained when PDF refinement was performed over a narrow range from 1.2 to 4.0 Å than over a range from 1.2 to 20.0 Å. Although we cannot exclude a possibility of the presence of anatase at the surface,⁵² a more plausible explanation could be that anatase is located in the flower center. This position of poorly crystalline anatase is consistent with its low quantity and also explains why it could not be observed by HRTEM. On the

Table 4. Anatase Content (%) in Pure and Fe-Doped TiO₂ Nanocrystals

% Fe	HRTEM	Rietveld	PDF	
			1.2–4.0 Å	1.2–20.0 Å
0	n.o. ^a	4.6 (7)	9 (3)	5 (3)
0.22	n.o.	n.o.	4 (3)	n.o.
0.47	n.o.	n.o.	5 (3)	n.o.
1.05	n.o.	6.1 (6)	8 (3)	6 (3)

^an.o. = not observed.

other hand, it is well-known that TiO₂—especially anatase structure in the form of nanorods or nanotubes—may contain few % of protons.⁵² If we consider that proton stabilizes anatase, this would suggest that the amorphous anatase is actually located at the surface of the rutile needles, since protonation is easier at the surface than in the core of the rod. However, HRTEM measurements did not reveal presence of anatase on rutile nanorod surface, and the samples were properly dried in vacuum at room temperature to a constant weight before all the experiments were carried out. The fraction of anatase obtained from PDF refinements over the range between 1.2 and 20.0 Å is in agreement with the Rietveld refinement results, as expected, since intermediate range order dominates the PDF in this case. With all these considerations in mind, we speculate that the most plausible scenario is the one in which small particles of anatase with low degree of crystallinity form initially, followed by further crystallization of rutile nanorods, finally resulting in formation of well-crystalline flowerlike aggregates. Iron concentration appears not to play role neither for the crystal morphology nor the rutile/anatase stability.

4. CONCLUSION

Industrial applicability of TiO₂ and Fe-doped TiO₂ nanocrystals critically depends on detailed knowledge of their size, strain, size distribution, particle morphology, cation distribution, and presence of defects. This motivated the study of Fe-doped TiO₂ nanocrystals to determine details of their structure and morphology. Rietveld and atomic PDF methods were applied on X-ray powder diffraction data. The analysis of the obtained XRPD patterns and Raman spectra revealed that synthesized samples with 0, 0.22, 0.47, and 1.05 at. % of iron ions in TiO₂ predominantly crystallized in rutile form, with a small contribution of anatase phase. High-resolution transmission electron microscopy and Raman spectroscopy revealed specific structure of flowerlike aggregates composed from rodlike shapes of rutile nanocrystallites, while SQUID magnetic measurements showed that Fe clusters were not formed. All techniques used are complementary, and when used in combination, they reveal useful information and provide a more complete picture about heterogeneity and disorder in Ti_{1-x}Fe_xO_{2-d} nanocrystal rutile-based flowerlike aggregates. The core of the nanocrystals (probably isometric) is made of anatase (presumably iron-rich), while the needlelike nanorods with rutile structure grow on the initially formed anatase, thus forming the rest of the flowerlike aggregate.

AUTHOR INFORMATION

Corresponding Author

*E-mail: akremen@EUnet.rs.

ACKNOWLEDGMENT

The Serbian Ministry of Science has financially supported this work under Contract No. III 45015. E.B. thanks Simon Billinge for discussions. Work at BNL was supported by the Office of Basic Energy Sciences, US Department of Energy, under Contract No. DE-AC02-98CH10886. Advanced Photon Source at the Argonne National Laboratory is supported under DOE Contract No. DE-AC02-06CH11357.

REFERENCES

- (1) Wang, X. H.; Li, J.-G.; Kamiyama, H.; Katada, M.; Ohashi, N.; Moriyoshi, Y.; Ishigaki, T. *J. Am. Chem. Soc.* **2005**, *127*, 10982–10990.
- (2) Chen, X.; Mao, S. S. *Chem. Rev.* **2007**, *107*, 2891–959.
- (3) Colomban, Ph. Raman/Rayleigh Study of Nanophases, Proc of the 27th Annual Cocoa Beach Conference and Exposition, Cocoa Beach, FL, 26–31 Jan 2003; Functional Ceramics Kriven, W. H., Lin, H. T., Eds. *Ceram. Eng. Sci. Proc.* **2003**, *24* (4), 41–50.
- (4) Gouadec, G.; Colomban, Ph. *Progr. Cryst. Growth. Charac. Mater.* **2007**, *53*, 1–56.
- (5) <http://www.gordonengland.co.uk>; <http://www.noodor.biz>, 2009.
- (6) ICSD data base, Version 2009-2, NIST and FIZ (136 different entries for TiO₂).
- (7) Huber, B.; Brodyanski, A.; Scheib, M.; Orendorz, A.; Ziegler, C.; Gnaser, H. *Thin Solid Films* **2005**, *472*, 114–124.
- (8) Abazović, N. D.; Čomor, M. I.; Zec, S.; Nedeljković, J. M.; Piscopiello, E.; Montone, A.; Antisari, M. V. *J. Am. Ceram. Soc.* **2009**, *92*, 894–896.
- (9) Cozzoli, P. D.; Kornowski, A.; Weller, H. *J. Am. Chem. Soc.* **2003**, *125*, 14539–14548.
- (10) Wu, J.-M.; Qi, B. *J. Phys. Chem. C* **2007**, *111*, 666–673.
- (11) Wu, J.-M. *Environ. Sci. Technol.* **2007**, *41*, 1723–1728.
- (12) Wu, J.-M.; Zhang, T.-W.; Zeng, Y.-W.; Hayakawa, S.; Tsuru, K.; Osaka, A. *Langmuir* **2005**, *21*, 6995–7002.
- (13) Kim, S. J.; Park, S. D.; Rhee, C. K.; Kim, W. W.; Park, S. *Scr. Mater.* **2001**, *44*, 1229–1233.
- (14) Bak, T.; Nowotny, J.; Nowotny, M. K. *J. Phys. Chem. B* **2006**, *110*, 21560–21567.
- (15) Nowotny, M. K.; Bak, T.; Nowotny, J.; Sorrell, C. *Phys. Status Solidi* **2005**, *242*, R88–R90.
- (16) Lee, K.; Lee, N. H.; Shin, S. H.; Lee, H. G.; Kim, S. J. *Mater. Sci. Eng., B* **2006**, *129*, 109–115.
- (17) Abazović, N. D.; Mirengi, L.; Janković, I. A.; Bibić, N.; Šojić, D. V.; Abramović, B. F.; Čomor, M. I. *Nanoscale Res. Lett.* **2009**, *4*, 518–525.
- (18) Hurum, D. C.; Gray, K. A.; Rajh, T.; Thurnauer, M. C. *J. Phys. Chem. B* **2005**, *109*, 977–980.
- (19) Abazović, N. D.; Montone, A.; Mirengi, L.; Janković, I. A.; Čomor, M. I. *J. Nanosci. Nanotechnol.* **2008**, *8*, 613–618.
- (20) Litter, M. I.; Navio, J. A. *J. Photochem. Photobiol. A* **1996**, *98*, 171–181.
- (21) Ding, Y.; Han, W. Q.; Lewis, L. H. *J. Appl. Phys.* **2007**, *102*, 123902.
- (22) Wang, C.; Bottcher, C.; Bahnmann, D. W.; Dorhmann, J. K. *J. Mater. Chem.* **2003**, *13*, 2322–2329.
- (23) Abazović, N. D.; Čomor, M. I.; Dramićanin, M. D.; Jovanović, D. J.; Ahrenkiel, S. P.; Nedeljković, J. M. *J. Phys. Chem. B* **2006**, *110*, 25366–25370.
- (24) Chupas, P. J.; Qiu, X.; Hanson, J. C.; Lee, P. L.; Grey, C. P.; Billinge, S. J. L. *J. Appl. Crystallogr.* **2003**, *36*, 1342–1347.
- (25) Chupas, P. J.; Chapman, K. W.; Lee, P. L. *J. Appl. Crystallogr.* **2007**, *40*, 463–470.
- (26) Egami, T.; Billinge, S. J. L. *Underneath the Bragg Peaks: Structural Analysis of Complex Materials*; Cahn, R. W., Ed.; Pergamon: New York, 2003.
- (27) Qiu, X.; Thompson, J. W.; Billinge, S. J. L. *J. Appl. Crystallogr.* **2004**, *37*, 678.

- (28) Oliver, P. M.; Watson, G. W.; Kelsey, E. T.; Parker, S. C. *J. Mater. Chem.* **1997**, *3*, 563–568.
- (29) Zhang, S.; Liu, C.-Y.; Liu, Y.; Zhang, Z.-Y.; Mao, L.-J. *Mater. Lett.* **2009**, *63*, 127–129.
- (30) Rodriguez-Carvajal, J. FullProf computer program <http://www.ill.eu/sites/fullprof/>, 2009.
- (31) Rodriguez-Carvajal, J. *Physica B* **1993**, *192*, 55–69.
- (32) Rodriguez-Carvajal, J. Recent Developments of the Program FULLPROF. In *Commission on Powder Diffraction (IUCr) Newsletter* **2001**, *26*, 12–19 (<http://journals.iucr.org/iucr-top/comm/cpd/Newsletters/>).
- (33) Balzar, D.; Audebrand, N.; Daymond, M. R.; Fitch, A.; Hewat, A.; Langford, J. L.; Le Bail, A.; Louer, D.; Masson, O.; McCowan, C. N.; Popa, N. C.; Stephens, P. W.; Toby, B. H. *J. Appl. Crystallogr.* **2004**, *37*, 911–924.
- (34) Farrow, C. L.; Juhás, P.; Liu, J. W.; Bryndin, D.; Bozin, E. S.; Bloch, J.; Proffen, Th.; Billinge, S. J. L. *J. Phys. Condens. Matter* **2007**, *19*, 335219–7p.p.
- (35) Ballirano, P.; Caminiti, R. *J. Appl. Crystallogr.* **2001**, *34*, 757–762.
- (36) Leinekugel-le-Cocq-Errien, A. Y.; Deniard, P.; Jobic, S.; Gautier, E.; Evain, M.; Aubin, V.; Bart, F. *J. Solid State Chem.* **2007**, *180* (1), 322–330.
- (37) Janisch, R.; Gopal, P.; Spaldin, N. A. *J. Phys.: Condens. Matter* **2005**, *17*, R657–R689.
- (38) (a) Kuljanin-Jakovljević, J.; Radoičić, M.; Radetić, T.; Konstatinović, Z.; Šaponjić, Z. V.; Nedeljković, J. *J. Phys. Chem. C* **2009**, *113*, 21029–21033. (b) Saponjić, Z. V.; Dimitrijević, N. M.; Poluektov, O. G.; Chen, L. X.; Wasinger, E.; Welp, U.; Tiede, D. M.; Zuo, X.; Rajh, T. *J. Phys. Chem. B* **2006**, *110* (50), 25441–25450.
- (39) (a) Rykov, A. I.; Nomura, K.; Sakuma, J.; Barrero, C.; Yoda, Y.; Mitsui, T. *Phys. Rev. B* **2008**, *77*, 014302. (b) Sangaletti, L.; Mozzati, M. C.; Drera, G.; Galinetto, P.; Azzoni, C. B.; Speghini, A.; Bettinelli, M. *Phys. Rev. B* **2008**, *78*, 075210.
- (40) Ohsaka, T.; Izumi, F.; Fujiki, Y. *J. Raman Spectrosc.* **1978**, *7*, 321–324.
- (41) Likodimos, V.; Stergiopoulos, T.; Falaras, P.; Kunze, J.; Schmuki, P. *J. Phys. Chem. C* **2008**, *112*, 12687–12696.
- (42) Swamy, V. *Phys. Rev. B* **2008**, *77*, 195414–4p.p.
- (43) Luca, V. *J. Phys. Chem. C* **2009**, *113*, 6367–6380.
- (44) Mazza, T.; Barborini, E.; Piseri, P.; Milani, P.; Cattaneo, D.; Li Bassi, A.; Bottani, C. E.; Ducati, C. *Phys. Rev. B* **2007**, *75*, 045416–5.
- (45) (a) Kosacki, I.; Petrosky, V.; Anderson, H.; Colomban, Ph. *J. Am. Ceram. Soc.* **2002**, *85*, 2646–2650. (b) Karlin, S.; Colomban, Ph. *J. Am. Ceram. Soc.* **1999**, *82*, 735–741.
- (46) Uribe, R.; Baudin, C.; Mazerolles, L.; Michel, D. *J. Mater. Sci.* **2001**, *36*, 5105–5113 and in Ph. Colomban *Imagerie mécanique et physico-chimique par microspectrométrie Raman, Techniques de l'Ingénieur, Innovation*, <http://www.techniques-ingenieur.fr/affichage/DispIntro.asp?nGcmID=RES>.
- (47) Baron, D. Computer program ASREL2 2009; <http://www.ladir.cnrs.fr/pagebaron.htm>.
- (48) Zukerman, R.; Vradman, L.; Titelman, L.; Zeiri, L.; Perkas, N.; Gedanken, A.; Landau, M. V.; Herskowitz, M. *Mater. Chem. Phys.* **2010**, *122*, 53–59.
- (49) Swamy, V.; Kuznetsov, A.; Dubrovinsky, L. S.; Caruso, R. A.; Shchukin, D. G.; Muddle, B. C. *Phys. Rev. B* **2005**, *71*, 184302–11.
- (50) Pokrant, S.; Irsen, S. *Microsc. Microanal.* **2008**, *14*, 354–355.
- (51) Colomban, Ph.; Mazerolles, L. *J. Mater. Sci.* **1991**, *26*, 3503–3510.
- (52) Lan, Y.; Gao, X.; Zhu, H.; Zheng, Z.; Yan, T.; Wu, F.; Ringer, S. P.; Song, D. *Adv. Funct. Mater.* **2005**, *15*, 1310–1318.

Spin-glass behavior of semiconducting $K_xFe_{2-y}S_2$

Hechang Lei (雷和畅), Milinda Abeykoon, Emil S. Bozin, and C. Petrovic

Condensed Matter Physics and Materials Science Department, Brookhaven National Laboratory, Upton, New York 11973, USA

(Received 28 January 2011; revised manuscript received 19 March 2011; published 16 May 2011)

We report the discovery of $K_xFe_{2-y}S_2$ single crystals, isostructural to $K_xFe_{2-y}Se_2$ superconductors. The sulfide compound is a small gap semiconductor and shows spin-glass behavior below 32 K. Our results indicate that stoichiometry, defects, and the local environment of FeCh (Ch = S, Se) tetrahedra have important effects on the physical properties of isostructural and isoelectronic $K_xFe_{2-y}Ch_2$ compounds.

DOI: [10.1103/PhysRevB.83.180503](https://doi.org/10.1103/PhysRevB.83.180503)

PACS number(s): 74.70.Xa, 74.70.Ad, 75.50.Lk, 74.72.Cj

Iron-based materials have been the focus of exploratory search for new superconductors since the discovery of $LaFeAsO_{1-x}F_x$ with a transition temperature T_c up to 26 K.¹ Several superconducting families were discovered soon after $RFePnO$ (R = rare earth; Pn = P or As, FePn-1111 type),²⁻⁴ including α -PbO-type FeCh (Ch = S, Se, Te; FeCh-11 type) materials that do not have any crystallographic layers in between puckered FeCh slabs.⁴ FeCh-11-type materials share a square-planar lattice of Fe with a tetrahedral coordination and Fermi surface topology similar to other iron-based superconductors.⁵ Under external pressure,^{6,7} T_c can be increased from 8 to 37 K and dT_c/dP can reach 9.1 K/GPa, the highest in all iron-based superconductors.⁷ The empirical rule proposed by Mizuguchi *et al.* proposes that the critical temperature is closely correlated with the anion height between Fe and Ch layers. There is an optimal distance around 0.138 nm with a maximum transition temperature $T_c \simeq 55$ K.⁸

Intercalation can change the local environment of the FeSe tetrahedron and introduce extra carriers. The intercalation could also decrease the dimensionality of the conducting bands. This is favorable for superconductivity since the presence of low-energy electronic collective modes in layered conductors helps to screen Coulomb interaction.⁹ This is seen in iron-based superconductors: T_c increases from FeCh-11 type to FePn-1111 type. Very recently the superconducting T_c was enhanced in iron selenide material to about 30 K not by external pressure but by inserting K, Rb, Cs, and Tl between the FeSe layers (AFSe-122 type), thus changing the crystal structure around the FeCh tetrahedra.¹⁰⁻¹³ Similar to pressure effects, the intercalation using elements with +1 valence decreases the Se height toward the optimum value.¹² The expanded FeSe interlayer distances could also contribute to reducing the dimensionality of the conducting bands and magnetic interactions. On the other hand, the insulating-superconducting transition can be induced in $(Tl_{1-x}K_x)Fe_{2-y}Se_2$ by tuning the Fe stoichiometry and implying that the superconductivity is in the proximity of an antiferromagnetic Mott-insulating state.¹³ Thus, exploring new oxychalcogenide and chalcogenide compounds containing similar FeCh layers would be instructive.

In this Rapid Communication, we report the discovery of $K_xFe_{2-y}S_2$ single crystals isostructural to 122 iron selenide superconductors. The structure analysis indicates that the anion height might not be essential for superconductivity. The resistivity and magnetic measurements suggest a spin-glass (SG) semiconductor ground state similar to that of the

$TlFe_{2-x}Se_2$ with high Fe deficiency, even though the anion heights are close to values found in iron-based superconductors with T_c above 20 K.^{13,14}

Single crystals of $K_xFe_{2-y}S_2$ were grown via the self-flux method¹⁵ with nominal composition K:Fe:S = 0.8:2:2. Prereacted FeS and K pieces were added into the alumina crucible with a partial pressure of argon gas. The quartz tubes were heated to 1030°C, kept at this temperature for 3 h, then cooled to 730°C. Platelike crystals up to $10 \times 10 \times 3$ mm³ can be grown. Powder x-ray diffraction (XRD) data were collected at 300 K using 0.3184-Å wavelength radiation (38.94 keV) at the X7B beamline of the National Synchrotron Light Source. The average stoichiometry was determined by energy-dispersive x-ray spectroscopy (EDX). Electrical transport, heat capacity, and magnetization measurements were carried out in Quantum Design PPMS-9 and MPMS-XL5.

Figure 1(a) shows powder XRD data at room temperature and structural refinements on $K_xFe_{2-y}S_2$ using General Structure Analysis System (GSAS).^{16,17} A model possessing tetragonal $ThCr_2Si_2$ structure and space group I4/mmm failed to explain the observed diffraction pattern due to the clear appearance of (110) and other superlattice reflections indicating symmetry lowering to I4/m. Data were successfully explained to within I4/m symmetry, incorporating the Fe vacancy order site, with lattice parameters $a = 8.3984(5)$ Å and $c = 13.5988(11)$ Å, which are appreciably smaller than those observed in the selenium counterpart.¹⁰ The c axis is particularly reduced due to the smaller ionic size of S^{2-} when compared to Se^{2-} . The ordered Fe vacancy is the same as in $K_xFe_{2-y}Se_2$.¹⁸ This may imply a similar origin of magnetic behavior for both compounds. Atomic positions with refined parameters are listed in Table I. Refinements yield that K1, K2, and Fe1 positions are partially occupied, while Fe2 positions are almost fully occupied. It should be noted that, when K1 and Fe1 positions are fully unoccupied while K2 and Fe2 are fully occupied, the corresponding chemical formula is $K_{0.8}Fe_{1.6}S_2$ and the Fe vacancy is completely ordered. The average atomic ratios from EDX are consistent with $K_{0.88(6)}Fe_{1.63(4)}S_{2.00(1)}$, indicating that there are both potassium and iron deficiencies from ideal 122 stoichiometry, in good agreement with XRD fitting results. It should be noted that 18.5% of the iron precipitates on the surface of the ingot on cooling. The iron precipitates are easy to remove and have no influence on the physical properties of $K_xFe_{2-y}S_2$.

The in-plane resistivity $\rho_{ab}(T)$ of the $K_xFe_{2-y}S_2$ single crystal rapidly increases with decreasing the temperature

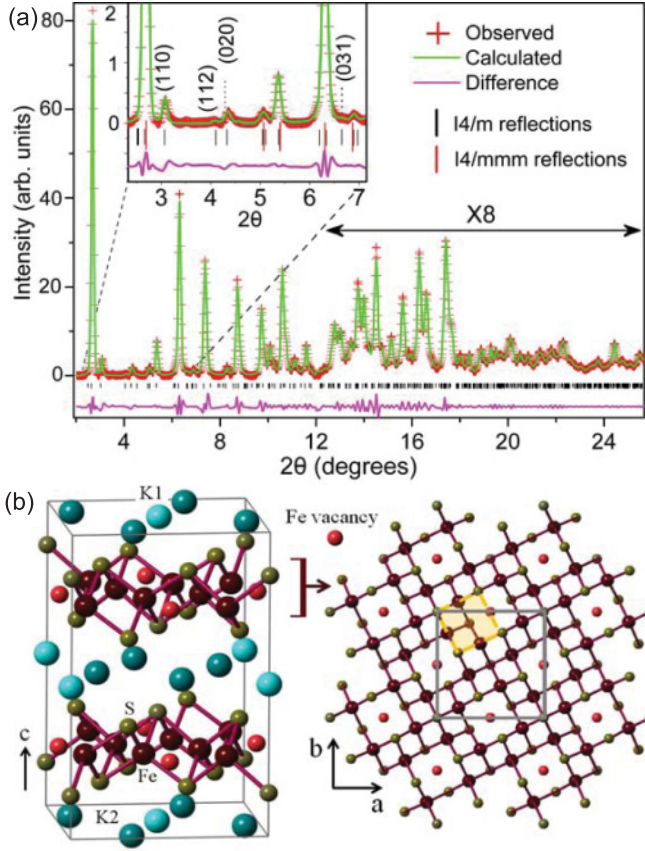


FIG. 1. (Color online) (a) Powder XRD patterns of $K_xFe_{2-y}S_2$ and fit using $I4/m$ model. Inset: low-scattering-angle part, emphasizing the presence of superlattice reflections characteristic of $I4/m$ symmetry. Enlarged isotropic thermal parameters, particularly in the potassium layer, are indicative of local disorder present in the structure. (b) Crystal structure of $K_xFe_{2-y}S_2$ in $I4/m$ unit cell with vacant Fe1 sites (small red circle) and K1 sites (light blue) (left). Sketch of the FeS slab (c -axis view) with ordered Fe vacancies (right). Small yellow and large gray squares illustrate $I4/mmm$ and $I4/m$ unit cells, respectively.

from $\rho_{ab}(300\text{ K}) \sim 100\text{ m}\Omega\text{ cm}$ and there is no obvious magnetoresistance (Fig. 2). The $\rho_{ab}(T)$ is thermally activated: $\rho = \rho_0 \exp(E_a/k_B T)$, where ρ_0 is a prefactor and k_B is the Boltzmann constant [inset (b) of Fig. 2]. Using the $\rho_{ab}(T)$ data from 70 to 300 K, we estimate $\rho_0 \sim 11.7(2)\text{ m}\Omega\text{ cm}$ and the activation energy $E_a = 51.8(2)\text{ meV}$. The semiconducting behavior might be at least partially ascribed to the deficiency of Fe in the Fe-Se plane that would introduce a random scattering potential, just like in highly Fe deficient $K_xFe_{2-y}Se_2$ and $TlFe_{2-x}Se_2$.^{13,14,19}

The magnetic susceptibility with $H \parallel ab$ is larger than with $H \parallel c$ [Fig. 3(a)], similar to the observed anisotropy in $TlFe_{2-x}Se_2$.¹⁴ The most interesting characteristics are the absence of Curie-Weiss behavior and the obvious bifurcation between the zero-field-cooling (ZFC) and field-cooling (FC) curves below 32 K. This might suggest the presence of low-dimensional short-range magnetic correlations and/or a long-range magnetic order above 300 K, and an antiferromagnetic phase transition at low temperatures. The $M(T)$ irreversible behavior below 32 K implies some ferromagnetic contribution

TABLE I. Structural parameters for $K_xFe_{2-y}S_2$ at room temperature.^a

Chemical formula		$K_{0.88}Fe_{1.63}S_2$			
Space group		$I4/m$			
a (Å)		8.3984(5)			
c (Å)		13.5988(11)			
V (Å ³)		959.17(11)			
Interatomic distance (Å)		Bond angle (deg)			
d_{Fe1-S2} [4]	2.4170(12)	$S2-Fe1-S2$ [2]	110.1(5)		
$d_{Fe1-Fe2}$ [4]	2.5914(16)	$S2-Fe1-S2$ [4]	109.2(3)		
d_{Fe2-S1} [1]	2.3647(11)	$S1-Fe2-S2$ [1]	103.9(5)		
d_{Fe2-S2} [1]	2.3369(11)	$S1-Fe2-S2$ [1]	109.8(3)		
d_{Fe2-S2} [1]	2.3005(11)	$S1-Fe2-S2$ [1]	111.0(3)		
d_{Fe2-S2} [1]	2.2660(11)	$S2-Fe2-S2$ [1]	105.3(3)		
$d_{Fe2-Fe2}$ [2]	2.6495(16)	$S2-Fe2-S2$ [1]	117.7(2)		
$d_{Fe2-Fe2}$ [1]	2.8135(17)	$S2-Fe2-S2$ [1]	108.7(5)		
		Anion heights (Å)			
S1 to Fe1	1.388(5)	S2 to Fe1	1.384(5)		
S1 to Fe2	1.334(5)	S2 to Fe2	1.439(5)		
Atom	x	y	z	Occ	U_{iso} (Å ²)
K1	0	0	0.5	0.84(12)	0.059(15)
K2	0.80(2)	0.418(6)	0.5000	0.89(3)	0.059(15)
Fe1	0	0.5	0.25	0.08(4)	0.0136(3)
Fe2	0.2954(5)	0.4111(5)	0.2460(16)	1.00(1)	0.0136(3)
S1	0	0	0.1479(5)	1.00(0)	0.0111(6)
S2	0.1113(4)	0.292(1)	0.3518(3)	1.00(0)	0.0111(6)

^aValues in brackets give the number of equivalent distances or angles of each type.

to magnetic susceptibility or a glassy transition where spins would be frozen randomly below the freezing temperature T_f . Similar magnetization was reported in $TlFe_{2-x}Se_2$ and

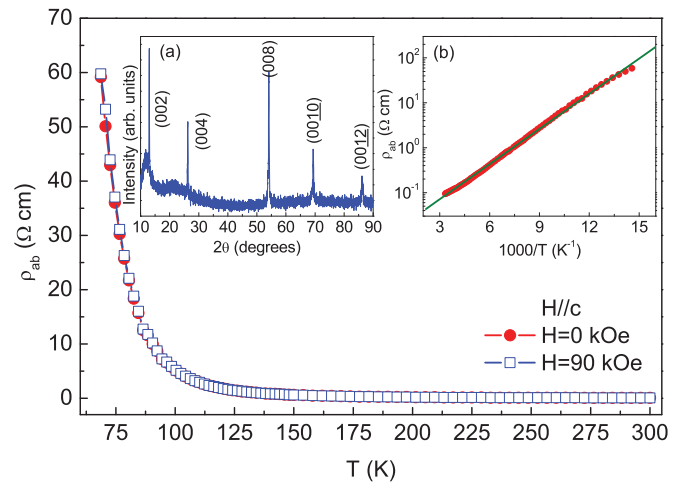


FIG. 2. (Color online) Temperature dependence of the in-plane resistivity $\rho_{ab}(T)$ with $H = 0$ [solid (red) circles] and 90 kOe [open (blue) squares]. Inset (a): single-crystal XRD pattern of $K_xFe_{2-y}S_2$ obtained using Rigaku Miniflex. The crystal surface is normal to the c axis with the plate-shaped surface parallel to the ab plane. Inset (b): fitting result using thermally activated model for $\rho_{ab}(T)$ in zero field.

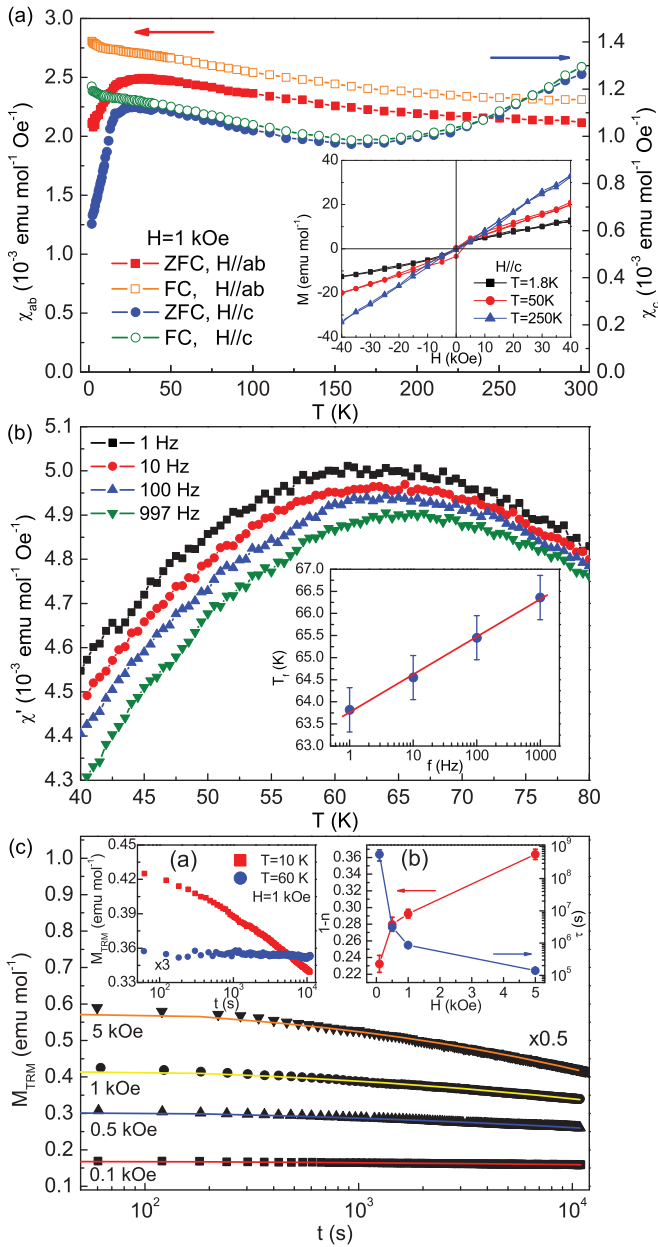


FIG. 3. (Color online) (a) ZFC and FC dc magnetic susceptibility with $H\parallel c$ and $H\parallel ab$ below 300 K. Inset: isothermal $M(H)$ for $H\parallel c$ at $T = 1.8, 50,$ and 250 K. (b) Temperature dependence of $\chi'(T)$ measured at several fixed frequencies. Inset: frequency dependence of T_f . The solid line is the linear fit to the T_f data. (c) M_{TRM} vs t at 10 K with various dc fields and $t_w = 100$ s. The solid lines are fits using a stretched exponential function. Inset (a): M_{TRM} vs t at 10 and 60 K with $H = 1$ kOe and $t_w = 100$ s. Inset (b): magnetic field dependence of $1 - n$ and τ .

$K\text{FeCuS}_2$.^{14,20} The inset in Fig. 3(a) shows the magnetization loops for $H\parallel c$. At 250 K, the M - H loop is almost linear and there is no hysteresis. However, an S-shaped M - H loop can be observed at 1.8 K, which is typical behavior of a SG system.¹⁴ The S-shaped M - H loop is present at $T = 50$ K, which indicates that short-range ferromagnetic interaction may exist above T_f . As shown in Fig. 3(b), the peak in the real part of ac susceptibility $\chi'(T)$ exhibits

strong frequency dependence in an ac magnetic field. When the frequency increases, the peak positions shift to higher temperatures whereas the magnitudes decrease, indicating typical SG behavior.²¹ By fitting the frequency dependence of the peak shift using $K = \Delta T_f / (T_f \Delta \log f)$, we obtained $K = 0.0134(5)$ [inset of Fig. 3(b)]. This is in agreement with values ($0.0045 \leq K \leq 0.08$) found in the canonical SG system, but much smaller than in a typical superparamagnet.²¹ Figure 3(c) shows the magnetic field dependence of the thermoremanent magnetization (TRM). The sample was cooled from $T = 60$ K (above T_f) in a magnetic field to $T = 10$ K (below T_f) and then kept at 10 K for $t_w = 100$ s. Then the magnetic field was removed and the magnetization decay $M_{TRM}(t)$ was measured. It can be seen that, below T_f ($T = 10$ K), $M_{TRM}(t)$ decays slowly so its value is nonzero even after several hours. This is another signature of the SG behavior, i.e., the existence of extremely slow spin relaxation below T_f .²¹ In contrast, above T_f , $M_{TRM}(t)$ quickly relaxes and does not show slow decay [inset (a) of Fig. 3(c)]. The magnetization decay can be explained well using a stretched exponential function commonly used to explain TRM behavior in SG systems, $M_{TRM}(t) = M_0 \exp[-(t/\tau)^{1-n}]$, where M_0 , τ , and $1 - n$ are the glassy component, the relaxation characteristic time, and the critical exponent, respectively. It can be seen [inset (b) of Fig. 3(c)] that τ decreases significantly with field but $1 - n$ increases slightly. On the other hand, the value of $1 - n$ is close to $1/3$, consistent with theoretical predictions and the experiments on traditional SG systems.^{22,23} The SG behavior could originate from Fe clusters induced by vacancies and disorder, and the exchange interactions between spins within a cluster would depend on the distribution of iron ions (Table I).²⁰ Indeed, in $\text{TlFe}_{2-x}\text{Se}_2$, the ground state is a reentrant spin glass if the content of Fe is less than 1.7.¹⁴ However, for x values larger than 1.7, $\text{TlFe}_{2-x}\text{Se}_2$ becomes a superconductor below 20 K.¹³ Therefore, superconductivity in $K_x\text{Fe}_{2-y}\text{S}_2$ might be induced for a smaller deficiency of Fe.

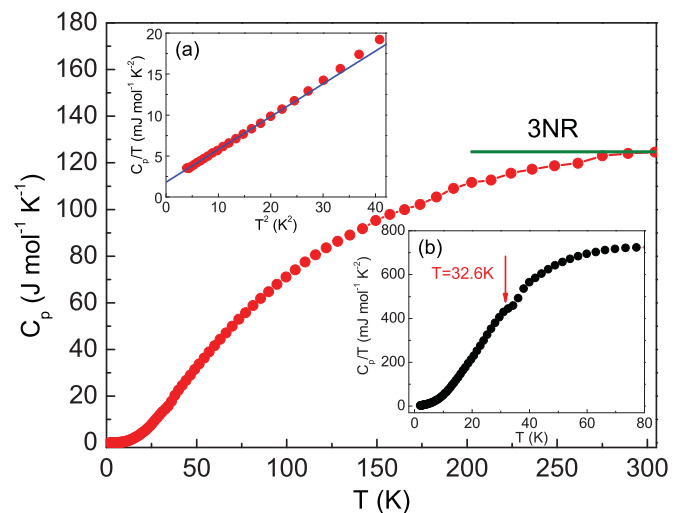


FIG. 4. (Color online) Temperature dependence of specific heat. Inset (a): low-temperature specific-heat data in the plot of C_p/T vs T^2 . The solid (blue) line is the fitting curve using the formula $C_p/T = \gamma_{SG} + \beta T^2$. Inset (b): enlarged area near the magnetic transition region of $C_p/T - T$.

The specific heat of $K_xFe_{2-y}S_2$ (Fig. 4) approaches the Dulong-Petit value of $3NR$ at high temperature, where N is the atomic number in the chemical formula ($N = 5$) and R is the gas constant. At low temperature, the specific heat can be fitted using $C_p = \gamma_{SG}T + \beta T^3$ [inset (a) of Fig. 4]. The variable γ_{SG} is commonly found in magnetic insulating SG systems, implying a constant density of states of the low-temperature magnetic excitations.^{24–26} The second term is due to phonon contribution. The obtained γ_{SG} is $1.58(6)$ mJ mol⁻¹ K⁻². The Debye temperatures Θ_D can be calculated from β through $\Theta_D = (12\pi^4NR/5\beta)^{1/3}$ to be $\Theta_D = 284.3(7)$ K. It should be noted that, as opposed to the usual λ anomaly, there is a very weak broad hump of C_p/T near $T = 32.6$ K [inset (b) of Fig. 4]. This is expected for bulk low-dimensional or glassy magnetic systems.^{24,27,28}

The discovery of $K_xFe_{2-y}S_2$ implies that it is possible to tune conductivity and magnetism by changing chalcogen elements (S and Se) in isostructural $K_xFe_{2-y}Ch_2$ materials. According to Table I, anion heights S1 to Fe1 and S1 to Fe2 in $K_{0.88(6)}Fe_{1.63(4)}S_{2.00(1)}$ are close to the alleged optimal value of 1.38 Å, comparable to distances in FePn-1111-type materials and lower than in $K_xFe_{2-y}Se_2$.^{8,12} Hence, if the anion height is the crucial parameter, the sulfide compound should be a

superconductor with higher T_c than that of $K_xFe_{2-y}Se_2$. However, it is a semiconductor, not a superconductor. We also note that in $K_xFe_{2-y}S_2$ there are two Fe sites and two corresponding anion heights. Our results indicate that the anion height values may be not essential parameters that govern superconductivity in AFeSe-122 compounds. In contrast, it suggests that disorder and site occupancies are significantly important.

In summary, we report the discovery of $K_xFe_{2-y}S_2$ single crystals isostructural to $T_c = 33$ K superconductor $K_xFe_{2-y}Se_2$ and exhibiting a similar width of formation and vacancies at both potassium and iron sites. Sulfide material is semiconducting and glassy magnetic, suggesting that the physical properties are governed by stoichiometry, defects, and local environment of Fe-S tetrahedra.

We thank S. L. Bud'ko for discussions, John Warren for help with scanning electron microscopy measurements, and John Hanson for help in facilitating the X7B experiment. The work at Brookhaven is supported by the US Department of Energy (DOE) under Contract No. DE-AC02-98CH10886 and in part by the Center for Emergent Superconductivity, an Energy Frontier Research Center funded by the DOE Office for Basic Energy Science.

- ¹Y. Kamihara, T. Watanabe, M. Hirano, and H. Hosono, *J. Am. Chem. Soc.* **130**, 3296 (2008).
- ²M. Rotter, M. Tegel, and D. Johrendt, *Phys. Rev. Lett.* **101**, 107006 (2008).
- ³X. C. Wang, Q. Q. Liu, Y. X. Lv, W. B. Gao, L. X. Yang, R. C. Yu, F. Y. Li, and C. Q. Jin, *Solid State Commun.* **148**, 538 (2008).
- ⁴F. C. Hsu, J. Y. Luo, K. W. Yeh, T. K. Chen, T. W. Huang, P. M. Wu, Y. C. Lee, Y. L. Huang, Y. Y. Chu, D. C. Yan, and M. K. Wu, *Proc. Natl. Acad. Sci. USA* **105**, 14262 (2008).
- ⁵A. Subedi, L. Zhang, D. J. Singh, and M. H. Du, *Phys. Rev. B* **78**, 134514 (2008).
- ⁶Y. Mizuguchi, F. Tomioka, S. Tsuda, T. Yamaguchi, and Y. Takano, *Appl. Phys. Lett.* **93**, 152505 (2008).
- ⁷S. Medvedev, T. M. McQueen, I. Trojan, T. Palasyuk, M. I. Erements, R. J. Cava, S. Naghavi, F. Casper, V. Ksenofontov, G. Wortmann, and C. Felser, *Nat. Mater.* **8**, 630 (2009).
- ⁸Y. Mizuguchi, Y. Hara, K. Deguchi, S. Tsuda, T. Yamaguchi, K. Takeda, H. Kotegawa, H. Tou, and Y. Takano, *Supercond. Sci. Technol.* **23**, 054013 (2010).
- ⁹A. Bill, H. Morawitz, and V. Z. Kresin, *Phys. Rev. B* **68**, 144519 (2003).
- ¹⁰J. Guo, S. Jin, G. Wang, S. Wang, K. Zhu, T. Zhou, M. He, and X. Chen, *Phys. Rev. B* **82**, 180520(R) (2010).
- ¹¹A. F. Wang, J. J. Ying, Y. J. Yan, R. H. Liu, X. G. Luo, Z. Y. Li, X. F. Wang, M. Zhang, G. J. Ye, P. Cheng, Z. J. Xiang, and X. H. Chen, *Phys. Rev. B* **83**, 060512(R) (2011).
- ¹²A. Krzton-Maziopa, Z. Shermadini, E. Pomjakushina, V. Pomjakushin, M. Bendele, A. Amato, R. Khasanov, H. Luetkens, and K. Conder, *J. Phys. Condens. Matter* **23**, 052203 (2011).
- ¹³M. H. Fang, H. D. Wang, C. H. Dong, Z. J. Li, C. M. Feng, J. Chen, and H. Q. Yuan, *Europhys. Lett.* **94**, 27009 (2011).
- ¹⁴J. J. Ying, A. F. Wang, Z. J. Xiang, X. G. Luo, R. H. Liu, X. F. Wang, Y. J. Yan, M. Zhang, G. J. Ye, P. Cheng, and X. H. Chen, e-print [arXiv:1012.2929](https://arxiv.org/abs/1012.2929).
- ¹⁵K. Kihou, T. Saito, S. Ishida, M. Nakajima, Y. Tomioka, H. Fukazawa, Y. Kohori, T. Ito, S. Uchida, A. Iyo, C. Lee, and H. Eisaki, *J. Phys. Soc. Jpn.* **79**, 124713 (2010).
- ¹⁶A. C. Larson and R. B. Von Dreele, Los Alamos National Laboratory Report No. LAUR 86-748, 1994.
- ¹⁷B. H. Toby, *J. Appl. Crystallogr.* **34**, 210 (2001).
- ¹⁸W. Bao, Q. Huang, G. F. Chen, M. A. Green, D. M. Wang, J. B. He, X. Q. Wang, and Y. Qiu, e-print [arXiv:1102.0830](https://arxiv.org/abs/1102.0830).
- ¹⁹D. M. Wang, J. B. He, T.-L. Xia, and G. F. Chen, *Phys. Rev. B* **83**, 132502 (2011).
- ²⁰M. Oledzka, K. V. Ramanujachary, and M. Greenblatt, *Mater. Res. Bull.* **31**, 1491 (1996).
- ²¹J. A. Mydosh, *Spin Glasses: An Experimental Introduction* (Taylor & Francis, London, 1993).
- ²²I. A. Campbell, *Phys. Rev. B* **37**, 9800 (1988).
- ²³D. Chu, G. G. Kenning, and R. Orbach, *Phys. Rev. Lett.* **72**, 3270 (1994).
- ²⁴C. Y. Huang, *J. Magn. Magn. Mater.* **51**, 1 (1985).
- ²⁵D. Meschede, F. Steglich, W. Felsch, H. Maletta, and W. Zinn, *Phys. Rev. Lett.* **44**, 102 (1980).
- ²⁶N. P. Raju, E. Gmelin, and R. K. Kremer, *Phys. Rev. B* **46**, 5405 (1992).
- ²⁷G. E. Brodale, R. A. Fisher, W. E. Fogle, N. E. Phillips, and J. van Curen, *J. Magn. Magn. Mater.* **31–34**, 1331 (1983).
- ²⁸L. O.-S. Martin, J. P. Chapman, L. Lezama, J. J. S. Garitaonandia, J. S. Marcos, J. Rodríguez-Fernández, M. I. Arriortua, and T. Rojo, *J. Mater. Chem.* **16**, 66 (2006).



Synthesis, crystal structure, and magnetism of β -Fe_{1.00(2)}Se_{1.00(3)} single crystals

Rongwei Hu (胡荣伟),^{1,*} Hechang Lei (雷和畅),¹ Milinda Abeykoon,¹ Emil S. Bozin,¹ Simon J. L. Billinge,^{1,2} J. B. Warren,³ Theo Siegrist,⁴ and C. Petrovic^{1,†}

¹Condensed Matter Physics and Materials Science Department, Brookhaven National Laboratory, Upton, New York 11973, USA

²Department of Applied Physics and Applied Mathematics, Columbia University, New York, New York 10027, USA

³Instrumentation Division, Brookhaven National Laboratory, Upton, New York 1197, USA

⁴Department of Chemical and Biochemical Engineering and National High Magnetic Field Laboratory, Florida State University, Tallahassee, Florida 32310, USA

(Received 13 May 2011; published 20 June 2011; publisher error corrected 8 July 2011)

Understanding iron-based superconductors requires high-quality impurity-free single crystals. So far they have been elusive for β -FeSe and extraction of intrinsic materials properties has been compromised by several magnetic-impurity phases. Here, we report synchrotron-clean β -FeSe superconducting single crystals grown via LiCl/CsCl flux method. Phase purity yields evidence for a defect-induced weak ferromagnetism that coexists with superconductivity below T_c . In contrast to Fe_{1+y}Te-based superconductors, our results reveal that the interstitial Fe(2) site is not occupied and that all contribution to density of states at the Fermi level must come from in-plane Fe(1).

DOI: [10.1103/PhysRevB.83.224502](https://doi.org/10.1103/PhysRevB.83.224502)

PACS number(s): 74.70.Xa, 74.62.Bf, 74.25.Ha, 74.62.Dh

I. INTRODUCTION

The physics of complex superconductors, such as the cuprates and iron-based superconductors, cannot be understood unless pure, high-quality materials are available that allow the intrinsic properties to be separated from extrinsic and impurity effects. In FeAs and Fe(Se)Te, just as in high- T_c cuprate and heavy-fermion materials, competing or coexisting magnetic order is closely associated with superconductivity.¹ This suggests proximity to a magnetic critical point and an unconventional origin of superconductivity where spin fluctuations may contribute to pairing.²⁻⁴ The observation of weakly localized rather than itinerant magnetism sensitive to structural changes raises the fundamental question of how strongly correlated are the charges in Fe superconductors and what is the origin of the magnetic order.⁵⁻⁷ Of particular interest is superconducting β -FeSe, a compensated semimetal without a crystallographic charge reservoir that superconducts at about 8 K without any carrier doping.⁸ It has a giant pressure coefficient of T_c of 9.1 K/GPa, enhancing T_c up to a maximum of 37 K, the third highest known critical temperature for any binary compound.⁹

A major obstacle in understanding intrinsic magnetism in β -FeSe has been the purity of the material itself. Magnetic impurities such as α -FeSe, Fe₇Se₈, Fe₃O₄, and elemental Fe are ubiquitous in all as-grown crystals and sometimes polycrystals.¹⁰⁻¹³ They contribute to the large ferromagnetic (FM) background, seen in the M - H loops below superconducting T_c . Modification of the original Fe-Se phase diagram near 1 : 1 stoichiometry suggested that β -FeSe is not stable at room temperature since it converts to hexagonal α -FeSe below 300 °C.^{12,14} Consequently, the absence of an exposed liquidus surface in the binary alloy phase diagram and the metastable nature of the superconducting FeSe are considered to be prohibitive and insurmountable factors for single-crystal preparation using standard synthesis methods.

Here, we describe a synthetic approach that yields stoichiometric and phase-pure materials and we report intrinsic structural and magnetic properties of superconducting β -FeSe.

These include evidence for defect-induced weak ferromagnetism (WFM) and the absence of interstitial Fe(2) whose occupancy governs the magnetic and structural phase diagram in isostructural Fe_{1+y}Te.⁷

II. EXPERIMENT

Powders of LiCl and CsCl, elemental Fe and Se were added together with the flux into an alumina crucible and sealed under partial Ar atmosphere. The ampoule was heated to a homogenization temperature of 715 °C, where it was kept for 1 h and then removed into a preheated furnace at 457 °C. After slow cooling to 300 °C, it was quenched in water.

Medium resolution, room temperature (300 K) x-ray diffraction measurements were carried out at X7B beamline at National Synchrotron Light Source (NSLS) at the Brookhaven National Laboratory, using a 0.5 mm² monochromatic beam of 38.92 keV ($\lambda = 0.3184$ Å). Pulverized sample was filled into a 1 mm diameter cylindrical Kapton capillary and the data collection was carried out in a forward-scattering geometry using a Perkin Elmer 2D detector mounted orthogonal to the beam path 378.3 mm away from the sample.

Single crystals of β -FeSe were also mounted on glass fibers for examination using an Oxford-Diffraction Xcalibur 2 charge-coupled device four-circle diffractometer with graphite-monochromated MoK α radiation. Elemental and microstructure analysis were performed on several β -FeSe crystals as well as on the particular crystals chosen for resistivity and magnetization using energy-dispersive x-ray spectroscopy in a JEOL JSM-6500 scanning-electron microscope (SEM).

Sample dimensions were measured with an optical microscope Nikon SMZ-800 with 10 μ m resolution and M/H values were corrected for straw background at each (T , H) of the measurement, real sample volume, and demagnetization factor. Thin Pt wires were attached to electrical contacts made of Epotek H20E silver epoxy for a standard four-probe measurement with current flowing in the (101) plane of the

tetragonal structure. Magnetization and resistivity measurements were carried out in a Quantum Design MPMS-5 and PPMS-9, respectively.

III. RESULTS

Figure 1 shows Fe-Se and LiCl-CsCl phase diagrams.^{14,15} The superconducting PbO-type β -FeSe is a low-temperature crystallographic phase that decomposes into Fe and hexagonal NiAs phase (α -FeSe) at 457 °C [Fig. 1(a)]. It coexists with hexagonal α -Fe₇Se₈ below 300 °C for certain Fe-Se stoichiometry.¹⁴ Previous attempts (for example, Refs. 10,11, and 16) to prepare single crystals of β -FeSe-involved nucleation and growth using KCl/NaCl flux or vapor transport reactions. We choose a LiCl-CsCl flux method of synthesis due to the presence of a low-temperature eutectic at 326 °C, well below the decomposition temperature of β -FeSe.¹⁵ The crystal growth possibly includes nucleation of Fe₇Se₈ above 700 °C and structural phase transition at low temperatures. As opposed to crystals grown in KCl,¹⁶ the low-temperature eutectic [Fig. 1(b)] allows for complete transition to tetragonal β -FeSe from 457–300 °C in a large fraction of crystals grown in a batch. Platelike FeSe crystals with the (101) plane exposed and elongated in one direction up to 1.5 × 0.5 × 0.05 mm³

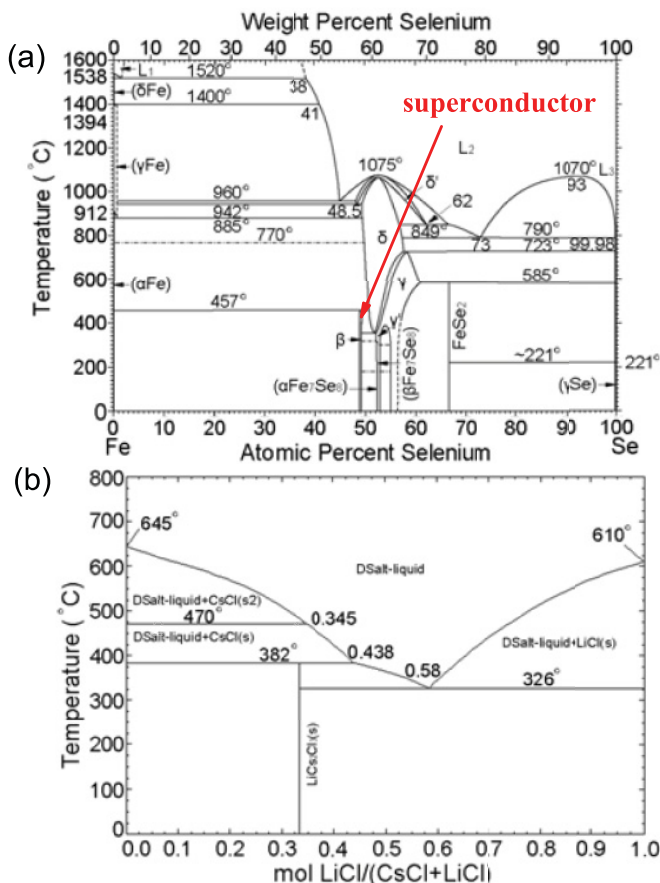


FIG. 1. (Color online) Fe-Se (a) and CsCl-LiCl phase diagrams (b). The presence of the low-temperature eutectics (b) enables long annealing in the liquid below 457 °C and complete transition from α -FeSe to β -FeSe in the large fraction of the crystals in a batch.

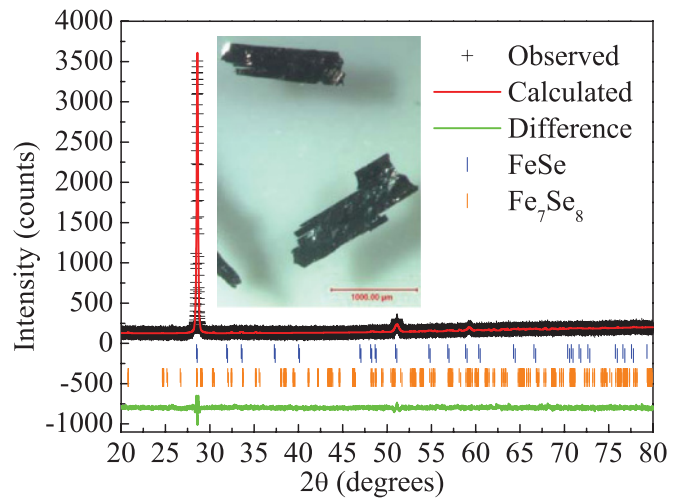


FIG. 2. (Color online) Powder x-ray diffraction spectra on a β -FeSe single crystal shows no impurity phases and (h0l) crystal orientation at 300 K. The data were shown by (+), the fit is given by the top solid line and the difference curve (bottom solid line) is offset for clarity. Allowed crystallographic reflections are given as vertical tick marks for β -FeSe (top line) and Fe₇Se₈ (bottom line). Bragg peak (201) for $2\theta = 51.1$ clearly distinguishes β -FeSe from Fe₇Se₈, in addition to magnetic properties. Inset shows typical β -FeSe single crystals.

can be separated by dissolving the flux in deionized water and rinsing in ethanol.

Crystals of β -FeSe were separated from α -Fe₇Se₈ by a combination of a permanent-magnet and a powder x-ray diffraction (XRD) spectra from a Rigaku Miniflex with CuK α radiation ($\lambda = 1.5418$ Å). We observed only (h0l) peaks (see Fig. 2) of the tetragonal phase in selected crystals for further analysis (see Fig. 2 inset). Crystals contaminated with Fe₇Se₈ and/or oxides showed additional peaks in the spectra.

Figures 3 and 4 show electron-density maps and elemental analysis of as-grown β -FeSe single crystals. The relative stoichiometry of multiple points on the as-grown crystals was measured and a composition of Fe_{0.99(4)}Se was obtained. Electron-density maps of these crystals confirmed a uniform distribution of Fe and Se

Crystals are moderately air sensitive. After one week of air exposure, a selenium oxide layer is visible on the crystal surface. After about a month of air exposure Fe₃O₄ is detectable in laboratory x-ray diffraction (XRD) and by the observation of a Verwey transition in $M(T)$.¹⁷ The first attempts to carry out synchrotron XRD experiments on samples that were exposed

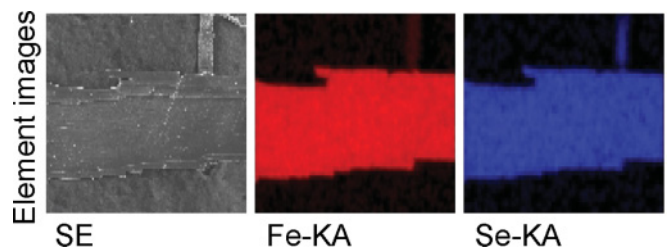


FIG. 3. (Color online) Microprobe electron density maps of as-grown β -FeSe single crystals.

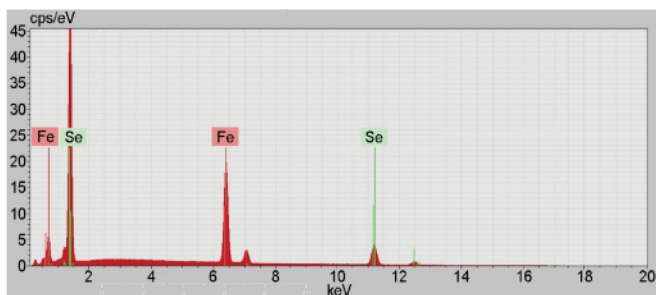


FIG. 4. (Color online) Elemental analysis of as-grown β -FeSe single crystals.

to air for several months revealed the presence of multiple additional phases including appreciable amounts of several selenium-oxide and iron-oxide phases. It has been found that while pure stoichiometric FeSe crystals can be grown, these tend to degrade through oxidation over the course of time. This suggests that the surface of FeSe crystals may be Se-terminated and that selenium oxide forms first, with further degradation involving iron-oxide phases or $\text{Fe}_2[\text{SeO}_3]_2\text{O}$ as well. Results reported here are based on samples whose exposure to air was minimized, and only traces of selenium oxide were found in crystals that were pulverized for the powder XRD experiments.

Synchrotron powder XRD data of FeSe sample were successfully refined using a two-phase structural model (see Fig. 5). The best fit contained 96.1 mol% (90.7 wt%) of FeSe of $P4/nmm$ space group, with $a = 3.7622(2)$ Å and $c = 5.5018(5)$ Å, with Se at $[1/4, 1/4, 0.2624(1)]$ and Fe at $(3/4, 1/4, 0)$. Compared to the high- T_c stoichiometric polycrystalline β -FeSe,^{12,18} the unit-cell parameters are reduced by 0.3% (a axis) or 0.4% (c axis), whereas c/a is smaller or identical. The anisotropic atomic-displacement-parameters

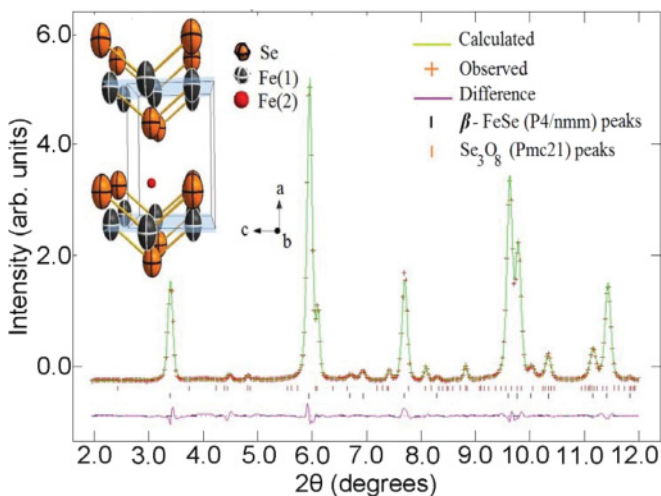


FIG. 5. (Color online) Structural refinement of FeSe synchrotron powder x-ray diffraction data over a narrow range of scattering angle, 2θ , taken at 300 K. Background-subtracted data are shown as (+), fit is given as a top solid line, and the difference curve (bottom solid line) is offset for clarity. Allowed crystallographic reflections are given as vertical tick marks: β -FeSe phase (bottom) and Se_3O_8 impurity phase (top) due to sample oxidation. Inset shows β -FeSe structure.

(ADP) ratio U_{33}/U_{11} is the ratio of thermal vibrations along crystallographic c and a axes in tetragonal structure. The U_{33}/U_{11} was 1.12 for Se and 1.41 for Fe. To illustrate this, anisotropic ADP's are shown as exaggerated thermal ellipsoids in Fig. 5 inset. In Van der Waals bonded crystals, such as FeSe, U_{33}/U_{11} ADP ratio is expected to be larger than 1 and the observed ratios are within the expected range. A somewhat larger ADP ratio of Fe, 1.41, suggests that it is underbonded and can move along the c axis. The FeSe_4 units are found to deviate from perfect tetrahedra, with an Fe-Se distance of $2.379(5)$ Å, and tetrahedral angles of $104.5(5)$ and $112.0(5)$ degrees. The anisotropic ADP ratio (tetrahedral angles) is smaller (equal) than the values obtained for β -FeSe polycrystals on powders containing several magnetic-impurity phases.^{12,19,20} However, the anisotropic ADP ratio observed here is similar to values found in pure $\text{Fe}_{1.08}\text{Te}$.²¹ As expected, the observed tetrahedral-bond angles deviate from the ideal tetrahedral angle found in iron-based superconductors with optimal T_c .²² The second phase, constituting 3.9 mol% (9.3 wt%), was found to be Se_3O_8 with $Pmc21$ space group with the refined lattice parameters $a = 4.977(1)$ Å, $b = 4.388(2)$ Å, and $c = 15.377(2)$ Å. No other phases were observed. Within the main phase, we investigated in detail the issue of stoichiometry and occupancy of the interstitial site, Fe(2) at $(3/4, 3/4, z)$ (see Fig. 5 inset). The stoichiometry was found to be $\text{Fe}_{1.00(2)}\text{Se}_{1.00(3)}$.

Difference Fourier analysis (DFA) is a standard method to find missing electron densities in refined atomic structures. In this technique, the difference between the observed and the calculated (model-based) Fourier maps is used to locate missing atoms in atomic structures. In this study, DFA did not reveal any appreciable electron density at the interstitial Fe(2) positions. Attempts to explicitly refine Fe(2)-site occupancy yielded 0.00(1), in agreement with the DFA and strongly suggesting that no iron resides on this site. However, DFA indicated a possibility for additional electron density in the vicinity of Se. This, along with the observation of relatively large anisotropic ADPs (U_{33}) of Se and Fe, may point to the presence of static and/or dynamic disorder associated with these sites. A small number of Se vacancies may lead to relaxation of the surrounding Fe atoms, resulting in static and/or dynamic disorder.

The resistivity $\rho(T)$ of LiCl/CsCl-flux-grown crystals smoothly changes to linear at low temperature where the onset of T_c and zero resistivity were observed at temperatures of about 1 K, or more, higher than in polycrystals (see Fig. 6).⁸ The residual-resistivity ratio (RRR) of 14 indicates good crystal quality whereas the single-crystal-diffraction pattern shows no impurities present. Reciprocal space planes ($hk0$) and ($h0l$) were reconstructed from several series of CCD frames (see inset in Fig. 6). A mosaic structure is observed perpendicular to the c axis, consistent with the arrangement of FeSe layers in the structure. The observed x-ray reflections are all consistent with the β -FeSe structure. M/H exhibits weak temperature dependence for both $H \perp (101)$ and $H \parallel (101)$ [see Fig. 7(a)]. Below 135 K, the M/H signal drops and then remains constant below the structural transition temperature ~ 100 K.⁸ This is more pronounced for $H \perp (101)$. Low-temperature M/H taken in $H = 10$ Oe confirms superconductivity [Fig. 7(b)] below 9.0(2) K. Extrapolation

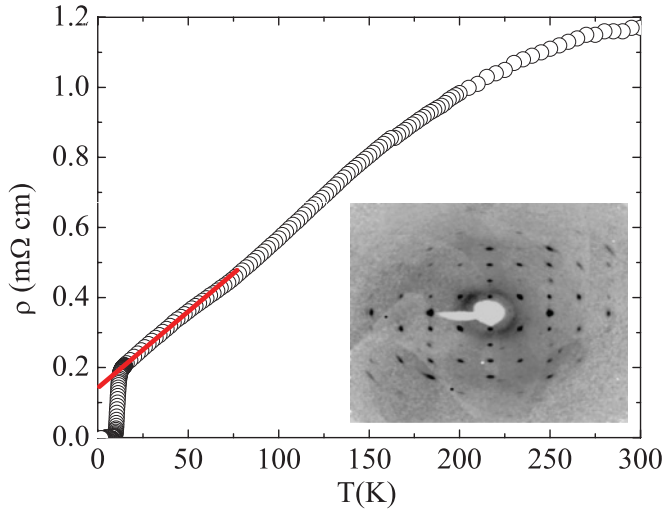


FIG. 6. (Color online) Temperature dependence of the resistivity for current in (101) plane with T_c onset and zero resistance of 12.0(1) and 9.2 (2) K, respectively. Inset shows precession pattern of the (101) plane of the same single crystal. All spots can be indexed within β -FeSe space group with no impurities present. The large mosaic is visible but the impurity-free unit-cell parameters are in agreement with the published (see text).

of $4\pi\chi$ data to $T = 0$ gives about 60% of diamagnetic screening. Complete ρ transition and partial superconducting volume fraction have been observed in $\text{SmFeAsO}_{1-x}\text{F}_x$ and $\text{CaFe}_{1-x}\text{Co}_x\text{AsF}$,^{4,23} where temperature-dependent magnetic moment coexists and inversely scales with the superconducting volume fraction.

In β -Fe_{1.01}Se polycrystals contaminated with magnetic impurity phases, a static moment was found above 1 GPa,²⁴ was ascribed to traces of Fe impurity at ambient pressure due to its weak nature,^{25,26} or was not detected.^{9,27} In our crystals, the *s* shape of $M(H)$ for $H \parallel (101)$ [see Fig. 8(a)] is typical of a type-II superconductor with a superimposed isotropic weak ferromagnetic (WFM) moment both above and below T_c .¹¹ In

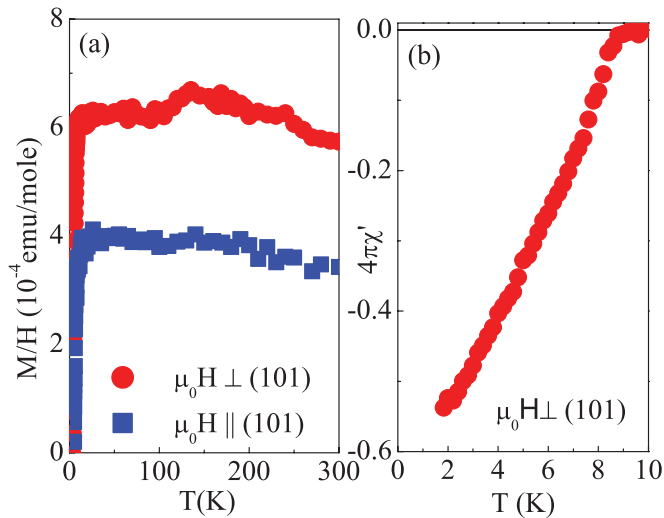


FIG. 7. (Color online) Anisotropy in high-temperature M/H for $H = 10$ kOe and superconducting volume fraction for $H \perp (101)$ measured in 10 Oe field.

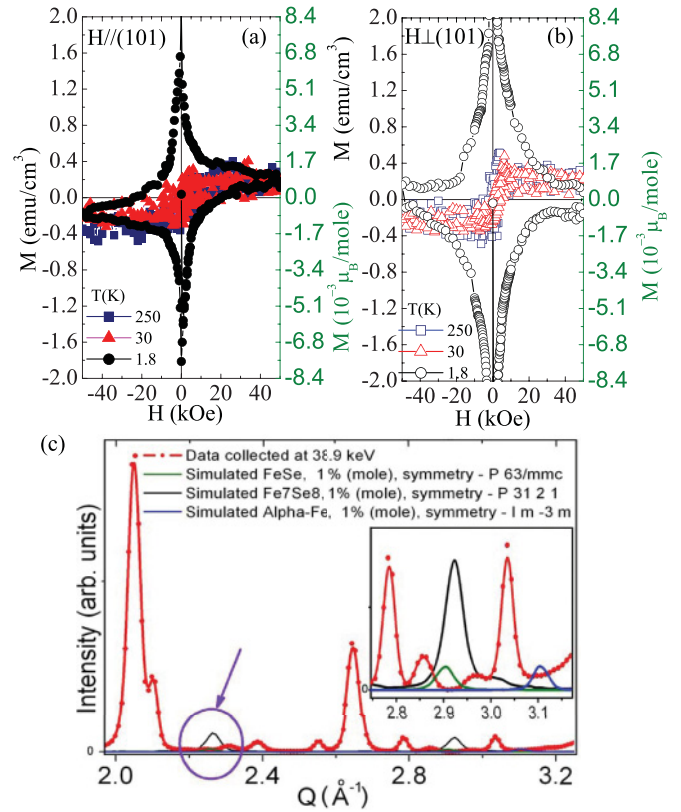


FIG. 8. (Color online) Magnetization isotherms below and above T_c for magnetic field parallel [$H \parallel (101)$] (a) and perpendicular to (101) plane [$H \perp (101)$] (b). Right-hand side scale shows magnetic moment assuming molar mass of β -FeSe (c) Comparison of background-subtracted diffraction data with simulated impurity phases at 300 K. Selected 2θ region is shown where simulated impurity peaks are clearly visible.

contrast, the $M(H)$ curves are symmetric for $H \perp (101)$ at $T = 1.8$ K [see Fig. 8(b)] within the experimental resolution (0.05 emu/cm^3) with no evidence for WFM below T_c .

IV. DISCUSSION

Is the observed WFM intrinsic or extrinsic? Figure 8(c) shows background-subtracted data compared to a simulated pattern for 1 mol% of commonly found magnetic phases. Based on the scattering power and distribution of peaks in our synchrotron powder XRD we can exclude contamination by α -FeSe and Fe_7Se_8 [see Fig. 8(c) and Appendix A], leaving only elemental Fe, or some unknown ferromagnetic phase with lattice periodicity commensurate with β -FeSe,²⁸ as a possible source of magnetic contamination. By focusing on information sensitive to the total number of Fe ions in a given volume we make several observations that support the intrinsic WFM scenario in as-grown crystals. Mössbauer quadrupole splittings and isomer shifts for binary Fe-Se materials differ by up to a factor of four whereas the signal component originating in the β -FeSe phase dominates the Mössbauer spectrum below room temperature in 50 kOe even for the sample containing more than 6 mol% of α -FeSe, Fe_3O_4 , and elemental Fe impurities.^{12,29,30} Moreover, the coercive field of bulk Fe or Fe nanoparticles [$\mu_0 H_c \leq (0.4\text{--}2.5) \text{ kOe}$] is several orders of

magnitude lower than in Figs. 8(a) and 8(b) (15 kOe).^{31,32} Furthermore, we observe the signature of the structural phase transition in the normal state [Fig. 7(a)], implying that a considerable fraction of the $M(T)$ signal must come from the β -FeSe. Finally, WFM due to an unknown Fe-based high- T_c ferromagnetic phase²⁸ is unlikely to have $\mu_0 H_c$ in the kOe range and is expected to provide an isotropic constant (or increasing) background (bias) to $M(H)$ loops both above and below T_c , as in Ref. 11. This is in contrast to anisotropic $M(H)$ below T_c [see Figs. 8(a) and 8(b)]. Note that $M(H)$ in Fig. 8(b) is symmetric with respect to the $M = 0$ line. This suggests that most of WFM signal in β -FeSe crystals is unrelated to extrinsic impurities. The WFM signal is well reproduced in several crystals grown in one batch and in crystals grown from multiple batches, whereas the magnitude of WFM increases in time (see Appendix B).

The proposed spin-density-wave (SDW) mechanism of magnetic order may not apply to iron chalcogenides and perhaps it could be more complex even for iron pnictides.^{33,34} Density-functional calculations indicate that a magnetic state with $0.15 \mu_B/\text{mol}$ is induced in Fe_{1-x}Se for $x = 0.0625$.³⁵ The saturation moment $|M_s|$ observed [see Figs. 8(a) and 8(b)] is about 1/150 smaller and would correspond to an Fe deficiency of less than 0.4 atomic%, a value below the resolution limit of our diffraction measurement. However, in this calculation,³⁵ the partial density of states (PDOS) of Fe(2) dominates the total density of states (DOS) and, more importantly, the stoichiometry variation. Negligible occupancy of Fe(2) within experimental error in our crystals implies that Fe nonstoichiometry is not the dominant mechanism of WFM. On the other hand, it is possible that some fraction of the WFM arises due to a Se-vacancy-induced magnetic cluster.³⁶ The Se-Se distances are Van der Waals distances and may produce Se-Se time-dependent bonding. We cannot distinguish between static and dynamic displacements but since the refinement results are giving 1 : 1 stoichiometry, vacancies could be equally distributed on both sites. In particular, theory predicts that the main effect of Se displacement would be to shift Fe(1) toward the vacant site, shifting the Fermi level E_F into a sharp peak in the DOS that would promote a more stable magnetic state than in a material without Se defects.³⁶ The net moment at 1.25 mol% Se deficiency is expected to be in the $10^{-2} \mu_B/\text{mol}$ range. This is arising from both Fe(1) and Fe(2) contributions. Since the theoretical contribution of Fe(2) PDOS at the Fermi level is about 50% of the total DOS,³⁶ the calculated moment is somewhat higher but generally in line with the observed $|M_s| \sim (1.0 \pm 0.5) \times 10^{-3} \mu_B/\text{mol}$ above T_c in our crystals with negligible Fe(2) occupancy. This is different from most FeAs superconductors where small-moment magnetic order from a SDW mechanism is found below the structural transition. This is also different from Fe_{1+y}Te where subtle crystal chemical effects, with both Fe(1) and Fe(2) occupied, induce WFM and structural and magnetic differences below the magnetostructural transition at 75–55 K.⁷ Since lattice distortions were also recently found³⁷ to induce both superconducting and magnetic phases in SrFe_2As_2 , this suggests that nanoscale defects and short-range structural features are important in a wider class of iron-based superconductors. Indeed, there is emerging evidence that both conducting and magnetic properties in the recently

discovered $\text{K}_x\text{Fe}_{2-y}\text{Se}_2$ superconductors are governed by Fe vacancies.^{38,39} In β -FeSe, defect-induced magnetism coexists with superconductivity that sets in far below T_c . Though rather unlikely, our analysis allows for some contribution of different impurity phase to WFM. The unknown high-temperature FM phase would be present in quantities too small to detect by diffraction and/or would have the lattice periodicity commensurate with β -FeSe and its moment would anisotropically diminish between 30 and 1.8 K.

In summary, single-phase superconducting single crystals of β -FeSe have been synthesized. Unlike isostructural Fe_{1+y}Te , the Fe(2) site is not occupied at all in these samples. The ADP anisotropy is consistent with dynamic disorder/defects associated with Fe and Se sites and/or Se vacancies. We present evidence for intrinsic defect-induced WFM, which anisotropically diminishes with an increase in the superconducting volume fraction.

ACKNOWLEDGMENTS

We thank Sang-Wook Cheong and Hai-Hu Wen for useful discussions and J. C. Hanson for help with XRD measurements. This work was carried out at the Brookhaven National Laboratory, which is operated for the US Department of Energy by Brookhaven Science Associates DE-Ac02-98CH10886. This work was in part supported by the US Department of Energy, Office of Science, Office of Basic Energy Sciences as part of the Energy Frontier Research Center (EFRC), and Center for Emergent Superconductivity (CES). A portion of this work was performed at the National High Magnetic Field Laboratory, which is supported by NSF Cooperative Agreement No. DMR-0654118, by the state of Florida, and by the DOE.

APPENDIX A: MAGNETIC IMPURITIES FROM DIFFRACTION

Magnetization measurements were performed on a sample volume $V = 4.532 \times 10^{-5} \text{ cm}^3$ ($a = 0.223476 \text{ cm}$, $b = 0.0555613 \text{ cm}$, and $c = 0.00365025 \text{ cm}$), corresponding to $(1.45 \pm 0.23) \times 10^{-5} \text{ emu}$ MPMS signal. Assuming that the magnetization (M) of β -FeSe is negligible when compared to impurity magnetization, we discuss possible magnetic-impurity levels.

First we assume that the sample contains 1 mol% of elemental α -Fe since any higher Fe content would have been detected [see Fig. 8(c)]. In order to obtain volume ratio, we need to multiply mole (i.e., formula unit) ratios of Fe and β -FeSe by (M/D) , where M is the molar mass and D is the density in g/cm^3 . Using $M(\text{Fe}) = 55.8 \text{ g}/\text{mol}$, $D(\text{Fe}) = 7.83 \text{ g}/\text{cm}^3$, $M(\beta\text{-FeSe}) = 134.8 \text{ g}/\text{mol}$, and $D(\beta\text{-FeSe}) = 5.72 \text{ g}/\text{mol}$, we get 0.3 volume%:

$$\frac{1 \text{ mol}(\text{Fe}) \times 7.12 \frac{\text{cm}^3}{\text{mol}}}{100 \text{ mol}(\beta\text{-FeSe}) \times 23.56 \frac{\text{cm}^3}{\text{mol}}} = 0.003 \quad (\text{A1})$$

That would correspond to a $1.37 \times 10^{-7} \text{ cm}^3$ volume of Fe in our sample. What would be its magnetic contribution? By dividing D/M we get $0.14 \text{ mol}/\text{cm}^3$ of Fe. In $1.37 \times 10^{-7} \text{ cm}^3$ iron volume, we have $1.92 \times 10^{-8} \text{ mol}$ Fe. The iron

saturation moment is $2.2 \mu_B/\text{mol}$, therefore that volume would have $M = 4.22 \times 10^{-8} \mu_B$. Using a conversion factor of $5585 \text{ emu}/\mu_B$ we obtain $M = 2.36 \times 10^{-4} \text{ emu}$. This is more than 100% of raw M (emu) signal in MPMS. Hence, it is possible that the Fe-impurity content in our crystal (mol% and consequently volume%) is below the detection capacity of synchrotron powder x-ray diffraction data since only a fraction of 1 mol% Fe would generate such a signal. This is about 0.05 atomic% of Fe.

Similarly, 1 mol% impurity of α -FeSe is approximately identical to 1% volume since α -FeSe has the identical molar mass M and 95% of β -FeSe density. Therefore 1 mol% α -FeSe impurity would correspond to $4.5 \times 10^{-7} \text{ cm}^3$ volume [using Eq. (1)]. Applying the same argument as above, $4.5 \times 10^{-7} \text{ cm}^3$ volume α -FeSe contains $1.9 \times 10^{-8} \text{ mol}$ α -FeSe. The α -FeSe saturation moment is $M_s \sim 0.2 \mu_B/\text{mol}$.⁴⁰ Therefore, such volume would contribute $M = 3.81 \times 10^{-9} \mu_B$. Using a conversion factor of $5585 \text{ emu}/\mu_B$ we obtain $M = 2.13 \times 10^{-5} \text{ emu}$. Our raw MPMS signal is 70% of that value. However, 0.7 mol% of α -FeSe would have been detected if present [70% of its peak height, see Fig. 8(c) in the main text].

Finally, 1 mol% of Fe_7Se_8 impurity [using $M(\text{Fe}_7\text{Se}_8) = 1022.59 \text{ g/mol}$, $D(\text{Fe}_7\text{Se}_8) = 6.43 \text{ g/cm}^3$, and Eq. (1)] would correspond to 6.75% of measured sample volume, which is $3.059 \times 10^{-6} \text{ cm}^3$. Since the expected Fe_7Se_8 saturation moment is $M_s \sim 80 \text{ (emu/cm}^3\text{)}$ ⁴¹ we would expect that such volume would contribute with $2.44 \times 10^{-4} \mu_B$. Our raw MPMS emu signal is 6% of that value, but still above the threshold of scattering-power detection in synchrotron experiments. If we multiply the observed intensity of 2.92 \AA^{-1} Fe_7Se_8 peak [see Fig. 8(c) in the main text] by 0.06, it is still above the background.

APPENDIX B: REPRODUCIBILITY, IMPURITIES, AND MAGNETIC SIGNAL OVER TIME

Figure 9 shows Rietveld refinement over the full 2θ range with only selenium oxide present due to oxidation.

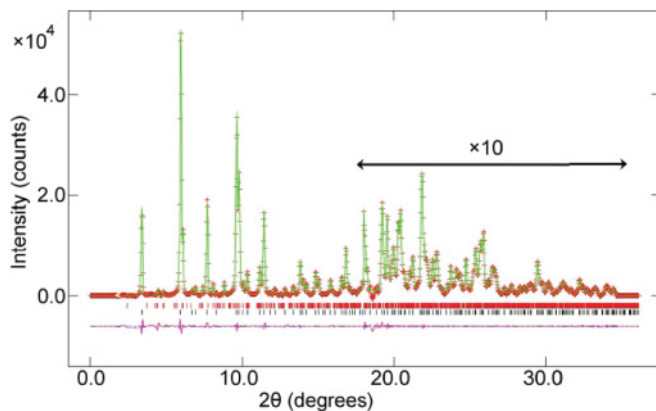


FIG. 9. (Color online) Structural refinement of FeSe synchrotron powder x-ray diffraction data over the full 2θ range taken at 300 K. Data (background subtracted) are shown as (+), fit is given as a top solid line, and the difference curve (bottom solid line) is offset for clarity. Bottom vertical tick marks represent reflections in the main β -FeSe phase ($P4/nmm$), while top tick marks denote reflections in Se_3O_8 ($Pmc21$).

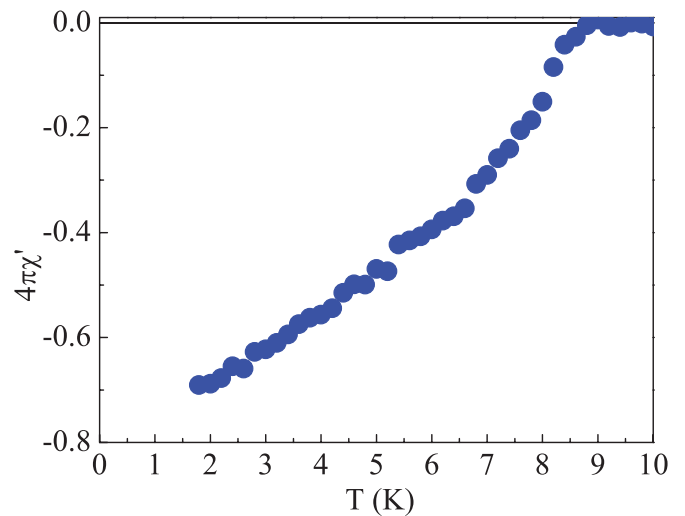


FIG. 10. (Color online) An example of superconducting T_c of independently grown crystal taken in 10 Oe field.

Powder x-ray diffraction taken on single crystals found no extrinsic peaks in ten out of ten crystals that were separated by a magnet. Only clean β -FeSe single crystals are used in further analysis. Samples that were contaminated by Fe_7Se_8 (from synthesis or oxidation) showed dominant FM hysteresis loop below T_c with only traces of type-II superconductor in M versus H . Resistivity and magnetization data were well reproduced in several independently grown crystals from multiple batches. Both bulk T_c , as measured by $4\pi\chi$ and resistive T_c (as defined in the text) varied by $\Delta T_c = \pm 1$ K. This variation is probably due to sample degradation induced by variable air exposure. However, the onset of resistive T_c was always above the bulk. Figure 10 shows an example of superconducting T_c and volume fraction for different, independently grown, samples. Figures 11(a) and 11(b) show hysteresis curves below T_c for an independently grown crystal from the same batch (sample 2) as the crystal used in the main text (sample 1). Unlike sample 1 (that was measured within a day from the moment of its synthesis),

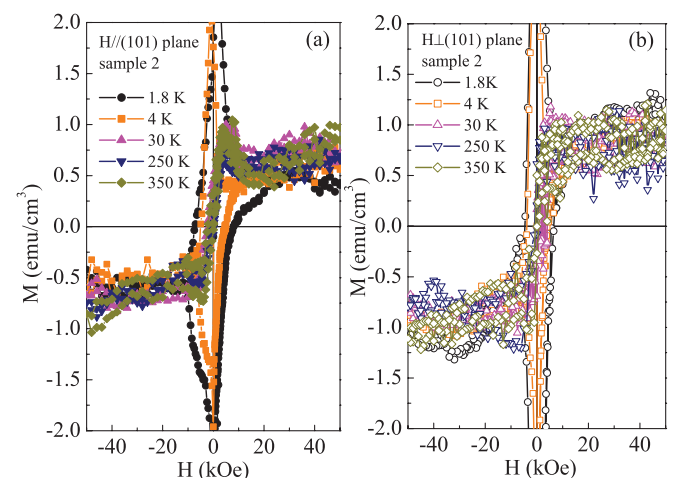


FIG. 11. (Color online) (a) Sample 2 M/H above and below T_c for $H \parallel (101)$ near $M = 0$. (b) Sample 2 M/H above and below T_c for $H \perp (101)$ near $M = 0$.

sample 2 was exposed to air for several days. In addition, it was slightly heated when sealing in quartz tube and kept in the low vacuum (several Torr) for about 3 months. Dominant type-II superconducting M -versus- H hysteresis is evident whereas small WFM is superimposed on the main signal. As expected, the magnitude of WFM signal is about two times larger in sample 2 than in crystal that was exposed to air for a shorter time [see Fig. 8(a) and 8(b), main text]. Based on our synchrotron powder x-ray results taken on samples that were exposed to air for several months, the larger WFM magnitude should also originate from Fe-based compounds (impurities) that form over a course of time (see main text). The thickness of sample 2 was identical and the ab plane was considerably smaller than in sample 1, hence the

crystal was more isotropic ($a = 0.1535$ cm, $b = 0.036$ cm, and $c = 0.0036$ cm). Larger irreversibility fields are expected when a geometric edge barrier for vortex penetration dwarfs pinning at the inhomogeneities of the material. If intrinsic, a larger WFM signal in sample 2 is expected to originate from more defects that would cause larger irreversibility field if the bulk pinning on inhomogeneities is dominant. However, for thin superconducting strips a geometric (specimen-shape-dependent) barrier is dominant and larger irreversibility fields are expected for more anisotropic samples.⁴² Both sample 1 and sample 2 are rather thin ($c/a = 0.016$ and $c/b = 0.06$ for sample 1 and $c/a = 0.023$ and $c/b = 0.1$ for sample 2, respectively), whereas sample 1 is more anisotropic and is expected to have a larger irreversibility field.

*Current address: Ames Laboratory US DOE and Department of Physics and Astronomy, Iowa State University, Ames, Iowa 50011, USA.

†petrovic@bnl.gov

¹I. I. Mazin, *Nature (London)* **464**, 183 (2010).

²I. I. Mazin, D. J. Singh, M. D. Johannes, and M. H. Du, *Phys. Rev. Lett.* **101**, 057003 (2008).

³K. Kuroki, S. Onari, R. Arita, H. Usui, Y. Tanaka, H. Kontani, and H. Aoki, *Phys. Rev. Lett.* **101**, 087004 (2008).

⁴A. J. Drew, Ch. Niedermayer, P. J. Baker, F. L. Pratt, S. J. Blundell, T. Lancaster, R. H. Liu, G. Wu, X. H. Chen, I. Watanabe, V. K. Malik, A. Dubroka, M. Rössle, K. W. Kim, C. Baines, and C. Bernhard, *Nat. Mater.* **8**, 310 (2009).

⁵V. Cvetkovic and Z. Tesanovic, *Europhys. Lett.* **83**, 47001 (2008).

⁶W. L. Yang, A. P. Sorini, C-C. Chen, B. Moritz, W.-S. Lee, F. Vernay, P. Olalde Velasco, J. D. Denlinger, B. Delley, J.-H. Chu, J. G. Analytis, I. R. Fisher, Z. A. Ren, J. Yang, W. Lu, Z. X. Zhao, J. van den Brink, Z. Hussain, Z.-X. Shen, and T. P. Devereaux, *Phys. Rev. B* **80**, 014508 (2009).

⁷Wei Bao, Y. Qiu, Q. Huang, M. A. Green, P. Zajdel, M. R. Fitzsimmons, M. Zhernenkov, S. Chang, Minghu Fang, B. Qian, E. K. Vehstedt, Jinhua Yang, H. M. Pham, L. Spinu, and Z. Q. Mao, *Phys. Rev. Lett.* **102**, 247001 (2009).

⁸F. C. Hsu, Jiu-Yong Luo, Kuo-Wei Yeh, Ta-Kun Chen, Tzu-Wen Huang, Phillip M. Wu, Yong-Chi Lee, Yi-Lin Huang, Yan-Yi Chu, Der Chung Yan, and Maw-Kuen Wu, *Proc. Natl. Acad. Sci. USA* **105**, 14262 (2008).

⁹S. Medvedev, T. M. McQueen, I. A. Troyan, T. Palasyuk, M. I. Erements, R. J. Cava, S. Naghavi, F. Casper, V. Ksenofontov, G. Wortmann, and C. Felser, *Nat. Mater.* **8**, 630 (2009).

¹⁰S. B. Zhang, X. D. Zhu, H. C. Lei, G. Li, B. S. Wang, L. J. Li, X. B. Zhu, Z. R. Yang, W. H. Song, J. M. Dai, and Y. P. Sun, *Supercond. Sci. Technol.* **22**, 075016 (2009).

¹¹U. Patel, J. Hua, S. H. Yu, S. Avci, Z. L. Xiao, H. Claus, J. Schlueter, V. V. Vlasko-Vlasov, U. Welp, and W. K. Kwok, *Appl. Phys. Lett.* **94**, 082508 (2009).

¹²T. M. McQueen, Q. Huang, V. Ksenofontov, C. Felser, Q. Xu, H. Zandbergen, Y. S. Hor, J. Allred, A. J. Williams, D. Qu, J. Checkelsky, N. P. Ong, and R. J. Cava, *Phys. Rev. B* **79**, 014522 (2009).

¹³D. Phelan, J. N. Millican, E. L. Thomas, J. B. Leão, Y. Qiu, and R. Paul, *Phys. Rev. B* **79**, 014519 (2009).

¹⁴H. Okamoto, *J. Phase Equilib.* **12**, 383 (1991).

¹⁵P. Chartrand and A. D. Pelton, *Can. Metall. Quart.* **39**, 405 (2000).

¹⁶B. H. Mok, S. M. Rao, M. C. Ling, K. J. Wang, C. T. Ke, P. M. Wu, C. L. Chen, F. C. Hsu, T. W. Huang, J. Y. Luo, D. C. Yan, K. W. Ye, T. B. Wu, A. M. Chang, and M. K. Wu, *Cryst. Growth Des.* **9**, 3260 (2009).

¹⁷J. Yang, M. Matsui, M. Kawa, H. Ohta, C. Michioka, C. Dong, H. Wang, H. Yuan, M. Fang, and K. Yoshimura, *J. Phys. Soc. Jpn.* **79**, 074704 (2010).

¹⁸Zhaofei Li, J. Ju, J. Tang, K. Sato, M. Watahiki, and K. Tanigaki, *Phys. Chem. Solids* **71**, 495 (2010).

¹⁹S. Margadonna, Y. Takabayashi, M. T. McDonald, K. Kasperkiewicz, Y. Mizuguchi, Y. Takano, A. N. Fitch, E. Suard, and K. Prassides, *Chem. Commun.* **43**, 5607 (2008).

²⁰S. Margadonna, Y. Takabayashi, Y. Ohishi, Y. Mizuguchi, Y. Takano, T. Kagayama, T. Nakagawa, M. Takata, and K. Prassides, *Phys. Rev. B* **80**, 064506 (2009).

²¹M. Onoda, Y. Kawasaki, M. Tsubokawa, and T. Koyano, *J. Phys. Condens. Matter* **22**, 505702 (2010).

²²S. A. J. Kimber, A. Kreyssig, Yu-Z. Zhang, H. O. Jeschke, R. Valenti, F. Yokaichiya, E. Colombier, J. Yan, T. C. Hansen, T. Chatterji, R. J. McQueeney, P. C. Canfield, A. I. Goldman, and D. N. Argyriou, *Nat. Mater.* **8**, 471 (2009).

²³S. Takeshita, R. Kadono, M. Hiraishi, M. Miyazaki, A. Koda, S. Matsuishi, and H. Hosono, *Phys. Rev. Lett.* **103**, 027002 (2009).

²⁴M. Bendele, A. Amato, K. Conder, M. Elender, H. Keller, H.-H. Klauss, H. Luetkens, E. Pomjakushina, A. Raselli, and R. Khasanov, *Phys. Rev. Lett.* **104**, 087003 (2010).

²⁵R. Khasanov, K. Conder, E. Pomjakushina, A. Amato, C. Baines, Z. Bukowski, J. Karpinski, S. Katrych, H.-H. Klauss, H. Luetkens, A. Shengelaya, and N. D. Zhigadlo, *Phys. Rev. B* **78**, 220510 (2008).

²⁶A. V. Fedorchenko, G. E. Grechnev, V. A. Desnenko, A. S. Panfilov, S. L. Gnatchenko, V. V. Tsurkan, J. Deisenhofer, H.-A. Krug von Nidda, A. Loidl, D. A. Chareev, O. S. Volkova, and A. N. Vasiliev, *Low Temp. Phys.* **37**, 83 (2011).

²⁷T. Imai, K. Ahilan, F. L. Ning, T. M. McQueen, and R. J. Cava, *Phys. Rev. Lett.* **102**, 177005 (2009).

- ²⁸P. K. Mang, S. Larochele, A. Mehta, O. P. Vajk, A. S. Erickson, L. Lu, W. J. L. Buyers, A. F. Marshall, K. Prokes, and M. Greven, *Phys. Rev. B* **70**, 094507 (2004).
- ²⁹Eng Chan Kim, S. G. Kang, I. H. Cho, Y. S. Hwang, H. G. Hwang, and J. G. Kim, *J. Appl. Phys.* **81**, 4131 (1997).
- ³⁰A. Blachowski, K. Ruebenbauer, J. Zukrowski, J. Przewoznik, K. Wojciechowski, and Z. M. Stadnik, *J. Alloys Compd.* **494**, 1 (2010).
- ³¹W. F. Brown, *Magnetic Materials, in the Handbook of Chemistry and Physics*, edited by E. U. Condon and H. Odishaw (McGraw-Hill, 1958).
- ³²J. Carvell, E. Ayieta, A. Gavrin, R. Cheng, V. R. Shah, and P. Sokol, *J. Appl. Phys.* **107**, 103913 (2010).
- ³³A. V. Balatsky and D. Parker, *Physics* **2**, 59 (2009).
- ³⁴W. G. Yin, Chi-Cheng Lee, and Wei Ku, *Phys. Rev. Lett.* **105**, 107004 (2010).
- ³⁵Yong-Feng Li, G.-B. Liu, L.-J. Shi, and B.-G. Liu, *Chin. Phys. Lett.* **26**, 127505 (2009).
- ³⁶K.-W. Lee, V. Pardo, and W. E. Pickett, *Phys. Rev. B* **78**, 174502 (2008).
- ³⁷S. R. Saha, N. P. Butch, K. Kirshenbaum, J. Paglione, and P. Zavalij, *Phys. Rev. Lett.* **103**, 037005 (2009).
- ³⁸Wei Bao, G. N. Li, Q. Huang, G. F. Chen, J. B. He, M. A. Green, Y. Qiu, D. M. Wang, J. L. Luo, and M. M. Wu, e-print [arXiv:1102.3674](https://arxiv.org/abs/1102.3674) (unpublished).
- ³⁹Wei Bao, Q. Huang, G. F. Chen, M. A. Green, D. M. Wang, J. B. He, X. Q. Wang, and Y. Qiu, e-print [arXiv:1102.0830](https://arxiv.org/abs/1102.0830) (unpublished).
- ⁴⁰T. Hirone and S. Chiba, *J. Phys. Soc. Jpn.* **11**, 666 (1956).
- ⁴¹T. Kamimura, K. Kamigaki, T. Hirone, and K. Sato, *J. Phys. Soc. Jpn.* **22**, 1235 (1967).
- ⁴²E. H. Brandt, *Physica C* **332**, 99 (2000).

Antiferromagnetism in semiconducting $\text{KFe}_{0.85}\text{Ag}_{1.15}\text{Te}_2$ single crystals

Hechang Lei(雷和畅), Emil S. Bozin, Kefeng Wang(王克锋), and C. Petrovic

Condensed Matter Physics and Materials Science Department, Brookhaven National Laboratory, Upton, New York 11973, USA

(Received 3 May 2011; published 16 August 2011)

We have synthesized single crystals of $\text{K}_{1.00(3)}\text{Fe}_{0.85(2)}\text{Ag}_{1.15(2)}\text{Te}_{2.0(1)}$. The material crystallizes in the ThCr_2Si_2 structure with $I4/mmm$ symmetry and without K and Fe/Ag deficiencies, unlike in $\text{K}_x\text{Fe}_{2-y}\text{Se}_2$ and $\text{K}_x\text{Fe}_{2-y}\text{S}_2$. Transport, magnetic, and heat-capacity measurements indicate that $\text{KFe}_{0.85}\text{Ag}_{1.15}\text{Te}_2$ is a semiconductor with long-range antiferromagnetic transition at $T_N = 35$ K.

DOI: [10.1103/PhysRevB.84.060506](https://doi.org/10.1103/PhysRevB.84.060506)

PACS number(s): 74.70.Xa, 74.10.+v, 75.50.Ee, 81.05.Zx

The discovery of superconductivity in $\text{LaFeAsO}_{1-x}\text{F}_x$ ¹ has stimulated substantial interest in iron-based high-temperature superconductors (Fe-HTSs). Until now, several Fe-HTSs were discovered. They can be divided into two classes. The first class is iron pnictide materials.^{1–3} They contain two-dimensional FePn (Pn = pnictogens) tetrahedron layers and atomic sheets (e.g., Ba, K) or complex blocks [e.g., La-O(F)] along the c axis. Another class is binary iron chalcogenides FeCh (Ch = chalcogens, FeCh-11 type).^{4–6} In contrast to the diversity of iron pnictide superconductors, FeCh-11-type materials do not have any atomic or complex layers between puckered FeCh sheets.

Very recently, the discovery of $\text{A}_x\text{Fe}_{2-y}\text{Se}_2$ ($\text{A} = \text{K}, \text{Rb}, \text{Cs},$ and Tl , FeCh-122 type) with $T_c \approx 30$ K raised T_c in Fe-HTS by introducing alkali metal atomic layers between FeCh sheets.^{7–10} Further studies indicate that in the new superconductors the T_c gets enhanced when compared to FeCh-11 materials, but there is also a set of distinctive physical properties. FeCh-122 materials are close to the metal-semiconducting crossover and antiferromagnetic (AFM) order.^{7–10} This is in contrast to other superconductors which are in close proximity to the spin-density wave state.¹¹ The Fermi surface in FeCh-122-type Fe-HTSs contains only electronlike sheets without the nesting features found in most other Fe-HTS.¹²

On the other hand, superconductivity in FeCh-11 materials is quite robust with respect to anion change, as seen on the example of FeSe_{1-x} , $\text{FeTe}_{1-x}\text{Se}_x$, and $\text{FeTe}_{1-x}\text{S}_x$.^{4–6} However, in FeCh-122 compounds, superconductivity is only observed in $\text{A}_x\text{Fe}_{2-y}\text{Se}_2$ or $\text{K}_x\text{Fe}_{2-y}\text{Se}_{2-z}\text{S}_z$,¹³ while pure $\text{K}_x\text{Fe}_{2-y}\text{S}_2$ is a semiconductor with spin-glass transition at low temperature.¹⁴ Moreover, the theoretical calculation indicates that the hypothetical KFe_2Te_2 , if synthesized, would have higher T_c than $\text{K}_x\text{Fe}_{2-y}\text{Se}_2$.¹⁵ Therefore, synthesis and examination of physical properties of FeCh-122 materials containing FeTe layers could be very instructive.

In this Rapid Communication we report discovery of $\text{K}_{1.00(3)}\text{Fe}_{0.85(2)}\text{Ag}_{1.15(2)}\text{Te}_{2.0(1)}$ single crystals. The resistivity and magnetic measurements indicate that this compound has the semiconducting long-range AFM order at low temperature, with no superconductivity down to 1.9 K.

Single crystals of $\text{K}(\text{Fe},\text{Ag})_2\text{Te}_2$ were grown by the self-flux method reported elsewhere in detail,^{14,16} with nominal composition $\text{K}:\text{Fe}:\text{Ag}:\text{Te} = 1:1:1:2$. Single crystals with

typical size $5 \times 5 \times 2$ mm³ can be grown. Powder x-ray diffraction (XRD) data were collected at 300 K using 0.3184-Å wavelength radiation (38.94 keV) at the X7B beamline of the National Synchrotron Light Source. The average stoichiometry was determined by examination of multiple points using an energy-dispersive x-ray spectroscopy (EDX) in a JEOL JSM-6500 scanning electron microscope. Electrical transport measurements were performed using a four-probe configuration on rectangular-shaped polished single crystals with current flowing in the ab plane of tetragonal structure. Thin Pt wires were attached to electrical contacts made of silver paste. Electrical transport, heat capacity, and magnetization measurements were carried out in Quantum Design PPMS-9 and MPMS-XL5.

Figure 1(a) shows powder XRD results and structural refinements of $\text{K}(\text{Fe},\text{Ag})_2\text{Te}_2$ using a general structure analysis system (GSAS).^{17,18} It can be seen that all reflections can be indexed in the $I4/mmm$ space group. The refined structure parameters are listed in Table I. The determined lattice parameters are $a = 4.3707(9)$ Å and $c = 14.9540(8)$ Å, which are reasonably smaller than those of $\text{CsFe}_x\text{Ag}_{2-x}\text{Te}_2$ [$a = 4.5058(4)$ Å and $c = 15.4587(8)$ Å],¹⁹ but much larger than those of $\text{K}_x\text{Fe}_{2-y}\text{Se}_2$ and $\text{K}_x\text{Fe}_{2-y}\text{S}_2$,^{7,14} due to the smaller ionic size of K^+ than Cs^+ and larger size of Ag^+ and Te^{2-} than Fe^{2+} and $\text{Se}^{2-}(\text{S}^{2-})$. On the other hand, a larger a -axis lattice parameter indicates that the Fe plane is stretched in $\text{K}(\text{Fe},\text{Ag})_2\text{Te}_2$ when compared to FeTe .²⁰ The crystal structure of $\text{K}(\text{Fe},\text{Ag})_2\text{Te}_2$ is shown in Fig. 1(b), where antiferrotype Fe/Ag-Te layers and K cation layers are stacked alternatively along the c axis. The XRD pattern of a single crystal [Fig. 1(c)] reveals that the crystal surface is normal to the c axis with the plate-shaped surface parallel to the ab plane. Figure 1(d) presents the EDX spectrum of a single crystal, which confirms the presence of the K, Fe, Ag, and Te. The average atomic ratios determined from EDX are $\text{K}:\text{Fe}:\text{Ag}:\text{Te} = 1.00(3):0.85(2):1.15(2):2.0(1)$. The value of $\text{Fe}/(\text{Ag} + \text{Fe})$ determined from XRD fitting (0.38) is close to that obtained from EDX (0.43), which suggests that Te compound prefers to contain more Ag. This might explain why pure KFe_2Te_2 cannot form, since large Ag^+ ions have to be introduced in order to match the rather large Te^{2-} anions and keep the stability of the structure. On the other hand, it should be noted that there are no K or Fe/Ag deficiencies in $\text{K}(\text{Fe},\text{Ag})_2\text{Te}_2$. This is rather different from $\text{K}_x\text{Fe}_{2-y}\text{Se}_2$ and $\text{K}_x\text{Fe}_{2-y}\text{S}_2$.^{7,14} Moreover, synchrotron powder X-ray

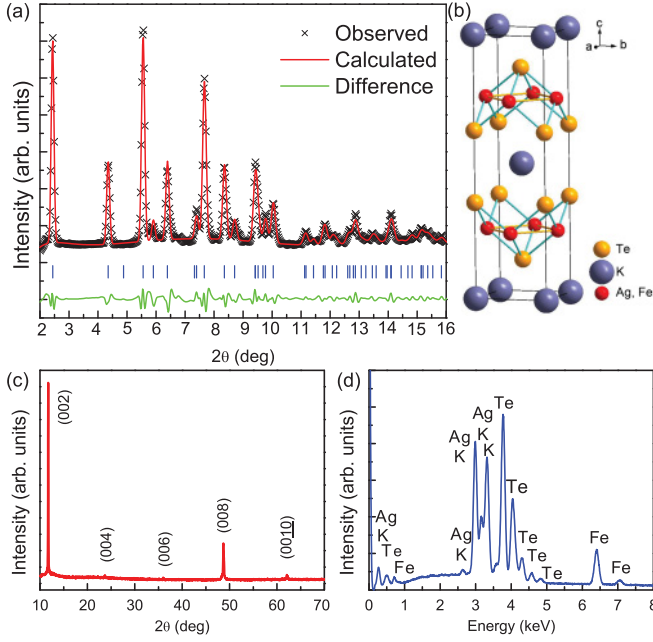


FIG. 1. (Color online) (a) Powder XRD patterns of $\text{KFe}_{0.85}\text{Ag}_{1.15}\text{Te}_2$. (b) Crystal structure of $\text{KFe}_{0.85}\text{Ag}_{1.15}\text{Te}_2$. The big blue, small red, and medium orange balls represent K, Fe/Ag, and Te ions. (c) Single-crystal XRD of $\text{KFe}_{0.85}\text{Ag}_{1.15}\text{Te}_2$. (d) The EDX spectrum of a single crystal.

refinement and EDX were consistent with either stoichiometric Te or not more than 5% vacancies (i.e., $\text{Te}_{1.9}$).

Figure 2 shows the temperature dependence of the in-plane resistivity $\rho_{ab}(T)$ of the $\text{KFe}_{0.85}\text{Ag}_{1.15}\text{Te}_2$ single crystal for $H = 0$ and 90 kOe. The resistivity increases with decreasing temperature, with a “shoulder” appearing at around 100 K. The room-temperature value ρ_{ab} is about 2.7 Ω cm, which is much larger than in superconducting $\text{K}_x\text{Fe}_{2-y}\text{S}_2$ and semiconduct-

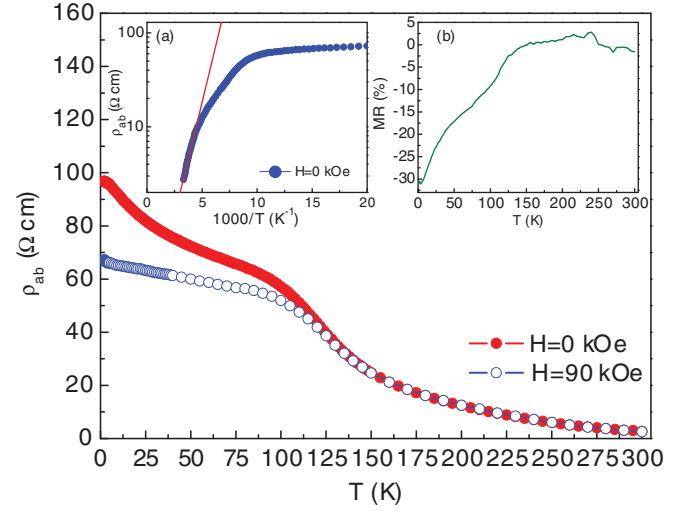


FIG. 2. (Color online) Temperature dependence of the in-plane resistivity $\rho_{ab}(T)$ of the $\text{KFe}_{0.85}\text{Ag}_{1.15}\text{Te}_2$ single crystal with $H = 0$ (closed red circle) and 90 kOe (open blue square, $H||c$). Inset (a) shows the fitted result using thermal activation model for $\rho_{ab}(T)$ at zero field where the red line is the fitting curve. Inset (b) exhibits the temperature dependence of MR(T) for $\text{KFe}_{0.85}\text{Ag}_{1.15}\text{Te}_2$.

ing $\text{K}_x\text{Fe}_{2-y}\text{S}_2$.^{14,16} The semiconducting behavior might be related to the random distribution of Fe and Ag ions in the Fe/Ag plane which induces a random scattering potential, similar to the effect of Fe deficiency in the FeSe or FeS plane.^{14,21} By fitting the $\rho_{ab}(T)$ at high temperature using the thermal activation model $\rho = \rho_0 \exp(E_a/k_B T)$, where ρ_0 is a prefactor and k_B is Boltzmann’s constant [inset (a) of Fig. 2], we obtained $\rho_0 = 71(6)$ m Ω cm and the activation energy $E_a = 96(2)$ meV in the temperature range above 200 K, which is larger than that of $\text{K}_x\text{Fe}_{2-y}\text{S}_2$.¹⁴ $\text{KFe}_{0.85}\text{Ag}_{1.15}\text{Te}_2$ exhibits large magnetoresistance [MR = $[\rho(H) - \rho(0)]/\rho(0)$] below about 100 K where the shoulder appears. As shown in inset (b) of Fig. 2, the negative MR is about 30% at 1.9 K for $H = 90$ kOe. This behavior is distinctively different from $\text{K}_x\text{Fe}_{2-y}\text{S}_2$, which does not show any MR in measured temperature range.¹⁴

Figure 3(a) presents the temperature dependence of magnetic susceptibility $\chi(T)$ of the $\text{KFe}_{0.85}\text{Ag}_{1.15}\text{Te}_2$ single crystal for $H = 1$ kOe along the ab plane and the c axis below 300 K with zero-field-cooling (ZFC) and field-cooling (FC). The $\chi_{ab}(T)$ is slightly larger than $\chi_c(T)$, and above 50 K, both can be fitted very well using Curie-Weiss law $\chi(T) = \chi_0 + C/(T - \theta)$, where χ_0 includes core diamagnetism, van Vleck and Pauli paramagnetism, C is the Curie constant, and θ is the Curie-Weiss temperature [solid lines in Fig. 3(a)]. The fitted parameters are $\chi_0 = 5.46(7) \times 10^{-6}$ emu $\text{g}^{-1} \text{Oe}^{-1}$, $C = 2.58(3) \times 10^{-3}$ emu $\text{g}^{-1} \text{Oe}^{-1} \text{K}$, and $\theta = -82(1)$ K for $H||ab$, and $\chi_0 = 3.5(1) \times 10^{-6}$ emu $\text{g}^{-1} \text{Oe}^{-1}$, $C = 2.92(5) \times 10^{-3}$ emu $\text{g}^{-1} \text{Oe}^{-1} \text{K}$, and $\theta = -100(2)$ K for $H||c$. The above values of C correspond to an effective moment of $\mu_{eff} = 3.60(2) \mu_B/\text{Fe}$ and $3.83(3) \mu_B/\text{Fe}$ for $H||ab$ and $H||c$, respectively. The values of μ_{eff} are smaller than for free Fe^{2+} ions ($4.7 \mu_B/\text{Fe}$) and Fe_{1+x}Te ($4.9 \mu_B/\text{Fe}$),²² but slightly larger than in $\text{K}_x\text{Fe}_{2-y}\text{S}_2$ ($3.31 \mu_B/\text{Fe}$).²³

TABLE I. Structural parameters for $\text{K}(\text{Fe},\text{Ag})_2\text{Te}_2$ at room temperature. Values in brackets give the number of equivalent distances or angles of each type. The occupancies of K and Te are fixed during fitting.

Chemical formula	$\text{K}_{1.00(3)}\text{Fe}_{0.85(2)}\text{Ag}_{1.15(2)}\text{Te}_{2.0(1)}$			
space group	$I4/mmm$			
a (\AA)	4.3707(9)			
c (\AA)	14.9540(8)			
V (\AA^3)	285.7(1)			
Interatomic distances (\AA)	Bond angles ($^\circ$)			
$d_{\text{Fe/Ag-Fe/Ag}}$ [4]	3.0906(4)	Te-Fe/Ag-Te [2]	104.44(3)	
$d_{\text{Fe/Ag-Te/Ag}}$ [4]	2.7651(5)	Te-Fe/Ag-Te [4]	112.05(4)	
Anion heights (\AA)	1.694(7)			
Atom	x	y	z	Occ. U_{iso} (\AA^2)
K	0	0	0	1.00 0.056(5)
Fe	0.5	0	0.25	0.76(8) 0.035(7)
Ag	0.5	0	0.25	1.24(8) 0.035(7)
Te	0.5	0.5	0.1367(5)	1.00 0.034(4)

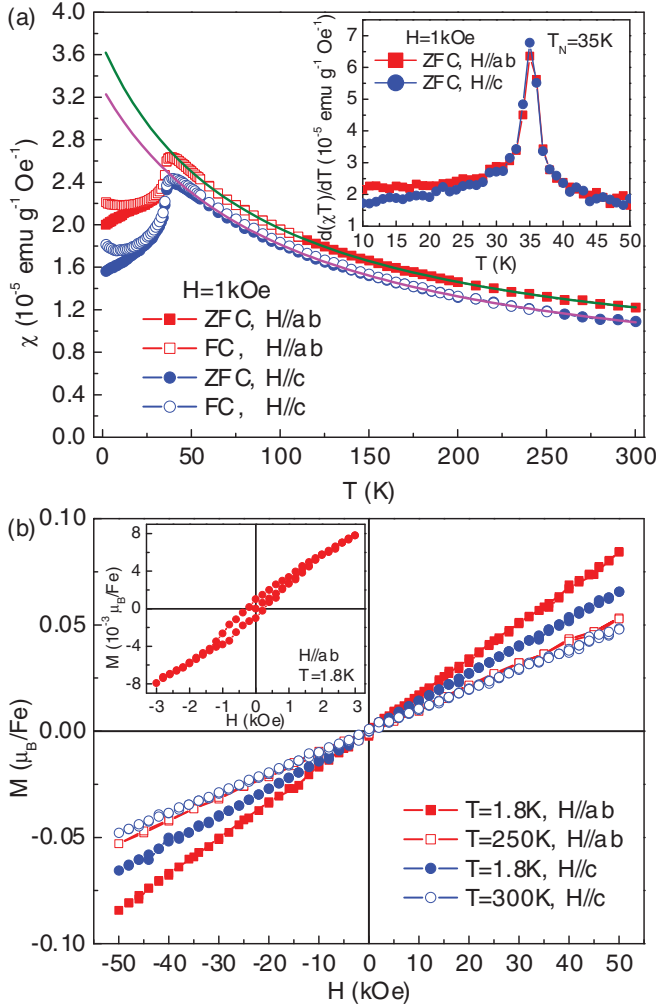


FIG. 3. (Color online) (a) Temperature dependence of DC magnetic susceptibility $\chi(T)$ with the applied field $H = 1$ kOe along the ab plane and c axis below 300 K under ZFC and FC mode. The inset shows the $d(\chi T)/dT$ result for both field directions. (b) Isothermal magnetization hysteresis loops $M(H)$ for $H\parallel ab$ and $H\parallel c$ at various temperatures.

We observe sharp drops below 35 K in both ZFC and FC curves, associated with the onset of long-range AFM order. The $T_N = 35$ K is determined from the peak of $d(\chi T)/dT$ [inset of Fig. 3(a)].²⁴ It should be noted that antiferromagnetism below 35 K and Curie-Weiss paramagnetism at higher temperature are obviously different from $K_x\text{Fe}_{2-y}\text{Se}_2$ and $K_x\text{Fe}_{2-y}\text{S}_2$.¹³ Figure 3(b) shows the magnetization loops for both field directions at various temperatures. It can be seen that all M-H loops exhibit almost linear field dependence and the $M(H)$ curve exhibits a very small hysteresis at 1.8 K with a small coercive field (~ 260 Oe).

Figure 4 shows the temperature dependence of heat capacity C_p for $\text{KFe}_{0.85}\text{Ag}_{1.15}\text{Te}_2$ single crystals measured between $T = 1.95$ and 300 K in a zero magnetic field. At high temperature heat capacity approaches the Dulong-Petit value of $3NR$, where N is the atomic number in the chemical formula ($N = 5$) and R is the gas constant ($R = 8.314 \text{ J mol}^{-1} \text{ K}^{-1}$). On the other hand, the low-temperature $C_p(T)$ curve can be fitted solely by a cubic term βT^3 . By neglecting antiferromagnon contribution,²⁵ from

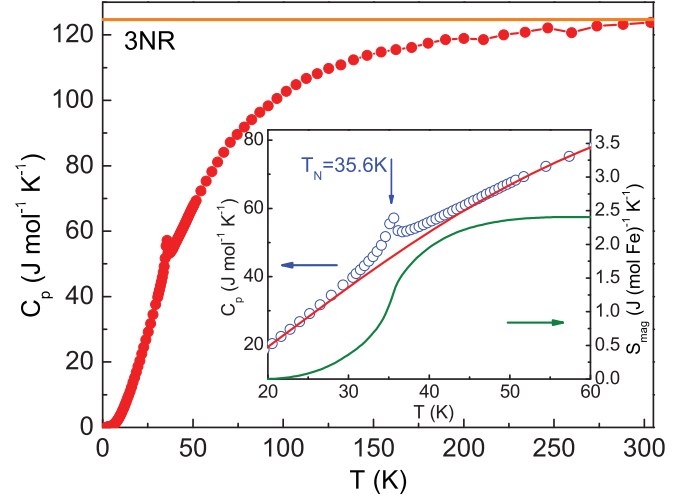


FIG. 4. (Color online) Temperature dependence of heat capacity for $\text{KFe}_{0.85}\text{Ag}_{1.15}\text{Te}_2$ single crystal. The orange solid line represents the classical value according to Dulong-Petit law at high temperature. The inset shows the enlarged area near the magnetic transition region of $C_p - T$. The red solid curve represents the lattice contribution, fitted by a polynomial. The right label denotes the magnetic entropy associated with the AFM transition.

the fitted value of $\beta = 3.11(2) \text{ mJ mol}^{-1} \text{ K}^{-4}$, the Debye temperature is estimated to be $\Theta_D = 146.2(3) \text{ K}$ using the formula $\Theta_D = (12\pi^4 NR/5\beta)^{1/3}$. This is much smaller than Θ_D of $K_x\text{Fe}_{2-y}\text{Se}_2$ and $K_x\text{Fe}_{2-y}\text{S}_2$ at least partially because of the larger atomic mass of Ag and Te in $\text{KFe}_{0.85}\text{Ag}_{1.15}\text{Te}_2$.^{14,26}

A λ -type anomaly at $T_N = 35.6 \text{ K}$ (shown in the inset of Fig. 4) confirms the bulk nature of the AFM order observed in the magnetization measurement shown in Fig. 3. The transition temperature is consistent with the values determined from $d(\chi T)/dT$ (35 K). Assuming that the total heat capacity consists of phonon (C_{ph}) and magnetic (C_{mag}) components, C_{mag} can be estimated by the subtraction of C_{ph} . Consequently, the magnetic entropy (S_{mag}) can be calculated using the integral $S_{mag}(T) = \int_0^T C_{mag}/T dT$. Because of the failure of the Debye model at $T > \Theta_D$, we estimated the lattice specific heat by fitting a polynomial to the $C_p(T)$ curve at temperatures well away from T_N . The obtained S_{mag} is about $2.4 \text{ J (mol Fe)}^{-1} \text{ K}^{-1}$ up to 60 K, which is only 18% of theoretical value ($R\ln 5 = 13.4 \text{ J (mol Fe)}^{-1} \text{ K}^{-1}$ for high-spin-state Fe^{2+} ions). Note that only about $1 \text{ J (mol Fe)}^{-1} \text{ K}^{-1}$ is released below T_N . This discrepancy may originate from an incorrect estimation of the lattice contribution to $C_{ph}(T)$, which can lead to reduced $S_{mag}(T)$ or a probable short-range order that may exist above the bulk three-dimensional AFM order occurring at T_N . This could also be supported by a much smaller $T_N = 35 \text{ K}$ compared to the Curie-Weiss temperature $\theta = -100(2) \text{ K}$ for $H\parallel c$.

There are two origins which could induce the negative MR effect in semiconductors: the reduction in spin disorder scattering due to the alignment of moments under a field, and the reduction of the gap arising from the splitting of the up- and down-spin subbands. The existence of AFM interaction could be related to this negative MR effect. The

temperature where MR effect becomes obvious is consistent with the Curie-Weiss temperature θ , which implies this MR effect could be related to the AFM interaction and due to the reduction in spin disorder scattering with field. When compared to $K_xFe_{2-y}Se_2$, substitution of Ag has an important influence on the magnetic and transport properties. It could reduce the exchange interaction between Fe atoms and thus suppress the T_N of $KFe_{0.85}Ag_{1.15}Te_2$ significantly. On the other hand, because of the near absence of vacancies in $KFeCuS_2$ and similar valence between Cu and Ag,²⁷ it is more meaningful to compare the physical properties between $KFeCuS_2$ and $KFe_{0.85}Ag_{1.15}Te_2$. The former has the larger E_a and room-temperature resistivity than the latter. This could be due to the smaller ionic sizes of Cu and S when compared to Ag and Te, which might lead to the smaller orbital overlap increasing E_a and resistivity. Both compounds exhibit Curie-Weiss law above 50 K and the fitted Curie-Weiss temperatures are also similar (176 K for $KFeCuS_2$). Moreover, $KFeCuS_2$ shows magnetic transition at 40 K, which is very close to the T_N of $KFe_{0.85}Ag_{1.15}Te_2$. However, the transition of $KFeCuS_2$ is spin glasslike, in contrast to the

long-range AFM order of $KFe_{0.85}Ag_{1.15}Te_2$. This implies that the distribution of Ag in $KFe_{0.85}Ag_{1.15}Te_2$ may be different from Cu in $KFeCuS_2$, which results in a different magnetic ground-state configuration with similar interaction strength.

In summary, we successfully synthesized the $K_{1.00(3)}Fe_{0.85(2)}Ag_{1.15(2)}Te_{2.0(1)}$ single crystals with $ThCr_2Si_2$ structure, identical to $K_{0.8}Fe_{2-y}Se_2$ at 600 K. Crystal structure and composition analysis indicate that there are no K, Fe/Ag, and Te vacancies within 3, 2, or 5 at. %, respectively. Transport, magnetic, and thermal measurements indicate that the $KFe_{0.85}Ag_{1.15}Te_2$ is a semiconductor with long-range AFM order below 35 K.

We thank John Warren for help with scanning electron microscopy measurements and Jonathan Hanson for help with x-ray measurements. Work at Brookhaven is supported by the US DOE under Contract No. DE-AC02-98CH10886 and in part by the Center for Emergent Superconductivity, an Energy Frontier Research Center funded by the US DOE, Office for Basic Energy Science.

- ¹Y. Kamihara, T. Watanabe, M. Hirano, and H. Hosono, *J. Am. Chem. Soc.* **130**, 3296 (2008).
- ²M. Rotter, M. Tegel, and D. Johrendt, *Phys. Rev. Lett.* **101**, 107006 (2008).
- ³X. C. Wang, Q. Q. Liu, Y. X. Lv, W. B. Gao, L. X. Yang, R. C. Yu, F. Y. Li, and C. Q. Jin, *Solid State Commun.* **148**, 538 (2008).
- ⁴F. C. Hsu, J. Y. Luo, K. W. Yeh, T. K. Chen, T. W. Huang, P. M. Wu, Y. C. Lee, Y. L. Huang, Y. Y. Chu, D. C. Yan, and M. K. Wu, *Proc. Natl. Acad. Sci. USA* **105**, 14262 (2008).
- ⁵K.-W. Yeh, T. W. Huang, Y. L. Huang, T. K. Chen, F. C. Hsu, P. M. Wu, Y. C. Lee, Y. Y. Chu, C. L. Chen, J. Y. Luo, D. C. Yan, and M. K. Wu, *Europhys. Lett.* **84**, 37002 (2008).
- ⁶Y. Mizuguchi, F. Tomioka, S. Tsuda, T. Yamaguchi, and Y. Takano, *Appl. Phys. Lett.* **94**, 012503 (2009).
- ⁷J. Guo, S. Jin, G. Wang, S. Wang, K. Zhu, T. Zhou, M. He, and X. Chen, *Phys. Rev. B* **82**, 180520(R) (2010).
- ⁸C.-H. Li, B. Shen, F. Han, X. Y. Zhu, and H.-H. Wen, *Phys. Rev. B* **83**, 184521 (2011).
- ⁹A. Krzton-Maziopa, Z. Shermadini, E. Pomjakushina, V. Pomjakushin, M. Bendele, A. Amato, R. Khasanov, H. Luetkens, and K. Conder, *J. Phys. Condens. Matter* **23**, 052203 (2011).
- ¹⁰M. H. Fang, H. D. Wang, C. H. Dong, Z. J. Li, C. M. Feng, J. Chen, and H. Q. Yuan, *EPL* **94**, 27009 (2011).
- ¹¹C. de la Cruz, Q. Huang, J. W. Lynn, J. Li, W. Ratcliff II, J. L. Zarestky, H. A. Mook, G. F. Chen, J. L. Luo, N. L. Wang, and P. Dai, *Nature* **453**, 899 (2008).
- ¹²Y. Zhang, L. X. Yang, M. Xu, Z. R. Ye, F. Chen, C. He, H. C. Xu, J. Jiang, B. P. Xie, J. J. Ying, X. F. Wang, X. H. Chen, J. P. Hu, M. Matsunami, S. Kimura, and D. L. Feng, *Nat. Mater.* **10**, 273 (2011).
- ¹³H. C. Lei, K. F. Wang, J. B. Warren, and C. Petrovic, e-print arXiv:1102.2434 (to be published 2011).
- ¹⁴H. C. Lei, M. Abeykoon, E. S. Bozin, and C. Petrovic, *Phys. Rev. B* **83**, 180503(R) (2011).
- ¹⁵I. R. Shein and A. L. Ivanovskii, *J. Supercond. Nov. Magn.* (online first) (2011).
- ¹⁶H. C. Lei and C. Petrovic, *Phys. Rev. B* **83**, 184504 (2011).
- ¹⁷A. C. Larson and R. B. Von Dreele, Los Alamos National Laboratory Report LAUR 86-748, 1994 (unpublished).
- ¹⁸B. H. Toby, *J. Appl. Crystallogr.* **34**, 210 (2001).
- ¹⁹J. Li, H.-Y. Guo, and R. A. Yglesias, *Chem. Mater.* **7**, 599 (1995).
- ²⁰E. E. Rodriguez, P. Zavalij, P.-Y. Hsieh, and M. A. Green, *J. Am. Chem. Soc.* **132**, 10006 (2010).
- ²¹D. M. Wang, J. B. He, T.-L. Xia, and G. F. Chen, *Phys. Rev. B* **83**, 132502 (2011).
- ²²Y. Liu, R. K. Kremer, and C. T. Lin, *Supercond. Sci. Technol.* **24**, 035012 (2011).
- ²³W. Bao, Q. Huang, G. F. Chen, M. A. Green, D. M. Wang, J. B. He, X. Q. Wang, and Y. Qiu, *Chin. Phys. Lett.* **28**, 086104 (2011).
- ²⁴M. E. Fisher, *Philos. Mag.* **7**, 1731 (1962).
- ²⁵J. van Kranendonk and J. H. van Vleck, *Rev. Mod. Phys.* **30**, 1 (1958).
- ²⁶B. Zeng, B. Shen, G. F. Chen, J. B. He, D. M. Wang, C. H. Li, and H. H. Wen, *Phys. Rev. B* **83**, 144511 (2011).
- ²⁷M. Oledzka, K. V. Ramanujachary, and M. Greenblatt, *Mater. Res. Bull.* **31**, 1491 (1996).

Detailed Mapping of the Local Ir^{4+} Dimers through the Metal-Insulator Transitions of CuIr_2S_4 Thiospinel by X-Ray Atomic Pair Distribution Function Measurements

E. S. Božin,^{1,*} A. S. Masadeh,^{2,3} Y. S. Hor,^{4,†} J. F. Mitchell,⁴ and S. J. L. Billinge^{1,5}

¹*Condensed Matter Physics and Materials Science Department, Brookhaven National Laboratory, Upton, New York 11973, USA*

²*Department of Physics and Astronomy, Michigan State University, East Lansing, Michigan 48824, USA*

³*Department of Physics, University of Jordan, Amman 11942, Jordan*

⁴*Materials Science Division, Argonne National Laboratory, Argonne, Illinois 60439, USA*

⁵*Department of Applied Physics and Applied Mathematics, Columbia University, New York, New York 10027, USA*

(Received 7 August 2010; published 24 January 2011)

The evolution of the *short-range* structural signature of the Ir^{4+} dimer state in CuIr_2S_4 thiospinel has been studied across the metal-insulator phase transitions as the metallic state is induced by temperature, Cr doping, and x-ray fluence. An atomic pair distribution function (PDF) approach reveals that there are no *local* dimers that survive into the metallic phase when this is invoked by temperature and doping. The PDF shows Ir^{4+} dimers when they exist, regardless of whether or not they are long-range ordered. At 100 K, exposure to a 98 keV x-ray beam melts the long-range dimer order within a few seconds, though the local dimers remain intact. This shows that the metallic state accessed on warming and doping is qualitatively different from the state obtained under x-ray irradiation.

DOI: 10.1103/PhysRevLett.106.045501

PACS numbers: 61.50.Ks, 61.05.cf, 71.30.+h

Local fluctuations in electronic and magnetic states are important in systems exhibiting colossal responses such as high temperature superconductors (HTS) [1,2] and colossal magnetoresistive (CMR) materials [3–5]. However, the ubiquity of these fluctuations and the exact role that they play in the rich observed physical phenomena are not understood. Part of the reason is that such fluctuations are extremely difficult to study because they are not long-range ordered [6,7]. In cases where there is strong electron-phonon coupling a signature of the local electronic states is evident in the local atomic structure and the electronic or magnetic states may be studied using a local structural probe [8,9] such as the atomic pair distribution function (PDF) analysis of powder diffraction data [10,11]. Here we use the PDF to study directly the existence or absence of Ir^{4+} dimer states in CuIr_2S_4 , which yields essential information to understand the unusual and poorly understood metal-insulator transitions in this system.

CuIr_2S_4 has generated significant interest recently because of its unusual magnetic, electronic and structural behavior [12–17]. It exhibits a metal-insulator (MI) transition, accompanied by a dramatic loss in magnetic susceptibility, charge ordering, and an accompanying structural phase transition, making it an important system for studying the interplay of electronic, magnetic, orbital and structural degrees of freedom. On cooling, crystallography indicates that the structural change in the insulating phase accompanies the formation of Ir^{4+} dimers (pairs of iridium ions move closer together by 0.5 Å [16]), which are presumably magnetic singlets explaining the loss of magnetic susceptibility. As well as the metallic phase appearing on warming, the material also becomes more metallic

when doped with Cr [18] and irradiated with optical [19] and x-ray [20,21] illumination.

The metallic state above the insulating ordered-dimer state in the phase diagram is unusual. It has a nonconventional conduction mechanism [22] and a recent observation of weak Fermi edges and broad peak features in ultraviolet photoemission spectra suggest that fluctuating dimers may survive in the high temperature metallic phase [23]. A PDF study can address this directly since the PDF is sensitive to the existence of the dimers whether or not they are ordered [23]. The local dimers are clearly evident in the PDF because of the large (0.5 Å) change in the Ir-Ir bond length in the dimer which separates this peak from any other nearby peak in the PDF. Here we show definitively that the dimers disappear abruptly from the local structure at the metal-insulator transition on warming [16]. They also disappear as the MI transition is crossed on doping Cr. However, they survive locally through an x-ray irradiation induced insulator-metal transition at low temperature [20,24]. These results provide essential input to guide theories of these interesting metal-insulator transitions [25,26].

CuIr_2S_4 and $\text{Cu}(\text{Ir}_{0.95}\text{Cr}_{0.05})_2\text{S}_4$ were prepared by solid state reaction in sealed, evacuated quartz ampoules. Stoichiometric quantities of the metals and elemental sulfur were thoroughly mixed, pelletized, and sealed under vacuum. The ampoules were slowly heated to 650–750 °C and held at this temperature for several weeks with intermediate grinding and pressing. The products were found to be single phase based on x-ray powder diffraction.

Total scattering experiments to obtain CuIr_2S_4 PDFs were performed at the 6-ID-D beam line at the Advanced Photon Source at Argonne National Laboratory, with

98.136 keV x rays using the rapid acquisition (RAPDF) mode [27]. The setup utilized a General Electric amorphous silicon-based area detector and Oxford Cryosystems cryostream for temperature variation with a sample to detector distance of 268.620 mm. Samples were packed in a kapton capillary 1 mm in diameter. The data were collected at various temperatures between 100 K and 300 K. The exposure time was varied as specified further in the text. The raw 2D data were integrated and converted to intensity versus 2θ using the software Fit2D [28], where 2θ is the diffraction angle. The integrated data were corrected for experimental artifacts, normalized, and Sine Fourier transformed (FT) to the PDF, $G(r)$, based on standard methods [11] using the program PDFGETX2 [29]. The upper limit of momentum transfer used in the FT of $Q_{\max} = 23.0 \text{ \AA}^{-1}$ was optimized such as to avoid large termination effects on the one hand and statistical noise on the other.

PDFs from CuIr_2S_4 are shown in Fig. 1. The peak in the PDF coming from the $\text{Ir}^{4+}\text{-Ir}^{4+}$ dimers (indicated by the arrow) is clearly apparent in the right-hand panels where the PDFs are shown on an expanded scale. The size of the distortion coupled with the fortuitous absence of other atomic distances at the same place allows us to study the dimer state in a model independent way using the PDF. Additionally, the changes in the next near-neighbor peak centered at 3.5 \AA clearly indicate that there is also an accompanying redistribution of PDF intensity from this peak to the dimer peak, lending confidence that the PDF is sensitive to the presence of local dimers. This is especially clear in the difference curve shown offset below. The 3.0 \AA PDF peak is not evident in the metallic state on warming [red curve in Fig. 1(a)] indicating that there are no local dimers in the metallic phase accessed by increasing temperature.

We now investigate the local structural changes on traversing the MI transitions. Figure 1(a) shows the effect of the temperature induced MI transition: experimental PDFs of CuIr_2S_4 in the metallic state at 230 K (red) and in the insulating state at 220 K (blue), 10 K apart, are dramatically different in the entire range, as evident from their difference curve (green) indicating that the structural change occurs at all length scales. Normal thermal effects have a much smaller effect on the PDF as is evident from Fig. 1(b), where the differences in the PDF due to a 10 K temperature change in the same structural phase (metallic state in this case), are within the estimated uncertainties of the measurement. There is clearly a significant structural modification in the local structure, as well as the average structure [16], at the MI transition. This may not seem surprising but this is not always the case, for example, in systems where distortions persist but become disordered at high temperature [30].

In Fig. 2 we show the detailed temperature dependence of the 3.0 \AA dimer peak as the sample goes through the MI

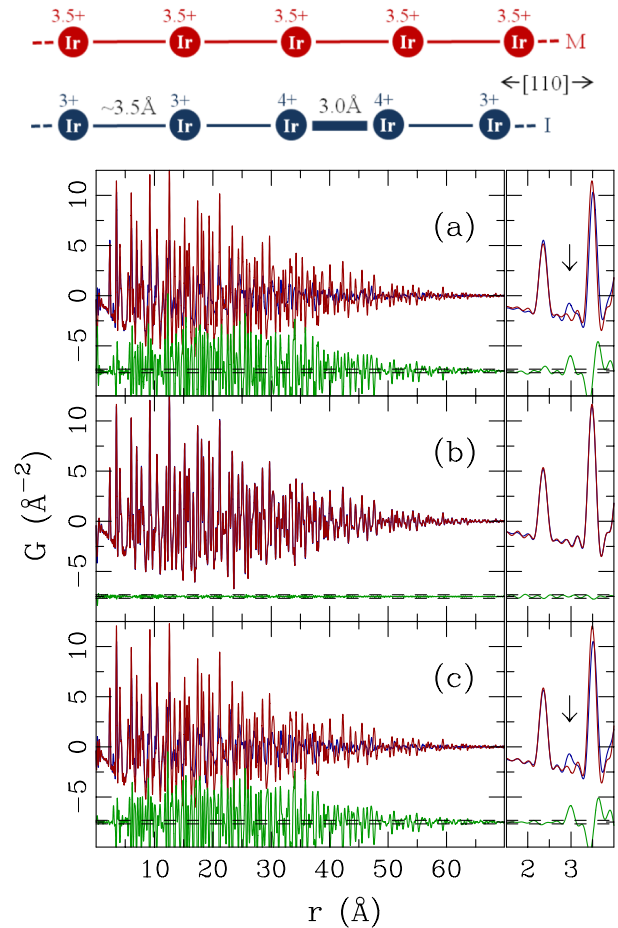


FIG. 1 (color online). Changes in PDF across the MI transition in CuIr_2S_4 when induced by temperature and Cr doping: experimental PDFs of (a) metallic 230 K (red) and insulating 220 K (blue), (b) metallic 230 K (red) and metallic 240 K (blue), (c) insulating undoped (blue) and metallic 5% Cr doped (red) at 200 K temperature. Difference curves are shown offset below (green). The corresponding side panels emphasize the short-range scale: the appearance of excess PDF intensity corresponding to the short $\text{Ir}^{4+}\text{-Ir}^{4+}$ dimer distance around 3.0 \AA in the insulating phase is indicated by arrows. The existence of this peak indicates the presence of local dimers. For reference, a sketch of Ir-chains in M and I phases is given on top. See text for details.

transition. The main panel shows the change in the peak maximum, defined as $\Delta G(T) = G(T) - G(230)$, versus temperature for both cooling (solid blue symbols) and warming (solid red symbols) cycles. To demonstrate the reproducibility of the data, the evolution of the dimer peak in the PDF itself is shown for cooling and warming cycles in lower left and upper right insets, respectively. Clean hysteretic behavior is observed, with a square loop that is about 10 K wide, in accord with hysteretic behavior observed in magnetic [31,32] and transport measurements [14,18,20,33,34]. Not only is long-range dimer order destroyed at the MI transition, but local dimers also disappear.

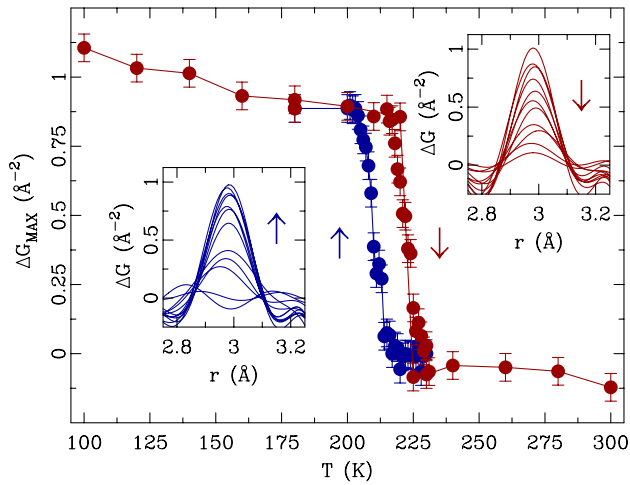


FIG. 2 (color online). Evolution of the short-range dimer structure across the MI transition in CuIr_2S_4 induced on cooling (blue) and warming (red) cycles. The insets show the evolution of the 3.0 Å dimer PDF peak on cooling (bottom left) and warming (up right). The main panel shows the excess height of this peak with respect to the 230 K data (see text for details).

The metallic state can also be reached from insulating CuIr_2S_4 by substituting a small percentage of Ir with Cr [18]. Inspection of Fig. 1(c), which shows the differences in two PDFs corresponding to insulating CuIr_2S_4 (blue solid line) and metallic (red solid line) at 200 K, indicates that the local dimers also disappear in the local structure in the metallic state accessed by 5% Cr-substitution at fixed temperature.

Here we extend the study to the destruction of the insulating ordered-dimer state by x-ray irradiation [19–21]. Photo-induced phase transitions, with an associated change in properties, are an important area of research because of the possibility of controlling properties optically [35,36]. The structural response to x-ray irradiation of our CuIr_2S_4 sample is summarized in Fig. 3 as the exposure time is varied at $T = 100$ K. Panels (a),(b),(c), and (d) each show a quarter of a full 2D diffraction pattern for exposures of 0.5, 1.0, 30.0, and 0.5 s, where the exposures were taken one after each other in the order (a)–(d) but with a 2 min gap between each where the sample was not being irradiated (shutter closed). The 1D diffraction patterns shown in panels (e) and (f) are obtained by integrating around the circular Debye-Scherrer rings on the 2D detector, evident in Figs. 3(a)–3(d). An extra peak can be seen in the diffraction pattern, indicated by the arrow in panel (b) and evident in the integrated data, inset in panel (f). This comes from long-range ordered dimers in the structure, but due to the limited reciprocal space resolution of the RAPDF measurement [27] it is formed from several superlattice peaks (SLP), including the strong $(3/2, 3/2, 3/2)$ peak. This is observed in all but image (c) that corresponds to the longest exposure time, reflecting the fact that the long-range dimer order is melted in this case. Notable also

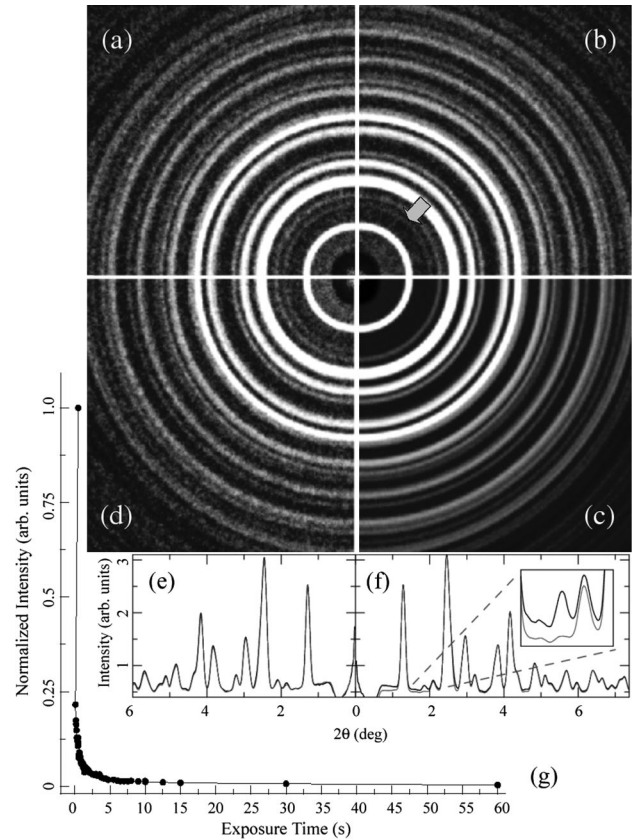


FIG. 3. Raw 2D diffraction data at 100 K of CuIr_2S_4 for successive (a) 0.5, (b) 1.0, (c) 30.0, and (d) 0.5 s exposures to x rays, with 2 min separations between the exposures. Notable is an extra diffraction ring indicated by the arrow in panel (b) present for all exposure times shown, except for 30 s. This corresponds to an unresolved multiplet of SLPs, including $(3/2, 3/2, 3/2)$, coming from long-range charge and dimer order. Panels (e) and (f) show the 1D powder diffraction pattern obtained by integrating around the rings from panels (a),(d) and (b),(c), respectively. The inset in panel (f) emphasizes the disappearance of the SLP multiplet. (g) Dependence of the normalized SLP intensity vs x-ray exposure time.

is an immediate recovery of the long-range order at 100 K in the successive 0.5 s exposure upon cessation of the exposure. Finally, in Fig. 3(g) we show the normalized integrated intensity of this multiplet SLP as a function of the x-ray exposure time. This establishes the behavior of the long-range dimer of our sample and has a behavior similar to other studies [20], but at a decay rate that is about 2 orders of magnitude faster than the one observed earlier. This may be a result of the different temperature of measurement (100 vs 10 K) or the different energy or flux of the irradiating x rays (100 vs 8 keV) [20].

The conductivity of the irradiated state increases over that of the insulating ground-state, though to a lesser degree than at the temperature or Cr induced MI transition [18]. We would like to see if the PDF yields information about the existence of local dimers in this more metallic

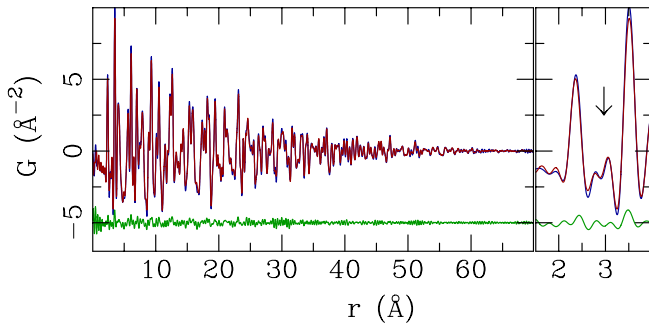


FIG. 4 (color online). Experimental PDFs of CuIr_2S_4 at 100 K corresponding to short (250 msec, blue) and long (30 sec, red) exposure times. The difference curve is offset below for clarity. The side panel emphasizes the short-range structure, with the arrow denoting the position of the 3.0 Å PDF peak corresponding to the local dimers. The differences are much smaller than seen in Fig. 1.

state induced by irradiation and so we compared the local structures after short and long x-ray exposures.

Figure 4 shows a comparison of the PDFs obtained in the first 250 ms of x-ray exposure, and after 30 sec of irradiation. As discussed above, the superstructure observed in the x-ray diffraction pattern coming from the dimer order is observed in the data from 250 ms but is completely destroyed in the data obtained after 30 s of irradiation. However, although the average structure behaves the same way at this MI transition, the behavior of the local structure is completely different between the irradiation induced and temperature or doping induced transitions. A comparison of Figs. 1 and 4 dramatically illustrates that the local structure is preserved on irradiation, where it is significantly changed at the temperature-doping transition. There is no loss in intensity of the dimer peak in the PDF after long irradiation suggesting that all charges remain localized resulting in distinct Ir^{3+} and Ir^{4+} sites, but further, that the localized holes remain bound in dimers. The increased conductivity in the irradiated sample [20,21] must be due to an increased hopping rate of localized charges bound in the dimer pairs that are no longer pinned to the lattice in an ordered arrangement and the irradiation must facilitate this pair hopping.

These PDF measurements allow us to measure directly if the Ir^{4+} - Ir^{4+} dimers exist regardless of whether or not they are long-range ordered. We show unambiguously that local dimers disappear in the metallic phases accessed on warming and on Cr doping, but they persist in the metallic state induced by irradiation with x rays.

We would like to thank P. Chupas and K. Chapman for their help in data collection. Work in the Billinge group was supported by the U.S. Department of Energy Office of Science (DOE-OS) under Contract No. DE-AC02-98CH10886. J.F.M.'s work at Argonne

National Laboratory (ANL), which is operated by UChicago Argonne LLC, and the APS facility, are supported under the U.S. DOE-OS Contract No. DE-AC02-06CH11357.

*bozin@bnl.gov

†Present address: Department of Physics, Missouri University of Science and Technology, Rolla, MO 65409, USA.

- [1] S. H. Pan *et al.*, *Nature (London)* **413**, 282 (2001).
- [2] S. Takeshita *et al.*, *Phys. Rev. Lett.* **103**, 027002 (2009).
- [3] E. Dagotto, *Science* **309**, 257 (2005).
- [4] J. Tao *et al.*, *Phys. Rev. Lett.* **103**, 097202 (2009).
- [5] S. J. L. Billinge *et al.*, *Phys. Rev. Lett.* **77**, 715 (1996).
- [6] S. J. L. Billinge and I. Levin, *Science* **316**, 561 (2007).
- [7] M. Hennion *et al.*, *Phys. Rev. Lett.* **94**, 057006 (2005).
- [8] J. Lee *et al.*, *Nature (London)* **442**, 546 (2006).
- [9] E. S. Božin *et al.*, *Phys. Rev. Lett.* **98**, 137203 (2007).
- [10] S. J. L. Billinge, *J. Solid State Chem.* **181**, 1695 (2008).
- [11] T. Egami and S. J. L. Billinge, *Underneath the Bragg Peaks: Structural Analysis of Complex Materials* (Pergamon Press, Elsevier, Oxford, England, 2003).
- [12] T. Furubayashi *et al.*, *J. Phys. Soc. Jpn.* **63**, 3333 (1994).
- [13] J. Matsuno *et al.*, *Phys. Rev. B* **55**, R15979 (1997).
- [14] S. Nagata *et al.*, *Phys. Rev. B* **58**, 6844 (1998).
- [15] H. Ishibashi *et al.*, *J. Magn. Magn. Mater.* **226–230**, 233 (2001).
- [16] P. G. Radaelli *et al.*, *Nature (London)* **416**, 155 (2002).
- [17] M. Croft *et al.*, *Phys. Rev. B* **67**, 201102 (2003).
- [18] R. Endoh, J. Awaka, and S. Nagata, *Phys. Rev. B* **68**, 115106 (2003).
- [19] K. Takubo *et al.*, *Phys. Rev. Lett.* **95**, 246401 (2005).
- [20] H. Ishibashi *et al.*, *Phys. Rev. B* **66**, 144424 (2002).
- [21] T. Furubayashi *et al.*, *Solid State Commun.* **126**, 617 (2003).
- [22] A. T. Burkov *et al.*, *Phys. Rev. B* **61**, 10049 (2000).
- [23] K. Takubo *et al.*, *Phys. Rev. B* **78**, 245117 (2008).
- [24] V. Kiryukhin *et al.*, *Phys. Rev. Lett.* **97**, 225503 (2006).
- [25] K. Kitamoto *et al.*, *Phys. Rev. B* **68**, 195124 (2003).
- [26] D. I. Khomskii and T. Mizokawa, *Phys. Rev. Lett.* **94**, 156402 (2005).
- [27] P. J. Chupas *et al.*, *J. Appl. Crystallogr.* **36**, 1342 (2003).
- [28] A. P. Hammersley *et al.*, *High Press. Res.* **14**, 235 (1996).
- [29] X. Qiu *et al.*, *J. Appl. Crystallogr.* **37**, 678 (2004).
- [30] H. J. Kim *et al.*, *Phys. Rev. Lett.* **96**, 226401 (2006).
- [31] P. Somasundaram *et al.*, *J. Appl. Phys.* **83**, 7243 (1998).
- [32] H. Suzuki *et al.*, *J. Phys. Soc. Jpn.* **68**, 2495 (1999).
- [33] S. Nagata *et al.*, *Physica (Amsterdam)* **194–196B**, 1077 (1994).
- [34] V. N. Andreev *et al.*, *Phys. Status Solidi B* **234**, 623 (2002).
- [35] S. Koshihara and S. Adachi, *J. Phys. Soc. Jpn.* **75**, 011005 (2006).
- [36] S. Iwai *et al.*, *Phys. Rev. Lett.* **96**, 057403 (2006).

Phase Diagram of $K_xFe_{2-y}Se_{2-z}S_z$ and the Suppression of its Superconducting State by an Fe2-Se/S Tetrahedron Distortion

Hechang Lei (雷和物),¹ Milinda Abeykoon,¹ Emil S. Bozin,¹ Kefeng Wang (王克锋),¹ J. B. Warren,² and C. Petrovic¹

¹Condensed Matter Physics and Materials Science Department, Brookhaven National Laboratory, Upton, New York 11973, USA

²Instrumentation Division, Brookhaven National Laboratory, Upton, New York 11973, USA

(Received 25 June 2011; published 19 September 2011)

We report structurally tuned superconductivity in a $K_xFe_{2-y}Se_{2-z}S_z$ ($0 \leq z \leq 2$) phase diagram. Superconducting T_c is suppressed as S is incorporated into the lattice, eventually vanishing at 80% of S. The magnetic and conductivity properties can be related to stoichiometry on a poorly occupied Fe1 site and the local environment of a nearly fully occupied Fe2 site. The decreasing T_c coincides with the increasing Fe1 occupancy and the overall increase in Fe stoichiometry from $z = 0$ to $z = 2$. Our results indicate that the irregularity of the Fe2-Se/S tetrahedron is an important controlling parameter that can be used to tune the ground state in the new superconductor family.

DOI: 10.1103/PhysRevLett.107.137002

PACS numbers: 74.62.Bf, 74.10.+v, 74.20.Mn, 74.70.Dd

The discovery of superconductivity in $K_xFe_{2-y}Se_2$ (AFeCh-122) with $T_c \approx 31$ K has triggered a renewed interest in the field of iron-based superconductors [1]. The crystal structure contains alkali metals and FeSe layers alternatively stacked along the c axis. When compared to other iron-based superconductors, AFeCh-122 show some distinctive features. Band structure calculations [2] and angle resolved photoemission spectroscopy measurements [3] indicate that the hole pockets are absent in the AFeCh-122 system. This is different from other iron-based superconductors where both electron and hole Fermi surfaces (FSs) are present [4], suggesting that unconventional pairing via FS nesting [5,6] might not be suitable for these materials. Experiments observed short and possibly long range magnetic order and its coexistence with superconductivity [7–9]. This is quite different from previous iron-based superconductors where superconductivity emerges when the spin density wave state is suppressed [10]. Finally, the role of the ordered Fe vacancy and its relations to the magnetic order, metallic state, and superconductivity remain unresolved.

Isovalent substitution is an effective way to study the relationship between structural parameters and physical properties. It is similar to pressure effects, because it should not change the carrier density. Unlike in the cuprates, superconductivity has been induced or enhanced by isovalent doping in iron-based superconductors, such as $BaFe_2(As_{1-x}P_x)_2$ and $FeTe_{1-x}Se_x$ [11,12]. Recently, it was discovered that $K_xFe_{2-y}S_2$, isostructural to $K_xFe_{2-y}Se_2$, exhibits a spin glass (SG) semiconductor ground state without superconducting transition [13]. Here, we report the evolution of physical properties and structural parameters of $K_xFe_{2-y}Se_{2-z}S_z$ ($0 \leq z \leq 2$) single crystals. The results indicate that suppression of superconducting T_c coincides with the increasing occupancy of Fe on both Fe1 and Fe2 sites with S substitution, in contrast to $(Tl, K)_xFe_{2-y}Se_2$ [14]. It is found that the regularity of

the Fe2-Ch (Ch = Se, S) tetrahedron is an important controlling parameter for electronic and magnetic properties and has a major influence on electron pairing, i.e., on T_c .

Single crystals of $K_xFe_{2-y}Se_{2-z}S_z$ were grown as described previously [13,15]. Powder X-ray diffraction (XRD) data were collected at 300 K using 0.3184 Å wavelength radiation (38.94 keV) at the X7B beam line of the National Synchrotron Light Source. Refinements of the XRD data were performed using General Structure Analysis System [16,17]. The average stoichiometry was determined by energy-dispersive x-ray spectroscopy in a JEOL JSM-6500 scanning electron microscope. Electrical transport and magnetization measurements were carried out in Quantum Design PPMS-9 and MPMS-XL5.

XRD patterns of all $K_xFe_{2-y}Se_{2-z}S_z$ show (110) and other superlattice reflections associated with $I4/m$ symmetry that incorporates an Fe ordered vacancy site [Fig. 1(a)]. The structure is shown in the inset of Fig. 1(b). The peak position of (110) shifts to a higher angle with increasing S content, which indicates that the lattice contracts gradually with S doping [Fig. 1(b) and Table I], due to the smaller ionic size of S^{2-} than Se^{2-} . The trend of lattice contraction approximately follows Vegard's law. The sum of Se and S stoichiometry in grown crystals is near 2.0, whereas both potassium and iron deviate from full occupancy (Table I) [13,15]. This is commonly found in all AFeCh-122 compounds [1,13,18]. It should be noted that the Fe content increases gradually with S doping, while the K content does not change monotonically. In addition, doping S into the Se site does not lead to random Fe occupation of Fe1 and Fe2 sites. The refinements show that the Fe1 site is poorly occupied, whereas the Fe2 site is almost fully occupied.

The superconductivity of $K_xFe_{2-y}Se_{2-z}S_z$ single crystals with $z < 1.58$ is confirmed by the magnetization measurement [Fig. 2(a)]. Zero-field-cooling (ZFC) superconducting transitions shift to low temperature with higher

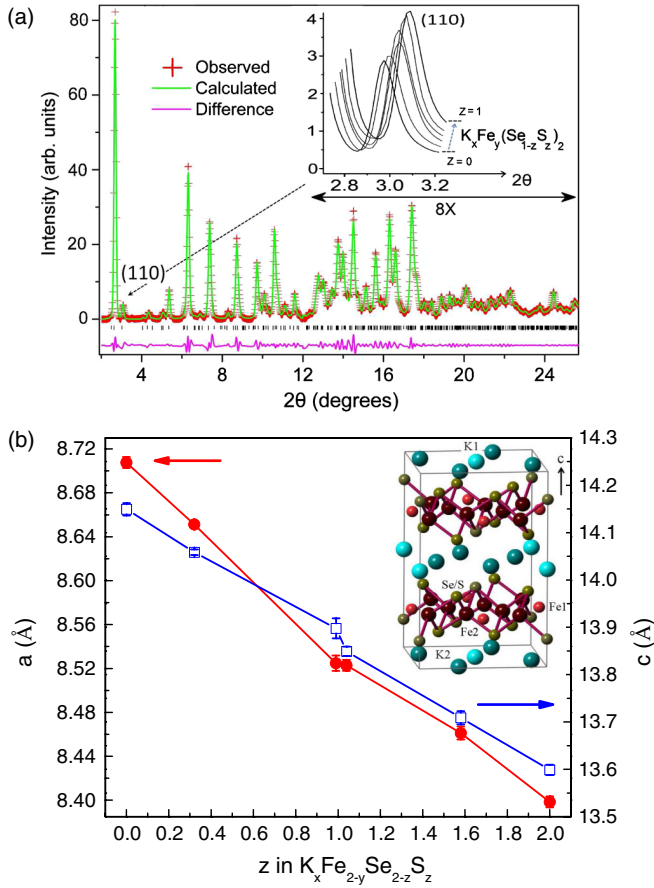


FIG. 1 (color online). (a) Powder XRD patterns of $K_xFe_{2-y}Se_{2-z}S_z$ at 300 K and fit using a $I4/m$ space group. Inset: (110) peak position with different S content. (b) Unit cell parameters as a function of the S substitution. Inset: Crystal structure of $K_xFe_{2-y}Se_{2-z}S_z$ in a $I4/m$ unit cell with vacant Fe1 sites marked light red (light grey) and Fe2 sites marked dark purple (dark grey).

S content. Field-cooling (FC) susceptibilities are very small [Fig. 2(a)], implying possible strong vortex pinning. The most interesting feature in the temperature dependence of magnetization is the absence of the Curie-Weiss law for all samples above 50 K as shown in Figs. 2(b) and 2(c) for $H \parallel ab$ and $H \parallel c$, respectively. Magnetic susceptibilities are weakly temperature dependent with no significant

anomalies above 50 K. This might suggest the presence of low dimensional short-range magnetic correlations and/or a long range antiferromagnetic order above 300 K. This has been observed in $K_xFe_{2-y}Se_2$ crystals with different K and Fe site occupancies [7,9]. Therefore, the magnetic interactions above 50 K are similar in the whole alloy series. On the other hand, nonsuperconducting samples show bifurcation between the ZFC and FC curves for both field orientations. The irreversible behavior suggests SG transition at low temperatures near $z = 2$ [13]. The spin glass freezing temperatures T_f for nonsuperconducting samples are determined from the maximum position of $\chi_{ab}(T)$ in ZFC curves and listed in Table I. The S-shape $M(H)$ curves [Fig. 2(d)] at 1.8 K for $z = 1.58$ and $z = 2$ are similar [13,19]. Hence, the SG state most likely persists in the $1.58 \leq z \leq 2$ range.

Besides $K_xFe_{2-y}S_2$, all other crystals show metallic behavior below a resistivity maximum ρ_{max} above the superconducting transition [Fig. 3(a)]. It should be noted that the temperature of ρ_{max} is not monotonic with the doping level of S (z), implying that the crossover may be influenced by the amount of both K and Fe deficiencies (Table I). On the other hand, the crystal with $z = 2$ is semiconducting even if the Fe deficiency is smaller than in other samples. In contrast to ρ_{max} , with the increase in S, the T_c is monotonically suppressed to a lower temperature and can not be observed above 2 K for $z \geq 1.58$ (Table I). We present the magnetic and superconducting phase diagram of $K_xFe_{2-y}Se_{2-z}S_z$ in Fig. 3(b). The semiconductor-metal crossover can be traced for $0 \leq z \leq 1.58$ at high temperature. In this region, $K_xFe_{2-y}Se_{2-z}S_z$ is a superconducting metal at low temperature. For $z = 1.58$, $\rho(T)$ is metallic with no superconducting T_c down to 2 K. For $1.58 \leq z \leq 2$, we observe a drop in $\chi - T$ curves that could be related to a SG transition. For $z = 2$, the $K_xFe_{2-y}Se_{2-z}S_z$ becomes a small gap semiconductor with no metallic crossover and with a SG transition below 32 K.

The gradual changes of T_c are difficult to explain by the slight variation of Fe and K contents, because the T_c variation found with S doping is rather different from T_c variations due to K and Fe differences [14,18,20]. It was shown that the superconductivity appears with higher

TABLE I. Structural, magnetic, and transport properties of $K_xFe_{2-y}Se_{2-z}S_z$. T_f is determined from a maximum position of $\chi_{ab}(T)$ in a zero-field-cooling curve. $T_{\rho_{max}}$, $T_{c,onset}$, and $T_{c,0}$ are obtained from resistivity data. Error bars for T_c , T_f , and $T_{\rho_{max}}$ reflect the standard deviation from the average temperatures measured on several crystals grown in one batch.

$K_xFe_{2-y}Se_{2-z}S_z$	a (Å)	c (Å)	$T_{c,onset}$ (K)	$T_{c,0}$ (K)	T_f (K)	$T_{\rho_{max}}$ (K)
$K_{0.64(4)}Fe_{1.44(4)}Se_{2.00(0)}$	3.911(2)	14.075(3)	33(1)	31(1)		132(6)
$K_{0.73(3)}Fe_{1.44(3)}Se_{1.68(6)}S_{0.32(5)}$	3.847(2)	14.046(4)	33(1)	31(1)		129(4)
$K_{0.70(7)}Fe_{1.55(7)}Se_{1.01(2)}S_{0.99(2)}$	3.805(2)	13.903(6)	24(2)	21(1)		203(20)
$K_{0.76(5)}Fe_{1.61(5)}Se_{0.96(4)}S_{1.04(5)}$	3.797(2)	13.859(3)	18(1)	16(2)		138(5)
$K_{0.80(8)}Fe_{1.64(8)}Se_{0.42(5)}S_{1.58(0.05)}$	3.781(2)	13.707(2)			17(1)	79(14)
$K_{0.80(1)}Fe_{1.72(1)}S_{2.00(1)}$	3.753(2)	13.569(3)			32(1)	

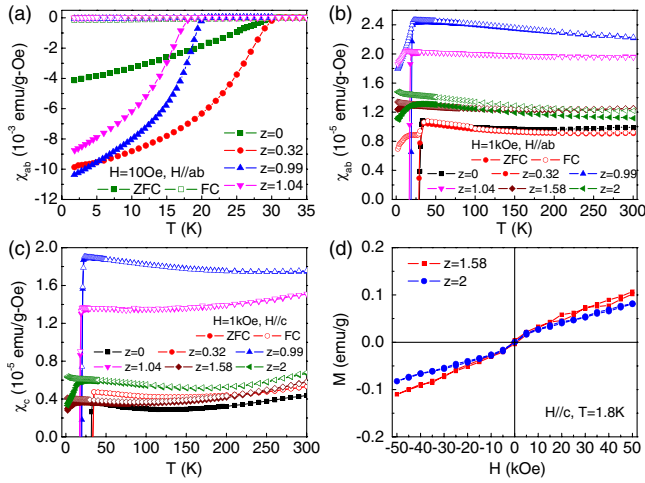


FIG. 2 (color online). (a) dc magnetic susceptibility of superconducting $K_xFe_{2-y}Se_{2-z}S_z$ samples below 35 K at $H = 10$ Oe for $H \parallel ab$ in ZFC and FC. (b) and (c) Temperature dependence of $\chi(T)$ of $K_xFe_{2-y}Se_{2-z}S_z$ at $H = 1$ kOe for $H \parallel ab$ and $H \parallel c$ in ZFC and FC, respectively. (d) M-H loops of nonsuperconducting samples at 1.8 K for $H \parallel c$.

Fe content when K content (x) < 0.85 [18,20]. As opposed to this trend, the $K_xFe_{2-y}Se_{2-z}S_z$ crystals with larger z values have higher Fe content but lower T_c .

Why is $K_xFe_{2-y}Se_2$ a superconductor whereas $K_xFe_{2-y}S_2$ is a semiconductor even though S is an isovalent substitution, similar to $FeTe_{1-x}Se_x$ [12]? This indicates that T_c is not only governed by K/Fe stoichiometry or vacancies. Below we show that superconductivity is in fact tuned by subtle structural effects induced by stoichiometry variation. The local environment of Fe profoundly changes with S, inducing the evolution of the band structure and changes of physical properties. In the $K_xFe_{2-y}Se_{2-z}S_z$ crystal structure, Fe atoms have a block-like distribution where every four Fe2 atoms form a square around a Se atom, making a cluster distinct from the Fe1 site with low occupancy [21,22]. Therefore there are Fe1-Fe2 distances as well as intra- and intercluster Fe2-Fe2 distances. The three types of distances are shown in Fig. 4(a). All cluster distances are unchanged with S doping whereas the Fe1-Fe2 distances decrease significantly [Fig. 4(a)]. Similar magnetization behavior above 50 K and rather different superconducting T_c 's as S content varies from 0 to 2 coincides with the nearly unchanged Fe2-Fe2 bond lengths. This shows that superconductivity is insensitive to the size of Fe2-Fe2 clusters whereas the unchanged high temperature magnetism could be related to the unchanged Fe2-Fe2 bond lengths. On the other hand, the SG behavior arising at the low temperature for non-superconducting samples can be explained by the nonzero random occupancy of the Fe1 (vacancy) site for higher S content [Fig. 4(b)], randomly changing the intercluster exchange interactions [23].

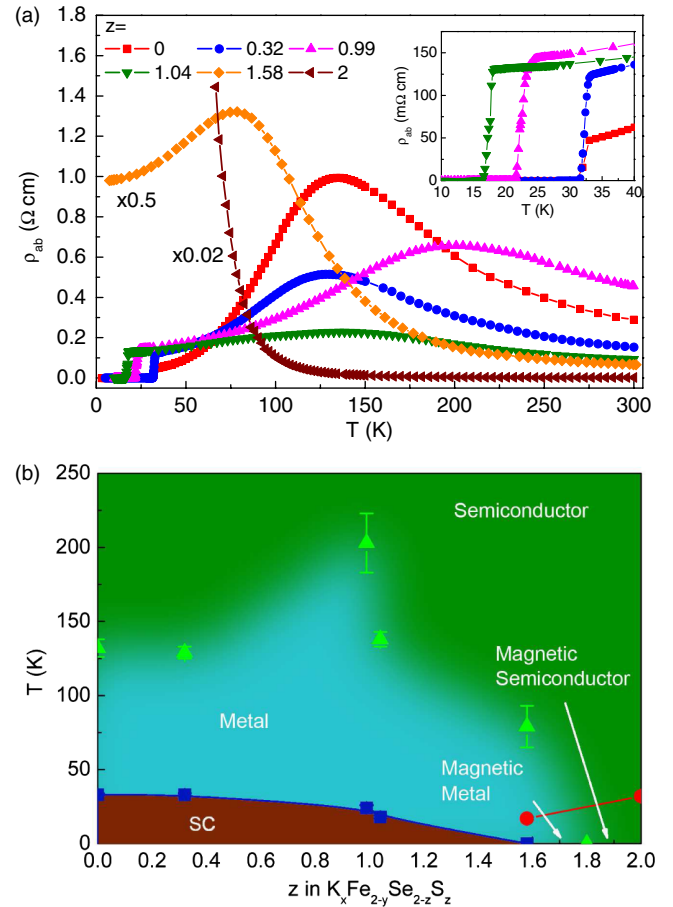


FIG. 3 (color online). (a) Temperature dependence of the in-plane resistivity $\rho_{ab}(T)$ of the $K_xFe_{2-y}Se_{2-z}S_z$ single crystals in a zero field. Inset: Temperature dependence of $\rho_{ab}(T)$ below 40 K for $0 \leq z \leq 1.2$. (b) Magnetic and superconducting phase diagram of $K_xFe_{2-y}Se_{2-z}S_z$. Green, blue, and orange colors show semiconducting, magnetic, and superconducting regions, respectively. Red symbols denote spin glass transitions.

According to the empirical rule proposed by Mizuguchi *et al.*, the critical temperature is closely correlated with the anion height between Fe and Pn (Ch) layers and there is an optimal distance (~ 1.38 Å) with a maximum transition temperature $T_c \sim 55$ K [24]. This is invalid in $K_xFe_{2-y}Se_{2-z}S_z$ materials, where there are two Fe and two Ch sites and four Fe-Ch heights. This is because there is no monotonic decrease as T_c is tuned to 0 [Fig. 4(c)], whereas both Se and S end members have rather similar anion heights.

The bond angle α between Pn(Ch)-Fe-Pn(Ch) is another important factor since T_c in iron pnictides is optimized when the Fe-Pn (Ch) tetrahedron is regular ($\alpha = 109.47^\circ$) [25]. In $K_xFe_{2-y}Se_{2-z}S_z$, the Ch2-Fe1-Ch2 angle changes towards the optimal value with increasing S [Fig. 4(d)], but the local environment of Fe2 exhibits an inverse trend. Among the six angles in the Fe2-Ch1(2) tetrahedron, three (Ch1-Fe2-Ch2) are nearly unchanged with S doping

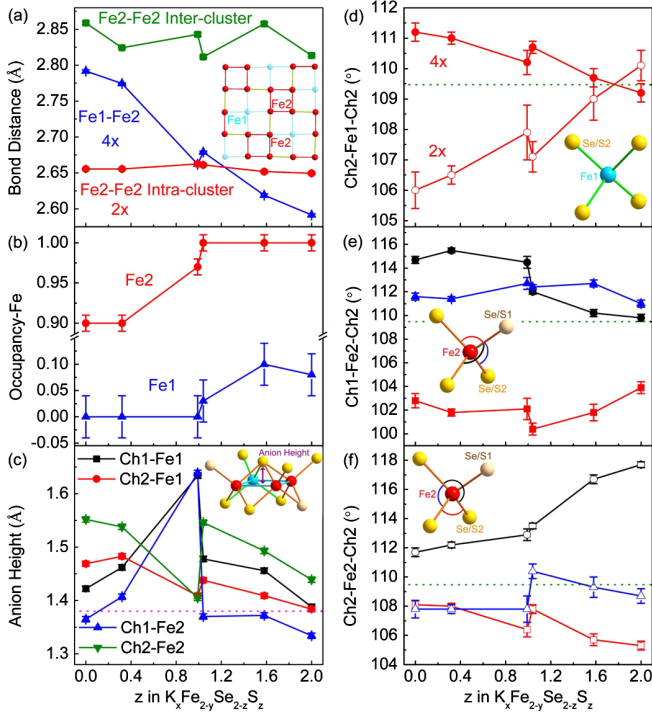


FIG. 4 (color online). (a) Bond lengths between Fe1(2) and Fe1(2). Inset shows top view of the Fe layer. (b) Occupancy of Fe1 and Fe2. (c) Anion height. Inset shows side view of Fe-Ch sheet. (d) Ch2-Fe1-Ch2, (e) Ch1-Fe2-Ch2, and (f) Ch2-Fe2-Ch2 bond angles of $K_xFe_{2-y}Se_{2-z}S_z$ as a function of S substitution, x . Insets of (d)–(f) show the Fe-Ch tetrahedron for Fe1-Ch1 and Fe2-Ch1(2). The dotted pink line in (c) shows the optimal bond lengths for T_c . The dotted green lines in (d)–(f) indicate the optimal angle for T_c .

[Fig. 4(e)]. The other three (Ch1-Fe2-Ch1) change significantly (maximum 6°) and deviate from the optimal value from the Se rich to the S rich side [Fig. 4(f)]. Hence, the increasing distortion of the Fe2-Ch tetrahedron with S doping is closely correlated to the suppression of T_c . This distortion may lead to carrier localization and/or a decrease in the density of states at the FS. Therefore, the regularity of the Fe2-Ch1(2) tetrahedron is the key structural factor in the formation of the metallic states in $K_xFe_{2-y}Se_{2-z}S_z$, and consequently, the T_c . The dispersion of tetrahedral angles from 109.47° increases with the S content increase.

We have demonstrated the structure tuning of superconductivity in $K_xFe_{2-y}Se_{2-z}S_z$ single crystals. For low S doping, the superconducting T_c is nearly the same as in the pure material. With the increase of S above $z = 1$, the T_c is gradually suppressed, finally vanishing at 80% of the S substitution. Conductivity and magnetic properties coincide with stoichiometry changes on the Fe1 site and with particular changes of the local environment of the Fe2 site. Nearly unchanged Fe2-Fe2 bond lengths result in the similar magnetic behavior. The suppression of

superconductivity with S doping could be traced to the increasing irregularity of the Fe2-Ch tetrahedron and to an increasing occupancy of the Fe1 site. These ultimately destroy superconductivity and bring about a glassy magnetic order and semiconducting ground state.

We thank Jonathan Hanson for help with the XRD experiment. Work at Brookhaven is supported by the U.S. DOE under Contract No. DE-AC02-98CH10886 and, in part, by the Center for Emergent Superconductivity, an Energy Frontier Research Center funded by the U.S. DOE, Office for Basic Energy Science.

- [1] J. Guo, S. Jin, G. Wang, S. Wang, K. Zhu, T. Zhou, M. He, and X. Chen, *Phys. Rev. B* **82**, 180520(R) (2010).
- [2] I. R. Shein and A. L. Ivanovskii, *Phys. Lett. A* **375**, 1028 (2011).
- [3] Y. Zhang, L. X. Yang, M. Xu, Z. R. Ye, F. Chen, C. He, J. Jiang, B. P. Xie, J. J. Ying, X. F. Wang, X. H. Chen, J. P. Hu, and D. L. Feng, *Nature Mater.* **10**, 273 (2011).
- [4] H. Ding, P. Richard, K. Nakayama, K. Sugawara, T. Arakane, Y. Sekiba, A. Takayama, S. Souma, T. Sato, T. Takahashi, Z. Wang, X. Dai, Z. Fang, G. F. Chen, J. L. Luo, and N. L. Wang, *Europhys. Lett.* **83**, 47001 (2008).
- [5] I. I. Mazin, D. J. Singh, M. D. Johannes, and M. H. Du, *Phys. Rev. Lett.* **101**, 057003 (2008).
- [6] K. Kuroki, S. Onari, R. Arita, H. Usui, Y. Tanaka, H. Kontani, and H. Aoki, *Phys. Rev. Lett.* **101**, 087004 (2008).
- [7] D. A. Torchetti, M. Fu, D. C. Christensen, K. J. Nelson, T. Imai, H. C. Lei, and C. Petrovic, *Phys. Rev. B* **83**, 104508 (2011).
- [8] V. Yu. Pomjakushin, D. V. Sheptyakov, E. V. Pomjakushina, A. Krzton-Maziopa, K. Conder, D. Chernyshov, V. Svitlyk, and Z. Shermadini, *Phys. Rev. B* **83**, 144410 (2011).
- [9] V. Yu. Pomjakushin, E. V. Pomjakushina, A. Krzton-Maziopa, K. Conder, and Z. Shermadini, *J. Phys. Condens. Matter* **23**, 156003 (2011).
- [10] C. de la Cruz, Q. Huang, J. W. Lynn, J. Y. Li, W. Ratcliff II, J. L. Zarestky, H. A. Mook, G. F. Chen, J. L. Luo, N. L. Wang, and P. C. Dai, *Nature (London)* **453**, 899 (2008).
- [11] S. Jiang, H. Xing, G. F. Xuan, C. Wang, Z. Ren, C. M. Feng, J. H. Dai, Z. A. Xu, and G. H. Cao, *J. Phys. Condens. Matter* **21**, 382203 (2009).
- [12] K.-W. Yeh, T. W. Huang, Y. L. Huang, T. K. Chen, F. C. Hsu, P. M. Wu, Y. C. Lee, Y. Y. Chu, C. L. Chen, J. Y. Luo, D. C. Yan, and M. K. Wu, *Europhys. Lett.* **84**, 37002 (2008).
- [13] H. C. Lei, M. Abeykoon, E. S. Bozin, and C. Petrovic, *Phys. Rev. B* **83**, 180503(R) (2011).
- [14] M. H. Fang, H. D. Wang, C. H. Dong, Z. J. Li, C. M. Feng, J. Chen, and H. Q. Yuan, *Europhys. Lett.* **94**, 27009 (2011).
- [15] H. C. Lei, and C. Petrovic, *Phys. Rev. B* **83**, 184504 (2011).

- [16] A. C. Larson and R. B. Von Dreele, Los Alamos National Laboratory, Report No. LAUR 86-748, 1994.
- [17] B. H. Toby, *J. Appl. Crystallogr.* **34**, 210 (2001).
- [18] D. M. Wang, J. B. He, T.-L. Xia, and G. F. Chen, *Phys. Rev. B* **83**, 132502 (2011).
- [19] J. J. Ying, A. F. Wang, Z. J. Xiang, X. G. Luo, R. H. Liu, X. F. Wang, Y. J. Yan, M. Zhang, G. J. Ye, P. Cheng, and X. H. Chen, [arXiv:1012.2929](https://arxiv.org/abs/1012.2929).
- [20] Y. J. Yan, M. Zhang, A. F. Wang, J. J. Ying, Z. Y. Li, W. Qin, X. G. Luo, J. Q. Li, J. P. Hu, and X. H. Chen, [arXiv:1104.4941](https://arxiv.org/abs/1104.4941).
- [21] W.-G. Yin, C.-H. Lin, and W. Ku, [arXiv:1106.0881](https://arxiv.org/abs/1106.0881).
- [22] W. Bao, G. N. Li, Q. Huang, G. F. Chen, J. B. He, M. A. Green, Y. Qiu, D. M. Wang, and J. L. Luo, [arXiv:1102.3674](https://arxiv.org/abs/1102.3674).
- [23] M. Oledzka, K. V. Ramanujachary, and M. Greenblatt, *Mater. Res. Bull.* **31**, 1491 (1996).
- [24] Y. Mizuguchi, Y. Hara, K. Deguchi, S. Tsuda, T. Yamaguchi, K. Takeda, H. Kotegawa, H. Tou, and Y. Takano, *Supercond. Sci. Technol.* **23**, 054013 (2010).
- [25] C.-H. Lee, A. Iyo, H. Eisaki, H. Kito, M. T. Fernandez-Diaz, T. Ito, K. Kihou, H. Matsuhata, M. Braden, and K. Yamada, *J. Phys. Soc. Jpn.* **77**, 083704 (2008).

Vacancy-induced nanoscale phase separation in $K_xFe_{2-y}Se_2$ single crystals evidenced by Raman scattering and powder x-ray diffraction

N. Lazarević,¹ M. Abeykoon,² P. W. Stephens,^{3,4} Hechang Lei (雷和畅),² E. S. Bozin,² C. Petrovic,² and Z. V. Popović¹

¹*Center for Solid State Physics and New Materials, Institute of Physics Belgrade, University of Belgrade, Pregrevica 118, 11080 Belgrade, Serbia*

²*Condensed Matter Physics and Materials Science Department, Brookhaven National Laboratory, Upton, New York 11973-5000, USA*

³*Department of Physics and Astronomy, State University of New York, Stony Brook, NY 11794-3800, USA*

⁴*Photon Sciences Directorate, Brookhaven National Laboratory, Upton, New York 11973-5000, USA*

(Received 7 May 2012; revised manuscript received 10 July 2012; published 6 August 2012)

Polarized Raman scattering spectra of $K_xFe_{2-y}Se_2$ were analyzed in terms of peculiarities of both $I4/m$ and $I4/mmm$ space group symmetries. The presence of the Raman active modes from both space group symmetries (16 Raman-active modes of the $I4/m$ phase and two Raman-active modes of the $I4/mmm$ phase) confirmed the existence of two crystallographic domains with different space group symmetry in a $K_xFe_{2-y}Se_2$ sample. High-resolution synchrotron powder x-ray diffraction structural refinement of the same sample confirmed the two-phase description, and determined the atomic positions and occupancies for both domains.

DOI: [10.1103/PhysRevB.86.054503](https://doi.org/10.1103/PhysRevB.86.054503)

PACS number(s): 78.30.-j, 74.25.-q, 61.05.cp, 61.72.jd

The recent discovery of block checkerboard antiferromagnetic order of superconducting materials $A_xFe_{2-y}Se_2$ ($A = K, Rb, Cs, \text{ and } Tl$) has invoked considerable debate in the scientific community.¹⁻⁶ It was shown that the appearance of antiferromagnetism is a consequence of the Fe vacancy ordering.^{7,8} These unique properties among the superconductors opened a question whether Fe vacancies stabilize or destroy the superconductivity. Very recently, scanning tunneling microscopy (STM) measurements,⁹ conducted on $K_xFe_{2-y}Se_2$ thin films grown by molecular beam epitaxy, revealed that the $K_xFe_{2-y}Se_2$ sample contains two distinct phases: an insulating phase with well defined $\sqrt{5} \times \sqrt{5}$ order of Fe vacancies, and a superconducting KFe_2Se_2 phase containing no Fe vacancies. It was found that the presence of a single Fe vacancy locally destroys superconductivity.⁹ Recent Angle-resolved photoemission spectroscopy (ARPES) and optical measurements combined with TEM analysis^{10,11} also show the presence of the nanoscale phase separation between superconducting and antiferromagnetic phases in bulk crystals.

Raman scattering (RS) measurements of $K_xFe_{2-y}Se_2$ were analyzed, to the best of our knowledge, only in Ref. 12. Zhang *et al.*¹² performed partial assignment: 11 out of 18 Raman-active modes predicted by factor-group analysis (FGA) within the $I4/m$ symmetry group. They found that only one mode around 180 cm^{-1} exhibits a change in frequency around T_c . However, the origin of this mode remained unclear.

In this paper, RS is used to determine the influence of vacancy ordering on phonon spectra of $K_xFe_{2-y}Se_2$ single crystals. The polarized Raman spectra were analyzed in terms of peculiarities of both the $I4/m$ and $I4/mmm$ space group symmetries. Sixteen out of eighteen Raman-active phonons of the $I4/m$ and two Raman-active phonons of the $I4/mmm$ phase, predicted by FGA for our measurement configuration, have been observed and assigned. This confirms the existence of two crystallographic domains in our sample. High-resolution powder x-ray diffraction (PXRD) measurements on the same sample also indicate that the sample has coexisting $I4/m$ and $I4/mmm$ regions.

Single crystals of $K_xFe_{2-y}Se_2$ were grown and treated by the post-annealing and quenching technique described elsewhere in detail.^{13,14} Before starting the RS measurements, the samples were cleaved in order to obtain a flat and shiny (001)-plane surface. The RS measurements were performed using a TriVista 557 Raman system in backscattering micro-Raman configuration. The 514.5 nm line of an Ar^+/Kr^+ mixed gas laser was used as an excitation source. The corresponding excitation power density was less than 0.2 kW/cm^2 . All measurements were performed in the vacuum by using a KONTI CryoVac continuous helium flow cryostat with a 0.5 mm thick window.

PXRD measurements at room temperature and $400 \text{ }^\circ\text{C}$ were carried out at the X16C beamline of the National Synchrotron Light Source at Brookhaven National Laboratory. The measurements were made on the same sample, several months after preparation and the Raman experiments. The sample was sealed in a 1 mm diameter glass capillary with Si as an internal standard and dilutant, and diffraction data collected at a wavelength of 0.5612 \AA from a channel-cut Si(111) monochromator and Ge(111) analyzer. PXRD results¹⁵ were Rietveld refined with TOPAS Academic software;¹⁶ see Fig. 1.

The sample's composition was previously measured by x-ray spectroscopy in an electron microscope to be $K_{0.64(4)}Fe_{1.44(4)}Se_2$.¹⁷ A PXRD pattern at $400 \text{ }^\circ\text{C}$ refined to a single phase of composition $K_{0.72(4)}Fe_{1.60(4)}Se_2$. While the results of these two measurements differ by more than the stated uncertainty, we do not believe they are in disagreement due to possible systematic errors in both measurement techniques. The room-temperature data were analyzed as a mixture of two phases: an $I4/mmm$ phase structurally identical to the high-temperature structure, and the Fe vacancy-ordered $\sqrt{5} \times \sqrt{5}$ $I4/m$ phase. This two-phase description is in agreement with the recent STM study.⁹ A fit to a single-phase model in $I4/m$ with partial vacancy ordering is significantly worse than the two-phase model ($\chi^2 = 2.88$ vs 2.28), and can therefore be excluded. The refined composition of the sample is $K_{0.68(2)}Fe_{1.57(3)}Se_2$, in satisfactory agreement with both the high-temperature PXRD and the x-ray spectroscopy results.

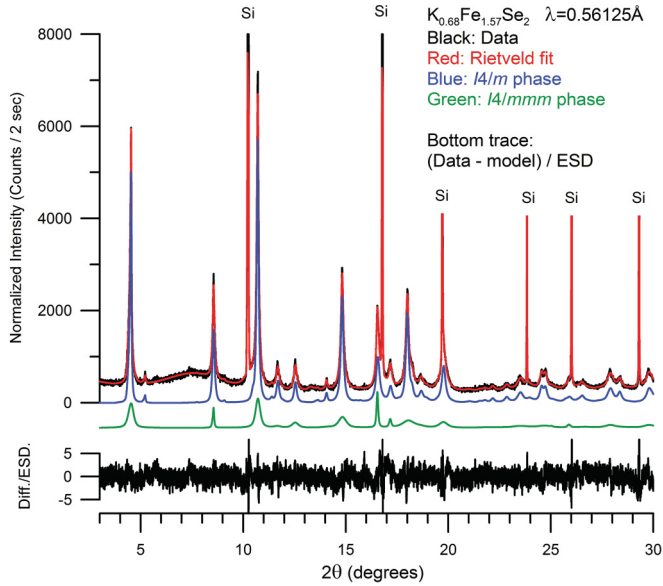


FIG. 1. (Color online) PXRD diffraction data with Rietveld fit, showing separate contributions from $I4/m$ and $I4/mmm$ phases. Peaks from the Si internal standard, in both the main plot and the scaled difference curve, are truncated. This fit has weighted R factor $R_{WP} = 5.90\%$ and $\chi^2 = 2.28$.

Unit cells for both phases are built up of interspersed FeSe slabs and nets of K, stacked along the z axis; see Fig. 2. Refined atomic positions and occupancies of both phases are listed in Table I. Note that the refined occupancy of the iron sites in the superconducting $I4/mmm$ phase is unity, within its standard uncertainty. On the other hand, neither Fe site in the $\sqrt{5} \times \sqrt{5}$ $I4/m$ phase is fully occupied.

One feature of note from the PXRD refinement (Fig. 1) is that the diffraction peaks of the $I4/mmm$ phase are substantially broader than those of the $I4/m$ phase. It is difficult to quantify the effect, because $I4/mmm$ peaks overlap the strongest $I4/m$ peaks and both phases exhibit significant anisotropic microstrain broadening; an estimate from the Scherrer equation leads to an $I4/mmm$ domain size on the order of 100 nm.

According to symmetry considerations one can expect four Raman-active phonons for the $I4/mmm$ phase and 27

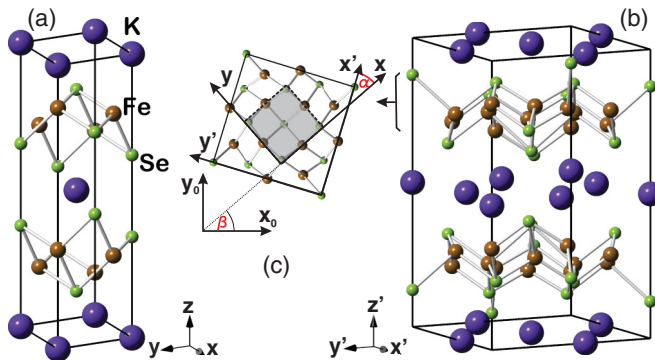


FIG. 2. (Color online) Crystal structure of $K_xFe_{2-y}Se_2$ in (a) $I4/mmm$ and (b) $I4/m$ unit cells (black lines). (c) FeSe slab in the (001) plane. The solid line illustrates the $I4/m$ unit cell and the shaded square illustrates the $I4/mmm$ unit cell.

TABLE I. Structural parameters for the $K_xFe_{2-y}Se_2$ two-phase powder sample at room temperature. Standard uncertainties given in parentheses are derived from counting statistics, and are generally smaller than plausible estimates of accuracy.

Phase I					
Space group $I4/mmm$					
Lattice $a = 3.898(1)$ Å, $c = 14.091(4)$ Å					
Mole fraction 19(1)%					
Atom	Site	x	y	z	Occ
K	2a	0	0	0	0.82(4)
Fe	4d	0	0.5	0.25	0.99(3)
Se	4e	0	0	0.354(1)	1
Phase II					
Space group $I4/m$					
Lattice $a = 8.703(3)$ Å, $c = 14.160(1)$ Å					
Mole fraction 81(1)%					
Atom	Site	x	y	z	Occ
K1	2b	0	0	0.5	1.00(6)
K2	8h	0.583(4)	0.242(2)	0.5	0.56(2)
Fe1	16i	0.296(1)	0.596(1)	0.247(1)	0.84(1)
Fe2	4d	0	0.5	0.25	0.33(2)
Se1	4e	0	0	0.139(1)	1
Se2	16i	-0.089(1)	0.302(1)	0.353(1)	1

Raman-active phonons for the $I4/m$ phase (Table II). When Raman scattering is measured at the (001) plane of the $K_xFe_{2-y}Se_2$ sample, two Raman-active phonons ($A_{1g} + B_{1g}$) of the $I4/mmm$ phase and 18 Raman-active phonons ($9A_g + 9B_g$) of the $I4/m$ phase can be observed. Here, one must have in mind that the x' and y' axes of the $I4/m$ phase are rotated by an angle α ($-\alpha$ for the twin domain),¹⁸ to the corresponding axes (x and y) of the $I4/mmm$ phase; see Fig. 2.

In general, the intensity of a given Raman-active phonon can be expressed as $I \sim |\mathbf{e}_s \hat{R} \mathbf{e}_i|^2$, where \mathbf{e}_i and \mathbf{e}_s are incident and scattered light polarization vectors.¹⁹ \hat{R} is Raman scattering tensor, a 3×3 complex matrix which describes the properties of the phonon with the respect to Raman scattering, expressed in the crystal principal axes basis. In order to obtain proper selection rules for $I4/mmm$ and $I4/m$ domains for the arbitrary crystal orientation (see Fig. 2), we have to transform the corresponding Raman tensors in terms of laboratory coordinate system $x_0y_0z_0$, $\hat{R}^{x_0y_0z_0} = \Phi \hat{R}^{xyz} \Phi^\dagger$. When measuring the Raman intensity of a phonon with polarization vectors \mathbf{e}_s and \mathbf{e}_i along the main axes of the Raman tensor, only the absolute value of one tensor component contributes to the Raman intensity. However, in other scattering geometries, where \mathbf{e}_s and \mathbf{e}_i are not parallel to the main axes of \hat{R} , the relative phase difference between Raman tensor elements influences the strength of the scattering process. For our scattering configuration in which $x_0 \parallel \mathbf{e}_s$ and $\Theta = \angle(\mathbf{e}_s, \mathbf{e}_i)$, the Raman intensities for the Raman tensors represented in Table II are given by

$$\begin{aligned}
 I_{A_g}(\theta) &\sim |a|^2 \cos^2 \theta, & I_{A_{1g}}(\theta) &\sim |a|^2 \cos^2 \theta, \\
 I_{B_g}(\theta) &\sim (c' \cos[\theta + 2(\beta \pm \alpha)] + d' \sin[\theta + 2(\beta \pm \alpha)])^2, \\
 I_{B_{1g}}(\theta) &\sim |c|^2 \cos^2(\theta + 2\beta).
 \end{aligned} \tag{1}$$

Figure 3(a) displays $I(\theta)$ according to Eqs. (1) for one arbitrary choice of parameters with $\alpha = 27^\circ$ and $\beta = 50^\circ$. As can be

TABLE II. The type of atoms together with their site symmetries, each site's contributions to the Γ point phonons, as well as Raman tensors, phonon activities and selection rules for both $I4/mmm$ and $I4/m$ phases.

$I4/mmm$ (D_{4h}^{17} and $Z^B = 1$)		$I4/m$ (C_{4h}^5 and $Z^B = 5$)	
Atoms (site symmetry)	Irreducible representations	Atoms (site symmetry)	Irreducible representations
K (D_{4h})	$A_{2u} + E_u$	K1 (C_{4h})	$A_u + E_u$
Fe (D_{2d})	$A_{2u} + B_{1g} + E_g + E_u$	K2 (C_s)	$2A_g + A_u + 2B_g + B_u + E_g + 2E_u$
Se (C_{4v})	$A_{1g} + A_{2u} + E_g + E_u$	Fe1 (C_1)	$3A_g + 3A_u + 3B_g + 3B_u + 3E_g + 3E_u$
		Fe2 (S_4)	$A_u + B_g + E_g + E_u$
		Se1 (C_4)	$A_g + A_u + E_g + E_u$
		Se2 (C_1)	$3A_g + 3A_u + 3B_g + 3B_u + 3E_g + 3E_u$

Raman tensors			
$\hat{R}_{A_{1g}}^{xyz} = \begin{pmatrix} a e^{i\varphi_a} & 0 & 0 \\ 0 & a e^{i\varphi_a} & 0 \\ 0 & 0 & b e^{i\varphi_b} \end{pmatrix}$	$\hat{R}_{B_{1g}}^{xyz} = \begin{pmatrix} c e^{i\varphi_c} & 0 & 0 \\ 0 & - c e^{i\varphi_c} & 0 \\ 0 & 0 & 0 \end{pmatrix}$	$\hat{R}_{A_g}^{x'y'z} = \begin{pmatrix} a' e^{i\varphi'_a} & 0 & 0 \\ 0 & a' e^{i\varphi'_a} & 0 \\ 0 & 0 & b' e^{i\varphi'_b} \end{pmatrix}$	$\hat{R}_{B_g}^{x'y'z} = \begin{pmatrix} c' e^{i\varphi'_c} & d' e^{i\varphi'_d} & 0 \\ d' e^{i\varphi'_d} & - c' e^{i\varphi'_c} & 0 \\ 0 & 0 & 0 \end{pmatrix}$

Activity and selection rules		Activity and selection rules	
$\Gamma_{\text{Raman}} = A_{1g}(\alpha_{xx+yy}, \alpha_{zz}) + B_{1g}(\alpha_{xx-yy}) + 2E_g(\alpha_{xz}, \alpha_{yz})$	$\Gamma_{\text{Raman}} = 9A_g(\alpha_{x'x'+y'y'}, \alpha_{zz}) + 9B_g(\alpha_{x'x'-y'y'}, \alpha_{x'y'}) + 9E_g(\alpha_{x'z}, \alpha_{y'z})$	$\Gamma_{\text{infrared}} = 2A_{2u}(\mathbf{E} \parallel \mathbf{z}) + 2E_u(\mathbf{E} \parallel \mathbf{x}, \mathbf{E} \parallel \mathbf{y})$	$\Gamma_{\text{infrared}} = 9A_u(\mathbf{E} \parallel \mathbf{z}) + 7B_u(\text{silent}) + 10E_u(\mathbf{E} \parallel \mathbf{x}', \mathbf{E} \parallel \mathbf{y}')$
$\Gamma_{\text{acoustic}} = A_u + E_u$	$\Gamma_{\text{acoustic}} = A_u + E_u$		

seen, modes of the B_g symmetry can be observed for every value of Θ , whereas the ones of the A_g and A_{1g} symmetry vanish for crossed polarization configuration, independently of the crystal orientation. The B_{1g} reaches maximum intensity for $\Theta = -2\beta$ and vanishes for $\Theta = 90^\circ - 2\beta$.

Figure 3(b) shows RS spectra of $K_x\text{Fe}_{2-y}\text{Se}_2$ single crystals measured at 85 and 270 K in parallel and crossed polarization configurations. First we will discuss the Raman modes of the high-symmetry phase $I4/mmm$. RS study of $(\text{Sr},\text{K})\text{Fe}_2\text{As}_2$,²⁰ isostructural to our high symmetry phase, revealed that the A_{1g} and B_{1g} symmetry modes appear at 185 and 210 cm^{-1} (at 20 K). According to this assignment the peaks at about 180 and 207 cm^{-1} (at 85 K, see Fig. 3) can be identified as the A_{1g} and B_{1g} symmetry vibrations of the As and Fe atoms of the high-symmetry phase, respectively. Appearance of the B_{1g} mode at similar energies in both $(\text{Sr},\text{K})\text{Fe}_2\text{As}_2$ (210 cm^{-1}) and $K_x\text{Fe}_{2-y}\text{Se}_2$ (207 cm^{-1}) is expected since the lattice parameter a for both crystal structures [$(\text{Sr},\text{K})\text{Fe}_2\text{As}_2$ and the $I4/mmm$ phase of $K_x\text{Fe}_{2-y}\text{Se}_2$] are nearly the same and, as shown,²⁰ the substitution of K for Sr does not significantly change the frequencies of Raman modes involving As and Fe atom vibrations. Replacement of the lighter As atom with the heavier Se atom at the C_{4v} site results only in a shift of the A_{1g} mode in $K_x\text{Fe}_{2-y}\text{Se}_2$ toward the lower energies (180 cm^{-1}), in comparison to the same mode in $(\text{Sr},\text{K})\text{Fe}_2\text{As}_2$ (185 cm^{-1}). The remarkable decrease of the B_{1g} mode relative intensity with lowering temperature can be Fe vacancy order/disorder related.

Raman modes of the lower-symmetry phase ($I4/m$), Fig. 3(b), at 163 and 203 cm^{-1} that are observed in parallel but not in crossed polarization configuration, are assigned as A_g symmetry modes. Three modes at about 194, 188, and 214 cm^{-1} , which appear for the crossed polarization configuration, are assigned as B_g modes.

Figure 4 shows Raman scattering spectra of $K_x\text{Fe}_{2-y}\text{Se}_2$ single crystals measured at 85 K in four different polarization configurations. A multiple peak structure has been observed for parallel polarization configuration in the low-energy region between 80 and 150 cm^{-1} . By comparison of this spectral

region with other polarization configurations (Fig. 4) we found that this structure consists of six Raman active modes, three of which (at about 107, 123, and 134 cm^{-1}) are of A_g symmetry (blue lines in the inset of Fig. 4) and the remaining (at about

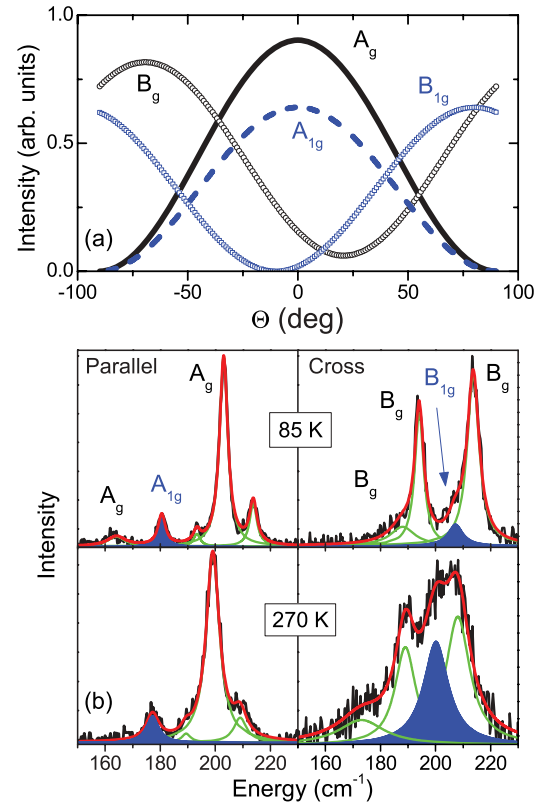


FIG. 3. (Color online) (a) Raman intensity angular dependencies of A_g , B_g , A_{1g} , and B_{1g} modes for arbitrary parameters in the single-domain case. (b) Raman scattering spectra of $K_x\text{Fe}_{2-y}\text{Se}_2$ single crystals measured in parallel and crossed polarization configurations. The sample was orientated so that $e_s \parallel 1/\sqrt{2}[1,1,0]$ of the $I4/mmm$ phase.

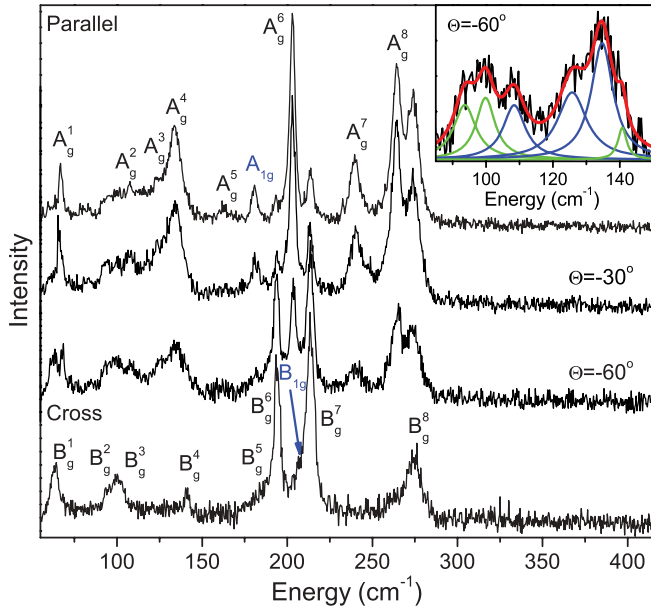


FIG. 4. (Color online) Raman scattering spectra of $K_xFe_{2-y}Se_2$ single crystals measured at 85 K in parallel ($\theta = 0^\circ$), $\theta = 30^\circ$, $\theta = 60^\circ$, and cross ($\theta = 90^\circ$) polarization configuration. Inset: Analysis of the $\theta = 60^\circ$ spectra low-energy region using Lorentz lineshapes.

94, 100, and 140 cm^{-1} are of B_g symmetry (green lines in the inset of Fig. 4). The lowest-energy modes appear at 63 cm^{-1} (B_g) and 67 cm^{-1} (A_g). Analysis of the high-energy spectral region of the Raman spectra of $K_xFe_{2-y}Se_2$ single crystals (above 230 cm^{-1}) showed three peaks, which we assigned as A_g symmetry modes (at about 240 and 264 cm^{-1}) and a B_g symmetry one (274 cm^{-1}).

Figure 5(a) shows Raman scattering spectra of $K_xFe_{2-y}Se_2$ single crystals in the $160\text{--}225\text{ cm}^{-1}$ spectral range measured at 85 K as a function of Θ . The relative intensities change of the analyzed modes as a function of Θ are presented in Fig. 5(b). The solid lines represent calculated spectra by using Eqs. (1) with one consistent set of parameters with the angle $\beta = 47(5)^\circ$, which confirms the supposed orientation of the sample (see the caption of Fig. 3). When analyzing the B_g mode relative intensity angular dependence, one must have in mind that $I4/m$ domains with the orientation α and $-\alpha$ appear with the same probability in the sample and both contribution must be taken into account. Analysis of the A_{1g} and B_{1g} modes' relative intensity angular dependences [Fig. 5(b)] also confirmed our previous assignment about the two-phase nature of the $K_xFe_{2-y}Se_2$ sample. Analysis of the 194 and 214 cm^{-1} modes' relative intensities (denoted as B_g^6 and B_g^7) confirmed the B_g nature of these modes. Additionally, we found that the angle between principal axes of the $I4/mmm$ and $I4/m$ phase domains in the (001) plane is about $\alpha = 29(6)^\circ$, which is in agreement with the expected value of $\sim 26.6^\circ$ for the $\sqrt{5} \times \sqrt{5}$ modulation.

In conclusion, Raman scattering was used to determine the influence of vacancy ordering on phonon spectra of $K_xFe_{2-y}Se_2$ single crystals. Polarized Raman spectra were analyzed in terms of peculiarities of both $I4/m$ and $I4/mmm$ symmetries. We have observed (at 85 K) $8A_g$ (67, 107, 123,

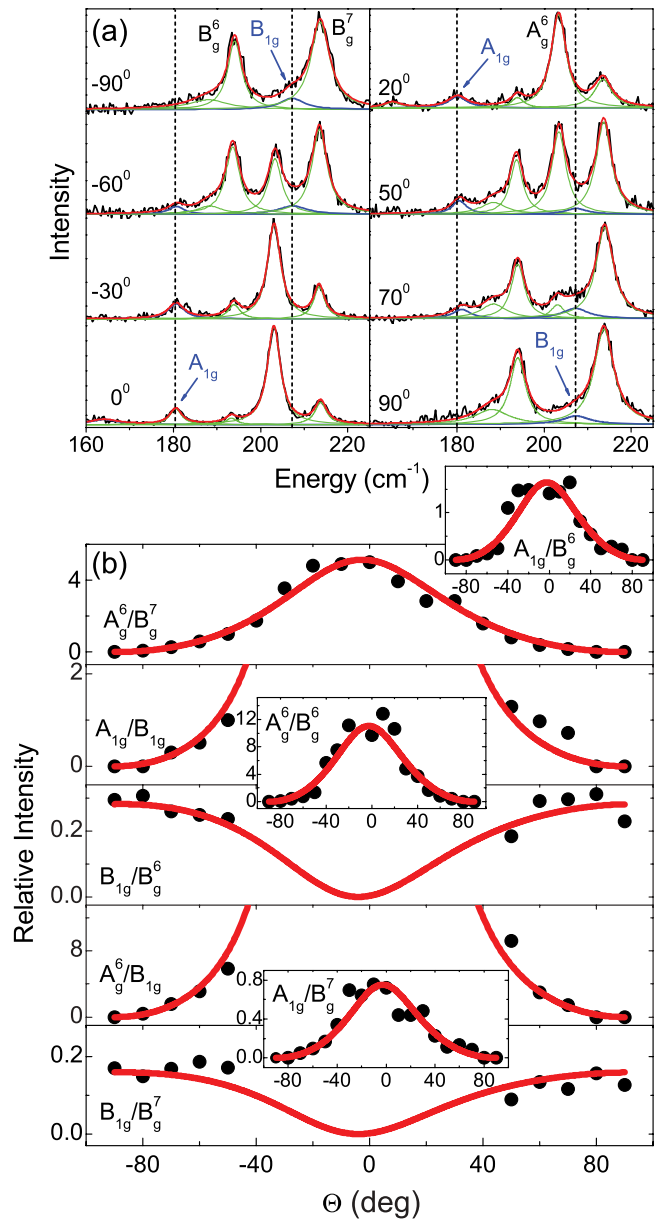


FIG. 5. (Color online) (a) Raman scattering spectra of $K_xFe_{2-y}Se_2$ single crystals measured at 85 K as a function of Θ . (b) Relative intensities of the Raman active modes as a function of Θ .

$134, 163, 203, 240,$ and 264 cm^{-1}) and $8B_g$ ($63, 94, 100, 140, 188, 194, 214,$ and 274 cm^{-1}) modes originating from the vibrations of the $I4/m$ phase and A_{1g} (180 cm^{-1}) and B_{1g} (207 cm^{-1}) modes originating from the vibrations of the $I4/mmm$ phase. This confirmed the two-phase nature of $K_xFe_{2-y}Se_2$ sample. The structural refinement of the PXR data of $K_xFe_{2-y}Se_2$ crystals confirmed the two-phase nature of the sample, as well as the fact that the Fe sites in the high-symmetry superconducting $I4/mmm$ phase are fully occupied, whereas there is a substantial density of Fe vacancies in the $\sqrt{5} \times \sqrt{5}$ $I4/m$ phase.

This work was supported by the Serbian Ministry of Education and Science under Projects No. ON171032 and

No. III45018. Work at Brookhaven is supported by the US Department of Energy (DOE) under Contract No. DE-AC02-98CH10886 (M.A. and E.S.B.) and in part by the Center

for Emergent Superconductivity, an Energy Frontier Research Center funded by the DOE Office for Basic Energy Science (H.L. and C.P.).

-
- ¹B. Wei, H. Qing-Zhen, C. Gen-Fu, M. A. Green, W. Du-Ming, H. Jun-Bao, and Q. Yi-Ming, *Chin. Phys. Lett.* **28**, 086104 (2011).
- ²G. M. Zhang, Z. Y. Lu, and T. Xiang, *Phys. Rev. B* **84**, 052502 (2011).
- ³F. Ye, S. Chi, W. Bao, X. F. Wang, J. J. Ying, X. H. Chen, H. D. Wang, C. H. Dong, and M. Fang, *Phys. Rev. Lett.* **107**, 137003 (2011).
- ⁴D. H. Ryan, W. N. Rowan-Weetaluktuk, J. M. Cadogan, R. Hu, W. E. Straszheim, S. L. Bud'ko, and P. C. Canfield, *Phys. Rev. B* **83**, 104526 (2011).
- ⁵V. Y. Pomjakushin, E. V. Pomjakushina, A. Krzton-Maziopa, K. Conder, and Z. Shermadini, *J. Phys.: Condens. Matter* **23**, 156003 (2011).
- ⁶Z. Shermadini, A. Krzton-Maziopa, M. Bendele, R. Khasanov, H. Luetkens, K. Conder, E. Pomjakushina, S. Weyeneth, V. Pomjakushin, O. Bossen, and A. Amato, *Phys. Rev. Lett.* **106**, 117602 (2011).
- ⁷P. Zavalij, W. Bao, X. F. Wang, J. J. Ying, X. H. Chen, D. M. Wang, J. B. He, X. Q. Wang, G. F. Chen, P.-Y. Hsieh, Q. Huang, and M. A. Green, *Phys. Rev. B* **83**, 132509 (2011).
- ⁸D. M. Wang, J. B. He, T.-L. Xia, and G. F. Chen, *Phys. Rev. B* **83**, 132502 (2011).
- ⁹W. Li, H. Ding, P. Deng, K. Chang, C. Song, K. He, L. Wang, X. Ma, J.-P. Hu, X. Chen, and Q.-K. Xue, *Nat. Phys.* **8**, 126 (2012).
- ¹⁰R. H. Yuan, T. Dong, Y. J. Song, P. Zheng, G. F. Chen, J. P. Hu, J. Q. Li, and N. L. Wang, *Sci. Rep.* **2**, 221 (2012).
- ¹¹F. Chen, M. Xu, Q. Q. Ge, Y. Zhang, Z. R. Ye, L. X. Yang, Juan Jiang, B. P. Xie, R. C. Che, M. Zhang, A. F. Wang, X. H. Chen, D. W. Shen, J. P. Hu, and D. L. Feng, *Phys. Rev. X* **1**, 021020 (2011).
- ¹²A. M. Zhang, K. Liu, J. H. Xiao, J. B. He, D. M. Wang, G. F. Chen, B. Normand, and Q. M. Zhang, *Phys. Rev. B* **85**, 024518 (2012).
- ¹³F. Han, B. Shen, Z.-Y. Wang, and H.-H. Wen, arXiv:1103.1347.
- ¹⁴H. Lei and C. Petrovic, *Phys. Rev. B* **84**, 212502 (2011).
- ¹⁵See Supplemental Material at <http://link.aps.org/supplemental/10.1103/PhysRevB.86.054503> for details of the powder crystal structure analysis.
- ¹⁶A. A. Coelho, TOPAS Academic v4.1 technical reference, www.topas-academic.net
- ¹⁷H. Lei, M. Abeykoon, E. S. Bozin, K. Wang, J. B. Warren, and C. Petrovic, *Phys. Rev. Lett.* **107**, 137002 (2011).
- ¹⁸V. Y. Pomjakushin, D. V. Sheptyakov, E. V. Pomjakushina, A. Krzton-Maziopa, K. Conder, D. Chernyshov, V. Svitlyk, and Z. Shermadini, *Phys. Rev. B* **83**, 144410 (2011).
- ¹⁹R. Loudon, *Adv. Phys.* **13**, 423 (1964).
- ²⁰A. P. Litvinchuk, V. G. Hadjiev, M. N. Iliev, B. Lv, A. M. Guloy, and C. W. Chu, *Phys. Rev. B* **78**, 060503 (2008).



Lattice dynamics reveals a local symmetry breaking in the emergent dipole phase of PbTe

Kirsten M. Ø. Jensen,¹ Emil S. Božin,² Christos D. Malliakas,³ Matthew B. Stone,⁴ Mark D. Lumsden,⁴ Mercouri G. Kanatzidis,^{3,5} Stephen M. Shapiro,² and Simon J. L. Billinge^{2,6}

¹*Center for Materials Crystallography, Department of Chemistry and iNano, Aarhus University, Denmark*

²*Condensed Matter Physics and Materials Science Department, Brookhaven National Laboratory, Upton, New York 11973, USA*

³*Department of Chemistry, Northwestern University, Evanston, Illinois 60208, USA*

⁴*Quantum Condensed Matter Division, Oak Ridge National Laboratory, Oak Ridge, Tennessee 37831, USA*

⁵*Materials Science Division, Argonne National Laboratory, Argonne, Illinois 60439, USA*

⁶*Department of Applied Physics and Applied Mathematics, Columbia University, New York, New York 10027, USA*

(Received 14 May 2012; published 20 August 2012)

Local symmetry breaking in complex materials is emerging as an important contributor to materials properties but is inherently difficult to study. Here we follow up an earlier structural observation of such a local symmetry broken phase in the technologically important compound PbTe with a study of the lattice dynamics using inelastic neutron scattering (INS). We show that the lattice dynamics are responsive to the local symmetry broken phase, giving key insights in the behavior of PbTe, but also revealing INS as a powerful tool for studying local structure. The new result is the observation of the unexpected appearance upon warming of a new zone center phonon branch in PbTe. In a harmonic solid the number of phonon branches is strictly determined by the contents and symmetry of the unit cell. The appearance of the new mode indicates a crossover to a dynamic lower symmetry structure with increasing temperature. No structural transition is seen crystallographically, but the appearance of the new mode in inelastic neutron scattering coincides with the observation of local Pb off-centering dipoles observed in the local structure. The observation resembles relaxor ferroelectricity, but since there are no inhomogeneous dopants in pure PbTe this anomalous behavior is an intrinsic response of the system. We call such an appearance of dipoles out of a nondipolar ground-state “emphanisis” meaning the appearance out of nothing. It cannot be explained within the framework of conventional phase transition theories such as soft-mode theory and challenges our basic understanding of the physics of materials.

DOI: [10.1103/PhysRevB.86.085313](https://doi.org/10.1103/PhysRevB.86.085313)

PACS number(s): 72.20.Pa, 63.20.dd, 73.22.Gk, 78.70.Nx

I. INTRODUCTION

The unexpected appearance, on warming, of local Pb off-centering dipoles was recently reported in PbTe.¹ No structural transition is seen in the average rock-salt crystal structure but is apparent in the local structure on warming above 100 K: the local symmetry is lowered, losing its centrosymmetry, upon warming. We refer to this as “emphanisis” meaning the appearance of something from nothing since it is fundamentally different from a normal ferroelectric transition where dipoles exist at low temperature but become disordered and fluctuating at high temperature. Here the dipoles *appear* upon warming from a ground state with no dipoles. In the original study¹ the dipoles were deemed to be fluctuating, but this could not be determined from the experiment itself. A recent inelastic neutron scattering (INS) study² noted the anharmonicity of certain phonons down to low temperature in PbTe. Here we present a detailed temperature-dependent INS study of the phonons in the temperature range where the local dipoles appear.¹ Below room temperature our results are in good agreement with earlier work on PbTe,^{3,4} and we also see the significantly anharmonic signal of the zone center transverse optical (TO) mode reported by Delaire *et al.*² However, the main result of this work is the characterization of the anharmonic features at ~ 6 meV as a new mode with a highly anomalous temperature dependence, growing rapidly in spectral weight with increasing temperature above 100 K, at the expense of the normal TO mode that is the incipient ferroelectric mode.⁴ The new mode and the original TO mode coexist over the entire temperature range measured to 600 K, resulting in an additional phonon branch in the Brillouin zone

indicative of a broken symmetry, though none is seen in the average structure. The new mode is broad with a short lifetime, but dispersive. It also hardens with increasing temperature. Since it appears over the same temperature range where local dipoles appear in the structure¹ we associate its appearance with the appearance of these objects that break the local, though not the average, centrosymmetric symmetry. Such behavior, observed in a pure binary alloy system, has not been described before and challenges our current understanding of the physics of materials.

II. RESULTS

We first consider the lattice dynamics at room temperature and below, and compare our measurements to earlier results in the literature^{2–4} to establish the quality of our sample and data. Figures 1(a)–1(c) show representative room temperature INS constant \vec{Q} scans, at three points in the Brillouin zone, collected on the HB3 triple axis spectrometer at Oak Ridge National Laboratory (ORNL). Details of the data collection are described in the Materials and Methods section below.

As illustrated in the inset to Fig. 1, the points in reciprocal space are (a) (033), which is a zone boundary K point⁵ in a position such that the instrument is sensitive to transverse polarized modes,⁶ (b) (2.5 2.5 2.5), which is a zone boundary L point sensitive to longitudinal modes, and (c) (133), which is a Brillouin zone center (Γ point) where both longitudinal and transverse modes can be measured. Certain phonon branches are expected based on the earlier work of Cochran *et al.*,³ the energy transfers of which are indicated by red dashed lines

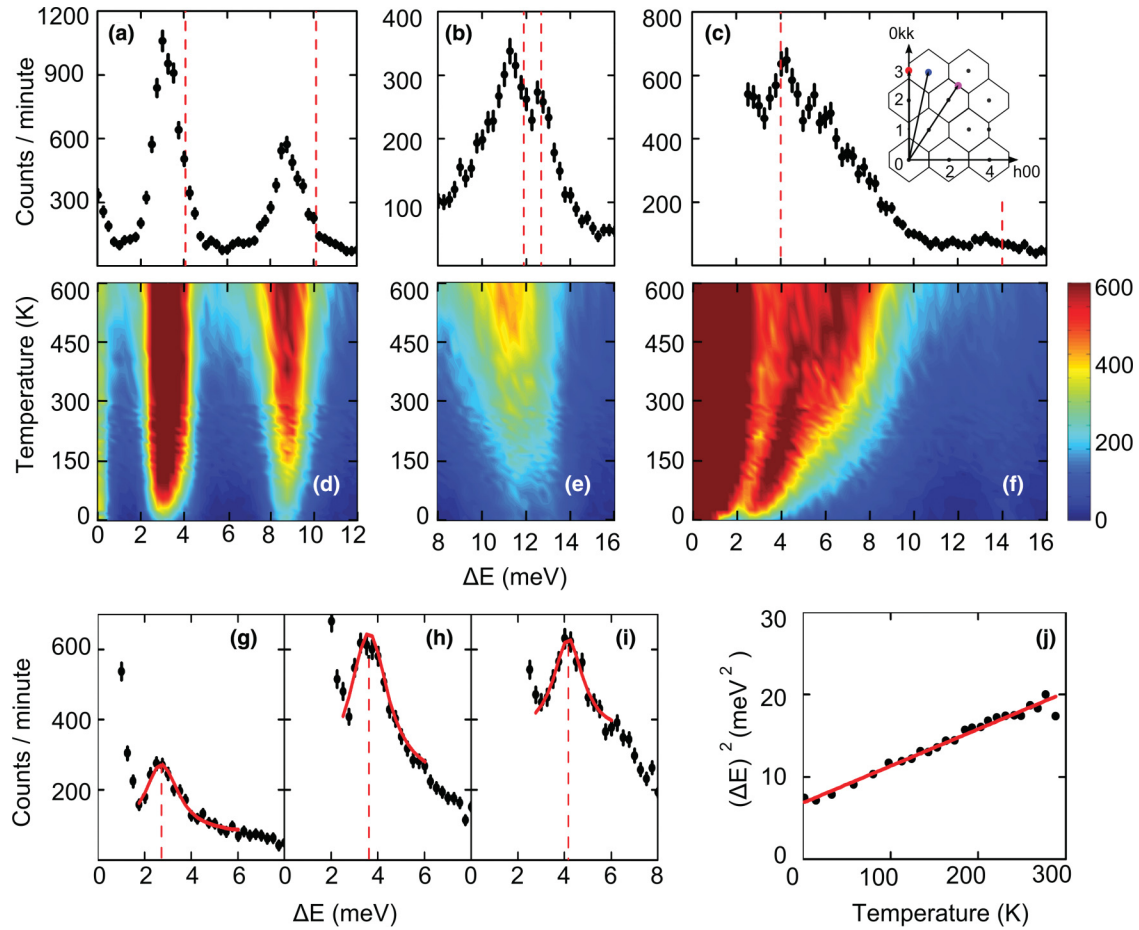


FIG. 1. (Color online) INS spectra of a PbTe single crystal at 288 K at different \vec{Q} points in reciprocal space: (a) $(0\ 3\ 3)$ zone edge, (b) $(2.5\ 2.5\ 2.5)$ zone edge, and (c) $(1\ 3\ 3)$ zone center. The red dashed lines indicate the phonon energies measured by Cochran *et al.* (Ref. 3) for comparison. The inset in (c) is a schematic of the plane of reciprocal space that the triple axis spectrometer was set to work in. The grey dots are the reciprocal lattice points, and the lines are Brillouin zone boundaries. The red, pink, and blue dots are the \vec{Q} points for the data shown in (a) (K point), (b) (L point), and (c) (Γ point), respectively. (d)–(f) show false color plots of the intensity (color axis) vs energy transfer, $\Delta E = \hbar\omega$, and temperature of the same modes shown in the panels above. (g)–(i) show representative fits of Lorentzian peaks (in red) to the TO mode at the $[133]$ zone center spectra: (g) 2 K, (h) 134 K, and (i) 231 K. The vertical dashed lines are the extracted mode energies ω . (j) ω^2 vs T for all the temperatures fit in the temperature range below 300 K with a straight line fit to the data shown in red.

in Fig. 1. There is good semiquantitative agreement with the earlier results. Figures 1(d)–1(f) shows a false-color plot of the scattered intensity as a function of temperature and energy transfer, $\Delta E = \hbar\omega$, for the same three \vec{Q} points. The K -point modes in Fig. 1(d) do not change energy at all vs temperature, neither do they broaden significantly. This is expected in a harmonic system, but even in a quasiharmonic approximation where lattice expansion is taken into account it is common to see softening with increasing temperature.⁷ The longitudinal acoustic/longitudinal optical (LA/LO) doublet at the L point shown in Fig. 1(e) does appear to broaden with increasing temperature though the peak contains two components that are both softening with increasing temperature. Fits to the line shapes suggest that there is little broadening of the individual lines. Qualitatively, the softening of these modes may be explained by a quasiharmonic analysis.

We now consider the zone-center TO mode in Figs. 1(c) and 1(f). This mode is the soft mode that indicates an incipient ferroelectric phase transition in PbTe.⁴ The mode softens with decreasing temperature (the opposite of the

L -point modes and opposite to early density functional theory (DFT) calculations⁸) but never reaches zero frequency. A softening to zero frequency would indicate the soft-mode transition temperature⁹ and a structural phase transition. It is immediately apparent that the mode is anomalously broad as pointed out recently.² The zone edge modes in Figs. 1(a) and 1(b) have a FWHM of around 1.5 meV which is close to the calculated energy resolution of the instrument, as described in Materials and Methods below. However, the high-energy tail on the zone center TO mode is of the order of ~ 5 meV. The temperature dependence of this scattering feature is shown in a false-color plot in Fig. 1(f). This feature in the scattering is seen to broaden dramatically with increasing temperature and is highly asymmetric and non-Gaussian.²

To study the temperature dependence of this mode in greater detail we have fit curves to the spectra at each temperature. We focus initially on the low-temperature region, $T < 300$ K. We would like to see if our data reproduce the earlier results of Alperin *et al.*⁴ Reasonable fits could be made to the scattering features by fitting a Lorentzian peak on a linear

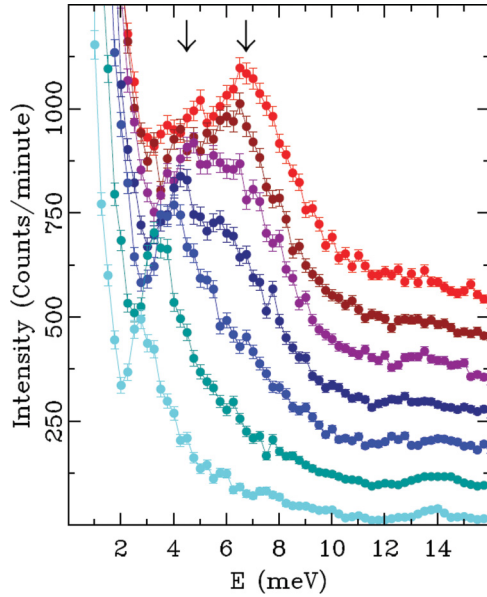


FIG. 2. (Color online) Plots of the INS spectrum at $\vec{Q} = (133)$. From the bottom (pale blue) the temperatures shown are 28, 99, 203, 299, 410, 486, and 601 K (topmost curve). Datasets are offset with respect to each other by 75 intensity units for clarity. The two arrows are guides to the eye, indicating the positions of the TO and the new mode at the highest temperature. Both modes soften upon cooling.

sloping background, and from this we extracted the mode frequency. Three of these fits are shown in Figs. 1(g)–1(i). The temperature dependence is shown in Fig. 1(j). For a mean-field, second order phase transition, the soft mode theory predicts that the frequency of the soft mode approaches zero as $(T - T_c)^{0.5}$,⁹ so a plot of ω^2 versus T will be linear and intercept the abscissa at transition temperature T_c . It is clear that the zone center mode softens upon cooling according to mean-field soft mode theory but still has a positive frequency at $T = 0$: PbTe is an incipient ferroelectric but, in the absence of alloying with Ge,¹⁰ does not undergo a ferroelectric phase transition upon cooling. There is excellent agreement with the earlier work.⁴ Extrapolating the line to the abscissa we obtain a putative phase transition temperature of -151 K. This is a little more negative in temperature than Alperin *et al.*⁴ (-135 K) but in good general agreement, and it establishes the purity of our crystal.

Having established that data from our sample are in good agreement with earlier work, we move to the main result of the current study. In Fig. 2 we show the temperature dependence of the zone center TO mode feature over a wide temperature range extending to high temperature.

Over a narrow temperature range beginning above ~ 100 K a new peak grows up rapidly but smoothly from the high energy tail of the TO mode, gaining spectral weight at the expense of the TO mode, but coexisting with it. Above room temperature the new peak becomes very strong, dominating the original TO feature. It indicates the presence of a new mode in the system that appears upon increasing temperature, which is highly anomalous.

The neutron scattering dynamic structure factor $S(\vec{Q}, \omega)$ is the normalized inelastic scattering intensity and is related to

the imaginary part of the dynamic susceptibility according to⁶

$$S(\vec{Q}, \omega) = \frac{\chi''(\vec{Q}, \omega)}{(1 - e^{-\frac{\hbar\omega}{k_B T}})}.$$

For a particular phonon mode in the s th branch at position $\vec{Q} = \vec{G} - \vec{q}$ in reciprocal space, where \vec{G} is a reciprocal lattice vector and \vec{q} is a vector that lies within a single Brillouin zone, $\chi''(\vec{Q}, \omega)$ is proportional to $|F(\vec{Q})|^2 / \omega_{\vec{q}s}$, where $F(\vec{Q})$ is the phonon dynamic structure factor. It is proportional to the Bragg scattering structure factor for zone center acoustic modes, but in general depends on the polarization of the vibrational mode and the atomic displacement vectors of the eigenfunction.

To obtain a quantity proportional to $\chi''(\vec{Q}, \omega)$, we multiply the measured intensity by the Bose-Einstein factor $C = (1 - e^{-\frac{\hbar\omega}{k_B T}})$. This removes the temperature dependent effects of phonon occupancy and allows us to track the changes in the phonon energy spectrum directly. The thus normalized data sets from $\vec{Q} = [331]$ were then fit with two damped harmonic oscillator functions to extract the different phonon dynamic susceptibilities. An additional Gaussian function was introduced to fit the intensity from the tail of the Bragg peak. Details of the fitting are in the Materials and Methods section. Representative examples of the fits to the data at various temperatures are shown in Figs. 3(a)–3(f).

The growth of the susceptibility of the new mode, at the expense of the TO mode, with increasing temperature is clearly apparent, as evident in Fig. 3(g). As well as growing, the new mode sharpens and hardens with increasing temperature. Rapid growth of the new mode spectral weight begins at around 100 K. The behavior is reminiscent of the power law growth of an order parameter in a Ginsburg-Landau theory of a conventional second order phase transition⁹ except in that case the order parameter grows upon cooling through the phase transition, not on warming as here. The temperature dependence of the mode susceptibility is reminiscent of the growth in the amplitude of the off-center Pb displacements observed in the atomic pair distribution function (PDF),¹ as shown in the inset. We have investigated the dispersion of the new mode in the $[h11]$ direction away from the zone center using the ARCS chopper spectrometer at ORNL. As is evident from Fig. 4, the mode clearly disperses to higher energy transfer moving away from the zone center, similar to the TO mode, and hardens with increasing temperature. Small features in the $h = 5.2$ spectra at an energy transfer around 5 meV are acoustic phonons, which cannot be resolved at lower momentum transfers, and should not be confused with the new mode which is dispersing towards higher momentum transfer.

The observation of additional modes implies a symmetry breaking in the system. The most trivial possibility is the appearance of a localized mode due to the presence of point defects in the material. Such modes are extremely weak and nondispersive but can become apparent, even for modest defect densities, when they interact with dispersing crystal modes.¹¹ This explanation can be ruled out by the temperature dependence. 100 K is too low a temperature for any significant thermally activated defect formation, and it is difficult to explain the power-law behavior of the susceptibility in this scenario. Also, the new mode is dispersive arguing

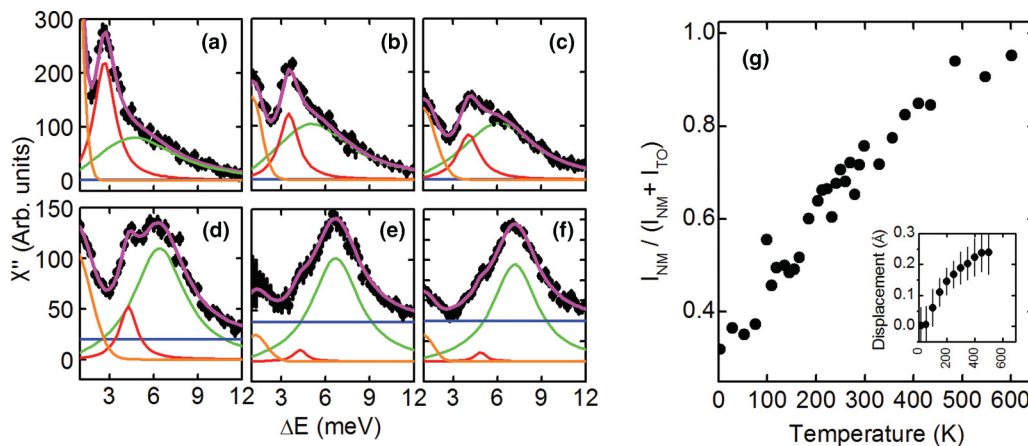


FIG. 3. (Color online) (a)–(f) Dynamic susceptibility obtained from the measured INS spectra (symbols) at representative temperatures with fits to the data shown as a pink line. There are two damped harmonic oscillator components, one for the TO mode (red) and one for the new mode (green). A Gaussian function was added to fit the intensity from the tail of the Bragg peak (orange). The horizontal blue line is a constant background component. (a) 2 K, (b) 98 K, (c) 203 K, (d) 299 K, (e) 482 K, and (f) 601 K. (g) shows the temperature dependence of the integrated weight in the new mode from the fits (black symbols). The inset shows the Pb off-centering displacement measured from the PDF measurement on PbTe reported in Ref. 1.

against this explanation. Similar arguments argue against another possibility which is the formation of thermally induced intrinsic local modes.¹² These are localized phonon modes that form due to nonlinear effects in a strongly driven system of oscillators¹³ and have been postulated to form due to thermal excitation in soft ionic systems.¹² An anharmonic coupling between the LA and TO modes has also been postulated to explain the breadth of the TO mode in PbTe,² but this does not explain the characteristic temperature dependence, and the clear observation of two distinct coexisting components in the vicinity of the TO mode. Also the LA mode is at zero frequency and far from the TO mode at the zone center where our data were measured. The most striking correspondence of the new mode is with the temperature dependent appearance of Pb off-centering structural dipoles

in the local structure reported from PDF measurements.¹ This observation was rationalized on thermodynamic grounds as the entropically stabilized appearance of a paraelectric phase above an undistorted nonferroelectric ground state. In this picture, the emergent dipoles break the local symmetry by removing the center of symmetry on the Pb site, even though there is no change in the long-range symmetry. This will result in short and long Pb-Te bonds, changing mode frequencies associated with the TO vibrations which are the intra-unit cell anti-phase vibrations of Pb and Te, just as observed here. If each off-center Pb atom is fluctuating independently, this would result in a flat nondispersing mode. The observation of dispersion implies that off-centered Pb ion displacements are correlated over some range of space, resulting in polar nanodomains similar to those observed in relaxor ferroelectrics

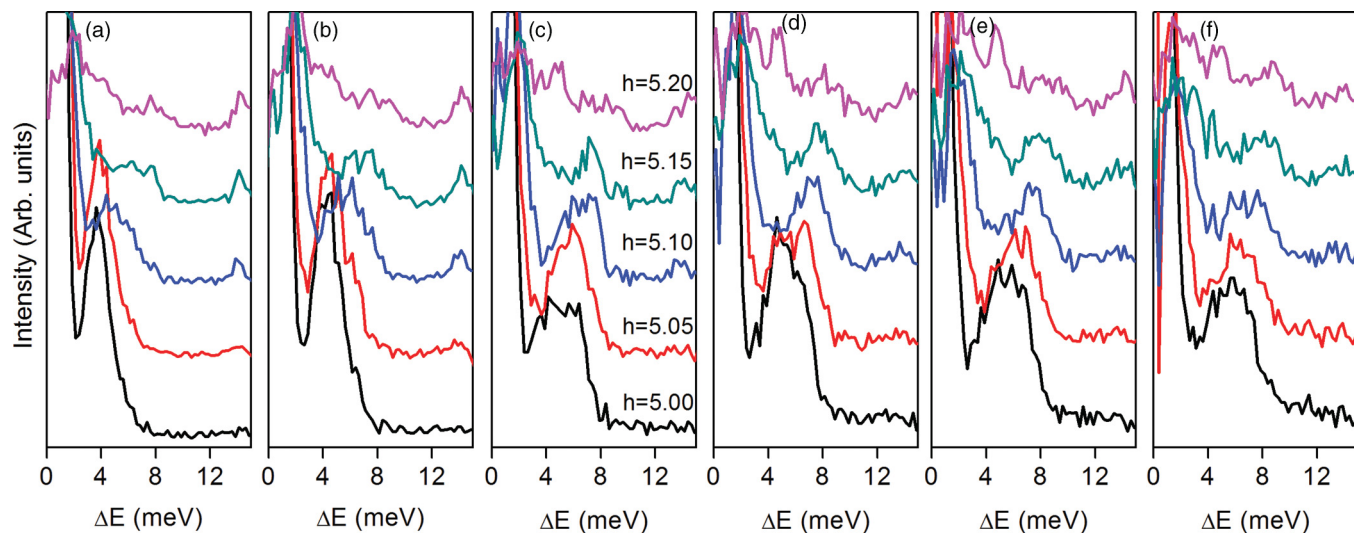


FIG. 4. (Color online) Neutron scattering intensity vs energy transfer from single crystal PbTe measured on the ARCS spectrometer. Curves in each panel are cuts along $[h11]$ for $5 < h < 5.2$ showing the dispersion of the modes. (a) 100 K, (b) 200 K, (c) 300 K, (d) 400 K, (e) 500 K, and (f) 600 K. At high temperature the intensity is almost exclusively coming from the new mode which is seen clearly dispersing to higher energy with increasing h .

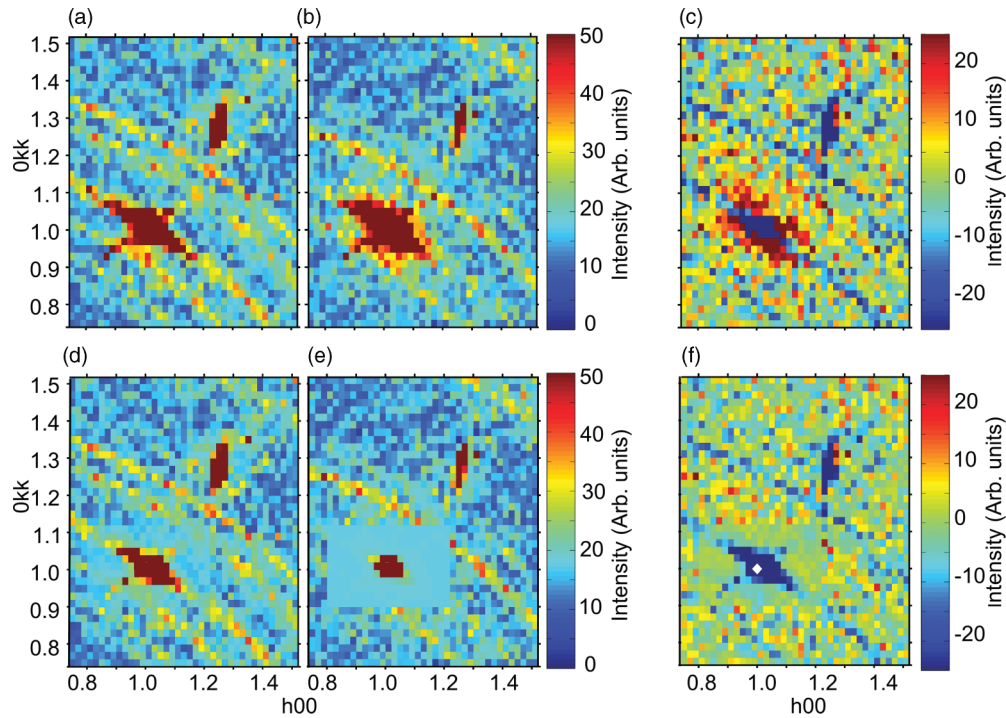


FIG. 5. (Color online) Elastic diffuse scattering around the $[h00],[0kk]$ plane of reciprocal space measured using the Triple axis spectrometer: (a) 16 K, (b) 482 K, (c) difference between the scans in (b) and (a): $I(482) - I(16)$. (d) and (e). As (a) and (b) but the intensities have been corrected to account for the change in phonon occupation of the acoustic modes that are within the energy resolution of the measurement. (f) The difference between the scans in (e) and (d).

below the Burns temperature.¹⁴ The new mode seen here is highly reminiscent of modes appearing in INS measurements of relaxor ferroelectrics that were attributed to polar nanodomains.¹⁵ However, the crucial distinction here is that PbTe is a pure material. In relaxors the polar nanodomains are stabilized by nanoscale chemical disorder whereas here they must be intrinsic. A physical explanation may lie in the partially localized optical phonon modes recently postulated by DFT and molecular modeling¹⁶ that result from partial covalency of the Pb and Te that competes with the electrostatic Madelung potential which prefers the high symmetry rock-salt structure. More work on the temperature dependence and the dispersion of these modes is needed to establish the true origin of this behavior.

We would like to establish if there is a static component to the short-range ordered nanoscale distortions by searching for diffuse scattering around the zone center in the elastic channel ($\omega = 0$). Indeed, we find there is a small increase in scattering at the base of the (111) Bragg peak at high temperature, which could be elastic diffuse scattering, as evident by comparing Figs. 5(a) and 5(b). The Bragg peak is evident as the strong scattering signal in dark red centered at (1.0,1.0,1.0). Another strong feature at (1.25,1.3,1.3) is a spurious feature of unknown origin. Powder diffraction lines are also evident coming from the aluminum cryostat windows, and for the line going through the Bragg peak, possibly some crystal mosaicity. The spurious features disappear (or rather appear with negative differential intensities) in the difference plot in Fig. 5(c) which shows the difference between the intensities at high (b) and low (a) temperature. We see some diffuse scattering intensity appearing at high temperature in this elastic

measurement, suggesting that the high temperature broken symmetry phase has a static component. This extra diffuse scattering component shows up as positive intensity around the (111) point in Fig. 5(c), whereas the Bragg features have a negative difference (dark blue) due to Debye-Waller effects. However, the most likely origin of the observed increase in elastic diffuse intensity is the finite energy resolution of our measurement resulting in a temperature dependent signal coming from the increase in population of the acoustic phonons that lie within the energy resolution window. Figs. 5(d) and 5(e) show scans that have been approximately corrected for phonon effects by dividing the region around the Bragg peak by the Bose factor appropriate for the phonon modes in the resolution window. This correction accounts for all of the observed diffuse scattering at high temperature in Fig. 5(c) [see Fig. 5(f)] suggesting that there is *no elastic diffuse scattering signal* from the dipoles and therefore they have no static component but are completely dynamic in nature, again consistent with the DFT prediction.¹⁶

The chemically simple binary PbTe compound continues to turn up surprises that challenge our understanding of condensed matter systems. We know of no other example of the appearance in a pure material of a new phonon mode with increasing temperature, and the characteristic temperature dependence of its dynamic susceptibility argues strongly that this is an intrinsic response of the system. The inelastic scattering is sensitive to the local symmetry which is broken at high temperature where the new mode is seen to coexist over a wide range of temperature with the original TO mode of the undistorted structure. A picture emerges of nanoscale regions where the local dipoles appear at high temperature and are

correlated and fluctuating. This lowering of local symmetry with rising temperature, betrayed by the emerging modes seen here and in the PDF,¹ may explain the long known anomalous temperature dependence of the semiconducting energy gap in PbTe.^{16,17} Unlike in conventional semiconductors where the energy gap is known to increase with falling temperature due to the reduction of the intensity of thermal vibrations, that of PbTe increases with increasing temperature up to as high as 600 K. It is this anomalous dependence that permits PbTe to exhibit delayed cross gap carrier excitations thereby sustaining a very high thermoelectric power factor at high temperatures. Coupled with the increased anharmonicity and phonon scattering from the same origin resulting in a very low thermal conductivity, this may help to explain the one two punch that propels PbTe to the top of its thermoelectric class.¹⁸

III. MATERIALS AND METHODS

A. Sample preparation

Stoichiometric amounts of Pb (rotometals, at 99.9% purity) and Te (plasmaterials, at 99.999% purity) were flame sealed in an evacuated ($<10^{-4}$ mTorr) fused silica tube. The mixture was heated to 1050 °C at a rate of 100 °C/h for 4 h and cooled down to room temperature at a rate of 20 °C/h. For the single crystal growth, ~ 20 g of PbTe were remelted using the Bridgman method. A 13 mm fused silica tube was loaded with PbTe and lowered at a rate of ~ 2.6 mm/h through a single zone vertical furnace that was set at 1050 °C. A cylindrical shaped crystal of 13 mm in diameter and ~ 60 mm in height was used for the inelastic neutron scattering experiment. The quality of the single crystal was evaluated using neutron Laue diffraction at SNS.

B. Triple axis inelastic neutron scattering experiments

The inelastic neutron experiments were performed at the HB3 triple axis instrument at the high flux isotope reactor (HFIR) located at Oak Ridge National Laboratory. All the experiments were performed with a fixed final energy $E_f = 14.7$ meV using pyrolytic graphite (PG) as a monochromator and analyzer and a PG filter after the sample to eliminate higher order contamination of the scattered beam. The neutron beam collimation was 48-20-40-90 before the monochromator, sample, analyzer, and detector, respectively. This yielded an energy resolution of 1.06 meV full width half maximum (FWHM) for zero energy transfer, increasing to 1.62 meV FWHM at $\omega = 12.0$ meV energy transfer. The sample was mounted to the cold-tip of a closed cycle He-4 based refrigerator (CCR). Data scans were made as a function of energy transfer at constant \vec{Q} points in reciprocal space at 35 different temperatures between 2.5 and 600 K.

C. Triple axis inelastic neutron scattering data curve fitting

Here we describe the method used to extract the dynamic structure factors of the modes at the (133) zone center from the TAS data. First the data are normalized to obtain the dynamic susceptibility $\chi''(\vec{Q}, \omega)$ as described in the main paper. Based on earlier work we expect two zone-center modes to be present at finite energy transfer (the acoustic modes are hidden under the elastic line at $\omega = 0$): the TO mode at around 4 meV and the LO mode around 14 meV. As the LO mode does

not overlap with either the TO or the new mode, we do not take this into account in the fit, which only includes the region from 1–12 meV. The TO mode is then fitted with a function representing a damped harmonic oscillator,⁶ with an additional constant background in the fit. Furthermore, a Gaussian function is added to take care of the tail of the Bragg peak which is present even after the normalization with the Bose factor. We then add an additional damped harmonic oscillator to account for the new mode. The spectra were then fit as a function of temperature sequentially with the starting model for each fit using the parameters obtained from the previous temperature point. Certain constraints were introduced in order to aid convergence, namely, the widths of TO and new mode curve and the background level were allowed to change by only $\pm 20\%$, between subsequent runs.

D. Triple axis elastic diffuse scattering measurements

Elastic scans were also taken on a grid of points in the Brillouin zone at 16 and 482 K to search for diffuse scattering from static disorder. The range $0.8 < h < 1.5$ was scanned in the $[h00]$ direction and $0.8 < k < 1.5$ in the $[0kk]$ direction to capture the region around the (111) reciprocal lattice point. This is a zone center and the PbTe Bragg peak is evident in Fig. 5(a) at the (111) point. There is an additional Bragg feature at around (1.25 1.3 1.3). We are not sure of the origin of this feature and think it is a spurious peak. It does not show any interesting temperature dependence and we neglect it in the analysis. In addition there are a number of powder Bragg lines evident. One goes through the (111) point and suggests some sample mosaicity. The other powder lines probably come from the aluminum sample environment.

In Figs. 5(d) and 5(e) we have applied a simple correction to account for the increased occupancy of acoustic phonons that lie within the energy resolution of the measurement. Based on the dispersion curves measured by Cochran *et al.*, we estimate the range of \vec{Q} that is affected by phonons within the energy resolution (of around 1 meV). We assume that the average phonon energy in that region is ~ 0.5 meV and so correct the intensities in this range of \vec{Q} by the Bose factor appropriate for a mode of that energy and the temperature in question. This is a highly simplified correction and is intended to estimate the scale of intensity coming from the increase mode population at high temperature rather than being a highly accurate correction. We see that this simple correction accounts for essentially 100% of the diffuse scattering seen at higher temperature in the elastic channel.

E. Chopper spectrometer inelastic neutron scattering experiments

Inelastic neutron scattering measurements were also performed using the ARCS direct geometry time-of-flight chopper spectrometer at the spallation neutron source (SNS) at the Oak Ridge National Laboratory. Single crystal measurements were performed with an incident energy of $E_i = 30$ meV with the sample mounted approximately in the $(hk0)$ scattering plane of the instrument. The sample was mounted to the cold tip of a closed cycle He-4 based refrigerator (CCR). Data were acquired by rotating the sample about the vertical axis by 40 degrees and collecting data in 1.875 degree increments. Empty

sample can measurements were performed for all data acquired at ARCS and subtracted from the data shown in the manuscript.

The resulting large five-dimensional data sets show the scattering intensity throughout much of (\vec{Q}, ω) space. The data are projected into a 4D space, and 3D slices and 2D cuts are made to extract features of interest using the DCS-mslice program within the DAVE¹⁹ software package.

ACKNOWLEDGMENTS

We would like to thank Simon Johnsen for help with growing the crystal and Nicola Spaldin and Petros Souvatzis

for helpful discussions. Work in the Billinge group was supported by the Office of Science, US Department of Energy (OS-DOE), under Contract No. DE-AC02-98CH10886. Work in the Kanatzidis group was supported as part of the Revolutionary Materials for Solid State Energy Conversion, an Energy Frontier Research Center funded by the US Department of Energy, Office of Science, Office of Basic Energy Sciences under Award No. DE-SC0001054. The neutron scattering measurements were carried out at the HFIR and SNS at Oak Ridge National Laboratory was sponsored by the Scientific User Facilities Division, Office of Basic Energy Sciences, US Department of Energy.

-
- ¹E. S. Božin, C. D. Malliakas, P. Souvatzis, T. Proffen, N. A. Spaldin, M. G. Kanatzidis, and S. J. L. Billinge, *Science* **330**, 1660 (2010).
- ²O. Delaire, J. Ma, K. Marty, A. F. May, M. A. McGuire, M.-H. Du, D. J. Singh, A. Podlesnyak, G. Ehlers, M. D. Lumsden, and B. C. Sales, *Nat. Mater.* **10**, 614 (2011).
- ³W. Cochran, R. A. Cowley, G. Dolling, and M. M. Elcombe, *Proc. R. Soc. London* **293**, 433 (1966).
- ⁴H. A. Alperin, S. J. Pickart, J. J. Rhyne, and V. J. Minkiewicz, *Phys. Lett.* **40**, 295 (1972).
- ⁵M. S. Dresselhaus, G. Dresselhaus, and A. Jorio, *Group Theory Application to the Physics of Condensed Matter* (Springer-Verlag, Berlin, 2008).
- ⁶G. Shirane, S. M. Shapiro, and J. M. Tranquada, *Neutron Scattering with a Triple Axis Spectrometer* (Cambridge University Press, Cambridge, 2002).
- ⁷B. T. Fultz, *Prog. Mater. Sci.* **55**, 247 (2010).
- ⁸J. M. An, A. Subedi, and D. J. Singh, *Solid State Commun.* **148**, 417 (2008).
- ⁹A. D. Bruce and R. A. Cowley, *Structural phase transitions* (Taylor and Francis, London, UK, 1981).
- ¹⁰W. Jantsch, in *Dynamical Properties of IV-VI Compounds*, edited by H. Bilz, A. Bussmann-Holder, W. Jantsch, and P. Vogl, *Springer Tracts in Modern Physics* (Springer Berlin/Heidelberg, 1983), Vol. 99, pp. 1–50.
- ¹¹R. M. Nicklow, W. P. Crummett, and J. M. Williams, *Phys. Rev. B* **20**, 5034 (1979).
- ¹²M. E. Manley, A. J. Sievers, J. W. Lynn, S. A. Kiselev, N. I. Agladze, Y. Chen, A. Llobet, and A. Alatas, *Phys. Rev. B* **79**, 134304 (2009).
- ¹³D. K. Campbell, S. Flach, and Y. S. Kivshar, *Phys. Today* **57**, 43 (2004).
- ¹⁴G. Burns, *Phys. Rev. B* **13**, 215 (1976).
- ¹⁵S. B. Vakhrushev and S. M. Shapiro, *Phys. Rev. B* **66**, 214101 (2002).
- ¹⁶Y. Zhang, X. Ke, P. R. C. Kent, J. Yang, and C. Chen, *Phys. Rev. Lett.* **107**, 175503 (2011).
- ¹⁷R. N. Tauber, A. A. Machonis, and I. B. Cadoff, *J. Appl. Phys.* **37**, 4855 (1966).
- ¹⁸Z. H. Dughaish, *Physica B* **322**, 205 (2002).
- ¹⁹R. T. Azuah, L. R. Kneller, Y. Qiu, P. L. W. Tregenna-Piggott, C. M. Brown, J. R. D. Copley, and R. M. Dimeo, *J. Res. Natl. Inst. Stand. Technol.* **114**, 341 (2009).

Local structure of ReO₃ at ambient pressure from neutron total-scattering studyE. S. Božin,¹ T. Chatterji,² and S. J. L. Billinge^{1,3}¹*Department of Condensed Matter Physics and Materials Science, Brookhaven National Laboratory, Upton, New York 11973, USA*²*Institut Laue-Langevin, 6 rue Jules Horowitz, Boîte Postale 156, Grenoble cedex 9, France*³*Department of Applied Physics and Applied Mathematics, Columbia University, New York, New York 10027, USA*

(Received 29 June 2012; published 18 September 2012)

A hypothesis that the local rotations of ReO₆ octahedra persist in the crystallographically untilted ambient phase of ReO₃ is examined by the high-resolution neutron time-of-flight total scattering based atomic pair distribution function analysis. Three candidate models were tested, $Pm\bar{3}m$, $P4/mbm$, and $Im\bar{3}$, for the local structure of ReO₃ at ambient pressure and 12 K, and both quantitative and qualitative assessments of the data were performed. No evidence for large local octahedral rotations was found, suggesting that the local and the average structures are the same ($Pm\bar{3}m$) as normally assumed.

DOI: [10.1103/PhysRevB.86.094110](https://doi.org/10.1103/PhysRevB.86.094110)

PACS number(s): 61.05.fg, 61.66.Fn, 65.40.De

I. INTRODUCTION

Among *d*-electron metallic conductors ReO₃ has a simple perovskitelike structure and its conductivity is comparable to that of a noble metal such as Ag.^{1,2} Although the electron-phonon coupling constant is not very small, ReO₃ surprisingly does not show superconductivity down to 20 mK.³ ReO₃ seems to belong to the normal class of conventional band Fermi liquids with electron-phonon interaction dominating the resistivity.³

ReO₃ crystallizes in the cubic space group $Pm\bar{3}m$ with the undistorted perovskitelike DO₉-type structure (ABO_3 , Fig. 1) comprised of a network of corner-shared ReO₆ octahedra and with an empty *A* site, and is in fact the simplest material containing BO_6 octahedra. ReO₃ is very special among the multitude of systems possessing the perovskite-based structure, in that its untilted cubic $Pm\bar{3}m$ structure is extremely stable at ambient pressure and at all temperatures from liquid-helium temperature⁴ up to its melting point at 673 K.^{5,6} Electronic band-structure calculations investigated this extraordinary structural stability⁶ and suggested that metallic bonding plays an important role.⁷ The open crystal structure makes ReO₃ suitable for doping or compression under high pressure. ReO₃ attracted considerable attention recently due to observation of weak negative thermal expansion (NTE) below room temperature.⁸ NTE is rarely found in metals, and in ReO₃ is rather sensitive to impurity-induced disorder.⁹

A structural phase transition was discovered in ReO₃ upon application of pressure when the pressure-induced anomaly in the Fermi surface was observed in measurements of de Haas–van Alphen frequencies,¹⁰ and was characterized in detail by means of x-ray and neutron diffraction.^{11–13} At room temperature ReO₃ undergoes a pressure-induced second-order phase transition at $p_c = 5.2$ kbar, to an intermediate tetragonal phase ($P4/mbm$) over a narrow pressure range, and further to a cubic ($Im\bar{3}$) phase that persists up to relatively high pressures while the ReO₆ octahedra remain almost undistorted,¹⁴ but considerably tilted.¹⁵ The driving force for the transition is argued to be the softening of the M3 phonon mode involving a rigid rotation of ReO₆ octahedra. It is a continuous transition with the rotation angle as an order parameter.¹³ The pressure-temperature phase diagram has been recently established,¹⁶ indicating that

the value of p_c decreases with decreasing temperature, leveling at around 2.4 kbar at base temperature. More recently, a study of the pressure-induced phase transition showed that in nanocrystalline ReO₃, the sequence of phases is different and with generally lower p_c values than for bulk samples.¹⁷

This canonical view has been challenged by the reexamination¹⁸ of the structural phase transition in ReO₃ using the x-ray absorption fine structure (XAFS) method sensitive to the nearest-neighbor information. This investigation suggests that even at ambient pressure the Re-O-Re bond angle deviates from 180° by about 8°. In this newly proposed view, ReO₃ only appears cubic in the analysis of the Bragg intensities, while the local structure is suggested to be heavily distorted. In this picture the phase transition at p_c is then a tilt order-disorder transition.¹⁸ Similar conclusions were drawn from the study of XAFS spectra of antiferrodistortive perovskites Na_{0.82}K_{0.18}TaO₃ and NaTaO₃.¹⁹ The results reported by Houser and Ingalls¹⁸ are in contrast to XAFS results reported earlier that suggested agreement between the local and the average structures,^{5,20,21} possibly due to the different approaches to XAFS data analysis taken in the different studies.^{18,22}

We have carried out a neutron total scattering study of ReO₃ at ambient pressure and low temperature. Based on the same data we performed both conventional Rietveld analysis, based on Bragg intensities, yielding the average crystallographic structure, and the atomic pair distribution function (PDF) analysis, which is a direct space method that includes both Bragg and diffuse scattering information, yielding structural information on local, intermediate, and long-range scales.^{23–25} This approach allows structure to be assessed on various length scales from the same data. Our analysis rules out the existence of large local tilt amplitudes in ReO₃.

II. EXPERIMENT

In this study we used 3 g of commercially available (Sigma-Aldrich) ReO₃ sample in the form of a loose powder. Neutron time-of-flight powder diffraction measurements were carried out using the high-resolution NPDF diffractometer at the Manuel Lujan Neutron Scattering Center at Los Alamos National Laboratory. The sample was sealed in a vanadium

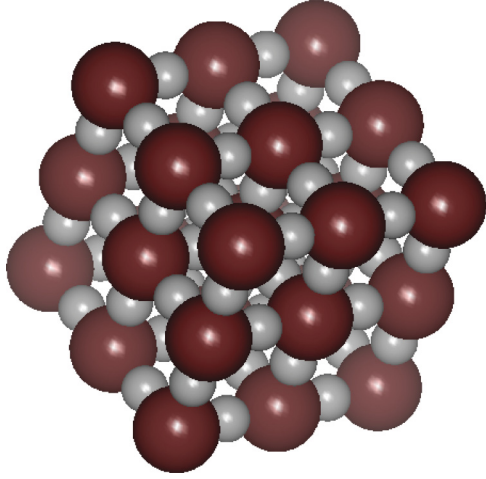


FIG. 1. (Color online) Structural motif of ReO_3 (space group $Pm\bar{3}m$): Re is shown as large spheres, while small spheres represent O.

tube with He exchange gas, and cooled down to 12 K using a closed cycle He refrigerator. Raw data were corrected for experimental effects such as sample absorption and multiple scattering using the program PDFGETN,²⁶ to obtain the total scattering structure function, $S(Q)$. This contains both Bragg and diffuse scattering and therefore information about atomic correlations on different length scales. The PDF, $G(r)$, is obtained by a Fourier transformation according to $G(r) = \frac{2}{\pi} \int_0^\infty Q[S(Q) - 1] \sin Qr dQ$, where Q is the magnitude of the scattering vector. The PDF gives the probability of finding an atom at a distance r away from another atom. The reduced total scattering structure function, $F(Q) = Q[S(Q) - 1]$, of ReO_3 at 12 K is shown in Fig. 2(a) and the resulting PDF, $G(r)$, in Fig. 2(b). PDFs refined in this study were produced using an upper limit of integration in Fourier transform Q_{max} of 32 \AA^{-1} .

The average crystal structure was verified by taking the standard Rietveld refinement approach in reciprocal space using the EXPGUI²⁷ platform operating the program GSAS.²⁸ The fit of the $Pm\bar{3}m$ model is shown as an inset to Fig. 2(a). The local structure was studied by refinements of structural models to the experimental PDF using the program PDFGUI.²⁹ The details of the PDF method are provided elsewhere.²³

The Rietveld refinements were carried out on the ambient structure model, $Pm\bar{3}m$ space group: Re at $1a$ (0,0,0) and O at $3d$ (0.5,0,0). The PDF local structural refinements were carried out over the range 1.5–10.0 \AA for three different candidate structures: conventional $Pm\bar{3}m$, and two models that allow rigid rotations of ReO_6 octahedra: $P4/m\bar{3}m$ [Re at $2b$ (0,0,0.5), O at $2a$ (0,0,0) and at $4h$ ($x, x + 0.5, 0.5$)], and $Im\bar{3}$ [Re at $8c$ (0.25,0.25,0.25), O at $24g$ (0, y, z)].

III. RESULTS AND DISCUSSION

The results of the Rietveld refinements are shown in the inset to Fig. 2(a) and Table I. They reproduce literature results well.^{9,11–13}

We now consider the local structure measured by the PDF. The fits are shown in Figs. 3(a)–3(c), and the results are summarized in Table I. The PDF does not presume

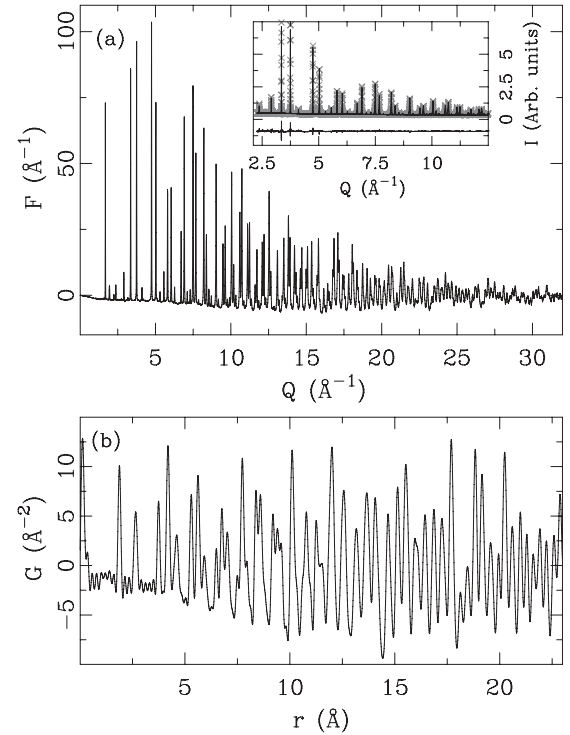


FIG. 2. Neutron experimental data of ReO_3 at 12 K and at ambient pressure: (a) reduced total scattering structure function, $F(Q)$, and (b) corresponding atomic PDF, $G(r)$. Inset shows Rietveld refinement using $Pm\bar{3}m$ model (solid line) of the normalized intensity (symbols) with the difference curve offset for clarity.

any periodicity and it is therefore possible to refine lower symmetry structures than the crystallographic model where it is warranted. This may be the case when the crystal structure is an average over local domains of lower symmetry, as, for example, in the ferroelectric BaTiO_3 .³⁰

TABLE I. Summary of structural refinements of ReO_3 data. Atomic displacement parameters, U , are in units of \AA^2 . Derived interatomic distances d and octahedral rotation angles φ are given at the bottom. Numbers in parentheses are estimated standard deviations (ESD) obtained from fitting.

	Rietveld	$Pm\bar{3}m$	$P4/m\bar{3}m$	$Im\bar{3}$
a (\AA)	3.7499(2)	3.7508(2)	5.3101(2)	7.5012(3)
c (\AA)			3.7430(3)	
U (Re)	0.0016(3)	0.0011(1)	0.0010(1)	0.0010(1)
x (O)			0.2400(6)	
y (O)				0.2520(7)
z (O)				0.2417(6)
U (O)	0.0057(5)	0.0053(3)	0.0031(3)	0.0031(3)
U_{par} (O)	0.0027(5)	0.0026(3)		
U_{perp} (O)	0.0073(3)	0.0061(2)		
R_{wp} (%)	2.97	7.89	7.87	8.21
$d_{1\text{Re-O}}$ (\AA)	1.8749(1)	1.8754(1)	1.8714(1)	1.8764(2)
$d_{2\text{Re-O}}$ (\AA)			1.8789(2)	
$d_{1\text{O-O}}$ (\AA)	2.6516(1)	2.6522(2)	2.6520(3)	2.6197(3)
$d_{2\text{O-O}}$ (\AA)			2.6572(4)	2.6855(3)
φ (deg)	0	0	2.3(2)	2.1(2)

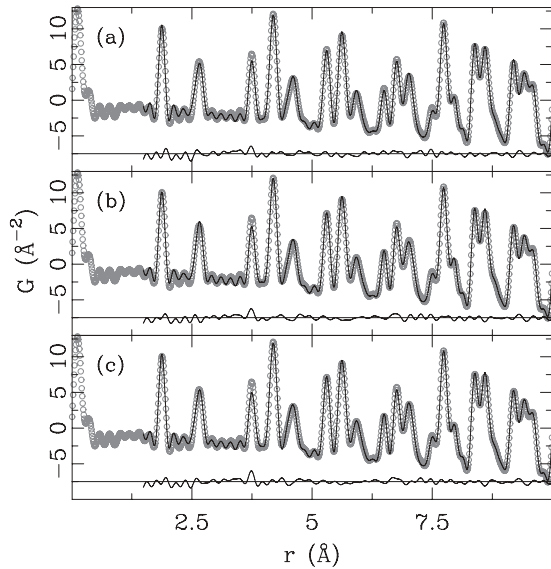


FIG. 3. Refinement of various models (solid black lines) to the 12 K neutron PDF data (open symbols): (a) $Pm\bar{3}m$ model, (b) $P4/mbm$ model, and (c) $Im\bar{3}$ model. The difference curves are offset for clarity.

As apparent from the figure, all three models provide good fits. The fact that the crystal structure model provides a good fit with a good agreement factor suggests that there is no evidence for a lower symmetry local structure. However, as evident in the table, the good fit benefits from the model being allowed to refine anisotropic atomic displacement parameters (ADP) which are significantly enlarged in directions perpendicular to the Re-O bond. It is therefore interesting to consider models that allow for rotations of the octahedral units such as the symmetry lowered phases observed at high pressure. The $Im\bar{3}$ model converges with finite tilts but yields larger R_{wp} values than the crystallographic model despite having one extra refined parameter. It does not find the minimum with zero tilts and the refined parameters $y(O)$ and $U(O)$ are 84% correlated, suggesting that this model is not correct. On the other hand, the tetragonal $P4/mbm$ model with isotropic ADPs imposed gives a comparable agreement to the one obtained using the crystallographic $Pm\bar{3}m$ model with anisotropic ADPs. However, in this model a and c lattice parameters are 95% correlated, again suggesting that the cubic model with anisotropic ADPs is sufficient. The fits to PDF data are shown in Figs. 3(a)–3(c) for $Pm\bar{3}m$, $P4/mbm$, and $Im\bar{3}$ models, respectively, and the results are presented in Table I.

The PDF measures the instantaneous structure and it is not possible to distinguish explicitly between local tilts that are static and those that are dynamic. If the tilts are dynamic as we presume here, the tilt angle extracted from the fits of the lower symmetry models yields an average tilt amplitude due to correlated motions of the atoms locally, i.e., rigid rotations of the octahedra, and is a useful quantitative measure of this amplitude. The octahedral rotation angles φ (Ref. 13) obtained from the PDF refinements are $2.3(2)^\circ$ and $2.1(2)^\circ$ for the $P4/mbm$ and $Im\bar{3}$ structures, respectively. These are much smaller than $\sim 4.9^\circ$ (equivalent to $\sim 8^\circ$ tilts) reported from XAFS,¹⁸ and smaller than values obtained in the pressure

stabilized tilted crystal structures.¹³ An estimate of the tilt angle implied by the ADPs obtained from both the $Pm\bar{3}m$ model fit by Rietveld and PDF yields $\sim 2.1(2)^\circ$ and $\sim 1.8(2)^\circ$, respectively. PDFs calculated with the EXAFS tilt angles gave qualitatively worse fits to the data. The values refined are sufficiently small to suggest that the local tilting is coming from dynamic fluctuations of a low-energy rigid unit tilting mode, as proposed as a mechanism for the observed negative thermal expansion.^{8,31}

We have further calculated the PDFs based on data published in the literature for the three models of interest,¹³ for comparison keeping the isotropic atomic displacement parameters and the scale factor the same as those from the PDF $Pm\bar{3}m$ refinement reported here. The structural parameters were taken for cases of ambient $Pm\bar{3}m$, 5.2 kbar $P4/mbm$ and $Im\bar{3}$, as well as for 7.3 kbar $Im\bar{3}$ that corresponds to the stable high-pressure phase case. These calculated PDFs, and the experimental PDF profile, are shown in Fig. 4, and reveal what kind of changes are to be expected in the PDF in the case of ReO_6 octahedral rotations being present locally. At room temperature, at 5.2 kbar average octahedral rotations of 3.0° were observed, while at 7.3 kbar the rotation angle value rises to 6.6° .¹³ It is quite apparent from the calculated PDFs shown in the figure that even for a small rotation angle there are appreciable changes in the local structure, and these are rather similar for the two models that allow tilting. While the first two PDF peaks do not change at all, reflecting the rigidity of the

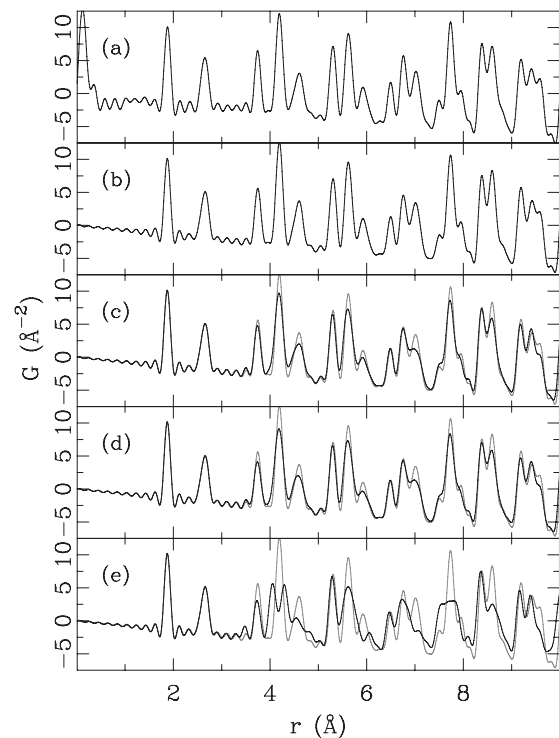


FIG. 4. Visual comparison of ReO_3 PDFs: (a) neutron PDF data, and various calculated PDFs of competing models: (b) ambient pressure $Pm\bar{3}m$, (c) 5.2 kbar $P4/mbm$ (average rotation angle 3°), (d) 5.2 kbar $Im\bar{3}$ (average rotation angle 3°), and (e) 7.3 kbar $Im\bar{3}$ (average rotation angle 6.6°). In panels (c)–(e) gray-line PDF profile is that of $Pm\bar{3}m$ shown in panel (b), and is given for comparison. See text for details.

ReO₆ octahedra,²¹ changes start to appear at higher distances as the ReO₆ network gets distorted. For a larger tilt magnitude, the changes in the local structure become much more dramatic [Fig. 4(e)]. By visual inspection and comparison of the features seen in the calculated PDFs, we can immediately rule out the larger tilt angle case, as there is no resemblance to the observed PDF.

IV. CONCLUSION

In summary, we used the PDF method to test a hypothesis from an earlier EXAFS study¹⁸ that the *local* rotations of ReO₆ octahedra persist in the ambient pressure, crystallographically untilted phase of ReO₃. The high-resolution neutron time-of-flight total scattering based atomic pair distribution function analysis was carried out on a dataset collected at 12 K under ambient pressure conditions. Three candidate models were tested, $Pm\bar{3}m$, $P4/mbm$, and $Im\bar{3}$, and quantitative and qualitative assessment of the data were performed. No evidence was found for local octahedral rotations of a magnitude comparable

to those seen in the distorted high-pressure phase and beyond what might be expected from thermal and quantum zero point motion, suggesting that the local and the average structure are the same ($Pm\bar{3}m$) as normally assumed. The PDF results shown here emphasize again the importance of using multiple complementary techniques in addressing delicate structural issues at the nanoscale.³²

ACKNOWLEDGMENTS

E.S.B. acknowledges useful discussions with John Provis, Efrain Rodriguez, and Anna Llobet. Work at Brookhaven National Laboratory was supported by the Office of Science, US Department of Energy (OS-DOE), under Contract No. DE-AC02-98CH10886. This work has benefited from the use of NPDF at the Lujan Center at Los Alamos Neutron Science Center, funded by DOE Office of Basic Energy Sciences. Los Alamos National Laboratory is operated by Los Alamos National Security LLC under DOE Contract No. DE-AC52-06NA25396.

¹A. Ferretti, D. B. Rogers, and J. B. Goodenough, *J. Phys. Chem. Solids* **26**, 2007 (1965).

²C. N. King, H. C. Kirsch, and T. H. Geballe, *Solid State Commun.* **9**, 907 (1971).

³P. B. Allen and W. W. Schulz, *Phys. Rev. B* **47**, 14434 (1993).

⁴A. Fujimori and N. Tsuda, *Solid State Commun.* **34**, 433 (1980).

⁵A. Kuzmin, J. Purans, G. Dalba, P. Fornasini, and F. Rocca, *J. Phys.: Condens. Matter* **96**, 9083 (1996).

⁶M. G. Stachiotti, F. Corà, C. R. A. Catlow, and C. O. Rodriguez, *Phys. Rev. B* **55**, 7508 (1997).

⁷W. Yu, J. Zhao, and C. Jin, *Phys. Rev. B* **72**, 214116 (2005).

⁸T. Chatterji, P. F. Henry, R. Mittal, and S. L. Chaplot, *Phys. Rev. B* **78**, 134105 (2008).

⁹E. E. Rodriguez, A. Llobet, T. Proffen, B. C. Melot, R. Seshadri, P. B. Littlewood, and A. K. Cheetham, *J. Appl. Phys.* **105**, 114901 (2009).

¹⁰F. S. Razavi, Z. Altounian, and W. R. Datars, *Solid State Commun.* **28**, 217 (1978).

¹¹J. E. Schirber and B. Morosin, *Phys. Rev. Lett.* **42**, 1485 (1979).

¹²J. D. Axe, Y. Fujii, B. Batlogg, M. Greenblatt, and S. Di Gregorio, *Phys. Rev. B* **31**, 663 (1985).

¹³J.-E. Jorgensen, J. D. Jorgensen, B. Batlogg, J. P. Remeika, and J. D. Axe, *Phys. Rev. B* **33**, 4793 (1986).

¹⁴J. E. Jorgensen, W. G. Marshall, R. I. Smith, J. S. Olsen, and L. Gerwald, *J. Appl. Crystallogr.* **37**, 857 (2004).

¹⁵J. E. Schirber, B. Morosin, R. W. Alkire, A. C. Larson, and P. J. Vergamini, *Phys. Rev. B* **29**, 4150 (1984).

¹⁶T. Chatterji and G. J. McIntyre, *Solid State Commun.* **139**, 12 (2006).

¹⁷K. Biswas, D. V. S. Muthu, A. K. Sood, M. B. Kruger, B. Chen, and C. N. R. Rao, *J. Phys.: Condens. Matter* **19**, 436214 (2007).

¹⁸B. Houser and R. Ingalls, *Phys. Rev. B* **61**, 6515 (2000).

¹⁹B. Rechav, Y. Yacoby, E. A. Stern, J. J. Rehr, and M. Newville, *Phys. Rev. Lett.* **72**, 1352 (1994).

²⁰B. Houser, R. Ingalls, and J. J. Rehr, *Physica B* **208-209**, 323 (1995).

²¹G. Dalba, P. Fornasini, A. Kuzmin, J. Purans, and F. Rocca, *J. Phys.: Condens. Matter* **7**, 1199 (1995).

²²A. Kuzmin, J. Purans, M. Benfatto, and C. R. Natoli, *Phys. Rev. B* **47**, 2480 (1993).

²³T. Egami and S. J. L. Billinge, *Underneath the Bragg Peaks: Structural Analysis of Complex Materials* (Pergamon Press, Elsevier, Oxford, England, 2003).

²⁴S. J. L. Billinge, *J. Solid State Chem.* **181**, 1698 (2008).

²⁵C. A. Young and A. L. Goodwin, *J. Mater. Chem.* **21**, 6464 (2011).

²⁶P. F. Peterson, M. Gutmann, T. Proffen, and S. J. L. Billinge, *J. Appl. Crystallogr.* **33**, 1192 (2000).

²⁷B. H. Toby, *J. Appl. Crystallogr.* **34**, 201 (2001).

²⁸A. C. Larson and R. B. Von Dreele, Los Alamos National Laboratory Report No. LAUR-86-748, 1987.

²⁹C. L. Farrow, P. Juhás, J. Liu, D. Bryndin, E. S. Božin, J. Bloch, T. Proffen, and S. J. L. Billinge, *J. Phys.: Condens. Matter* **19**, 335219 (2007).

³⁰G. H. Kwei, S. J. L. Billinge, S.-W. Cheong, and J. G. Saxton, *Ferroelectrics* **164**, 57 (1995).

³¹U. D. Wdowik, K. Parlinski, T. Chatterji, S. Rols, and H. Schober, *Phys. Rev. B* **82**, 104301 (2010).

³²S. J. L. Billinge and I. Levin, *Science* **316**, 561 (2007).

Electronic thermoelectric power factor and metal-insulator transition in FeSb₂Qing Jie,^{1,*} Rongwei Hu (胡荣伟),^{1,†} Emil Bozin,¹ A. Llobet,² I. Zaliznyak,¹ C. Petrovic,^{1,‡} and Q. Li^{1,§}¹Condensed Matter Physics and Materials Science Department, Brookhaven National Laboratory, Upton, New York 11973, USA²Lujan Neutron Scattering Center, LANL, MS H805, Los Alamos, New Mexico 87545, USA

(Received 23 May 2012; published 14 September 2012)

We show that synthesis-induced metal-insulator transition (MIT) for electronic transport along the orthorhombic c axis of FeSb₂ single crystals has greatly enhanced electrical conductivity while keeping the thermopower at a relatively high level. By this means, the thermoelectric power factor is enhanced to a new record high $S^2\sigma \sim 8000 \mu\text{W K}^{-2} \text{cm}^{-1}$ at 28 K. We find that the large thermopower in FeSb₂ can be rationalized within the correlated electron model with two bands having large quasiparticle disparity, whereas MIT is induced by subtle structural differences. The results in this work testify that correlated electrons can produce extreme power factor values.

DOI: [10.1103/PhysRevB.86.115121](https://doi.org/10.1103/PhysRevB.86.115121)

PACS number(s): 72.20.Pa, 71.27.+a, 71.30.+h, 72.80.Sk

I. INTRODUCTION

The efficiency of thermoelectric (TE) material at temperature T is evaluated by the figure of merit $ZT = (S^2/\rho\kappa)T$, where S is the thermopower, ρ is the electrical resistivity, and κ is the thermal conductivity. There are two distinct approaches to increasing the ZT : either by κ reduction or by power factor (S^2/ρ) enhancement. Techniques such as alloying, “phonon glass electron crystal” (PGEC) approach, and nanostructure engineering have been used to reduce the phonon mean free path, reduce lattice κ , and produce high Z , at or above the room temperature.^{1–5} Reduction of the phonon mean free path has limitations since it cannot be reduced below the interatomic spacing and therefore other mechanisms for high ZT are sought after.⁶ Tuning the carrier density by doping is often inadequate since lower ρ comes with higher carrier concentration that favors lower S .⁷

The most favorable TE electronic structure is the one that has a resonance in the density of states centered about $2-3k_B T$ away from the Fermi energy (ϵ_F).⁸ Kondo insulators (KI) represent a close approximation of such an ideal case. In a strongly correlated electron system, and, in particular, in a KI, localized f or d states hybridize with conduction electron states leading to the formation of a small hybridization gap. The density of states just below and just above the hybridization gap becomes very large. The thermopower is very sensitive to variations in density of states in the vicinity of the ϵ_F , hence very large absolute values of $|S| > 100 \mu\text{V/K}$ can be expected and are reported in KI.⁹ The materials include not only rare-earth-based compounds but also FeSi.^{10–15}

FeSb₂ crystallizes in $Pnmm$ orthorhombic structure and has been characterized as an example of a strongly correlated noncubic Kondo insulator-like material with $3d$ ions.^{16–18} Similar to FeSi, heavy fermion states were discovered in FeSb₂ by doping-induced metallization.^{19,20} Colossal values of thermopower up to $\sim 45 \text{ mV/K}$ at 10 K and a record high thermoelectric power factor (TPF) of $\sim 2300 \mu\text{W/K}^2 \text{cm}$ were observed.²¹ This is two orders of magnitude larger than in best Bi₂Te₃-based materials and one order of magnitude larger than any reported value in correlated electron systems. Crystals in Refs. 19 and 21 exhibit semiconductor behavior and small resistivity anisotropy with relatively high resistivity for current directed along all three principal crystalline axes. In contrast, single crystals used in Kondo insulator studies showed high

anisotropy of the resistivity: electric transport along the a and b axes is semiconducting, while the c axis is metallic at high temperatures and exhibits metal-insulator transition (MIT) at 40 K.^{16,17,22}

Here we investigated the TPF in two FeSb₂ crystals, with (crystal 1) and without (crystal 2) MIT. We show that large S enhancement can be attributed to electronic correlations in multiple charge and heat carrying bands. We also provide evidence for structural origin of MIT in correlated electron bands that reduces ρ by several orders of magnitude around 30 K in crystal 1 and results in a new record high TPF.

II. EXPERIMENT

Single crystals of FeSb₂ with MIT have been prepared as in Refs. 16 and 17 by decanting at 650 °C. Single crystals of FeSb₂ without MIT have been prepared by the method described in Refs. 19 and 21, i.e., by decanting at 690 °C, after a cool down from high temperatures to 640 °C. Crystals were oriented using a Laue camera and cut into $0.6 \times 0.5 \times 4.5$ ($a \times b \times c$) mm³ samples for two probe thermopower measurements with two ends soldered on disk-shape leads using indium. Resistivity $\rho(T)$ was determined by a standard four-point ac method. Heat and current transport along the orthorhombic c axis were measured using the Quantum Design PPMS platform. A magnetic field was applied along the crystallographic a axis. Sample dimensions were measured with an optical microscope Nikon SMZ-800 with 10 μm resolution. Consequently the relative errors on the electrical resistivity and thermal conductivity are 4% and for the Hall coefficient, 2%. Since the Seebeck coefficient does not depend on the sample geometry the main source of error is the sample uniformity and the accuracy of crystal orientation which introduces the measurement error of up to 5%.

The atomic pair distribution (PDF) method, based on the total scattering approach, yields structural information on different length scales.²³ X-ray scattering experiments for PDF analysis were carried out at the 11-ID-C beamline of the Advanced Photon Source using high energy beam ($E = 114.82 \text{ keV}$, $\lambda = 0.108 \text{ \AA}$, $0.5 \text{ mm} \times 0.5 \text{ mm}$ size). Both PDF, $G(r)$, and its algebraic relative, radial distribution function (RDF), $R(r)$, were considered in this study. Experimental PDF, $G(r)$ is obtained from the measured reduced total scattering structure factor, $F(Q) = Q[S(Q) - 1]$, via sine Fourier transform

$G(r) = G(r) = (2/\pi) \int_0^\infty [F(Q)\sin(Qr)dQ]$. In practice, the upper limit of integration is some finite value Q_{\max} . RDF, $R(r)$ is obtained from $G(r)$ through $R(r) = rG(r) + 4\pi r^2 \rho_0$, where ρ_0 is the average number density. Experimental setup for total scattering x-ray experiments utilized a Cryo Industries of America cryostat and Perkin-Elmer image plate detector. Finely ground samples in cylindrical polyimide capillaries were placed in a low-temperature sample changer, and the data for the two samples were successively collected for 4 min at each temperature in probed range between 5 and 300 K. PDFs were obtained up to $Q_{\max} = 26 \text{ \AA}^{-1}$ momentum transfer using standard protocols, and intermediate length scale structure modeled over $(1.7\text{--}45.0) \text{ \AA}^{-1}$ range with $Pnmm$ structural model using the program PDFGUI.²⁴ Preliminary reference neutron total scattering based PDF's were obtained using a time-of-flight HIPD instrument at Los Alamos Neutron Scattering Center.

III. RESULTS AND DISCUSSIONS

The ρ_c for crystal 1 is metallic down to the onset of MIT (T_{MIT}), as opposed to crystal 2 [Fig. 1(a)].^{16,17,21,22} Above 80 K and up to 300 K, $\rho_c(T)$ of crystal 2 is insensitive to magnetic field and is semiconducting. Interestingly, the logarithmic derivative, $d[\ln \rho_c(T)]/dT$ reveals an underdeveloped anomaly at T_{MIT} in crystal 2 which points to the intrinsic nature of this temperature scale [Figs. 1(b) and 1(c)]. Arrhenius analysis assuming thermally activated behavior leads to a number of distinct energy scales valid for limited subranges of this temperature interval (Table I), allowing only approximate estimation of the gap values. The absolute value $|d\{\ln[\rho(T)]\}/dT|$ in the metallic and insulating states is very similar, which is reminiscent of the universality observed near the MIT in low-dimensional electron gas systems.²⁵ Below

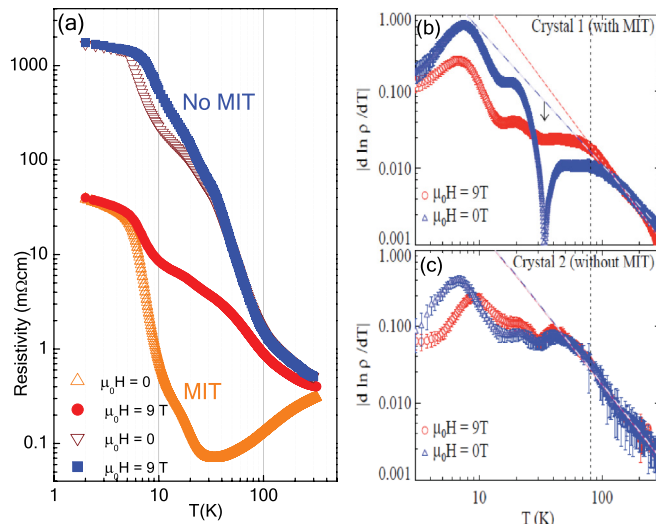


FIG. 1. (Color online) (a) Comparison of c -axis resistivity for two crystals. In 9 T $\rho(T)$ in crystal 1 above 80 K is consistent with semiconducting thermally activated transport with an activation gap of 120 K. (b),(c) Temperature regime(s) where $\rho(T)$ is dominated by thermally activated transport. The arrow in (b) marks the MIT in crystal 1, where $d[\ln(\rho)]/dT$ changes sign. Broken lines in both panels are linear fits to activation-type behavior.

TABLE I. Approximate (see text) energy gap from electronic transport, the ratio of quasiparticle weights and scattering times in the valence and conduction bands $Z\Gamma = ((Z_v^2 \tau_v^{5/2})/\Gamma_v)/((Z_c^2 \tau_c^{5/2})/\Gamma_c)$ and $\epsilon_F \sim \ln(\mu_c/\mu_v)$ for a crystal with MIT (top) and a crystal with no MIT (bottom row). The huge difference of fitting parameters between crystals 1 and 2 may be rationalized by the fact that the mobility difference of two bands for crystals with MIT is $10^8\text{--}10^9$, while the one for crystals without MIT is ~ 10 , whereas both show similar large Seebeck coefficients.

(2–5) K	(10–30) K	(80–100) K	$Z\Gamma$	ϵ_F
0.14(1) meV	6.2(1) meV	Metallic	6.2×10^{-8}	3.4 meV
0.08(1) meV	4.1(1) meV	14.7(1) meV	38	0.8 meV

5 K electrical transport is dominated by extrinsic impurity states and is governed by a very small activation gap, similar for both crystals. Distinct energy scales and indirect gaps are in agreement with optical spectroscopy studies and *ab initio* calculations.^{18,21,26,27} The large activation gap observed above 80 K in crystal 2 is not observed in the metallic phase of crystal 1, but its size argues against contribution of impurity states.

The Hall resistivity $\rho_{xy}(B)$ (current flowing along the c axis) for both crystals [Figs. 2(a) and 2(b)] is nonlinear, confirming the presence of two carrier bands. In the absence of skew scattering we proceed to the analysis of the data in the two-band picture. In a two-carrier system²⁸ the Hall coefficient is $R_H = \rho_{xy}/H = \rho_0(\alpha_2 + \beta_2 H^2)/(1 + \beta_3 H^2)$, where $\alpha_2 = f_1 \mu_1 + f_2 \mu_2$, $\beta_2 = (f_1 \mu_2 + f_2 \mu_1) \mu_1 \mu_2$, and $\beta_3 = (f_1 \mu_2 + f_2 \mu_1)^2$, where $\rho_0 = \rho(B = 0)$, $f_i = |n_i \mu_i|/\sum |n_i \mu_i|$ is the f factor, and n_i and μ_i are individual carrier band concentrations

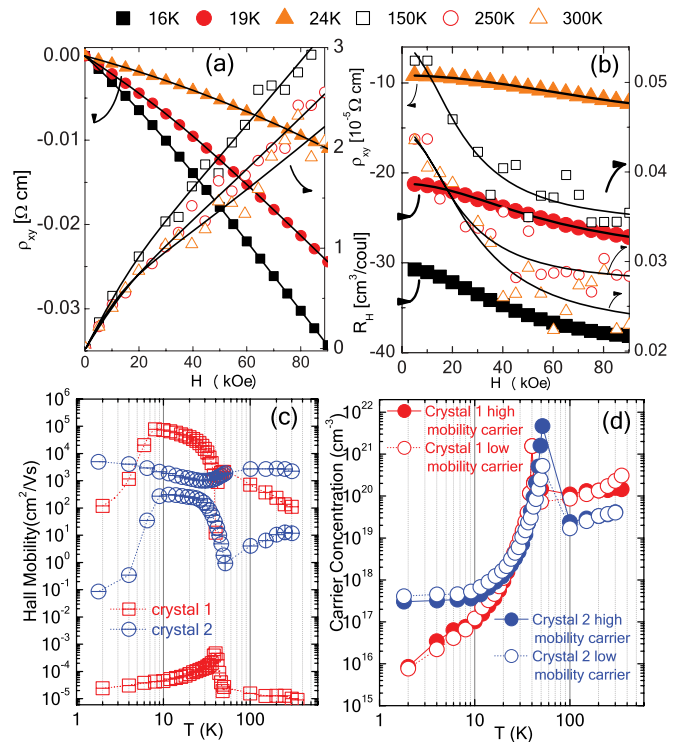


FIG. 2. (Color online) The ρ_{xy} (a) and Hall constant (b) for crystal 2. Hall mobility (c) where the hole (electron) carriers are denoted by + (–) and carrier concentrations of high and low mobility carriers (d) as a function of temperature for both crystals.

and mobilities. The agreement with the model is excellent and we obtain carrier band concentrations and mobilities for crystal 2 while also showing data for crystal 1 for comparison.²⁹ In the model “carrier” denotes a set of carriers with identical mobility associated with only one energy and/or one degenerate energy level and is different from the conventional electron or hole carriers that correspond to a continuous energy band. The low mobility carriers in crystal 2 are hole type [$\mu(2)_L \sim 10 \text{ cm}^2/\text{V s}$] and they are an order of magnitude less mobile when compared to hole carriers in crystal 1 at 300 K. Note that hole carriers in crystal 1 at room temperature constitute high mobility band [$\mu(1)_H \sim 10^2 \text{ cm}^2/\text{V s}$]. Yet, just like $\mu(1)_H$, the $\mu(2)_L$ band exhibits sign change below 50 K, having identical temperature dependence when compared to $\mu(1)_H$ with up to three orders of magnitude lower nominal values. The $\mu(2)_H$ carriers are electron type in crystal 2. They show little change in magnitude and do not change sign. The most striking difference between crystals 1 and 2 is the ratio of nominal mobility values. The large mobility difference is absent in crystal 2. Moreover, there is about or less than one order of magnitude between $\mu(2)_H$ and $\mu(2)_L$ in the high thermopower region from 10 to 40 K. The low and high carrier concentrations in both crystals have nearly identical values, suggesting a compensated nature of electronic transport at all temperatures. The carrier concentrations $n_2(H)$ and $n_2(L)$ are rather close at 300 K but they are both about an order of magnitude lower and have the same temperature dependence as carrier concentrations $n_1(H)$ and $n_1(L)$ in crystal 1. Carrier concentrations in crystals 1 and 2 are nearly identical in the temperature region of high thermopower, whereas in the impurity regime below 10 K crystal 2 (no MIT) shows much higher carrier concentrations. Values of carrier mobilities for crystal 2 ($\sim 10^{-3} \text{ cm}^2/\text{V s}$) are in general agreement with mobility values at low temperatures obtained using a two-band model (4–25 K) on crystals with no MIT.³⁰

Using carrier concentrations and Hall mobilities from a large number of measured $\rho_{xy}(B)$ isotherms we obtain $S(T)$ for both crystals in the framework of a two-band noninteracting semiconductor^{31–33} model where thermopower $S = (S_e\sigma_e + S_h\sigma_h)/(\sigma_e + \sigma_h)$ and

$$S_{e,h} = (k_B/e) \left[\frac{[(5/2) + s] F_{(3/2)+s}(\xi_{e,h})}{[(3/2) + s] F_{(1/2)+s}(\xi_{e,h})} \right] - \xi_{e,h}, \quad (1)$$

where $F_j(\xi) = \int_0^\infty \frac{x^j dx}{1+\exp(x-\xi)}$. The scattering exponent s represents the energy dependence of the relaxation time $\tau = \tau_0 e^s$, $\xi = \epsilon_F/(k_B T)$ are the reduced Fermi energies for electrons and holes ξ_e and ξ_h (as measured from the bottom of the conduction band for electrons and from the top of the valence band for holes), and $\epsilon_F = h^2/(2m^*)(N/V)^{(2/3)}(3/8\pi)^{(2/3)}$. Hence, for semimetals $\epsilon_{Fe} = -(\epsilon_{Fh} + \epsilon_0)$ and $\xi_e = -\xi_h - \epsilon_0/(k_B T)$, where ϵ_0 is the overlap energy, and for semiconductors $\epsilon_{Fe} = -\epsilon_{Fh} + \epsilon_g$ and $\xi_e = -\xi_h - \epsilon_0/(k_B T)$, where ϵ_g is the energy gap for semiconductors. In this model we used value $s = -1/2$ assuming that acoustic phonon scattering is dominant at all temperatures and $m^* = m_e$. The two-band noninteracting semiconductor model adequately describes crystal 2 above 50 K and below 5 K, whereas it fails to explain $|S(T)|$ for crystal 1 in its metallic state (Fig. 3). While the similar shape of calculated and measured thermopower for both crystals

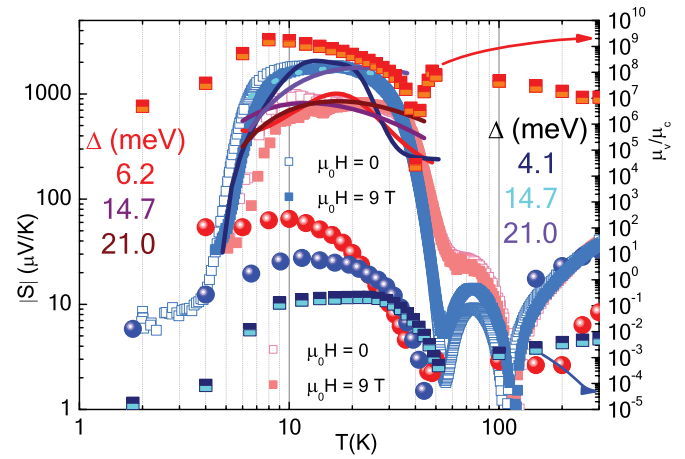


FIG. 3. (Color online) (a) $|S(T)|$ for FeSb₂ crystals 1 (red) and 2 (blue squares). Red and blue balls show fits to the two-band noninteracting semiconductor model. Fits to the correlated electron model for crystal 1 are shown by red, purple, and brown (crystal 1) and dark blue, light blue, and violet (crystal 2) solid lines that correspond to increasing values of fixed energy gap Δ (see text). The ratio of individual band mobilities in a two-carrier model is shown by the red/orange (crystal 1) and dark/light blue squares (crystal 2).

between 10 and 40 K in the noninteracting model argues in favor of the two-band approach, such calculation does not explain the amplification of $|S(T)|$ observed in the (10–30) K range. The prime suspect for discrepancy is strong correlations, which can have a significant impact on carriers in $3d$ bands.

In a correlated electronic system with two bands separated by a gap, S depends not only on the gap size but also on the anisotropy or asymmetry in the transport function:³⁴

$$S = \frac{1}{|e|T} \left(\epsilon_F - \frac{\Delta}{2} \delta\lambda \right) - \frac{5k_B}{2|e|} \delta\lambda, \quad (2)$$

where ϵ_F is the chemical potential, Δ is the gap, and $\delta\lambda = (\lambda_c - \lambda_v)/(\lambda_c + \lambda_v)$ is the asymmetry parameter. The asymmetry parameter carries the information on band specific correlation strengths since $\lambda_{c,v} = Z_{c,v}^2 m_{c,v}^{*(5/2)} e^{-\beta\mu} / \Gamma_{c,v} m_0^2$, where $Z_{c,v}$ are quasiparticle weights, $\Gamma_{c,v}$ are scattering amplitudes, and $m_{c,v}^*$ is the effective mass of carriers in conduction and valence bands. In addition, in real materials the $|S(T)|_{\max}$ rapidly diminishes with the increase in impurity concentration due to the increase of scattering amplitude, as recently observed in FeSb₂.^{34–36} Bandwidth narrowings $m_{c,v}^*$ influence $S(T)$ not only through the asymmetry parameter $\delta\lambda$ but also via chemical potential since $\epsilon_F = (3k_B T/4) \ln(m_v^*/m_c^*)$.³⁴ Finally, the presence of impurities can have considerable effect on both $|S(T)|_{\max}$ and $S(T)$. The $S(T)$ magnitude at a given temperature depends on the ability of impurity carriers to put the Fermi level in the optimal position for thermopower enhancement.³⁴

Both crystals have similar $S(T)$ and nearly identical magnetothermopower $MT = [S(9T) - S(0)]/S(0)$ in the region of high S (Fig. 3). In contrast to differences in $\rho(T)$, thermopower $S(T)$ for heat flow along the c axis is rather similar above 120 K and below 8 K. Thermopower changes sign from positive to negative above 100 K in both crystals, indicating the presence of two carrier types. Since $m_{c,v}^* = e\tau_{c,v}/\mu_{c,v}$,

where $\tau_{c,v}$ is the scattering time and $\mu_{c,v}$ is the mobility in conduction and valence bands, we use mobility values for individual bands obtained from the fits of the R_H in the two-band model. The value of $Z^2\tau^{5/2}/\Gamma$ then becomes a fit parameter for each carrier band, in addition to the chemical potential ϵ_F . Fits to the above equation for a fixed value of the gap which corresponds to the correlated electron temperature region (10–30) K are shown in Fig. 3(a) as red (crystal 1) and blue (crystal 2) solid lines. The best fits are obtained for the gap values of $\sim(15\text{--}20)$ meV (Table I), suggesting that the large enhancement of S is due to the strong electronic correlations associated with a smaller indirect gap.^{18,26} Note that this is within the extremal limits in the asymmetric case when the chemical potential is near the edge of the valence band ($|S(T)e| \leq \Delta/T + 5/2k_B$).³⁴ For large Γ or for similar λ_c and λ_v (symmetric multiband effects) $S \rightarrow 0$. This is observed: S sign change is at $T = (120 \pm 4)$ K, for both crystals 1 and 2. This implies that correlation effect on $S(T)$ vane at high temperatures.

The phonon drag is unlikely to have a significant contribution to S since isostructural RuSb_2 and FeAs_2 have larger κ and much smaller values of $|S(T)|_{\text{max}}$, due to different temperature dependence of S and Nernst coefficient.^{18,37–39} The $|S(T)|$ rises below 40 K, reaching values of 1 mV/K (crystal 1) and 1.9 mV/K (crystal 2) in the (10–20) K range (Fig. 4). The $S^2\sigma$ of crystal 1 ($7800 \mu\text{W K}^{-2} \text{cm}^{-1}$) is maximized at $T_{\text{max}} = 28$ K, which is higher than in crystal 2 ($T_{\text{max}} = 20$ K) and close to T_{MIT} . The maximum value we find is three times larger than the TPF previously observed²¹ in FeSb_2 and occurs at 16 K higher temperature.

The central finding of the above analysis is that large thermopower in both FeSb_2 crystals can be rationalized within the correlated electron model with two bands having the large disparity of quasiparticle properties. This is best illustrated by the ratio of carrier mobilities in the conduction and valence bands. While the mobility of the valence band carriers in crystal 1 greatly exceeds that of the conduction carriers, they are practically immobilized in crystal 2 where conduction carriers have higher mobility. A key observation here is that despite great disparity in absolute values, mobilities of the

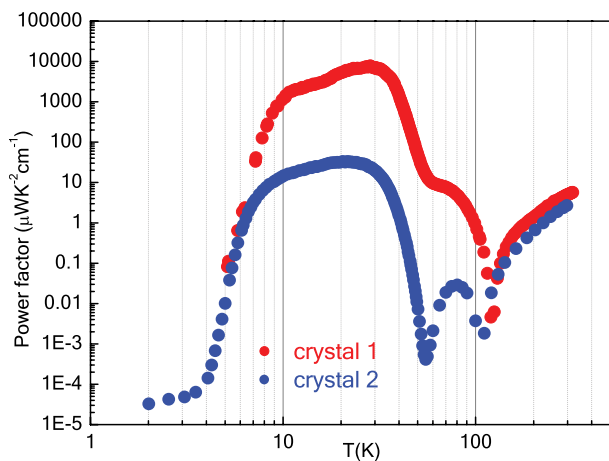


FIG. 4. (Color online) The low resistivity around MIT leads to a record high TPF. Crystal 1 has two orders of magnitude higher TPF between 8 and 100 K.

valence-band carriers in two crystals show strikingly similar temperature dependence with a pronounced anomaly at MIT. Most importantly, in both cases there is a change in the nature of valence charge carriers, which are holes at temperatures above MIT and electrons at lower temperatures. As we discuss later, this observation reveals the likely nature of the MIT and of its absence in crystal 2.

Now we turn to the quasi-one-dimensional (quasi-1D) metallic conductivity¹⁶ and the MIT in crystal 1 which is the key for colossal TPF. For a large concentration of impurities the chemical potential can go into the valence/conduction band, producing metallic $\rho(T)$.³⁴ While an order of magnitude disparity in the number of charge carriers observed in crystals 1 and 2 above ~ 100 K would be consistent with such a scenario, it cannot be reconciled with the closely compensated nature of the carrier content. Below 10 K, where conductivity is governed by impurities, there are more carriers in crystal 2 than in crystal 1. Finally, impurity bands cannot account for the quasi-1D metallic conductance. Band structure suggests that the likely origin of the quasi-1D transport is the nonbonding d_{xy} band, where the overlaps of Fe d_{xy} orbitals are along the chains of edge-sharing octahedra parallel to the c axis, with little or no overlaps between orbitals in different chains [Fig. 5(a)].^{27,40,41} Hall data shows that quasi-1D metallic conductance in sample 1 at temperatures above 40 K is provided by a small number of mobile holes, which implies a nearly filled valence band. Such a nonbonding band must be narrow and strongly correlated, and should be described

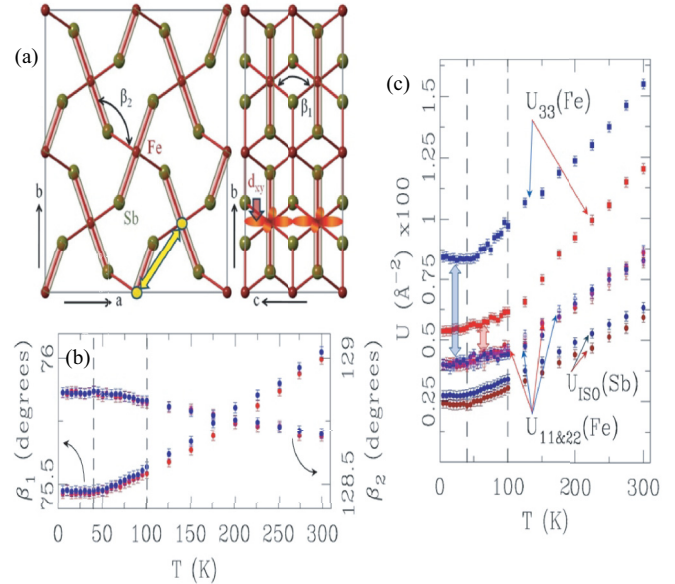


FIG. 5. (Color online) Structural unit of FeSb_2 (a) shows $2 \times 2 \times Pnmm$ unit cell as seen from the top of the c axis (left), and from the top of the a axis (right). Shaded rectangles denote short Fe-Sb distances within the FeSb_6 octahedra. Intrachain and interchain Fe-Sb-Fe angles are denoted as β_1 and β_2 , respectively. Next-nearest-neighbor interchain Fe-Fe distance is indicated by the double arrow. (b) Temperature dependence of β_1 and β_2 for crystal 1 (red) and crystal 2 (blue). (c) ADP factors for Fe (anisotropic) and Sb (isotropic) for crystal 1 (red) and crystal 2 (blue). Vertical dashed lines in (b) and (c) at 40 and 100 K indicate temperatures of insulator-metal transition and change of the nature of the charge carriers, respectively.

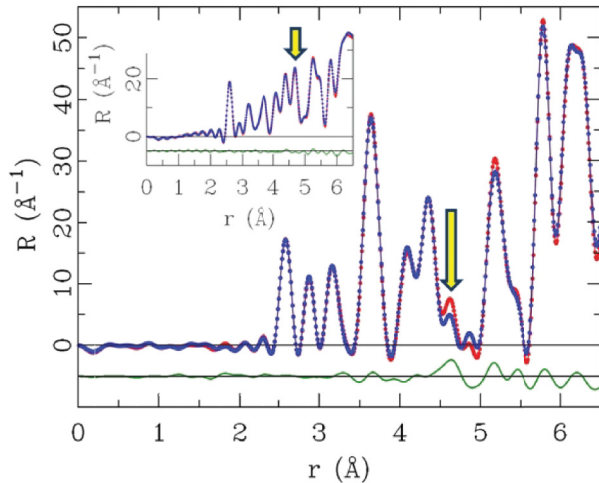


FIG. 6. (Color online) Experimental neutron RDF data (inset) at 20 K reveals no detectable difference, suggesting that the disorder observed in x-ray experiment probably originates from the charge sector.

by the 1D Hubbard model.⁴² The low-dimensional transport in such band is sensitive to disorder and MIT is expected at half filling. Can it be the origin of the MIT observed in crystal 1 that d_{xy} band is depleted with the decreasing temperature, attaining half-filling at T_{MIT} ? Could it then be that a small additional disorder in crystal 2 induces localization of the quasi-1D charge carriers?

In order to answer this question, we performed the PDF analysis of the x-ray data taken on powder samples of crystals 1 and 2 (Figs. 5 and 6). The PDF provides insight into the crystal structure on short and intermediate length scales and allows quantifying subtle structural features such as bond properties and local disorder. Intrachain and interchain Fe-Sb-Fe angles, $\beta_1(T)$ and $\beta_2(T)$, respectively, shown in Fig. 5(b), are very similar, with a small difference developing in β_1 above 100 K. This may indicate charge redistribution involving d_{xy} bands since the presence of Fe d_{xy} charge will result in a somewhat larger β_1 angle.⁴¹ Atomic displacement factors (ADP) [Fig. 5(c)] of Fe atoms are rather anisotropic: mean-square atomic displacements along the a and b axes, U_{11} and U_{22} , are nearly equal for both crystals, while those along the c axis, U_{33} , are noticeably enhanced in crystal 2 at all temperatures, being 0.0084 \AA^2 (crystal 2) and 0.0054 \AA^2 (crystal 1) at 10 K. Enhanced ADPs are typical indication of disorder. In this case disorder is markedly 1D, precisely along the c axis and significantly higher in crystal 2.

It is clear from the difference curves (Fig. 6) in the x-ray RDF (Refs. 23 and 24) that the average local environments on the length scale of about one $Pnmm$ unit cell (reflected in the first several RDF peaks up to 4.5 \AA) are indistinguishable. On larger length scales structural features start to differ. The RDF peak at about 4.65 \AA , denoted by a vertical arrow in Fig. 6, is markedly broader and less intense for crystal 2 at all temperatures studied. This peak corresponds to the next-nearest-neighbor Fe-Fe distance [FeSb₆ interchain distance, double arrow in Fig. 5(a)], with no other contributions. Such a discrepancy could have several origins arising in a difference in

Fe-Fe bond-length distribution, amount of Fe in the structures of the two crystals, charge state of Fe between the two crystals, or a combination of these effects.

Low-dimensional ρ is very sensitive to disorder which, in the simplest picture, suppresses metallic state by inducing strong localization. More generally, the disorder can impact the d_{xy} overlap and the band structure, the orbital character of the electronic states responsible for conduction, the occupancy of Fe d_{xy} orbitals, and even the orbital-dependent Hubbard U interaction strength in a d_{xy} quasi-1D band of itinerant states that forms with sufficient d_{xy} overlap. As opposed to this “self-generated” impurity level arising from Fe d orbitals in crystals with MIT, extrinsic impurity levels cannot produce metallic resistivity near or close to room temperature as in crystals with MIT and are significant only at low temperatures.^{29,30}

Crystals with MIT were cooled slowly from $1000 \text{ }^\circ\text{C}$ to $650 \text{ }^\circ\text{C}$ and were decanted at that temperature from the liquid Sb flux. On the other hand, crystals with no MIT were cooled to $640 \text{ }^\circ\text{C}$, closer to Sb solidification temperature and were subsequently decanted at $690 \text{ }^\circ\text{C}$. There are two main factors that could contribute to increased crystallographic disorder in crystals with no MIT. FeSb₂ melts and decomposes at $738 \text{ }^\circ\text{C}$ to FeSb and Sb. Hence, crystallization occurs over a rather narrow temperature window. Crystals decanted at $690 \text{ }^\circ\text{C}$ are much closer to the melting point when compared to crystals decanted at $650 \text{ }^\circ\text{C}$. This could contribute to increased disorder in Fe-Sb chemical bonds. In addition, crystals cooled to $640 \text{ }^\circ\text{C}$ are closer to solidification line and are likely to experience more stress from the flux. This is consistent with observed structural differences, suggesting that MIT in FeSb₂ crystals is governed by subtle structural differences tunable by synthesis procedure. Greatly increased conductivity near MIT, combined with significant electronic TEP, leads to a new record high thermoelectric power factor.

IV. CONCLUSION

In summary, we report the highest known TPF induced by the synthesis-controlled MIT in the correlated electron semiconductor FeSb₂. The large thermopower enhancement can be understood within the electronic model, whereas MIT likely originates in quasi-1D and strongly correlated narrow bands of itinerant states very sensitive to disorder. This is further supported by the recent observation of quasi-1D magnetism in isostructural CrSb₂.⁴³

ACKNOWLEDGMENTS

We thank T. M. Rice and Simon Billinge for useful discussions and Milinda Abeykoon and Pavol Juhas for help with x-ray experiments. This work was carried out at the Brookhaven National Laboratory, which is operated for the US Department of Energy by Brookhaven Science Associates DE-AC02-98CH10886. The Advanced Photon Source at Argonne National Laboratory, operated by UChicago Argonne LLC, is supported under the US DOE-OS Contract No. DE-AC02-06CH11357. Neutron PDF experiments were carried out on HIPD at LANSCE, funded by DOE BES; LANL is operated by Los Alamos National Security LLC under DE-AC52-06NA25396.

*Present address: Department of Physics, Boston College, Chestnut Hill, MA 02467.

†Present address: Department of Physics, University of Maryland, College Park, MD 20742-4111.

‡petrovic@bnl.gov

§qiangli@bnl.gov

- ¹A. F. Ioffe, *Physics of Semiconductors* (Academic, New York, 1960), p. 282.
- ²B. C. Sales, D. Mandrus, B. C. Chakoumakos, V. Keppens, and J. R. Thompson, *Phys. Rev. B* **56**, 15081 (1997).
- ³G. S. Nolas, J. L. Cohn, G. A. Slack, and S. B. Schujman, *Appl. Phys. Lett.* **73**, 178 (1998).
- ⁴W. Kim, J. Zide, A. Gossard, D. Klenov, S. Stemmer, A. Shakouri, and A. Majumdar, *Phys. Rev. Lett.* **96**, 045901 (2006).
- ⁵B. Poudel, Q. Hao, Y. Ma, Y. Lan, A. Minnich, B. Yu, X. Yan, D. Wang, A. Muto, D. Vashaee, X. Chen, J. Liu, Mildred S. Dresselhaus, G. Chen, and Zhifeng Ren, *Science* **320**, 634 (2008).
- ⁶D. G. Cahill, S. K. Watson, and R. O. Pohl, *Phys. Rev. B* **46**, 6131 (1992).
- ⁷G. D. Mahan, B. Sales, and J. Sharp, *Phys. Today* **50** (3), 42 (1997).
- ⁸G. D. Mahan and J. O. Sofo, *Proc. Natl. Acad. Sci. USA* **93**, 7436 (1996).
- ⁹T. Takabatake, T. Sasakawa, J. Kitagawa, T. Suemitsu, Y. Echizen, K. Umeo, M. Sera, and Y. Bando, *Physica B* **328**, 53 (2003).
- ¹⁰B. C. Sales, E. C. Jones, B. C. Chakoumakos, J. A. Fernandez-Baca, H. E. Harmon, J. W. Sharp, and E. H. Volckmann, *Phys. Rev. B* **50**, 8207 (1994).
- ¹¹C. D. W. Jones, K. A. Regan, and F. J. DiSalvo, *Phys. Rev. B* **58**, 16057 (1998).
- ¹²C. D. W. Jones, K. A. Regan, and F. J. DiSalvo, *Phys. Rev. B* **60**, 5282 (1999).
- ¹³H. Sato, Y. Abe, H. Okada, T. D. Matsuda, K. Abe, H. Sugawara, and Y. Aoki, *Phys. Rev. B* **62**, 15125 (2000).
- ¹⁴K. Abe, H. Sato, T. D. Matsuda, T. Namiki, H. Sugawara, and Y. Aoki, *J. Phys.: Condens. Matter* **14**, 11757 (2002).
- ¹⁵S. R. Harutyunyan, V. H. Vardanyan, A. S. Kuzanyan, V. R. Nikoghosyan, S. Kunii, K. S. Wood, and A. M. Gulian, *Appl. Phys. Lett.* **83**, 2142 (2003).
- ¹⁶C. Petrovic, J. W. Kim, S. L. Bud'ko, A. I. Goldman, P. C. Canfield, W. Choe and G. J. Miller, *Phys. Rev. B* **67**, 155205 (2003).
- ¹⁷C. Petrovic, Y. Lee, T. Vogt, N. Dj. Lazarov, S. L. Bud'ko, and P. C. Canfield, *Phys. Rev. B* **72**, 045103 (2005).
- ¹⁸A. Perucchi, L. Degiorgi, Rongwei Hu, C. Petrovic, and V. F. Mitrovic, *Eur. Phys. J. B* **54**, 175 (2006).
- ¹⁹A. Bentien, G. K. H. Madsen, S. Johnsen, and B. B. Iversen, *Phys. Rev. B* **74**, 205105 (2006).
- ²⁰J. F. DiTusa, K. Friemelt, E. Bucher, G. Aeppli, and A. P. Ramirez, *Phys. Rev. B* **58**, 10288 (1998).
- ²¹A. Bentien, S. Johnsen, G. K. H. Madsen, B. B. Iversen, and F. Steglich, *Europhys. Lett.* **80**, 17008 (2007).
- ²²Rongwei Hu, K. J. Thomas, Y. Lee, T. Vogt, E. S. Choi, V. F. Mitrovic, R. P. Hermann, F. Grandjean, P. C. Canfield, J. W. Kim, A. I. Goldman, and C. Petrovic, *Phys. Rev. B* **77**, 085212 (2008).
- ²³S. J. L. Billinge and T. Egami, *Underneath the Bragg Peaks: Structural Analysis of Complex Materials* (Pergamon Press–Elsevier, Oxford, England, 2003).
- ²⁴C. L. Farrow, P. Juhas, J. W. Liu, D. Bryndin, E. S. Bozin, J. Bloch, T. Proffen, and S. J. L. Billinge, *J. Phys.: Condens. Matter* **19**, 335219 (2007).
- ²⁵S. L. Sodhi, S. M. Girvin, J. P. Carini, and D. Shahar, *Rev. Mod. Phys.* **69**, 315 (1997).
- ²⁶A. Herzog, M. Marutzky, J. Sichelschmidt, F. Steglich, S. Kimura, S. Johnsen, and B. B. Iversen, *Phys. Rev. B* **82**, 245205 (2010).
- ²⁷A. V. Lukoyanov, V. V. Mazurenko, V. I. Anisimov, M. Sigrist, and T. M. Rice, *Eur. Phys. J. B* **53**, 205 (2006).
- ²⁸J. S. Kim, *J. Appl. Phys.* **86**, 3187 (1999).
- ²⁹Rongwei Hu, V. F. Mitrovic, and C. Petrovic, *Appl. Phys. Lett.* **92**, 182108 (2008).
- ³⁰H. Takahashi, R. Okazaki, Y. Yasui, and I. Terasaki, *Phys. Rev. B* **84**, 205215 (2011).
- ³¹G. A. Saunders and O. Oktu, *J. Phys. Chem. Solids* **29**, 327 (1968).
- ³²E. H. Putley, *The Hall Effect in Semiconductor Physics* (Dover, New York, 1968).
- ³³V. Jovicic and J. P. Heremans, *Phys. Rev. B* **77**, 245204 (2008).
- ³⁴Jan M. Tomczak, K. Haule, T. Miyake, A. Georges, and G. Kotliar, *Phys. Rev. B* **82**, 085104 (2010).
- ³⁵A. Bentien, G. K. H. Madsen, S. Johnsen, and B. B. Iversen, *Phys. Rev. B* **74**, 205105 (2006).
- ³⁶H. Takahashi, Y. Yasui, I. Terasaki, and M. Sato, *J. Phys. Soc. Jpn.* **80**, 054708 (2011).
- ³⁷N. Lazarevic, Z. V. Popovic, Rongwei Hu, and C. Petrovic, *Phys. Rev. B* **81**, 144302 (2010).
- ³⁸P. Sun, N. Oeschler, S. Johnsen, B. B. Iversen, and F. Steglich, *Appl. Phys. Express* **2**, 091102 (2009).
- ³⁹Peijie Sun, Niels Oeschler, Simon Johnsen, Bo Brummerstedt Iversen, and F. Steglich, *Phys. Rev. B* **79**, 153308 (2009).
- ⁴⁰J. B. Goodenough, *J. Solid State Chem.* **5**, 144 (1972).
- ⁴¹F. Hulliger, *Struct. Bonding (Berlin)* **4**, 83 (1967).
- ⁴²F. H. L. Essler, *The One Dimensional Hubbard Model* (Cambridge University Press, Cambridge, 2005).
- ⁴³M. B. Stone, M. D. Lumsden, S. E. Nagler, D. J. Singh, J. He, B. C. Sales, and D. Mandrus, *Phys. Rev. Lett.* **108**, 167202 (2012).

Magnetism in $\text{La}_2\text{O}_3(\text{Fe}_{1-x}\text{Mn}_x)_2\text{Se}_2$ tuned by Fe/Mn ratio

Hechang Lei (雷和畅),¹ Emil S. Bozin,¹ A. Llobet,² V. Ivanovski,³ V. Koteski,³ J. Belosevic-Cavor,³ B. Cekic,³ and C. Petrovic¹

¹Condensed Matter Physics and Materials Science Department, Brookhaven National Laboratory, Upton, New York 11973, USA

²Lujan Neutron Scattering Center, Los Alamos National Laboratory, MS H805, Los Alamos, New Mexico 87545, USA

³Institute of Nuclear Sciences Vinca, University of Belgrade, Belgrade 11001, Serbia

(Received 26 June 2012; revised manuscript received 22 August 2012; published 17 September 2012)

We report the evolution of structural and magnetic properties in $\text{La}_2\text{O}_3(\text{Fe}_{1-x}\text{Mn}_x)_2\text{Se}_2$. Heat capacity and bulk magnetization indicate an increased ferromagnetic component of the long-range magnetic order and possible increased degree of frustration. Atomic disorder on Fe(Mn) sites suppresses the temperature of the long-range order whereas intermediate alloys show a rich magnetic phase diagram.

DOI: [10.1103/PhysRevB.86.125122](https://doi.org/10.1103/PhysRevB.86.125122)

PACS number(s): 74.25.Wx, 74.25.F–, 74.25.Op, 74.70.Dd

I. INTRODUCTION

Parent materials of cuprates and iron-based superconductors are layered transition metal (TM) compounds with an antiferromagnetic (AFM) ground state due to a dissimilar magnetic mechanism and with rather different electronic conductivity.¹ The local environment of TM is intimately connected with this since puckering of iron pnictide crystallographic layers promotes higher conductivity in parent materials of iron superconductors, as opposed to cuprates.^{2,3} Recently, a family of layered TM oxychalcogenides $\text{Ln}_2\text{O}_3\text{TM}_2\text{Ch}_2$ (Ln = rare earth, TM = Mn, Fe, Co, and Ch = S, Se) and its analogs $\text{A}_2\text{F}_2\text{TM}_2\text{OCh}_2$ (A = Sr, Ba)(2322) has received more attention.^{4–16} They have anti- CuO_2 -type $[\text{TM}_2\text{OCh}_2]^{2-}$ layers and the local environment of TM bears much more resemblance to manganites or cuprates than to iron-based superconductors. This typically results in a semiconducting or Mott-insulating ground state with AFM transition.^{5,8} Within the $[\text{TM}_2\text{OCh}_2]^{2-}$ layers transition metal atoms are located at the distorted octahedral environment due to the different distances of TM-Ch and TM-O, whereas the TM-Ch(O) octahedrons are face sharing. This distortion lifts the degeneracy of e_g and t_{2g} levels in a nondistorted octahedral crystal field. The $[\text{TM}_2\text{OCh}_2]^{2-}$ layers in the crystal structure harbor three principal competing interactions: the nearest neighbor (NN) J_3 interaction of the closest TM atoms in the crystallographic ab plane, next nearest neighbor (NNN) superexchange interaction J_2 of nearly 90° TM-Ch-TM, and (NNN) J_1 superexchange interaction of 180° TM-O-TM.^{4,6,8,14} Theoretical calculation and neutron diffraction results indicate that the AFM transition stems from the competition of three interactions in an unusual frustrated AFM checkerboard spin-lattice system.^{6–10,14,16} Frustrated magnetic order on checkerboard lattices hosts rich magnetic ground states and could be relevant to physics of colossal magnetoresistance manganites and iron-based and cuprates superconducting materials.^{17–21} Therefore it is of interest to address the nature of magnetic order and frustration in 2322 materials since it shares some characteristics of all the above mentioned compounds.

Among 2322 materials, $\text{La}_2\text{O}_3\text{Mn}_2\text{Se}_2$ (Mn-2322) exhibits a faint specific heat anomaly at AFM transition and two-dimensional (2D) short-range magnetic correlations that lock magnetic entropy far above the temperature of the bulk long-range AFM transition.^{14,15} A weak ferromagnetic (FM) component superimposed on the paramagnetic background in

M(H) loops at 2 K proposed to arise due to spin reorientation and/or spin canting below the AFM transition,¹⁴ might also come from magnetic impurities such as Mn_3O_4 .¹⁶ Mn-2322 has a G-type AFM structure with the ordered moment along the c -axis direction and where NN Mn ions have opposite spins with dominant AFM $J_3 < 0$ and fully frustrated $|J_1| < J_2$ with $J_1 < 0$ and $J_2 > 0$.^{14,16} On the other hand, $\text{La}_2\text{O}_3\text{Fe}_2\text{Se}_2$ (Fe-2322) adopts magnetic structure similar to FeTe where half of the J_3 , J_2 , and J_1 are frustrated^{9,16,22} and different from the theoretical predictions.⁸ This is different from other compounds with the same structure, in which J_1 is the dominant term.¹⁰

In this work we tuned the magnetism on Fe/Mn checkerboard lattice by varying TM content and examined the magnetic ground states of the $\text{La}_2\text{O}_3(\text{Fe}_{1-x}\text{Mn}_x)_2\text{Se}_2$ series. We find that Mn substitution leads to the increase of activation energies for the electrical transport energy gap E_a and has a strong effect on the magnetic phase diagram and the spin entropy release above the temperature of the long-range magnetic order.

II. EXPERIMENT

$\text{La}_2\text{O}_3(\text{Fe,Mn})_2\text{Se}_2$ [(Fe,Mn)-2322] polycrystals were synthesized by solid-state reaction from high purity materials ($\geq 99\%$). Dried La_2O_3 powder, Mn lump, and Fe and Se powders were mixed and ground in an agate mortar. The mixture was pressed into pellets and sealed in a quartz tube backfilled with pure argon gas. The ampule was heated to 1273 K and reacted for 24 h followed by furnace cooling. This was repeated several times to ensure homogeneity. The color of the final product is yellowish green for Mn-2223 and black for Fe-2322.

Powder x-ray diffraction (XRD) patterns of the ground samples were taken with $\text{Cu } K_\alpha = 0.1458$ nm using a Rigaku Miniflex x-ray machine. The structural parameters were obtained by Rietveld refinement using RIETICA software.²³ Single crystal x-ray data were collected in a Bruker Kappa Apex II single crystal x-ray diffractometer at room temperature with $\text{Mo } K_\alpha = 0.071073$ nm on a 20- μm single crystal isolated from the polycrystalline powder. Single crystal unit cell refinement was performed with the Bruker APEX 2 software package. Time-of-flight neutron diffraction measurements were carried out at 300 K on the high intensity powder diffractometer (HIPD) of the Lujan Neutron Scattering Center

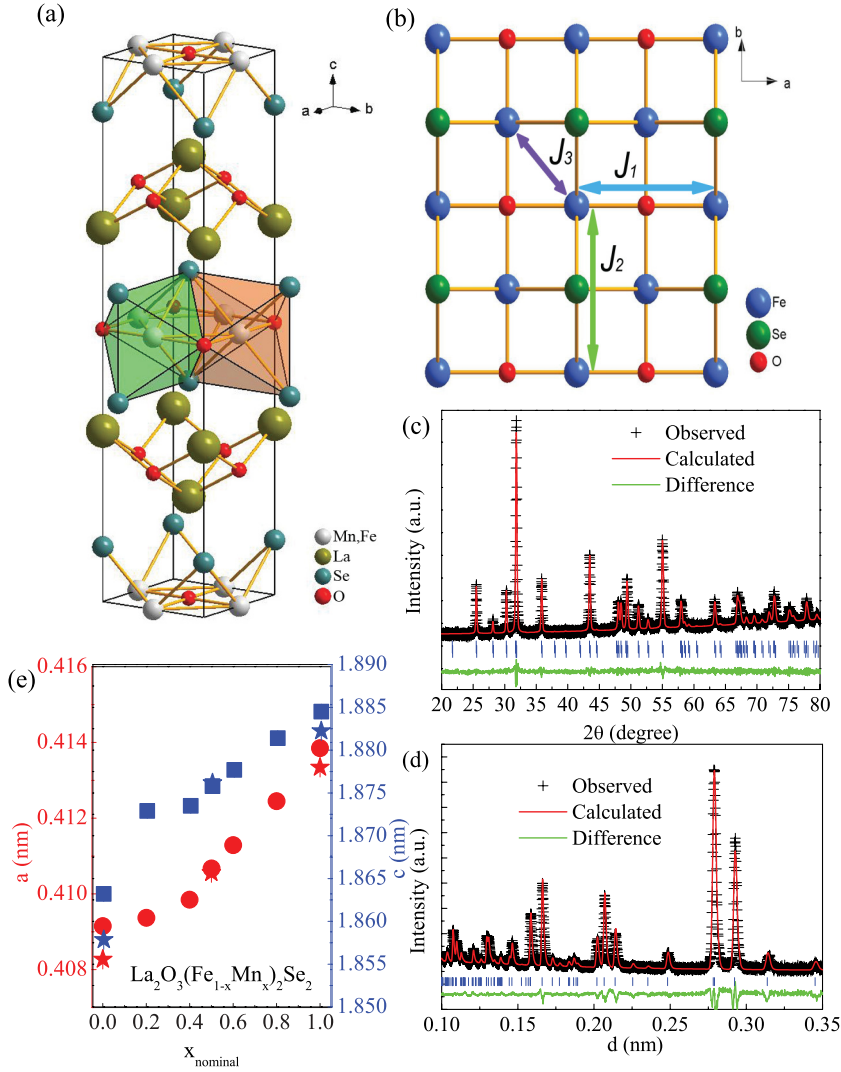


FIG. 1. (Color online) (a) Crystal structure of $(\text{Fe,Mn})\text{-2322}$. (b) TM-O planes shown for $\text{TM} = \text{Fe}$. Se atoms (green) are puckered above and below the plane, with Se-Fe-Se angle 97.04° along both a and b crystallographic axes. (c) and (d) XRD and neutron powder diffraction results at room temperature for the Mn-2322 polycrystal, respectively. (e) Lattice parameters for $(\text{Fe,Mn})\text{-2322}$ determined from neutron diffraction (stars) and XRD (circles).

at the Los Alamos National Laboratory. Pulverized samples were loaded in extruded vanadium containers in helium atmosphere and sealed. Data were collected for 1 h for each sample. Rietveld refinements of the data were carried out using GSAS software^{24,25} within the $I4/mmm$ space group.

Mössbauer spectra were taken in transmission mode with the $^{57}\text{Co}(\text{Rh})$ source at 294 K and the parameters were obtained using WINNORMOS software.²⁶ Calibration of the spectrum was performed by laser and isomer shifts were given with respect to $\alpha\text{-Fe}$.

Thermal, transport, and magnetic measurements were carried out in a Quantum Design PPMS-9 and MPMS-5. The samples were cut into rectangular parallelepipeds and thin Pt wires were attached for four probe resistivity measurements. Sample dimensions were measured with an optical microscope Nikon SMZ-800 with $10\text{-}\mu\text{m}$ resolution.

III. RESULTS AND DISCUSSIONS

Crystal structure of $(\text{Fe,Mn})\text{-2322}$ and principle magnetic interactions $J_1\text{-}J_3$ are shown in Figs. 1(a) and 1(b). Both XRD and neutron reflections can be indexed using a tetragonal unit cell [Figs. 1(c) and 1(d)], indicating a continuous solid solution between Mn-2322 and Fe-2322. The unit cell of Mn-2322

single crystal determined from the single crystal x-ray experiment was $I4/mmm$ with $a = 0.417(3)$ nm and $c = 1.89(2)$ nm, in agreement with the powder data. Powder x-ray and neutron lattice parameters are shown in Fig. 1(e) and details of the crystal structure extracted from the neutron data, listed in Tables I–III, are consistent with the reported values.^{8,14} For Mn-2322, using obtained Mn-Se and Mn-O bond lengths (shown in Table I), we calculate the valence of Mn ions using the bond

TABLE I. Structural parameters for $\text{La}_2\text{O}_3\text{Fe}_2\text{Se}_2$ at 300 K.

Chemical Formula		$\text{La}_2\text{O}_3\text{Fe}_2\text{Se}_2$			
Interatomic Distances (nm)		Bond Angles ($^\circ$)			
$d_{\text{Fe-O}}$	0.20413(1)	O-Fe-O	180		
$d_{\text{Fe-Se}}$	0.27129(8)	Se-Fe-Se	97.61(4)/82.39(4)		
$d_{\text{Fe-Fe}}$	0.28869(1)	Se-Fe-O	90		
Atom	x	y	z	Occ	U_{iso} (10^{-2} nm ²)
La	0.5	0.5	0.1843(1)	1	0.0026(2)
O1	0.5	0	0.25	1	0.0059(3)
O2	0.5	0.5	0	1	0.0124(5)
Fe	0.5	0	0	1	0.0059(2)
Se	0	0	0.0962(1)	1	0.0032(2)

TABLE II. Structural parameters for $\text{La}_2\text{O}_3(\text{Fe}_{0.5}\text{Mn}_{0.5})_2\text{Se}_2$ at 300 K.

Chemical Formula						$\text{La}_2\text{O}_3(\text{Fe}_{0.5}\text{Mn}_{0.5})_2\text{Se}_2$					
Interatomic Distances (nm)						Bond Angles ($^\circ$)					
$d_{\text{Fe}/\text{Mn}-\text{O}}$		0.20528(1)		O-Fe-O		180					
$d_{\text{Fe}/\text{Mn}-\text{Se}}$		0.27641(12)		Se-Fe-Se		95.92(6)/84.08(6)					
$d_{\text{Fe}/\text{Mn}-\text{Fe}/\text{Mn}}$		0.29031(1)		Se-Fe/Mn-O		90					
Atom	x	y	z	Occ	U_{iso} (10^{-2} nm^2)						
La	0.5	0.5	0.1851(1)	1	0.0057(3)						
O1	0.5	0	0.25	1	0.0051(5)						
O2	0.5	0.5	0	1	0.0100(7)						
Fe	0.5	0	0	1	0.0058(8)						
Se	0	0	0.0987(1)	1	0.0044(4)						

valence sum (BVS) formalism in which each bond with a distance d_{ij} contributes a valence $v_{ij} = \exp[(R_{ij} - d_{ij})/0.37]$ with R_{ij} as an empirical parameter and the total of valences of atom i , V_i equals $V_i = \sum_j v_{ij}$.^{27,28} The calculated valence of Mn ions is +2.03, consistent with the apparent oxidation state (+2) for Mn atoms. With an increase in Mn content, the lattice parameters increase gradually for both a and c axes, hence the unit cell of Mn-2322 is larger than Fe-2322, which itself is larger than the unit cell of $\text{La}_2\text{O}_2\text{Co}_2\text{OSe}_2$ (Co-2322).^{4,7} This trend can be explained by the larger ionic size of Mn^{2+} when compared to Fe^{2+} and Co^{2+} ions, giving some insight in the spin state of Mn^{2+} ions. The lattice parameters should be proportional to the ionic size, $r_{\text{TM}^{2+}}$, of transition metals TM^{2+} (TM = Mn, Fe, and Co). Therefore from the observation $a_{\text{Mn}} = 0.41334 \text{ nm} > a_{\text{Fe}} = 0.40788 \text{ nm} > a_{\text{Co}} = 0.40697 \text{ nm}$ and $c_{\text{Mn}} = 1.88221 \text{ nm} > c_{\text{Fe}} = 1.86480 \text{ nm} > c_{\text{Co}} = 1.84190 \text{ nm}$ we conclude that $r_{\text{Mn}^{2+}} > r_{\text{Fe}^{2+}} > r_{\text{Co}^{2+}}$. Mössbauer spectra and theoretical calculations for Fe-2322 and Co-2322 suggest that Fe^{2+} and Co^{2+} are in the high spin state.^{6,10} This is in agreement with $r_{\text{Fe}^{2+}}(0.0780 \text{ nm}) > r_{\text{Co}^{2+}}(0.0745 \text{ nm})$ for the high spin (HS) state (coordination number = 6). Therefore, the Mn^{2+} ions should be in the HS state since $r_{\text{Mn}^{2+}}(\text{LS}) = 0.067 \text{ nm}$ (LS = low spin) and $r_{\text{Mn}^{2+}}(\text{HS}) = 0.083 \text{ nm}$ for Mn^{2+} with sixfold coordination.

Mössbauer isomer shifts δ are sensitive on the electron density on a nucleus. Electric quadrupole splitting Δ arises due to interaction between electric field gradient and nuclear

TABLE III. Structural parameters for $\text{La}_2\text{O}_3\text{Mn}_2\text{Se}_2$ at 300 K.

Chemical Formula						$\text{La}_2\text{O}_3\text{Mn}_2\text{Se}_2$					
Interatomic Distances (nm)						Bond Angles ($^\circ$)					
$d_{\text{Mn}-\text{O}}$		0.2667(1)		O-Mn-O		180					
$d_{\text{Mn}-\text{Se}}$		0.28030(1)		Se-Mn-Se		95.01(1)/84.99(1)					
$d_{\text{Mn}-\text{Mn}}$		0.29227(1)		Se-Fe-O		90					
Atom	x	y	z	Occ	U_{iso} (10^{-2} nm^2)						
La	0.5	0.5	0.1866(2)	1	0.0042(5)						
O1	0.5	0	0.25	1	0.0057(7)						
O2	0.5	0.5	0	1	0.0015(8)						
Mn	0.5	0	0	1	0.0086(8)						
Se	0	0	0.1006(1)	1	0.0020(5)						

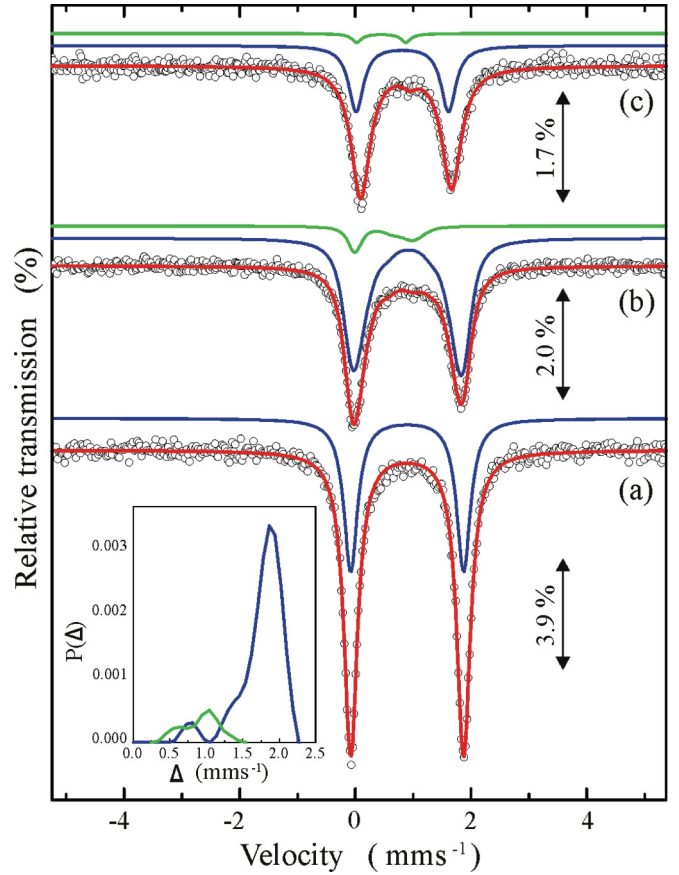


FIG. 2. (Color online) Mössbauer spectra of $\text{La}_2\text{O}_3(\text{Fe}_{1-x}\text{Mn}_x)_2\text{Se}_2$ for $x = 0$ (a), $x = 0.2$ (b), and $x = 0.5$ (c), respectively. Vertical arrows denote relative positions of peaks with respect to the background. The data were shown by open circles and the fit is given by the red solid line. The doublets of the main (blue) and impurity (green) phases are offset for clarity. Inset shows the distributions of the electrical quadrupole splitting at the ^{57}Fe spectrum of $\text{La}_2\text{O}_3(\text{Fe}_{0.8}\text{Mn}_{0.2})_2\text{Se}_2$.

quadrupole moment. The δ and Δ provide information of the oxidation, spin state, chemical bonding, and site symmetry. Mössbauer spectra of Fe-2322 [Fig. 2(a)] shows a single doublet, consistent with a single inequivalent $4c$ position of Fe in $I4/mmm$ space group of the unit cell. Isomer shifts $\delta = 0.895(1) \text{ mm/s}$ and quadrupole splitting [$\Delta = 1.952(1) \text{ mm/s}$] (Table IV) are well in agreement with the high spin $S = 2$ of Fe^{2+} in the D_{2h} symmetry site of FeO_2Se_2 octahedra.¹¹ However, the $v = 0.3 \text{ mm/s}$ discrepancy between the experimental and theoretical fits and the mild asymmetry of peak intensities suggest that another interaction is superimposed on the main doublet. The Fe^{2+} experiences either an additional doublet or sextet due to an impurity phase or a high

TABLE IV. Mössbauer isomer shifts δ and electric field quadrupole splittings Δ for $\text{La}_2\text{O}_3(\text{Fe}_{1-x}\text{Mn}_x)_2\text{Se}_2$ at 294 K.

Chemical formula	$\delta(\text{mm/s})$	$\Delta(\text{mm/s})$	$\Gamma(\text{mm/s})$
$\text{La}_2\text{O}_3\text{Fe}_2\text{Se}_2$	0.895(1)	1.952(1)	0.287(2)
$\text{La}_2\text{O}_3(\text{Fe}_{0.8}\text{Mn}_{0.2})_2\text{Se}_2$	0.90(4)	1.756	0.309
$\text{La}_2\text{O}_3(\text{Fe}_{0.5}\text{Mn}_{0.5})_2\text{Se}_2$	0.812(6)	1.60(1)	0.309(7)

temperature magnetism in the sample with magnetic dipole interaction of $\mu_0 H \ll eV_{zz} Q$ magnitude. However, no known impurity phase, including LaFeO_3 , was able to explain the experimental spectra. In contrast, Mössbauer spectra in both $\text{La}_2\text{O}_3(\text{Fe}_{0.5}\text{Mn}_{0.5})_2\text{Se}_2$ and $\text{La}_2\text{O}_3(\text{Fe}_{0.8}\text{Mn}_{0.2})_2\text{Se}_2$ detected Fe-Se phase impurity with $\delta = 0.45(7)$ mm/s, $\Delta = 0.8(1)$ mm/s. When Mn substitutes Fe in a 1:4 ratio [Fig. 2(b)] there are eight Fe^{2+} ions in the first two coordination spheres which contribute to 10 different combinations after the substitution if all combinations are of equal probability. The most important contribution to hyperfine interactions is from the first coordination sphere. With 1:4 Mn to Fe ratio there are three different combinations: with 0, 1, or 2 Mn on four Fe sites. The ratio of these combinations is 17:20:3, respectively. Distribution of electric quadrupole splittings centered at 1.756 mm/s, with 0.309 mm/s standard deviation and pronounced tail near the smaller values confirms uniform distribution of Mn. The main doublet and minority phase (or interaction) are also present when one-half of Fe^{2+} is replaced by Mn^{2+} in $\text{La}_2\text{O}_3(\text{Fe}_{0.5}\text{Mn}_{0.5})_2\text{Se}_2$ [Fig. 2(c)]. The atomic positions where half of Fe ions were substituted by Mn are symmetric within the first coordination sphere around Fe^{2+} that contains FeO_2Se_2 and four closest Fe ions in the Fe-O planes [Fig. 1(a)]. This is confirmed by the rather small widening of the doublet lines [$\Gamma = 0.309(7)$ mm/s]. Decreased values of isomer shift δ suggest a change in the charge density on the Fe^{2+} and substantial decrease of the octahedra (Table IV).⁴

In order to complement the Mössbauer measurements, we performed density functional theory (DFT) calculations using the WIEN2K all-electron full-potential APW + lo code.²⁹ For La, Fe, Mn, Se, and O atoms the muffin-tin sphere radii were set to 2.38, 1.86, 1.86, 2.5, and 1.62 a.u. The basis set functions were expanded up to $R_{\text{mt}}K_{\text{max}} = 7$. We used the LDA-Fock-0.25 hybrid functional,^{10,30} which provides a viable alternative to the LDA + U approach in describing the electron correlations in this system. Starting from the Fe-2322 and Mn-2322 pure structures, we constructed $2 \times 2 \times 1$ supercells of $\text{La}_2\text{O}_3(\text{Fe}_{0.25}\text{Mn}_{0.75})_2\text{Se}_2$, $\text{La}_2\text{O}_3(\text{Fe}_{0.5}\text{Mn}_{0.5})_2\text{Se}_2$, and $\text{La}_2\text{O}_3(\text{Fe}_{0.75}\text{Mn}_{0.25})_2\text{Se}_2$ to approximate the mixed Fe-Mn systems. Figure 3 shows the total density of states (DOS) as calculated for the FM state of the investigated compounds.

The LDA-Fock-0.25 hybrid functional correctly predict the Mott-insulating behavior of (Fe, Mn)-2322. The band gaps are similar but decrease somewhat from pure Fe-2322 (about 0.4 eV) to pure Mn-2322 (about 0.25 eV). The overall shape of the DOS across this group is very similar, one significant distinction being the band-gap shift of the minority DOS towards lower energies with increased Mn content. In our checkerboard AFM LDA-Fock-0.25 calculations (carried out only for the end compounds, not shown here), the band gaps of Fe-2322 and Mn-2322 are found to be 1.85 and 0.99 eV, respectively. Our calculations indicate that the AFM state is more stable than the FM state by 0.75 eV in Fe-2322 and 0.43 eV in Mn-2322. The supercell approach also enabled us to calculate the electric field gradient (EFG) and isomer shift (IS) at Fe situated in several different local coordinations. In Fig. 4 we compare the results of our calculations with the values extracted from Mössbauer spectroscopy. While our calculations were able to reproduce the values of the measured EFGs, the ISs are found to be smaller than the experimental

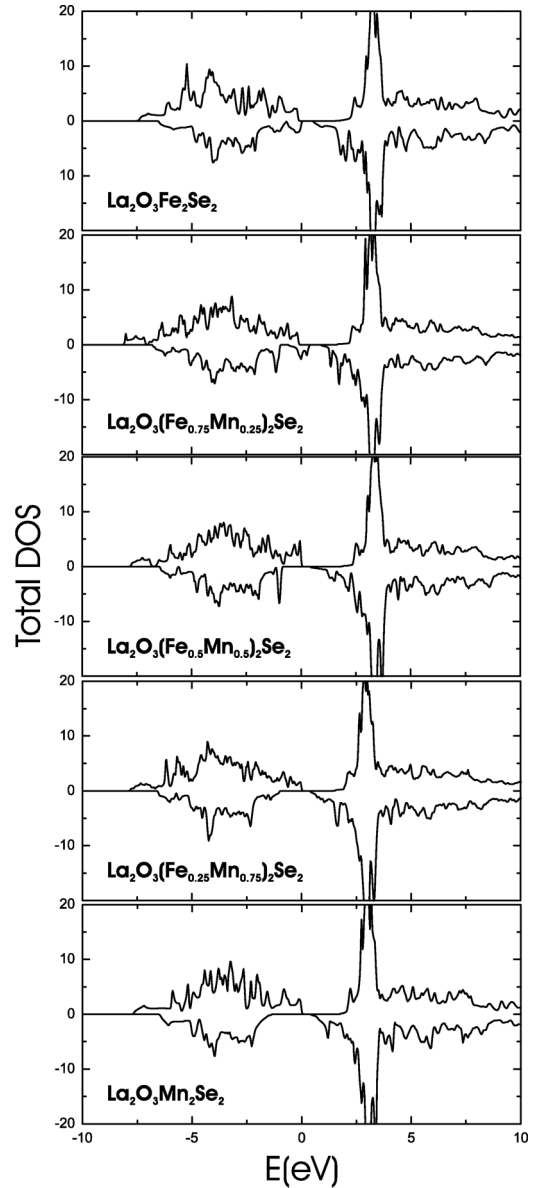


FIG. 3. Total DOS per formula unit for the FM state of (Fe, Mn)-2322. The Fermi level is set to zero energy. There is a band-gap shift of the minority DOS towards lower energies as Mn substitutes Fe in the lattice.

values by up to 20%. The discrepancy is because experimental Mössbauer includes second-order Doppler shift and chemical isomer shift due to electronic density whereas the theoretical parts involves only the latter. The calculated EFG of 11.6×10^{21} V/m² in pure Fe-2322 agrees very well with the EFG obtained in similar DFT calculations.³¹

Neglecting grain boundaries, Mn-2322 resistivity at room temperature is about $2 \times 10^4 \Omega \text{ cm}$. This is two orders of magnitude smaller than Co-2322.⁷ The resistivities of (Fe, Mn)-2322 exhibit activated behavior, $\rho = \rho_0 \exp(E_a/k_B T)$, where ρ_0 is the prefactor, E_a is the activation energy, k_B is the Boltzmann's constant, and T is temperature [Figs. 5(a) and 5(b)]. By fitting the $\rho(T)$ data from 210 to 320 K we obtain the activation energy $E_a = 0.2425(2)$ eV for Mn-2322. This is substantially smaller than the activation energy of Co-2322⁷ and consistent

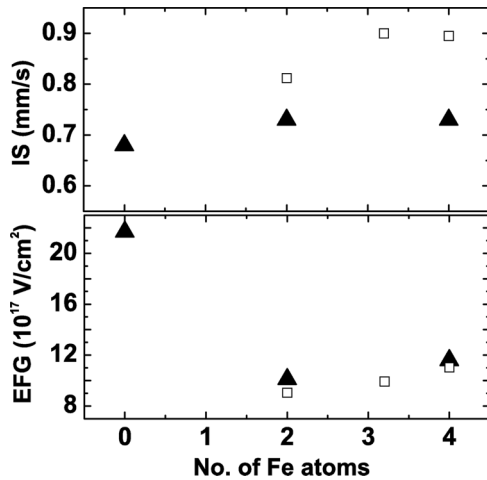


FIG. 4. Calculated (solid triangles) and measured (open squares) EFGs and ISs plotted as a function of the number of (in-plane) neighboring Fe atoms. Our $2 \times 2 \times 1$ supercells did not allow for geometries with one and three Fe atoms. The experimental EFGs and ISs are plotted against the average number of neighboring Fe atoms in $\text{La}_2\text{O}_3(\text{Fe}_{0.5}\text{Mn}_{0.5})_2\text{Se}_2$, $\text{La}_2\text{O}_3(\text{Fe}_{0.8}\text{Mn}_{0.2})_2\text{Se}_2$, and Fe-2322.

with the recently reported value.¹⁶ The E_a decreases rapidly by $x = 0.5$ (0.1814(3) eV), then gradually as the Mn/Fe ratio is tuned to Fe-2322 [0.1796(3) eV]. The value of E_a for Fe-2322 is close to that reported in the literature.⁸ The residual resistivity values (ρ_0) exhibit the same trend. These results indicate that the band gap of (Fe,Mn)-2322 decreases with the contraction of lattice parameters. Narrowing of the band gap is also consistent with sample color changes from yellowish green in Mn-2322 to black in Fe-2322. Gap values obtained for Mn-2322 are in agreement with LDA calculations (Fig. 3), however, for Fe-2322 and for intermediate alloys there is a disagreement. This suggests increased importance of strong electronic correlations for increased Fe site occupancy of (Fe, Mn)-2322 alloys.

Temperature dependence of dc magnetic susceptibility $\chi(T) = M/H$ taken in 50 kOe magnetic field for (Fe,Mn)-2322 with zero field cooling (ZFC) is shown in Fig. 6(a). For Fe-2322, there is AFM transition at $T_N = 90$ K, consistent with previous results.⁸ With Mn doping, this AFM transition shifts to lower temperature quickly and disappears in Mn-2322. On the other hand, there is other FM-like transition emerging and shifting to higher temperature when Mn enters the lattice. Finally, for Mn-2322, the $\chi(T)$ curves of Mn-2322 [inset of Fig. 6(a)] exhibit three features: one broader maximum, T_{Max} and two anomalies, T_{M1} and T_{M2} . T_{Max} (~ 275 K) with no Curie-Weiss behavior up to 350 K implies that there is a stronger two-dimensional short-range spin correlation in Mn-2322 than in Fe-2322 at high temperature, reflecting the frustrated nature of the magnetic structure in Mn-2322.^{14,16} From the sharp minimum of the $d(\chi T)/dT$ curves [Fig. 6(b)] we extract $T_{M1} \sim 164$ K, in agreement with previous results.¹⁴⁻¹⁶ The T_{M1} anomaly is field independent and therefore should have considerable ferromagnetic component due to canting and/or magnetocrystalline anisotropy possibly induced by frustration.¹⁴ The second anomaly {minimum in $d(\chi T)/dT$ at $T_{M2} = 122$ K [inset of Fig. 6(a)]} is also field

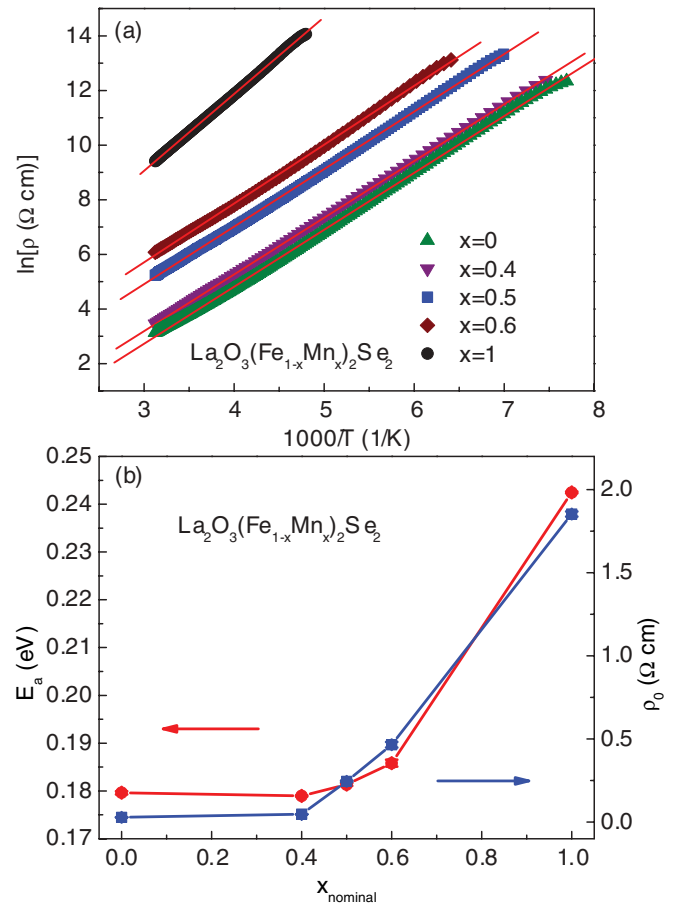


FIG. 5. (Color online) (a) Temperature dependence of the resistivity for (Fe,Mn)-2322 polycrystals. (b) Activation energies using $\rho = \rho_0 \exp(E_a/k_B T)$ and the relation between ρ_0 , E_a , and x_{nominal} .

independent, however, it is strongly suppressed in high fields. This is in agreement with its proposed spin reorientation origin.¹⁴ The ZFC and field cooling (FC) $\chi(T)$ curves split at $T_{M1,2}$ but gradually overlap with magnetic field increase [Fig. 6(c)]. This implies the presence of either magnetic frustration or magnetocrystalline anisotropy. On the other hand, $\chi(T)$ of Mn-2322 show a hump around $T_N = 42$ K at 1 kOe with the ZFC mode (blue curve), similar to previous results.^{14,16} It could be due to superparamagnetic Mn_3O_4 nanoparticle contamination below our diffraction resolution limit.¹⁶ Overall, the substantial shift of the cusp with x and the evolution of an FM-like increase of magnetization above the cusp temperature point to development of intrinsic magnetic interactions from Fe-2322 to Mn-2322. With Mn doping, the part of magnetic entropy that contributes to the long-range order rapidly shifts to lower temperature whereas the frustration-induced FM (or canting, anisotropic exchange interactions) component of magnetization increases and high temperature two-dimensional short-range magnetic order becomes stronger as the magnetic system is tuned toward the lattice with full Mn occupation.

The specific heat of (Fe,Mn)-2322 (Fig. 7) approaches the value of $3NR$ at 300 K, where N is the atomic number in the chemical formula ($N = 9$) and R is the gas constant ($R = 8.314 \text{ J mol}^{-1} \text{ K}^{-1}$), consistent with the Dulong-Petit law.

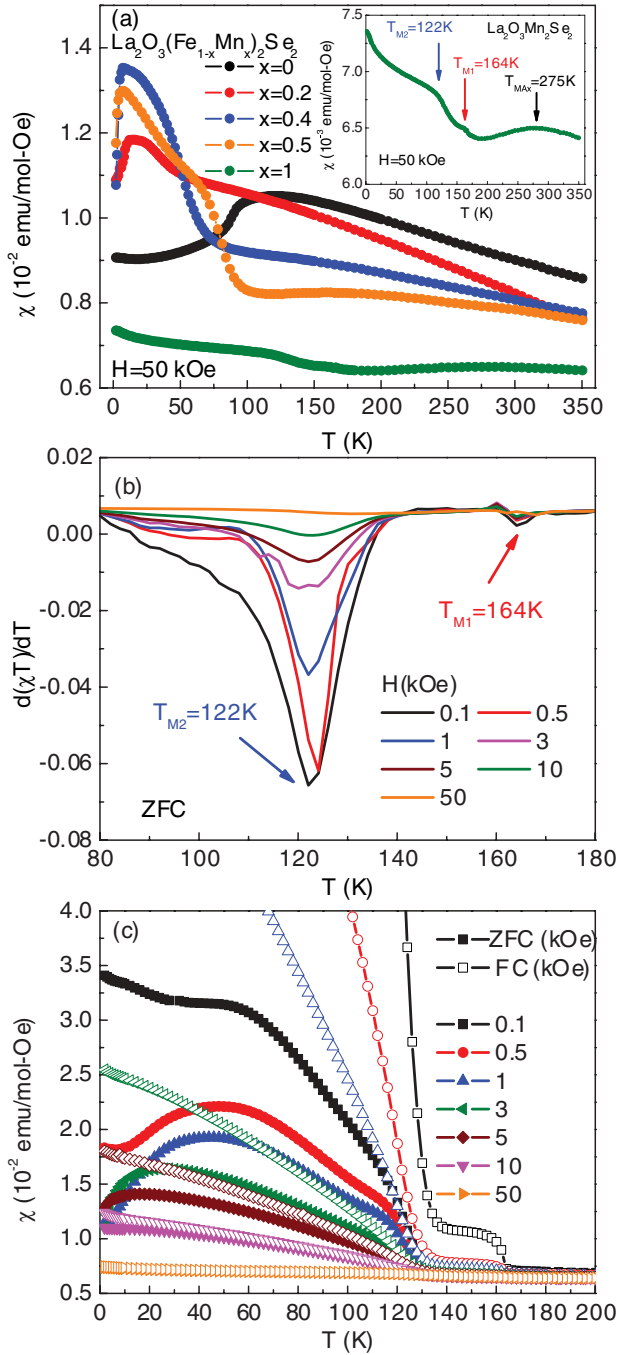


FIG. 6. (Color online) (a) Temperature dependence of the magnetic susceptibility $\chi(T)$ for (Fe,Mn)-2322 taken in 50 kOe. Inset shows enlarged $\chi(T)$ for Mn-2322. (b) $d(\chi T)/dT$ of Mn-2322 at various magnetic fields for ZFC magnetization. (c) ZFC and FC curves of Mn-2322 near magnetic transitions.

On the other hand, Fe-2322 specific heat shows a λ -type anomaly at $T = 89$ K for Fe-2322 in agreement with the result in the literature.¹¹ This anomaly is due to a long-range three-dimensional antiferromagnetic (AFM) ordering of the Fe^{2+} . After subtraction of the phonon contribution (C_{ph}) fitted using a polynomial for the total specific heat, we obtain the magnetic contribution (C_{mag}) and calculate the magnetic entropy using $S_{\text{mag}}(T) = \int_0^T C_{\text{mag}}/T dt$. The derived S_{mag} is 3.23 J/mol-K at

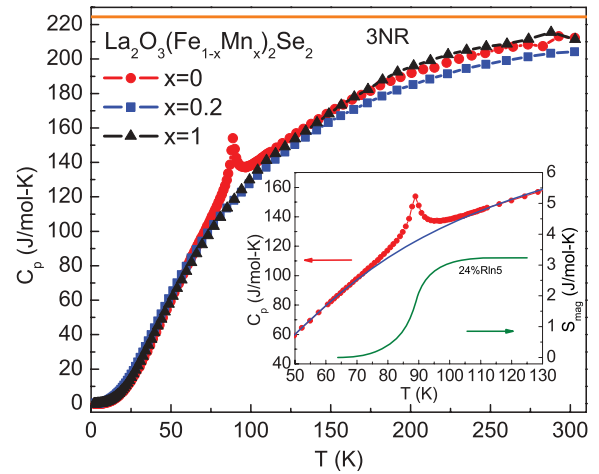


FIG. 7. (Color online) Temperature dependence of specific heat for (Fe,Mn)-2322 polycrystals. Inset shows the specific heat of Fe-2322 data between 50 K and 130 K. The solid curve represents the phonon contribution fitted by a polynomial. The right axis and its associated solid curve denote the magnetic entropy related to the AFM transition of Fe-2322.

120 K, which is much smaller than the expected value [$\sim 24\% R \ln(2S + 1) = R \ln 5$] for Fe^{2+} ions with the high spin state (inset of Fig. 7). Note that only about half of that value is released below T_N . It suggests that a substantial fraction of magnetic entropy is locked at high temperatures due to possible 2D short-range magnetic order before long-range correlations develop at T_N .¹⁴ In contrast, there is no λ -type anomaly for Mn-2322 at the temperature of magnetic transitions ($T_{M1} = 164$ K and $T_{M2} = 122$ K), which is consistent with the previous result and can be ascribed to the overwhelming release of magnetic entropy due to the existence of 2D short-range order above magnetic transitions.¹⁴ The 20% Mn doping in Fe-2322 has already resulted in complete release of magnetic entropy above T_N . If the entropy is released via the high temperature frustration mechanism, this suggests that frustration effects are considerably enhanced with Mn doping. This could explain the absence of Curie-Weiss law in $M(T)$ above T_N [Fig. 6(a)].

IV. CONCLUSION

$\text{La}_2\text{O}_3(\text{Fe}_{1-x}\text{Mn}_x)_2\text{Se}_2$ compounds are magnetic with the high spin state for $\text{Fe}^{2+}/\text{Mn}^{2+}$. Intermediate alloys exhibit long-range magnetic order and release magnetic entropy at high temperature due to possible magnetic frustration. Further neutron scattering experiments are necessary to provide microscopic information on how principle competing interactions evolve in this alloy series. FM component of magnetically ordered ground state and possibly the degree of magnetic frustration both raise rapidly as Mn enters the lattice. In (Fe,Mn)-2322 compounds long-range magnetic order competes with disorder induced by geometric spin frustration. Atomic disorder on Fe/Mn sites tips this balance and promotes frustration. Since the balance of all three principle interactions J_1 - J_3 can be tuned by the Fe/Mn ratio, this system might be mapped to the 2D pyrochlore where charge order and the metal-to-insulator transition have been predicted at half filling.^{32,33}

ACKNOWLEDGMENTS

Part of this work was carried out at Brookhaven National Laboratory which is operated for the US Department of Energy (DOE) by Brookhaven Science Associates under Grant No. DE-Ac02-98CH10886. A portion of this work benefited from the use of a high-intensity powder diffractometer at the

Lujan Center at Los Alamos Neutron Science Center, funded by DOE Office of Basic Energy Sciences. Los Alamos National Laboratory is operated by Los Alamos National Security LLC under DOE Contract No. DE-AC52-06NA25396. This work was also supported by Grant No. 45018 from the Serbian Ministry of Education and Science.

-
- ¹I. I. Mazin, *Nature (London)* **464**, 183 (2010).
²V. Cvetkovic and Z. Tesanovic, *Europhys. Lett.* **85**, 37002 (2009).
³M. M. Qazilbash, J. J. Hamlin, R. E. Baumbach, L. Zhang, D. J. Singh, M. B. Maple, and D. N. Basov, *Nature Phys.* **5**, 647 (2009).
⁴J. M. Mayer, L. F. Schneemeyer, T. Siegrist, J. V. Waszczak, and B. Van Dover, *Angew. Chem., Int. Ed. Engl.* **31**, 1645 (1992).
⁵S. J. Clarke, P. Adamson, S. J. C. Herkelrath, O. J. Rutt, D. R. Parker, M. J. Pitcher, and C. F. Smura, *Inorg. Chem.* **47**, 8473 (2008).
⁶H. Kabbour, E. Janod, B. Corraze, M. Danot, C. Lee, M. H. Whangbo, and L. Cario, *J. Am. Chem. Soc.* **130**, 8261 (2008).
⁷C. Wang, M. Q. Tan, C. M. Feng, Z. F. Ma, S. Jiang, Z. A. Xu, G. H. Cao, K. Matsubayashi, and Y. Uwatoko, *J. Am. Chem. Soc.* **132**, 7069 (2010).
⁸J. X. Zhu, R. Yu, H. Wang, L. L. Zhao, M. D. Jones, J. Dai, E. Abrahams, E. Morosan, M. Fang, and Q. Si, *Phys. Rev. Lett.* **104**, 216405 (2010).
⁹D. G. Free and J. S. O. Evans, *Phys. Rev. B* **81**, 214433 (2010).
¹⁰H. Wu, *Phys. Rev. B* **82**, 020410 (2010).
¹¹Y. Fuwa, M. Wakeshima, and Y. Hinatsu, *J. Phys.: Condens. Matter* **22**, 346003 (2010).
¹²Y. Fuwa, T. Endo, M. Wakeshima, Y. Hinatsu, and K. Ohoyama, *J. Am. Chem. Soc.* **132**, 18020 (2010).
¹³E. E. McCabe, D. G. Free, B. G. Mendis, J. S. Higgins, and J. S. O. Evans, *Chem. Mater.* **22**, 6171 (2010).
¹⁴N. Ni, E. Climent-Pascual, S. Jia, Q. Huang, and R. J. Cava, *Phys. Rev. B* **82**, 214419 (2010).
¹⁵R. H. Liu, J. S. Zhang, P. Cheng, X. G. Luo, J. J. Ying, Y. J. Yan, M. Zhang, A. F. Wang, Z. J. Xiang, G. J. Ye, and X. H. Chen, *Phys. Rev. B* **83**, 174450 (2011).
¹⁶D. G. Free, N. D. Withers, P. J. Hickey, and J. S. O. Evans, *Chem. Q Mater.* **23**, 1625 (2011).
¹⁷C. D. Ling, J. E. Millburn, J. F. Mitchell, D. N. Argyriou, J. Linton, and H. N. Bordallo, *Phys. Rev. B* **62**, 15096 (2000).
¹⁸U. Löw, V. J. Emery, K. Fabricius, and S. A. Kivelson, *Phys. Rev. Lett.* **72**, 1918 (1994).
¹⁹T. Yildirim, *Phys. Rev. Lett.* **101**, 057010 (2008).
²⁰Q. Si and E. Abrahams, *Phys. Rev. Lett.* **101**, 076401 (2008).
²¹M. J. Han, Q. Yin, W. E. Pickett, and S. Y. Savrasov, *Phys. Rev. Lett.* **102**, 107003 (2009).
²²S. Li, C. de la Cruz, Q. Huang, Y. Chen, J. W. Lynn, J. Hu, Y. L. Huang, F. C. Hsu, K. W. Yeh, M. K. Wu, and P. C. Dai, *Phys. Rev. B* **79**, 054503 (2009).
²³B. Hunter, *Int. Un. of Cryst. Comm. Newsletter* **20** (1998).
²⁴A. C. Larson, and R. B. Von Dreele, General structure analysis system, Report No. LAUR-86-748, Los Alamos National Laboratory, Los Alamos, NM (2000).
²⁵B. H. Toby, *J. Appl. Crystallogr.* **34**, 201 (2001).
²⁶R. A. Brand, WinNormos Mössbauer fitting program, Universität Duisburg, 2008.
²⁷I. D. Brown and D. Altermatt, *Acta Crystallogr. Sect. B* **41**, 244 (1985).
²⁸N. E. Brese and M. O'Keefe, *Acta Crystallogr. Sect. B* **47**, 192 (1991).
²⁹P. Blaha, K. Schwarz, G. Madsen, D. Kvasnicka, and J. Luitz, Compter program WIEN2K, an augmented plane wave + local orbitals program for calculating crystal properties (Karlheinz Schwarz, Technische Universität Wien, Austria, 2001).
³⁰F. Tran, P. Blaha, K. Schwarz, and P. Novák, *Phys. Rev. B* **74**, 155108 (2006).
³¹F. Yayoi, W. Makoto, and H. Yukio, *J. Phys.: Condens. Matter* **22**, 346003 (2010).
³²S. Fujimoto, *Phys. Rev. Lett.* **89**, 226402 (2002).
³³S. Fujimoto, *Phys. Rev. B* **67**, 235102 (2003).



Iron chalcogenide superconductors at high magnetic fields

Hechang Lei, Kefeng Wang, Rongwei Hu, Hyejin Ryu, Milinda Abeykoon, Emil S Bozin & Cedomir Petrovic

To cite this article: Hechang Lei, Kefeng Wang, Rongwei Hu, Hyejin Ryu, Milinda Abeykoon, Emil S Bozin & Cedomir Petrovic (2012) Iron chalcogenide superconductors at high magnetic fields, *Science and Technology of Advanced Materials*, 13:5, 054305, DOI: [10.1088/1468-6996/13/5/054305](https://doi.org/10.1088/1468-6996/13/5/054305)

To link to this article: <https://doi.org/10.1088/1468-6996/13/5/054305>



© 2012 National Institute for Materials Science



Published online: 28 Dec 2012.



Submit your article to this journal [↗](#)



Article views: 1171



View related articles [↗](#)



Citing articles: 5 View citing articles [↗](#)

TOPICAL REVIEW

Iron chalcogenide superconductors at high magnetic fields

Hechang Lei¹, Kefeng Wang¹, Rongwei Hu^{1,3}, Hyejin Ryu^{1,2},
Milinda Abeykoon¹, Emil S Bozin¹ and Cedimir Petrovic^{1,2}

¹ Condensed Matter Physics and Materials Science Department, Brookhaven National Laboratory, Upton, NY 11973, USA

² Department of Physics and Astronomy, Stony Brook University, Stony Brook, NY 11794-3800, USA

E-mail: hlei@bnl.gov and petrovic@bnl.gov

Received 31 May 2012

Accepted for publication 12 November 2012

Published 28 December 2012

Online at stacks.iop.org/STAM/13/054305

Abstract

Iron chalcogenide superconductors have become one of the most investigated superconducting materials in recent years due to high upper critical fields, competing interactions and complex electronic and magnetic phase diagrams. The structural complexity, defects and atomic site occupancies significantly affect the normal and superconducting states in these compounds. In this work we review the vortex behavior, critical current density and high magnetic field pair-breaking mechanism in iron chalcogenide superconductors. We also point to relevant structural features and normal-state properties.

Keywords: iron chalcogenide superconductors, upper critical fields, vortex physics, critical current density

1. Introduction

The discovery of superconductivity in La(O,F)FeAs with superconducting transition temperature $T_c = 26$ K [1] stimulated intensive research on related materials. This resulted in the discovery of several families of iron-based superconductors with the highest $T_c = 56$ K [1–23], including REOFePn (RE = rareearth; Pn = P or As, FePn-1111 type) [1–7], AFe₂As₂ (A = alkaline or alkaline-earth metal, FeAs-122 type) [8–10], AFeAs (FeAs-111 type) [11, 12], (Sr₄M₂O₆)(Fe₂Pn₂) (M = Sc, Ti or V, FePn-42622 type) [13, 14], FeCh (Ch = S, Se, Te, FeCh-11 type) [15–17] and A_xFe_{2–y}Se₂ (AFech-122 type) [18–23].

The crystal structure of FeCh and AFech-122 systems features a square-planar lattice of Fe with tetrahedral coordination, which is the common ingredient found in all iron-based superconductors, but they also have some distinctive characteristics. For example, FeCh-11 type materials have a rather simple crystal structure without the

charge reservoir layer. FeSe exhibits a significant pressure effect [24]: under external pressure, the T_c can be increased from 8 to 37 K and the dT_c/dP can reach 9.1 K GPa⁻¹, the highest increase in all iron-based superconductors. Fe(Te,Se) and Fe(Te,S) contain strongly magnetic excess Fe in Fe(2) site that provides local moments and tunes details of magnetic structure depending upon the amount of excess Fe [25, 26]. On the other hand, in AFech-122 materials the hole Fermi surfaces (FSs) are absent [27, 28], which is different from other iron-based superconductors where both electron and hole FSs are present [29], suggesting pairing symmetry other than s_{\pm} [30]. There are also vacancies in the Fe plane that order at $T = 578$ K resulting in long-range antiferromagnetic (AFM) order at $T_N = 559$ K [31]. Finally, one of the most distinctive features in AFech-122 is the proximity of semiconducting state [23], which is magnetic but is spatially separated and coexists with superconducting regions on the 10–100 nm length scale [32–38]. This is different from iron pnictides where superconductivity emerges when the spin density wave (SDW) state is suppressed [39].

On the other hand, because of large upper critical fields $\mu_0 H_{c2}$ and small lower critical fields, iron-based

³ Present address: Center for Nanophysics, and Advanced Materials, and Department of Physics, University of Maryland, College Park, MD 20742-4111, USA.

superconductors exhibit rich vortex phenomena in the mixed state and exotic temperature dependences of $\mu_0 H_{c2}(T)$. There are also some promising technical application perspectives due to high T_c and large $\mu_0 H_{c2}$. The distinctive features of iron chalcogenides will lead to the pronounced differences of the superconducting properties in magnetic fields when compared to pnictides, such as the different contributions of multiband and spin paramagnetic effects which will determine the temperature dependence of the $\mu_0 H_{c2}(T)$, the different strengths of vortex thermal fluctuations in mixed state and the different behaviors of critical current density J_c in magnetic fields.

In this paper, we review the superconducting properties of iron chalcogenide superconductors in high magnetic fields, while comparing these properties with those of iron pnictide superconductors. In section 2, we address vortex physics, especially thermally activated flux flow. Section 3 describes the J_c , and in section 4, we describe the important features of $\mu_0 H_{c2}$ and compare $\mu_0 H_{c2}$ in iron pnictide and iron chalcogenide superconductors. Finally, in section 5, we summarize the main results we discussed and outline general perspectives of this field.

2. Vortex physics in iron chalcogenide superconductors

Iron-based superconductors are extreme type-II superconductors with $\kappa \sim 100$ and a large range of magnetic field penetration in the mixed state of $\mu_0 H$ - T phase diagram. Hence, rich vortex physics is expected in all iron-based superconductors. In the mixed state the thermal fluctuation effects on the vortex behavior can be quantified by the Ginzburg number G_i

$$G_i = \frac{1}{2} \left(\frac{k_B T_c}{\mu_0 H_c^2(0) \xi_{ab}^2(0) \xi_c(0)} \right)^2, \quad (1)$$

where k_B is Boltzmann constant, μ_0 is vacuum permeability, $\mu_0 H_c(0) = \phi_0 / 2\sqrt{2}\pi \lambda_{ab}(0) \xi_{ab}(0)$ is the thermodynamic critical field (ϕ_0 is magnetic flux quantum), $\lambda_{ab}(0)$ is the London penetration depth in the ab plane, and $\xi_{ab}(0)$ and $\xi_c(0)$ are the coherence lengths in the ab plane and c -axis, at $T = 0$ K, respectively. Here we assume $\xi_a(0) = \xi_b(0) = \xi_{ab}(0)$, which is consistent with the tetragonal lattice symmetry of iron-based superconductors. The G_i is basically the squared ratio of the thermal energy to the condensation energy in the volume occupied by the Cooper pair [40]; it can be rewritten as [40]

$$G_i \propto \gamma_m^{4/3} m^4 T_c^4 n^{-8/3}, \quad (2)$$

where γ_m is the mass anisotropy in a uniaxial crystal, $\gamma_m = m_c/m_{ab} = (\xi_{ab}/\xi_c)^2 = (H_{c2,ab}/H_{c2,c})^2$, and m is the effective mass and n is carrier density. The G_i can be increased strongly if (i) T_c increases, (ii) effective mass increases, (iii) mass anisotropy increases or (iv) carrier density decreases. In the layered cuprate oxide superconductors vortex behavior can be affected dramatically by thermal fluctuation ($G_i \sim 10^{-3} - 1$) because of high T_c

and large γ_m when compared to conventional Bardeen–Cooper–Schrieffer (BCS) superconductors where vortex thermal fluctuation is negligible ($G_i \sim 10^{-10} - 10^{-6}$) [40]. In iron-based superconductors, thermal fluctuation effects ($G_i \sim 10^{-4} - 10^{-2}$) also influence vortex properties [40]. Some iron-based superconductors exhibit significant vortex fluctuations similar to those in the cuprates with smallest anisotropy, such as $\text{YBa}_2\text{Cu}_3\text{O}_{7-x}$ (YBCO), despite smaller T_c and γ_m . Relatively large thermal fluctuation effects may be related to the low n and large m [41–43]. In FeCh-11 superconductors, T_c is smaller at ambient pressure as compared to FeAs-122 materials but the G_i ($\sim 10^{-3}$) is larger than the latter one ($G_i \sim 10^{-4}$) [40], which could be ascribed to the significant mass enhancement [41]. Therefore, thermally activated vortex dynamics is expected even at low temperatures.

2.1. Thermally activated flux flow

Thermal fluctuations in FeCh-11 superconductors can result in the thermally activated flux flow (TAFF) behavior where the vortex bundles hop between neighboring pinning centers. According to the TAFF theory, the resistivity in TAFF region can be expressed as [44–46]

$$\rho = (2v_0 L B / J) \exp(-J_{c0} B V L / T) \sinh(J B V L / T), \quad (3)$$

where v_0 is an attempt frequency for a flux bundle hopping, L is the hopping distance, B is the magnetic induction, J is the applied current density, J_{c0} is the critical current density in the absence of flux creep, V is the bundle volume and T is the temperature. If J is small enough and $J B V L / T \ll 1$, we obtain

$$\rho = (2\rho_c U / T) \exp(-U / T) = \rho_{0f} \exp(-U / T), \quad (4)$$

where $U = J_{c0} B V L$ is the thermal activation energy and $\rho_c = v_0 L B / J_{c0}$, which is usually considered to be temperature independent. For cuprate superconductors, the prefactor $2\rho_c U / T$ is usually assumed as a constant ρ_{0f} [45], therefore, $\ln \rho(T, \mu_0 H) = \ln \rho_{0f} - U(T, \mu_0 H) / T$. On the other hand, according to the condensation model [46], $U(T, \mu_0 H) = (\mu_0 H_c(t))^2 \xi^n(t)$, where $\mu_0 H_c$ is the thermodynamic critical field, ξ is the coherence length, $t = T / T_c$, and n depends on the dimensionality of the vortex system with the range from 0 to 3. Since $\mu_0 H_c \propto 1 - t$, and $\xi \propto (1 - t)^{-1/2}$ near T_c [47], it is obtained that $U(T, \mu_0 H) = U_0(\mu_0 H)(1 - t)^q$, where $q = 2 - n/2$. It is generally assumed that $U(T, \mu_0 H) = U_0(\mu_0 H)(1 - t)$, i.e. $n = 2$, and the $\ln \rho - 1/T$ becomes Arrhenius relation

$$\ln \rho(T, \mu_0 H) = \ln \rho_0(\mu_0 H) - U_0(\mu_0 H) / T, \quad (5)$$

where $\ln \rho_0(\mu_0 H) = \ln \rho_{0f} + U_0(\mu_0 H) / T_c$ is a temperature-independent term and $U_0(\mu_0 H)$ is the apparent activation energy. Furthermore, it can be concluded that $-\partial \ln \rho(T, \mu_0 H) / \partial T^{-1} = U_0(\mu_0 H)$. Hence, the $\ln \rho$ versus $1/T$ should be linear in the TAFF region. The slope is $U_0(\mu_0 H)$ and its y-intercept represents $\ln \rho_0(\mu_0 H)$.

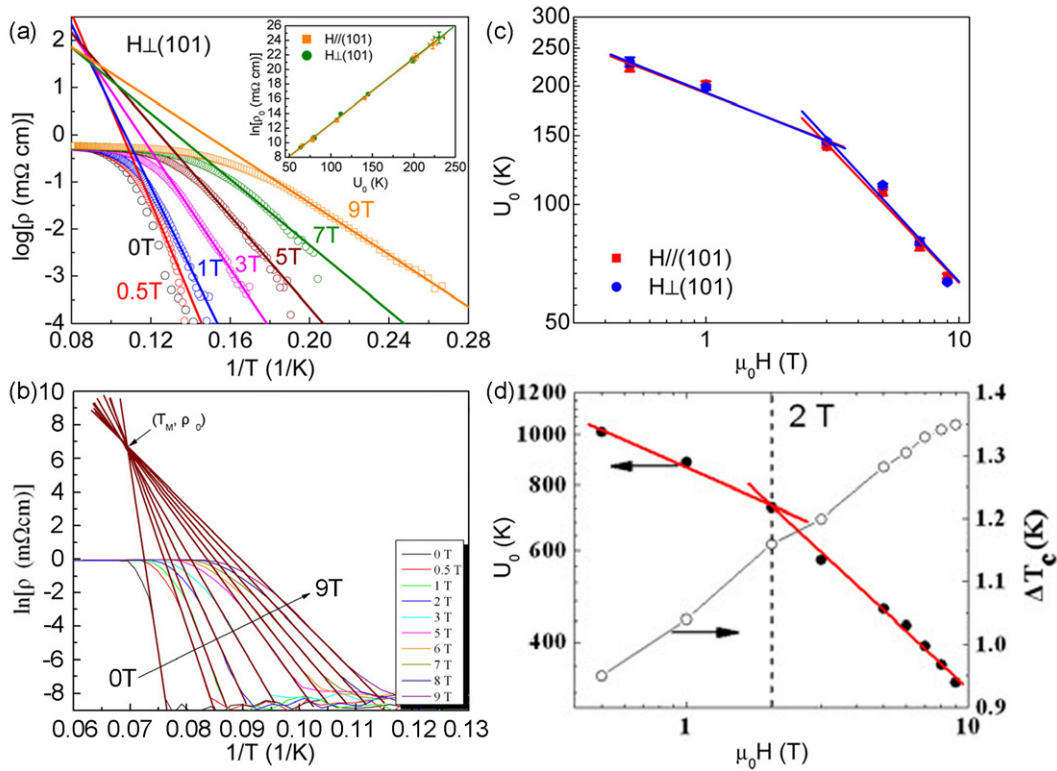


Figure 1. Arrhenius plots for resistivity in various fields for (a) FeSe single crystal with $H \perp (101)$ and (b) $\text{Fe}_{1.03}\text{Te}_{0.55}\text{Se}_{0.45}$ single crystals with $H \parallel c$. The corresponding solid lines are fitting results from the Arrhenius relation. Inset of (a): $\ln \rho_0(\mu_0 H)$ versus $U_0(\mu_0 H)$ derived from the Arrhenius relation for both field directions. The solid lines are linear fitting results. (c) and (d) Field dependence of $U_0(\mu_0 H)$ for FeSe and $\text{Fe}_{1.03}\text{Te}_{0.55}\text{Se}_{0.45}$, respectively. The solid lines are power-law functions $U_0(\mu_0 H) \sim (\mu_0 H)^{-\alpha}$. (a) Reprinted with permission from [48]. Copyright 2012 by the American Physical Society. (b) Reprinted with permission from [49]. Copyright 2010 by the Elsevier.

As shown in figures 1(a) and (b), the experimental data can be fitted using the Arrhenius relation very well for both FeSe and $\text{Fe}_{1.03}\text{Te}_{0.55}\text{Se}_{0.45}$ (Se-45) single crystals [48, 49]. The good linear behavior indicates that the temperature dependence of $U(T, \mu_0 H)$ is approximately linear, i.e. $U(T, \mu_0 H) = U_0(\mu_0 H)(1 - t)$ [45, 46]. The $\log \rho(T, \mu_0 H)$ lines for compounds extrapolate to the same temperature T_{cross} , which should be equal to T_c [50]. For FeSe single crystal, the extrapolated temperatures are about 11.1 K for both $H \parallel (101)$ and $H \perp (101)$. This behavior has also been observed in $\text{NdFeAsO}_{0.7}\text{F}_{0.3}$ single crystals for $H \parallel c$, however, it is not the case for $H \parallel ab$ [51]. For FeSe single crystal, the obtained U_0 are similar for $H \parallel (101)$ and $H \perp (101)$ (inset of figure 1(a)) and much smaller than in $\text{Fe}(\text{Te}, \text{Se})$ [49, 52]. Moreover, $\ln \rho_0(\mu_0 H) - U_0(\mu_0 H)$ is linear for both field directions (inset of figure 1(a)). Fits using $\ln \rho_0(\mu_0 H) = \ln \rho_{0f} + U_0(\mu_0 H)/T_c$ yielded values of ρ_{0f} and T_c as 37(1) m Ω cm and 11.2(1) K for $H \parallel (101)$ and 39(2) m Ω cm and 11.2(1) K for $H \perp (101)$. The T_c values are consistent with the values of T_{cross} within the error bars. As shown in figures 1(c) and (d), the field dependence of $U_0(H)$ exhibits a power-law behavior for both FeSe and Se-45, i.e. $U_0(\mu_0 H) \sim (\mu_0 H)^{-\alpha}$. There are two types of power-law behavior at low and high fields. For FeSe, $\alpha \sim 0.25$ for $\mu_0 H < 3$ T and $\alpha \sim 0.7$ for $\mu_0 H > 3$ T. Se-45 exhibits similar behavior to FeSe ($\alpha \sim 0.25$ for $\mu_0 H < 2$ T and $\alpha \sim 0.55$ for $\mu_0 H > 2$ T). The weak power-law dependence of $U_0(\mu_0 H)$ at low fields implies that single-vortex pinning dominates in this region [44], followed

by a quicker decrease of $U_0(\mu_0 H)$ at high fields where the vortex spacing becomes significantly smaller than penetration depth in higher fields and a crossover to a collective-pinning regime occurs. In this region, the $U_0(\mu_0 H)$ becomes strongly dependent on the field [53]. A similar crossover has been observed in $\text{Nd}(\text{O}, \text{F})\text{FeAs}$ single crystals [51]. Because $\alpha = 0.5$ and 1 correspond to a planar-defect pinning and a point-defect pinning, respectively [54], for FeSe, the fitted α values vary between 0.5 and 1, suggesting that the pinning centers may be mixed with point and planar defects. On the other hand, for Se-45, the fitted α values are close to 0.5, implying that the vortices are mainly pinned by the collective point defects in the high-field region.

Large fitting errors occur for $\text{Fe}_{1.14}\text{Te}_{0.91}\text{S}_{0.09}$ (S-09) single crystal when using the Arrhenius relation in the TAFF region (solid lines), especially for $H \parallel ab$ (figures 2(a) and (b)). Deviation from the Arrhenius relation indicates that the assumptions of constant ρ_{0f} and linear temperature dependence of $U(T, \mu_0 H)$ could be invalid in S-09. If $U(T, \mu_0 H) = U_0(\mu_0 H)(1 - t)$ and $\rho_{0f} = \text{const}$, this will result in $-\partial \ln \rho(T, \mu_0 H)/\partial T^{-1} = U_0(\mu_0 H)$, and $U_0(\mu_0 H)$ should be a set of horizontal lines as shown in figures 2(c) and (d). The limited lengths of horizontal lines correspond to the temperature interval used for estimating $U_0(\mu_0 H)$ in the Arrhenius relation. It can be seen that $-\partial \ln \rho(T, \mu_0 H)/\partial T^{-1}$ increases sharply with decreasing temperature, which was also observed in Bi-2212 thin films [55]. The center of each $U_0(\mu_0 H)$ horizontal line approximately intersects the

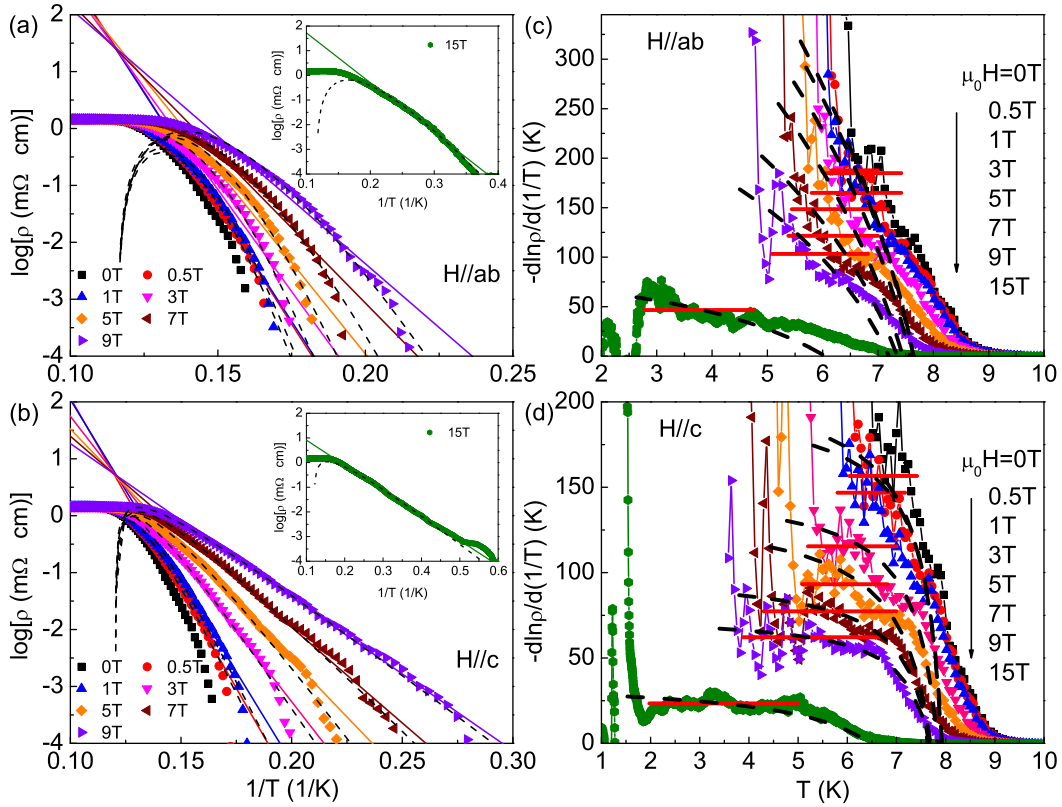


Figure 2. (a) and (b) Temperature dependence of longitudinal resistivities $\log \rho(T, \mu_0 H)$ of $\text{Fe}_{1.14}\text{Te}_{0.91}\text{S}_{0.09}$ in various magnetic fields for $H \parallel ab$ and $H \parallel c$, respectively. The corresponding solid and black dashed lines are fitting results from the Arrhenius relation (equations (5) and (6)). (c) and (d) Experimental $-\partial \ln \rho / \partial T^{-1}$ data in the TAFF region for $H \parallel ab$ and $H \parallel c$, respectively. The red solid horizontal lines correspond to $U_0(\mu_0 H)$ obtained from the Arrhenius relation and the blue dashed lines are plotted using equation (7). The parameters are determined via fitting equation (6) to the corresponding experimental resistivity data shown in panels (a) and (b). Reprinted with permission from [50]. Copyright 2010 by the American Physical Society.

$-\partial \ln \rho(T, \mu_0 H) / \partial T^{-1}$ curve, and therefore each $U_0(\mu_0 H)$ is only the average value of its $-\partial \ln \rho(T, \mu_0 H) / \partial T^{-1}$ in the fitting temperature region. Hence, the $U(T, \mu_0 H)$ determined using the Arrhenius relation does not reflect the true evolution of thermal activation energy with temperature in S-09, particularly for $H \parallel ab$.

If $\rho_{0f} = 2\rho_c U(T, \mu_0 H) / T$ is temperature dependent due to the term $U(T, \mu_0 H) = U_0(\mu_0 H)(1-t)^q$ and q can be different from 1, then it can be shown from equation (4) [56] that

$$\begin{aligned} \ln \rho = & \ln(2\rho_c U_0(\mu_0 H)) + q \ln(1-t) \\ & - \ln T - U_0(\mu_0 H)(1-t)^q / T \end{aligned} \quad (6)$$

and thus

$$-\partial \ln \rho / \partial T^{-1} = [U_0(\mu_0 H)(1-t)^q - T][1 + qt / (1-t)], \quad (7)$$

where q , ρ_c and $U_0(\mu_0 H)$ are temperature-independent free parameters, and T_c derived from the Arrhenius relation is used for fitting. Figures 2(a) and (b) reveal that all fitting curves (dashed lines) agree well with experimental data and the results are better than the Arrhenius relation, especially for $H \parallel ab$. Figures 2(c) and (d) clearly show the advantage of equation (7) over the Arrhenius relation. It can effectively capture the upturn trend of $-\partial \ln \rho / \partial T^{-1}$ with decreasing

temperature. As shown in figure 3(a), the $U_0(\mu_0 H)$ values obtained using equation (6) are comparable to that in FeSe but smaller than in Fe(Te,Se) [48, 49, 52]. Similar to FeSe and Fe(Te,Se), there are also two ranges in the field dependence of $U_0(H)$ curves with different α for both field directions in S-09. For $H \parallel ab$, $\alpha = 0.12(2)$ for $\mu_0 H < 5$ T and $\alpha = 1.7(3)$ for $\mu_0 H > 5$ T; For $H \parallel c$, $\alpha = 0.21(3)$ for $\mu_0 H < 5$ T and $\alpha = 1.3(2)$ for $\mu_0 H > 5$ T. In the low-field region, the small α suggests that single-vortex pinning dominates, similar to FeSe and Fe(Te,Se). At high fields α is larger than 1, implying that the material enters a collective pinning regime and the pinning centers are point defects [54]. On the other hand, the values of q change from about 1 for $H \parallel c$ to 2 for $H \parallel ab$, independent on the field intensity for both directions (figure 3(b)). The value of $q = 2$ has also been observed in many cuprates superconductors [55–57]. The nonlinear temperature dependence of $U_0(T, \mu_0 H)$ and non-constant prefactor ρ_{0f} are also common to other iron-based superconductors [58, 59].

It should be noted that the low volume fraction of superconductivity in Fe(Te,S) should not significantly affect the analysis of TAFF. Because of the inhomogeneity of crystals, the conductivity can be expressed as $\sigma = \sigma_{sc} + \sigma_{normal}$, where σ_{sc} is the conductivity of superconducting fraction and σ_{normal} is the conductivity of the normal fraction

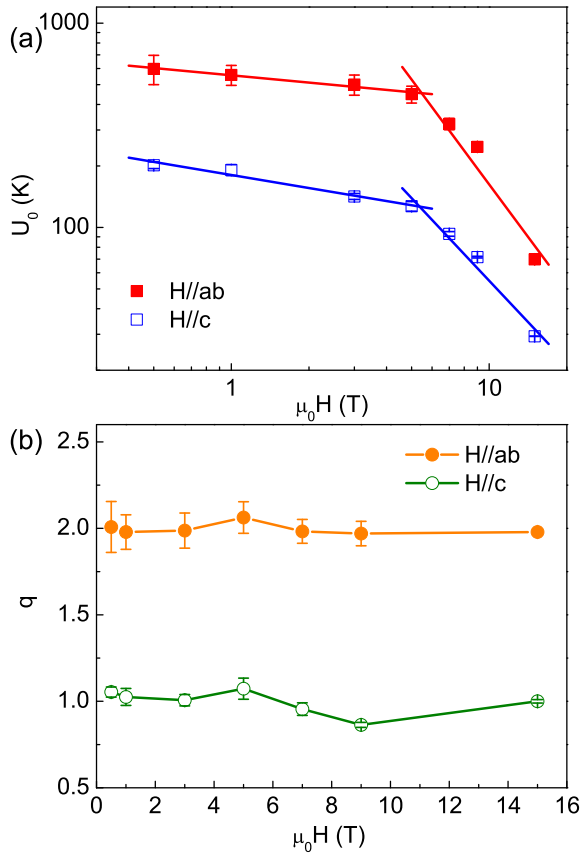


Figure 3. Magnetic field dependences of (a) U_0 and (b) q obtained from fitting the resistivity in the TAFF region using equation (6) for $\text{Fe}_{1.14}\text{Te}_{0.91}\text{S}_{0.09}$. The open and filled squares represent $U_0(\mu_0 H)$ for $H//c$ and $H//ab$, respectively, while the open and filled circles show corresponding q , respectively. The solid lines in (a) are power-law functions $U_0(\mu_0 H) \sim (\mu_0 H)^{-\alpha}$. Reprinted with permission from [50]. Copyright 2010 by the American Physical Society.

of the crystal. When $T < T_{c,\text{zero}}$, $\sigma = \sigma_{\text{sc}} = \infty$, i.e. $\rho = 0$ and the normal-state part of sample is short-circuited. On the other hand, the resistivity in the TAFF regime is about one to three orders of magnitude less than in the normal state [45, 46]. It means that although the conductivity σ_{sc} in this range is finite, it is still much larger than σ_{normal} , and we can approximate $\sigma \approx \sigma_{\text{sc}}$.

In $\text{K}_{0.64}\text{Fe}_{1.44}\text{Se}_2$ and $\text{Tl}_{0.58}\text{Rb}_{0.42}\text{Fe}_{1.72}\text{Se}_2$ single crystals, as shown in figure 4, the good linear behavior of $\ln \rho(T, \mu_0 H)$ versus $1/T$ in a wide temperature range for both field directions indicates that the temperature dependence of $U(T, \mu_0 H)$ is approximately linear [60], i.e. $q = 1$, and the ρ_{0f} is constant, similar to FeSe and Fe(Te,Se) [48, 49]. For $\text{K}_{0.64}\text{Fe}_{1.44}\text{Se}_2$, fitting by the function $\ln \rho_0(\mu_0 H) = \ln \rho_{0f} + U_0(\mu_0 H)/T_c$ yields $\rho_{0f} = 5.3(1)$ and $12.4(1) \Omega \text{ cm}$ and $T_c = 31.8(3)$ and $32.3(2)$ K for $H//ab$ and $H//c$, respectively (inset of figure 4(a)). On the other hand, the $\log \rho(T, \mu_0 H)$ lines for different fields extrapolate to one temperature $T_{\text{cross}} \sim 32$ K for both field directions, consistent with the values of T_c within the error bars. The $U_0(\mu_0 H)$ values obtained for both superconductors are much larger than in FeCh-11 materials; they are comparable to that in polycrystalline $\text{NdFeAsO}_{0.7}\text{F}_{0.3}$ [51], but are still

much smaller than in polycrystalline $\text{SmFeAsO}_{0.9}\text{F}_{0.1}$ [58]. The power-law fitting yields $\alpha = 0.78(2)$ and $0.84(2)$ for $H//ab$ and $H//c$ in $\text{K}_{0.64}\text{Fe}_{1.44}\text{Se}_2$ and $\alpha = 0.27(2)$ for $H//ab$ and $0.22(2)$ for $H//c$ in $\text{Tl}_{0.58}\text{Rb}_{0.42}\text{Fe}_{1.72}\text{Se}_2$ (insets of figures 4(b)–(d)). For both materials, the field dependencies of $U_0(\mu_0 H)$ are similar for both field directions, indicating that the pinning forces weakly depend on orientation [60]. But the values of α are rather different. For $\text{K}_{0.64}\text{Fe}_{1.44}\text{Se}_2$, the values of α are similar to those in FeSe, suggesting that both point and planar defects act as the pinning centers. On the other hand, the much smaller values of α in $\text{Tl}_{0.58}\text{Rb}_{0.42}\text{Fe}_{1.72}\text{Se}_2$ imply that the single-vortex pinning mechanism is dominant in fields up to 15 T.

3. Critical current density

Since the discovery of iron-based superconductors, the combination of rather high T_c and high $\mu_0 H_{c2}$ has induced great interests for application. For practical applications of superconductors, however, high J_c is another key parameter that needs to be investigated. YBCO has superior current-carrying properties but the stringent weak-link effect of grain boundaries (GBs) restricts the range of applications and increases the cost of fabrication [61]. In iron-based superconductors (figures 5(a) and (b)) [62], the high $\mu_0 H_{c2}$ gives some promise for applications at high fields, where low-temperature Nb_3Sn superconductor is at disadvantage because of low $\mu_0 H_{c2}$ [40].

Iron chalcogenide superconductors crystallize in a relatively simple crystal structure, but often with defects and relatively large range of stoichiometry. In addition, there is a sensitivity to atmosphere in AFeCh-122. However, lower anisotropy γ of $\mu_0 H_{c2}$ when compared to iron pnictide superconductors is advantageous for applications such as superconducting wires for high-field magnets.

3.1. J_c and flux pinning in FeCh-11 and AFeCh-122 single crystals

Figure 6 shows the J_c of FeSe, $\text{FeTe}_{0.61}\text{Se}_{0.39}$ and $\text{FeTe}_{0.9}\text{S}_{0.1}$ single crystals at various fields and temperatures [48, 63, 64]. At $T \sim 5$ K, the J_c of FeSe is about $2.4 \times 10^3 \text{ A cm}^{-2}$ for $H \perp (101)$ at zero field. This is lower than J_c in $\text{FeTe}_{0.61}\text{Se}_{0.39}$ and $\text{FeTe}_{0.9}\text{S}_{0.1}$, which is about 2×10^5 and $3 \times 10^5 \text{ A cm}^{-2}$ for $H//c$, respectively. $\text{FeTe}_{0.61}\text{Se}_{0.39}$ shows relative high J_c and it remains above $7 \times 10^4 \text{ A cm}^{-2}$ at $\mu_0 H = 5$ T. Moreover, the T_c of optimally doped Fe(Te,Se) ($\text{Se} \sim 0.4 - 0.5$) is about 14 K, which is higher than in Fe(Te,S) and FeSe. It implies that the optimally doped Fe(Te,Se) might be suitable for applications. On the other hand, the anisotropy γ_{J_c} of J_c ($\gamma_{J_c} = J_c^{H \parallel (101)}/J_c^{H \perp (101)}$ or $J_c^{H // ab}/J_c^{H // c}$) is about 4–5 for FeSe and $\text{FeTe}_{0.9}\text{S}_{0.1}$ [48, 64].

When compared to FeCh-11 superconductors, the much higher T_c and $\mu_0 H_{c2}$ of AFeSe-122 superconductors immediately raise a question whether the J_c values of these materials are more promising for practical applications. As shown in figure 7(a), however, the early studies indicate that J_c of $\text{K}_x\text{Fe}_{2-y}\text{Se}_2$ is rather low ($\sim (0.7-2.6) \times 10^3 \text{ A cm}^{-2}$ at

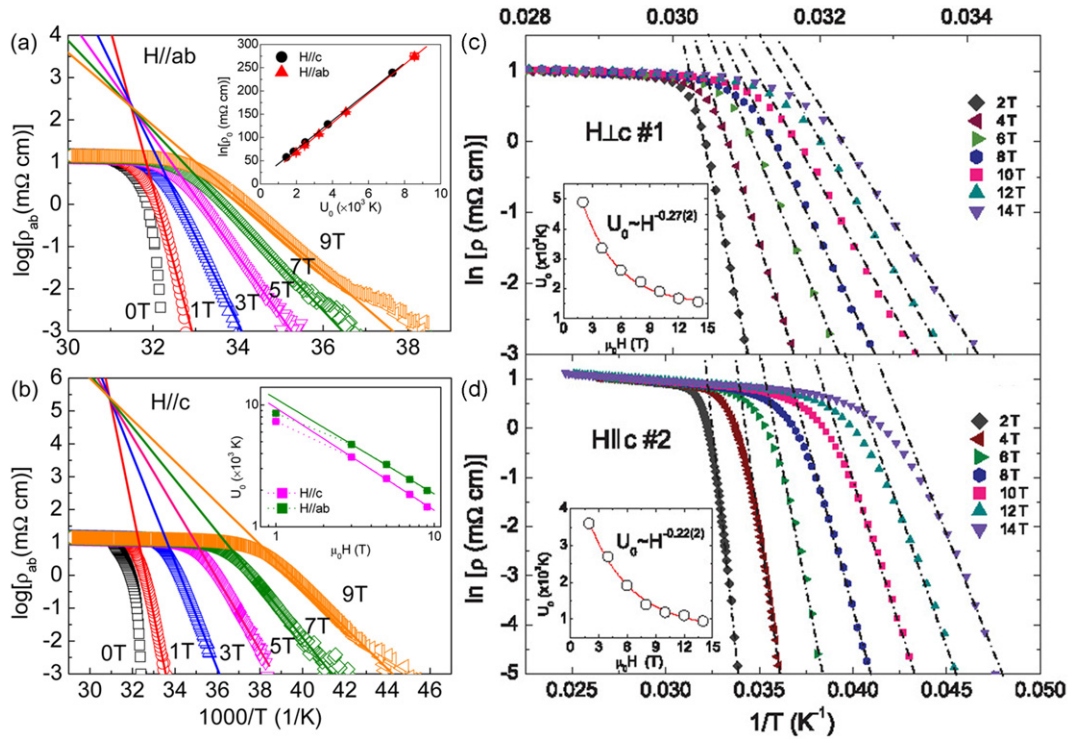


Figure 4. Arrhenius plot for resistivity at various fields of $K_{0.64}Fe_{1.44}Se_2$ for (a) $H\parallel ab$ and (b) $H\parallel c$ and $Tl_{0.58}Rb_{0.42}Fe_{1.72}Se_2$ for (c) $H\parallel ab$ and (d) $H\parallel c$. The corresponding solid lines are fitting results from the Arrhenius relation. Inset of (a): $\ln(\rho_0)$ versus $U_0(\mu_0H)$ derived from the Arrhenius relation for $K_{0.64}Fe_{1.44}Se_2$. The solid lines are linear fitting results. Inset of (b): field dependence of $U_0(\mu_0H)$ of $K_{0.64}Fe_{1.44}Se_2$. Insets of (c) and (d): field dependences of $U_0(\mu_0H)$ in $Tl_{0.58}Rb_{0.42}Fe_{1.72}Se_2$ for $H\parallel ab$ and $H\parallel c$, respectively. The solid lines in the insets of (b–d) are power-law functions $U_0(\mu_0H) \sim (\mu_0H)^{-\alpha}$. Panels (c) and (d) reprinted with permission from [60]. Copyright 2012 by the American Physical Society.

5 K) [65, 66], even lower than that of FeSe [48]. Therefore, it is important to explore pathways for the enhancement of J_c in AFeCh-122 compounds.

It was soon found that sulfur doping can remarkably enhance the J_c of $K_xFe_{2-y}Se_{2-z}S_z$ [67]. As shown in figure 7(a), the $J_c^{ab}(\mu_0H)$ ($H\parallel c$) exhibits a small increase in the high-field region for $z = 0.32$ when compared to the $z = 0$ sample. On the other hand, the enhancement is about one order of magnitude for $z = 0.99$ ($J_c^{ab}(0) = 7.4 \times 10^3 \text{ A cm}^{-2}$ at 1.8 K) in the entire magnetic-field range. For higher S content, the $J_c^{ab}(0)$ is still much larger than in $z = 0$ sample, but the $J_c^{ab}(\mu_0H)$ at high fields is smaller. It should be noted that the T_c decreases significantly when $z > 0.32$. When compared to $z = 0$ ($T_{c, \text{onset}} = 33.0 \text{ K}$), the $z = 0.99$ crystal has $T_{c, \text{onset}} = 24.6 \text{ K}$, whereas $z = 1.04$ corresponds to $T_{c, \text{onset}} = 18.2 \text{ K}$ [68]. Therefore, the sample with $z = 0.99$ exhibits the best performance among sulfur-doped samples investigated. Moreover, the ratio of $J_c^c(\mu_0H)/J_c^{ab}(\mu_0H)$ is approximately 1 and is smaller than in FeCh-11 superconductors. Although the J_c of $z = 0$ sample is much larger than in $K_xFe_{2-y}Se_2$ and also larger than in FeSe, it is still smaller than in $FeTe_{0.61}Se_{0.39}$ and $FeTe_{0.9}S_{0.1}$.

Metallic and superconducting state was induced by post-annealing and quenching treatment in as-grown and insulating $K_xFe_{2-y}Se_2$ crystals, which is a notable improvement in superconducting properties [69]. Therefore, some effects of this process on the J_c are also expected [70]. Post-annealing and quenching process can further

increase $J_c^{ab}(0)$ to $7.4 \times 10^3 \text{ A cm}^{-2}$ at 1.8 K which is about 50 times larger than that of the as-grown sample (figure 4(a)). This cannot be simply ascribed to the improvement of the superconducting volume fraction, because the volume fraction of the quenched crystal is only about four times larger than that of the as-grown crystal. It could also be related to the enhanced flux pinning force due to the post-annealing and quenching treatment. The J_c in the quenched crystal is also slightly higher than that in $K_xFe_{2-y}Se_2$ crystals grown using the one-step technique [71] and are the highest known J_c values among AFeCh-122 type materials until now. The quenched sample also exhibits a good performance at high fields. The $J_c^{ab}(\mu_0H = 4.8 \text{ T})$ for the quenched sample is still larger than 10^4 A cm^{-2} at 1.8 K, whereas for the as-grown sample, it has already decreased about one order of magnitude.

As shown in figure 7(b), detailed studies on the temperature and field dependences of the vortex pinning force $F_p = \mu_0HJ_c$ show that it follows the Dew-Huges [72] scaling law: $f_p \propto h^p(1-h)^q$, where $f_p = F_p/F_p^{\text{max}}$ is the normalized vortex pinning force, F_p^{max} corresponds to the maximum pinning force and $h = H/H_{\text{irr}}$ is the reduced field. The results indicate that there is a dominant pinning mechanism. The obtained p and q is 0.86(1) and 1.83(2), respectively and the value of $h_{\text{fit}}^{\text{max}} = p/(p+q) \approx 0.32$ is consistent with the peak positions ($h_{\text{exp}}^{\text{max}} \approx 0.33$) of the experimental curves at different temperatures. Those values are close to the expected values for core normal point-like

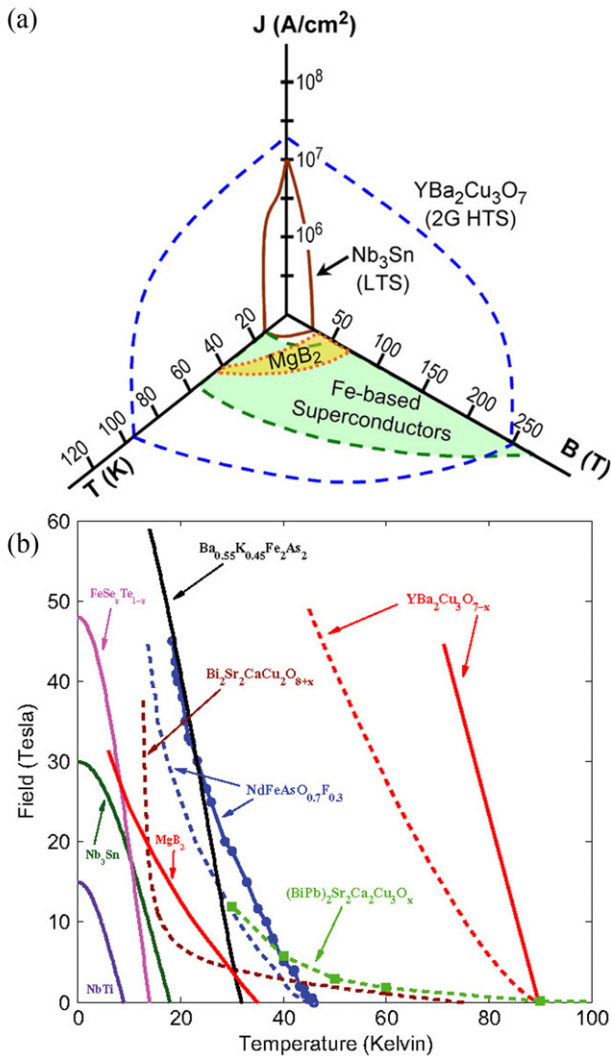


Figure 5. (a) J_c - T_c - $\mu_0 H_{c2}$ contour lines of Nb_3Sn , $\text{YBa}_2\text{Cu}_3\text{O}_{7-x}$, MgB_2 and iron-based superconductors. (b) T_c - H phase diagrams for various superconductors. The solid and dashed lines show the $\mu_0 H_{c2}$ and the irreversibility fields H^* for $H \parallel c$, respectively. (a) Reprinted with permission from [62]. (b) Reprinted with permission from [40]. Copyright 2011 by the IOP Publishing.

pinning ($p = 1$, $q = 2$ and $h_{\text{fit}}^{\text{max}} = 0.33$) [69]. These point-like pinning centers might come from the random distribution of iron vacancies after quenching, similar to FeAs -122 type materials [73, 74]. On the other hand, the F_p^{max} can be fitted using $F_p^{\text{max}} \propto (\mu_0 H_{\text{irr}})^{\alpha}$ with $\alpha = 1.67(1)$ (inset of figure 4(b)), close to the theoretical value ($\alpha = 2$) for the core normal point-like pinning [72]. Moreover, as shown in figure 7(c), the temperature dependence of $\mu_0 H_{\text{irr}}$ can be fitted with equation $\mu_0 H_{\text{irr}}(T) = \mu_0 H_{\text{irr}}(0)(1 - t)^{\beta}$, and we obtained $\beta = 1.21(1)$, close to the characteristic value of 3D giant flux creep ($\beta = 1.5$) [53]. For type-II superconductors, vortices interact with pinning centers either via the spatial variations in the T_c (δT_c pinning) or by scattering of charge carriers with reduced mean free path l near defects (δl pinning) [44]. These two pinning types result in the different temperature dependences of $J_c(t)$ in the single vortex pinning regime i.e. low-field and zero-field regions. For δT_c pinning, $J_{c,H=0}^{\delta T_c}(t) = J_{c,H=0}(0)(1 - t^2)^{7/6}(1 + t^2)^{5/6}$

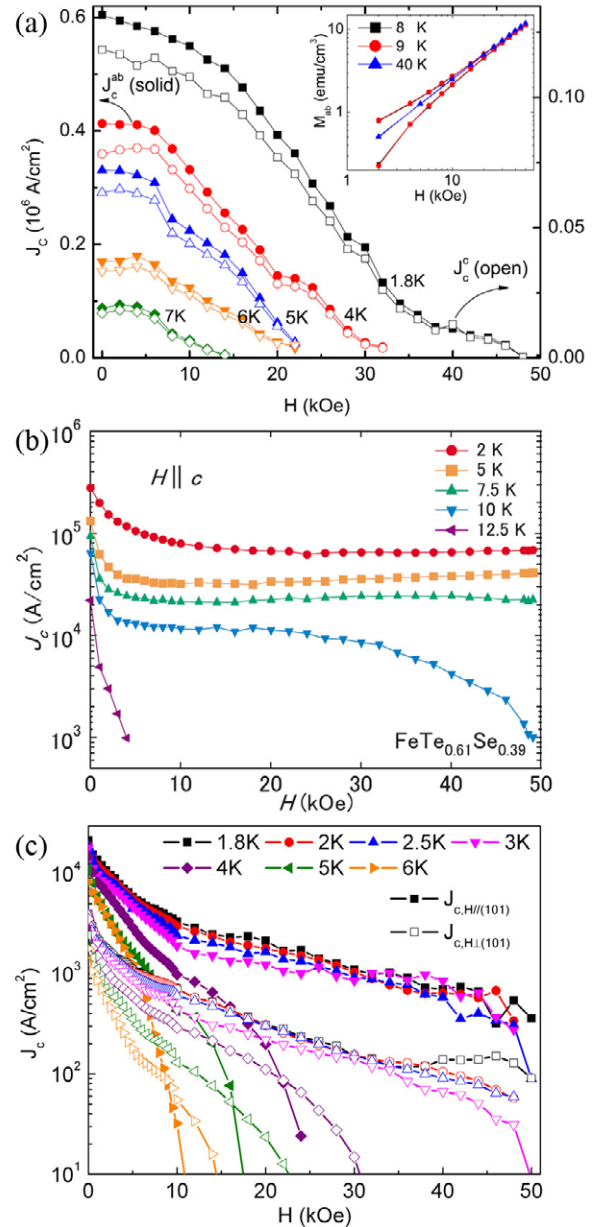


Figure 6. $J_c(T, \mu_0 H)$ at various temperatures and fields for (a) $\text{FeTe}_{0.9}\text{S}_{0.1}$, (b) $\text{FeTe}_{0.61}\text{Se}_{0.39}$ and (c) FeSe . (a) Reprinted with permission from [64]. (b) Reprinted with permission from [63]. Copyright 2009 by the American Physical Society.

while for δl pinning, $J_{c,H=0}^{\delta l}(t) = J_{c,H=0}(0)(1 - t^2)^{5/2}(1 + t^2)^{-1/2}$ [77]. As shown in figure 3(c), the $J_{c,H=0}(t)$ is between the two curves corresponding to δT_c and δl pinnings, respectively, but much closer and similar in shape to the δT_c -pinning curve. Using $J_{c,H=0}(t) = x J_{c,H=0}^{\delta T_c}(t) + (1 - x) J_{c,H=0}^{\delta l}(t)$, the experimental data can be fitted very well with $x = 0.74(2)$, suggesting that both δT_c and δl pinnings play roles in the quenched $\text{K}_x\text{Fe}_{2-y}\text{Se}_2$ single crystals, but the former mechanism is dominant. The dominant effect of δT_c pinning also implies that the main pinning centers lead to the distribution of T_c in their vicinity or might even be non-superconducting, like Y_2O_3 and Y-Cu-O precipitates in $\text{YBa}_2\text{Cu}_3\text{O}_{7-x}$ thin films [78]. Although the

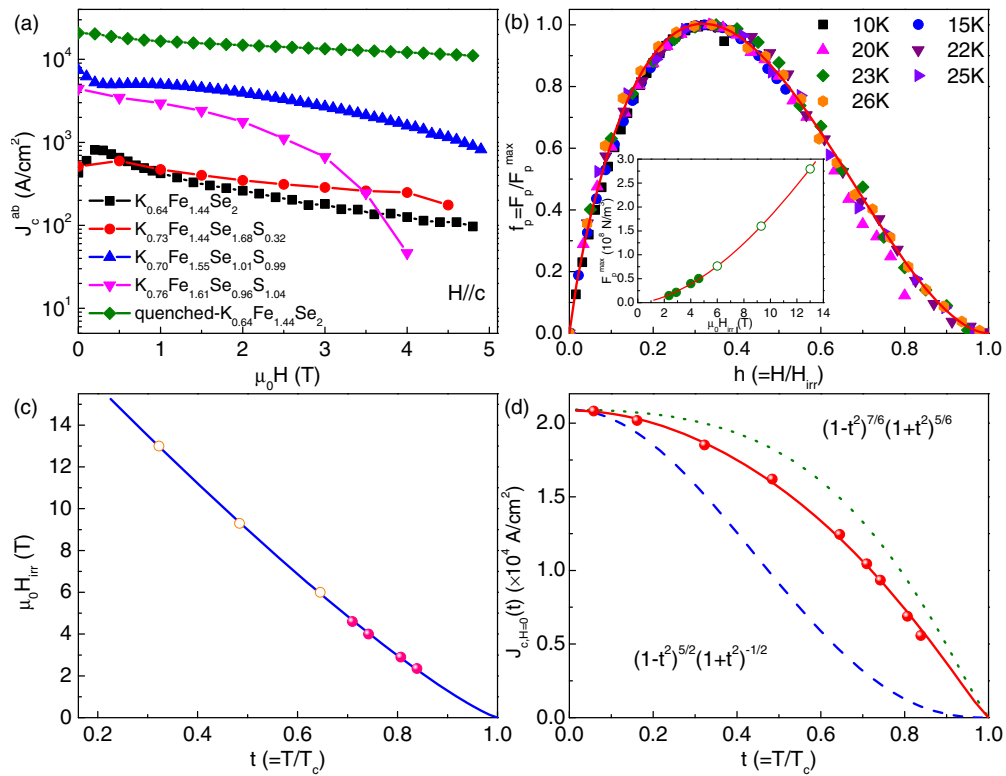


Figure 7. (a) Field dependences of $J_c^{ab}(\mu_0 H)$ of sulfur-doped $K_xFe_{2-y}Se_{2-z}S_z$ and quenched $K_xFe_{2-y}Se_2$ single crystals at 1.8 K. (b) Reduced field dependence of $f_p(h)$ at various temperatures for quenched $K_xFe_{2-y}Se_2$ single crystal. Solid line is fitting curve using $f_p = Ah^p(1-h)^q$. Inset: F_p^{max} as a function of H_{irr} . The fitting result using $F_p^{max} = A(\mu_0 H_{irr})^\alpha$ is shown as solid lines. (c) Reduced temperature dependence of $\mu_0 H_{irr}(t)$ with the fitting result using the $(1-t)^\beta$ law (solid line) for quenched $K_xFe_{2-y}Se_2$ single crystal. (d) Reduced temperature dependence of the $J_c(t)$ at zero field for quenched $K_xFe_{2-y}Se_2$ single crystal. The solid line shows the fitting result using $J_c(0)(1-t)^\gamma$. The measured and estimated $\mu_0 H_{irr}$ are shown as filled and open circles in inset of (b) and (c). Reprinted with permission from [70]. Copyright 2011 by the American Physical Society.

J_c^{ab} of quenched $K_xFe_{2-y}Se_2$ single crystals is enhanced significantly when compared to the as-grown samples, it is still smaller than in $FeTe_{0.61}Se_{0.39}$ and other iron pnictide superconductors [73, 74]. There might be more room to improve the current-carrying capacity for AFeCh-122 superconductors in the future using methods such as A site ionic disorder and nanometer-scale second phases.

It should be noted that if the phase separation scale is microns or even larger, the insulating region could have some effect on the calculation of the absolute values of J_c . This is because the volume of insulating phase has been used to calculate the J_c from $M-H$ curve, i.e., the real J_c values might be even larger than the calculated ones. However, the phase separation should have minor effects on the field and temperature dependences of J_c , i.e. the pinning mechanism should not be affected by this type of phase separation. If the phase separation is in the nanometer range, as it has been observed in $K_xFe_{2-y}Se_2$ by transmission electron microscopy [75], the effects on J_c are similar to what has been discussed above regarding the pinning mechanism. The insulating second phase can be considered as the pinning center, similar to nanometer-scale $BaZrO_3$ inclusions in YBCO coatings on metals [76].

3.2. GBs properties of iron-based superconductors

For practical applications, especially for fabrication of superconducting wires and tapes, superconductors are usually made in the polycrystalline bulk or thin-film form. Therefore, besides enhancement of J_c by various artificial pinning centers in the grains, i.e. enhancement of intragrain properties, the GBs properties are also of great interest for the applications of iron-based superconductors.

There are two studies so far on the $Ba(Fe,Co)_2As_2$ epitaxial thin films deposited on bicrystal substrates (figure 8) [79, 80]. Both show that the J_c across bicrystal grain boundary (BGB) has an exponential dependence on GB misorientation angle θ , indicating a weak-link effect for high-angle BGBs. However, the critical GB misorientation angles θ_c are different: about 6° and about 10° [79, 80]. According to the study of Katase *et al*, the slopes of the exponential decay are much smaller than those for YBCO BGBs, and the critical angle is approximately $9-10^\circ$, which is substantially larger than that of YBCO ($\sim 3-5^\circ$, inset of figure 8(a)) [80, 81]. Larger critical angle suggests smaller constraints for the in-plane orientation for substrate or buffer layers to obtain high- J_c iron-based superconducting films on flexible metal substrates. This observation will certainly be advantageous for tape applications. Similar study is lacking in

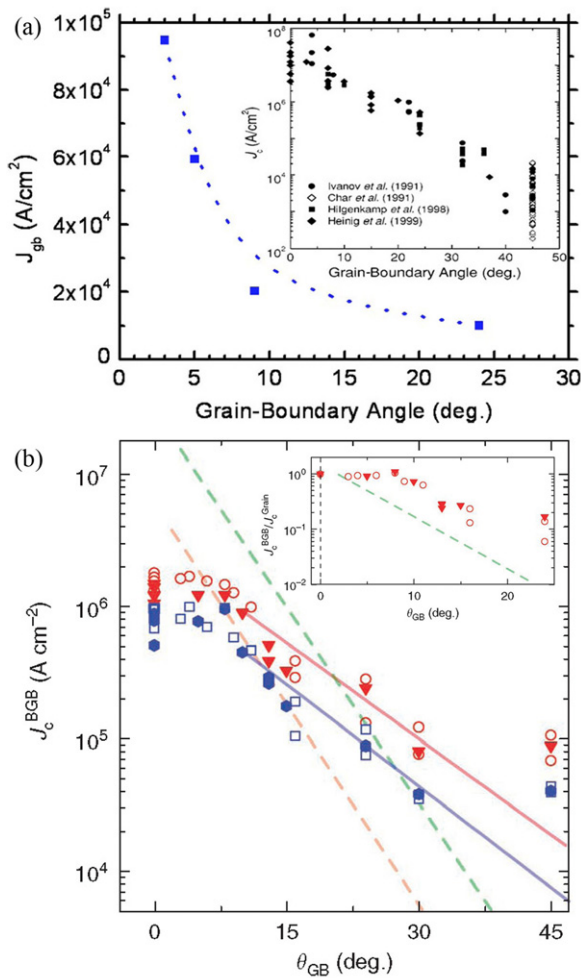


Figure 8. (a) Dependence of the intergrain $J_{c,gb}$ (12 K, 0.5 T, θ) on the misorientation angle θ for $\text{Ba}(\text{Fe},\text{Co})_2\text{As}_2$ BGB junction. Inset shows the $J_{c,gb}(\theta)$ for YBCO. (b) $J_{c,gb}(\theta)$ for $\text{Ba}(\text{Fe},\text{Co})_2\text{As}_2$ BGB junctions grown on [001]-tilt bicrystal substrates of MgO (open symbols) and $(\text{La},\text{Sr})(\text{Al},\text{Ta})\text{O}_3$ (filled symbols) at 4 K (red symbols) and 12 K (blue symbols). The red and blue solid lines are fitted to the empirical equation of $J_{c,gb} = J_{c0} \exp(-\theta_{GB}/\theta_c)$. The average data of the YBCO BGB junctions taken at 4 and 77 K are indicated by the green and orange dashed lines, respectively. The inset shows the ratio of the intragrain $J_{c,g}$ and $J_{c,gb}$ to θ_{GB} at 4 K on MgO (open circle) and $(\text{La},\text{Sr})(\text{Al},\text{Ta})\text{O}_3$ (filled triangle) bicrystals, respectively. The dashed green line shows the result of the YBCO BGB junctions. (a) Reprinted with permission from [79]. Copyright 2009 by the American Institute of Physics. (b) Reprinted with permission from [80]. Copyright 2011 by the Macmillan Publishers Ltd: Nature Commun.

iron selenide superconductors, and therefore related studies on FeCh-11 or AFeCh-122 films will be of interest to understand the GB properties.

3.3. Iron chalcogenide superconducting wires and tapes

After the discovery of iron-based superconductors, the trials for fabrication of iron-based superconducting wires were immediately carried out [82–84]. There are two methods to prepare iron-based superconducting wires and tapes, power-in-tube (PIT) and coated conductor techniques.

PIT technique has been used widely in Bi-based cuprate oxide wires (first-generation high-temperature superconductor (HTS) wires) and MgB_2 [85, 86]. Ozaki *et al* [87] fabricated $\text{Fe}(\text{Se},\text{Te})$ wires by an *ex situ* PIT method with the transport $J_c(0)$ of about 64 A cm^{-2} at 4.2 K. Recently, chemical-transformation PIT method was used to fabricate FeSe wires with a transport $J_c(0)$ of 588 A cm^{-2} at 4.2 K for a three-core wire (figure 9(a)) [88]. Although the J_c is enhanced considerably, it is much smaller than that of iron arsenic superconducting wires prepared using PIT method. For example in $(\text{Ba},\text{K})\text{Fe}_2\text{As}_2$ the $J_c(0)$ reaches $1 \times 10^4 \text{ A cm}^{-2}$ at 4.2 K [89]. But it should be noted that the J_c for both iron chalcogenide and iron arsenic superconducting wires fabricated using PIT method are much smaller than those of single crystals [48, 63, 74], implying that the texturing of grains in wires is important due to the GB weak-link effect.

Coated conductor technique has been successfully developed for the YBCO coated conductors (second-generation HTS wires) to overcome the weak-link effect [61]. The $\text{FeSe}_{0.5}\text{Te}_{0.5}$ thin films deposited on Hastelloy substrates, on which an MgO buffer layer has been formed by ion beam assisted deposition (IBAD), exhibit a nearly isotropic $J_c(0)$ exceeding $2 \times 10^5 \text{ A cm}^{-2}$ at 4.2 K and still higher than $1 \times 10^4 \text{ A cm}^{-2}$ at a magnetic field as high as 25 T (figure 9(b)) [90]. This gives the superior property in high fields ($\geq 20 \text{ T}$) when compared to Nb_3Sn or Ni–Ti wires. The fitting of field dependency of the F_p using Dew-Huges scaling law yields $q \sim 2$ and $p \sim 1$ (figure 9(c)), similar to $\text{K}_x\text{Fe}_{2-y}(\text{Se},\text{S})_2$ and quenched $\text{K}_x\text{Fe}_{2-y}\text{Se}_2$ [67, 70]. This suggests that the point-defect core pinning is dominant due to the inhomogeneous distribution of Se and Te [90]. In the core-pinning regime, F_p is a product of the individual $F_{p,ind}$ and the pinning center density n . This implies that the J_c of $\text{FeSe}_{0.5}\text{Te}_{0.5}$ thin films can still be enhanced by simply adding more defects to act as pinning centers [90]. Moreover, the weak-link effect of $\text{FeSe}_{0.5}\text{Te}_{0.5}$ may not be as severe as that of YBCO. Although the IBAD substrates have many low-angle GBs in the textured MgO template, the $J_c(0)$ of $\text{FeSe}_{0.5}\text{Te}_{0.5}$ thin films on IBAD-MgO with in-plane misorientation angle $\Delta\phi = 4.5^\circ$ is just a little lower than that of thin films deposited on LaAlO_3 single-crystal substrate [90]. These results should be confirmed with further studies of the thin films grown on controlled bicrystal substrates. On the other hand, depositing $\text{FeSe}_{0.5}\text{Te}_{0.5}$ thin films directly on textured metal tapes may be possible because $\text{FeSe}_{0.5}\text{Te}_{0.5}$ thin films are prepared in vacuum unlike YBCO-coated conductors. This considerably simplifies the synthesis procedure and reduces production costs [62]. A similar study on the $\text{Ba}(\text{Fe},\text{Co})_2\text{As}_2$ thin films deposited on IBAD-MgO-buffered Hastelloy substrates shows that the $J_c(0)$ is $(1.2\text{--}3.6) \times 10^6 \text{ A cm}^{-2}$ at 2 K with $\Delta\phi \sim 3^\circ$, regardless of the larger $\Delta\phi$ ($5.5\text{--}7.3^\circ$) of the MgO buffer layers [91]. It is much larger than that of $\text{Ba}(\text{Fe},\text{Co})_2\text{As}_2$ wire prepared by PIT method and comparable to that on MgO single crystals and remains at $1 \times 10^6 \text{ A cm}^{-2}$ at $T \leq 10 \text{ K}$ [89, 91]. This observation is consistent with the fact that the $\Delta\phi$ of $\text{Ba}(\text{Fe},\text{Co})_2\text{As}_2$ is much smaller than the $\theta_c = 9^\circ$ [91]. These results demonstrate that the coated conductors

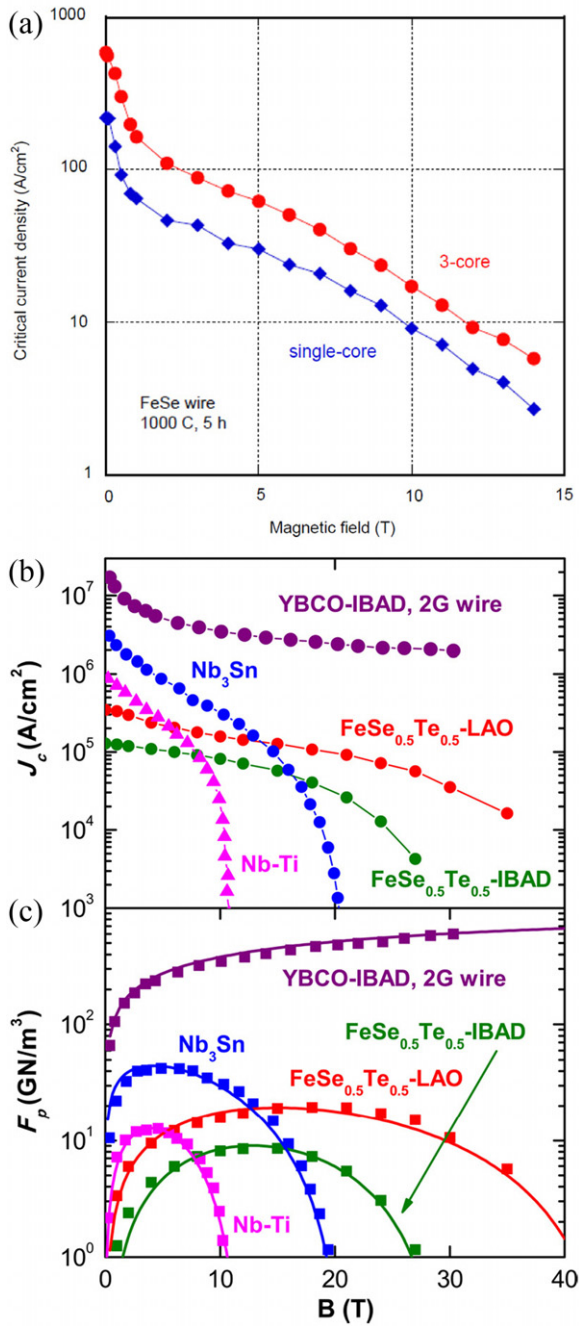


Figure 9. (a) Field dependence of $J_c(B)$ for single-core and three-core FeSe wires. (b) $J_c(B)$ and (c) $F_p(B)$ of FeSe_{0.5}Te_{0.5} thin films at 4.2 K compared with the results of other superconducting wires or tapes. Solid lines in (c) are the fitting results using the Dew-Hughes's scaling law. (a) Reprinted with permission from [88]. Copyright 2011 by the IOP Publishing. (b) Reprinted with permission from [90]. Copyright 2011 by the American Institute of Physics.

technique is a promising method to fabricate iron-based superconducting tapes for high field applications.

4. Upper critical fields

The upper critical field $\mu_0 H_{c2}$ is one of the most important superconducting parameters which provides valuable

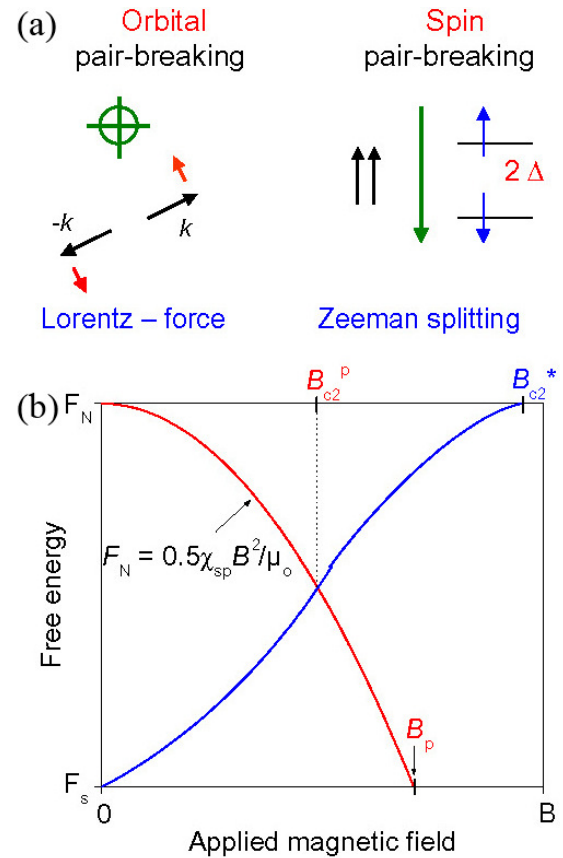


Figure 10. (a) Schematics of depairing mechanism of a singlet Copper pair via the external magnetic field. (b) Schematic field dependences of the Gibbs free energies of the normal state and superconducting state in a type-II superconductor. The free-energy curve of the normal state without Zeeman energy is the upper horizontal line, crossing the free-energy curve of a type-II superconductor at B_{c2}^* . The free-energy curve of the normal state including Zeeman energy is the red line, crossing the free-energy curve of a type-II superconductor at B_{c2}^p and the zero-field free-energy curve of the superconducting state (lower horizontal line) at the Pauli limiting field B_p . Reprinted with permission from [92]. Copyright 2009 by the IOP Publishing.

information on fundamental superconducting properties, such as coherence length, anisotropy, details of underlying electronic structures and dimensionality of superconductivity as well as insights into the pair-breaking mechanism. Iron-based superconductors usually have very high $\mu_0 H_{c2}$ and exhibit rich variety of temperature dependence of $\mu_0 H_{c2}(T)$.

4.1. Pair breaking mechanisms and multiband effects on $\mu_0 H_{c2}$

The s wave Cooper pair is formed by two electrons that attract together with opposite spins and momenta. External magnetic fields contributes to depairing via two primary mechanisms (figure 10(a)) [92]. One is the orbital pair breaking mechanism. The Lorentz force acts on paired electrons with opposite momenta and the superconductivity is destroyed when the kinetic energy exceeds the condensation energy of the Cooper pairs. Another mechanism

is the Pauli paramagnetic pair breaking. When the Pauli spin susceptibility energy (Zeeman energy) exceeds the condensation energy as shown in figure 10(b), the singlet pair with opposite spins is broken into unbound triplet along the field direction (Zeeman effect, also called spin-paramagnetic effect).

Through the Maki parameters α (see below) and λ_{so} [93], the effects of Pauli spin paramagnetism and spin-orbital scattering have been included in the Werthamer–Helfand–Hohenberg (WHH) theory for a single-band *s* wave weak-coupled type-II superconductor in the dirty limit [94]. The $\mu_0 H_{c2}(T)$ is given by

$$\ln \frac{1}{t} = \left(\frac{1}{2} + \frac{i\lambda_{so}}{4\gamma} \right) \psi \left(\frac{1}{2} + \frac{h + \lambda_{so}/2 + i\gamma}{2t} \right) + \left(\frac{1}{2} - \frac{i\lambda_{so}}{4\gamma} \right) \psi \left(\frac{1}{2} + \frac{h + \lambda_{so}/2 - i\gamma}{2t} \right) - \psi \left(\frac{1}{2} \right), \quad (8)$$

where $\psi(x)$ is digamma function, $\gamma \equiv [(\alpha h)^2 - (\lambda_{so}/2)^2]^{1/2}$ and

$$h = \frac{4\mu_0 H_{c2}(T)}{\pi^2 T_c (-d\mu_0 H_{c2}(T)/dT)_{T=T_c}} \quad (9)$$

If the orbital effect is dominant ($\alpha = 0$) and the spin-orbital scattering is negligible ($\lambda_{so} = 0$), the equation can be simplified as

$$\ln \frac{1}{t} = \psi \left(\frac{1}{2} + \frac{h}{2t} \right) - \psi \left(\frac{1}{2} \right), \quad (10)$$

which describes the temperature dependence of orbital limited upper critical field $\mu_0 H_{c2}^*(T)$. At zero temperature it becomes

$$\mu_0 H_{c2}^*(0) = -0.693 T_c (d\mu_0 H_{c2}(T)/dT)_{T=T_c}. \quad (11)$$

On the other hand, if we only consider the spin-paramagnetic effect alone, the zero-temperature Pauli limiting field $\mu_0 H_p(0)$ (Chandrasekhar–Clogston limit field for a weakly coupled superconductor) is [95, 96]

$$\mu_0 H_p(0)[T] = \Delta / \sqrt{2} \mu_B = 1.86 T_c, \quad (12)$$

where Δ is the *s* wave superconducting gap. Including strong-coupling corrections in the BCS theory due to electron–phonon and electron–electron interactions gives [92, 97]

$$\mu_0 H_p(0)[T] = 1.86(1 + \lambda_{ep})^\varepsilon \eta_\Delta \eta_{ib} (1 - I). \quad (13)$$

Here η_Δ describes the strong coupling intraband correction for the gap, I is the Stoner factor $I = N(E_F)J$, $N(E_F)$ is the electronic density of states (DOS) per spin at the Fermi energy E_F , J is an effective exchange integral, η_{ib} is introduced to describe phenomenologically the effect of the gap anisotropy, λ_{ep} is electron–phonon coupling constant and $\varepsilon = 0.5$ or 1 [92, 97, 98].

When compared to the orbital pair breaking effect, the relative contribution of the Pauli paramagnetic pair breaking effect is quantified by the Maki parameter

$\alpha = \sqrt{2} H_{c2}^*(0) / H_p(0)$. When $\alpha > 1$, the spin-paramagnetic effect becomes essential [93] and the actual upper critical field $\mu_0 H_{c2}(0)$ is given by

$$\mu_0 H_{c2}(0) = \mu_0 H_{c2}^*(0) / \sqrt{1 + \alpha^2}. \quad (14)$$

In the single-band clean limit, the Maki parameter α is given by [40]

$$\alpha = \frac{\pi^2 \Delta m}{4 E_F m_0}, \quad H \parallel c, \quad (15)$$

$$\alpha = \frac{\pi^2 \Delta m v_{ab}}{4 E_F m_0 v_c}, \quad H \parallel ab, \quad (16)$$

where v_{ab} and v_c are the Fermi velocities in the *ab* plane and along the *c*-axis, respectively, m is the electron effective mass and m_0 is free electron mass. For conventional single-band BCS superconductors, because of $m \sim m_0$, $v_{ab} \sim v_c$, and low T_c , the α is usually small, i.e. the orbital pair breaking mechanism is dominant. On the other hand, for some exotic superconductors, such as heavy fermion superconductors with $m \gg m_0$ or organic superconductors with large ratio of v_{ab}/v_c , the condition of $\alpha > 1$ can be easily satisfied and the spin-paramagnetic effect is dominant. When α is large enough and superconductors are in the clean limit, the Fulde–Ferrell–Larkin–Ovchinnikov (FFLO) state may appear, resulting in a non-zero momentum of the Cooper pairs and the spatial oscillations of the superconducting order parameter [99, 100].

On the other hand, for the superconductors with several disconnected Fermi surfaces, the multiband effects on the $\mu_0 H_{c2}$ should be considered. The most famous example is MgB_2 where the $\mu_0 H_{c2}$ can be described successfully using the two-band BCS model in the dirty limit [101, 102].

In the dirty limit, taking into account both orbital and spin-paramagnetic effect with interband and intraband scattering contributions, the $\mu_0 H_{c2}(T)$ is given by

$$(\lambda_0 + \lambda_i)(\ln t + U_+) + (\lambda_0 - \lambda_i)(\ln t + U_-) + 2w(\ln t + U_+)(\ln t + U_-) = 0, \quad (17)$$

where $t = T/T_{c0}$, and

$$\lambda_0 = (\lambda_-^2 \pm 4\lambda_{12}\lambda_{21})^{1/2}, \quad (18)$$

$$\lambda_i = [(\omega_- + \gamma_-)\lambda_- - 2\lambda_{12}\gamma_{21} - 2\lambda_{21}\gamma_{12}] / \Omega_0, \quad (19)$$

$$\lambda_\pm = \lambda_{11} \pm \lambda_{22}, \quad (20)$$

$$\omega_\pm = (D_1 \pm D_2)\pi \mu_0 H_{c2} / \Phi_0, \quad (21)$$

$$\gamma_\pm = \gamma_{12} \pm \gamma_{21}, \quad (22)$$

$$\Omega_0 = [(\omega_- + \gamma_-)^2 + 4\gamma_{12}\gamma_{21}]^{1/2}, \quad (23)$$

$$w = \lambda_{11}\lambda_{22} - \lambda_{12}\lambda_{21}, \quad (24)$$

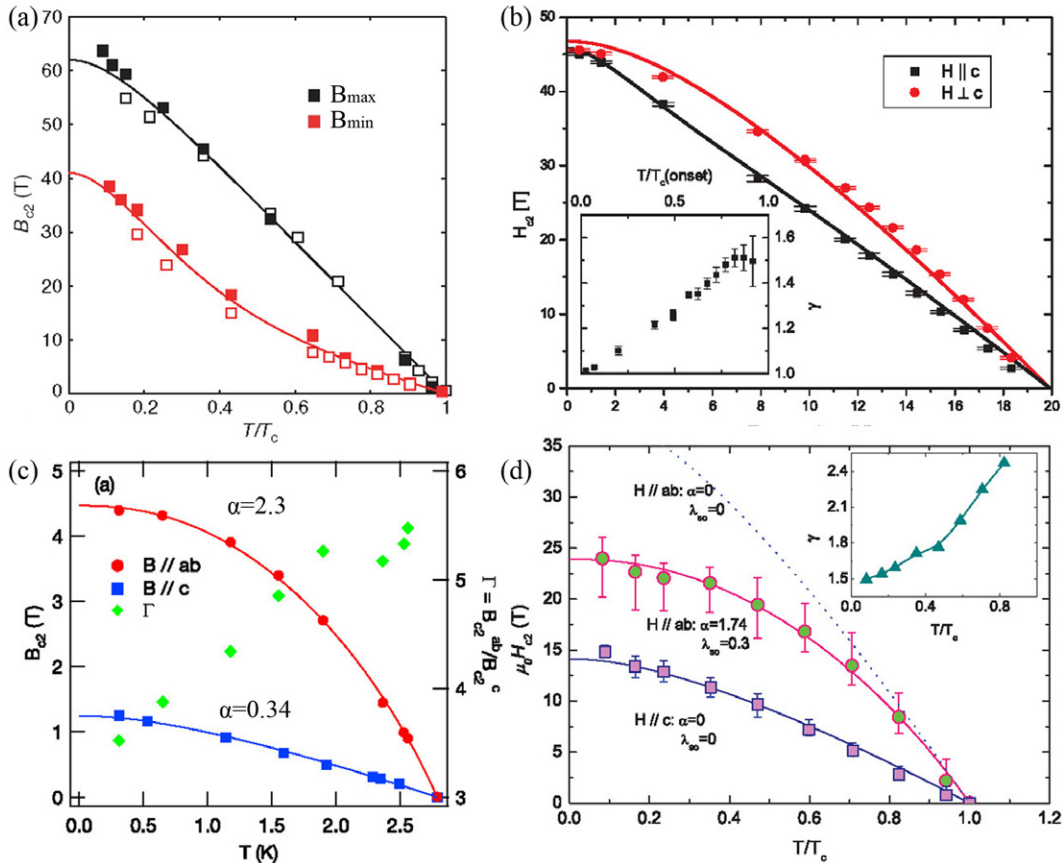


Figure 11. Temperature dependence of $\mu_0 H_{c2}(T)$ for (a) polycrystalline $\text{LaFeAsO}_{0.89}\text{F}_{0.11}$, (b) $\text{Sr}(\text{Fe},\text{Co})\text{As}_2$ thin film, (c) KFe_2As_2 single crystal and (d) LiFeAs single crystal. (a) Reprinted with permission from [104]. Copyright 2011 by the Macmillan Publishers Ltd: Nature. (b) Reprinted with permission from [106]. Copyright 2009 by the American Physical Society. (c) Reprinted with permission from [108]. Copyright 2009 by the Physical Society of Japan. (d) Reprinted with permission from [109]. Copyright 2011 by the American Physical Society.

$$U_{\pm} = \text{Re} \left[\psi \left(\frac{1}{2} + \frac{\Omega_{\pm} + i\mu_B H_{c2}}{2\pi T} \right) - \psi \left(\frac{1}{2} \right) \right], \quad (25)$$

$$2\Omega_{\pm} = \omega_{\pm} + \gamma_{\pm} \pm \Omega_0. \quad (26)$$

D_1 and D_2 are intraband diffusivities of the bands 1 and 2; λ_{11} and λ_{22} are the intraband couplings in the bands 1 and 2, and λ_{12} and λ_{21} describe the interband couplings between bands 1 and 2; γ_{12} and γ_{21} are interband scattering rates between band 1 and 2. If neglecting interband scattering ($\gamma_{12} = \gamma_{21} = 0$), we obtain

$$(\lambda_0 + \lambda_-)(\ln t + U[(k+i)h]) + (\lambda_0 - \lambda_-)(\ln t + U[(\eta k+i)h]) + 2w(\ln t + U[(k+i)h])(\ln t + U[(\eta k+i)h]) = 0, \quad (27)$$

where $U[x] = \text{Re} \left[\psi \left(\frac{1}{2} + x \right) - \psi \left(\frac{1}{2} \right) \right]$, $h = \mu_0 H_{c2} D_0 / (2\Phi_0 T)$, $D_0 = \mu_B \Phi_0 / \pi = \hbar^2 / 2m$ is quantum diffusivity, $k = D_1 / D_0$, $\eta = D_2 / D_1$. When the spin-paramagnetic effect is negligible ($D_0 \ll D_{1,2}$), H_{c2} can be simplified to

$$(\lambda_0 + \lambda_-)(\ln t + U[kh]) + (\lambda_0 - \lambda_-)(\ln t + U[\eta kh]) + 2w(\ln t + U[kh])(\ln t + U[\eta kh]) = 0. \quad (28)$$

Moreover, for $\eta = 1$, equation (28) can be further reduced to equation (10) [93, 94].

4.2. Features of $\mu_0 H_{c2}(T)$ in iron arsenic superconductors

All parameters of equations (15) and (16) that might lead to a large α exist in iron-based superconductors [40], therefore the spin-paramagnetic effect needs to be considered. Furthermore, there are several disconnected electron and hole sheets at the FS that originate from the hybridized d-orbitals of iron [29]. This suggests that the multiband effect on the $\mu_0 H_{c2}(T)$ should also be taken into account. For iron arsenic superconductors, due to the different contributions of multiband and spin-paramagnetic effects, there are various temperature dependences of $\mu_0 H_{c2}(T)$ for different systems (see the review paper about this topic [103] and references therein). Figure 11 shows several typical $\mu_0 H_{c2}(T)$ dependences in iron arsenic superconductors. FePn-1111 system ($\text{LnFeAs}(\text{O},\text{F})$, figure 11(a)) shows a pronounced upturn curvature in $\mu_0 H_{c2,c}(T)$ at low temperatures. In contrast, $\mu_0 H_{c2,ab}(T)$ exhibits a downturn curvature with decreasing temperature [51, 104]. Both can be explained within a two-band theory with a high diffusivity ratio of electron band to hole band, but the spin-paramagnetic effect also needs to be considered, especially for $H \parallel ab$ [51, 104, 105]. For the FeAs-122 system ($\text{A}(\text{Fe},\text{Co})_2\text{As}_2$, figure 11(b)), the upturn curvature of $\mu_0 H_{c2,c}(T)$ present in FeAs-1111 system does not appear, but it still shows a positive curvature

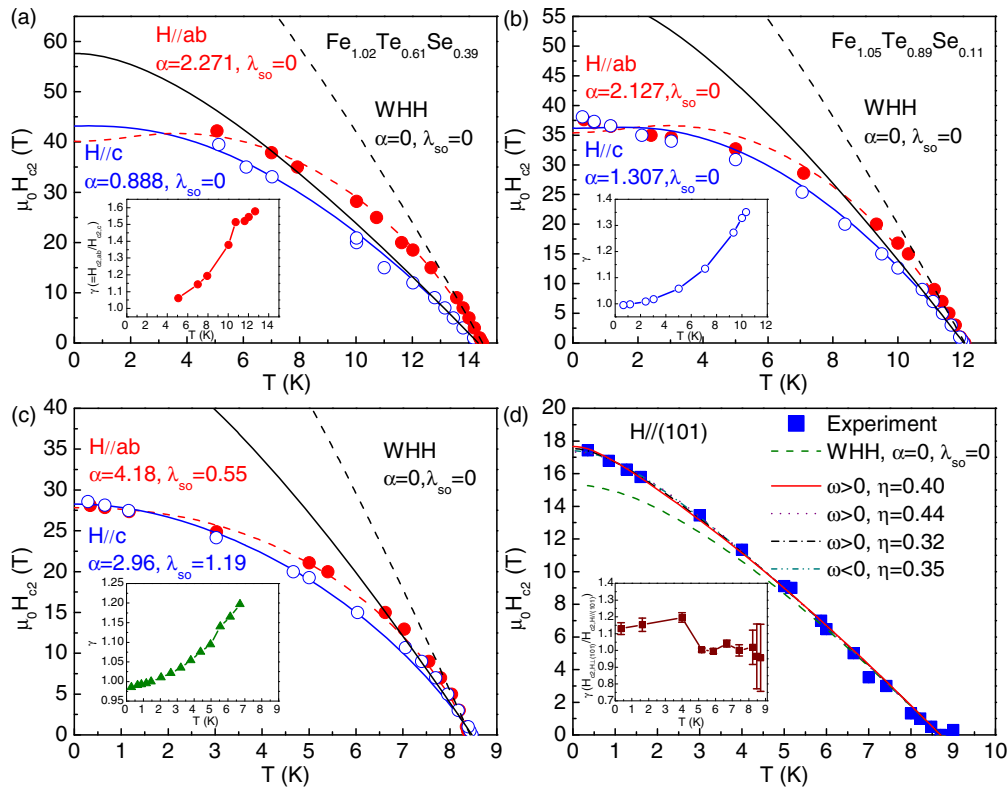


Figure 12. Temperature dependence of $\mu_0 H_{c2}(T)$ for (a) $\text{Fe}_{1.02}\text{Te}_{0.61}\text{Se}_{0.39}$, (b) $\text{Fe}_{1.05}\text{Te}_{0.89}\text{Se}_{0.11}$, (c) $\text{Fe}_{1.14}\text{Te}_{0.91}\text{S}_{0.09}$ and (d) FeSe single crystals. Insets: the anisotropy γ of $\mu_0 H_{c2}(T)$. (a) and (b) Reprinted with permission from [110]. Copyright 2010 by the American Physical Society. (c) Reprinted with permission from [117]. Copyright 2010 by the American Physical Society. (d) Reprinted with permission from [119]. Copyright 2012 by the American Physical Society.

at temperatures far below T_c without saturation. On the other hand $\mu_0 H_{c2,ab}(T)$ tends to saturate with decreasing temperature [106, 107]. This can also be interpreted using a two-band theory with a larger diffusivity ratio of two bands when compared to FePn-1111 system [106, 107]. Similar to FePn-1111 system, the spin-paramagnetic effect may also have some effect on the $\mu_0 H_{c2,ab}(T)$ [107]. For KFe_2As_2 and LiFeAs (figures 11(c) and (d)), both $\mu_0 H_{c2,ab}(T)$ and $\mu_0 H_{c2,c}(T)$ show saturation trends at low temperatures with different negative curvatures. The former can be ascribed to the spin-paramagnetic effect and the latter is mainly determined by the orbital-limited field in the one-band scenario [108, 109].

4.3. Features of $\mu_0 H_{c2}(T)$ in iron chalcogenide superconductors

Both multiband and spin-paramagnetic effects contribute to $\mu_0 H_{c2}(T)$ in iron chalcogenide superconductors. However, the multiband effect is much weaker when compared to iron arsenides, and the spin-paramagnetic effect is usually the dominant factor.

In $\text{Fe}(\text{Te},\text{Se})$ (as shown on examples of $\text{Fe}_{1.02}\text{Te}_{0.61}\text{Se}_{0.39}$ (Se-39) and $\text{Fe}_{1.05}\text{Te}_{0.89}\text{Se}_{0.11}$ (Se-11) in figures 12(a) and (b)) both $\mu_0 H_{c2}(T)$ for $H\parallel ab$ and $H\parallel c$ can be explained well using the WHH model with spin-paramagnetic effect when neglecting spin-orbital scattering. It indicates that the spin-paramagnetic effect is the dominant

pair-breaking mechanism for both $H\parallel ab$ and $H\parallel c$ [110, 111, 114]. For the $\text{Fe}(\text{Te},\text{Se})$ in the clean limit (grown by Bridgman–Stockbarger technique) the $\mu_0 H_{c2}(T)$ is Pauli limited. This may suggest the emergence of the FFLO state at low temperatures [114]. The dominance of spin-paramagnetic effect in $\text{Fe}(\text{Te},\text{Se})$ may be due to the disorder induced by $\text{Te}(\text{Se})$ substitution/vacancies and excess Fe in $\text{Fe}(2)$ site [92, 115]. For Se-39, more Se doping introduces more disorder than in Se-11. This effect could contribute to the larger $\alpha_{H\parallel ab}$ of Se-39 when compared to Se-11. However, it cannot explain the inverse trend of $\alpha_{H\parallel c}$. Therefore, another effect must compete with disorder. It may be the effect of excess Fe in $\text{Fe}(2)$ position, which is the unique feature of 11-system, different from other Fe pnictide superconductors. The $\text{Fe}(2)$ has larger local magnetic moment than $\text{Fe}(1)$ in $\text{Fe}(\text{Te},\text{Se})$ layers. The $\text{Fe}(2)$ moment is present even if the SDW antiferromagnetic ordering of the Fe plane is suppressed by doping or pressure, contributing to $N(E_F)$ [25]. According to equation (13), $\mu_0 H_p(0)$ can be decreased if the Stoner factor increases via enhancement of J or $N(E_F)$. Excess Fe in $\text{Fe}(2)$ site with local magnetic moment could interact with itinerant electron in Fe layer, resulting in exchange-enhanced Pauli paramagnetism or Ruderman–Kittel–Kasuya–Yosida (RKKY) interaction, thus enhancing J . Hence, higher content of excess Fe in Se-11, could lead to larger $\alpha_{H\parallel c}$ than in Se-39. Another possibility may be that the $N(E_F)$ is decreased with increasing the content of Se [116]. This trend

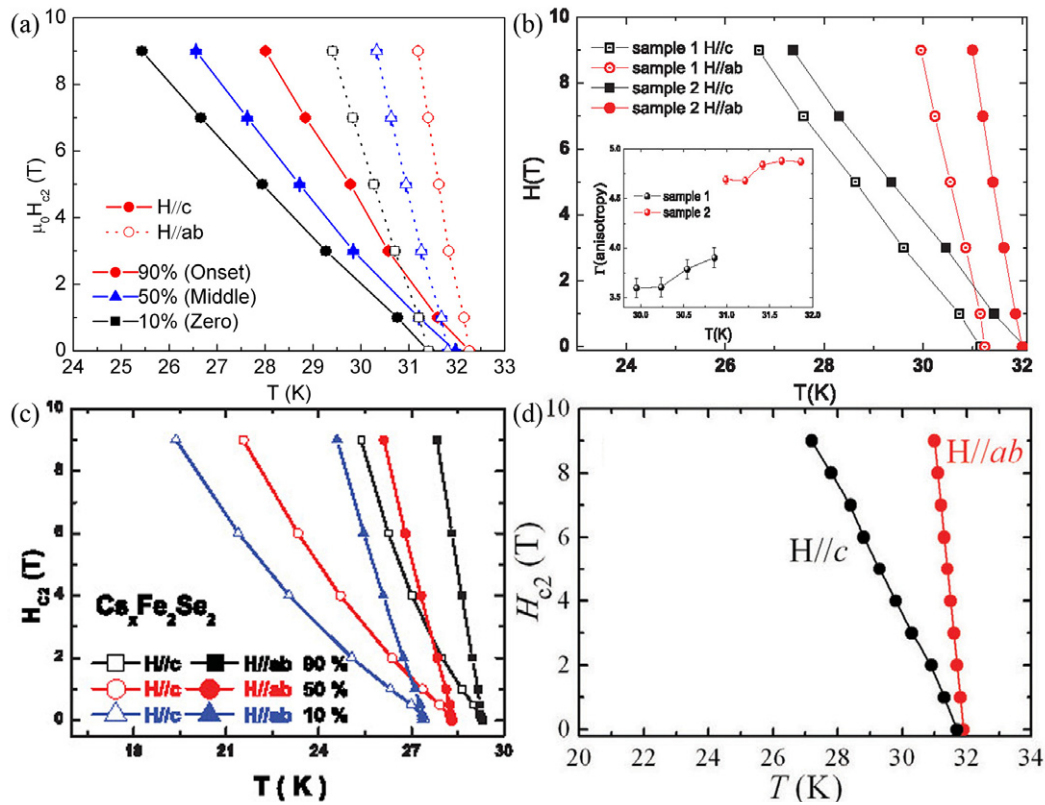


Figure 13. Temperature dependence of $\mu_0 H_{c2}(T)$ near T_{c0} for (a) $K_{0.64}Fe_{1.44}Se_2$, (b) $Rb_{0.8}Fe_{1.68}Se_2$, (c) $Cs_{0.81}Fe_{1.61}Se_2$ and (d) $Tl_{0.58}Rb_{0.42}Fe_{1.72}Se_2$ single crystals. (b) Reprinted with permission from [123] and (c) Reprinted with permission from [124]. Copyright 2011 by the American Physical Society. (d) Reprinted with permission from [123]. Copyright 2011 by the European Physical Society.

will also enhance the Pauli-limited field, i.e. suppress the spin-paramagnetic effect.

As shown in figure 12(c), spin-paramagnetic effect is also dominant in $\mu_0 H_{c2}(T)$ of S-09 with larger α and obvious spin-orbital scattering [117], when compared to Se-39 and Se-11. The spin-paramagnetic effect should have the same origin as in Se-39 and Se-11 due to disorder. Moreover, since the $N(E_F)$ of FeS is larger than that of FeSe, [116], it is likely that the $N(E_F)$ of S-09 is larger than that of Fe(Te,Se) with the same doping content. This will lead to the smaller $\mu_0 H_p(0)$, i.e. larger α . On the other hand, non-zero λ_{so} can also be explained via increasing Kondo-like scattering from excess Fe in Fe(2) site, consistent with the definition of λ_{so} , which is proportional to the spin-flip scattering rate [93, 94]. It is also consistent with the Kondo behavior of S-09 in the normal state, related to the excess Fe in Fe(2) that act as the Kondo-like impurities [117]. The presence of Kondo-type interactions in binary iron chalcogenides, first inferred from the normal-state scattering and $\mu_0 H_{c2}(T)$ behavior, has later been confirmed by the neutron scattering measurements [118].

Furthermore, the evaluated mean free path of S-09, $l = 1.35$ nm using the Drude model $l = \hbar(3\pi^2)^{1/3}/(e^2\rho_0n^{2/3})$, suggests that S-09 is a dirty-limit superconductor since $l/\xi(0) = 0.396$ [117]. Therefore, the FFLO state at high fields is unlikely in S-09 because the short mean free path will remove any momentum anisotropy [99, 100].

The $\mu_0 H_{c2,H\parallel(101)}(T)$ of FeSe single crystal at low temperatures is larger than the value evaluated from the

WHH theory with $\alpha = 0$ and $\lambda_{so} = 0$ (figure 12(d)) [119], which is distinctively different from Fe(Te,Se) and Fe(Te,S) where the WHH curve is far above the experimental data. The enhancement of the $\mu_0 H_{c2}(T)$ at low temperatures and high fields implies that the multiband effect is not negligible. By using the coupling constants, determined from muon spin resonance (μSR) experiment with very small interband coupling [120], the $\mu_0 H_{c2,H\parallel(101)}(T)$ data from both rf and resistivity measurements can be very well explained using a two-band model with $\eta = 0.40$. It is similar to the value of FeAs-122 but much larger than that of other two-band iron-based superconductors, such as FeAs-1111 [51, 104]. Large η leads to the absence of the upturn of $\mu_0 H_{c2}(T)$ at low temperatures, which is observed in FeAs-1111 superconductors [51, 104], but not in FeAs-122 compounds [106]. We have also performed simulations for different values of coupling constants: (i) dominant intraband coupling, $w > 0$ and (ii) dominant interband coupling, $w < 0$. The different sets of fitting parameters results in almost identical result, fitting the experimental data well (figure 12(d)). The derived η is in the range of 0.32–0.44, suggesting that the fitting results are insensitive to the choice of coupling constants. Thus, either interband and intraband coupling strength are comparable or their difference is below the resolution of our experiment. On the other hand, assuming $\mu_0 H_{c2}(T = 0.35 \text{ K}) \approx \mu_0 H_{c2}(0)$, the $\mu_0 H_{c2}(0)$ are 17.4(2) and 19.7(4) T for $H\parallel(101)$ and $H\perp(101)$, respectively. Given the electron–phonon coupling

parameter $\lambda_{e-ph} = 0.5$ (typical value for weak-coupling BCS superconductors) [121], the Pauli limiting field $\mu_0 H_p(0) = 1.86 T_c (1 + \lambda_{e-ph})^{1/2}$ is 19.8 T [97]. This is nearly the same as the $\mu_0 H_{c2,H\perp(101)}(T = 0.35 \text{ K})$ and larger than value for $H\parallel(101)$. It suggests that the spin-paramagnetic effect might also have some influence on the $\mu_0 H_{c2}(T)$, but should not be the dominant effect. The situation is rather different in Fe(Te,Se) and Fe(Te,S) where the spin-paramagnetic effect governs $\mu_0 H_{c2}(T)$ [110, 117]. The existence of two bands is also confirmed from the Hall measurement [119].

The anisotropy of $\mu_0 H_{c2}(T)$, $\gamma(T)$ ($= H_{c2,ab}(T)/H_{c2,c}(T)$) (insets of figures 12(a)–(c)) decreases with decreasing temperature, reaching ~ 1 for all Fe(Te,Se) and Fe(Te,S) compounds. Similar results have been reported in the literature [66, 122]. These results show that Fe(Te,Se) and Fe(Te,S) are high-field isotropic superconductors. When T is close to T_c , the γ of Se-11 is smaller than that of Se-39 but larger than in Fe(Te,S). Although the behavior of $\gamma(T)$ is similar in Fe(Te,Se)/Fe(Te,S) and FeAs-based superconductors, the value is smaller in the former compounds [103]. For FeSe, the $\gamma(T)$ ($= H_{c2,H\perp(101)}(T)/H_{c2,H\parallel(101)}(T)$) is nearly constant and close to 1, but it is difficult to compare this with other FeCh-11 superconductors due to the differences of the orientation.

In AFeCh-122 superconductors, the slopes of $\mu_0 H_{c2}(T)$ near T_{c0} , $d\mu_0 H_{c2}(T)/dT|_{T=T_c}$ ($\sim 6\text{--}10 \text{ TK}^{-1}$) are similar to those in FeCh-11 materials for $H\parallel ab$ but are much smaller ($\sim 1\text{--}3 \text{ TK}^{-1}$) than in the latter for $H\parallel c$ (figure 13) [60, 110, 117, 123–125]. The larger T_c compared to FeCh-11 superconductors leads to the significantly larger $H_{c2}(0)$ evaluated from equation (11) for $H\parallel ab$. The $\mu_0 H_{c2}(0)$ values are usually $\sim 125\text{--}275 \text{ T}$ and $\sim 30\text{--}60 \text{ T}$ for $H\parallel ab$ and $H\parallel c$, respectively [60, 123, 125].

Recent studies on the $\mu_0 H_{c2}(T)$ of $\text{K}_{0.8}\text{Fe}_{1.76}\text{Se}_2$ and $\text{Tl}_{0.58}\text{Rb}_{0.42}\text{Fe}_{1.72}\text{Se}_2$ single crystals up to 60 T show that $\mu_0 H_{c2}(T)$ for $H\parallel c$ presents an almost linear temperature dependence and slight upturn at low temperatures, whereas the curve of $\mu_0 H_{c2}(T)$ for $H\parallel ab$ has a convex curvature with a much larger value and gradually tends to saturate at low temperatures (figure 14) [60, 126]. The $\mu_0 H_{c2}(T)$ for $H\parallel c$ is slightly larger than the value predicted with equation (11) at low temperatures, but is smaller than the theoretical one for $H\parallel ab$. For $H\parallel ab$, fitting with equation (8) yields $\alpha = 5.6$ and $\lambda_{so} = 0.3$, indicating that the spin-paramagnetic effect may play an important role in suppressing superconductivity for $H\parallel ab$ [60]. On the other hand, the enhancement of $\mu_0 H_{c2}(T)$ for $H\parallel c$ at low temperatures may be related to the multiband effect [60]. These behaviors are very similar to those of FeAs-1111 and FeAs-122, but not FeCh-11 compounds. In $\text{K}_{0.8}\text{Fe}_{1.76}\text{Se}_2$, the $\gamma(T)$ increases with temperature and finally decreases gradually with decreasing temperature. But in $\text{Tl}_{0.58}\text{Rb}_{0.42}\text{Fe}_{1.72}\text{Se}_2$, the $\gamma(T)$ decreases with temperature in the entire measurement range with larger values when compared to $\text{K}_{0.8}\text{Fe}_{1.76}\text{Se}_2$. Similar to other iron-based superconductors, the decrease of $\gamma(T)$ with temperature may be related to the multiband effect or to the gradual setting in of pair breaking by the spin-paramagnetic effect, which

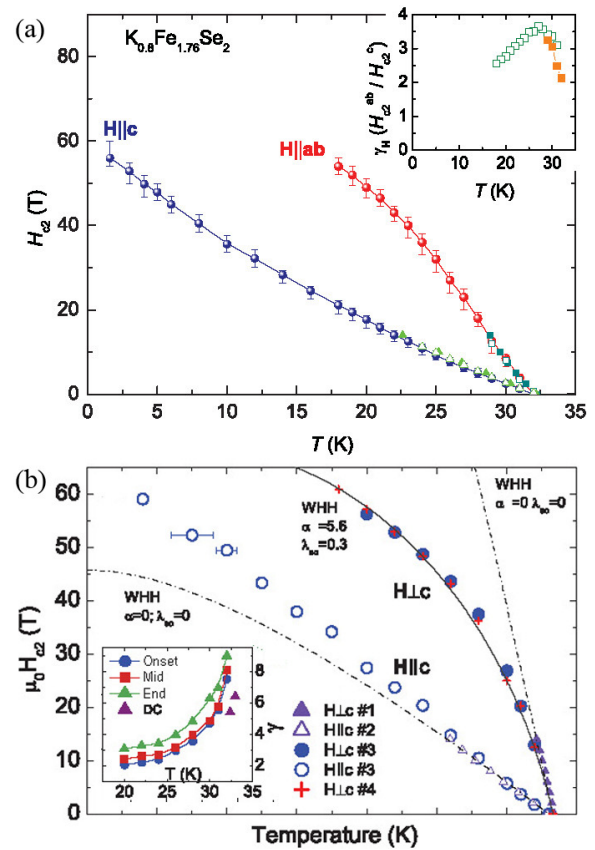


Figure 14. Temperature dependence of $\mu_0 H_{c2}(T)$ up to 60 T for (a) $\text{K}_{0.8}\text{Fe}_{1.76}\text{Se}_2$ and (b) $\text{Tl}_{0.58}\text{Rb}_{0.42}\text{Fe}_{1.72}\text{Se}_2$ single crystals. (a) Reprinted with permission from [126]. Copyright 2011 by the American Physical Society. (b) Reprinted with permission from [60]. Copyright 2012 by the American Physical Society.

requires $\mu_0 H_{c2,ab} = \mu_0 H_{c2,c}$ in the low-temperature and high-field limit [103]. On the other hand, the $\gamma(T)$ values in $\text{K}_{0.8}\text{Fe}_{1.76}\text{Se}_2$ and $\text{Tl}_{0.58}\text{Rb}_{0.42}\text{Fe}_{1.72}\text{Se}_2$ are much larger than those in FeCh-11 materials. This difference could be related to the decrease of dimensionality when compared to FeCh-11 superconductors.

For both FeCh-11 and AFeCh-122 superconductors, doping on Fe site is usually detrimental for superconductivity [127, 128]. On the contrary, in FeAs-based superconductors doping on Fe site is beneficial as it induces superconductivity in compounds such as $\text{Ba}(\text{Fe},\text{Co})_2\text{As}_2$ [8]. In FeCh-11 materials, doping on Ch site enhances superconductivity [16, 17], whereas it has an opposite trend in AFeCh-122 where S and Te doping decreases T_c [68, 129]. However, the suppression of superconductivity is far less strong when compared to doping on Fe site.

As shown in figure 15(a), the lattice parameters decrease with S doping due to the smaller ionic size of S^{2-} than Se^{2-} . The trend of lattice contraction approximately follows the Vegard's law. In addition, doping S into Se site does not lead to random Fe occupation of Fe1 and Fe2 sites. The refinements within single-phase I4/m crystallographic space group show that the Fe1 site has a low occupancy, whereas the Fe2 site is almost fully occupied. Besides $\text{K}_x\text{Fe}_{2-y}\text{S}_2$, all

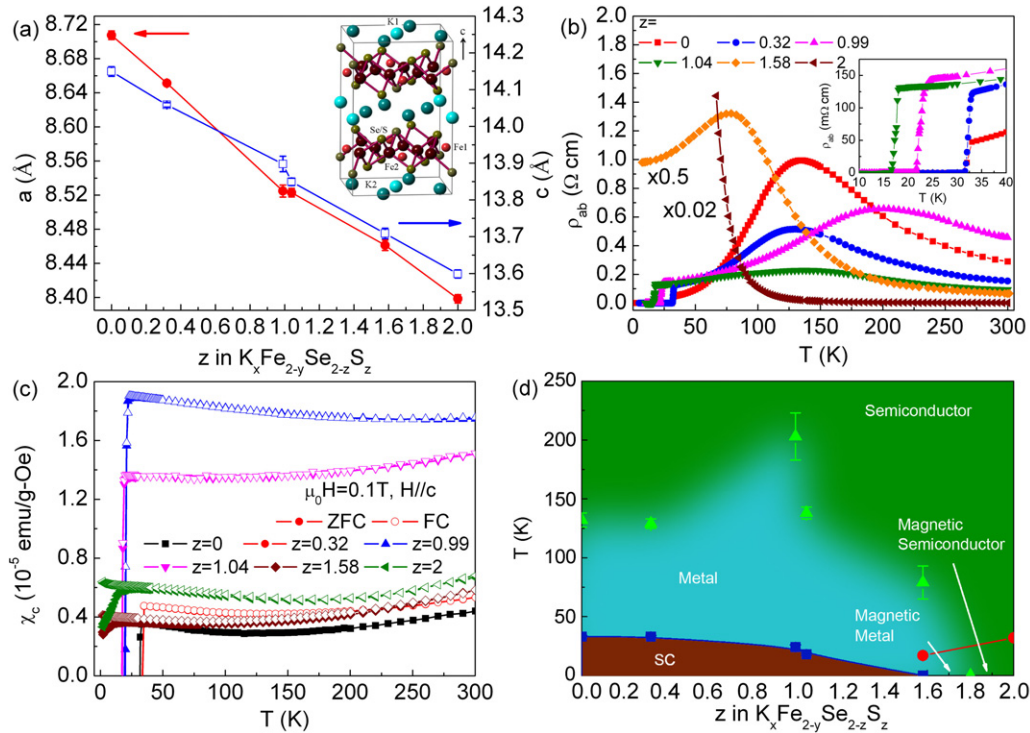


Figure 15. (a) Unit cell parameters as a function of S substitution. Inset: crystal structure of $K_xFe_{2-y}Se_{2-z}S_z$ in $I4/m$ unit cell with vacant Fe1 sites marked light red and Fe2 sites marked dark purple. (b) Temperature dependence of the in-plane resistivity $\rho_{ab}(T)$ of the $K_xFe_{2-y}Se_{2-z}S_z$ in zero field. Inset: temperature dependence of $\rho_{ab}(T)$ below 40 K for $0 \leq z \leq 1.2$. (c) Temperature dependence of $\chi(T)$ at $\mu_0 H = 0.1$ T for $H \parallel c$ for zero-field cooling (ZFC) and FC, respectively. (d) Magnetic and superconducting phase diagram of $K_xFe_{2-y}Se_{2-z}S_z$. Green, blue and orange colors show semiconducting, magnetic and superconducting regions, respectively. Red symbols denote spin glass transitions. Reprinted with permission from [68]. Copyright 2011 by the American Physical Society.

other crystals show metallic behavior with resistivities below ρ_{max} at temperatures above T_c (figure 15(b)). It should be noted that the temperature of ρ_{max} varies non-monotonically with the doping level of S(z), implying that the temperature of crossover may be influenced by both K and Fe deficiencies. Shoemaker *et al* [130] found that the temperature dependence of resistivity in the normal state can be described well by a two-phase model containing metallic and insulating phases. This result suggests that the metal-semiconductor crossover can be also partially related to the two-phase coexistence in $K_xFe_{2-y}Se_2$, i.e. the phase separation in the samples, which has been observed by various measurement technique [32–38]. On the other hand, the crystal with $z = 2$ is semiconducting even if the Fe deficiency is smaller than in the other samples. Whether there is also phase separation in $K_xFe_{2-y}S_2$ needs to be investigated in the future.

The changes in the ground state phase diagram of $K_xFe_{2-y}Se_{2-z}S_z$ are due to the sulfur doping and should not be influenced by the microscopic phase separation. If $K_xFe_{2-y}Se_2$ shows superconducting behavior, the T_c is always above 30 K and is never below 30 K [75]. It means that the T_c is not sensitive to the compositional fluctuation of K or Fe once superconductivity appears. So, the gradual decrease of T_c in $K_xFe_{2-y}Se_{2-z}S_z$ is difficult to ascribe to compositional fluctuations due to the phase separation. In contrast to ρ_{max} , the T_c is monotonically suppressed to lower temperature with the increase in S and cannot be observed above 2 K for $z \geq 1.58$. The

superconductivity of $K_xFe_{2-y}Se_{2-z}S_z$ single crystals with $z < 1.58$ is confirmed by the magnetization measurement (figure 15(c)). The Curie–Weiss temperature dependence is absent for all samples above 50 K as shown in figure 15(c). Magnetic susceptibilities are weakly temperature dependent with no significant anomalies above 50 K. This suggests the presence of low-dimensional short-range magnetic correlations and/or a long-range AFM order above 300 K. Interestingly, non-superconducting samples show bifurcation between the ZFC and FC curves for both field directions, suggesting spin glass (SG) transition at low temperatures in the $1.58 \leq z \leq 2$ range. The magnetic and superconducting phase diagram of $K_xFe_{2-y}Se_{2-z}S_z$ is shown in figure 15(d). Semiconductor-metal crossover can be traced for $0 \leq z \leq 1.58$ at high temperatures. In this z region, $K_xFe_{2-y}Se_{2-z}S_z$ is a superconducting metal at low temperatures. For $z = 1.58$, $\rho(T)$ is metallic with no superconducting T_c down to 2 K. For $1.58 \leq z \leq 2$, we observe a drop in $\chi - T$ curves that could be related to a SG transition. For $z = 2$, the $K_xFe_{2-y}Se_{2-z}S_z$ becomes a small-gap semiconductor with no metallic crossover and with a SG transition below 32 K.

The gradual changes of T_c are difficult to explain only by the slight variation of Fe and K contents, because usually the superconductivity appears with higher Fe content when K content (x) < 0.85 [131, 75]. As opposed to this trend, the $K_xFe_{2-y}Se_{2-z}S_z$ crystals with larger z values have higher Fe contents but lower T_c , indicating that T_c is not only governed by K/Fe stoichiometry or vacancies. The local environment

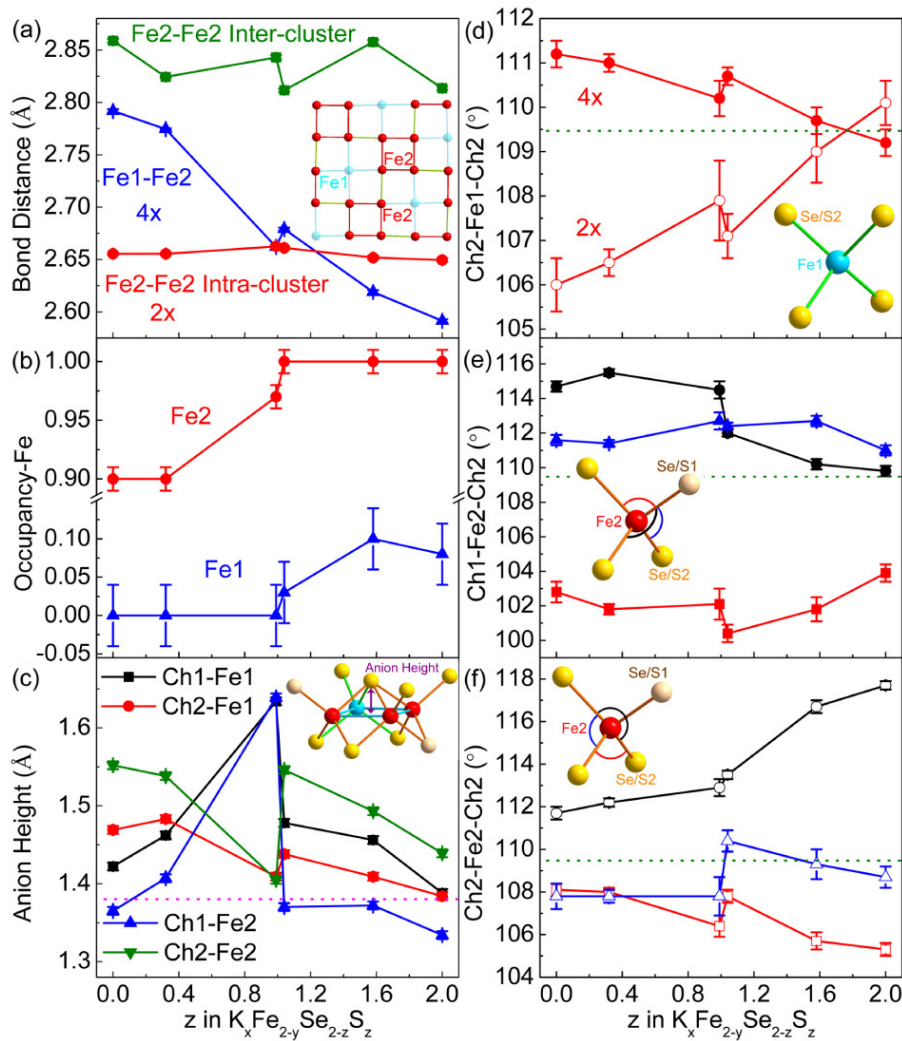


Figure 16. (a) Bond lengths between Fe sites. Inset shows top view of Fe layer. (b) Occupancy of Fe1 and Fe2 sites. (c) Anion height. Inset shows side view of Fe–Ch sheet. (d) Ch2–Fe1–Ch2, (e) Ch1–Fe2–Ch2 and (f) Ch2–Fe2–Ch2 bond angles of $K_xFe_{2-y}Se_{2-z}S_z$ as a function of S substitution, x . Insets of (d–f) show Fe–Ch tetrahedron for Fe1–Ch1 and Fe2–Ch1(2). The dotted pink line in (c) shows the optimal bond lengths for T_c . The dotted green lines in (d–f) indicate the optimal angle for T_c . Reprinted with permission from [68]. Copyright 2011 by the American Physical Society.

of Fe profoundly changes with S doping, inducing the changes in band structure and physical properties. In the $K_xFe_{2-y}Se_{2-z}S_z$ crystal structure refined in $I4/m$ space group, Fe atoms have block-like distribution where four Fe2 sites form a square around Se atom, making a cluster distinct from Fe1 site with low occupancy (inset of figure 15(a)) [31]. Therefore there are Fe1–Fe2 distances as well as intra- and inter-cluster Fe2–Fe2 distances. All cluster distances are unchanged with S doping whereas the Fe1–Fe2 distances decrease significantly (figure 16(a)). A similar magnetization behavior above 50 K and rather different superconducting T_c values as S content varies from 0 to 2 coincide with the nearly unchanged Fe2–Fe2 bond lengths. This result shows that superconductivity is insensitive to the size of Fe2–Fe2 clusters whereas the unchanged high-temperature magnetism could be related to the unchanged Fe2–Fe2 bond lengths. On the other hand, the SG behavior arising at low temperatures for non-superconducting samples can be explained by the non-zero random occupancy of Fe1 (vacancy) site for a higher

S content (figure 16(b)), randomly changing the inter-cluster exchange interactions [132].

The correlation of T_c with the anion height between Fe and Pn (Ch) layers was empirically observed. There is an optimal distance ($\sim 1.38 \text{ \AA}$) with a maximum $T_c \sim$ of 55 K [133]. This seems to be invalid in $K_xFe_{2-y}Se_{2-z}S_z$ materials, where there are two Fe and two Ch sites and four Fe–Ch heights. There is no monotonic decrease as T_c is tuned to 0, whereas both Se and S end members have rather similar anion heights (figure 16(c)). The bond angle α between Pn(Ch)–Fe–Pn(Ch) is more instructive since T_c in iron pnictides is optimized when Fe–Pn (Ch) tetrahedron is regular ($\alpha = 109.47^\circ$) [134]. In $K_xFe_{2-y}Se_{2-z}S_z$, the Ch2–Fe1–Ch2 angle changes toward the optimal value with increasing S content (figure 16(d)), but the local environment of Fe2 site exhibits inverse trend. Among six angles in the Fe2–Ch1(2) tetrahedron, three (Ch1–Fe2–Ch2) are nearly unchanged with S doping (figure 16(e)). The other three (Ch1–Fe2–Ch1) change significantly (maximum 6°) and deviate from optimal

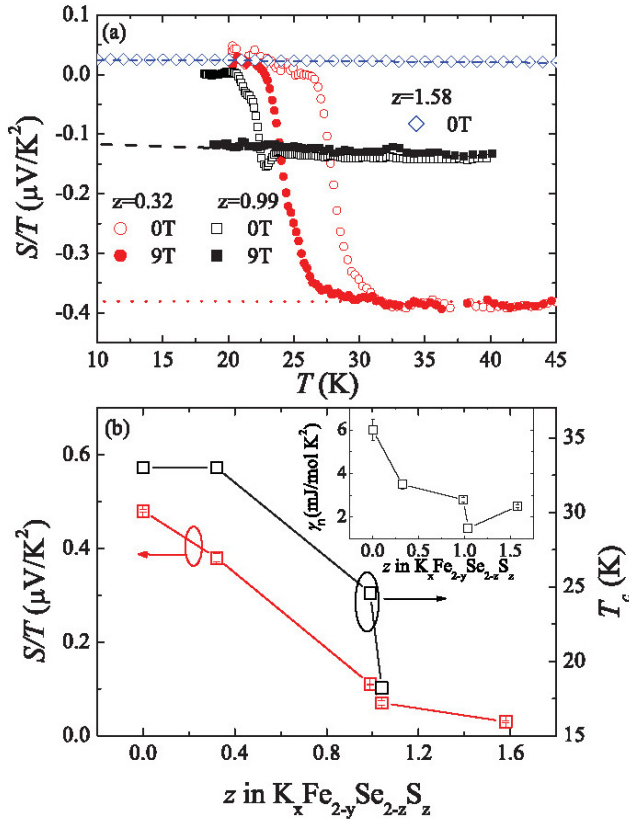


Figure 17. (a) Temperature dependence of the Seebeck coefficient divided by T , S/T , for $\text{K}_x\text{Fe}_{2-y}\text{Se}_{2-z}\text{S}_z$ with $z = 0.32, 0.99$ and 1.58 under 0 T (open symbols) and 9 T (solid symbols), respectively. The dashed lines are the linear fitting results. (b) The relationship between the zero-temperature extrapolated value of S/T (open circle) and T_c (open square) to S concentration z . The inset shows the relationship between the Sommerfeld coefficient γ_n and z . Reprinted with permission from [136]. Copyright 2011 by the American Physical Society.

value from Se-rich to S-rich side (figure 16(f)). Hence, the increasing distortion of Fe2–Ch tetrahedron with S doping is closely correlated to the suppression of T_c . This distortion may lead to carrier localization, decreasing the density of states at the Fermi energy, which is confirmed by the measurement of thermal properties as discussed below. Therefore, the regularity of Fe2–Ch1(2) tetrahedron is an important structural factor governing the formation of the metallic states in $\text{K}_x\text{Fe}_{2-y}\text{Se}_{2-z}\text{S}_z$, and consequently the T_c .

Thermal properties indicate that the density of states at the Fermi energy decreases with S doping, resulting in the suppression of correlation strength [135, 136]. As shown in figure 17(a), the suppression of T_c with the increase of sulfur concentration is confirmed by the shift of transition temperature where the Seebeck coefficient S becomes 0 because Cooper pairs carry no entropy in the superconducting state. The diffusive Seebeck response of a Fermi liquid dominates and is expected to be linear versus temperature in the zero-temperature limit, with a magnitude proportional to the strength of electron correlations in the simple Boltzmann picture [137]. This is similar to the temperature linearity of electronic specific heat, $C_e/T = \gamma$. In a one-band system both

can be described by

$$S/T = \pm \frac{\pi^2 k_B}{2} \frac{1}{e} \frac{1}{T_F} = \pm \frac{\pi^2}{3} \frac{k_B^2}{e} \frac{N(E_F)}{n}, \quad (29)$$

$$\gamma_n = \frac{\pi^2}{2} k_B \frac{n}{T_F} = \frac{\pi^2}{3} k_B^2 N(E_F), \quad (30)$$

where e is the electron charge and T_F is the Fermi temperature, which is related to E_F and $N(E_F)$ ($= 3n/2E_F = 3n/k_B T_F$) [137]. For superconducting crystals, the Seebeck coefficient in the normal state is independent of magnetic field and exhibits a linear relationship with temperature which can be fitted using equation (29) very well in the low-temperature range (figure 17(a)). With S doping, S/T is suppressed from $-0.48 \mu\text{V K}^{-2}$ to a very small value of $\sim 0.03 \mu\text{V K}^{-2}$ for crystals without superconducting transition. Similar to S/T , the electronic Sommerfeld coefficient in the normal state γ_n is also gradually suppressed with the increase in sulfur content (inset of figure 17(b)). According to equations (29) and (30), S/T and γ_n are related to n and $N(E_F)$. Since sulfur has an identical electronic configuration to selenium, there should be no simple change in the carrier concentration with sulfur doping because the elemental analysis is consistent with full occupancy of Se (S) sites [68]. The absolute value of the dimensionless ratio of the Seebeck coefficient to specific heat, $q = N_{\text{Av}} e S/T \gamma_n$, where N_{Av} is the Avogadro number, gives the carrier density n . The values of q do not exhibit significant change [136]. Therefore, the suppressions of S/T and γ_n reflects a suppression of $N(E_F)$.

The ratio of T_c to T_F characterizes the correlation strength in superconductors. In unconventional superconductors, such as CeCoIn_5 and $\text{YBa}_2\text{Cu}_3\text{O}_{6.67}$, this ratio is about 0.1, but it is only ~ 0.02 in BCS superconductors, such as $\text{LuNi}_2\text{B}_2\text{C}$ [135]. In $\text{Fe}_{1+y}\text{Te}_{1-x}\text{Se}_x$, T_c/T_F it is also near 0.1, pointing to the importance of electronic correlations [138]. The ratio $T_c/T_F \sim 0.04$ for $\text{K}_{0.64}\text{Fe}_{1.44}\text{Se}_2$ implies a weakly correlated superconductor [135] when compared to $\text{Fe}_{1+y}\text{Te}_{1-x}\text{Se}_x$. A theoretical study pointed out that the ordered Fe vacancies could induce band narrowing and consequently decrease the correlation strength needed for the Mott transition [139]. With increasing sulfur content, the value of T_c/T_F decreases further [136]. This implies a suppression of electron correlation strength as the system is tuned toward semiconducting states. The effective mass m , derived from $k_B T_F = \hbar^2 k_F^2 / 2m$, is also suppressed with the increase in S content, consistent with the decrease of correlation strength with S doping [136].

S doping affects not only T_c and properties in the normal state, but also $\mu_0 H_{c2}(T)$. As shown in figure 18(a), with S doping, for $\text{K}_{0.70}\text{Fe}_{1.55}\text{Se}_{1.01}\text{S}_{0.99}$ (S-99), $d\mu_0 H_{c2}(T)/dT|_{T=T_c}$ is $2.74(7)$ and $0.649(7) \text{ T K}^{-1}$ for $H \parallel ab$ and $H \parallel c$, respectively, and for $\text{K}_{0.76}\text{Fe}_{1.61}\text{Se}_{0.96}\text{S}_{1.04}$ (S-104), $d\mu_0 H_{c2}(T)/dT|_{T=T_c}$ is $3.15(4)$ and $0.499(4) \text{ T K}$ for $H \parallel ab$ and $H \parallel c$, respectively [140]. Both are much smaller than in $\text{K}_{0.64}\text{Fe}_{1.44}\text{Se}_2$ (S-0). Therefore, the $\mu_0 H_{c2}(T)$ values obtained with equation (10) are significantly smaller than those in S-0 for both field directions. Using $\lambda_{e-\text{ph}} = 0.5$, the Pauli limiting field $\mu_0 H_p(0) = 1.86 T_c (1 + \lambda_{e-\text{ph}})^{1/2}$ is 53.5 and

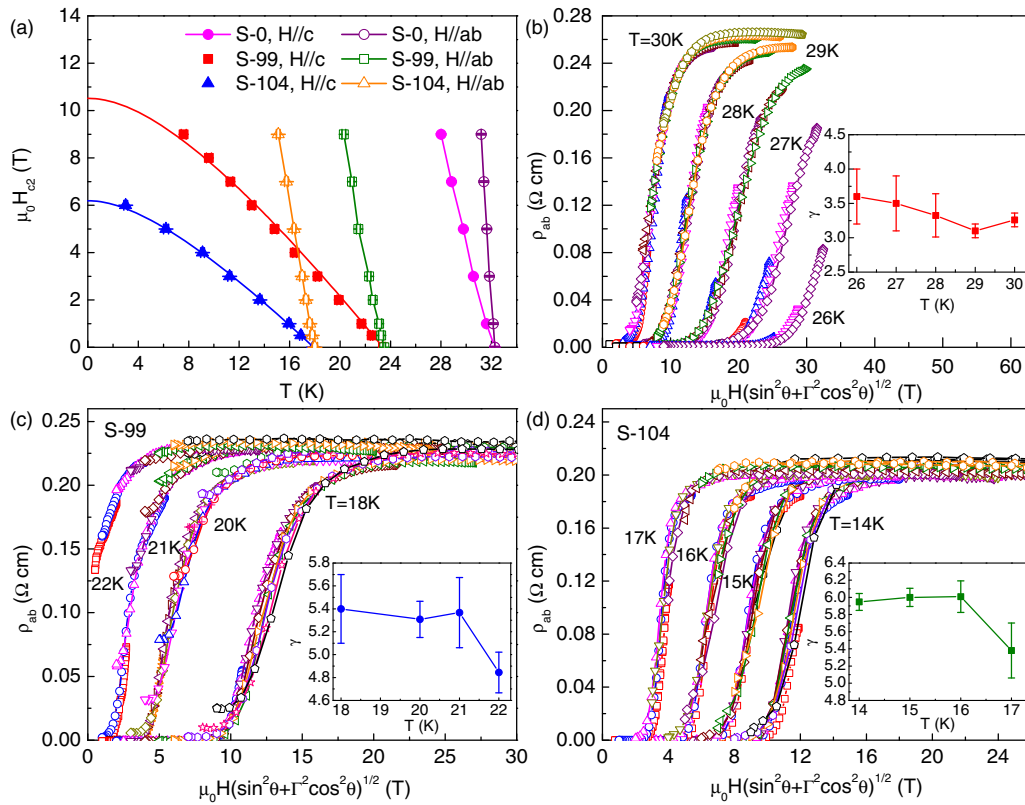


Figure 18. (a) Temperature dependence of $\mu_0 H_{c2}(T)$ for $\text{K}_{0.64}\text{Fe}_{1.44}\text{Se}_2$ (S-0), $\text{K}_{0.70}\text{Fe}_{1.55}\text{Se}_{1.01}\text{S}_{0.99}$ (S-99) and $\text{K}_{0.76}\text{Fe}_{1.61}\text{Se}_{0.96}\text{S}_{1.04}$ (S-104) single crystals. Scaling behavior of the $\rho_{ab}(T, \mu_0 H)$ versus $\mu_0 H_s = \mu_0 H (\cos^2 \theta + \gamma^2 \sin^2 \theta)^{1/2}$ for (b) S-0, (c) S-99 and (d) S-104 at different magnetic fields and temperatures. The insets in (b–d) show the temperature dependence of $\gamma(T)$ determined using GL theory for S-0, S-99 and S-104, respectively. Reprinted with permission from [140]. Copyright 2011 by the European Physical Society.

41.0 T for S-99 and S-104, respectively. Both values are larger than extrapolated $\mu_0 H_{c2,c}(0)$ using equation (11) for S-99 and S-104. It should be noted that for the $\mu_0 H_{c2,c}(T)$ of S-99 and S-104, there is no upturn at low temperatures when compared to undoped AFeSe-122 materials [60, 126]. Moreover, the fits using simplified WHH theory are rather satisfactory for temperatures far below T_c for $H//c$ for both S doped samples. All this implies that for S-99 and S-104 the spin-paramagnetic and multiband effects are negligible when the magnetic field is applied along the c -axis. This is different from undoped AFeSe-122 materials [60, 126]. The changes of the $\mu_0 H_{c2,c}(T)$ with S doping could be due to the changes of band structure. Experiments in higher field and lower temperature are needed to shed more light on the behaviors of $\mu_0 H_{c2,ab}(T)$.

To characterize the evolution of the anisotropy $\gamma(T)$ with S doping near T_c , the angular-dependent resistivity $\rho_{ab}(\theta, \mu_0 H, T)$ is measured at various magnetic fields and temperatures, where θ is the angle between the direction of external field and the c -axis of the samples. According to the anisotropic Ginzburg–Landau (GL) model, the effective upper critical field $\mu_0 H_{c2}^{\text{GL}}(\theta)$ can be represented as [141]

$$\mu_0 H_{c2}^{\text{GL}}(\theta) = \mu_0 H_{c2,ab} / (\sin^2 \theta + \gamma^2 \cos^2 \theta)^{1/2}, \quad (31)$$

where $\gamma = H_{c2,ab} / H_{c2,c} = (m_c / m_{ab})^{1/2} = \xi_{ab} / \xi_c$. Since the resistivity in the mixed state depends on the effective field $H / H_{c2}^{\text{GL}}(\theta)$, the resistivity can be scaled with $H / H_{c2}^{\text{GL}}(\theta)$ and

data should collapse onto one curve in different magnetic fields at a certain temperature when a proper $\gamma(T)$ value is chosen [141]. Figures 18(b)–(d) show the relation between resistivity and scaling field $\mu_0 H_s = \mu_0 H (\sin^2 \theta + \gamma^2 \cos^2 \theta)^{1/2}$ for S-0, S-99 and S-104, respectively. Good scaling is obtained by adjusting $\gamma(T)$. The temperature dependence and value of $\gamma(T)$ for S-0 (the inset of figure 18(b)) are similar to reported results [126]. For S-99 and S-104, the $\gamma(T)$ exhibits the same trend as that for S-0, i.e. increasing with temperature. However, the value increases gradually with increasing S content (figures 18(c) and (d)). It changes from ~ 3 for S-0 to ~ 6 for S-104. The larger anisotropy with increasing S content may suggest that the two-dimensional Fermi surface is becoming less warped with S doping [123].

4.4. Spin-paramagnetic effect in iron-based superconductors

According to equation (14), the Maki parameter α can be calculated as $\alpha = [(H_{c2}^*(0) / H_{c2}(0))^2 - 1]^{1/2}$. It can be also obtained from the fitting using equation (8) or (27). We summarize the α of iron-based superconductors reported in the literature for $H//ab$ and $H//c$ (figure 19). There are three general trends for α : (i) $\alpha_{H//ab}$ are larger than $\alpha_{H//c}$ for all of superconductors, indicating that the spin-paramagnetic effect is weaker for $H//c$ than $H//ab$. (ii) FeCh-11 shows the largest α for both field directions with $\alpha > 1$, reflecting that the spin-paramagnetic effect is the dominant pair-breaking effect

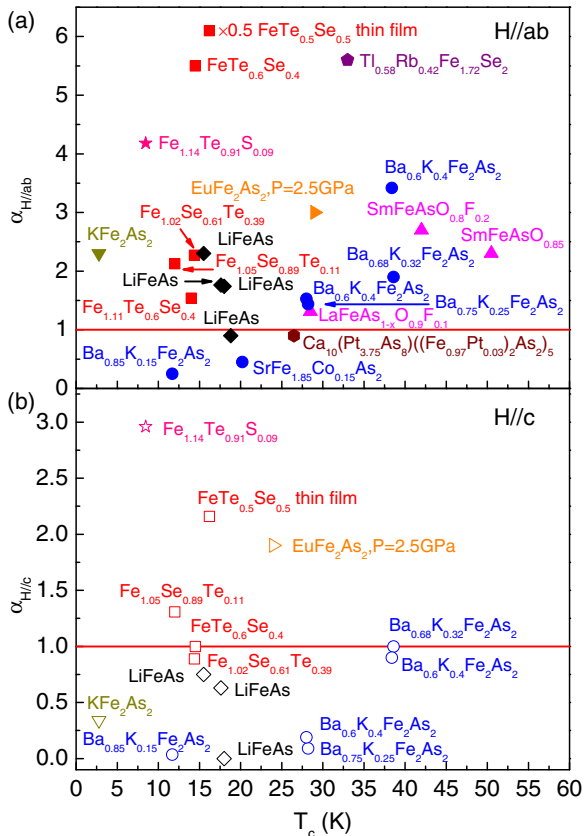


Figure 19. Maki parameters α obtained from $\alpha = [(H_{c2}^*(0)/H_{c2}(0))^2 - 1]^{1/2}$ or fitting using equation (8) or (13) in various iron-based superconductors for (a) $H\parallel ab$ and (b) $H\parallel c$: $\text{Ti}_{0.58}\text{Rb}_{0.42}\text{Fe}_{1.72}\text{Se}_2$ [60], $\text{SmFeAsO}_{0.8}\text{F}_{0.2}$ [105], $\text{SmFeAsO}_{0.85}$ [105], KFe_2As_2 [108], $\text{Fe}_{1.02}\text{Se}_{0.61}\text{Te}_{0.39}$ [110], $\text{Fe}_{1.05}\text{Se}_{0.89}\text{Te}_{0.11}$ [110], $\text{FeTe}_{0.6}\text{Se}_{0.4}$ [112], $\text{LaO}_{0.9}\text{F}_{0.1}\text{FeAs}_{1-x}$ [115], $\text{Fe}_{1.14}\text{Te}_{0.91}\text{S}_{0.09}$ [117], $\text{Fe}_{1.11}\text{Te}_{0.6}\text{Se}_{0.4}$ [122], $\text{Ba}_{0.68}\text{K}_{0.32}\text{Fe}_2\text{As}_2$ [144], $\text{SrFe}_{1.85}\text{Co}_{0.15}\text{As}_2$ [145], LiFeAs [109, 146–148], EuFe_2As_2 [149], $\text{FeSe}_{0.5}\text{Te}_{0.5}$ thin film [150], $(\text{Ba,K})\text{Fe}_2\text{As}_2$ [150], $\text{Ba}_{0.6}\text{K}_{0.4}\text{Fe}_2\text{As}_2$ [151] and $\text{Ca}_{10}(\text{Pt}_4\text{As}_8)((\text{Fe}_{0.97}\text{Pt}_{0.03})_2\text{As}_2)_5$ [152].

for both field directions. (iii) For FeAs-based superconductors where the spin-paramagnetic effect is considered, the $\alpha_{H\parallel ab}$ are usually larger than 1 but the $\alpha_{H\parallel c}$ are usually smaller than 1, implying that the spin paramagnetic effect is dominant for $H\parallel ab$. The larger $\alpha_{H\parallel ab}$ when compared to $\alpha_{H\parallel c}$ can be understood from equations (15) and (16). When assuming other parameters are the same for $H\parallel ab$ and $H\parallel c$, if v_{ab} is larger than v_c it will lead to the larger $\alpha_{H\parallel ab}$ than $\alpha_{H\parallel c}$. Theoretical calculations confirms this assumption [42, 142]. On the other hand, assuming that the relaxation time of the conduction electrons τ is isotropic and independent of Fermi velocities, the anisotropy of resistivity in the normal state $\gamma_\rho(0)$ is proportional to $\langle v_{ab}^2 \rangle_{\text{FS}} / \langle v_c^2 \rangle_{\text{FS}}$, where $\langle \dots \rangle_{\text{FS}}$ denotes the average on the FS [143]. The experimental results of $\gamma_\rho(0)$ also confirmed that v_{ab} is larger than v_c [143]. Briefly, because of $v_i = \partial\epsilon_k / \partial k_i$, the cylinder-like Fermi surface in iron-based superconductors will usually result in $v_{ab} \gg v_c$, therefore $\alpha_{H\parallel ab}$ larger than $\alpha_{H\parallel c}$. Moreover, in the case of a cylinder-like Fermi surface, the open electronic orbits along the c -axis at low temperatures will also make the orbitally limiting upper critical field unlikely [60].

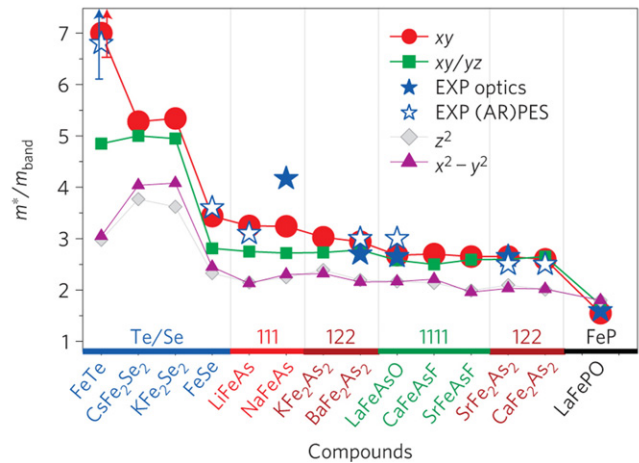


Figure 20. The mass enhancement m^*/m_{band} of the iron 3d orbitals in the paramagnetic state, calculated with the density functional theory and cellular dynamical mean field theory (DFT+CDMFT), and the low-energy effective mass enhancement obtained from optical spectroscopy experiments and (angle-resolved) photoemission spectroscopy experiments. Reprinted with permission from [41]. Copyright 2011 by the Macmillan Publishers Ltd: Nature Mat.

On the other hand, the evolution of spin-paramagnetic effect in iron-based superconductors (FeCh-11 , $\text{AFeCh-122} > \text{FeAs-111} > \text{FeAs-122} > \text{FeAs-1111}$) can be partially related to the evolution of the enhancement of effective mass in these materials according to equations (15) and (16) (figure 20) [41]. Moreover, the low carrier density n in iron-based superconductors [42, 43], resulting in the smaller E_F according to the free electron model, will also lead to the larger α .

We now comment on the recently discovered phase separation in $\text{K}_x\text{Fe}_{2-y}\text{Se}_2$ crystals [32–38]. Since the wide-gap semiconducting phase is locked at high temperatures, (super)conductivity originates from the volume fraction of the sample that is conducting below the high-temperature structural transition. This should not have a major effect on $\mu_0 H_{c2}(T)$ phase diagrams, fits and estimate of mechanism of pair breaking in high fields. The values of J_c could be affected to some extent because the Bean model was applied to inhomogeneous samples. Yet, due to the rather small scale of phase separation and Josephson coupling that bridges insulating nanoislands [35], values of J_c represent a lower estimate of J_c and should be close to the intrinsic values for the superconducting phase. A similar argument can be applied for diffusion thermopower S and conclusions based on the correlation strength in the normal state since S does not depend on the sample geometry. In contrast, resistivity values represent the upper limit of ρ for the superconducting phase, similar to polycrystalline samples with grain boundary contributions.

5. Conclusions

In summary, iron chalcogenide superconductors now have T_c and $\mu_0 H_{c2}$ values that are comparable to those of iron pnictide superconductors. Whereas the J_c are still

low in $K_x\text{Fe}_{2-y}\text{Se}_2$ when compared to ternary arsenide superconductors, the μ_0H_{c2} values are in similar range. Because of the strong correlations present in the normal state and/or in the parent materials, spin-paramagnetic effects on $\mu_0H_{c2}(T)$ are significant in binary FeCh-11 superconductors, probably masking multiband evolution of $\mu_0H_{c2}(T)$. Enhanced spin-paramagnetic effects most likely originate from a Kondo-like interaction with the more localized Fe orbitals. This is in contrast to ternary AFeCh-122 materials where electronic correlations in the normal state are weaker and where much of the $\mu_0H_{c2}(T)$ and vortex behavior is still unexplored due to extremely large upper critical fields and complex structural features.

Acknowledgments

We thank T P Murphy, E S Choi, D Graf and S W Tozer for useful discussions and experiment support at NHMFL and J B Warren for help with scanning electron microscopy measurement at Brookhaven Nation Laboratory. This work was carried out at the Brookhaven National Laboratory, which is operated for the US Department of Energy by Brookhaven Science Associates DE-Ac02-98CH10886. This work was in part supported by the US Department of Energy, Office of Science, Office of Basic Energy Sciences as part of the Energy Frontier Research Center (EFRC), Center for Emergent Superconductivity (CES) (HL and CP). A portion of this work was performed at the National High Magnetic Field Laboratory, which is supported by NSF Cooperative Agreement no DMR-0084173, by the State of Florida, and by the US Department of Energy.

References

- [1] Kamihara Y, Watanabe T, Hirano M and Hosono H 2008 *J. Am. Chem. Soc.* **130** 3296
- [2] Kamihara Y, Hiramatsu H, Hirano M, Kawamura R, Yanagi H, Kamiya T and Hosono H 2006 *J. Am. Chem. Soc.* **128** 10012
- [3] Chen X H, Wu T, Wu G, Liu R H, Chen H and Fang D F 2008 *Nature* **453** 761
- [4] Chen G F, Li Z, Wu D, Li G, Hu W Z, Dong J, Zheng P, Luo J L and Wang N L 2008 *Phys. Rev. Lett.* **100** 247002
- [5] Ren Z-A *et al* 2008 *Europhys. Lett.* **82** 57002
- [6] Wang C *et al* 2008 *Europhys. Lett.* **83** 67006
- [7] Wen H-H, Mu G, Fang L, Yang H and Zhu X Y 2008 *Europhys. Lett.* **82** 17009
- [8] Sefat A S, Jin R Y, McGuire M A, Sales B C, Singh D J and Mandrus D 2008 *Phys. Rev. Lett.* **101** 117004
- [9] Rotter M, Tegel M and Johrendt D 2008 *Phys. Rev. Lett.* **101** 107006
- [10] Chen G F, Li Z, Li G, Hu W Z, Dong J, Zhang X D, Zheng P, Wang N L and Luo J L 2008 *Chin. Phys. Lett.* **25** 3403
- [11] Wang X C, Liu Q Q, Lv Y X, Gao W B, Yang L X, Yu R C, Li F Y and Jin C Q 2008 *Solid State Commun.* **148** 538
- [12] Chu C W, Chen F, Gooch M, Guloy A M, Lorenz B, Lv B, Sasmal K, Tang Z J, Tapp J H and Xue Y Y 2009 *Physica C* **469** 326
- [13] Ogino H, Matsumura Y, Katsura Y, Ushiyama K, Horii S, Kishio K and Shimoyama J I 2009 *Supercond. Sci. Technol.* **22** 075008
- [14] Zhu X Y, Han F, Mu G, Cheng P, Shen B, Zeng B and Wen H-H 2009 *Phys. Rev. B* **79** 220512
- [15] Hsu F C *et al* 2008 *Proc. Natl Acad. Sci. USA* **105** 14262
- [16] Yeh K-W *et al* 2008 *Europhys. Lett.* **84** 37002
- [17] Mizuguchi Y, Tomioka F, Tsuda S, Yamaguchi T and Takano Y 2009 *Appl. Phys. Lett.* **94** 012503
- [18] Guo J, Jin S, Wang G, Wang S, Zhu K, Zhou T, He M and Chen X 2010 *Phys. Rev. B* **82** 180520
- [19] Mizuguchi Y, Takeya H, Kawasaki Y, Ozaki T, Tsuda S, Yamaguchi T and Takano Y 2011 *Appl. Phys. Lett.* **98** 042511
- [20] Krzton-Maziopa A, Shermadini Z, Pomjakushina E, Pomjakushin V, Bendele M, Amato A, Khasanov R, Luetkens H and Conder K 2011 *J. Phys.: Condens. Matter* **23** 052203
- [21] Wang A F *et al* 2011 *Phys. Rev. B* **83** 060512
- [22] Li C-H, Shen B, Han F, Zhu X Y and Wen H-H 2011 *Phys. Rev. B* **83** 184521
- [23] Fang M H, Wang H D, Dong C H, Li Z J, Feng C M, Chen J and Yuan H Q 2011 *Europhys. Lett.* **94** 27009
- [24] Medvedev S, McQueen T M, Trojan I, Palasyuk T, Erements M I, Cava R J, Naghavi S, Casper F, Ksenofontov V, Wortmann G and Felser C 2009 *Nature Mater.* **8** 630
- [25] Zhang L J, Singh D J and Du M H 2009 *Phys. Rev. B* **79** 012506
- [26] Bao W *et al* 2009 *Phys. Rev. Lett.* **102** 247001
- [27] Shein I R and Ivanovskii A L 2011 *Phys. Lett. A* **375** 1028
- [28] Zhang Y *et al* 2011 *Nature Mater.* **10** 273
- [29] Ding H *et al* 2008 *Europhys. Lett.* **83** 47001
- [30] Mazin I I, Singh D J, Johannes M D and Du M H 2008 *Phys. Rev. Lett.* **101** 057003
- [31] Bao W, Huang Q, Chen G F, Green M A, Wang D M, He J B, Wang X Q and Qiu Y 2011 *Chin. Phys. Lett.* **28** 086104
- [32] Wang Z, Song Y J, Shi H L, Wang Z W, Chen Z, Tian H F, Chen G F, Guo J G, Yang H X and Li J Q 2011 *Phys. Rev. B* **83** 140505
- [33] Li W *et al* 2012 *Nature Phys.* **8** 126
- [34] Chen F *et al* 2012 *Phys. Rev. X* **1** 021020
- [35] Yuan R H, Dong T, Song Y J, Zheng P, Chen G F, Hu J P, Li J Q and Wang N L 2012 *Sci. Rep.* **2** 1
- [36] Ricci A *et al* 2011 *Phys. Rev. B* **84** 060511
- [37] Rici A *et al* 2011 *Supercond. Sci. Technol.* **24** 082292
- [38] Wang C N *et al* 2012 *Phys. Rev. B* **85** 214503
- [39] de la Cruz C *et al* 2008 *Nature* **453** 899
- [40] Gurevich A 2011 *Rep. Prog. Phys.* **74** 124501
- [41] Yin Z P, Haule K and Kotliar G 2011 *Nature Mater.* **10** 932
- [42] Singh D J and Du M-H 2008 *Phys. Rev. Lett.* **100** 237003
- [43] Chen G F *et al* 2008 *Phys. Rev. Lett.* **101** 057007
- [44] Blatter G, Feigelman M V, Geshkenbein V B, Larkin A I and Vinokur V M 1994 *Rev. Mod. Phys.* **66** 1125
- [45] Palstra T T M, Batlogg B, Schneemeyer L F and Waszczak J V 1988 *Phys. Rev. Lett.* **61** 1662
- [46] Palstra T T M, Batlogg B, van Dover R B, Schneemeyer I F and Waszczak J V 1990 *Phys. Rev. B* **41** 6621
- [47] Brandt E H 1995 *Rep. Prog. Phys.* **58** 1465
- [48] Lei H C, Hu R and Petrovic C 2012 *Phys. Rev. B* **84** 014520
- [49] Ge J Y, Cao S X, Shen S X, Yuan S J, Kang B J and Zhang J C 2010 *Solid State Commun.* **150** 1641
- [50] Lei H C, Hu R, Choi E S and Petrovic C 2010 *Phys. Rev. B* **82** 134525
- [51] Jaroszynski J *et al* 2008 *Phys. Rev. B* **78** 174523
- [52] Yadav C S and Paulose P L 2009 *New J. Phys.* **11** 103046
- [53] Yeshurun Y and Malozemoff A P 1988 *Phys. Rev. Lett.* **60** 2202
- [54] Chin C C and Morishita T 1993 *Physica C* **207** 37
- [55] Zhang Y Z, Wang Z, Lu X F, Wen H H, de Marneffe J F, Deltour R, Jansen A G M and Wyder P 2005 *Phys. Rev. B* **71** 052502
- [56] Zhang Y Z, Wen H H and Wang Z 2006 *Phys. Rev. B* **74** 144521
- [57] Wang Z H and Cao X W 1999 *Solid State Commun.* **109** 709

- [58] Zhang Y Z, Ren Z A and Zhao Z X 2009 *Supercond. Sci. Technol.* **22** 065012
- [59] Song Y J, Kang B, Rhee J-S and Kwon Y S 2012 *Europhys. Lett.* **97** 47003
- [60] Jiao L *et al* 2012 *Phys. Rev. B* **85** 064513
- [61] Larbalestier D, Gurevich A, Feldmann D M and Polyanskii A 2001 *Nature* **414** 368
- [62] Li Q, Si W D and Dimitrov I K 2011 Films of iron chalcogenide superconductors *Rep. Prog. Phys.* **74** 124510
- [63] Taen T, Tsuchiya Y, Nakajima Y and Tamegai T 2009 *Phys. Rev. B* **80** 092502
- [64] Hu R, Bozin E S, Warren J B and Petrovic C 2009 *Phys. Rev. B* **80** 214514
- [65] Lei H C and Petrovic C 2011 *Phys. Rev. B* **83** 184504
- [66] Hu R, Cho K, Kim H, Hodovanets H, Straszheim W E, Tanatar M A, Prozorov R, Bud'ko S L and Canfield P C 2011 *Supercond. Sci. Technol.* **24** 065006
- [67] Lei H C and Petrovic C 2011 *Phys. Rev. B* **84** 052507
- [68] Lei H C, Abeykoon M, Bozin E S, Wang K F, Warren J B and Petrovic C 2011 *Phys. Rev. Lett.* **107** 137002
- [69] Han F, Shen B, Wang Z-Y and Wen H-H 2012 *Phil. Mag.* **92** 2553
- [70] Lei H C and Petrovic C 2011 *Phys. Rev. B* **84** 212502
- [71] Gao Z S, Qi Y P, Wang L, Yao C, Wang D L, Zhang X P and Ma Y W 2011 arXiv:1103.2904
- [72] Dew-Hughes D 1974 *Phil. Mag.* **30** 293
- [73] Yamamoto A *et al* 2008 *Appl. Phys. Lett.* **94** 062511
- [74] Sun D L, Liu Y and Lin C T 2009 *Phys. Rev. B* **80** 144515
- [75] Yan Y J, Zhang M, Wang A F, Ying J J, Li Z Y, Qin W, Luo X G, Li J Q, Hu J P and Chen X H 2011 *Sci. Rep.* **2** 212
- [76] Yamada Y *et al* 2005 *Appl. Phys. Lett.* **87** 132502
- [77] Griessen R, Wen H-H, van Dalen A J J, Dam B, Rector J, Schnack H G, Libbrecht S, Osquiguil E and Bruynseraede Y 1994 *Phys. Rev. Lett.* **72** 1910
- [78] Ijaduola A O, Thompson J R, Feenstra R, Christen D K, Gapud A A and Song X 2006 *Phys. Rev. B* **73** 134502
- [79] Lee S *et al* 2009 *Appl. Phys. Lett.* **95** 212505
- [80] Katase T, Ishimaru Y, Tsukamoto A, Hiramatsu H, Kamiya T, Tanabe K and Hosono H 2011 *Nature Commun.* **2** 409
- [81] Hilgenkamp H and Mannhart J 2002 *Rev. Mod. Phys.* **74** 485
- [82] Gao Z S, Wang L, Qi Y P, Wang D L, Zhang X P, Ma Y W, Yang H and Wen H H 2008 *Supercond. Sci. Technol.* **21** 112001
- [83] Qi Y P, Wang L, Wang D L, Zhang Z Y, Gao Z S, Zhang X P and Ma Y W 2010 *Supercond. Sci. Technol.* **23** 055009
- [84] Mizuguchi Y, Deguchi K, Tsuda S, Yamaguchi T, Takeya H, Kumakura H and Takano Y 2009 *Appl. Phys. Express* **2** 083004
- [85] Goyal A, Specht E D, Kroeger D M, Mason T A, Dingley D J, Riley G N and Rupich M W 1995 *Appl. Phys. Lett.* **66** 2903
- [86] Glowacki B A, Majoros M, Vickers M, Evetts J E, Shi Y and McDougall I 2001 *Supercond. Sci. Technol.* **14** 193
- [87] Ozaki T, Deguchi K, Mizuguchi Y, Kumakura H and Takano Y 2011 *IEEE Trans. Appl. Supercond.* **21** 2858
- [88] Mizuguchi Y, Izawa H, Ozaki T, Takano Y and Miura O 2011 *Supercond. Sci. Technol.* **24** 125003
- [89] Togano K, Matsumoto A and Kumakura H 2011 *Appl. Phys. Express* **4** 043101
- [90] Si W, Zhou J, Jie Q, Dimitrov I, Solovyov V, Johnson P D, Matias V, Sheehan C and Li Q 2011 *Appl. Phys. Lett.* **98** 262509
- [91] Katase T, Hiramatsu H, Matias V, Sheehan C, Ishimaru Y, Kamiya T, Tanabe K and Hosono H 2011 *Appl. Phys. Lett.* **98** 242510
- [92] Fuchs G *et al* 2009 *New J. Phys.* **11** 075007
- [93] Maki K 1966 *Phys. Rev.* **148** 362
- [94] Werthamer N R, Helfand E and Hohenberg P C 1966 *Phys. Rev.* **147** 295
- [95] Chandrasekhar B S 1962 *Appl. Phys. Lett.* **1** 7
- [96] Clogston A M 1962 *Phys. Rev. Lett.* **9** 266
- [97] Orlando T P, McNiff E J Jr, Foner S and Beasley M R 1979 *Phys. Rev. B* **19** 4545
- [98] Schossmann M and Carbotte J P 1989 *Phys. Rev. B* **39** 4210
- [99] Fulde P and Ferrel R A 1964 *Phys. Rev.* **135** A550
- [100] Larkin A I and Ovchinnikov Y N 1964 *Zh. Eksp. Teor. Fiz.* **47** 1136
Larkin A I and Ovchinnikov Y N 1965 *Sov. Phys.—JETP* **20** 762 (Engl. transl.)
- [101] Gurevich A 2003 *Phys. Rev. B* **67** 184515
- [102] Gurevich A 2007 *Physica C* **456** 160
- [103] Zhang J L, Jiao L, Chen Y and Yuan H Q 2011 *Front. Phys.* **6** 463
- [104] Hunte F, Jaroszynski J, Gurevich A, Larbalestier D C, Jin R, Sefat A S, McGuire M A, Sales B C, Christen D K and Mandrus D 2008 *Nature* **453** 903
- [105] Lee H-S, Bartkowiak M, Park J-H, Lee J-Y, Kim J-Y, Sung N-H, Cho B K, Jung C-U, Kim J S and Lee H-J 2009 *Phys. Rev. B* **80** 144512
- [106] Baily S A, Kohama Y, Hiramatsu H, Maiorov B, Balakirev F F, Hirano M and Hosono H 2009 *Phys. Rev. Lett.* **102** 117004
- [107] Kano M, Kohama Y, Graf D, Balakirev F, Sefat A S, McGuire M A, Sales B C, Mandrus D and Tozer S W 2009 *J. Phys. Soc. Japan* **78** 084719
- [108] Terashima T, Kimata M, Satsukawa H, Harada A, Hazama K, Uji S, Harima H, Chen G-F, Luo J-L and Wang N-L 2009 *J. Phys. Soc. Japan* **78** 063702
- [109] Zhang J L, Jiao L, Balakirev F F, Wang X C, Jin C Q and Yuan H Q 2011 *Phys. Rev. B* **83** 174506
- [110] Lei H C, Hu R W, Choi E S, Warren J B and Petrovic C 2010 *Phys. Rev. B* **81** 094518
- [111] Kida T, Matsunaga T, Hagiwara M, Mizuguchi Y, Takano Y and Kindo K 2009 *J. Phys. Soc. Japan* **78** 113701
- [112] Khim S, Kim J W, Choi E S, Bang Y, Nohara M, Takagi H and Kim K H 2010 *Phys. Rev. B* **81** 184511
- [113] Klein T *et al* 2010 *Phys. Rev. B* **82** 184506
- [114] Gebre T, Li G, Whalen J B, Conner B S, Zhou H D, Grissonnanche G, Kostov M K, Gurevich A, Siegrist T and Balicas L 2011 *Phys. Rev. B* **84** 174517
- [115] Fuchs G *et al* 2008 *Phys. Rev. Lett.* **101** 237003
- [116] Subedi A, Zhang L, Singh D J and Du M H 2008 *Phys. Rev. B* **78** 134514
- [117] Lei H C, Hu R, Choi E S, Warren J B and Petrovic C 2010 *Phys. Rev. B* **81** 184522
- [118] Zalitznyak A I, Xu Z, Tranquada J M, Gu G, Tsvelik A M and Stone M B 2011 *Phys. Rev. Lett.* **107** 216403
- [119] Lei H C, Graf D, Hu R, Ryu H J, Choi E S, Tozer S W and Petrovic C 2012 *Phys. Rev. B* **85** 094515
- [120] Khasanov R, Bendele M, Amato A, Conder K, Keller H, Klauss H-H, Luetkens H and Pomjakushina E 2010 *Phys. Rev. Lett.* **104** 087004
- [121] Allen P B 1999 *Handbook of Superconductivity* ed C P Poole Jr (New York: Academic) p 478
- [122] Fang M H, Yang J H, Balakirev F F, Kohama Y, Singleton J, Qian B, Mao Z Q, Wang H D and Yuan H Q 2010 *Phys. Rev. B* **81** 020509
- [123] Li C-H, Shen B, Han F, Zhu X Y and Wen H-H 2011 *Phys. Rev. B* **83** 184521
- [124] Ying J J *et al* 2011 *Phys. Rev. B* **83** 212502
- [125] Wang H-D, Dong C-H, Li Z-J, Mao Q-H, Zhu S-S, Feng C-M, Yuan H Q and Fang M H 2011 *Europhys. Lett.* **93** 47004
- [126] Mun E D, Altarawneh M M, Mielke C H and Zapf V S 2011 *Phys. Rev. B* **83** 100514
- [127] Zhang Z T, Yang Z R, Li L, Zhang C J, Pi L, Tan S and Zhang Y H 2011 *J. Appl. Phys.* **109** 07E113
- [128] Tan D *et al* 2011 *Phys. Rev. B* **84** 014502

- [129] Gu D C, Sun L L, Wu Q, Zhang C, Guo J, Gao P W, Wu Y, Dong X L, Dai X and Zhao Z X 2012 *Phys. Rev. B* **85** 174523
- [130] Shoemaker D P, Chung D Y, Claus H, Francisco M C, Avci S, Llobet A and Kanatzidis M G 2012 *Phys. Rev. B* **86** 184511
- [131] Wang D M, He J B, Xia T-L and Chen G F 2011 *Phys. Rev. B* **83** 132502
- [132] Oledzka M, Ramanujachary K V and Greenblatt M 1996 *Mater. Res. Bull.* **31** 1491
- [133] Mizuguchi Y, Hara Y, Deguchi K, Tsuda S, Yamaguchi T, Takeda K, Kotegawa H, Tou H and Takano Y 2010 *Supercond. Sci. Technol.* **23** 054013
- [134] Lee C-H, Iyo A, Eisaki H, Kito H, Fernandez-Diaz M T, Ito T, Kihou K, Matsuhata H, Braden M and Yamada K 2008 *J. Phys. Soc. Japan* **77** 083704
- [135] Wang K F, FLei H C and Petrovic C 2011 *Phys. Rev. B* **83** 174503
- [136] Wang K F, Lei H C and Petrovic C 2011 *Phys. Rev. B* **84** 054526
- [137] Behnia K, Jaccard D and louquet J 2004 *J. Phys.: Condens. Matter* **16** 5187
- [138] Pourret A, Malone L, Antunes A B, Yadav C S, Paulose P L, Fauque B and Behnia K 2011 *Phys. Rev. B* **83** 020504
- [139] Yu R, Zhu J-X and Si Q 2011 *Phys. Rev. Lett.* **106** 186401
- [140] Lei H C and Petrovic C 2011 *Europhys. Lett.* **95** 57006
- [141] Blatter G, Geshkenbein V B and Larkin A I 1992 *Phys. Rev. Lett.* **68** 875
- [142] Zeng B, Mu G, Luo H Q, Xiang T, Mazin I I, Yang H, Shan L, Ren C, Dai P C and Wen H-H 2010 *Nature Commun.* **1** 112
- [143] Nakamura H, Machida M, Koyama T and Hamada N 2009 *J. Phys. Soc. Japan* **78** 123712
- [144] Gasparov V A, Drigo L, Audouard A, Sun D L, Lin C T, Bud'ko S L, Canfield P C, Wolff-Fabris F and Wosnitza J 2011 *JETP Lett.* **93** 667
- [145] Khim S, Kim J S, Kim J W, Lee S H, Balakirev F F, Bang Y and Kim K H 2010 *Physica C* **470** S317
- [146] Khim S, Lee B, Kim J W, Choi E S, Stewart G R and Kim K H 2011 *Phys. Rev. B* **84** 104502
- [147] Kurita N, Kitagawa K, Matsubayashi K, Kismarahardja A, Choi E S, Brooks J S, Uwatoko Y, Uji S and Terashima T 2011 *J. Phys. Soc. Japan* **80** 013706
- [148] Cho K, Kim H, Tanatar M A, Song Y J, Kwon Y S, Coniglio W A, Agosta C C, Gurevich A and Prozorov R 2011 *Phys. Rev. B* **83** 060502
- [149] Kurita N, Kimata M, Kodama K, Harada A, Tomita M, Suzuki H S, Matsumoto T, Murata K, Uji S and Terashima T 2011 *Phys. Rev. B* **83** 100501
- [150] Tarantini C, Gurevich A, Jaroszynski J, Balakirev F, Bellingeri E, Pallescchi I, Ferdeghini C, Shen B, Wen H H and Larbalestier D C 2011 *Phys. Rev. B* **84** 184522
- [151] Yuan H Q, Singleton J, Balakirev F F, Baily S A, Chen G F, Luo J L and Wang N L 2009 *Nature* **457** 565
- [152] Mun E, Ni N, Allred J M, Cava R J, Ayala O, McDonald R D, Harrison N and Zapf V S 2012 *Phys. Rev. B* **85** 100502

Quantitative nanostructure characterization using atomic pair distribution functions obtained from laboratory electron microscopes

Milinda Abeykoon^I, Christos D. Malliakas^{II}, Pavol Juhás^{III}, Emil S. Božin^I, Mercouri G. Kanatzidis^{II, IV} and Simon J. L. Billinge^{*, I, III}

^I Condensed Matter Physics and Materials Science Department, Brookhaven National Laboratory, P.O. Box 5000, Upton, New York 11973, USA

^{II} Department of Chemistry, Northwestern University, 2145 Sheridan Road, Evanston, IL, 60208, USA

^{III} Department of Applied Physics and Applied Mathematics, Columbia University, 500 West 120th Street, New York, 10027, USA

^{IV} Materials Science Division, Argonne National Laboratory, Chicago, Illinois 60439, USA

Received December 17, 2011; accepted February 10, 2012

Pair distribution function / Electron diffraction / Nanomaterials / Polycrystalline films

Abstract. Quantitatively reliable atomic pair distribution functions (PDFs) have been obtained from nanomaterials in a straightforward way from a standard laboratory transmission electron microscope (TEM). The approach looks very promising for making electron derived PDFs (ePDFs) a routine step in the characterization of nanomaterials because of the ubiquity of such TEMs in chemistry and materials laboratories. No special attachments such as energy filters were required on the microscope. The methodology for obtaining the ePDFs is described as well as some opportunities and limitations of the method.

1. Introduction

One of the great challenges of nanoscience is to obtain the quantitative structures of nanoparticles [4, 18]. The atomic pair distribution function (PDF) method has recently emerged as a powerful tool for doing this [13, 19, 3, 28, 27, 21, 24, 22, 29], but obtaining the required high quality diffraction data to a High momentum transfer with good statistics generally requires synchrotron X-ray or spallation neutron data from a national user facility. Here we show that data of sufficient quality for quantitative analysis of nanoparticle structure using the PDF can be obtained from transmission electron microscopes (TEM) available at many research institutions. Quantitative structural models were applied to PDFs of several nanoparticle systems showing that electron PDFs can be modeled with the powerful emerging modeling tools for studying PDFs in general [15, 25, 32, 5]. This approach complements medium and high resolution imaging methods for studying nanoparticles in the TEM. The ease of data collection and ubiquity of TEMs will make this an important tool in the characterization of nanostructured materials.

A challenge when using electrons as a probe is that they scatter strongly [11, 9] and not according to the weak scattering kinematical scattering equations on which the PDF analysis is based [12, 34]. This would appear to rule out electrons as a source of diffraction data for PDFs except in the cases of very dilute, such as gas-phase [31], samples. However, kinematical, or nearly kinematical, scattering is obtained from electrons when sample volumes are sufficiently small that multiple scattering events are not of high probability before the electrons exit the sample (typically a few nm of thickness), or when the scattering from the samples is highly incoherent, for example the scattering from amorphous materials and away from zone axes in a crystal [35]. In these latter cases, there is still significant multiple scattering, but it should be sufficiently incoherent that it can be treated as a background and subtracted and the resulting coherent signal can be treated kinematically. This has been discussed in detail in a number of publications [7, 2, 1, 20]. This is used in the rapidly growing field of electron crystallography [35], and has been demonstrated in previous work of electron diffraction (ED) from glasses and amorphous materials [23, 8, 7, 17, 26], though little has been done in the way of quantitative modeling in those studies. In these respects, the study of small nanoparticles is particularly favorable. The samples are inherently thin, limited to the diameter of the nanoparticles when they are dispersed as a sub-mono-layer on a holey carbon support, and the structure is typically less coherent than from crystals because of the finite size effects that significantly broaden Bragg peaks and the often lower symmetries of nanoparticle structures due to surface and bulk relaxations. In fact fortuitously, the scattering is most kinematical precisely for the small nanoparticles (<10 nm) that are most beneficially studied using PDF methods [13, 19, 3, 28, 27, 21, 24, 22, 29].

Here we show how to obtain PDFs from a normal transmission electron microscope (TEM) found in many research labs. We find that the resulting electron PDFs (ePDFs) can be modeled to extract quantitative structural information about the local structure using PDF refine-

* Correspondence author (e-mail: sb2896@columbia.edu)

ment programs such as PDFgui [15]. This opens the door to broader application of PDF methods for nanostructure characterization since TEM is already a routine part of the nanoparticle characterization process [33, 36]. With this development, as well as obtaining low and high resolution TEM *images* of nanoparticles, quantitative structural information, similar to that normally obtained from a Rietveld refinement [30, 37] in bulk materials, is also available from nanoparticles with little additional effort. This approach also complements high resolution TEM by getting an average signal from a large number of nanoparticles rather than giving information from a small part of the sample that may not be representative. The fact that the real-space images and the diffraction data suitable for structural analysis can be obtained at the same time and from the same region of material is also a large advantage, resulting in more complete information for the characterization of the sample. In some cases, the small quantity of material required for ePDF, compared to X-ray and neutron PDF measurements (xPDFs and nPDFs, respectively), may also be a major advantage, as well as the ability to study thin films.

Theoretical background

The Fourier transform of X-ray or neutron powder diffraction data yields the PDF, $G(r)$ according to [14]

$$G(r) = (2/\pi) \int_{Q_{\min}}^{Q_{\max}} Q[S(Q) - 1] \sin(Qr) dQ, \quad (1)$$

where the structure function, $S(Q)$, is the properly normalized powder diffraction intensity and Q , for elastic scattering, is the magnitude of the scattering vector, $Q = 4\pi \sin(\theta)/\lambda$. [34, 13] The PDF is also related to the atomic structure through

$$G(r) = \frac{1}{Nr} \sum_{ij} \frac{f_i(0)f_j(0)}{\langle f(0) \rangle^2} \delta(r - r_{ij}) - 4\pi r Q_o, \quad (2)$$

where the sum goes over all pairs of atoms i and j separated by r_{ij} in the model. The form factor of atom i is $f_i(Q)$ and $\langle f(Q) \rangle$ is the average over all atoms in the sample. In Eq. (2), the scattering factors are evaluated at $Q = 0$, which in the case of X-rays is the atomic number of the atom. The double sums are taken over all atoms in the sample. For a multicomponent system, $S(Q)$ can be written in terms of the concentrations, c_i , of the atoms [34, 13]

$$S(Q) = 1 + \frac{I(Q) - \sum c_i |f_i(Q)|^2}{|\sum c_i f_i(Q)|^2}. \quad (3)$$

In the case of electrons as a probe, the equations are the same, providing the scattering can be treated kinematically [9]; however, the form factor must be appropriate for electrons, $f_e(Q)$, which is the Fourier transform of the electronic potential distribution of an atom. Note that in the electron diffraction literature, it is common to use $s = 2 \sin(\theta)/\lambda = Q/2\pi$ instead of Q for the independent variable in the scattering. The electron form factor, $f_e(Q)$, is different to, but closely related to, the X-ray form factor

of the same atom, $f_x(Q)$, which is the Fourier transform of the electron density. A useful relationship between $f_e(Q)$ and $f_x(Q)$ is [9]

$$f_e(Q) = \frac{m_e e^2}{2\hbar^2} \left(\frac{Z - f_x(Q)}{Q^2} \right), \quad (4)$$

where m_e and e are the mass and charge of the electron, respectively, \hbar is Plank's constant, and Z the atomic number. This equation does not give a definite value for $f_e(Q)$ at $Q = 0$, but $f_e(0)$ can be calculated by extrapolation or by using

$$f_e(0) = 4\pi^2 \frac{m_e^2}{3\hbar^2} (Z \langle r_e^2 \rangle), \quad (5)$$

where $\langle r_e^2 \rangle$ is the mean square radius of the electronic shell of the atom [9]. Figure 1 shows a comparison between X-ray and electron form factors, $f_x(Q)$ and $f_e(Q)$ of Au. This form for the electron form factor is approximate and these approximations may introduce additional uncertainties in resulting atomic displacement parameters (ADPs) obtained from modeling resulting PDFs. However, we believe that these errors will be smaller than those introduced due to unaccounted for multiple scattering effects, as discussed later, and can probably be neglected, though this is not definitely established.

In the case of single crystal ED, a rule of thumb is that when the crystal thickness is greater than ~ 300 – 400 Å, data reduction must be done based on the dynamical diffraction theory which assumes the presence of coherent multiple scattering components of electrons [9]. Depending on the energy of the electrons, this thickness limit may even fall below these numbers in the presence of heavy elements [9], and in the case of electron powder diffraction, the average thickness of crystallites in the specimen should also be less than a few hundred Ångströms to avoid dynamical scattering effects [10]. Coherent multiple scattering changes the relative intensities of Bragg peaks from the kinematical structure factor values, redistributes intensity to the weaker peaks at higher values of Q [8] and can allow symmetry disallowed peaks to appear in the pattern. If Γ is the elastic mean free path of the electron, it

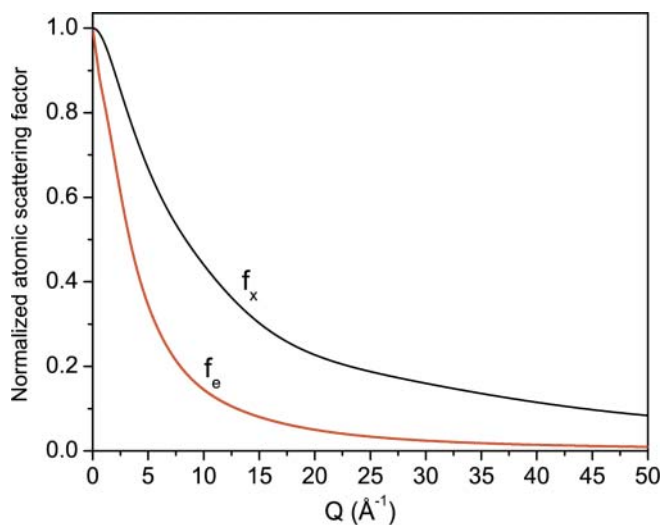


Fig. 1. A comparison between normalized (to $f(0)$) X-ray and electron form factors, $f_x(Q)$ and $f_e(Q)$ of Au.

has been shown that a PDF determined from a polycrystalline Pt sample does not affect the positions of the PDF peaks for $D/\Gamma \leq 5$, where D is the particle size, but it does affect the determination of coordination numbers [2]. Here we show that model fits may be good, even in the presence of significant multiple scattering, while refined thermal factors are underestimated, though it is desirable to optimize experimental conditions such as to minimize multiple scattering.

Incoherent multiple scattering can be observed in ED patterns in the form of increased background [9] which does not affect the relative intensities of the Bragg peaks. This is why, in the case of a less coherent structure, dynamical scattering effects are less important.

In this study, all the specimens used were nanosized samples: thin films, discrete nanoparticles, or agglomerates of nanoparticles. In this case, the hope was that multiple scattering would not introduce undue aberrations into the kinematical diffraction pattern and a reliable PDF will result. We found this to be largely true with an exception we discuss below.

2. Experimental

Nanocrystalline thin film, or dispersed nanoparticulate samples, were distributed on a holey carbon grid and ED data taken with a short camera length, to give the widest Q -range, and a relatively large beam-size (2–5 μm diameter) on the sample, to obtain the best possible powder average. To improve the powder average different regions of the sample were illuminated by translating the sample under the beam. In other respects, the TEM was used in a standard configuration using a CCD detector with no energy filtering and operated at 200 keV (wavelength, $\lambda = 0.025079 \text{ \AA}$).

All selected area ED experiments were carried out at room temperature on a Hitachi H8100 200 KeV transmission electron microscope equipped with a Gatan Orius SC600 CCD Camera (24 \times 24 mm active area). Typical exposure time per frame was around 0.3 s. Formvar coated 300 mesh copper grids (Electron Microscopy Sciences) stabilized with an evaporated carbon film were used to support the metallic films and nanoparticles. Deposition of gold on the carbon coated side of the TEM grid was performed with a Denton Vacuum DeskIII sputterer gave a uniform film. The thickness of the film was measured in real time during the sputtering process with the aid of a thickness monitor (Maxtek, Inc TM-350). Part of the grid was masked during the deposition and this masked area was used to extract the diffraction intensity of the support. No differences were found in the diffraction intensity data of the background (carbon and polymer films) between different grids. Deposition on the side of the grid that was coated with the polymer gave Au nanoparticles with a wide range of sizes up to 100 nm. NaCl nanoparticles were deposited on a TEM grid by a radio-frequency thermal evaporation method.

For comparison, X-ray measurements on Au nanoparticles were carried out in the rapid acquisition mode

(RAPDF) [6] using a Perkin Elmer amorphous silicon 2D detector at beamline X7B at National Synchrotron Light Source (NSLS) at Brookhaven National Laboratory (BNL). Nanoparticles in ethanol solution were loaded in a 1 mm diameter kapton tube sealed at both ends, and mounted perpendicular to the X-ray beam. The data were collected at room temperature using the X-ray energy of $\sim 38 \text{ keV}$ ($\lambda = 0.3196 \text{ \AA}$). The data were collected in a multiple 4 s exposures for a total collection time of 5 min.

To calibrate the conversion from detector coordinates to scattering angle, it is necessary to measure the ED pattern from a standard of known lattice parameters. The software for reducing the data to 1D, Fit2D [16] uses this to optimize the effective sample-detector distance, find the center of the Scherrer rings on the detector, and correct for aberrations such as any deviation from orthogonality of the detector and the scattered beam. Typical standards used by the program are Al_2O_3 , CeO_2 , LaB_6 , NaCl and Si . However, for the ED experiment it is necessary to have a nano-sample standard to obtain a good powder average. For this, gold nanoparticles of diameter $\sim 100 \text{ nm}$ were used and a literature value of 4.0782 \AA for the lattice parameter. The effective sample-detector distance depends on the settings of the magnetic lenses used in the microscope. We assumed that the energy of the electrons, 200 keV, is well known (resulting in $\lambda = 0.025079 \text{ \AA}$), though for the most accurate results the electron wavelength should be calibrated using standard methods. Once these calibration quantities are known, they are fixed and the same values are used to convert the sample data. From this perspective, it is essential that the sample is measured under identical conditions as the standard, including camera length and focus. We found that even scanning around a sample to find a different viewing area resulted in a small variation in the position on the detector of the center of the resulting diffraction pattern. It was thus necessary to run a separate calibration run on each diffraction pattern to determine the center of the rings, while keeping the camera-length from the Au calibration.

3. Data analysis

The 2D ED images were read and integrated into 1D powder diffraction patterns, after subtracting a properly scaled background measurement of the empty holey carbon grid and masking the missing beam stop region. The data have to be further processed to obtain the PDF. Other corrections were applied to the raw data to account for experimental effects and properly normalized and divided by $\langle F_e(Q) \rangle^2$ [13], resulting in the total scattering structure function, $S(Q)$. The kernel of the Fourier transform is the reduced structure function, $F(Q) = Q[S(Q) - 1]$. We used a home-written program, PDFgetE, to carry out these steps. The PDF is then straightforwardly obtained as the Fourier transform of $F(Q)$ according to Eq. (1), which is also carried out in PDFgetE. Once the PDFs are obtained, they can be modeled using existing PDF modeling programs. Here we used PDFgui [15].

4. Results

A low resolution TEM image of the 2.7 nm thick Au film is shown in Fig. 2a. The film is uniform and featureless in the image, but a region at the edge of the film was selected for imaging so that the edge of the film gives a visual cue to its presence. An ED pattern from a position away from the edge of the film is shown in Fig. 2b. We can see a series of concentric circles due to the Scherrer powder diffraction rings in transmission geometry. The resulting 1D ED pattern, obtained by integrating around the rings in the 2D pattern is shown in Fig. 2c. Broad diffuse features are observed that are consistent with the nanocrystallinity of the sample. Weak features are clearly evident up to $Q = 12 \text{ \AA}^{-1}$ (Fig. 2c inset), but less apparent beyond that point.

The $F(Q)$ from the same data after correction is shown in Fig. 3a and the resulting ePDFs in Fig. 3c, with the calculated PDF from a model of the gold fcc structure plotted on top in red. For comparison, in Fig. 3b and d we show the X-ray derived $F(Q)$ and xPDF, respectively. Unfortunately this is not a direct comparison between identical samples. We were not able to collect X-ray data from the same film as the ePDF as it was too thin to get a sufficient signal in the X-ray measurement.

The structure functions of the electron and X-ray data (Fig. 3a and b, respectively) are clearly highly similar. Features in the $eF(Q)$ are broader than the X-ray case but the features are all recognizable and have the correct relative intensities. Likewise, the e- and xPDFs (Fig. 3c and d, respectively) are highly similar, with the features in the ePDF of the nanoscale film being broader. The quality of the fits is comparable for both the ePDF and xPDF curves, with the ePDF giving a slightly lower (better) agreement factor. The refined parameters are presented in Table 1. The breadth of the ePDF peaks are accommodated in the model by giving gold very large ADPs, twice as large as those in the X-ray measured gold nanoparticles that are already large. This indicates the presence of significant atomic scale disorder in the film and is not com-

Table 1. Refined parameters for 2.7 nm thick nanoparticulate Au film, ~ 100 nm diameter nanoparticles (NP) from ePDFs and from a gold nanoparticle sample from xPDFs. The structure model is the fcc bulk gold structure, space-group $Fm\bar{3}m$. It was not possible to measure the nanoparticle size from the ePDFs as we were not able to calibrate the intrinsic Q -space resolution of the ED measurement allowing us to separate the instrumental resolution and particle size effects in the ePDFs.

	ePDF (film)	ePDF (NP)	xPDF
Q_{\max} (\AA^{-1})	15.25	15.25	15.25
Fit range (\AA)	1–20	1–20	1–20
Cell parameter (\AA)	4.075(3)	4.076(2)	4.058(1)
U_{iso} (\AA^2)	0.033(4)	0.006 (3)	0.014(1)
Diameter (\AA)	$\sim 27^a$	$\sim 1000^b$	24.51(9)
Q -damp (\AA^{-1})	0.095(5)	0.095(5)	0.047(2)
R_w (%)	17	24	20

a: film thickness measured during deposition

b: NP diameter estimated directly from the TEM image

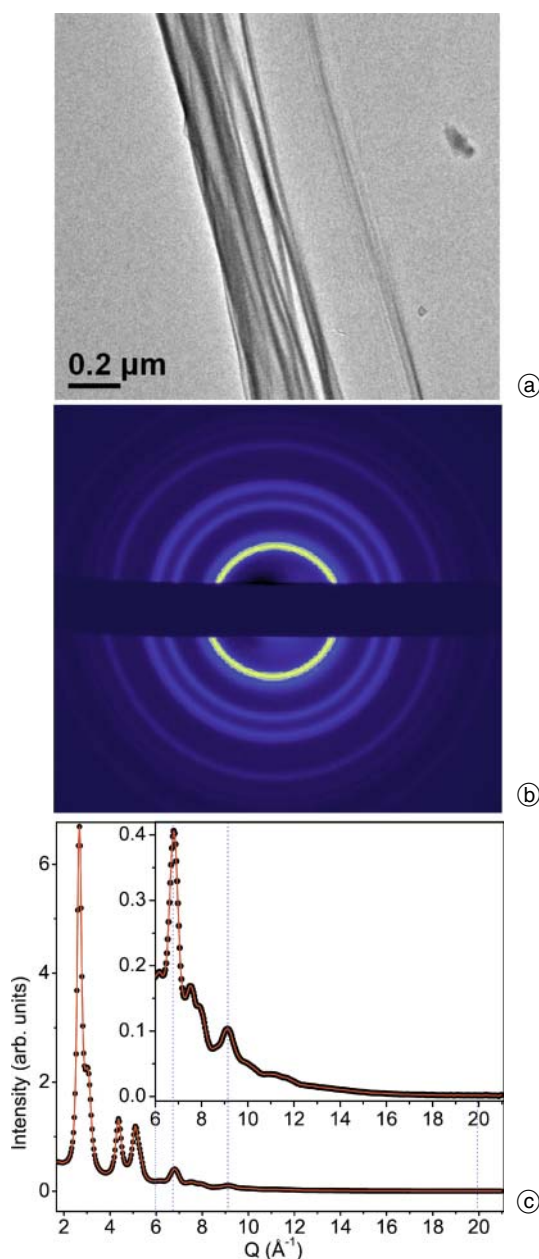


Fig. 2. (a) A TEM image of the 2.7 nm thick Au film used for ED. (b) A false-color 2D ED pattern collected on this sample using 200 keV electrons. Lighter colors indicate higher intensity. The dark bar across the middle of the image is the shadow of the beam-stop. (c) 1D Au electron powder diffraction pattern obtained by integrating around the rings in 2b. The inset shows the high Q region of the ED pattern on an expanded y-scale. The dotted lines are guides to the eye.

ing from the ePDF measurement itself. This is discussed in greater detail below.

These results clearly demonstrate that quantitatively reliable ePDFs can be obtained from nanocrystalline materials in a standard laboratory TEM. The counting statistics from the electron data compare favorably to those from the X-ray measurements (Fig. 3a and b), despite the much shorter measurement time, suggesting that ePDF determination could become a useful general characterization tool during nanoparticle synthesis. Two effects are clearly evident in the Q -space data: low Q -space resolution and the rapid diminishing of the amplitude of scattered features

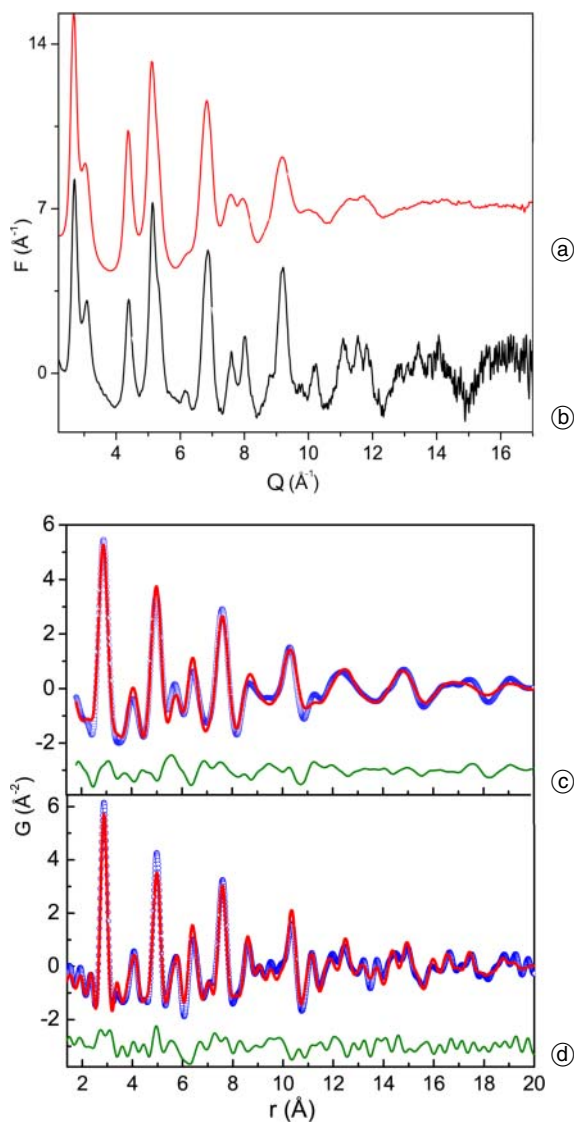


Fig. 3. (a) Reduced structure function, $F(Q)$, of Au obtained from the integrated ED pattern in Fig. 2(c), (b) An $F(Q)$ of Au nanoparticles calculated from an XRD pattern collected at X7B at the NSLS. (c) Au bulk structure model fit to the resulting ePDF from 3(a). (d) Au bulk structure model fit to the resulting xPDF from 3(b). Observed and calculated PDFs are presented with blue circles and a solid red line, respectively. The difference between observed and calculated is offset below (green solid lines). In both cases $Q_{\max} = 15.25 \text{ \AA}^{-1}$.

with increased Q . The latter is likely to reflect real differences in the samples, with the range of structural coherence being lower in the gold film than the gold nanoparticles used in the X-ray experiment. The lower Q -space resolution could be either a sample or a measurement effect but this cannot be disentangled without having a well characterized, kinematically scattering, nanoparticle standard for ED, which doesn't currently exist. The sputtered gold film has an fcc gold structure, like the bulk, but with significantly more disorder and a nanometer range for the structural coherence.

The ED data were taken with a standard CCD camera and no filtering of inelastically scattered electrons. This is the most straightforward protocol for data collection as it is the standard setup in most laboratory TEMs. It is expected to result in lower quality PDFs than those meas-

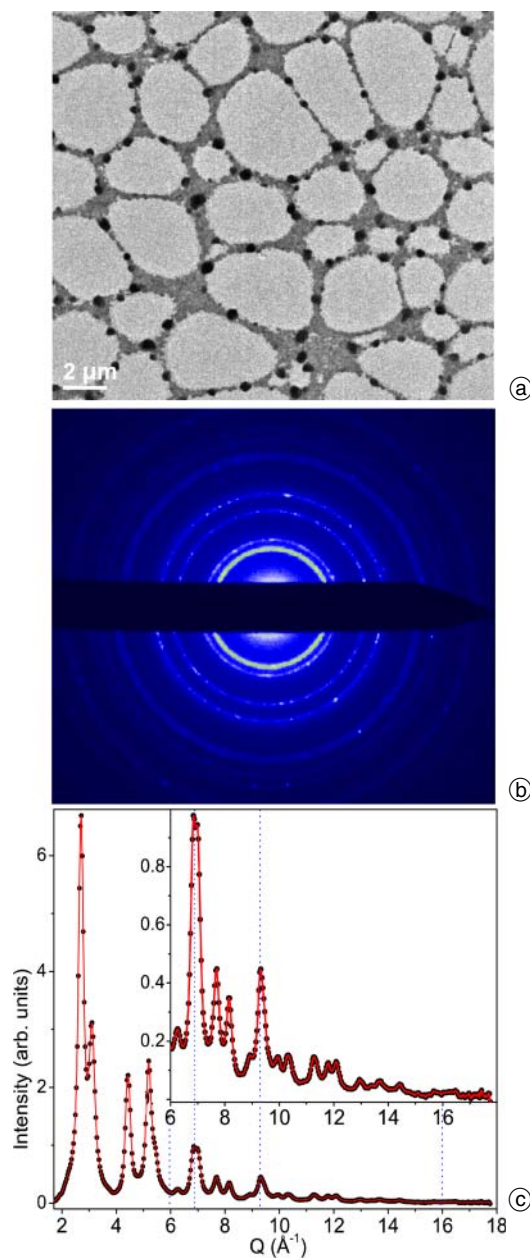


Fig. 4. (a) A TEM image of $\sim 100 \text{ nm}$ Au nanoparticles used for ED. Black dots are the nanoparticles on the grid and the large white areas are the holes in the grid. (b) A background subtracted ED image, collected from the same region of the sample using 200 keV electrons. (c) The 1D ED pattern obtained by integrating around the rings in 4(b). The inset shows a magnified region of the integrated ED pattern as indicated by the dotted lines.

ured with energy filtered electrons because of the higher backgrounds due to inelastically scattered electrons [8]. ED data collected with an image plate detector are also expected to be higher quality due to the low intrinsic detector noise and better dynamic range of that detector technology. Thus, the resulting PDF shown in Fig. 3c represents the baseline of what is possible without specialized instrumentation. The resulting $F(Q)$ shows excellent signal to noise up to the maximum accessible Q -range of 17 \AA^{-1} , as evident in Fig. 3a.

To explore the size limits for Au NPs to scatter kinematically, we collected data from larger, 100 nm Au nano-

particles, and the results are also given in Table 1 and Figs 4 and 5. Comparing the integrated 1D diffraction patterns of the large NPs and the thin Au film, Figs. 4c and 2c, respectively, we see similar features, but in the case of the NPs, the amplitudes of the scattered intensities extend to much higher Q values, as if there is a much smaller Debye-Waller factor for the data. This can be clearly observed by comparing the $eF(Q)$ of the large nanoparticles in Fig. 5a with those from X-ray diffraction data, $xF(Q)$ in Fig. 5b. The enhancement in the high- Q features is large and is almost certainly due to significant coherent multiple scattering in this sample. The resulting ePDF from the NPs has peaks that are correspondingly sharp compared to the gold thin film the xPDFs of gold NPs. Regardless of the presence of significant multiple scattering, a model was refined against the ePDF of the 100 nm Au nanoparticles to see the extent that the refined structural model parameters are affected. The structure refinement

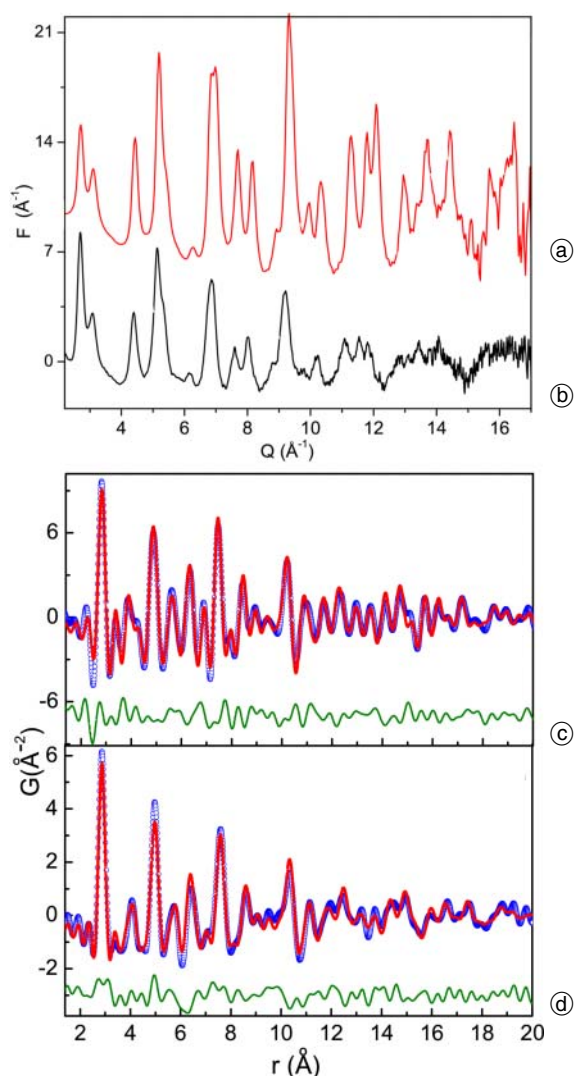


Fig. 5. (a) The reduced structure function, $F(Q)$, of Au calculated from the integrated ED pattern in Fig. 4(c). (b) An $F(Q)$ generated from an integrated Au NP XRD pattern from a 2D data set collected at X7B at the NSLS. (c) Au bulk structure model fit to the resulting ePDF from 5(a). (d) Au bulk structure model fit to the resulting xPDF from 5(b). Observed and calculated PDFs are presented with blue circles and a solid red lines, respectively. The difference between observed and calculated is offset below (green solid lines).

gave fits that were slightly worse but comparable in quality to the xPDF fits (see Table 1), $R_w = 0.24$. The refined values were similar also, except for much smaller atomic displacement parameters (ADPs), due to the artificially sharpened PDF peaks. It is somewhat remarkable that, in this case, the dynamical scattering produces features in the $F(Q)$ with approximately the correct relative amplitude, but extending to much higher- Q . Not only are the PDF peaks in the right position [2], but have the right relative amplitudes. Gold may be a special case because the structure factors are all either ones or zero's.

This clearly shows that for a strong scatterer such as Au, 100 nm nanoparticles already give significant dynamical

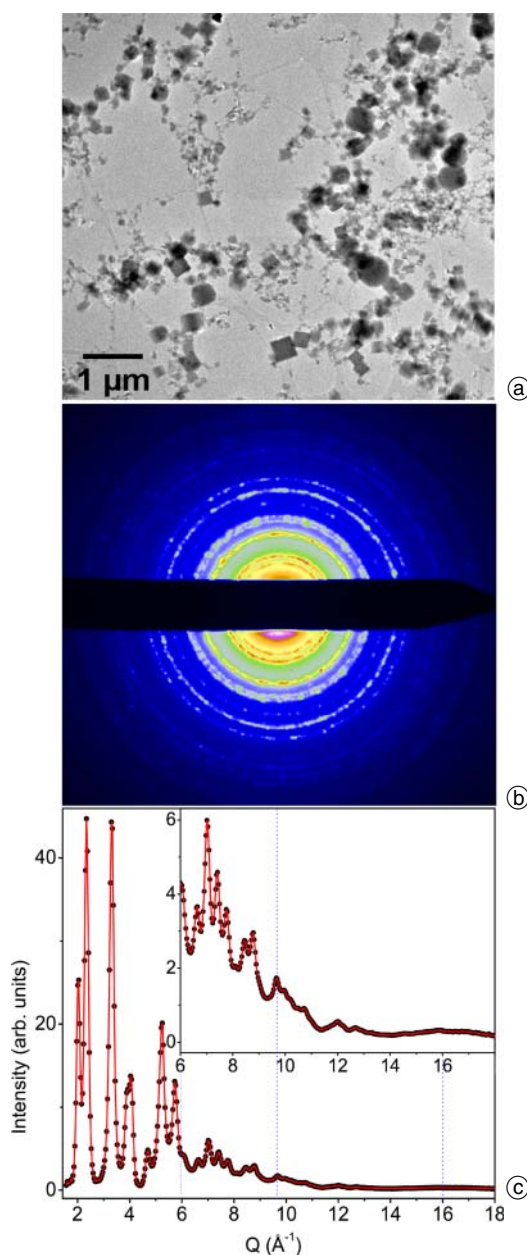


Fig. 6. (a) A TEM image of the NaCl film used for ED. (b) A false-color 2D ED image collected from this sample using 200 keV electrons. Lighter colors indicate higher intensity. The black bar across the middle of the image is the shadow of the beam-stop. (c) The 1D ED pattern obtained by integrating around the rings in 6(b). The inset shows the high Q region of the ED pattern on an expanded y-scale. The dotted lines are guides to the eye.

cal effects. The resulting PDFs give useful semi-quantitative and qualitative information but the refined thermal parameters are not reliable. Indeed, the effect of the multiple scattering to increase the real-space resolution by boosting the intensities of the high- Q peaks makes the PDF peaks sharper with the result that bond-lengths can be extracted with greater precision from the ePDF data than in this case. When accurate PDF peak positions rather than quantitative peak intensities are desired, this could be a significant advantage of the ePDF method, for example, when looking for small peak splittings, or resolving peak overlaps, to aid in structure solution.

A less trivial structure factor is obtained from binary compounds such as the NaCl studied here. The TEM image of the sample in Fig. 6a shows that it consists of nanoscale crystallites, some of which have a cubic habit and others that have no particular morphology. The correspond-

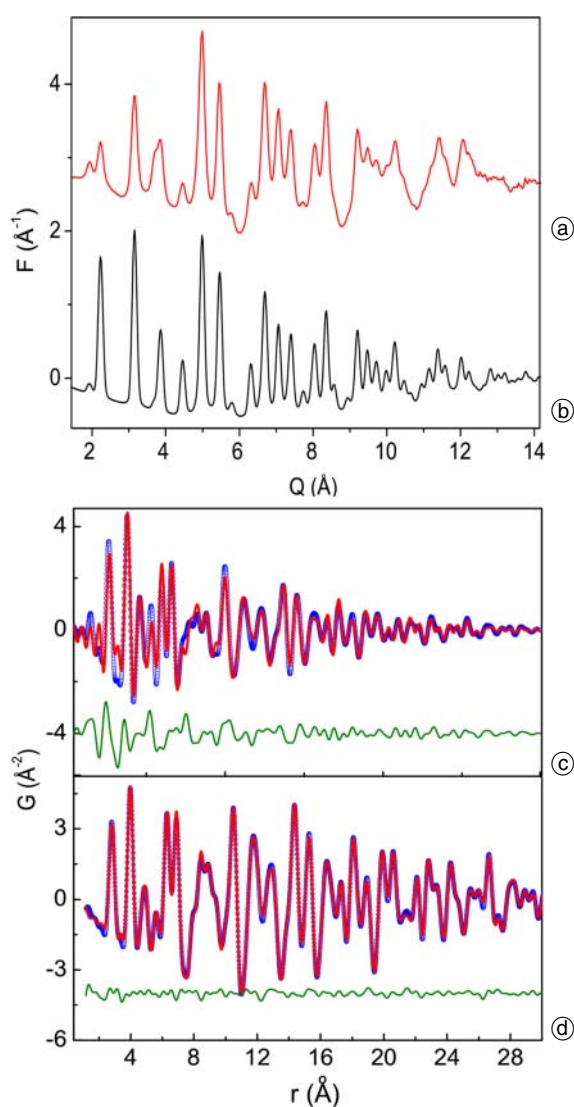


Fig. 7. (a) The reduced structure function, $F(Q)$, of NaCl obtained from the integrated ED pattern in Fig. 6(c). (b) An $F(Q)$ of NaCl calculated from an X-ray data set. (c) NaCl bulk structure model fit to the resulting ePDF from 7(a). (d) NaCl bulk structure model fit to the resulting xPDF from 7(b). Observed and calculated PDFs are presented with blue circles and solid red lines, respectively. The difference between observed and calculated is offset below (green solid lines). In both cases $Q_{\max} = 13.6 \text{ \AA}^{-1}$.

Table 2. Refined parameters for nanoparticulate NaCl from ePDFs and for a bulk powder of NaCl from the xPDF. The structure model is the fcc rock-salt structure, space-group $Fm\bar{3}m$. It was not possible to measure the nanoparticle size from the ePDFs as we were not able to calibrate the intrinsic Q -space resolution of the ED measurement allowing us to separate the instrumental resolution and particle size effects in the ePDFs.

	ePDF	xPDF
Q_{\max} (\AA^{-1})	13.6	13.6
Fit range (\AA)	0.2–30	0.2–30
Cell parameter (\AA)	5.62(2)	5.63(1)
$U_{\text{iso}} - \text{Na}$ (\AA^2)	0.007(5)	0.027(1)
$U_{\text{iso}} - \text{Cl}$ (\AA^2)	0.004(4)	0.016(1)
Q -damp (\AA^{-1})	0.095(5)	0.06(1)
R_w %	33	6

ing ED pattern in Fig. 6b shows clear and fairly uniform rings, with some spottiness from an imperfect powder average, which may contribute to the observed discrepancies in the rock-salt model fit to the ePDF. Figure 6c shows the integrated ED pattern. The $F(Q)$ and the resulting ePDF obtained from this data set is shown in Figs. 7a and c, respectively. For comparison, an $xF(Q)$ and an xPDF obtained from a bulk crystalline NaCl sample are also shown in Fig. 7b and d.

The rock-salt structure model fits to the PDFs are shown in Fig. 7c and d and the results are presented in Table 2. The e- and xPDFs are qualitatively highly similar, with all features in the xPDF easily recognizable in the ePDF. Notably, the relative intensities of adjacent peaks are similar between the e- and xPDFs. Peaks in the ePDF die out in amplitude with increasing r more quickly, due to the broader features in the ED pattern. The overall quality of the fit to the ePDF is worse than the xPDF of bulk NaCl. Refined lattice constants agree well within the experimental uncertainty. The ePDF refined thermal parameters are much smaller than those obtained from the X-ray data. This is unlikely to be a real effect as both the X-ray and electron data were measured at room temperature, and it is rather implausible that the nanoparticulate samples have *less* static structural disorder than bulk NaCl. We therefore assume that this is the effect of multiple scattering in the data, similar to that observed for large Au NPs. Clearly, ADPs refined from ePDFs present a lower bound on actual sample ADPs. They are accurate in the case where multiple scattering is negligible, but underestimate the thermal motions and static disorder in the presence of multiple scattering.

5. Discussion and conclusions

The Au and NaCl examples establish that quantitatively, or semi-quantitatively, reliable PDFs can be obtained from nanomaterials using electron diffraction data obtained on a standard laboratory TEM, without the use of filtering. Because of the ease and speed of collecting such data and the ubiquity of such instruments in chemistry and materials laboratories, if the barriers to data processing could be overcome making the whole process straightforward, this

could become a broadly applicable standard and useful characterization method for nanoparticles and thin films.

This work also explores the experimental parameters for obtaining good data for reliable ePDFs from nanomaterials. Principally, samples should be thin enough or, for the case of nanoparticles, have a sufficiently small diameter. What this diameter depends on the average atomic number of the sample. For Au, 100 nm diameter NPs gave significant coherent multiple scattering, 2.7 nm thick films did not. For all materials we expect that 10 nm and smaller particles will scatter kinematically; and these are precisely in the size-range of nanoparticles that benefit the most from a PDF analysis [22]. Obtaining a good powder average is also a very important part of powder diffraction regardless of the probing technique, XRD, ND or ED. This can be easily achieved by using a large sample volume in ND and spinning the sample in XRD. However, in ED, both of these methods become difficult due to the limitations of the configuration and careful sample preparation in this regard is very helpful. Again, for the particular application in nanoparticle structure characterization, the small size of the particles means that better powder averages can be obtained even from small sample volumes. However, the quality of the powder average should be checked by visual inspection of the ED images from the CCD, which is readily done as is evident in the figures in this paper. The powder average can be improved by increasing the beam-spot size on the sample and also by taking multiple images from different regions of the sample and averaging them. It is also important that samples be free of texture for PDF analysis in the current implementation. This may be particularly relevant in the case of polycrystalline thin films that are prone to texture, though less so for nanoscale and amorphous films and mono (or few) layer coverages of nanoparticles on a surface. The raw data on the 2D detector should be carefully assessed for the effects of texture. Texture in the plane of the film can be searched for by looking for systematic intensity variations around the diffraction rings on the detector. Perpendicular texture could be assessed by taking diffraction patterns of the film with it tilted at different angles with respect to the beam and comparing the resulting ring intensities. For a highly textured film a 2D rather than a 3D PDF transform may be more appropriate. In the future we plan to develop and make available software for checking for texture and where possible correcting for it. The maximum attainable Q_{\max} is determined by the operational energy, camera length, dimensions of the detector and the diameter of the microscope, but in general should be maximized. Our electron microscope configuration equipped with a CCD camera limited Q_{\max} to $\sim(17-18)$ Å. The advantage of using a higher Q_{\max} is the better real space resolution that results in the ePDF. However, standard microscope configurations naturally give sufficiently high Q_{\max} values for most applications. Thus there seems to be no impediment to the use of ED from standard laboratory electron microscopes for quantitative nanoparticle structural characterization using the PDF.

Acknowledgements. We would like to acknowledge helpful discussions with Michael Thorpe. We also thank Jon Hanson for allowing

access to the X7B beamline at NSLS, which is supported by DOE-BES under contract No DE-AC02-98CH10886. Work in the Billinge group was supported by DOE-BES through account DE-AC02-98CH10886. Work in the Kanatzidis group was supported by NSF through grant DMR-1104965.

References

- [1] Ankele, J.; Mayer, J.; Lamparter, P.; Steeb, S.: Quantitative electron diffraction data of amorphous materials. *Z. Naturforsch. A* **60A** (2005) 459–68.
- [2] Anstis, G. R.; Liu, Z.; Lake, M.: Investigation of amorphous materials by electron diffraction: the effects of multiple scattering. *Ultramicroscopy* **26** (1988) 65–69.
- [3] Billinge, S. J. L.: Nanoscale structural order from the atomic pair distribution function (PDF): There's plenty of room in the middle. *J. Solid State Chem.* **181** (2008) 1698–1703.
- [4] Billinge, S. J. L.; Levin, I.: The problem with determining atomic structure at the nanoscale. *Science* **316** (2007) 561–565.
- [5] Cervellino, A.; Giannini, C.; Guagliardi, A.: DEBUSSY: a Debye user system for nanocrystalline materials. *J. Appl. Crystallogr.* **43** (2010) 1543–1547.
- [6] Chupas, P. J.; Qiu, X.; Hanson, J. C.; Lee, P. L.; Grey, C. P.; Billinge, S. J. L.: [Rapid acquisition pair distribution function analysis \(RA-PDF\)](#). *J. Appl. Crystallogr.* **36** (2003) 1342–1347.
- [7] Cockayne, D. J. H.: The study of nanovolumes of amorphous materials using electron scattering. *Annu. Rev. Mater. Res.* **37** (2007) 159–187.
- [8] Cockayne, D. J. H.; McKenzie, D. R.: Electron diffraction analysis of polycrystalline and amorphous thin films. *Acta Crystallogr. A* **44**(6) (Nov 1988) 870–878.
- [9] Cowley, J. M.: *Electron Diffraction Techniques*, 1st ed., vol. 1. Oxford University Press, 1992.
- [10] Cowley, J. M.: *Diffraction Physics*, 3rd ed. Elsevier, Amsterdam, 1995.
- [11] Cowley, J. M.: Applications of electron nanodiffraction. *Micron* **35** (2004) 345–360.
- [12] Debye, P.: Dispersion of Röntgen rays. *Annalen der Physik (Berlin, Germany)* **46** (1915) 809–823.
- [13] Egami, T.; Billinge, S. J. L.: *Underneath the Bragg peaks: structural analysis of complex materials*. Pergamon Press, Elsevier, Oxford, England, 2003.
- [14] Farrow, C. L.; Billinge, S. J. L.: Relationship between the atomic pair distribution function and small angle scattering: implications for modeling of nanoparticles. *Acta Crystallogr. A* **65**(3) (2009) 232–239.
- [15] Farrow, C. L.; Juhás, P.; Liu, J.; Bryndin, D.; Božin, E. S.; Bloch, J.; Proffen, T.; Billinge, S. J. L.: PDFfit2 and PDFgui: Computer programs for studying nanostructure in crystals. *J. Phys: Condens. Mat.* **19** (2007) 335219.
- [16] Hammersley, A. P.; Svenson, S. O.; Hanfland, M.; Hauserman, D.: Two-dimensional detector software: from real detector to idealised image or two-theta scan. *High Pressure Res.* **14** (1996) 235–248.
- [17] Hirotsu, Y.; Ohkubo, T.; Bae, I.-T.; Ishimaru, M.: Electron diffraction structure analysis for amorphous materials. *Mater. Chem. Phys.* **81** (2003) 360–363.
- [18] Jadzinsky, P. D.; Calero, G.; Ackerson, C. J.; Bushnell, D. A.; Kornberg, R. D.: Structure of a thiol monolayer-protected gold nanoparticle at 1.1 Å resolution. *Science* **318**(5849) (2007) 430–433.
- [19] Juhás, P.; Cherba, D. M.; Duxbury, P. M.; Punch, W. F.; Billinge, S. J. L.: Ab initio determination of solid-state nanostructure. *Nature* **440**(7084) (2006), 655–658.
- [20] Karle, J.: Structure determination of gaseous and amorphous substances by diffraction methods: philosophical concepts and their implementation (a review). *Proc. Natl. Acad. Sci. USA* **74** (1977) 4707–4713.
- [21] Kodama, K.; Iikubo, S.; Taguchi, T.; Shamoto, S.: Finite size effects of nanoparticles on the atomic pair distribution functions. *Acta Crystallogr. A* **62** (2006) 444–453.
- [22] Masadeh, A. S.; Božin, E. S.; Farrow, C. L.; Paglia, G.; Juhás, P.; Karkamkar, A.; Kanatzidis, M. G.; Billinge, S. J. L.: Quantitative size-dependent structure and strain determination of CdSe

- nanoparticles using atomic pair distribution function analysis. *Phys. Rev. B* **76** (2007) 115413.
- [23] Moss, S. C.; Graczyk, J. F.: [Evidence of voids within the as-deposited structure of glassy silicon](#). *Phys. Rev. Lett.* **23** (1969) 1167–1171.
- [24] Neder, R. B.; Korsunskiy, V. I.; Chory, C.; Müller, G.; Hofmann, A.; Dembski, S.; Graf, C.; Rühl, E.: Structural characterization of II–VI semiconductor nanoparticles. *Phys. Status Solidi C* **4**(9) (2007) 1610–1634.
- [25] Neder, R. B.; Proffen, T.: *Diffuse Scattering and Defect Structure Simulations A cook book using the program DISCUS*. Oxford University Press, Oxford, 2008.
- [26] Nörenberg, H.; Säverin, R.; Hoppe, U.; Holzhüter, G.: Estimation of radial distribution functions in electron diffraction experiments: physical, mathematical and numerical aspects. *J. Appl. Crystallogr.* **32** (1999) 911–916.
- [27] Page, K.; Proffen, T.; Terrones, H.; Terrones, M.; Lee, L.; Yang, Y.; Stemmer, S.; Seshadri, R.; Cheetham, A. K.: [Direct observation of the structure of gold nanoparticles by total scattering powder neutron diffraction](#). *Chem. Phys. Lett.* **393** (2004) 385–388.
- [28] Petkov, V.; Gateshki, M.; Niederberger, M.; Ren, Y.: Atomic-scale structure of nanocrystalline $\text{Ba}_x\text{Sr}_{1-x}\text{TiO}_3$ ($x = 1, 0.5, 0$) by X-ray diffraction and the atomic pair distribution function technique. *Chem. Mater.* **18** (2006) 814.
- [29] Petkov, V.; Ohta, T.; Hou, Y.; Ren, Y.: Atomic-scale structure of nanocrystals by high-energy X-ray diffraction and atomic pair distribution function analysis: Study of $\text{Fe}_x\text{Pd}_{100-x}$ ($x = 0, 26, 28, 48$) nanoparticles. *J. Phys. Chem. C* **111**(2) (2007) 714–720.
- [30] Rietveld, H. M.: A profile refinement method for nuclear and magnetic structures. *J. Appl. Crystallogr.* **2** (1969), 65–71.
- [31] Schooss, D.; Blom, M. N.; Parks, J. H.; von Issendorff, B.; Haberland, H.; Kappes, M. M.: The structures of Ag_{55}^+ and Ag_{55}^- : Trapped ion electron diffraction and density functional theory. *Nano Lett.* **5** (2005) 1972–1977.
- [32] Tucker, M. G.; Keen, D. A.; Dove, M. T.; Goodwin, A. L.; Hui, Q.: RMCProfile: reverse Monte Carlo for polycrystalline materials. *J. Phys.: Condens. Mat.* **19** (2007) 335218.
- [33] Wang, Z. L.: Transmission electron microscopy of shape-controlled nanocrystals and their assemblies. *J. Phys. Chem. B* **104**(6) (2000) 1153–1175.
- [34] Warren, B. E.: *X-ray Diffraction*. Dover, New York, 1990.
- [35] Weirich, T. E.; Lábár, J. L.; Zuo, X.; Eds.: *Electron Crystallography: Novel approaches for structure determination of nanosized materials*, Springer Amsterdam, 2006.
- [36] Won, J. H.; Sato, K.; Ishimaru, M.; Hirotsu, Y.: Transmission electron microscopy study on FeSi_2 nanoparticles synthesized by electron-beam evaporation. *J. Appl. Phys.* **100** (July 2006) 4307.
- [37] Young, R. A.: *The Rietveld Method*, vol. 5 of *International Union of Crystallography Monographs on Crystallography*. Oxford University Press, Oxford, 1993.

Metastability and Structural Polymorphism in Noble Metals: The Role of Composition and Metal Atom Coordination in Mono- and Bimetallic Nanoclusters

Sergio I. Sanchez,[†] Matthew W. Small,[†] Emil S. Bozin,[‡] Jian-Guo Wen,[†] Jian-Min Zuo,[§] and Ralph G. Nuzzo^{†,§,*}

[†]Department of Chemistry and the Frederick Seitz Materials Research Laboratory and [§]Department of Materials Science and Engineering, University of Illinois at Urbana—Champaign, Urbana, Illinois 61801, United States and [‡]Condensed Matter Physics and Materials Science Department, Brookhaven National Laboratory, Upton, New York 11973, United States

ABSTRACT This study examines structural variations found in the atomic ordering of different transition metal nanoparticles synthesized *via* a common, kinetically controlled protocol: reduction of an aqueous solution of metal precursor salt(s) with NaBH₄ at 273 K in the presence of a capping polymer ligand. These noble metal nanoparticles were characterized at the atomic scale using spherical aberration-corrected scanning transmission electron microscopy (C_s-STEM). It was found for monometallic samples that the third row, face-centered-cubic (fcc), transition metal [(3M)—Ir, Pt, and Au] particles exhibited more coherently ordered geometries than their second row, fcc, transition metal [(2M)—Rh, Pd, and Ag] analogues. The former exhibit growth habits favoring crystalline phases with specific facet structures while the latter samples are dominated by more disordered atomic arrangements that include complex systems of facets and twinning. Atomic pair distribution function (PDF) measurements further confirmed these observations, establishing that the 3M clusters exhibit longer ranged ordering than their 2M counterparts. The assembly of intracolumn bimetallic nanoparticles (Au—Ag, Pt—Pd, and Ir—Rh) using the same experimental conditions showed a strong tendency for the 3M atoms to template long-ranged, crystalline growth of 2M metal atoms extending up to over 8 nm beyond the 3M core.



KEYWORDS: nanoparticle · atomic structure · noble metals · bimetallic · core—shell · pair distribution function · aberration corrected electron microscopy

Progress in recent years has seen important advances made in nanoscience toward the development of useful new forms of nanotechnology.^{1–8} One recurring theme found in research is controlling structures with nanometer precision.^{9–12} The difficulty with synthesizing ever-smaller structures is that the outcome of a reaction is dictated by a complex interplay of thermodynamics and kinetics. Kinetically favored products may or may not be the same as those preferred thermodynamically. Under different conditions the most stable structure of a material may in fact also be size-dependent and change from a single-crystalline habit to one that exhibits twinning or is amorphous.^{13,14} Because of this, and the broader utility of

crafting structures at the atomic scale, it is imperative to understand both kinetic and thermodynamic contributions to materials synthesis.

It is now well understood that catalytic properties of nanoscale metal clusters depend markedly on the structure of their exposed surfaces.^{15–18} Vertex and edge atom sites are known to bind more strongly to molecules and reactive intermediates, doing so in ways that broadly impact reaction rates.^{19–21} A notable study by Bratlie *et al.*¹⁵ demonstrated that different nanocrystal morphologies can wholly dictate the outcome of a prototypical catalytic reaction. Cubic Pt crystals defined by {100} planes, for example, are selective for the hydrogenation of benzene to cyclohexane,

* Address correspondence to r-nuzzo@illinois.edu.

Received for review November 15, 2012 and accepted December 28, 2012.

Published online December 28, 2012
10.1021/nn305314m

© 2012 American Chemical Society

while cuboctahedral structures (defined by {100} and {111} planes) yield a mixture of cyclohexene and cyclohexane under similar conditions.¹⁵ Such data motivate this work to better understand the factors that control nanocrystal growth.

Research has shown that different avenues exist by which materials growth chemistry can generate desired nanostructures.²² The stabilities of structures produced using chemically controlled procedures can vary in complex ways depending on size and the presence of other species.^{18,22–27} Theoretical calculations, predict that fcc, single-crystalline nanoparticles will assume a truncated octahedron confined by the {111} and {100} families of planes as their equilibrium thermodynamic shape.²⁴ The formation of such a shape, however, embeds costly energetic motifs due to the presence of undercoordinated atoms.²⁸ Conversely, particles not composed of a single crystal domain (and therefore containing multiple twins) adopt an icosahedral or decahedral crystal morphology, where the faceting is exclusively defined by low energy {111} terminating facets.²⁸ Ultimately, it is these planes that assist in the formation of a low energy structure, albeit at the cost of increased internal strain.^{13,23,28} In these scenarios the mediating effects of surface energy dictate the nanoparticle's stable geometry. Theoretical calculations predict that a crystal bound by high index crystal planes will ultimately minimize the surface energy by reconstructing and assuming more favorable, lower index faceting, namely, the {111}, {100}, and {110} families of planes.^{22,23}

The energetic driving force for the reconstruction to lower index planes arises from the instability associated with undercoordinated atoms.^{29,30} With nanoparticles this behavior is complicated by the curvature adopted to minimize the exposed surface area. Creating a rounded structure from a collection of facets inevitably applies increased strain to atoms residing at the edges and vertices of adjoining crystal planes.^{19,31–33} Because these atoms have fewer neighbors than those situated on a flat surface, the coordination environment is more extreme.^{19,31} As a result, they have more unsatisfied bonds and are less stable.^{31–33} In discriminating the different surface truncation energies, it is easy to see why a high atomic density (111) surface is intrinsically more stable than a lower atomic density (100) surface.³⁴

Despite the significant role thermodynamics plays in directing the attributes of nanostructures, kinetics cannot be neglected as a complex and often competing contributor. It is frequently found that adjusting experimental parameters (*i.e.*, capping agent, reducing agent, temperature, *etc.*) can yield products with specific morphological features,^{2,3,22,35,36} crystal sizes,^{3,22,37–39} and catalytic activity.^{25–27,40–43} In such cases the geometry of a nanocrystal is not solely determined by the

minimization of its surface energy (thermodynamic minimum). Instead one must consider the possible formation of metastable structures possessing a conversion potential well too deep to overcome.^{13,24} In such cases, the reactions result in the formation of thermodynamically unfavorable features.²³ Therefore a balance exists in that the metastable structure formed may reside far away from the global energetic minimum.

We report the results of an investigation of the synthesis of polyvinylpyrrolidone (PVP) capped nanoparticles grown in solution from six noble metal precursors (Rh, Pd, Ag, Ir, Pt, Au) using NaBH₄ as a reducing agent. Because of the high reduction potential of NaBH₄, this growth is very rapid, proceeding from a burst of nucleation events and is known to produce a large number of very small nanoparticles (~1 nm).⁴⁴ Generally speaking, the synthetic approach illustrates growth occurring under conditions of kinetic control. Our results show clear structural differences between the 2 and 3M nanostructures investigated that cannot be explained merely by thermodynamic arguments and indicates that there is a distinct, electronic structural sensitivity. Using C_s-STEM we characterize the atomistic details that differentiate the 2 and 3M nanoparticle structures formed and define size-dependent patterns related to their stability. Conclusions supported by the C_s-STEM data agree fully with measurements made using high-energy X-ray diffraction (XRD). The latter XRD data confirm that a dilation of the lattice constant occurs for the 2M nanoparticles whereas the 3M series presents more bulk-like values. We further compare the PDF measurements to assess the levels of coherence/crystallinity present in these materials. Most revealing are features observed for the intracolumn bimetallic (Au–Ag, Pt–Pd, and Ir–Rh) structures, where the 3M metal atoms of a growth-nucleating core impart their bonding structure onto 2M atoms in core–shell habits to very large cluster diameters—essentially directing the overall growth of the 2M atoms—whereas without their presence disordered crystal morphologies dominate.

RESULTS AND DISCUSSION

Structural and Crystallographic Analysis of Single-Element Nanocrystals. Figure 1 shows representative C_s-STEM micrographs of metals in the 3M series of nanocrystals (Au, Pt, and Ir). The Au samples (Figure 1a–c), for the synthetic protocols used here, presented with a relatively wide distribution of particle sizes (2.2 ± 1.7 nm; Supporting Information (S.I.) Figure 1) with some appearing single crystalline and others being symmetrically twinned (S.I. Figure 2). Although only single crystals are depicted in Figure 1, it was generally observed that both the single and polycrystalline particles revealed an atomic structure in which Au atoms could be identified up to the terminating edges. Fast Fourier transforms (FFTs) of the micrographs

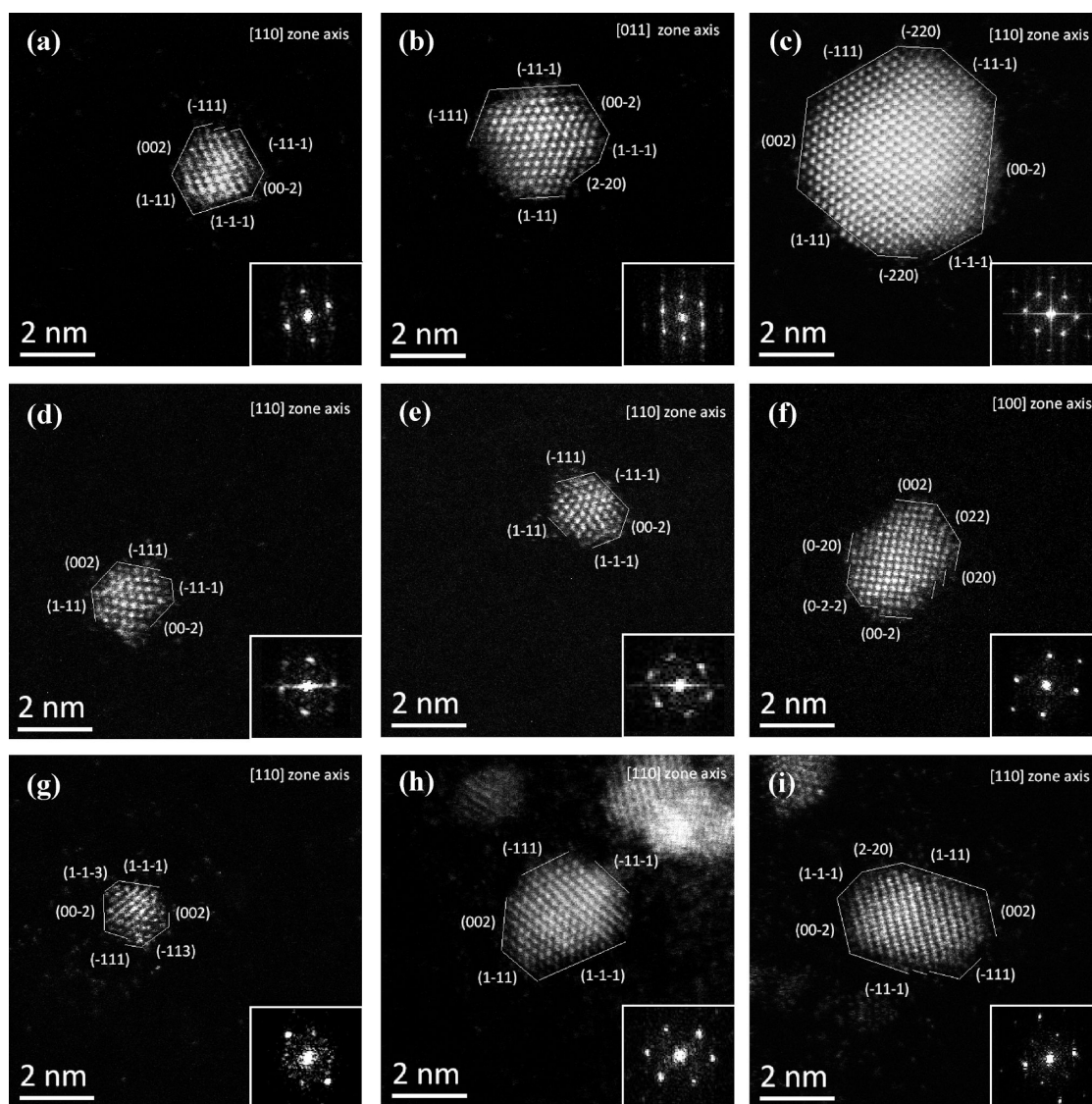


Figure 1. Representative C_v -STEM micrographs of the 3M nanocrystals, Au (a–c), Pt (d–f), Ir (g–i). Facets and crystal orientation corresponding to the inset FFT are annotated directly on the micrographs.

(i.e., the power spectra) are given as insets in the lower right of Figure 1a–c. The spatial frequencies associated with the periodic placement of atoms in the crystal make it possible to identify the zone axis of the cluster and index their bounding facet structure. This analysis was easier to carry out for larger crystals within the size distribution since they were more frequently found to be crystalline. In addition to identifying an approximate zone axis, the FFT also made it possible to determine an apparent lattice constant for the Au particles ($4.05 \pm 0.12 \text{ \AA}$, in close agreement with the literature value of 4.08 \AA for bulk Au).⁴⁵ The values obtained using the FFT tend to lack high precision because nanocrystals are rarely perfectly oriented along a zone axis and for this reason many of these projection-limited values must be averaged. Table 1 shows that with adequate sampling the lattice constants so deduced can still be accurate—in the present

work the values so obtained for all metals investigated were found to compare very favorably with bulk reference values. As expected, low-index planes define a common feature of the crystals' facet structures.¹⁶

Figure 1d–f shows representative images of Pt nanocrystals taken from a sample with a size distribution of $1.5 \pm 0.6 \text{ nm}$ (S.I. Figure 1). The atomic ordering evident within the images allowed lattice parameters and facet structures for these nanocrystals to be assigned. An estimated lattice parameter of $3.90 \pm 0.09 \text{ \AA}$ closely matches the literature value of 3.92 \AA for bulk Pt (Table 1).⁴⁵ Unlike Au, which exhibited frequent twinning, the Pt samples were predominantly single-crystalline.

The Ir specimens (Figure 1g–i) resemble the Pt samples with the exception of being highly susceptible to aggregation (not sintering). Although the mean particle size ($1.6 \pm 0.8 \text{ nm}$, S.I. Figure 1) was on the

TABLE 1. Comparison of Lattice Parameters Determined by C_s -STEM and High-Energy XRD Tabulated with Literature Values

element	lattice constants		
	microscopy – experimental value (Å)	X-ray diffraction – experimental value (Å)	literature value (Å)
Ag	4.16 ± 0.05^a	4.12 ± 0.06	4.09
Au	4.05 ± 0.12	4.05 ± 0.02	4.08
Pt	3.90 ± 0.09	3.92 ± 0.05	3.92
Pd	4.00 ± 0.15	3.95 ± 0.04	3.89
Ir	3.84 ± 0.09	3.84 ± 0.13	3.84
Rh	3.90 ± 0.19	3.89 ± 0.16^b	3.80

^a The apparent disorder exhibited by the majority of Ag particles limited the amount of sampling for analysis by microscopy. ^b The Rh XRD data only presented two discernible Bragg peaks with which to calculate the lattice constant (the (200) and the (333)) peaks.

order of Pt and Au, Ir particles were seldomly found in isolation. As with the other 3M metals, the Ir nanocrystals bounding edges were often assignable using the spectral data from the FFT of the image. Surprisingly, unlike the other 3M structures, Ir crystals experienced an increase in twinning defects at larger sizes (S.I. Figure 3). As shown in Table 1, our analysis indicates an average lattice parameter of 3.84 ± 0.09 nm for the Ir clusters, in agreement with that of bulk fcc Ir (3.84 Å).⁴⁵

Figure 2 shows a collection of C_s -STEM micrographs for the 2M (Ag, Pd, and Rh) nanoparticles. Dimensional analysis of the Ag nanoparticles revealed a mean particle diameter of 3.4 ± 2.8 nm (S.I. Figure 1), thus allowing a broad distribution of cluster sizes to be structurally characterized. With few exceptions, the Ag particles observed appeared highly disordered, lacking both well-defined boundaries and long-ranged atomic periodicity (Figure 2a–c). In contrast to the 3M specimens, C_s -STEM imaging of the Ag samples revealed no apparent correlation between size and the emergence of a more ordered habit over the particle sizes present. The absence of spatial frequencies in the power spectra (inset in the Ag nanocrystal micrographs) supports this finding, where the presence of a bright ring is generally found in place of distinct spatial frequencies. As in diffraction, a sharp ring structure would indicate a polycrystalline material (here all contributing crystals are within a single image) and an increasing diffuse component in the ring(s) indicates a move toward an amorphous structure. Given the disorder present in this sample, only a limited number of clusters provided the structural information given in Table 1.

Imaging of the Pd specimens (Figure 2d–f; 1.6 ± 0.8 nm, S.I. Figure 1) also revealed the presence of a generalized trend toward structures that looked more disordered. Unlike the case for Ag, Pd nanoclusters strongly evidenced size-dependent behavior. Increasing cluster sizes led to a propensity for adoption of an ordered habit. The ordering seen, however, was not generally found to be associated with single crystals until reaching relatively large sizes (as illustrated by representative examples shown in Figure 2d–f). Most strikingly, we found no examples in which Pd particles

smaller than ~ 3 nm exhibited crystallographic data amenable to the assignment of a single lattice, although this does not rule out their existence. Nonetheless, the trends observed *via* electron microscopy and the absence of crystalline Pd particles below 3 nm in a multitude of images surveyed indicate that they must be rare. Interestingly, the observation of significant twinning within these structures agrees with results from our previous work⁴⁶ even though the synthesis methods differ.

Structural properties similar to Pd were observed for the Rh nanocrystals (1.5 ± 0.5 nm, S.I. Figure 1). Smaller Rh crystals (< 2.6 nm) were not found to adopt geometries with an organized packing structure. They appeared as collapsed clusters of atoms showing no evidence of the spatial frequencies expected for an fcc crystal (Figure 2g,h). Particles exceeding this apparent threshold limit began to display evidence of crystallinity, as revealed in the FFT data. Multigrained nanoparticles were often found in which multiple crystal domains could be observed. It is clear that, for both the 2 and 3M clusters, there exist size-dependent variances in metal atom bonding that affect the final level of disorder.

Lattice constants calculated for the 2M samples, as determined by microscopy, are listed in Table 1 for the Ag, Pd and Rh nanoclusters. A comparison with literature values (Table 1) reveals a trend toward dilation of the lattice constants for these three samples with respect to their values in bulk. The fact that tensile (noncompressive) strains are present is very surprising, and contrasts with the common notion of surface atom relaxation in the atomic structures of metal nanoparticles.^{29,30} In this regard the 2 and 3M series of metals are very different. For the case of Au, Pt, and Ir, the atomically resolved micrographs show bonding comparable to the bulk. Both the Pt and Au nanocrystals, as might be expected, seem to show slight relaxations of their lattice parameters based on the microscopy.

Unfortunately, electron microscopy only provides a localized description of the features observed for the overall specimen. To verify that the trends observed

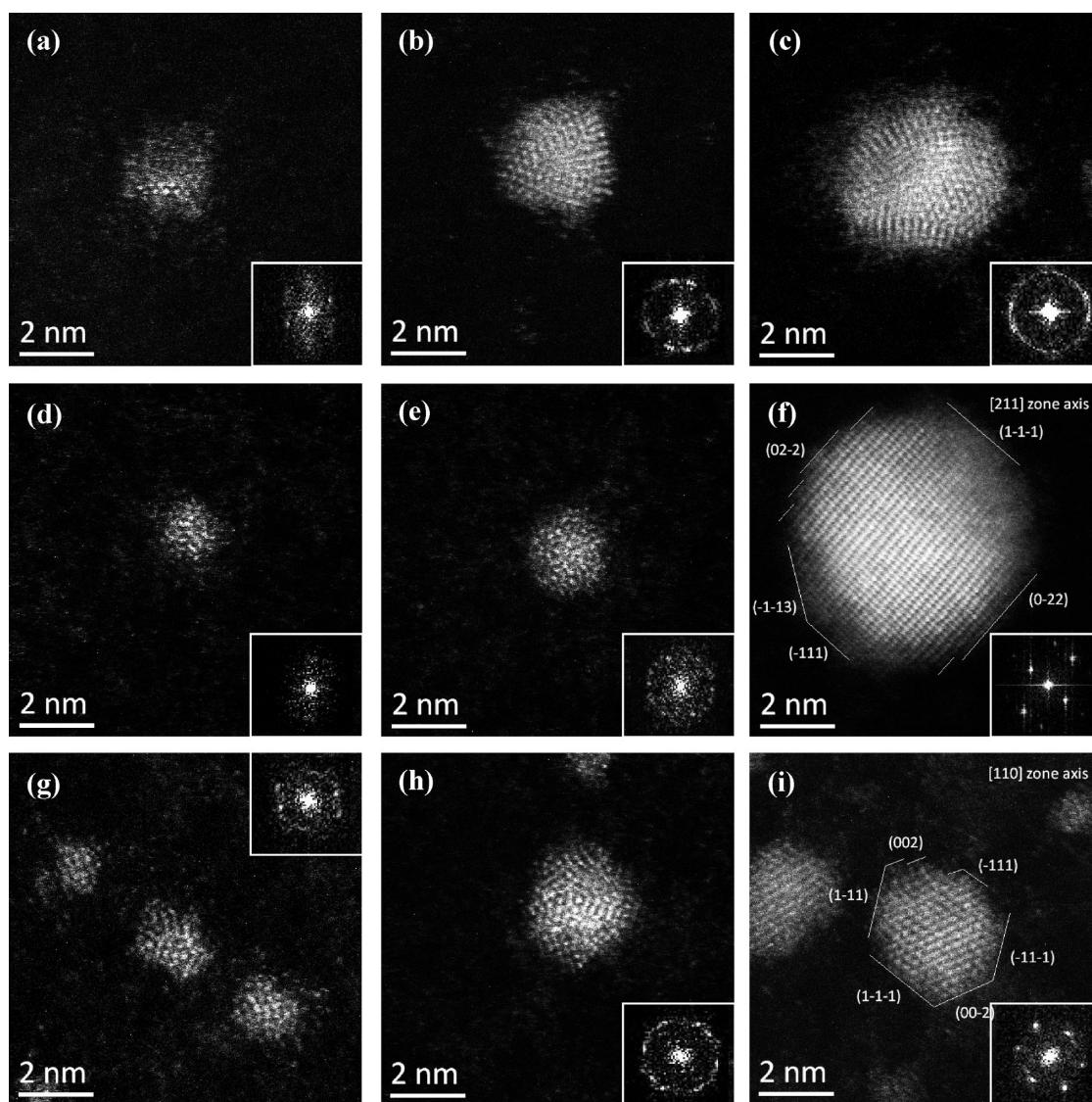


Figure 2. Representative C_s -STEM micrographs of the 2M nanocrystals, Ag (a–c), Pd (d–f), Rh (g–i). Facets and crystal orientation are annotated only in instances where the nanocrystal and inset FFT indicated a faceting structure.

are not caused by selective sampling, a bulk analytical technique was used to provide independent analysis and support the structural interpretations reached above. Data from high-energy XRD measurements were collected to provide a comprehensive structural assessment of the samples. Lattice parameters were determined from the Bragg peak reflections in the diffraction profiles and are presented in Table 1. A comparison of the lattice constants from the XRD measurements with those obtained from C_s -STEM shows close agreement. Significantly, the trend in which small 2M clusters exhibit a dilation of their lattice parameters compared to those bulk materials was reaffirmed. On the basis of the XRD data, the Ag, Pd, and Rh nanoparticles all have average lattice constants showing slight tensile strains in agreement with the values deduced *via* microscopy. Similar findings have been reported in other studies of Ag,⁴⁷ Pd,^{48–51} and

Rh⁵¹ nanoparticles. These studies attributed the observed strains to changes in structure that result variously because of the surrounding medium,⁴⁷ the presence of low-coordination number surface atoms,⁵¹ and the disorder of surface atoms.⁴⁸ The C_s -STEM data support a comprehensive structural feature embracing such attributes, but with a more complex underpinning. More specifically, the inability to terminate the 2M nanocrystal surfaces with well-defined facets may induce a tensile strain in the core atoms as they attempt to accommodate the disorder present at the surface.⁴⁸

At this point it is important to define what structural features are encompassed by the term “disorder” in the context of this study. Although it was mentioned that some of the particles undergo twinning (*e.g.*, Au, Ir, Rh, etc.) this does not preclude the possibility of forming definable planes (S.I. Figure 2 and 3). In the same

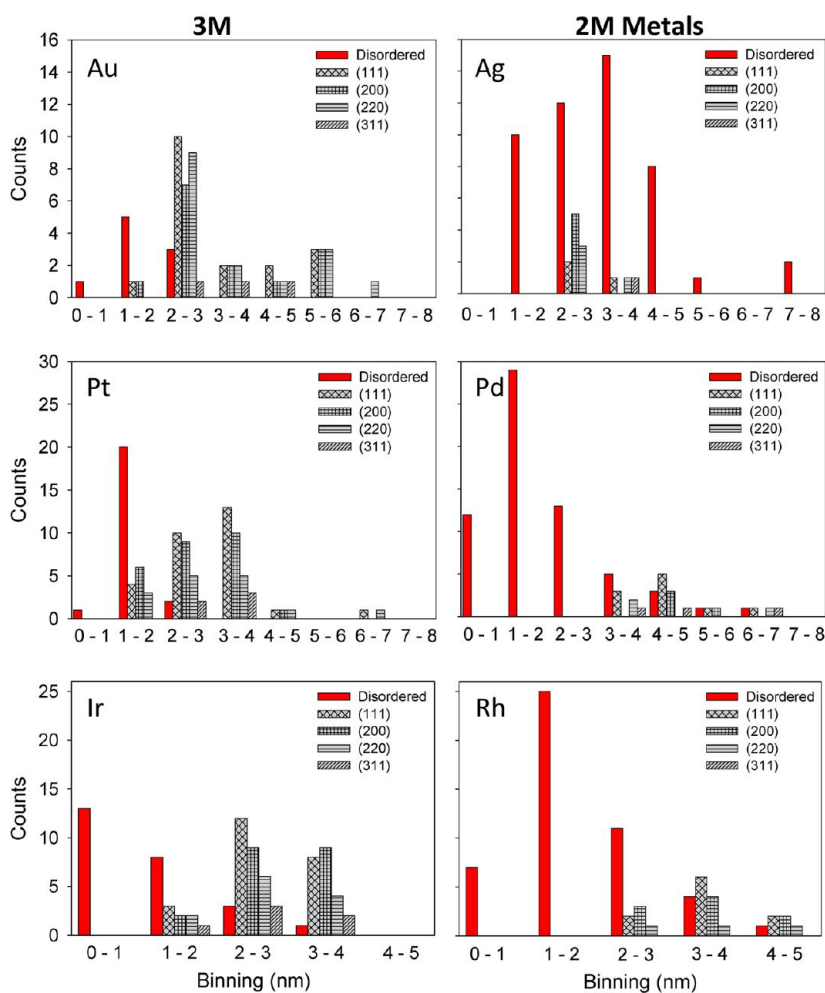


Figure 3. Binned histograms defining the size-dependent nature of crystallinity for the 3M (Au, Pt, Ir) and 2M (Ag, Pd, Rh) metals. The red bars represent “disordered” clusters such that atomically resolved images showed no extended structure across the particle. The hatched bars tally the frequency of crystal planes defined by FFT. Note: The frequencies of the binned data do not reflect the size distributions of the samples.

respect, a particle may exhibit crystallinity at the core even if the periodic nature of the atom packing does not extend to its surface. By “disordered” nanoparticles we refer to an organization of the atoms such that an extended, periodic packing structure is not present in the cluster. These are, in effect, amorphous states that embed large strains. The power spectra of such disordered clusters will not exhibit the spatial frequencies expected for an ordered habit and yield an amorphous pattern due to the disorder present. Nevertheless, interpretation of such “disorder” should be undertaken cautiously since even crystalline clusters along non-zone axes may exhibit projections that satisfy the above criterion.

To better understand if the microscopy results were truly indicating disorder we examined a large number of clusters for each sample. If no preferred orientation exists, all the samples should present equivalent rates of crystalline/disordered structures. Figure 3 presents the frequency of exposed surfaces (*e.g.*, the (111), (200), *etc.*) occurring for each sample as well as the

abundance of disordered particles (lacking any observable lattice structure) quantified and binned with respect to size (*e.g.*, 0–1, 1–2, 2–3 nm, *etc.*). One notes that the occurrence of definable planes is strongly related to particle size for the 3M specimens. Below particle sizes of ~ 1 nm there were no clusters for which such assignments could be made. In the 1–2 nm regime, however, the onset of crystallinity is noted by the emergence of well-defined truncating planes. With increasing size of the 3M nanocrystals, the presence of the {111}, {100}, {110}, and {311} family of planes becomes more numerous and ultimately dominates the observed crystal geometries. The behaviors for the 2M structures are more complex and show an extended range in which disordered morphologies prevail. The Ag nanoclusters showed no size-dependent crystallinity as noted by the abundant distribution of disordered particles throughout the binned data. The Pd and Rh clusters exhibited a more conventional behavior with disordered structures becoming less common for larger particles. The onset of ordering in

the 2M samples appears to occur most prominently in the size range between 2 and 4 nm. Even so, disordered particle habits persist to very large sizes (e.g., Rh (4–5 nm), Pd (6–7 nm), and Ag (7–8 nm)), values much larger than is seen for their 3M counterparts (e.g., Ir (3–4 nm), Pt (2–3 nm), and Au (2–3 nm)).

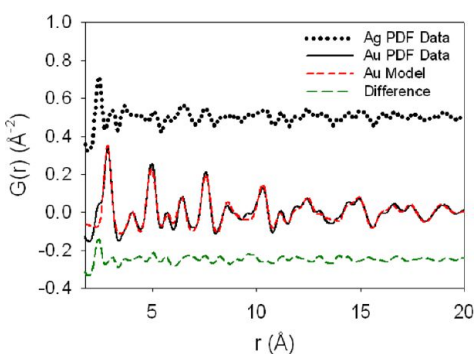


Figure 4. Atomic PDFs comparing Au (solid black line) and Ag (dotted line), with the Ag profile vertically displaced by $+0.5 \text{ \AA}^{-2}$ for clarity. The red curve is the fit modeling the experimental PDF data to a spherically shaped fcc Au crystal. The difference profile (green curve) between the experimental data and fit is vertically displaced by -0.25 \AA^{-2} .

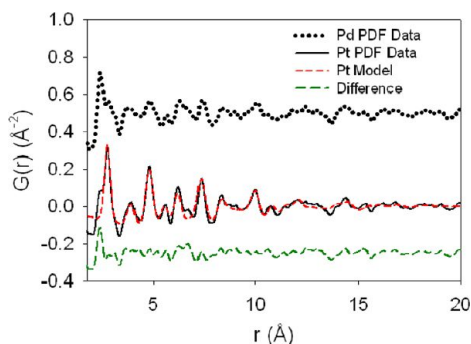


Figure 5. Atomic PDFs comparing Pt (solid black line) and Pd (dotted line), with the Pd profile vertically displaced by $+0.5 \text{ \AA}^{-2}$ for clarity. The red curve is the fit modeling the experimental PDF data to a spherically shaped fcc Pt crystal. The difference profile (green curve) between the experimental data and fit is vertically displaced by -0.25 \AA^{-2} .

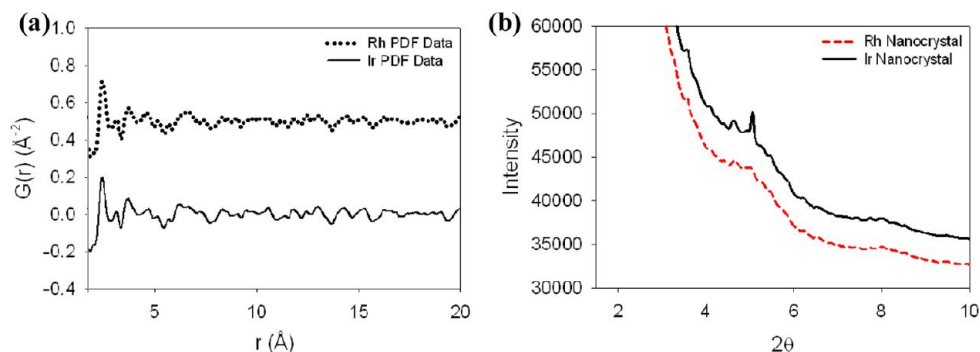


Figure 6. (a) Atomic PDFs comparing Ir (solid black line) and Rh (dotted line), with the Ir profile vertically displaced by $+0.5 \text{ \AA}^{-2}$ for clarity. (b) Un-normalized raw XRD data showing the presence of Bragg reflections in the Ir data and correspondingly absent in the Rh data.

Atomic PDF Analysis of Single-Element Nanocrystals. To ensure that the nature of the observed structural features in the 2 and 3M series can be interpreted in terms of crystallinity, we employed a total X-ray scattering based PDF technique.^{52–54} Since the PDF includes both Bragg peaks and the diffuse components of the diffraction pattern, its Fourier transform reflects both the local and average atomic structure. It is particularly sensitive to the atomic short-ranged ordering since the scattered intensities are weighted by the magnitude of their wave vectors. This makes the PDF method suitable for characterizing materials in cases where deviations from the average structure are present, such as aperiodic distortions in bulk crystal structures, nanoporous materials, and, most importantly here, finite-size, nanomaterial systems.^{52,53}

Figures 4–6 show the atomic PDF results for the six monometallic samples examined in our study. Comparing the PDFs of the 2 and 3M nanoparticles it is immediately evident that there exists a difference in the long-range order of the atom pair distances. Figure 4 directly compares the measured PDFs for the specific case of Au and Ag. The Au PDF displays multiple peaks at specific atom-pair distances extending beyond 20 Å, a value consistent with the mean particle size of the Au clusters (2.2 nm). Conversely, the PDF for Ag (dashed black line) lacks any features with significant intensity denoting recurrent atom pair distances being present in the sample. This observation is somewhat surprising considering the average particle size of the Ag specimen (3.4 nm) would lead one to expect more bulk-like structural features in clusters of this size (*i.e.*, long-ranged order, well-defined, intense pair-distance peaks, *etc.*). The lack of well-defined atom-pair contributions for the Ag samples precluded PDF modeling. The Au PDF data, however, allowed full modeling, as shown by the red curve overlying the experimental data (solid black line) in Figure 4. The structural model used in this fit was that of bulk Au, conforming to $Fm\bar{3}m$ space group constraints. Assuming a spherical particle, a spherical shape-function envelope was used to account for the effects of the

nanoparticle's finite dimensions on the PDF profile. The model structure indicated an fcc Au particle measuring 2.8 ± 0.1 nm in diameter, a value consistent with the microscopy data for this sample (2.3 ± 1.7 nm, S.I. Figure 1). The lattice parameter deduced from the fit was 4.06 ± 0.01 Å, also in excellent agreement with the microscopy and XRD findings (Table 1).

The data in Figure 5 compare the PDFs collected for the Pt and Pd samples. The Pt crystals produced multiple peaks at specific atom-pair distances extending to ~ 14 Å. The resolvable peak intensities for the Pt data (solid black line) allowed modeling of the PDF (solid red line). Similar to the case of the Au nanocrystals, a best fit was obtained for the Pt nanocrystals by refining a structure based on that of bulk Pt. A spherically shaped particle morphology was again assumed, and a spherical shape-function envelope used while considering the constraints imposed by the $Fm\bar{3}m$ space group symmetry. The particle diameter of 1.8 ± 0.1 nm calculated from the model closely matches the results obtained by microscopy (1.5 ± 0.6 nm). The lattice parameter obtained was 3.93 ± 0.01 Å, again in close agreement with the data in Table 1. The PDF of the Pd nanocrystals extends to 1.6 nm and shows lower intensity peaks (dashed black line) and less coherence with increasing r . As with the Ag data, the weaker Pd signal precludes analysis beyond assignments providing qualitative agreement with the trends observed by microscopy. It is also worth mentioning that past studies assessing the atomic structure of Pd nanoparticles using atomic PDFs also show that significant levels of disorder are present in clusters of this size.⁵⁵

The Ir and Rh data produced more complex PDF patterns than were observed for any of the other samples (Figure 6a). Although not obvious in the PDFs, the raw XRD data (Figure 6b) unambiguously shows

that the Ir nanocrystals yield more intense Bragg reflections than is seen for the Rh clusters. Even so, the data in each case precluded analysis by fitting the PDF function. On the basis of the microscopy data alone, we conclude that Ir nanoclusters are the least crystalline of the 3M metals (notably because of the significance of twinning), yet have a more coherent atomic bonding structure than its similarly sized 2M analogue.

Kinetic Analysis of the Nanocrystal Synthesis. We next considered the importance of metastable states that result from the methods of synthesis used. To do so we synthesized samples using two different methods, with one proceeding at elevated temperatures. The only similarities between the methods used were the metals investigated and the use of PVP as the capping agent. Our first procedure is based on the protocol of Tsunoyama *et al.*⁵⁶ and uses rapid reduction to produce nanomaterials with reasonably well controlled dimensions at 273 K (see Experimental Methods, Preparation of Nanocrystals). The second method used a softer reduction, where an ethylene glycol solution containing a metal salt and PVP was heated to over 415 K (S.I. Experimental Details). This should result in more thermodynamically controlled structures since the reduction proceeds more slowly and the higher temperatures allow the clusters to sample a larger structural phase space.⁵⁷ Despite these differences, no significant impacts on the structural trends were observed for the samples investigated (monometallic samples only, S.I. Figures 4 and 5). The results confirmed the structural behavior of Pt and Pd described in a previous study using C_s -STEM and XRD.⁴⁶

Chemical and Crystallographic Analysis of Binary Nanocrystals. We conducted a simultaneous reduction of neighboring metal atoms (Au–Ag, Pt–Pd, and Ir–Rh) to form intracolumn, bimetallic particles. Figure 7a shows

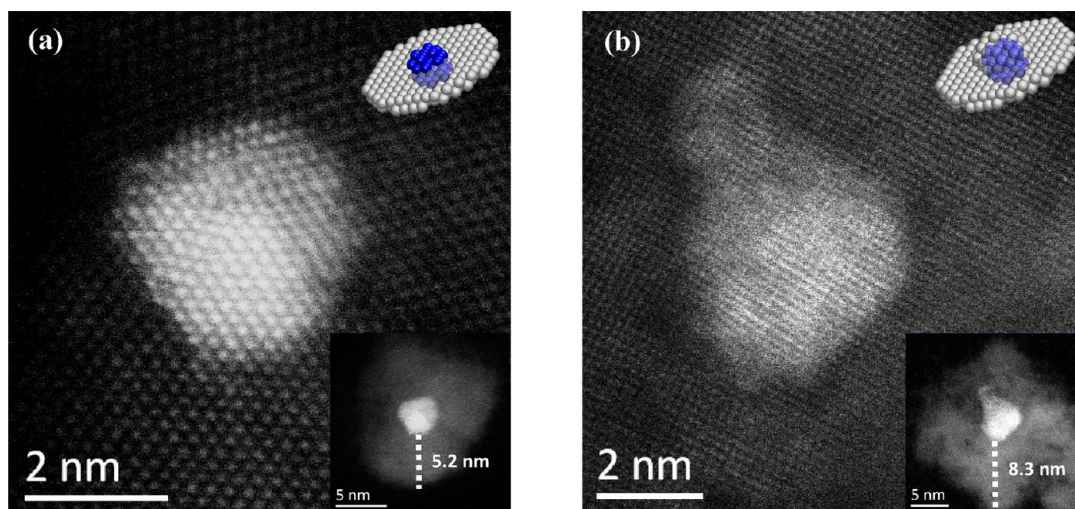


Figure 7. C_s -STEM micrographs of the bimetallic (a) Au–Ag and (b) Pt–Pd nanocrystals showing the organized atomic structure of the 2M metals (Ag and Pd) in the presence of their 3M counterparts (Au and Pt). Lower magnification images are inset in the lower right and a schematic illustration is inset on the top right. The dashed lines in the insets illustrate the extent to which the 2M metal atoms grow from the high-Z scattering 3M cluster.

that the combination of Au and Ag forms a phase-segregated structure. Energy dispersive X-ray spectroscopy (EDX) measurements indicated the presence of both Au and Ag in the individual nanoparticles (S.I. Figure 6a). In addition, the Z-contrast (achieved as a function of Rutherford scattering⁵⁸) allows discrimination of the Au and Ag enriched regions. The high intensity regions of the micrograph are due to a predominance of Au ($Z_{\text{Au}} = 79$) atoms while the less intense regions are due principally to Ag ($Z_{\text{Ag}} = 47$) atoms. Similar qualitative analytical schemes have been observed and applied in other systems.^{46,59,60} The bimetallic Pt–Pd nanocrystals (Figure 7b) show similar intensity patterns in the micrograph, where the high scattering element (Pt) was concentrated at the core and surrounded by lower scattering Pd atoms. EDX measurements further confirmed the presence of both species (S.I. Figure 6b).

Although these phase-segregated structures were frequently observed in the Au–Ag system, alloyed clusters were also found to be present (S.I. Figure 7). Interestingly, FFT analysis of the sample indicated two sets of lattice values despite the apparent coherency in the packing of the atoms. Evaluation of data from the high contrast region containing the Au core yielded a lattice parameter of $4.07 \pm 0.05 \text{ \AA}$, consistent with the quantities obtained for the monometallic Au nanocrystals (Table 1). The power spectra acquired in the low contrast regions yielded an average value of $4.14 \pm 0.01 \text{ \AA}$, closely matching the expanded lattice value determined by microscopy for monometallic Ag. Using the same FFT analysis on the homogeneously mixed Au–Ag alloys (S.I. Figure 7) a mean lattice parameter of $4.05 \pm 0.03 \text{ \AA}$ was found. This latter measurement further supports the assertion that the Ag atoms adopt the bonding habits of Au atoms when the metals are combined.

The bimetallic Pt–Pd crystals formed a series of phase-segregated structures analogous to those observed for the Au–Ag specimens (Figure 7b and S.I. Figure 8). The Pd atoms are arranged periodically

radiating away from the nucleating Pt center to distances that can exceed 8 nm (inset of Figure 7b). The lattice constants, as determined from the micrograph, were $\sim 3.92 \pm 0.04 \text{ \AA}$ and an abnormally high $4.09 \pm 0.05 \text{ \AA}$, corresponding to the high-Z and low-Z regions of the micrograph, respectively. The lattice value for the high-Z region was in line with expectations for Pt (Table 1). For the surrounding Pd atoms, however, the calculated lattice parameter far exceeded literature values for bulk Pd as well as the experimental values obtained here for the monometallic Pd nanoclusters (Table 1).

Contrary to the phase-segregated structures observed for Pt–Pd and Au–Ag, the Ir–Rh specimens exhibited only homogeneously mixed nanocrystals (S.I. Figure 9). EDX measurements confirmed the presence of both Ir and Rh within individual nanoparticles indiscriminate of cluster size. Examination of multiple images demonstrated that the qualitative features of monometallic Ir nanocrystals are prominent despite the presence of Rh atoms. Most notably, the tendency of the bimetallic nanocrystals to form a defined crystal structure at sizes below 2 nm is observed (S.I. Figure 9), with twinning emerging as the particle sizes increased. FFT analysis of the Ir–Rh crystals revealed a lattice parameter of $3.84 \pm 0.12 \text{ \AA}$. Despite the high uncertainty associated with the approximation, it does agree favorably with the lattice constant of the monometallic Ir nanocrystals (Table 1). Although the Ir–Rh system does not generate the same phase-segregated nanostructures as the Pt–Pd or Ag–Au systems, the data do re-emphasize that the presence of 3M atoms strongly affects the bonding structure exhibited by the binary composition nanocrystal.

Atomic PDF Analysis of Binary Nanocrystals. Detailed PDF modeling was carried out to shed further light on the nature of atomic bonding present in select binary compositions. Figure 8a shows the comparison in PDF profiles between the monometallic Au and the Au–Ag data (vertically shifted by $+3 \text{ \AA}^{-2}$). The arrows indicate the emergence of resolvable peaks in the bimetallic

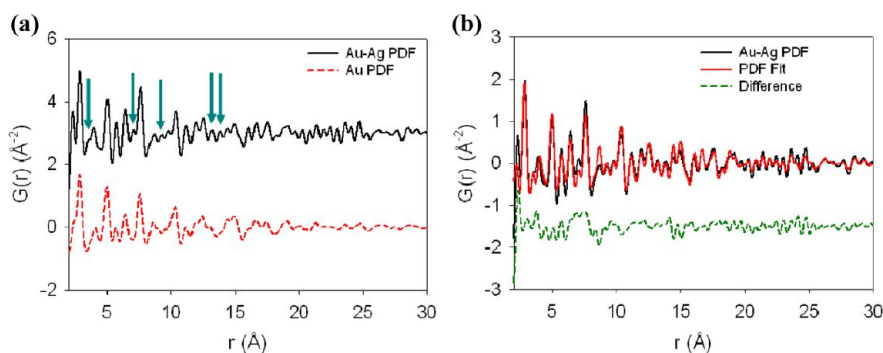


Figure 8. (a) Comparison of the atomic PDFs for the bimetallic Au–Ag (vertically displaced by $+3 \text{ \AA}^{-2}$) and the monometallic Au samples. Arrows in the bimetallic PDF highlight the emergence of new atom-pair contributions to the Au–Ag profile. (b) The experimental PDF data for the Au–Ag nanocrystals (in black) is modeled (in red) with a difference profile also shown (in green, vertically displaced by -1.5 \AA^{-2}).

sample. This indicates the attendant contributions from separate atom-pair distances not found in the elementally pure Au system, which in this case can be ascribed to the presence of Au–Ag atom pairs.

Atomic PDF modeling is essential to elucidate the role of Ag in the Au–Ag PDF profile. Although the structure in Figure 7a suggests a phase-segregated nanoparticle habit, alloy structures were also observed, necessitating consideration of both motifs during the PDF analysis. Of the two structures, PDF modeling indicated a slight preference for the formation of a biphasic system. From a more qualitative standpoint, the data indicate that the amorphous-like packing observed for the monometallic Ag is no longer present. Instead, the analysis revealed a well-ordered material analyzable using a two-phase refinement, where the model considers the crystal structure and relative scale while assuming a 1:1 ratio of each metal. The resultant fit with a two-phase model system is shown in Figure 8b accompanied by the difference profile.

The modeling results afforded measurements of the lattice parameters for both metallic species. For the Au phase a lattice constant of $4.04 \pm 0.02 \text{ \AA}$ was found, whereas the Ag phase is characterized by a lattice spacing of $4.09 \pm 0.02 \text{ \AA}$. These values agree favorably with those of bulk Ag and Au (Table 1, 4.09 and 4.08 \AA , respectively). The experimental results for the Au phase in this case suggest a compressive strain is present. The fit results indicated a mean particle diameter for the clusters of $5.3 \pm 0.2 \text{ nm}$. This value is surprising since microscopy suggests an average diameter of $12.6 \pm 4.8 \text{ nm}$ if the low-Z element is included. Interestingly, if only the diameter of the high-Z component is considered, the mean particle diameter shrinks to $5.6 \pm 1.4 \text{ nm}$ and more closely matches the value deduced in the PDF modeling.

Comparison between the monometallic Pt and the bimetallic Pt–Pd specimens revealed multiple pair distances unassignable to bulk, fcc Pt, indicated by the arrows in Figure 9a. As with the Au–Ag system, these aberrant peaks are assigned to bimetallic, Pt–Pd,

bonding. As in the earlier case, using a two-phase system for the PDF modeling (Figure 9b) produced a quality fit. Lattice constants calculated from the fit were $3.93 \pm 0.02 \text{ \AA}$ and $3.95 \pm 0.02 \text{ \AA}$ for the Pt and Pd components, respectively. Table 1 shows that the Pt fit value closely matches the bulk Pt lattice parameter. Conversely, the Pd data show a 1.5% dilation of the lattice parameter compared to the literature value of 3.89 \AA . This tensile strain was also found in the Pd microscopy and XRD derived lattice constants (Table 1) though of varying magnitude. Like Ag in the Au–Ag samples, Pd now adopts an extended, ordered habit instead of an amorphous one. PDF fit results indicated a mean particle diameter of $2.1 \pm 0.2 \text{ nm}$. Inclusion of the low-Z component when measuring the average size with microscopy gives a size of $20.7 \pm 8.2 \text{ nm}$ for the Pt–Pd nanostructures which is nearly an order of magnitude larger. This value does however closely approximate that of the high-Z Pt cluster core ($3.5 \pm 1.4 \text{ nm}$, Figure 7b).

The discrepancies in the bimetallic cluster sizes predicted for both Au–Ag and Pt–Pd when using C_s -STEM and PDF modeling are unexpected. There are two likely reasons why discrepancies of this sort might arise. First, if part of the structure lacks order it will present a broadened (and for this reason difficult to distinguish) signal in the PDF analysis, even for large nanocrystals. Given that the 2M metal shells appear in the C_s -STEM data to have structures that are very similar to the 3M cores, this prospective complication can be safely discounted. The second reason that the 2M metal shell might not contribute to the cluster size determined by the PDF analysis is if bonding present in the shell contributes a much smaller fraction of bonds at a given distance relative to those present in the 3M core. To investigate this possibility we carried out additional quantitative analyses of the binary crystal C_s -STEM micrographs.

Structural Analysis of Binary Nanocrystals. The atomic strains evidenced in the structure of the 2M metal components for the bimetallic samples of Au–Ag and

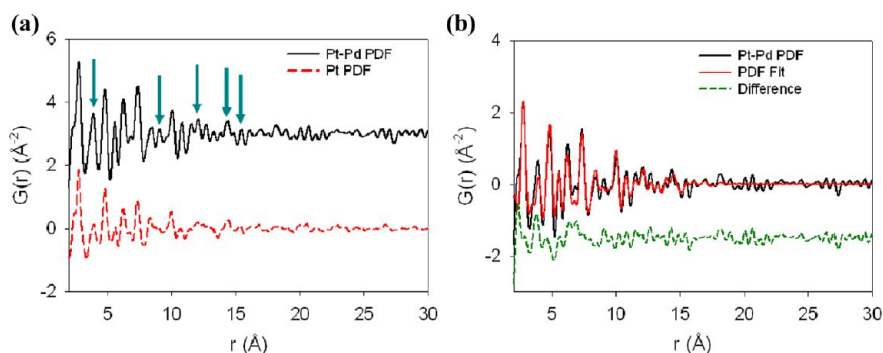


Figure 9. (a) Comparison of the atomic PDFs for the bimetallic Pt–Pd (vertically displaced by $+3 \text{ \AA}^{-2}$) and the monometallic Pt samples. Arrows in the bimetallic PDF highlight the emergence of atom-pair contributions unaccounted for in the monometallic Pt profile. (b) The experimental PDF data for the Au–Ag nanocrystals (in black) is modeled (in red) with a difference profile also shown (in green, vertically displaced by -1.5 \AA^{-2}).

Pt–Pd warrant further discussion. The atomic PDF analysis of the Au–Ag system indicated a particle size of 5.35 ± 0.2 nm. As mentioned above, this value was only appropriate if the particle dimensions were defined by the Au component of the nanostructure. To determine why structures synthesized using a 1:1 ratio of Au to Ag—and presenting such an extended structure—had such unusual behavior, an atom quantification study was conducted on these samples.

The intensity (I) observed in C_s -STEM micrographs is produced from an atomic volume (V) by a number of atoms (N) projected onto an image. This intensity scales with atomic number ($\sim Z^{1.6}$) such that,⁶¹

$$N_X \times V_X \times Z_X^{1.6} = \frac{I}{K}$$

where X represents a particular atomic species and K is a constant of proportionality. If we consider the high-contrast region to isotropically fill three-dimensions we can correlate the diameter to an approximate number of atoms. This was done by calculating the dependence of the number of atoms with respect to the diameter (S.I. Figure 10) of the monometallic Au nanocrystals (Figure 1a–c) as outlined in a previous work.⁴⁶ In doing so, we are able to correlate an atom count to an expected particle diameter. With N_{Au} , the volume of a Au atom (V_{Au} where $V_X = 4/3\pi r^3$ and $r = 0.135$ nm for the radius of a Au (or Pt) atom), and the measured I in place, N_{Ag} can be determined by equating

$$\frac{I_{Au}}{N_{Au} \times V_{Au} \times Z_{Au}^{1.6}} = \frac{I_{Ag}}{N_{Ag} \times V_{Ag} \times Z_{Ag}^{1.6}}$$

where the volume of a Ag atom (V_{Ag} ; where $r = 0.160$ nm (0.140 nm) for the Ag (Pd) atom) and atomic number (Z ; where $Z_{Au} = 79$, $Z_{Pt} = 78$, $Z_{Ag} = 47$, and $Z_{Pd} = 46$) can be obtained using literature values. The value for I_{Ag} can be determined by integrating the intensity from a region containing the low- Z component as seen in S.I. Figure 11a. Once calculated, N_{Ag} provides a scaled numerical value representing the same total volume encompassed by the integrated area. With proper background subtraction this provides a comparative method of determining whether or not the exhibited intensities are demonstrative of a similar number of atoms. The comparison can then be expanded so that aspects of structure can be inferred.

For the Au–Ag sample it was consistently found that the volume of intensity for the high intensity regions (presumably Au) encompassed a greater number of atoms than the low intensity regions (presumably Ag). This may seem intuitive as the stronger scattering Au atoms would have a greater likelihood of generating a signal into the dark-field detector. However, this highlights the significance of scaling the results by the atomic number ($Z^{1.6}$) to account for the difference in scattering power of the two elements.⁶¹ We have thus accounted for differences in the scattering

TABLE 2. Comparison of the Calculated Number of Ag Atoms to Those Determined for Au for Measured Nanoparticle. The Measured Particle Size Was Determined from the High-Z Component of the Binary Structures

atom quantification for the binary Au–Ag system		
measured particle size (nm)	no. of Au atoms, N_{Au}	calcd no. of Ag atoms, N_{Ag}
2.68	1250	394
3.75	2200	1450
3.84	2700	888
4.7	5400	1511
5.2	8300	5245
5.45	8700	2336

TABLE 3. Comparison of the Calculated Number of Pd Atoms to Those Determined for Pt for Measured Nanoparticle. The Measured Particle Size Was Determined from the High-Z Component of the Binary Structures

atom quantification for the binary Pt–Pd system		
measured particle size (nm)	no. of Pt atoms, N_{Pt}	calcd no. of Pd atoms, N_{Pd}
2.2	680	2696
2.65	700	915
4.3	3000	2015
5.3	4600	3168
5.94	5000	3033
6.55	7000	4102

strength as the source in variation between N_{Au} and N_{Ag} and present our estimates in Table 2 (N_{Pt} and N_{Pd} in Table 3). The considerable drop in atom count (going from N_{Au} to N_{Ag}) means that there are less Ag atoms inhabiting the same volume as the Au core. On the basis of the data in Table 2 we infer that the Ag atoms must adopt a low aspect ratio structure, projecting from a facet of the pre-existing Au nanocrystal (top right inset, Figure 7a). Incidentally, Figure 7a shows the presence of a twin boundary on the Au nanocrystal from which the Ag atom growth propagates. Although a more globular morphology might be expected for a solution-based synthesis, it should be noted that both Au and Ag have been shown to form nanoplates under certain growth conditions.²² In contrast, analysis of the Pt–Pd nanostructures (S.I. Figure 11b) shows growth that appears to be more globular; with the Pd sites nucleating more heterogeneously on the Pt core cluster.

Analysis of Contributions to Nanoparticle Shape. When considering the degree of crystallinity exhibited by nanoparticles, various factors are frequently implicated for the final structure observed. Some common reasons given for an observed morphology are the reduction rate, the stacking fault energy of the metal, the surface energy of the metal, and/or the presence of adsorbates. In the first case, the reduction will yield more amorphous/twinned particles or single

TABLE 4. Reduction Potentials for Ions from the Metal Salts Used in This Study^a

reaction	reduction potential (eV)
$\text{BH}_4^- + 8\text{OH}^- \leftrightarrow \text{H}_2\text{BO}_3^- + 5\text{H}_2\text{O} + 8\text{e}^-$	1.24
$\text{AuCl}_4^- + 3\text{e}^- \leftrightarrow \text{Au} + 4\text{Cl}^-$	1.002
$\text{Ag}^+ + \text{e}^- \leftrightarrow \text{Ag}$	0.7996
$\text{IrCl}_6^{2-} + \text{e}^- \leftrightarrow \text{IrCl}_6^{3-}$	0.8665
$\text{IrCl}_6^{3-} + 3\text{e}^- \leftrightarrow \text{Ir} + 4\text{Cl}^-$	0.77
$\text{PtCl}_6^{2-} + 2\text{e}^- \leftrightarrow \text{PtCl}_4^{2-} + 2\text{Cl}^-$	0.68
$\text{PtCl}_4^{2-} + 2\text{e}^- \leftrightarrow \text{Pt} + 2\text{Cl}^-$	0.755
$\text{PdCl}_4^{2-} + 2\text{e}^- \leftrightarrow \text{Pd} + 4\text{Cl}^-$	0.591
$\text{RhCl}_6^{3-} + 3\text{e}^- \leftrightarrow \text{Rh} + 6\text{Cl}^-$	0.431

^a All data were obtained from: Lide, D. R. *CRC Handbook of Chemistry and Physics*, 87th ed.; CRC Press: Boca Raton, FL, 2006. ^b RhCl_3 has multiple hydrated forms when in aqueous solution. The form given is one of the most common.

crystalline particles depending on the degree of kinetic control.^{22,23} The relative importance of kinetic formation *versus* thermodynamic stability should be reflected in how quickly the different metals are reduced.²³ Reduction potentials for the various metal ion reactants are given in Table 4.⁴⁵ A ranking of the reduction potentials that result in a metallic state gives the relative order: Au > Ag > Ir > Pt > Pd > Rh. From this it can be seen that the 3M metal atoms tend to have a higher reduction potential and are therefore expected to nucleate more quickly than the 2M metal atoms. Consequently, it would be expected that they would also be the structures most impacted by kinetics and form an array of structures. As the data above show, this is not the case.

A second possible cause for the observed trends is the stacking fault energies of the metals. Pt has a high stacking fault energy (322 mJ/m²) and is 280 mJ/m² higher than that of Au (42 mJ/m²),⁶² meaning that a higher energetic cost would be required to induce a dislocation/deformation process in a Pt crystal. This can explain why Au is seen to produce symmetrically twinned structures in particles as large as ~6 nm (S.I. Figure 2). Somewhat oddly, the stacking fault energy of Ir (480 mJ/m²)⁶² is significantly higher than that of Pt, making it more energetically costly to introduce structural imperfections into the Ir lattice despite our observation that twinning becomes more common at larger sizes. Similarly, the qualitative features seen for the Ag clusters can be explained by the relatively low stacking fault energy of Ag (20 mJ/m²), lowest among all the metals examined here) when compared to Rh (750 mJ/m²) and Pd (180 mJ/m²).⁶² Not only does the stacking fault energy of Rh exceed that of Pd, but it also does so for all of the other metals investigated (S.I. Figure 13). Yet Figure 2 shows that the 580 mJ difference in stacking fault energy (between Rh and Pd) does not lead to markedly dissimilar nanostructures. While stacking fault energies might underpin some of our observations, there clearly remain other factors that can contribute to the degree of disorder present within a nanocluster.

That leads us to consider the role that surface energies may play in dictating the final structure. Both experimental^{34,63} and theoretical³⁴ evidence confirm that the intracolumn surface energies (where surface energy is defined as the energy required to create a surface)²² of the 2M metals are lower than those of their intracolumn 3M counterparts (S.I. Figure 14). For example, the experimentally determined surface energy for the (111) surface of Au is 1.506 J/m², a value greater than that of the 1.246 J/m² found for (111) Ag.⁶³ Related differences in physical properties have also been documented in comparisons made between Pt and Pd (2.489 and 2.003 J/m², respectively)⁶³ and between Ir and Rh (3.048 and 2.659 J/m², respectively).⁶³ Theoretical studies have further extended these trends to the (100) and (110) surfaces where it has been convincingly established that the 3M specimens consistently have higher surface energies than their 2M counterparts.³⁴ It is interesting to note that the metal with the highest surface energies (Ir, *e.g.*, 3.048 J/m² for the (111) plane) readily overcomes the energetic barrier to the formation of facets, whereas the metal with the lowest surface energies (Ag, *e.g.*, 1.246 J/m² for the (111) plane) does not. Although the properties of nanomaterials will undoubtedly differ from those in a bulk state, we think it reasonable to presume that the surface energy trends will maintain their relative order even in the nanoregime. This is an important point as, to some degree, it mitigates the argument that the difference in lattice structure between the 2 and 3M nanoparticles is entirely driven by surface energetics. If this is the case, surface energetics alone cannot entirely explain the variances in crystallinity observed.

Lastly, in view of the noted effects of heteroepitaxy, the role of adsorbed species on the structures observed herein must also be taken into consideration.¹⁸ For instance, it has been shown that the chemisorption of O₂ can result in the expansion of the lattice parameter for Ag.⁶⁴ The introduction of an adsorbed species would likely reduce the surface energy required to distort/expand the relative atom pair distances.⁶⁴ Adsorbed species could be used to explain the disorder exhibited by some of the nanocrystals except that, in the presence of a secondary metal, such disorder was absent in several cases. As can be strongly inferred from the data in Figure 7a and b, adsorbed species cannot be responsible for the morphology of the particles formed.

What then is the origin of the mesoscopic structural dichotomy between the 2 and 3M particles? We believe that the differences seen in the metal-atom bonding reflect impacts on electronic structure due to relativistic effects. Briefly recounted, the inner electrons of heavy elements experience a large nuclear charge such that they must reach levels approaching the speed of light to sustain a balance with the embedded, electrostatic potential. The acceleration

results in an increase in the electron's relativistic mass and contraction of the 1s orbital.⁶⁵ These effects propagate such that they lead to a contraction of the 6s orbital, an expansion of the 5d orbitals and, consequently, impacting the use of the 5d electrons for the purposes of bonding.⁶⁵ This difference in bonding nature does not necessarily reflect a difference in bond strength; rather, it serves to rationalize the tendency for the 3M metal atoms to undergo directional bonding. This would then establish a correlation with the barrier heights associated with metal atom placements occurring at locally high symmetry (*i.e.*, directional) or more disordered sites. The correlations suggested here have in fact been used by others to account for the ground-state energetics of both nano- and surface-structural features. Regarding the former cases, experimental^{4,66} observations and theoretical calculations⁶⁷ invoking relativistic effects explain why atomic chains of the 3M metals can be formed while ones comprising metals of the 2M series cannot. Relativistic effects have also been used to explain the complex dynamics evidenced in surface reconstructions. Most notable in this regard are the now well established motifs seen in the reconstruction of the (110) and (111) facets of 3M metal crystals—structural behaviors not evidenced in crystals of the 2M metals.^{65,68}

When taken together, the current results suggest that the presence of a 3M metal atom can be used to impart its patterns of bonding to other metal atoms. This strongly implicates that the critical barriers for growth in ordered habits are strongly tied to the electronic structure, and, hence, the surface and twinning energies of the 3M atoms present. Referring back to Figure 2a–c as an exemplary case, we note the disordered structural behaviors seen in monometallic Ag nanoclusters (where both atomic PDF measurements and microscopy results both confirmed the lack of a defined crystal structure for these clusters). Introducing Au into the reaction induced (locally) ordered Ag–Ag bonding that propagates more than 5 nm beyond the critical nucleus (inset of Figure 7a). A similar pattern of order being imparted onto a growing 2M metal cluster by a 3M metal is also seen in the Pt–Pd bimetallic sample (Figure 7b). Although the bimetallic samples possess sizes larger than the range of monometallic samples investigated, the epitaxial growth exhibited here has also been observed for both bulk-like Pt–Pd structures in work by Habas *et al.*¹ and

in 2–4 nm Pt–Pd nanoparticles by Sanchez, *et al.*⁴⁶ Indeed, the latter work also revealed instances of nonuniform growth dependent upon the nucleation center. In light of the present work, we can posit that the structures seen in those works were driven by the higher surface and stacking fault energies of Pt even in the case where the shell layer was Pt. At the small sizes that we have examined, this templating appears to be true irrespective of whether the system is formed *via* thermodynamic or kinetic control.

CONCLUSIONS

This study presents information regarding the dynamics of metal atom bond formation in nanoscale materials growth. We note trends that distinguish the nanostructures formed by second and third row, fcc, transition metal series. Complex physicochemical effects underpin the formation of the distinct bonding motifs seen. The present data strongly suggest that the 3M metals function far more effectively in imparting ordered bonding characteristics than their 2M counterparts through relativistic effects that manifest themselves as surface and stacking fault energies. Specifically, the intrinsic electronic nature of Au, Pt, and Ir atoms promotes a more uniform bonding network that is sustained by additional growth species even if their natural state is more disordered. What remains unclear, at present, is the size of the critical nucleus that might be involved in this regard: the number of metal atoms that need be present in a cluster and how the complex solution phase environment comprising the growth media might serve to perturb/stabilize these structures. It remains an interesting and particular challenge to develop experimental means to explore the structural dynamics of metal atom clusters of this size at atomic resolution in the complex (and evolving) chemical environments as are found in the nucleation processes mediating growth.

Finally we note that the results reported here have important implications beyond crystal growth. Most notably, the complex nature of the bond strains seen in metal clusters of varied form (and significant deviations from bulk bonding habits) might lead to correlated impacts on the energetics of reactions carried out using materials of this form as catalysts. Such features remain very poorly understood within the current literature and form, we believe, an important forward going opportunity for future progress in research.

EXPERIMENTAL METHODS

Preparation of Nanocrystals. HAuCl₄ (FW = 339.79 g/mol), RhCl₃ (FW = 209.26 g/mol), and H₂PtCl₆·6H₂O (FW = 517.92 g/mol) were purchased from Strem Chemicals. The H₂IrCl₆·6H₂O (FW = 406.93 g/mol), AgNO₃ (FW = 169.8 g/mol), Na₂PdCl₄

(FW = 294.19 g/mol) precursors, polyvinylpyrrolidone (PVP; FW = 40 000 g/mol) and reagent grade NaBH₄ (FW = 37.83 g/mol) were purchased from Sigma-Aldrich.

The protocol used to produce the nanocrystals was adapted from the work of Tsunoyama *et al.*⁵⁶ To summarize, a typical reaction began by chilling a 0.3 mM solution of PVP in deionized

water (~50 mL) to 0 °C using an ice bath. To this solution was added 0.05 mmol of the desired metal precursor. The subsequent solution was purged with N₂ (g) for 30 min under vigorous magnetic stirring. A separate 5 mL solution of 0.1M NaBH₄ (aq) was prepared and rapidly added to the existing PVP/H₂O/metal precursor solution. The system was then allowed to react for 1 h while being maintained at 0 °C with N₂ (g) bubbling. Following synthesis, the solvent was evaporated, the samples dried, and then resuspended in ethanol and stored at ambient conditions.

In the case of the bimetallic samples the synthetic approach was unchanged with the exception that the two separate metals were simultaneously introduced into the reaction vessel. In place of the 0.05 mmol addition of one metal precursor, two 0.025 mmol equivalents of each of the different metal precursors were added to the chilled 0.3 mM PVP/H₂O solution.

Electron Microscopy. C_s-STEM samples were prepared by the dropwise addition of the prepared nanoparticle suspensions onto ultrathin holey carbon films supported on Cu-framed grids (Ted Pella, Inc.). C_s-STEM images were collected on a JEOL model 2200FS electron microscope operated at 200 keV capable of sub-angstrom resolution.⁶⁹ To prevent localized buildup of carbonaceous species (also known as “contamination”) the beam was defocused by lowering the sample height as far as possible and the sample was irradiated at low magnification for ~30 min before acquiring images for each sample. The inner-cutoff angle of the annular dark-field detector at a 60 cm camera length was 100 mrad, to ensure that no diffracted beams would interfere with the measured images. A 20 or 30 μm aperture was generally used during image acquisition to minimize the damage due to excessive radiation exposure. These aperture sizes limited the beam current to 13 and 30 pA, respectively. Additionally, the fast Fourier transform (FFT) of low magnification (~1.0 × 10⁶ times magnification, S.I. Figure 12a) images were compared to the FFT of high magnification (15.0 × 10⁶ times magnification, S.I. Figure 12b) images prior to image capture as a precautionary step to prevent the possibility of confusing beam-induced restructuring with the as-prepared structure of the nanocrystals. The microscope was also supplied with an Oxford INCA ATW detector (40 mm²) for chemically sensitive energy dispersive X-ray spectroscopy measurements.

High-resolution STEM image evaluation, FFT, or power spectrum analysis, approximation of lattice parameters, and size distribution histograms were done using DigitalMicrograph (Gatan Inc.) software. Zone axis assignments were determined by measuring the ratio of the different spatial frequencies attendant within a FFT of a micrograph and comparing them to the diffraction patterns of an fcc crystal. After establishing crystal orientation the spatial frequencies were subsequently used to index and annotate the crystal planes on the corresponding micrograph. Mean lattice parameters were calculated by using the average distances measured from the central peak to a particular spatial frequency and evaluated with respect to the indexed crystal planes. Particle sizes were determined by measuring the diameter cross-section of many individual nanoparticles.

5.2.3. High-Energy X-ray Data Collection. For the monometallic samples, X-ray total scattering measurements were carried out at beamline 11-IDC at the Advanced Photon Source (APS), Argonne National Laboratory (ANL), with high energy X-rays ($E_0 = 114.82$ keV, $\lambda = 0.108$ Å) using the rapid acquisition mode.⁷⁰ The setup utilized a 2-D image plate detector (Perkin-Elmer) positioned perpendicular to the beam path 297.14 mm away from the mounted samples. Ethanol suspensions of the nanocrystals were sealed in cylindrical kapton capillary tubes (Cole-Palmer) 1 mm in diameter. The data were collected at 300 K. The exposure time was set for 250 s for each sample.

The bimetallic samples were collected at beamline X-7B at the National Synchrotron Light Source (NSLS), Brookhaven National Laboratory (BNL), with high-energy X-ray ($E_0 = 38.94$ keV, $\lambda = 0.3184$ Å), utilizing a 2-D image plate detector (Perkin-Elmer). The detector was placed orthogonal to the beam path at distance 116.18 mm away from the mounted samples. These ethanol-suspended samples were loaded in kapton cylindrical tubes measuring 1 mm in diameter. Owing to the lower flux of

the X-ray radiation at beamline X-7B, exposure time was set for 900 s to improve the statistics of the collected data.

In both sets of experiments blank tubes (kapton) and tubes containing ethanol were simultaneously submitted for measurement for purposes of background removal.

X-ray Diffraction Analysis. For XRD analysis, the normalized, integrated data were examined without being sine Fourier transformed. Peak positions were identified using the radiation energy ($\lambda = 0.108$ Å), Bragg's law,

$$\lambda = 2d \sin\theta$$

and the inverse relationship in an fcc solid between the lattice constant, a , and interplanar distances, d

$$d = \frac{a}{\sqrt{h^2 + k^2 + l^2}}$$

where h , k , and l are the Miller indices of the corresponding Bragg planes. The h , k , and l values were determined by assignment of the spatial frequencies in the acquired power spectra.

Atomic Pair Distribution Function Analysis. The raw 2D data were integrated and converted to intensity versus 2θ using the software Fit2D,⁷¹ with 2θ as the angle of diffraction. The integrated data were corrected for experimental artifacts, normalized, and sine Fourier transformed to the PDF, $G(r)$, based on standard methods⁵⁴ using the program PDFgetX2.⁷² Modeling was performed using the PDFgui program.⁷³ The upper limit in the Fourier transform, $Q_{\text{MAX}} = 20.0$ Å⁻¹, was optimized to avoid large termination effects and to reasonably minimize the introduction of noise. This was critical since the signal-to-noise ratio decreases with increasing Q .

Conflict of Interest: The authors declare no competing financial interest.

Acknowledgment. This work was sponsored in part by the United States Department of Energy Grant No. DE-FG02-03ER15476. Experiments were conducted in part at the Frederick Seitz Materials Research Laboratory Central Facilities, University of Illinois at Urbana–Champaign, which is partially supported by the United States Department of Energy under Grant Nos. DE-FG02-07ER46453 and DE-FG02-07ER46471. Work at Brookhaven National Laboratory, which is operated for the U.S. Department of Energy by Brookhaven Science Associates, is supported by Grant No. DE-AC02-98CH10886. Research was also carried out at the Advanced Photon Source (APS) at Argonne National Laboratory. Use of APS was supported by the United States Department of Energy, Office of Science, Office of Basic Energy Sciences, under Grant No. DE-AC02-06CH11357

Supporting Information Available: Additional information was referred to at various points in the text (e.g., additional micrographs mentioned in the body of the text, energy dispersive X-ray spectra, size distribution histograms, and methodologies used to synthesize the high temperature noble metal nanoparticles). This material is available free of charge via the Internet at <http://pubs.acs.org>.

REFERENCES AND NOTES

- Habas, S.; Lee, H.; Radmilovic, V.; Somorjai, G. A.; Yang, P. Shaping Binary Metal Nanocrystals through Epitaxial Seeded Growth. *Nature* **2007**, *6*, 692–697.
- Lee, H.; Habas, S. E.; Kweskin, S.; Butcher, D.; Somorjai, G. A.; Yang, P. Morphological Control of Catalytically Active Platinum. *Angew. Chem., Int. Ed.* **2006**, *45*, 7824–7828.
- Narayanan, R.; El-Sayed, M. A. Catalysis with Transition Metal Nanoparticles in Colloidal Solution: Nanoparticle Shape Dependence and Stability. *J. Phys. Chem. B* **2005**, *109*, 12663–12676.
- Ohnishi, H.; Kondo, Y.; Takayanagi, K. Quantized Conductance through Individual Rows of Suspended Gold Atoms. *Nature* **1998**, *395*, 780–783.
- Rao, C. N. R.; Sood, A. K.; Subrahmanyam, K. S.; Govindaraj, A. Graphene: The New Two-Dimensional Nanomaterial. *Angew. Chem., Int. Ed.* **2009**, *48*, 7752–7777.

6. Gao, H.; Ji, B.; Jager, I. L.; Artz, E.; Fratzl, P. Materials Become Insensitive to Flaws at Nanoscale: Lessons from Nature. *Proc. Natl. Acad. Sci. U.S.A.* **2003**, *100*, 5597–5600.
7. Nel, A. E.; Madler, L.; Velegol, D.; Xia, T.; Hoek, E. M. V.; Somasundaran, P.; Klaessig, F.; Castranova, V.; Thompson, M. Understanding Biophysicochemical Interactions at the Nano-Bio Interface. *Nature* **2009**, *8*, 543–557.
8. Rogers, J. A.; Lagally, M. G.; Nuzzo, R. G. Synthesis, Assembly and Applications of Semiconductor Nanomembranes. *Nature* **2011**, *477*, 45–53.
9. Roder, H.; Hahn, E.; Brune, H.; Bucher, J.-P.; Kern, K. Building One- and Two-Dimensional Nanostructures by Diffusion-Controlled Aggregation at Surfaces. *Nature* **1993**, *366*, 141–143.
10. Brune, H.; Giovannini, M.; Bromann, K.; Kern, K. Self-Organized Growth of Nanostructure Arrays on Strain-Relief Patterns. *Nature* **1998**, *394*, 451–453.
11. Goldberger, J.; He, R.; Zhang, Y.; Lee, S.; Yan, H.; Choi, H.-J.; Yang, P. Single-Crystal Gallium Nitride Nanotubes. *Nature* **2003**, *422*, 599–602.
12. Tian, Z. R.; Voigt, J. A.; Liu, J.; Mckenzie, B.; Mcdermott, M. J. Biomimetic Arrays of Oriented Helical ZnO Nanorods and Columns. *J. Am. Chem. Soc.* **2002**, *124*, 12954–12955.
13. Marks, L. D. Experimental Studies of Small Particle Structures. *Rep. Prog. Phys.* **1994**, *57*, 603–649.
14. Sato, K.; Huang, W. J.; Bohra, F.; Sivaramakrishnan, S.; Tedjasaputra, A. P.; Zuo, J. M. Size-Dependent Structural Transition from Multiple-Twinned Particles to Epitaxial fcc Nanocrystals and Nanocrystal Decay. *Phys. Rev. B* **2007**, *76*, 144113.
15. Bratlie, K. M.; Lee, H.; Komvopoulos, K.; Yang, P.; Somorjai, G. A. Platinum Nanoparticle Shape Effects on Benzene Hydrogenation Selectivity. *Nano Lett.* **2007**, *7*, 3097–3101.
16. Chen, J.; Lim, B.; Lee, E.; Xia, Y. Shape-Controlled Synthesis of Platinum Nanocrystals for Catalytic and Electrocatalytic Applications. *Nano Today* **2009**, *4*, 81–95.
17. Narayanan, R.; Tabor, C.; El-Sayed, M. A. Can the Observed Changes in the Size or Shape of a Colloidal Nanocatalyst Reveal the Nanocatalysis Mechanism Type: Homogeneous or Heterogeneous? *Top. Catal.* **2008**, *48*, 60–74.
18. An, K.; Somorjai, G. A. Size and Shape Control of Metal Nanoparticles for Reaction Selectivity in Catalysis. *ChemCatChem* **2012**, *4*, 1512–1524.
19. Huang, W. J.; Sun, R.; Tao, J.; Menard, L. D.; Nuzzo, R. G.; Zuo, J. M. Coordination-Dependent Surface Atomic Contraction in Nanocrystals Revealed by Coherent Diffraction. *Nat. Mater.* **2008**, *7*, 308–313.
20. Sanchez, S. I.; Small, M. W.; Sivaramakrishnan, S.; Wen, J. G.; Zuo, J. M.; Nuzzo, R. G. Visualizing Materials Chemistry at Atomic Resolution. *Anal. Chem.* **2010**, *82*, 2599.
21. Sanchez, S. I.; Menard, L. D.; Bram, A.; Kang, J. H.; Small, M. W.; Nuzzo, R. G.; Frenkel, A. I. The Emergence of Nonbulk Properties in Supported Metal Clusters: Negative Thermal Expansion and Atomic Disorder in Pt Nanoclusters Supported on Γ - Al_2O_3 . *J. Am. Chem. Soc.* **2009**, *131*, 7040.
22. Xia, Y.; Xiong, Y.; Lim, B.; Skrabalak, S. E. Shape-Controlled Synthesis of Metal Nanocrystals: Simple Chemistry Meets Complex Physics? *Angew. Chem., Int. Ed.* **2009**, *48*, 60–103.
23. Tao, A. R.; Habas, S.; Yang, P. Shape Control of Colloidal Metal Nanocrystals. *Small* **2008**, *4*, 310–325.
24. Henry, C. R. Morphology of Supported Nanoparticles. *Prog. Surf. Sci.* **2005**, *80*, 92–116.
25. Huang, X.; Tang, S.; Mu, X.; Dai, Y.; Chen, G.; Zhou, Z.; Ruan, F.; Yang, Z.; Zheng, N. Freestanding Palladium Nanosheets with Plasmonic and Catalytic Properties. *Nat. Nanotechnol.* **2011**, *6*, 28–32.
26. Jiang, H.-L.; Akita, T.; Ishida, T.; Haruta, M.; Xu, Q. Synergistic Catalysis of Au@Ag Core-Shell Nanoparticles Stabilized on Metal–Organic Framework. *J. Am. Chem. Soc.* **2011**, *133*, 1304–1305.
27. Shao, M. H.; Huang, T.; Liu, P.; Zhang, J.; Sasaki, K.; Vukmirovic, M. B.; Adzic, R. R. Palladium Monolayer and Palladium Alloy Electrocatalysts for Oxygen Reduction. *Langmuir* **2006**, *22*, 10409–10415.
28. Negreiros, F. R.; Soares, E. A.; de Carvalho, V. E. Energetics of Free Pure Metallic Nanoclusters with Different Motifs by Equivalent Crystal Theory. *Phys. Rev. B* **2007**, *76*, 205429–1/205429–11.
29. Mays, C. W.; Vermaak, J. S.; Wilsdorf, D. K. On Surface Stress and Surface Tension: II. Determination of the Surface Stress of Gold. *Surf. Sci.* **1968**, *12*, 134–140.
30. Vermaak, J. S.; Mays, C. W.; Kuhlmann-Wilsdorf, D. On Surface Stress and Surface Tension: I. Theoretical Calculations. *Surf. Sci.* **1968**, *12*, 128–133.
31. Callister, W. *Materials Science and Engineering—An Introduction*, 7th ed. ed.; Wiley: New York, 2006; p 84.
32. Stokes, R. J.; Evans, D. F. *Fundamentals of Interfacial Engineering*; Wiley-VCH: New York, 1997.
33. Van Hove, M. A.; Tong, S. Y. *The Structure of Surfaces*; Springer: New York, 1985; p 435.
34. Vitos, L.; Ruban, A. V.; Skriver, H. L.; Kollar, J. The Surface Energy of Metals. *Surf. Sci.* **1998**, *411*, 186–202.
35. Yang, Y.; Matsubara, S.; Xiong, L.; Hayakawa, T.; Nogami, M. Solvothermal Synthesis of Multiple Shapes of Silver Nanoparticles and Their SERS Properties. *J. Phys. Chem. C* **2007**, *111*, 9095–9104.
36. Zhu, J.; Shen, Y.; Xie, A.; Qiu, L.; Zhang, Q.; Zhang, S. Photoinduced Synthesis of Anisotropic Gold Nanoparticles in Room-Temperature Ionic Liquid. *J. Phys. Chem. C* **2007**, *111*, 7629–7633.
37. Templeton, A. C.; Chen, S.; Gross, S. M.; Murray, R. W. Water-Soluble, Isolable Gold Clusters Protected by Tiopronin and Coenzyme a Monolayers. *Langmuir* **1999**, *15*, 66–76.
38. Frenkel, A. I.; Nemzer, S.; Pister, I.; Soussan, L.; Harris, T.; Sun, Y.; Rafailovich, M. H. Size-Controlled Synthesis and Characterization of Thiol-Stabilized Gold Nanoparticles. *J. Chem. Phys.* **2005**, *123*, 184701–1–184701–6.
39. Teranishi, T.; Hosoe, M.; Miyake, M. Formation of Mono-dispersed Ultrafine Platinum and Their Electrophoretic Deposition on Electrodes. *Adv. Mater.* **1997**, *9*, 65–67.
40. Baker, L. R.; Kennedy, G.; Krier, J. M.; Van Spronsen, M.; Onorato, R. M.; Somorjai, G. A. The Role of an Organic Cap in Nanoparticle Catalysis: Reversible Restructuring of Carbonaceous Material Controls Catalytic Activity of Platinum Nanoparticles for Ethylene Hydrogenation and Methanol Oxidation. *Catal. Lett.* **2012**, *142*, 1286–1294.
41. Dykeman, R. R.; Yuan, Y.; Yan, N.; Asakura, H.; Teramura, K.; Tanaka, T.; Dyson, P. J. Rational Design of a Molecular Nanocatalyst-Stabilizer That Enhances Both Catalytic Activity and Nanoparticle Stability. *ChemCatChem* **2012**, *4*, 1907–1910.
42. Krier, J. M.; Michalak, W. D.; Baker, L. R.; An, K.; Komvopoulos, K.; Somorjai, G. A. Sum Frequency Generation Vibrational Spectroscopy of Colloidal Platinum Nanoparticle Catalysts: Disordering versus Removal of Organic Capping. *J. Phys. Chem. C* **2012**, *116*, 17540–17546.
43. Peng, Z.; Yang, H. Synthesis and Oxygen Reduction Electrocatalytic Property of Pt-on-Pd Bimetallic Heteronanostructures. *J. Am. Chem. Soc.* **2009**, *131*, 7542–7543.
44. Grzelczak, M.; Perez-Juste, J.; Mulvaney, P.; Liz-Marzan, L. M. Shape Control in Gold Nanoparticle Synthesis. *Chem. Soc. Rev.* **2008**, *37*, 1783–1791.
45. *CRC Handbook of Chemistry and Physics*, 75 ed.; CRC Press: Boca Raton, 1995.
46. Sanchez, S.; Small, M.; Zuo, J.-M.; Nuzzo, R. G. Structural Characterization of Pt–Pd and Pd–Pt Core–Shell Nanoclusters at Atomic Resolution. *J. Am. Chem. Soc.* **2009**, *131*, 8683–8689.
47. Yang, X. C.; Dubiel, M.; Brunsch, S.; Hofmeister, H. X-Ray Absorption Spectroscopy Analysis of Formation and Structure of Ag Nanoparticles in Soda-Lime Silicate Glass. *J. Non-Cryst. Sol.* **2003**, *328*, 123–136.
48. Sun, Y.; Frenkel, A. I.; Isseroff, R.; Shonburn, C.; Forman, M.; Shin, K.; Koga, T.; White, H.; Zhang, L.; Zhu, Y.; Rafailovich, M. H.; Sokolov, J. C. Characterization of Palladium Nanoparticles by Using X-ray Reflectivity, EXAFS, and Electron Microscopy. *Langmuir* **2006**, *22*, 807–816.
49. Lamber, R.; Wetjen, S.; Jaeger, N. I. Size Dependence of the Lattice Parameter of Small Palladium Particles. *Phys. Rev. B* **1995**, *51*, 10968–10971.

50. Teranishi, T.; Miyake, M. Size Control of Palladium Nanoparticles and Their Crystal Structures. *Chem. Mater.* **1998**, *10*, 594–600.
51. Jeon, Y. T.; Lee, G. H. Magnetism of the fcc Rh and Pd Nanoparticles. *J. Appl. Phys.* **2008**, *103*, 094313–1–094313–5.
52. Petkov, V.; Billinge, S. J. L.; Heising, J.; Kanatzidis, M. G. Application of Atomic Pair Distribution Function Analysis to Materials with Intrinsic Disorder. Three-Dimensional Structure of Exfoliated-Restacked WS_2 : Not Just a Random Turbostratic Assembly of Layers. *J. Am. Chem. Soc.* **2000**, *122*, 11571–11576.
53. Billinge, S. J. L.; Kanatzidis, M. G. Beyond Crystallography: The Study of Disorder, Nanocrystallinity and Crystallography Challenged Materials with Pair Distribution Functions. *Chem. Commun.* **2004**, 749–760.
54. Egami, T.; Billinge, S. J. L. *Underneath the Bragg Peaks: Structural Analysis of Complex Materials*; Pergamon Press: Oxford, 2003; Vol. 7.
55. Petkov, V.; Ohta, T.; Hou, Y.; Ren, Y. Atomic-Scale Structure of Nanocrystals by High-Energy X-ray Diffraction and Atomic Pair Distribution Function Analysis: Study of Fe_xPd_{100-x} ($x = 0, 26, 28, 48$) Nanoparticles. *J. Phys. Chem. C* **2007**, *111*, 714–720.
56. Tsunoyama, H.; Sakurai, H.; Negishi, Y.; Tsukuda, T. Size-Specific Catalytic Activity of Polymer-Stabilized Gold Nanoclusters for Aerobic Alcohol Oxidation in Water. *J. Am. Chem. Soc.* **2005**, *127*, 9374–9375.
57. Wiley, B.; Sun, Y.; Xia, Y. Synthesis of Silver Nanostructures with Controlled Shapes and Properties. *Acc. Chem. Res.* **2007**, *40*, 1067–1076.
58. Williams, D. B.; Carter, B. C. *Transmission Electron Microscopy: Basics*; Springer Science+Business Media Inc.: New York, 1996.
59. Rosenthal, S.; McBride, J.; Pennycook, S.; Feldman, L. Synthesis, Surface Studies, Composition and Structural Characterization of CdSe, Core/Shell and Biologically Active Nanocrystals. *Surf. Sci. Rep.* **2007**, *62*, 111.
60. Wang, J. X.; Inada, H.; Wu, L.; Zhu, Y.; Choi, Y.-M.; Liu, P.; Zhou, W.-P.; Adzic, R. R. Oxygen Reduction on Well-Defined Core–Shell Nanocatalysts: Particle Size, Facet, and Pt Shell Thickness Effects. *J. Am. Chem. Soc.* **2009**, *131*, 17298–17302.
61. Krivanek, O. L.; Chisholm, M. F.; Nicolosi, V.; Pennycook, T. J.; Corbin, G. J.; Dellby, N.; Murfitt, M. F.; Own, C. S.; Szilagy, Z. S.; Oxley, M. P.; Pantelides, S. T.; Pennycook, S. J. Atom-by-Atom Structural and Chemical Analysis by Annular Dark-Field Electron Microscopy. *Nature* **2010**, *464*, 571.
62. Rosengaard, N. M.; Skriver, H. L. Calculated Stacking-Fault Energies of Elemental Metals. *Phys. Rev. B* **1993**, *47*, 12865–12873.
63. Tyson, W. R.; Miller, W. A. Surface Free Energies of Solid Metals: Estimation from Liquid Surface Tension Measurements. *Surf. Sci.* **1977**, *62*, 267–276.
64. Hu, J.; Cai, W.; Li, C.; Gan, Y.; Chen, L. *In Situ* X-ray Diffraction Study of the Thermal Expansion of Silver Nanoparticles in Ambient Air and Vacuum. *Appl. Phys. Lett.* **2005**, *86*, 151915–1–151915–3.
65. Bond, G. C. Relativistic Effects in Coordination, Chemisorption and Catalysis. *J. Mol. Catal. A* **2000**, *156*, 1–20.
66. Smit, R. H. M.; Untiedt, C.; Yanson, A. I.; van Ruitenbeek, J. M. Common Origin for Surface Reconstruction and the Formation of Chains of Metal Atoms. *Phys. Rev. Lett.* **2001**, *87*, 266102.
67. Bahn, S. R.; Jacobson, K. W. Chain Formation of Metal Atoms. *Phys. Rev. Lett.* **2001**, *87*, 266101.
68. Takeuchi, N.; Chan, C. T.; Ho, K. M. Reconstruction of the (100) Surfaces of Au and Ag. *Phys. Rev. B* **1991**, *43*, 14363–14370.
69. Wen, J.-G.; Mabon, J.; Lei, C. H.; Burdin, S.; Sammann, E.; Petrov, I.; Shah, A. B.; Chobpattana, V.; Zhang, J.; Ran, K.; Zuo, J.-M.; Mishina, S.; Aoki, T. The Formation and Utility of Sub-angstrom to Nanometer-Sized Electron Probes in the Aberration-Corrected Transmission Electron Microscope at the University of Illinois. *Microsc. Microanal.* **2010**, *16*, 183–193.
70. Chupas, P. J.; Qiu, X.; Hanson, J. C.; Lee, P. L.; Grey, C. P.; Billinge, S. J. L. Rapid Acquisition Pair Distribution Function Analysis (RA-PDF). *J. Appl. Crystallogr.* **2003**, *36*, 1342–1347.
71. Hammersley, A. P.; Svenson, S. O.; Hanfland, M.; Hauserman, D. Two-Dimensional Detector Software: From Real Detector to Idealised Image or Two-Theta Scan. *High Press. Res.* **1996**, *14*, 235.
72. Qiu, X.; Thompson, J. W.; Billinge, S. J. L. PDFgetX2: A Gui-Driven Program to Obtain the Pair Distribution Function from X-ray Powder Diffraction Data. *J. Appl. Crystallogr.* **2004**, *37*, 678.
73. Farrow, C. L.; Juhas, P.; Liu, J. W.; Bryndin, D.; Bozin, E. S.; Bloch, J.; Proffen, T.; Billinge, S. J. L. PDFfit2 and PDFgui: Computer Programs for Studying Nanostructure in Crystals. *J. Phys.: Condens. Matter* **2007**, *19*, 335219–1–335219–7.

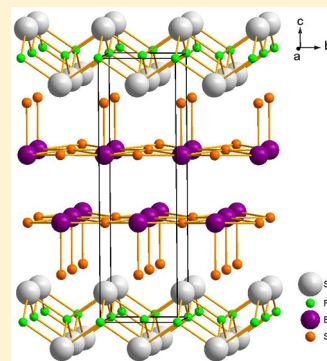
New Layered Fluorosulfide SrFBiS₂

Hechang Lei, Kefeng Wang, Milinda Abeykoon, Emil S. Bozin, and Cedomir Petrovic*

Condensed Matter Physics and Materials Science Department, Brookhaven National Laboratory, Upton, New York 11973, United States

Supporting Information

ABSTRACT: We have synthesized a new layered BiS₂-based compound, SrFBiS₂. This compound has a similar structure to LaOBiS₂. It is built up by stacking up SrF layers and NaCl-type BiS₂ layers alternatively along the *c* axis. Electric transport measurement indicates that SrFBiS₂ is a semiconductor. Thermal transport measurement shows that SrFBiS₂ has a small thermal conductivity and large Seebeck coefficient. First principle calculations are in agreement with experimental results and show that SrFBiS₂ is very similar to LaOBiS₂, which becomes a superconductor with F doping. Therefore, SrFBiS₂ may be a parent compound of new superconductors.



INTRODUCTION

Low-dimensional superconductors with layered structure have been extensively studied and still attract much interest due to their exotic superconducting properties and mechanism when compared to conventional BCS superconductors. The examples include high *T_c* cuprates,¹ Sr₂RuO₄,² Na_xCoO₂·H₂O,³ and iron-based superconductors.⁴ The discovery of LnOFePn (Ln = rare earth elements, Pn = P, As) in particular revitalizes the study of layered compounds with mixed anions, paving a way to materials with novel physical properties. For example, Ln₂O₂TM₂OCh₂ (TM = transition metals, Ch = S, Se) show strong electron–electron interactions and Mott insulating state on the two-dimensional (2D) frustrated antiferromagnetic (AFM) checkerboard spin–lattice.^{5–9} Very recently, bulk superconductivity was found in BiS₂-type layered compounds with mixed anions: Bi₄O₄S₃ and Ln(O,F)BiS₂.^{10–12} Experimental and theoretical studies indicate that these materials exhibit multiband behaviors with dominant electron carriers originating from the Bi *6p_x* and *6p_y* bands in the normal state.^{13–16} On the other hand, compounds with mixed anions exhibit remarkable flexibility of structure. Different two-dimensional (2D) building blocks, such as [LnO]⁺, [AEF]⁺ (AE = Ca, Sr, Ba), [Ti₂OPn₂]²⁻, [FePn]⁻, and [TM₂OCh₂]²⁻, can sometimes be integrated to form new materials.^{4,17–21} Individual building blocks often keep their structural and electronic properties after being combined together.¹⁹

In this work, we report the discovery of a new BiS₂-based layered compound, SrFBiS₂. It contains a NaCl-type BiS₂ layer and shows semiconducting behavior with relatively large thermopower. Theoretical calculations indicate that this compound is very similar to LnOBiS₂.

EXPERIMENT SECTION

Synthesis. SrFBiS₂ polycrystals were synthesized by a two-step solid-state reaction. First, Bi₂S₃ was prereacted by reacting Bi needles (purity 99.99%, Alfa Aesar) with sulfur flakes (purity 99.99%, Aldrich) in an evacuated quartz tube at 600°C for 10 h. Then Bi₂S₃ was mixed with stoichiometric SrF₂ (purity 99%, Alfa Aesar) and SrS (purity 99.9%, Alfa Aesar) and intimately ground together using an agate pestle and mortar. The ground powder was pressed into 10 mm diameter pellets. We used a maximum pressure of 5 tons. The pressed pellet was loaded in an alumina crucible and then sealed in quartz tubes with Ar under the pressure of 0.15 atm. The quartz tubes were heated to 600°C in 10 h and kept at 600°C for another 10 h.

Structure and Composition Analysis. Phase identity and purity were confirmed by powder X-ray diffraction carried out by a Rigaku Miniflex X-ray machine with Cu K α radiation ($\lambda = 1.5418 \text{ \AA}$). Structural refinement of powder SrFBiS₂ sample was carried out by using Rietica software.²² Synchrotron X-ray experiment was conducted at 300 K on a X17A beamline of the National Synchrotron Light Source (NSLS) at Brookhaven National Laboratory (BNL). The setup utilized a X-ray beam 0.5 mm \times 0.5 mm in size and $\lambda = 0.1839 \text{ \AA}$ ($E = 67.4959 \text{ keV}$), conditioned by two-axis focusing with a one-bounce sagittally bent Laue crystal monochromator and Perkin-Elmer image plate detector mounted perpendicular to the primary beam path. A finely pulverized sample packed in a cylindrical polyimide capillary 1 mm in diameter was placed 204 mm away from the detector. Multiple scans were performed to a total exposure time of 120 s. The 2D diffraction data were integrated and converted to intensity versus 2θ using the software FIT2D.²³ The intensity data were corrected and normalized and converted to atomic pair distribution function (PDF), $G(r)$, using the program PDFgetX2.²⁴ The average stoichiometry of a SrFBiS₂ polycrystal was determined by examination of multiple points using an energy-dispersive X-ray spectroscopy (EDX) in a JEOL JSM-6500 scanning electron microscope.

Received: July 14, 2013

Published: August 29, 2013

Electrical and Thermal Transport Measurements. The sample pellets were cut into rectangular bars, and the surface is polished by sandpaper. Thin Pt wires were attached using silver epoxy for four probe resistivity measurements. Electrical and thermal transport measurements were carried out in quantum design physical property measurement system (PPMS-9).

Band Structure Calculations. First principle electronic structure calculations were performed using experimental crystallographic parameters within the full-potential linearized augmented plane wave (LAPW) method²⁵ implemented in the WIEN2k package.²⁶ The general gradient approximation (GGA) of Perdew et al.,²⁷ was used for exchange-correlation potential. The LAPW sphere radius were set to 2.5 Bohr for all atoms, and the converged basis corresponding to $R_{\min}k_{\max} = 7$ with additional local orbital were used, where R_{\min} is the minimum LAPW sphere radius and k_{\max} is the plane wave cutoff.

RESULTS AND DISCUSSION

Structure and Composition. Figure 1(a) shows the powder XRD pattern of SrFBiS₂ measured by Rigaku Miniflex. Almost all of reflections can be indexed using the $P4/nmm$ space group. The unidentified peaks belong to the second phase of Bi₂S₃. Using two-phase Le Bail fitting, the refined lattice parameters of SrFBiS₂ are $a = 4.084(2)$ Å and $c = 13.798(2)$ Å. When compared to LaOBiS₂, the a -axial lattice parameter is larger, and the c -axial one is slightly smaller.¹¹ The PDF structural analysis was carried out using the program PDFgui.²⁸ The SrFBiS₂ data are explained well within the model having $P4/nmm$ symmetry with $a = 4.079(2)$ Å and $c = 13.814(5)$ Å ($R_{\text{wp}} = 0.138$, $\chi^2 = 0.024$). It is consistent with the fitting results obtained from Miniflex. The final fit is shown in Figure 1(b), and the results are summarized in Table 1. In addition to the principal phase, the sample is found to have ~16(1) wt % of Bi₂S₃ impurity with $Pnma$ symmetry, which is also observed in Figure 1(a). The structure of SrFBiS₂ is similar to LaOBiS₂, which is built up by stacking the rock salt-type BiS₂ layer and fluorite-type SrF layer alternatively along the c axis as shown Figure 1(c). The EDX spectrum of polycrystal confirms the presence of Sr, F, Bi, and S. The average atomic ratios determined from EDX are Sr:F:Bi:S = 1.00(4):1.00(9):1.03(5):1.88(4) when setting the content of Sr as 1. It confirms the formula of obtained compound is SrFBiS₂.

Electrical Properties. As shown in Figure 2, the resistivity $\rho(T)$ of SrFBiS₂ polycrystalline shows a semiconducting behavior in the measured temperature region (1.9–300 K). It should be noted that Bi₂S₃ polycrystal shows metallic behavior because of sulfur deficiency.²⁹ The impurity may have some minor influence on the absolute value of resistivity, but the semiconducting behavior should be intrinsic. Neglecting the grain boundary contribution, the room-temperature resistivity $\rho(300 \text{ K})$ is about 0.5 Ω cm. Using the thermal activation model $\rho_{\text{ab}}(T) = \rho_0 \exp(E_a/k_B T)$ (ρ_0 is a prefactor, E_a thermal activated energy, and k_B the Boltzmann's constant) to fit the $\rho(T)$ at high temperature (75–300 K) (inset of Figure 2), we obtain $E_a = 31.8(3)$ meV. The semiconductor behavior is consistent with theoretical calculation result shown below. On the other hand, theoretical calculations have indicated that undoped LaOBiS₂ is also a semiconductor, which is partially consistent with the experimental result.^{13,30} The transport measurement indicates that LaOBiS₂ shows semiconducting behavior at $T < 200$ K but exhibit an upturn of resistivity at higher temperature. The origin of the upturn is unclear. Therefore, the replacement of LaO by SrF should not change the band structure and thus physical properties too much,

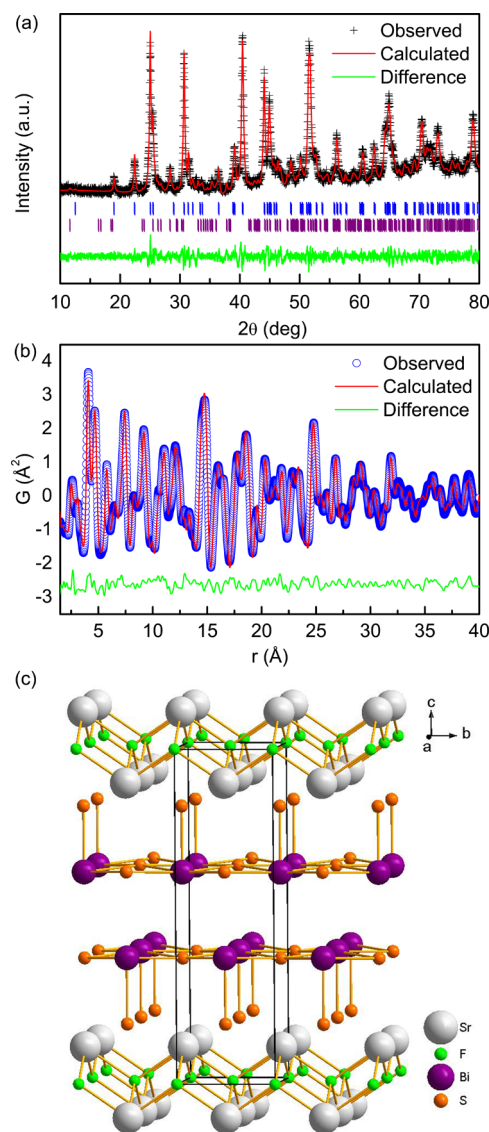


Figure 1. (a) Powder XRD pattern of SrFBiS₂ and the fitted result using two-phase Le Bail fitting. Crosses are experimental data. Red line is fitted spectra. Green line is the difference between experimental data and fitted spectra. Vertical lines are calculated Bragg positions for SrFBiS₂ (upper) and Bi₂S₃ (lower), respectively. (b) Synchrotron PDF refinement of data taken at room temperature. (c) Crystal structure of SrFBiS₂. The biggest white, big purple, medium orange, and small green balls represent Sr, Bi, S, and F ions, respectively.

especially at low temperature, similar to the relation between SrFFeAs and LaOFeAs.^{18,31} The slight differences between LaOBiS₂ and SrFBiS₂, such as larger a -axial and smaller c -axial lattice parameters, could result in changing of physical properties at higher temperature. Note that the semiconducting $\rho(T)$ in LaOBiS₂ and SrFBiS₂ are different from those in parent compounds of iron pnictide superconductors. The latter show metallic behaviors at high temperature and a semiconducting-like upturn in the resistivity curve related to the spin density wave (SDW) transition. There is no significant magnetoresistance in SrFBiS₂ up to 90 kOe magnetic field.

Thermal Transport Properties. The temperature dependences of the thermal conductivity $\kappa(T)$ and thermoelectric power (TEP) $S(T)$ for SrFBiS₂ in zero field between 2 and 350 K are shown in Figure 3. The electronic thermal conductivity

Table 1. Crystallographic Data for SrFBiS₂ Obtained from Synchrotron Powder XRD

chemical formula	SrFBiS ₂				
formula mass (g/mol)	379.73				
crystal system	tetragonal				
space group	P4/nmm (No. 129)				
<i>a</i> (Å)	4.079(2)				
<i>c</i> (Å)	13.814(5)				
<i>V</i> (Å ³)	229.8(3)				
<i>Z</i>	2				
density (g/cm ³)	5.51				
atom	site	<i>x</i>	<i>y</i>	<i>z</i>	<i>U</i> _{eq} (Å ²) ^a
Sr	2c	1/4	1/4	0.1025(2)	0.0069(4)
F	2a	3/4	1/4	0	0.033(2)
Bi	2c	1/4	1/4	0.6286(5)	0.0183(3)
S1	2c	1/4	1/4	0.379(3)	0.060(2)
S2	2c	1/4	1/4	0.811(2)	0.019(1)

^a*U*_{eq} is defined as one-third of the orthogonalized *U*_{ij} tensor.

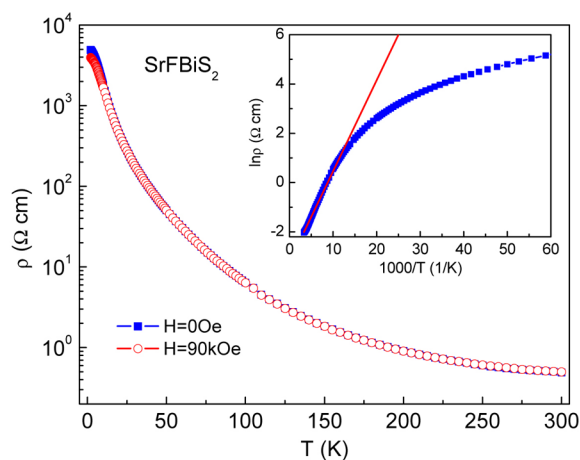


Figure 2. Temperature dependence of the resistivity $\rho(T)$ of the SrFBiS₂ at $H = 0$ (closed blue squares) and 90 kOe (open red circles). Inset shows the fitted result using thermal activation model for $\rho(T)$ at zero field, where the red line is the fitting curve.

$\kappa_e(T)$ estimated from the Wiedemann–Franz law using a value for the Lorenz number of $2.44 \times 10^{-8} \text{ W } \Omega/\text{K}^2$ was less than 5×10^{-6} of $\kappa(T)$. Therefore, lattice thermal conductivity dominates $\kappa_e(T)$, which exhibits a peak at around 60 K (Figure 1(a)). The peak in $\kappa(T)$ commonly arises because different phonon scattering processes usually dominate in different temperature ranges. Umklapp scattering dominates at high temperatures, while boundary and point-defect scattering dominate at low and intermediate temperatures, respectively.³² On the other hand, the $\kappa(T)$ of SrFBiS₂ shows similar behavior to Bi₄O₄S₃ but with different peak position and absolute value.¹⁶ For TEP $S(T)$ of SrFBiS₂, there is a reversal in sign at about 11 K, i.e., hole-like carrier changes into electron-like carrier, which is dominant at room temperature. According to two band model, $S = |S_h|\sigma_h - |S_e|\sigma_e/(\sigma_e + \sigma_h)$.¹⁶ If we assume that S_h and S_e are temperature independent, it suggests that electron and hole conductivities change dramatically with temperature: at low temperature, $\sigma_h > \sigma_e$ whereas $\sigma_e > \sigma_h$ above 11 K. Hole-like carriers may originate from defect induced p-type doping. With increasing temperature, electron-like carriers due to intrinsic band excitation increase significantly, finally leading to $\sigma_e > \sigma_h$ and a sign change in $S(T)$. Similar behavior was observed in LaOZnP and p-type Si.^{33,34} Even though the $S(T)$ in SrFBiS₂ is significant and not much smaller than in classic thermoelectric materials,³⁵ its low electrical conductivity makes its figure of merit ZT ($ZT = \sigma S^2 T/\kappa$) extremely small.

Electronic Structure. First principle calculations (Figure 4) confirm that SrFBiS₂ is a semiconductor with a direct band gap of 0.8 eV located at *X* point. This is similar to LaOBiS₂ where the energy gap was found to be 0.82 eV.³⁶ The calculation confirms the results of transport measurement. Similar to LaOBiS₂,^{13,36} both S 3*p* and Bi 6*p* states are located around the Fermi level (−2.0 to 2.0 eV) in SrFBiS₂. Thus there is a strong hybridization between S 3*p* and Bi 6*p* states. The absence of dispersion along Γ –*Z* line suggests quasi two-dimensional character of the band structure in SrFBiS₂ (Figure 4(b)). In LaOBiS₂, F doping results in metallic states and superconductivity at low temperature. The main influence of F substitution is a carrier doping that shifts the Fermi level and has only a minor effect on the lowest conduction band. Because of the similarity between SrFBiS₂ and LaOBiS₂, new superconductors could be obtained by chemical substitution.

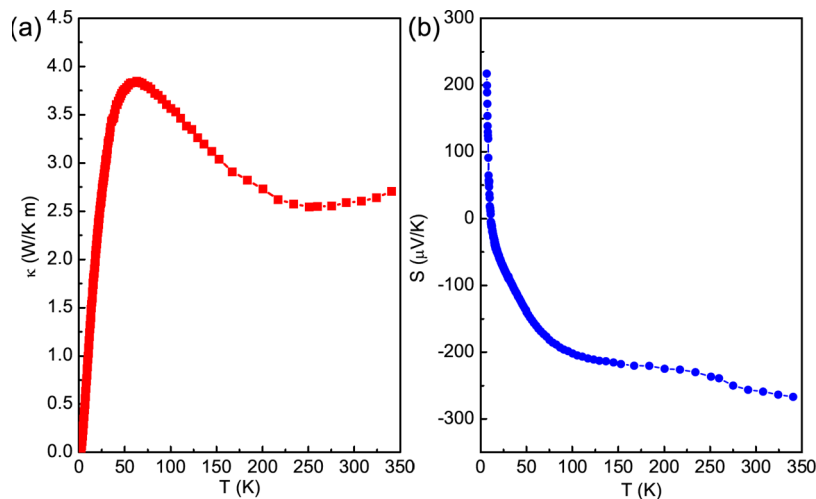


Figure 3. Temperature dependence of (a) thermal conductivity and (b) thermoelectric power for SrFBiS₂ under zero magnetic field within a temperature range from 2 to 340 K.

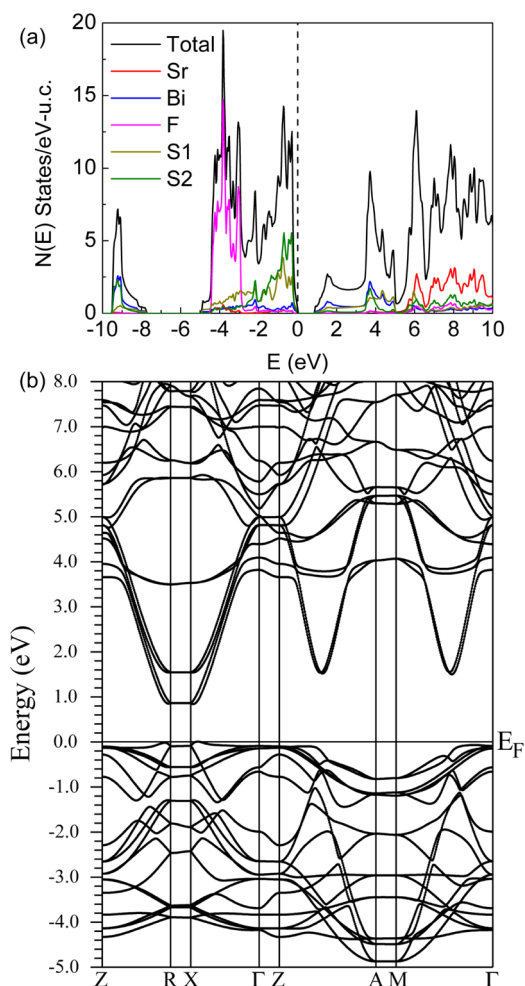


Figure 4. (a) Total and atom resolved density of states and (b) band structure of SrFBiS₂.

CONCLUSION

In summary, we report a discovery of a new layered fluorosulfide, SrFBiS₂. It contains a NaCl-type BiS₂ layer similar to Bi₄O₄S₃ and Ln(O,F)BiS₂ superconductors. SrFBiS₂ polycrystals show semiconducting behavior between 2 and 300 K. We observe rather small thermal conductivity and large TEP with sign reversal at low temperature. Theoretical calculation confirms the semiconducting behavior and indicates a similar DOS and band structure to undoped LaOBiS₂. Because of the similarity between SrFBiS₂ and the parent compound of BiS₂-based superconductors, it is of interest to investigate the doping effects on physical properties of SrFBiS₂. It could pave a way to new members in this emerging family of BiS₂-based superconductors.

ASSOCIATED CONTENT

Supporting Information

Data as mentioned in the text. This material is available free of charge via the Internet at <http://pubs.acs.org>.

AUTHOR INFORMATION

Corresponding Author

*E-mail: petrovic@bnl.gov.

Notes

The authors declare no competing financial interest.

ACKNOWLEDGMENTS

We thank John Warren for help with SEM measurements. Work at Brookhaven is supported by the U.S. DOE under Contract No. DE-AC02-98CH10886 and in part by the Center for Emergent Superconductivity, an Energy Frontier Research Center funded by the U.S. DOE, Office for Basic Energy Science (H.L. and C.P.). This work benefited from usage of X17A beamline of the National Synchrotron Light Source at Brookhaven National Laboratory. We gratefully acknowledge Zhong Zhong and Jonathan Hanson for their help with the X17A experiment setup.

REFERENCES

- Bednorz, J. G.; Müller, K. A. *Z. Physik B* **1986**, *64*, 189.
- Maeno, Y.; Hashimoto, H.; Yoshida, K.; Nishizaki, S.; Fujita, T.; Bednorz, J. G.; Lichtenberg, F. *Nature* **1994**, *372*, 532.
- Takada, K.; Sakurai, H.; Takayama-Muromachi, E.; Izumi, F.; Dilanian, R. A.; Sasaki, T. *Nature* **2003**, *422*, 53.
- Kamihara, Y.; Watanabe, T.; Hirano, M.; Hosono, H. *J. Am. Chem. Soc.* **2008**, *130*, 3296.
- Mayer, J. M.; Schneemeyer, L. F.; Siegrist, T.; Waszczak, J. V.; Van Dover, B. *Angew. Chem., Int. Ed. Engl.* **1992**, *31*, 1645.
- Wang, C.; Tan, M. Q.; Feng, C. M.; Ma, Z. F.; Jiang, S.; Xu, Z. A.; Cao, G. H.; Matsubayashi, K.; Uwatoko, Y. *J. Am. Chem. Soc.* **2010**, *132*, 7069.
- Zhu, J.-X.; Yu, R.; Wang, H.; Zhao, L. L.; Jones, M. D.; Dai, J.; Abrahams, E.; Morosan, E.; Fang, M.; Si, Q. *Phys. Rev. Lett.* **2010**, *104*, 216405.
- Ni, N.; Climent-Pascual, E.; Jia, S.; Huang, Q.; Cava, R. J. *Phys. Rev. B* **2010**, *82*, 214419.
- Free, D. G.; Withers, N. D.; Hickey, P. J.; Evans, J. O. *Chem. Mater.* **2011**, *23*, 1625.
- Mizuguchi, Y.; Fujihisa, H.; Gotoh, Y.; Suzuki, K.; Usui, H.; Kuroki, K.; Demura, S.; Takano, Y.; Izawa, H.; Miura, O. *Phys. Rev. B* **2012**, *86*, 220510(R).
- Mizuguchi, Y.; Demura, S.; Deguchi, K.; Takano, Y.; Fujihisa, H.; Gotoh, Y.; Izawa, H.; Miura, O. *J. Phys. Soc. Jpn.* **2012**, *81*, 114725.
- Demura, S.; Mizuguchi, Y.; Deguchi, K.; Okazaki, H.; Hara, H.; Watanabe, T.; Denholme, S. J.; Fujioka, M.; Ozaki, T.; Fujihisa, H.; Gotoh, Y.; Miura, O.; Yamaguchi, T.; Takeya, H.; Takano, Y. *J. Phys. Soc. Jpn.* **2013**, *82*, 033708.
- Usui, H.; Suzuki, K.; Kuroki, K. *Phys. Rev. B* **2012**, *86*, 220501(R).
- Li, S.; Yang, H.; Tao, J.; Ding, X.; Wen, H.-H. Multi-Band Exotic Superconductivity in the New Superconductor Bi₄O₄S₃. <http://arxiv.org/abs/1207.4955>.
- Singh, S. K.; Kumar, A.; Gahtori, B.; Shruti, G.; Sharma, S.; Patnaik; Awana, V. P. S. *J. Am. Chem. Soc.* **2012**, *134*, 16504.
- Tan, S. G.; Li, L. J.; Liu, Y.; Tong, P.; Zhao, B. C.; Lu, W. J.; Sun, Y. P. *Phys. C* **2012**, *483*, 94.
- Matsui, S.; Inoue, Y.; Nomura, T.; Yanagi, H.; Hirano, M.; Hosono, H. *J. Am. Chem. Soc.* **2008**, *130*, 14428.
- Han, F.; Zhu, X. Y.; Mu, G.; Cheng, P.; Wen, H.-H. *Phys. Rev. B* **2008**, *78*, 180503.
- Kabbour, H.; Cario, L.; Boucher, F. *J. Mater. Chem.* **2005**, *15*, 3525.
- Liu, R. H.; Zhang, J. S.; Cheng, P.; Luo, X. G.; Ying, J. J.; Yan, Y. J.; Zhang, M.; Wang, A. F.; Xiang, Z. J.; Ye, G. J.; Chen, X. H. *Phys. Rev. B* **2011**, *83*, 174450.
- Liu, R. H.; Song, Y. A.; Li, Q. J.; Ying, J. J.; Yan, Y. J.; He, Y.; Chen, X. H. *Chem. Mater.* **2010**, *22*, 1503.
- Hunter B. Rietica: A Visual Rietveld Program. International Union of Crystallography Commission on Powder Diffraction Newsletter No. 20, Summer, 1998. <http://www.rietica.org>.
- Hammersley, A. P.; Svenson, S. O.; Hanfland, M.; Hauserman, D. *High Pressure Res.* **1996**, *14*, 235.

- (24) Qiu, X.; Thompson, J. W.; Billinge, S. J. L. *J. Appl. Crystallogr.* **2004**, *37*, 678.
- (25) Weinert, M.; Wimmer, E.; Freeman, A. J. *Phys. Rev. B* **1982**, *26*, 4571.
- (26) Blaha, P.; Schwarz, K.; Madsen, G. K. H.; Kvasnicka, D.; Luitz, J. *WIEN2k: An Augmented Plane Wave + Local Orbitals Program for Calculating Crystal Properties*; Technische Universitat Wien: Austria, 2001; ISBN: 3-9501031-1-2.
- (27) Perdew, J. P.; Burke, K.; Ernzerhof, M. *Phys. Rev. Lett.* **1996**, *77*, 3865.
- (28) Farrow, C. L.; Juhas, P.; Liu, J. W.; Bryndin, D.; Bozin, E. S.; Bloch, J.; Proffen, Th.; Billinge, S. J. L. *J. Phys.: Condens. Mater.* **2007**, *19*, 335219.
- (29) Chen, B.; Uher, C.; Iordanidis, L.; Kanatzidis, M. G. *Chem. Mater.* **1997**, *9*, 1655.
- (30) Awana, V. P. S.; Kumar, A.; Jha, R.; Kumar, S.; Kumar, J.; Pal, A. *Solid State Commun.* **2013**, *157*, 31–23.
- (31) Dong, J.; Zhang, H. J.; Xu, G.; Li, Z.; Li, G.; Hu, W. Z.; Wu, D.; Chen, G. F.; Dai, X.; Luo, J. L.; Fang, Z.; Wang, N. L. *EPL* **2008**, *83*, 27006.
- (32) Yang, J.; Morelli, D. T.; Meisner, G. P.; Chen, W.; Dyck, J. S.; Uher, C. *Phys. Rev. B* **2002**, *65*, 094115.
- (33) Seeger, K. In *Semiconductor Physics: An Introduction*; Springer-Verlag, Berlin, 2004.
- (34) Kayanuma, K.; Hiramatsu, H.; Hirano, M.; Kawamura, R.; Yanagi, H.; Kamiya, T.; Hosono, H. *Phys. Rev. B* **2007**, *76*, 195325.
- (35) Rowe, D. M. In *Thermoelectrics Handbook: Macro to Nano*; Taylor & Francis: London, 2006.
- (36) Wan, X.; Ding, H.-C.; Savrasov, S. Y.; Duan, C.-G. *Phys. Rev. B* **2013**, *87*, 115124.

PAPER

An integrated study of thermal treatment effects on the microstructure and magnetic properties of Zn–ferrite nanoparticles

To cite this article: Bratislav Antic *et al* 2013 *J. Phys.: Condens. Matter* **25** 086001

View the [article online](#) for updates and enhancements.

You may also like

- [Progressive freezing of interacting spins in isolated finite magnetic ensembles](#)
Kakoli Bhattacharya, Veronique Dupuis, Damien Le-Roy *et al.*
- [Synthesis and temperature dependent magnetic properties of nanocrystalline \$Ni_{1-x}Zn_xFe_2O_4\$ ferrites](#)
Muhammad Atif
- [Non-equilibrium relaxation and aging in the dynamics of a dipolar fluid quenched towards the glass transition](#)
Ricardo Peredo-Ortiz, Pablo F Zubieta Rico, Ernesto C Cortés-Morales *et al.*

An integrated study of thermal treatment effects on the microstructure and magnetic properties of Zn–ferrite nanoparticles

Bratislav Antic¹, Marija Perovic¹, Aleksandar Kremenovic²,
Jovan Blanusa¹, Vojislav Spasojevic¹, Predrag Vulic², Lotfi Bessais³ and
Emil S Bozin⁴

¹ Condensed Matter Physics Laboratory, Institute of Nuclear Sciences ‘Vinča’, University of Belgrade, PO Box 522, 11001 Belgrade, Serbia

² Laboratory of Crystallography, Faculty of Mining and Geology, University of Belgrade, Djusina 7, 11001 Belgrade, Serbia

³ CMTR, ICMPE, UMR 7182, CNRS-Université Paris 12, 2 à 8 Rue Henri Dunant, F-94320 THIAIS, France

⁴ Condensed Matter Physics and Materials Science Department, Brookhaven National Laboratory, Upton, NY 11973, USA

E-mail: bantic@vinca.rs

Received 18 September 2012, in final form 3 January 2013

Published 23 January 2013

Online at stacks.iop.org/JPhysCM/25/086001

Abstract

The evolution of the magnetic state, crystal structure and microstructure parameters of nanocrystalline zinc–ferrite, tuned by thermal annealing of ~ 4 nm nanoparticles, was systematically studied by complementary characterization methods. Structural analysis of neutron and synchrotron x-ray radiation data revealed a mixed cation distribution in the nanoparticle samples, with the degree of inversion systematically decreasing from 0.25 in an as-prepared nanocrystalline sample to a non-inverted spinel structure with a normal cation distribution in the bulk counterpart. The results of DC magnetization and Mössbauer spectroscopy experiments indicated a superparamagnetic relaxation in ~ 4 nm nanoparticles, albeit with different freezing temperatures T_f of 27.5 K and 46 K, respectively. The quadrupole splitting parameter decreases with the annealing temperature due to cation redistribution between the tetrahedral and octahedral sites of the spinel structure and the associated defects. DC magnetization measurements indicated the existence of significant interparticle interactions among nanoparticles (‘superspins’). Additional confirmation for the presence of interparticle interactions was found from the fit of the $T_f(H)$ dependence to the AT line, from which a value of the anisotropy constant of $K_{\text{eff}} = 5.6 \times 10^5 \text{ erg cm}^{-3}$ was deduced. Further evidence for strong interparticle interactions was found from AC susceptibility measurements, where the frequency dependence of the freezing temperature $T_f(f)$ was satisfactory described by both Vogel–Fulcher and dynamic scaling theory, both applicable for interacting systems. The parameters obtained from these fits suggest collective freezing of magnetic moments at T_f .

(Some figures may appear in colour only in the online journal)

1. Introduction

Nanocrystalline ferrites with the AB_2X_4 spinel structure are the most frequently investigated systems due to the broad range of their technological applications. These span

diverse areas such as catalysis [1] and medical applications (treatment by magnetic hyperthermia, use as a drug delivery system in cancer therapy, and as contrast agents in MRI diagnostics) [2], and are also used in high-density magnetic recording media [3], as ferrofluids [4], and as sensors [4],

among other applications. Furthermore, with the development of experimental and theoretical tools they have become of great interest as model systems in fundamental research. Nanocrystalline ferrites are characterized by unique properties such as superparamagnetism, core/shell structure, and very often exhibit appreciable enhancement of their physical properties (e.g. magnetization, permeability, resistivity, etc) compared to their bulk counterparts [4–6].

The magnetic properties of magnetic nanocrystalline materials are often considered as a superposition of the intrinsic properties of nanoparticles (e.g. structure, magnetic moments, different types of anisotropies, etc) and interparticle interactions among them like dipole–dipole and exchange ones. In ferromagnetic zinc–ferrite each single-domain nanoparticle possesses a large magnetic moment (‘superspin’). Depending on the interaction strength among the superspins, magnetic systems can be subdivided into two general types with different behaviors. When interparticle interactions are negligible, a superparamagnetic (SP) state occurs [5–7], where the superspins belonging to each nanoparticle oscillate between their easy magnetization directions, and block along these directions below the so called blocking temperature T_B . In the case of sufficiently strong interactions among superspins, they do not relax independently, but in a collective way. It has to be noted that the interactions usually have a high degree of frustration. This frustration is a consequence of particle size distribution, different particle shapes and interparticle distances. All these factors lead to the formation of the so called superspin-glass (SSG) state below a certain freezing temperature T_f [8]. It is common that $T_B < T_f$, since the contribution of magnetic particle interaction is superimposed on the blocking process.

There are several experimental signatures of SP or SSG behavior and we shall mention three of them, used in this paper. The first one is $M(T)$ measurement under the field-cooled (FC) regime, where for an SP system below T_B , the magnetization constantly increases with temperature decrease, unlike for the SSG state, where below T_f , the magnetization shows flatness or decreases [9]. Also, it is well known that the blocking or freezing temperatures shift to lower temperatures with increase of the magnetic field strength. This temperature decrease can be described, in the mean field picture, by so called AT lines which represent the boundaries between paramagnetic and spin-glass phases. In the T – H phase diagram this can be written as [9]

$$T_{\max} = T_f[1 - (H/H_a)^\alpha], \quad (1)$$

where H_a is the anisotropy field, T_{\max} and T_f are the freezing temperatures in the magnetic fields H and $H = 0$, respectively. The parameter α depends on the interaction strength and distinguishes the SP and SSG cases. For noninteracting particles $\alpha = 2$ [10], while for interacting systems this parameter is close to $2/3$ [11].

AC susceptibility measurements, $\chi'(T)$ and $\chi''(T)$, for different frequencies f (different time window) represent a valuable method for investigation of the spin relaxations. There are several models describing the dependence of the relaxation time τ on different parameters like the anisotropy

barrier $E_a = K_{\text{eff}}V$ (K_{eff} is the effective anisotropy constant, V is the particle volume) and the interparticle interaction, which is presented as the characteristic temperature T_0 . For noninteracting particles $T_0 = 0$ and in that case the superparamagnetic relaxation τ is given by the Néel–Brown expression $\tau = \tau_0 \exp(KV/k_B T)$, where τ_0 is typically in the range of 10^{-11} – 10^{-9} s, k_B is the Boltzmann constant, and T is the temperature [12]. Other models which take into account the influence of the interparticle interactions on the magnetic relaxation are considered in section 3.3.3.

Zinc–ferrite, ZnFe_2O_4 , crystallizes in the spinel type structure, represented by the general formula AB_2X_4 , space group (S.G.) $Fd\bar{3}m$. Cations occupy tetrahedral 8a (A) and octahedral 16d (B) sites, while oxygen is in the 32e crystallographic position. Nanocrystalline ZnFe_2O_4 has a mixed, metastable, cation distribution with some percentage of Zn^{2+} residing at 16d sites instead of 8a sites, and a corresponding concentration of Fe^{3+} then occupies 8a sites. This is often described as inverted spinel with formula $(\text{Zn}_{1-\alpha}\text{Fe}_\alpha)_\text{A}[\text{Zn}_\alpha\text{Fe}_{2-\alpha}]_\text{B}$, where the inversion parameter α depends on the sample preparation method and the thermal treatment [13]. Consequently, ZnFe_2O_4 with a metastable cation distribution is suitable for studying the effects of thermal annealing on the inversion parameter.

It is well known that three kinds of interactions, A–A, B–B, and A–B superexchange interactions, exist in spinel ferrites, in which the A–B interaction is much stronger than the others. In bulk ZnFe_2O_4 having normal spinel structure, the absence of magnetic ions at A sites (populated by nonmagnetic Zn) results in weak antiferromagnetic exchange interactions within Fe atoms at B sites, making bulk ZnFe_2O_4 antiferromagnetic below 10 K. Due to the partial inversion of Zn^{2+} and Fe^{3+} cation distributions in nanocrystalline zinc–ferrite, a superexchange interaction between the iron ions at A and B sublattice sites occurs, leading to ferrimagnetic long range ordering at much higher temperatures. This greatly enhances the saturation magnetization.

Here we report results of a systematic study using multiple complementary techniques on a series of ZnFe_2O_4 nanoparticle samples obtained using thermal annealing protocols. Inter- and intra-particle interactions in the ZnFe_2O_4 nanoparticle system are studied by analysis of DC magnetization and AC susceptibility data. Details of the structure and microstructure for nanocrystalline ZnFe_2O_4 depending on variable thermal annealing protocols are assessed using synchrotron x-ray and neutron diffraction data. Two independent methods were combined: the Rietveld method in reciprocal space and the atomic pair distribution function (PDF) method in direct space. The effects of thermal annealing on the magnetic properties and magnetic states at low temperatures are investigated by combining Mössbauer spectroscopy, DC magnetization and AC susceptibility measurements. Using these methods we have established a relationship between the structure/microstructure and magnetism.

2. Experimental details

Nanocrystalline ZnFe_2O_4 was prepared by a low temperature chemical co-precipitation method using aqueous solutions of nitrate precursors. Details of the synthesis procedure are given in [14, 15]. Chemical quantitative analysis was performed by inductively coupled plasma optical emission spectroscopy, ICP-OES (Spectroflame ICP, 2.5 kW, 27 MHz). The ratio of Zn:Fe found was close to 1:2, indicating the cation stoichiometry of the samples. An as-prepared sample, denoted by S1, was annealed at 400 °C (S2) and 500 °C (S3) in order to monitor the effects of thermal annealing on the structural, microstructural and magnetic properties. Bulk ZnFe_2O_4 (S4) was prepared by a ceramic procedure. The starting compounds, Fe_2O_3 and ZnO, were mixed in stoichiometric ratios, pressed and heated at 1200 °C for 24 h.

Structural and microstructural analyses were carried out on three nanocrystalline zinc-ferrite samples (S1, S2 and S3), and on one bulk reference sample (S4) using synchrotron based high-energy x-ray powder diffraction data. The measurements were performed at 300 K at the 6-ID-D beam-line of the Advanced Photon Source at Argonne National Laboratory, utilizing the image plate (IP) detector MAR345. Samples were packed in cylindrical polyimide capillaries 1.0 mm in diameter sealed at both ends. A monochromatic incident x-ray beam of 0.5 mm \times 0.5 mm in size was used, conditioned using a Si(311) monochromator to have an energy of 86.84 keV ($\lambda = 0.1428 \text{ \AA}$). The IP detector was mounted orthogonally to the beam path with a sample to detector distance of 230.274 mm, as calibrated by using a ceria standard sample [16]. Multiple scans were performed on each sample to a total exposure time of 600 s. This approach avoids detector saturation while allowing sufficient statistics to be obtained. To reduce the background scattering, lead shielding was placed before the sample with a small opening for the incident beam. The 2D diffraction data were integrated and converted to intensity versus 2θ using the software FIT2D [17], where 2θ is the angle between the incident and scattered x-ray beams. The integrated data were normalized by the average monitor counts. These intensity data were subsequently used in the Rietveld analysis. For the PDF analysis the data were further processed. The intensity data were corrected and normalized [18] using the program PDFgetX2 [19] to obtain the total scattering structure function, $F(Q)$, and its sine Fourier transform, i.e. the atomic PDF, $G(r)$. In the Fourier transform of $F(Q)$ to obtain $G(r)$, the data were truncated at a finite maximum value of the momentum transfer, $Q = Q_{\text{max}}$. Q_{max} was optimized so as to avoid large termination effects and to reasonably minimize the introduced noise level as the signal to noise ratio decreased with the increased Q value. Here, $Q_{\text{max}} = 25.0 \text{ \AA}^{-1}$ was found to be optimal.

Time-of-flight (TOF) neutron diffraction data were collected on nanocomposed and bulk samples at 295 K on the SEPD diffractometer at the Intense Pulsed Neutron Source at Argonne National Laboratory and at 15 K on the NPDF diffractometer at Los Alamos Neutron Scattering Center at Los Alamos National Laboratory. Nanocrystalline and

finely pulverized bulk samples were loaded into an extruded vanadium container under He-atmosphere, and sealed using indium wire. A closed cycle displax cooling system was used to control the temperature. The data were collected for 6 h to obtain good statistics.

^{57}Fe Mössbauer spectroscopy was used as a local magnetic microstructure probe in the temperature interval of 10–298 K. The Mössbauer spectra for nanosized and bulk ZnFe_2O_4 samples were collected in the transmission configuration, in constant acceleration mode with the radioactive source of ^{57}Co embedded in a rhodium matrix. The room temperature spectrum of α -iron foil was used for spectrometer calibration.

Magnetic measurements were performed on an MPMS XL-5 SQUID magnetometer and a PPMS magnetometer. Magnetization versus temperature, $M(T)$, was measured in the 1.8–350 K temperature range, under zero-field-cooled (ZFC) and field-cooled (FC) regimes, in different applied fields. Hysteresis loops were measured at 5 K in FC and ZFC regimes.

3. Results and discussion

3.1. The structure/microstructure of Zn-ferrites from Rietveld and PDF approaches

The crystal structure and microstructure properties of samples S1–S4 were investigated by x-ray diffraction. The analysis of the experimental data was carried out by both Rietveld and PDF approaches. While the Rietveld analysis obtains the crystal structure solely from the Bragg reflections, the PDF method utilizes both Bragg and diffuse scattering signals to extract structural information.

Rietveld refinement was carried out by using Fullprof software [20], in which a TCH Pseudo-Voigt function was chosen to describe the profile of the diffraction maxima in order to resolve the microstructure parameters (crystallite size and microstrain). As expected, better refinement reliability factors were obtained for the bulk sample structure than for those derived from refinement of the as-prepared sample structure (figures 1(a), (b)).

In addition, the crystal structure for the S1 and S4 samples was studied using TOF neutron powder diffraction data. In figure 2, fully converged Rietveld refinements of S1 sample data at 295 K are shown. Rietveld refinement of TOF data of nonmagnetic structures was carried out on nanocomposed and bulk samples at 295 K as a multipattern refinement in Fullprof software. The function used to model the peak shapes represents convolution of a pseudo-Voigt function with a pair of back-to-back exponentials. As in the case of refinement of the synchrotron data, the refinement residuals are higher in the case of the bulk sample ($\chi^2 \sim 4.0$) compared to the nanosized sample ($\chi^2 \sim 1.8$). The obtained structure parameters are given in table 1. They are in good agreement with the results of the refinement of the data from the synchrotron experiment for samples S1 and S4. The bulk sample is found to be almost normal (non-inverted) spinel, while the S1 nanocomposed sample shows approximately 25% of inversion.

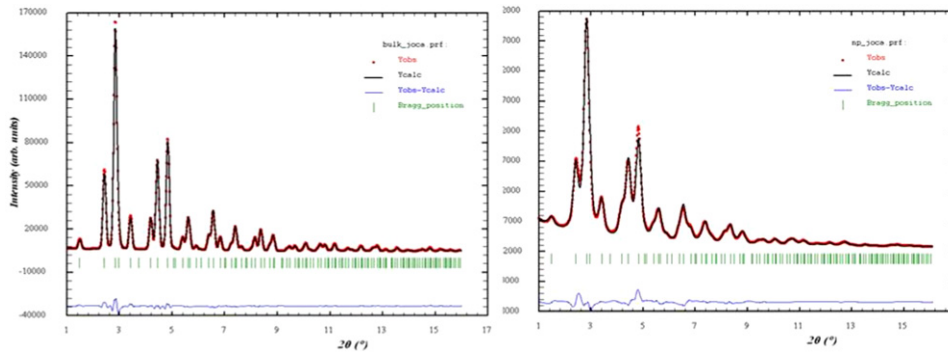


Figure 1. The refined diffraction patterns of (a) the bulk and (b) the as-prepared sample. The bottom line indicates the difference between the data and the calculated pattern.

Table 1. The structure parameters obtained from Rietveld and PDF analyses.

		S1	S2	S3	S4
Lattice (Å)	Rietveld	8.440 18(101)	8.449 13(48)	8.432 22(45)	8.4298(6)
	PDF	8.441 2(2)	8.443 2(4)	8.426 1(2)	8.4328(3)
	TOF	8.442(4)	—	—	8.4287(2)
$x(O)$	Rietveld	0.254 67(34)	0.256 72(20)	0.258 87(22)	0.2600(2)
	PDF	0.258 0(3)	0.258 6(2)	0.259 0(2)	0.2604(2)
	TOF	0.257 6(6)	—	—	0.2603(1)
Zn occupation number	Rietveld	0.740(13)	0.722(8)	0.840(8)	1
	TOF	0.748(20)	—	—	0.982(3)

The atomic PDF represents a total scattering based function in direct space that provides a distribution of interatomic distances r in a material. The PDF is a well suited method for structural assessment in bulk materials with nanometer scale inhomogeneities, and crystallographically challenged materials, such as nanoparticles [21]. Figure 3 illustrates 15 K TOF data from the NPf for bulk sample S4 (gray) and as-prepared nanocrystalline sample S1 (red). In figure 3(a) a comparison of the reduced total scattering functions, $F(Q)$, is shown. Notably, there is an appreciable broad diffuse scattering component in the data for sample S1. As can be seen in the inset that shows $F(Q)$ on an expanded scale, the Bragg peaks in the data for the nanocrystalline sample are much broader than the corresponding peaks for the bulk counterpart, as expected. Comparison of the corresponding PDFs, $G(r)$, is given in figure 3(b). While the PDF of the bulk sample exhibits excellent crystallinity and long range order, the structural coherence abruptly degrades for the as-prepared sample as r increases, reflected in an abrupt decay of the PDF intensity as a length scale comparable to the nanoparticle size is approached, as sketched by the dashed red line that serves as a guide to the eye. The PDF analysis was carried out using the program PDFgui [22]. A model corresponding to an average cubic structure within the $Fd\bar{3}m$ space group was used and had seven parameters: the lattice parameter, the x -fractional coordinate of the oxygen, isotropic thermal parameters for Zn, Fe and O, the spherical particle diameter, and an overall scale factor. The refinements for all samples were carried out on 300 K x-ray data over the 1.5–65.0 Å range, with reasonably low agreement factors, r_{WP} , between the data and the model, ranging from 0.11 to

0.12. The final fits are shown in figure 4 for as-prepared sample S1 (a), sample S2 (b), sample S3 (c), and bulk sample S4 (d). By visual comparison of the data one can immediately notice a gradual but rapid loss of PDF intensity for the S1–S3 samples, compared to the bulk S4, reflecting the loss of structural coherence in the nanocrystalline samples. Additional decay of the PDF intensity originating from the limited Q -space resolution of the x-ray measurement setup is also present, and can most notably be seen in the data of the bulk sample, as well as in the data obtained for a crystalline Ni reference, shown in figure 4(e).

The values of the structural parameters obtained from the PDF analysis, lattice parameters and oxygen coordinates, shown in table 1, are in reasonably good agreement with those determined from the Rietveld refinement of the x-ray and neutron data.

Inspection of the difference curves for the PDF refinements shown in figures 4(a)–(d) and 5(a), and the low values of the agreement factors, indicate that the cubic $Fd\bar{3}m$ model explains the structure of all the samples reasonably well. However, a closer examination of the difference curves in these figures reveals the existence of discrepancies in the low- r region of the PDFs for the nanocrystalline samples. Further, comparison of the atomic displacement parameters (ADPs) obtained from broad range refinements of the nanocrystalline data relative to those obtained for the bulk (inset to figure 5(a)) indicates enlarged values of the ADPs for all three atomic species for the as-prepared sample. This enlargement systematically decreases as the NP size increases towards bulk. Evaluation of the cubic fit to the data of the S1 sample in the low- r range, figure 5(b), provides a clue as to

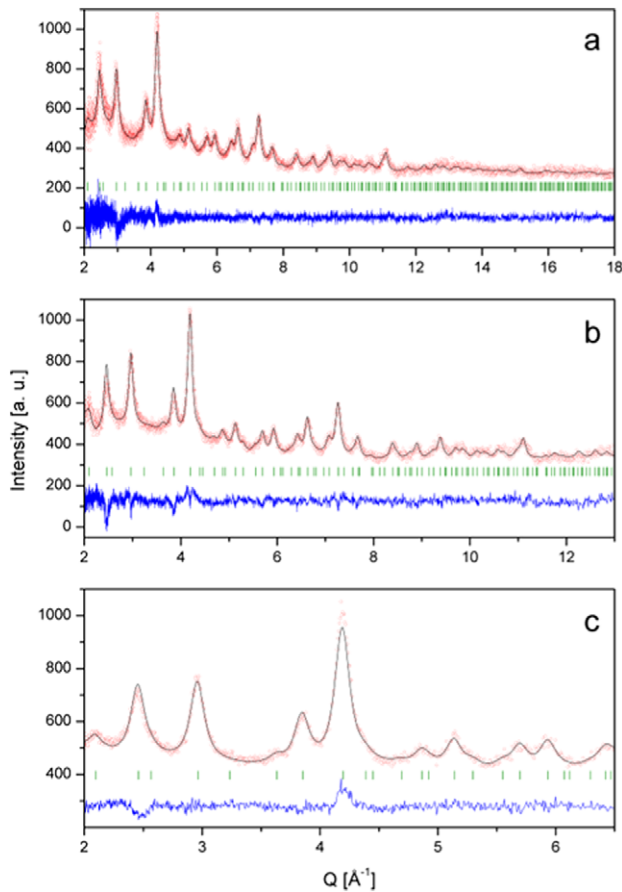


Figure 2. The final Rietveld plots of the nanocomposed sample at 295 K: (a) region 1, (b) region 2, and (c) region 3. The dots denote the observed step intensities; the line represents the corresponding calculated values. The difference curve between the observed and calculated values is given at the bottom. The vertical lines represent peak positions for the nuclear structure.

why the ADPs are enlarged. While the cubic model explains the data well over a broad range, it misses the positions of the PDF peaks centered at around ~ 3.0 and ~ 3.5 \AA . The two peaks correspond to the near-neighbor Fe–Fe and Zn–Zn distances in the $Fd\bar{3}m$ structure, respectively. As is apparent from figure 5(b), the data indicate that the Fe–Fe distance is longer than the average model predicts, while the Zn–Zn distance is shorter than that predicted by the average model. By considering published ionic radii of the species involved [23], the observed effect can be understood by simple coordination chemistry arguments. As mentioned earlier, in a normal spinel structure the Fe occupy 16d sites on the pyrochlore sublattice of corner-shared Fe-tetrahedra, and are octahedrally coordinated by O, while the Zn occupy 8a sites that are tetrahedrally coordinated by oxygen. The ionic radii of Zn^{2+} are 0.6 \AA for tetrahedral coordination and 0.74 \AA for octahedral coordination, and those of Fe^{3+} are 0.49 \AA for tetrahedral coordination in the HS configuration and 0.645 \AA for octahedral coordination in the HS configuration (0.55 \AA in the LS configuration). When inversion occurs, with a fraction of Zn atoms occupying Fe sites and vice versa, local structural distortions can be expected. An octahedral site subject to inversion would host a larger Zn^{2+} ion substituting

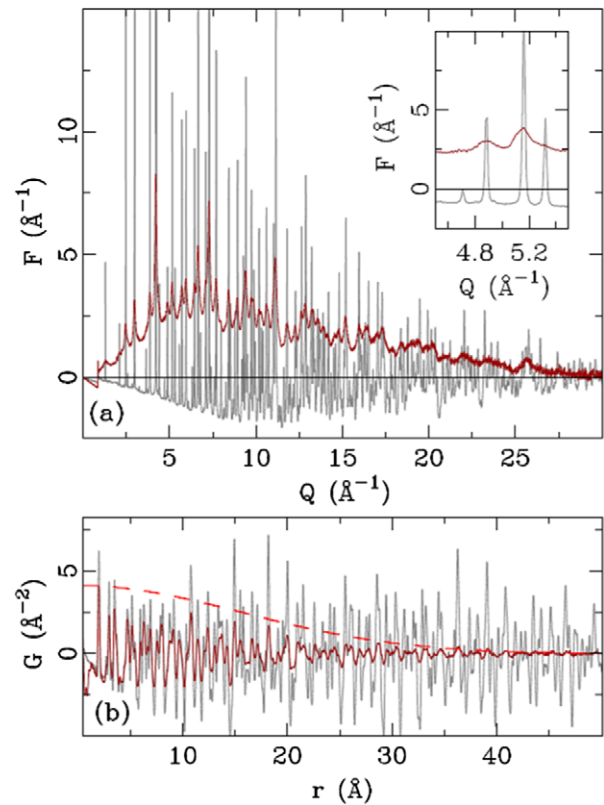


Figure 3. (a) The reduced neutron total scattering structure function, $F(Q)$, at 15 K for the bulk S4 sample (gray) and the as-prepared S1 nanocrystalline sample (red). The inset shows a small region on an expanded scale. (b) The corresponding atomic PDF for samples S4 (gray) and S1 (red). The dashed red line illustrates damping of the PDF for the nanoparticle sample due to its finite size. See the text for details.

for a smaller Fe^{3+} , accounting for the observed enlarged near-neighbor distance between two 16d sites. Conversely, a tetrahedral site subject to inversion would host a smaller Fe^{3+} ion substituting for a larger Zn^{2+} ion, resulting in a decrease of the near-neighbor distance between two 8a sites, in qualitative agreement with observed behavior. Hence, the observed effect in as-prepared nanocrystalline sample S1 can be understood to be a consequence of inversion, in good agreement with earlier results of EXAFS [24] and XANES [25]. This renders PDF a useful tool for observing inversion through associated structural defects, which is of particular importance in cases where inversion cannot be easily detected directly and reliably due to, for example, modest scattering contrast. One unique advantage of the PDF approach compared to EXAFS is that PDF probes the structure on various length scales, in contrast to EXAFS that provides information normally limited to the first few coordination shells. PDF can therefore be utilized to estimate the spatial extent of the inversion-induced distortions. From the difference curve in figure 5(a) it is clear that in the case of ZnFe_2O_4 the distortions are rather localized and do not propagate in a correlated fashion beyond the nearest-neighbor distances involved. This is in accord with the notion that the inversion is a random process. Spatially averaged distortions are then well described by the average structure cubic model

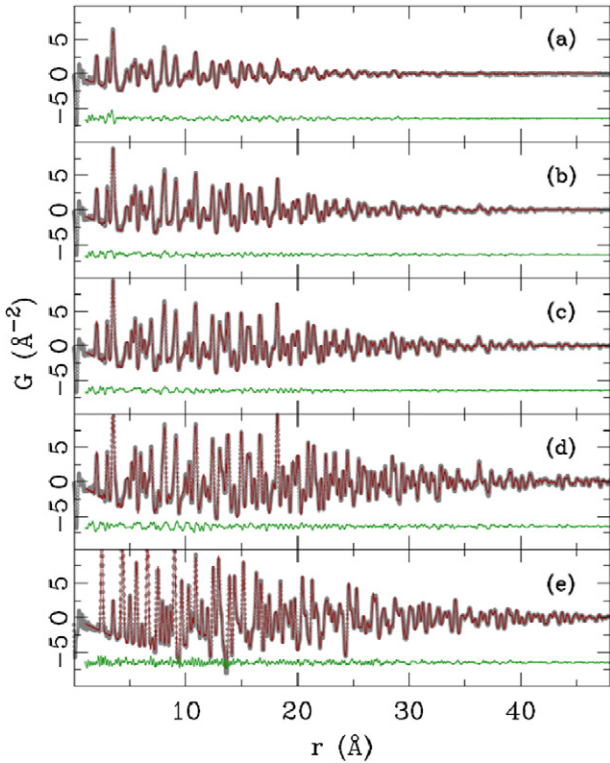


Figure 4. Refinements of the $Fd\bar{3}m$ model to the experimental x-ray PDF data collected at 300 K for (a) as-prepared Zn-ferrite nanoparticles (S1) as well as those annealed at 400 °C (S2) (b) and 500 °C (S3) (c). For comparison, the structure of bulk Zn-ferrite (d) was also refined over a wide r -range. Data are shown as open symbols, model profiles as solid lines, and corresponding difference curves are shown offset below for clarity. Nickel standard data and the corresponding structure model fit are also shown (e) to illustrate the damping effect of Q -space resolution on the PDF. See the text for details.

with enlarged ADP parameters. The evolution of inversion and associated distortions with change of the nanoparticle size is summarized in figure 5(c) which features the experimental radial distribution function, $R(r)$. On going from as-prepared sample S1 towards bulk sample S4, the distortion decreases and the features in the local structure relax towards the non-inverted spinel structure. The evolution with particle size of the relative local displacements (compared to bulk) is estimated from model independent Gaussian fits to the $R(r)$ data and is illustrated in the inset to figure 5(c).

The occupation number of Zn ions at the A site was determined by Rietveld refinement, showing the change of Zn ion occupation ratio over A and B sites. The results show that the bulk sample resembles a normal spinel structure, while about 25% of inversion is found in S1 and S2. This is in qualitative agreement with the evolution of the observed local structural distortions in the PDF. However, the values of the inversion parameter from Rietveld refinement, particularly for the S2 sample, may be less reliable due to poor scattering contrast. This emphasizes the importance of using multiple complementary methods when studying challenging nanocrystalline systems.

Microstructure analysis of the S1, S2 and S3 samples was performed on x-ray diffraction data by the Rietveld

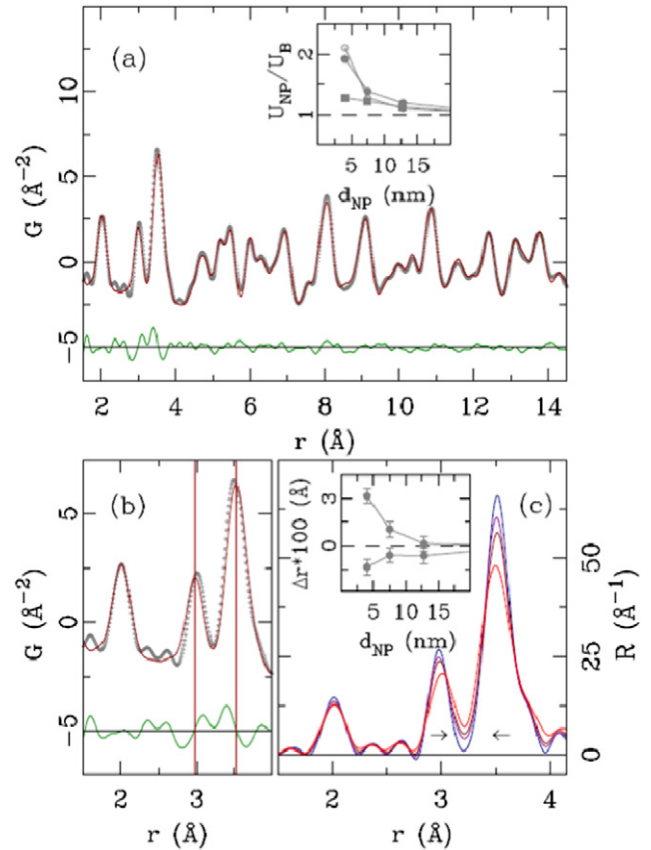


Figure 5. (a) A fit of the cubic $Fd\bar{3}m$ model (solid line) to the as-prepared S1 nanocrystalline sample PDF data (open symbols). The difference is offset for clarity. The inset shows the 300 K evolution of the relative ADPs for Zn (solid circles), Fe (open circles) and O (solid squares) with nanoparticle size compared to their values obtained for the bulk sample (S4). (b) Close-up of the fit shown in (a). The vertical lines indicate the positions of peaks obtained from the fully converged cubic model. (c) A comparison of the 300 K x-ray short range radial pair distribution functions (RDF), $R(r)$, for all samples: S1 (light red), S2 (dark red), S3 (purple) and S4 (blue). The arrows indicate inversion-induced local distortion. The inset shows the evolution of the local distortion with nanoparticle size. See the text for details.

method and by using Ni powder standard to determine the instrumental line broadening. The results for particle size and microstrain are shown in table 2. Both parameters were refined using an isotropic (spherical) particle shape model and an isotropic microstrain (random defect distribution), providing satisfactory agreement with the experimental data. The Rietveld-obtained values for particle size are also compared to those obtained from the PDF, and good agreement was found for all samples. Since the size characterization by the PDF is in principle sensitive to both the core and the shell regions, while the Rietveld results merely denote the dimensions of the crystalline core, the agreement implies that any coherent shell region in the studied samples is probably very thin. Whilst this does not exclude the possibility of the existence of a disordered amorphous-like shell, no discrepancies in the low- r region of the modeled PDF were seen, beyond those ascribed to inversion that would indicate the presence of an amorphous-like surface region.

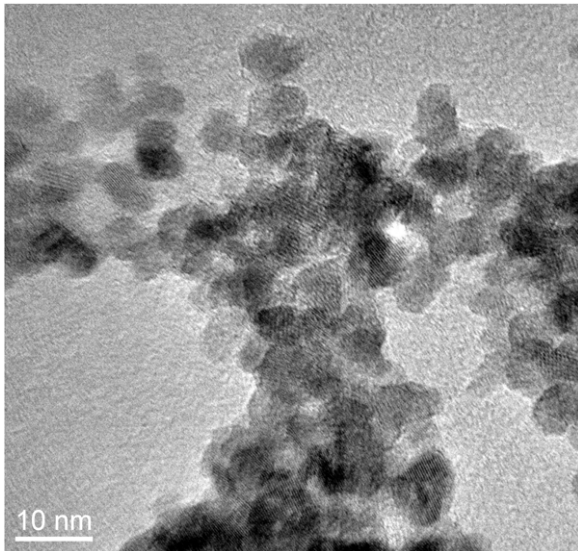


Figure 6. TEM image of S1.

Table 2. Particle size and microstrain for nanoparticle samples obtained from Rietveld refinement and the PDF.

		S1	S2	S3
Particle size (Å)	Rietveld	34	77	129
	PDF	39(1)	75(1)	128(2)
Microstrain ($\times 10^{-4}$)		55	29	—

3.2. Particle shape, particle morphology and crystallite size

The particle size and morphology of the as-prepared sample were characterized by transmission electron microscopy. A typical image of the S1 sample is shown in figure 6. TEM analysis reveals that the particles are isotropic, with a relatively uniform size distribution. Inspection indicates that the mean particle size is in the 4–6 nm range, suggesting that on average one grain is composed of one crystallite. This implies that the produced nanomaterial is well crystallized and free of defects. A more detailed TEM analysis enabled us to clarify the morphology of the synthesized particles. The particles are nearly spherical in shape.

3.3. The magnetization of Zn-ferrites

3.3.1. Magnetization versus temperature. The temperature dependences of ZFC and FC magnetization (1.8–300 K) for the investigated nanoparticles (S1–S3) were measured in different fields, from $H = 10$ Oe up to 5 kOe. As an example, the result of measurements for S3 in a field of 100 Oe is shown in figure 7 (main panel). It can be seen that the ZFC and FC magnetization curves separate below the irreversibility temperature T_{irr} , indicating the presence of a certain degree of magnetic anisotropy which is still significant in a field of 2 kOe, but is overcome in a field of 5 kOe (not shown). The ZFC branch exhibits a pronounced maximum which is characteristic for both the SP and SG states. However, the FC branch below T_{max} decreases, deviating from SP behavior,

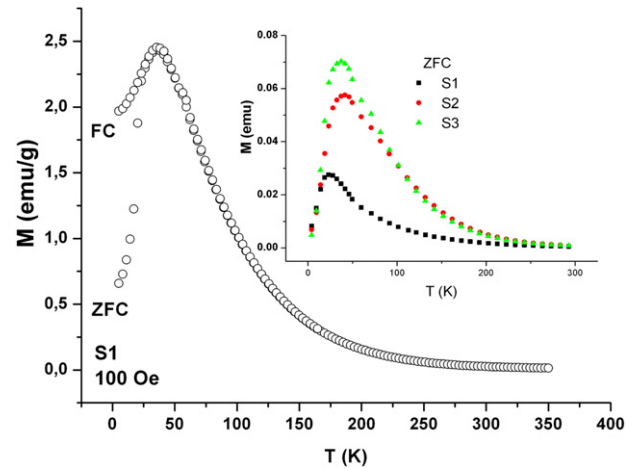


Figure 7. Temperature dependence on magnetization for sample S1 measured after ZFC and FC in an applied field of 100 Oe. Inset: ZFC magnetization versus temperature for samples S1–S3.

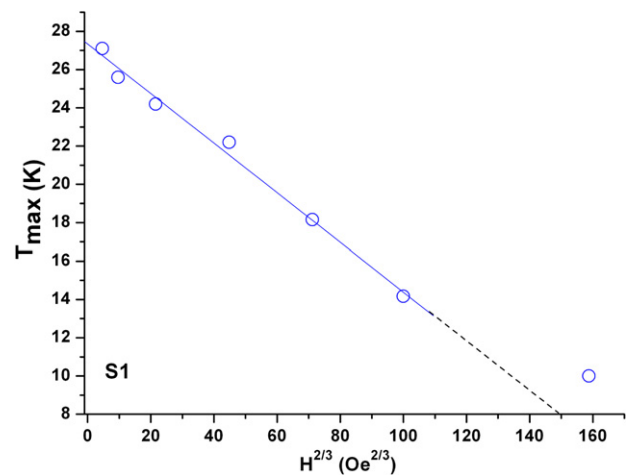


Figure 8. T_{max} versus $H^{2/3}$ for sample S1. The line is a fit to the Almeida–Thouless (AT) line.

where the FC magnetization constantly increases. The decrease of FC magnetization at low temperatures is caused by interparticle interactions among nanoparticle superspins. In a case of strong interactions T_{max} would represent the freezing temperature which is a superposition of the blocking process of nanoparticle moments and interactions among them. The blocking temperature is lower than T_{max} , and depending on the strength of the interparticle interactions, can be several times less than the freezing temperature for $H = 0$ [26].

In order to further investigate the nature of the magnetic state below T_{max} , temperature dependence $T_{max}(H)$ was measured from 10 Oe to 5 kOe for sample S1. A significant shift of T_{max} to lower temperature with increase of the applied field H can be seen in figure 8, where T_{max} versus $H^{2/3}$ is depicted. The full line in the T – H phase diagram is the fit to the Almeida–Thouless (AT) line, given by equation (1) [27]. This line represents the boundary between the superparamagnetic and SSG states. Good agreement with experimental values is achieved in the range from 10 to

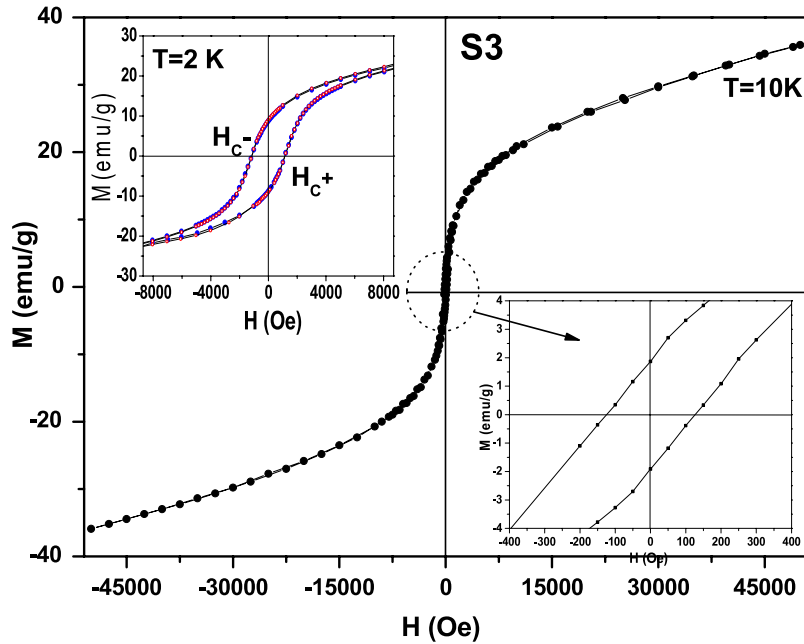


Figure 9. The hysteresis loop for the S3 sample at 10 K. Lower inset: enlargement of the low-field region. Upper inset: overlapping hysteresis loops measured at 2 K after FC and ZFC (see text).

1000 Oe, but above this range a certain deviation is observed. This implies that collective behavior exists for low applied fields, while for higher fields this collective state is suppressed or even erased [28]. From this fit the freezing temperature $T_f = (27.5 \pm 0.1)$ K and anisotropy field $H_a = (4200 \pm 100)$ Oe are obtained. By using the relation $H_a = 2K_{\text{eff}}/\rho M_s$ [26], the effective anisotropy constant $K_{\text{eff}} = 5.6 \times 10^5$ erg cm $^{-3}$. In this relation M_s is the saturation magnetization obtained from $M(H)$ measurements ($M_s = 50$ emu g $^{-1}$, see the next paragraph) and ρ is the density of the sample. The density $\rho = 5.93$ g cm $^{-3}$ was calculated as m/V , where V is the volume of the crystal cell (calculated from the obtained cell parameters, see table 1), with eight formula units in it ($Z = 8$). The obtained effective anisotropy constant K_{eff} is one order of magnitude higher than in the isostructural bulk ferrites [29]. From the obtained value of K_{eff} and by using the expression $K_{\text{eff}}V = 25k_B \langle T_B \rangle$, the mean blocking temperature $\langle T_B \rangle$ can be estimated. If we take the mean value for the particle size obtained for the S1 sample by the Rietveld and PDF methods ($\langle d \rangle = 3.6$ nm, see table 2), $\langle T_B \rangle = (4 \pm 1)$ K is obtained. This value is about six times lower than the freezing temperature $T_f = 27.5$ K, showing a high contribution of interparticle interaction to the freezing temperature.

The validity of the AT behavior has been found in many different nanostructure systems in which interparticle exchange interactions are present, such as in layered $\text{LiNi}_{0.4}\text{Mn}_{0.4}\text{Co}_{0.2}\text{O}_2$ [30], nanocrystalline Ni–ferrite with a core/shell morphology of nanoparticles [31], single crystalline ZnMn_2As_2 [32], and epitaxial BiFeO_3 (BFO) thin films grown on (111) SrTiO_3 substrates [33].

3.3.2. Magnetization versus field. The $M(H)$ measurements were performed at several temperatures in the range of

2–300 K, in both the zero-field-cooled and field-cooled regimes. The hysteresis loop for the S3 sample at 10 K is shown in figure 9, with the low-field region enlarged (lower inset to figure 9) to show the hysteresis symmetry. One of the remarkable features of the magnetization curve is its increase with applied field and the absence of saturation even in a field of 5 T (the maximum field strength achievable on an XL-5 SQUID magnetometer) or 9 T (measurements on a PPMS). The observed behavior should be mainly addressed to the canting of spins in the ferrimagnetically ordered particle core due to strong A–B superexchange interactions. Nevertheless, the non-saturation could be also an indication of the presence of spin disorder at the particle surface. In the upper inset in figure 9 the hysteresis loops are shown at 2 K in both the FC and ZFC regimes. The same results were observed in two other samples (S1 and S2). The observed non-saturation and symmetry of the magnetization loops in the FC regime is indicative of the nanoparticles having core/shell structure, with a smaller effect of the magnetic moments in the shell [34]. The result of PDF/Fullprof analyses referring to the shell and the above results suggest that the shell is not significant in size and is probably not crystalline.

To further explore the existence of interparticle interactions, we consider the reduced remanence, M_R/M_S . The theoretically predicted M_R/M_S value of 0.5 for noninteracting single-domain particles with their easy axis randomly oriented has been confirmed experimentally in some noninteracting nanoparticle systems, such as CoFe_2O_4 [7]. A value of 0.15 at 5 K was reported for Fe_3O_4 with interparticle interactions [35]. Further lowering of this value may also be induced by internal strain [36]. The results of our size/strain analysis point to the existence of non-negligible strain (table 1). The values of M_R/M_S obtained for sample S3 at different temperatures were 0.21 (2 K), 0.11 (6 K) and

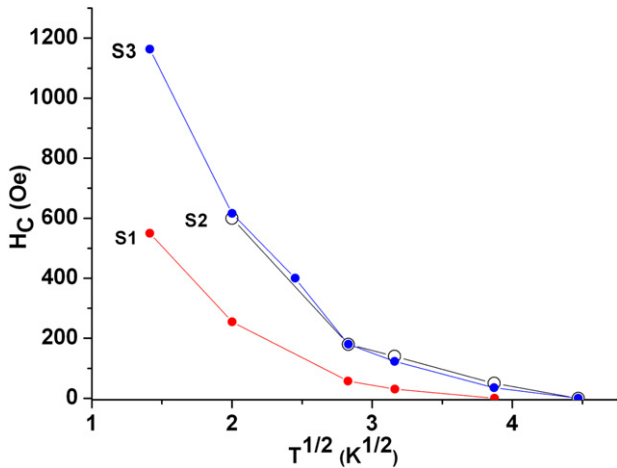


Figure 10. The variation of coercivity with temperature for samples S1–S3.

0.05 (10 K). These reduced values are most probably induced by both internal strain and interparticle interactions.

The change of H_C (ZFC) with temperature for S1–S3 is presented in figure 10. The coercivity develops below the freezing temperature and its value decreases non-linearly with increasing temperature. The presented results show the values of H_C and their dependence on particle size. We note that although the values of H_C for S2 and S3 are very similar, there is a difference in the size of these particles (table 2). In noninteracting single-domain nanoparticles with uniaxial anisotropy, the $H_C(T)$ dependence should obey the relation $H_C = H_{C0}[1 - (T/T_B)^{1/2}]$ [37], where H_{C0} denotes the coercivity at $T = 0$ K and T_B is the blocking temperature. The observed deviation in linearity

of the $H_C(T^{1/2})$ curves (figure 10) is attributed to the existence of interparticle interactions. Further investigation of the interparticle interactions was carried out by $M(H)$ measurements at different temperatures in SPM regions. Figure 11 shows the reduced magnetization (M/M_S) versus H/T for three selected temperatures, 100, 200 and 300 K, for the S1 sample (main panel). The values of the saturation magnetization M_S were obtained by extrapolating M versus $1/H$ at $1/H = 0$. Non-overlapping curves have been found in superspin-glass systems [8], and indicate the existence of interparticle interactions. For two other samples, S2 and S3, the $M(H)$ curves at 300 K are presented in the inset of figure 11. They show S-shapes with zero values of coercivity and remanence, which is typical for SPM systems.

Concerning the value of the saturation magnetization, it was found to be around 50 emu g^{-1} for S3 at 10 K (figure 9) and about 20 emu g^{-1} at room temperature (the inset of figure 11). The value depends on the cation distribution, surface and core particle spin canting, inter- and intra- particle interactions, different kinds of anisotropies, and parasite phases. Brief inspection of the literature points to a broad range of reported values of the magnetization of Zn–ferrite nanoparticles, from 11 to 88 emu g^{-1} as was reported in [38]. A partial migration of Fe atoms from A to B sites yields ferrimagnetic clusters due to the strong A–B superexchange interactions. This partial inversion has been invoked as the source of the much larger magnetization in ZnFe_2O_4 fine particles [41] or the room temperature ferrimagnetic behavior observed in ZnFe_2O_4 thin films [39, 40].

We have used DC magnetization measurements in order to examine the existence of core/shell structure of Zn–ferrite nanoparticles, to correlate the obtained results with PDF/Rietveld results (section 3.1), and to extract

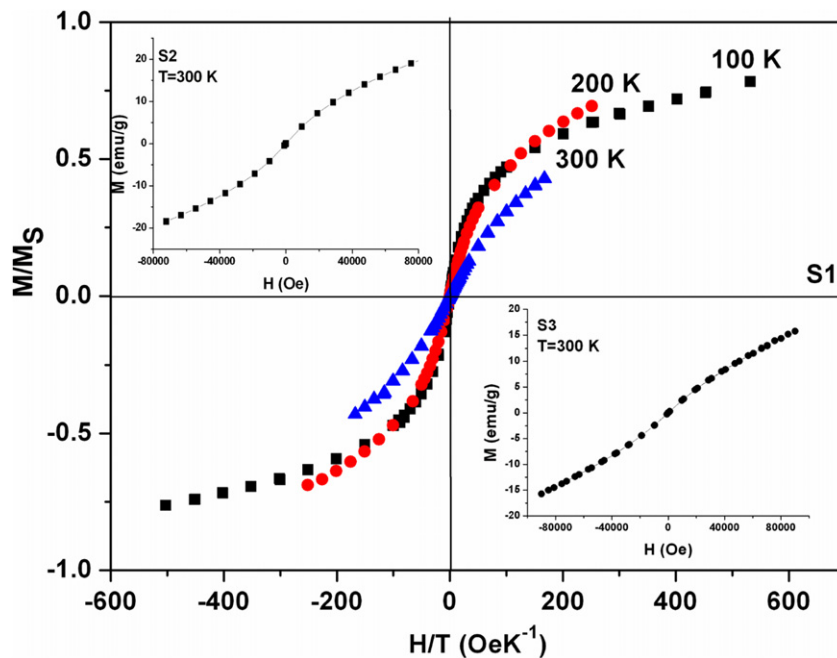


Figure 11. Normalized magnetization versus H/T for S1 at 100, 200 and 300 K. Inset: magnetization versus field for S2 and S3 at 300 K.

information on the interparticle interactions. The shell was found to be thin in all samples studied. The results of DC magnetization measurements suggest a picture of interacting ferrite nanoparticles.

3.3.3. The AC susceptibility of Zn-ferrite nanoparticles. In order to get a better insight into the nature of the magnetic state at low temperatures, the magnetic dynamics was investigated by AC susceptibility measurements as described in section 2. Figure 12(a) shows the in-phase part χ' and the out-of-phase part χ'' of the dynamic susceptibility $\chi_{ac} = \chi' - i\chi''$ for sample S3 measured at different frequencies, f in an oscillating field of 5 Oe. As can be seen, at the peak values of the $\chi'(T, f)$ curves, T_f increases and shifts to lower temperatures with decreasing frequency. $\chi''(T, f)$ also shows a maximum whose amplitude and position depend on the frequency of the AC field. The obtained dependences of the χ' and χ'' maxima are characteristic for superspin-glass (SSG) as well as for SPM systems [41, 42].

Information about the magnetic state was first extracted from the relative shift of the maximum peak temperature T_f per decade of frequency, i.e. $\Psi = (\Delta T_f / T_f) / \Delta(\log f)$, for the in-phase part χ' . For spin-glasses Ψ has a value in the range $\sim 10^{-3} - 10^{-2}$ [41, 42]. In the case of a superparamagnet (noninteracting magnetic particles) the Ψ parameter is 10^{-1} [41]. The obtained value of $\Psi = 0.027$ suggests that the investigated system is a superspin-glass, rather than a superparamagnet.

To analyze the obtained frequency shift of the temperature $T_f(f)$ we used two approaches usually used for ensembles of interacting nanoparticles: (i) the Vogel-Fulcher law and (ii) dynamic scaling theory. The empirical Vogel-Fulcher law, given by the following expression, is widely used in cluster-glass systems [42]:

$$f = f_0 \exp(-E_a / (T_f - T_0)), \quad (2)$$

where the parameter T_0 is a measure of the interparticle interaction strength, and E_a denotes an energy barrier parameter. $E_a = K_{eff}V$, where K_{eff} and V denote the anisotropy and particle volume, respectively. The frequency parameter f_0 is connected with the relaxation time τ of the magnetization vector in the region $T \rightarrow T_f^+$ by the relation $\tau = 1/f_0$. To precisely determine the T_f as a maximum value in $\chi'(T, f)$ we fitted the experimental values near maxima by a polynomial function. The observed T_f for different frequencies in the range of 1–1000 Hz was fitted using equation (2), see figure 12(b). The obtained best-fit values of the parameters were $E_a = 255$ K, $T_0 = 26.4$ K and $f_0 = 1.3 \times 10^{12}$ Hz. The relaxation time τ was found to cover a wide range of values, from 10^{-6} s [43] to 10^{-13} s [44] in spin-glasses and from 10^{-9} to 10^{-11} s in SPM systems [35]. The observed $\tau = 7.6 \times 10^{-13}$ s indicates a spin-glass-like behavior.

In the second approach, the in-phase component χ' of the AC susceptibility was analyzed according to conventional power-law dynamics. In the $T \rightarrow T_f^+$ temperature region, the relaxation time τ of the magnetic moments shows a critical slowing-down described by the relation $\tau = \tau_0 \varepsilon^{-z\nu}$,

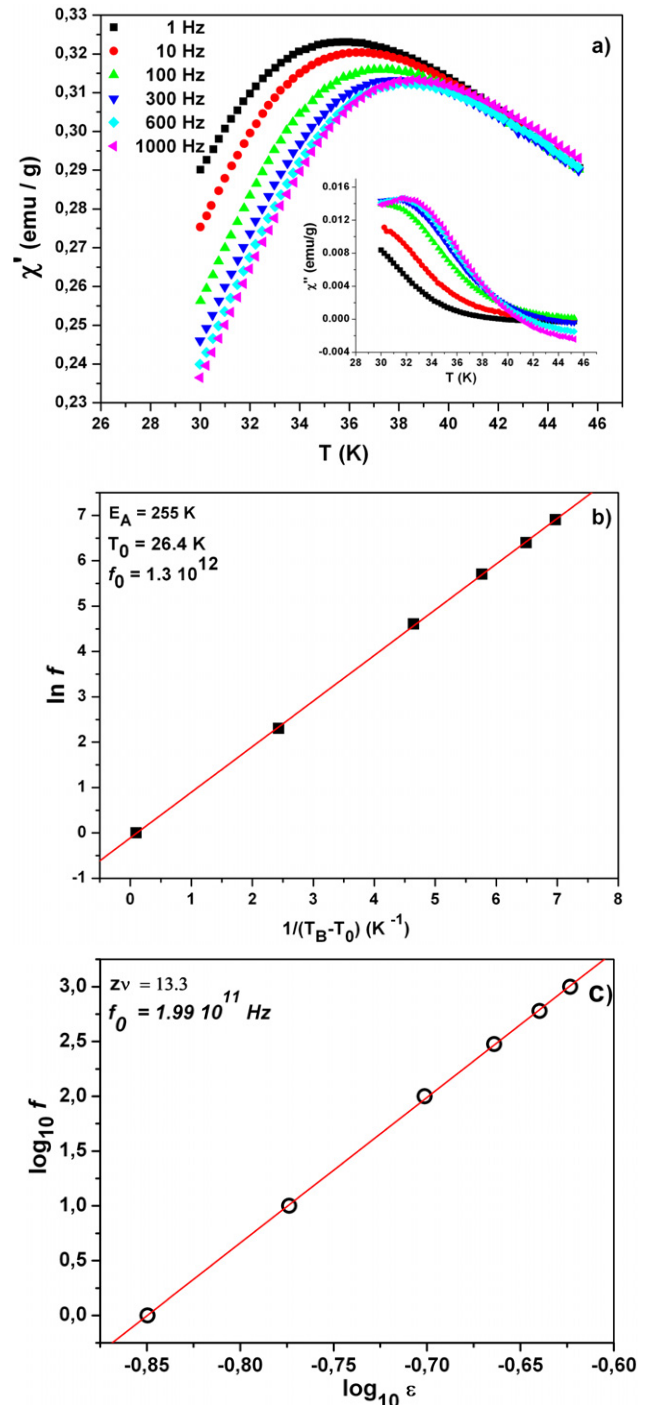


Figure 12. (a) The real, χ' , and imaginary, χ'' , (inset) components of the AC susceptibility as a function of temperature and frequency for the Zn-ferrite annealed at 500 °C (S3); (b) a plot of $\ln f$ versus $1/(T_f - T_0)$; and (c) a log-log plot of the reduced temperature $\varepsilon = (T - T_f)/T_f$ versus the driven frequency for sample S3.

where $\varepsilon = (T - T_f)/T_f$ denotes a reduced temperature, τ_0 is the microscopic relaxation time, z is the dynamical scaling exponent, and ν is the correlation-length scaling exponent [41, 45]. Thus, the frequency-dependent maxima should follow the expression

$$f = f_0 \varepsilon^{z\nu}. \quad (3)$$

A log–log plot of $f(\varepsilon)$ gives an excellent linear dependence, as shown in figure 12(c). The best-fit values of the parameters are $f_0 = 1.99 \times 10^{11}$ Hz, $z\nu = 13.3$ and $T_f = 31$ K. For canonical spin-glasses such as CuMn and AuMn, typical f_0 values are within the 10^{11} – 10^{12} Hz range [41]. The obtained value of the critical exponent $z\nu$ is larger in comparison with those found in diluted magnetic semiconductors [46, 47] and other spin-glasses, where the $z\nu$ parameters are in the range of 4–10 [41]. However, some works on magnetic nanoparticles with strong interactions, high local disorder and/or broad particle size distributions have reported power-law dynamics near T_f , with exponents $z\nu$ within the $10 \leq z\nu < 24$ range [48, 49].

It is well known that, for systems of noninteracting, single-domain magnetic particles, the frequency dependence of the blocking temperature $T_B(f)$ can be well described by the Néel–Arrhenius law [50]. Our experimental data were also fitted to the Arrhenius law, but unphysical values were obtained.

3.4. Mössbauer spectroscopy study of Zn–ferrites

Mössbauer spectra for zinc–ferrite sample S1, recorded in the temperature interval (10, 298) K, are shown in figure 13. The relative area of doublet components decreases with reducing temperature in favor of sextet components, showing behavior characteristic of superparamagnetic relaxation in nanoparticle systems. A transition to a magnetically ordered state occurs over a wide temperature range. The estimated freezing temperature is $T_f = 46$ K, suggesting that for the nanoparticle sample the ordering temperature is much higher than the Néel temperature reported for bulk samples ($T_N = 9$ K) [51, 52]. In bulk ZnFe_2O_4 normal spinel, all Fe^{3+} ions are octahedrally coordinated with O (sites B) and weak BB superexchange interactions among them are responsible for AF magnetic ordering at the Néel temperature. Due to the partial inversion of the Zn^{2+} and Fe^{3+} cation distributions in nanocrystalline zinc–ferrite, superexchange interaction between iron ions in tetrahedral and octahedral sites occurs, leading to ferrimagnetic long range ordering at much higher temperatures. The degree of cation inversion can be estimated from the low temperature Mössbauer spectrum, with the assumption that the recoilless fractions for Fe^{3+} in tetrahedrally and octahedrally coordinated sites (A and B) are almost the same [53]. Within this assumption, the areas of the A and B site components can be considered as proportional to the iron occupancy in the A and B sites. An inversion degree of 0.27 was estimated from the fit of the Mössbauer spectrum recorded at 10 K.

The fit of the 10 K spectrum is based on the superposition of three sextets with different values of the hyperfine field. The lower isomer shift parameter (IS) of one component suggests that it corresponds to the Fe^{3+} in tetrahedral surroundings (A sites). On the other hand, the invariance of the isomer shift values for the other two components indicates that both of them describe iron nuclei in octahedral site B. The usage of two components represents an approximation made in order to describe different local environments of Fe^{3+} ions

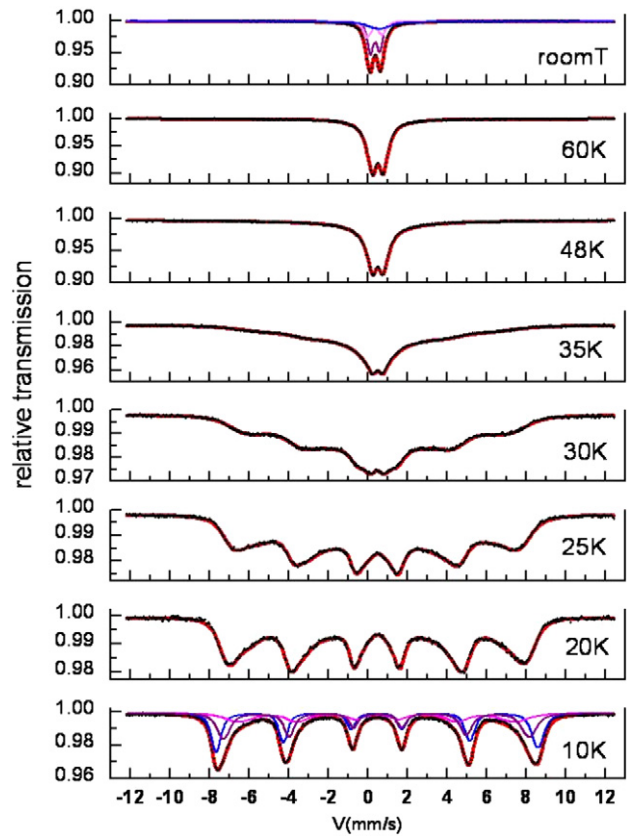


Figure 13. Fitted ^{57}Fe Mössbauer spectra of nanoparticle ZnFe_2O_4 sample S1 from 10 K to room temperature.

in B sites. Due to the lack of resolution, determination of the exact number of such components represents a difficult task. Different values of their hyperfine fields B_{hf} originate from a variety of different environments that Fe nuclei can be found in within this spinel structure. Due to the strong overlap of A and B site components, it is very difficult to make a clear distinction between various subspectra corresponding to different magnetic Fe surroundings. The use of in-field Mössbauer spectroscopy would undoubtedly confirm the existence (or otherwise) of distinct positions of Fe^{3+} in such an inverted spinel structure.

With increasing temperature the three sextet components collapse into the slightly asymmetric doublets obtained in the room temperature Mössbauer spectrum. Collapsing of the components occurs in a wide temperature interval due to the distribution of particle size in the nanoparticle ZnFe_2O_4 S1 sample. Superparamagnetic relaxation spectra recorded at intermediate temperatures show a complex hyperfine structure with a quadrupole doublet superimposed on a magnetically split pattern. The values of the IS obtained from the fit of Mössbauer spectra clearly confirm the absence of the Fe^{2+} valence state (see table 3). A comparison of room temperature Mössbauer spectra for bulk and nanocrystalline zinc–ferrite samples, as well as for nanoparticle samples annealed at 400 and 500 °C is shown in figure 14.

The room temperature Mössbauer spectrum recorded for the bulk sample was fitted as a superposition of two symmetric doublets. The invariant values of the IS, corresponding to

Table 3. Mössbauer parameters extracted from the fit of Mössbauer spectra at different temperatures.

Temperature/sample description	Component	IS (mm s ⁻¹)	QS (mm s ⁻¹)	B _{hf} (T)	Area (%)
10 K S1	S ₁	0.45	0.02	50.49	35.8
	S ₂	0.45	0.07	47.96	37.1
	S ₃	0.42	0.01	43.28	27.1
298 K S1	D ₁	0.36	0.49		67.6
	D ₂	0.39	0.75		32.4
298 K S2	D ₁	0.36	0.45		71.6
	D ₂	0.37	0.79		28.4
298 K S3	D ₁	0.35	0.40		76.4
	D ₂	0.35	0.70		23.6
298 K S4	D ₁	0.35	0.33		44.5
	D ₂	0.35	0.40		55.6

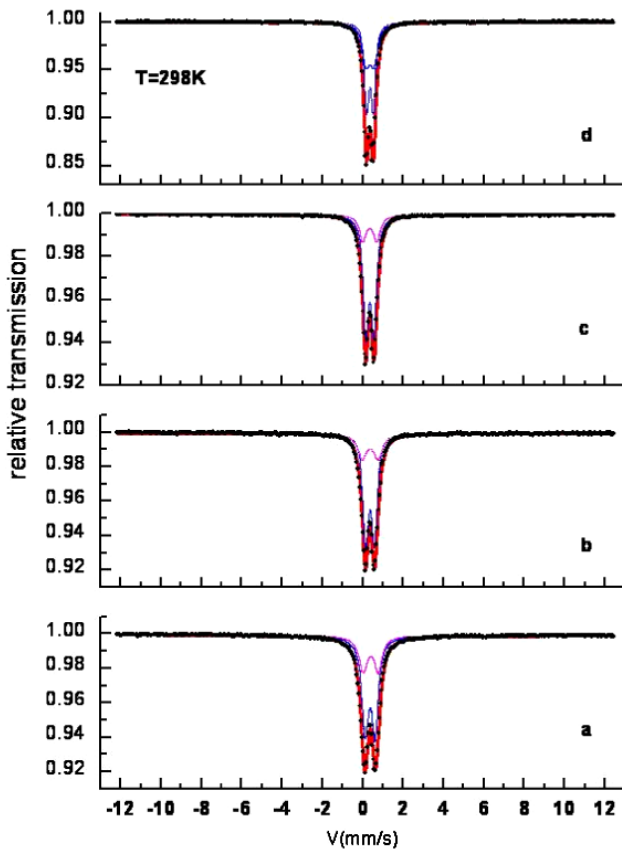


Figure 14. Room temperature Mössbauer spectra for ZnFe₂O₄: (a) S1, (b) nanoparticle S2, (c) S3 and (d) bulk counterpart.

Fe³⁺ ions octahedrally surrounded by oxygen, confirm that the components describe crystallographically the same iron site (B), table 3 [53]. In the case of the nanoparticle sample, an increase of the quadrupole splitting (QS) parameter is evident in comparison to the values obtained for the bulk sample. The disorder in the local field leading to such an increase of the QS in the nanocrystalline sample has several different origins. Firstly, due to the cation redistribution on A and B sites observed by Rietveld and PDF analyses, it is reasonable to expect that the local bond symmetry is changed. Also, a higher degree of defects in nanoparticle samples and a considerable fraction of Fe ions located at the surface of the grains exhibiting spin canting due to the surface anisotropy

could be alternative and/or additional reasons for the observed increase of the QS [54–56].

The annealing treatment of the nanoparticle ZnFe₂O₄ sample at 400 and 500 °C causes structural changes towards higher crystallinity. The increase of the crystallite size by heating lowers the surface contribution and partially reduces the amount of defects, hence reducing the disorder in the local field. The QS parameter exhibits a decreasing trend with increasing nanoparticle size, although an annealing temperature of 500 °C was still insufficient to achieve higher crystallinity compared to that of the bulk sample [57].

4. Conclusions

Multiple complementary techniques were employed in order to study the magnetism, structure and microstructure of a series of Zn–ferrite nanoparticles obtained by thermal treatment (the particle sizes were 4, 7.5 and 13 nm). The crystal structure was refined by both Rietveld and PDF methods using neutron and x-ray data. Small discrepancies between the Rietveld and PDF results were found for the values of the lattice parameters, in which case those derived from the PDF can be considered as more reliable due to the fact that the PDF is based on a total scattering approach including both Bragg and diffuse scattering components, while Rietveld relies on Bragg intensities alone. PDF modeling and the Rietveld method gave comparable values for the crystallite size, suggesting that the nanoparticles (if we consider them as core/shell structured) probably have rather thin shell regions; this was confirmed by FC *M(H)* measurements. The results of DC magnetization and AC susceptibility measurements imply that the investigated Zn–ferrite nanoparticle system can be well described within the SSG picture. Experimental results such as the observation of the Almeida–Thouless line for low-field magnetization data (*T*_{max} versus *H*^{2/3}), the difference in *M*/*M*_S versus *H*/*T* curves above *T*_{max} (temperature of the maximum in ZFC magnetization), the non-linearity in *H*_C versus *T*^{1/2} and the remanence/saturation ratio value *M*_R/*M*_S suggest that the behavior is typical of that of interacting nanoparticle systems. The effective anisotropy constant for the nanoparticle samples, *K*_{eff} = 5.6 × 10⁵ erg cm⁻³, was found to be an order of magnitude higher than the *K*_{eff} for isostructural bulk ferrites. The thermal treatment affected

the magnetic parameters, such as the freezing temperature, coercivity, saturation magnetization and quadrupole splitting observed in Mössbauer spectroscopy measurements.

Acknowledgments

The Serbian Ministry of Education and Science has financially supported this work under contract No. III 45015. We would like to thank Professor Vladimir Srdic for sample preparation. The work at the Brookhaven National Laboratory was supported by the US DOE under Contract No. DE-AC02-98CH10886. The experiments at the Advanced Photon Source at the Argonne National Laboratory were supported by the US DOE Contract No. DE-AC02-06CH11357, and those at LANSCE at Los Alamos National Laboratory under Contract No. DEAC52-06NA25396.

References

- [1] Lee H, Jung J C, Kim H, Chung Y-M, Kim T J, Lee S J, Oh S-H, Kim Y S and Song I K 2008 *Catal. Lett.* **122** 281–6
- [2] Barcena C, Sra A K, Chaubey G S, Khemtong C, Liu J P and Gao J 2008 *Chem. Commun.* **19** 2224–6
- [3] Piraux L et al 1994 *Appl. Phys. Lett.* **65** 2484–6
- [4] De Heer W A 2000 *Nanomagnetism Characterization of Nanophase Materials* ed Z L Wang (Germany: Wiley-VCH)
- [5] Kodama R H, Berkowitz A E, McNiff E J and Foner S 1996 *Phys. Rev. Lett.* **77** 394–7
- [6] Kodama R H 1999 *J. Magn. Magn. Mater.* **200** 359–72
- [7] Tung L D, Kolesnichenko V, Caruntu D, Chou N H, O'Connor J and Spinu L 2003 *J. Appl. Phys.* **93** 7486–8
- [8] Kremenovic A, Antic B, Spasojevic V, Vucinic-Vasic M, Jaglicic Z, Pirnat J and Trontelj Z 2005 *J. Phys.: Condens. Matter* **17** 4285–99
- [9] Suzuki M, Fullem S I, Suzuki I S, Wang L and Zhong C-J 2009 *Phys. Rev. B* **79** 024418
- [10] El-Hilo M, O'Grady K and Chantrell R W 1992 *J. Magn. Magn. Mater.* **114** 307
- [11] Mamiya H and Nakatani I 1998 *J. Magn. Magn. Mater.* **177** 966–7
- [12] Néel L 1949 *Ann. Geophys.* **5** 99–136
- [13] Antic B, Kremenovic A, Nikolic A S and Stoilkjovic M 2004 *J. Phys. Chem. B* **108** 12646–51
- [14] Maletin M, Moshopoulou E G, Kontos A G, Devlin E, Delimitis A, Zaspalis V T, Nalbandian L and Srdic V V 2007 *J. Eur. Ceram. Soc.* **27** 4391–4
- [15] Maletin M, Moshopoulou E G and Srdic V V 2008 *Phys. Status Solidi a* **205** 1831–4
- [16] Chupas P J, Qiu X, Hanson J C, Lee P L, Grey C P and Billinge S J L 2003 *J. Appl. Crystallogr.* **36** 1342–7
- [17] Hammersley A P, Svenson S O, Hanfland M and Hauserman D 1996 *High Pressure Res.* **14** 235–48
- [18] Egami T and Billinge S J L 2003 *Underneath the Bragg Peaks: Structural Analysis of Complex Materials* (New York: Pergamon)
- [19] Qiu X, Thompson J W and Billinge S J L 2004 *J. Appl. Crystallogr.* **37** 678
- [20] Rodriguez-Carvajal J 2003 *FullProf.2k [Version 2.40-May 2003-LLB JRC] Computer program www-llb.ccea.fr/fullweb/fp2k/fp2k.htm*
- [21] Billinge S J L and Levin I 2007 *Science* **316** 561–5
- [22] Farrow C L, Juhas P, Liu J W, Bryndin D, Bozin E S, Bloch J, Proffen Th and Billinge S J L 2007 *J. Phys.: Condens. Matter* **19** 335219
- [23] Shannon R D 1976 *Acta Crystallogr. A* **32** 751–67
- [24] Nakashima S et al 2007 *Phys. Rev. B* **75** 174443
- [25] Ammar S et al 2004 *J. Non-Cryst. Solids* **345/346** 658–62
- [26] Spasojevic V, Mrakovic A, Perovic M, Kusigerski V and Blanus J 2011 *J. Nanopart. Res.* **13** 763–71
- [27] de Almeida J R L and Thouless J J 1978 *J. Phys. A: Math. Gen.* **11** 983–90
- [28] Garcia del Muro M, Battle X and Labarta A J 2000 *J. Magn. Magn. Mater.* **221** 26–31
- [29] Hamdeh H H, Xia Z, Foehrweiser R and McCormick B J 1994 *J. Appl. Phys.* **76** 1135
- [30] Du F, Bie X, Chen Y, Wei Y, Liu L, Wang C, Zou G and Chen G 2009 *J. Appl. Phys.* **106** 053904
- [31] Martinez B, Obradors X, Balcells L, Rouanet A and Monty C 1998 *Phys. Rev. Lett.* **80** 181–4
- [32] Laue I, Vanacken J, Nateprov A N, Herlach F, von Ortenberg M and Arushanov E K 2006 *Phys. Status Solidi b* **185** 245–55
- [33] Singh M K, Katiyar R S, Prellier W and Scott J F 2009 *J. Phys.: Condens. Matter* **21** 042202
- [34] Muroi M, Street R, McCormick P G and Amighian J 2001 *Phys. Rev. B* **63** 184414
- [35] Goya G F, Berquó T S, Fonseca F C and Morales M P 2003 *J. Appl. Phys.* **94** 3520–8
- [36] Ammar S et al 2001 *J. Mater. Chem.* **11** 186–92
- [37] Stoner E C and Wohlfarth E P 1948 *Phil. Trans. R. Soc. A* **240** 599–642
- [38] Yao C, Zeng Q, Goya G F, Torres T, Liu J, Wu H, Ge M, Zeng Y, Wang Y and Jiang J Z 2007 *J. Phys. Chem. C* **111** 12274–8
- [39] Lorenz M, Brandt M, Mexner K, Brachwitz K, Ziese M, Esquinazi P, Hochmuth H and Grundmann M 2011 *Phys. Status Solidi RRL* **5** 438–40
- [40] Raghavender A T 2011 *Mater. Lett.* **65** 3636–8
- [41] Mydosh J A 1993 *Spin Glasses: An Experimental Introduction* (London: Taylor and Francis)
- [42] Antic B, Goya G F, Rechenberg H R, Kusigerski V, Jovic N and Mitric M 2004 *J. Phys.: Condens. Matter* **16** 651–9 and references therein
- [43] Bhowmik R N and Ranganathan R 2001 *J. Magn. Magn. Mater.* **237** 27–40
- [44] Pejakovic D A, Manson J L, Miller J S and Epstein A 2000 *Phys. Rev. Lett.* **85** 1994–7
- [45] Gunnarsson K, Svedlindh P, Norbald P and Lundgren L 1988 *Phys. Rev. Lett.* **61** 754–7
- [46] Goya G F and Sagredo V 2001 *Phys. Rev. B* **64** 235208
- [47] Bontemps N, Rajchenbach J, Chamberlin R V and Orbach R 1984 *Phys. Rev. B* **30** 6514–20
- [48] Kleemann W, Petravic O, Binek Ch, Kakazei G N, Pogorelov Yu G, Sousa J B, Cardoso S and Freitas P P 2001 *Phys. Rev. B* **63** 134423
- [49] De Toro J A, López de la Torre M A, Arranz M A, Riveiro J M, Martínez J L, Palade P and Filoti G 2001 *Phys. Rev. B* **64** 094438
- [50] Dorman J L, Bessais L and Fiorani D 1988 *J. Phys. C: Solid State Phys.* **21** 2015–34
- [51] Li F S, Wang L, Wang J B, Zhou Q G, Zhou X Z, Kunkel H P and Williams G 2001 *J. Magn. Magn. Mater.* **268** 332–9
- [52] Wang L, Zhou Q and Li F 2004 *Phys. Status Solidi* **2** 377–82
- [53] Battle J, Clark T and Evans B J 1997 *J. Physique IV* **7** C1–257
- [54] Stewart S J, Figueroa S J A, Sturla M B, Scorzelli R B, Garcia F and Requejo F G 2007 *Physica B* **389** 155–8
- [55] Li F, Wang H, Wang L and Wang J 2007 *J. Magn. Magn. Mater.* **309** 295–9
- [56] Chinnasamy C N, Narayanasamy A, Ponpandian N, Chattopadhyay K, Guerault H and Greneche J-M 2001 *Scr. Mater.* **44** 1407–10
- [57] Potzel W, Schäfer W and Kalvius G M 2000 *Hyperfine Interact.* **130** 241–73

Thermal Evolution of Cation Distribution/Crystallite Size and Their Correlation with the Magnetic State of Yb-Substituted Zinc Ferrite Nanoparticles

M. Vucinic-Vasic,[†] E. S. Bozin,[‡] L. Bessais,[§] G. Stojanovic,[†] U. Kozmidis-Luburic,[†] M. Abeykoon,[‡] B. Jancar,^{||} A. Meden,[⊥] A. Kremenovic,^{#,∇} and B. Antic^{*,#}

[†]Faculty of Technical Sciences, University of Novi Sad, Trg D. Obradovica 6, 21000 Novi Sad, Serbia

[‡]Condensed Matter Physics and Materials Science Department, Brookhaven National Laboratory, Upton, New York 11973, United States

[§]ICPME, UMR 7075 CNRS and Université Pierre and Marie Curie, 94230 Thiais, France

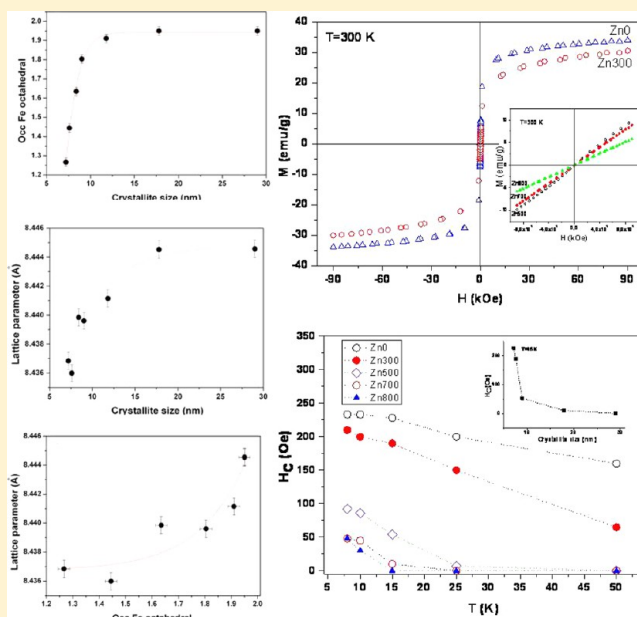
^{||}Jožef Štefan Institute, Jamova 39, 1000 Ljubljana, Slovenia

[⊥]Faculty of Chemistry and Chemical Technology, University of Ljubljana, 1000 Ljubljana, Slovenia

[#]Institute of Nuclear Sciences "Vinča", University of Belgrade, P.O. Box 522, 11001 Belgrade, Serbia

[∇]Faculty of Mining and Geology, Laboratory for Crystallography, University of Belgrade, P.O. Box 162, 11001 Belgrade, Serbia

ABSTRACT: Evolution of the structural and magnetic properties of $\text{ZnFe}_{1.95}\text{Yb}_{0.05}\text{O}_4$ nanoparticles, prepared via a high-energy ball milling route and exposed to further thermal annealing/heating, was assessed in detail and correlation of these properties explored. While as-prepared spinel nanoparticles possess a high degree of inversion, heating of the sample to $\sim 500^\circ\text{C}$ is found to rapidly alter the cation distribution from mixed to normal, in agreement with the known cation preferences. Under the same conditions the crystallite size only slowly grows. By further thermal treatment at higher temperatures, the crystallite size is changed more appreciably. An interrelationship among the lattice parameter, octahedral site occupancy, and crystallite size has been established. The observations are (a) both the site occupancy of Fe^{3+} at octahedral 16d spinel sites ($N_{16d}(\text{Fe}^{3+})$) and the cubic lattice parameter rapidly increase with an initial increase of the crystallite size, (b) the lattice parameter increases with increasing occupancy, $N_{16d}(\text{Fe}^{3+})$, and (c) there appears to be a critical nanoparticle diameter (approximately 15 nm) above which both the site occupancy and lattice parameter values are saturated. The magnetic behavior of the annealed samples appears to be correlated to the evolution of both the cation distribution and crystallite size, as follows. As-prepared samples and those annealed at lower temperatures show superparamagnetic behavior at room temperature, presumably as a consequence of the Fe^{3+} distribution and strong $\text{Fe}^{3+}(8a)-\text{O}-\text{Fe}^{3+}(16d)$ superexchange interactions. Samples with a nanoparticle diameter greater than 12 nm and with almost normal distributions exhibit the paramagnetic state. The coercive field is found to decrease with an increase of the crystallite size. Partial $\text{Yb}^{3+}/\text{Fe}^{3+}$ substitution is found to increase the inversion parameter and saturation magnetization. Detailed knowledge of the thermal evolution of structural/microstructural parameters allows control over the cation distribution and crystallite size and hence the magnetic properties of nanoferrites.



1. INTRODUCTION

For many years ferrites have been one of the most studied materials, particularly in the form of nanopowders and thin films. They crystallize in a simple spinel structure and often serve as model systems. Their broad industrial applications require development of controlled methods for their synthesis, which would supply the targeted characteristics of the material. Another

possibility to optimize the physical properties of a ferrite is a partial substitution of cations by 3d and 4f elements. The rare earth (4f) ions are larger than the hosts; hence, they often create

Received: April 8, 2013

Revised: May 12, 2013

Published: May 15, 2013

structural distortions and have significant influence on the crystallite strain. Binary ferrites (MFe_2O_4 ; $M = Zn, Mn, Fe, Ni, Cr$) are often doped/substituted to improve their magnetic properties. It is noteworthy that a series of $Fe_{2.85}RE_{0.15}O_4$ ($RE = Gd, Dy, Ho, Tm, \text{ and } Yb$) samples have recently been prepared by high-energy ball milling (HEBM) protocols, and a correlation between the magnetic and structure properties has been reported.¹ One of the goals of this study is to investigate the effect of partial substitution of Fe ions with Yb in the zinc ferrite nanoparticle system on the magnetic properties of the parent compound.

Ferrites crystallize in a spinel-type cubic structure, which is traditionally divided into two different ideal structure types, normal and inverse. In normal spinels, M ions of ferrites MFe_2O_4 are solely located on tetrahedral (8a) sites and Fe ions solely on octahedral (16d) sites within the $Fd\bar{3}m$ space group. Inverse spinels have half of the Fe ions residing on tetrahedral sites, while the rest of the Fe ions and all the M ions occupy the octahedral sites. At the nanoscale, the cation distribution is often found to be mixed (between these two ideal structure types), and this is then quantified by the inversion parameter, which corresponds to the fraction of M ions residing on the octahedral sites. Bulk $ZnFe_2O_4$ is known to have an almost normal spinel structure with Zn^{2+} ions located on tetrahedral sites and Fe^{3+} ions located on the octahedral sites. On the other hand, the nanosized counterpart has a mixed cation distribution $(Zn_{1-\alpha}Fe_{\alpha})_{8a}[Zn_{\alpha}Fe_{2-\alpha}]_{16d}$, where the inversion parameter α is found to vary, depending on the sample preparation method and the thermal treatment.²

The aims of this work were (i) the synthesis of Yb-substituted zinc ferrite by the HEBM method, (ii) an investigation of the thermal evolution of structural and microstructural parameters by both in situ and ex situ X-ray diffraction techniques, (iii) the determination of the magnetic properties of as-prepared and annealed samples, and (iv) an investigation of the relationship between the structure/microstructure and the magnetic properties.

2. EXPERIMENTAL SECTION

2.1. Mechanochemical Synthesis. The starting compounds for mechanochemical synthesis of the title compound were ZnO, Fe_2O_3 , and Yb_2O_3 . They were mixed in appropriate molar ratios according to the stoichiometry $ZnFe_{1.95}Yb_{0.05}O_4$. The mixture was milled in air using a planetary ball Fritch “pulverizette 4” mill equipped with tungsten carbide bowls and balls. The milling parameters were a ball-to-powder mass ratio of 20:1, a rotation speed of the main disk of 400 rpm, and a rotation speed of the planets of 1300 rpm. Balls 10 mm in diameter and a 250 mL bowl were used. The time of milling was approximately 10 h.

As-prepared $ZnFe_{1.95}Yb_{0.05}O_4$ (Zn0) from the same batch was then annealed at different temperatures (300, 400, 500, 600, 700, and 800 °C) for 6 h each. The annealed samples are labeled as Zn300, Zn400, Zn500, Zn600, Zn700, and Zn800, where the numbers denote the corresponding annealing temperature.

2.2. Experimental Methods: X-ray Diffraction (XRD), Transmission Electron Microscopy (TEM), and Electrical and Magnetization Measurements. X-ray powder diffraction (XRPD) data were collected on a PANalytical X'pert PRO diffractometer equipped with an Anton Paar HTK-1200N using $Cu K\alpha_1$ radiation. Data were collected in the 2θ range from 16.995° to 89.976° in steps of 0.053° for in the situ regime and from 15.019° to 119.941° in steps of 0.067° for the ex situ regime. In situ measurements were made at room temperature and in the temperature interval of 100–600 °C in steps of 100 °C. Separately, after annealing at temperatures of 300, 400, 500, 600,

700, and 800 °C, the diffraction patterns on such obtained samples were collected at room temperature (ex situ regime).

The synchrotron X-ray experiment was conducted on ex situ samples at 300 K on the 11-IDC beamline of the Advanced Photon Source (APS) at Argonne National Laboratory (ANL). The setup utilized an X-ray beam 0.5 mm \times 0.5 mm in size with a wavelength of 0.108 Å ($E = 114.82$ keV) and a Perkin-Elmer amorphous silicon image plate detector mounted perpendicular to the primary beam path. Finely pulverized samples packed in a cylindrical polyimide capillary 1 mm in diameter were placed 357.84 mm away from the detector. Multiple scans were performed on each sample to a total exposure time of 250 s to improve the counting statistics. The 2D diffraction data were integrated and converted to intensity versus 2θ data using the software FIT2D.³ The intensity data were corrected and normalized⁴ and converted to an atomic pair distribution function (PDF), $G(r)$, using the program PDFgetX2.⁵ Data up to $Q_{\max} = 26 \text{ \AA}^{-1}$ were used in the Fourier transform, an optimal value found for this set of measurements balancing the trade-off between the signal-to-noise ratio and the counting statistics, to produce good-quality PDFs.⁴

Transmission electron micrographs were collected with a Jeol JEM 2100 transmission electron microscope operating at 200 kV. The samples were prepared by dispersing the powders in acetone and dropping the suspension on a lacey carbon film supported on a 300-mesh copper grid.

Magnetic measurements were performed on a PPMS magnetometer. Magnetization vs field, $M(H)$, data were measured in the 10–300 K temperature range under the zero-field-cooled (ZFC) regime up to a field of 9 T.

3. RESULTS AND DISCUSSION

3.1. Crystal Structure Determination of $ZnFe_{1.95}Yb_{0.05}O_4$ by Rietveld Refinement and PDF Modeling. The prepared sample was checked using the collected XRD data. All the reflections in the diffraction pattern were indexed in the expected $Fd\bar{3}m$ space group and the spinel structure type. However, some low-intensity reflections were noticed originating from hematite and tungsten carbide. Contamination of tungsten carbide derived from the bowls and balls that were used in the synthesis process.

X-ray diffraction data collected at room temperature for as-prepared $ZnFe_{1.95}Yb_{0.05}O_4$ and annealed samples were used to refine the structure parameters to study their thermal evolution (ex situ studies). The evolution of the structure parameters with heating of the as-prepared Zn0 sample was also investigated using the in situ diffraction technique in the temperature range of 25–600 °C.

Due to the presence of hematite and tungsten carbide besides the main spinel phase, we have used a three-phase Rietveld refinement in the Fullprof computer program⁶ to refine the crystal structure parameters. The refinement ascertained the weight fraction for both hematite and tungsten carbide (WC) phases together to be less than 1.5 wt % (ex situ). Figure 1 shows the graphical result of the Rietveld refinement procedure for Zn0 with a comparison between observed and calculated intensities. Tungsten carbide reflections were not visible in the diffraction pattern of samples annealed at 500 °C and higher temperatures (ex situ studies) or at temperatures above 500 °C (in situ studies). It is well-known that tungsten carbide powder burns in air. Oxidation of WC powder starts at 500 °C, and WC can be burned completely at 529 °C.⁷ Structural parameters of the main ferrite phase that were refined were the lattice parameter, isotropic temperature factors, and occupation numbers.

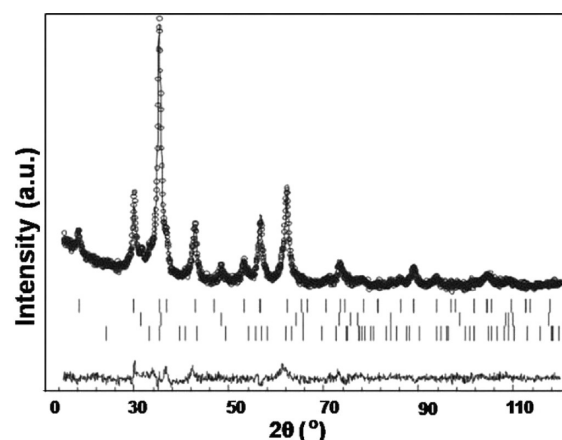


Figure 1. Representative final Rietveld refinement for the ZnO sample, showing the comparison between observed (○) and calculated (solid line) step intensities, as well as their difference. The vertical bars indicate the positions of the crystallographic reflections for the individual phases used. From top to bottom, the first row of tick marks corresponds to the ferrite phase, the second to tungsten carbide, and the third to hematite.

The cation distribution was determined by refinement of site occupancies in the Rietveld approach. The starting model for Rietveld refinement was a random cation distribution of Zn^{2+} and Fe^{3+} ions at octahedral and tetrahedral sites. All Yb^{3+} ions were placed in octahedral sites and fixed there, due to the known Yb^{3+} preference for the octahedral site as well as due to the relatively small atomic fraction of Yb in $\text{ZnFe}_{1.95}\text{Yb}_{0.05}\text{O}_4$. Site occupancies of Zn and Fe were constrained to keep the stoichiometric ratio. Refined cation site occupancy values for the as-prepared sample denoted a mixed distribution, $(\text{Zn}_{0.32}\text{Fe}_{0.68})_{8a}[\text{Zn}_{0.68}\text{Fe}_{1.27}\text{Yb}_{0.05}]_{16d}$. The found inversion parameter of 0.68 denotes a very high level of inversion. It is important to note that in ZnFe_2O_4 prepared following the same protocols the inversion parameter was found to be 0.43.⁸ In mechanochemical synthesis of ferrites, cations can be distributed against their known site preferences (in a large percentage), influencing the physical properties significantly; see, e.g., ref 9. The influence of partial substitution of Fe^{3+} by Yb^{3+} on the cation distribution probably is one of the main reasons for high inversion. To overcome the shortcomings of the Rietveld method for determination of the cation distribution, computed cation–anion bond lengths (based on the values of the Shannon ionic radii) were then compared with those obtained from the refined structure geometry parameters. Final distributions were established when satisfactory agreement between the bond lengths calculated using the two approaches was achieved.

The thermal evolution of the cation distribution is shown in Figure 2 using the values of the occupation number for Fe in octahedral 16d positions. Both ex situ and in situ values show the same tendency to change. Specifically, the distribution appears to exhibit significant changes from mixed toward normal with annealing/heating at lower temperatures (up to 500 °C). With further increasing the annealing temperature to 800 °C, the distribution is slowly changed to normal.

In addition to the crystallographic approach, another approach to analyze the effects of thermal annealing on the structural parameters was used. The experimental PDFs of as-prepared and annealed samples are shown in Figure 3a. As can be seen, the intensity is attenuated at high values of r due to the finite particle size. As the particle size grows, the PDF peaks become more intense at high r and the features propagate further. The PDF structural analysis was carried out using the program PDFgui.⁵

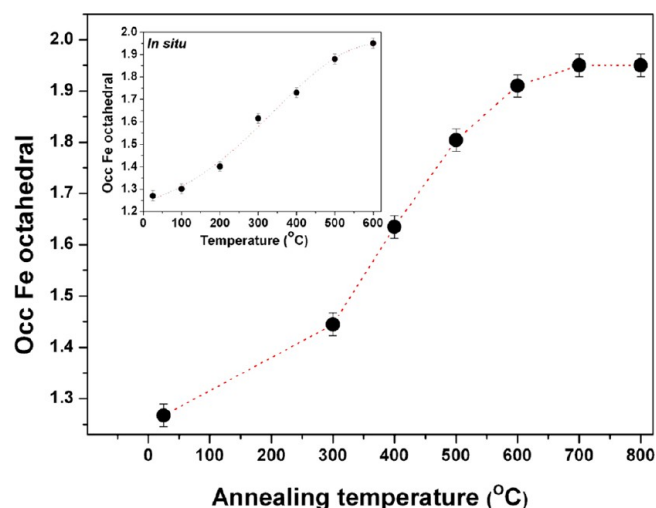


Figure 2. Occupation parameter of Fe^{3+} ions at octahedral sites versus the annealing temperature. The main panel corresponds to room temperature values obtained for the ex situ regime, while the inset shows this evolution in the in situ regime. Dashed lines are guides for the eyes.

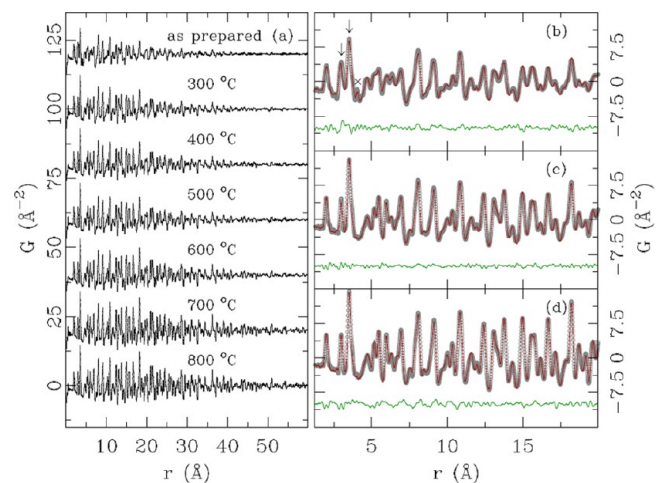


Figure 3. (a) Comparison of experimental PDFs at 300 K obtained from the ex situ experiment on the as-prepared and annealed samples. The annealing temperatures are noted next to the PDF profiles to which they correspond. (b) Fit of the two-phase model (cubic $Fd\bar{3}m$ phase and the WC impurity phase discussed in the text) to the data of the as-prepared sample. Open symbols are the data, the red solid curve is the model, and the green line is the difference that is offset for clarity. Features marked by arrows and a times sign are discussed in the text. (c) and (d) show single-phase $Fd\bar{3}m$ model fits to the data of the samples annealed at 400 and 800 °C, respectively.

The data for all samples are explained reasonably well within the cubic spinel model having $Fd\bar{3}m$ symmetry. The model utilizing eight independent parameters (lattice parameter, oxygen fractional coordinate, iron occupancy in the 16d position, three isotropic atomic displacement parameters, nanoparticle diameter assuming a spherical particle shape, and an overall scale factor) was refined over the 1.2–50 Å range. The occupancy of the 16d site was set to values obtained from the combined approach described above and kept fixed. Representative final fits over a selected range are shown in Figure 3 b–d for the as-prepared sample and samples annealed at 400 and 800 °C, respectively. The fit to the data of the as-prepared sample was substantially worse than the others. A two-phase fit was necessary to account

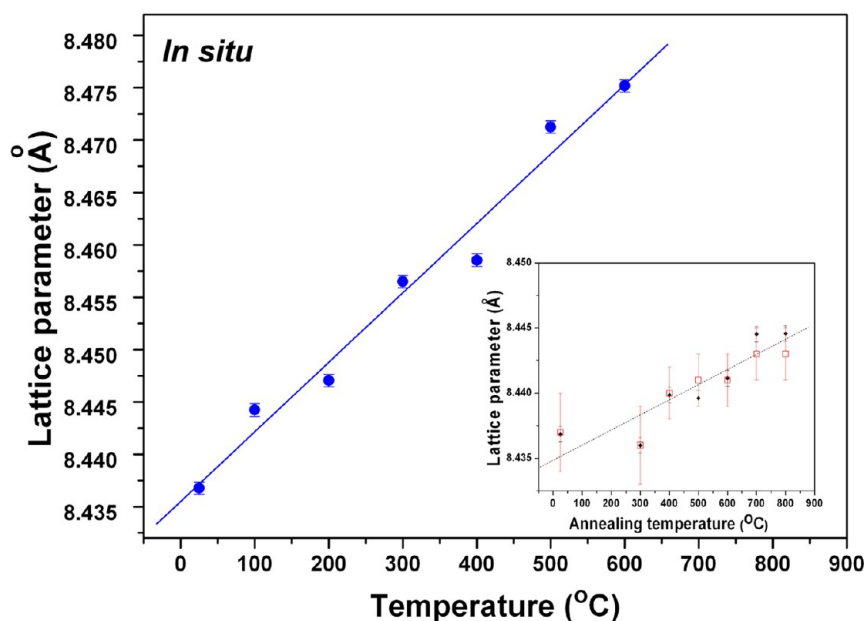


Figure 4. Linear fit to the lattice parameter for as-prepared $\text{ZnFe}_{1.95}\text{Yb}_{0.05}\text{O}_4$ as a function of temperature (in situ) and annealing temperature in the inset (ex situ, Rietveld results are presented by squares, PDF results by tilted squares).

for the presence of the tungsten carbide residue. A feature from this phase can be seen in Figure 3 b marked by a times sign. Closer examination of the difference curve reveals the existence of discrepancies in the low- r region of the PDF for the as-prepared nanocrystalline sample that the $Fd\bar{3}m$ model does not capture correctly. Furthermore, comparison of atomic displacement parameters (ADPs) obtained from broad-range refinement of the as-prepared sample data relative to those obtained for the annealed samples indicates enlarged values of ADPs for all three atomic species in the as-prepared specimen. This is also observed as markedly broader PDF peaks in Figure 3 b compared to the corresponding peaks seen in the data shown in Figure 3 c,d. While the cubic model in principle explains the data over a broad range, it misses the positions of the PDF peaks centered at around ~ 3.0 and ~ 3.5 Å, marked by arrows in Figure 3 b. The two peaks correspond to the near-neighbor Fe–Fe (16d–16d) and Zn–Zn (8a–8a) distances in the $Fd\bar{3}m$ structure, respectively. This is a known local structural effect caused by an appreciable degree of inversion, as seen in zinc ferrites by the extended X-ray absorption fine structure (EXAFS),¹⁰ X-ray absorption near-edge structure (XANES),¹¹ and PDF,¹² and was discussed in detail elsewhere.¹² This effect is not observed in the data of the annealed samples. Also, the WC impurity is not observed in the data of these samples.

In Figure 4, the change of the lattice parameter with thermal annealing/heating is shown. The lattice parameter of the as-prepared sample shows an approximately linear dependence on the temperature (main panel). The parameters of linear tendency $a = a_0 + kt$ were $a_0 = 8.435(2)$ Å and $k = 6.6(5) \times 10^{-5}$ Å/°C. Lattice parameter changes for the in situ regime are related to (i) simple thermal expansion, (ii) the changes in the cation distribution, (iii) the crystallite size effects (grain–surface relaxation effect), and (iv) the valence of the polyvalent ions. The inset of Figure 4 shows the room temperature lattice parameters determined by the Rietveld and PDF approaches of the annealed samples (ex situ regime). The unit cell changes in this case are related to effects ii–iv. The change of lattice parameter due to changes in the cation distribution is based on

migration of cations between tetrahedral and octahedral sites. The lattice parameter of the spinel lattice depends on the complex interplay between the size of the ions and their distribution. Ionic radii for tetrahedral (IV) and octahedral (VI) coordination are $\text{Fe}^{3+}(\text{IV}) = 0.49$ Å, $\text{Fe}^{3+}(\text{VI}) = 0.645$ Å, $\text{Zn}^{2+}(\text{IV}) = 0.60$ Å, $\text{Zn}^{2+}(\text{VI}) = 0.745$ Å, $\text{Yb}^{3+}(\text{VI}) = 0.858$ Å, and $\text{O}^{2-}(\text{IV}) = 1.38$ Å.¹³ The unit cell parameters of most nanocrystalline materials can also be significantly different from the coarse-grain or single-crystal counterparts due to the grain–surface relaxation effect.¹⁴ The possible reduction of iron from the +3 to the +2 state could also influence the lattice parameter due to the difference in their ionic radius. The difference in the values of the lattice parameter of the annealed sample at a certain temperature and the as-prepared sample heated at the same temperature is a result of thermal expansion and partial differences in the distribution of cations in the 8a and 16d sites. The relative difference between the occupancies of iron at octahedral sites for the two regimes (in situ and ex situ) is equal to or smaller than 5%, except at a temperature of 300 °C, for which the difference is about 10%. Using the obtained values of the lattice parameter for the in situ regime, we can calculate the linear thermal expansion coefficient. The obtained value is $\alpha = 6.4(6) \times 10^{-6}$ °C⁻¹. Literature data for the linear thermal expansion coefficient of bulk and nanocrystalline ZnFe_2O_4 are 6.959×10^{-6} °C⁻¹¹⁵ and 7.1×10^{-6} °C⁻¹,⁹ respectively. The coefficient of volume thermal expansion, $\beta = 3\alpha = 1.9(1) \times 10^{-5}$ °C⁻¹, is in reasonably good agreement with the value (2.056×10^{-5} °C⁻¹) calculated using Ottonello's empirical formula with the oxygen fractional coordinate set to $u = 0.385$.¹⁶

3.2. Microstructure Analysis and Correlations between Structure–Microstructure Parameters. Crystallite size values were obtained by standard line profile analysis of the XRPD data using the Fullprof program. X-ray line broadening was analyzed by refining regular TCH-pV function parameters (isotropic effects).¹⁷ The annealing temperature dependent crystallite size is shown in Figure 5, with the corresponding temperature dependence for the in situ regime shown in the inset. While the crystallite sizes of the samples annealed at

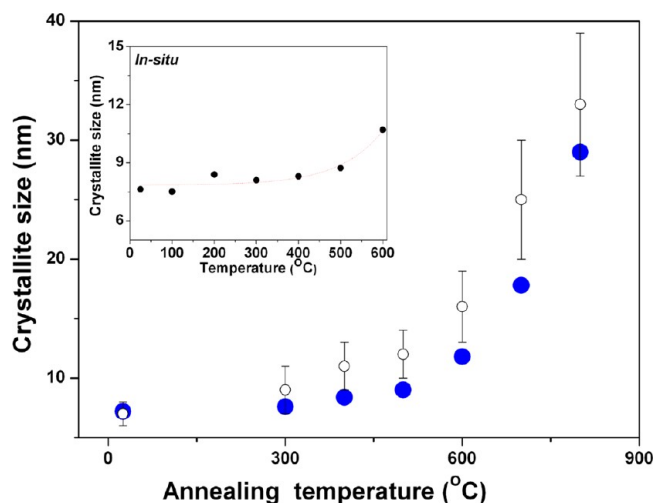


Figure 5. Dependence of the crystallite size for $\text{ZnFe}_{1.95}\text{Yb}_{0.05}\text{O}_4$ on the annealing temperature (●, Rietveld results; ○, PDF results). Inset: evolution of the crystallite size of the as-prepared sample with temperature (in situ studies). The line is a guide for the eyes.

temperatures up to 500 °C are found to be rather similar, slowly increasing between ~ 7 and 9 nm, for the samples annealed at higher temperatures the crystallite size increases much more rapidly. Such a tendency in the evolution of the crystallite size with the annealing conditions assessed from room temperature data was obtained by both the Rietveld and PDF approaches. The in situ assessment by heating the as-prepared sample is in agreement with this, revealing that the crystallite size is almost constant (7.5–8.7 nm) up to 500 °C and then shows an increasing tendency at higher temperature.

To better understand the physical properties of the studied nanoparticles, it is of importance to compare side by side the details of the temperature evolution of various structural–microstructural parameters, including the crystallite size, cation distribution, and lattice parameters, and explore their correlations. At lower heating/annealing temperatures the crystallite size increases rather slowly. In contrast, in the same temperature regime, the migration of cations happens quite quickly. Variation of the lattice parameter with temperature appears to be linear. Thus, for samples annealed at lower temperatures, the dominant effect on the physical properties is likely due to the cation redistribution. On the other hand, at higher processing temperatures the cation distribution becomes close to normal and does not change appreciably anymore, so the samples annealed at temperatures at and above 600 °C can be used to examine the effects of the particle size on the observed physical properties. Figure 6 summarizes the relationship between the crystallite size and the corresponding cation distribution and lattice parameters, as derived from structural refinements of data in the ex situ regime. This analysis reveals that the crystallite size has a rather dramatic effect on both the cation distribution and lattice parameters for sizes below ~ 10 nm, Figure 6 a,b. On the other hand, values of the occupancies and lattice parameters appear to be saturated to approximately their bulk-counterpart values for crystallites larger than ~ 15 nm. It is tempting to speculate that ~ 15 nm is a threshold diameter beyond which the size effect on the cation distribution and lattice parameters becomes less important. With increasing particle size, migration of the cations happens very quickly. Figure 6c shows a trend of increasing lattice parameters with increasing population of the

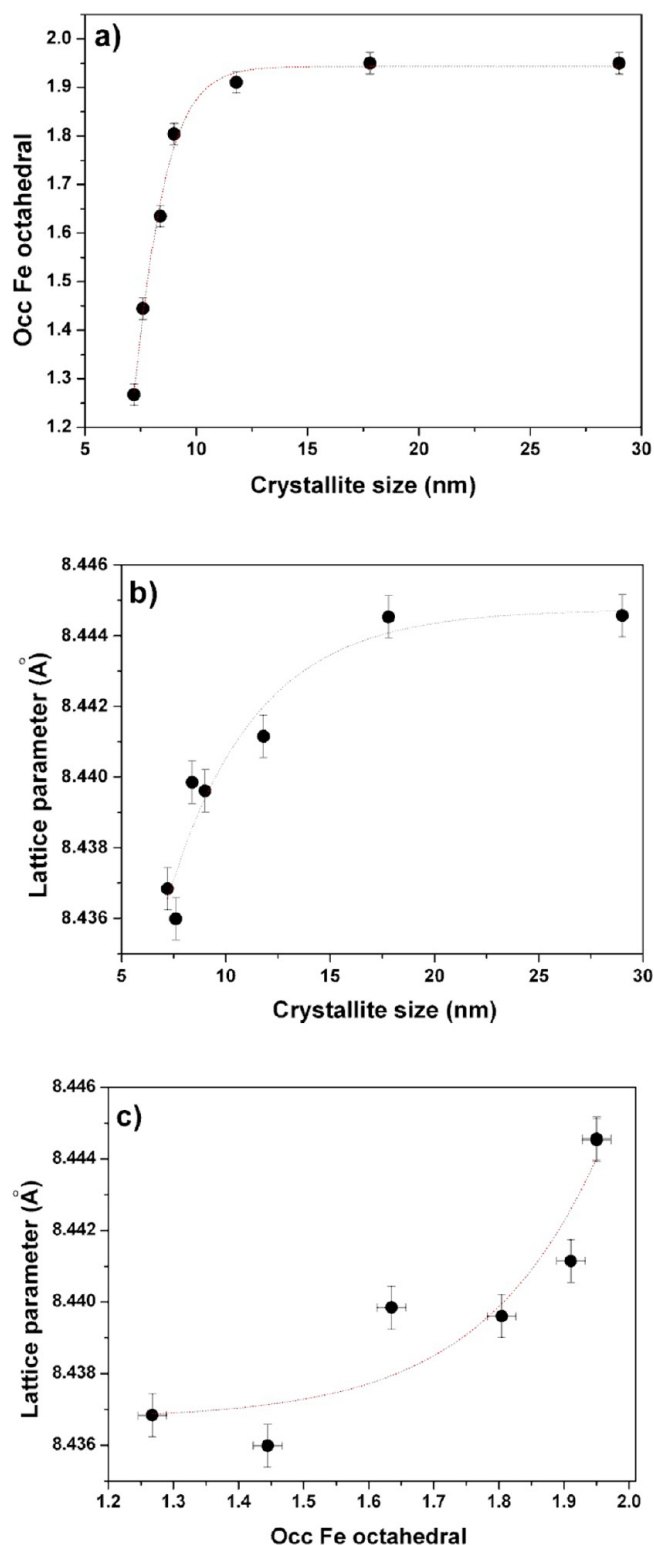


Figure 6. Relationship between (a) the occupation parameter of Fe^{3+} ions at octahedral sites and the crystallite size, (b) the lattice parameter and the crystallite size, and (c) the lattice parameter and the occupation parameter of Fe^{3+} ions at octahedral sites. Refined structural parameters of the annealed samples are used. The lines are guides for the eyes.

octahedral sites by iron ions, reflecting the difference in the respective zinc and iron ionic radii involved in cation rearrangement between the octahedral and tetrahedral sites in the spinel.

The morphology and particle size for the samples studied (ex situ, Zn0–Zn800) were assessed by TEM. These results are illustrated by selected TEM images of Zn0, Zn500, and Zn800 samples, shown in Figure 7. The particles appear to be nearly

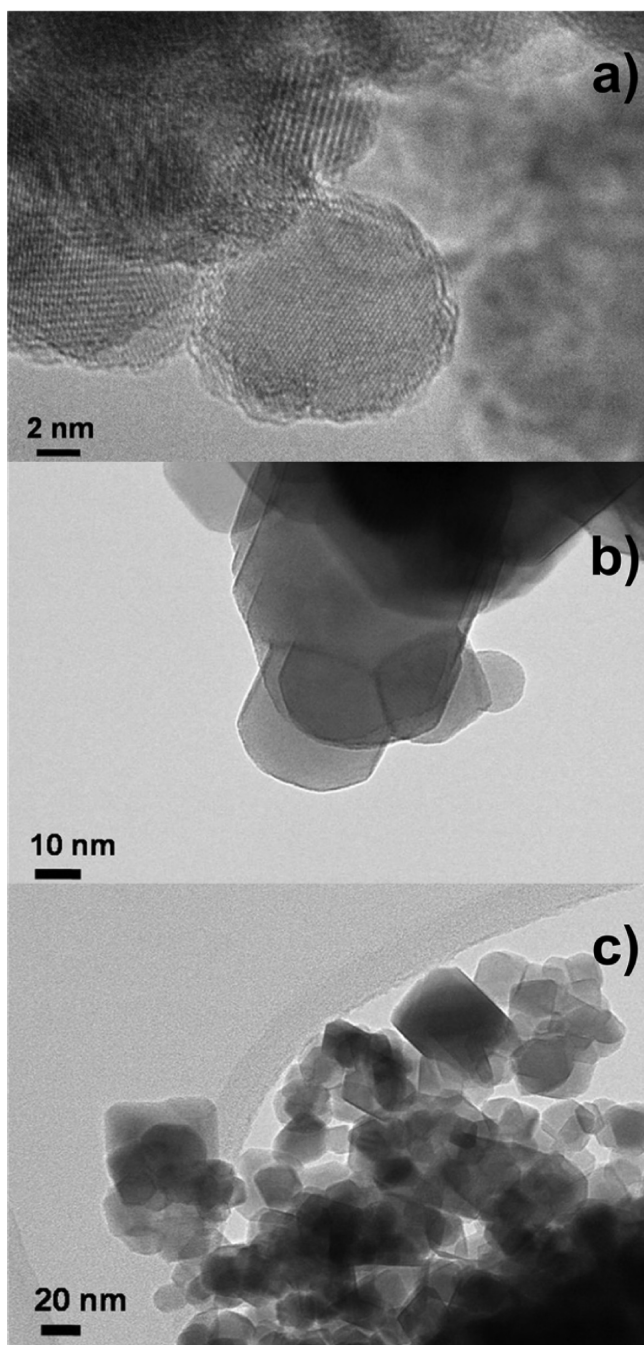


Figure 7. Representative TEM images of selected samples: (a) as-prepared, (b) annealed at 500 °C, and (c) annealed at 800 °C.

spherical in shape, with an average particle size of approximately 20 nm for samples Zn0–Zn300 and approximately 30 nm for samples Zn500–Zn800. Comparison of the Zn0–Zn800 results from TEM imaging, which reveals the overall particle shape and morphology (including conglomeration), and XRPD, which is sensitive to coherent structural cores of underlying nanocrystallites, suggests that as-prepared and annealed nanoparticles are composed of a few crystallites.

3.3. Hysteresis Loops in $\text{ZnFe}_{1.95}\text{Yb}_{0.05}\text{O}_4$. Magnetic hysteresis loops, $M(H)$, for the as-prepared sample (Zn0) as well as for a subset of the annealed samples (Zn300, Zn500, Zn700, Zn800) were recorded at 300 K, Figure 8. Observed

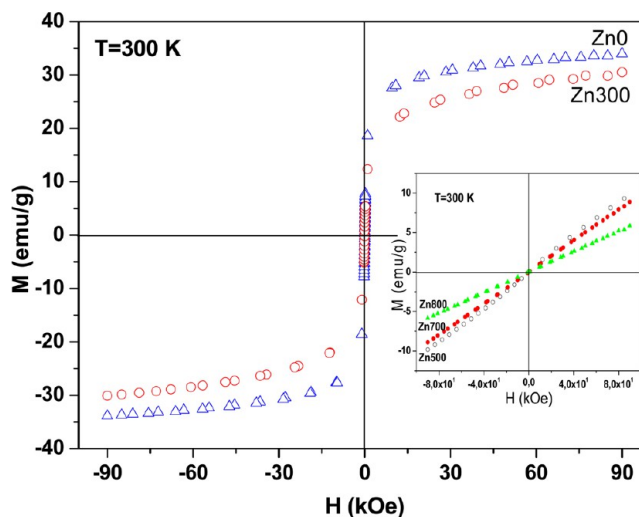


Figure 8. Magnetization versus applied magnetic field at 300 K for $\text{ZnFe}_{1.95}\text{Yb}_{0.05}\text{O}_4$ nanoparticles after annealing at different temperatures (see the text).

differences in $M(H)$ highlight the dependence of the magnetism of the studied system on the particle size and cation distribution. The S-shaped hysteresis loops with zero coercivity and remanence for the Zn0 and Zn300 samples point to their superparamagnetic behavior. For these samples magnetization is not saturated up to the maximum field of 9 T, which indicates enhanced magnetic anisotropy. The value of saturation magnetization, M_s , at room temperature was found to be 35 emu/g for Zn0, bigger than for mechanochemically synthesized zinc ferrite reported earlier, where M_s was found to be 30 emu/g.¹⁸ Incorporation of a ytterbium ion in zinc ferrite influences the magnetocrystalline anisotropy and the value of the observed magnetization. Chinnasamy et al. have proposed that large magnetocrystalline anisotropy influences canting of the core spins and hence the magnetization value.¹⁹ On the other hand, the $M(H)$ curves for the other three samples studied (Zn500, Zn700, and Zn800 corresponding to higher annealing temperatures) are typical for paramagnetic materials. We further elaborate on the $M(H)$ results to explore possible correlations between the magnetism and the structure–/microstructure.

It is well-known that bulk zinc ferrite shows antiferromagnetic behavior because of its normal spinel structure, with magnetic Fe^{3+} ions residing exclusively at 16d sites. However, in small-sized particles, cation redistribution occurs between 8a and 16d, sites leading to a mixed distribution, $(\text{Zn}_{1-x}\text{Fe}_x)_{8a}[\text{Zn}_x\text{Fe}_{2-x}]_{16d}$. In that case magnetic behavior is determined by $(\text{Fe}^{3+})_{8a}$ –O– $(\text{Fe}^{3+})_{16d}$ -type interactions. In the case of as-prepared $\text{ZnFe}_{1.95}\text{Yb}_{0.05}\text{O}_4$, a rather large fraction of Fe^{3+} occupies 8a sites (as observed in Figure 2), causing ferrimagnetic order within single-domain nanoparticles. With annealing the sample at lower temperatures, this distribution is rapidly changed toward normal, while the particle size remains almost unchanged (Figure 5). Simultaneously, as observed, the magnetic behavior changes from superparamagnetic (Zn0, Zn300) to paramagnetic (Zn500, Zn700, Zn800). Correlation between the particle size and magnetism has been intensively investigated in a number of studies.¹² These results suggested that there is a critical

particle diameter at which they become single domain and display superparamagnetic behavior. As the particle size decreases, the surface effects become significant and impact the observed magnetic properties appreciably.²⁰ In sufficiently small particles, such as those studied in this work, a large fraction of spins are expected to be on the particle surface, and these spins have an influence on the net magnetic moment. The observed magnetic behavior is a consequence of both particle size and cation distribution effects. As shown in Figure 6, when the particle diameter reaches values on the order of ~ 15 nm, the cation distribution and lattice parameter become saturated. Interestingly, as the particle size is changed, the crossover in the observed magnetic properties where superparamagnetic behavior is seen appears to coincide with the characteristic diameter considered in structural–microstructural analysis. This indirectly points to the existence of correlation between the structural and magnetic properties.

To further understand the influence of the cation distribution and crystallite/particle size on the magnetism, we explored the temperature dependence of the coercivity, H_C , of these samples in the 10–300 K temperature range, as shown in Figure 9. For

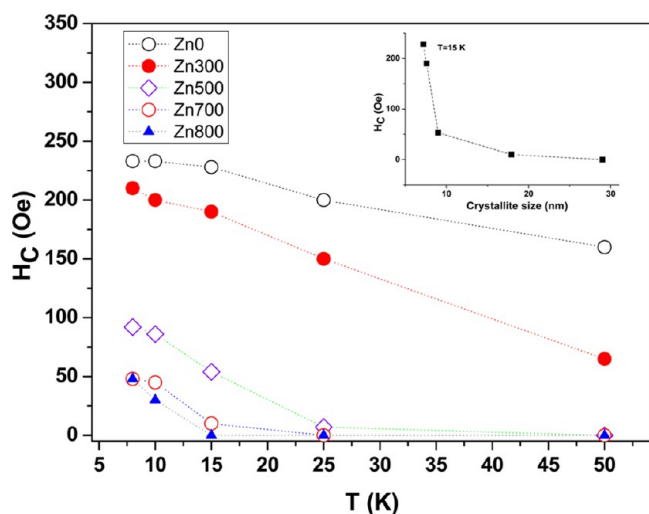


Figure 9. Coercive field (H_C) versus T for $\text{ZnFe}_{1.95}\text{Yb}_{0.05}\text{O}_4$ nanoparticles after annealing at various temperatures. The lines are guides for the eyes. Inset: dependence of H_C on the crystallite size at 15 K.

samples Zn0 and Zn300 coercivity has no zero value in this temperature range. Coercivity becomes zero at $25 \text{ K} < T < 50 \text{ K}$ for Zn500, at $15 \text{ K} < T < 25 \text{ K}$ for Zn700, and at $10 \text{ K} < T < 15 \text{ K}$ for Zn800, as can be seen in Figure 9. If the results are compared for two samples with approximately the same size, Zn300 and Zn500, the conclusion can be derived that the cation distribution dominates the particle size effects in its impact on the observed magnetic properties. To establish the particle size effect on the observed H_C value, a comparison can be made at fixed low temperature for all the samples studied. For this purpose we selected 15 K as a reference: at this temperature the H_C value sharply decreases with an increase of the crystallite size from Zn0 to Zn500 and becomes zero for Zn700. This is shown in the inset of Figure 9, where H_C is plotted versus the particle size at 15 K. For single-domain particles it is well-known that H_C initially increases with an increase of the crystallite size, but above specific characteristic dimensions, when the particles become multi-domain, H_C decreases.²¹ However, the opposite behavior of H_C vs particle size has also been observed, as in, for example, nickel ferrite.²² The enhancement of H_C in smaller nickel ferrite

particles was attributed to the effect of spin canting that dominates the effect of the cation distribution.²² The relationship between the crystallite size and coercivity in single-domain ferrite particles studied in this work is due to surface effects, possible structural disordering, and the cation distribution. Additionally, interparticle interactions also have a large effect on the magnetism. Their presence in the studied ensembles of ferrite nanoparticles is an inevitable reality.

4. CONCLUSION

$\text{ZnFe}_{1.95}\text{Yb}_{0.05}\text{O}_4$ nanoparticles were prepared using an inexpensive and simple mechanochemical procedure at room temperature. Successful substitution of Yb^{3+} for Fe^{3+} in a small percentage has been achieved. Although Yb^{3+} substitution into the spinel structure was done in a relatively small amount, the observed effects on the structural and magnetic properties are rather substantial, compared to those of the pure zinc ferrite system. Combined in situ and ex situ X-ray diffraction techniques, as well as two modeling approaches, Rietveld and PDF, were applied to determine the crystal structure and microstructure and to investigate their evolution with thermal treatment. For annealing/heating temperatures below $500 \text{ }^\circ\text{C}$, the cation distribution rapidly changes, while the crystallite size increases rather slowly. The opposite trend is seen for the processing temperatures in the range between 500 and $800 \text{ }^\circ\text{C}$. Knowledge of this structure–microstructure evolution allows tailoring the cation distribution and the crystallite size by application of appropriate thermal treatment of the as-prepared ferrite sample. Concerning the correlation of the structure–microstructure parameters and the magnetic properties, it was found that the cation distribution has a dominating influence on the magnetization and coercive field values over the particle size effects. Furthermore, this nanoparticle system appears to have an associated characteristic diameter of about 15 nm influencing the displayed magnetic properties. Particles with a larger diameter have saturated values of the cation distribution and lattice parameter. The results of this study also emphasize the importance of taking a systematic approach and combining multiple experimental techniques aimed at better understanding of complex nanocrystalline systems.

AUTHOR INFORMATION

Corresponding Author

*E-mail: bantic@vinca.rs.

Notes

The authors declare no competing financial interest.

ACKNOWLEDGMENTS

The Serbian Ministry of Education and Science has financially supported this work under Contract No. III45015. Work at Brookhaven National Laboratory was supported by the U.S. Department of Energy, Office of Science, Office of Basic Energy Sciences, under Contract No. DE-AC02-98CH10886. This work benefited from usage of the 11-IDC beamline of the APS at ANL. Use of the APS is supported by the U.S. Department of Energy, Office of Science, under Contract No. DE-AC02-06CH11357.

REFERENCES

- (1) Cvejic, Z.; Antic, B.; Kremenovic, A.; Rakic, S.; Goya, G. F.; Rechenberg, H. R.; Jovalekic, C.; Spasojevic, V. Influence of Heavy Rare Earth Ions Substitution on Microstructure and Magnetism of Nanocrystalline Magnetite. *J. Alloys Compd.* **2009**, *472*, 571–575.

(2) Antic, B.; Kremenovic, A.; Nikolic, A. S.; Stoiljkovic, M. Cation Distribution and Size-Strain Microstructure Analysis in Ultrafine Zn–Mn Ferrites Obtained from Acetylacetonato Complexes. *J. Phys. Chem. B* **2004**, *108*, 12646–12651.

(3) Hammersley, A. P.; Svenson, S. O.; Hanfland, M.; Hauserman, D. Two-Dimensional Detector Software: From Real Detector to Idealised Image or Two-Theta Scan. *High Pressure Res.* **1996**, *14*, 235–248.

(4) Egami, T.; Billinge, S. L. J. *Underneath the Bragg Peaks: Structural Analysis of Complex Materials*; Pergamon Press: Oxford, U.K., 2004.

(5) Qiu, X.; Thompson, J. W.; Billinge, S. J. L. PDFgetX2: A GUI Driven Program To Obtain the Pair Distribution Function from X-ray Powder Diffraction Data. *J. Appl. Crystallogr.* **2004**, *37*, 678–678.

(6) Rodriguez-Carvajal, J. FullProf computer program, 2009. <http://www.will.eu/sites/fullprof/> (accessed January 2010).

(7) Newkirk, A. E. The Oxidation of Tungsten Carbide. *J. Am. Chem. Soc.* **1955**, *77* (17), 4521–4522.

(8) Hofmann, M.; Campbell, S. J.; Ehrhardt, H.; Feyerherm, R. The Magnetic Behaviour of Nanostructured Zinc Ferrite. *J. Mater. Sci.* **2004**, *39*, 5057–5065.

(9) Philip, J.; Gnanaprakash, G.; Panneerselvam, G.; Antony, M. P.; Jayakumar, T.; Ray, B. Effect of Thermal Annealing under Vacuum on the Crystal Structure, Size, and Magnetic Properties of ZnFe₂O₄ Nanoparticles. *J. Appl. Phys.* **2007**, *102*, 054305.

(10) Ammar, S.; Jouini, N.; Fiévet, F.; Stephan, O.; Marhic, C.; Richard, M.; Villain, F.; Cartier dit Moulin, Ch.; Brice, S.; Sainctavit, Ph. Influence of the Synthesis Parameters on the Cationic Distribution of ZnFe₂O₄ Nanoparticles Obtained by Forced Hydrolysis in Polyol Medium. *J. Non-Cryst. Solids* **2004**, *345–346*, 658–662.

(11) Nakashima, S.; Koji Fujita, K.; Tanaka, K.; Hirao, K.; Yamamoto, T.; Tanaka, I. First-Principles XANES Simulations of Spinel Zinc Ferrite with a Disordered Cation Distribution. *Phys. Rev. B* **2007**, *75*, 174443.

(12) Antic, B.; Perovic, M.; Kremenovic, A.; Blanus, J.; Spasojevic, V.; Vulic, P.; Bessais, L.; Bozin, E. S. An Integrated Study of Thermal Treatment Effects on the Microstructure and Magnetic Properties of Zn-Ferrite Nanoparticles. *J. Phys.: Condens. Matt.* **2013**, *25*, 086001.

(13) Shanon, R. D. Revised Effective Ionic Radii and Systematic Studies of Interatomic Distances in Halides and Chalcogenides. *Acta Crystallogr., A* **1976**, *32*, 751–767.

(14) Gleiter, H. Nanostructured Materials: Basic Concepts and Microstructure. *Acta Mater.* **2000**, *48*, 1–29.

(15) Šepelák, V.; Becker, K. D. Comparison of the Cation Inversion Parameter of the Nanoscale Milled Spinel Ferrites with That of the Quenched Bulk Materials. *Mater. Sci. Eng., A* **2004**, *375–377*, 861–864.

(16) Ottonello, G. Energetics of Multiple Oxides with Spinel Structure. *Phys. Chem. Mineral.* **1986**, *13*, 79–90.

(17) Honkimäki, V.; Surotti, P. In *Defect and Microstructure Analysis by Diffraction*; Snyder, R. L., Fiala, J., Bunge, H. J., Eds.; Oxford University Press: New York, 1999; pp 41–58.

(18) Lemine, O. M.; Bououdina, M.; Sajieddine, M.; Al-Saie, A. M.; Shafi, M.; Khatab, A.; Al-hilali, M.; Henini, H. Synthesis, Structural, Magnetic and Optical Properties of Nanocrystalline ZnFe₂O₄. *Physica B* **2001**, *406*, 1989–1994.

(19) Chinnasamy, C. N.; Narayanasamy, A.; Ponpandian, N.; Chattopadhyay, K.; Shinoda, K.; Jeyadevan, B.; Tohji, K.; Nakatsuka, K.; Furubayashi, T.; Nakatani, I. Mixed Spinel Structure in Nanocrystalline NiFe₂O₄. *Phys. Rev. B* **2001**, *63*, 184108–1–6.

(20) Yao, C.; Zeng, Q.; Goya, G. F.; Torres, T.; Liu, J.; Wu, H.; Ge, M.; Zeng, Y.; Wang, Y.; Jiang, J. Z. ZnFe₂O₄ Nanocrystals: Synthesis and Magnetic Properties. *J. Phys. Chem. C* **2007**, *111*, 12274–12278.

(21) Malik, R.; Annapoorni, S.; Lamba, S.; Sharma, P.; Inoue, A. Competing Magnetic Interactions in Nickel Ferrite Nanoparticle Clusters: Role of Magnetic Interactions. *J. Appl. Phys.* **2008**, *104*, 064317 and references therein.

(22) Šepelák, V.; Bergmann, L.; Feldhoff, A.; Heitjans, P.; Krumeich, F.; Menzel, D.; Litterst, F. J.; Campbell, S. J.; Becker, K. D. Nanocrystalline Nickel Ferrite, NiFe₂O₄: Mechanosynthesis, Nonequilibrium Cation Distribution, Canted Spin Arrangement, and Magnetic Behavior. *J. Phys. Chem. C* **2007**, *111*, 5026–5033.

Local structural evidence for strong electronic correlations in spinel LiRh_2O_4

K. R. Knox,^{1,*} A. M. M. Abeykoon,¹ H. Zheng,² W.-G. Yin,¹ A. M. Tsvelik,¹ J. F. Mitchell,² S. J. L. Billinge,^{1,3} and E. S. Bozin¹

¹*Department of Condensed Matter Physics and Materials Science, Brookhaven National Laboratory, Upton, New York 11973, USA*

²*Materials Science Division, Argonne National Laboratory, Argonne, Illinois 60439, USA*

³*Department of Applied Physics and Applied Mathematics, Columbia University, New York, New York 10027, USA*

(Received 12 April 2013; revised manuscript received 21 June 2013; published 25 November 2013)

The local structure of the spinel LiRh_2O_4 has been studied using atomic-pair distribution function analysis of powder x-ray diffraction data. This measurement is sensitive to the presence of short Rh-Rh bonds that form due to dimerization of Rh^{4+} ions on the pyrochlore sublattice, independent of the existence of long-range order. We show that structural dimers exist in the low-temperature phase, as previously supposed, with a bond shortening of $\Delta r \sim 0.15 \text{ \AA}$. The dimers persist up to 350 K, well above the insulator-metal transition, with Δr decreasing in magnitude on warming. Such behavior is inconsistent with the Fermi-surface nesting-driven Peierls transition model. Instead, we argue that LiRh_2O_4 should properly be described as a strongly correlated system.

DOI: [10.1103/PhysRevB.88.174114](https://doi.org/10.1103/PhysRevB.88.174114)

PACS number(s): 61.50.Ks, 61.05.cp, 71.30.+h

I. INTRODUCTION

The interplay of charge, spin, orbital, and lattice degrees of freedom driven by electron correlation is a unifying principle across a wide range of transition-metal systems.¹⁻³ Such a picture provides the framework for the understanding needed when one-electron physics is inadequate. In this paper, we argue, based on structural principles, that the spinel LiRh_2O_4 , whose coupled spin, charge, and lattice behaviors have been understood in terms of single-particle physics [band Jahn-Teller transition and charge density wave (CDW) formation],⁴ is better described as a strongly correlated system.

LiRh_2O_4 , discovered in 2008,⁴ belongs to a class of spinels described by the common formula AB_2X_4 . Like LiRh_2O_4 , these systems often exhibit interesting phenomena such as spin frustration, charge, spin, and orbital ordering, and metal-insulator transitions (MITs).⁵⁻¹⁴ For example, spinels with Ti or Ir on the B site undergo a symmetry lowering phase transition from a high-temperature metallic phase into a low-temperature insulating B - B dimerized state. This transition has been explained using a band Jahn-Teller model,⁴ with dimerization the result of a Peierls transition associated with CDW formation.¹⁵ The pyrochlore sublattice of corner shared B_4 tetrahedra, composed of intersecting chains of B ions, as shown in Fig. 1(a), contains electronically active valence electrons in the t_{2g} orbitals of the d shell. In the metallic high-temperature cubic (HTC) phase, these orbitals are triply degenerate,¹⁶ while in the low-temperature insulating phase, a band Jahn-Teller transition breaks this degeneracy.

In LiRh_2O_4 , the MIT occurs in two stages⁴ and it has been suggested that the two-step nature of the transition could shed light on the mechanism of the transition. At $T_{c1} = 225 \text{ K}$, there is a structural phase transition to an intermediate-temperature tetragonal (ITT) phase that breaks the degeneracy of the t_{2g} levels and changes the electron filling of the orbitals oriented along different crystallographic directions. At $T_{c2} = 170 \text{ K}$, a second transition occurs into a low-temperature orthorhombic (LTO) phase. This state is insulating with, presumably, a CDW along the chains. In related materials, the CDW is seen in average⁸ and local¹⁷ structural measurements as a very short metallic B - B bond, although it has not been experimentally established in LiRh_2O_4 before this work.

The nominal charge of Rh in LiRh_2O_4 is $3.5+$, implying that, on average, there are 5.5 electrons in the t_{2g} manifold since the e_g levels are at higher energy and unpopulated. If the charge were distributed evenly, there would be 0.5 holes per Rh atom shared among the t_{2g} levels [Fig. 1(b)(i)]. Charge can disproportionate between the available orbitals in two distinct ways. First, it can separate between the three t_{2g} orbitals, d_{xy} , d_{yz} , and d_{xz} , on a single atomic site [subband disproportionation; Fig. 1(b)(ii)]. Second, the charge may distribute itself unevenly between atoms along the chain directions, forming a CDW, regardless of the partitioning of charge between orbitals on an individual atom [Fig. 1(b)(iii)]. In this paper, we will use CDW, dimerization, and short bond interchangeably to describe this since they highlight different aspects of the same phenomenon. In the extreme case, this would result in $3+$ and $4+$ Rh ions along the chain.⁴ The LTO structure in LiRh_2O_4 has not been solved, but in a similar system, CuIr_2S_4 , the pattern of charge is nominally $-(3+) - (3+) - (4+) - (4+) -$ (Ref. 18) with the $4+$ ions dimerizing.

The main result of this work is the observation of short Rh-Rh distances over a wide temperature range, which includes all three structural phases. This means that in LiRh_2O_4 , the dimers are confirmed to exist at low temperature, but also well above the LTO insulating state. Thus, the ITT-to-LTO transition may be thought of as a crystallization of dimers from a liquid formed at higher temperatures in the metallic phase. We argue that, taken together, all of the experimental data are at odds with the existing understanding¹⁵ where the phase transitions in AB_2X_4 systems are explained by the Peierls mechanism driven by Fermi-surface effects.

II. METHODS

LiRh_2O_4 was synthesized using a solid-state reaction under high-pressure oxygen. High-purity Rh_2O_3 was mixed with a 10 weight-percent excess of Li_2O_2 . The mixed powders were fired at $900 \text{ }^\circ\text{C}$ for 20 hours under an oxygen pressure of 0.6 MPa . The resulting powder was found to be single phase by laboratory x-ray diffraction. DC susceptibility data were measured on cooling in a 1 T field using a Quantum Design

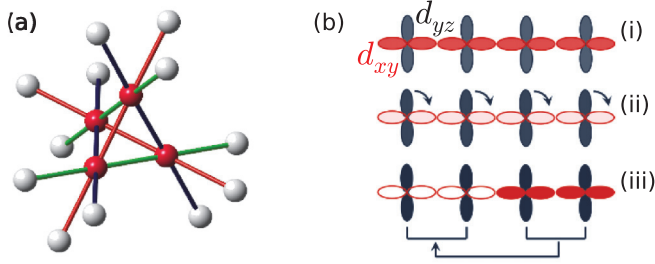


FIG. 1. (Color online) (a) Structural motif of Rh-pyroxhlore sublattice. Red atoms denote single Rh_4 tetrahedron. Red, blue, and green colored bonds differentiate independent chain directions. (b) Two-dimensional sketch of different charge distributions in d_{xy} (red) and d_{yz} (blue) orbitals of the t_{2g} manifold with charge filling represented by color intensity: (i) homogeneous, (ii) subband disproportionated (band Jahn-Teller effect), and (iii) CDW. Arrows denote disproportionation of charge.

Physical Property Measurement System (PPMS). Resistivity was measured using a standard four-terminal technique.

X-ray total scattering data were collected at the X17A beam line (beam energy 67.42 keV) of the National Synchrotron Light Source (NSLS) at Brookhaven National Laboratory (BNL) in the 80–500 K temperature range using standard protocols.^{17,19,20} Experimental pair distribution functions (PDFs) of LiRh_2O_4 were obtained by Fourier transforming the reduced total scattering structure function, $F(Q)$, over a broad range of momentum transfer, Q ($Q_{\text{max}} = 28 \text{ \AA}^{-1}$).

Lattice parameters were obtained using a Le Bail fit to the diffraction data using the General Structure Analysis System (GSAS),²¹ utilizing $Fd\bar{3}m$ (HTC), $I4_1/amd$ (ITT), and $Fm\bar{m}m$ (LTO) models from the literature.⁴ Structural refinement of PDF data was carried out using PDFgui.²²

III. RESULTS

A. Sample characterization

Our sample exhibits resistivity, magnetic susceptibility, and average structural changes (shown in Fig. 2) consistent with earlier reports.⁴ The structural phase transitions are clearly observed, with corresponding changes in resistivity and magnetization.

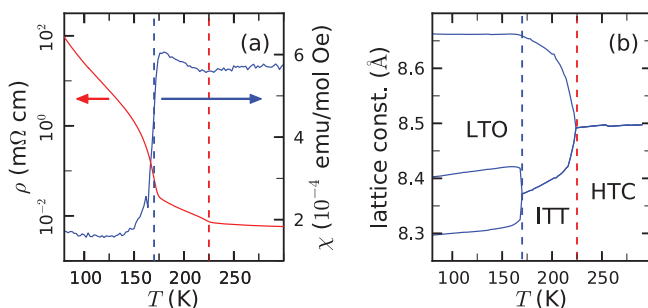


FIG. 2. (Color online) (a) Temperature dependence of LiRh_2O_4 resistivity (red) and magnetic susceptibility (blue). (b) Lattice parameters determined from Le Bail fit of the x-ray data. Vertical dashed lines denote structural phase transitions at 170 K (blue) and 225 K (red).

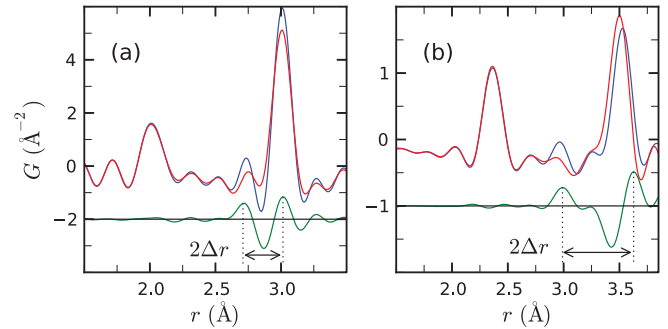


FIG. 3. (Color online) Comparison of experimental PDFs at 240 K (red) and 160 K (blue) for (a) LiRh_2O_4 and (b) CuIr_2S_4 . Difference curves (green) are offset for clarity. Dotted lines indicate r position of short (dimerized) and long (undimerized) peaks. Δr , defined as half the distance between the long and short bonds, is used as a measure of the distortion associated with dimerization.

B. PDF analysis

Despite the lack of a low-temperature crystallographic model, evidence of a dimerized state can be immediately seen by comparing high- and low-temperature experimental LiRh_2O_4 PDFs in the low- r regime. Figure 3(a) shows the low- r region of the LiRh_2O_4 PDF in the LTO and HTC phases along with a difference curve. Since the atomic number of Rh is significantly larger than those of Li and O, the PDF intensity in this region is dominated by Rh-O (2.0 \AA peak) and Rh-Rh (3.0 \AA peak) atomic-pair correlations. In the average HTC model, there is only one nearest-neighbor Rh-Rh distance, corresponding to the sharp PDF peak at 3.0 \AA , whereas in the LTO phase, the orthorhombic distortion splits the near-neighbor Rh-Rh distance into three average distances. From the lattice parameters obtained from our Le Bail fit of the x-ray data [Fig. 2(b)], it is straightforward to calculate these three distances as 2.95 \AA , 3.0 \AA , and 3.02 \AA . However, an additional contribution to the PDF clearly appears at $\sim 2.7 \text{ \AA}$ in the LTO phase. A similar observation has been made in CuIr_2S_4 [Fig. 3(b)] where the presence of dimers in the low-temperature phase is well established.^{8,17} The formation of dimers along one-dimensional (1D) chains is characterized by the redistribution of PDF intensity into short (dimerized) and long (nondimerized) bonds. This occurs with a concomitant loss of intensity at the position of the *average* bond along the 1D dimerizing chain, indicating a transfer of intensity from the principal peak to the long- and short-bond peaks. This redistribution of intensity emerges in Fig. 3 as a signature M shape in the difference curve.

In CuIr_2S_4 , dimerization occurs along the shorter of two inequivalent Ir chains, which contains the active electronic orbitals that are available for dimerization.⁸ Similarly, in LiRh_2O_4 , dimerization is expected to occur along the shortest of the three Rh chains.⁴ Thus, as seen in Fig. 3, the characteristic M shape in the LiRh_2O_4 difference curve is centered at the position of the shortest average Rh-Rh bond (at the leading edge of the large peak at 3.0 \AA). The associated structural distortion, Δr , is $\sim 0.15 \text{ \AA}$ in LiRh_2O_4 and $\sim 0.45 \text{ \AA}$ in CuIr_2S_4 . This unambiguously establishes the presence of dimers in the LTO phase of LiRh_2O_4 , experimentally confirming prior

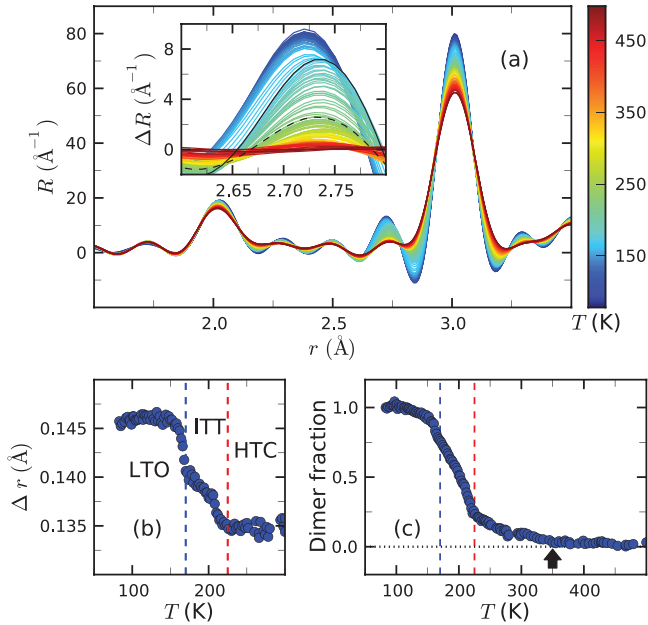


FIG. 4. (Color online) (a) Plot of temperature evolution of LiRh_2O_4 RDF in the 1.5–3.5 \AA range. Inset displays differential RDF near the dimer peak obtained by subtracting a reference RDF at 500 K with black lines at 170 K (solid line), and 225 K (dashed line) denoting differential RDFs at phase-transition temperatures. (b),(c) Results of differential RDF analysis: (b) distortion, Δr , (c) integrated intensity of short-bond peak normalized to its low- T value, representing the dimer fraction. Black arrow indicates observed break in slope at 350 K. Horizontal dotted line, drawn at zero, is a guide to the eye. Vertical dashed lines indicate phase-transition temperatures.

speculation based on anomalies in transport and susceptibility and by analogy with CuIr_2S_4 .^{23,24}

We now turn our attention to the temperature evolution of the Rh dimers, which is observable in the raw data. Figure 4(a) shows the temperature evolution of the radial distribution function (RDF), $R(r)$, a related form of $G(r)$,²⁰ $R(r)dr$ represents the number of bonds with lengths between r and $r + dr$. While the region surrounding the peak at 2 \AA is largely unchanged, a significant redistribution of PDF intensity occurs in the 2.5–3.25 \AA range with increasing temperature. It is clear from a careful examination of the inset to Fig. 4(a) that this redistribution does not occur abruptly at T_{c2} . Rather, the short bond lengthens slightly on warming from 160 to 170 K. Then, as the sample is heated through the ITT phase and into the HTC phase, intensity is gradually transferred from the 2.7 \AA region to the leading edge of the large peak at 3 \AA . This implies that the dimer does not disappear at the LTO-to-ITT phase transition. Rather, it survives into the ITT and HTC phases with gradually diminishing intensity.

The temperature evolution of the dimers is further quantified by tracking the peak position and integrated intensity of the relevant $R(r)$ features. The size of the distortion associated with the dimer formation, Δr (see Fig. 3), is determined by subtracting a reference RDF at 500 K from all measured RDFs and analyzing the resulting difference curves. As evident from Fig. 4(b), Δr is nearly

constant as the sample is heated through the LTO phase. Then, it changes rapidly in the 160–170 K range, decreasing from ~ 0.146 to 0.14 \AA as the LTO/ITT phase transition is approached. As temperature is further increased through the ITT phase, Δr changes smoothly, gradually decreasing until it stabilizes at 0.133 \AA at the ITT/HTC phase boundary.

An estimate of the number of dimers present in the sample is obtained by following the integrated intensity of the short-bond peak in the RDF difference curve. As shown in Fig. 4(c), the dimer fraction is relatively stable through the LTO phase. A rapid drop is observed between 160 and 170 K. Notably, the dimer fraction does not drop to zero at T_{c2} , but decreases gradually through the ITT phase. It survives even into the HTC phase, disappearing at ~ 350 K.

Further confirmation of our results is obtained by model-dependent analysis of the LiRh_2O_4 PDFs. Figure 5(a) shows a best fit of the ITT model to the LiRh_2O_4 PDF at 200 K in the 1.5 \AA to 20 \AA range. The fit is poor throughout the entire refinement range, but significantly poorer in the shaded region below 5 \AA , as evident from the difference curve. However, this should not come as a surprise if dimers exist in the ITT phase; the $I4_1/amd$ model does not allow for the presence of a nearest-neighbor Rh-Rh bond that is significantly shorter than the average bond. The average tetragonal distortion obtained

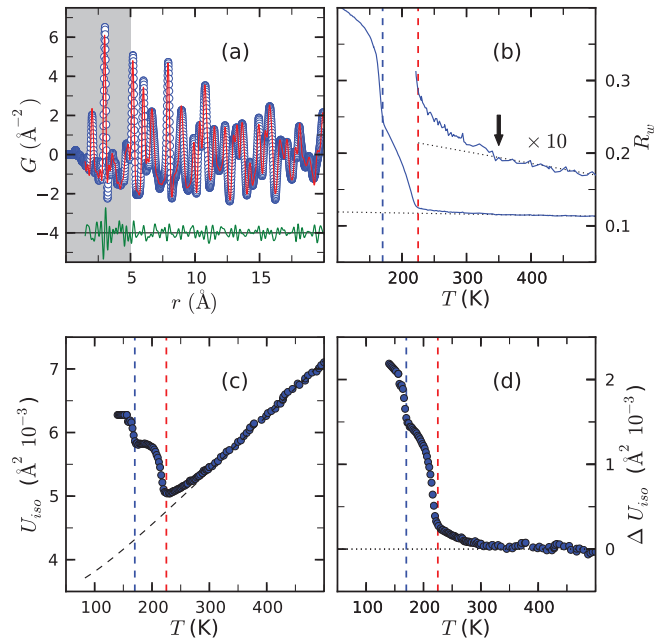


FIG. 5. (Color online) (a) Best fit (red line) to LiRh_2O_4 PDF (blue circles) at 200 K in the 1.5–20 \AA range using $I4_1/amd$ model. Difference curve (green) is offset for clarity. Shaded area denotes poorly fit region. (b) Refinement residual, R_w , for the entire temperature range. Black dotted line is a linear fit to the high-temperature tail. Inset shows expanded view in the 200–500 K range, with observed break in slope at 350 K indicated by arrow. (c) Temperature dependence of the isotropic atomic displacement parameter (ADP), U_{iso} , of Rh obtained from the fits. Black dashed line represents a fit of the Debye model to the high-temperature tail. (d) Differential ADP, ΔU_{iso} , obtained from data shown in (c) by subtracting the Debye model values from the refined ADPs at all temperatures. Vertical dashed lines in (b)–(d) denote phase transitions.

by Le Bail fitting results in a small splitting (less than 0.02 Å) of the nearest-neighbor Rh-Rh distance, but cannot account for the significantly shorter Rh-Rh bond that is associated with dimer formation, which corresponds to a distortion that is nearly an order of magnitude larger.

Fits of the $I4_1/amd$ structural model to experimental PDFs were carried out throughout the temperature range studied. Since the dimers cannot be accounted for by this model, their presence will result in an increase in the refinement residual, R_w . Assuming that the short-bond distortion is the major contributor to the poor fit, R_w , which is a sensitive measure of the goodness of fit, can be used to track this distortion. Figure 5(b) shows $R_w(T)$ over the entire temperature range. As expected from the inadequacy of the $I4_1/amd$ model to describe the low-temperature state, its value is high in the LTO phase. After an abrupt drop upon crossing into the ITT phase, R_w remains unusually large and decreasing with T throughout the ITT phase, consistent with the observations that the local structure is not explained by the average crystallographic model. While reaching reasonably small values in the HTC phase, $R_w(T)$ exhibits a sudden change in slope at ~ 350 K [Fig. 5(b)], reminiscent of the dimer fraction shown in Fig. 4(c). Notably, both $R_w(T)$ and the dimer fraction [Fig. 4(c)] resemble $\rho(T)$ [Fig. 2(a)], suggesting that the transport behavior is marked by the evolution of the dimers.

Another sensitive measure of the presence of dimers is the isotropic atomic displacement parameter associated with the Rh crystallographic site. This is shown in Fig. 5(c). The canonical temperature dependence of ADPs in materials on cooling is their gradual *decrease* with decreasing temperature, reflecting the decrease in thermal motion. However, this trend is not observed in the Rh-ADP obtained from our structural refinement; instead, the Rh-ADP is seen to increase with decreasing temperature in the ITT and LTO phases, indicating that the $I4_1/amd$ model is inadequate to describe these phases. Additionally, although the refined Rh-ADP decreases on cooling through the HTC phase, it deviates from canonical Debye behavior [see Eq. (1)] between 300 and 350 K.

The temperature dependence of ADPs is often described by a Debye-type model as

$$U^2(T) = \frac{3h^2}{4\pi^2 m k_B \Theta_D} \left(\frac{\Phi(\Theta_D/T)}{\Theta_D/T} + \frac{1}{4} \right) + U_0^2, \quad (1)$$

where

$$\Phi(x) = \frac{1}{x} \int_0^x \frac{x' dx'}{e^{x'} - 1}. \quad (2)$$

Any deviation from this behavior is typically ascribed either to overall inadequacy of the structural model or to the presence of nanoscale features that deviate from the average structure. Thus, the presence of dimers that are not long-range ordered and, hence, unaccounted for by the average structural model would result in anomalous behavior of the associated ADP. The dashed black line in Fig. 5(c) represents a fit of the Debye model to the high-temperature tail of the Rh $U_{iso}(T)$ curve. As can be seen in the figure, the fit is reasonable at high temperature. However, the data deviate from the canonical behavior described by the model, while the sample is still in the HTC phase. In Fig. 5(d), we show the difference between the ADP data and the high-temperature Debye fit. Again, the

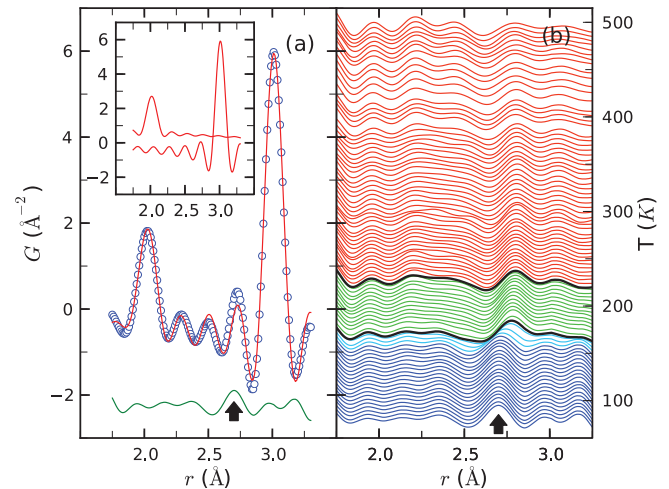


FIG. 6. (Color online) (a) Gaussian fit (red) to 80 K LiRh_2O_4 PDF (blue circles) in the 1.5–3.5 Å range. Difference curve (green) is offset for clarity. Inset shows fit components. (b) Temperature evolution of the difference curve shown in (a). Arrows in (a) and (b) indicate the short-bond peak which is unaccounted for in the two-Gaussian model. Crystallographic phases are color coded (LTO blue, ITT green, HTC red), while the black profiles mark the phase transitions.

characteristic curve shows up, reminiscent of $\rho(T)$, $R_w(T)$, and the dimer fraction temperature dependence.

To confirm the temperature evolution of the short Rh-dimer bond, a structural model-independent assessment of the experimental PDFs was performed; the low- r portion of the LiRh_2O_4 PDFs were fit with Gaussians convolved with Sinc functions to account for termination effects.²⁰ The Gaussians were used to fit the range from 1.5 Å to 3.5 Å to account for the peaks at 2.0 Å and 3.0 Å [inset to Fig. 6(a)]. The short-bond peak associated with dimerization was intentionally left out of this model, and any unaccounted PDF intensity (such as from the Rh-dimer peak) shows up in the difference curve. In this way, the evolution of the dimer peak may be followed directly by plotting the difference curve obtained by subtracting the best fit of the two-Gaussian model from the data. A representative fit to the 80 K PDF profile is shown in Fig. 6(a), with the unaccounted dimer peak in the difference curve marked with an arrow. The temperature evolution of this difference curve is shown in Fig. 6(b). As the sample is warmed through the LTO phase, it is clear that the short-bond peak is roughly constant in both position and intensity until 160 K, at which point it rapidly moves towards higher r in advance of the phase transition at 170 K. The peak then persists through the ITT phase and well into the HTC phase with gradually diminishing intensity.

C. Specific-heat analysis

Figure 7(a) compares the specific heat, C , of LiRh_2O_4 (obtained from Ref. 4) with that of CuIr_2S_4 (obtained from Ref. 25). Both are expressed as functions of the renormalized temperature, T/Θ_D , where Θ_D was obtained by fitting the data over the whole temperature range from 0 to 300 K with the Debye specific-heat expression

$$C = 9NR \left(\frac{T}{\Theta_D} \right)^3 \int_0^{\Theta_D/T} \frac{x^4 e^x}{(e^x - 1)^2} dx. \quad (3)$$

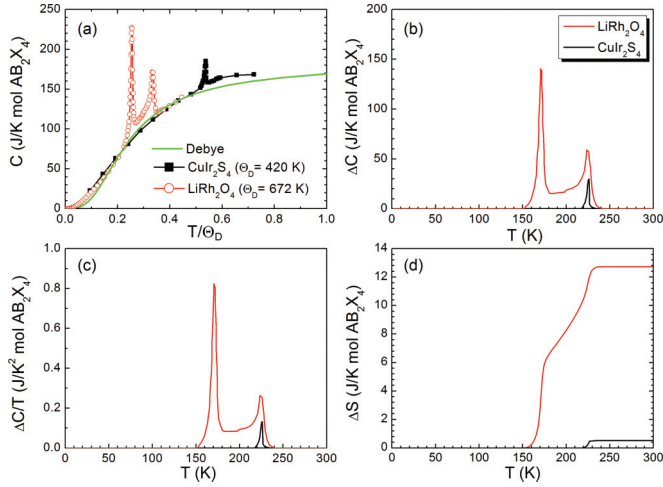


FIG. 7. (Color online) (a) Renormalized-temperature dependence of the specific heat for LiRh_2O_4 (red circles) and CuIr_2S_4 (black squares), compared with the Debye model (green line). (b) ΔC , the contribution to the specific heat coming from the phase transitions for LiRh_2O_4 (red line) and CuIr_2S_4 (black line). (c) $\Delta C/T$. (d) The corresponding entropy, $\Delta S(T) = \int_0^T \Delta C/T dT$.

The fitted Debye temperatures are $\Theta_D = 420$ K for CuIr_2S_4 and 672 K for LiRh_2O_4 . The larger value of Θ_D for LiRh_2O_4 can be ascribed to the smaller atomic masses of Li, Rh, and O as compared to Cu, Ir, and S, respectively.

It is clear that, after scaling, the C curves of LiRh_2O_4 and CuIr_2S_4 differ only at the peaks around the transition temperatures. This indicates that the phonon contributions to the specific heat of these materials are rather similar. Additionally, their values at 300 K are close to $3NR = 174.6 \text{ J mol}^{-1} \text{ K}^{-1}$ where $N = 7$ (the number of atoms in the chemical formula) and $R = 8.314 \text{ J mol}^{-1} \text{ K}^{-1}$ (the universal gas constant), which indicates that phonon contributions dominate C in this temperature regime. Indeed, it is clear that both curves closely follow the Debye model away from the transition temperatures.

Since C only deviates substantially from the Debye curve near the transition temperatures, it is straightforward to extract the electronic contributions. This was done by subtracting a linear background from the peaks near the transition temperatures, as shown in Fig. 7(b). Figures 7(c) and 7(d) compare $\Delta C/T$ and the electronic contribution to the entropy, $\Delta S(T) = \int_0^T \Delta C/T dT$, respectively. Integrating C/T for these peaks shows a significantly larger entropy increase for LiRh_2O_4 than for CuIr_2S_4 . Since the phonon contributions have already been accounted for, this difference can only arise from contributions to the entropy from the electronic system, including the charge, spin, and orbital degrees of freedom.

It is useful to express the entropy change in the familiar units of $R \ln 2$, which would be appropriate for a system of localized objects with spin $\frac{1}{2}$;³¹ this is also the value of the entropy change of the Verwey transition in Fe_3O_4 .²⁶ The entropy associated with the transition in CuIr_2S_4 is $0.03 R \ln 2$, confirming its weakly correlated nature. However, the corresponding entropy change in LiRh_2O_4 is about $R \ln 2$ for the low- T transition and an additional $R \ln 2$ for the high- T transition. This large electronic entropy indicates the existence of many degenerate states above the transition, a hallmark

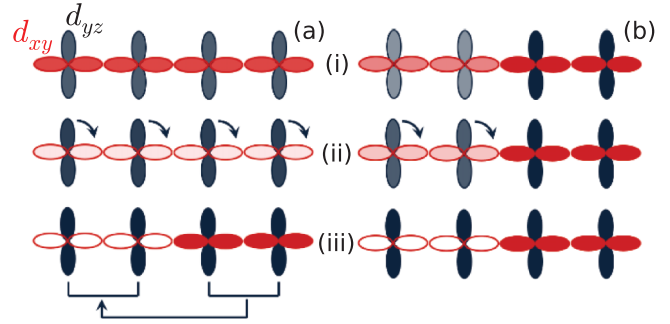


FIG. 8. (Color online) (a) LiRh_2O_4 charge distribution model based on band Jahn-Teller scenario: (i) homogeneous charge distribution, (ii) subband charge disproportionation, and (iii) CDW. (b) Alternative model based on experimental observations made in this work, with CDW existing in all three phases. As in Fig. 1(b), color intensity corresponds to the average amount of charge, while arrows denote charge disproportionation.

of strong electron correlation. Although the origin of this large entropy is unclear at this moment (and calls for further theoretical and experimental investigation), it is reasonable to conclude that LiRh_2O_4 and CuIr_2S_4 belong to two different regimes in terms of electron correlation.

IV. CONCLUSION

These results indicate a complicated and unexpected evolution of the local dimers with temperature. The observation of the dimer signal in the PDF gives direct evidence for the presence of the CDW along the chains in all the phases, distinct from the subband disproportionation that leads to an overall lowering of the cubic symmetry. This is illustrated in Fig. 8(a) and contrasted with the previous view in Fig. 8(b). This behavior is different from that observed in CuIr_2S_4 where the dimers disappear in both the average and local structure at the MIT.¹⁷ This difference may be explained by electron correlation effects in LiRh_2O_4 , which are not present in CuIr_2S_4 . This view is also supported by a comparison of the specific heat and entropy of CuIr_2S_4 and LiRh_2O_4 . The electronic contribution to the entropy is found to be $2.2 R \ln 2$ in LiRh_2O_4 , which is significantly larger than $0.03 R \ln 2$ in CuIr_2S_4 , but comparable to $R \ln 2$ in Fe_3O_4 .²⁶

Additionally, an explanation for the different behavior of the magnetic susceptibility, χ , in LiRh_2O_4 as compared to CuIr_2S_4 may reside in our PDF data. In the HTC phase of LiRh_2O_4 , the sample contains few dimers and a balance of itinerant spins; thus it is weakly metallic and χ is roughly constant with decreasing T . At the HTC-to-ITT phase transition, the spins localize, but many are initially unpaired, resulting in a slight upturn in χ . Then, on cooling through the ITT phase, dimers gradually freeze-out. However, significant undimerized Rh^{4+} ions remain [as evidenced by the dimer fraction plotted in Fig. 4(c)], which contribute to the paramagnetic response and overcome the decrease in χ due to dimer formation from the other Rh^{4+} ions, thus leading to the observed increase in χ . This coexistence of dimerized and undimerized Rh^{4+} ions in

LiRh_2O_4 is consistent with the presence of significant electron correlations, leading to frustration in this system.

Our results point to an interesting aspect of the pyrochlore sublattice, namely, the corner shared B_4 tetrahedra consisting of intersecting quasi-1D chains of B ions [Fig. 1(a)]. This sublattice plays host to a competition between one-dimensional (1D) and three-dimensional (3D) physics. In a more metallic spinel, such as CuIr_2S_4 , the system can lower its dimensionality through orbital ordering along the chains of B ions, resulting in a 1D chain that is unstable to the formation of a CDW. On the other hand, in a less metallic spinel, such as Fe_3O_4 , the physics is driven by the geometric frustration of ordering different partial charges ($\pm\delta$) on the vertices of the 3D network of tetrahedra.^{27–30} LiRh_2O_4 lies between these extremes, where the effects of intersite Coulomb interaction

and kinetic energy are comparable, resulting in a competition that leads to the unusual behavior observed in this material.

ACKNOWLEDGMENTS

Sample preparation and characterization work at Argonne National Laboratory was supported by the U.S. Department of Energy, Office of Science, Office of Basic Energy Sciences (DOE-BES) under Contract No. DE-AC02-06CH11357. PDF x-ray experiments, data analysis, and modeling were carried out at Brookhaven National Laboratory, supported by DOE-BES under Contract No. DE-AC02-98CH10886. Use of the National Synchrotron Light Source, Brookhaven National Laboratory, was supported by the DOE-BES under Contract No. DE-AC02-98CH10886.

*kknox@bnl.gov

¹A. J. Millis, *Nature (London)* **392**, 147 (1998).

²E. Dagotto, *Science* **309**, 257 (2005).

³A. Georges, L. de'Medici, and J. Mravlje, *Annu. Rev. Condens. Matter Phys.* **4**, 137 (2013).

⁴Y. Okamoto, S. Niitaka, M. Uchida, T. Waki, M. Takigawa, Y. Nakatsu, A. Sekiyama, S. Suga, R. Arita, and H. Takagi, *Phys. Rev. Lett.* **101**, 086404 (2008).

⁵J. Matsuno, T. Mizokawa, A. Fujimori, D. A. Zatsopin, V. R. Galakhov, E. Z. Kurmaev, Y. Kato, and S. Nagata, *Phys. Rev. B* **55**, R15979 (1997).

⁶J. Rodriguez-Carvajal, G. Rousse, C. Masquelier, and M. Hervieu, *Phys. Rev. Lett.* **81**, 4660 (1998).

⁷H. Ishibashi, T. Y. Koo, Y. S. Hor, A. Borissov, P. G. Radaelli, Y. Horibe, S. W. Cheong, and V. Kiryukhin, *Phys. Rev. B* **66**, 144424 (2002).

⁸P. G. Radaelli, Y. Horibe, M. J. Gutmann, H. Ishibashi, C. H. Chen, R. M. Ibberson, Y. Koyama, Y. S. Hor, V. Kiryukhin, and S. W. Cheong, *Nature (London)* **416**, 155 (2002).

⁹M. Schmidt, W. Ratcliff II, P. G. Radaelli, K. Refson, N. M. Harrison, and S. W. Cheong, *Phys. Rev. Lett.* **92**, 056402 (2004).

¹⁰S. Di Matteo, G. Jackeli, C. Lacroix, and N. B. Perkins, *Phys. Rev. Lett.* **93**, 077208 (2004).

¹¹K. Takubo, S. Hirata, J.-Y. Son, J. W. Quilty, T. Mizokawa, N. Matsumoto, and S. Nagata, *Phys. Rev. Lett.* **95**, 246401 (2005).

¹²V. Kiryukhin, Y. Horibe, Y. S. Hor, H. J. Noh, S. W. Cheong, and C. H. Chen, *Phys. Rev. Lett.* **97**, 225503 (2006).

¹³H. D. Zhou, B. S. Conner, L. Balicas, and C. R. Wiebe, *Phys. Rev. Lett.* **99**, 136403 (2007).

¹⁴D. Errandonea, R. S. Kumar, F. J. Manjon, V. V. Ursaki, and I. M. Tiginyanu, *J. Appl. Phys.* **104**, 063524 (2008).

¹⁵D. I. Khomskii and T. Mizokawa, *Phys. Rev. Lett.* **94**, 156402 (2005).

¹⁶P. G. Radaelli, *New J. Phys.* **7**, 53 (2005).

¹⁷E. S. Božin, A. S. Masadeh, Y. S. Hor, J. F. Mitchell, and S. J. L. Billinge, *Phys. Rev. Lett.* **106**, 045501 (2011).

¹⁸M. Croft, W. Caliebe, H. Woo, T. A. Tyson, D. Sills, Y. S. Hor, S. W. Cheong, V. Kiryukhin, and S.-J. Oh, *Phys. Rev. B* **67**, 201102 (2003).

¹⁹P. J. Chupas, X. Qiu, J. C. Hanson, P. L. Lee, C. P. Grey, and S. J. L. Billinge, *J. Appl. Crystallogr.* **36**, 1342 (2003).

²⁰T. Egami and S. J. L. Billinge, *Underneath the Bragg Peaks: Structural Analysis of Complex Materials*, 2nd ed. (Elsevier, Amsterdam, 2013).

²¹A. C. Larson and R. B. Von Dreele, Los Alamos National Laboratory, Report No. LAUR-86-748, 1987 (unpublished).

²²C. L. Farrow, P. Juhás, J. Liu, D. Bryndin, E. S. Božin, J. Bloch, T. Proffen, and S. J. L. Billinge, *J. Phys.: Condens. Matter* **19**, 335219 (2007).

²³S. Okamoto, S. Ishihara, and S. Maekawa, *Phys. Rev. B* **61**, 14647 (2000).

²⁴Y. Nakatsu, A. Sekiyama, S. Imada, Y. Okamoto, S. Niitaka, H. Takagi, A. Higashiya, M. Yabashi, K. Tamasaku, T. Ishikawa *et al.*, *Phys. Rev. B* **83**, 115120 (2011).

²⁵L. Zhang, Z. Qu, L. Pi, S. Huang, S. Tan, and Y. Zhang, *J. Magn. Magn. Mater.* **321**, 4092 (2009).

²⁶J. P. Shepherd, J. W. Koenitzer, Ricardo Aragón, C. J. Sandberg, and J. M. Honig, *Phys. Rev. B* **31**, 1107 (1985).

²⁷P. W. Anderson, *Phys. Rev.* **102**, 1008 (1956).

²⁸M. S. Senn, J. P. Wright, and J. P. Attfield, *Nature (London)* **481**, 173 (2012).

²⁹M. Coey, *Nature (London)* **430**, 155 (2004).

³⁰D. Volja, W.-G. Yin, and W. Ku, *Europhys. Lett.* **89**, 27008 (2010).

³¹Note that we do not wish to imply by this that LiRh_2O_4 contains localized spins.

Crystal-Field Splitting and Correlation Effect on the Electronic Structure of $A_2\text{IrO}_3$

H. Gretarsson,¹ J. P. Clancy,¹ X. Liu,² J. P. Hill,² Emil Bozin,² Yogesh Singh,³ S. Manni,⁴ P. Gegenwart,⁴ Jungho Kim,⁵ A. H. Said,⁵ D. Casa,⁵ T. Gog,⁵ M. H. Upton,⁵ Heung-Sik Kim,⁶ J. Yu,⁶ Vamshi M. Katukuri,⁷ L. Hozoi,⁷ Jeroen van den Brink,⁷ and Young-June Kim^{1,*}

¹*Department of Physics, University of Toronto, 60 St. George Street, Toronto, Ontario M5S 1A7, Canada*

²*CMP&MS Department, Brookhaven National Laboratory, Upton, New York 11973, USA*

³*Indian Institute of Science Education and Research Mohali, Sector 81, SAS Nagar, Manauli PO 140 306, Punjab, India*

⁴*I. Physikalisches Institut, Georg-August-Universität Göttingen, D-37077 Göttingen, Germany*

⁵*Advanced Photon Source, Argonne National Laboratory, Argonne, Illinois 60439, USA*

⁶*Department of Physics and Astronomy, Seoul National University, Seoul 151-747, Korea*

⁷*Institute for Theoretical Solid State Physics, IFW Dresden, Helmholtzstrasse 20, 01069 Dresden, Germany*

(Received 21 September 2012; published 13 February 2013)

The electronic structure of the honeycomb lattice iridates Na_2IrO_3 and Li_2IrO_3 has been investigated using resonant inelastic x-ray scattering (RIXS). Crystal-field-split d - d excitations are resolved in the high-resolution RIXS spectra. In particular, the splitting due to noncubic crystal fields, derived from the splitting of $j_{\text{eff}} = 3/2$ states, is much smaller than the typical spin-orbit energy scale in iridates, validating the applicability of j_{eff} physics in $A_2\text{IrO}_3$. We also find excitonic enhancement of the particle-hole excitation gap around 0.4 eV, indicating that the nearest-neighbor Coulomb interaction could be large. These findings suggest that both Na_2IrO_3 and Li_2IrO_3 can be described as spin-orbit Mott insulators, similar to the square lattice iridate Sr_2IrO_4 .

DOI: [10.1103/PhysRevLett.110.076402](https://doi.org/10.1103/PhysRevLett.110.076402)

PACS numbers: 71.70.Ej, 75.10.Jm, 75.25.Dk, 78.70.Ck

The intense interest in iridium oxides, or iridates, arises from a number of competing interactions of similar magnitude [1–9]. While the on-site Coulomb interaction is the dominant energy scale in $3d$ transition metal oxides, the spin-orbit coupling (SOC) is largely ignored. On the other hand, for $5d$ elements such as Ir, the SOC becomes significant and in fact plays a dominant role. A good example is Sr_2IrO_4 , whose electronic states are well described by $j_{\text{eff}} = 1/2$ states arising from the spin-orbit-split t_{2g} levels [2,3,8].

One of the most intensely scrutinized families of iridates is the honeycomb lattice family $A_2\text{IrO}_3$ ($A = \text{Na}, \text{Li}$) [5,7,10–14]. Originally thought of as Mott [4] or topological insulators [5], these materials are now believed to be Mott insulators [10,11]. A recent calculation, though, suggests that uniaxial strain might still drive the system to topological insulating behavior [15]. Furthermore, these materials could be described with the Kitaev-Heisenberg model [7,11,12], in which bond-dependent Kitaev interactions are realized and support various types of topological phases. The applicability of such intriguing theoretical possibilities to a real system crucially depends on the j_{eff} physics arising from strong SOC. However, the experimental situation seems to be far from clear. In particular, structural refinements find a sizable trigonal distortion of the IrO_6 octahedra [16,17], which will produce crystal-field splittings within the t_{2g} manifold. If the splitting is comparable to the SOC, the $j_{\text{eff}} = 1/2$ states will mix with $j_{\text{eff}} = 3/2$ states [18] and the relevant microscopic model becomes quite different from the ideal j_{eff} physics [14,19],

preventing the Kitaev-Heisenberg model from being realized [7,11,13]. Recent theoretical studies have even suggested that the ground state has a large contribution from the $j_{\text{eff}} = 3/2$ state [20].

Therefore, it is of great importance to elucidate the underlying electronic structure of Na_2IrO_3 experimentally. In particular, the spectroscopic investigation of excitations between spin-orbit-split j_{eff} states can provide us with direct information regarding the size of the crystal-field splitting with respect to the typical SOC energy scale in iridates (0.4–0.5 eV) [21,22]. In the case of Sr_2IrO_4 , such excitations from $j_{\text{eff}} = 3/2$ to $j_{\text{eff}} = 1/2$ were observed around 0.6–0.8 eV in the resonant inelastic x-ray scattering (RIXS) data [8], which are accounted for in the quantum chemical calculation by Katukuri *et al.* [23]. The splitting within these “spin-orbit” excitations arises due to nonzero tetragonal crystal fields and is much smaller (~ 0.1 eV) than the SOC, justifying the j_{eff} description of Sr_2IrO_4 .

In this Letter, we present a comprehensive picture of the low energy electronic structure of Na_2IrO_3 and Li_2IrO_3 , based on Ir L_3 -edge RIXS experiments. Our high-resolution RIXS measurements allow us to resolve the crystal-field splitting of the $j_{\text{eff}} = 3/2$ states due to the trigonal distortion, which is determined to be about 110 meV in both compounds. This energy scale agrees very well with quantum chemical calculations and is much smaller than the typical value for SOC, validating the j_{eff} picture in these compounds. We have also studied the momentum dependence of the insulating gap; the observed flat dispersion of the insulating gap is consistent

with what is expected from a significant Coulomb interaction in both compounds. Taken together, we argue that, just as Sr_2IrO_4 , the honeycomb A_2IrO_3 iridates can be described as spin-orbit Mott insulators [2,15,19,24].

The RIXS experiment was carried out at the Advanced Photon Source using the 30ID MERIX and the 9ID RIXS spectrometer. A spherical (1 m radius) diced Si(844) analyzer and a Si(844) secondary monochromator were used to obtain the overall energy resolution (FWHM) of ~ 35 meV [25]. To minimize the elastic background, most of the measurements were carried out in a horizontal scattering geometry near $\mathbf{Q} = (0\ 0\ 6.7)$, for which the scattering angle 2θ was close to 90° . We use the $C2/m$ notation for the lattice [16,17]. A single crystal of Na_2IrO_3 and a polycrystalline sample of Li_2IrO_3 were grown by the solid-state synthesis method, previously described in detail [10,11]. The Na_2IrO_3 crystal was platelike with a flat shiny surface; the surface normal was in the (001) direction.

The RIXS process at the L_3 edge of Ir (or any other d electron system) is a second order process consisting of two dipole transitions ($2p \rightarrow 5d$ followed by $5d \rightarrow 2p$). Therefore, it is especially valuable for detecting excitations between the d levels and has been extensively utilized in the study of $3d$ transition metal compounds [26–32]. Recent instrumental advances have made it possible to measure collective magnetic excitations [8,33]. In A_2IrO_3 , Ir^{4+} ions are in the $5d^5$ configuration in a slightly distorted octahedral environment of oxygen ions, with the edge-sharing IrO_6 octahedra forming a honeycomb net. Due to the octahedral crystal field, there exists a fairly large splitting ($10Dq$) between the t_{2g} and e_g states. Since the $5d$ orbitals are spatially more extended than the $3d$ orbitals, the $10Dq$ value is expected to be much larger. Indeed, in our RIXS investigations of various iridium compounds, well-separated t_{2g} and e_g states have been observed, with the $10Dq$ value typically about 3 eV [34].

In Fig. 1, a representative high-resolution RIXS spectrum of Na_2IrO_3 is plotted on a wide energy scale. This scan was obtained at room temperature and plotted as a function of energy loss ($\hbar\omega = E_i - E_f$). The incident energy, $E_i = 11.217$ keV, was chosen to maximize the resonant enhancement of the spectral features of interest below 1 eV. A broad and strong feature is observed at 2–4 eV, and other sharper features are observed below 1 eV, corresponding to $d-d$ transitions from occupied t_{2g} states into the empty e_g and t_{2g} levels, respectively. Also plotted in the figure are the room temperature data of polycrystalline Li_2IrO_3 . A lack of significant momentum dependence of these $d-d$ excitations (shown later in Fig. 2) allows one to directly compare the peak positions between the single crystal and powder samples. The spectra were fit to five peaks (labeled A–E), as shown by the dashed black lines. The low energy excitations can be fit to three peaks, two Gaussians (B and C) of the same width and one Lorentzian peak (A) on top of a broad background (Gaussian). Two

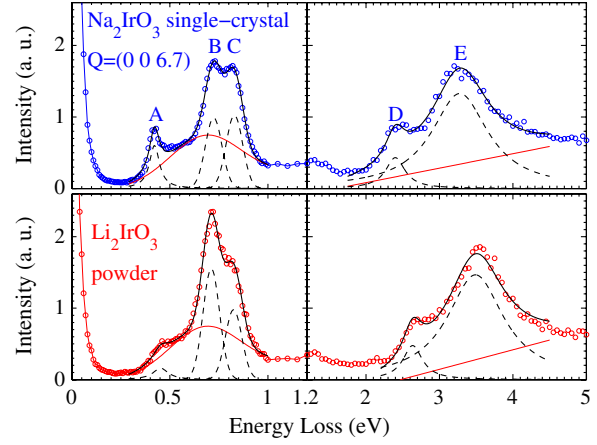


FIG. 1 (color online). Top: Wide energy range RIXS spectrum for a single-crystal sample of Na_2IrO_3 at $\mathbf{Q} = (0\ 0\ 6.7)$ obtained with $E_i = 11.217$ keV. Note the different scale used for the left and right panels. Bottom: RIXS spectrum for the Li_2IrO_3 powder sample at $|\mathbf{Q}| \approx 8 \text{ \AA}^{-1}$, obtained with the same E_i . All spectra were measured at room temperature. The dashed black curves are the result of a fit (see the text), and the thin solid red lines represent the background.

Lorentzian functions with sloping background were used to fit the higher energy excitations (D and E). The resulting peak positions are listed in Table I.

To clarify the nature of the excitations revealed by RIXS, we have carried out multiconfiguration self-consistent-field and multireference configuration-interaction (MRCI) calculations [35] on clusters consisting of one central IrO_6 octahedron, all adjacent Na or Li ions, and the three nearest-neighbor IrO_6 octahedra (see Ref. [23] and the Supplemental Material [36] for details). Local $d-d$ transitions are computed only for the central IrO_6 octahedron, while the nearest-neighbor octahedra are explicitly included in the cluster for providing an accurate description of the nearby charge distribution. Two different lattice configurations are considered: i.e., the $C2/c$ structure [10,37] and also the $C2/m$ arrangement proposed more recently [16,17,38].

The results of the spin-orbit MRCI (MRCI + SOC) calculations using the $C2/m$ configuration [16] are listed for Na_2IrO_3 in the third column of Table I. The MRCI + SOC data fit the experiment reasonably well, with peaks B and C corresponding to $j_{\text{eff}} = 3/2$ to $j_{\text{eff}} = 1/2$ electronic transitions. Above 2.5 eV, the MRCI + SOC results indicate multiple t_{2g} to e_g excitations displaying a two-peak structure reminiscent of the D and E features in the RIXS spectra. Although direct comparison is difficult due to the broad spectral widths of D and E arising from multiple excitations, MRCI + SOC seems to overestimate somewhat the relative energies of those latter features. Interestingly, for the alternative $C2/c$ structure of Na_2IrO_3 [10], the splitting between the two doublets originating from the $j_{\text{eff}} = 3/2$ quartet is much larger and the position of the

TABLE I. RIXS and MRCI + SOC excitation energies ($C2/m$ structure) for 213 iridates (eV).

	Na213 RIXS	Na213 MRCI	Li213 RIXS	Li213 MRCI
Peak A	0.42(1)	...	0.45(2)	...
Peak B	0.72(2)	0.82	0.72(2)	0.80
Peak C	0.83(2)	0.89	0.83(2)	0.97
Peak D	2.4(1)	2.8–3.4	2.6(1)	3.1–3.7
Peak E	3.3(1)	3.8–4.1	3.5(1)	4.1–5.0

C peak is overestimated by 0.25 eV in the MRCI + SOC treatment. Since the deviations from the experimental data are in this case larger, the MRCI + SOC results for $C2/c$ symmetry are not listed in Table I. The t_{2g} splittings in calculations with no SOC are in fact as large as 0.6 eV for the $C2/c$ structure of Na_2IrO_3 , which gives rise to a highly uneven admixture of t_{2g} components in the spin-orbit calculations. In contrast, for the $C2/m$ configuration, the t_{2g} splittings are about 0.1 eV and the three different t_{2g} hole configurations contribute with similar weight to the spin-orbit ground-state wave function (see Table II).

For Li_2IrO_3 , the calculations correctly reproduce the shift to higher energies of the t_{2g} to e_g transitions relative to those in Na_2IrO_3 . The discrepancy between the experimental values and the MRCI + SOC results (e.g., peak C) could be caused by the uncertainty in the structural model used for this calculation ($C2/m$ from Ref. [38]). Since local structural disorder is not easily captured in the regular diffraction data, local structure probes such as pair-distribution-function (PDF) measurements can sometimes be useful for clarifying the structural details. We have carried out x-ray PDF studies on Li_2IrO_3 and Na_2IrO_3 powder samples. Details of these measurements and the comparison of the two structures are reported in the Supplemental Material [36]. Except for the overall lattice contraction, the Li_2IrO_3 PDF seems to be well described by the $C2/m$ symmetry, eliminating the local structural disorder as a possible explanation. The most likely cause of the structural uncertainty is the oxygen position, since x-ray structural probes are not particularly sensitive to light elements like oxygen [37,38]. We note that the latest refinements using both powder neutron and single-crystal x-ray data on Na_2IrO_3 do show important differences compared to earlier x-ray powder diffraction data and

TABLE II. Percentage contributions of the different Ir $5d^5$ configurations to the lowest on-site $d-d$ excited states in Na_2IrO_3 , as obtained from MRCI + SOC calculations.

Energy (eV)	0	0.82	0.89
$d_{xy}^2 d_{yz}^2 d_{zx}^1$	38.7	24.3	32.2
$d_{xy}^2 d_{yz}^1 d_{zx}^2$	34.7	60.3	24.7
$d_{xy}^1 d_{yz}^2 d_{zx}^2$	26.6	15.4	43.1

that the MRCI + SOC results are very different for the two structures. Better structural refinements using neutron diffraction would reduce the oxygen position uncertainty in Li_2IrO_3 and could improve the agreement between our MRCI + SOC calculation and the experiment.

One of our main findings is that the splitting of the strong RIXS peak located at 0.7–0.8 eV is due to the trigonal distortion which is well corroborated with our MRCI + SOC calculations. The fact that this splitting (110 meV) is much smaller than a SOC of 0.4–0.5 eV [21,22] strongly supports that these excitations are transitions from crystal-field-split $j_{\text{eff}} = 3/2$ levels to the $j_{\text{eff}} = 1/2$ state (labeled as a spin-orbit exciton in Ref. [8]). Given that the optical gap in this material is about 350 meV [24] and that there is no such excitation in the MRCI + SOC calculations, which only look at on-site $d-d$ excitations, it is reasonable to associate feature A at low energy as arising from the excitation of a particle and hole pair across the charge gap. Additional periodic density functional theory (DFT) calculations using generalized-gradient approximations (GGA) show that a moderate size U and SOC can indeed open a (Mott) gap of 300–400 meV, in accordance with the experimental observation (see the Supplemental Material [36]).

The nature of the charge excitation gap can be further revealed by its momentum dependence. In Fig. 2, we plot the momentum dependence of the low energy peaks ($A-C$) in Na_2IrO_3 . In the honeycomb plane, the magnetic ordering doubles the unit cell [39], and correspondingly the first Brillouin zone (BZ) becomes smaller. Two different BZ schemes are illustrated in the inset of Fig. 2(a) to aid the comparison. We will use the rectangular BZ notation. Note that the two high symmetry directions of interest, the $\mathbf{q} = (h 0)$ and $\mathbf{q} = (0 k)$ in rectangular notation, correspond to the $\Gamma-K$ and $\Gamma-M$ directions in the honeycomb plane, respectively. One can see that the overall momentum dependence of the excitation spectrum is very small, except for peak A . To investigate the behavior of peak A in detail, the low energy portion of the spectra was fit to a Lorentzian peak. Since the peak seems to disappear at $\mathbf{q} = (1 0)$, we have used the spectrum at this \mathbf{q} as an empirical background. The fitting results for peak positions, widths, and intensities are shown in Figs. 2(b) and 2(c). The width and peak position remain almost unchanged (≈ 10 meV dispersion), but the intensity is strongly peaked around the BZ center. This can be clearly seen in the pseudocolor plot of the spectra shown in Fig. 2(d), in which a strong peak around $\mathbf{q} = (0 0)$ and 0.42 eV is contrasted with the \mathbf{q} -independent features $B + C$. In addition, one can see that the spectral weight changes abruptly around 0.4 eV, confirming that this is the particle-hole continuum boundary. Based on our RIXS results, the electronic excitations in A_2IrO_3 can be summarized, as is shown in Fig. 2(e).

It is clear from this observation that the insulating gap is direct (minimum gap at Γ). The relatively flat dispersion

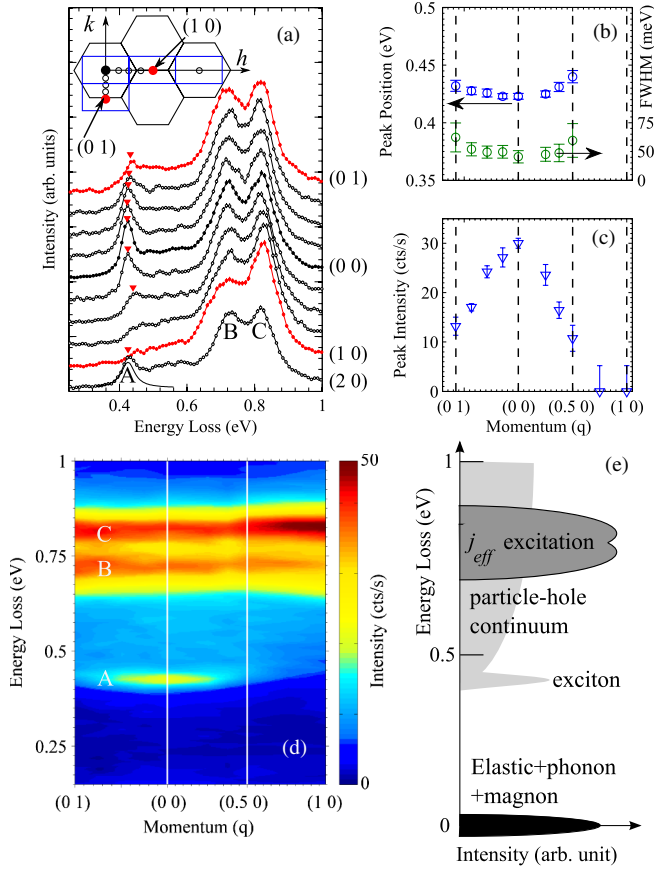


FIG. 2 (color online). (a) Momentum dependence of the low energy RIXS spectra of Na_2IrO_3 obtained at $T = 9$ K. The inset shows a schematic diagram of the $(hk0)$ reciprocal space plane. The BZs corresponding to the monoclinic unit cell are blue rectangles. For comparison, we also plot the BZ of the honeycomb net in black. The circles are the points where RIXS spectra are taken. The low energy peaks denoted with red triangles are fit to a Lorentzian, and the momentum dependence of (b) the peak position and width and (c) the peak intensity are shown. (d) The same data are plotted in a false color scale. (e) Schematics of electronic excitations in $A_2\text{IrO}_3$ determined from our RIXS measurements.

observed in our data is also consistent with the DFT calculation, which suggests that the bandwidth is about 50% (40%) for the GGA + SOC (GGA + SOC + U) result compared to the GGA-only case, leading to an almost dispersionless charge gap. Both the sharpness in energy and the momentum dependence of peak A are quite reminiscent of the excitonic behavior of the BZ center particle-hole excitation across the charge-transfer gap in the insulating cuprate La_2CuO_4 [40]. This suggests that an extra nearest-neighbor Coulomb interaction V (in addition to the on-site interaction U) might be important for modeling this material [41,42]. Sizable V could promote the tendency toward exciton binding and also further narrow the bandwidths. The smaller intensity of the charge gap feature in Li_2IrO_3 compared to Na_2IrO_3 could be due to the

fact that the Li_2IrO_3 data are powder averaged. However, one cannot rule out the possibility of weaker V in Li_2IrO_3 as compared to Na_2IrO_3 .

Another interesting aspect of our data is that the dispersion of the gap appears to follow the underlying honeycomb lattice rather than the crystallographic or magnetic unit cell. This is clearly observed by the spectrum obtained at $\mathbf{q} = (2\ 0)$. While $(2\ 0)$ is the next BZ center along the Γ - K direction (in honeycomb notation), $(1\ 0)$ is on the zone boundary; peak A disappears at $(1\ 0)$ but recovers its intensity at the $\mathbf{q} = (2\ 0)$ position. Additional momentum dependence data, reported in the Supplemental Material [36], show the lack of momentum dependence along the L direction (perpendicular to the honeycomb plane). Therefore, the electronic structure of Na_2IrO_3 seems to be quite well described as that of a 2D honeycomb lattice.

It is worth comparing the observed low energy RIXS spectrum with that of Sr_2IrO_4 . In Sr_2IrO_4 , a low energy magnon was observed below 200 meV, while highly dispersive excitations were observed between 0.4 and 0.8 eV. This latter band of excitations is composed of particle-hole excitation across the Mott gap and spin-orbit excitations from the $j_{\text{eff}} = 3/2$ to the $j_{\text{eff}} = 1/2$ states. Because of the smaller single-particle bandwidth in $A_2\text{IrO}_3$ (see the DFT calculations in Ref. [15]), the “ j_{eff} excitation” in Na_2IrO_3 is almost dispersionless, unlike the highly dispersive counterpart in Sr_2IrO_4 . Perhaps an even more significant difference is the well-separated energy scale of the j_{eff} excitation and the particle-hole continuum in Na_2IrO_3 . These two energy scales are very similar in Sr_2IrO_4 , but the large separation in Na_2IrO_3 allows one to investigate these two types of excitation separately.

To summarize, we have carried out resonant inelastic x-ray scattering investigations of electronic excitations in Na_2IrO_3 and Li_2IrO_3 . We observe three well-defined features below 1 eV and a broad two-peak feature at 2–5 eV. By comparing our observation with quantum chemical and density functional theory calculations, we associate these features with d - d transitions. Specifically, the high energy excitations are from t_{2g} to e_g excitations, while the low energy excitations around 0.7–0.8 eV are excitations from $j_{\text{eff}} = 3/2$ to $j_{\text{eff}} = 1/2$ states. The splitting of the latter feature arising from the trigonal crystal field is about 110 meV, much smaller than the spin-orbit-coupling energy scale of Ir compounds, which validates the applicability of j_{eff} physics in $A_2\text{IrO}_3$. In addition, we observe a lower energy excitation around 0.4 eV, which shows very little momentum dependence and is associated with the particle-hole excitation across the Mott gap; the “excitonic” behavior of this peak suggests the nearest-neighbor Coulomb interaction V is sizable. We conclude that the electronic structures of both Na_2IrO_3 and Li_2IrO_3 are similar and that these systems can be described as spin-orbit Mott insulators.

We would like to thank Y. B. Kim and S. Bhattacharjee for fruitful discussions and Doug Robinson for technical assistance during the PDF measurements. Research at the University of Toronto was supported by the NSERC, CFI, and OMRI. This research benefited from the RIXS Collaboration, which is supported by the Computational Materials and Chemical Sciences Network (CMCSN) Program of the Division of Materials Science and Engineering, U.S. Department of Energy, Grant No. DE-SC0007091. Use of the APS was supported by the U.S. DOE Office of Science, under Contract No. DE-AC02-06CH11357. Work performed at Brookhaven National Laboratory was supported by the DOE, Office of Science, Division of Materials Science, under Contract No. DE-AC02-98CH10886. Y.-J. Kim was supported by the KOFST through the Brainpool Program. H.-S. Kim and J. Yu were supported by the NRF through the ARP (R17-2008-033-01000-0). H.-S. Kim would like to acknowledge the support from the KISTI Supercomputing Center through the strategic support program for supercomputing application research (No. KSC-2010-S00-0005). S. Manni acknowledges support from the Erasmus Mundus Eurindia Project.

*yjkim@physics.utoronto.ca

- [1] Y. Okamoto, M. Nohara, H. Aruga-Katori, and H. Takagi, *Phys. Rev. Lett.* **99**, 137207 (2007).
- [2] B. J. Kim *et al.*, *Phys. Rev. Lett.* **101**, 076402 (2008).
- [3] B. J. Kim, H. Ohsumi, T. Komesu, S. Sakai, T. Morita, H. Takagi, and T. Arima, *Science* **323**, 1329 (2009).
- [4] G. Jackeli and G. Khaliullin, *Phys. Rev. Lett.* **102**, 017205 (2009).
- [5] A. Shitade, H. Katsura, J. Kuneš, X.-L. Qi, S.-C. Zhang, and N. Nagaosa, *Phys. Rev. Lett.* **102**, 256403 (2009).
- [6] D. Pesin and L. Balents, *Nat. Phys.* **6**, 376 (2010).
- [7] J. Chaloupka, G. Jackeli, and G. Khaliullin, *Phys. Rev. Lett.* **105**, 027204 (2010).
- [8] J. Kim *et al.*, *Phys. Rev. Lett.* **108**, 177003 (2012).
- [9] J. P. Clancy, N. Chen, C. Y. Kim, W. F. Chen, K. W. Plumb, B. C. Jeon, T. W. Noh, and Y.-J. Kim, *Phys. Rev. B* **86**, 195131 (2012).
- [10] Y. Singh and P. Gegenwart, *Phys. Rev. B* **82**, 064412 (2010).
- [11] Y. Singh, S. Manni, J. Reuther, T. Berlijn, R. Thomale, W. Ku, S. Trebst, and P. Gegenwart, *Phys. Rev. Lett.* **108**, 127203 (2012).
- [12] J. Chaloupka, G. Jackeli, and G. Khaliullin, [arXiv:1209.5100v1](https://arxiv.org/abs/1209.5100v1).
- [13] J. Reuther, R. Thomale, and S. Trebst, *Phys. Rev. B* **84**, 100406(R) (2011).
- [14] I. I. Mazin, H. O. Jeschke, K. Foyevtsova, R. Valentí, and D. I. Khomskii, *Phys. Rev. Lett.* **109**, 197201 (2012).
- [15] C. H. Kim, H. S. Kim, H. Jeong, H. Jin, and J. Yu, *Phys. Rev. Lett.* **108**, 106401 (2012).
- [16] S. K. Choi *et al.*, *Phys. Rev. Lett.* **108**, 127204 (2012).
- [17] F. Ye, S. Chi, H. Cao, B. C. Chakoumakos, J. A. Fernandez-Baca, R. Custelcean, T. F. Qi, O. B. Korneta, and G. Cao, *Phys. Rev. B* **85**, 180403 (2012).
- [18] X. Liu *et al.*, *Phys. Rev. Lett.* **109**, 157401 (2012).
- [19] S. Bhattacharjee, S.-S. Lee, and Y. B. Kim, *New J. Phys.* **14**, 073015 (2012).
- [20] S. W. Lovesey and A. N. Dobrynin, *J. Phys. Condens. Matter* **24**, 382201 (2012).
- [21] B. Andlauer, J. Schneider, and W. Tolksdorf, *Phys. Status Solidi B* **73**, 533 (1976).
- [22] K. W. Blazey and F. Levy, *Solid State Commun.* **59**, 335 (1986).
- [23] V. M. Katukuri, H. Stoll, J. van den Brink, and L. Hozoi, *Phys. Rev. B* **85**, 220402 (2012).
- [24] R. Comin *et al.*, *Phys. Rev. Lett.* **109**, 266406 (2012).
- [25] Y. J. Kim, J. P. Hill, J. Kim, and D. Casa, *Synchrotron Radiation News* **25**, 3 (2012).
- [26] M. M. Sala *et al.*, *New J. Phys.* **13**, 043026 (2011).
- [27] G. Ghiringhelli, M. Matsubara, C. Dallera, F. Fracassi, A. Tagliaferri, N. Brookes, A. Kotani, and L. Braicovich, *Phys. Rev. B* **73**, 035111 (2006).
- [28] A. Uldry, F. Vernay, and B. Delley, *Phys. Rev. B* **85**, 125133 (2012).
- [29] G. Ghiringhelli, N. Brookes, E. Annese, H. Berger, C. Dallera, M. Grioni, L. Perfetti, A. Tagliaferri, and L. Braicovich, *Phys. Rev. Lett.* **92**, 117406 (2004).
- [30] L. J. P. Ament, M. van Veenendaal, T. P. Devereaux, J. P. Hill, and J. van den Brink, *Rev. Mod. Phys.* **83**, 705 (2011).
- [31] M. Z. Hasan, E. D. Isaacs, Z. X. Shen, L. L. Miller, K. Tsutsui, T. Tohyama, and S. Maekawa, *Science* **288**, 1811 (2000).
- [32] J. Schlappa, K. Wohlfeld, K. J. Zhou, M. Mourigal, M. W. Haverkort, V. N. Strocov, L. Hozoi, C. Monney, S. Nishimoto, S. Singh *et al.*, *Nature (London)* **485**, 82 (2012).
- [33] L. Braicovich *et al.*, *Phys. Rev. Lett.* **102**, 167401 (2009).
- [34] H. Gretarsson, J. Kim, D. Casa, T. Gog, K. R. Choi, S. W. Cheong, and Y.-J. Kim, *Phys. Rev. B* **84**, 125135 (2011).
- [35] T. Helgaker, P. Jørgensen, and J. Olsen, *Molecular Electronic-Structure Theory* (Wiley, Chichester, 2000).
- [36] See Supplemental Material at <http://link.aps.org/supplemental/10.1103/PhysRevLett.110.076402> for detailed description of the electronic structure and quantum chemical calculations, additional RIXS spectra, and PDF experiments.
- [37] H. Kobayashi, M. Tabuchi, M. Shikano, H. Kageyama, and R. Kanno, *J. Mater. Chem.* **13**, 957 (2003).
- [38] M. J. O'Malley, H. Verweij, and P. M. Woodward, *J. Solid State Chem.* **181**, 1803 (2008).
- [39] X. Liu, T. Berlijn, W.-G. Yin, W. Ku, A. Tsvelik, Y.-J. Kim, H. Gretarsson, Y. Singh, P. Gegenwart, and J. P. Hill, *Phys. Rev. B* **83**, 220403 (2011).
- [40] D. S. Ellis, J. Hill, S. Wakimoto, R. Birgeneau, D. Casa, T. Gog, and Y.-J. Kim, *Phys. Rev. B* **77**, 060501 (2008).
- [41] J. van den Brink, M. B. J. Meinders, J. Lorenzana, R. Eder, and G. A. Sawatzky, *Phys. Rev. Lett.* **75**, 4658 (1995).
- [42] R. Neudert, M. Knupfer, M. S. Golden, J. Fink, W. Stephan, K. Penc, N. Motoyama, H. Eisaki, and S. Uchida, *Phys. Rev. Lett.* **81**, 657 (1998).

Evidence for Short-Range-Ordered Charge Stripes Far above the Charge-Ordering Transition in $\text{La}_{1.67}\text{Sr}_{0.33}\text{NiO}_4$

A. M. Milinda Abeykoon,¹ Emil S. Božin,¹ Wei-Guo Yin,¹ Genda Gu,¹ John P. Hill,¹
John M. Tranquada,¹ and Simon J. L. Billinge^{1,2}

¹*Condensed Matter Physics and Materials Science Department, Brookhaven National Laboratory, Upton, New York 11973, USA*

²*Department of Applied Physics and Applied Mathematics, Columbia University, New York, New York 10027, USA*

(Received 31 May 2013; revised manuscript received 17 July 2013; published 30 August 2013)

The temperature evolution of structural effects associated with charge order (CO) and spin order in $\text{La}_{1.67}\text{Sr}_{0.33}\text{NiO}_4$ has been investigated using neutron powder diffraction. We report an anomalous shrinking of the c/a lattice parameter ratio that correlates with T_{CO} . The sign of this change can be explained by the change in interlayer Coulomb energy between the static-stripe-ordered state and the fluctuating-stripe-ordered state or the charge-disordered state. In addition, we identify a contribution to the mean-square displacements of Ni and in-plane O atoms whose width correlates quite well with the size of the pseudogap extracted from the reported optical conductivity, with a non-Debye-like component that persists below and well above T_{CO} . We infer that dynamic charge-stripe correlations survive to $T \sim 2T_{\text{CO}}$.

DOI: [10.1103/PhysRevLett.111.096404](https://doi.org/10.1103/PhysRevLett.111.096404)

PACS numbers: 71.27.+a, 61.05.F-, 71.45.Lr, 74.72.Kf

The phenomenology of charge and spin stripes has been of considerable interest in a broad range of strongly correlated electron systems [1–6], and in particular with regard to the problem of high-temperature superconductivity in cuprates [7–9]. Although static charge-stripe-order (CO) and spin-order (SO) have been detected by diffraction techniques only in select cuprate materials [10–12], stripe-like modulations of electronic states have been detected at the surface of cleavable cuprates by scanning tunneling spectroscopy [13–15], and a new type of charge correlation has recently been identified in $\text{YBa}_2\text{Cu}_3\text{O}_{6+x}$ [16–20]. When static charge-stripe order occurs in $\text{La}_{2-x}\text{Ba}_x\text{CuO}_4$ [21], it competes with Josephson coupling between the superconducting layers [22–25]. Dynamic stripes may have a broader relevance to superconductivity in the cuprates [26]; however, there is not yet any direct, incontrovertible evidence for dynamic charge stripes in cuprates.

$\text{La}_{2-x}\text{Sr}_x\text{NiO}_4$ has served as a model system for studying stripe order [27]. Charge-stripe order can occur at relatively high temperatures, reaching a maximum of $T_{\text{CO}} = 240$ K at $x = 1/3$ [28,29]. While the stripe order is more classical than in the cuprates, with quantum fluctuations being unimportant, there is the possibility that dynamical stripes might exist above T_{CO} . Inelastic neutron scattering studies have already shown that spin-stripe correlations survive above both T_{SO} and T_{CO} [30]. An x-ray scattering study was able to follow critical scattering associated with charge-stripe correlations to temperatures slightly above T_{CO} , but ran out of signal by $T_{\text{CO}} + 20$ K [31]. In contrast, measurements of optical conductivity have demonstrated the absence of a dominant Drude peak, the signature of a conventional metallic state, to temperatures as high as $2T_{\text{CO}}$ [32]. The fact that the optical conductivity remains peaked at finite frequency suggests that the charge carriers are quasilocated, which might

be the result of fluctuating charge stripes persisting at high temperature.

In this Letter, we use neutron scattering from a polycrystalline sample to investigate the structural response associated with charge-stripe correlations in $\text{La}_{1.67}\text{Sr}_{0.33}\text{NiO}_4$ (LSNO). This might appear to be a surprising approach, as even in the stripe-ordered state the superlattice peaks associated with stripe order are too weak to detect by powder diffraction. Nevertheless, we observe distinct signatures in the temperature-dependent scattering associated with the loss of static charge stripe order at T_{CO} and the gradual attenuation of fluctuating stripes at much higher temperatures.

The $\text{La}_{1.67}\text{Sr}_{0.33}\text{NiO}_4$ sample studied here was initially prepared as a single crystal by the traveling-solvent floating-zone method; a portion of the crystal was then ground to powder form. Neutron diffraction measurements on a piece of the starting crystal have confirmed that $T_{\text{CO}} = 240$ K, consistent with previous work [28,29,31]. Time-of-flight neutron powder diffraction measurements were carried out at the NPDF beam line [33] of the Los Alamos Neutron Scattering Center at Los Alamos National Laboratory. Data were converted to the pair distribution function (PDF) using PDFgetN [34] and the PDF was modeled using PDFgui [35]. Rietveld refinements were performed using GSAS+EXPGUI [36,37]. The tetragonal space group $I4/mmm$ was used in the refinements [38]. More details of the experiments and data reduction may be found in the Supplemental Material [39].

Representative Rietveld and PDF fits to the 80 K data are shown in Fig. 1. The model fit to the data is the undistorted tetragonal structure, which does not allow for the average atomic displacements associated with charge ordering. The fits are good, which indicates that any structural modification due to the charge ordering is small, consistent with

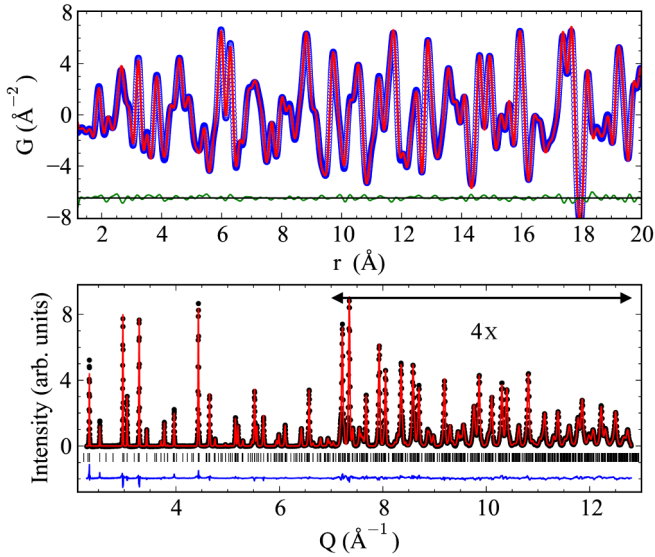


FIG. 1 (color online). PDF (top) and Rietveld (bottom) fits to 80 K data. In both panels, structure models are shown as red solid lines, while the data are shown as circles. Difference curves are offset for clarity.

earlier studies [38]. No charge or spin superlattice peaks are evident in the data; even in the best case of a nickelate with 3D long-range order, the superlattice intensities are no more than 10^{-4} relative to strong fundamental reflections [40], which is beyond the dynamic range for powder diffraction. While we do not detect the average atomic displacements associated with charge ordering, the transition is revealed by a modification of the tetragonality of the unit cell. The unit cell volume varies smoothly with temperature, as shown in Fig. 2 by the blue circles, in agreement with earlier studies [41]; however, the c/a ratio exhibits a strong anomaly at T_{CO} . This anomaly results from a contraction in the c and an elongation in the a directions in a way that preserves the total unit cell volume. To the best of our knowledge, this is the first time an anomaly in the LSNO unit cell constants at T_{CO} has been reported. It correlates well with anomalies in the sound velocity [28] and thermal conductivity [42].

We can define an order parameter based on this structural response by quantifying how the c/a ratio deviates from a smooth extrapolation of the high-temperature behavior. We use the T dependence of the unit cell volume for this purpose, which we rescale to lie on top of the c/a curve in the high-temperature region. Taking the difference and normalizing the signal to a jump of unity, the resulting order parameter is shown in the inset of Fig. 2. Plotted with it is the normalized single crystal CO peak intensity [31], which is proportional to the square of the conventional order parameter for the charge-ordering transition. Both show the same T dependence, indicating that the anomaly in c/a originates from the development of long-range charge order.

The observed charge stripes in the low- T phase of LSNO for $x = 1/3$ lie in the NiO_2 plane and are diagonal with

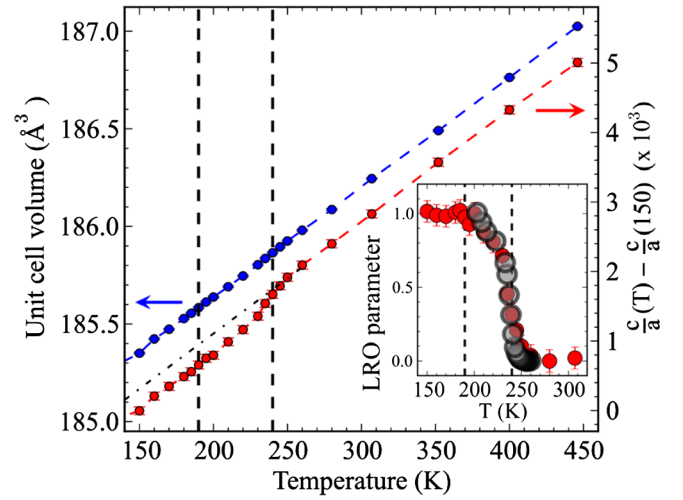


FIG. 2 (color online). The temperature evolution of c/a ratio (bottom curve with red solid circles) in comparison with the volume expansion (top curve with blue solid circles). Dotted lines indicate $T_{SO} = 190$ K and $T_{CO} = 240$ K. In the inset, the red solid circles represent a normalized long-range-order (LRO) parameter calculated from c/a , and the black open circles represents the T evolution of the normalized integrated intensity of the single crystal CO peak from Du *et al.* [31].

respect to the nearest neighbor nickel ions. This pattern of charge order is consistent with the Wigner-crystal model from electrostatic considerations. It is interesting to examine whether the same considerations could account for the c/a anomaly. To understand how charge ordering may couple to the lattice parameters, we consider three extremes: (1) ordered stripes, with a staggered stacking as observed experimentally, (2) ordered stripes, without any stacking order along the c axis, and (3) uniform charge in layers. Evaluating the interlayer Coulomb energy for these three configurations, we find that minimization of the Coulomb energy is consistent with an anomalous reduction of the c/a ratio at T_{CO} . (Details are presented in the Supplemental Material [39].)

We now turn our attention to the local structure. Atomic displacements associated with charge stripes, whether static or dynamic, should contribute to measures of disorder relative to the tetragonal model. From the Rietveld refinement of the diffraction pattern, we obtain atomic displacement parameters (ADPs), where the ADP for a particular atomic site in the unit cell can be written as $U_{ii} = \langle u_i^2 \rangle$, where u_i is the instantaneous displacement of such an atom along direction i and the average is over time and configuration. In the PDF, disorder will impact the widths of contributions for individual interatomic distributions (although these may overlap and interfere). For well-behaved materials, the temperature dependence of the ADPs is well explained [43] by the simple Debye model [44]. Deviations from this behavior may indicate the appearance of underlying structural distortions [45,46]. The temperature-dependent anisotropic ADPs

from various atoms in the LSNO structure obtained from Rietveld refinements are shown in Fig. 3. The thermal evolution of various other ADPs are shown in Fig. 3(a) while the ADPs that lie along in-plane nickel-oxygen bonds are shown in Fig. 3(b). In each case the dashed lines (not vertical) represent Debye-model fits to the low-temperature region of the data (with an explanation of the Debye model given in the Supplemental Material [39]). The directions of the different ADPs are indicated in the inset of Fig. 3(a).

For the examples in Fig. 3(a), the measured ADPs lie on, or close to, the Debye curves at all temperatures, suggesting that the behavior is dominated by conventional disorder due to harmonic motion. The ADPs for oxygen atoms in directions perpendicular to the Ni-O bonds, $O_a U_{11}$ and $O_p U_{33}$, are significantly larger in amplitude than the other ADPs in Fig. 3(a), yielding lower Debye temperatures in the fits, suggesting lower-energy rotational motions of the NiO_6 octahedra, as expected in structures based on the perovskite motif, and as noted before.

In contrast, the ADPs for the in-plane O and Ni atoms in directions *parallel* to the in-plane Ni-O bonds, shown in Fig. 3(b), exhibit large deviations from conventional behavior. These ADPs are the ones we anticipate should have substantial contributions associated with stripe order below T_{CO} [40]. Each ADP should involve a sum of two contributions, one from the stripe-related displacements and another from the usual vibrational motion. Indeed, we see that the ADPs asymptotically approach a Debye curve at high temperature. We infer that the excess magnitude of each ADP above the shifted Debye curve (dotted lines) is associated with stripe correlations. Intriguingly, there is no dramatic change at T_{CO} where static stripe order disappears. Instead, the low-temperature behavior can be characterized by a distinct Debye curve, with downward deviations beginning near the T_{SO} . The stripe-related disorder above T_{CO} is presumably dynamic, given the effective disappearance of elastic diffuse scattering in single-crystal neutron-scattering experiments.

We can define a measure of local stripe correlations as

$$\Delta(T) = \sqrt{U_{ii}^A(T)} - \sqrt{U_{Dii}^A(T)}, \quad (1)$$

where A indicates the atomic species and U_{Dii} represents the Debye approximation to the high-temperature behavior. The “order” parameters from in-plane Ni U_{11} and O U_{22} , normalized to unity, are shown in the inset of Fig. 3(b). There is essentially identical temperature dependence for the Ni and O sites.

To make a connection with the electronic properties, one can compare the temperature dependence of the local order parameters with the optical conductivity data from Katsufuji *et al.* [32]. The energy gap for finite conductivity closes at T_{CO} , but this provides no measure of the correlations that survive above T_{CO} . To better capture the effective pseudogap, we have evaluated the energy at which the

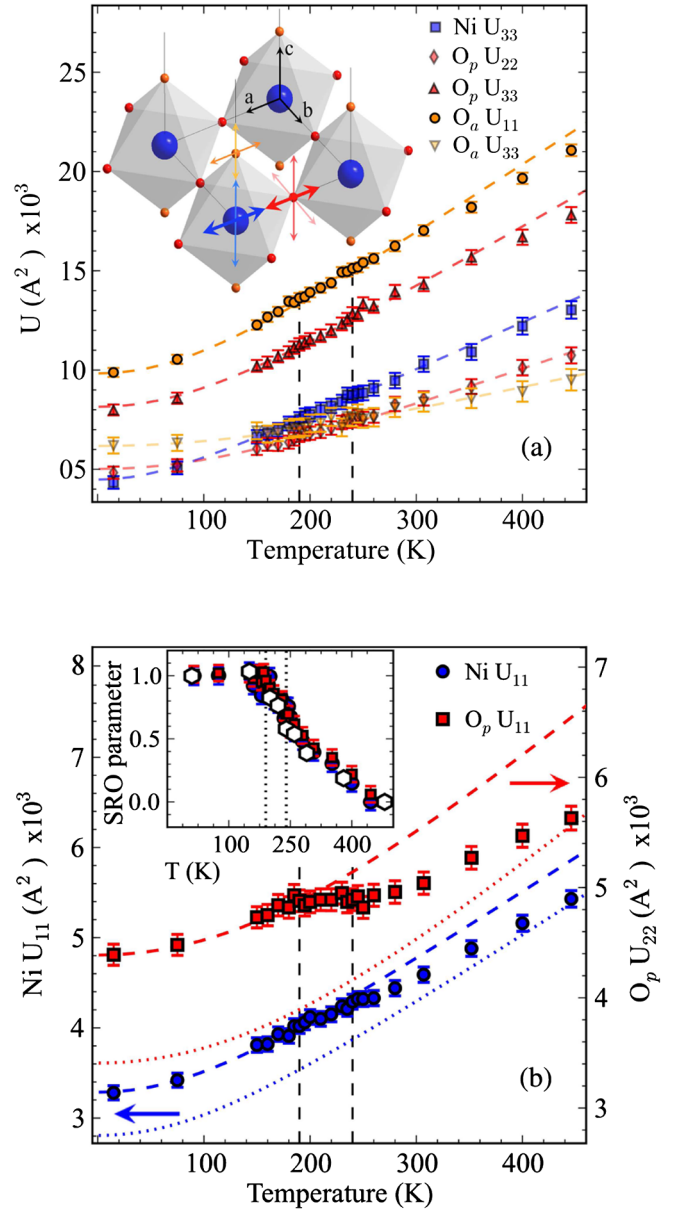


FIG. 3 (color online). Anisotropic ADPs that are not along in-plane Ni-O bonds are shown in (a), while the ADPs that lie along these bonds are shown in (b). The structure is shown in the inset of (a) to illustrate the atoms and the directions of the different anisotropic ADPs that are plotted in the main panels, with Ni in blue, apical oxygen (O_a) in orange, and in-plane oxygen (O_p) in red. Vertical dotted lines indicate the spin- and charge-ordering temperatures, T_{SO} and T_{CO} . Dashed lines represent calculated Debye behavior. The dotted lines in (b) represent calculated Debye behavior with different offsets that are appropriate to fit the high- T ADPs. The inset contains the same ADP data converted to a short-range-order (SRO) parameter, which is the normalized difference from the high- T Debye fit as described in the text, where the symbols used are the same as in the main panel. Plotted on top is a similar SRO parameter for the energy of the pseudogap as determined from optical conductivity measurements as described in the text.

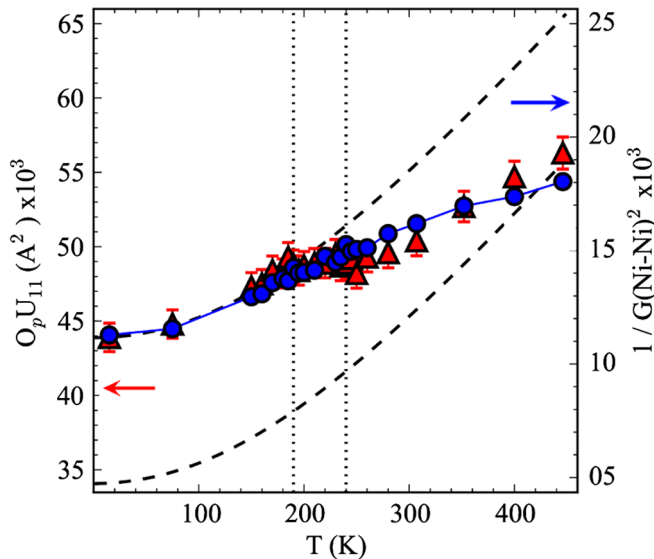


FIG. 4 (color online). Comparison of the temperature evolution of the squared inverse height of the nearest neighbor Ni-Ni PDF peak (blue solid circles) and of the in-plane oxygen U_{22} (red triangles).

optical conductivity falls to half of its peak value at each temperature. With normalization at low temperature, this quantity is plotted in the inset of Fig. 3(b) using open symbols. A remarkable resemblance is observed between the local order parameters from the ADPs and the temperature evolution of the energy gap, which directly links the pseudogap behavior in LSNO and the presence of stripe correlations in the local structure.

The local structural response can also be extracted from PDF analysis. To keep the analysis simple, we focus on just the correlations for atoms separated by the a lattice parameter (3.83 Å), corresponding to the near-neighbor O-O distance that also includes Ni-Ni neighbors. The area of this peak stays essentially constant with temperature, but the width varies. The inverse square PDF peak height is proportional to the square width, or ADP, of that correlation and so is a sensitive and model-independent way of interrogating the data for this parameter. The temperature evolution of the inverse square PDF peak height is shown in Fig. 4 as blue solid circles. For comparison, the in-plane oxygen ADP along the Ni-O bond, U_{22} , is indicated by red triangles. The inverse square PDF peak height shows the same T dependence. A clear break in slope can be observed in the T evolution of the inverse square PDF peak height at T_{SO} , indicating its sensitivity to stripe order, and the behavior closely follows the Rietveld ADP for the in-plane oxygen along the bond. Thus, the PDF, which is a model-independent complementary measure of the evolution of CO, confirms the Rietveld result.

In summary, we have presented a temperature-dependent neutron powder diffraction study of LSNO, which is known to show robust charge-stripe order below 240 K. We have shown that the tetragonality shows an

anomalous change at T_{CO} . In contrast, a local order parameter determined from mean-square displacements of Ni and in-plane O sites, or equivalently from squared PDF peak widths, shows a temperature dependence that correlates quite well with the pseudogap in the optical conductivity [32]. From this behavior, we have inferred that charge-stripe correlations survive to temperatures far above T_{CO} , and only gradually become attenuated. These results provide support for the idea that short-range-ordered, and presumably fluctuating, stripes could underlie electronic features, such as pseudogap and nematic and smectic phases seen in the related cuprates [26,47].

This work was supported by the Office of Basic Energy Sciences, Division of Materials Sciences and Engineering, U.S. Department of Energy through account No. DE-AC02-98CH10886. This work has benefited from the use of NPDF at LANSCE, funded by DOE Office of Basic Energy Sciences. LANL is operated by Los Alamos National Security LLC under DOE Contract No. DE-AC52-06NA25396.

- [1] N. Ikeda, H. Ohsumi, K. Ohwada, K. Ishii, T. Inami, K. Kakurai, Y. Murakami, K. Yoshii, S. Mori, Y. Horibe, and H. Kito, *Nature (London)* **436**, 1136 (2005).
- [2] M. Coey, *Nature (London)* **430**, 155 (2004).
- [3] M.S. Senn, J.P. Wright, and J.P. Attfield, *Nature (London)* **481**, 173 (2012).
- [4] H. Ulbrich and M. Braden, *Physica (Amsterdam)* **481C**, 31 (2012).
- [5] M. Hücker, *Physica (Amsterdam)* **481C**, 3 (2012).
- [6] T. Wu, H. Mayaffre, S. Kramer, M. Horvatic, C. Berthier, W.N. Hardy, R. Liang, D.A. Bonn, and M.-H. Julien, *Nature (London)* **477**, 191 (2011).
- [7] S.A. Kivelson, I.P. Bindloss, E. Fradkin, V. Oganesyan, J.M. Tranquada, A. Kapitulnik, and C. Howald, *Rev. Mod. Phys.* **75**, 1201 (2003).
- [8] M. Vojta, *Adv. Phys.* **58**, 699 (2009).
- [9] J. Zaanen, O.Y. Osman, H.V. Kruis, Z. Nussinov, and J. Tworzydło, *Philos. Mag. B* **81**, 1485 (2001).
- [10] M. Hücker, *Physica (Amsterdam)* **481C**, 3 (2012).
- [11] P. Abbamonte, E. Demler, J.S. Davis, and J.-C. Campuzano, *Physica (Amsterdam)* **481C**, 15 (2012).
- [12] M. Fujita, *Physica (Amsterdam)* **481C**, 23 (2012).
- [13] J.A. Robertson, S.A. Kivelson, E. Fradkin, A.C. Fang, and A. Kapitulnik, *Phys. Rev. B* **74**, 134507 (2006).
- [14] Y. Kohsaka, C. Taylor, K. Fujita, A. Schmidt, C. Lupien, T. Hanaguri, M. Azuma, M. Takano, H. Eisaki, H. Takagi, S. Uchida, and J.C. Davis, *Science* **315**, 1380 (2007).
- [15] C.V. Parker, P. Aynajian, E.H. da Silva Neto, A. Pushp, S. Ono, J. Wen, Z. Xu, G. Gu, and A. Yazdani, *Nature (London)* **468**, 677 (2010).
- [16] G. Ghiringhelli, M. Le Tacon, M. Minola, S. Blanco-Canosa, C. Mazzoli, N.B. Brookes, G.M. De Luca, A. Frano, D.G. Hawthorn, F. He, T. Loew, M.M. Sala, D.C. Peets, M. Salluzzo, E. Schierle, R. Sutarto, G.A. Sawatzky, E. Weschke, B. Keimer, and L. Braicovich, *Science* **337**, 821 (2012).

- [17] J. Chang, E. Blackburn, A. T. Holmes, N. B. Christensen, J. Larsen, J. Mesot, R. Liang, D. A. Bonn, W. N. Hardy, A. Watenphul, M. v. Zimmermann, E. M. Forgan, and S. M. Hayden, *Nat. Phys.* **8**, 871 (2012).
- [18] E. Blackburn, J. Chang, M. Hücker, A. T. Holmes, N. B. Christensen, R. Liang, D. A. Bonn, W. N. Hardy, U. Rütt, O. Gutowski, M. v. Zimmermann, E. M. Forgan, and S. M. Hayden, *Phys. Rev. Lett.* **110**, 137004 (2013).
- [19] S. Blanco-Canosa, A. Frano, T. Loew, Y. Lu, J. Porras, G. Ghiringhelli, M. Minola, C. Mazzoli, L. Braicovich, E. Schierle, E. Weschke, M. Le Tacon, and B. Keimer, *Phys. Rev. Lett.* **110**, 187001 (2013).
- [20] V. Thampy, S. Blanco-Canosa, M. García-Fernández, M. P. M. Dean, G. D. Gu, M. Först, B. Keimer, M. Le Tacon, S. B. Wilkins, and J. P. Hill, *Phys. Rev. B* **88**, 024505 (2013).
- [21] M. Hücker, M. v. Zimmermann, G. D. Gu, Z. J. Xu, J. S. Wen, G. Xu, H. J. Kang, A. Zheludev, and J. M. Tranquada, *Phys. Rev. B* **83**, 104506 (2011).
- [22] S. Tajima, T. Noda, H. Eisaki, and S. Uchida, *Phys. Rev. Lett.* **86**, 500 (2001).
- [23] Q. Li, M. Hücker, G. D. Gu, A. M. Tsvelik, and J. M. Tranquada, *Phys. Rev. Lett.* **99**, 067001 (2007).
- [24] E. Berg, E. Fradkin, S. A. Kivelson, and J. M. Tranquada, *New J. Phys.* **11**, 115004 (2009).
- [25] C. C. Homes, M. Hücker, Q. Li, Z. J. Xu, J. S. Wen, G. D. Gu, and J. M. Tranquada, *Phys. Rev. B* **85**, 134510 (2012).
- [26] S. A. Kivelson, E. Fradkin, and V. J. Emery, *Nature (London)* **393**, 550 (1998).
- [27] H. Ulbrich and M. Braden, *Physica (Amsterdam)* **481C**, 31 (2012).
- [28] A. P. Ramirez, P. L. Gammel, S.-W. Cheong, D. J. Bishop, and P. Chandra, *Phys. Rev. Lett.* **76**, 447 (1996).
- [29] S.-H. Lee and S.-W. Cheong, *Phys. Rev. Lett.* **79**, 2514 (1997).
- [30] S.-H. Lee, J. M. Tranquada, K. Yamada, D. J. Buttrey, Q. Li, and S.-W. Cheong, *Phys. Rev. Lett.* **88**, 126401 (2002).
- [31] C.-H. Du, M. E. Ghazi, Y. Su, I. Pape, P. D. Hatton, S. D. Brown, W. G. Stirling, M. J. Cooper, and S.-W. Cheong, *Phys. Rev. Lett.* **84**, 3911 (2000).
- [32] T. Katsufuji, T. Tanabe, T. Ishikawa, Y. Fukuda, T. Arima, and Y. Tokura, *Phys. Rev. B* **54**, R14230 (1996).
- [33] T. Proffen, T. Egami, S. J. L. Billinge, A. K. Cheetham, D. Louca, and J. B. Parise, *Appl. Phys. A* **74**, s163 (2002).
- [34] P. F. Peterson, M. Gutmann, T. Proffen, and S. J. L. Billinge, *J. Appl. Crystallogr.* **33**, 1192 (2000).
- [35] C. L. Farrow, P. Juhás, J. Liu, D. Bryndin, E. S. Božin, J. Bloch, T. Proffen, and S. J. L. Billinge, *J. Phys. Condens. Matter* **19**, 335219 (2007).
- [36] A. C. Larson and R. B. Von Dreele, Los Alamos National Laboratory Report No. LAUR-86-748, 2004.
- [37] B. H. Toby and S. J. L. Billinge, *Acta Crystallogr. Sect. A* **60**, 315 (2004).
- [38] G. Wu, J. J. Neumeier, C. D. Ling, and D. N. Argyriou, *Phys. Rev. B* **65**, 174113 (2002).
- [39] See Supplemental Material at <http://link.aps.org/supplemental/10.1103/PhysRevLett.111.096404> for a description of the sample preparation method, neutron powder diffraction measurements, and the details of the theory used in the main text to explain the results. The Supplemental Material also contains a plot of the bond length ratio, (Ni-Oa)/(Ni-Op).
- [40] J. M. Tranquada, J. E. Lorenzo, D. J. Buttrey, and V. Sachan, *Phys. Rev. B* **52**, 3581 (1995).
- [41] G. Wu, J. J. Neumeier, C. D. Ling, and D. N. Argyriou, *Phys. Rev. B* **65**, 174113 (2002).
- [42] C. Hess, B. Büchner, M. Hücker, R. Gross, and S.-W. Cheong, *Phys. Rev. B* **59**, R10397 (1999).
- [43] S. J. L. Billinge, P. K. Davies, T. Egami, and C. R. A. Catlow, *Phys. Rev. B* **43**, 10340 (1991).
- [44] P. Debye, *Ann. Phys. (Berlin)* **344**, 789 (1912).
- [45] S. J. L. Billinge, R. G. DiFrancesco, G. H. Kwei, J. J. Neumeier, and J. D. Thompson, *Phys. Rev. Lett.* **77**, 715 (1996).
- [46] E. S. Božin, C. D. Malliakas, P. Souvatzis, T. Proffen, N. A. Spaldin, M. G. Kanatzidis, and S. J. L. Billinge, *Science* **330**, 1660 (2010).
- [47] M. J. Lawler, K. Fujita, J. Lee, A. R. Schmidt, Y. Kohsaka, C. K. Kim, H. Eisaki, S. Uchida, J. C. Davis, J. P. Sethna, and E.-A. Kim, *Nature (London)* **466**, 347 (2010).

Confirmation of disordered structure of ultrasmall CdSe nanoparticles from X-ray atomic pair distribution function analysis

Cite this: *Phys. Chem. Chem. Phys.*, 2013, **15**, 8480

Xiaohao Yang,^a Ahmad S. Masadeh,^b James R. McBride,^c Emil S. Božin,^d Sandra J. Rosenthal^c and Simon J. L. Billinge^{*ad}

The atomic pair distribution function (PDF) analysis of X-ray powder diffraction data has been used to study the structure of small and ultra-small CdSe nanoparticles. A method is described that uses a wurtzite and zinc-blende mixed phase model to account for stacking faults in CdSe particles. The mixed-phase model successfully describes the structure of nanoparticles larger than 2 nm yielding a stacking fault density of about 30%. However, for ultrasmall nanoparticles smaller than 2 nm, the models cannot fit the experimental PDF showing that the structure is significantly modified from that of larger particles and the bulk. The observation of a significant change in the average structure at ultra-small size is likely to explain the unusual properties of the ultrasmall particles such as their white light emitting ability.

Received 9th January 2013,
Accepted 11th March 2013

DOI: 10.1039/c3cp00111c

www.rsc.org/pccp

1 Introduction

Semiconductor CdSe nanoparticles have been extensively studied.¹ Their size can be well controlled providing a good platform for studying the nanoparticle size dependence of their various properties.² Significant deviations from the bulk properties have been reported for nanoparticles smaller than 5 nm.^{3,4} Among them, the optical properties provide a size-tunability with potential applications in solar cells and lighting applications.^{3,5} Recently, it has become possible to synthesize ultra-small CdSe nanoparticles which were found to exhibit an extremely broad emission spectrum rather than the blue shifted monochromatic light emission of still small but larger nanoparticles.^{6–10}

Accurate determination of atomic structure is important for understanding the fundamental properties of nanoparticles. However, due to the absence of Bragg peaks when scattering from very small particles, traditional crystallography breaks down:¹¹ the so-called “nanostructure problem”.¹² As an alternative, the atomic pair distribution function (PDF) method is a powerful tool for studies of nanoscale structure,^{13,14} as it uses total scattering data and does not require long-range periodicity. Recently, progress in both data collection¹⁵ and modeling tools^{13,16,17} has allowed the

PDF method to be successfully applied to the study of nanoparticle structure.^{18–22}

An early understanding of the structure of CdSe nanoparticles suggested using X-ray diffraction and transmission electron microscopy (TEM) indicated that their structure is an intermediate status between wurtzite and zinc-blende.^{23–25} This was confirmed in more recent studies where the PDFs of different sizes of II–VI semiconductor nanoparticles were fit with models of the wurtzite structure with significant stacking faults.^{19,25,26}

For ultrasmall nanoparticles below 2 nm, conventional TEM methods fail due to the poor contrast of nanoparticles to the carbon supporting film.⁸ However, images may be obtained from aberration-corrected atomic number contrast scanning transmission electron microscopy (Z-STEM). Z-STEM studies on ultra-small CdSe nanoparticles suggested the presence of a highly distorted crystal structure where it was difficult to assign a wurtzite or zinc-blende structure.^{8,27} A study combining density functional theory and quantum mechanical molecular dynamics suggested a dynamic disordered structure for ultra-small nanoparticles that changes with time under electron radiation.²⁸ The strong interaction of the high energy electrons with the particles may be expected to produce a significant perturbation to the system. It is therefore not clear from this measurement what the structural ground-state of the particles is, though it is clear that it is not highly stable. Is the ground-state disordered as observed under the electron beam, or is it ordered but disorders under the electron beam?

^a Department of Applied Physics and Applied Mathematics, Columbia University, New York, New York 10027, USA

^b Department of Physics, The University of Jordan, Amman 11942, Jordan

^c Department of Chemistry, Vanderbilt University, Nashville, Tennessee 37235, USA

^d Condensed Matter Physics and Materials Science Department, Brookhaven National Laboratory, Upton, NY 11973, USA. E-mail: sb2896@columbia.edu

In this paper, we have revisited the same ultra-small nanoparticles that were studied by Pennycook *et al.*,²⁸ however, using X-ray PDF analysis. The X-rays are much less strongly interacting than the electrons and should not perturb the nanoparticle structure yielding a view of the structural ground-state, at least at the ensemble average level. We find that even in the X-ray measurements reported here the structure of the ultra-small particles is significantly modified from the faulted wurtzite seen at larger sizes, being more disordered than the structure in the $D > 2$ nm particles. This suggests that the actual stable, or metastable, state of these ultrasmall nanoparticles is significantly disordered. Although in principle it is possible to solve the structure of nanoparticles from PDF data,¹⁸ it has so far not been possible in this case because of their high level of disorder which limits the information content in the PDF.

Despite the fact that the structure model of the ultrasmall particles is unknown, we could extract information about the homogeneous and inhomogeneous strain in these nanoparticles from the position and width, respectively, of the first peak in the PDF, quantitative information that is not available from the TEM study. We find considerably enhanced compressive homogeneous strain and increased inhomogeneous strain in the bond-length distribution, the latter reflecting the observed disorder of these samples.

In larger nanoparticles that have a faulted wurtzite structure we introduce a new method for estimating the stacking fault density rapidly in the nanoparticles using a wurtzite–zinc-blende mixed-phase model fit only over the local structure. This replaces the approximate method introduced in Masadeh *et al.*¹⁹ and is a rapid, high-throughput alternative to the more time-consuming, though more accurate, approach using big-box models containing large ensembles with many atoms.^{20,25,26} For the samples studied we found the density to be about 30%.

2 Experimental details

2.1 Sample preparation

CdSe nanocrystal samples were synthesized and purified as reported by Bowers *et al.*⁷ and were characterized using UV-visible spectroscopy. Dry nanocrystals powders were packed into Kapton tubing for X-ray powder diffraction experiments. Four nanoparticle sizes, CdSe417 (ultra-small), CdSe470 (small), CdSe552 (medium) and CdSe586 (large), were used for this study, as well as a bulk CdSe sample as a reference. The numbers in the sample name here are referring to their associated center-band-edge absorption wavelength.

The absorption data in Fig. 1 was used to characterize the size of the nanocrystals following the equation provided by Yu *et al.*²⁹ The presence of multiple peaks in the absorption spectra for each nanocrystal is an indication of their low polydispersity and high symmetry.

2.2 High-energy X-ray diffraction experiments

X-ray powder diffraction experiments were performed at the 6IDD beamline at the Advanced Photon Source (APS) at Argonne National Laboratory. Diffraction data were collected

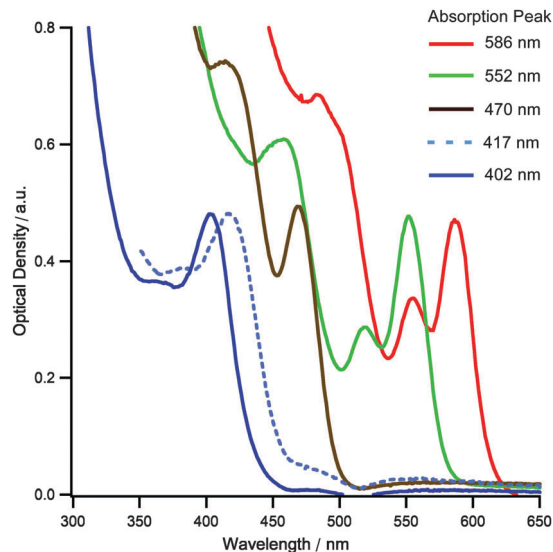


Fig. 1 UV-Vis emission spectra of the CdSe nanoparticles used in this study. The ultra-small nanoparticles that had an absorption maximum at 402 nm were redshifted to 417 nm after washing, as indicated by the blue dashed curve.

using the rapid acquisition pair distribution function (RAPDF) technique.¹⁵ Data were collected at room temperature with an X-ray energy of 98.111 keV ($\lambda = 0.12637$ Å). A 2D image plate camera (Mar345) was used with a sample to detector distance of 229.967 mm, as calibrated by using a silicon standard sample.¹⁵ The scattering signal from the surfactant (TOPO) was measured independently and subtracted as a background in the data reduction.

2D diffraction data were integrated and converted to intensity *versus* 2θ using the FIT2D³⁰ program. These data were further processed to obtain the PDF as described below.

2.3 The atomic PDF method

The atomic PDF, $G(r)$, gives the probability of finding a pair of atoms at a distance of r ,

$$G(r) = 4\pi r [\rho(r) - \rho_0], \quad (1)$$

where $\rho(r)$ is the atomic pair-density, ρ_0 is the average atomic number density and r is the radial distance.³¹ Experimentally, the PDF is obtained from a sine Fourier transformation according to³²

$$G(r) = \frac{2}{\pi} \int_{Q_{\min}}^{\infty} Q[S(Q) - 1] \sin Qr \, dQ, \quad (2)$$

where Q is the magnitude of the scattering vector and $S(Q)$ is the total scattering structure function which is the properly corrected and normalized powder diffraction intensity obtained in a diffraction experiment. Here the data were truncated at $Q_{\max} = 19.0$ Å⁻¹ which was found to be optimal to avoid large termination effects as well as minimizing the statistical noise level, due to the decreasing signal to noise ratio with increasing Q value. The data were processed using the program PDFGetX3.³³

Representative examples of the reduced total scattering function $F(Q)$ and PDFs from our samples are shown in Fig. 2(a) and (b), respectively. We can see that for the larger

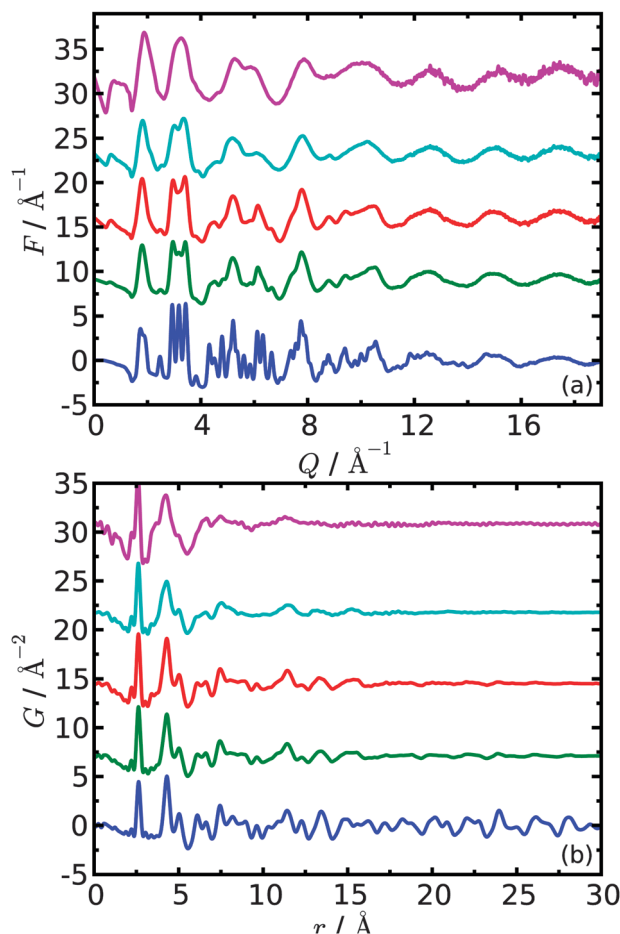


Fig. 2 (a) The experimental reduced structure function $F(Q)$ of CdSe nanoparticles with different diameters and (b) the corresponding PDFs, $G(r)$, obtained by Fourier transformation of the data in (a) with $Q_{\max} = 19.0 \text{ \AA}^{-1}$. The curves are arranged from smallest to largest moving from top to bottom: CdSe417, CdSe470, CdSe552, CdSe586, and CdSeBulk. See text for an explanation of the nomenclature.

nanoparticles the features in the PDF of bulk wurtzite are clearly evident in the PDFs, albeit diminishing in amplitude with increasing- r due to the finite size of the nanoparticles. The CdSe417 PDF has some similarities, but careful inspection shows that the broad peaks in the PDF at higher- r are not aligned well with those from the larger nanoparticles suggesting a modified structure for these ultra-small nanoparticles.

Quantitative structural information can be extracted from the PDF by comparing the experimental PDF and PDF calculated from models.¹³ We used the program SrFit³⁴ to fit a structural model to the experimental PDF. SrFit is a structure refinement program that searches for the structure that is most consistent with the experimental PDF by varying parameters in the model using a user selectable regression method, here least-squares minimization. The agreement of the calculated PDF to the experimental one is characterized by the residual function,

$$R_w = \sqrt{\frac{\sum_{i=1}^N [G_{\text{obs}}(r_i) - G_{\text{calc}}(r_i; \vec{p})]^2}{\sum_{i=1}^N G_{\text{obs}}^2(r_i)}}, \quad (3)$$

where G_{obs} is the PDF extracted from the diffraction data, G_{calc} is the PDF calculated from the model and \vec{p} is the list of variables (*i.e.*, parameters that vary) in the model.

3 Results and discussion

The PDF represents the atomic order within the nanoparticle. For nanoparticles, as r increases, features in the PDF die due to finite particle size effects. The value of r where obvious structure disappears from the PDF places a lower bound on the diameter of the nanoparticles. By visual inspection of the experimental PDF, we can directly set this lower limit as 3.4, 2.8, 2.4, and 1.3 nm for CdSe586, CdSe552, CdSe470, and CdSe417, respectively. This parameter will be refined more precisely later, taking into account the finite resolution of the measurement, by fitting models to the experimental data.

3.1 Mixed-phase model for structure of CdSe

Semiconductor alloys such as sulfides and selenides may crystallize in either the hexagonal wurtzite structure or in the cubic zinc-blende structure.³⁵ The wurtzite and zinc-blende structures have identical corner-shared tetrahedral building blocks but have a different stacking sequence. The layer stacking of wurtzite is ABABAB... along its [001] direction and the stacking of zinc-blende is ABCABC... along the same structural direction, which is [111] in the cubic unit cell, as seen in Fig. 3. The two structures give identical PDFs for the first few neighbors, but differences emerge for higher neighbor pairs. Two structure models, wurtzite (space group $P6_3mc$) and zinc-blende (space group $F\bar{4}3m$), were fit to our PDF data. In the refinement, we constrain both models to have isotropic atomic displacement factors (ADPs). The R_w value and refined results are shown in Table 1 and Fig. 4. Clearly, the wurtzite model gives a better fit

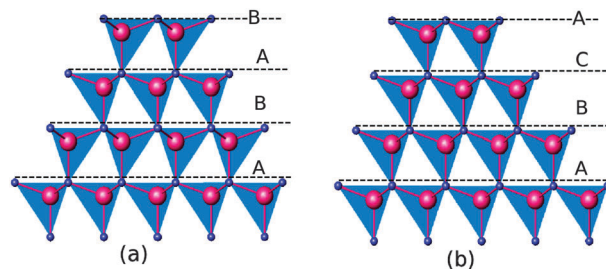


Fig. 3 Fragments from the (a) wurtzite structure, space group ($P6_3mc$) with (ABAB...) layer sequence and (b) zinc-blende structure, space group ($F\bar{4}3m$) with (ABCABC...) sequence.

Table 1 The agreement factor, R_w , obtained from PDF refinements with the wurtzite, zinc-blende, and mixed phase models. Isotropic ADPs were used for all fits

	Zinc-blende	Wurtzite	Mix phases
CdSebulk	0.66	0.16	0.12
CdSe586	0.35	0.19	0.16
CdSe552	0.38	0.28	0.22
CdSe470	0.39	0.32	0.28
CdSe417	0.59	0.49	0.41

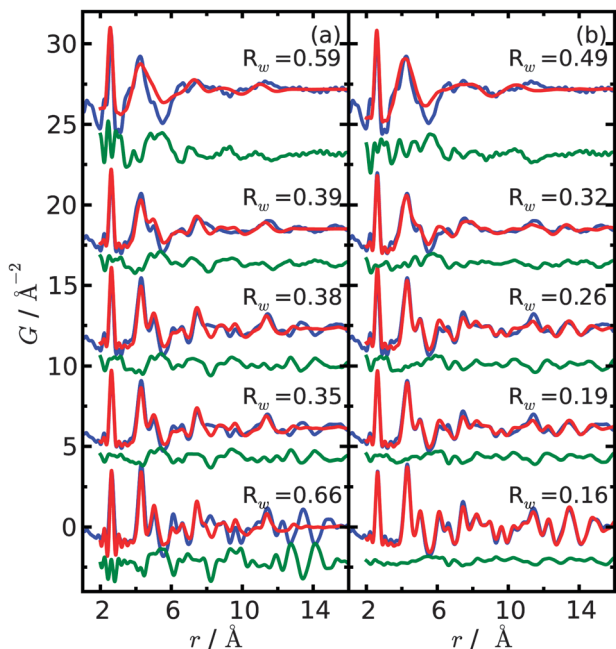


Fig. 4 The experimental PDF, $G(r)$, with $Q_{\max} = 19.0 \text{ \AA}^{-1}$ (blue line) and the calculated PDF from the refined structural model (red line), with the difference curve offset below (green line). PDF data are fitted using zinc-blende model (a) and wurtzite model (b). From top to the bottom: CdSe417, CdSe470, CdSe552, CdSe586, CdSeBulk.

for the bulk data. However, in the nanoparticles the fit quality of these two models is comparable. Although both models give reasonable fit, neither of them can fully reproduce the features in experimental PDF, which indicates that the structure of CdSe quantum dots is not purely wurtzite or zinc-blende, but an intermediate structure between these two, as has been reported.^{19,23}

In the earlier work of Masadeh *et al.*,¹⁹ a model based on wurtzite but containing stacking faults gave a better fit to the data and solved the problem of the unphysically large U_{33} ADP of Se found in their models refined with anisotropic ADPs. The model is based on a wurtzite superlattice with stacking faults along the c -axis and has a fixed stacking fault density. Here we introduce a way of extracting the stacking fault density in a straightforward way directly from modeling the local structure in the PDF.

An interesting possibility of fitting PDFs is that the fitting may be constrained to take place over different ranges of r . We notice that the difference between the wurtzite and zinc-blende structures is only evident on reaching the third layer in the stacking direction. Both stacking sequences begin AB, with wurtzite appending an A whereas zinc-blende appends a C layer. If we take wurtzite as the reference structure, and we define $P(C)$ as the probability of the third layer being a C with respect to the previous two layers defined as AB, we see that wurtzite is the case where $P(C) = 0$ and zinc-blende is $P(C) = 1$. In the presence of stacking faults, we will have, in general, $0 < P(C) < 1$. The stacking fault density (with respect to wurtzite) will be given by $P(C)$.

We can simulate this in the modeling by fitting the PDF over a range that only includes 3 layers and fitting a two-phase model of wurtzite and zinc-blende where we allow the proportion of the wurtzite phase, f , to vary between zero and one (and the proportion of the other phase to be $(1-f)$). This proportion gives $P(C)$ directly. For this to work the model must be suitably constrained so that no other structural parameters can account for the stacking faults, for example, the wurtzite and zinc-blende models must be constrained to have isotropic ADPs since stacking fault effects can be accounted for by enlarged U_{33} parameters in the wurtzite model.¹⁹ To reduce the degrees of freedom it is also possible to add additional constraints, such as enforcing the ADPs of atoms in each of the two phases to be the same as each other, and the volume of the primitive cell of the two phase to be the same as each other.

The fitting results of the mixed phase model are shown in Table 2 and plotted in Fig. 5. Here we used a two step refinement strategy to obtain the stacking fault density. First a refinement with fitting range up to 40 \AA was performed to obtain the diameter of nanoparticles. Then we fixed the size of the nanoparticles and performed a fit over the r range up to 10 \AA which is the approximate range of three stacking layers, to obtain the stacking fault density. The two step refinement is used due to the fact that a large fitting range is required for obtaining reliable size information but is undesirable for refining the stacking fault density. We see from the figure, and the R_w values in the table, that the fits for all but the smallest nanoparticles are quite good and from comparison in Table 1, the mixed-phase model gives a better fit than any single phase model. This is illustrated in Fig. 6 which shows a

Table 2 The refined values obtained from fitting with the mixed-phase model. The ADPs of the two models were constrained to be same as each other and the lattice parameter of the zinc-blende phase was calculated according to the volume of the primitive cell which was constrained to be equal to that of the wurtzite phase

	CdSebulk	CdSe586	CdSe552	CdSe470	CdSe417
Wurtzite a (\AA)	4.2986(3)	4.288(1)	4.290(1)	4.288(2)	3.73(3)
Wurtzite c (\AA)	7.0134(6)	6.999(2)	6.977(3)	6.865(6)	7.53(9)
Zinc-blende a (\AA)	6.0773(5)	6.063(1)	6.059(2)	6.024(3)	5.66(5)
Cd U_{iso}	0.0232(3)	0.0299(4)	0.032(1)	0.058(3)	0.23(6)
Se U_{iso}	0.0223(5)	0.0373(9)	0.030(2)	0.052(4)	0.19(7)
Se Z-frac.	0.3752(2)	0.3728(4)	0.3750(6)	0.3799(9)	0.306(2)
NP diameter (nm)	∞	35.8(3)	29.9(3)	24.0(5)	13.2(3)
Stacking fault density (%)	8.3(2)	27.2(3)	30.7(3)	29.2(9)	68(2)
R_w (wur)	0.12	0.16	0.22	0.28	0.41

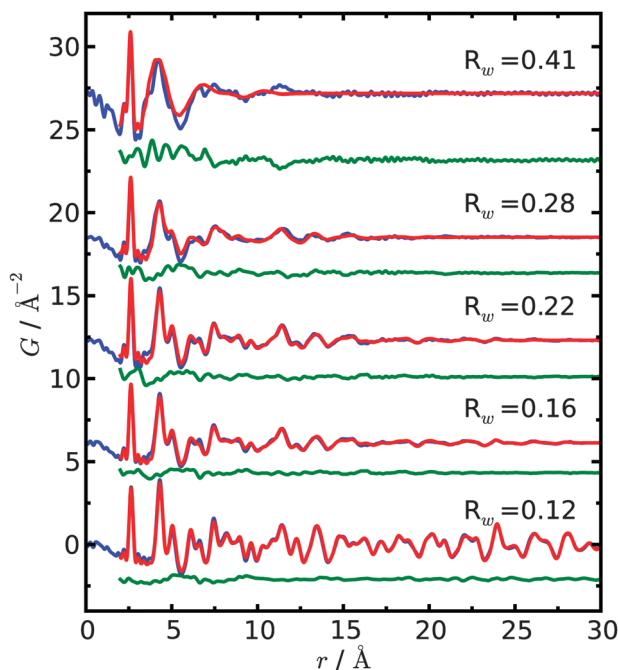


Fig. 5 The experimental PDF, $G(r)$, with $Q_{\max} = 19.0 \text{ \AA}^{-1}$ (blue line) and the calculated PDF from the refined structural model (red line), with the difference curve offset below (green line). The PDF data are fitted using the mixed-phase model. From top to bottom: CdSe417, CdSe470, CdSe552, CdSe586, CdSeBulk.

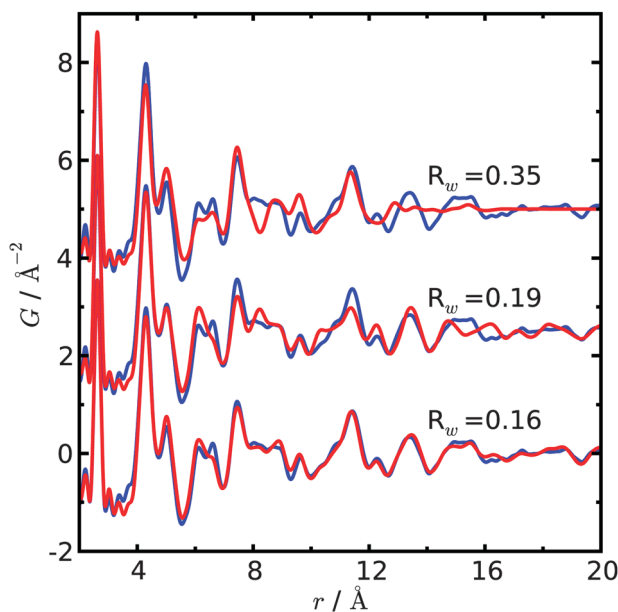


Fig. 6 Comparison of fits from different models to the PDF of the largest nanoparticle. The experimental PDF from CdSe586 (blue line) and calculated PDF (red line), with zinc-blende model (top), wurtzite model (middle), and mixed-phase model (bottom).

comparison of the three fitting results of CdSe586. The resulting R_w values are higher than can be obtained from crystalline samples with well defined structures,¹³ but are comparable to small-box fits to nanoparticles.¹⁹ The mixed-phase model clearly gives the best fit suggesting that our mixed-phase model is successful in modeling

the stacking faults. Indeed, it does a much better job of explaining the high- r region of the PDF than either end-member model even though a mixed-phase model does not strictly describe random stacking faults in this region.

One advantage of the mixed-phase model method for is we can refine the stacking fault density directly and rapidly rather than having to specify a fixed stacking fault density based on wurtzite superlattice.¹⁹ The refined stacking fault density with respect to the wurtzite structure is about 8% for bulk CdSe and about 30% for the three larger nanoparticles, as indicated in Table 2. As was found in earlier studies,^{19,36} there are significantly higher stacking fault densities in small CdSe nanoparticles than in the bulk and the structures can be thought of as being intermediate between wurtzite and zinc-blende.

We should point out that the mixed-phase model has its limitations. Strictly speaking it can only simulate the stacking faults accurately up to three layers of tetrahedra (about 10 Å in the wurtzite c -axis direction) because beginning from the fourth layers, we may encounter multiple different stacking sequences such as AXXC (e.g., ABAC) which is inconsistent with either wurtzite stacking ABAB or zinc-blende stacking ABCAB. However the PDF measures the average structure of large numbers of nanoparticles. Although there are small differences that exist in the high- r , there is little information in the PDF that suggests a preference for a particular stacking superstructure, but rather a random statistical distribution.

Once we have a good fit such as from the mixed-phase model, we can obtain the size of the nanoparticles following the same procedure described in ref. 19. The refined diameters are 3.6, 3.2, 2.5 nm respectively for the CdSe586, CdSe552, CdSe470. We see a decreasing particles size as the absorption peak shifts towards the blue. We will discuss the results for the smallest nanoparticles, CdSe417, below.

3.2 Ultrasmall nanoparticles

The PDF of CdSe417 suggests a different structure from the larger diameter samples. In Fig. 2(b), while it still has a sharp first peak, the second and third peaks are heavily distorted and merge into one broad peak. The significant modification of the PDF for CdSe417 is evidence of a structural modification for the smallest nanoparticles.

The modified structure is not simply a broadened and strained version of the structure of the larger nanoparticles. When fitted to the mixed-phase model, we see significantly poorer fitting quality for the CdSe417 as indicated by the larger R_w and by direct observation of the fit in Fig. 5 (top curve): the wurtzite–zinc-blende mixture model is placing intensity in the wrong positions in the PDF. In order to get even this good of an agreement many of the fitting parameters had to refine to unphysical values, such as the lattice parameter change of about 0.5 \AA^{-1} compared to CdSe470, ADPs increasing to unphysical values. The poor fitting of mixed-phase model to CdSe417 but good fitting to larger particles indicates that the structure of ultrasmall nanoparticles are different from larger nanoparticles. This was also seen in an earlier Z-STEM

measurement,²⁸ and is now confirmed in a less perturbing X-ray measurement.

3.2.1 Information beyond the structure model. The mixed-phase model cannot give good structural information for the smallest nanoparticles. However, we still can extract some structure-model independent information from the PDF. Since all nanoparticles have a sharp first peak, which comes from the nearest neighboring atomic pairs, we can extract information about internal strains from the position and shape of the first peak. The homogeneous strain in nanoparticles causes a uniform compression or extension for all bonds, *i.e.* the first peak of the PDF shifts to lower- or higher- r .¹⁹ On the other hand, inhomogeneous strain causes non-uniform bond length changes, which result in an additional peak broadening of the first PDF peak other than broadening caused by thermal vibration.

Here we fit the first PDF peak of all the nanoparticles with a Gaussian profile to obtain the peak position and peak width. The results are shown in Fig. 7 and Table 3. As the nanoparticle size decreases, we see the first peak gradually shift to lower- r , *i.e.* there is an increasing compressive homogeneous strain inside the nanoparticles. This homogeneous strain increases rapidly for the smallest nanoparticles indicating that they have a significant compressive strain. Similar behavior is seen with increases in the peak broadening with decreasing size indicating that the inhomogeneous strain, or width of the bond-length distribution in the nanoparticles, also increases.

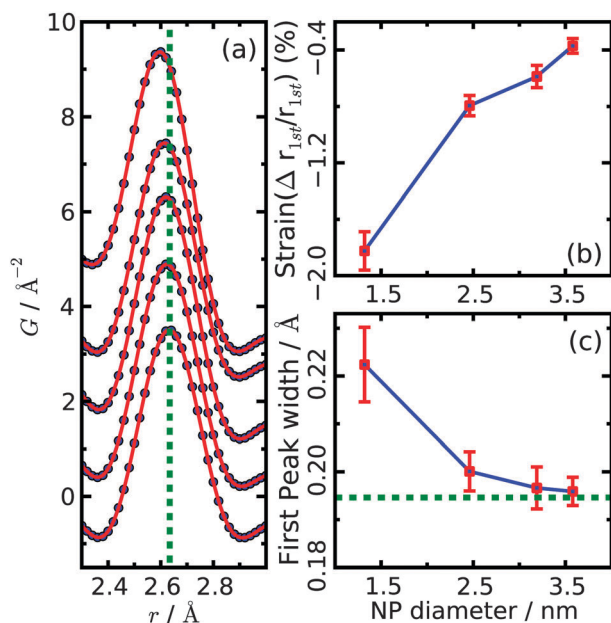


Fig. 7 (a) Fits of Gaussians to the first PDF peak. Experimental PDFs are blue dotted lines and the best fit Gaussians shown in red. From top to bottom CdSe417, CdSe470, CdSe552, CdSe586, and CdSeBulk. The green dotted line indicates the first peak position of the bulk sample for comparison. (b) Homogeneous strain, ($\Delta r_{1st}/r_{1st}$) (%), as measured from the first PDF peak coming from the Cd–Se bond vs. nanoparticle size. (c) Width of the first PDF peak vs. nanoparticle size. The green dotted line indicates the width of the peak of the bulk sample, for comparison.

Table 3 The first PDF peak position (FPP) and width (FPW) for different CdSe nanoparticles and the bulk

	PDF FPP (Å)	PDF FPW (Å)
CdSe-bulk	2.634(1)	0.194(2)
CdSe586	2.625(1)	0.196(3)
CdSe552	2.619(2)	0.197(4)
CdSe470	2.614(2)	0.200(4)
CdSe417	2.586(3)	0.222(8)

The rapid increase in inhomogeneous strain for the smallest nanoparticles is consistent with the increased structural disorder they exhibit, though since we are probing here only the first PDF peak, it indicates that the disorder is also affecting the direct Cd–Se bond lengths and is not just a disordered arrangement of higher- r motifs with fully relaxed near-neighbor bonds.

4 Conclusion

The PDF method was used to characterize the structure of a series of CdSe nanoparticles. Except for the smallest nanoparticles, the model of faulted wurtzite successfully describes the atomic structure. We describe a rapid approximate approach for extracting the stacking fault density by fitting wurtzite–zinc-blende two-phase models to the low- r region of the PDF. The resulting stacking fault density of the nanoparticles extracted from the model was around $\sim 30\%$ for larger nanoparticles. The PDF of the smallest nanoparticle (~ 1.3 nm) has a different structure altogether and cannot be fit with a disordered wurtzite model. The compressive homogeneous and inhomogeneous strain was extracted as a function of particle size. Both parameters increased significantly in the ultra-small nanoparticles, with a large homogeneous strain of 2.0% at the smallest particle size.

Acknowledgements

We would like to acknowledge help from Pavol Juhas, Mouath Shatnawi, HyunJeong Kim and Christos Malliakas for help in collecting data. The X-ray data collection and analysis were supported as part of the Center for Re-Defining Photovoltaic Efficiency Through Molecule Scale Control, an Energy Frontier Research Center funded by the U.S. Department of Energy, Office of Science, Office of Basic Energy Sciences under Award Number DE-SC0001085. Data were collected at the 6IDD beamline of the MUCAT sector at the Advanced Photon Source (APS). Use of the APS is supported by the U.S. DOE, Office of Science, Office of Basic Energy Sciences, under Contract No. W-31-109-Eng-38.

References

- 1 S. J. Rosenthal, J. McBride, S. J. Pennycook and L. C. Feldman, *Surf. Sci. Rep.*, 2007, **62**, 111–157.
- 2 S. H. Tolbert and P. A. Alivisatos, *Science*, 1994, **265**, 373.
- 3 M. Bruchez, M. Moronne, P. Gin, S. Weiss and A. P. Alivisatos, *Science*, 1998, **281**, 2013–2016.

- 4 L. S. Li and A. P. Alivisatos, *Phys. Rev. Lett.*, 2003, **90**, 097402.
- 5 V. L. Colvin, M. C. Schlamp and A. P. Alivisatos, *Nature*, 1994, **370**, 354–357.
- 6 M. J. Bowers, J. R. McBride and S. J. Rosenthal, *J. Am. Chem. Soc.*, 2005, **127**, 15378–15379.
- 7 M. J. I. Bowers, J. R. McBride, M. D. Garrett, J. A. Sammons, A. D. Dukes III, M. A. Schreuder, T. L. Watt, A. R. Lupini, S. J. Pennycook and S. J. Rosenthal, *J. Am. Chem. Soc.*, 2009, **131**, 5730.
- 8 J. R. McBride, A. D. Dukes III, M. A. Schreuder and S. J. Rosenthal, *Chin. Phys. Lett.*, 2010, **498**, 1–9.
- 9 O. E. Rayevska, G. Y. Grodzyuk, V. M. Dzhagan, O. L. Stroyuk, S. Y. Kuchmiy, V. F. Plyusnin, V. P. Grivin and M. Y. Valakh, *J. Phys. Chem. C*, 2010, **114**, 22478–22486.
- 10 T. E. Rosson, S. M. Claiborne, J. R. McBride, B. S. Stratton and S. J. Rosenthal, *J. Am. Chem. Soc.*, 2012, **134**, 8006–8009.
- 11 S. J. L. Billinge and I. Levin, *Science*, 2007, **316**, 561–565.
- 12 S. J. L. Billinge, *Physics*, 2010, **3**, 25.
- 13 T. Egami and S. J. L. Billinge, *Underneath the Bragg peaks: structural analysis of complex materials*, Elsevier, Amsterdam, 2nd edn, 2012.
- 14 S. J. L. Billinge and M. G. Kanatzidis, *Chem. Commun.*, 2004, 749–760.
- 15 P. J. Chupas, X. Qiu, J. C. Hanson, P. L. Lee, C. P. Grey and S. J. L. Billinge, *J. Appl. Crystallogr.*, 2003, **36**, 1342–1347.
- 16 C. L. Farrow, P. Juhás, J. Liu, D. Bryndin, E. S. Božin, J. Bloch, T. Proffen and S. J. L. Billinge, *J. Phys.: Condens. Matter*, 2007, **19**, 335219.
- 17 R. B. Neder and T. Proffen, *Diffuse Scattering and Defect Structure Simulations: A cook book using the program DISCUS*, Oxford University Press, Oxford, 2008.
- 18 P. Juhás, D. M. Cherba, P. M. Duxbury, W. F. Punch and S. J. L. Billinge, *Nature*, 2006, **440**, 655–658.
- 19 A. S. Masadeh, E. S. Božin, C. L. Farrow, G. Paglia, P. Juhás, A. Karkamkar, M. G. Kanatzidis and S. J. L. Billinge, *Phys. Rev. B: Condens. Matter Mater. Phys.*, 2007, **76**, 115413.
- 20 R. B. Neder and V. I. Korsunskiy, *J. Phys.: Condens. Matter*, 2005, **17**, S125–S134.
- 21 V. Petkov, Y. Peng, G. Williams, B. Huang, D. Tomalia and Y. Ren, *Phys. Rev. B: Condens. Matter Mater. Phys.*, 2005, **72**, 195402.
- 22 M. J. Cliffe, M. T. Dove, D. A. Drabold and A. L. Goodwin, *Phys. Rev. Lett.*, 2010, **104**, 125501.
- 23 M. G. Bawendi, A. R. Kortan, M. L. Steigerwald and L. E. Brus, *J. Chem. Phys.*, 1989, **91**, 7282–7290.
- 24 C. B. Murray, D. J. Norris and M. G. Bawendi, *J. Am. Chem. Soc.*, 1993, **115**, 8706–8715.
- 25 R. B. Neder, V. I. Korsunskiy, C. Chory, G. Müller, A. Hofmann, S. Dembski, C. Graf and E. Rühl, *Phys. Status Solidi C*, 2007, **4**, 1610–1634.
- 26 C. Kumpf, R. B. Neder, F. Niederdraenk, P. Luczak, A. Stahl, M. Scheuermann, S. Joshi, S. K. Kulkarni, C. Barglik-Chory, C. Heske and E. Umbach, *J. Chem. Phys.*, 2005, **123**, 224707.
- 27 J. Jasieniak, C. Bullen, J. van Embden and P. Mulvaney, *J. Phys. Chem. B*, 2005, **109**, 20665–20668.
- 28 T. J. Pennycook, J. R. McBride, S. J. Rosenthal, S. J. Pennycook and S. T. Pantelides, *Nano Lett.*, 2012, **12**, 3038–3042.
- 29 W. W. Yu, L. Q. W. Guo and X. Peng, *Chem. Mater.*, 2010, **15**, 2854–2860.
- 30 A. P. Hammersley, S. O. Svenson, M. Hanfland and D. Hauserman, *High Pressure Res.*, 1996, **14**, 235–248.
- 31 B. E. Warren, *X-ray Diffraction*, Dover, New York, 1990.
- 32 C. L. Farrow and S. J. L. Billinge, *Acta Crystallogr., Sect. A: Fundam. Crystallogr.*, 2009, **65**, 232–239.
- 33 P. Juhas, T. Davis, C. L. Farrow and S. J. L. Billinge, *ArXiv e-prints*, 2012.
- 34 C. L. Farrow, P. Juhás and S. J. L. Billinge, unpublished.
- 35 I. Kikuma and M. Furukoshi, *J. Cryst. Growth*, 1985, **71**, 136–140.
- 36 V. I. Korsunskiy, R. B. Neder, A. Hofmann, S. Dembski, C. Graf and E. Rühl, *J. Appl. Crystallogr.*, 2007, **40**, 975–985.

PAPER

Physical properties of $K_xNi_{2-y}Se_2$ single crystals

To cite this article: Hechang Lei *et al* 2014 *J. Phys.: Condens. Matter* **26** 015701

View the [article online](#) for updates and enhancements.

You may also like

- [Photoelectric Properties of Pulse Electrodeposited \$CdIn_2Se_4\$ Films](#)
Kollegal Ramakrishna Murali
- [Pyridine intercalated \$Bi_2Se_3\$ heterostructures: controlling the topologically protected states](#)
I S S de Oliveira and R H Miwa
- [Effect of substrate temperature on the optical, structural and morphological properties of \$In_2Se_3\$ thin films grown by a two-step process](#)
Clavijo J, Romero E and Gordillo G

Physical properties of $K_xNi_{2-y}Se_2$ single crystals

Hechang Lei^{1,5}, Milinda Abeykoon¹, Kefeng Wang¹, Emil S Bozin¹,
Hyejin Ryu^{1,2}, D Graf³, J B Warren⁴ and C Petrovic^{1,2}

¹ Condensed Matter Physics and Materials Science Department, Brookhaven National Laboratory, Upton, NY 11973, USA

² Department of Physics and Astronomy, State University of New York, Stony Brook, NY 11794-3800, USA

³ NHMFL/Physics, Florida State University, Tallahassee, FL 32310, USA

⁴ Instrumentation Division, Brookhaven National Laboratory, Upton, NY 11973, USA

E-mail: petrovic@bnl.gov

Received 19 September 2013, in final form 29 October 2013

Published 29 November 2013

Abstract

We have synthesized $K_{0.95(1)}Ni_{1.86(2)}Se_2$ single crystals. The single crystals contain K and Ni deficiencies not observed in KNi_2Se_2 polycrystals. Unlike KNi_2Se_2 polycrystals, the superconductivity is absent in single crystals. The detailed physical property study indicates that the $K_{0.95}Ni_{1.86}Se_2$ single crystals exhibit heavy-fermion-like characteristics. The transition to a heavy fermion state below $T \sim 30$ K results in an enhancement of the electron-like carrier density whereas the magnetic susceptibility shows little anisotropy and suggests the presence of both itinerant and localized Ni orbitals.

(Some figures may appear in colour only in the online journal)

1. Introduction

Even before the discovery of the superconducting $T_c = 26$ K in $LaFeAsO_{1-x}F_x$ [1], some nickel pnictide materials (such as $LaONiP$) [2] had already been found to become superconducting (SC) at low temperatures. Examples of nickel pnictide superconductors also include $LaONiAs$, $LaO_{1-x}NiBi$, $BaNi_2P_2$ and $SrNi_2P_2$ [3–6]. However, all nickel pnictide SCs have much lower T_c (<5 K) when compared to iron pnictide SCs, of which the T_c values are mostly well above 5 K [7]. The possible reason leading to this difference could be due to different superconducting mechanisms or to different values of material parameters relevant for superconductivity which are not optimized for the nickel pnictides even if the pairing mechanism were to be identical [7].

On the other hand, iron chalcogenide SCs have also been discovered, including $FeCh$ ($Ch = S, Se, Te$) [8–10], and $A_xFe_{2-y}Se_2$ ($A = K, Rb, Cs, Tl/K$ and Tl/Rb) [11–16]. In contrast to iron chalcogenide SCs, however, corresponding

nickel chalcogenide SCs were still missing until recently. $NiSe$ has a $NiAs$ -type structure with space group $P63/mmc$ and this structure is isostructural to hexagonal $FeSe$ (high-temperature phase). $NiSe$ is a non-superconducting metal with ferromagnetic fluctuations [17]. Similarly, $TlNi_2Se_2$ is a Pauli paramagnet without a superconducting transition down to 2 K [18]. However, very recently, it was reported that KNi_2Se_2 polycrystals are superconducting with $T_c = 0.80(1)$ K [19]. Moreover, KNi_2Se_2 single crystals feature a heavy-fermion-like state with an increased carrier mobility and enhanced effective electronic band mass below about 40 K. This state should emerge from the proposed local charge density wave (CDW) state, which persists up to 300 K [19].

A study of single crystals is necessary in order to elucidate the anisotropy in intrinsic physical properties of KNi_2Se_2 and eliminate the influence of grain boundaries and ferromagnetic Ni impurities. Hence, in this work we report the physical properties of $K_{0.95(1)}Ni_{1.86(2)}Se_{2.00(1)}$ single crystals. Unexpectedly, we found no evidence for a superconducting transition down to 0.3 K in resistivity measurements. Magnetic, Hall, thermodynamic and thermal measurements suggest that the heavy-fermion-like properties of $K_xNi_{2-y}Se_2$ arise from dominant electron-like carriers. The

⁵ Present address: Frontier Research Center, Tokyo Institute of Technology, 4259 Nagatsuta, Midori, Yokohama 226-8503, Japan.

Table 1. Structural parameters for $\text{K}_{0.948}\text{Ni}_{1.86}\text{Se}_2$ at room temperature.

Chemical formula	$\text{K}_{0.95(1)}\text{Ni}_{1.86(2)}\text{Se}_{2.00(1)}$			
Space group	$I4/mmm$			
a (Å)	3.8707(5)			
c (Å)	13.591(4)			
V (Å ³)	203.62(7)			
Atom	x	y	z	U_{iso} (Å ²)
K	0	0	0	0.062(5)
Ni	0	0.5	0.25	0.0206(18)
Se	0	0	0.352 38(28)	0.0177(13)

onset of the heavy-fermion-like state below 30 K coincides with the increased electron-like carrier concentration below $T \sim 30$ K.

2. Experiment

Single crystals of KNi_2Se_2 were grown by a self-flux method similar to $\text{K}_x\text{Fe}_{2-y}\text{Se}_2$ [20] with a nominal composition K:Ni:Se = 1:2:2. Briefly, pre-reacted NiSe and K pieces were added into an alumina crucible with a partial pressure of argon gas. The quartz tubes were heated to 1030 °C, kept at this temperature for 3 h, then cooled to 730 °C at a rate of 6 °C h⁻¹. Platelike dark pink colored single crystals with typical size $5 \times 5 \times 2$ mm³ can be grown. A high-energy synchrotron x-ray experiment at 300 K was conducted on X7B beamline of the National Synchrotron Light Source (NSLS) at Brookhaven National Laboratory (BNL). The setup utilized an x-ray beam 0.5 mm \times 0.5 mm in size with a wavelength of 0.3196 Å ($E = 38.7936$ keV) configured with a focusing double-crystal bent Laue monochromator and a PerkinElmer amorphous silicon image plate detector mounted perpendicular to the primary beam path. A finely pulverized sample packed in a cylindrical polyimide capillary 1 mm in diameter was placed 377.81 mm away from the detector. Multiple scans were performed to a total exposure time of 240 s. The 2D diffraction data were integrated and converted to intensity versus 2θ using the software FIT2D [21]. Structural refinements were carried out using the GSAS modeling program [22] operated by the EXPGUI platform [23]. The elemental analysis was performed using energy-dispersive x-ray spectroscopy (EDX) in a JEOL JSM-6500 scanning electron microscope. Electrical and thermal transport, heat capacity, and magnetization measurements were carried out in Quantum Design PPMS-9 and MPMS-XL5. The in-plane resistivity $\rho_{ab}(T)$ was measured using a four-probe configuration on cleaved rectangularly shaped single crystals with the current flowing in the ab -plane of tetragonal structure. Thin Pt wires were attached to electrical contacts made of silver paste. Thermal transport properties were measured in a Quantum Design PPMS-9 from 2 to 350 K using the one-heater two-thermometer method. The relative error was $\frac{\Delta\kappa}{\kappa} \sim 5\%$ and $\frac{\Delta S}{S} \sim 5\%$, based on a Ni standard measured under identical conditions.

3. Results and discussion

Refinement of the synchrotron x-ray diffraction data of KNi_2Se_2 reveals that the sample is constituted of 97% by weight of KNi_2Se_2 (space group $I4/mmm$) and 3% by weight of SeO_2 impurity (space group $P42/mbc$). The SeO_2 impurity phase arises due to sample preparation. Most likely, the oxidation process of KNi_2Se_2 is similar to β -FeSe [24]. The fit is shown in figure 1(a) and the refinement results are summarized in table 1. The determined lattice parameters are $a = 3.8707(5)$ Å and $c = 13.591(4)$ Å. The value for the a axis is somewhat smaller whereas the c axis lattice parameter is larger when compared to polycrystalline samples with full occupancies of K and Ni ($a = 3.9098(8)$ Å and $c = 13.4142(5)$ Å [25]). This is in agreement with a previous study which indicated that the deviation from full occupancy can increase the c lattice parameter with only a minor effect on the a lattice parameter [25]. On the other hand, both the a and c lattice parameters are smaller than those in $\text{K}_x\text{Fe}_{2-y}\text{Se}_2$ ($a = 3.9109$ Å and $c = 14.075$ Å [20]). It could be due to the smaller ionic radius of Ni^{2+} (0.55 Å) than Fe^{2+} (0.63 Å) with four-fold coordination [26]. The antiferromagnetic state in $\text{K}_x\text{Fe}_{2-y}\text{Se}_2$ can increase the lattice parameters further when compared to the non-magnetic state according to the theoretical calculation [27]. The crystal structure of KNi_2Se_2 is shown in figure 1(b), where antifluorite-type Ni–Se layers and K cation layers are piled up alternately along the c axis. XRD pattern of a single crystal (figure 1(c)) reveals that the crystal surface is normal to the c axis with the plate-shaped surface parallel to the ab -plane. Figure 1(d) shows the EDX spectrum of a single crystal of KNi_2Se_2 , confirming the presence of the K, Ni, and Se. The EDX results for several single crystals with multiple measuring points indicate that the crystals are rather homogeneous and the determined average atomic ratios are K:Ni:Se = 0.95(1):1.86(2):2.00(1) when fixing the Se stoichiometry to be 2. Although the number of deficiencies is smaller when compared to $\text{K}_x\text{Fe}_{2-y}\text{Se}_2$ crystals [20], it is noticeably higher when compared to KNi_2Se_2 polycrystals which feature full occupancies of K, Ni and Se atomic sites [25]. The vacancies of K and Fe should be randomly distributed, otherwise the symmetry of the structure (space group: $I4/mmm$) should be lower. This is the case for $\text{K}_x\text{Fe}_{2-y}\text{Se}_2$, where the space group changes from $I4/mmm$ to $I4/m$ [20]. On the other hand, the deficiencies should have minor effect on the heavy fermion behavior, as

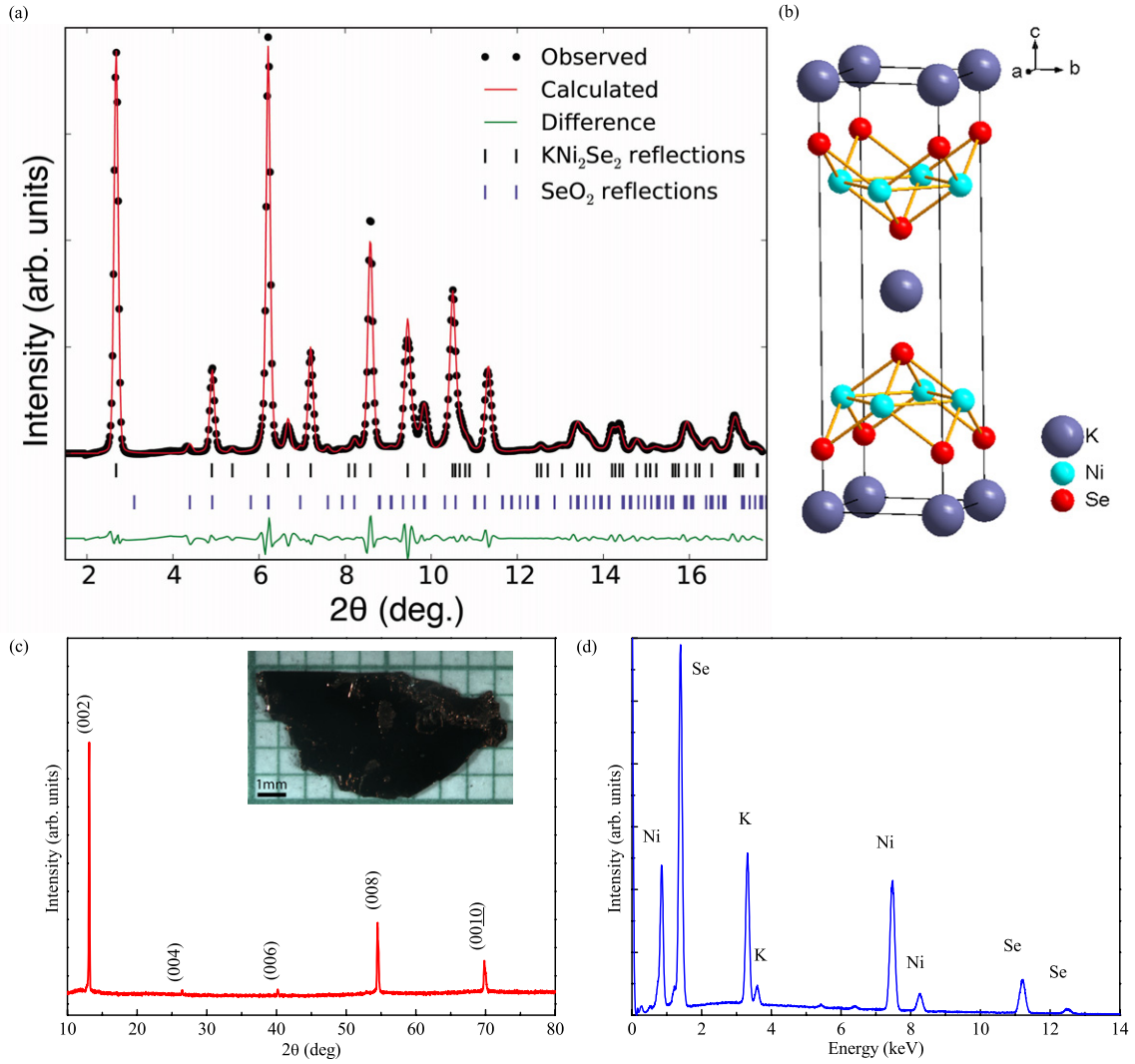


Figure 1. (a) Refinement of synchrotron x-ray diffraction data of $\text{K}_{0.95}\text{Ni}_{1.86}\text{Se}_2$: data (solid symbols), structural model (red solid line), difference curve (green solid line, offset for clarity). Vertical tickmarks denote reflections in the main phase (black, top row) and the secondary SeO_2 phase (blue, bottom row). (b) Crystal structure of KNi_2Se_2 . The large purple, medium cyan and small red balls represent K, Ni and Se ions. (c) Single crystal XRD of $\text{K}_{0.948}\text{Ni}_{1.86}\text{Se}_2$. The inset shows a photo of a typical single crystal of KNi_2Se_2 . (d) The EDX spectrum of a single crystal.

shown below, because this behavior is still observed in the polycrystal sample without significant deficiencies. However, the deficiencies might have a significant influence on the superconductivity which appears in the polycrystal sample.

The temperature dependence of the in-plane resistivity $\rho_{ab}(T)$ of the $\text{K}_{0.95}\text{Ni}_{1.86}\text{Se}_2$ single crystal exhibits metallic behavior with the residual resistivity ratio (RRR) $\rho_{ab}(295\text{ K})/\rho_{ab}(0.3\text{ K}) = 5$. The room-temperature value $\rho_{ab}(295\text{ K})$ ($256\ \mu\Omega\text{ cm}$) is slightly smaller than the value in polycrystals ($350\ \mu\Omega\text{ cm}$). However, the RRR value is much smaller than that in polycrystals (RRR ~ 175). Larger residual resistivity ρ_0 in crystals could come from the increased impurity scattering due to the deficiencies. The most striking feature is the absence of a superconducting transition down to 0.3 K in $\text{K}_{0.948}\text{Ni}_{1.86}\text{Se}_2$ single crystals when compared to KNi_2Se_2 polycrystals with $T_c = 0.80(1)\text{ K}$ [19]. The absence of superconductivity in single crystals could be related to the deficiencies of K and Ni, implying that the superconductivity

in KNi_2Se_2 is very sensitive to the atomic ratio. There is no metal-insulating transition (MIT) in KNi_2Se_2 and the absolute values of resistivity are much smaller when compared to $\text{K}_x\text{Fe}_{2-y}\text{Se}_2$ [20], indicating that Ni orbitals in the former material are more itinerant when compared to Fe orbitals in the latter material. Surprisingly, as shown in the inset of figure 2(b), the $\rho_{ab}(T) \sim T^2$ dependence is observed up to 20 K at temperatures where other types of scattering (e.g. electron-phonon) are usually active or dominant. From the fit using $\rho_{ab}(T) = \rho_0 + AT^n$, we obtain the residual resistivity $\rho_0 = 50.282(2)\ \mu\Omega\text{ cm}$, the coefficient of the quadratic resistivity term $A = 0.0079(5)\ \mu\Omega\text{ cm K}^{-2}$, and $n = 1.96(2)$.

Figure 3 presents the temperature dependence of magnetic susceptibility $\chi(T)$ of the $\text{K}_{0.95}\text{Ni}_{1.86}\text{Se}_2$ single crystal for $H = 1\text{ kOe}$ along the ab plane and c axis below 300 K. It can be seen that the $\chi_c(T)$ is larger than the $\chi_{ab}(T)$ at high temperature. The susceptibility can be fitted

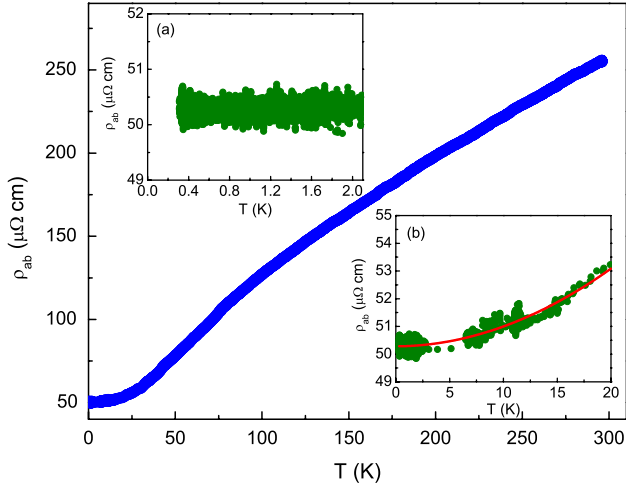


Figure 2. Temperature dependence of the in-plane resistivity $\rho_{ab}(T)$ of the $\text{K}_{0.95}\text{Ni}_{1.86}\text{Se}_2$ single crystal from 0.3 to 295 K. The inset (a) shows the enlarged part of $\rho_{ab}(T)$ below 2 K. The inset (b) shows the fitted result from 0.3 to 20 K using $\rho_{ab}(T) = \rho_0 + AT^n$, where the red line is the fitting curve.

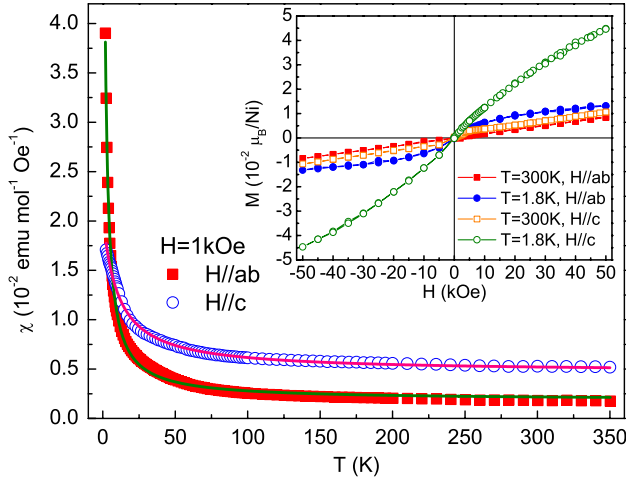


Figure 3. (a) Temperature dependence of magnetic susceptibility $\chi(T)$ with the applied field $H = 1$ kOe along the ab plane and the c axis below 300 K. The inset shows the isothermal magnetization hysteresis loops $M(H)$ for $H \parallel ab$ and $H \parallel c$ at 300 and 1.8 K.

using the Curie–Weiss law $\chi(T) = \chi_0 + C/(T - \theta)$ when a temperature-independent contribution χ_0 is accounted for. Here, χ_0 includes core diamagnetism, Landau diamagnetism, and Pauli paramagnetism, C is the Curie constant and θ is the Curie–Weiss temperature (solid lines in figure 3). The fitted values for χ_0 are $1.87(5) \times 10^{-3}$ and $4.69(4) \times 10^{-3}$ emu mol f.u. $^{-1}$ Oe $^{-1}$ for $H \parallel ab$ and $H \parallel c$, which are much larger than the value in the literature [25]. Because the core diamagnetism is typically on the order of 10^{-6} – 10^{-5} emu mol $^{-1}$ Oe $^{-1}$ [28], and $\chi_{\text{Landau}} \approx -1/3\chi_{\text{Pauli}}$, such large χ_0 values strongly imply there is an enhanced Pauli paramagnetism, i.e. the significant pileup of the density of states at the Fermi level due to $\chi_{\text{Pauli}} \approx \mu_B^2 N(E_F)$. On the other hand, the obtained local moment is about $0.463(3)$ and $0.615(7)$ μ_B/Ni for $H \parallel ab$ and $H \parallel c$. This is unlikely

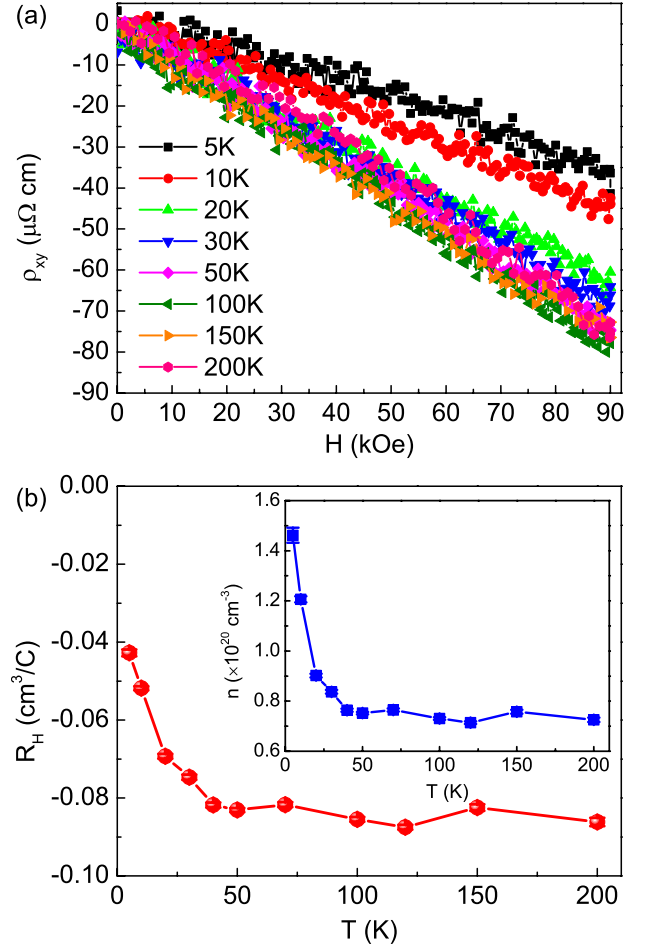


Figure 4. (a) Field dependence of $\rho_{xy}(H)$ at various temperatures. (b) Temperature dependence of the Hall coefficient R_H of $\text{K}_{0.95}\text{Ni}_{1.86}\text{Se}_2$ single crystal. Inset: temperature dependence of the carrier density $n = 1/|eR_H|$ calculated from R_H based on the single-band model.

to be due to impurities such as Ni^{2+} with $S = 1$ because the corresponding molar fraction would be 16.4(1) and 29.7(3) mol% for $H \parallel ab$ and $H \parallel c$, respectively. Such a large amount of impurities should have been detected in the XRD pattern, hence the origin of low-temperature susceptibility rise should be intrinsic. The contribution of impurity is revealed (figure 3 (inset)) in the magnetization loops for both field directions at 300 and 1.8 K. There is a ferromagnetic component superposed on the paramagnetic background with a very small magnetic moment ($\sim 10^{-2}$ μ_B/Ni). After subtracting the paramagnetic part from the curve for $H \parallel ab$ at 1.8 K, the saturated moment would correspond to ~ 0.2 mol% Ni^{2+} or ~ 1 mol% Ni impurities. The above analysis indicates that Ni orbitals in NiSe_4 tetrahedra are at the boundary of itinerancy and Mott localization with a possible orbital dependent correlation strength, similarly to iron orbitals in iron based superconductors [29].

As shown in figure 4(a), the transverse resistivity $\rho_{xy}(H)$ shows an approximately linear relation against the magnetic field and is negative at all measuring temperatures, indicating that the electron-type carrier is dominant. From the linear fitting of $\rho_{xy}(H) - H$ relation, we obtain the Hall

coefficients $R_H = \rho_{xy}(H)/H$ at different temperatures, which is shown in figure 4(b). It can be seen that R_H is weakly temperature dependent when $T > 30$ K and then decreases with temperature. In a single-band scenario, this change suggests that the carrier density increases at about $T = 30$ K, since $R_H = 1/ne$ (Inset of figure 4(b)). This temperature is close to the observed crossover from the proposed local CDW state to the heavy fermion state in stoichiometric KNi_2Se_2 polycrystals [19]. On the other hand, the change can also be ascribed to the multiband effect, which has been observed in classic two-band materials such as MgB_2 as well as in iron based material $\text{Nd}(\text{O}, \text{F})\text{FeAs}$ [30, 31]. A multiband electronic structure at the Fermi level is also supported by the density function calculations [32]. However, the observed temperature dependence is much weaker than that in $\text{Nd}(\text{O}, \text{F})\text{FeAs}$ single crystal, which exhibits significant multiband behavior. It implies the multiband behavior should be weaker in KNi_2Se_2 when compared to iron based superconductors. From the obtained R_H , the corresponding carrier density at 300 K is $\sim 4 \times 10^{-3}$ carrier per Ni, increasing up to $\sim 8 \times 10^{-3}$ carrier per Ni. The carrier density is very low, even one order lower than in iron based superconductors, such as $\text{LaFeAsO}_{0.89}\text{F}_{0.11}$ ($\sim 10^{21} \text{ cm}^{-3}$) [33]. Moreover, from the measured resistivity at 5 K ($\rho_{ab}(5 \text{ K}) = 4.74 \times 10^{-5} \Omega \text{ cm}$) and the derived carrier density at same temperature ($n(5 \text{ K}) = 1.46 \times 10^{20} \text{ cm}^{-3}$), the carrier mobility at 5 K can be roughly estimated using $\sigma = ne\mu$ and is about $905 \text{ cm}^2 \text{ V}^{-1} \text{ S}^{-1}$. It is close to the result derived from magnetoresistance measurements of polycrystals ($1070 \text{ cm}^2 \text{ V}^{-1} \text{ S}^{-1}$), implying that KNi_2Se_2 has a high carrier mobility. On the other hand, as discussed below, the electron specific heat is large at low temperature, indicating the increased effective mass. Because μ is proportional to the mean scattering time and inversely proportional to the effective mass, the mean scattering time could be rather large at low temperatures [19].

Figure 5 shows the temperature dependence of thermoelectric power (TEP) $S(T)$ for $\text{K}_{0.95}\text{Ni}_{1.86}\text{Se}_2$ single crystals measured between $T = 2$ and 350 K. At high temperature, the $S(T)$ is negative, consistent with dominant negative charge carriers. It is interesting that the value of the $S(T)$ decreases with decreasing temperature and then becomes positive at about $T_1 = 64$ K. The sign change implies multiband transport. Even though the Hall coefficient R_H is unchanged in that temperature range, the sign of $S(T)$ might change since they have a different dependence on carrier density n_e (n_h), mobility μ_e (μ_h), and S_e (S_h) in the two-band model ($R_H = \frac{1}{e} \frac{n_h\mu_h^2 - n_e\mu_e^2}{(n_h\mu_h + n_e\mu_e)^2}$, $S = \frac{S_en_e\mu_e + S_hn_h\mu_h}{n_e\mu_e + n_h\mu_h}$) [34]. With further decreasing temperature, $S(T)$ shows a peak at around $T_m = 27$ K and then decreases with temperature. Finally it becomes negative again and the temperature corresponding to the second sign reverse is about $T_2 = 12$ K. The temperature of T_m is very close to the temperature where the change of slope in R_H appears. As we discuss below, the second sign change of $S(T)$ could be related to the heavy fermion state, where the Fermi surface becomes large with increasing carrier density in electron-type bands.

Figure 6(a) shows the relation between C_p/T and T^2 for $\text{K}_{0.95}\text{Ni}_{1.86}\text{Se}_2$ single crystal at low temperature. It

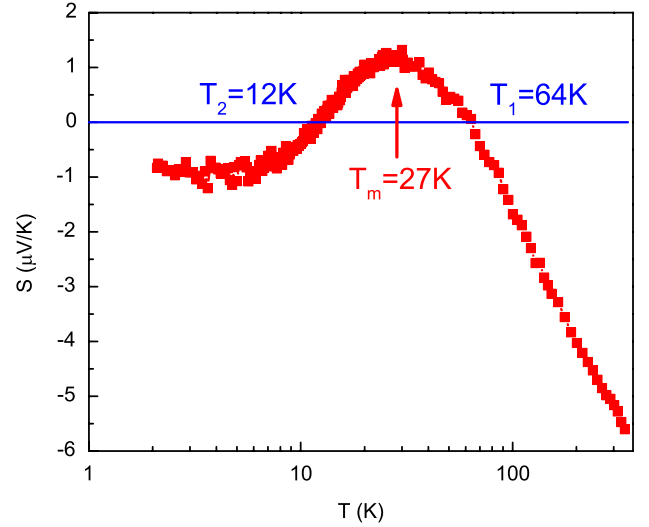


Figure 5. Temperature dependence of thermoelectric power $S(T)$ for $\text{K}_{0.95}\text{Ni}_{1.86}\text{Se}_2$ single crystal from 2 to 350 K.

can be seen that there is an upturn in the specific heat as $T < 3$ K. This upturn could not be related to the superconducting transition or to a nuclear Schottky anomaly since it appears at much higher temperatures. This might be an intrinsic effect related to magnetic fluctuations due to the deficiencies of K and Ni. Similar behavior has been observed in $\text{Ca}(\text{Fe}_{0.1}\text{Co}_{0.9})_2\text{P}_2$ and $\text{Ca}(\text{Fe}_{1-x}\text{Ni}_x)_2\text{P}_2$ ($x = 0.5$ and 0.6) [35]. In order to obtain the electronic specific heat and Debye temperature, we fit the $C_p/T - T^2$ curve between 5 and 10 K by using the formula $C_p/T = \gamma + \beta_3 T^2 + \beta_5 T^4$. We obtain $\gamma = 48(2) \text{ mJ mol}^{-1} \text{ K}^{-2}$, $\beta_3 = 1.06(8) \text{ mJ mol}^{-1} \text{ K}^{-4}$, and $\beta_5 = 5.4(6) \mu\text{J mol}^{-1} \text{ K}^{-6}$. The Debye temperature is estimated to be $\Theta_D = 209(5) \text{ K}$ using the formula $\Theta_D = (12\pi^4 NR/5\beta)^{1/3}$, where N is the atomic number in the chemical formula ($N = 5$) and R is the gas constant ($R = 8.314 \text{ J mol}^{-1} \text{ K}^{-1}$). The Debye temperature Θ_D and electronic specific heat γ are close to the results obtained on the KNi_2Se_2 polycrystals [19]. The large γ implies the mass enhancement at low temperatures and heavy-fermion-like behavior [19]. Moreover, the Θ_D is also similar to that of $\text{K}_x\text{Fe}_{2-y}\text{Se}_2$ ($\sim 212 \text{ K}$) [36], which could be ascribed to the similar structure and atomic weight.

As shown in figure 6(b), at high temperature the heat capacity approaches the Dulong–Petit value of $3NR$ ($124.71 \text{ J mol}^{-1} \text{ K}^{-1}$), implying that the electronic specific heat at high temperature is not enhanced when compared to that at low temperature. In order to evaluate the temperature evolution of the electronic specific heat, the $C_p(T)$ curve is fitted using double-Debye model in different ranges from T ($5 \text{ K} < T < 52 \text{ K}$) to 300 K, similar to the discussion for the KNi_2Se_2 polycrystalline sample [19]. For the double-Debye model, the total specific heat can be expressed by [19]:

$$C_p(T) = \gamma T + 9R(N - s) \left(\frac{T}{\Theta_{D1}} \right)^3 \int_0^{\Theta_{D1}/T} \frac{x^4 e^x}{(e^x - 1)^2} dx + 9Rs \left(\frac{T}{\Theta_{D2}} \right)^3 \int_0^{\Theta_{D2}/T} \frac{x^4 e^x}{(e^x - 1)^2} dx \quad (1)$$

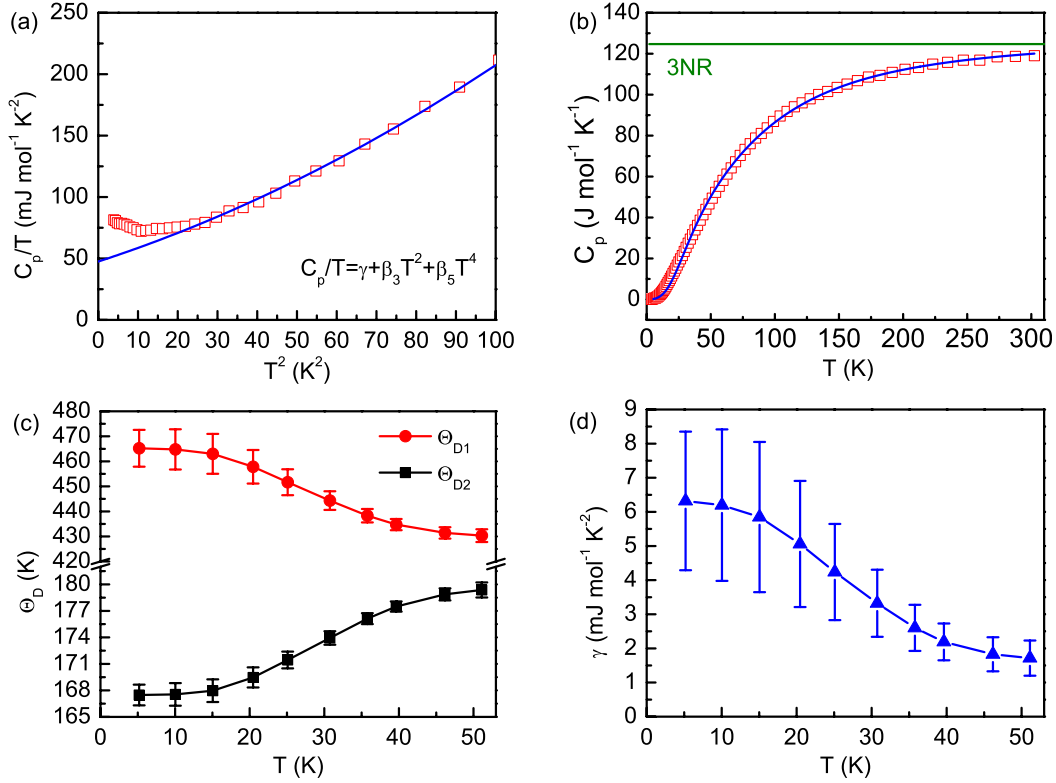


Figure 6. (a) The relation between C_p/T and T^2 for $\text{K}_{0.948}\text{Ni}_{1.86}\text{Se}_2$ single crystal at low temperature. The solid curve represents the fitting result using the formula $C_p/T = \gamma + \beta_3 T^2 + \beta_5 T^4$. (b) The temperature dependence of $C_p(T)$ for the entire measured temperature range. The green solid line represents the classical value according to the Dulong–Petit law at high temperature and the blue line shows the fitting result by using the double-Debye model between 5 and 300 K. (c) The fitted Debye temperatures Θ_{Di} and (d) γ using the double-Debye model at various temperature ranges between T and 300 K.

where Θ_{Di} is the Debye temperature for each sublattice and s the number of oscillators in one sublattice. We set $s = 2$, the same as that for the polycrystalline sample. The $C_p(T)$ curve can be fitted well by using this model (figure 6(b)) and the obtained Θ_{Di} and γ are shown in figures 6(c) and (d), respectively. It can be seen that Θ_{D1} increases with decreasing T and Θ_{D2} has the inverse trend, consistent with the result for the polycrystalline sample. On the other hand, the γ values are much smaller than that obtained from the low-temperature fit. Moreover, the γ is about $2.5 \text{ mJ mol}^{-1} \text{K}^{-2}$ when $T > 35 \text{ K}$ and increases monotonically up to about $6.3 \text{ mJ mol}^{-1} \text{K}^{-2}$ for $T = 5 \text{ K}$. The crossover temperature is close to 35 K. The above results imply that the effect of electronic mass enhancement is very weak at high temperature, while it gains strength when cooling below about 30–40 K. Temperature-dependent mass enhancement is consistent with the results for polycrystals [19].

The phonon drag contribution to $S(T)$ gives an $\sim T^3$ dependence for $T \ll \Theta_D$, $\sim 1/T$ for $T \geq \Theta_D$ (where Θ_D is the Debye temperature) and a peak structure for $\Theta_D/5$ [37, 38]. The estimated Debye temperature of our crystals is about 210 K. Since $S(T)$ (figure 5) is nearly constant for $T \ll \Theta_D$, is linear for $T \geq \Theta_D$, and shows no peak structure at $\Theta_D/5 = 42 \text{ K}$, it is unlikely that the sign change in thermoelectric power is related to the phonon drag effect.

From the obtained A and γ , the Kadowaki–Woods (KW) ratio $A/\gamma^2 = 3.43(6) \times 10^{-6} \mu\Omega \text{ cm mol}^2 \text{K}^2 \text{mJ}^{-2}$. This

is somewhat smaller than the value for KNi_2Se_2 polycrystals ($1.2 \times 10^{-5} \mu\Omega \text{ cm mol}^2 \text{K}^2 \text{mJ}^{-2}$) [19], and from the universal value observed in strongly correlated heavy fermion systems ($1 \times 10^{-5} \mu\Omega \text{ cm mol}^2 \text{K}^2 \text{mJ}^{-2}$) [39]. However, it is still larger than that in many intermediate valence Yb-based and several Ce-based compounds with large γ ($A/\gamma^2 \sim 0.4 \times 10^{-6} \mu\Omega \text{ cm mol}^2 \text{K}^2 \text{mJ}^{-2}$) [39]. On the other hand, from the fitted temperature-independent susceptibility χ_0 ($1.87(5) \times 10^{-3}$ and $4.69(4) \times 10^{-3} \text{ emu mol f.u.}^{-1} \text{Oe}^{-1}$ for $H \parallel ab$ and $H \parallel c$) and the relation of $\chi_{\text{Landau}} \approx -1/3 \chi_{\text{Pauli}}$ when ignoring the core and orbital diamagnetism, $\chi_{\text{Pauli}} \approx 2.81 \times 10^{-3}$ and $7.04 \times 10^{-3} \text{ emu mol f.u.}^{-1} \text{Oe}^{-1}$ for $H \parallel ab$ and $H \parallel c$. The estimate of the Wilson’s ratio ($R_W = \frac{\pi^2 k_B^2}{3\mu_B^2} \frac{\chi_{\text{Pauli}}}{\gamma}$) gives large values $R_W = 4.26$ and 10.68 for $H \parallel ab$ and $H \parallel c$. This value is also larger than that derived from polycrystalline ($R_W = 1.7$) [19]. Such large values have been usually found in the heavy Fermi liquids ($R_W = 1-6$) [40]. However, large R_W values also occur in systems with a magnetic instability or a strong exchange enhanced paramagnetic state [41].

4. Conclusion

In summary, we synthesized $\text{K}_{0.95}\text{Ni}_{1.86}\text{Se}_2$ single crystals using the self-flux method. Different from polycrystals, there are small K and Ni deficiencies, similar to the iron based counterpart $\text{K}_x\text{Fe}_{2-y}\text{Se}_2$. Resistivity measurements indicate

that the $K_{0.95}Ni_{1.86}Se_2$ single crystal does not exhibit a superconducting transition down to 0.3 K, in contrast to polycrystals. Therefore, the superconducting state is rather sensitive to K and Ni stoichiometry, similar to KFe_2Se_2 . Our results suggest a transition to a heavy fermion state at low temperature.

Acknowledgments

Work at Brookhaven is supported by the US DOE under Contract No. DE-AC02-98CH10886. This work has benefited from using the X7B beamline of the National Synchrotron Light Source at Brookhaven National Laboratory (MA and EB). Work at the National High Magnetic Field Laboratory is supported by the DOE NNSA DEFG52-10NA29659 (DG), by the NSF Cooperative Agreement No. DMR-0654118, and by the State of Florida.

References

- [1] Kamihara Y, Watanabe T, Hirano M and Hosono H 2008 *J. Am. Chem. Soc.* **130** 3296
- [2] Watanabe T, Yanagi H, Kamiya T, Kamihara Y, Hiramatsu H, Hirano M and Hosono H 2007 *Inorg. Chem.* **46** 7719
- [3] Watanabe T, Yanagi H, Kamihara Y, Kamiya T, Hirano M and Hosono H 2008 *J. Solid State Chem.* **181** 2117
- [4] Kozhevnikov V L, Leonidova O N, Ivanovskii A L, Shein I R, Goshchitskii B N and Karkin A E 2008 *JETP Lett.* **87** 649
- [5] Mine T, Yanagi H, Kamiya T, Kamihara Y, Hirano M and Hosono H 2008 *Solid State Commun.* **147** 111
- [6] Ronning F, Bauer E D, Park T, Baek S-H, Sakai H and Thompson J D 2009 *Phys. Rev. B* **79** 134507
- [7] Ronning F, Bauer E D, Park T, Kurita N, Klimczuk T, Movshovich R, Sefat A S, Mandrus D and Thompson J D 2009 *Physica C* **469** 396
- [8] Hsu F C et al 2008 *Proc. Natl Acad. Sci. USA* **105** 14262
- [9] Yeh K-W et al 2008 *Europhys. Lett.* **84** 37002
- [10] Mizuguchi Y, Tomioka F, Tsuda S, Yamaguchi T and Takano Y 2009 *Appl. Phys. Lett.* **94** 012503
- [11] Guo J, Jin S, Wang G, Wang S, Zhu K, Zhou T, He M and Chen X 2010 *Phys. Rev. B* **82** 180520
- [12] Wang A F et al 2011 *Phys. Rev. B* **83** 060512
- [13] Li C-H, Shen B, Han F, Zhu X Y and Wen H-H 2011 *Phys. Rev. B* **83** 184521
- [14] Liu R H et al 2011 *Europhys. Lett.* **94** 27008
- [15] Krzton-Maziopa A, Shermadini Z, Pomjakushina E, Pomjakushin V, Bendele M, Amato A, Khasanov R, Luetkens H and Conder K 2011 *J. Phys.: Condens. Matter* **23** 052203
- [16] Fang M H, Wang H D, Dong C H, Li Z J, Feng C M, Chen J and Yuan H Q 2011 *Europhys. Lett.* **94** 27009
- [17] Umeyama N, Tokumoto M, Yagi S, Tomura M, Tokiwa K, Fujii T, Toda R, Miyakawa N and Ikeda S-I 2012 *Japan. J. Appl. Phys.* **51** 053001
- [18] Newmark A R, Huan G, Greenblatt M and Croft M 1989 *Solid State Commun.* **71** 1025
- [19] Neilson J R, Llobet A, Stier A V, Wu L, Wen J, Tao J, Zhu Y, Tesanovic Z B, Armitage N P and McQueen T M 2012 *Phys. Rev. B* **86** 054512
- [20] Lei H C and Petrovic C 2011 *Phys. Rev. B* **83** 184504
- [21] Hammersley A P, Svenson S O, Hanfland M, Fitch A N and Hauserman D 1996 *High Press. Res.* **14** 235
- [22] Larson A C and Von Dreele R B 1994 *Los Alamos National Laboratory Report No.* LAUR 86-748
- [23] Toby B H 2001 *J. Appl. Crystallogr.* **34** 210
- [24] Hu R, Lei H C, Abeykoon M, Bozin E S, Billinge S J L, Warren J B, Siegrist T and Petrovic C 2011 *Phys. Rev. B* **83** 224502
- [25] Neilson J R and McQueen T M 2012 *J. Am. Chem. Soc.* **134** 7750
- [26] Speight J G 2005 *Lange's Handbook of Chemistry* 16th edn (London: McGraw-Hill) pp 1.153–1.154
- [27] Cao C and Dai J-H 2011 *Chin. Phys. Lett.* **28** 057402
- [28] Carlin R L 1986 *Magnetochemistry* (New York: Springer)
- [29] Yin Z P, Haule K and Kotliar G 2011 *Nature Mater.* **10** 932
- [30] Yang H et al 2008 *Phys. Rev. Lett.* **101** 067001
- [31] Cheng P, Yang H, Jia Y, Fang L, Zhu X, Mu G and Wen H-H 2008 *Phys. Rev. B* **78** 134508
- [32] Lu F, Zhao J Z and Wang W-H 2012 *J. Phys.: Condens. Matter* **24** 495501
- [33] Sefat A S, McGuire M A, Sales B C, Jin R, Howe J Y and Mandrus D 2008 *Phys. Rev. B* **77** 174503
- [34] Smith R A 1978 *Semiconductors* (Cambridge: Cambridge University Press)
- [35] Jia S, Chi S, Lynn J W and Cava R J 2010 *Phys. Rev. B* **81** 214446
- [36] Zeng B, Shen B, Chen G F, He J B, Wang D M, Li C H and Wen H H 2011 *Phys. Rev. B* **83** 144511
- [37] Barnard D 1972 *Thermoelectricity in Metals and Alloys* (London: Taylor and Francis)
- [38] Cohn J L, Wolf S A, Selvamannickam V and Salama K 1991 *Phys. Rev. Lett.* **66** 1098
- [39] Tsujii N, Yoshimura K and Kosuge K 2003 *J. Phys.: Condens. Matter* **15** 1993
- [40] DeLong L E, Guertin R P, Hasanain S and Fariss T 1985 *Phys. Rev. B* **31** 7059
- [41] Julian S R, Mackenzie A P, Lonzarich G G, Bergemann C, Haselwimmer R K W, Maeno Y, NishiZaki S, Tyler A W, Ikeda S and Fujita T 1999 *Physica B* **259–261** 928

ARTICLE

Received 9 Jun 2014 | Accepted 5 Nov 2014 | Published 8 Dec 2014

DOI: 10.1038/ncomms6761

Intra-unit-cell nematic charge order in the titanium-oxypnictide family of superconductors

Benjamin A. Frandsen^{1,*}, Emil S. Bozin^{2,*}, Hefei Hu^{2,†}, Yimei Zhu², Yasumasa Nozaki³, Hiroshi Kageyama³, Yasutomo J. Uemura¹, Wei-Guo Yin² & Simon J.L. Billinge^{2,4}

Understanding the role played by broken-symmetry states such as charge, spin and orbital orders in the mechanism of emergent properties, such as high-temperature superconductivity, is a major current topic in materials research. That the order may be within one unit cell, such as nematic, was only recently considered theoretically, but its observation in the iron-pnictide and doped cuprate superconductors places it at the forefront of current research. Here, we show that the recently discovered BaTi₂Sb₂O superconductor and its parent compound BaTi₂As₂O form a symmetry-breaking nematic ground state that can be naturally explained as an intra-unit-cell nematic charge order with *d*-wave symmetry, pointing to the ubiquity of the phenomenon. These findings, together with the key structural features in these materials being intermediate between the cuprate and iron-pnictide high-temperature superconducting materials, render the titanium oxypnictides an important new material system to understand the nature of nematic order and its relationship to superconductivity.

¹Department of Physics, Columbia University, New York, New York 10027, USA. ²Condensed Matter Physics and Materials Science Department, Brookhaven National Laboratory, Upton, New York 11973, USA. ³Department of Energy and Hydrocarbon Chemistry, Graduate School of Engineering, Kyoto University, Nishikyō, Kyoto 615-8510, Japan. ⁴Department of Applied Physics and Applied Mathematics, Columbia University, New York, New York 10027, USA. * These authors contributed equally to this work. † Present address: Intel Corporation, Folsom, California 95630, USA. Correspondence and requests for materials should be addressed to S.J.L.B. (email: sb2896@columbia.edu).

Rather than being an anomalous side effect in one or two cuprate systems, broken-symmetry states are now thought to be widespread in strongly correlated electron systems and other complex materials. Extensive study of the manganites^{1,2}, cuprates^{3,4}, iron pnictides⁵ and a variety of other systems has made it increasingly evident that local and global symmetry breaking in the charge, orbital, lattice and spin degrees of freedom are associated with the appearance of emergent phenomena, such as colossal magnetoresistance and high-temperature superconductivity (HTSC), but the exact relationship is not understood. Historically, the study of such broken-symmetry states has been very challenging. Taking the cuprates as an example, 8 years elapsed from the initial discovery of superconductivity to the first observation of symmetry-broken charge order (stripes) in one system⁶, another 7 years passed before hints were found in others^{7,8} and only within the last 3 years has charge order begun to emerge as a possibly ubiquitous feature of the cuprates^{9,10}.

Several possibilities arise when considering the symmetries that can be broken by these states. Most charge-/spin-density waves (C/SDWs) break the translational symmetry of the lattice, folding the Brillouin zone and resulting in superlattice diffraction peaks. On the other hand, orbital ordering, where charge transfers between orbitals centred at the same site, can break the metric rotational symmetry without lowering the translational symmetry. Examples are charge-nematic¹¹ and loop-current^{12,13} orders in the doped cuprates. In this context, nematic order is defined as one that breaks the rotational point group symmetry while preserving the lattice translational symmetry. The fact that nematic symmetry-broken states have recently been discovered experimentally in both the cuprate¹¹ and iron-based¹⁴ superconductors raises the importance and relevance of this observation to HTSC. It is, therefore, critically important to understand the role and ubiquity of symmetry breaking, including intra-unit-cell nematicity, to the superconducting phenomenon.

Standard theoretical treatments of HTSC, such as the effective single-band t - J model, have typically ignored the possibility of intra-unit-cell orders¹⁵. When multiple atoms per unit cell are explicitly included in the theory, qualitatively different ground-state solutions may be found¹⁶, underscoring the subtlety and importance of accounting correctly for this phenomenon. Hence, finding related but distinct systems that exhibit this phenomenon is expected to shed new light on this critical question.

Very recently, superconductivity was discovered^{17–19} in titanium-oxypnictide compounds, such as ATi_2Pn_2O ($A = \text{Na}_2, \text{Ba}, (\text{SrF})_2, (\text{SmO})_2$; $Pn = \text{As}, \text{Sb}, \text{Bi}$), which are close structural and chemical cousins to the cuprates and iron-pnictides^{20–24}. In particular, in isovalent $\text{BaTi}_2(\text{Sb}_{1-x}\text{Bi}_x)_2\text{O}$ and aliovalent $\text{Ba}_{1-x}\text{Na}_x\text{Ti}_2\text{Sb}_2\text{O}$ (ref. 25), muon spin rotation and heat capacity measurements point to fully-gapped s -wave superconductivity^{26–28}. Interestingly, a number of compounds in this family also show strong anomalies in resistivity and/or magnetic susceptibility that are thought to be signatures of symmetry-breaking charge- or spin-ordered ground states^{21,24,25,29,30}, suggesting that these materials are excellent candidates for studying the interplay between broken-symmetry states and superconductivity. In light of these strong transport anomalies, it is then quite surprising that subsequent experiments have failed to uncover any direct evidence for a conventional spin- or charge-density wave ground state^{26,27,31}, leaving open the question of whether these materials do possess symmetry-broken ground states.

Here, we show that superconducting $\text{BaTi}_2\text{Sb}_2\text{O}$, and its non-superconducting parent compound $\text{BaTi}_2\text{As}_2\text{O}$, do indeed undergo a tetragonal-orthorhombic phase transition, corresponding to a C_4 - C_2 symmetry lowering, that occurs at

the temperature of the transport anomaly. On the other hand, high-sensitivity electron diffraction measurements failed to detect any superlattice peaks in the bulk at low temperature, indicating that this transition does not break translational symmetry. The low-temperature phase, therefore, constitutes a nematic state. In light of the pronounced upturn in resistivity accompanying this nematic transition, together with the absence of any ordered SDW²⁶, we attribute the nematicity to an intra-unit-cell charge order with d -wave symmetry by charge transfer between neighbouring Ti sites—similar to that between neighbouring oxygen sites in cuprate superconductors—and find that it naturally explains the temperature dependence of the lattice constants. These results establish this family of materials as another playground for studying symmetry-breaking electronic phases and their relationship to superconductivity.

Results

Structural and electronic properties of $\text{BaTi}_2Pn_2\text{O}$. The basic structural unit of $\text{BaTi}_2Pn_2\text{O}$ is a planar square net of titanium and oxygen, in analogy with the cuprates (Fig. 1a,b), with the crucial difference that the positions of the metal and oxygen ions are switched between the structures (the complete titanate structure is shown as an inset in Fig. 2b). In Fig. 1, the square net is shown by solid lines along the nearest neighbour bonds, with dashed lines showing the net joining second neighbour ions. This second-nearest-neighbour square net connects oxygen ions in the cuprates, but metal ions in the titanate compounds and also in the iron-based superconductors (Fig. 1c). Thus, in terms of chemistry and structure, the titanate compounds bridge between the ferrous and cuprate superconductors. The Ti $3d$ orbitals are occupied by one electron per Ti atom, which is found to reside in a nominally $1/4$ -filled band formed via hybridization of the d_{xy} and $d_{y^2-z^2}/d_{x^2-z^2}$ orbitals for the Ti(1)/Ti(2) ions (defined in Fig. 1b). The local geometry of the Ti(1) site is shown in Fig. 1d and the arrangement of the d -energy levels is shown in Fig. 1e.

Furthermore, the phase diagram (Fig. 2b) is highly reminiscent of the cuprates and iron-based superconductors, with superconductivity appearing on doping and transport behaviour that is strongly suggestive of a competing electronic transition such as the formation of a CDW or SDW^{21,24}. The transport is metallic at high temperature²¹, with a positive resistivity slope versus temperature (Fig. 2a). However, on cooling, a pronounced upturn in the resistivity is found for all x in the solid solution $\text{BaTi}_2\text{As}_{1-x}\text{Sb}_x\text{O}$. The feature occurs at a temperature T_a that decreases monotonically from 200 K for $x=0$ to 50 K for $x=1$, with superconductivity appearing below ~ 1 K for the antimony endmember and increasing to 5 K for $\text{BaTi}_2\text{Bi}_2\text{O}$ (refs 19,24). Anomalies in the magnetic susceptibility and specific heat are also observed²¹ at T_a .

Density functional theory (DFT) calculations for $\text{BaTi}_2\text{Sb}_2\text{O}$ predicted an instability towards a bicollinear SDW formation^{32,33} or a commensurate CDW ground state driven by an unstable phonon mode that doubles the unit cell by distorting the Ti squares and preserves the tetragonal symmetry³⁴. The possibility of SDW formation in $\text{BaTi}_2(\text{As,Sb})_2\text{O}$, either commensurate or incommensurate, was subsequently ruled out by muon spin relaxation and ^{121/123}Sb nuclear resonance measurements, which show conclusively that no magnetic order develops at any temperature probed^{26,27,31}. On the other hand, a conventional CDW should be evident through an associated structural distortion. However, initial electron and neutron diffraction studies on the Sb endmember²⁶ found no broken symmetry or any signature of superlattice formation at low temperatures, nor was a CDW gap formation observed in angle-resolved photoemission measurements of the nested Fermi surfaces

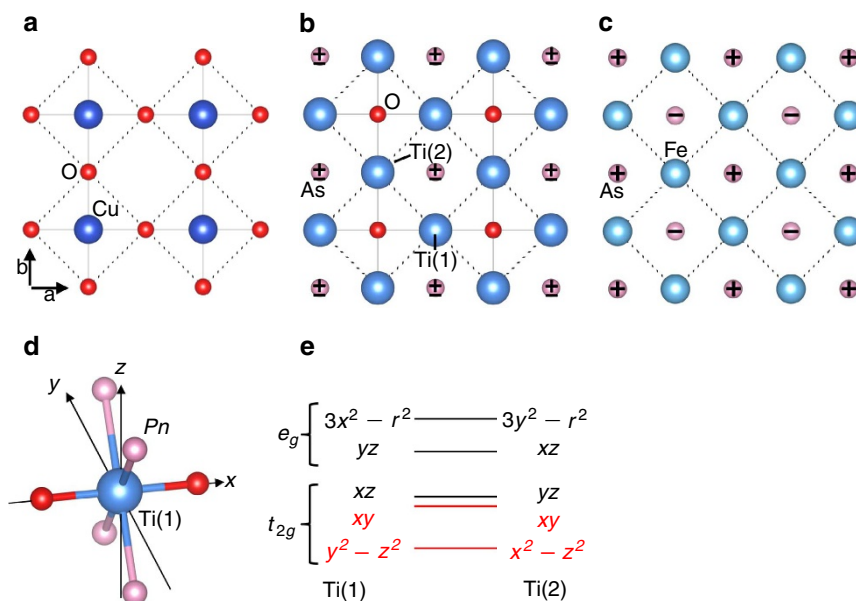


Figure 1 | Planar geometries of cuprate, titanium-oxypnictide, and iron-pnictide superconducting families. (a–c) Planar motifs in cuprates, titanium oxypnictides and iron pnictides, respectively. Solid grey lines show the metal-anion square net, and dotted black lines show the square net of second-nearest-neighbour atoms. The + and – signs in **b** and **c** denote As atoms that are above and below the plane, respectively. **(d)** TiO₂Pn₄ octahedral motif found in BaTi₂Pn₂O. **(e)** Schematics of the Ti 3d-orbital energy levels for the two distinct Ti sites labelled in **b**, Ti(1) and Ti(2). The two lowest-lying orbitals marked in red form two bands occupied by one electron per Ti.

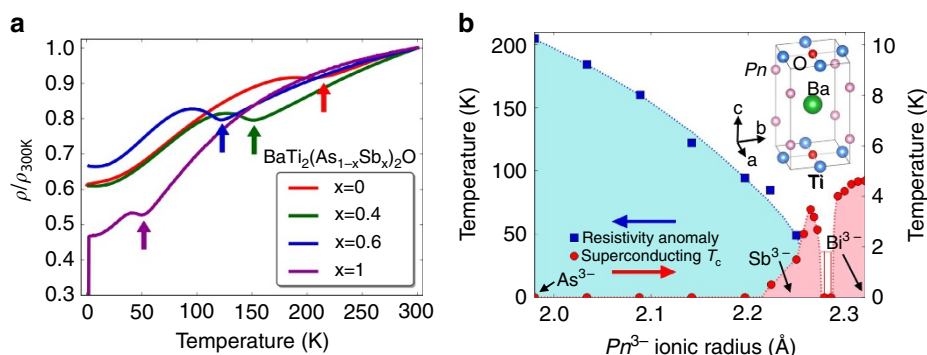


Figure 2 | Transport characteristics and phase diagram of BaTi₂Pn₂O with Pn = As, Sb, Bi. (a) Electrical resistivity of BaTi₂(As_{1-x}Sb_x)₂O, normalized by the room temperature resistivity. Arrows indicate the anomaly discussed in the text. (b) Phase diagram of BaTi₂Pn₂O shown as a function of Pn³⁻ ionic diameter. Broken lines are guides to the eye. The error bars accompanying the red circles arise from the instrumental low-temperature limit of 1.8 K. Inset: tetragonal crystal structure of BaTi₂Pn₂O.

(although a slight depression of the density of states at other momenta was found to correlate in temperature with the resistivity anomaly³⁵). The possibility of an incommensurate CDW was also ruled out by ^{121/123}Sb nuclear resonance measurements³¹.

Neutron powder diffraction measurements. In the absence of evidence for a long-range ordered CDW, we undertook a neutron diffraction and total scattering measurement on BaTi₂Sb₂O with a dense set of temperature points to search for evidence for a possible short-range ordered CDW^{36,37}. We also extended the investigation to the previously unstudied BaTi₂As₂O endmember. Unexpectedly, we found a long-range structural phase transition at T_a . Room temperature measurements of BaTi₂As₂O confirm the tetragonal $P4/mmm$ space-group symmetry previously reported from X-ray diffraction²¹. However, on cooling through T_a , we observe a distinct splitting of the (200)/(020) and

(201)/(021) Bragg peaks, representing the first observation of a symmetry lowering at the same temperature as the resistivity anomaly in BaTi₂As₂O. This is shown in Fig. 3, which compares the high- and low-temperature Bragg peaks in panel (a) and displays their temperature evolution in panel (b). The (200) peak at 2.02 Å begins to broaden below 200 K, coinciding with T_a , and appears to split at the lowest temperatures. Similarly, the (201) peak at 1.94 Å displays apparent splitting as the temperature is lowered. These observations demonstrate that BaTi₂As₂O undergoes a long-range ordered structural phase change at T_a , lowering its symmetry from tetragonal to orthorhombic.

To investigate the structural transition in greater detail, we performed Le Bail³⁸ refinements at all temperatures. We used the parent $P4/mmm$ model for $T \geq 200$ K. The simplest possible symmetry-breaking distortion mode of the parent $P4/mmm$ structure consistent with the observed peak splitting is a mode that breaks the degeneracy of the a - and b -axes without otherwise shifting atoms within the unit cell, resulting in a space-group

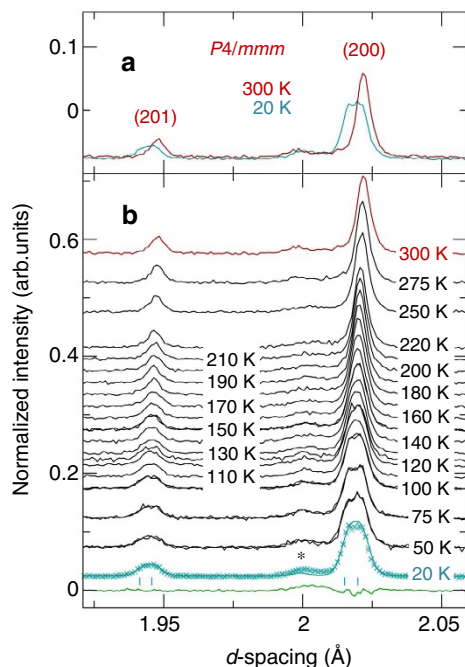


Figure 3 | Temperature evolution of BaTi₂As₂O neutron diffraction pattern. (a) Comparison of normalized intensities of 300 K (red) and 20 K (blue) data around (200) and (201) reflections in *P4/mmm* setting. (b) Waterfall plot across the temperature range studied. The 20 K data (blue symbols) are shown with a fit (blue solid line) of the refined *Pmmm* model. The corresponding difference curve is shown as the green solid line below. The asterisk marks the (200)/(020) reflections of the BaTiO₃ impurity phase.

symmetry of *Pmmm*, which was used for $T < 200$ K. We also explored other candidate orthorhombic structures with lower symmetry, but since these structures do not improve the fit quality within the resolution limitations of the current data, *Pmmm* is the most appropriate choice. We display the results of these refinements in Fig. 4. As seen in panel (b), the tetragonal *a* axis clearly splits below $T \sim 200$ K, with a maximum orthorhombic splitting of ~ 0.01 Å. The orthorhombicity parameter $\eta = 2 \times (a-b)/(a+b)$ is shown in the inset of panel (a), indicating a maximum orthorhombicity of $\sim 0.22\%$. Panel (a) also displays the temperature dependence of the *c* axis parameter, which exhibits an upturn below the structural transition deviating from the linear thermal contraction trend seen for $T > 200$ K. This same type of *c* axis response also accompanies long-range ordered stripe formation in the nickelates³⁶. Additional details regarding Rietveld refinement of BaTi₂As₂O can be found in Supplementary Note 1. The superconducting BaTi₂Sb₂O shows qualitatively the same behaviour, albeit with an amplitude decreased by a factor of ~ 5 , with an orthorhombic splitting (0.05%) and a small but observable *c* axis upturn appearing on cooling through $T_a = 50$ K. The undistorted *P4/mmm* model can be used with moderate success at all temperatures, but the *Pmmm* model yields a better fit below 50 K (see Supplementary Note 2). Pair distribution function analysis is consistent with these observations for both compounds and can be found in Supplementary Note 3.

These results offer compelling evidence that the observed structural response is intimately related to the transport anomaly and may be driven by a broken symmetry of the electronic system forming at that temperature. The small distortion amplitude in BaTi₂Sb₂O explains why this long-range structural phase change escaped notice in previous neutron diffraction measurements²⁶.

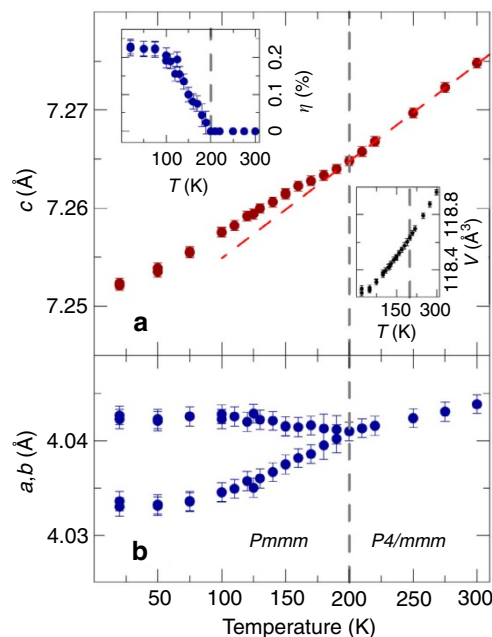


Figure 4 | Temperature evolution of BaTi₂As₂O structural parameters. (a) Lattice parameter *c* (red). (b) Lattice parameters *a*, *b* (blue). Insets: orthorhombicity $\eta = 2 \times (a-b)/(a+b)$ (left) and unit cell volume (right). Vertical dashed grey line indicates transition temperature. Dashed red line is a guide for the eyes. Error bars represent the estimated standard deviation of the corresponding refined parameter.

Electron diffraction measurements. Since CDW formation is implicated, we made a special effort to search for the appearance of weak superlattice peaks associated with a finite CDW wave-vector in electron diffraction (ED) patterns below T_a . The original study on the antimony endmember failed to observe superlattice peaks²⁶. Here, we concentrated on the arsenic endmember where the structural distortion is five times larger, and the ED patterns were heavily overexposed to search for any weak response at intensities close to background. Despite these efforts, the ED patterns taken along the [001] and [011] directions revealed no superlattice peaks in the bulk at low temperature, as shown in Fig. 5. However, in a very small fraction of the sample in the immediate vicinity of grain boundaries, weak superlattice peaks with $\mathbf{Q} = (1/2, 0, 0)$ are observed at low temperature. This non-bulk behaviour is explored further in Supplementary Note 4.

Discussion

A picture emerges of a C_4 - C_2 symmetry breaking occurring with an accompanying strong upturn in resistivity, but with no corresponding CDW superlattice peaks appearing. The resistivity upturn is larger than would be expected as a passive response of the electronic system to the structural transition, borne out by a standard DFT calculation with the observed orthorhombicity parameter $\eta = 0.22\%$, which showed that merely 0.0003 electrons are transferred from Ti(1) to Ti(2). Therefore, in common with earlier discussion^{18,21}, we propose that the structural transition is a response to an instability of the electronic system. The earlier muon spin relaxation results^{26,27}, together with the ED measurements, allow us to rule out the existing proposals of SDW formation^{32,33} or a phonon-driven CDW³⁴. Instead, an intra-unit-cell charge-nematic electronic symmetry breaking is implicated, similar to that proposed for doped cuprates³⁹.

In the current case, a charge redistribution between the on-site orbital states at the Fermi level, $d_{x^2-z^2}/d_{y^2-z^2}$ to d_{xy} , does not

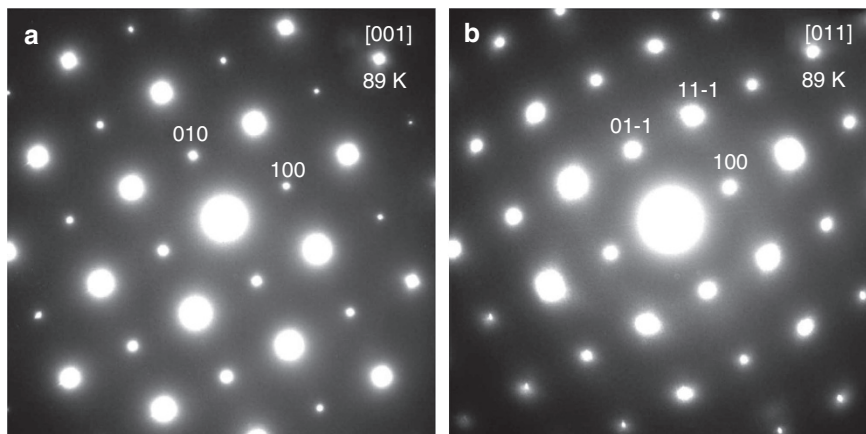


Figure 5 | Electron diffraction patterns of BaTi₂As₂O. (a) Diffraction pattern with the incident beam along the [001] and (b) along the [011] directions. No superlattice peaks are observed at low temperature even after heavy overexposure.

break the rotational symmetry, so can be ruled out. Instead, a simple but novel intra-unit-cell charge order (IUC-CO) naturally explains the observed phenomenology. A transfer of charge from Ti(1) to Ti(2) (see Fig. 1b) lowers the rotational symmetry of the Ti₂O plaquette locally from C_4 to C_2 , with the effect on the overall lattice symmetry depending on the ordering pattern of the distinct Ti ions in neighbouring unit cells. Repeating the symmetry-lowered plaquette uniformly along the a and b directions results in no change of the unit cell, but breaks the metric symmetry from C_4 in $P4/mmm$ to C_2 in $Pmmm$, as observed experimentally. This arrangement of charges can accordingly be described as a nematic IUC-CO. Our data are therefore consistent with the formation of this type of charge order on cooling through T_a . Such a model is also consistent with the breaking of C_4 symmetry at the Pn site that has been observed from ^{121/123}Sb nuclear resonance measurements³¹.

This nematic IUC-CO is energetically favoured on Coulombic grounds if the on-site Hubbard energy U is sufficiently small, which is a reasonable assumption as the system is a metal rather than a Mott insulator. The small Hubbard U arises from significant screening due to the solvation effect of the high polarizabilities of the As³⁻ and Sb³⁻ anions, which are an order of magnitude larger than that of O²⁻. Moreover, the As and Sb ions reside on a lower symmetry site in the $Pmmm$ structure, which enhances the effects of their polarizabilities. This physics was proposed in an earlier study of the iron-pnictide superconductors⁴⁰. Returning to the present system, the transfer of a charge of δ from Ti(1) to Ti(2) will result in a lowering of the electrostatic energy, $V(1-\delta)(1+\delta) = V(1-\delta^2)$, where V is the screened Coulombic interaction between Ti sites and is positive. The result is charge order with a d -wave symmetry⁴¹ with the sign of the modulated charge density varying as $- + - +$ around the plaquette. From plaquette to plaquette, the orientation of the axis of the distortion can be parallel or perpendicular, forming a ferro- or anti-ferro- type ordering, which would preserve or break translational symmetry, respectively. The former is consistent with the experimental observations in this material. We suggest that the rather rigid face-shared octahedral topology in each layer favours the uniform ferro- over the anti-ferro- ordering. It is noteworthy that this V is the counterpart of the Coulombic repulsion V_{pp} between neighbouring oxygen atoms in the CuO₂ plane, which was shown to drive IUC nematic order in nonstoichiometric doped cuprates⁴². Hence, the present results obtained on these stoichiometric materials (thus having less ambiguity such as disorder effects) yield insight into the origin of IUC nematic order in the cuprates.

This nematic IUC-CO naturally explains the observed changes in the a - and c -lattice parameters. The transfer of charge from the Ti(1) $d_{y^2-z^2}$ orbital to Ti(2) $d_{x^2-z^2}$ results in increased electrostatic repulsion between the charge-rich $d_{x^2-z^2}$ orbitals extending along the a axis, breaking the tetragonal degeneracy of the a and b axes and leading to the observed orthorhombic distortion. Furthermore, a uniform stacking of the IUC-CO in each layer can also explain the response of the c -lattice parameter, which expands upon entering the charge-ordered state (Fig. 4a). This lattice expansion may be attributed in part to increased electrostatic repulsion between inter-layer Ti ions from the transferred charge. The net energy contribution is $V'[(1+\delta)^2 + (1-\delta)^2] = V'(2+2\delta^2)$, where V' is the inter-layer screened Coulombic interaction. This acts in addition to other elastic energy contributions.

The structural effects observed on cooling are much smaller in BaTi₂Sb₂O than BaTi₂As₂O, suggesting that the IUC-CO is relatively suppressed both in amplitude and temperature. This may be a result of the larger unit cell in the Sb compound, due to its larger Sb³⁻ ionic diameter (2.25 versus 1.98 Å for As³⁻; ref. 18), resulting in a smaller V .

To identify the microscopic driving force of this nematic instability, we present a symmetry-based zero-order analysis in which only the leading energy scales are retained. Ti atoms reside at the centre of a distorted octahedron with oxygen at the apices and pnictide atoms around the equatorial plane, as shown in Fig. 1d for Ti(1). The Ti $3d$ -energy levels are illustrated in Fig. 1e, similar to the case of nearly isostructural (LaO)₂CoSe₂O (ref. 43). The nominal electron occupation is one electron per Ti atom, which would have been assigned to the locally lowest-lying $d_{y^2-z^2}$ and $d_{x^2-z^2}$ orbitals on the Ti(1) and Ti(2) ions, respectively. However, the σ -bonding between the Ti(1) and Ti(2) d_{xy} orbitals forms a relatively wide band that overlaps the locally lowest level. Therefore, the minimum model for the titanium oxypnictides involves the two orbitals: $d_{y^2-z^2}$ and d_{xy} on Ti(1) and $d_{x^2-z^2}$ and d_{xy} on Ti(2). Since the d_{xy} orbital has the same impact on both the a and b direction, the C_4 - C_2 symmetry lowering around the central oxygen atom is mainly determined by the charge imbalance between the quasi-one-dimensional $d_{y^2-z^2}$ band on Ti(1) and $d_{x^2-z^2}$ on Ti(2) as a result of the Stoner instability⁴². No doubt this mechanism will be complicated by hybridization and other issues, but this symmetry-based analysis provides the appropriate realistic starting point. Since the proposed nematic intra-unit-cell charge order elegantly explains all the observed structural effects, it is anticipated to be the electronic ground state of BaTi₂Pn₂O.

Methods

Neutron powder diffraction. Powder specimens of $\text{BaTi}_2\text{As}_2\text{O}$ and $\text{BaTi}_2\text{Sb}_2\text{O}$ were prepared via conventional solid state reaction methods. Details of the synthesis are provided in a previous study²⁶. Time-of-flight neutron total scattering experiments were performed at the Neutron Powder Diffractometer at Los Alamos Neutron Science Center (LANSCE) at Los Alamos National Laboratory. Data were collected using a closed-cycle He refrigerator at temperatures ranging from 10–300 K in steps of 10 K near the structural transition and 25 K away from the transition over a wide range of momentum transfer Q . Le Bail³⁸ fits to the intensity profiles were performed with GSAS⁴⁴ on the EXPGUI platform⁴⁵. Pair distribution function (PDF) profiles were obtained by Fourier transforming the measured total scattering intensity up to a maximum momentum transfer of $Q_{\text{max}} = 24 \text{ \AA}^{-1}$ using established protocols^{46,47} as implemented in the programme PDFgetN⁴⁸. The Le Bail fits were used to extract lattice parameters and space-group symmetry, the PDF fits to extract atomic displacement parameters. Symmetry mode analysis using the programme ISODISTORT⁴⁹ was conducted to identify candidate distorted structures.

Electron diffraction and DFT calculations. Electron diffraction patterns were recorded using a JEOL ARM 200CF transmission electron microscope (TEM), operated at 200 keV, at Brookhaven National Laboratory. The TEM samples were prepared by crushing powder specimens into thin flakes transparent to the electron beam, which were supported by a lacey carbon copper grid. DFT calculations were performed within the generalized gradient approximation implemented in the Wien2k software package⁵⁰.

References

- Dagotto, E. *et al.* *Nanoscale phase separation and colossal magnetoresistance* (Springer-Verlag, 2003).
- Dagotto, E. Complexity in strongly correlated electronic systems. *Science* **309**, 257–262 (2005).
- Orenstein, J. & Millis, A. J. Advances in the physics of high-temperature superconductivity. *Science* **288**, 468–474 (2000).
- da Silva Neto, E. H. *et al.* Ubiquitous interplay between charge ordering and high-temperature superconductivity in cuprates. *Science* **343**, 393–396 (2014).
- Fernandes, R., Chubukov, A. & Schmalian, J. What drives nematic order in iron-based superconductors? *Nat. Phys.* **10**, 97–104 (2014).
- Tranquada, J. M., Sternlieb, B. J., Axe, J. D., Nakamura, Y. & Uchida, S. Evidence for stripe correlations of spins and holes in copper oxide superconductors. *Nature* **375**, 561–563 (1995).
- Hoffman, J. E. *et al.* A four unit cell periodic pattern of quasi-particle states surrounding vortex cores in $\text{Bi}_2\text{Sr}_2\text{CaCu}_2\text{O}_{8+\delta}$. *Science* **295**, 466–469 (2002).
- Vershinin, M. *et al.* Local ordering in the pseudogap state of the high- T_c superconductor $\text{Bi}_2\text{Sr}_2\text{CaCu}_2\text{O}_{8+\delta}$. *Science* **303**, 1995–1998 (2004).
- Chang, J. *et al.* Direct observation of competition between superconductivity and charge density wave order in $\text{YBa}_2\text{Cu}_3\text{O}_{6.67}$. *Nat. Phys.* **8**, 871–876 (2012).
- Comin, R. *et al.* Charge order driven by Fermi-arc instability in $\text{Bi}_2\text{Sr}_{2-x}\text{La}_x\text{CuO}_{6+\delta}$. *Science* **343**, 390–392 (2014).
- Lawler, M. J. *et al.* Intra-unit-cell nematicity of the high- T_c copper-oxide pseudogap states. *Nature* **466**, 374–377 (2010).
- Varma, C. Non-Fermi-liquid states and pairing instability of a general model of copper oxide metals. *Phys. Rev. B* **55**, 14554 (1997).
- Li, Y. *et al.* Hidden magnetic excitation in the pseudogap phase of a high- T_c superconductor. *Nature* **468**, 283–285 (2010).
- Chuang, T. *et al.* Nematic electronic structure in the ‘parent’ state of the iron-based superconductor $\text{Ca}(\text{Fe}_{1-x}\text{Co}_x)_2\text{As}_2$. *Science* **327**, 181–184 (2010).
- Lee, P. A., Nagaosa, N. & Wen, X.-G. Doping a mott insulator: Physics of high-temperature superconductivity. *Rev. Mod. Phys.* **78**, 17–85 (2006).
- Fernandes, R., Chubukov, A., Knolle, J., Eremin, I. & Schmalian, J. Preemptive nematic order, pseudogap, and orbital order in the iron pnictides. *Phys. Rev. B* **85**, 024534 (2012).
- Yajima, T. *et al.* Synthesis and physical properties of the new oxybismuthides $\text{BaTi}_2\text{Bi}_2\text{O}$ and $(\text{SrF})_2\text{Ti}_2\text{Bi}_2\text{O}$ with a d^1 square net. *J. Phys. Soc. Jpn* **82**, 013703 (2013).
- Yajima, T. *et al.* Two superconducting phases in the isovalent solid solutions $\text{BaTi}_2\text{Pn}_2\text{O}$ ($\text{Pn} = \text{As}, \text{Sb}, \text{and Bi}$). *J. Phys. Soc. Jpn* **82**, 033705 (2013).
- Zhai, H.-F. *et al.* Superconductivity, charge- or spin-density wave, and metal-nonmetal transition in $\text{BaTi}_2(\text{Sb}_{1-x}\text{Bi}_x)_2\text{O}$. *Phys. Rev. B* **87**, 100502 (2013).
- Ozawa, T. C. & Kauzlarich, S. M. Chemistry of layered d -metal pnictide oxides and their potential as candidates for new superconductors. *Sci. Technol. Adv. Mater.* **9**, 033003 (2008).
- Wang, X. F. *et al.* Structure and physical properties for a new layered pnictide-oxide: $\text{BaTi}_2\text{As}_2\text{O}$. *J. Phys. Condens. Mater.* **22**, 075702 (2010).
- Liu, R. H. *et al.* Structure and physical properties of the layered pnictide-oxides: $(\text{SrF})_2\text{Ti}_2\text{Pn}_2\text{O}$ ($\text{Pn} = \text{As}, \text{Sb}$) and $(\text{SmO})_2\text{Ti}_2\text{Sb}_2\text{O}$. *Chem. Mater.* **22**, 1503–1508 (2010).
- Johrendt, D., Hosono, H., Hoffmann, R.-D. & Pöttgen, R. Structural chemistry of superconducting pnictides and pnictide oxides with layered structures. *Z. Kristallogr.* **226**, 435–446 (2011).
- Yajima, T. *et al.* Superconductivity in $\text{BaTi}_2\text{Sb}_2\text{O}$ with a d^1 square lattice. *J. Phys. Soc. Jpn* **81**, 103706 (2012).
- Doan, P. *et al.* $\text{Ba}_{1-x}\text{Na}_x\text{Ti}_2\text{Sb}_2\text{O}$ ($0.0 \leq x \leq 0.33$): a layered titanium-based pnictide oxide superconductor. *J. Am. Chem. Soc.* **134**, 16520–16523 (2012).
- Nozaki, Y. *et al.* Muon spin relaxation and electron/neutron diffraction studies of $\text{BaTi}_2(\text{As}_{1-x}\text{Sb}_x)_2\text{O}$: Absence of static magnetism and superlattice reflections. *Phys. Rev. B* **88**, 214506 (2013).
- von Rohr, F., Schilling, A., Nesper, R., Baines, C. & Bendele, M. Conventional superconductivity and charge-density-wave ordering in $\text{Ba}_{1-x}\text{Na}_x\text{Ti}_2\text{Sb}_2\text{O}$. *Phys. Rev. B* **88**, 140501 (2013).
- Gooch, M. *et al.* Weak coupling BCS-like superconductivity in the pnictide oxide $\text{Ba}_{1-x}\text{Na}_x\text{Ti}_2\text{Sb}_2\text{O}$ ($x = 0$ and 0.15). *Phys. Rev. B* **88**, 064510 (2013).
- Axtell, III E. A., Ozawa, T., Kauzlarich, S. M. & Singh, R. Phase transition and spin-gap behavior in a layered tetragonal pnictide oxide. *J. Solid State Chem.* **134**, 423–426 (1997).
- Liu, R. H. *et al.* Physical properties of the layered pnictide oxides $\text{Na}_2\text{Ti}_2\text{P}_2\text{O}$ ($\text{P} = \text{As}, \text{Sb}$). *Phys. Rev. B* **80**, 144516 (2009).
- Kitagawa, S., Ishida, K., Nakano, K., Yajima, T. & Kageyama, H. s -wave superconductivity in superconducting $\text{BaTi}_2\text{Sb}_2\text{O}$ revealed by $^{121/123}\text{Sb}$ -NMR/nuclear quadrupole resonance measurements. *Phys. Rev. B* **87**, 060510 (2013).
- Singh, D. J. Electronic structure, disconnected fermi surfaces and antiferromagnetism in the layered pnictide superconductor $\text{Na}_x\text{Ba}_{1-x}\text{Ti}_2\text{Sb}_2\text{O}$. *New J. Phys.* **14**, 123003 (2012).
- Wang, G., Zhang, H., Zhang, L. & Liu, C. The electronic structure and magnetism of $\text{BaTi}_2\text{Sb}_2\text{O}$. *J. Appl. Phys.* **113**, 243904 (2013).
- Subedi, A. Electron-phonon superconductivity and charge density wave instability in the layered titanium-based pnictide $\text{BaTi}_2\text{Sb}_2\text{O}$. *Phys. Rev. B* **87**, 054506 (2013).
- Xu, H. C. *et al.* Electronic structure of the $\text{BaTi}_2\text{As}_2\text{O}$ parent compound of the titanium-based oxypnictide superconductor. *Phys. Rev. B* **89**, 155108 (2014).
- Abeykoon, M. *et al.* Evidence for short-range-ordered charge stripes far above the charge-ordering transition in $\text{La}_{1.67}\text{Sr}_{0.33}\text{NiO}_4$. *Phys. Rev. Lett.* **111**, 096404 (2013).
- Božin, E. S., Billinge, S. J. L., Takagi, H. & Kwei, G. H. Neutron diffraction evidence of microscopic charge inhomogeneities in the CuO_2 plane of superconducting $\text{La}_{2-x}\text{Sr}_x\text{Cu}_4$ ($0 \leq x \leq 0.30$). *Phys. Rev. Lett.* **84**, 5856–5859 (2000).
- Le Bail, A., Duroy, H. & Fourquet, J. L. *Ab-initio* structure determination of LiSbWO_6 by X-ray powder diffraction. *Mater. Res. Bull.* **23**, 447–452 (1987).
- Fujita, K. *et al.* Direct phase-sensitive identification of a d -form factor density wave in underdoped cuprates. *Proc. Natl Acad. Sci. USA* **111**, E3026–E3032 (2014).
- Sawatzky, G., Elfimov, I., van den Brink, J. & Zaanen, J. Heavy-anion solvation of polarity fluctuations in pnictides. *Europhys. Lett.* **86**, 17006 (2009).
- Fradkin, E., Kivelson, S. A., Lawler, M. J., Eisenstein, J. P. & Mackenzie, A. P. Nematic fermi fluids in condensed matter physics. *Annu. Rev. Condens. Matter Phys.* **1**, 153 (2010).
- Fischer, M. H. & Kim, E.-A. Mean-field analysis of intra-unit-cell order in the Emery model of the CuO_2 plane. *Phys. Rev. B* **84**, 144502 (2011).
- Wu, H. Electronic structure, spin state, and magnetism of the square-lattice mott insulator $\text{LaCo}_2\text{Se}_2\text{O}_3$ from first principles. *Phys. Rev. B* **82**, 020410(R) (2010).
- Larson, A. C. & Von Dreele, R. B. *General structure Analysis System*. Report No. LAUR-86-748, 87545 (Los Alamos National Laboratory, 1994).
- Toby, B. H. EXPGUI, a graphical user interface for GSAS. *J. Appl. Crystallogr.* **34**, 201–213 (2001).
- Egami, T. & Billinge, S. J. L. *Underneath the Bragg Peaks: Structural Analysis of Complex Materials* 2nd edn (Elsevier, 2012).
- Chupas, P. J. *et al.* Rapid acquisition pair distribution function analysis (RA-PDF). *J. Appl. Crystallogr.* **36**, 1342–1347 (2003).
- Peterson, P. F., Gutmann, M., Proffen, T. & Billinge, S. J. L. PDFgetN: a user-friendly program to extract the total scattering structure function and the pair distribution function from neutron powder diffraction data. *J. Appl. Crystallogr.* **33**, 1192–1192 (2000).
- Campbell, B., Stokes, H., Tanner, D. & Hatch, D. ISODISPLACE: an internet tool for exploring structural distortions. *J. Appl. Crystallogr.* **39**, 607–614 (2006).
- Blaha, P., Schwarz, K., Madsen, G., Kvasnicka, D. & Luitz, J. *WIEN2k: An Augmented Plane Wave Plus Local Orbitals Program for Calculating Crystal Properties* (Vienna University Technology, 2001).

Acknowledgements

Work at Brookhaven National Laboratory was supported by the U.S. Department of Energy, Office of Basic Energy Sciences, under contract No. DE-AC02-98CH10886.

Work at Columbia University was supported by the U.S. National Science Foundation (NSF) Partnership for International Research and Education (PIRE) Super-PIRE project (grant OISE-0968226). Y.J.U. also acknowledges support from NSF DMR-1105961, the Japan Atomic Energy Agency Reimei project, and the Friends of Todai Inc. The work at Kyoto University was supported by the FIRST program, Japan Society of the Promotion of Science (JSPS). Neutron scattering experiments were carried out on NPDF at LANSCE, funded by DOE Office of Basic Energy Sciences. LANL is operated by Los Alamos National Security LLC under DOE Contract No. DE-AC52-06NA25396.

Author contributions

Y.J.U., S.J.L.B. and B.A.F. initiated this work. Y.N. and H.K. carried out sample preparation and characterization. E.S.B. carried out the neutron diffraction measurements and analysed the data with assistance from B.A.F. H.H. performed the electron diffraction measurements with help from Y.Z. W.-G.Y. proposed the charge-ordering

model and provided theoretical support. B.A.F., W.-G.Y. and S.J.L.B. wrote the paper, with input from all the authors.

Additional information

Supplementary Information accompanies this paper at <http://www.nature.com/naturecommunications>

Competing financial interests: The authors declare no competing financial interests.

Reprints and permission information is available online at <http://npg.nature.com/reprintsandpermissions/>

How to cite this article: Frandsen, B. A. *et al.* Intra-unit-cell nematic charge order in the titanium-oxypnictide family of superconductors. *Nat. Commun.* 5:5761 doi: 10.1038/ncomms6761 (2014).

Local off-centering symmetry breaking in the high-temperature regime of SnTeK. R. Knox,¹ E. S. Bozin,¹ C. D. Malliakas,^{2,3} M. G. Kanatzidis,^{2,3} and S. J. L. Billinge^{1,4}¹*Department of Condensed Matter Physics and Materials Science, Brookhaven National Laboratory, Upton, New York 11973, USA*²*Department of Chemistry, Northwestern University, Evanston, Illinois 60208, USA*³*Materials Science Division, Argonne National Laboratory, Argonne, Illinois 60439, USA*⁴*Department of Applied Physics and Applied Mathematics, Columbia University, New York, New York 10027, USA*

(Received 5 November 2013; published 3 January 2014)

The local structure of SnTe has been studied using atomic pair distribution function analysis of x-ray and neutron data. Evidence is found for a locally distorted high-temperature state, which emerges *on warming* from an undistorted rocksalt structure. The structural distortion appears rapidly over a relatively narrow temperature range from 300 to 400 K. A similar effect has been reported in PbTe and PbS and dubbed *emphanis*; here we report on *emphanis* in a compound that does not contain Pb. The analysis suggests that this effect is unrelated to the low-temperature ferroelectric state in SnTe.

DOI: [10.1103/PhysRevB.89.014102](https://doi.org/10.1103/PhysRevB.89.014102)

PACS number(s): 61.50.Ks, 61.05.cf, 61.05.fg, 77.84.—s

I. INTRODUCTION

In the canonical view of structural transformations, a low-symmetry ground state evolves into a higher symmetry state on warming.^{1–7} However, it is not uncommon to observe broken-symmetry states in the high-temperature phase which are spatially disordered and/or fluctuating.^{8–12} These states often arise as a legacy of the low-symmetry ground state as such systems pass through an order-disorder phase transition, e.g., in LaMnO₃,^{13,14} BaTiO₃,^{15–18} and GeTe.^{19,20} However, the emergence of a locally broken symmetry state from a high-symmetry state is rare and unusual. Recently, an example of such an exception was found in the high performance thermoelectric PbTe and its relative PbS—an unexpected appearance of local fluctuating Pb displacements *on warming*.²¹ Here, we show that SnTe exhibits this phenomenon as well, revealing insights into its origin.

The rocksalt structure of these materials (PbTe, PbS, and SnTe) is undistorted near room temperature but becomes locally distorted on warming, though without a corresponding change in the average crystal structure. This phenomenon is unique among high-symmetry systems and has been called *emphanis*,²¹ meaning the appearance of a low-symmetry state from a high-symmetry state on warming by virtue of a well defined displacement of atoms from their centrosymmetric positions. *Emphanis* may explain some anomalies seen in these systems,²² such as the unusual temperature dependence of the band gap²³ and the very low lattice thermal conductivity.²⁴ However, since its discovery, a controversy has developed regarding the existence, origin, and ubiquity of *emphanis*. Atomic pair distribution function (PDF) analysis, which simultaneously probes both average and local atomic structure, revealed a local off-centering of Pb in PbTe and PbS as large as 0.25 Å.²¹ This picture was supported by maximum entropy analysis of single-crystal diffraction data²⁵ as well as *ab initio* molecular dynamics calculations.^{26,27} On the other hand, a recent extended x-ray-absorption fine-structure study²⁸ found no evidence of Pb off-centering within the resolution of the measurements. Based on first-principles calculations²⁹ and inelastic neutron scattering (INS) measurements³⁰ it has been suggested that lattice anharmonicity is behind the effect in PbTe. However, INS studies have also revealed the appearance

of a new phonon mode on warming, suggestive of dynamic symmetry breaking.³¹

Since PbTe is an incipient ferroelectric,^{32,33} it was speculated that the *emphanitic* regime resembles the paraelectric-dipole-like state often found above a ferroelectric ground state.²¹ Hartree-Fock and density functional calculations have supported this notion, revealing the existence of a second minimum in the energy landscape of PbS, with a ferroelectric α -GeTe-type structure.³⁴ However, a complete understanding of the true nature of the *emphanitic* distortion remains elusive.

Here, we present a detailed temperature-dependent x-ray and neutron PDF structural study on SnTe. Not only is SnTe isostructural to PbTe at room temperature, but it also displays a low-temperature ferroelectric phase.^{35,36} We show that SnTe exhibits a crossover to an *emphanitic* phase above 300 K, displaying clear signatures of off-centering displacements in the high-temperature regime. This crossover occurs over a relatively narrow temperature range of approximately 100 K, with no appreciable further evolution of the underlying distortions above 400 K. This temperature dependence strongly supports the notion that *emphanis* is truly a novel transformation from a higher to a lower local symmetry rather than thermal motion of atoms in a single-welled anharmonic potential. The results further suggest that the *emphanitic* behavior is not related to the ferroelectric state, but is a completely distinct phenomenon.

II. METHODS

Stoichiometric amounts of Sn and Te (~10 g) were combined in a 13-mm fused silica tube, which was then evacuated to 10⁻⁴ mbar and flame sealed before being placed in a computer-controlled furnace. The reactants were heated to 1273 °C over 24 h, held at 1273 °C for 2 h, rocked for ~5 s to ensure a homogeneous melt, and then cooled to room temperature in 24 h. The resulting polycrystalline samples were ground into powders for x-ray and neutron total scattering experiments, performed at the X17A beam line of the National Synchrotron Light Source (NSLS) at Brookhaven National Laboratory (BNL) and at the Neutron Powder Diffractometer (NPDF)³⁷ at Los Alamos Neutron Science Center (LANSCE) at Los Alamos National Laboratory, respectively. Data were collected in the 15–500 K temperature range in 3 and 50 K

steps for x-ray and neutron data, respectively. High-resolution PDFs were obtained via Fourier transform of the measured total scattering structure functions up to $Q_{\max} = 26 \text{ \AA}^{-1}$ using standard protocols.^{38,39} Data reduction to obtain the PDFs was carried out using the programs PDFgetX3 (Ref. 40) and PDFgetN (Ref. 41) for x-ray and neutron data, respectively. The radial distribution function (RDF), $R(r)$, was also calculated by standard methods.³⁸ The RDF has the useful property that bonds between atoms moving in harmonic potentials are represented by Gaussian peaks with zero offset.

III. RESULTS AND DISCUSSION

The low-temperature ferroelectric phase of SnTe is rhombohedral ($R3m$), transforming to cubic ($Fm\bar{3}m$) at $\sim 100 \text{ K}$ on warming (the exact value of the transition temperature is dependent on carrier concentration⁴²). GeTe is the only other known ferroelectric binary chalcogenide, with a [111]-type atomic off-centering as large as 0.3 \AA .⁴³ The symmetry of the ferroelectric phase in SnTe is identical, but with atomic displacements an order of magnitude smaller.⁴²

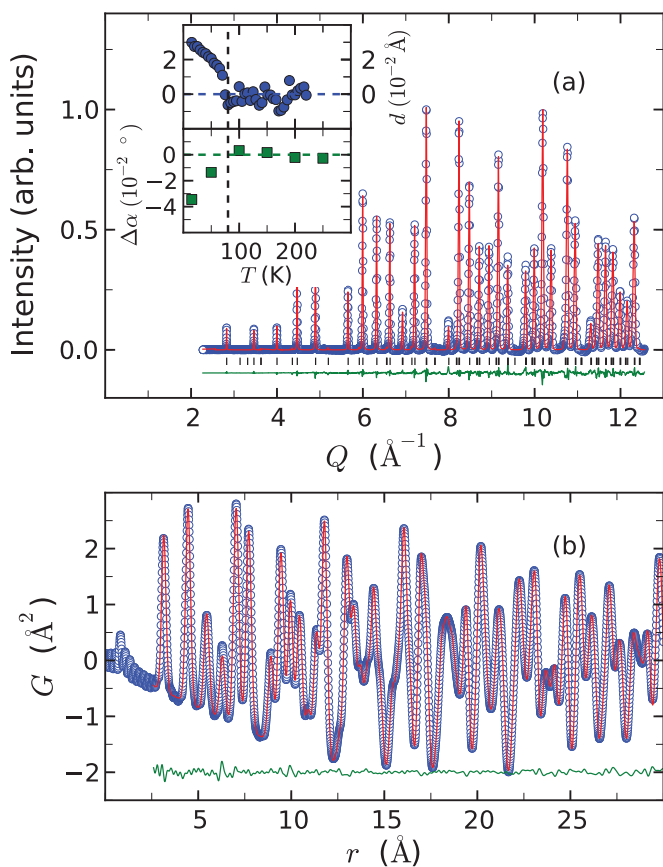


FIG. 1. (Color online) Best fits (red lines) at 150 K using $Fm\bar{3}m$ model to (a) background subtracted raw neutron data and (b) x-ray PDF data. Data are shown as open blue circles. Difference curves (green) are offset for clarity. Allowed reflections are shown in panel (a) in black. Inset to (a): measures of temperature dependence of rhombohedral distortion obtained from $R3m$ fits. Top: [111] sublattice displacement d from x-ray PDF data. Bottom: Angle $\Delta\alpha$, measuring deviation from a cubic unit cell, from raw neutron data.

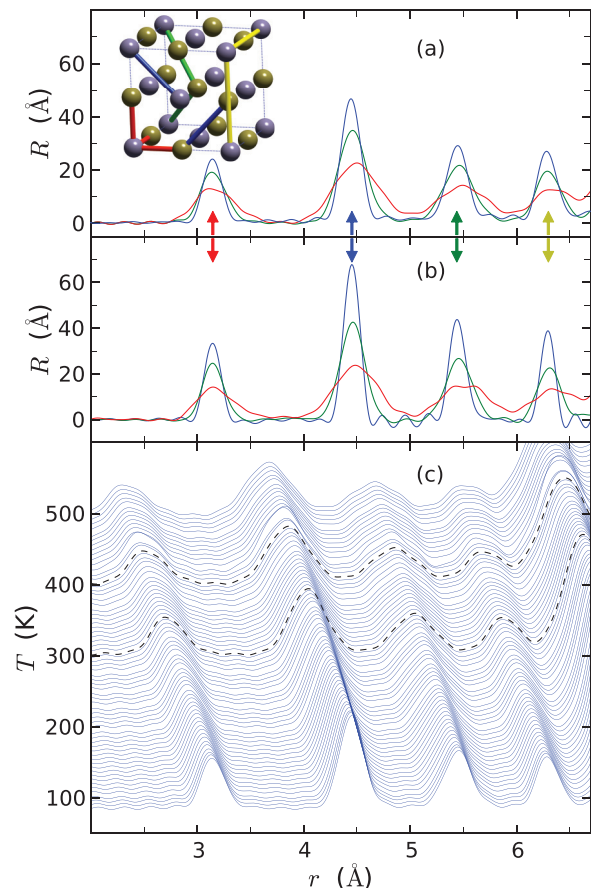


FIG. 2. (Color online) RDF, $R(r)$, in the 2.7–6.7- \AA range for SnTe obtained from (a) x-ray measurements at 10 K (blue), 150 K (green), and 500 K (red) and (b) neutron measurements at 10 K (blue), 150 K (green), and 450 K (red). (c) Waterfall plot of $R(r)$ obtained from x-ray measurements. Data are offset for clarity. Inset to (a): $Fm\bar{3}m$ model with contributions to $R(r)$ color coded. Sn (Te) atoms shown as gray (brown) spheres.

Despite the small distortion, the ferroelectric transition can be clearly seen in our data in both the local and average structures with a T_c of $\sim 80 \text{ K}$, as shown in the inset to Fig. 1(a). Above T_c both the local and average structures become cubic as shown by the fits in Fig. 1. The fits are exceptionally good, which vouches for the high quality of our data and lends confidence to the claim that the cubic model accurately describes the average and local structure at this temperature.

We now consider the evolution of the *local* structure with temperature in SnTe. Figure 2(a) shows the first four peaks of the x-ray RDF at selected temperatures. 10 and 150 K are representative of the rhombohedral and cubic phases, respectively. At 150 K the RDF peaks are at the characteristic positions for a rocksalt structure with the first peak coming from Sn-Te nearest-neighbor pairs, the second from next-nearest-neighbor pairs (Sn-Sn and Te-Te), etc. [see inset to Fig. 2(a)]. At this temperature the peaks are Gaussian functions convolved with a sinc function coming from the finite-range Fourier transform.³⁸ The Gaussian line shape is characteristic of quasiharmonic thermal motion around a single average bond length.³⁸ Note that the first peak appears slightly asymmetric

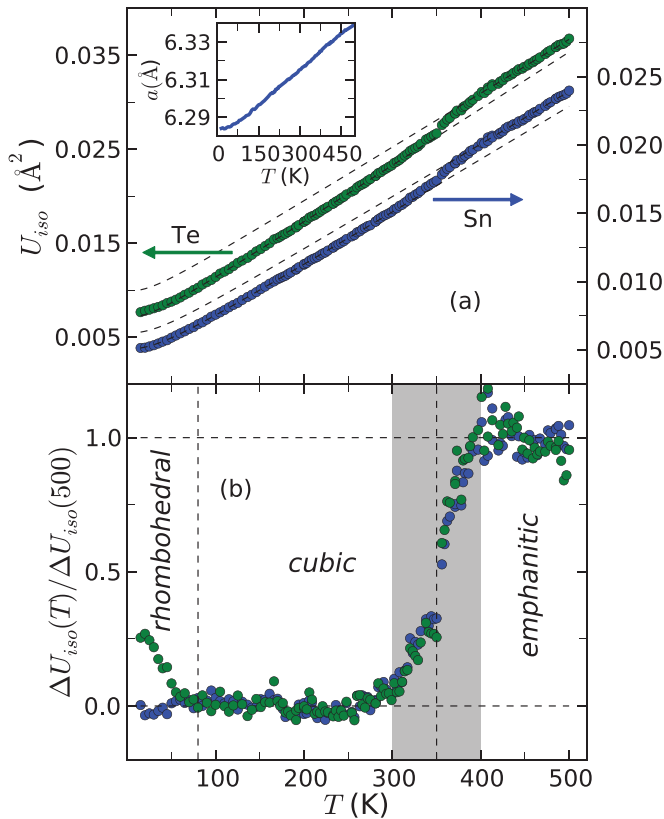


FIG. 3. (Color online) (a) $U_{150}(T)$ for Sn (blue) and Te (green) extracted by fitting an $Fm\bar{3}m$ model to SnTe x-ray PDFs over the entire temperature range studied. Dashed black lines represent best fits to the 100–300-K range and 400–500-K range using the Debye model. (b) Normalized difference between measured data and Debye model, $\Delta U_{150} = U_{150}^{\text{obs}} - U_{150}^{\text{calc}}$. Vertical dashed lines indicate rhombohedral and emphanitic transformation temperatures. Inset to (a): temperature dependence of SnTe lattice parameter.

with additional weight on the high- r side of the peak. However, the higher- r peaks are more symmetric—this is typical of anharmonic motion of atoms in a single wellled potential.

The RDF at 10 K is similar; the first four peaks appear symmetric and Gaussian. The peaks are narrower and taller, with larger termination ripples, which is expected from the reduced thermal motion. That the rhombohedral distortion does not dramatically alter the peak shapes at this temperature is not surprising given the size of the atomic displacements; the local distortion is quite small (the relative sublattice shift is ~ 0.02 Å) and cannot be casually noticed at this length scale without careful fitting.

The RDF at 500 K, however, differs dramatically from those at 15 and 150 K. It is clear that the first peak is not only asymmetric, but is composed of two or more incompletely resolved peaks. In fact, each of the first four peaks appears to be multicomponent. As noted above, a non-Gaussian nearest-neighbor peak shape may be ascribed to anharmonicity in a single-welled potential. However, the appearance of the first four RDF peaks at 500 K indicates the existence of *multiple*, incompletely resolved long and short bond peaks, consistent with the presence of local atomic displacements away from the average rocksalt arrangement. The multivalued

peaks are similar to what was observed in PbTe,²¹ though the effects appear much more pronounced in the current case. RDFs obtained from neutron data [Fig. 2(b)] confirm these observations—the low- r peaks at 15 and 150 K are highly symmetric, while the 450-K RDF clearly shows peak splitting in each of the first four peaks.

In order to determine the temperature at which these distortions to the local structure emerge we show the evolution of the first four x-ray RDF peaks in a waterfall plot from 100 to 500 K [Fig. 2(c)]. Visual inspection of the data shows that the peaks broaden but remain mostly symmetric up to ~ 300 K. Above 300 K peak splitting becomes apparent—most noticeably, the third peak grows both high- r and low- r shoulders and the fourth peak splits into two peaks. By 400 K these effects appear to saturate and the distortion does not grow appreciably from 400 to 500 K.

To quantify the temperature dependence of this local distortion the x-ray PDFs were fit with a cubic model ($Fm\bar{3}m$) from 2.5 to 30 Å over the entire temperature range studied. Although excellent fits were obtained for all temperatures, anomalies were observed in the isotropic atomic displacement parameters (ADPs), U_{150} , which are intended to capture thermal motion, but can also record static atomic displacements that are not allowed by the model. Figure 3(a) shows the temperature dependence of U_{150} for Sn and Te obtained from the fits. Both curves follow linear trends in the 100–300-K range. However, below 100 K and above 300 K there is an upward deviation.

The canonical behavior of ADPs is often described by a Debye model⁴⁴ with two free parameters: the Debye temperature Θ_D and an effective offset that is sensitive to static or nonthermal disorder in the material. Best fits to the experimental U_{150} curves were made for the 100–300-K range; these are represented as dashed black lines in Fig. 3(a). The resulting Debye temperatures were 178(1) and 139(2) K for Sn and Te, respectively, in agreement with earlier reports.^{45,46}

The deviation below 100 K can be readily explained by the phase transition to a long-range-ordered rhombohedral structure. When an incorrect structural model is used to fit PDF data the fit will respond by setting the ADPs to anomalously large values. However, the remarkable result of this experiment is the observation of a similar upward deviation in U_{150} occurring *on warming* near room temperature, although there is no long-range structural phase transition at 300 K or above. At temperatures above 400 K the U_{150} curves match the slopes of those below 300 K, but with offsets larger by $0.002(1)$ Å² and $0.003(1)$ Å² for Sn and Te, respectively, corresponding to root-mean-square local atomic displacements of ~ 0.05 Å. Models explicitly allowing for local distortions produced still larger atomic off-centering of 0.1–0.2 Å in the saturation region (400–500 K). The temperature response and distortion size are similar to what was observed in the emphanitic phase of PbTe and PbS.²¹

The crossover behavior may be isolated from the underlying thermal effects by subtracting the lower offset Debye curve from the experimental data as shown in Fig. 3(b). Doing so clearly defines two transformations: a phase transition at 80 K where both the local and average structures simultaneously change, and a crossover above 300 K that we ascribe to emphanic, where the sample becomes locally distorted while the global symmetry remains cubic. These transformations

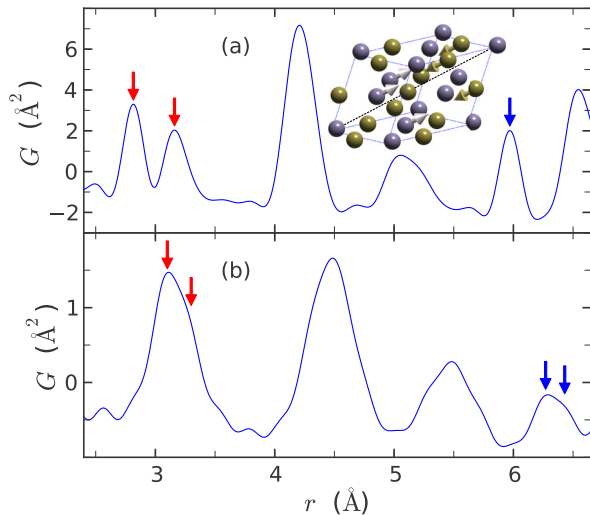


FIG. 4. (Color online) $G(r)$ for (a) GeTe at 100 K and (b) SnTe at 400 K. Red arrows indicate splitting of nearest-neighbor peak due to rhombohedral distortion in GeTe and emphanitic distortion in SnTe. Blue arrows indicate lattice repeat distance which is split in SnTe, but not in GeTe. Inset to (a): $R3m$ distortion to cubic structure (not to scale). Arrows indicate sublattice motion along [111] direction (dashed black line).

are separated by 200 K, suggesting that the emphanitic and ferroelectric phases are not closely related. Additionally, the emphanitic phase shows local atomic off-centering that is an order of magnitude larger than that observed in the ferroelectric phase. Thus, the emphanitic phase does not appear to be a re-entrant phenomenon.

Further evidence that the emphanitic distortion is unrelated to ferroelectricity comes from a comparison of the symmetries of the two regimes. In the absence of a specific model for the emphanitic phase, it is useful to directly compare raw PDF data. As previously mentioned, the symmetry of the ferroelectric phase is the same as that found in α -GeTe—the unit cell undergoes a rhombohedral distortion and the sublattices separate along the [111] direction. As shown in Fig. 4(a) for GeTe this distortion splits the nearest-neighbor PDF peak by ~ 0.3 Å, but leaves the lattice repeat distance at $r = 6$ Å unchanged, a general feature of the $R3m$ ferroelectric distortion in binary chalcogenides. As shown in Fig. 4(b) a similar splitting is observed in the nearest-neighbor peak in the emphanitic phase of SnTe. However, in this case the lattice

repeat distance also appears split by nearly 0.2 Å. This provides model independent evidence that the emphanitic distortion in SnTe does not share the same [111] symmetry as the low-temperature ferroelectric phase, in agreement with earlier PDF and diffraction results from PbTe.^{21,25} Several models allowing for atomic off-centering were applied to the SnTe PDFs to determine the correct symmetry of the emphanitic phase. Although none of the distorted structures exactly reproduced all the low- r features of the emphanitic PDFs the best approximation was a [100] PbO-like distortion;⁴⁷ this structure was identified as the most likely symmetry of the emphanitic state in PbTe.^{21,25}

IV. CONCLUSION

The nature of the emphanitic behavior in SnTe allows us to answer key questions about the effect. First, it is not, as previously supposed,²¹ related to fluctuations of the incipient ferroelectric state of the material. Second, as indicated by the abrupt temperature response, it is unlikely to originate from simple anharmonic effects.³⁰ Pb and Sn both possess an electron lone pair (LP) which can be in an active (LPA: resulting in a low-symmetry structure) or inactive (LPI: resulting in a high-symmetry structure) state depending on the compound in question.^{48–51} A possible explanation for emphanitis is a crossover from an LPI state at low temperature to an LPA state at high temperature, brought on by the dramatic lattice expansion in these materials. Our results suggest that there may be a broad class of compounds that display emphanitic behavior, prompting further studies to identify these materials. Additionally, theoretical calculations and modeling of the physical properties of the IV–VI materials already identified should take the emphanitic behavior into account.

ACKNOWLEDGMENTS

Data collection, analysis, and modeling were supported by US DOE, Office of Science, Office of Basic Energy Sciences (DOE-BES) under Contract No. DE-AC02-98CH10886. NSLS is operated by BNL under the same Contract No. Sample preparation and characterization were supported by DOE-BES under Contract No. DE-AC02-06CH11357. Neutron PDF experiments were carried out on NPDF at LANSCE, funded by DOE BES; Los Alamos National Laboratory is operated by Los Alamos National Security LLC under Contract No. DE-AC52-06NA25396.

¹J. F. Scott, *Rev. Mod. Phys.* **46**, 83 (1974).

²A. D. Bruce and R. A. Cowley, *Structural Phase Transitions* (Taylor and Francis, London, UK, 1981).

³R. M. Hazen and L. W. Finger, *Comparative Crystal Chemistry: Temperature, Pressure, Composition and the Variation of Crystal Structure* (Wiley, New York, 1982).

⁴A. Bray, *Adv. Phys.* **43**, 357 (1994).

⁵D. Khomskii, *Basic Aspects of the Quantum Theory of Solids: Order and Elementary Excitations* (Cambridge University Press, Cambridge, England, 2010).

⁶S. Filatov, *Crystallogr. Rep.* **56**, 953 (2011).

⁷U. Müller, *Symmetry Relationships Between Crystal Structures: Applications of Crystallographic Group Theory in Crystal Chemistry* (Oxford University Press, Oxford, 2013), Vol. 18.

⁸A. D. Bruce, K. A. Müller, and W. Berlinger, *Phys. Rev. Lett.* **42**, 185 (1979).

⁹W. David, R. Ibberson, T. Dennis, J. Hare, and K. Prassides, *Europhys. Lett.* **18**, 219 (1992).

¹⁰H. Kim, M. Kaviani, J. C. Thomas, A. Van der Ven, C. Uher, and B. Huang, *Phys. Rev. Lett.* **105**, 265901 (2010).

- ¹¹L. Cañadillas Delgado, O. Fabelo, J. A. Rodríguez-Velamazán, M.-H. Lemée-Cailleau, S. A. Mason, E. Pardo, F. Lloret, J.-P. Zhao, X.-H. Bu, V. Simonet, C. V. Colin, and J. Rodríguez-Carvajal, *J. Am. Chem. Soc.* **134**, 19772 (2012).
- ¹²A. M. Milinda Abeykoon, E. S. Božin, W.-G. Yin, G. Gu, J. P. Hill, J. M. Tranquada, and S. J. L. Billinge, *Phys. Rev. Lett.* **111**, 096404 (2013).
- ¹³J. Rodríguez-Carvajal, M. Hennion, F. Moussa, A. H. Moudden, L. Pinsard, and A. Revcolevschi, *Phys. Rev. B* **57**, R3189 (1998).
- ¹⁴X. Qiu, Th. Proffen, J. F. Mitchell, and S. J. L. Billinge, *Phys. Rev. Lett.* **94**, 177203 (2005).
- ¹⁵K. Itoh, L. Zeng, E. Nakamura, and N. Mishima, *Ferroelectrics* **63**, 29 (1985).
- ¹⁶G. H. Kwei, A. C. Lawson, S. J. L. Billinge, and S.-W. Cheong, *J. Phys. Chem.* **97**, 2368 (1993).
- ¹⁷B. Zalar, V. V. Laguta, and R. Blinc, *Phys. Rev. Lett.* **90**, 037601 (2003).
- ¹⁸E. A. Stern, *Phys. Rev. Lett.* **93**, 037601 (2004).
- ¹⁹E. Steigmeier and G. Harbeke, *Solid State Commun.* **8**, 1275 (1970).
- ²⁰T. Matsunaga, P. Fons, A. Kolobov, J. Tominaga, and N. Yamada, *Appl. Phys. Lett.* **99**, 231907 (2011).
- ²¹E. S. Božin, C. D. Malliakas, P. Souvatzis, T. Proffen, N. A. Spaldin, M. G. Kanatzidis, and S. J. L. Billinge, *Science* **330**, 1660 (2010).
- ²²Y. Y. Peter and M. Cardona, *Fundamentals of Semiconductors: Physics and Materials Properties* (Springer, New York, 2010).
- ²³R. N. Tauber, A. A. Machonis, and I. B. Cadoff, *J. Appl. Phys.* **37**, 4855 (1966).
- ²⁴A. F. Joffe, *Can. J. Phys.* **34**, 1342 (1956).
- ²⁵S. Kastbjerg, N. Bindzus, M. Søndergaard, S. Johnsen, N. Lock, M. Christensen, M. Takata, M. A. Spackman, and B. B. Iversen, *Adv. Funct. Mater.* **23**, 5477 (2013).
- ²⁶Y. Zhang, X. Ke, P. R. C. Kent, J. Yang, and C. Chen, *Phys. Rev. Lett.* **107**, 175503 (2011).
- ²⁷H. Kim and M. Kaviani, *Phys. Rev. B* **86**, 045213 (2012).
- ²⁸T. Keiber, F. Bridges, and B. C. Sales, *Phys. Rev. Lett.* **111**, 095504 (2013).
- ²⁹T. Shiga, J. Shiomi, J. Ma, O. Delaire, T. Radzynski, A. Lusakowski, K. Esfarjani, and G. Chen, *Phys. Rev. B* **85**, 155203 (2012).
- ³⁰O. Delaire, J. Ma, K. Marty, A. F. May, M. A. McGuire, M.-H. Du, D. J. Singh, A. Podlesnyak, G. Ehlers, M. D. Lumsden, and B. C. Sales, *Nat. Mater.* **10**, 614 (2011).
- ³¹K. M. Ø. Jensen, E. S. Božin, C. D. Malliakas, M. B. Stone, M. D. Lumsden, M. G. Kanatzidis, S. M. Shapiro, and S. J. L. Billinge, *Phys. Rev. B* **86**, 085313 (2012).
- ³²R. Bate, D. Carter, and J. Wrobel, *Phys. Rev. Lett.* **25**, 159 (1970).
- ³³H. Burkhard, O. Bauer, and A. Lopez-Otero, *J. Opt. Soc. Am.* **67**, 943 (1977).
- ³⁴D. Zagorac, K. Doll, J. C. Schön, and M. Jansen, *Chem. Eur. J.* **18**, 10929 (2012).
- ³⁵G. Pawley, W. Cochran, R. Cowley, and G. Dolling, *Phys. Rev. Lett.* **17**, 753 (1966).
- ³⁶L. Brillson, E. Burstein, and L. Muldower, *Phys. Rev. B* **9**, 1547 (1974).
- ³⁷T. Proffen, T. Egami, S. J. L. Billinge, A. K. Cheetham, D. Louca, and J. B. Parise, *Appl. Phys. A* **74**, s163 (2002).
- ³⁸T. Egami and S. J. L. Billinge, *Underneath the Bragg Peaks: Structural Analysis of Complex Materials*, 2nd ed. (Elsevier, Amsterdam, 2013).
- ³⁹P. J. Chupas, X. Qiu, J. C. Hanson, P. L. Lee, C. P. Grey, and S. J. L. Billinge, *J. Appl. Crystallogr.* **36**, 1342 (2003).
- ⁴⁰P. Juhas, T. Davis, C. L. Farrow, and S. J. L. Billinge, *J. Appl. Crystallogr.* **46**, 560 (2013).
- ⁴¹P. F. Peterson, M. Gutmann, T. Proffen, and S. J. L. Billinge, *J. Appl. Crystallogr.* **33**, 1192 (2000).
- ⁴²P. Littlewood, *J. Phys. C: Solid State Phys.* **13**, 4875 (1980).
- ⁴³M. J. Polking, M. Han, A. Yourdkhani, V. Petkov, C. F. Kisielowski, V. V. Volkov, Y. Zhu, G. Caruntu, A. P. Alivisatos, and R. Ramesh, *Nat. Mater.* **11**, 700 (2012).
- ⁴⁴P. Debye, *Ann. Phys. (Berlin, Ger.)* **344**, 789 (1912).
- ⁴⁵G. J. Kemerink, N. Ravi, and H. de Waard, *J. Phys. C: Solid State Phys.* **19**, 4897 (1986).
- ⁴⁶W. Keune, *Phys. Rev. B* **10**, 5057 (1974).
- ⁴⁷W. J. Moore, Jr. and L. Pauling, *J. Am. Chem. Soc.* **63**, 1392 (1941).
- ⁴⁸I. Lefebvre, M. A. Szymanski, J. Olivier-Fourcade, and J. C. Jumas, *Phys. Rev. B* **58**, 1896 (1998).
- ⁴⁹U. V. Waghmare, N. A. Spaldin, H. C. Kandpal, and R. Seshadri, *Phys. Rev. B* **67**, 125111 (2003).
- ⁵⁰A. Walsh and G. W. Watson, *J. Phys. Chem.* **109**, 18868 (2005).
- ⁵¹Y. Du, H.-C. Ding, L. Sheng, S. Y. Savrasov, X. Wan, and C.-G. Duan, *J. Phys.: Condens. Matter* **26**, 025503 (2014).

Low-temperature structural and transport anomalies in Cu₂Se

Hang Chi,¹ Hyoungchul Kim,^{2,7} John C. Thomas,³ Guangsha Shi,³ Kai Sun,³ Milinda Abeykoon,⁴ Emil S. Bozin,⁴ Xiaoya Shi,⁴ Qiang Li,⁴ Xun Shi,⁵ Emmanouil Kioupakis,³ Anton Van der Ven,^{3,6} Massoud Kaviani,² and Ctirad Uher^{1,*}

¹*Department of Physics, University of Michigan, Ann Arbor, Michigan 48109, USA*

²*Department of Mechanical Engineering, University of Michigan, Ann Arbor, Michigan 48109, USA*

³*Department of Materials Science and Engineering, University of Michigan, Ann Arbor, Michigan 48109, USA*

⁴*Condensed Matter Physics and Materials Science Department, Brookhaven National Laboratory, Upton, New York 11973, USA*

⁵*State Key Laboratory of High Performance Ceramics and Superfine Microstructure, Shanghai Institute of Ceramics, Chinese Academy of Sciences, 1295 Dingxi Road, Shanghai 200050, China*

⁶*Materials Department, University of California, Santa Barbara, California 93106, USA*

⁷*High-Temperature Energy Materials Research Center, Korea Institute of Science and Technology, Seoul 136-791, Republic of Korea*

(Received 14 March 2014; revised manuscript received 7 May 2014; published 28 May 2014; corrected 10 June 2014)

Through systematic examination of symmetrically nonequivalent configurations, first-principles calculations have identified a new ground state of Cu₂Se, which is constructed by repeating sextuple layers of Se-Cu-Cu-Cu-Cu-Se. The layered nature is in accord with electron and x-ray diffraction studies at and below room temperature and also is consistent with transport properties. Magnetoresistance measurements at liquid helium temperatures exhibit cusp-shaped field dependence at low fields and evolve into quasilinear field dependence at intermediate and high fields. These results reveal the existence of weak antilocalization effect, which has been analyzed using a modified Hikami, Larkin, and Nagaoka model, including a quantum interference term and a classical quadratic contribution. Fitting parameters suggest a quantum coherence length L of 175 nm at 1.8 K. With increasing temperature, the classical parabolic behavior becomes more dominant, and L decreases as a power law of $T^{-0.83}$.

DOI: [10.1103/PhysRevB.89.195209](https://doi.org/10.1103/PhysRevB.89.195209)

PACS number(s): 71.55.Ht, 72.15.Rn, 72.80.Jc

Transition metal chalcogenides (TMCs) allow fruitful research in contemporary condensed matter physics, leading to intriguing discoveries and promising applications [1]. For example, the silver chalcogenides (e.g., Ag₂Te) are renowned for their extraordinary large magnetoresistance (MR) [2] and have been recently identified as a new class of binary topological insulators (TI) with a highly anisotropic Dirac cone [3]. Additionally, transition metal dichalcogenides (TMDCs) MX_2 , where M is a transition metal element and X is a chalcogen atom (S, Se, or Te), are well known for their two-dimensional (2D) structures formed by X - M - X layers with strong in-plane bonding and weak out-of-plane interactions. The unique intrinsic 2D nature of TMDCs has stimulated the search for novel states of matter, for instance, by offering a coexistence of superconductivity and the Mott commensurate charge density wave (CCDW) phase in 1T-TaS₂ [4]. Furthermore, the electronic band structures of TMDCs are believed to host exotic spin-orbit phenomena such as the systematic crossover from weak antilocalization (WAL) to weak localization (WL) [5,6].

As an important member of the TMC family, the superionic Cu₂Se has also received heightened attention in recent developments of thermoelectrics [7] and optoelectronics [8] due to the unique transport properties associated with its structural phase transition occurring at ~ 400 K. The exact temperature of this well-known reversible second-order phase transition from the ordered room temperature (RT) monoclinic α phase to the disordered high temperature (HT) cubic β phase depends on the Cu deficiency in the metal sublattice [9] and is found to be tunable upon iodine doping on the selenium sites [10]. It is generally accepted that the disordered

HT β phase of Cu₂Se [space group $Fm\bar{3}m(O_h^5, \#225)$] is constructed by statistically distributing Cu atoms over the $8c$ tetrahedral sites in a face-centered cubic (fcc) matrix formed by Se atoms. However, the structural determination of the ordered phase(s) still remains controversial [11]. Furthermore, despite some rare reports on samples with quite high Cu deficiency (e.g., Cu_{2-x}Se, $0.20 \leq x \leq 0.25$) [12], a detailed study of the transport properties of stoichiometric Cu₂Se at low temperatures is still desirable. In this paper, we report first-principles determination of the ground state along with several unexpected experimental findings regarding the low-temperature transport properties of Cu₂Se, which may indicate an intrinsic 2D quantum behavior.

The ground state of Cu₂Se was obtained via structural relaxation of the cubic HT β phase. In order to determine the most stable structure, Cu atoms were randomly distributed onto the $32f$ trigonal sites in the fcc Se matrix, which form tetrahedrons around the $8c$ tetrahedral sites. Note that for stoichiometric Cu₂Se, only one-quarter of the $32f$ sites are occupied by Cu atoms. Symmetrically distinct configurations with up to eight Cu atoms have been studied based on the Cu occupancy on the sublattice [13]. Subsequent density functional theory (DFT) calculations of the formation energy have allowed us to identify stable configurations of Cu₂Se. The DFT-based energies were obtained using the Vienna *Ab initio* Simulation Package (VASP) [14] within the Perdew-Burke-Ernzerhof (PBE) parameterization of the generalized gradient approximation (GGA) for exchange and correlation [15] and using the projector-augmented wave (PAW) method [16,17]. The electronic band structure and density of states (D_e) were calculated using more advanced Heyd-Scuseria-Ernzerhof (HSE06) hybrid functional [18,19]. VASP and PHONON [20] codes were then used for the *ab initio* phonon calculations.

*Corresponding author: cuh@umich.edu

TABLE I. Calculated properties of Cu_2Se . The literature results are also listed. ΔE_0 (eV/u.f.), E_g (eV), $u_{p,g,A}$ (m/s), c_{ij} (GPa), and c_p (J/mol-K, at 300 K) are the formation energy per unit formula with respect to the proposed structure, electronic band gap, averaged acoustic phonon group velocity, elastic constants, and specific heat capacity.

	ΔE_0		E_g	$u_{p,g,A}$	c_p	c_{11}	c_{22}	c_{33}	c_{44}
Cu_2Se	0		1.03	2635	72.1	11.14	102.49	88.62	36.75
Literature	0.003 ^a	0.046 ^b	1.20 ^c	2918 ^d	81.6 ^e	—	—	—	—
	c_{55}	c_{66}	c_{12}	c_{13}	c_{23}	c_{15}	c_{25}	c_{35}	c_{46}
Cu_2Se	14.65	12.82	6.81	6.90	42.37	-5.10	14.51	22.42	11.30
Literature	—	—	—	—	—	—	—	—	—

^a $P2_1/c$ structure, from Ref. [23].

^b $C2/c$ structure, from Ref. [10].

^cFrom Ref. [21].

^dFrom Ref. [7].

^eFrom Ref. [22].

The total energy and Hellmann-Feynman (HF) forces were found starting from the fully relaxed configuration, such that initial ionic forces were less than 10^{-5} eV/Å. The ionic displacements of 0.03 Å of selected atoms were sampled along the x , y , and z directions. All phonon and thermodynamic properties were predicted using a fit of interatomic force constant tensors to the calculated HF forces. Diagonalization of the dynamical matrix yields the phonon dispersion from which the density of states (D_p) was obtained. Physical properties of Cu_2Se are summarized in Table I, with the literature results also listed [21,22].

The proposed ground state of Cu_2Se crystallizes in space group $P2_1/c(C_{2h}^5, \#14)$, with optimized lattice parameters $a = 7.453$ Å, $b = 4.322$ Å, $c = 6.880$ Å, $\alpha = 90.00^\circ$, $\beta = 70.62^\circ$, $\gamma = 90.00^\circ$, and atomic occupation Cu1 (0.06111, 0.58259, 0.15164), Cu2 (0.80599, 0.92292, 0.05310), and Se (0.28070, 0.93855, 0.25485). As shown in Fig. 1(a), the ground state of Cu_2Se has quasi-2D characteristics typified by the Se-Cu-Cu-Cu-Cu-Se type of sextuple layers (thickness $t = 3.95$ Å), which are interconnected via weak Se-Se bonds (gap $\delta = 3.08$ Å). Compared with recent literature results using rather different approaches, the monoclinic structure of Cu_2Se obtained here has lower formation energy per unit formula (Table I) [10,23]. The proposed structure is also dynamically stable due to the absence of the soft modes in the phonon spectrum, as is evident in Fig. 1(d). As shown in Fig. 1(e), the monoclinic Cu_2Se is confirmed to be semiconducting, and the electronic band gap E_g (using HSE) is found to be 1.03 eV, which agrees very well with the experimental value of 1.20 eV [21] and is the best first-principles result in comparison to the existing literature values [24].

Polycrystalline Cu_2Se samples were prepared following the recipes described elsewhere [10]. Powdered samples were used for the temperature-dependent x-ray diffraction (XRD) experiments at the X17A beamline of the National Synchrotron Light Source at the Brookhaven National Laboratory. The setup utilized cylindrical geometry with an x-ray beam of 67.42 keV ($\lambda = 0.1839$ Å), a Perkin-Elmer image plate detector placed perpendicular to the primary beam path $d = 204.134$ mm away from the Kapton capillary containing the pulverized sample, and an Oxford Cryosystem 700 for temperature control. A JEOL 2010F transmission electron microscope (TEM) operating at 200 kV was used to

collect selected area electron diffraction (SAED) patterns for the analysis of the detailed microstructure. Simulated SAED patterns were obtained using the CrystalKit software package.

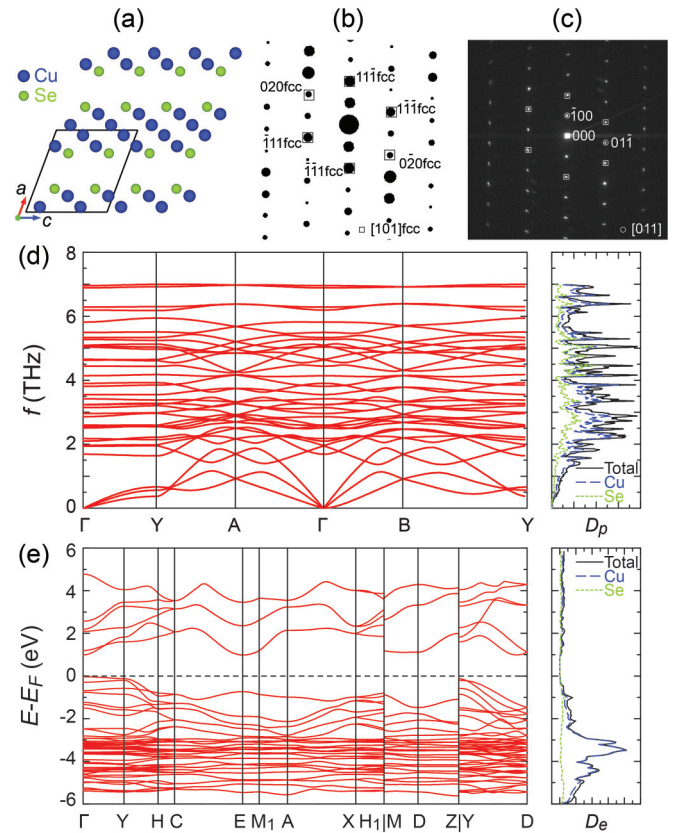


FIG. 1. (Color online) (a) Projected (along the monoclinic b axis) *ab initio* ground state structure of Cu_2Se formed by repeating sextuple layers of Se-Cu-Cu-Cu-Cu-Se. (b) Simulated SAED pattern along the zone axis $[011]$ of the monoclinic phase and the $[101]_{\text{fcc}}$ with the diffractions from the fcc structure labeled as squares. (c) The experimental SAED pattern along the $[011]$ zone axis of the monoclinic phase. (d) The calculated phonon band structure and density of states (D_p) indicate the proposed structure is dynamically stable. (e) The electronic band structure and density of states (D_e) calculated using HSE hybrid functional suggests that Cu_2Se is a semiconductor with band gap $E_g = 1.03$ eV.

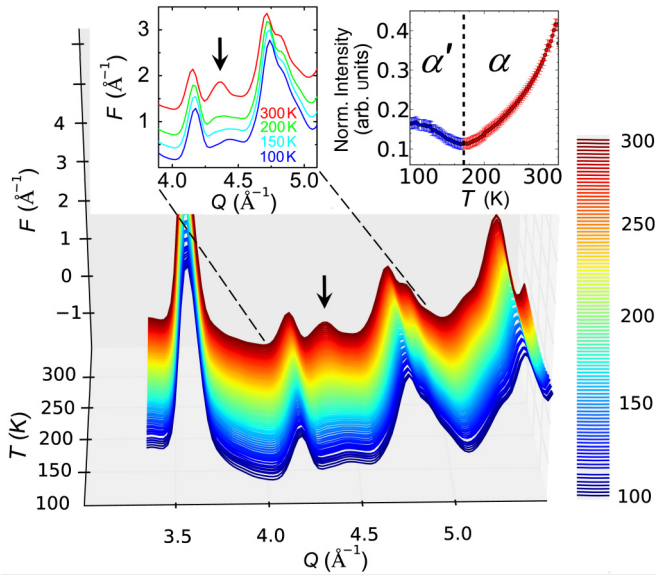


FIG. 2. (Color online) Reduced total scattering XRD structure function, $F(Q) = Q[S(Q) - 1]$, where $S(Q)$ is the total scattering structure function and Q is the momentum transfer, in the 100–300 K range (main panel). Temperature evolution of the normalized intensity around (400) reflection in cubic notation, marked with an arrow in the upper left inset ($Q \sim 4.3 \text{ \AA}^{-1}$). This region is sensitive to subtle structural changes and evidences the α' to α superstructure transition at around 175 K, as denoted by a vertical dashed line (upper right inset). Red symbols denote the evolution with temperature of the intensity peaked at $Q \sim 4.362 \text{ \AA}^{-1}$, while the blue symbols show the evolution of the intensity peaked at $Q \sim 4.436 \text{ \AA}^{-1}$.

The chemical composition analyses were conducted using energy dispersive spectrometry (EDS). The low-temperature transport property measurements were carried out in the temperature range of 1.8–300 K on samples with dimensions $6 \times 2 \times 1 \text{ mm}^3$ in a Quantum Design Magnetic Property Measurement System (MPMS) (magnetic field up to 5.5 T) using a Linear Research ac bridge with 16 Hz excitation.

The EDS analysis on the TEM specimen indicates it contains 66.3 at.% Cu and 33.7 at.% Se, which verifies the Cu_2Se chemical composition. The simulated SAED pattern along the monoclinic [011] zone axis is presented in Fig. 1(b), where the monoclinic [011] axis of the proposed ground state is equivalent to an fcc [101] axis. Spots labeled by the square symbols are indexed according to the fcc diffraction pattern, which corresponds to the SAED pattern of the HT cubic β phase [10]. Figure 1(c) displays the experimental SAED pattern along the monoclinic [011] axis. The agreement between the experimental and theoretical patterns has verified the predicted layered structure of the ground state. Additional superstructural diffraction spots/strips have been also observed along other zone axes. This may result from the different packing order of the sextuple layers and/or Cu-vacancy ordering at finite temperature when thermal energy starts to affect the structure [25].

To further understand the structure, low-temperature XRD measurements have been performed. In line with earlier reports [12,25–28], a reversible α to α' superstructure transition is also evident in the sample studied here via an intensity

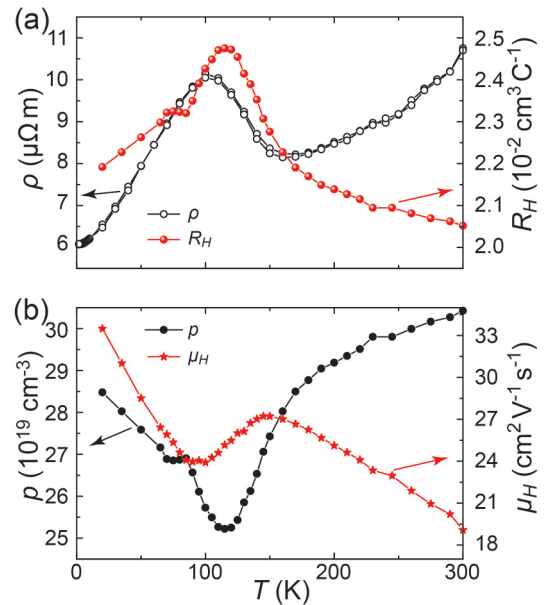


FIG. 3. (Color online) Low-temperature transport profile of stoichiometric Cu_2Se as a function of temperature. (a) Electrical resistivity ρ and Hall coefficient R_H show anomalies at 100–150 K, where ρ measurements overlap upon either warm-up or cooldown in the temperature. (b) Hall density ρ and Hall mobility μ_H .

rearrangement of the multiplet of superlattice peaks located in the Q region close to the (400) reflection in cubic notation (Fig. 2). This is found from the assessment of the systematic temperature-dependent XRD data, collected in the 100–300 K range upon warming. The transfer of intensity occurs at around 175 K (upper right inset in Fig. 2).

We were interested to find out what the impact is of such structural changes on the transport properties. As shown in Fig. 3, the above mentioned α to α' type of transition has a strong imprint on the temperature dependence of the electrical resistivity (20% effect) and the Hall effect. The electrical resistivity of Cu_2Se exhibits a highly anomalous behavior in the 100–150 K temperature range, which is also accompanied by a large peak in the Hall effect. We speculate that such features might represent a possible charge density wave (CDW) transition [29] as a result of the distortion/redistribution of the sextuple layers upon temperature change. However, further theoretical and experimental efforts are needed to clarify the issue. We note that in spite of looking for accompanying anomalies in the Seebeck effect, thermal conductivity, and the specific heat, we found none. The anomalous behavior seems to be limited to galvanomagnetic transport only.

At even lower temperatures (1.8–30 K), the MR of Cu_2Se is extraordinary, as shown in Fig. 4(a). The semiclassical transport theory predicts a quadratic field-dependent MR in the low-field range, which saturates in high fields. In distinct contrast to the traditional theory, the MR of Cu_2Se at low temperatures exhibits a WAL-like cusp, which is suppressed when the temperature increases. In addition, at high fields, the MR increases with the increasing field in a linear fashion with no sign of saturation up to $B = 5 \text{ T}$.

We account for the field dependence of differential magnetoconductance (MC) over the entire range of fields and

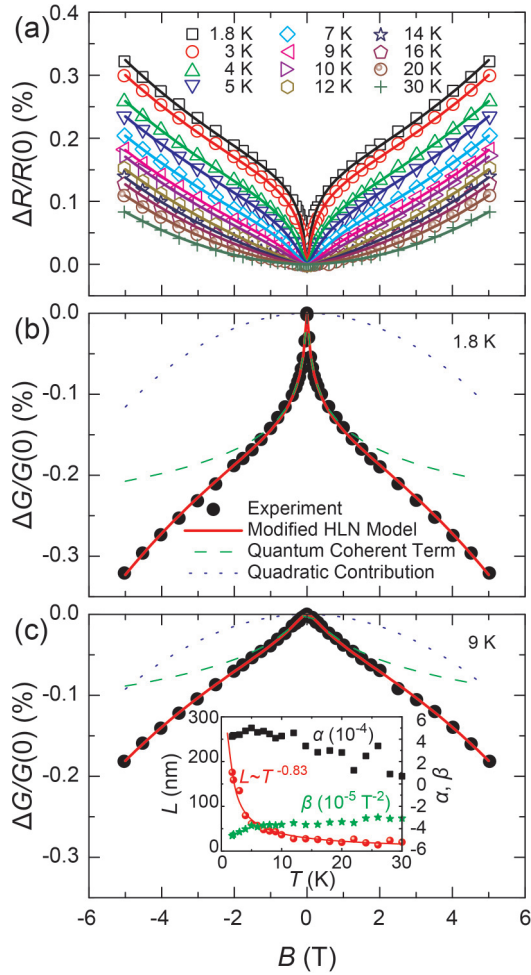


FIG. 4. (Color online) (a) Magnetoresistance profile (as a function of magnetic field intensity) of Cu_2Se at various temperatures (1.8–30 K) indicating evolution of weak antilocalization behavior as the temperature is lowered to 1.8 K. Theoretical fitting to differential magnetoconductance using a modified HLN model at selected temperatures (b) 1.8 K and (c) 9 K. The inset of (c) depicts the fitting parameters showing a power law behavior ($\sim T^{-0.83}$) of the quantum interference length.

temperatures with a modified Hikami, Larkin, and Nagaoka (HLN) quantum interference model [30,31]:

$$\begin{aligned}
 MC &\equiv \frac{G(B) - G(0)}{G(0)} \\
 &= -\alpha \left[\psi \left(\frac{\hbar}{4eL^2B} + \frac{1}{2} \right) - \ln \left(\frac{\hbar}{4eL^2B} \right) \right] + \beta B^2,
 \end{aligned} \tag{1}$$

where ψ is the digamma function. The original formalism of the simple HLN model was developed to characterize the transport properties of a 2D system where the conductance quantum ($2e^2/h$) naturally comes into play. In order to compensate for the bulk effects of this quasi-2D layered structure of Cu_2Se , we have normalized the conductance using the zero field value and introduced a dimensionless fitting parameter α . Here L is the phase coherence length, and β is the quadratic coefficient arising from additional scattering terms. The HLN model has been successfully used in explaining the magnetotransport phenomena in various 2D material systems like Bi_2Se_3 [32,33], $\text{Bi}_2\text{Se}_2\text{Te}$ [34], and $\text{Bi}_2\text{Te}_2\text{Se}$ thin films [31]. It is worth emphasizing that such a modified model simultaneously accounts for the quantum phase interference cusp at low fields as well as the linearlike MR at high fields. It is shown that the additional quadratic term compensates the logarithmic dependence of the quantum interference at high fields, leading to an intermediate linear field dependence of MR. The overall fitting result, along with the corresponding quantum interference term and quadratic term, is shown in Figs. 4(b) and 4(c) for $T = 1.8$ K and 9 K, respectively. In the present sample, the phase coherence length L is 175 nm at 1.8 K and decreases following a power law of $T^{-0.83}$ temperature dependence. The successful application of the HLN model in Cu_2Se is advocating for the 2D quantum nature of the new phase and likely provides another candidate of bulk materials with monolayer behavior, apart from the newly discovered ReS_2 [35].

In summary, the ground state of Cu_2Se , typified by Se-Cu-Cu-Cu-Cu-Cu-Se sextuple layers, has been identified using *ab initio* calculations. Upon cooldown to liquid nitrogen temperatures, the transport property measurements along with the structural analyses have confirmed the existence of yet another phase transition of possible CDW character. The unusual manifestation of the WAL-type of MR profile at liquid helium temperatures indicates the quantum nature of such a phase of Cu_2Se , which may promote further interest in this member of the TMCs.

This work was supported as part of the Center for Solar and Thermal Energy Conversion, an Energy Frontier Research Center funded by the U.S. Department of Energy, Office of Science, Basic Energy Sciences under Award No. DE-SC-0000957. The JEOL 2010F TEM was funded by the National Science Foundation (Grant No. DMR-9871177) and operated by the Electron Microbeam Analysis Laboratory at the University of Michigan. Work at Brookhaven National Laboratory was supported by the DOE, Office of Science, Division of Materials Science (Contract No. DE-AC02-98CH10886). Work at the Shanghai Institute of Ceramics was supported by the National Natural Science Foundation of China (NSFC) (Award No. 51121064 and 51222209).

- [1] Q. H. Wang, K. Kalantar-Zadeh, A. Kis, J. N. Coleman, and M. S. Strano, *Nat. Nano* **7**, 699 (2012).
 [2] R. Xu, A. Husmann, T. F. Rosenbaum, M. L. Saboungi, J. E. Enderby, and P. B. Littlewood, *Nature* **390**, 57 (1997).

- [3] W. Zhang, R. Yu, W. X. Feng, Y. G. Yao, H. M. Weng, X. Dai, and Z. Fang, *Phys. Rev. Lett.* **106**, 156808 (2011).
 [4] B. Sips, A. F. Kusmartseva, A. Akrap, H. Berger, L. Forro, and E. Tutis, *Nat. Mater.* **7**, 960 (2008).

- [5] H.-Z. Lu, W. Yao, D. Xiao, and S.-Q. Shen, *Phys. Rev. Lett.* **110**, 016806 (2013).
- [6] H. Yuan, M. S. Bahramy, K. Morimoto, S. Wu, K. Nomura, B.-J. Yang, H. Shimotani, R. Suzuki, M. Toh, C. Kloc, X. Xu, R. Arita, N. Nagaosa, and Y. Iwasa, *Nat. Phys.* **9**, 563 (2013).
- [7] H. Liu, X. Shi, F. Xu, L. Zhang, W. Zhang, L. Chen, Q. Li, C. Uher, T. Day, and G. J. Snyder, *Nat. Mater.* **11**, 422 (2012).
- [8] S. C. Riha, D. C. Johnson, and A. L. Prieto, *J. Am. Chem. Soc.* **133**, 1383 (2010).
- [9] X. Xiao, W. Xie, X. Tang, and Q. Zhang, *Chin. Phys. B* **20**, 087201 (2011).
- [10] H. Liu, X. Yuan, P. Lu, X. Shi, F. Xu, Y. He, Y. Tang, S. Bai, W. Zhang, L. Chen, Y. Lin, L. Shi, H. Lin, X. Gao, X. Zhang, H. Chi, and C. Uher, *Adv. Mater.* **25**, 6607 (2013).
- [11] Landolt-Börnstein, in *Non-Tetrahedrally Bonded Elements and Binary Compounds I*, Vol. 41C (Springer, Berlin, Heidelberg, 1998), p. 1.
- [12] T. Ohtani, Y. Tachibana, J. Ogura, T. Miyake, Y. Okada, and Y. Yokota, *J. Alloys Compd.* **279**, 136 (1998).
- [13] H. Chi, H. Kim, J. C. Thomas, X. Su, S. Stackhouse, M. Kaviani, A. Van der Ven, X. Tang, and C. Uher, *Phys. Rev. B* **86**, 195209 (2012).
- [14] G. Kresse and J. Furthmüller, *Phys. Rev. B* **54**, 11169 (1996).
- [15] J. P. Perdew, K. Burke, and M. Ernzerhof, *Phys. Rev. Lett.* **77**, 3865 (1996).
- [16] P. E. Blöchl, *Phys. Rev. B* **50**, 17953 (1994).
- [17] G. Kresse and D. Joubert, *Phys. Rev. B* **59**, 1758 (1999).
- [18] J. Heyd, G. E. Scuseria, and M. Ernzerhof, *J. Chem. Phys.* **118**, 8207 (2003).
- [19] A. V. Krukau, O. A. Vydrov, A. F. Izmaylov, and G. E. Scuseria, *J. Chem. Phys.* **125**, 224106 (2006).
- [20] K. Parlinski, PHONON software package (Cracow, 2008).
- [21] G. K. Padam, *Thin Solid Films* **150**, L89 (1987).
- [22] V. P. Kubaschewski and J. Nölting, *Berich. Bunsen. Gesell.* **77**, 70 (1973).
- [23] M. C. Nguyen, J.-H. Choi, X. Zhao, C.-Z. Wang, Z. Zhang, and K.-M. Ho, *Phys. Rev. Lett.* **111**, 165502 (2013).
- [24] M. Råsander, L. Bergqvist, and A. Delin, *J. Phys.: Condens. Matter* **25**, 125503 (2013).
- [25] N. Frangis, C. Manolikas, and S. Amelinckx, *Phys. Status Solidi A* **126**, 9 (1991).
- [26] A. L. N. Stevels and F. Jellinek, *Recueil* **90**, 273 (1971).
- [27] M. A. Korzhuev, V. F. Bankina, B. F. Gruzinov, and G. S. Bushmarina, *Sov. Phys. Semicond.* **23**, 959 (1989).
- [28] S. A. Danilkin, M. Avdeev, T. Sakuma, R. Macquart, and C. D. Ling, *J. Alloys Compd.* **509**, 5460 (2011).
- [29] J. S. Rhyee, K. H. Lee, S. M. Lee, E. Cho, S. Il Kim, E. Lee, Y. S. Kwon, J. H. Shim, and G. Kotliar, *Nature* **459**, 965 (2009).
- [30] S. Hikami, A. I. Larkin, and Y. Nagaoka, *Prog. Theor. Phys.* **63**, 707 (1980).
- [31] B. A. Assaf, T. Cardinal, P. Wei, F. Katmis, J. S. Moodera, and D. Heiman, *Appl. Phys. Lett.* **102**, 012102 (2013).
- [32] J. Chen, H. J. Qin, F. Yang, J. Liu, T. Guan, F. M. Qu, G. H. Zhang, J. R. Shi, X. C. Xie, C. L. Yang, K. H. Wu, Y. Q. Li, and L. Lu, *Phys. Rev. Lett.* **105**, 176602 (2010).
- [33] M. Liu, J. Zhang, C.-Z. Chang, Z. Zhang, X. Feng, K. Li, K. He, L.-l. Wang, X. Chen, X. Dai, Z. Fang, Q.-K. Xue, X. Ma, and Y. Wang, *Phys. Rev. Lett.* **108**, 036805 (2012).
- [34] L. Bao, L. He, N. Meyer, X. Kou, P. Zhang, Z. Chen, A. V. Fedorov, J. Zou, T. M. Riedemann, T. A. Lograsso, K. L. Wang, G. Tuttle, and F. Xiu, *Sci. Rep.* **2**, 726 (2012).
- [35] S. Tongay, H. Sahin, C. Ko, A. Luce, W. Fan, K. Liu, J. Zhou, Y.-S. Huang, C.-H. Ho, J. Yan, D. F. Ogletree, S. Aloni, J. Ji, S. Li, J. Li, F. M. Peeters, and J. Wu, *Nat. Commun.* **5**, 3252 (2014).

Probing IrTe₂ crystal symmetry by polarized Raman scattering

N. Lazarević,¹ E. S. Bozin,² M. Šćepanović,¹ M. Opačić,¹ Hechang Lei (雷和畅),² C. Petrovic,² and Z. V. Popović¹

¹*Center for Solid State Physics and New Materials, Institute of Physics Belgrade, University of Belgrade, Pregrevica 118, 11080 Belgrade, Serbia*

²*Condensed Matter Physics and Materials Science Department, Brookhaven National Laboratory, Upton, New York 11973-5000, USA*
(Received 7 April 2014; revised manuscript received 26 May 2014; published 16 June 2014)

Polarized Raman scattering measurements on IrTe₂ single crystals carried out over the 15–640 K temperature range, and across the structural phase transition, reveal different insights regarding the crystal symmetry. In the high temperature regime three Raman active modes are observed at all of the studied temperatures above the structural phase transition, rather than two as predicted by the factor group analysis for the assumed $P\bar{3}m1$ symmetry. This indicates that the actual symmetry of the high temperature phase is lower than previously thought. The observation of an additional E_g mode at high temperature can be explained by doubling of the original trigonal unit cell along the c axis and within the $P\bar{3}c1$ symmetry. In the low temperature regime (below 245 K) the other Raman modes appear as a consequence of the symmetry lowering phase transition and the corresponding increase of the primitive cell. All of the modes observed below the phase transition temperature can be assigned within the monoclinic crystal symmetry. The temperature dependence of the Raman active phonons in both phases is mainly driven by anharmonicity effects. The results call for reconsideration of the crystallographic phases of IrTe₂.

DOI: [10.1103/PhysRevB.89.224301](https://doi.org/10.1103/PhysRevB.89.224301)

PACS number(s): 78.30.-j, 74.25.Kc, 61.05.cp, 64.60.-i

I. INTRODUCTION

Although known for some time [1,2], the interest in IrTe₂ has been renewed recently with the discovery of superconductivity [3–6]. By doping this layered compound with Pt, Pd, and Cu, the phase transition which occurs at low temperatures [7] is suppressed and superconductivity emerges [3–6,8]. At room temperature IrTe₂ has a trigonal symmetry with edge-sharing IrTe₆ octahedra forming layers stacked along the c axis [7], as shown in Fig. 1. As temperature is decreased, the system undergoes a symmetry lowering phase transition in the temperature range between 220 and 280 K, with the exact transition temperature T_{PT} presumably depending on the sample form (powder versus single crystal) and the thermal cycle details (cooling or warming) [3–7,9]. The phase transition is accompanied by a hump in electrical resistivity and a drop in magnetic susceptibility [10], anomalies reminiscent of those associated with the onset of a charge-density-wave (CDW) state observed in other TX_2 systems [11]. However, the exact nature of the low temperature phase remains controversial, since no signatures of the CDW gap in IrTe₂ have been seen in angle resolved photoemission and optical spectroscopy studies [5,9,10]. Recent band structure calculations combined with x-ray absorption spectroscopy measurements suggest that the dramatic change in the interlayer and intralayer hybridizations could play an important role in the structural phase transition of IrTe₂ [6]. More recently, it has also been suggested that the depolymerization of the polymeric Te-Te bonds might be responsible for the structural phase transition [9].

Although prior crystallographic analyses showed that the IrTe₂ crystal structure changes from trigonal to monoclinic with decreasing temperature, the low temperature structure is still a subject of debate [7]. It was argued that the initially assigned monoclinic $C2/m$ symmetry cannot fully describe the structure below the phase transition [11–13]. Consequently, the proposed crystal symmetry was further lowered down to

triclinic $P\bar{1}$ [11] and even $P1$ [13]. Moreover, it was also suggested that the trigonal and monoclinic structures coexist intrinsically below the phase transition [12]. The nature of the phase transition as well as the symmetry of the low temperature phase therefore still remain open questions.

Important information concerning the symmetry of the crystal system can be obtained by utilizing the properties of Raman spectroscopy and by performing the measurements in different polarization configurations whereby one can probe different scattering channels. Raman spectroscopy also emerges as a valuable tool for detecting the intrinsic phase separation [14].

Here we present results of a systematic Raman scattering study on IrTe₂ single crystals. The spectra were collected in different scattering geometries at various temperatures. The room temperature Raman spectra were analyzed within the trigonal crystal symmetry. Three instead of two peaks, which are predicted by the factor group analysis (FGA) for the $P\bar{3}m1$ space group, are observed in the Raman spectra, suggesting a different crystal symmetry of IrTe₂ in the high temperature phase from that previously assumed. The same phonon structure persists at $T \gg T_{PT}$, indicating that it is a true characteristic of the high temperature phase. At temperatures below $T_{PT} = 245$ K, the clear fingerprint of the first order structural phase transition is observed in the Raman spectra. The observed modes are interpreted within the monoclinic crystal symmetry. No signatures of the trigonal unit cell presence have been detected in the low temperature Raman scattering spectra. All temperature induced effects in both phases are mostly anharmonic. These observations provide important insights and constraints for possible crystal symmetries of this system in different temperature regimes.

II. EXPERIMENT

Single crystals of IrTe₂ were prepared by the self-flux method. Ir and Te were mixed in an 18:82 stoichiometric

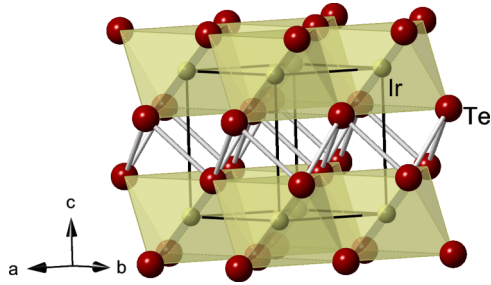


FIG. 1. (Color online) Crystal structure of IrTe₂ in the trigonal phase. Solid lines represent a single $P\bar{3}m1$ unit cell, with yellow (red) spheres indicating the positions of Ir (Te).

ratio, heated in alumina crucibles under an Ar atmosphere up to 1160 °C, kept at that temperature for 24 h, and then cooled to 400 °C over 130 h. Excess Te flux was removed at 400 °C by centrifugation. Platelike mm-size crystals were obtained. Magnetization and resistivity data were measured by warming the sample from 5 K. They are in good agreement with published values [3].

Raman scattering measurements were performed using a JY T64000 Raman system with 1800/1800/1800 grooves/mm gratings and a TriVista 557 Raman system with the 900/900/1800 grooves/mm gratings combination, both in a backscattering micro-Raman configuration. The 514.5 nm line of a mixed Ar⁺/Kr⁺ gas laser was used as an excitation source. High temperature measurements were performed in an Ar environment by using a Linkam THGS600 heating stage. Low temperature measurements were performed using a KONTI CryoVac continuous flow cryostat with a 0.5 mm thick window in the warming regime. Complementary atomic pair distribution function (PDF) measurements at 300 K were performed on a finely pulverized sample at the X17A beamline of the National Synchrotron Light Source (NSLS) at Brookhaven National Laboratory, utilizing a 67.42 keV x-ray beam within a commonly used rapid-acquisition setup [15] featuring a sample to detector distance of 204.25 mm, and with access to a wide momentum transfer range up to 28 Å⁻¹. Standard corrections, PDF-data processing, and structure modeling protocols were utilized, as described in detail elsewhere [16].

III. RESULTS AND DISCUSSION

IrTe₂ crystallizes in a trigonal type of structure ($P\bar{3}m1$ space group) with one molecular unit per unit cell (Fig. 1) [7,18]. The crystal structure consists of IrTe₂ layers which are made up of edge-sharing IrTe₆ octahedra. Short Te-Te bonds between adjacent IrTe₂ result in three-dimensional polymeric networks, thereby reducing the c/a ratio in comparison with the standard hexagonal closed packing of the CdI₂ structure [1,9,19]. This is related to the Ir⁺³ state and the fractional oxidation state of Te anions (Te^{-1.5}) [2,9].

A. High temperature phase

Figure 2 shows the room temperature polarized Raman scattering spectra of IrTe₂ single crystals measured from the (001) plane of the sample. Although the FGA for the

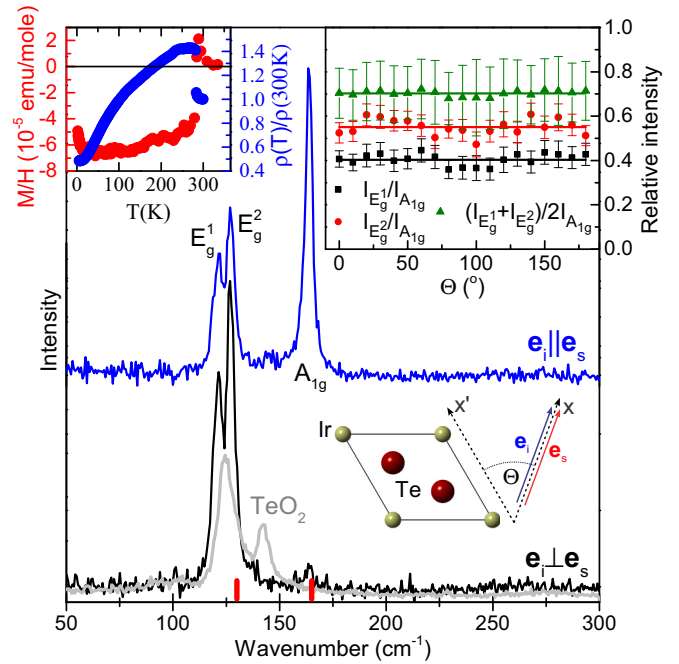


FIG. 2. (Color online) Room temperature Raman scattering spectra of IrTe₂ measured using a JY T64000 Raman system in different polarization configurations. Gray lines represent the spectra of TeO₂ with scaled intensity. Red markers represent phonon energies at Γ point calculated by Cao *et al.* [11]. Inset on the left: Magnetization and resistivity data measured by warming the sample from the base temperature. Inset on the right: Relative intensities of the Raman active modes measured in a parallel polarization configuration for different orientations of the sample with respect to the laboratory axis.

$P\bar{3}m1$ space group predicts only two Raman active modes ($A_{1g} + E_g$) to be observed in the scattering experiment, three peaks are clearly distinguished in the data. A contribution to the Raman spectra originating from scattering on possible TeO₂ impurities can be safely excluded (see Fig. 2). According to the selection rules for the trigonal system, summarized in Table I, the A_{1g} mode can only be observed in a parallel but not in a crossed polarization configuration, whereas the E_g mode can be observed in both parallel and crossed polarization configurations. Consequently, the peak at about 164 cm⁻¹, which is indeed observed in a parallel but not in a cross polarization configuration, is attributed to the A_{1g} symmetry mode. The energy of this mode is in very good agreement with the calculated value [11] (red mark in Fig. 2). Whereas the numerical calculations [11] further predict a single E_g mode at about 130 cm⁻¹ to be observed in the Raman scattering experiment, two peaks at about 121 and 126 cm⁻¹ are unambiguously observed in the data in this energy range (see Fig. 2). These modes are observed in both parallel and cross polarization configurations, which suggests their E_g symmetry. The appearance of two modes in the energy range where only one mode is expected indicates that the original crystal symmetry assignment for the high temperature phase may be inadequate, and that the actual symmetry is in fact lower. We consider the issue of the symmetry of the high temperature phase in more detail next.

TABLE I. Considerations of Raman tensors for three different crystal systems and the Raman mode distribution in the Γ point and various space groups of interest for IrTe₂.

Crystal system	Raman tensors [17]		Raman modes
Trigonal ($O_z \parallel C_3$ $O_y \parallel C_2$)	$\hat{R}_{A_{1g}} = \begin{pmatrix} a & 0 & 0 \\ 0 & a & 0 \\ 0 & 0 & b \end{pmatrix}$	$\hat{R}_{E_g} = \begin{pmatrix} -c & 0 & 0 \\ 0 & c & 0 \\ 0 & 0 & 0 \end{pmatrix}, \begin{pmatrix} 0 & c & 0 \\ c & 0 & 0 \\ 0 & 0 & 0 \end{pmatrix}$	$\Gamma_{P\bar{3}m1} = A_{1g} + E_g$ $\Gamma_{P\bar{3}c1} = A_{1g} + A_{2g}(\text{silent}) + 2E_g$
Monoclinic ($O_y \parallel C_2$)	$\hat{R}_{A_g} = \begin{pmatrix} b & 0 & d \\ 0 & c & 0 \\ d & 0 & a \end{pmatrix}$	$\hat{R}_{B_g} = \begin{pmatrix} 0 & f & 0 \\ f & 0 & e \\ 0 & e & 0 \end{pmatrix}$	$\Gamma_{C2/m} = 2A_g + B_g$
Triclinic	$\hat{R}_A = \hat{R}_{A_g} = \begin{pmatrix} a & d & e \\ d & b & f \\ e & f & c \end{pmatrix}$		$\Gamma_{P\bar{1}} = 21A_g$ $\Gamma_{P1} = 222A$

The first possibility is that the IrTe₂ symmetry is lowered at room temperature to some t subgroup of the $P\bar{3}m1$ [20]. This would imply splitting of a double degenerate E_g mode into an A_g - B_g doublet [21]. Hereby the obtained modes would display different angular Raman intensity dependencies as the sample orientation is varied in a parallel polarization configuration (see Fig. 2). On the contrary (as can be seen in the inset of Fig. 2), both modes at 121 and 126 cm⁻¹ exhibit the same angular intensity dependence, thereby excluding the possibility of the E_g mode splitting, i.e., symmetry lowering to some t subgroup of the $P\bar{3}m1$. Furthermore, it confirms the E_g nature of the 121 and 126 cm⁻¹ modes since, for a trigonal system (see Table I), both A_{1g} and E_g mode intensities are independent on the sample orientation when measured in a parallel polarization configuration.

The second possibility which could explain the observed appearance of the two E_g modes instead of a single E_g mode is the symmetry change to some k subgroup of $P\bar{3}m1$ [20]. The simplest option is $P\bar{3}c1$ ($Z = 2$) with Ir atoms located on the $2b$ site and Te atoms at the $4d$ site. The $P\bar{3}c1$ unit cell is built by doubling of the $P\bar{3}m1$ unit cell along the c axis (see Fig. 1). The FGA for the $P\bar{3}c1$ predicts three Raman active modes to be observed in the Raman scattering experiment ($A_{1g} + 2E_g$), which is in complete agreement with our findings. To further verify the plausibility of this assumption, we performed a structural analysis of room temperature x-ray PDF data of IrTe₂ using the $P\bar{3}c1$ model. The fit results are shown in Fig. 3 and summarized in Table II.

Importantly, the observed phonon structure and, consequently, the crystal $P\bar{3}c1$ symmetry persist at temperatures

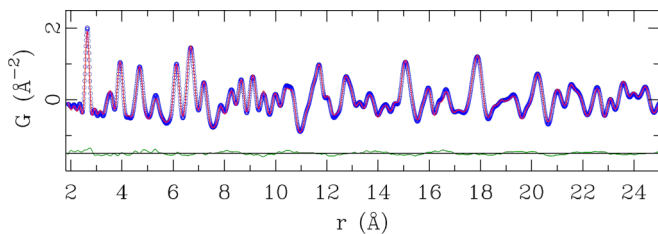


FIG. 3. (Color online) Room temperature x-ray PDF of IrTe₂: Experimental data (blue open symbols), $P\bar{3}c1$ model (red solid line), and difference curve (green solid line) which is offset for clarity. Structural parameters are summarized in Table II.

$T \gg T_{PT}$ deep in the high temperature regime, as is evident from Fig. 4, indicating that these are the characteristics of the high temperature phase. As the temperature is increased, all of the modes are shifted toward lower energies and become progressively broader (see the inset of Fig. 4). All of the changes of the spectra induced by a temperature increase are in accordance with the well known anharmonicity model [22–24].

B. Low temperature phase

By lowering the temperature, IrTe₂ undergoes the phase transition in the range between 220 and 280 K [7,11,13]. The origins of the phase transition as well as the crystal symmetries of IrTe₂ at low temperatures are still under vigorous debate [7,11–13].

Polarized Raman scattering spectra of IrTe₂ measured at low temperatures (between 15 and 300 K) in parallel and cross polarization configurations are presented in Fig. 5. Significant changes in the spectra in both polarization configurations are observed around 245 K. A lower transition temperature is a consequence of the local heating effects of the sample by the laser beam. Unlike in the case of a canonical CDW phase transition where additional modes gradually appear [25], the observed sudden change in the phonon spectra suggests the first order character of the phase transition. The existence of at least 11 peaks in the low temperature phase indicates lowering of the symmetry and/or an increase of the unit cell size.

Figure 6 shows polarized Raman scattering spectra of IrTe₂ measured at 15 K in parallel and cross polarization configurations. A significant difference in the spectra measured in the parallel and crossed polarization configurations

TABLE II. Structural parameters for the $P\bar{3}c1$ phase obtained from PDF analysis at 300 K. The lattice parameters are $a = b = 3.929(4)$ Å, $c = 10.805(2)$ Å. U_{ij} (Å² × 10³) are nonzero components of the displacement tensor.

Atom	x	y	z	$U_{11} = U_{22}$	U_{33}
Ir	0	0	0	6(2)	6(3)
Te	1/3	2/3	0.126(1)	7(2)	9(4)
$\chi^2 = 0.002$					
$R_{wp} = 0.106$					

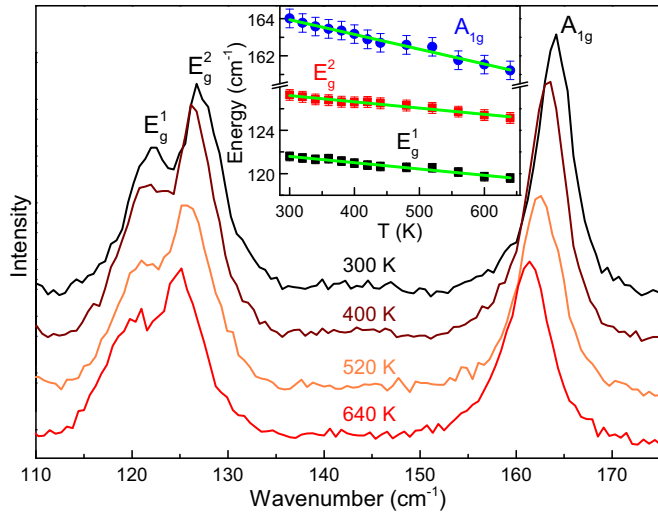


FIG. 4. (Color online) Raman scattering spectra of IrTe₂ single crystals measured at various temperatures, as indicated, in the high temperature regime using a TriVista 557 Raman system. Inset: Energy temperature dependence of the A_{1g}, E_g¹, and E_g² Raman active modes. The solid green lines represent calculated spectra by using the standard three-phonon anharmonicity model [22], where [ω₀ = 123.4(2) cm⁻¹, C = 0.26(2) cm⁻¹], [ω₀ = 129.0(2) cm⁻¹, C = 0.27(2) cm⁻¹], and [ω₀ = 160.4(2) cm⁻¹, C = 0.48(3) cm⁻¹] are the best fit parameters for the E_g¹, E_g², and A_{1g} Raman active modes, respectively.

indicates the existence of the two separate scattering channels in the low temperature phase. Symmetry arguments suggest that in the case of the triclinic crystal structure only one channel can be observed. Due to the proposed orientation of the triclinic lattice [11,13] in relation to the trigonal lattice,

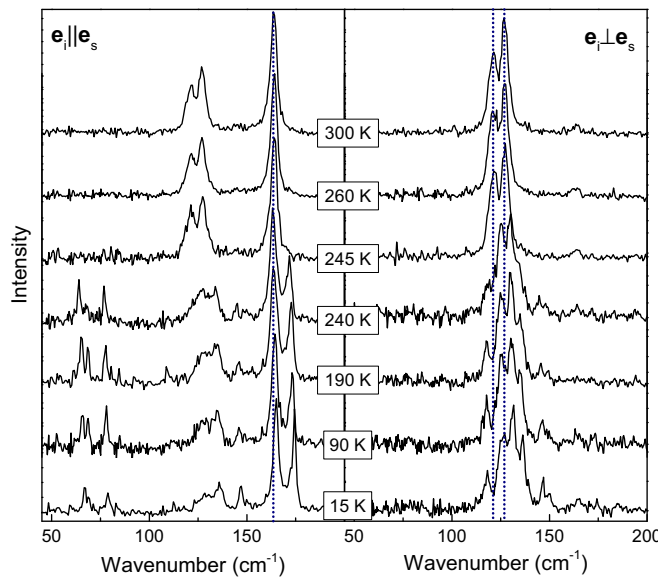


FIG. 5. (Color online) Polarized Raman scattering spectra of IrTe₂ measured at various temperatures, as indicated, in the low temperature regime using a JY T64000 Raman system in parallel and cross polarization configurations. The spectra were measured by warming the sample from 15 K. Dotted vertical lines represent a guide to the eyes.

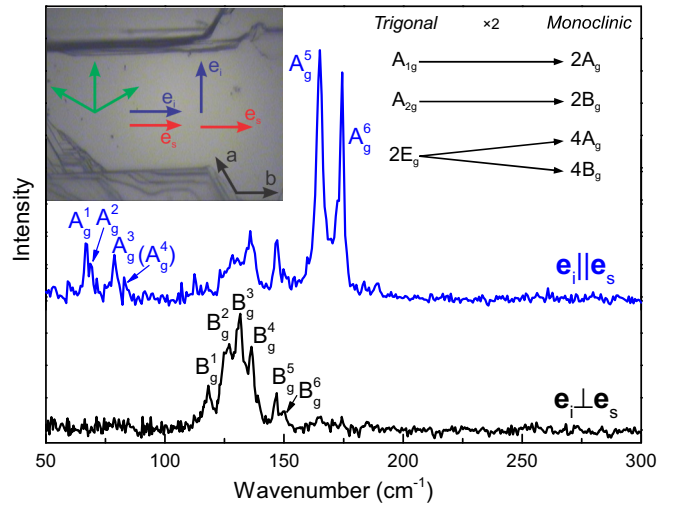


FIG. 6. (Color online) Polarized Raman scattering spectra of IrTe₂ measured at 15 K using a JY T64000 Raman system in parallel and cross polarization configurations. Inset on the left: Image of the IrTe₂ sample. Inset on the right: Correlation diagram connecting Raman active phonons for trigonal and monoclinic types of structures.

the contribution to the scattering intensity (in our scattering geometry) would come from nearly all the components of the Raman tensor (see Table I) and the cancellation of some Raman modes in different polarization configurations is highly unlikely. Furthermore, for both *P*1 and *P*1̄ space groups, a substantially larger number of Raman modes is expected to be observed in the measured spectra. All this suggests that the IrTe₂ crystal symmetry in the low temperature phase should be higher than triclinic (*P*1 or *P*1̄). The next crystal system with two different scattering channels is monoclinic (see Table I). The obtained spectra may be interpreted within the monoclinic crystal symmetry provided that the optical axis of the low temperature phase is orthogonal to the direction of incident light in the Raman scattering experiment, i.e., if it lies in the (001) plane of the trigonal phase. This is consistent with the picture proposed by Matsumoto *et al.* [7]. At this point one should have in mind that symmetry breaking may occur along three equivalent directions, as indicated by the green arrows in the left inset of Fig. 6. For generality we assume the contributions from all three possible orientations. Consequently, one may expect the appearance of the B_g modes in both parallel and cross polarization configurations. Although the A_g modes may be also observed in both parallel and cross polarization configurations (with the assumption of twinning), in the crossed polarization configuration the intensity of the A_g modes depends on the |*b* - *c*|² and the cancellation can be easily achieved.

Following the previous arguments, the peaks at about 67, 69, 79, 165, and 174 cm⁻¹ which can be observed in parallel but not in cross polarization configurations may be assigned as the A_g symmetry modes. We believe that the weak structure at about 83 cm⁻¹ may also be the A_g symmetry mode, however, very low intensity prevents unambiguous assignment. Six peaks at about 118, 126, 131, 136, 148, and 150 cm⁻¹ that can be observed in both parallel and crossed polarization configurations are assigned as the B_g symmetry modes.

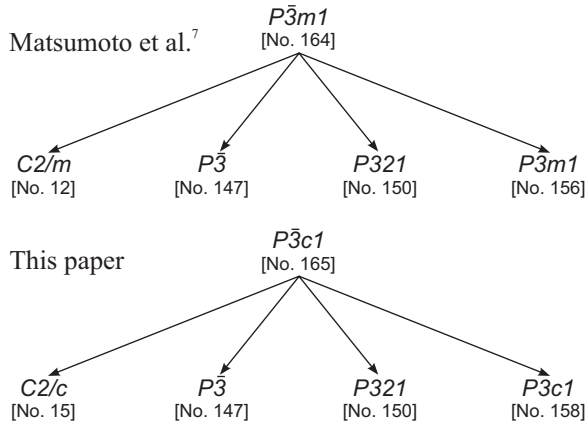


FIG. 7. Schematics of maximal nonisomorphic subgroup relations of the space group $P\bar{3}m1$ [7] (upper panel) and $P\bar{3}c1$ (lower panel) for the t subgroup. The number of the space group is given in the parentheses.

Although the properties of the observed Raman modes can, in principle, be interpreted within the monoclinic crystal system, the proposed [7] unit cell of the $C2/m$ symmetry group with $Z = 2$ cannot account for the number of observed Raman modes. According to FGA for $C2/m$ ($Z = 2$), only three modes are expected to be observed in the Raman scattering experiment (see Table I). Consequently, a larger unit cell within the monoclinic crystal system is needed to reproduce the observed Raman spectra. Following the previous arguments and the discussion regarding the symmetry of the high temperature phase, we may conclude that the space group symmetry of IrTe₂ at low temperatures should be searched for within the monoclinic $C2/c$ space group or some of its t subgroups (see Fig. 7) [20].

The temperature evolution of the Raman spectra (see Fig. 5) across the phase transition can be seen as the splitting of the two E_g modes into A_g (A_g^1 - A_g^4) and B_g (B_g^1 - B_g^4) quartets due to symmetry lowering and (at least) a two times increase of the primitive cell size (see the right inset in Fig. 6). The A_g^5 and A_g^6 most likely originate from the A_{1g} mode whereas the B_g^5 and B_g^6 originate from the A_{2g} mode of the trigonal phase. The absence of the E_g^1 and E_g^2 modes (within our experimental resolution), characteristic for the trigonal phase, in the low temperature Raman spectra of IrTe₂ suggests the absence of the trigonal lattice at low temperatures [12].

The temperature dependence of the energy and linewidth for the highest intensity Raman modes is shown in Fig. 8. A clear fingerprint of the first order phase transition is observed in both the energy and the linewidth of the observed modes. The solid lines represent the calculated spectra for the low temperature phase by using the three-phonon anharmonicity model [22]. Good agreement with the experimental data confirms that anharmonicity plays a major role in the temperature dependence of the temperature phase phonon self-energy below T_{PT} .

IV. CONCLUSION

A Raman scattering study of IrTe₂ single crystals has been presented. At room temperature, three instead of two

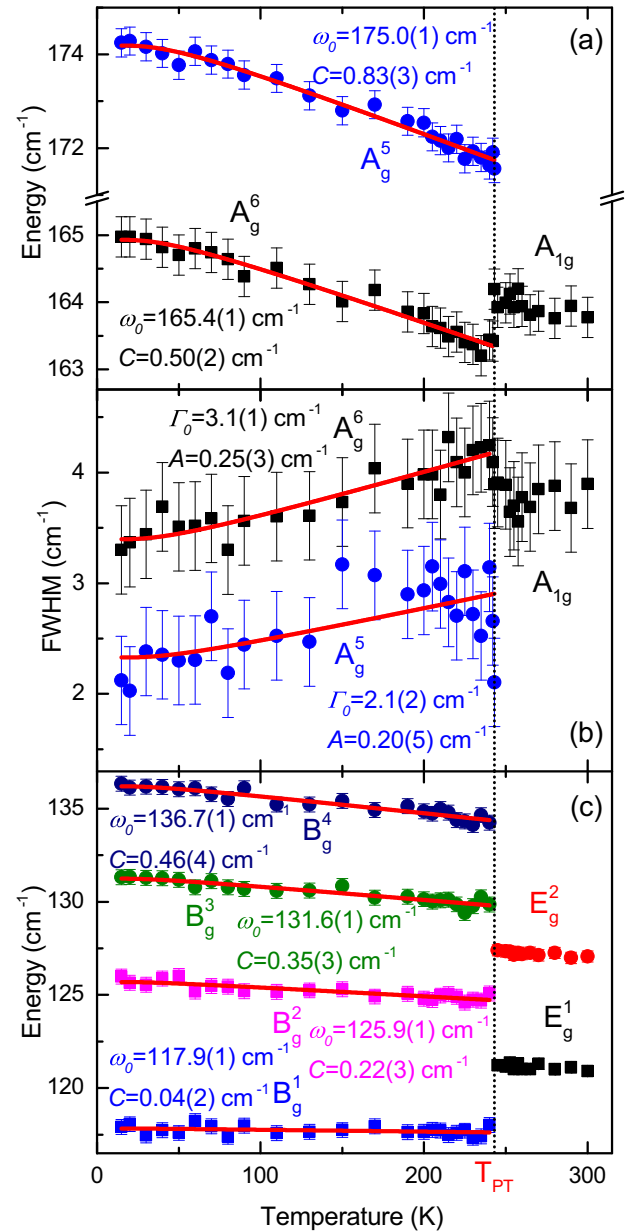


FIG. 8. (Color online) Temperature dependence of the highest intensity Raman mode energy (a) and (c) and linewidth (b). Solid lines represent the calculated spectra by using the standard three-phonon anharmonicity model [22]. The spectra were measured by warming the sample from 15 K.

Raman active modes predicted by the factor group analysis for the $P\bar{3}m1$ symmetry group are observed. The Raman data showed that the $P\bar{3}c1$ rather than the $P\bar{3}m1$ crystal symmetry is needed to describe the phonon structure of IrTe₂ at room temperature. The sudden change in the Raman spectra below $T_{PT} = 245$ K revealed the first order structural phase transition. The properties of the phonon spectra below T_{PT} are well interpreted within the monoclinic crystal symmetry. The splitting of the E_g modes at the T_{PT} comes from the symmetry lowering and the increase in the size of the unit cell. We believe that the space group symmetry of IrTe₂ at low temperatures should be searched for within the monoclinic $C2/c$ space group or some of its t subgroups. Further structural

investigations of both trigonal and monoclinic phases of IrTe₂ are needed. Apart from the symmetry change at T_{PT} , the temperature dependence of the energy and linewidth of the Raman active modes of IrTe₂ is mostly anharmonic.

ACKNOWLEDGMENTS

We gratefully acknowledge discussions with R. Hackl. This work was supported by the Serbian Ministry of Educa-

tion, Science and Technological Development under Projects No. ON171032 and No. III45018, as well as the Serbian-Germany bilateral project “Interplay of Fe-vacancy ordering and spin fluctuations in iron-based high temperature superconductors.” Part of this work was carried out at the Brookhaven National Laboratory which is, as well as the NSLS facility, operated for the Office of Basic Energy Sciences, US Department of Energy by Brookhaven Science Associates, under Contract No. DE-AC02-98CH10886.

-
- [1] S. Jobic, P. Deniard, R. Brec, J. Rouxel, A. Jouanneaux, and A. N. Fitch, *Z. Anorg. Allg. Chem.* **598**, 199 (1991).
- [2] S. Jobic, R. Brec, and J. Rouxel, *J. Solid State Chem.* **96**, 169 (1992).
- [3] J. J. Yang, Y. J. Choi, Y. S. Oh, A. Hogan, Y. Horibe, K. Kim, B. I. Min, and S.-W. Cheong, *Phys. Rev. Lett.* **108**, 116402 (2012).
- [4] S. Pyon, K. Kudo, and M. Nohara, *J. Phys. Soc. Jpn.* **81**, 053701 (2012).
- [5] D. Ootsuki, Y. Wakisaka, S. Pyon, K. Kudo, M. Nohara, M. Arita, H. Anzai, H. Namatame, M. Taniguchi, N. L. Saini, and T. Mizokawa, *Phys. Rev. B* **86**, 014519 (2012).
- [6] M. Kamitani, M. S. Bahramy, R. Arita, S. Seki, T. Arima, Y. Tokura, and S. Ishiwata, *Phys. Rev. B* **87**, 180501 (2013).
- [7] N. Matsumoto, K. Taniguchi, R. Endoh, H. Takano, and S. Nagata, *J. Low Temp. Phys.* **117**, 1129 (1999).
- [8] A. Kiswandhi, J. S. Brooks, H. B. Cao, J. Q. Yan, D. Mandrus, Z. Jiang, and H. D. Zhou, *Phys. Rev. B* **87**, 121107 (2013).
- [9] Y. S. Oh, J. J. Yang, Y. Horibe, and S.-W. Cheong, *Phys. Rev. Lett.* **110**, 127209 (2013).
- [10] A. F. Fang, G. Xu, T. Dong, P. Zheng, and N. L. Wang, *Sci. Rep.* **3**, 1153 (2013).
- [11] H. Cao, B. C. Chakoumakos, X. Chen, J. Yan, M. A. McGuire, H. Yang, R. Custelcean, H. Zhou, D. J. Singh, and D. Mandrus, *Phys. Rev. B* **88**, 115122 (2013).
- [12] L. Zhang, X. Zhu, L. Ling, C. Zhang, L. Pi, and Y. Zhang, *Philos. Mag.* **94**, 439 (2014).
- [13] G. L. Pascut, K. Haule, M. J. Gutmann, S. A. Barnett, A. Bombardi, S. Artyukhin, D. Vanderbilt, J. J. Yang, S.-W. Cheong, and V. Kiryukhin, [arXiv:1309.3548](https://arxiv.org/abs/1309.3548).
- [14] N. Lazarević, M. Abeykoon, P. W. Stephens, H. Lei, E. S. Bozin, C. Petrovic, and Z. V. Popović, *Phys. Rev. B* **86**, 054503 (2012).
- [15] P. J. Chupas, X. Qiu, J. C. Hanson, P. L. Lee, C. P. Grey, and S. J. L. Billinge, *J. Appl. Cryst.* **36**, 1342 (2003).
- [16] T. Egami and S. J. L. Billinge, *Underneath the Bragg Peaks: Structural Analysis of Complex Materials*, 2nd ed. (Elsevier, Amsterdam, 2012).
- [17] H. Kuzmany, *Solid-State Spectroscopy: An Introduction* (Springer, Berlin, 2009).
- [18] C. Souillard, P. Petit, P. Deniard, M. Evain, S. Jobic, M.-H. Whangbo, and A.-C. Dhaussy, *J. Solid State Chem.* **178**, 2008 (2005).
- [19] E. Canadell, S. Jobic, R. Brec, J. Rouxel, and M.-H. Whangbo, *J. Solid State Chem.* **99**, 189 (1992).
- [20] T. Hahn, U. Shmueli, A. A. J. C. Wilson, and E. Prince, *International Tables for Crystallography* (Reidel, Dordrecht, 2005).
- [21] W. G. Fateley, F. R. Dollish, N. T. McDevitt, and F. F. Bentley, *Infrared and Raman Selection Rules for Molecular and Lattice Vibrations: The Correlation Method* (Wiley-Interscience, New York, 1972).
- [22] M. Balkanski, R. F. Wallis, and E. Haro, *Phys. Rev. B* **28**, 1928 (1983).
- [23] N. Lazarević, Z. V. Popović, R. Hu, and C. Petrovic, *Phys. Rev. B* **81**, 144302 (2010).
- [24] N. Lazarević, M. Radonjić, M. Šćepanović, H. Lei, D. Tanasković, C. Petrovic, and Z. V. Popović, *Phys. Rev. B* **87**, 144305 (2013).
- [25] N. Lazarević, Z. V. Popović, R. Hu, and C. Petrovic, *Phys. Rev. B* **83**, 024302 (2011).



OPEN

SUBJECT AREAS:

ELECTRONIC PROPERTIES
AND MATERIALSSTRUCTURE OF SOLIDS AND
LIQUIDSPHASE TRANSITIONS AND
CRITICAL PHENOMENA

Received

12 December 2013

Accepted

28 January 2014

Published

12 February 2014

Correspondence and
requests for materials
should be addressed to
E.S.B. (bozin@bnl.gov)

* current address:

Department of Physics,
Missouri University of
Science and
Technology, Rolla, MO
65409, USA

$\text{Cu}(\text{Ir}_{1-x}\text{Cr}_x)_2\text{S}_4$: a model system for studying nanoscale phase coexistence at the metal-insulator transition

E. S. Božin¹, K. R. Knox¹, P. Juhás¹, Y. S. Hor^{2*}, J. F. Mitchell² & S. J. L. Billinge^{1,3}

¹Condensed Matter Physics and Materials Science Department, Brookhaven National Laboratory, Upton, NY 11973, ²Materials Science Division, Argonne National Laboratory, Argonne, Illinois 60439, ³Department of Applied Physics and Applied Mathematics, Columbia University, New York, NY 10027.

Increasingly, nanoscale phase coexistence and hidden broken symmetry states are being found in the vicinity of metal-insulator transitions (MIT), for example, in high temperature superconductors, heavy fermion and colossal magnetoresistive materials, but their importance and possible role in the MIT and related emergent behaviors is not understood. Despite their ubiquity, they are hard to study because they produce weak diffuse signals in most measurements. Here we propose $\text{Cu}(\text{Ir}_{1-x}\text{Cr}_x)_2\text{S}_4$ as a model system, where robust local structural signals lead to key new insights. We demonstrate a hitherto unobserved coexistence of an Ir^{4+} charge-localized dimer phase and Cr-ferromagnetism. The resulting phase diagram that takes into account the short range dimer order is highly reminiscent of a generic MIT phase diagram similar to the cuprates. We suggest that the presence of quenched strain from dopant ions acts as an arbiter deciding between the competing ground states.

Metals-insulator transitions (MITs)^{1,2} remain one of the most fascinating phenomena in condensed matter physics^{3,4}, especially in cases where emergent behavior appears close to the transition⁵ resulting in colossal effects, such as high-temperature superconductivity^{6,7} and colossal magnetoresistance⁸. For a remarkably broad range of materials, a similar phase diagram emerges with loss of a long-range ordered state crossing over to a homogeneous metallic state, but with a broad region where complex behavior, heterogeneous states, difficult to detect broken local symmetries and nanoscale fluctuations become important^{9–11}. It is often precisely in this intermediate region where the interesting emergent behaviors occur. One of the major challenges is to study this complex region experimentally since the important physics seems to be closely related to details of the nature and interactions⁵ of the competing nano-scale heterogeneous phases, which cannot be easily studied using bulk average experimental probes. New insights can be obtained from experimental probes that are spatially resolved with nanoscale resolution^{12–20} and from probes that are sensitive to the local structure such as the atomic pair distribution function (PDF) analysis^{21–25} and extended x-ray absorption fine structure spectroscopy^{26–30}. The important cuprates are especially challenging in this regard because of the small response of the lattice to the heterogeneous electronic states.

Among the wide variety of materials displaying MITs is a class of transition metal spinels with partially filled t_{2g} orbitals³¹. Exotic types of orbital and charge ordering, spin dimerization, and associated superstructures emerge in the low temperature insulating phases, such as octamers in CuIr_2S_4 ³², helices in MgTi_2O_4 ³³, and heptamers in AlV_2O_4 ³⁴. Appearance of these complex motifs is accompanied by a decrease in the magnetic susceptibility. This behavior is understood first in CuIr_2S_4 as the formation of Ir^{4+} - Ir^{4+} structural dimers which results in the spins on the dimerized iridium ions forming a singlet ($S = 0$) state. The interesting isomeric patterns that form in the different spinels depend on details of the chemistry and structure of the specific system and come about from different orderings of the dimers on the pyrochlore sublattice of corner shared tetrahedra of transition metal ions (Fig. 1(a))³², but through a careful analysis of the local structure and properties in CuIr_2S_4 we show that the important physics driving the MIT is the charge localization and dimer formation itself rather than the dimer ordering and isomerization.

The structural dimerization is shown schematically in Fig. 1. In CuIr_2S_4 the iridium ions are 3.5+ on average and sit on the corners of a 3D array of corner-shared tetrahedra, forming 3 degenerate sublattices, as shown in Fig. 1(a). On cooling, a tetragonal distortion breaks the degeneracy of the three sublattices (Fig. 1(b)). One sublattice is then half filled and this band may lower its energy by forming a particularly short “dimer” bond

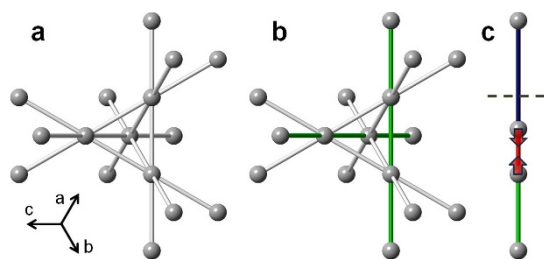


Figure 1 | Structural effect of dimerization in spinels. (a) Regular pyrochlore sublattice in the high temperature cubic phase of transition metal spinels. All near neighbor transition metal distances (grey) are of equal average length (t_{2g} are degenerate). The metal-metal bonds are shown, indicating degenerate interpenetrating 1D chains of ions. (b) Structural distortion (for example tetragonal along c -axis) lifts the degeneracy (making the (110)-type directions (green) special). (c) Dimerization along the (110)-type chains occurring in the low temperature insulating phases results in a redistribution of bond-lengths: each dimer converts two average distances to a pair of short (red) and long (blue) distances. Details of the three dimensional ordering of the dimers then depend on the specifics of the transitional metal spinel family.

(Fig. 1(c)). This is known in the undoped end-member because the dimers order over long-range giving rise to an easily measured structural phase transition, which correlates in temperature with changes in the conductivity and magnetic susceptibility. The state of ordered dimers that disappear on warming is analogous to the antiferromagnetic (AF) state of the undoped end-member in the cuprate high temperature superconductors in that a long range ordered (LRO) broken symmetry insulating state is seen at low temperature. It is thus interesting to see what happens in this system on doping. This has been studied³⁵ in the case of Cr doping and a crossover to a metallic state, a MIT, where the metallic state has ferromagnetic LRO.

Although the MIT that takes place on warming in pure CuIr_2S_4 is quite well understood^{31,32,36–40}, the MIT on doping $\text{Cr}^{35,41,42}$ is not. The phase diagram as it is understood currently is shown in Fig. 2³⁵. The long range dimer order is quickly suppressed with Cr doping and a metallic state emerges with ferromagnetic order appearing at higher doping, presumably involving the Cr spins. On the other hand, here we show that the *local* structure shows greater complexity with a crossover region in which a competition is taking place between different ground-states leading to a nano-scale phase separation with a diamagnetic disordered-dimer phase coexisting with a ferromagnetically long-range ordered phase. This is qualitatively similar to behavior in metal-insulator transitions in systems such as cuprate superconductors^{17,43–49} and nickelates^{50–56} where hidden broken symmetry phases and nanoscale phase separation are seen in the vicinity of the MIT, though much easier to study here because of the robust signal of the dimers in the local structure. The results represent the first observation of nanoscale phase coexistence in irridates. We believe that generic lessons learned in the CuIr_2S_4 system can guide our understanding of MITs in these other systems since CuIr_2S_4 exhibits a similar generic phase diagram, sketched in the inset to Fig. 2. The generic picture is that of a competition between two competing states, a paramagnetic metallic state and a diamagnetic insulating charge-localized dimer state. The localized state is destabilized with respect to the delocalized metallic state on increased doping, but shows reentrant behavior that we explain due to dopant induced quenched disorder favoring the charge-localized dimer state. The material finally crosses over to a ferromagnetic metallic state at the Cr rich end of the phase diagram, but the metallic and insulating states coexist on the nanoscale over a wide range of doping and temperature, which can be well quantified in this system since the signal from the charge-localized dimer state has a distinctive local structural signature.

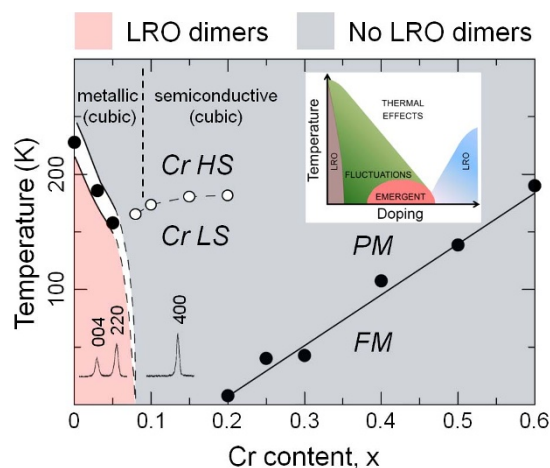


Figure 2 | $\text{Cu}(\text{Ir}_{1-x}\text{Cr}_x)_2\text{S}_4$ average phase diagram. This is the canonical phase diagram largely reproduced from Endoh *et al.*³⁵. Regions with long range dimer order present (absent) are shaded in red (grey). A first order MIT is observed only close to the CuIr_2S_4 end, with Cr-doping quickly suppressing the LRO. Insets at lower left show low temperature diffraction patterns for $x = 0$ (trigonal $\text{P}\bar{1}$) and $x = 0.15$ (cubic $\text{Fd}\bar{3}\text{m}$) that clearly indicate the change in crystallographic symmetry going from the diamagnetic insulating (red) to the paramagnetic metallic, PM, (grey) phases. White symbols denote the onset of anomalies observed in resistivity and susceptibility for the intermediate x -range, originally attributed to Cr high spin (HS) to low spin (LS) transition³⁵. For $x \geq 0.2$ the asymptotic ferromagnetic (FM) Weiss temperature increases linearly with increasing Cr-content (black circles). Inset at top right: a generic phase diagram discussed in the introduction.

Approach

The local structure of the material was measured as a function of doping and temperature over a wide range using the atomic pair distribution function analysis (PDF) of X-ray diffraction data⁵⁷. High resolution PDFs, $G(r)$, where r is the interatomic distance, were obtained by a Fourier transformation of powder diffraction data collected with short wavelength, high energy X-rays, according to $G(r) = \frac{2}{\pi} \int_{Q_{\min}}^{Q_{\max}} Q[S(Q) - 1] \sin Qr dQ$ ⁵⁸. The integrated data were corrected for experimental artifacts and normalized, to obtain the total scattering structure function, $S(Q)$. This contains both Bragg and diffuse scattering and therefore information about atomic correlations on different length scales^{23,24,59,60}. The data were analyzed by considering the evolution of features in the data-PDFs, in particular peaks in the PDF that are sensitive to the presence or otherwise of the structural dimers, and by fitting structural models to the data. This local structural information was then correlated with property measurements.

Results

Evolution of dimers with doping. In the low temperature insulating phase of CuIr_2S_4 pairs of Ir^{4+} dimerize by moving closer together by a large 0.5 \AA^{32} distance, resulting in the appearance of a distinct peak in the PDF at 3.0 \AA^{40} . This is shown in Fig. 3(a). The low temperature PDF clearly displays an additional peak at around 3.0 \AA and this feature disappears in the high temperature data. A signature M-shape in the difference curve can also be observed, originating from the redistribution of PDF intensity from the position of the undistorted bonds before dimerization into short (dimerized) and long (non-dimerized) bonds, in accord with the dimerization invoked bond-length redistribution sketched in Fig. 1(c).

This rather strong structural response allows the presence or absence of Ir^{4+} dimers to be easily probed by a direct observation

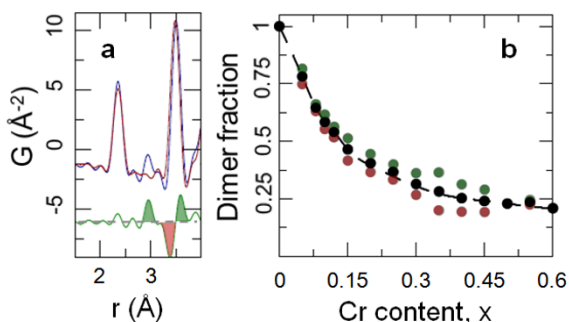


Figure 3 | Dimer signal in the PDF and estimate of the fraction of dimerized Ir^{4+} . (a) Comparison of experimental PDFs at 300 K (red) and 10 K (blue) over a narrow r -range for CuIr_2S_4 , with the difference curve (green) offset for clarity. Shaded features in the difference curve (color coded by green for dimer and red for loss peaks) are used in the dimer fraction evaluation. (b) Evolution of the dimer fraction with Cr-doping: the color code corresponds to that used for marking the features in the difference curve in (a), that were considered in the numeric integration analysis described in the Supplementary Material. Solid black symbols represent an arithmetic average of green and red values, while the dashed line is a guide to the eye.

of this dimer peak⁴⁰, and the M-shaped feature in difference curve. Dimers reveal themselves through this additional peak in the PDF irrespective of the length-scale of their ordering, allowing us to see the presence of localized charges even when they are only *local* in nature. For CuIr_2S_4 this is demonstrated in the upper left panel of Fig. 4⁴⁰. Although the low temperature long-range dimer order is swiftly suppressed by Cr-substitution resulting in an average cubic structure (Fig. 2), the PDF analysis reveals that *on the nanoscale* dimers exist at low temperature within the entire composition range studied, since the dimer peak, indicated by an arrow in Fig. 4, and the characteristic M-shaped difference curve, can be seen, albeit diminishing in amplitude with increasing doping, in all the low- T data-sets. Furthermore, careful quantitative analysis of the dimer signal in the difference curves of properly normalized PDFs enables an estimate of the dimer fraction to be carried out relative to the undoped end-member, as shown in Fig. 3(b). The details of this estimation procedure are provided in the Supplementary Material. While the concentration of dimers decreases with doping, the distortion amplitude appears to be doping independent within the accuracy of our measurement. The PDF analysis presented here is based on total scattering data that do not discriminate between the elastic and inelastic scattering channels, and hence PDF does not distinguish whether the dimers are static or dynamic, though their observation in the local, but not average, structure establishes that they are not long-range ordered.

Correlation length of dimer order. Here, we explore the correlation length of local dimer order across the phase diagram. Since the PDF provides structural information on different lengthscales, this may be done by carrying out a variable r -range fit to the PDF of carefully chosen models²³. Here, we utilize the fact that the cubic spinel model, which describes the global structure well, fails for the dimer case. The observation of local dimers implies that the global cubic symmetry comes from an average over incoherent domains of locally ordered dimers where there is a lower symmetry within the domain. We expect the cubic model to work well on lengthscales much larger than the local domain size, but to fail for short lengthscales dominated by the intra-domain signal. In Fig. 5(a) and (b) fits of the cubic model to the low temperature data of 0% Cr (exhibiting long range ordered dimers) and 40% Cr (no long range ordered dimers, dimer signal relatively weak) samples are shown, respectively. The model fails for CuIr_2S_4 on all lengthscales, as

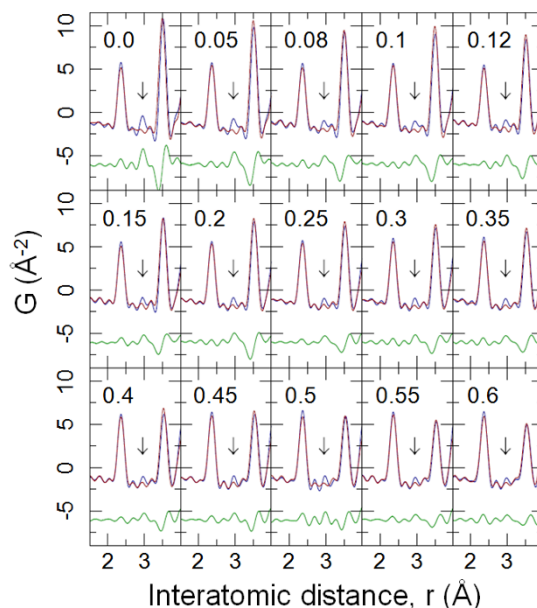


Figure 4 | Observation of doping dependence of the PDF dimer signature at low temperature. Comparison of experimental PDFs at 300 K (red) and 10 K (blue) over a narrow r -range for $\text{Cu}(\text{Ir}_{1-x}\text{Cr}_x)_2\text{S}_4$ ($0 \leq x \leq 0.6$), with difference curve (green) offset for clarity. Each panel corresponds to a single composition x , as indicated. Arrows denote the position of the dimer PDF peak. The dimer signature clearly persists to $x = 0.6$, though the signal is getting weaker.

expected. On the other hand, for the 40% Cr sample with $\text{Fd}\bar{3}m$ global symmetry the cubic model fails only on lengthscales shorter than ~ 1 nm, as evident from the difference curve extending out of the 2σ uncertainty parapet in Fig. 5(b). The correlation length determined in this way for all the samples is plotted in the inset to Fig. 5(b), where the error bars indicate a range of uncertainty associated with determining this crossover marked as the grey band in Fig. 5(b), with further discussion of how this was obtained provided in the Supplementary Material. No significant temperature variation of this bound could be established within the accuracy of our measurement. Although our analysis does not explicitly address the nature of the dimer order, it is interesting to contemplate what such short range dimer order may include. While the observed correlation length bound extends only to near neighbor dimers along the (110)-chains, it encompasses both near neighbor and next near neighbor dimers spanning the octamers, suggesting a three dimensional character of the dimer correlations.

Evolution of dimers with temperature. Next we address the temperature dependence of the dimer existence. This may be accomplished by plotting relevant structural parameters, such as lattice parameter, atomic displacement parameters (ADPs, U_{iso}), and cubic model fit residual, R_{wp} , obtained from average structure fits to the PDF data. While the average crystallographic model does not see the broken symmetry state directly, anomalous behavior of these parameters is to be expected as the nanoscale state sets in, and can be a sensitive indirect confirmation of their presence⁵⁶.

For example, R_{wp} will increase when the local structure is not well explained by the cubic model. The temperature evolution of the cubic lattice parameter and Ir U_{iso} from the 40% Cr sample on cooling are shown in Fig. 5(c) and (d), respectively. On cooling down from 300 K (grey region) both parameters evolve smoothly displaying canonical behavior, as evident from the linear fit to the lattice parameter, and the Debye model fit to the ADP of Ir (see Supplementary Material). However, dramatic deviations from these trends are observed at

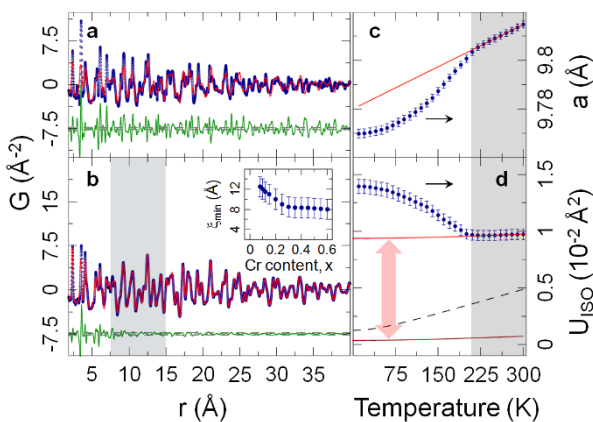


Figure 5 | Deviations from cubic $Fd\bar{3}m$ structure. (a) CuIr_2S_4 data at 10 K (open blue symbols), the best fit cubic model (solid red line), and the difference curve (green solid line) offset for clarity. Dashed lines are experimental uncertainties on the 2σ level. (b) Same as (a) but for 40% Cr sample. The grey area marks the r -region where the crossover from local to average behavior occurs. The temperature dependencies of the lattice parameter and Ir isotropic atomic displacement parameter (U_{iso}) for the 40% Cr sample are shown in (c) and (d), respectively. Light red solid lines represent fits to the high temperature region of (c) (fit with a linear function) and (d) (fit with the Debye model). Deviations of the data from these trends are clearly observed at low temperature. (d) The Debye model with static offset (represented by the double arrow) set to zero (dark solid red line). The black dashed line represents the Debye model fit to Ir U_{iso} for CuIr_2S_4 data. An appreciably larger static offset for the 40% Cr doped sample reflects the higher level of quenched disorder as compared to CuIr_2S_4 . The inset to (b) shows the doping dependence of the lower r -boundary where deviations from the cubic model become apparent at low temperature.

~ 180 K, with the lattice parameter decreasing rapidly and U_{iso} of Ir exhibiting an upturn. These deviations mark the onset temperature of the local dimer formation on cooling.

Using this same approach it is then possible to determine the evolution of the dimer formation across the whole phase diagram. In Fig. 6 we plot the evolution of different system parameters vs. doping and temperature. For example, the existence of a global cubic structure may be found by excluding the low- r region of the PDF from fits of the cubic model. This is shown in Fig. 6(b) and is in good agreement with previous crystallographic results displayed in Fig. 6(a)³⁵. However, if we include the low- r region of the PDF in the fit a very different picture emerges (Fig. 6(c)): the *nanoscale* phase diagram of $\text{Cu}(\text{Ir}_{1-x}\text{Cr}_x)_2\text{S}_4$ that maps out the (x, T) evolution of local dimers. A similar picture emerges from other measures of the local dimers such as the differential lattice parameter, Δa , and differential Ir isotropic atomic displacement parameter, ΔU_{iso} (Fig. 6(d) and (e)). These quantities are obtained by subtracting the observed behavior of the parameters from the expected behavior in the absence of local dimer formation, as determined by an extrapolation to low temperature of the high-temperature behavior using standard assumptions such as Debye behavior for the ADPs. All these measures reveal a previously undetected dome of local dimers appearing, roughly peaked at ~ 200 K at around $x = 0.3$. These strategies for searching for the presence of local broken symmetry states carry over, in principle, to other material systems of interest such as the cuprates and nickelates.

Discussion

The new information provided by this study leads to a completely different interpretation to the standard one³⁵ of the phase line close to 180 K in the intermediate doping regime, marked by white symbols

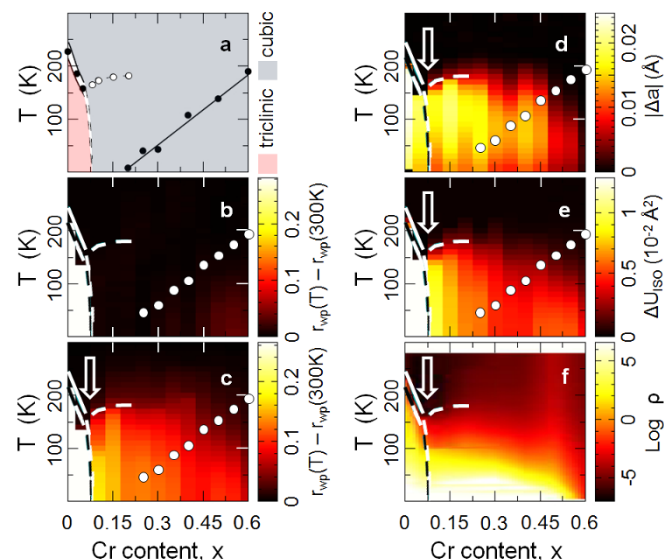


Figure 6 | Reassessment of the (x, T) phase diagram of $\text{Cu}(\text{Ir}_{1-x}\text{Cr}_x)_2\text{S}_4$. (a) Average $\text{Cu}(\text{Ir}_{1-x}\text{Cr}_x)_2\text{S}_4$ phase diagram shown in Fig. 2³⁵. (b) (x, T) dependence of the cubic model fit residual, R_{wp} , for the $Fd\bar{3}m$ cubic model fit over the high- r 15–40 Å PDF range, reproducing the behavior in (a). (c) Same as (b) but for the PDF refinements including the low- r region, revealing the local dimers in the R_{wp} parameter. (d) (x, T) dependence of the differential $Fd\bar{3}m$ lattice parameter. (e) (x, T) dependence of the differential Ir U_{iso} . See text for definitions. (f) (x, T) dependence of $\text{Log } \rho$, after reference 35. In (b)–(e): Weiss temperature of our samples is shown as white solid symbols. Dashed lines reproduce phase lines discussed in Fig. 2. Vertical arrow denotes a feature discussed in the text.

in Figs. 2 and 6(a), and by dashed white lines in Figs. 6(b)–(f). This was originally interpreted from analysis of magnetic susceptibility data as coming from a low spin (LS, $s = 1/2$) to high spin (HS, $s = 3/2$) crossover of the doped Cr ions³⁵. It is clear from this work that the anomalous loss in magnetic susceptibility in doped samples on cooling is actually due to the formation of local dimers that are not apparent in the average structure.

It is interesting to ask whether it is the global or local structure which is more important for determining the transport properties of the material. To explore this, we plot the resistivity vs x and T in Fig. 6(f). The resemblance of this to the local phase diagram suggests that the local structure is very important for determining (and understanding) the transport properties. On warming the dimer state is replaced by the charge delocalized paramagnetic metallic state. However, on doping at low temperature, as we show here, it is replaced by a disordered or short-range ordered dimer phase.

One of the most interesting parts of the phase diagram occurs around $x = 0.07$ and $T \sim 175$ K (marked by an arrow in Fig. 6 (c)–(f)) where local dimers disappear on doping, but are re-entrant at higher doping. The doping quickly destabilizes the ordered dimer phase yielding the paramagnetic metallic phase, and indeed the dimers are destroyed even in the local structure, but on further doping the localized, but now disordered, dimers are again preferred. There are elastic strain costs associated with localizing charges as dimers when they are not ordered over long range. It may be possible to explain the reentrant behavior if local lattice strain fields around doped Cr ions may be utilized by dimers to form without paying an additional strain energy cost. It is not known if the doped Cr is in the $3+$ or $4+$ state because copper can also alter its valence to maintain charge neutrality. However, either way the doped Cr is smaller (0.615 Å and 0.55 Å for Cr^{3+} or as Cr^{4+} , respectively) than the Ir that it replaces (0.68 Å and 0.625 Å for Ir^{3+} or as Ir^{4+} , respectively). This is in line with the observation in $\text{Cu}(\text{Ir}_{1-x}\text{Cr}_x)_2\text{S}_4$ that the

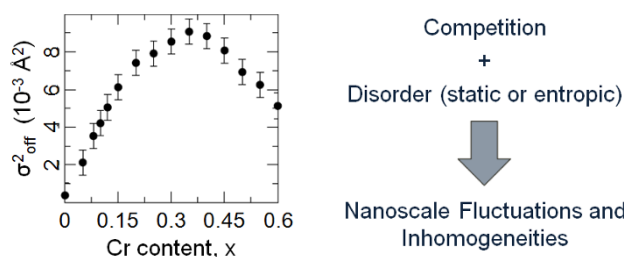


Figure 7 | Measure of quenched disorder in $\text{Cu}(\text{Ir}_{1-x}\text{Cr}_x)_2\text{S}_4$. The Debye model offset parameter, a sensitive measure of quenched disorder, versus Cr-doping, as obtained from the fits of this model to the Ir $U_{iso}(T)$ (left). Schematic of ingredients leading to nanoscale fluctuations and inhomogeneities (right).

average lattice parameter decreases on doping with Cr³⁵. The doped Cr ions therefore result in a compressive strain of the lattice in their vicinity. The dimer formation also results in a decrease in the unit cell volume^{32,41}, and also pressure stabilizes the charge-localized dimer state^{61,62}. It is thus plausible that dimers will form preferentially in the compressive strain field of the quenched defects.

As the phase diagram is traversed at 175 K, at a doping high enough to destroy dimer long range order, but still low, there are many dimers to be accommodated but few Cr ions and the paramagnetic metallic phase becomes energetically preferred. However, with increased Cr doping the increase in the number of Cr sites and the decrease in the number of dimers to be accommodated presumably are better matched, and the charge-localized dimer state may be again stabilized locally, though without the dimers ordering over long range. This would explain the reentrant and dome-like behavior of the local dimer state that we observe and is also consistent with the doping dependence of the static disorder as measured from the offset parameter in the Debye model fits to the Ir $U_{iso}(T)$ shown in the left panel of Fig. 7 (see Supplementary Material for details). The electrical properties are sensitive to the local dimer state and the conductivity of the sample results in a similar dome-like behavior to the local-dimer state (Fig. 6(f)), reinforcing the importance of characterizing the local nature of the material to understand the properties. This strain-biasing effect can be expected to be broadly applicable to a wide range of systems exhibiting doping induced MITs and generic-

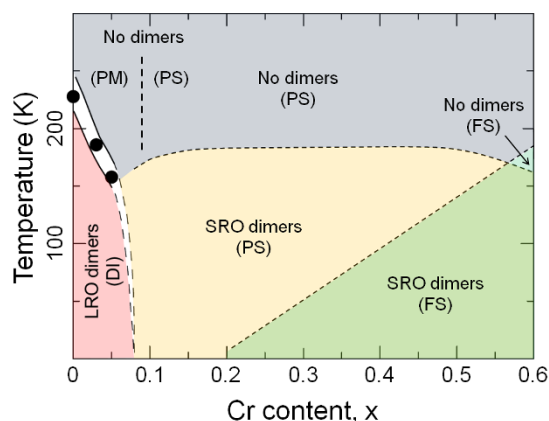


Figure 8 | Revised phase diagram for $\text{Cu}(\text{Ir}_{1-x}\text{Cr}_x)_2\text{S}_4$. Regions with dimers being long range ordered (LRO), short range ordered (SRO), and absent are identified. Dominant magnetic and transport characteristics are also noted, with D = diamagnetic, P = paramagnetic, F = ferromagnetic, M = metallic, I = insulating, and S = semiconducting. The average structure is triclinic in the diamagnetic insulating phase, and cubic elsewhere. The local structure is distorted on a nanometer lengthscale in regions where SRO dimers exist.

ally shows how the competition between ground-states, in the presence of quenched disorder, can lead to a nanoscale coexistence of both of the competing phases (Fig. 7). It just requires that the competing phases have slightly different average bond lengths and the dopant ions introduce local strains into the lattice⁶³.

A ferromagnetic metallic state appears in the region of high Cr doping³⁵, introducing a third competing state into the picture. Our PDF measurements cannot distinguish the paramagnetic metallic phase seen at low doping and the ferromagnetic metallic state seen at higher doping, but the ferromagnetic signal is also detected in our magnetization measurements for as low as $x = 0.25$, implying that there is a wide region of coexistence of the charge-localized dimer and ferromagnetic states at low temperature, which can only be explained as a nanoscale coexistence of insulating charge-localized dimer and metallic ferromagnetic phases.

In summary, this study provides a revised $\text{Cu}(\text{Ir}_{1-x}\text{Cr}_x)_2\text{S}_4$ phase diagram, Fig. 8, and shows how enormous insight into the physics of doped systems with MITs can be obtained from a systematic study of local structure over wide ranges of temperature and doping. $\text{Cu}(\text{Ir}_{1-x}\text{Cr}_x)_2\text{S}_4$ can serve as a model system for this because of the robustness of the structural signal associated with the charge-localized dimer state. The general notion that broken symmetry states can persist, undetected, in probes of average structure over wide ranges of doping and temperature and may explain anomalies in bulk properties such as transport and magnetization, is likely to be carried over to other doped systems at the metal-insulator boundary.

Methods

Sample synthesis and characterization. Polycrystalline samples of $\text{Cu}(\text{Ir}_{1-x}\text{Cr}_x)_2\text{S}_4$ with $0 \leq x \leq 0.6$ were prepared by a standard solid state route in sealed, evacuated quartz ampoules. Stoichiometric quantities of the metals and elemental sulfur were thoroughly mixed, pelletized, and sealed under vacuum. The ampoules were slowly heated to 650–750 °C and held at this temperature for several weeks with intermediate grinding and pressing. The products were found to be single phase based on laboratory x-ray powder diffraction. DC susceptibility data were measured on cooling in a 1 T field using a Quantum Design PPMS. Resistivity was measured using a standard four-terminal technique.

Total scattering experiments. PDF data for $10 \text{ K} \leq T \leq 300 \text{ K}$ were obtained using standard protocols⁵⁷ from synchrotron x-ray total scattering experiments carried out at the 11-IDC beamline of the Advanced Photon Source at Argonne National Laboratory. The setup utilized a 114.82 keV x-ray beam ($\lambda = 0.108 \text{ \AA}$) and a Perkin Elmer amorphous silicon detector, and a closed cycle helium refrigerator. The raw 2D data were integrated and converted to intensity versus Q using the software Fit2D⁶⁴, where Q is the magnitude of the scattering vector. Data reduction and Sine Fourier transform of measured total scattering structure functions up to a high momentum transfer of $Q_{max} = 27 \text{ \AA}^{-1}$ was carried out using the PDFgetX3⁶⁵ program. PDF structure refinements were carried out using the PDFgui program suite⁶⁶.

- Mott, N. F. *Metal-Insulator Transitions* (Taylor & Francis, London, 1974).
- Zaenen, J., Sawatzky, G. A. & Allen, J. W. Band gaps and electronic structure of transition metal compounds. *Phys. Rev. Lett.* **55**, 418 (1985).
- Imada, M., Fujimori, A. & Tokura, Y. Metal-insulator transitions. *Rev. Mod. Phys.* **70**, 1039 (1998).
- Taguchi, M. *et al.* Bulk screening in core-level photoemission from Mott-Hubbard and charge transfer systems. *Phys. Rev. B* **71**, 155102 (2005).
- Georges, A., de'Medici, L. & Mravlje, J. Strong correlations from Hund's coupling. *Annu. Rev. Condens. Matter Phys.* **4**, 137–178 (2013).
- Bednorz, J. G. & Müller, K. A. Possible high- T_c superconductivity in the Ba-La-Cu-O system. *Z. Phys. B Con. Mat.* **64**, 189 (1986).
- Kamihara, Y. *et al.* Iron-based layered superconductor: LaOFeP . *J. Am. Chem. Soc.* **128**, 10012 (2006).
- Jonker, G. H. & van Santen, J. H. Ferromagnetic compounds of manganese with perovskite structure. *Physica* **16**, 337–49 (1950).
- Dagotto, E. Complexity in strongly correlated electronic systems. *Science* **309**, 257–262 (2005).
- Dubi, Y., Meir, Y. & Avishai, Y. Nature of the superconductor-insulator transition in disordered superconductors. *Nature* **449**, 876–880 (2007).
- Dagotto, E., Yunoki, S., Sen, C., Alvarez, G. & Moreo, A. Recent developments in the theoretical study of phase separation in manganites and underdoped cuprates. *J. Phys.: Condens. Mat.* **20**, 434224 (2008).
- Pan, S. H. *et al.* Microscopic electronic inhomogeneity in the high- T_c superconductor $\text{Bi}_2\text{Sr}_2\text{CaCu}_2\text{O}_{8+\delta}$. *Nature* **413**, 282 (2001).



13. Kohsaka, Y. *et al.* Imaging nanoscale electronic inhomogeneity in the lightly doped Mott insulator $\text{Ca}_{2-x}\text{Na}_x\text{CuO}_2\text{Cl}_2$. *Phys. Rev. Lett.* **93**, 097004 (2004).
14. Hanaguri, T. *et al.* A ‘checkerboard’ electronic crystal state in lightly hole-doped $\text{Ca}_{2-x}\text{Na}_x\text{CuO}_2\text{Cl}_2$. *Nature* **430**, 1001–1005 (2004).
15. Kohsaka, Y. *et al.* An intrinsic bond-centered electronic glass with unidirectional domains in underdoped cuprates. *Science* **315**, 1380–1385 (2007).
16. Kohsaka, Y. *et al.* How Cooper pairs vanish approaching the Mott insulator in $\text{Bi}_2\text{Sr}_2\text{CaCu}_2\text{O}_{8+\delta}$. *Nature* **454**, 1072–1078 (2008).
17. Lawler, M. J. *et al.* Intra-unit-cell nematicity of the high- T_c copper-oxide pseudogap states. *Nature* **466**, 374–377 (2010).
18. Fratini, M. *et al.* Scale-free structural organization of oxygen interstitials in $\text{La}_2\text{CuO}_{4+y}$. *Nature* **466**, 841–844 (2010).
19. Tao, J. *et al.* Direct imaging of nanoscale phase separation in $\text{La}_{0.55}\text{Ca}_{0.45}\text{MnO}_3$: relationship to colossal magnetoresistance. *Phys. Rev. Lett.* **103**, 097202 (2009).
20. Tao, J. *et al.* Role of structurally and magnetically modified nanoclusters in colossal magnetoresistance. *Proc. Natl. Acad. Sci. USA* **108**, 20941 (2011).
21. Božin, E. S., Billinge, S. J. L., Takagi, H. & Kwei, G. H. Neutron diffraction evidence of microscopic charge inhomogeneities in the CuO_2 plane of superconducting $\text{La}_{2-x}\text{Sr}_x\text{Cu}_4$ ($0 \leq x \leq 0.30$). *Phys. Rev. Lett.* **84**, 5856–5859 (2000).
22. Jeong, I.-K. *et al.* Direct observation of the formation of polar nanoregions in $\text{Pb}(\text{Mg}_{1/3}\text{Nb}_{2/3})\text{O}_3$ using neutron pair distribution function analysis. *Phys. Rev. Lett.* **94**, 147602 (2005).
23. Qiu, X., Proffen, T., Mitchell, J. F. & Billinge, S. J. L. Orbital correlations in the pseudocubic O and rhombohedral R-phases of LaMnO_3 . *Phys. Rev. Lett.* **94**, 177203 (2005).
24. Božin, E. S. *et al.* Understanding the insulating phase in CMR manganites: Shortening of the Jahn-Teller long-bond across the phase diagram of $\text{La}_{1-x}\text{Ca}_x\text{MnO}_3$. *Phys. Rev. Lett.* **98**, 137203 (2007).
25. Malavasi, L. *et al.* Local structural investigation of $\text{SmFeAsO}_{1-x}\text{F}_x$ high temperature superconductors. *J. Phys. Condens. Mat.* **23**, 272201 (2011).
26. Booth, C. H. *et al.* Direct relationship between magnetism and MnO_6 distortions in $\text{La}_{1-x}\text{Ca}_x\text{MnO}_3$. *Phys. Rev. Lett.* **80**, 853–856 (1998).
27. Jiang, Y., Bridges, F., Downward, L. & Neumeier, J. J. Relationship between macroscopic physical properties and local distortions of low-doping $\text{La}_{1-x}\text{Ca}_x\text{MnO}_3$: An EXAFS study. *Phys. Rev. B* **76**, 224428 (2007).
28. Sundaram, N. *et al.* Local structure of $\text{La}_{1-x}\text{Sr}_x\text{CoO}_3$ determined from EXAFS and neutron pair distribution function studies. *Phys. Rev. Lett.* **102**, 026401 (2009).
29. Booth, C. H. *et al.* Electronic structure and f-orbital occupancy in Yb-substituted CeCoIn_5 . *Phys. Rev. B* **83**, 235117 (2011).
30. Haskel, D. *et al.* Pressure tuning of the spin-orbit coupled ground state in Sr_2IrO_4 . *Phys. Rev. Lett.* **109**, 027204 (2012).
31. Radaelli, P. G. Orbital ordering in transition-metal spinels. *New J. Phys.* **7**, 53 (2005).
32. Radaelli, P. G. *et al.* Formation of isomorphous Ir^{3+} and Ir^{4+} octamers and spin dimerization in the spinel CuIr_2S_4 . *Nature* **416**, 155–158 (2002).
33. Schmidt, M. *et al.* Spin singlet formation in MgTi_2O_4 : Evidence of a helical dimerization pattern. *Phys. Rev. Lett.* **92**, 056402 (2004).
34. Horibe, Y. *et al.* Spontaneous formation of vanadium “molecules” in a geometrically frustrated crystal: AlV_2O_4 . *Phys. Rev. Lett.* **96**, 086406 (2006).
35. Endoh, R., Awaka, J. & Nagata, S. Ferromagnetism and the metal-insulator transition in the thiospinel $\text{Cu}(\text{Ir}_{1-x}\text{Cr}_x)_2\text{S}_4$. *Phys. Rev. B* **68**, 115106 (2003).
36. Croft, M. *et al.* Metal-insulator transition in CuIr_2S_4 : XAS results on the electronic structure. *Phys. Rev. B* **67**, 201102 (2003).
37. Khomskii, D. I. & Mizokawa, T. Orbital induced Peierls state in spinels. *Phys. Rev. Lett.* **94**, 156402 (2005).
38. Yagasaki, K. *et al.* Hopping conductivity in CuIr_2S_4 spinel compound: I. empirical model for electronic configuration and mechanism of metal-insulator transition. *J. Phys. Soc. Jpn* **75**, 074706 (2006).
39. Okamoto, Y. *et al.* Band Jahn-Teller instability and formation of valence bond solid in a mixed-valent spinel oxide LiRh_2O_4 . *Phys. Rev. Lett.* **101**, 086404 (2008).
40. Božin, E. S., Masadeh, A. S., Hor, Y. S., Mitchell, J. F. & Billinge, S. J. L. Detailed mapping of the local Ir^{4+} dimers through the metal-insulator transitions of CuIr_2S_4 thiospinel by x-ray atomic pair distribution function measurements. *Phys. Rev. Lett.* **106**, 045501 (2011).
41. Furubayashi, T., Matsumoto, T., Hagino, T. & Nagata, S. Structural and magnetic studies of metal-insulator transition in thiospinel CuIr_2S_4 . *J. Phys. Soc. Jpn* **63**, 3333–3339 (1994).
42. Nagata, S. Metal-insulator transition in the thiospinel CuIr_2S_4 . *Chin. J. Phys.* **43**, 722 (2005).
43. Tranquada, J. M., Sternlieb, B. J., Axe, J. D., Nakamura, Y. & Uchida, S. Evidence for stripe correlations of spins and holes in copper oxide superconductors. *Nature* **375**, 561 (1995).
44. Reznik, D. *et al.* Electron-phonon coupling reflecting dynamic charge inhomogeneity in copper-oxide superconductors. *Nature* **440**, 1170 (2006).
45. Xia, J. *et al.* Polar Kerr-effect measurements of the high-temperature $\text{YBa}_2\text{Cu}_3\text{O}_{6+x}$ superconductor: Evidence for broken symmetry near the pseudogap temperature. *Phys. Rev. Lett.* **100**, 127002 (2008).
46. Mesáros, A. *et al.* Topological defects coupling smectic modulations to intra-unit-cell nematicity in cuprates. *Science* **333**, 426–430 (2011).
47. Wu, T. *et al.* Magnetic-field-induced charge-stripe order in the high-temperature superconductor $\text{YBa}_2\text{Cu}_3\text{O}_y$. *Nature* **477**, 191–194 (2011).
48. Ghiringhelli, G. *et al.* Long-range incommensurate charge fluctuations in $(\text{Y,Nd})\text{Ba}_2\text{Cu}_3\text{O}_{6+x}$. *Science* **337**, 821–825 (2011).
49. Torchinsky, D. H., Mahmood, F., Bollinger, A. T., Božović, I. & Gedik, N. Fluctuating charge density waves in a cuprate superconductor. *Nat. Mater.* **12**, 387–391 (2013).
50. Tranquada, J. M., Buttrey, D. J. & Rice, D. E. Phase separation, charge-density waves, and magnetism in $\text{La}_2\text{NiO}_4+d$ with $d = 0.105$. *Phys. Rev. Lett.* **70**, 445 (1993).
51. Tranquada, J. M., Lorenzo, J. E., Buttrey, D. J. & Sachan, V. Cooperative ordering of holes and spins in $\text{La}_2\text{NiO}_{4.125}$. *Phys. Rev. B* **52**, 3581 (1995).
52. Wochner, P., Tranquada, J. M., Buttrey, D. J. & Sachan, V. Neutron-diffraction study of stripe order in $\text{La}_2\text{NiO}_4+d$ with $d = 2/15$. *Phys. Rev. B* **57**, 1066 (1998).
53. Li, J., Zhu, Y., Tranquada, J. M., Yamada, K. & Buttrey, D. J. Transmission-electron-microscopy study of charge-stripe order in $\text{La}_{1.725}\text{Sr}_{0.275}\text{NiO}_4$. *Phys. Rev. B* **67**, 012404 (2003).
54. Hucker, M. *et al.* Oxygen and strontium codoping of La_2NiO_4 : Room-temperature phase diagrams. *Phys. Rev. B* **70**, 064105 (2004).
55. Hucker, M. *et al.* Unidirectional diagonal order and three-dimensional stacking of charge stripes in orthorhombic $\text{Pr}_{1.67}\text{Sr}_{0.33}\text{NiO}_4$ and $\text{Nd}_{1.67}\text{Sr}_{0.33}\text{NiO}_4$. *Phys. Rev. B* **74**, 085112 (2006).
56. Abeykoon, M. *et al.* Evidence for short-range ordered charge stripes far above the charge-ordering transition in $\text{La}_{1.67}\text{Sr}_{0.33}\text{NiO}_4$. *Phys. Rev. Lett.* **111**, 096404 (2013).
57. Egami, T. & Billinge, S. J. L. *Underneath the Bragg peaks: structural analysis of complex materials* (Elsevier, Amsterdam, 2012), 2nd edn.
58. Farrow, C. L. & Billinge, S. J. L. Relationship between the atomic pair distribution function and small angle scattering: implications for modeling of nanoparticles. *Acta Crystallogr. A* **65**, 232–239 (2009).
59. Božin, E. S. *et al.* Entropically stabilized local dipole formation in lead chalcogenides. *Science* **330**, 1660 (2010).
60. Knox, K. R. *et al.* Local structural evidence for strong electronic correlations in spinel LiRh_2O_4 . *Phys. Rev. B* **88**, 174114 (2013).
61. Oomi, G., Kagayama, T., Yoshida, I., Hagino, T. & Nagata, S. Effect of pressure on the metal-insulator transition temperature in thiospinel CuIr_2S_4 . *J. Magn. Magn. Mater.* **140–144**, 157 (1995).
62. Garg, A. B., Vijayakumar, V., Godwal, B. K., Choudhury, A. & Hochheimer, H. D. Reentrant high-conduction state in CuIr_2S_4 under pressure. *Solid State Commun.* **142**, 369 (2007).
63. Billinge, S. J. L. & Duxbury, P. M. Structural compliance, misfit strain and stripe nanostructures in cuprate superconductors. *Phys. Rev. B* **66**, 064529 (2002).
64. Hammersley, A. P., Svenson, S. O., Hanfland, M. & Hauserman, D. Two-dimensional detector software: from real detector to idealised image or two-theta scan. *High Pressure Res.* **14**, 235–248 (1996).
65. Juhas, P., Davis, T., Farrow, C. L. & Billinge, S. J. L. PDFgetX3: A rapid and highly automatable program for processing powder diffraction data into total scattering pair distribution functions. *J. Appl. Crystallogr.* **46**, 560–566 (2013).
66. Farrow, C. L. *et al.* PDFfit2 and PDFgui: Computer programs for studying nanostructure in crystals. *J. Phys. Condens. Mat.* **19**, 335219 (2007).

Acknowledgments

Work at Brookhaven National Laboratory (data collection, analysis and modeling) is supported by the U.S. Department of Energy Office of Science (DOE-OS) under Contract no. DE-AC02-98CH10886. Work at Argonne National Laboratory, which is operated by UChicago Argonne LLC, and the Advanced Photon Source (APS) facility, (materials synthesis and characterization) is supported under the U.S. DOE-OS Contract No. DE-AC02-06CH11357. This work has benefited from using the 11-IDC beamline of the APS.

Author contributions

E.S.B. and S.J.L.B. designed this work; Y.S.H. and J.F.M. synthesized the samples and carried out magnetic characterizations; E.S.B. and P.J. carried out total scattering experiments and PDF data reduction; E.S.B., P.J. and K.R.K. performed PDF analysis; E.S.B. and S.J.B. wrote the paper; all the authors participated in discussions of the results as well as preparing the manuscript.

Additional information

Supplementary information accompanies this paper at <http://www.nature.com/scientificreports>

Competing financial interests: The authors declare no competing financial interests.

How to cite this article: Božin, E.S. *et al.* $\text{Cu}(\text{Ir}_{1-x}\text{Cr}_x)_2\text{S}_4$: a model system for studying nanoscale phase coexistence at the metal-insulator transition. *Sci. Rep.* **4**, 4081; DOI:10.1038/srep04081 (2014).



This work is licensed under a Creative Commons Attribution-NonCommercial-NoDerivs 3.0 Unported license. To view a copy of this license, visit <http://creativecommons.org/licenses/by-nc-nd/3.0>